TETR: A Tokamak Engineering Test Reactor to Qualify Materials and Blanket Components for Early DT Fusion Power Reactors

B. Badger, G.L. Kulcinski, R.W. Conn, C.W. Maynard, K. Audenaerde, H. Avci, D. Blackfield, R.W. Boom, E. Cheng, J.R. Conrad, S. Dalhed, G.A. Emmert, B. Feinberg, Y. Gohar, S. Hong, J. Kesner, E. Larsen, P.F. Michaelson, K. Okula, M. Ragheb, E. Ramer, J. Scharer, D. Schluderberg, T. Sung, I.N. Sviatoslavsky, D.K. Sze, W.F. Vogelsang, P. Wilkes, W.R. Wilkes, L. Wittenberg, J. Wrazel, T. Wu, T. Yang, J. Young, and W.C. Young

February 1977

UWFDM-191

FUSION TECHNOLOGY INSTITUTE

UNIVERSITY OF WISCONSIN

MADISON WISCONSIN

TETR - A Tokamak Engineering Test Reactor to Qualify Materials and Blanket Components for Early DT Fusion Power Reactors

B. Badger
G.L. Kulcinski
R.W. Conn
C.W. Maynard
K. Audenaerde
H. Avci
D. Blackfield
R.W. Boom
E. Cheng
J.R. Conrad
S. Dalhed
G.A. Emmert
B. Feinberg
Y. Gohar
S. Hong
J. Kesner
E. Larsen
P.F. Michaelson
K. Okula
M.M.H. Ragheb
E. Ramer
J. Scharer
D. Schluderberg[a]
T. Sung
I. Sviatoslavsky
D.K. Sze
W.F. Vogelsang
P. Wilkes
W.R. Wilkes[b]
L. Wittenberg[b]
J. Wrazel
T. Wu
T. Yang
J. Young[c]
W.C. Young

Fusion Research Program
Nuclear Engineering Department
University of Wisconsin
Madison, Wisconsin 53706
U.S.A.

June 1977

Revised December 1977

(a) Babcock and Wilcox Company, Lynchburg, VA
(b) Mound Laboratory, Monsanto Corporation, Miamisburg, OH
(c) Battelle Pacific Northwest Laboratory, Richland, WA

Funding for this project came from the Department of Energy, Division of Magnetic Fusion Energy, and from the Wisconsin Electric Utilities Research Foundation. Their support is gratefully acknowledged and appreciated.

Preface

The idea of a fusion materials and engineering test reactor has been on the minds of those engaged in fusion technology studies since the late 1960's. Following the promising physics results of the early 70's and the difficulties pointed out by the fusion reactor designs of the mid-1970's, it became clear that such a test facility was sorely needed. The first group to propose such a research reactor chose the mirror concept but with the evidence that a beam driven tokamak facility could be built and was, in fact, made a keystone of the U.S. fusion program, several ideas about a beam driven DT tokamak fusion reactor appeared. We have extended those preliminary ideas into a specific reactor design which, we feel, fills a gaping hole in the present ERDA program to fusion reactor commercialization. The Tokamak Engineering Test Reactor (TETR) described here is designed to be built with state of the art plasma physics, engineering, and materials information of the 1980's. It is intended to provide materials damage and engineering design data for the Demonstration Power Reactor of the 1990's.

This report is hopefully the first in a series of even more in-depth design analyses for such a test facility. We certainly recognize that in a fast moving field such as fusion technology, many of the ideas presented here will become obsolete even as the report is issued. However, we are constantly reassessing our ideas and will continue to update certain parts of the ideas developed in this document. These will appear in future University of Wisconsin Fusion Design Memos (UWFDM's).

The authors wish to acknowledge the financial support for this work which was provided by the Division of Magnetic Fusion Energy under the

direction of Dr. E. Kintner. We are particularly indebted to Drs. J. Williams, F. Coffman, R. Kostoff and B. Twinning whose interest and constructive criticism of this work provided us with continual incentive.

We are also very appreciative of the professionalism and dedication of the editorial and secretarial staff at the University of Wisconsin without whose help this report could not be issued. Those primarily responsible for this fine effort are Mr. Richard Vacca, Ms. Connie Linehan, Ms. Gail Herrington, Ms. Bonnie Smart, and Ms. Linda Kraft. Mr. Dennis Bruggink also helped in the production.

G. L. Kulcinski

R. W. Conn

C. W. Maynard

TABLE OF CONTENTS

Preface and Acknowledgement
Table of Contents

I. Overview

A. Design Philosophy and General Parameters of TETR	I-1
B. Plasma Physics	I-12
C. Plasma Heating	I-22
D. Magnet Systems	I-29
E. Blanket & Shield Design	I-38
F. Neutronics	I-42
G. Thermal Hydraulics	I-48
H. Radiation Damage to TETR Components	I-55
I. Materials Test Facilities	I-64
J. The Lithium Test Modules	I-70
K. The Tritium System	I-72
L. Radioactivity and Safety	I-78
M. Plant Layout	I-82
N. Resources & Cost	I-88

II. Design Philosophy

A. Background	II-1
B. Approach	II-2
C. Major Constraints for the Design of TETR	II-10
D. Usefulness of TETR as a Materials Test Facility vis-à-vis Other Proposed Materials Test Facilities	II-15

III. Plasma Physics Analysis

A. Introduction	III-1
B. MHD Equilibria for Plasmas in TETR	III-1
1. The Description of the MHD Code	III-20
2. Calculational Results	III-21
C. Feedback Stabilization System for TETR Plasma Position Control	III-46
1. Dispersion Relation without Feedback	III-46
2. Dispersion Relation with Feedback	III-53
3. Effect of Time Delay in the Feedback Loop	III-56
4. Minimization of the Required Power	III-60
5. Application to TETR	III-62
D. Plasma Startup Analysis for TETR	III-68
E. Global and Space-Time Analysis of Plasma Operating Conditions	III-83
1. Introduction and General Considerations	III-83
a. Fraction of Tritium in Target	III-83
2. Global Balance Calculations	III-88
3. Spatially Dependent Transport Calculations	III-91
a. Calculation of a Plasma Bounded by a Divertor	III-93
b. Neutral Recycle	III-101
4. Beam Penetration Calculations	III-108

III. Plasma Physics Analysis (continued)
F. Analysis of Thermal Stability in TETR III-113
1. Introduction and Global Analysis III-113
2. One Dimensional Space-Time Analysis of Thermal Stability III-122
3. Summary III-133
G. Primary Vacuum System III-135
1. General Description III-135
2. System Design, Capacity, and Base Pressure III-137
3. Regeneration and Cryogenic Requirement III-144
4. Initial Pumpdown III-144

IV. Plasma Heating IV-1
A. Introduction IV-1
B. Positive Ion Source System IV-4
1. Overview IV-4
2. Ion Source Requirements IV-6
3. Layout IV-9
4. Molecular Species Removal IV-13
5. Neutralizer Cell and Direct Convertor IV-16
6. Gas Flow and Vacuum Pumping IV-19
a. Gas Loads IV-19
b. Pressure Profile IV-22
c. Conductances IV-24
d. Flow Balance Equations IV-28
7. Power Flow IV-32
8. Molecular Species Rejection at Low Energy IV-36
C. Negative Ion Source System IV-49
D. Summary IV-51
E. Supplementary RF Electron Heating of TETR Neutral Beam Heated Plasma IV-55
1. Introduction IV-55
2. Fast Alfvén Wave Electron Heating of TETR Plasma IV-57
F. Vacuum Pumps IV-70

V. Magnet System V-1
A. Introduction and General Description of System V-1
B. Toroidal Field Magnets V-2
1. Materials V-4
2. Specifications V-7
3. Construction Techniques V-7
4. Dewar Design V-13
5. Lateral Support and Structural Safety V-14
6. AC Losses in TF Coils and Shielding V-17
7. Magnet Safety and Protection V-21
C. Vertical Field Coils V-24
1. General Description V-24
2. Coil Specifications V-26
3. Structural Considerations V-33

V. Magnet System (continued)
D. Ohmic Heating Coils V-36
1. General Considerations V-36
2. Coil Description V-38
3. Stress Analysis of OH Coils V-40
4. Cryogenic Considerations V-45
5. Losses V-46
E. Refrigeration Requirements V-50
1. TF Coils V-50
2. Ohmic Heating Coil V-50
3. Cryosorption Pump Requirements V-50
F. Power Requirements V-51
1. TF Coils V-51
2. OH and VF Coils V-51

VI. Blanket and Shield Design VI-1
A. Introduction VI-1
B. General Description and Specifications VI-2
C. First Wall Stresses VI-9
1. Thermal Stresses VI-11
2. Pressure Stresses VI-13
3. Mechanical Support Stresses VI-13
4. Cyclic Stresses VI-16
D. Disassembly and Maintenance VI-20

VII. Neutronics VII-1
A. Introduction VII-1
B. Calculations VII-4
C. Blanket and Shield Performance VII-17
D. Two-Dimensional Analysis VII-47
References VII-83

VIII. Heat Transfer and Cooling VIII-1
A. Introduction VIII-1
B. Thermal Hydraulic Design and Calculations for the Blanket VIII-4
1. Temperature Range VIII-4
2. Burnout Considerations VIII-4
3. Coolant Flow Arrangement VIII-7
C. Annealing Requirements VIII-11
D. First Wall Protection by Curtain to a Plasma Dump VIII-12
1. Mathematical Formulation VIII-13
2. Results and Discussion VIII-15
E. Heat Rejection System VIII-27
F. Design Considerations for Collector Plates VIII-30
1. Thermal Input VIII-31
2. Structural Material VIII-32
3. Cooling Scheme VIII-33
4. Sputtering Considerations VIII-38

IX. Radiation Damage Considerations IX-1
A. Introduction and Perspective IX-1
B. Radiation Environment IX-1
1. Neutron Flux and Energy Spectra IX-1
a. Poloidal Variation IX-1
b. Variation Through Blanket and Shield IX-6
c. Neutron Flux Variations in Neutral Beam Injector Port and Shield IX-13
2. Particle Flux to Solid Surfaces IX-13
a. Flux to Carbon Curtain IX-13
b. Flux to Divertor Surface IX-16
C. Response Rates in TETR Materials IX-16
1. Displacement Rate IX-16
a. Stainless Steel IX-16
i. Poloidal Variation IX-16
ii. Two-Dimensional Variation IX-21
iii. Displacement Variation Along Neutral Beam Ports IX-24
2. Gas Production Rates IX-24
a. Poloidal Variation IX-24
b. Two-Dimensional Variation of Helium Gas Production IX-24
3. Parametric Representation of the Damage Environment IX-27
a. He/dpa Ratio IX-27
b. Temperature Plots IX-27
c. Stress IX-27
4. Transmutation Rate in 316 Stainless Steel First Walls IX-30

IX. Radiation Damage Considerations (continued)

D. Effect of Irradiation on TETR 316 SS Components IX-36
1. Introduction IX-36
2. Swelling Due to Void Formation IX-36
3. Fatigue Life IX-40
4. Tensile Properties IX-40
5. Creep-Rupture Life IX-44
6. Crack Growth Rates IX-44
7. Conclusions IX-47

E. Effect of Irradiation on Non-Structural Compounds of TETR IX-49
1. Introduction IX-49
2. Carbon Curtain IX-49
a. Neutron Effects in Carbon at High Temperatures IX-49
b. Physical Sputtering of the Carbon Curtain IX-52
3. Chemical Sputtering of Carbon in a DT Environment IX-52
4. Sputtering Damage to the Particle Collector Plates in the Divertor IX-54
5. Radiation Damage to the Tungsten Shield Material IX-54
6. Radiation Damage in the Boron Carbide Neutron Absorber Material IX-54
7. Radiation Effects to Magnet Materials IX-57
a. Damage in Cu Stabilizer IX-57
b. Radiation Effects in the NbTi Superconductor IX-57
c. Radiation Damage to the Mylar Thermal Insulation IX-62
d. Radiation Damage to the Electrical Insulator Materials in the TF Coil IX-62
e. Radiation Damage to the Electrical Insulation in the VF Coil IX-62
f. Radiation Damage to the OFHC Copper in the VF Coil IX-62

F. Summary of Radiation Damage Problems in the Non Test Cell Area of TETR IX-6
References IX-6

X. Test Modules for Structural Materials
A. Introduction X-1
B. The Test Requirements X-2
1. Wall and Blanket Materials X-2
C. Materials Choice X-6
D. Test Matrix Philosophy X-7
E. Test Matrix Details X-9
1. Test Facilities X-9
2. Test Volume Requirements X-11
3. Data Extrapolation and Optimization X-12
4. The Test Matrix for Environmental Variables X-14
F. Individual Test Facilities X-14
1. Creep Tests X-14
2. Biaxial Creep Testing X-18
3. Fatigue Tests X-20
4. Crack Propagation Tests X-21
5. Specimens for Post Irradiation Study X-22
6. Temperature Control X-23
7. Instrumentation X-23
8. Shield and Leakage Containment X-23
9. Test Access Requirements X-24
G. Summary X-24
References X-25

XI. Engineering Test Modules for Liquid Breeders and Heat Transfer Fluids XI-1
A. Introduction XI-1
B. Module I: Liquid Lithium XI-2
1. Review of Lithium Corrosion Studies XI-2
2. Proposal for the Study of Lithium Corrosion XI-13
3. Structural Materials for a Liquid Lithium Test Module XI-14
a. Modular Design XI-14
b. Structural Materials for Module Specimens XI-18
4. Temperature Control of the Module XI-33
5. Sampling System XI-36
a. Isolation of In-Run Samples XI-36
b. Post-Run Sample Isolation XI-41
6. Sample Analysis XI-42
a. Analysis of Samples Taken During a Run XI-42
b. Post-Run Sample Analysis (316 Stainless Steel Analysis) XI-59
c. Summary: Sample Examination Techniques XI-65
7. Lithium Loop Procedures XI-67
a. Startup Procedures in the Lithium Loop XI-67
b. In-Run Procedures XI-68
c. Loop Shutdown Procedures XI-72
8. Alternative Studies in the Liquid Lithium Loop XI-75
C. Solid Lithium Compounds: Modular Experimentation XI-77
1. Introduction XI-77
2. Proposal for the Examination of Solid Breeders in Modular Testing XI-95
3. Static Sample Experimentation XI-99
a. Sample Preparation XI-99
b. Containment in Static Sample Experimentation XI-107
c. Temperature Control in the Static Breeder Module XI-111
d. Determination and Purification of Product Gases XI-113
e. Static Sample Loop Experiments XI-120

XII. The Tritium Cycle XII-1
A. Introduction XII-1
1. General Comments XII-1
2. Parameters Governing the Fuel Cycle XII-2
3. Fuel Flow Rates XII-2
B. Tritium-Deuterium Separation XII-6
1. The Fuel Separation System XII-6
2. The Isotope Separation Strategy XII-11
C. Tritium Control System for UW TETR XII-24
1. Introduction XII-24
2. Plasma Fuel and Exhaust System XII-24
3. Primary Containment System XII-25
4. Secondary Containment System XII-25
5. Tertiary Containment System XII-32
6. Tritium Permeation Into Cooling Water XII-36
7. Tritium Permeation Into Modular Coolant XII-41
8. Tritium Permeation Into the Divertor Coolant XII-42
9. Removal of Tritium from the Divertor Coolant XII-48
10. Tritium Storage Room XII-54
11. Summary XII-54

XIII. Radioactivity and Safety XIII-1
A. Introduction XIII-1
1. Method of Calculation XIII-1
2. Geometry of the System and Material Composition XIII-8
B. Buildup of Activity in TETR-A XIII-11
C. Activity Following Shutdown in TETR-A XIII-14
D. Activity Following Shutdown in Final Design XIII-29
1. Two-Dimensional Effects XIII-36

XIV. Plant Layout XIV-1
A. Introduction XIV-1
B. General Building Plot Plan XIV-1
C. Reactor and Auxiliary Buildings XIV-6

XV. Resources and Cost XV-1
A. Introduction XV-1
B. Materials Inventory for the Nuclear Island of TETR XV-1
C. Capital Costs of TETR XV-3
D. Operating and Maintenance Costs for TETR XV-30
1. Salaries XV-30
2. Miscellaneous Supplies and Equipment XV-32
3. Outside Support Services XV-32
4. Miscellaneous Costs XV-32

XV. Resources and Cost (continued)
5. General and Administrative Costs XV-32
6. Coolant Makeup XV-33
7. Cost of Electrical Power XV-33
8. Unusual Maintenance Items XV-34
9. Total O and M Costs XV-35
E. Fuel Costs for TETR XV-36
F. Total Operating Costs for TETR XV-39
G. Summary of TETR Cost Analysis XV-40

XVI. Conclusions XVI-1
A. Design Philosophy XVI-1
B. Plasma Physics XVI-1
C. Plasma Heating XVI-2
D. Magnets XVI-2
E. Blanket and Shield XVI-2
F. Neutronics XVI-3
G. Thermal Hydraulics XVI-3
H. Radiation Damage to TETR Components XVI-4
I. Test Modules for Structural Materials XVI-5
J. Lithium Test Modules XVI-5
K. Tritium System XVI-5
L. Radioactivity XVI-6
M. Plant Layout XVI-6
N. Resources and Cost XVI-6

A. Appendix A - Basis of the Calculations Used to Derive the Detailed Cost Data of Chapter XV A-1

Chapter I - Overview

The following represents a very condensed version of the information contained in Chapters II thru XV. No attempt is made to justify or document specific points given here and the necessary detail and references can be found in the body of the report.

I-A. Design Philosophy and General Parameters of TETR

There is a curious mixture of optimism and urgency developing in the fusion community. Recent successes in plasma physics have removed most of the doubts as to "if" the breakeven stage can be achieved; now the question is "when?" Counter to this optimism is the realization that time is not necessarily on our side in solving the long range energy problem. Projections of 30 to 50 years before a "commercial" reactor will be available are not very conducive to large scale funding, especially when viewed in light of more pressing short range problems. Reduced funding and efforts will only further extend the time scale for commercialization such that society may in fact opt for other solutions.

The above picture provides a very convincing argument for accelerating the fusion program to get early results even though they may not in fact change the overall deployment strategy very much. One key element in such an accelerated program is the limit to which materials and engineering systems can be safely pushed. The determination of that limit requires extensive (and expensive) test facilities at the earliest possible date. In fact, if one follows the Logic III approach of the 1976 ERDA Fusion Program Plan, it is realized that such a technology test facility is needed in the mid to late 1980's if one wishes to have any meaningful demonstration of a moderate sized electrical production plant in this century. If such a test facility is to be built in this timeframe, then it must be designed in the early 1980's. The purpose of this report is to describe how we feel such a facility can be designed and built within the boundary conditions and fit into the scenario of a vigorous, but reasonable, program to commercialization of fusion power.

An example of how we think this Tokamak Engineering Test Reactor (TETR) fits into such an accelerated program is shown in Figure I-A-1. The TETR would be designed with state of the art physics from PLT, T-10, PDX, Alcator, TFTR a la 1980. It would capitalize on the tritium handling experience from building the Tritium Facility at LASL, the Toroidal Test Assembly for superconducting magnets at ORNL and the High Flux Neutron Source at HEDL. The TETR would not impact an Experimental Power Reactor (EPR) significantly but it would be generating data directly for the Demonstration Power Reactor (DPR).

The design requirements and constraints for TETR are given in Table I-A-1. The reason for these limits is explained in Chapters II and III. The technical

Figure I-A-1

TIME FRAME IN WHICH TO CONSIDER TETR (AFTER LOGIC III)

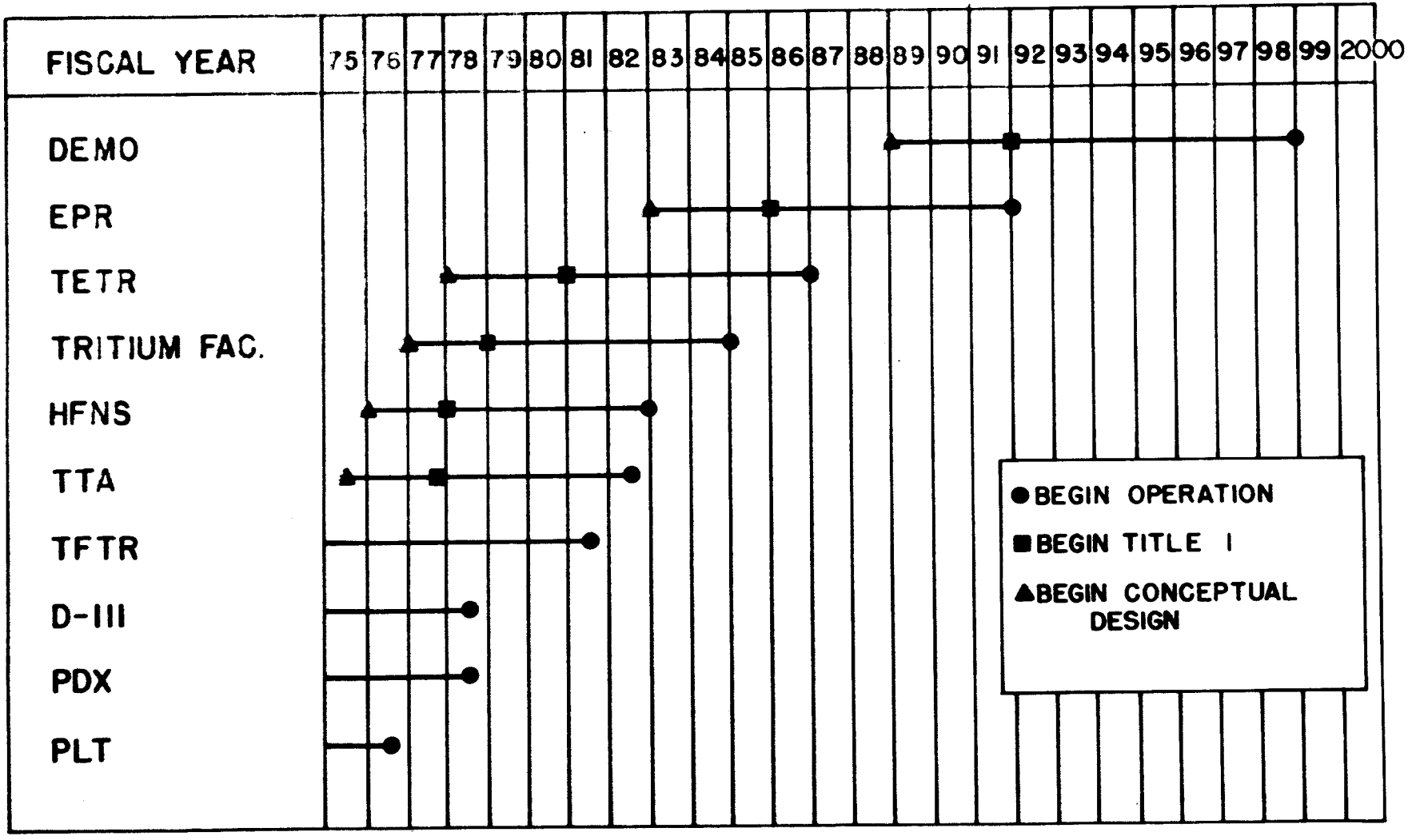

Table I-A-1

Design Requirements and Contraints for TETR

(1) TFTR state of the art plasma physics (beam driven)

(2) Neutral beams of no greater than 200 KeV, 50 A/module or 150 KeV, 100 A/module

(3) Superconducting TF coils (TiNb) No pulses superconductors.

(4) Stainless steel structure (except for test modules)

(5) Does not have to produce net electrical power (no requirement for high temperatures)----Can have power cycle attached to test loop

(6) Limited tritium breeding (in special test modules only)

(7) Must produce "characteristic" Tokamak environment in test zone at the rate of 1 MW/m^2 per year (integrated)

(8) Equilibrium tritium release rate <10 curie/day and total release less than allowed for LWR in 10-CF-R50

(9) Cost on the order of 550 million dollars (1977)

(10) Operating expense <100 million dollars a year (1977)

(11) Must be able to build in <6 years from start of construction and sited "within the fence" at a federal site

---

constraints were all felt to be achievable in the 1980 timeframe with a minimum extension of the scientific and industrial base of the world while the financial limits were felt to be within those set by an enlightened society with respect to the energy crisis. The environmental constraints are all within those already accepted in the fission power industry.

The usefulness of this device in just one area, material testing, is briefly summarized in Table I-A-2 and Figures I-A-2 and I-A-3. In Table I-A-2, we compare existing or proposed neutron producing facilities for the US in terms of the maximum damage and helium gas production rates in steel, test volume, operating plant factor, and operating date. It is seen that while both the displacement rates and helium production rates in TETR are not the highest attainable, such a reactor does have the largest test volume by almost a factor of 1000. The product of the accumulated test damage and test volume is shown in Figures I-A-2,3 and these figures reveal that a reactor like TETR is far superior to either fast neutron test facilities or thermal neutron reactors. Using the best estimate of what will be needed to freeze design of DPR by 1991, we find that even if the TETR does not operate until 1987, the data reported here (and in Chapter II) could be available in time for the DPR. The conclusion of this analysis, supported by the documentation in Chapters II-XV is that a device like TETR is feasible and perhaps even vital to the demonstration of the commercial feasibility of fusion in this century.

Table I-A-2

Possible Test Facilities To Provide Instrumented Data on Fe-Cr-Ni Alloys For Fusion For A DPR

Facility (Flux)	dpa/yr*	appm He/yr*	Instrumented High Flux Test Volume cm^3	PF %	Op Date
RTNS-UG (2×10^{13})	1.3	50	1	90	Jan '78
INS (10^{14})	6.5	250	3	80	Jan '81
D-Li (10^{15})	65	1000	10	80	Jan '83
D-Li (10^{14})	6.5	100	300	80	Jan '83
D-Li (5×10^{13})	3.3	50	1000	80	Jan '83
ORR	10	150**	1000	70	Jan '78
FFTF	40	4	4000	70	Jan '80
TETR	11	200	2,000,000	70	Jan '87

*100% PF, average over flux

**First Year

FIGURE I-A-2 -- CUMULATIVE DAMAGE TEST VOLUME THAT CAN BE PROVIDED BY CTR INSTRUMENTED IRRADIATION FACILITIES

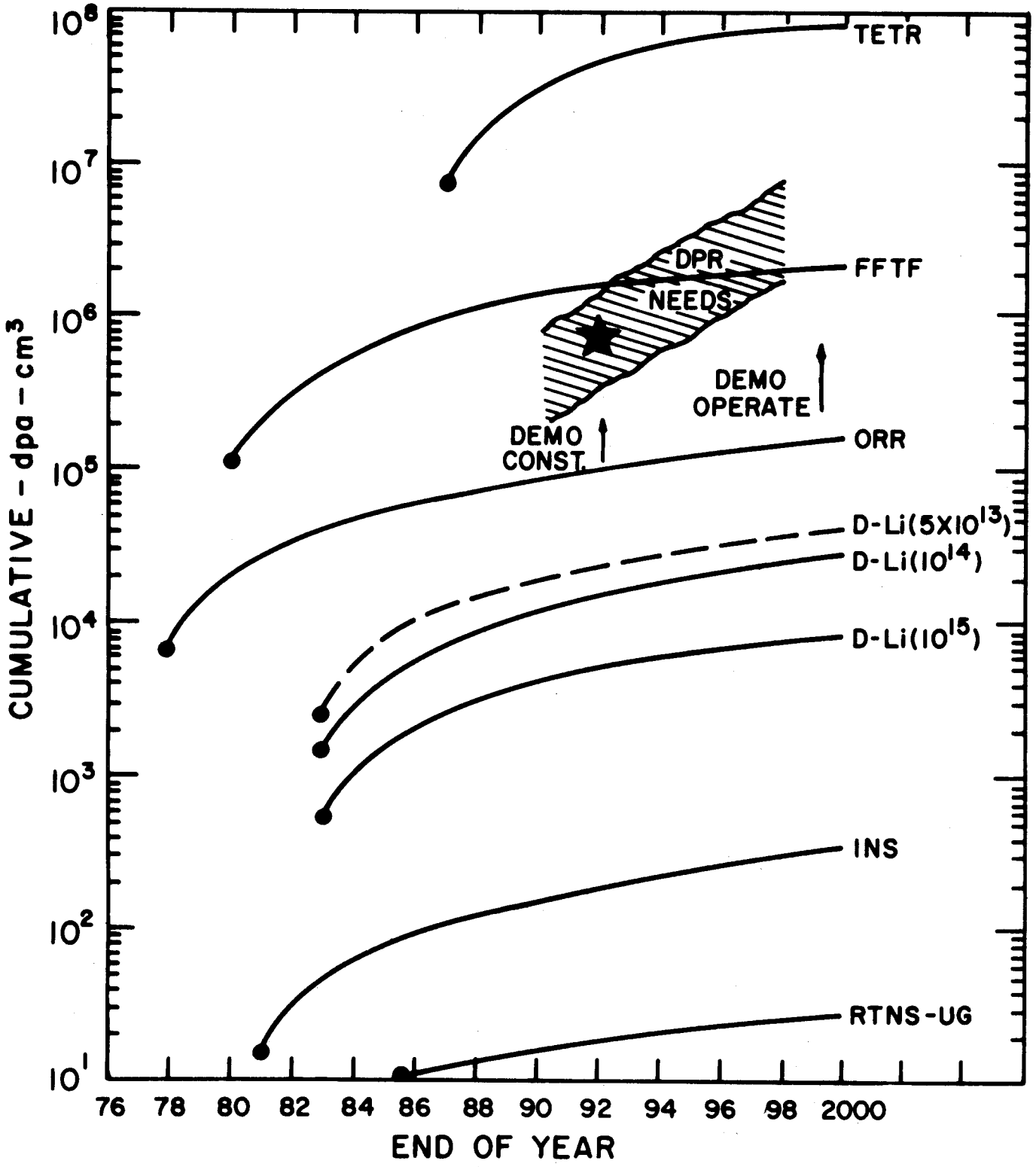

FIGURE I-A-3 -- CUMULATIVE DAMAGE TEST VOLUME THAT CAN BE PROVIDED BY POTENTIAL CTR INSTRUMENTED IRRADIATION FACILITIES

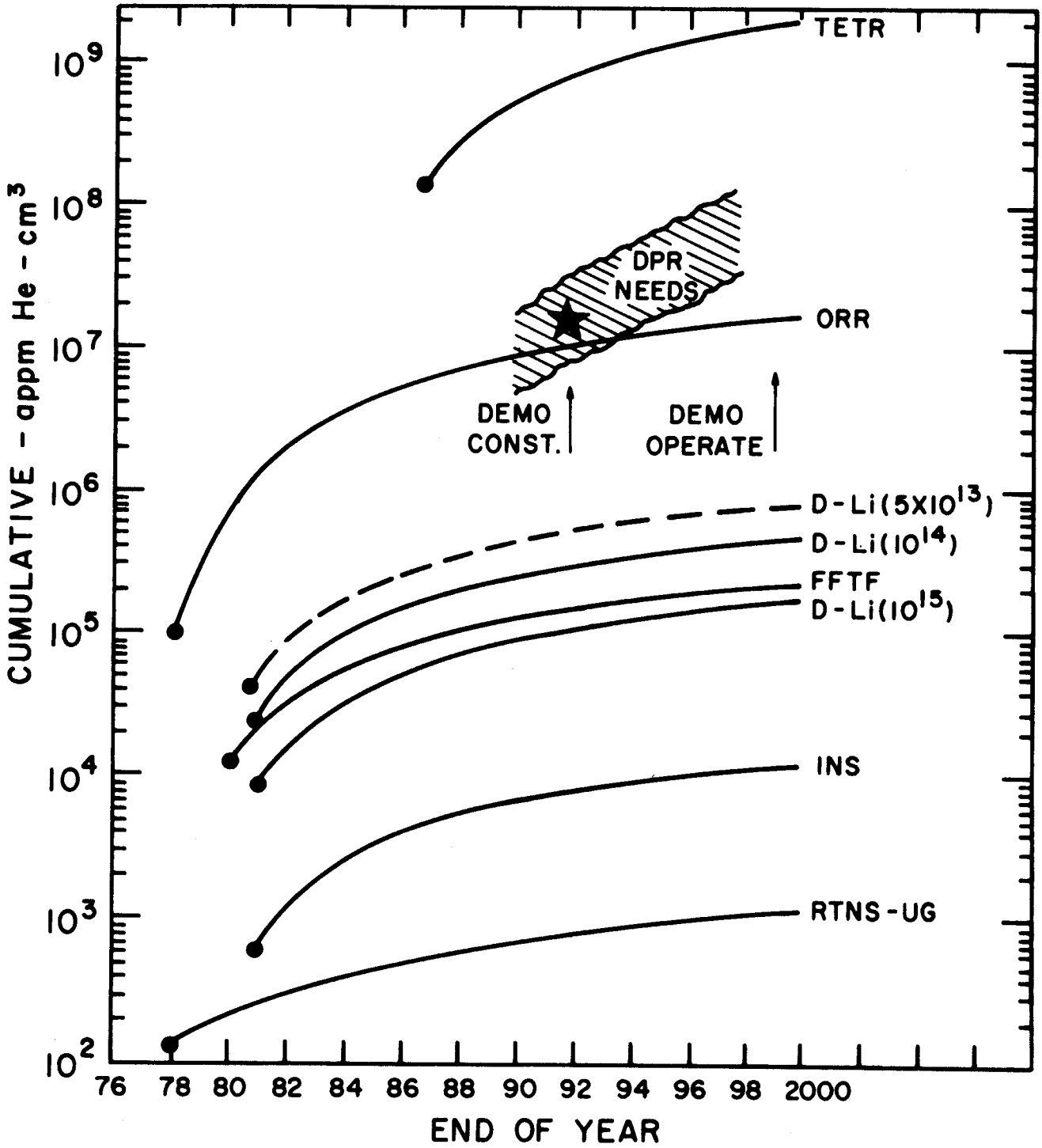

An isometric view of TETR is given in Figure I-A-4 emphasizing the prominent spacial requirements of the neutral beam injectors and revealing the access ports to the 16 main test modules. A more detailed cross section is shown in Figure I-A-5 and the main operating parameters of TETR are listed in Table I-A-3. The reactor generates 360 MW of thermal power from DT fusions in addition to 150 MW of injected power from the neutral beams, 162 MW of waste heat from the injectors, and 90 MW of heat from the resistive loss in the OH and VF coils. There is no breeding of tritium and approximately 9.9 kg must be supplied per year from an external source.

The plasma shape is a "triangular shaped D" with a half width of 0.6 meters and a height to width ratio of 2.0. The major radius of the plasma is only 3.25 meters and the operating current is 2.52 MA with an overall beta of 6.6%. Impurity control is accomplished by a double null divertor and a thin carbon curtain between the plasma and the first wall. Approximately 150 MW of neutral beam power is injected during the 60 second burn and the duty cycle is 83%. The magnetic field on axis is 41.9 kG from 16 superconducting NbTi Ti coils. A maximum field of 85 kG occurs on the inner windings of the TF coils. The OH coils are cryogenically cooled aluminum and the VF coils are copper cooled with ambient temperature water.

The main structural material of the "permanent" structure is 316 SS operated at a maximum temperature of 300°C. The first wall is cooled with steam while helium is used to cool the test modules (which run at higher temperatures) and water is used to cool the divertor collector plates (see Figure I-A-6). The neutron wall loading in the test cell area is $\sim$1 MW/m^2 averaged over a calendar year and is instanteously at the 1.2-1.4 MW/m^2 level. This flux is incident on $\sim$20 m^2 of test area which is 10 cm thick providing a test volume of $\sim$2 m^3. A testing matrix for austenitic steels as well as advanced alloys of Ti and refractory metals has been worked out and it is shown that the appropriate high fluence, large volume combination can be achieved to provide a considerable data base from which to design the Demonstration Power Reactor in the later 1990's.

There is presently no provision for TETR to generate electricity (although it could be accomplished at a modest cost) and the average thermal electrical power demand is 480 MWe over the 60 second burn time. The capital costs of TETR are estimated to be 628 million dollars and the annual operating costs are in the neighborhood of 85 million dollars per year.

ISOMETRIC VIEW OF TETR

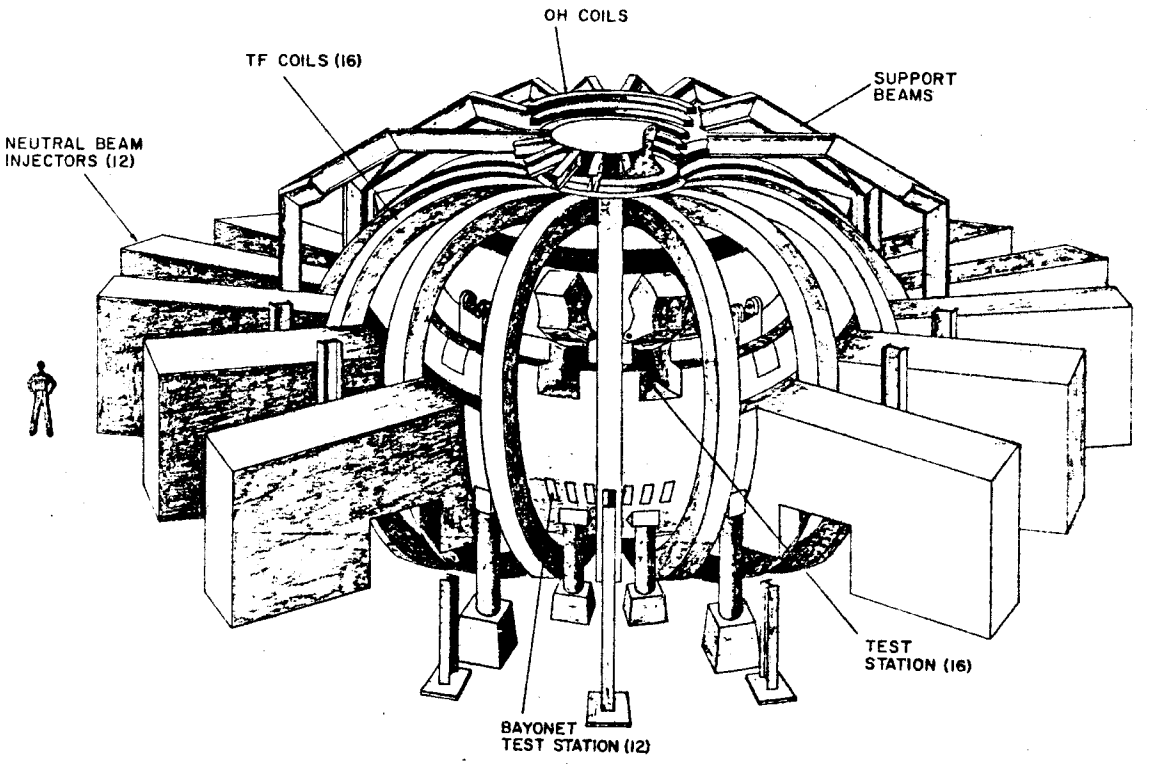

FIGURE I-A-4

CROSS SECTION VIEW OF TETR

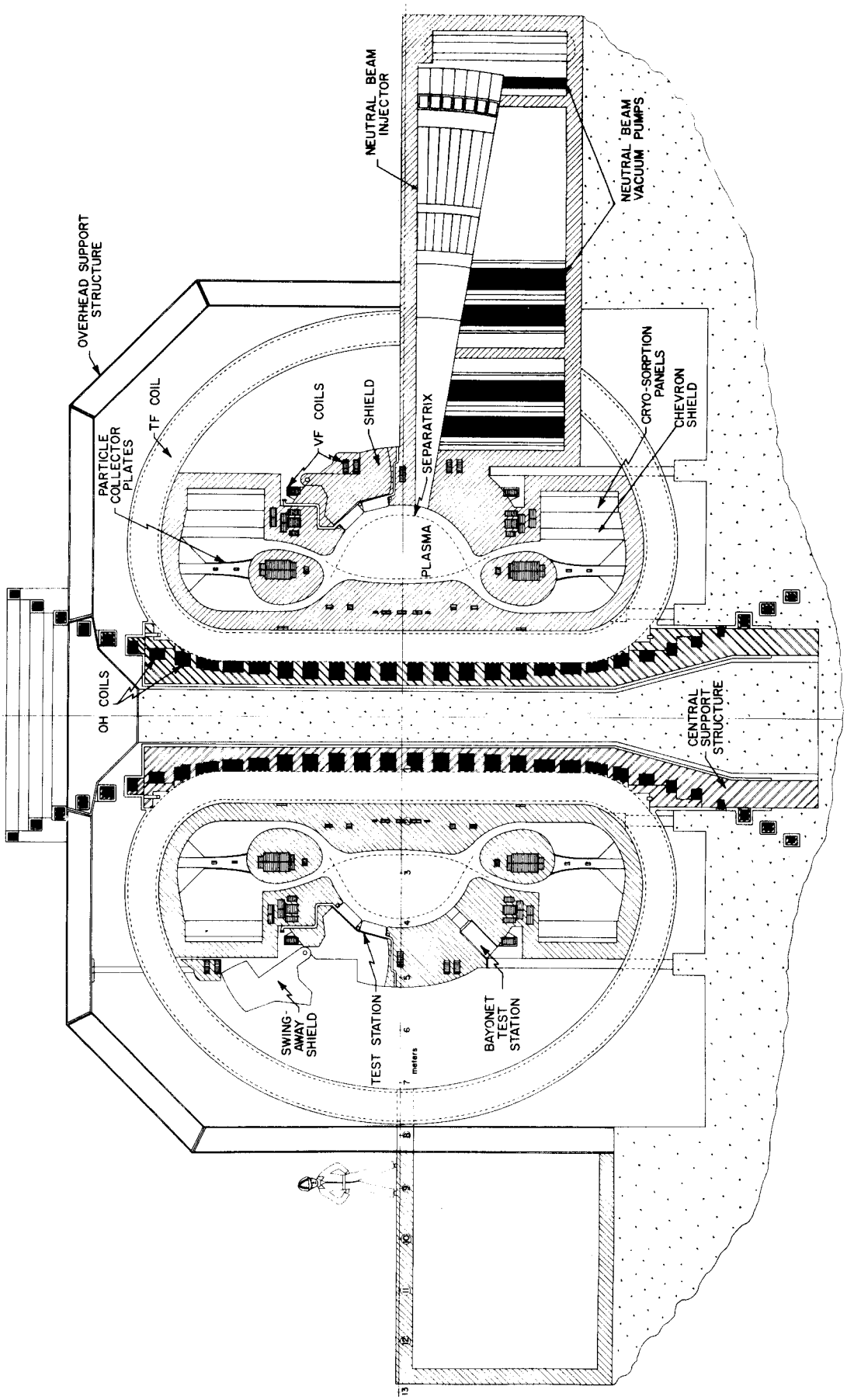

FIGURE I-A-5

Table I-A-3

Major Operating Characteristics of TETR

Fusion Power	360 MW
Fuel Cycle	D+T (TCT Mode)
Tritium Source	External (9.9 kg/yr)
Plasma Dimensions	
Major Radius	3.25 m
Half Width	0.6 m
Height to Width Ratio	2.0
Shape	"Triangular D"
Plasma Current	2.52 MA
Total Beta	6.6%
Impurity Control	Divertor + C Curtain
Plasma Heating Method	150 MW - Neutral Beams
Burn Time	60 sec
Duty Cycle	83%
Plant Factor	70%
No. of TF coils	16
Superconductor	NbTi
Field on Axis/Max. Field	41.9 kG/85 kG
OH Coils	Cryogenic Copper
VF Coils	Water Cooled Copper
"Permanent Structure"	316 SS
Maximum O.D. Temp.	300°C
Coolant	First Wall - Steam Test Cell - He Divertor Plates - H_2O
First Wall Life	~10 MW-yr/m^2
Neutron Wall Loading	
Test Cell (ave)	~1 MW/m^2 (cal. year)
Test Cell (inst)	1.2-1.4 MW/m^2
High Flux Test Volume	2,000,000 cm^3
Electrical Requirements	480 MW_e during burn
Est. Capital Costs	628 million dollars
Est. Annual Operating Costs	85 million dollars

Summary of Major TETR Systems

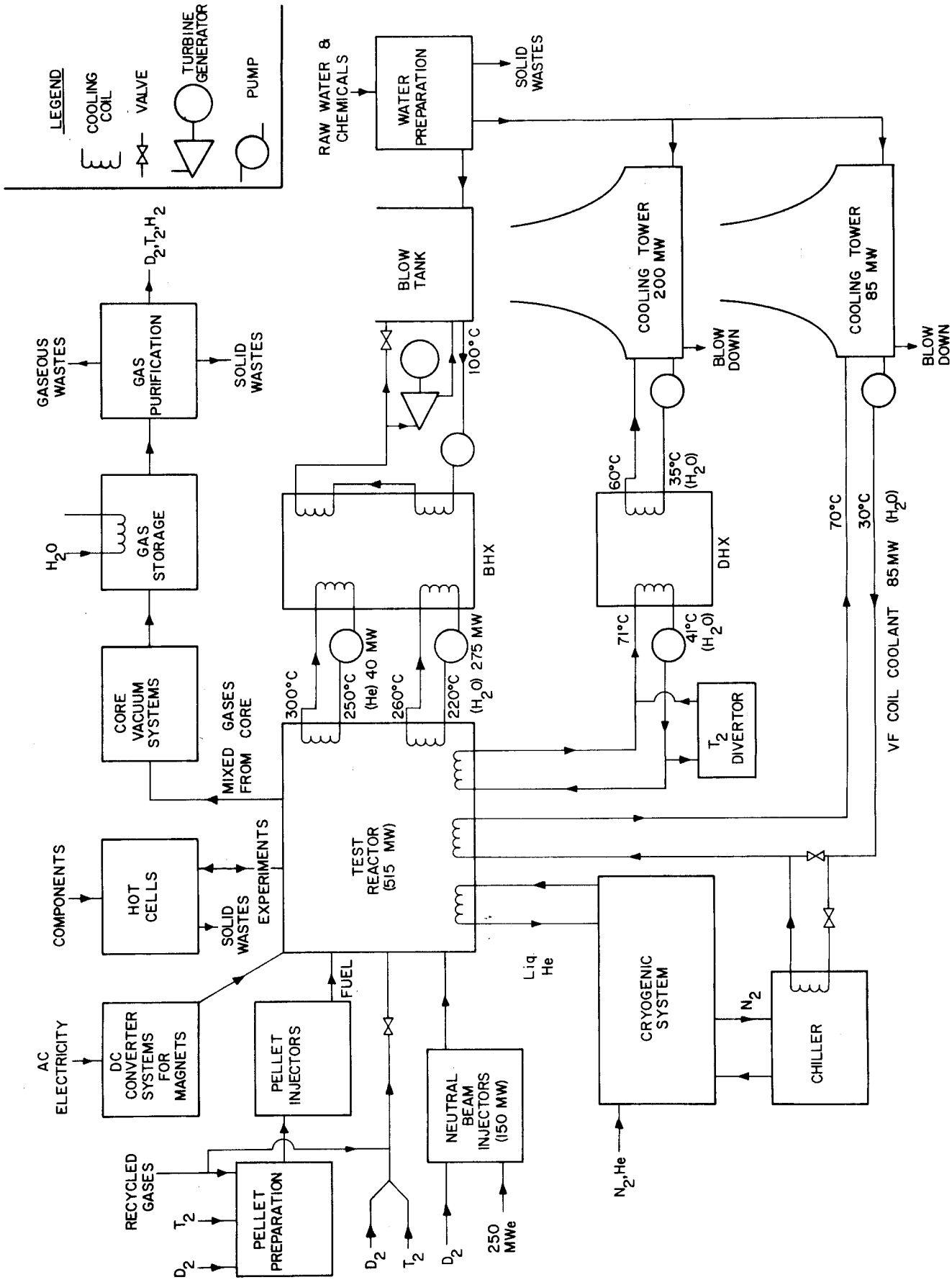

Figure I-A-6

I-B. Plasma Physics

The TETR is designed to operate as a neutral beam driven, two component tokamak with $n\tau_E \sim 10^{13}$ cm^{-3} sec rather than as an ignition device. It is also designed with a divertor which serves to both pump the chamber and maintain a sufficiently pure plasma with a high enough tritium concentration. The main problem is, as with all devices, to find a configuration that is sufficiently MHD stable while at the same time achieving the design goals as outlined in I-A.

The basic model for TETR is a "D" or triangularly shaped plasma that admits the inclusion of a double null poloidal divertor. This shape fills most optimally the available space inside the TF coils. A series of MHD calculations have been carried out, and a plot of the surfaces on constant ψ is shown by Fig. I-B-1. An optimized system of poloidal field coils has been developed that produces an elongated "D" shaped MHD equilibrium plasma with a current of 2.52 MA, an axial toroidal field of 4.2 T, a shape factor of 1.54 at a poloidal β of 3.8. The aspect ratio is 5.4. This system can produce sufficient power to generate neutron wall loadings above 1 MW/m^2 and has ready accessibility to meet the design goals of TETR. A feedback stabilization system based on the existing EF coils is required to provide overall vertical stability of the current loop since the vacuum vertical field has a negative decay index. A summary of the plasma parameters from the MHD equilibrium analysis is given on Table I-B-1.

The vertical magnetic field in TETR has the wrong curvature for vertical stability for reasons just discussed. The vertical position can, however, be feedback stabilized to keep the plasma properly centered as has been accomplished, for example, in the Versator experiment. The plasma position is stable in the horizontal direction although variations in the plasma current or pressure may, however, cause the plasma to sit off-center horizontally. It is becoming common practice in present Tokamaks to include a feedback loop to keep the plasma centered horizontally. This is technologically not very different from stabilization of the vertical position. A linear stability analysis of the vertical position, including the effect of eddy currents in the conducting wall surrounding the plasma, has been completed to determine the necessary characteristics of the feedback system.

To provide the radial feedback field, a small change in the current of eight of the divertor coils is made. Typical values of ΔI in these coils produce a radial magnetic field of 50 G and corresponds to a stored magnetic energy of 5 kJ for the feedback field. A summary of the feedback parameters for TETR is given in Table I-B-2.

The operating cycle for TETR from startup to shutdown is summarized on Table I-B-3. During the one second startup, the single turn loop voltage around the plasma ring reaches a maximum of 25.3 volts at about 0.1 second . The average electron density for these calculations is taken to be 10^{13} cm^{-3}, less than the final density of 7.5×10^{13} cm^{-3} which will be achieved after the startup phase by gas injection.

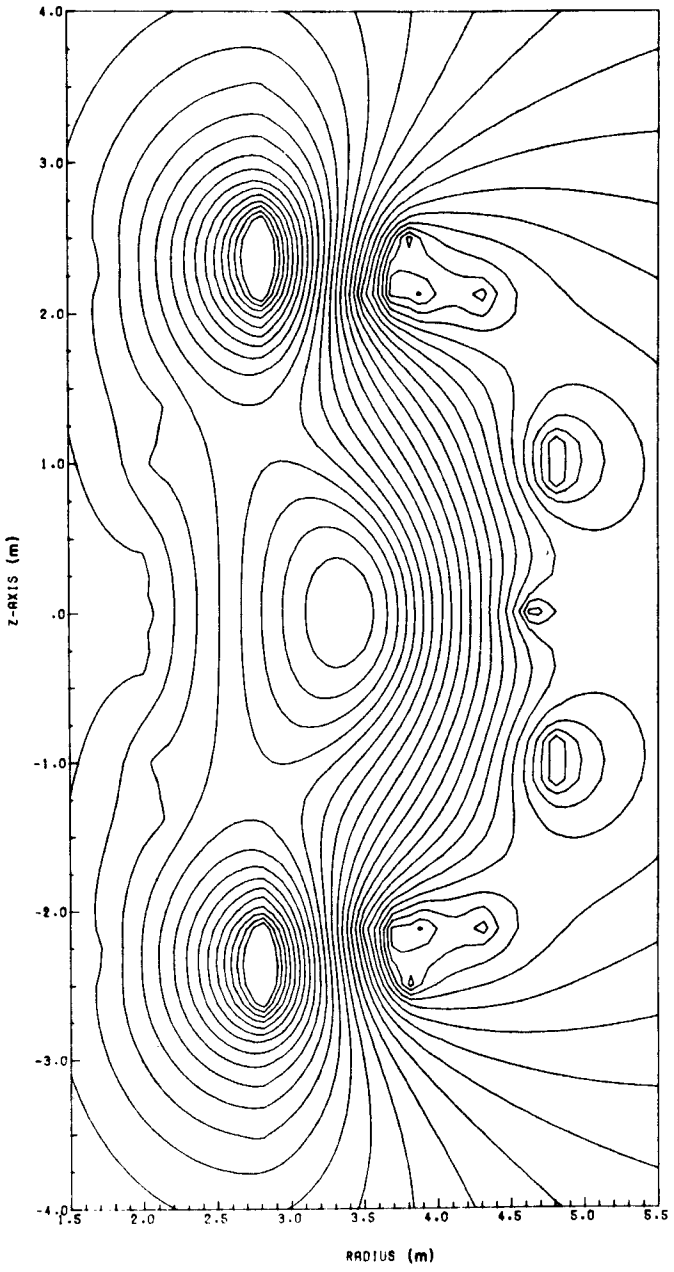

Figure I-B-1 - Flux Surfaces for the Final TETR Plasma Design

Table I-B-1

Final Plasma Parameters for TETR from MHD Analysis

R_o = 3.25 m

R_m = 3.37 m

R_{in} = 2.65 m

R_{out} = 3.85 m

a = 0.6

b = 1.20

b/a = 2.0

S = 1.53

A = 5.42

V_p = 41.6 m^3

A_w = 115 m^2

B_T = 41.9 KG

B_{max} = 85 KG (at R = 1.60 m)

β_θ = 3.8

q_o = 0.95

q_{max} = 2.5

I_p = 2.52 MA

n = -2.0

B_θ = 3.7 KG

$\bar{p}$ = 0.49 x 10^6 joules/m^3

β(total) = 0.066

Table I-B-2

Feedback Parameters of TETR

Growth Rate - no shell, γ_o	7.3 x 10^5 sec^{-1}
Growth Rate with shell	1.3 x 10^3 sec^{-1}
Frequency of high frequency modes	5 x 10^5 sec^{-1}
β (L/R time of shell)	1.9 x 10^{-3} sec
Skin Time ($\frac{1}{2}\mu_o \sigma \delta^2$)	2.8 x 10^{-6} sec
Minimum gain for stabilization	18.5 Gauss/cm
Design Gain	28 Gauss/cm
Maximum allowable delay time	.74 msec.
Design delay time	.33 msec.
Required power @ $\epsilon(0)$ = 3 cm	90 MW
Maximum excursion for $\epsilon(0)$ = 3 cm	4.6 cm

Table I-B-3

TETR Operating Cycle

Time (seconds)	Phase Description
0-1	Startup: plasma and divertor currents rise to full maximum; transformer currents begin to drop; plasma ohmically heats to T_e = 2.1 keV.
1-61	Burn: gas injection to full density; neutral beam injection to maximum temperature; transformer currents drop to maximum negative values.
61-62.5	Shutdown: beam injection discontinued; current in transformer reversed; plasma and divertor currents drop to zero.
62.5-72.5	Recharge: plasma cool-down; residual gas pumped out; chamber refilled with fresh fuel; transformer currents reset to initial values.

The initial temperature and current used in the calculations were 100 eV and 20 kA, respectively. Several calculations done for startup conditions have shown the results to be relatively insensitive to the initial temperature. The choice of an initial current physically represents current due to preionization and soak of a skin effect current, if formed. The results are also relatively insensitive to this choice. Based on the TFTR calculations and interpretation of TFR results, it appears entirely possible that either one or both of preionization and supplementary heating will be necessary for discharge formation.

During the final, or recharge phase, neutral gas influx cools the plasma. Minimum time for this phase is dictated by mechanical pumping requirements, and is chosen to be 10 seconds. During this recharge phase, the transformer must be reset to its initial current for the beginning of a new cycle. The electric field generated will be approximately 0.3 mV/cm, which will induce a current in the chamber. If the pressure is low enough, an avalanche breakdown could occur. However, by having the divertor coils carry a nominal current, field lines can be diverted to intersect the walls, and the particles will be deposited on the walls. Maximum energy flux to the first wall during this period will be less than 1 Joule/m^2/sec, which is negligible.

A series of transport calculations were made to study the temperature and density profiles in TETR during plasma burn; the purpose was to understand the impact that these profiles would have on the design of such a tokamak and to determine operating parameters. We also carried out a global model analysis and have compared the results with those from the space-time model.

The resulting temperature and density profiles are shown in Fig. I-B-2 and I-B-3, respectively. Note the very peaked density profiles typical of divertor boundary conditions in the presence of trapped particle scaling. The plasma separatrix (edge) density is quite low ($\sim 2 \times 10^{12}$ cm^{-3}) which indicates that the divertor may not be very useful as a screen to impurities which come from the first solid surfaces.

Mean plasma parameters for TETR are shown in Table I-B-4 together with parameters determined from a global model analysis that assumes parabolic spatial profiles. The steady state neutron flux at the wall is ~ 1.3 MW/m^2 and the mean energy and particle containment times are $\tau_E = 52$ and $\tau_p = 31$ ms, respectively. These times are quite small if we consider that present tokamaks show energy containment times up to 50 ms although they are smaller in size. The reason for these short times is related to the rapid increase in transport coefficients predicted for the trapped ion mode at the high temperatures that are generated in this very strongly driven device. Less pessimistic scaling laws would predict a larger τ_E, considerably higher temperatures and, therefore, an enhanced TCT fusion probability. However, larger values of τ_E and mean temperature would drive up beta and the MHD determined beta limit would then necessitate a decrease in the injected power. This indicates that we are near the peak

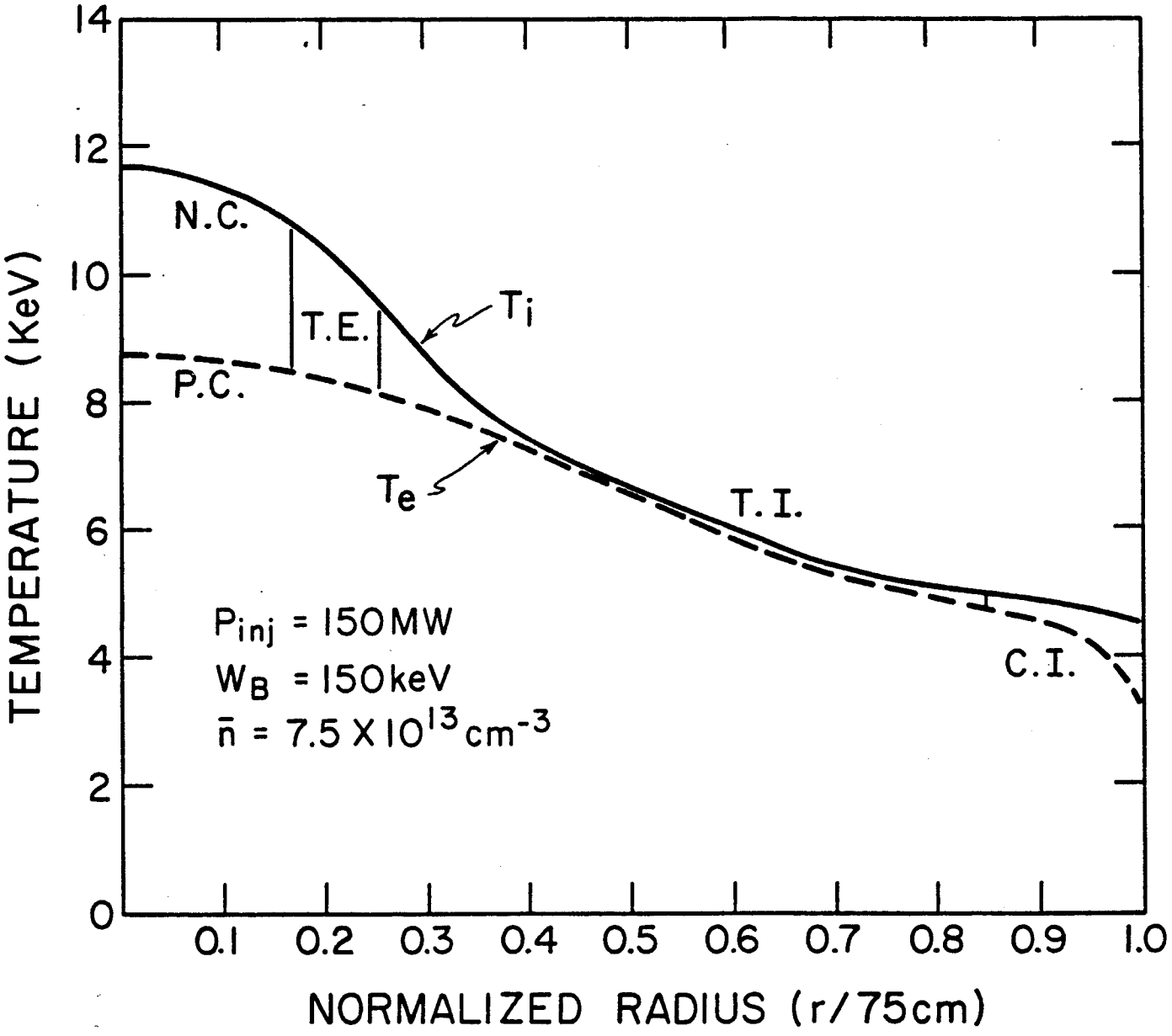

Figure I-B-2 - Equilibrium TETR Temperature Profiles for Ions and Electrons. Dominant Diffusion Mechanisms in Various Regions are Indicated.

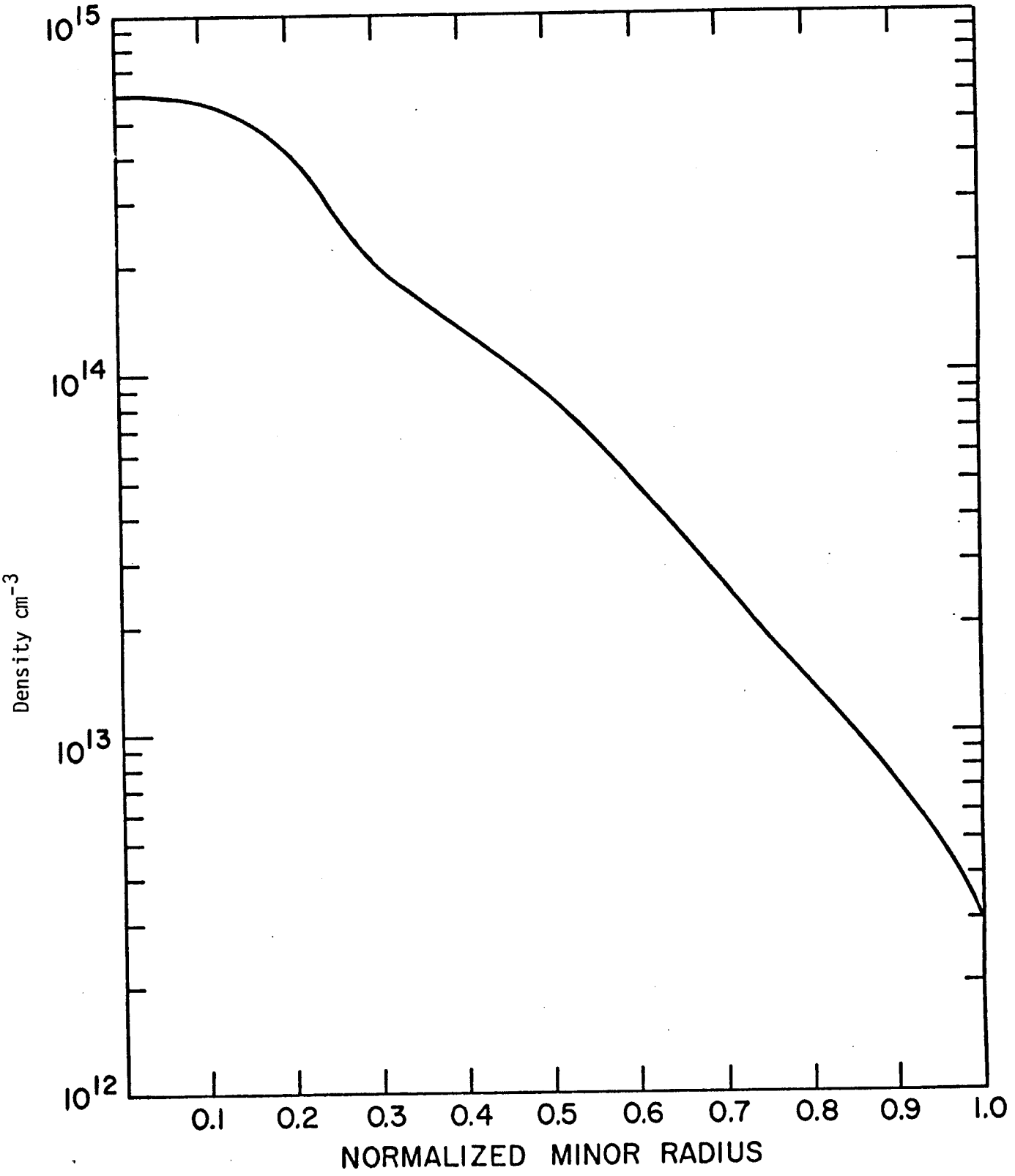

Figure I-B-3 - Equilibrium TETR Density Profile. The Sharp Density Decrease is Typical of Divertor Bounded Tokamaks.

Table I-B-4

Final Plasma Parameters of TETR from Energy Balance Analysis

	Global Model	Space-Time Analysis
Major Radius (m)	3.24	3.24
Poloidal Beta	2.8	3.2
Toroidal Current (MA)	2.54	2.52
Volume (m^3)	37.8	36.
Toroidal Magnetic Field (kG)	41.8	41.9
q(a)	2.4	2.4
Plasma Circumference/Inscribed Circle	1.55	1
Half Width	0.60	0.75
Half Height	1.20	0.75
Electron Density (cm^{-3})	7.7×10^{13}	7.5×10^{13}
Mean Electron Temp. (keV)	11.3	7.4
Mean Ion Temp. (keV)	12.2	8.6
Amplification Factor - Q	1.78	1.62
Neutron Flux at Wall (MW/m^2)	1.44	1.31
Γ	.36	1.0
Energy Containment Time (ms)	80	52
Power to Divertor (MW)	203	198
$n\tau_E$	6.2×10^{12}	3.9×10^{12}
Beam Slowing Down Time (ms)	160	
Particle Containment Time (ms)		31
Pellet Source (#/cm^3-sec)		2.4×10^{15}
Injected Power (MW)	150	150
Injection Energy (keV)	150	150

in neutron energy density attainable in a fixed β tokamak system. We may be helped here by the fact that the q profile is frozen into the plasma, which will serve to raise the beta limitation. Furthermore, the fusion probability is also proportional to the fraction of tritium in the plasma which decreases approximately linearly with the particle containment time. It may be noted that as the fraction of tritium drops to near 50%, the thermal fusion contribution increases, but this will not make up for the decrease in beam plasma fusions. Therefore, one would ideally like to increase τ_E somewhat while keeping τ_p less than about 100 ms. (We find for τ_p = 100 ms, the fraction of tritium in the plasma is 83%. The total poloidal beta of the beam and plasma is 3.2 which indicates a beta of 4.6%.)

In summary, analyses reveal that although the assumed (trapped particle) scaling laws predict a very short energy and particle containment time, the plasma in TETR will be sufficiently hot to produce the levels of neutron flux we require. Longer values of τ_E would enhance neutron production but would necessitate the need for high β equilibria. Longer particle containment times would cause a dilution of the tritium fraction in the target and thereby reduce neutron production. It would, however, have the advantage of lessening the fueling, tritium handling and pumping problems.

The vacuum system in TETR makes use of both cryocondensation and cryosorption pumps. Limited space in the divertor zone and high gas loads typical of Tokamak reactors led us to use a new and innovative idea in pump design. The idea is to build two pumps back to back, fitted into a cylindrical body such that one pump can be on line while the other is being regenerated (see Figure I-B-4). As soon as the pump on line is saturated, the pump pair is rotated 180° and a freshly regenerated pump is in place to commence pumping. More pumps can be fitted into available space in this way than previously.

There are 66 pump pairs in the divertor zone in TETR with a total pumping area of 57.42 m^2. The pumping speed for D&T is 1.94 x 10^6 ℓ/sec and for He, 0.48 x 10^6 ℓ/sec, taking into account a water cooled chevron shield intended to protect the pumps from neutron streaming. Expected pressure in the divertor zone is $P_{D\&T}$ = 3.7 x 10^{-4} torr and P_{He} = 1 x 10^{-5} torr.

The neutral beam tubes will use primarily cryocondensation pumps because the main gas load is deuterium. There are four pump stations with 12 pumps in each beam tube with a cumulative pumping speed for deuterium of 2.6 x 10^6 ℓ/sec. The anticipated pressure at the tube inlet to the chamber is 1 x 10^{-5} torr.

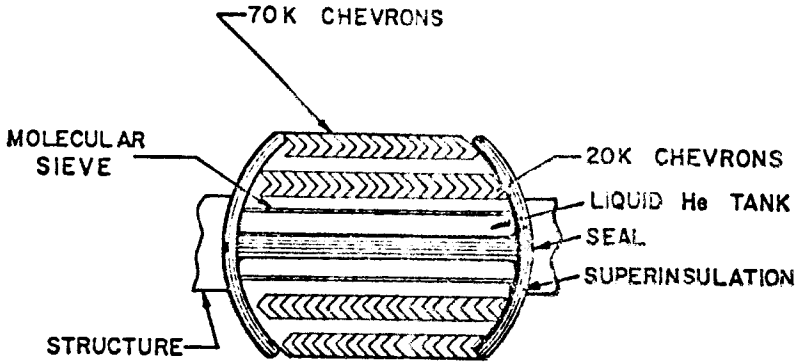

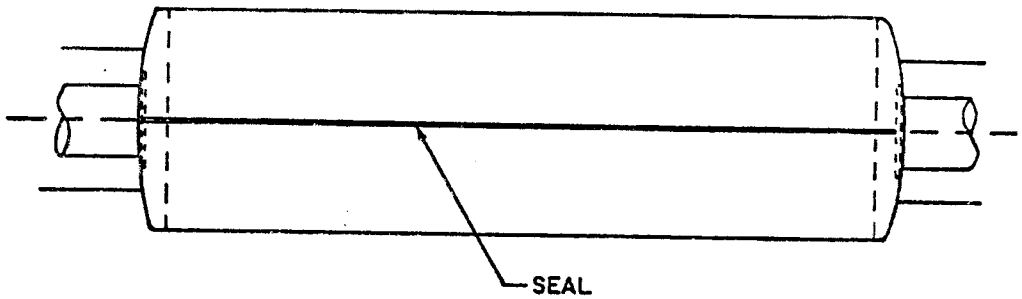

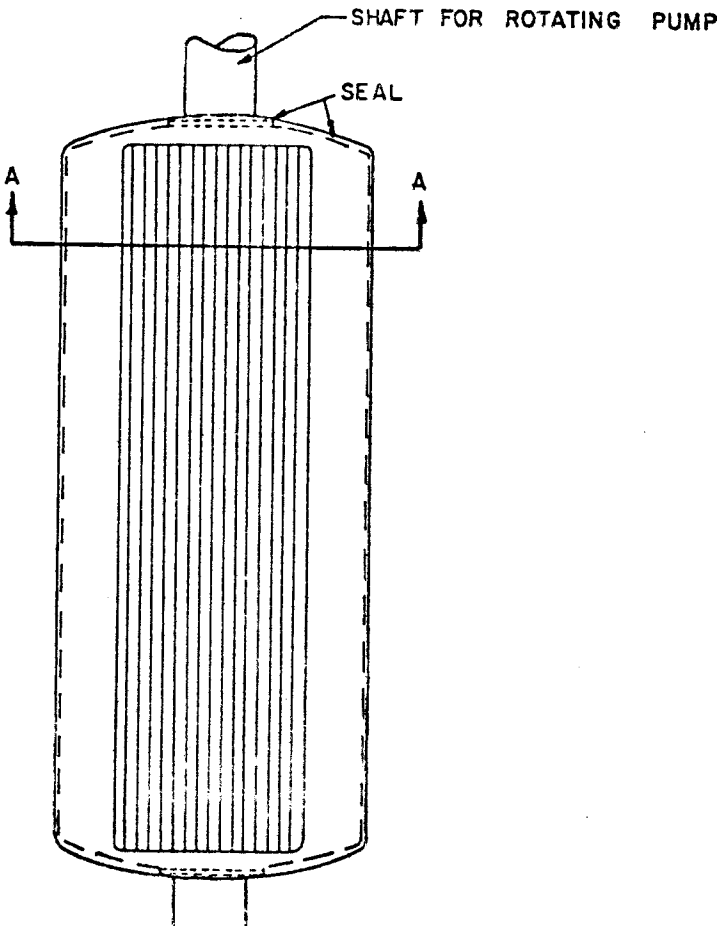

Figure I-B-4

Sketch of Proposed Rotatable Cryo-Sorption Pump

I-C. Plasma Heating

The neutral beam system for TETR provides 1000A (equivalent) of neutral atomic deuterium (D°) at 150 keV for a total injected power of 150 MW. Since TETR operates in the beam driven two component mode, the beams are on for the full 60 sec burn time.

The base case design for the neutral beam system is a 1980's state of the art positive ion system. The layout of this system is shown in Figure I-C-1. The system consists of 12 beam lines, half of which are aimed in the clockwise direction, half in the counterclockwise direction in order to avoid imparting a net plasma momentum. Each beam line contains 7 positive ion sources of the Berkeley type for a total of 84 sources.

The ion beam extracted from the source consists of 75% D^+, 15% D_2^+, and 10% D_3^+. The molecular fraction, if left in the beam, would dissociate in the gas neutralizer cell, and give birth to neutrals at one-half and one-third of the peak injection energy. The less energetic neutrals would not effectively penetrate the plasma, and thus would produce enhanced wall loading and decreased efficiency of the neutral beam system. To eliminate these undesirable effects, the molecular species are removed by passing the beam through a transverse magnetic field upstream from the neutralizer cell. This approach has the additional advantage of placing the ion source in a position which is out of direct line of sight of the fusion neutrons. The molecular species removal places stringent demands on the vacuum pumping system in order to minimize premature neutralization of the beam in the bending magnet region. Optimization of the pumping system leads to required pumping speeds in the range of 3×10^5 l/sec. in the various chambers.

In order to achieve reasonable electrical efficiency, the power in both the molecular fraction of the source output, as well as the un-neutralized fraction of the beam which exits the neutralizer cell must be recovered by direct converters. An analysis of the power flow for the base case system yields an overall injector electrical efficiency of 48% with the assumed 75% atomic source fraction. Considerable improvement in efficiency could be achieved by increasing the atomic fraction of the source output. The principal design parameters for the positive ion base case system are summarized in Table I-C-1.

While it is unlikely that negative ion source technology will have progressed to the level required for TETR size beams by the mid-1980's, a negative ion source system was considered briefly in order to demonstrate the potential advantages. For example, a negative ion system employing electron photo-detachment neutralization has an electrical efficiency of 81% at 150 keV. A summary of various options considered for TETR is given in Table I-C-2.

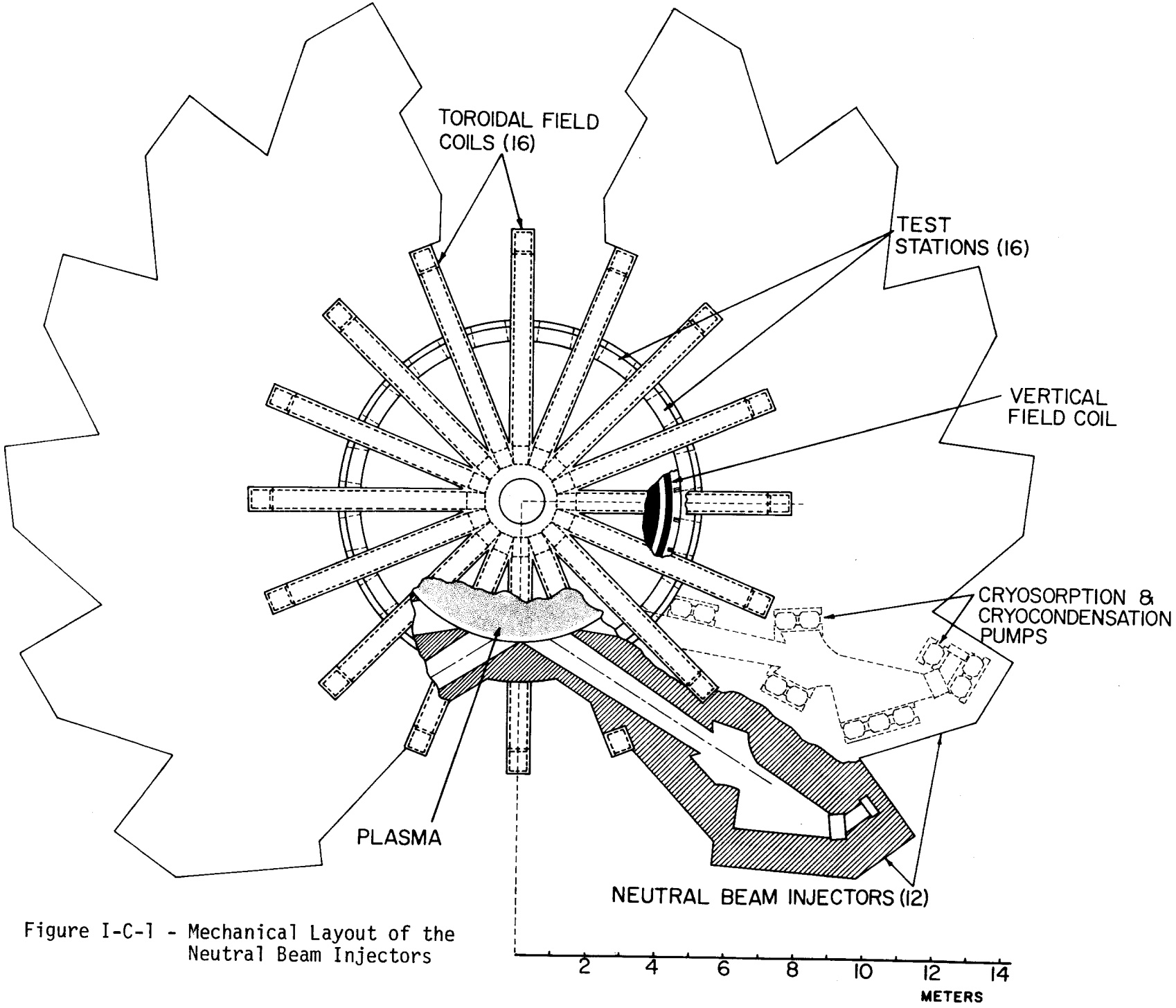

Figure I-C-1 - Mechanical Layout of the Neutral Beam Injectors

Table I-C-1

Summary of Design Parameters for Positive Ion Source System Proposed for TETR

Total injection power (D^0)	150 MW
Beam energy	150 keV
Total injected current	1000 A equivalent
Number of beam lines	12
Sources per beam line	7
Total number of sources	84
Total extracted current (all species)	4460 A
Extracted current per source	53.1 A
Source species composition:	
D^+	75%
D_2^+	15%
D_3^+	10%
Source extraction area	400 cm^2
Source current density	133 mA/cm^2
Source extraction power density	20 kW/cm^2
Beam dimensions at blanket:	
Vertical	24 cm
Horizontal	96 cm
Neutralizer type	D_2 gas target
Neutralizer target thickness	1.66×10^{16} molecules/cm^2
Neutralization efficiency	0.324
Source gas efficiency	0.4
Source gas input per beam line	188 Torr-ℓ/sec
Neutralizer gas input per beam line	97 Torr-ℓ/sec
Direct converter type	In-line, space charge controlled
Direct converter efficiency	0.9
Net electrical input power	312 MW
Net electrical efficiency	0.48

Table I-C-2

Power Requirements for Various Neutral Beam Options on TETR - 150 keV Injection Energy

Option	Ion Source Type	Neutralizer	Energy (keV) at Which Molecular Species are Removed	Neutralization Efficiency η_n	Net Input Power (MW)	Electrical Efficiency η_e
1	positive	gas target	150	0.324	312	0.48
2	positive	gas target	15	0.324	260	0.58
3a	negative	gas target	-	0.61	207	0.73
3b	negative	photodetachment	-	0.90	186	0.81

We also considered the alternative roles that radiofrequency (RF) heating of driven tokamaks (such as TETR) might play. They can be broken down into two major categories: (1) wave heating which provides direct ion heating without other supplementary heating such as neutral beams. (2) radiofrequency heating schemes to compliment primary neutral beam heating of driven tokamaks. We excluded wave heating which primarily heats electrons such as electron cyclotron resonance heating and fast low frequency Alfvén wave heating from the first category for TETR plasma. This is because the objectives of high neutron yield and fusion Q require relatively short plasma density and energy confinement times which do not allow sufficient equilibration time for the heated electrons to heat the ions and produce copious amounts of fusion reactions.

The remaining wave heating schemes which fall under the first category are:

(a) heating the tritium ions at the first cyclotron harmonic ($\omega = 2\omega_{CT}$) with the first magnetosonic wave with a deuterium blanket.

(b) two-ion hybrid wave heating with a minority species of fundamental resonance.

(c) ion heating by means of lower hybrid waves.

While some experimental experience exists for all three schemes in deuterium plasmas, these are still preliminary and further work on PLT and TFTR is felt to be required before they could be considered as the primary supplementary heating means for a TETR device.

In the area of radiofrequency heating techniques to compliment neutral beam heating, we considered two major subcategories:

(a) RF ion clamping neutral beam heated plasmas, and

(b) supplementary electron heating of neutral beam heated plasmas.

Possibilities of RF clamping of neutral beam generated ions include lower hybrid wave heating at the fundamental or first harmonic of the ion cyclotron beam frequency. It was felt that much more theoretical and experimental work is required before these methods can be seriously considered for a TETR design. Finally, we considered supplementary electron heating of neutral beam heating plasmas.

Due to the assumed near term timeframe of the TETR machine, we have decided to consider only radiofrequency heating techniques which complement primary neutral beam supplementary heating. The concept of RF clamping of neutral beam heated plasmas seems attractive, but the analysis is complex and no theoretical work on the subject has been published. We therefore decided to concentrate our work on a study of the effect of RF electron heating on the neutral beam heated plasma. Our initial rationale was that by heating the electrons to a sufficiently high temperature, one could improve the efficiency of beam plasma fusions. The beam could have a higher probability of slowing down on the tritium ions rather than the electrons.

The main wave heating modes which can achieve this are the electron Landau damping of the low frequency fast Alfvén wave and electron cyclotron damping. Since the sources for the electron cyclotron resonance heating are gyrotrons which are in the development stage and are expected to have efficiencies $\eta \leq 30\%$ in the high frequency range required for a machine such as TETR, we rule out this technique for such a near term machine requiring up to 50 MW power levels. The fast Alfvén wave, however, would be launched at a low frequency ($f \sim 300$ kHz) so that multi-megawatt sources can be seriously considered. Stix has provided a preliminary treatment of plasma heating by this mode and among its advantages are the avoidance of impurity ion acceleration, the use of electron Landau damping as the absorption of a single eigenmode allowing wave enhancement in the plasma zone and lessening arcing problems for a given power input at the antenna. This mode would require a set of poloidal coils made of short sections which are located just inside the torus wall and shielded by a magnetic or mechanical limiter. The complete mechanical, heat transfer and radiation damage analyses were not considered here.

An example of the effectiveness of supplemental RF heating of electrons is shown in Figure I-C-2. It was concluded that supplemental RF heating was only important if the scaling is such that neutral beams cannot heat the electrons above 8 keV. With the present scaling laws (e.g. trapped ion scaling) in TETR, the efficient use is made of the fast Alfvén wave to heat the electrons and provide more fusion output power from the neutral beam heated plasma.

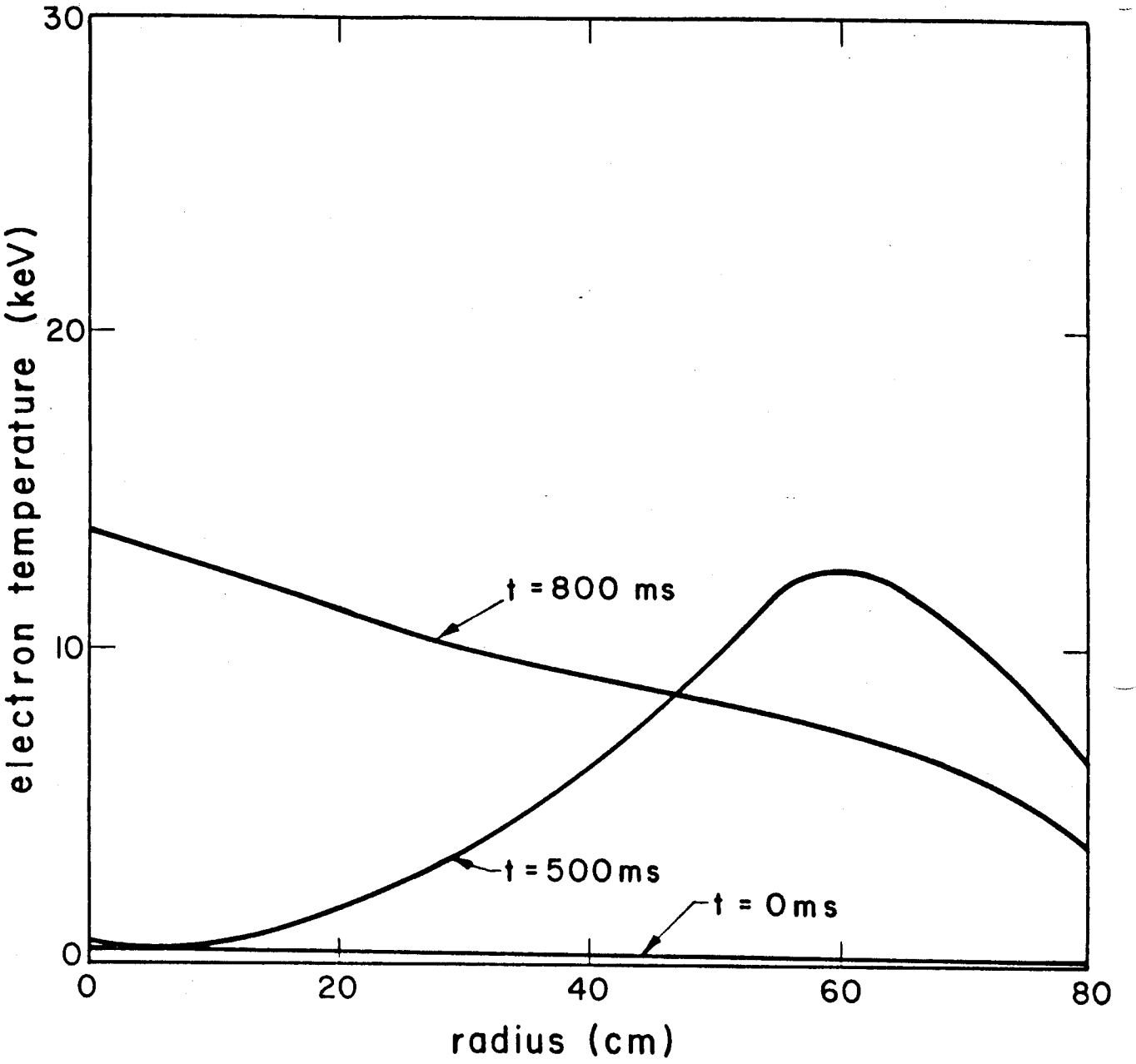

Electron temperature profile when 50 MW of RF power is supplied in the initial 500 ms of heating. After 500 ms, the RF is turned off and 150 MW of neutral beams are injected. In the RF phase $k_{\parallel} = 10^{-3}cm^{-1}$, $\omega = 10^{-2}\omega_{CD}$ and the m=1 mode was assumed.

Figure I-C-2

I-D-Magnet System

The basic design philosophy for the toroidal field (TF), ohmic heating (OH) and vertical field (VF) coils is very similar to that in UWMAK-I, II, and III. There have been only a few changes due to the limited space available and short rise times of the OH and VF coils. The general relationship of the 16 TF, 32 OH and 49 VF coils is shown in Figure I-D-1 and more details are given below.

I-D-Magnet Systems

The toroidal field coils are of a pure constant tension "D" shape design obtained from the analytical formulation by Moses which corrects the magnetic forces for variations in field due to the discreteness of the finite number of coils and the shape of the cross section. Embedded conductors in structural disks (Figure I-D-2) are employed in order to hold the conductors rigidly within the supporting structure. The coils are cryogenically stable with NbTi superconducting filaments in an OFHC Copper Stabilizer and produce a maximum field of 8.5 T and an axial field of 4.19 T at R = 3.25 m.

The TF coils are shielded from the pulsed vertical field (which has a rise time of one second) with high purity aluminum at 4.2 °K (Figure I-D-3). The shell structure between the TF magnets is designed in conjunction with the magnet dewars to sustain the lateral loads due to the pulsed fields from the VF coils, the plasma current, and the much larger loads produced if one adjacent TF magnet should lose current.

The limited space near the central core prevented the provision of enough redundancy and reliability of operation for a current higher than the design current. Safety protection is provided by a dump resistor applied to the 16 magnets in series, not just to a defective magnet. High purity aluminum has been considered as an alternative stabilizer which could provide a measure of redundancy in terms of current capacity. A complete list of specifications for the toroidal field coils is given in Table I-D-1.

The outstanding feature of the poloidal magnetic field system is that the coils are non-superconducting. There is a total of 32 ohmic heating coils in TETR. They are made of thin strips of high purity aluminum, laminated together to suppress eddy currents from the time varying fields. Stainless steel structure is used to contain the soft high purity aluminum and to transfer the turn to turn forces to the central support structure. The coils are cooled in a pool of boiling liquid helium at 4.2 °K.

A resistivity of 3.7×10^{-9} ohm-cm was used for the high purity aluminum and the heat flux is <0.1 watts/cm^2. Maximum current in the conductor is 32 kA at a current density of <4250 A/cm^2. Stresses in the conductor are kept below 2×10^7 N.m^2 (3000 psi) except in a few localized areas on the innermost turns of several coils. OH coils not contained within the central support structure will have additional stainless steel reinforcing.

A total of 25.9 tonnes of high purity aluminum and 36.8 tonnes of stainless steel are needed for the OH coils. The total heat loss in the system is 99.6 kW at 4.2 K. Table I-D-2 gives the main features of the OH system.

Figure I-D-1

Cross Section of TETR with Numbered VF and OH Coils

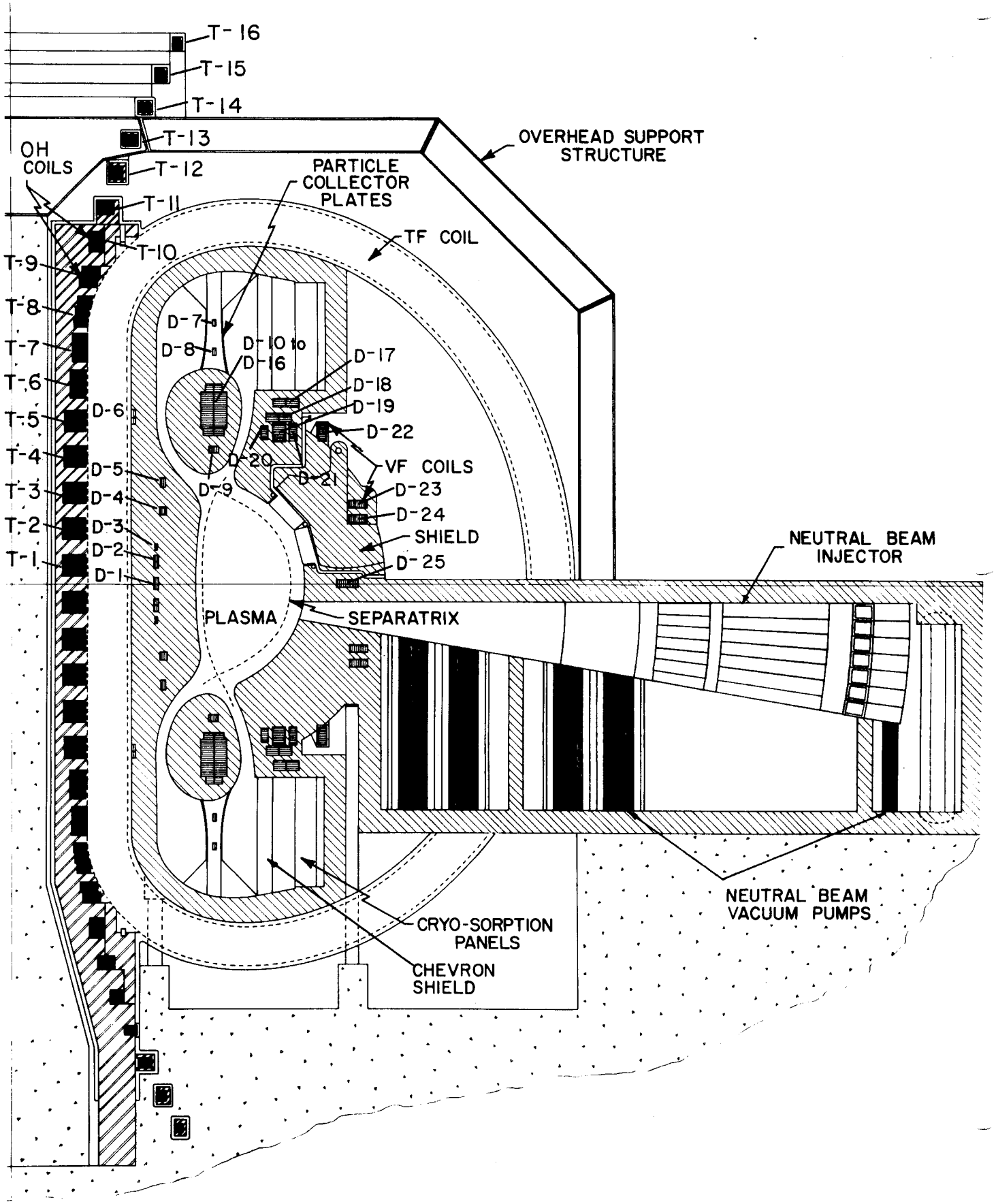

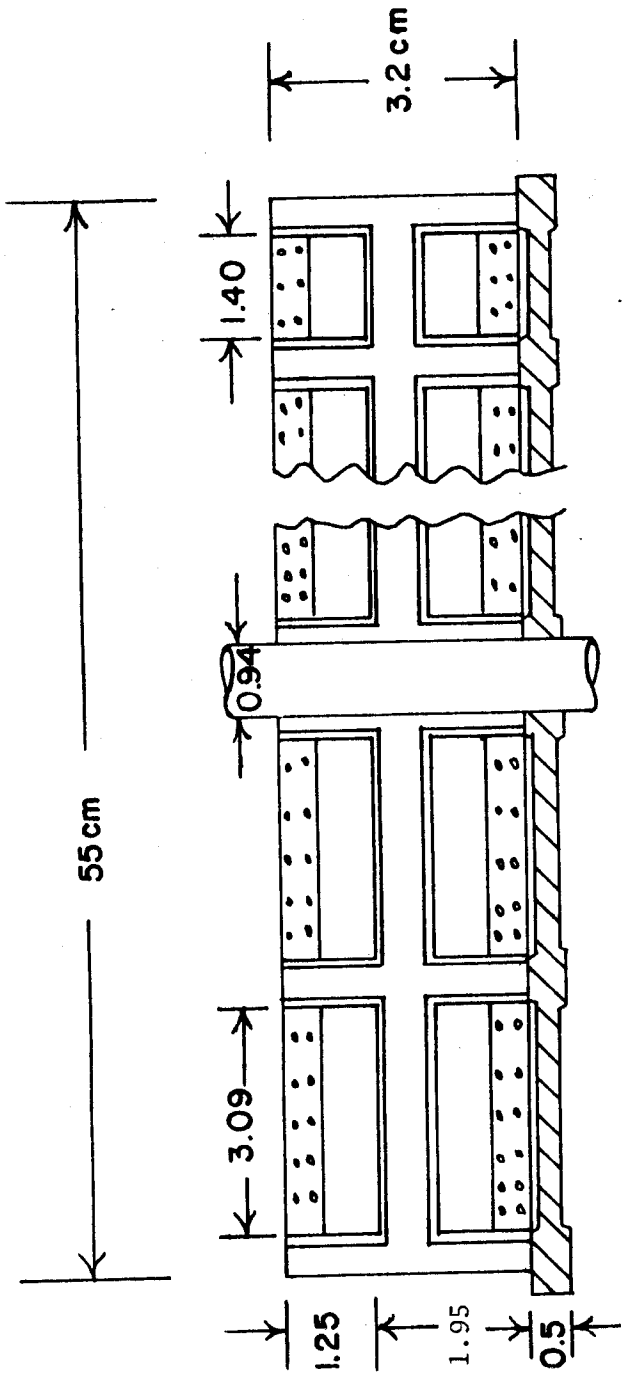

Figure I-D-2

Cross Section of TF Magnet Disk

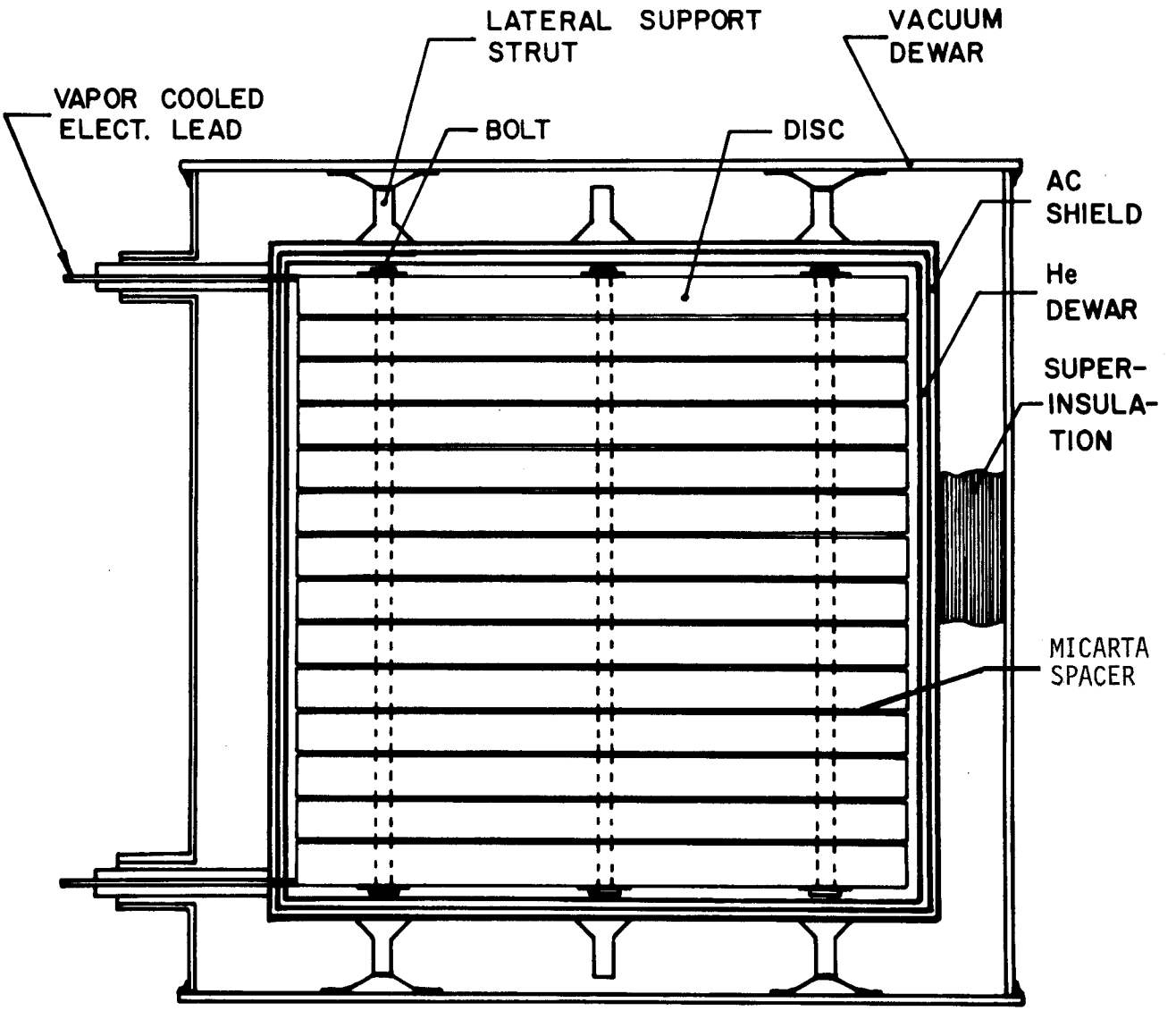
LATERAL SUPPORT STRUT
VACUUM DEWAR
VAPOR COOLED ELECT. LEAD
BOLT
DISC
AC SHIELD
He DEWAR
SUPER-INSULA-TION
MICARTA SPACER

Figure I-D-3

Summary of TF Coil Specifications for TETR

(a)	Field Specifications		
	On axis field	B_o = 4.19 tesla at R = 3.25 m	
	Maximum field at conductor	B_m = 8.5 tesla at R = 1.6 m	
	Total energy stored	6.3GJ = 1.75 MWh	
	Field ripple along the far edge of plasma	2%	
(b)	Magnet Components		
	Number of magnets	16	
	Number of disks per magnet	12	
	Superconductor	NbTi with filament diameter 40 μm and twist pitch 15 cm	
	Spacer between disks	0.5 cm micarta	
	Insulation between conductor and structure	0.1 cm epoxy fiberglass	
	Disk cross section	3.2 x 55 cm	
		Option I	Option II
	Stabilizer	OFHC copper	High purity Al
	Structure	316 SS	2219 Al
	Maximum structure design stress	1.03×10^8 N/m^2	1.5×10^8 N/m^2
	Maximum design strain	0.05%	0.19
	Conductor current (A)	9838	8050
	Number of turns/disk	36	44
	Conductor size	3.09 x 1.35 cm on inside turn, tapers to 1.40 x 1.35 cm on outer-most turn	1.41 x 1.25 cm
	Aluminum alloy bolts to fasten the discs together	375	375
	Lateral support between the magnet and dewar (reinforced epoxy struts each side cross section)	3000 cm^2	3000 cm^2
	Each magnet weight	45 Mtons	15.3 Mtons
(c)	Total Materials Required		
	NbTi superconductor	37.5 Mtons	37.5 Mtons
	Stabilizer	447 Mtons	110 Mtons
	Structure	230 Mtons	110 Mtons
	Insulation (epoxy)	15 Mtons	15.4 Mtons
	Micarta spacers	11.7 Mtons	11.7 Mtons
	Dewar (inner)	22 Mtons	22 Mtons
	Epoxy struts	1.2 Mtons	1.2 Mtons
	Aluminum alloy bolts	0.7 Mtons	0.7 Mtons
	Aluminum shielding	12.5 Mtons	12.5 Mtons
	Cryogenic Insulation	803 m^2	803 m^2

Table I-D-2

Summary of Ohmic Heating Coils For TETR

Number of Coils	32
Type of Conductor	High Purity Aluminum
Cooling	Pool Boiling Liquid Helium
Maximum current in conductor	32 kA
Maximum current density	4250 A/cm^2
Maximum heat flux	<0.1 W/cm^2
Mass of high purity aluminum	25.9 tonnes
Mass of stainless steel	36.8 tonnes
Assumed resistivity of conductor	3.7×10^{-9} ohm cm
Total heat loss	99.6 kW at 4.2°K

Table I-D-3

Summary of Vertical Field Coil System

Number of coils	48
Type of conductor	10% CW OFHC copper
Type of cooling	Forced water cooling
Maximum current density	1743 A/cm^2
Current range	66kA - 477kA
Maximum operating temperature	77°C
Mass of OFHC copper	160 tons
Power dissipated	76 MW
Water flow	29×10^3 liters/sec.

There are 49 vertical field coils with a current range of 66kA to 477kA in the VF coil system. They are made of 10% cold worked OFHC copper with integral water cooling channels. The conductor is in the form of a rectangular bar with multiple cooling holes and is insulated with silicate impregnated glass or mica tape. Joints in the copper are made with induction brazing using a silver alloy filler.

Operating stresses in the conductor are kept below 13×10^7 N/m^2 (19,000 psi). The maximum current density is 1743 A/cm^2 and the maximum operating temperature is 77°C. Cooling water enters at 30°C and exits at 70°C.

A total of 160 tons of OFHC copper is used in the VF coil system. Maximum power dissipated is 76 MW and the water flow is 29×10^3 liters/sec. Table I-D-3 lists the main features of the VF coils.

The charge, discharge and power cycle curves for TETR are shown in Fig. I-D-4 and I-D-5. During the initial 1 sec startup period, the VF coils are charged while the OH coils are discharged. The maximum total stored energy in the poloidal system is 128 kW. Unlike UWMAK-I, II and III, the stored energy in the VF coils is small compared to the OH coils, and consequently a large amount of instantaneous power, 890 MW, is released from the poloidal field coils which could be sent back to the power grid. The maximum power required is 370 MW at the end of reset. Since it has been assumed that a maximum of 500 MW can be purchased directly from the electric utilities, a single 370 MW ac/dc bridge is needed. The time average resistive loss in the OH coil system is 82.7 kW and the peak value is 600 kW. The time average resistive loss in the VF coils is 63 MW while the maximum is 84 MW during the burn period.

The total amount of power required by the cryogeneration for both the magnet and the vacuum system is 118 kW at 4.2 K, or about 35.4 MW at 300 K. There is an additional 84 MW or more for the VF coils. If we compare this to all the other requirements for TETR (mainly the beams) then the total power required for the magnets is ~25% of the total power required (480 MW_e).

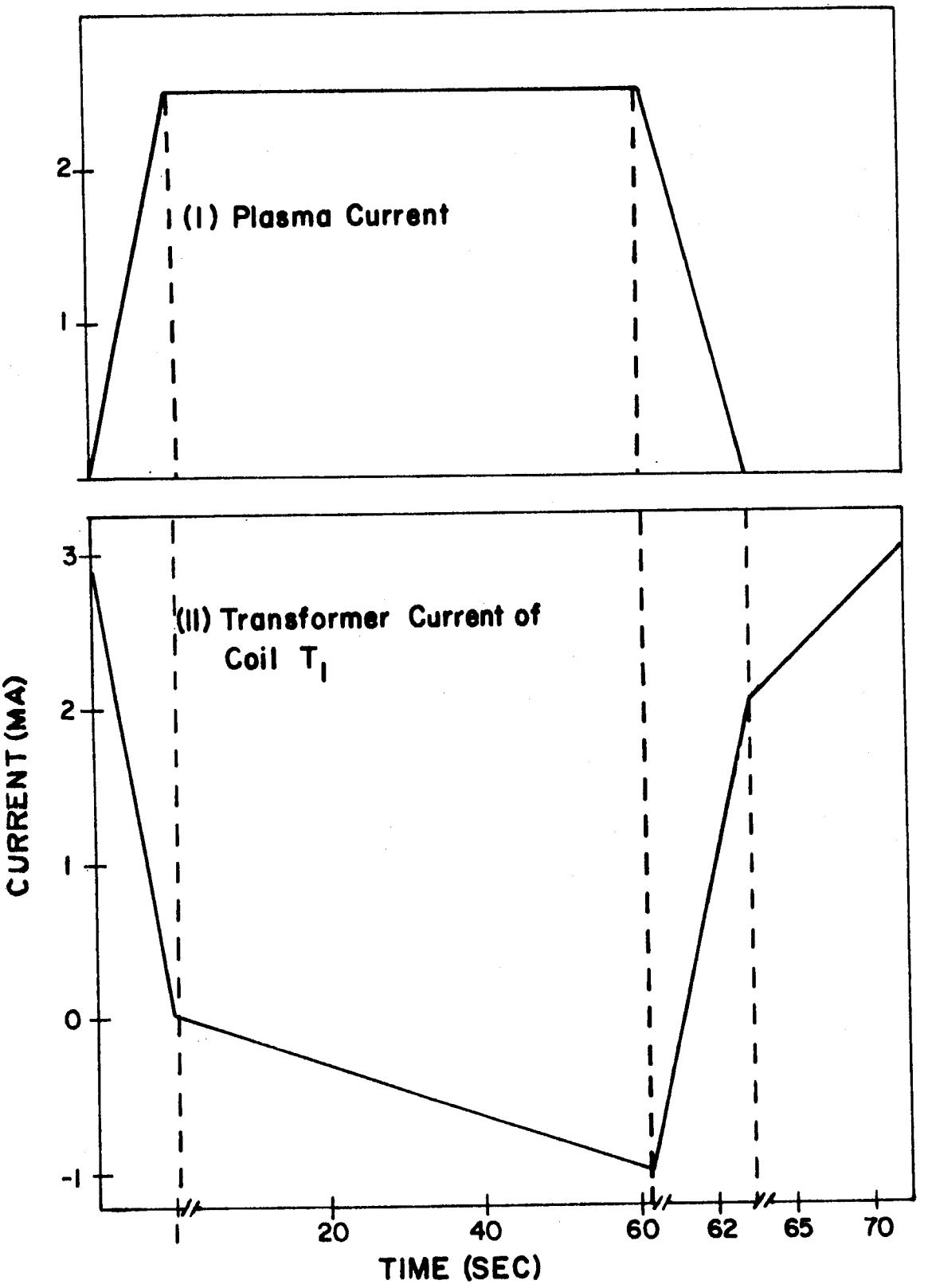

Figure I-D-4

Time Variation of Plasma Current and Representative Coil Current

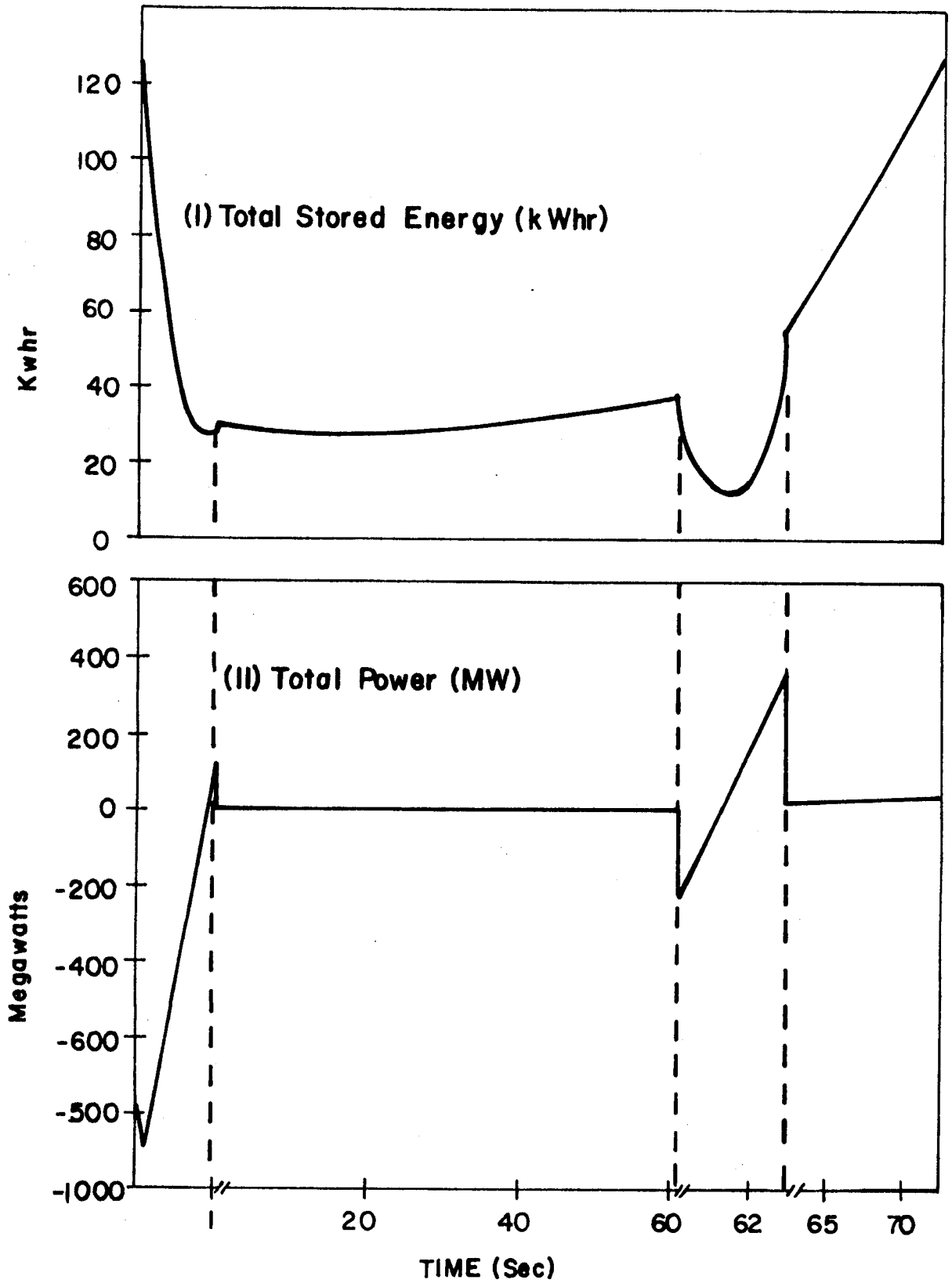

Figure I-D-5

Power Requirements for TETR Magnet System

I-E. Blanket and Shield Design

TETR will not have an energy conversion system nor will it contain breeding material (except in the test stations) and therefore, it will not have a blanket in the strict sense. Instead it will have a water cooled first wall which is also the primary vacuum barrier and will be immediately followed by the shield.

The first wall consists of a bank of squashed stainless steel tubes (Figure I-E-1) attached to a heavier stainless steel sheet and the entire assembly is then covered with a thin corrugated stainless steel sheet which conforms to the shape of the tubes. The cooling tubes are oriented in the poloidal direction and the supply and return manifold in the toroidal direction. This type of structure which has an effective thickness of 0.78 cm is very stiff and provides redundancy against first wall leaks. It is supported on the shield by rectangular rods spaced 20 cm apart which are locked to the shield with mechanical latches. Peripheral welds on the inside of the plasma chamber seal adjacent sections to each other. Figure I-E-2 is a toroidal and poloidal view of the first wall, manifold, shield latches and a joint between adjacent sections. The entire first wall is covered with a graphite liner which is attached to the first wall by stainless steel studs and graphite nuts.

The shield is designed with a combination of box beams and ribs oriented in the radial direction. The box beams are filled with shielding material and surround the plasma chamber circumferentially along the outer divertor slot to provide the hoop strength needed to balance the bending moments from the shield overhang and the compressive forces due to the atmospheric loading on the chamber. Heavy radial ribs running in the poloidal direction join the box beams together and provide the stiffness needed to make the shield self-supporting.

The upper half of the reactor contains the test stations (Figure I-E-3). These locations have specially designed shield sections which are hinged to allow quick and easy access to the test stations. Removal of a test station makes the plasma chamber accessible for possible maintenance, repair or routine first wall replacement. Visual inspection with optical instruments can be made through the bayonette test stations located on the lower half of the reactor.

Stresses in the first wall have been kept low with the intention of maximizing the fatigue life. Cyclic stresses occurring between burn periods are small due to the thermal inertia of the graphite liner which prevents excessive cooling of the first wall. Table I-E-1 gives the main parameters of the blanket and shield.

Figure I-E-1 - Cross Section of First Wall Showing Variation in Tube Width

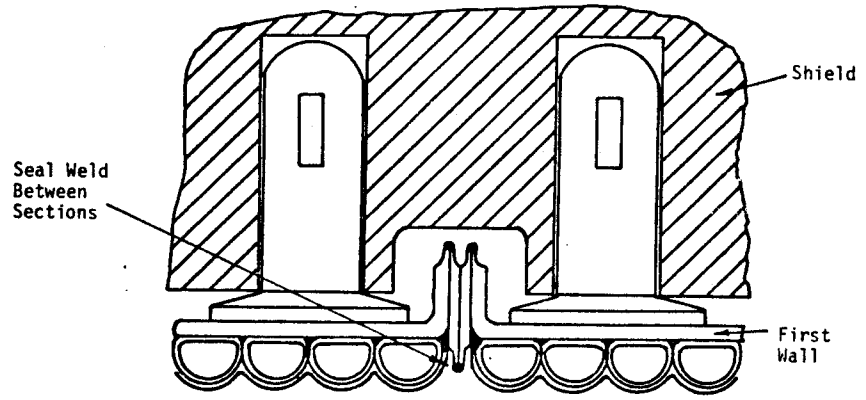

Poloidal View of a Joint Between First Wall Sections

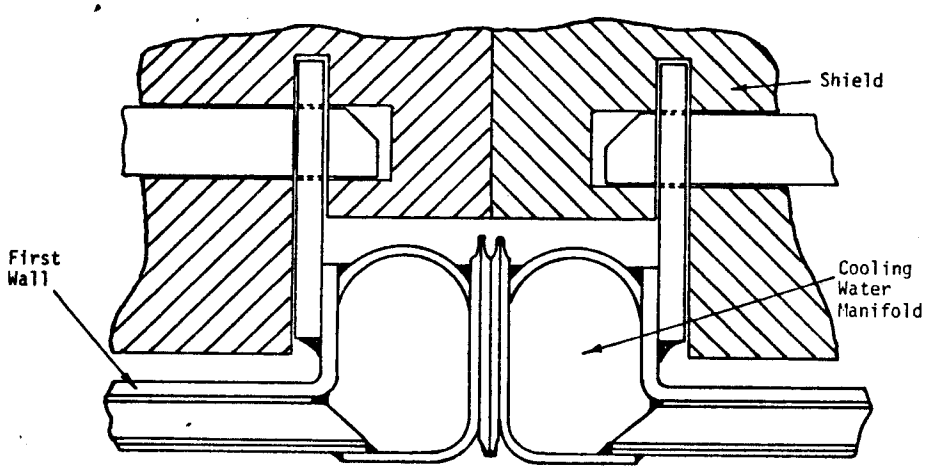

Toroidal View of a Joint Between First Wall Sections Showing Cooling Water Manifolds

Figure I-E-2

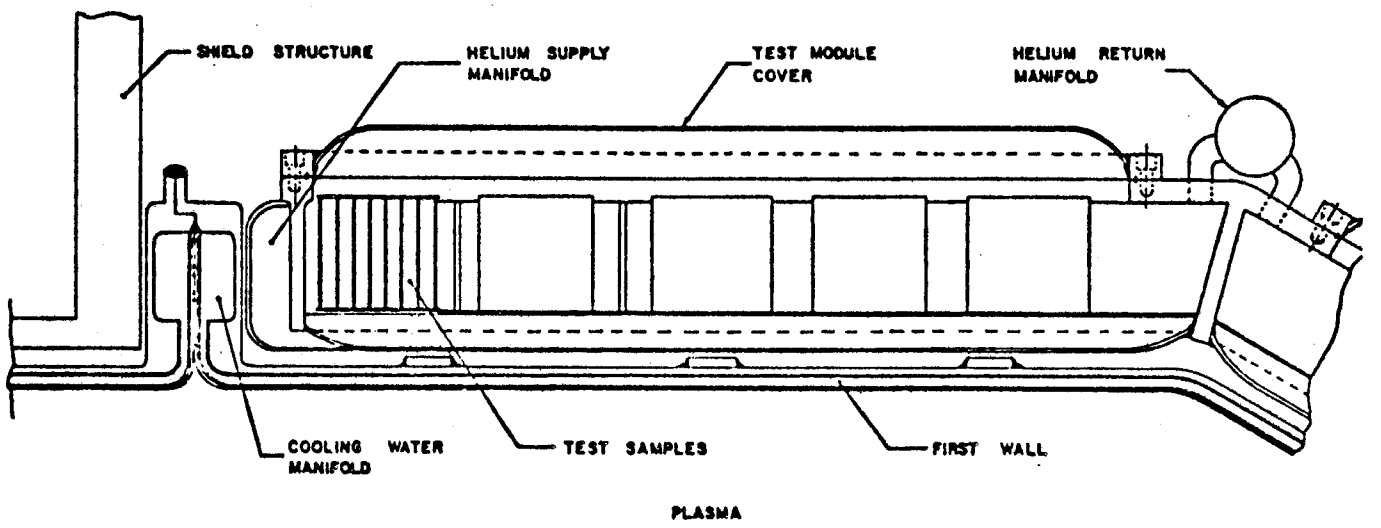

Toroidal View

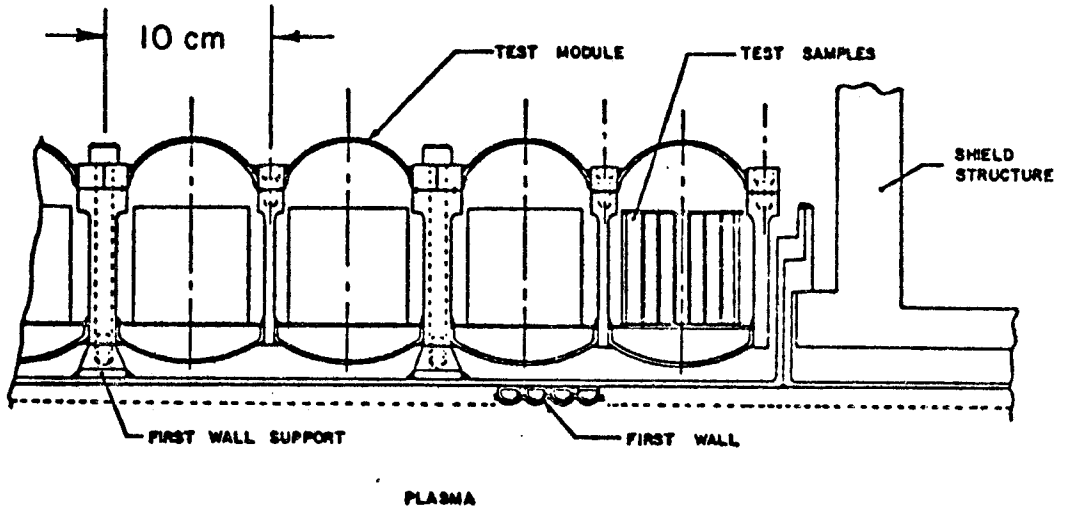

Poloidal View

Figure I-E-3 - Toroidal and Poloidal Cross Sections of a Typical Test Module

Table I-E-1

First Wall and Shield Specifications

Total surface area covered by first wall	300 m^2
Initial outer diameter of cooling tube	1.2 cm
Thickness of cooling tube wall	0.1 cm
Thickness of back-up sheet	0.4 cm
Thickness of front corrugated sheet	0.1 cm
Spacing between tubes:	
Maximum	1.7 cm
Minimum	1.3 cm
Maximum pressure in tubes	3.43×10^6 Pa (500 psi)
Maximum stress in first wall	5.1×10^7 Pa (7400 psi)
Spacing between first wall supports	20 cm
Spacing between graphite liner supports	60 cm
Thickness of graphite liner	1 cm
Weight of stainless steel in first wall	18.5 MT
Weight of graphite liner	3.4 MT
Maximum operating temperature of first wall	300°C
Maximum operating temperature of graphite liner	1100°C
Total weight of shield (including VF coils)	9081 MT
Mass of stainless steel in shield	792 MT
Mass of H_2O in shield	25 MT
Mass of W in shield	3310 MT
Mass of B_4C in shield	237 MT
Mass of Pb in shield	4560 MT
Mass of Cu in VF coils	157 MT

I-F. Neutronics

The neutronics design calculations have been done in greater detail than in any of our previous studies. This is principally due to the need to know the entire radiation environment for the benefit of the experimental program. However, it was also regarded as vital that we assure access to the regions surrounding the reactor which in turn required the study of all openings to the reaction chamber. Finally, the detail seemed desirable in a study of a reactor proposed for serious near term consideration.

Two design decisions fixed the essential nature of the neutronics design. First, the decision to neither breed tritium nor produce electrical power meant that we were designing only a shield. No lithium is required and coolant choice is not constrained by potential reactions with lithium. Second, the ability to thermally isolate the test modules and the rapid adjustment of the radiation to that characteristic of the module meant that the temperature and composition of the shield could be chosen without serious consequences for the user of the facility. Thus, low temperature operation of the first zone is possible allowing a stainless steel first wall to potentially last the life of the facility. This in turn should improve the reactor availability greatly. Simple water cooling may also be employed.

The problem is thus defined essentially as a pure shielding one with few constraints. There are several special shielding problems posed by particular design features. The near term feature requiring the time varying field coils to be normal poses special shielding problems particularly in the case of the vertical field coils. The relatively large penetrations due to the use of a small driven machine increases the special shielding problems behind the neutral beam penetration. Further, the desire for good access to the facility requires considerably greater radiation attenuation than in our previous design studies.

With these problems and goals in mind, specific design constraints were formulated. These include limits on radiation exposure of insulators and nuclear heating in normal and superconducting coils and radiation levels at the back of the shields. One-dimensional survey calculations were then carried out to check the performances of various shield materials. The survey covered a wide range of designs and the case referred to as the basic design described in Figure I-F-1 and Table I-F-1 was chosen. It is more expensive than the other designs due to the large quantity of tungsten, but meets all design criteria but one and even there poses a reasonable problem in replacement or use of alternative materials. The key design limits from the nuclear standpoint and the calculated results are given in Table I-F-2.

It was found that only the radiation damage to the fiberglass insulation of the outer vertical field coil exceeded our design criteria. The implication of that effect is explored in Chapter IX and we have concluded that more radiation damage resistant insulators are required.

Figure I-F-1

Schematic of Blanket and Shield Design-TETR

Inner Blanket (midplane)

Composition	I	II	III	IV	V	VI	VII	VI	V	VIII	V	VI	IX	VII	XI
Thickness -cm	55	1	3	1	5	5	11.5	5	5	7	7.5	7.5	34.5	1.5	0.5
Zone	1	2	3	4	5	6	7	8	9	10	11	12	13	14	15

Plasm

150 cm

Outer Blanket (Midplane)

	XI	VII	IX	VI	V	VIII	V	VI	VII	V	VI	
Plasma →	0.5	1.5	28	7.5	7.5	30	5	5	15	5	5	
	17	18	19	20	21	22	23	24	25	26	27	

110 cm

Key for Figure I-F-1

Zone Compositions for the Basic TETR Design at the Midplane

Composition*	Volume Percent	Material
I	57.65	Cu
	30.65	St.St.
	10.11	NbTi
	1.59	Insulation
II	100	Al
III	5	Mylar (H_9 C_{10} O_4)
IV	100	St.St.
V	87.4	B_4C
	4	St.St.
	4	H_2O
VI	92	Pb
	4	St.St.
	4	H_2O
VII	96	St.St.
	4	H_2O
VIII	75	Cu
	20	H_2O
	5	Insulation
IX	87.6	W
	4	St.St.
	4	H_2O
X	40	St.St.
	50	H_2O
XI	100	C
XII	100	Vacuum

*St.St. = 316 Stainless Steel

Table I-F-1

Dimensions per Zone for the Basic TETR Design of the Midplane

Zone Number	Radius (cm)		Thickness (cm)
	Inner	Outer	
1	105.0	160.0	55
2	160.0	161.0	1
3	161.0	164.0	3
4	164.0	165.0	1
5	165.0	170.0	5
6	170.0	175.0	5
7	175.0	186.5	11.5
8	186.5	191.5	5.0
9	191.5	196.5	5.0
10	196.5	203.5	7
11	203.5	211	7.5
12	211	218.5	7.5
13	218.5	253.0	34.0
14	253.0	254.5	1.5
15	254.5	255.0	0.5
16	255	405	150
17	405	405.5	0.5
18	405.5	407	1.5
19	407	435	28
20	435	442.5	7.5
21	442.5	450.0	7.5
22	450.0	480	30
23	480	485	5
24	485	490	5
25	490	505	15
26	505	510	5
27	510	515	5

Table I-F-2

Key Criteria for TETR Blanket and Shield

Design Basis	Design Limit	Result for Basic Design[a]
Resistivity limit in the stabilizer of the toroidal field windings	Less than 5.7×10^{-5} dpa/yr.	1.2×10^{-5} dpa/yr.
Cryogenic refrigeration load due to nuclear heating	Less than 1.5×10^{-3} w/cm^3	4.7×10^{-5} w/cm^3
Radiation damage to the super insulation	Less than 1.13×10^{7} Rad/yr.	1.3×10^{7} Rads/yr
Coolant Limits in vertical field coils due to nuclear heating	Less than 0.1 W/cm^3	(Inner) 0.01 W/cm^3 (Outer) 0.05
Radiation damage to vertical field coil fiberglass	Less than 2.65×10^{8} Rad/yr	(Inner) 2.5×10^{8} Rad/yr (Outer) 9.6×10^{8}

(a) Does not account for streaming of radiation

The two-dimensional neutronics analysis in R-Z geometry of the system revealed a number of new problems. It was necessary to modify the divertor slots to meet design limits in the toroidal field coils. These limits were satisfied in the one-dimensional studies which simulate the midplane results but, the two-dimensional results revealed the maximum damage behind the divertor slots is ~10 times higher. The modified slot was successful in protecting the toroidal coil everywhere. The original and modified slots are shown in Figure I-F-2. In addition, the streaming through the neutral beam injection port quantified the need for a shadow shield around the injector system. Detailed analysis of the contour effects is given in Chapter IX on radiation damage.

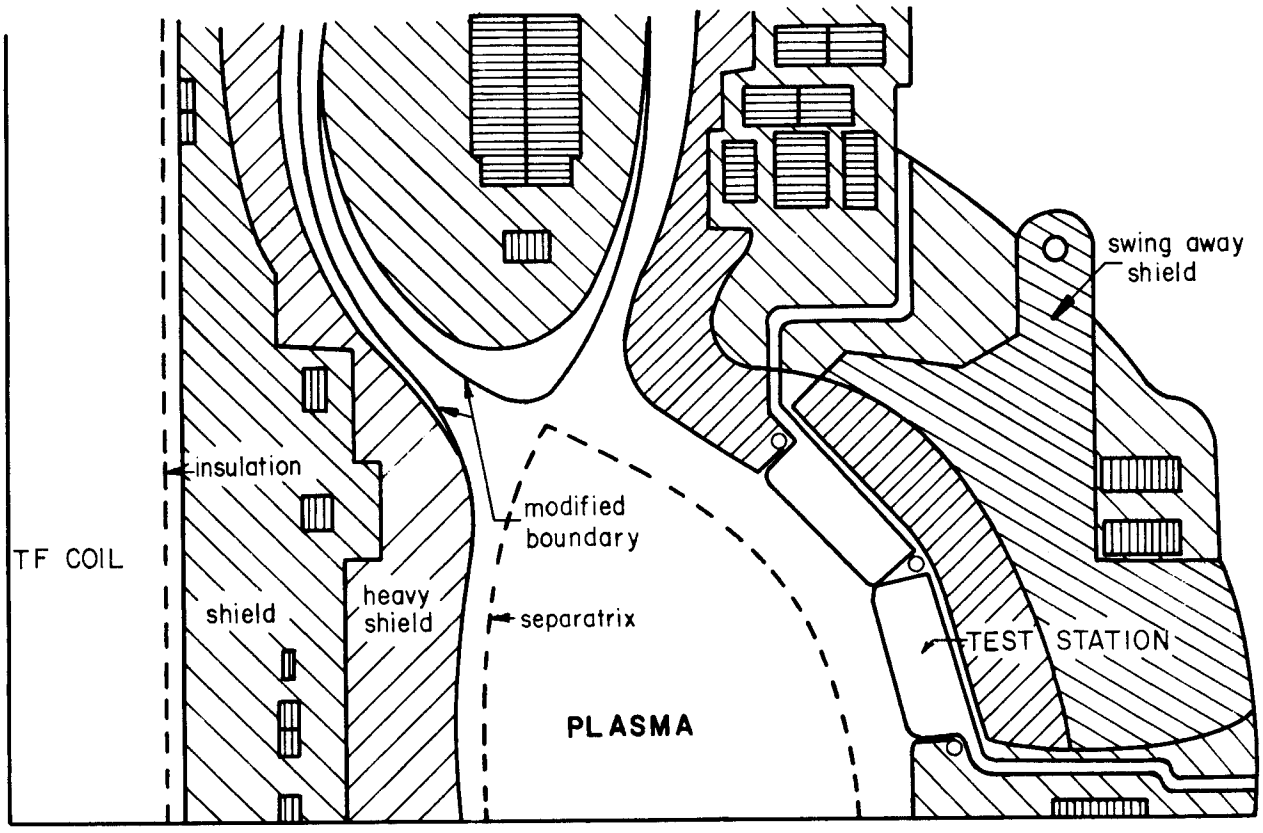

Fig I-F-2 A schematic diagram of TETR showing modified divertor slots

I-G. Thermal Hydraulics

The analysis of the cooling systems in TETR is completely different than those performed for power stations. In the present design, no attempt is to be made to utilize the high temperature coolant to make electricity or to provide high pressure coolants. In this respect, the analyses for TETR is easier than in earlier designs. On the other hand, more attention must be paid to removing the high heat loads to the divertor section and to, as always, protecting the first wall from a "burn through" by a localized plasma dump.

There are three separated coolant loops for the TETR. The first wall and blanket are cooled by boiling water ~250°C. Boiling water is used to minimize the effect of thermal cycling. The testing module requires an inert coolant at a moderately high temperature so high purity helium is used. The coolant for the collector plates has to handle a large thermal flux while keeping the plate structure at a moderate temperature. High velocity water is used as the coolant for this region. The cooling regimes, the coolant and their temperature ranges are shown on Table I-G-1.

Table I-G-1

Summaries of Blanket Cooling Schemes

Regime	Coolant	Temperature	Thermal Energy
First Wall and Blanket	Boiling Water	220 to 260°C	275 MW
Testing Module	He (300 psi)	250 to 300°C	40 MW
Collector Plate	Water	66 to 71°C	200 MW

The temperature rise of the coolant from the collector plate is very small due to the high velocity required. To facilitate the heat exchanger design, only a fraction of the coolant is directed to the heat exchanger and cooled to 45°C. The return stream will be united to the hot stream and the resultant temperature is 66°C which is then fed to the collector plate.

Power generation is not the primary function of this reactor so that a power conversion system is not included. The temperature of the blanket coolant is high enough, however, that a low pressure steam turbine may be included to demonstrate the power conversion from fusion reaction. The heat exchangers have been designed keeping this in mind so that the water from the heat exchangers is hot enough for power conversion with a thermal efficiency of about 20% if desired. In the normal operations, the thermal energy will be dumped to a cooling tower.

A summary of the heat exchanger designs are shown on Table I-G-2. All three designs are point designs and no optimization was attempted. The fourth column is for the magnet coolant. No intermediate coolant is required for this loop. Three different cooling towers are required for the blanket and testing section, for the collector plate, and for the magnet, respectively.

Table I-G-2

Summary For The Heat Exchanger Designs

	Main Blanket	Testing Section	Collector	Magnets
Q, MW	275	40	200	70
Coolant	Steam	He (300 psi)	Water	Water
Tin, °C	220	250	45	30
Tout, °C	260	300	71	65
Flow Rate, $\frac{kg}{hr}$	7500	5.56×10^5	6.6×10^6	2×10^6
Secondary Coolant	H_2O	H_2O	H_2O	None
T, °C	100 to 200	100 to 200	35 to 60	---
Flow Rate, $\frac{kg}{hr}$	2.4×10^6	3.4×10^5	6.9×10^6	---
U $\frac{watt}{cm^2\text{-}°C}$	.78	.37	.90	---
ΔTm, °C	80	125	10.5	---
Area, m^2	440	90	2200	---
ID, HX m	2.0	1.0	3.65	---
Length, HX m	4.4	3.6	6	---
Weight, kg	25,000	6000	110,000	
Cost@ $30/kg	$.75 \times 10^6$	$.18 \times 10^6$	3.3×10^6	

Total Cost 4.23×10^6

The possibilities of having to remove 5 to 20 MW/m^2 from the collection plates in the divertor means that "traditional" methods of energy collection in this region (i.e. liquid Li films)are no longer possible. After considerable investigation, a new scheme was proposed which utilizes a Ta-10 W structural material cooled by a high velocity stream of water. This material represents the best combination of yield strength, thermal conductivity, expansion coefficient, Young's Modulus, sputtering coefficient, and corrosion resistance of all the metals considered.

The total energy collected by the Ta-10W plates is 200 MW and by a proper geometrical arrangement, we have been able to reduce the maximum energy flux to 6.67 MW/m^2 if the particles leave the plasma in equal amounts in the four divertor slots (see Figure I-D-1). However, it may be possible for slight plasma perturbations to alter the symmetry of escaping particles and one should design

for the possibility of having all the particles escape down one divertor slot for short periods of time. This means that values in excess of 20 MW/m^2 may have to be handled. The details of the proposed collector plate design can be found in Chapter VIII and a summary of the critical features of the collector plate design is given in Table I-G-3. The Ta-10W does not exceed 295°C during normal operation nor are the stresses excessive (14,000 MN/m^2 - 20,000 psi). The biggest problem with this system is the relatively short lifetime of the material due to sputtering. This lifetime (determined by 20% of the original 1 mm removed) could be from 1.5 to 7.5 months depending on the sputtering coefficient.

The problem of first wall protection from a plasma dump was examined and it was shown that in addition to protecting the plasma from high Z impurities and the first wall from particle erosion, a 1 mm carbon curtain provides enough thermal inertia to smooth out the temperature fluctuations in the first wall between burns and to protect against inadvertent plasma dumps. A measure of the protection can be seen in Figures I-G-1 and I-G-2 where the unprotected and 1 cm thick carbon curtain protected 316 SS wall temperature is given as a function of energy density and time. Without the carbon curtain the temperature increase in the first wall will be ~1000°C after 0.2 sec of a 1500 $watt/cm^2$ plasma dump. (This represents a concentration of all the plasma to ~ 5 % of the surface area). Placing a 1 cm thick carbon curtain in front of the wall reduces the ultimate first wall temperature increase to levels below melting and greatly extends the time over which one can control the malfunction. Of course, the curtain will also get hot and in Figure I-G-3 we see that within 10 seconds the curtain will vaporize for all power levels above 1000 $watts/cm^2$. But again, the time during which proper corrective action can be taken is greatly extended.

The conclusion of the above analysis is that even if the carbon curtain were not needed for plasma or first wall wall erosion wall reasons, its role in protecting the first wall against inadvertent melting from plasma dumps would be important enough to consider its use in tokamaks.

Table I-G-3

Summary of Collector Plate Design

Material	Ta-10 W
Coolant	H_2O
Coolant Pressure	140 $\frac{MN}{m^2}$ (200 psi)
Coolant Velocity	30 m/sec
Coolant Inlet Temperature	65°C
Coolant Exit Temperature	71°C
Maximum Film ΔT	70°C
Maximum Structure Temperature	295°C
Coolant Pressure Drop	35 $\frac{MN}{m^2}$ (50 psi)
Coolant Tube I. D.	1 cm
Coolant Tube Wall Thickness	1 mm
Maximum Stress	14,000 $\frac{MN}{m^2}$ (20,000 psi)
Safety Factor	6
Plate Life	1.5 months at S = .05
	7.5 months at S = .01

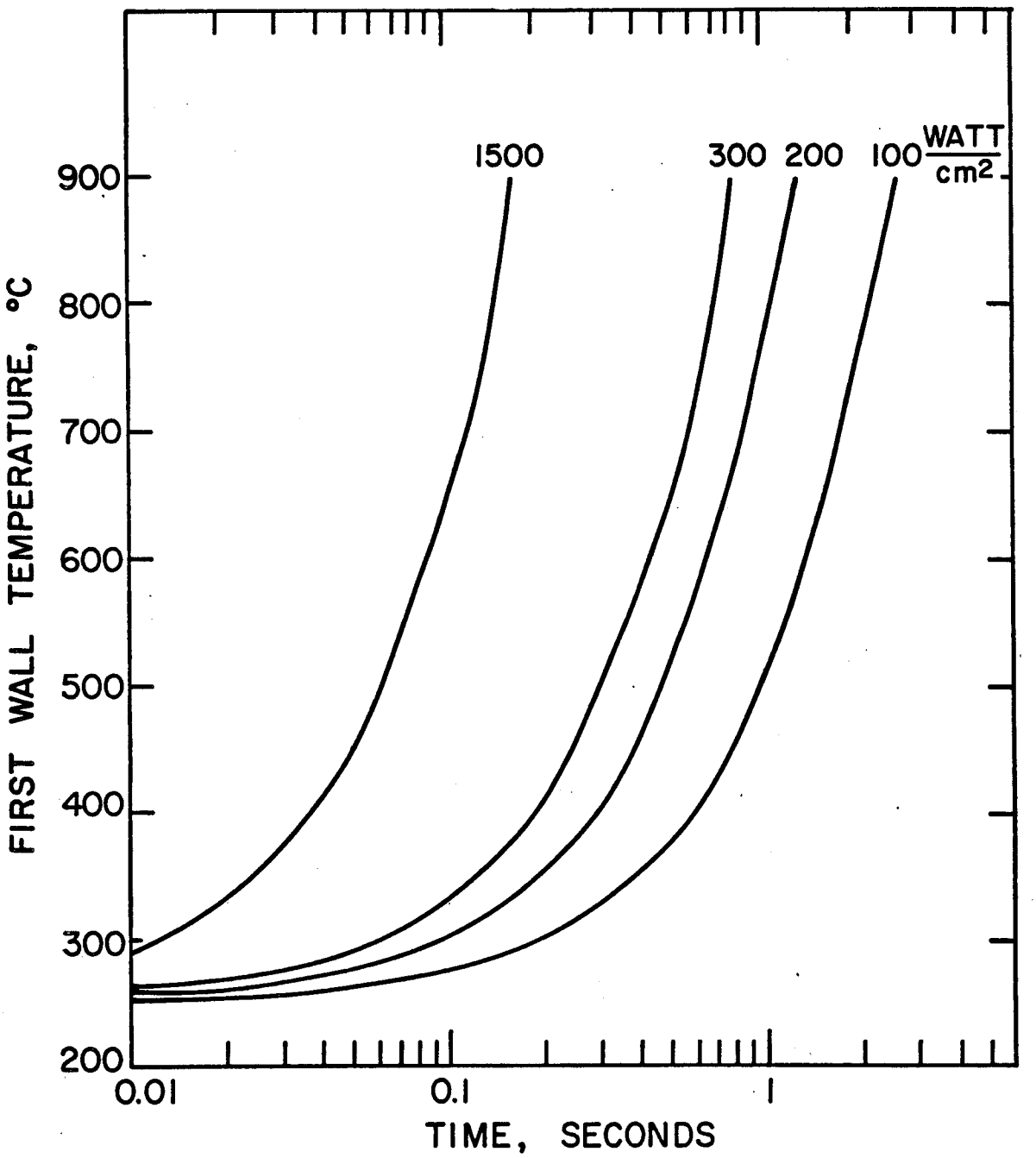

Figure I-G-1 -- Temperature Response of Unprotected First Wall

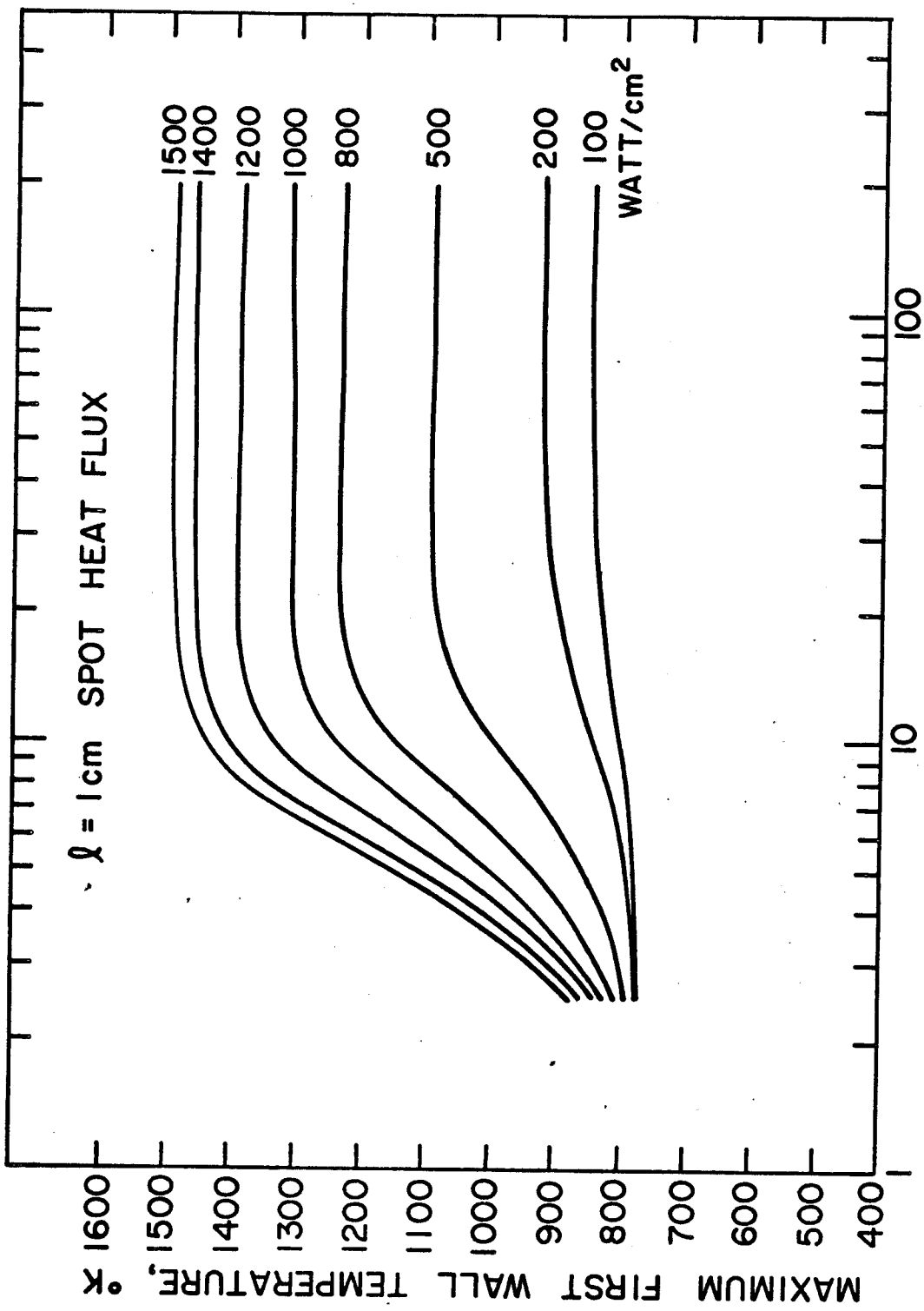

Figure I-G-2 - Temperature Response of First Wall Protected by a 1 cm Thick Curtain

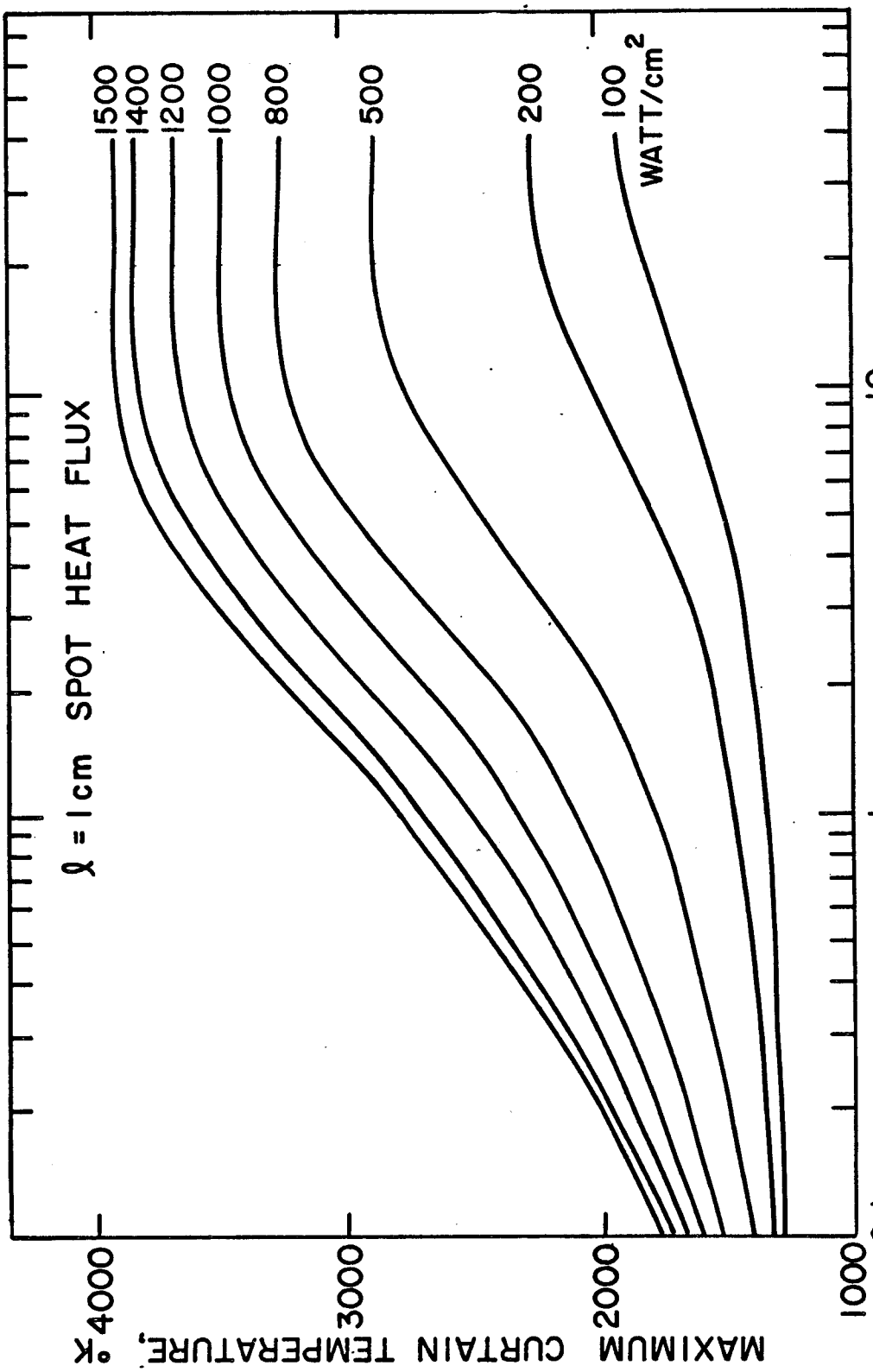

Figure I-G-3 - Temperature Response of a 1 cm Thick Curtain

I-H. Radiation Damage to TETR Components

In the process of providing a test bed to irradiate samples for future commercial facilities, many of the permanent components of the TETR reactor will suffer damage from the high energy neutrons and energetic ions environment. It is convenient to class these problems in 6 major areas.

- Neutron damage to the 316 SS structure
- Neutron and energetic hydrogenic ion damage in the graphite liner
- Surface damage to the Ta-10W particle collector plates in the divertor zone
- Radiation induced resistivity changes in the TF coil materials
- Degradation of electrical and thermal insulators for the TF and VF coils
- Other components such as W, B_4, C, Pb, etc.

The main feature of the damage environment for these areas are given in Table I-H-1. A brief summary of the important problems resulting from those damage rates is given below and the reader is referred to Chapter IX for more details.

Before we discuss the reactor itself it is important to note the reason for placing the test cells off the midplane of the reactor. Figures I-H-1a shows a cross sectional view of the TETR and Figure 1-H-1b shows how the displacement and helium production rates vary with the poloidal angle. It is obvious that to get the highest damage rates, one must be in the 20-75° region. Note also that the damage gradient varies slowly in the poloidal direction compared to the size of a typical specimen (~ several mm's).

Turning to the rest of the reactor we find that we have an important advantage in the analysis of TETR components over assessments done for previous UWMAK reactors because of the two-dimensional description of the damage environment (see Chapter VII for more details). An example of the damage flux and displacement rates for the lower half of the TETR is shown in Figures I-H-2a, b, and c. Such detail is extremely helpful in pinpointing "hot spots" where peculiar leakage and geometry effects produce damage rates much higher than indicated by more traditional one-dimensional analyses. The 2-D studies also revealed anomolies in transmutation rates such as the production of helium and hydrogen.

Our assessments of the swelling, fatigue, creep-rupture, and fracture behavior of the first walls reveal that it should be possible to attain a 10 MW-y/m^2 lifetime if the steel is kept at ~300°C. It is important to note that we have not done a finite element analysis of the stresses but at a nominal 4000 psi (30 MPa) stress variation, some 3 x 10^5 times per year,

Table I-H-1

Summary of Radiation Damage Environment for Non Test Cell Components - TETR

	Component	Maximum Temperature	Maximum Radiation Damage Level/yr (70% PF)
1)	316 SS First Wall	300°C	9.5 dpa 210 appm He
2)	Carbon Curtain	1200°C	6.7 dpa 1.5×10^{23} D,T,He neutral particles/cm^2 (3.8 keV)
3)	Ta-10W Particle Collector Plates	300°C	7×10^{24} D,T,He ions cm^{-2} (10.3 keV)
4)	Copper Stabilizer and NbTi S/C in TF coils	4.2°K	3×10^{-4} dpa
5)	Epoxy Fiberglass and Mylar Insulation-TF coil	4.2°K	10^8 rad.
6)	Epoxy Fiberglass Insulation	70°C	10^9 rad (most TF coils) 2×10^{11} rad (D-9 coil)

Fig. I-H-1a

LOCATION OF POLOIDAL COORDINATES FOR TETR NEUTRONICS CALCULATIONS

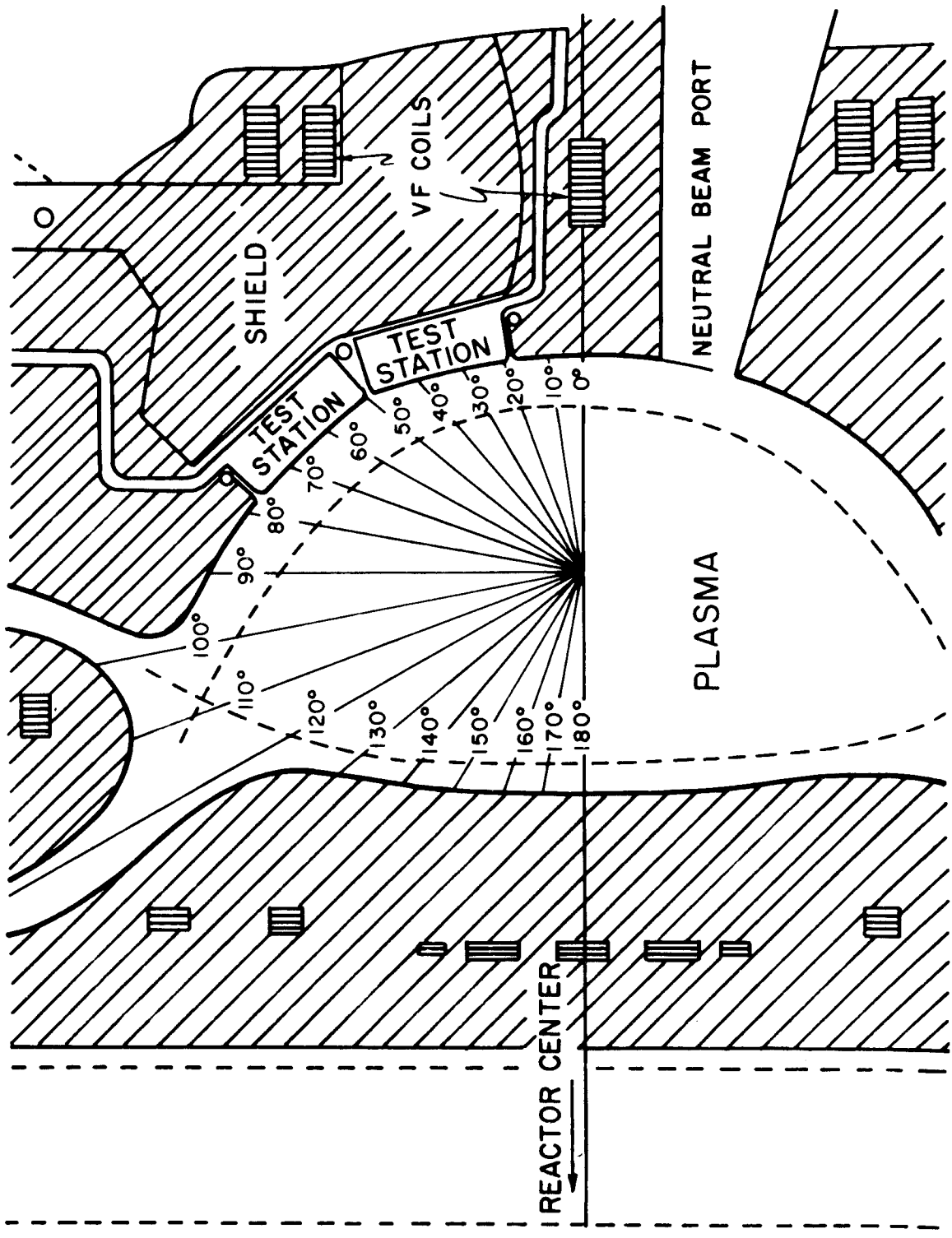

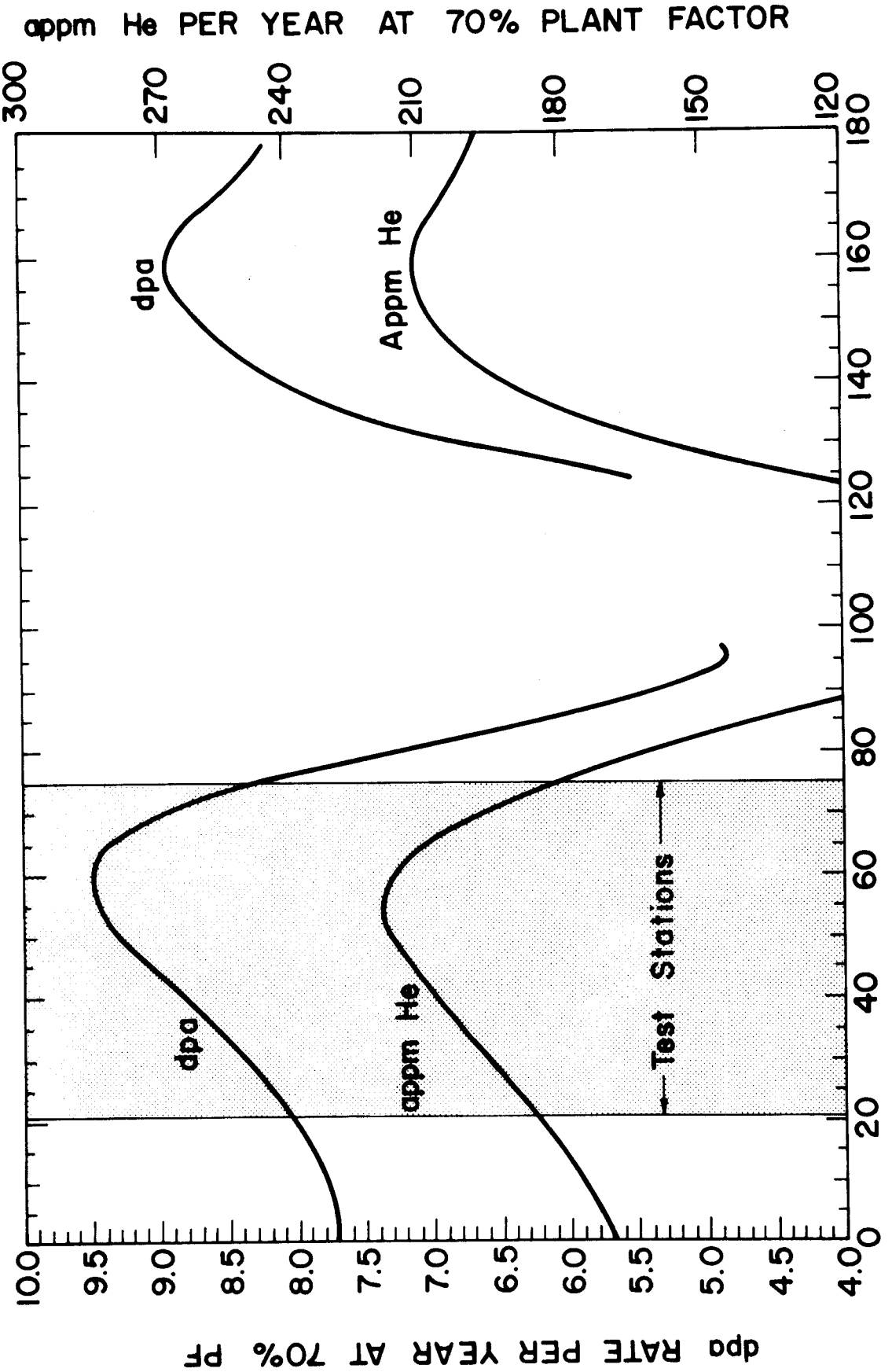
Poloidal Variation of Displacement and Gas Production Rates in TETR
dpa RATE PER YEAR AT 70% PF
appm He PER YEAR AT 70% PLANT FACTOR
θ - POLOIDAL ANGLE
dpa
appm He
Test Stations
dpa
Appm He
10.0
9.5
9.0
8.5
8.0
7.5
7.0
6.5
6.0
5.5
5.0
4.5
4.0
300
270
240
210
180
150
120
0
20
40
60
80
100
120
140
160
180

Fig. I-H-1b

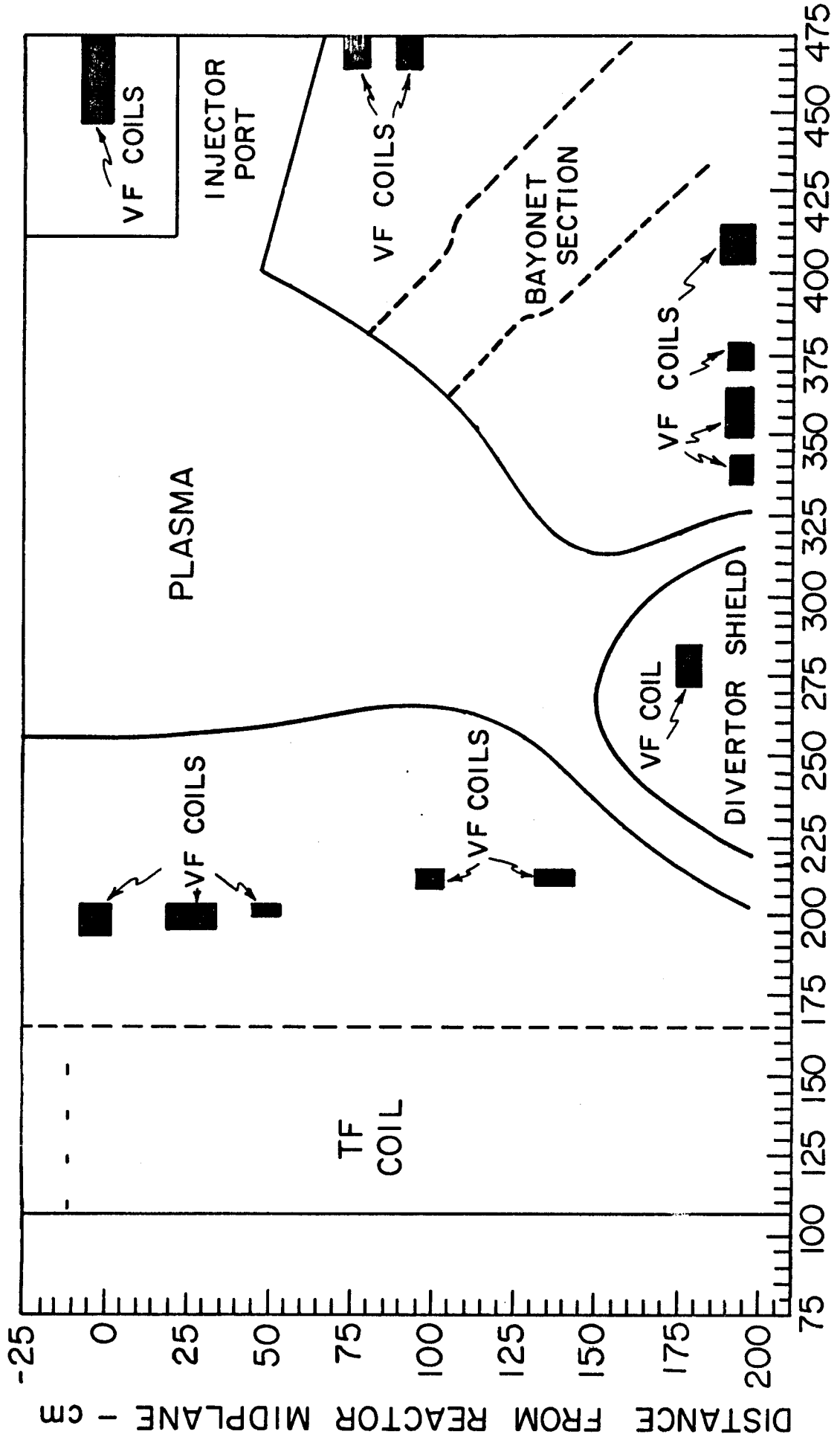

FIGURE I-H-2a SCHEMATIC OF TETR USED FOR NEUTRONICS CALCULATIONS

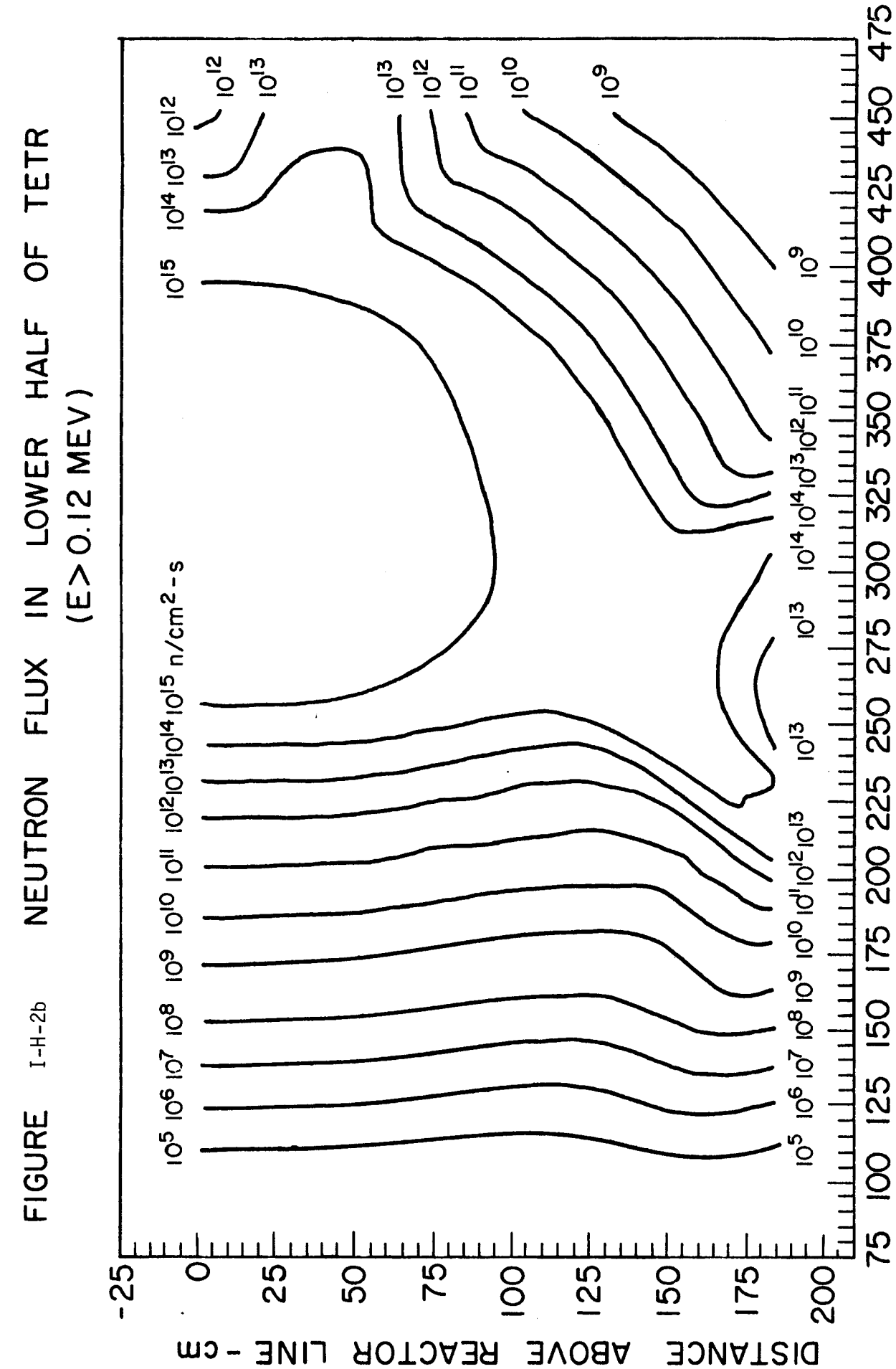
FIGURE I-H-2b NEUTRON FLUX IN LOWER HALF OF TETR
(E>0.12 MEV)
DISTANCE ABOVE REACTOR LINE - cm
DISTANCE FROM REACTOR CENTER - cm
-25
0
25
50
75
100
125
150
175
200
75
100
125
150
175
200
225
250
275
300
325
350
375
400
425
450
475
10^5 10^6 10^7 10^8 10^9 10^{10} 10^{11} 10^{12} 10^{13} 10^{14} 10^{15} n/cm^2-s
10^{15} 10^{14} 10^{13} 10^{12}
10^{12}
10^{13}
10^{13}
10^{12}
10^{11}
10^{10}
10^9
10^5 10^6 10^7 10^8 10^9 10^{10} 10^{11} 10^{12} 10^{13}
10^{13}
10^{13} 10^{14} 10^{14} 10^{13} 10^{12} 10^{11} 10^{10} 10^9

FIGURE I-H-2c HELIUM GAS PRODUCTION CONTOURS IN TETR

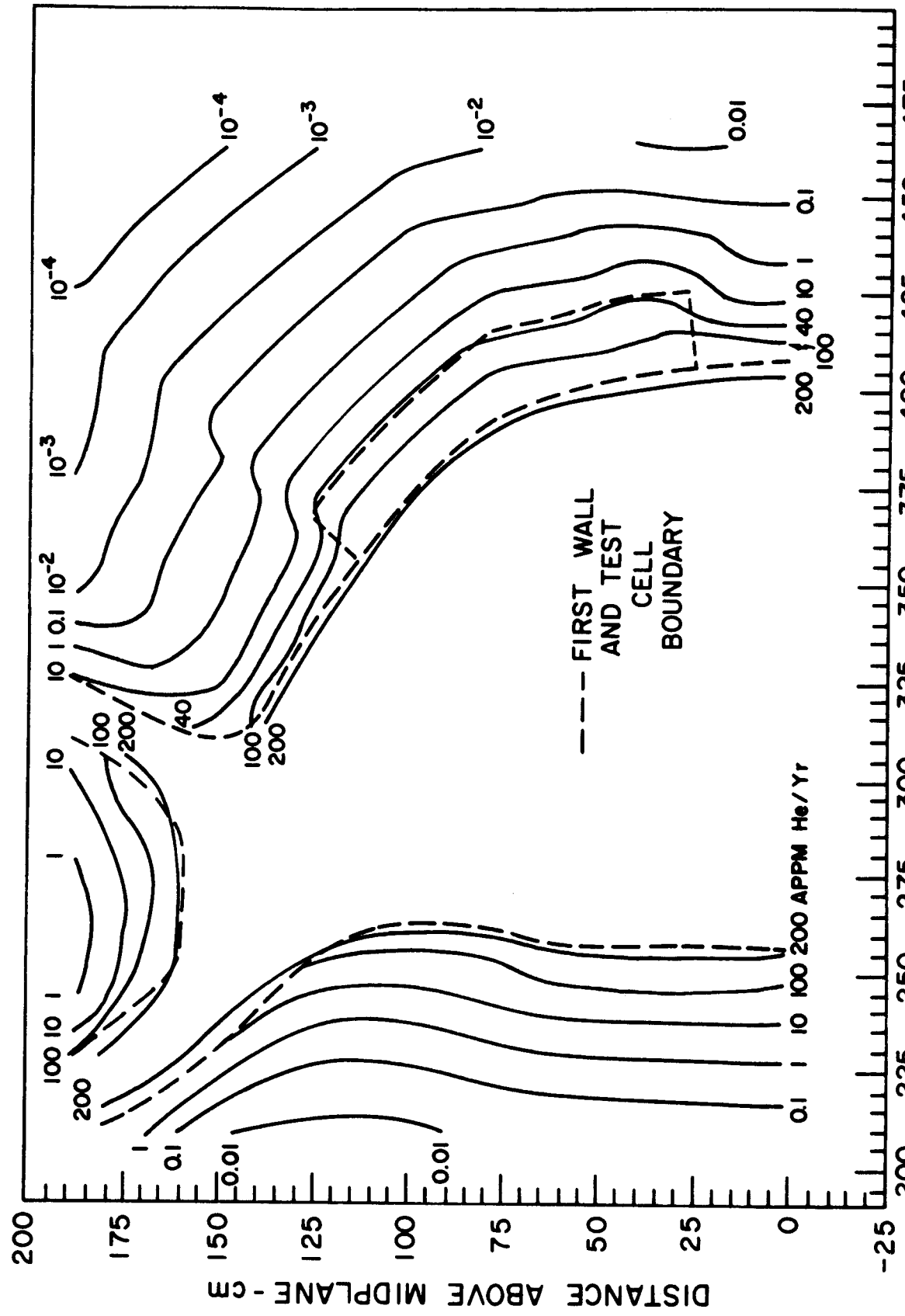

there appears to be no major problems in crack propagation. If the stress values were to increase substantially, fatigue life would then become important. Also we find that the nominal swelling will be in the 5% range after 10 MW-y/m^2 based on EBR-II irradiated material. If helium assisted nucleation alters that substantially, we could have local stress gradients that might also changes the above analysis.

The carbon curtain is expected to shrink by ~8% in ~1 year of irradiation, thereafter it will expand by ~34% after 10 MW-y/m^2. Because the curtain is of a weave construction, it is expected that it will be able to accommodate such a dimensional change without compromising the plasma operation.

A more severe problem is envisioned with the chemical and physical sputtering of the carbon curtain. Calculations reveal that the erosion due to physical sputtering might be as high as 0.1 mm/yr and that due to chemical sputtering 0.2 to 0.6 mm/yr. The effect of such large amounts of carbon on the cryopumps in the vacuum system or the steel first walls needs to be studied further.

The collection of the particles diverted from the plasma has always been a difficult problem and TETR is no exception. We feel we have a design which can take the high heat loads (see Chapter VIII) but the physical sputtering rate is quite severe. It is calculated that we may have to replace the Ta-10W tubes after less than 1 month of operation. Such a frequent repair is clearly not consistent with a high plant factor and we feel that this may be the most serious problem yet to be solved for Tokamaks with divertors.

The radiation damage to the TF coils was one of our prime concerns in the design of TETR because of the difficulty of doing repairs on such massive components in an intense radiation field. The one-dimensional calculations showed that we could keep the damage level down to acceptable values and by using a combination of periodic room temperature anneal (~ once a year) and thicker Cu stabilizer regions in the high damage regions we could meet all design requirements. However, the 2-D analyses revealed that the neutrons streaming down the diverter slots caused some "hot spots" which may cause the copper resistivity to increase by 6-fold within a year and the critical current density of the NbTi to be degraded by ~20% or more. We feel that once noted, these problems could be alleviated by a slight redesign of the blanket and therefore present no fundamental barriers.

The electrical and thermal insulation of the TF coils is also subjected to some rather severe radiation levels (10^7 to 10^8 rad/yr) and it is questionable whether the mylar insulation in the "hot spots" can in fact survive a 10 year exposure (~10^9 rads). It may be necessary to use inorganic thermal insulation in some parts of the TF coil for this reason. The epoxy fiberglass appears to be useable for 10 years from the standpoint of compressive strength and electrical properties.

Probably the most severe insulator problem occurs in the verticle field coils labeled D-9 in Figure I-D-1. The radiation exposure here is ~ 2 x 10^{11} rad/year and it is questionable whether even the epoxy fiberglass can stand such levels for 10 years. Therefore, it is recommended that perhaps some inorganic electrical insulators will be required for those components.

In summary we have isolated a few problems which will require further work before a completely acceptable design is attained, but the majority of the TETR components appear to be useable for the minimum 10 MW-y/m^2 exposure required. Such an optimistic view is based on only fragmentary information from currest test facilities and one must always allow for the fact that once we start using high energy neutron test facilities, we may have to reassess the present position. This is, in fact, one of the strongest arguments for getting a large volume high flux test facility like TETR in place at the earliest possible moment.

I-I. Materials Test Facilities

Since one of the main reasons for proposing TETR is to test materials, the impact of the design features on the available test area is crucially important. Although TETR is a rather "small" reactor from the designer's point of view, the basic space limitations on the coils prevent the building of a device which would be "small" by radiation materials testing standards. Compared with fast reactor facilities TETR provides a very large test volume. For example, compared with a large fast reactor test facility like FFTF, TETR provides an order of magnitude increase in usable volume for in-situ testing.

Furthermore, TETR has been designed to provide a true fusion environment so that the large test volume provides conditions typical of the DPR, removing the uncertainties of simulation entirely. The result is that with TETR, the U.S. fusion community will be able to complete a thorough alloy development program and provide hard design data for the DPR.

The test facilities in TETR are housed in 16 test stations, Table I-I-1, with a smaller number of bayonet test sites to permit a few samples to be tested in the plasma vacuum. Each test station has 1 m^2 of wall area and the test sites lie immediately behind the first wall.

Six test stations were chosen for primary alloy testing, a further two for the backup alloy and two more for refractory metals, titanium alloys and other first wall candidates. This gives a 10 m^2 testing area facing the plasma dedicated to mechanical property and structural testing of alloys. In addition, one test station will have facilities to place alloys in the vacuum facing the plasma so that surface effects can be studied in the primary and backup alloys.

Since it is likely that carbon linings and reflectors will be important in reactors one complete test station is given over to testing this material. A further test station will be used for testing for corrosion of stainless steels and super alloys in Li and the behavior of leaks. The remaining three test stations are reserved for testing T breeding, alternative coolants and various blanket designs and repair mechanisms.

An area of 10 cm x 10 cm was chosen for each test module (there are 100 test modules per test station) with up to five simultaneous tests proceeding in each one. The test modules are independent, each with its own coolant flow and instrumentation. Modules were designed so that the useful testing region extends 10 centimeters behind the first wall.

Table I-I-1

TETR Test Station Usage

Station #	Material Tested	In Situ Study	Post Irradiation
1-6	Primary Alloy	Mech. Props.	Swelling & Mech. Props.
7	Primary Alloy	Surface Effects	Swelling & Mech. Props.
8	Carbon	Plasma Int.	Swelling & Mech. Props.
9	Steel-Li	Leakage	Corrosion
10		Dynamic Testing of Defected Blanket Designs	
11		Non-Li Coolants	
12		T_2 Breeder & n-multipliers	
13,14	Backup Alloy		
15,16	Refractory & Reactive Metals & Other Advanced Materials	Mech. Props.	Corrosion

The properties of swelling and microstructural development, fatigue, creep and fracture toughness crack properties are recognized as the principal problems for first wall materials. Swelling and microstructure will be studied outside the reactor and most of the fracture toughness testing and crack propagation measurements will also be conducted ex reactor. However, fatigue and creep testing will be conducted entirely in situ. These tests will be fully instrumented and run at controlled temperatures.

The creep tests proposed are of two types viz. tensile creep (Figure I-I-1) and biaxial pressurized tubes. Testing is proposed of equal numbers of tensile creep and fatigue specimens and about half as many biaxial tubes and a similar proportion of crack propagation/fracture toughness samples. A few crack propagation measurements in situ are proposed but most tests of this property will be conducted outside the reactor.

Taking into account the number of tests per module (which differs for different tests) we have identified over 2900 tests proceeding simultaneously (Tables I-I-2, I-I-3).

There will be two environments for these tests, a) helium and b) flowing liquid lithium. In addition a small number of tests actually in the plasma vacuum are proposed using the small bayonet test sites and one test station for post-irradiation testing of surface damage.

In accord with current assessments by the materials community, the first choice of alloy is 316 stainless steel with a nickel base super alloy as a backup. However, titanium alloys may, in fact, be a better choice for backup alloys depending on current experimental results. Testing on these alloys will be conducted in a 3:1 ratio with a similar number of alternative alloy tests being conducted as for the backup alloy.

Between four and five alloy or heat variations have been selected for the primary alloy and in all alloy cases, tests are assumed to cover both weld and base metals. For the primary alloy five different temperatures of testing are proposed in the range 200-500^{0}C and up to five stress ranges depending on the type of test. A redundancy of two has been assumed throughout.

Even though the proposed program has many specific features, it has been designed to be flexible to incorporate the latest results of such testing facilities which would precede TETR. However, they do serve to illustrate the magnitude of the testing program that can be accommodated in TETR. Such a program could strongly reduce the risks and guesswork involved in building the DPR in the time frame of this century.

Figure I-I-1

BELLEVILLE SPRING WASHER CREEP RIG

MATERIAL: Ti ALLOY

SCALE:
APPROX 2 X FULL SIZE

OVERALL HEIGHT 2'-4"
O.D 1 1/8"

LOADING NOTE-
LOAD APPLIED BY SEPARATE TOOL TO SPRING WASHERS AND UPPER COMPRESSION RING SCREWED DOWN INTO PLACE. THE LOAD IS THEN RELEASED & TAKEN UP BY RING PUTTING SPECIMEN IN TENSION

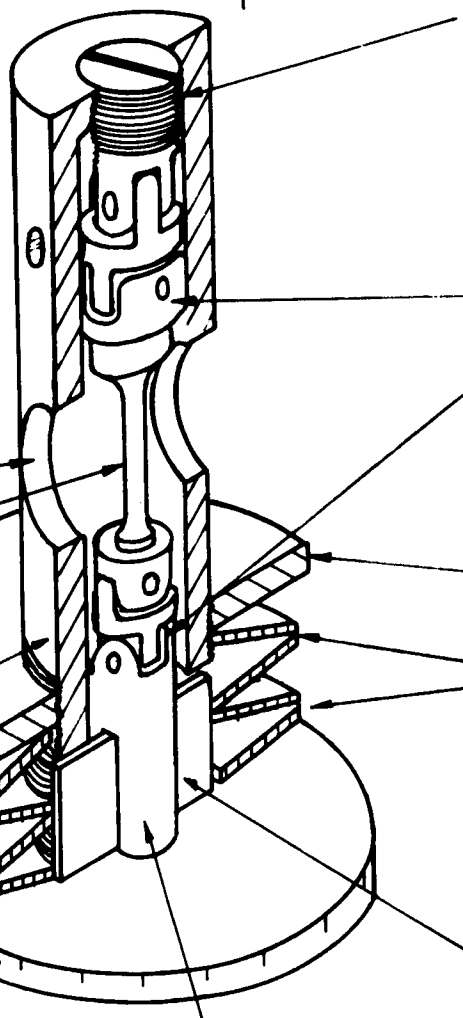

Table I-I-2

Use Of Mechanical Property Test Stations

Alloy	# of Test Stations	# In He	# In Li	# of Modules	# of Creep Modules	# of Creep Tests	# of Fatigue Modules	# of Fatigue Tests	# of Biaxial Modules	# of Biaxial Tests	# of Crack Propgn. Modules	# of Crack Propgn. Tests	# of Ex Reactor Test Modules	# Ex Reactor Test Specimens
Primary	6	4	2	600	144	720	240	720	62	291*	15	15+	139	1112
Backup	2	$1\frac{2}{3}$	$\frac{1}{3}$	200	48	240	80	240	21	98*	5	5+	91	728
Refractory Metals & Adv. Matls.	2	$1\frac{1}{3}$	$\frac{2}{3}$	200	48	240	80	240	21	98*	5	5+	91	728
Totals	10	11	5	1000	304	1200	400	1200	104	487	25	25	321	2568

*10% of these tests with instrumented pressure lines for leak testing.

+These tests instrumented for crack opening measurements in-situ.

Total of simultaneously irradiated mech. props specimens = 5480

Total in-situ simultaneous tests = 2912

Table I-I-3

Test Matrix At The Base Fluence of 1 MW-Yr/m^2

Material & Test		Environment	Base Metal + Weld	Alloy Variation and Heats	Stress Ranges	Temp. Ranges	Redundancy	Totals
Primary Alloy	creep	1.5(a)	2	4.8(c)	5	5	2	720
	fatigue	1.5	2	4.8	5	5	2	720
	biaxial	1.5	2	4.85	2	5	2	291
	cracking	1.5	2	1	2.5	2	1	15
	ex reactor	1.5	2	5	1	5	14(g)	1112
Backup Alloy	creep	1.2(d)	2	$3\frac{1}{8}$(f)	4	4	2	240
	fatigue	1.2	2	$3\frac{1}{8}$(f)	4	4	2	240
	biaxial	1.2	2	3.4	2	3	2	98
	cracking	1.2	2	3.4	2	3		5
	ex reactor	1.2	2	$3\frac{1}{8}$	1	5	19.4(g)	728
Refractories Metals & Advanced Materials	creep	1.5(a)	2	2.5	4	4	2	240
	fatigue	1.5	2	2.5	4	4	2	240
	biaxial	1.5	2	2.72	2	3	2	98
	cracking	1.5	2	2.72	2	3	2	5
	ex reactor	1.5	2	2.5	1	5	19.4(g)	728

a) Helium and liquid lithium, with twice as many in He.

b) 500°C, 450°C, 400°C, 300°C, 200°C.

c) For example 5 variants tested in ratio 5:5:5:5:4. (giving 4.80 average)

d) Tests' ratio 5 in He to 1 in Li.

e) Tests' ratio 2 in He to 1 in Li.

f) Tests' ratio for 4 alloy variants 3.5:3:3:3.

g) This redundancy allows for different tests; tensile, fracture toughness, etc.

Total number of simultaneous tests 2912

The total for each horizontal line is obtained by multiplying all the factors in the line.

I-J. The Lithium Test Modules

The lithium test modules examine the chemical interactions of breeding and structural materials in future CTR blanket designs. This study is divided into two sections; module I is concerned with the interaction of liquid lithium and structural materials of interest in CTR designs and module II is concerned with the evolution of tritium bred in solid lithium compounds and the effects of blanket design on tritium production.

The corrosive action of liquid lithium on materials of containment is a major drawback to its use. In module I, the nature of this corrosion is characterized by examining a pumped liquid lithium loop for an extended period of time (~ 1 year). This discussion concerns a 316 stainless steel containment for low temperature liquid lithium (< 500°C), as well as other materials of containment. Alternative materials suggested are TZM or Nb-1Zr (for their high lithium resistance and refractivity) and titanium-vanadium-aluminum alloys or elementally-tailored stainless steels (for their low levels of induced radioactivity).

Lithium will be sampled and analyzed for metallic impurities leached from the containment, nonmetallic impurities, and impurities activated either before or after dissolution in the lithium and tritium. Oxygen and hydrogen will be monitored on line. Samples of containment material inserted in the lithium at the start of the run will be available during periodic shutdowns of the reactor. After the experiment, an examination of activity deposited around the loop and a chemical radiometric and microscopic study of the containment surfaces exposed to lithium will be made.

The loop will consist of piping running alongside the swingaway shield into and out of the in-reactor test sections. The temperature of the in-reaction will be controlled by a combination of helium cooling and electrical heating and the out-of-reactor piping will be heated electrically. As the loop simulates a breeding blanket design, a heat exchanger is included, but all heat generated in the loop will be dumped. The loop is expected to contain about 2.5 m^3 of surface area in contact with lithium and about 12.5 l (1.5 kg) of lithium.

Module II will examine tritium breeding and evolution in solid lithium compounds and the effect of various design features and of extensive lithium burnup (about 5%/year) on tritium production. Stainless steel, refractories and low activity materials are suggested for containment. The experiments will study the effect of fabrication density, temperature and containment on the tritium species involved from both static and mobile

lithium-bearing ceramics in a design which will permit the burnup of 5% of the lithium per year. This discussion centers around static lithium oxide and lithium aluminate samples and mobile lithium oxide samples, but other breeding materials can be incorporated into the study. Additional studies will examine sintering and abrasion where appropriate.

Since the loop simulates a CTR breeding blanket, the temperature of the breeder is controlled by pressurized helium flowing around the tritium-bearing lines to a heat exchanger. No tritium is carried in the helium coolant except that which escapes from the tritium-bearing lines by permeation through the material of containment. The tritium separation and purification system will collect condensible tritium species over low temperature molecular sieves or dessicants and noncondensible tritium species on cryogenic plates or metal hydride bids depending on the power requirements of the system. The solid breeder loopis not yet parameterized as to tritium production and processing flow rates but the loop is expected to require about 4.8 kg of lithium aluminate and 1.1 kg of lithium oxide fabricated into 1 cm thick plates of about 85% of theoretical density (or the equivalent in close-packed microspheres).

I-K. The Tritium System

The separation and purification system for tritium is based on the cryogenic collection and continuous delivery of hydrogen isotopes to the distillation system. Since the reactor does not burn fuel continuously, the fuel flow rates are adjusted according to the fraction of the time the reactor is actually burning fuel. Figure I-K-1 is a summary of the flow rates of all the hydrogenic isotopes. The burn cycle duty factor is 83% and the plant duty factor, including both burn cycle down time and reactor down time, is 70%. At a 70% plant factor, the average tritium flow rate is 3.175×10^{-2} g-atom/sec and, at a burnup rate of 0.33%, 9.9 Kg of tritium is burned per year at a cost of 49.6 million dollars.

At an 83% duty factor, the tritium flow rate is 3.765×10^{-2} g-atom/sec. The plasma consists of 3.7:1 mixture of tritium and deuterium so the deuterium flow rate is 1.016×10^{-2} g-atom/sec. There is one fuel reprocessing system for each quadrant of the torus. Cryosorption pumps evacuate the plasma chamber after the burn. Solid debris are separated by filtration or by a cyclone separator and the remining non-hydrogenic impurities are removed by the passage of the fuel stream through a Pd-Ag diffuser.

A three-column cryogenic distillation system is used to separate and purify tritium and deuterium (95% purity). Storage is provided by hydride beds or low pressure cylinders. The three column system requires about 100 watts of refrigeration power per quadrant. The total fuel separation system is expected to cost about $1,000,000 with a $280,000 operating cost for refrigeration power.

The tritium containment system consists of a three-level barrier system. Primary containment consists of those high-integrity components and pipes which enclose tritium-bearing materials. Secondary containment is provided by gloveboxes containing a circulating helium atmosphere surrounding large pieces of equipment subject to frequent attention. Primary system pipes are enclosed within large diameter pipes whose atmosphere is monitored for tritium. The glovebox atmosphere is continuously detritiated under normal conditions but is diverted to the high capacity Tritium Efficient Removal System (TERS) under off-normal conditions. Tertiary containment is provided by the reactor hall and associated buildings and under off-normal conditions, this atmosphere is diverted to the Emergency Tritium Containment System (ETCS).

Tritium permeation to the modular coolant is insignificant over a five year period (.25 Ci) and small to the 10^5 ℓ reactor coolant water (27.4 Ci). Disposal of the reactor water after five years is possible either by dilution with fresh water and dumping or by packaging for burial at a cost of $400,000. The large tritium leakage to the divertor coolant water (~8 g/day) necessitates the use of a purification system. When the tritium concentration in the 16,000 ℓ inventory of water reaches that of "heavy water" in natural water (~40 ppm of tritiated water, or 60 Ci/ℓ), a side stream is purified by isotopic exchange with pure water. The divertor water is processed at 1.0232 ℓ/min and 8 g.day of tritium is removed by the system. Electrolysis is used to generate a mixture of hydrogen isotopes from the highly concentrated (30,000 Ci/ℓ) product water from the divertor water purification system. The estimated capital costs of such a system is $1,000,000 with a yearly operating expense of $208,000.

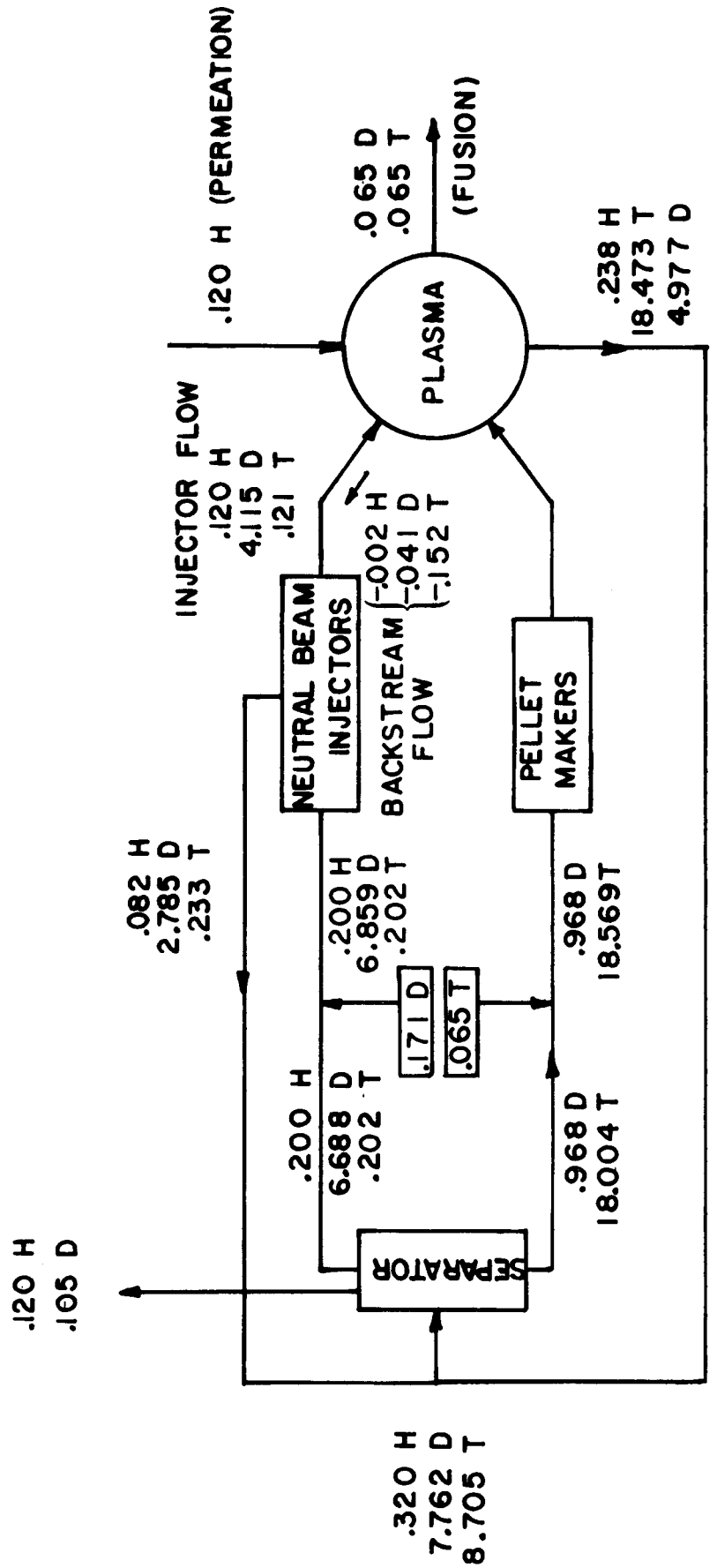
TETR FUEL CYCLE
.120 H (PERMEATION)
.065 D
.065 T
(FUSION)
PLASMA
.238 H
18.473 T
4.977 D
INJECTOR FLOW
.120 H
4.115 D
.121 T
NEUTRAL BEAM INJECTORS
BACKSTREAM FLOW
-.002 H
-.041 D
-.152 T
PELLET MAKERS
.082 H
2.785 D
.233 T
.200 H
6.859 D
.202 T
.171 D
.065 T
.968 D
18.569T
.200 H
6.688 D
.202 T
.968 D
18.004 T
SEPARATOR
.120 H
.105 D
.320 H
7.762 D
18.705 T
ALL FLOWS ARE IN m-mol/sec
PURITY OF EACH FUEL STREAM ≥ 95 %

Figure I-K-1

Tables I-K-1 through I-K-5 summarize the important parameters of the tritium system including cost and fuel inventories. The largest single item is the cost of tritium burnup (Table I-K-5) and the second most expensive item is the tritium containment system including waste water disposal (~$19,000,000).

Table I-K-1

TETR Fueling Summary

Fueling Data	
Burn Time	60 sec
Down Time	12.5 sec
Burn Efficiency	0.33%
Thermonuclear Power Output	396 $MW_{(th)}$
Neutral Beam Injector Energy	150 KeV
Beam Power	150 MW
Beam Efficiency	60%
Purity of Tritium Pellets	95%
Purity of Deuterium Injected	95%
Q	1.78
n	$7.7 \times 10^{13} cm^{-3}$
τ_e	92 msec
Plasma Volume	41.6 m^3
Burn Cycle Duty Factor	83%
Plant Duty Factor (Including Reactor Down Time)	70%
Fuel Flow Rates During Burn	
Tritium Flow Rate	4.536×10^{-2} g-atom/sec
Deuterium Flow Rate	1.224×10^{-2} g-atom/sec
Fuel Flow Rate Averaged Over Burn Cycle	
Tritium	3.765×10^{-2} g-atom/sec
Deuterium	1.016×10^{-2} g-atom/sec
Fuel Flow Rate Averaged Over Plant Operation	
Tritium	3.175×10^{-2} g-atom/sec
Deuterium	0.857×10^{-2} g-atom/sec
Fuel Consumption (0.33% burnup, 70% plant factor)	
Tritium	1.047×10^{-4} g-atom/sec
Deuterium	1.047×10^{-4} g-atom/sec
Yearly Fuel Consumption (70% plant factor)	
Tritium	9.90 Kg
Deuterium	6.60 Kg

Table I-K-2

Tritium Inventory* in TETR

Cryosorption Pumps	1.52 Kg
Injector Pumps	.01 Kg
Storage (1 day's supply of tritium)	9.76 Kg
Distillation Columns	.19 Kg
Divertor Coolant	.10 Kg
TOTAL	11.58 Kg

*83% Duty Factor

Table I-K-3

Tritium Losses in TETR

Permeation to Water Coolant	.015 Ci/day
Loss Over 5 Year Lifetime	27.4 Ci
Permeation to Modular Coolant (5 Year)	.25 Ci
Permeation to Divertor Coolant @ 83% duty factor	8.23 g/day

Table I-K-4

Tritium System Costs in TETR

	Capital (10^6\$)	Operating (10^6\$)
Isotope Separation System		
Debris Separation	0.02	?
Impurity Separation (Pd Diffusers & Methane Cracking)	0.14	?
Distillation Columns	0.20	?
Tritium Control (Gloveboxes, Emergency Storage, Control Systems)	0.64	?
Refrigeration Power		0.28
Tritium Containment System		
Gloveboxes	4.72	
Secondary Containment		
Atmosphere Purification		
(normal conditions)	2.50	?
(off-normal conditions)	6.00	?
Tertiary Containment (atmosphere purification under off-normal conditions)	4.00	?
Divertor Coolant Purification	1.05	.21
Waste Water Disposal	.40	
	18.67	

Table I-K-5

Fueling Costs For TETR

	Cost (10^6\$)
Tritium ($5000/g)	
Consumed	49.6
Decay	3.0
Deuterium ($40/Kg)	
Consumed	~0

I-L. Radioactivity and Safety

The design of TETR went through several modifications and changes in concept. One of the main considerations was whether a carbon ISSEC was to be used. Although it was finally decided that it was not necessary, this decision came rather late in the design process and consequently most of the radioactivity calculations were performed using the carbon ISSEC. Nevertheless, many of the results of the calculations qualitatively hold for the final design. In particular, it was noted that the use of tungsten in the design has rather interesting effects from a radioactivity standpoint in addition to the other shielding and cost effects. The principle effect noted was that while the use of tungsten gave a radioactivity (or afterheat) value higher than that of stainless steel, the isotopes produced in tungsten have shorter lifetimes than those produced in stainless steel and are in fact dominated by the longest lived isotope produced i.e. W^{185} ($t_{1/2}$ = 75 days). The result is that after about a year of decay, the radioactivity is dominated by that of the stainless steel structure even though it is only a few percent by volume of the material present. The analysis also shows that in stainless steel, the effects of the alloying elements, especially molybdenum and nickel, are most important in determining the long lived activity of the blanket. If choices may be made to eliminate some of these elements, the activity, afterheat or BHP may be greatly reduced.

The final design of the outer blanket and shield at midplane of the reactor is shown in Fig. I-L-1. Indicated are the primary case and two alternative cases, namely SS in which all of the tungsten is replaced by stainless steel and WAL in which the stainless steel in the last two regions is replaced by aluminum. The activity following shutdown after two years of operation is shown in Fig. I-L-2 for the outer blanket. The base case (WSS) shows behavior typical of previous systems using stainless steel. The activity at shutdown is dominated by the tungsten in Zone 4 (specifically W^{185}) but after about a year, only the stainless steel is contributing. The subsequent decay is slow with the very long lived activity due to Ni^{59}. The afterheat and BHP of the system is similar to previous studies with the primary differences being a somewhat higher afterheat at shutdown than in previous studies primarily because of the large amount of radioactive material in the non-breeding blanket. The effects of substituting stainless steel for tungsten are noted in the SS case in which all tungsten is replaced by stainless. The principal effects are a reduction in activity at shutdown by about a factor of two and a somewhat smaller decrease in afterheat and BHP. The long lived activity is however increased by about an order of magnitude.

In order to assess the maintenance problem, the dose was calculated outside the blanket and shield. The results are presented in Table I-L-1. For the base case WSS, it is seen that the dose rates are high following shutdown and it would require about a day before any work could be done. To reduce the dose further would require waiting for over a month. When stainless steel is substituted for tungsten, the dose rates are much higher due to the reduced effectiveness of stainless as a shield material. The WAL case in which the stainless in the two outer regions of the shield is replaced by aluminum was considered because previous work indicated that in a well designed shield most of the dose comes

Figure I-L-1 - Schematic Diagram of TETR Outer Blanket

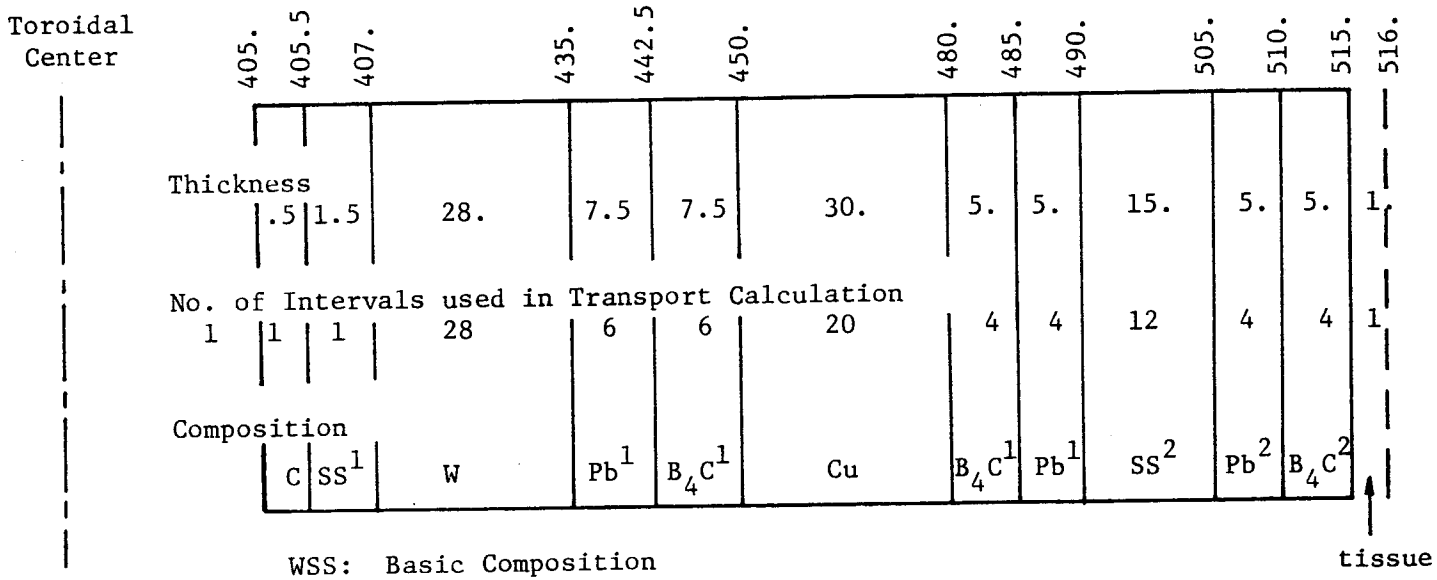

WSS: Basic Composition

SS^1	40 % 316 SS + 50 % H_2O
SS^2	96 % 316 SS + 4 % H_2O
W	4 % 316 SS + 4 % H_2O + 92 % W*
Pb^1, Pb^2	4 % 316 SS + 4 % H_2O + 92 % Pb
B_4C^1, B_4C^2	4 % 316 SS + 4 % H_2O + 92 % B_4C*
Cu	75 % Cu + 20 % H_2O + 5 % Insulator

*Density Factor

0.95 for W and B_4C

SS: Alternative A - Same as basic case except

W	96 % 316 SS + 4 % H_2O

WAL: Alternative B - Same as basic case except

Pb^2	4 % Al + 4 % H_2O + 92 % Pb
B_4C^2	4 % Al + 4 % H_2O + 92 % B_4C*

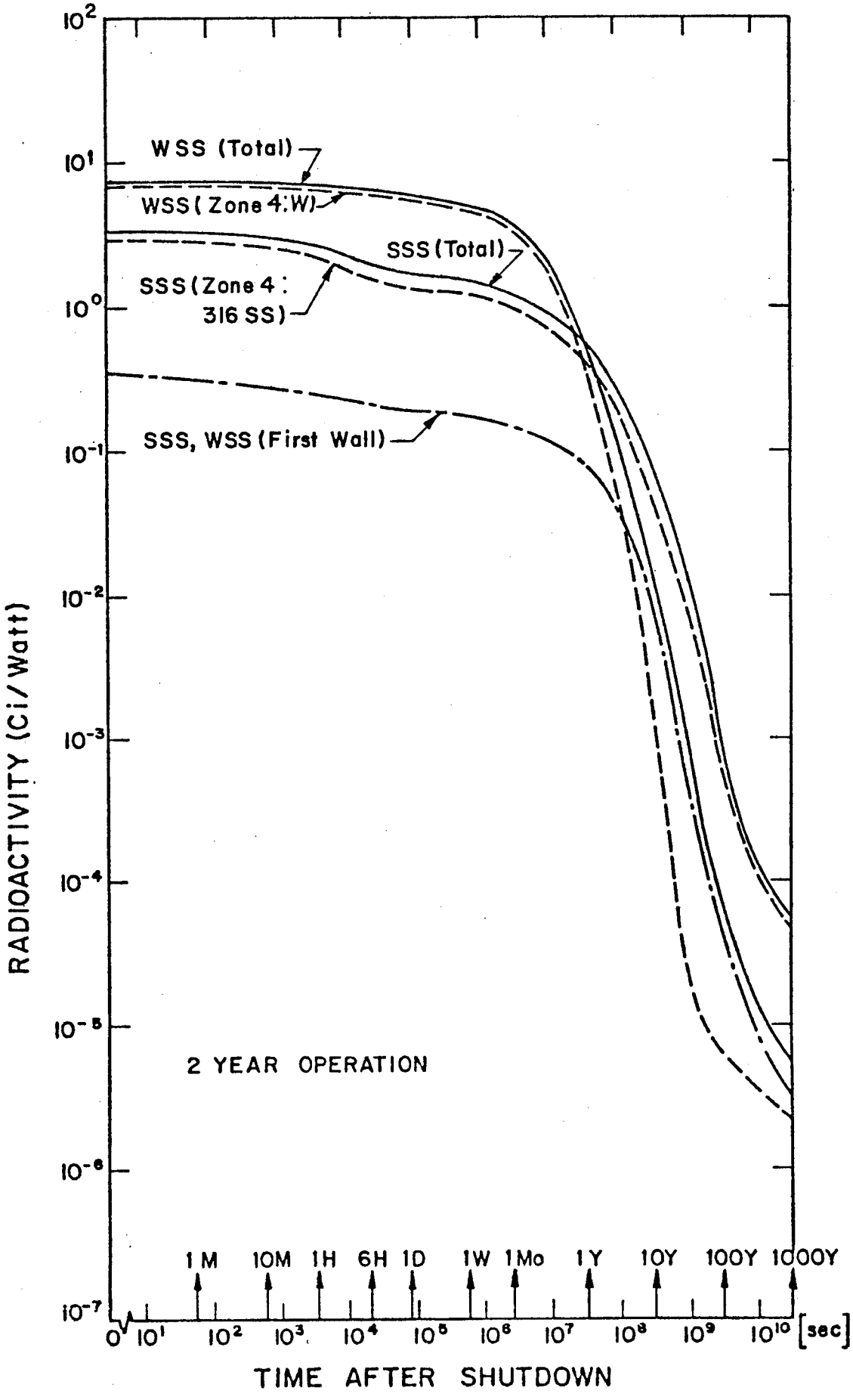

Figure I-L-2 - Decay of TETR Outer Blanket Activity

from the outer part of the shield. It is seen here that the initial doses are higher than the base case and remain so until the Na^{24} activity has decayed. After that time, the doses are quite low allowing maintenance work to be performed. These doses are calculated behind the main shielding sections and could be modified significantly by the presence of the penetration for the neutral beam sources.

Table I-L-1

Calculated Dose Rate Outside the Shield

Neutron Wall Loading	WSS	SS	WAL
Time After Shutdown		1.10 MW/m^2	
		Dose Rate, mrem/hr	
0	683.2	1,875.1	826.9
1 min.	666.7	1,829.3	758.0
10 min.	598.3	1,625.9	551.8
1 hr.	474.2	1,311.6	438.6
6 hr.	143.5	390.6	181.9
1 day	27.9	69.3	46.9
1 week	24.0	59.8	3.5
1 month	21.0	51.9	3.1
1 yr.	7.7	18.7	1.5
10 yr.	1.3	3.1	1.5
100 yr.	7.8×10^{-5}	2.1×10^{-4}	3.3×10^{-1}
1000 yr.	2.9×10^{-5}	8.1×10^{-5}	3.7×10^{-5}

I-M. Plant Layout

The physical layout of the TETR facility is shown in Figures I-M-1 and I-M-2. The main unique features of this plan are:

1.) Underground siting to reduce shielding requirements for the reactor building.

2.) Much reduced size compared to normal reactor plants due to the lack of turbine building and associated electrical generating equipment.

3.) Adjacent hot cell and auxiliary buildings for experimental equipment and handling of test specimens.

4.) An external control and maintenance building for both reactor and experimental test assemblies.

5.) Three external cooling towers.

The layout of the Reactor and Auxiliaries building is shown in Figure I-M-3 and in addition to the dome shaped 32 m diameter reactor building, there are hot cells for both reactor equipment and experiments, heat exchanger rooms, tritium handling facilities, vacuum equipment rooms as well as pump rooms, helium storage facilities and room for auxiliary maintenance. Finally, room has been set aside for the installation of a small (~80 MWe) turbine generator should one become desirable during the course of operation.

Further detailed considerations await Architect participation in the program.

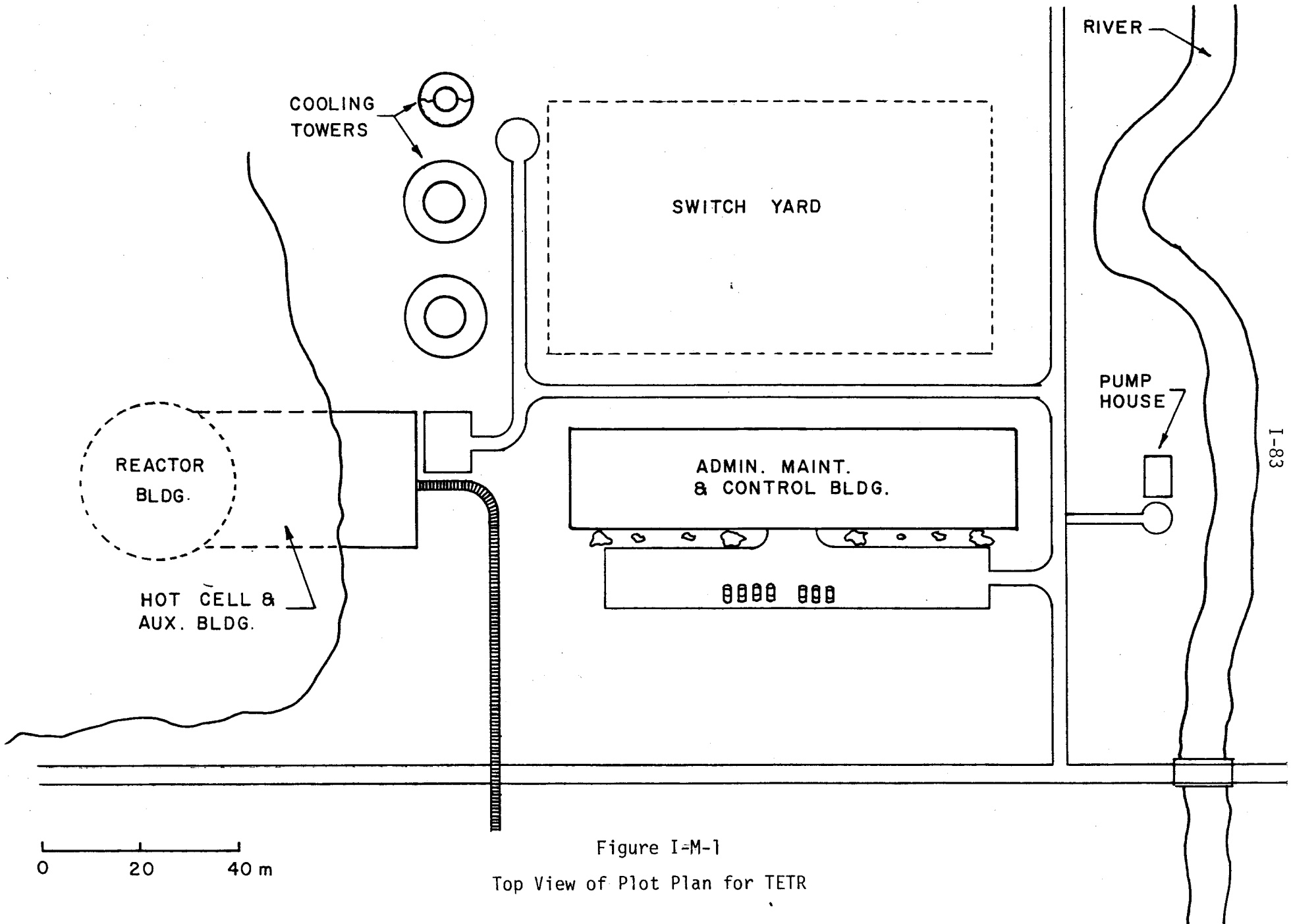

Figure I-M-1

Top View of Plot Plan for TETR

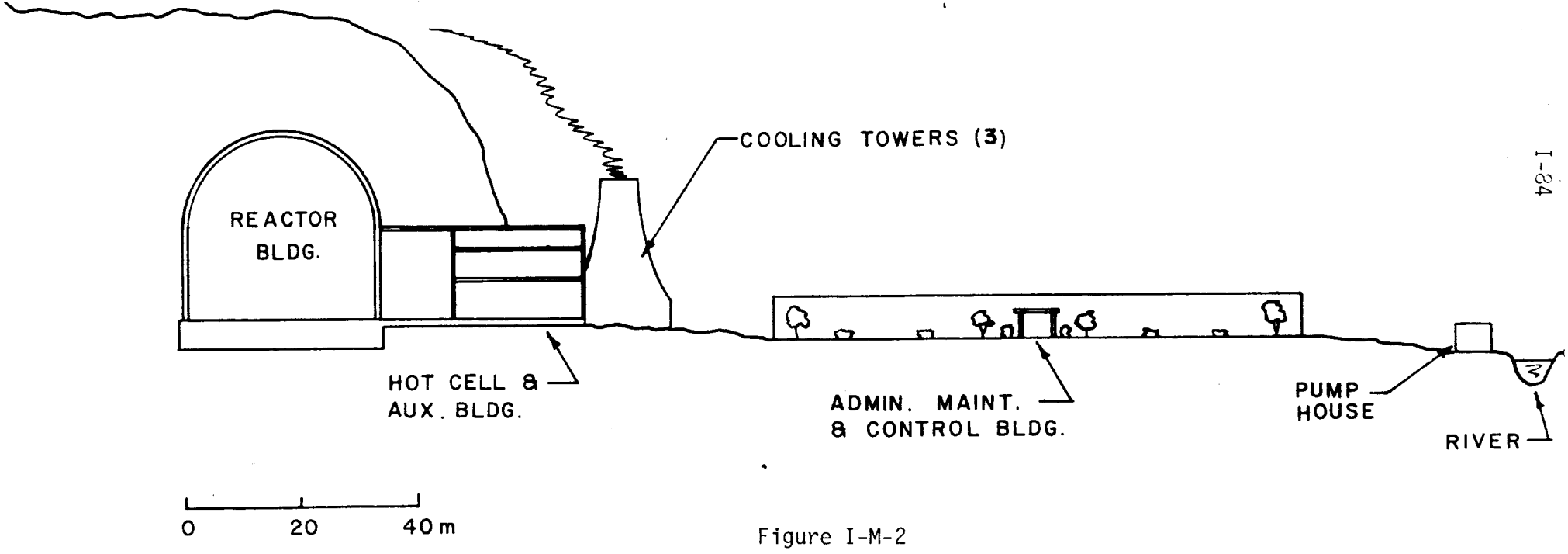

Figure I-M-2

Side View of Plot Plan for TETR

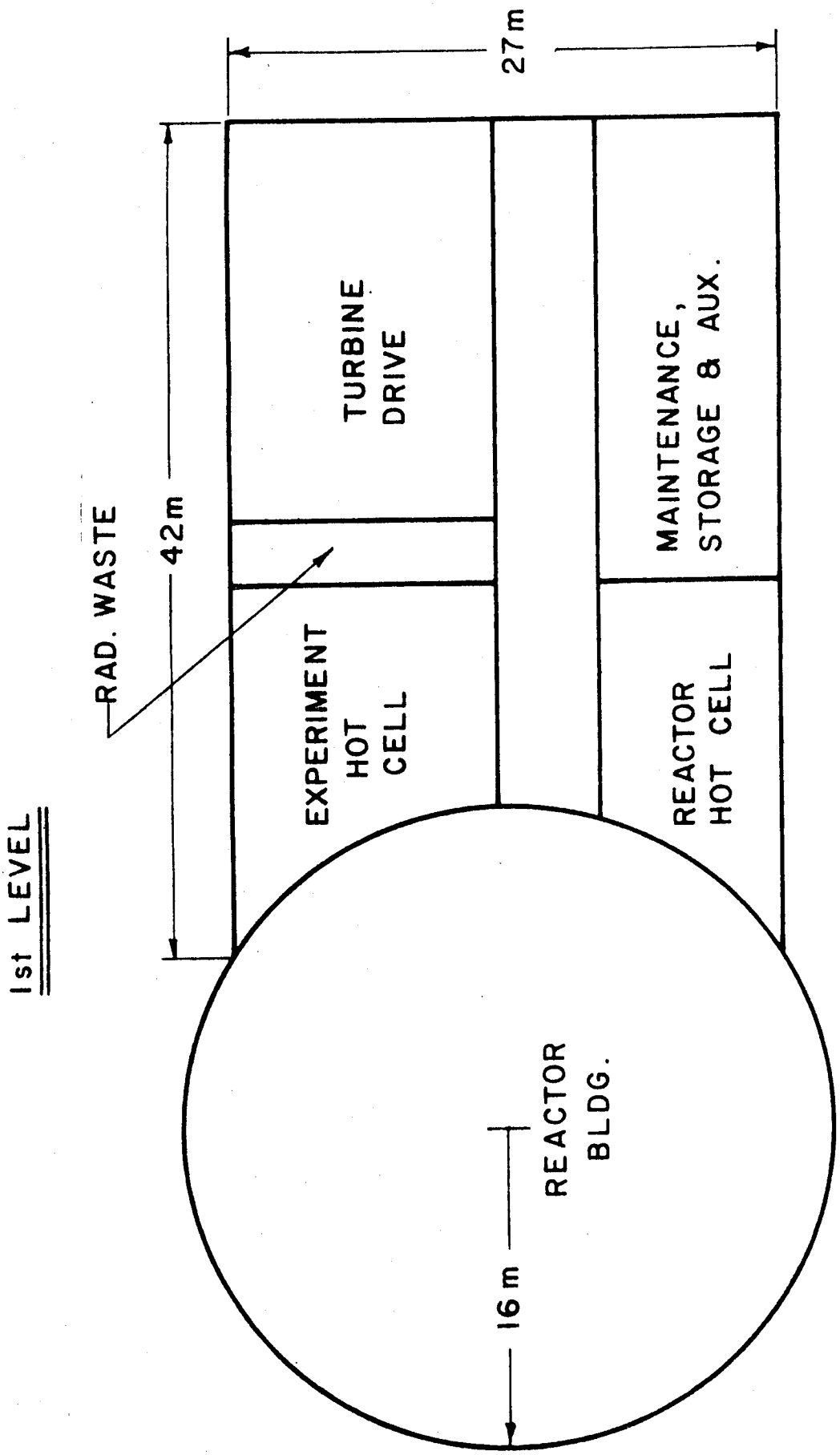

Figure I-M-3a - Cross Section of Reactor and Auxiliary Building for TETR

2nd LEVEL (7 m above 1st level)

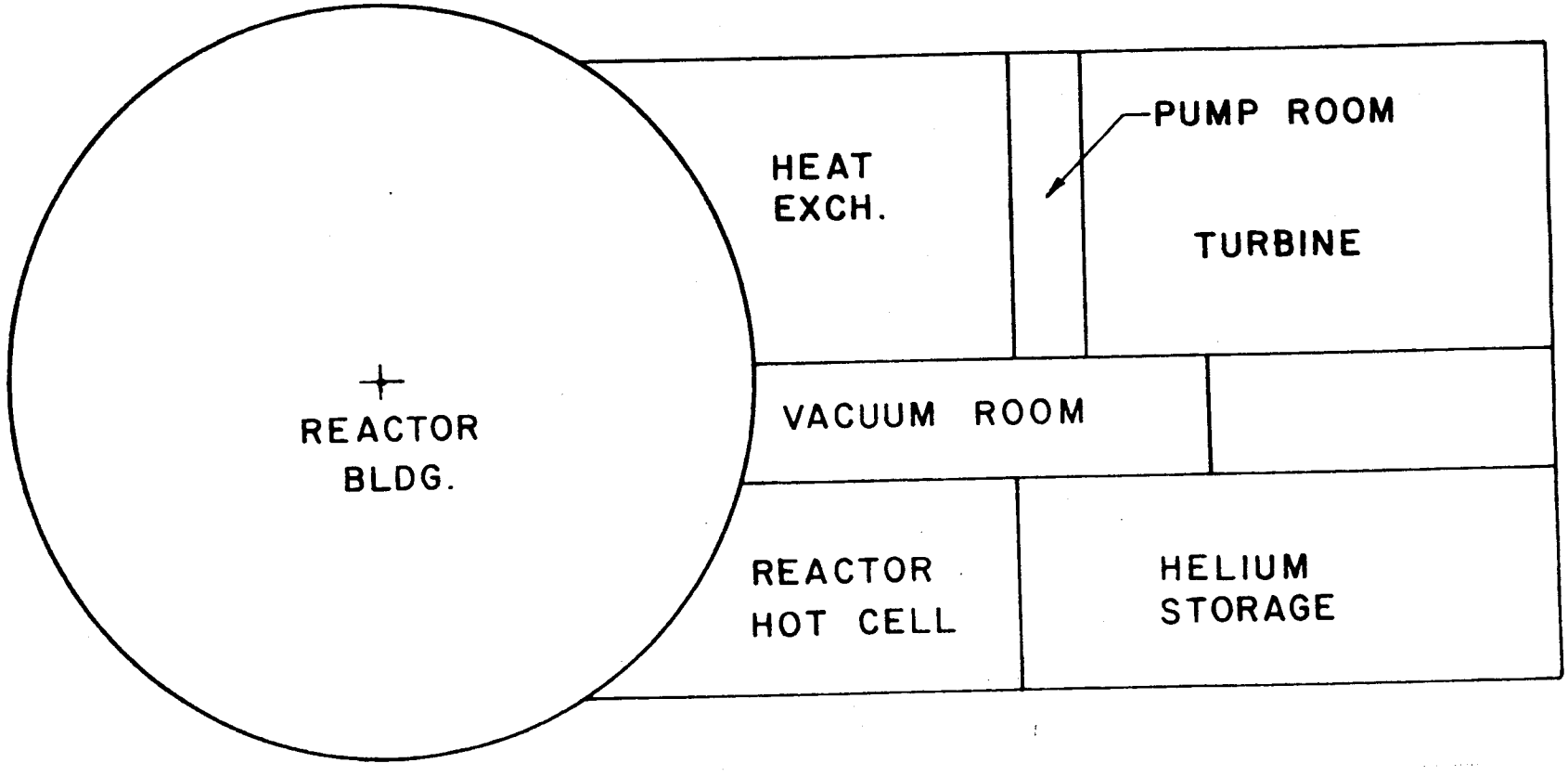

Figure I-M-3b

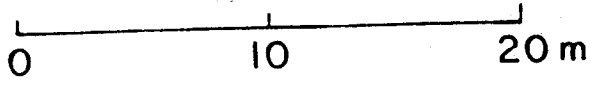

3rd LEVEL (5 m above 2nd level)

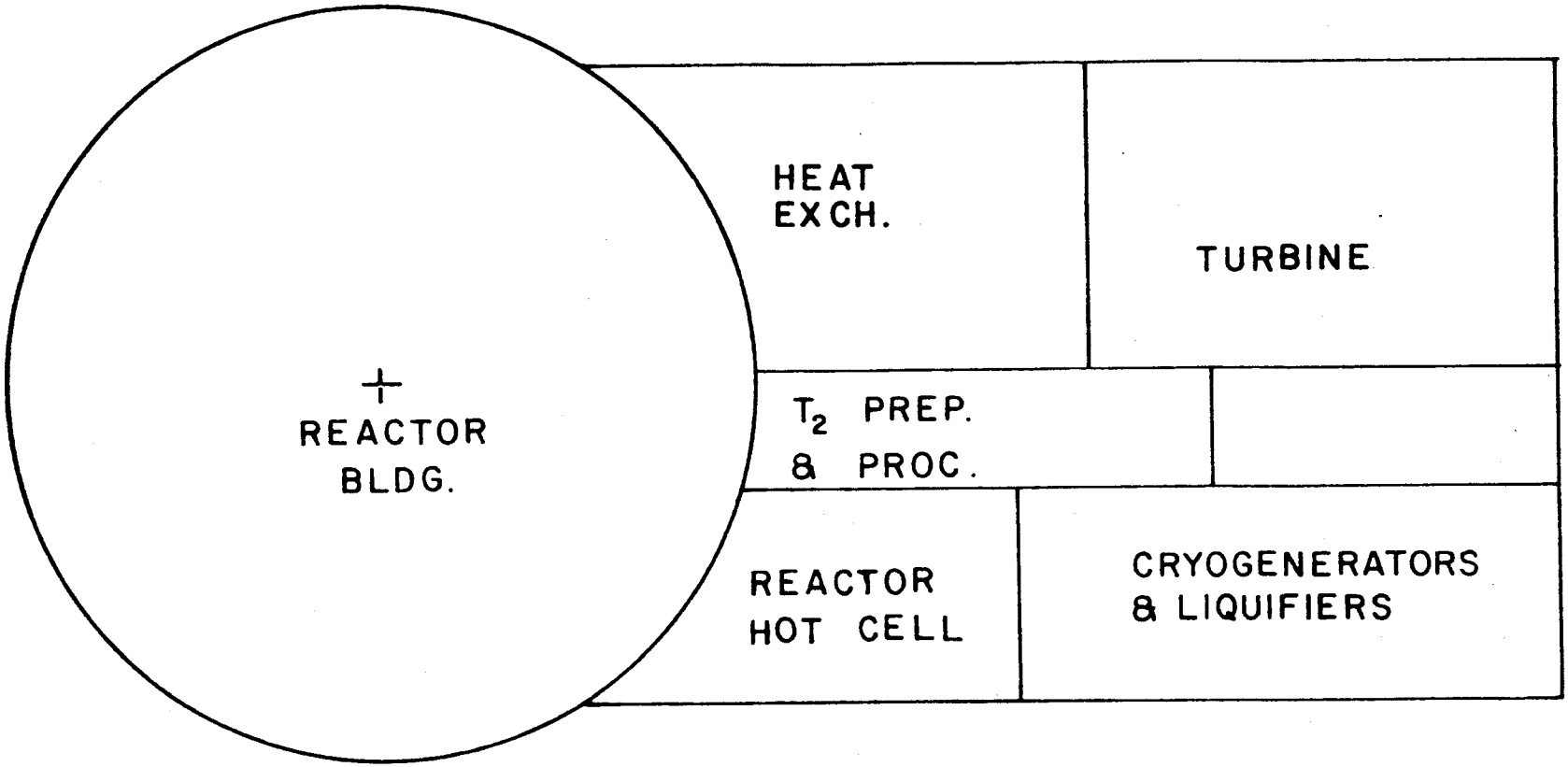

Figure I-M-3c

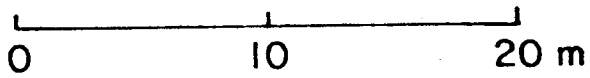

I-N. Resources and Cost

The fact that TETR is a "one of a kind" reactor means that materials resources do not have quite the same importance as in a generic design for a power reactor. Nevertheless, the cost of the reactor is closely aligned with the amount, form and type of materials used to make up the nuclear island as well as in auxiliary areas. Therefore, it is important to establish a clear inventory of those materials so that analyses can determine the effect of design modifications.

Table I-N-1 contains the materials inventory for the TETR Nuclear Island (blanket, shield, test modules, magnets, neutral beam injectors, vacuum pumps, etc.). There are 6 features of this table which are worth noting;

1. The largest single demand for any element is for Pb (4560 tonnes).
2. The amount of W required is 3310 tonnes.
3. The shield accounts for more than 90% of the mass of the nuclear island.
4. Over 1300 tonnes of stainless steel are required.
5. The requirement for boron carbide is over 200 tonnes.
6. The total nuclear island material requirement is over 10,000 tonnes.

None of the requirements will place a great strain on the US mining or mill capacity. Even the W requirement is only 1% of the US production in 1970. Therefore, we conclude that resources will not be a problem for one TETR.

We have chosen to follow the approach of J. R. Young "Economic Information Requirements - Fusion Reactor Design Studies" (to be published) in determining the capital costs for TETR. It can be seen from Table I-N-2 that the major direct cost item in TETR is the reactor plant equipment. It constitutes 86% of all the direct costs. Investigating this category in more detail, we find the following contributing factors to Account 22. (For more detail see Table XV-C-3 and Appendix A in Chapter XV).

Account	Item	Million of Dollars	%
221	Reactor Equipment	260.303	69
222	Main Heat Transfer & Transport System	9.677	3
223	Auxiliary Cooling Systems	67.325	18
224	Radioactive Waste Treatment and Disposal	0.120	--
225	Fuel Handling and Storage Systems	3.156	1
226	Other Reactor Plant Equipment	32.255	9
227	Instrumentation and Control	3.744	1
		377.856	

Table I-N-1

Element	Blanket				Shield	Magnets			Central Support Structure	N. Beam Injectors	Vacuum System	Total (Tonnes)	Tonnes MW_t
	Inner	Central	Outer	Test Stations	Supports	TF & Dewars	OH & Dewars	VF					
Al	0.05	0.025	0.07	0.03		144.31	26.34		1.7	0.28	0.65	173.455	0.337
B					185							185	0.359
C	0.46	0.22	0.60	0.27	52							53.55	0.104
Cr	0.97	0.46	1.26	0.56	158.4	45.72	7.89	2.66	30.6	5	11.7	265.22	0.515
Nb						25						25	0.049
Cu	0.05	0.025	0.07	0.03		450	0.44	159.52	1.7	0.28	0.65	612.77	1.19
He						1.5	0.4				2.75	4.65	0.009
Fe	3.35	1.59	4.34	1.93	522.7	156.2	27.19	8.78	105.4	17.2	40.3	888.98	1.726
Pb					4560							4560	8.854
Mn	0.11	0.05	0.14	0.06	15.8	5	0.88	0.27	3.4	0.55	1.3	27.56	0.054
Mo	0.11	0.05	0.14	0.06		5	0.88		3.4	0.55	1.3	11.49	0.022
Ni	0.76	0.36	0.98	0.44	95	35.28	6.13	1.50	23.8	3.88	9.1	177.33	0.344
Ti						12						12	0.023
W					3310							3310	6.427
Mg						0.56						0.56	0.001
Total	5.86	2.78	7.6	3.38	8898.9	880.57	70.15	172.83	170	27.74	67.75	10,307	20.014
Components													
316 SS	5.4	2.56	7.0	3.11		252	43.82		170	27.76	65	576.65	
304 SS					792			13.3				805.3	
B_4C					237							237	
Graphite	0.46	0.22	0.6	0.27								1.55	
NbTi						37.5						37.5	
Al (6061)T-6						121.2						121.2	
High Purity Al						25.4	25.9					51.3	
OFHC Copper						447		159.52				606.52	
Pb (Shield)					4560							4560	
W (Shield)					3310							3310	
												10,307	

Table I-N-2

Summary of Costs for TETR

(June 1, 1977 dollars)

Account Number	Title	$
	Direct Costs	
20	Land	1,000,000
26	Spec. Mat.	1,020,000
21	Structure and Site	16,847,000
22	Reactor Plant Equip.	377,856,000
23	Heat Disposal Equip.	9,510,000
24	Electric Plant Equip.	30,820,000
25	Miscellaneous Equip.	3,120,000
	Sub Total Direct	440,173,000
Indirect Costs	(Based on Direct Minus W)	
91	Construction Facilities (15%)	48,648,000
92	Engr. & Const. Maint. (20%)	64,865,000
93	Other Cost (8%)	25,946,000
	Sub Total Indirect	139,459,000
	Total Reactor	579,632,000
	Contingency (15% of Direct)	48,648,000
	Total Cost Incl. Cont.	628,280,000

Aside from the reactor plant equipment, we see that a major cost item is the cryogenic cooling systems for OH coils ($58,125,000). This cost arises from the I^2R loss in the cryogenic Al coils and could be reduced by going to superconducting coils. The increased cost of the S/C coils would be minimal (< a few million dollars) so that our conservative assumptions that pulsed superconducting coils would not be available for TETR contributes approximately 13% to the overall cost of the reactor.

Another major cost item of the Reactor Plant Equipment is the ventilation and cleanup system used to protect against large T_2 leaks. This cleanup system amounts to $17,200,000 or 4% of the total plant costs.

Within the reactor equipment we find the following breakdown of costs.

Account	Item	Million of Dollars	%
221.1	Blanket	0.552	0.2
221.2	Shield	133.547	51
221.3	Magnets	30.565	12
221.4	Neutral Beam Injection	60.00	23
221.5	Test Modules	17.639	7
221.6	Control Devices	18.000	7
		260.303	

The surprising thing about the above table is that the shield is the dominant cost item (51%) and it is 4 times the cost of the magnets. Even the 150 MW of neutral beams (at 40¢/watt) is twice as expensive as the magents. Hence, it is apparent that the magnets do not pace the total cost of the reactor as is normally assumed by most people.

Turning back to the costs of the shield, we see that they are divided as follows.

Shield Component	Millions of Dollars	%
304 SS	11.880	9
Tungsten	115.850	87
B_4C	3.081	2
Pb	2.736	2
	133.547	

The data above reveals that over 87% of the shield costs stems from our use of W as a shield material. This choice is necessary to protect the magnets from damage. The tungsten could be replaced with lead and more than 100 million dollars could be saved on the direct costs or approximately 16% of the total costs of the reactor. However, replacing the W with Pb in the inner shield and along the divertor slots would not be acceptable from a radiation damage standpoint to the insulators. This obviously points

out a fruitful area of research, namely, the development of a more radiation damage resistant insulator material. The other option is to build a much bigger device to allow more room in the inner shield for neutron attenuation. This would tend to increase the cost of the rest of the reactor and the exact optimum has not yet been determined.

It is instructive to rank the major cost items in TETR so as to understand what is contributing to the total costs. This is done in Table I-N-3. This table again shows that the most costly item in TETR is the shield (30%) followed by the neutral beams (14%), cyrogenic cooling for OH coils (13%), DC convertors (7%), magnets (7%), control (4%), test modules (4%), air purification (4%) and vacuum equipment (3%). This table again points out the great cost that is incurred by having to use W to protect the electrical insulator in the TF coils.

The total indirect costs came to $139,459,000 which bring the reactor costs to $579,632,000. Adding a 15% contingency allowance brings the total reactor cost to roughly 630 million dollars, slightly more than desired but not out of reason. A perspective on this value can be obtained by noting that up through the completion date of the FFTF the amount spent will be $540 x 10^6. It should be noted that the true cost of FFTF in 1977 dollars would be much higher than 540 million when adjusted for inflation (FFTF started in the mid-1960's).

Finally, it is interesting to note that we could produce electricity with TETR quite easily by adding a 40 million dollar turbine generator in the reactor auxiliary building (see Chapter XIV). The 275 MW_{th} of 260°C heat could be converted to approximately 60-70 MW_e without increasing the TETR cost to over $700 million dollars. Such an attractive feature should be investigated further.

A summary of all the O & M costs is given in Table I-N-4. The annual requirement is $33,734,000, which is dominated by the cost of electricity (85%). It is important to note that the major contributor to the cost of electricity is the operation of the neutral beams which constitute 69% of the electrical requirements and 57% of the total O and M costs.

Since TETR is a net consumer of tritium we must include the cost of tritium in the total operating costs. Assuming $5000 /g for tritium and inventory of over 11 kg we calculate the following costs for T_2 in TETR.

TOTAL ANNUAL FUEL COSTS TETR

		Dollars
1)	Tritium Burned	49,662,000
2)	Tritium Decayed	2,935,000
3)	Deuterium	10,000
		52,607,000

Table I-N-3

Summary of Major Cost Items - TETR

Item	Millions of Dollars	% of Direct
Shield & Blanket	133.1	31
(304SS)	(11.88)	(3)
(W)	(115.850)	(26)
(B_4C)	(3.081)	(1)
(Pb)	(2.736)	(1)
Neutral Beams	60.00	14
Cryogenic Cooling	58.125	13
DC Converters	30.82	7
Magnets	30.565	7
Control	18.0	4
Test Modules	17.64	4
Air Purification	17.2	4
Vacuum Equipment	12.035	3

Table I-N-4

SUMMARIZED O AND M COSTS

Cost Item		Annual Cost
Salaries		$ 1,440,000
Miscellaneous Supplies and Equipment		800,000
Outside Support Services		180,000
Miscellaneous Costs		120,000
	Sub-Total	2,540,000
General and Administrative (20%)		510,000
Electricity (480 MW, 70% plant factor)		29,434,000
Coolant Makeup (20% He per year)		250,000
Unusual Maintenance Items		1,000,000
		$33,734,000

Note: This does not include the labor and material costs for preparing test assemblies.

Adding this cost of tritium to the other operating costs we find (Table I-N-5) that the total annual operating cost is in the neighborhood of $85,000,000/year, well under our target of $100,000,000/year.

Table I-N-5

SUMMARY TOTAL ANNUAL OPERATING COST TETR

Item	Dollars
Fuel	52,607,000
Electricity	29,434,000
Other O & M	4,300,000
	85,114,000

It is obvious that two of the major design decisions have had a great impact on the operating costs of TETR. The decisions not to breed tritium and opeate in the driven mode constitute 88% of the operating costs. The magnitude of these cost items features could be reduced by two not totally unreasonable governmental actions:

1) Association of TETR with a captive hydroelectric station producing power at 4 mills/KWh as is the case for the Northwest US.

2) Dedication of an existing thermal production reactor to the production of T_2 for TETR. This, associated with other cost-saving features, could lower the cost of Tritium. However, it is unlikely that the optimistic combination of the above factors would reduce the annual operating costs by more than a factor of two to approximately $40,000,000/year.

We conclude from this analysis that one TETR could be built without imposing any unrealistic demands on the United States or world resources. The total capital costs should be between $600,000,000 - $700,000,000, and the annual operating costs in the $85,000,000 a year level. Several key areas of TETR should be studied for the potential of reducing these costs; development of radiation damage resistant electrical insulators for magnets (to reduce the need for W), low cost neutral beams, dedicated tritium-producing facilities, pulsed superconductors and coupling with cheap hydroelectric power. We did not examine the construction schedule in detail, but it appears reasonable that such a facility could be built and operating in five to seven years after authorization.

II.) Design Philosophy

II-A.) Background

There is currently a curious mixture of optimism and urgency developing in the fusion community. On the one hand, recent successes in Alcator, PLT, T-10, IIX-2B, and in the inertial confinement area have removed most of the doubts from the physics community as to "if" the breakeven stage can be achieved; now the question is "when?" Most scientists in the field feel that the breakeven stage will be achieved in the next 5-10 years (i.e. before 1982 to 1987). Counter to this optimism is the realization that time is not necessarily on our side in solving the long range energy problem. Recent difficulties of the LMFBR program and some deemphasis of the LWR program have raised the serious question of just how we are to bridge the gap from our present dependence on fossil fuels to a future reliance on "inexhaustible" fuels.

In this climate, there is a strong temptation to try to accelerate the fusion program from its traditional goal of commercialization in the early 21st century to a demonstration of electricity generation in the 1980's with commercial systems appearing around the turn of the century. Such a philosophy means that much of the normal sequencial experiments would have to be done in parallel. Reactors operating on a DT fuel would then have to be built without the benefit of prior testing of fueling, heating, and confinement schemes in the extremely harsh environment of a DT plasma. Materials testing in the appropriate neutron spectrum would also have to be accomplished simultaneous to the full scale operation of the reactor. Such a practice is risky at best and could well be disastrous in the event of a primary pressure boundary failure.

Somewhere between the orderly but admittedly long time development of fusion power and the "Manhattan Project" approach is a scenario which carries some risk but, in fact, can be defended in view of our impending energy crisis. The main elements of such an approach were discussed in a recent ERDA report[1] which outlined five logical paths to commercial fusion. While not endorsing all the ideas put forth in that document but at the same time accepting the basic concept of logic III,[1] we have attempted to design an Engineering Test Reactor which can have maximum benefit to the magnetic fusion program. The timing of such a facility is such that it will be the test bed for many engineering systems and structural materials required for use in the Demonstration Power Reactors (DPRs) of the late 1990's. To fulfill this requirement, such a facility needs to be built and be operating by the 1985 to 1987 period so that information from the test reactor can be reasonably incorporated in the design phase of the first large scale, relatively high plant factor DPR. This last requirement means that the design of the test facility must be made on the basis of what is known about the physics and engineering in the early 1980's. The purpose of this report is to describe how we feel such a facility can be designed with the above boundary conditions and fit into the scenario of a reasonable and vigorous program to the commercialization of fusion power.

II-B.) Approach

One of the overall guidelines of our work has been that the test facility should give as much information about the ultimate engineering systems as possible while requiring a minimum of extrapolation of 1980 technology. When assessing the most likely form of the first DPR, we have come to the conclusion that it is

most likely to be a Tokamak or closely related system. Therefore, our design is a Tokamak Engineering Test Reactor (TETR) for short.

The first question to face is when is the information for the DPR required. We have used the information in reference 1 for logic III to illustrate when conceptual design, Title 1 activities, and the start of operation is to commence for DPR (see Figure II-B-1). Other important supporting facilities such as the Experimental Power Reactor (EPR), the tritium facility at LASL, the High Flux Neutron Facility (HFNS) at HEDL, the Toridal Test Assembly (TTA) at ORNL, the Toroidal Fusion Test Reactor (TFTR) at PPPL, the Doublet III (D-III) at General Atomic, the Poloidal Divertor Experiment (PDX) at PPPL and the Princeton Large Torus (PLT) at PPPL are shown in Figure II-B-1. The anticipated time frame in which to consider TETR is also included.

It can be seen that under the ERDA logic III philosophy, conceptual design of the DPR would begin in 1988 with title 1 construction, starting 1991. The reactor would be ready to operate in 1999 under this schedule. In viewing figure II-B-1, it is apparent that the last time new information can have a significant impact on the DPR is 1991 when construction begins. It is true that small design changes could be made for a few years after that date but it would be very difficult to meet the 1999 operating date with any significant changes in materials. Therefore we will use the date of 1991 as the time when final decisions on the DPR materials will have to be made. Working backwards, we find that if TETR is to take advantage of PLT, PDX, D-III, and to some degree TFTR, TTA, and the HFNS it cannot start Title 1 construction before FY 1981 (only four years from the time of this writing). Given a six year construction time after Title 1 activity commences,

Figure II-B-1

TIME FRAME IN WHICH TO CONSIDER TETR (AFTER LOGIC III)

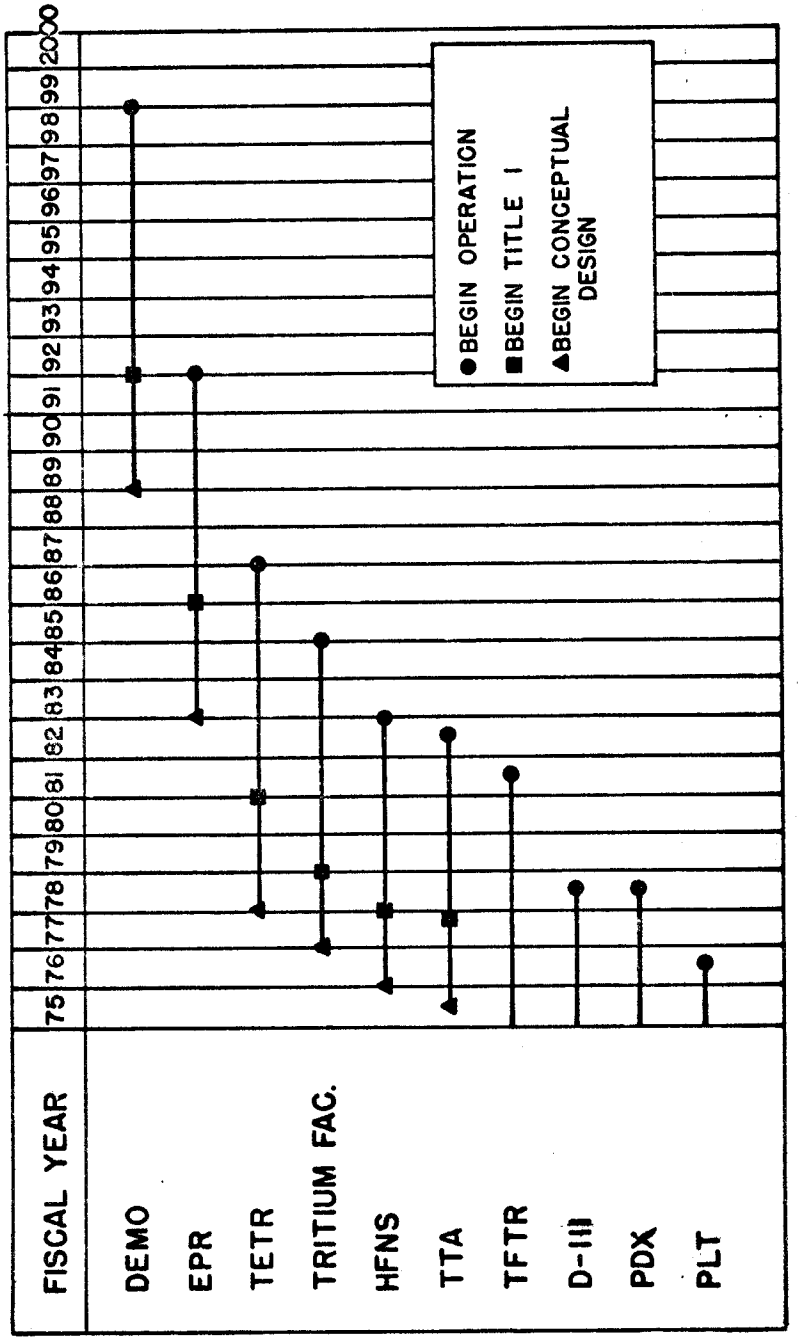

this would put the TETR in operation about FY 1987. Thus it would have four years to 'debug', run tests and analyze the data before the 'deadline' date of 1991 for the DPR.

Turning now to the DPR itself, we then set out to anticipate just what materials and engineering information might be needed. This involves a bit of crystal ball gazing which must constantly be reassessed as new research developments are brought to light. The reader may not agree exactly with our perception of what the DPR might look like but we hope we have been broad enough so as to include the majority of opinions.

It is most likely that any demonstration power reactor would have to produce several hundred MW_e of net power if it is to be called a true demonstration of economic feasibility (note, we do not think the DPR <u>will</u> be economic, only that it will <u>demonstrate</u> the potential for economic feasibility). Considering that it will probably be of a nominal efficiency, ~30%, this would indicate that a power level of 1000 MW_t is reasonable.

The reactor itself must run in a semi-continuous mode and a plant factor of ~50% would probably be considered as a minimum target by most utility representatives. Assuming that such a DPR will be plagued with numerous 'bugs' for some time after startup which might require 2-3 months per year to correct, we have placed a minimum duty cycle of 70% $(\frac{\text{burn time}}{\text{cycle time}})$ on the DPR. The length of the burn time cannot be set exactly but it should be in the order of 100 seconds. A value of 10 seconds for the burn may not be sufficient to achieve a 70% duty cycle because it would allow less than 3 seconds between shots to accomplish the pumping, reset of the coils, refueling, etc. On the other hand, a thousand second burn would probably overburden the DPR with power supplies and require much larger OH and VF coils than would be necessary for a high power production demonstration.

The next major choice (as it concerns the TETR) is choice of structure and

coolant. There have been many combinations suggested and we have listed some of them in Table II-B-1. In our opinion, the most likely coolant for the DPR (which is assumed to have to have a breeding ratio of greater than 1.0) is lithium. It will solve the breeding and cooling problem quite nicely as has been demonstrated in several reactor designs in the past, and it does so with an acceptable pumping power and pressure. The corrosion problems can be minimized by running at moderate temperatures, which as we shall see later, are also required for radiation damage reasons.

The use of helium introduces complications with respect to high pressures (hence highly stressed components) and the net efficiency is not attractive if we run at moderate temperatures to avoid serious radiation damage problems. The use of He would also require a separate breeding loop which presents problems from radiation damage and possible breeding difficulties if a solid breeder is used.

It is quite possible that selected components would be water cooled, such as the first wall or regions which would be hard to replace if they failed. Therefore the possibility of even lower temperatures than normally required for efficient electricity generation must be considered.

When all factors were weighed it was the judgement of this design group that the austenitic stainless steel-lithium combination was the most likely for the DPR. The reasons for the choice of this combination were detailed in ou UWMAK-I report.[2] The major points are: presence of an established mining and milling industry which can deliver fabricable and weldable components which satisfy established design code criteria, and a wealth of experimental data on the behaviour of at least 304 and 316 steels after high fluence and high temperature neutron irradiation. It is conceivable that titanium alloys may be a serious contender for the primary alloy[3] but the lack of sufficient irradiation

Table II-B-1

Possible Structure Coolant Combination for Late 1990's DPR

Coolant	Structure
Lithium	Austenitic steel, Titanium alloy, Vanadium alloy
Helium	Austenitic steel, Titanium alloy, Vanadium alloy, Graphite, High Nickel Base Alloys
Water (selected positions)	Austenitic Steel, Titanium alloys, Zirconium

data would probably prohibit their use in early reactors. The long term promise of these alloys is bright due to their low induced activity and good fatigue resistance, and they will be serious contenders for the first generation of commercial reactors.

The next closely associated parameter to determine is the operating temperature of the DPR. It is the present opinion of this design group that one does not have to demonstrate fusion at very high efficiences in the early development years. This,coupled with the need to obtain longer component lifetimes led us to think that operating temperatures of 400-450°C would be sufficient for the DPR. The choice of final temperature will be made once the complete damage-temperature-stress matrix is understood, which is, in fact, the function of a project such as TETR.

The neutron wall loading will probably be in the 1-2 MW/m^2(ave) region with peak values at ~3 MW/m^2 due to geometry considerations. Values above 5 MW/m^2 would be difficult to handle from the heat flux alone to say nothing about the radiation damage. Values below 1 MW/m^2 will probably not be very economically attractive so we will assume that we must gear our test matrix to a 2 ± 1 MW/m^2 level.

A final point is that there is likely to be some form of impurity control in the DPR such as divertors and/or low Z lines materials. The use of carbon for this application has been suggested[4] and recent EPR designs[5] all have used C or Be either as 2-dimensional curtains, 3-dimension plates or coatings. Therefore one of the functions of TETR should be to clearly establish the long term viability of such materials in a fusion environment.

A summary of what we perceive the engineering DPR operating conditions to be is given in Table II-B-2 and we outline how we intend to provide data for this set of conditions in section D of this chapter and chapters X and XI.

Table II-B-2

Anticipated DPR Operating Conditions

1) Data Needed by 1991
2) Thermal Power Output ~1000 MW
3) Plant Factor ~50%
4) Duty Factor ~70%
5) Stainless Steel Structure
6) Lithium Coolant - Steam Power Cycle
7) Maximum Coolant Temperature -400°C
8) Maximum Structure Temperature -450°C
9) Use of Low Z Materials to Control Impurities
10) Neutron Wall Loading 2 ± 1 MW/m^2

II-C). Major Constraints for the Design of TETR

Before we began to design the TETR we agreed on a set of 12 requirements and/or constraints. These are listed in Table II-C-1 and we will briefly touch on the reasoning behind them in the rest of this section. The reader should certainly recognize that a great deal more thought went into these ideas than appears in this report.

The first requirement stems from the fact that we doubt that ignition physics will be the state of the art in 1980-82. When we freeze the design of this facility, this ignition physics consideration, coupled with the desire to build as small a reactor as is consistent with the engineering goals we have set (for example, high neutron wall loading) dictates that we only consider a driven reactor. We therefore will assume that TETR is designed with TFTR state of the art plasma physics. The implications of this are discussed in more detail in Chapter III.

The next design constraint for TETR is that it must use neutral beams of energy no greater than 200 KeV and have current ratings no more than 50 amperes per module, or, 150 KeV and 100 amperes per module. The higher energy beams would no doubt have to come from negative ion sources while the latter would most likely come from positive ion sources. We felt that the 150 KeV positive ion source technology is a reasonable extrapolation from the TETR requirements in 1982 and that there is a good possibility of reaching the lower current, 200 KeV source in the late 1980's.

It was felt that no toroidal or vertical field magnet technology beyond that supplied by the TTA in 1982 should be expected. That facility will test superconducting TF coils with NbTi superconductor. We did not think it is reasonable to anticipate higher field Nb_3Sn superconducting coils even though they would have considerably increased the attainable neutron wall

TABLE II-C-1

Design Requirements and Constraints for TETR

(1) TFTR state of the art plasma physics (beam driven)

(2) Neutral beams of no greater than 200 KeV, 50 A/module or 150 Kev, 100 A/module

(3) Superconducting TF coils (TiNb) No Pulsed Superconductors.

(4) Stainless steel structure (except for test modules)

(5) Does not have to produce net electrical power (no requirement for high temperatures)---- Can have power cycle attached to test loop

(6) Limited tritium breeding (in special test modules only)

(7) Must produce "characteristic" Tokamak environment in test zone at the rate of 1 MW/m^2 per year (integrated)

(8) Equilibrium tritium release rate <10 curie/day and total release less than allowed for LWR in 10-CF-R50

(9) Cost on the order of 550 million dollars (1977)

(10) Operating expense <100 million dollars a year (1977)

(11) Must be able to be build in <6 years from start of construction and sited "within the fence" at a federal site

loadings. We also have assumed that we will not have mastered the technology of operating fast pulsed superconducting coils by 1980. This means that we will have to use cryogenic OH coils despite their power consumption.

We have limited the structure of this reactor to austenitic stainless steel (not necessarily 316 SS) because it is the only material that we have extensive radiation damage information on, even though it is from fission reactors. We also felt that despite its high induced radioactivity- the cost, available industry, and fabricability far out-weighed the radiation hazards. However, we do leave the possibility open to the use of other materials in the test cell area.

The TETR is not required to produce electricity. This decision allows us to drastically lower the temperature of the blanket and has allowed us to run the first wall and rest of the blanket at temperatures of 300^{o}C or lower. Such a design was radically new a few years ago but now is being followed by many reactor designers. The lack of electricity production obviously will increase the operation costs but it will also reduce the capital costs and greatly simplify reactor start up, shut down and arbitrary power changes during operation. We point out however, that the TETR could easily produce electricity even with 250 - 300^{o}C heat and it could do so at a modest incremental cost. (However the overall cost per unit of electricity would be quite uneconomical.)

We have also removed the requirement to be self-sufficient in tritium. Obviously such a decision greatly increases the operating costs but it will lower the capital costs and may simplify the safety design of the reactor building. This constraint also removes the need for Li in the blanket (except that it will be included in special test modules to study pumping, corrosion, on line extraction systems, etc.)

The main function of the TETR is to produce a "characteristic" test environment where the yearly averaged neutron wall loading is 1 MW/m^2. The word characteristic is meant to include such items as duty cycle, charged particle - neutron synergistic effects, stresses due to vacuum loading, dead weight, coolant pressures, swelling gradients, etc. The value of a yearly average neutron wall loading of 1 MW/m^2 is important to correlate with the 2 MW/m^2 - 50% PF anticipated operating conditions of the DPR. This choice obviously means that a high premium will be placed on a high plant factor for TETR so as to reduce the instantaneous wall loading to as close to 1 MW/m^2 as possible. For example, a 3 MW/m^2 - 33% PF combination for TETR is probably not feasible due to the difficulty in getting such high wall loadings.

It was felt that the tritium release rates in TETR would have to be kept at the 10 curie/day or less level and the total release of all radioisotopes (including T_2) would have to be less than that allowed for LWR's in 10-CF-R50. It is difficult to guess what future restrictions on the release of radioactivity might be but it was felt that if we kept within today's limits, we could not be too far off for the period of 10 years from now. It may in fact be shown that the only radioisotope released from a facility like TETR would be T_2 and the limits may then be relaxed to a total activity release of less than the current total for LWR's but higher than 10 curies/day. However, we will use the conservative limits in our design.

We have placed a total capital cost goal for TETR at roughly 550 million dollars (at 1977 rates). It was felt that while a lower figure was desirable, it was not realistic in today's construction market. It is

noted that the Fast Flux Test Facility at Hanford is projected to cost 540 million dollars (at 1965 to 197? rates) without the supporting materials test program. On the other hand, it was felt that if the costs were in the one billion dollar level, the U.S. government might not be able to justify such a large facility along with other physics and technology devices.

The annual operating cost target was ≤100 million dollars per year (1977 rates). This value is high compared to previous fission test facilities even when the cost of fuel and waste storage is considered. We feel that trading capital costs and an early operating date for increased operating cost is a reasonable compromise to make at this time and that the fusion program would be willing to pay roughly 1/3 of its present operating budget (and presumably somewhat less of increased future budgets) for the ability to put a workable demonstration reactor on line by the end of the century.

Finally, we felt that the TETR is needed as soon as possible if the community is serious about a 1998-99 DPR date. The only way we think that the TETR could be designed, built, and operating in the 1986-87 period is to be built on government land behind the 'fence' at a remote national laboratory. The placement of this one-of-a-kind facility in one of these restricted areas should reduce much of the delay currently encountered by public hearings for nuclear facilities such as LWR's, LMFBR's, processing plants, etc.

It is within the above design requirements and constraints that we set off to put together a credible design for TETR. The rest of this report is concerned with the details of that facility and in the rest of this chapter we will briefly discuss the materials testing aspects of a facility like TETR versus other fission reactors, or proposed solid and liquid target DT facilities.

II-D. Usefulness of TETR as a Materials Test Facility Vis-À-Vis Other Proposed Materials Test Facilities

If we just speak to the primary function of TETR, that is, to provide an adequate amount of high quality, high fluence data on as many materials as possible, subjected to as many conditions as possible, then we need to examine four main parameters.

1.) Test volume.

2.) Integrated damage rates per unit of time.

3.) Ability to simulate the unique features of fusion neutron damage.

4.) Ability to alter the irradiation environment so as to test in realistic temperature, stress and damage rate conditions.

It is obvious that the examination of such topics here is getting ahead of our story but it is worthwhile to consider such a topic divorced from the details presented in Chapters X and XI.

As noted in several previous publications[4,6-8] there are at least six types of potential neutron irradiation facilities that could be used to test potential CTR specimens in-situ.

1.) The Rotating Target Neutron Source (RTNS) at the Lawrence Livermore Laboratory. An upgraded version producing 2×10^{13} n $cm^{-2} s^{-1}$ (14 MeV) in a small ($\sim$1 cm^3) volume is currently under construction and scheduled for operation in 1978.

2.) The Intense Neutron Source (INS) at the Los Alamos Scientific Laboratory. This source will produce up to 10^{14} n cm^{-2} s^{-1} (14 MeV) in a volume of few cubic centimeters and it may be operational in 1981.

3.) A neutron stripping source such as the D-Li source proposed by workers at Brookhaven National Laboratory. The neutron spectrum is rather broad and the testing volume can be stated as a function of the flux of

total neutrons. Table II-D-1 shows that ~10 cm^3 can be subjected to 10^{15} total neutrons cm^{-2} s^{-1} whereas a volume of ~300 cm^3 will experience fluxes above 10^{14} n cm^{-2} s^{-1} and ~1000 cm^3 will see a flux of 5×10^{13} n cm^{-2} s^{-1}. This source is presently being designed and if funded in the U.S., may operate in 1983 at HEDL.

4.) Because of the production of helium by thermal neutrons in Ni containing alloys one can consider the use of thermal test reactors. Our requirement that such facilities have sufficient testing space for in situ studies narrows the number of reactors down to those like the Advanced Test Reactor (ATR) in Idaho Falls or the Oak Ridge Research Reactor (ORR) at the Oak Ridge National Laboratory. The flux levels here are not too meaningful because of different neutron spectra but on a displacement basis, such thermal reactors can produce damage at a rate three times higher than the RTNS and produce helium at ~6 times the rate in RTNS. These values combined with a thousand cm^3 of high flux testing volume show the utility of such facilities. It would be relatively easy to modify such reactors for in situ testing in a year and such facilities could be operating in 1978.

5.) Fast fission test facilities, such as EBR-II or DFR can provide very high displacement rates but are characterized by low helium production rates[6]. Unfortunately, such facilities were not designed for in situ testing and they are almost exclusively dedicated to the LMFBR programs in various countries. Future facilities such as FFTF will have even higher fluxes and larger test volumes. It is conceivable that the CTR community might be able to obtain some of the test space in those facilities for testing. Unfortunately the FFTF is not anticipated to be available until 1980.

6.) A typical DT fusion reactor spectra could be provided by a driven (power and tritium consuming) tokamak reactor similar to the Tokamak Engineering Test Reactor (TETR) described here or the mirror FERF at Lawrence Livermore Laboratory. The displacement rates are comparable or slightly less than in fission reactors. The dpa rates in the DT devices are roughly 1/4 of those in fast neutron reactors but the helium production rates are 5 to 10 times those in steel. However, such a DT facility could provide a very large (a few million cm^3) volume for in situ testing. The drawback of this device is that even if the plasma physics and technology systems behave as anticipated it would be ~1987 before such a reactor could start to provide data.

When one combines the instantaneous damage rates with the anticipated plant factors and projected starting dates, it is possible to estimate the maximum cumulative damage levels that can be achieved. Such information is plotted in figure II-D-1 and II-D-2 and given in table II-D-1. As a point of reference we compare this information with what might be required by designers of DPRs as outlined earlier in this chapter. It is reasonable that these designers would want information about at least one year of operation in a DPR and this information should be available by the start of construction of the reactor. Applying such criteria to the DPR we see that dpa requirements are ~15 dpa and 300 appm He would be required by 1991. The interesting point about figures II-D-1 and II-D-2 is that all of the sources considered for the DPRs and all except the TETR for EPRs, can produce the displacement damage levels required by the proposed date of reactor construction and all except the FFTF can produce the helium levels. The appropriate displacement damage and helium production levels can be produced by the times listed in Table II-D-2 for the two types of reactors.

FIGURE II-D-1 CUMULATIVE DISPLACEMENT DAMAGE IN STEEL FOR POTENTIAL CTR INSTRUMENTED IRRADIATION FACILITIES

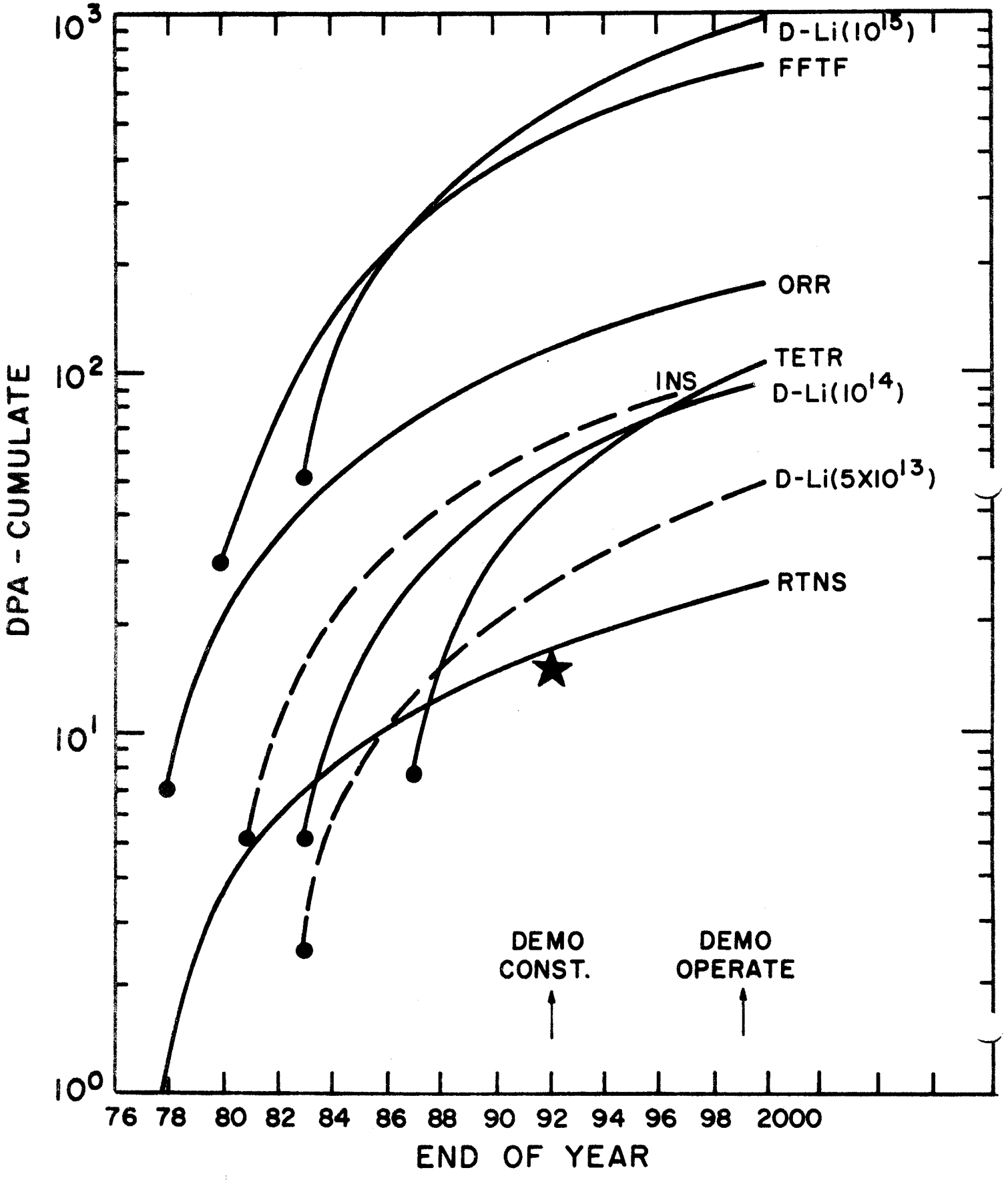

FIGURE II-D-2 CUMULATIVE HELIUM PRODUCTION IN STEEL FOR POTENTIAL CTR INSTRUMENTED IRRADIATION FACILITIES

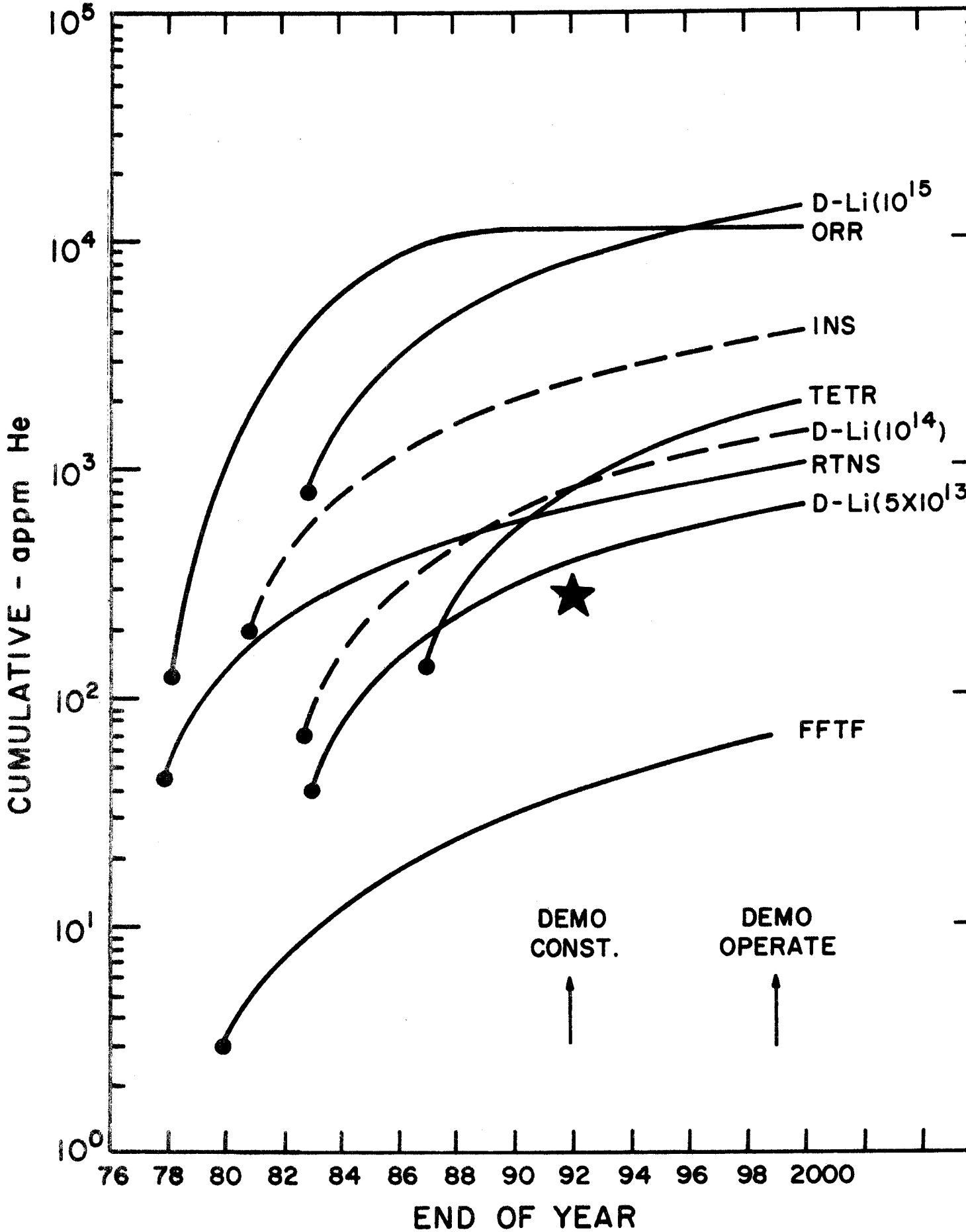

Table II-D-1

Possible Test Facilities To Provide Instrumented Data on Fe-Cr-Ni Alloys For Fusion For A DPR

Facility (Flux)	dpa/yr*	appm He/yr*	Instrumented High Flux Test Volume cm^3	PF %	Op Date
RTNS-UG (2×10^{13})	1.3	50	1	90	Jan '78
INS (10^{14})	6.5	250	3	80	Jan '81
D-Li (10^{15})	65	1000	10	80	Jan '83
D-Li (10^{14})	6.5	100	300	80	Jan '83
D-Li (5×10^{13})	3.3	50	1000	80	Jan '83
ORR	10	150**	1000	70	Jan '78
FFTF	40	4	4000	70	Jan '80
TETR	11	200	2,000,000	70	Jan '87

*100% PF, average over flux

**First Year

Table II-D-2

Date When 1 Year Equivalent Insitu For The DPR Could Be Produced (End of Year) By Projected Neutron Facilities For At Least One Specimen of Stainless Steel

	DPR	
	Max dpa	Max appm He
RTNS-UG	1990	1983
INS	1983	1982
D-Li (10^{15})	1983	1983
D-Li (10^{14})	1985	1986
D-Li ($5x10^{13}$)	1988	1990
ORR	1982	1979
FFTF	1980	not in reasonable lifetime
TETR	1988	1988

However, just achieving the appropriate damage level is not sufficient for a successful materials test program. Many temperatures, environments, stresses, alloy variations and back up samples must be tested in order to obtain a clear picture of the material's response to irradiation and to develop theoretical models. It is impossible at this time to establish a specific value for the number of samples that need to be tested and the total cumulative volume required for those tests. As outlined in this report, approximately 5000 different samples would need to be tested to provide a proper base to construct a DPR. At an average of 10 cm^3 per test (some post irradiation tests would require only a few cm^3 and some complex in situ tests might require 20-50 cm^3), this translates into a requirement for a damage-test volume product of about 10^6 dpa - cm^3 and $\sim 2 \times 10^7$ appm He-cm^3 by 1991. Such a number could be off by a factor of 2 in either direction but it is doubtful whether it is off by as much as a factor of 10. The anticipated DPR requirements are plotted in figure II-D-3 and II-D-4 along with the cumulative damage-test volume product of the facilities listed in Table II-D-1. The first obvious point in these figures is that none of the currently proposed facilities can provide all the necessary data by 1991. The RTNS-UG is woefully inadequate in this respect and although such facilities cost only ~1-5% of the other facilities, even 20-100 such devices would not solve the problem. The next point is that a single INS is not adequate and more than 1000 would be required to produce the desired number of test specimens. The various D-Li combinations are much better suited to provide this damage-volume product but again even under the best of circumstances, the product is a factor of 10 to 100 too low. The thermal reactors are somewhat better with regard to displacement damage and can provide data at least four years before stripping sources are constructed. The fast reactor test facility,

FIGURE II-D-3 CUMULATIVE DAMAGE TEST VOLUME THAT CAN BE PROVIDED BY CTR INSTRUMENTED IRRADIATION FACILITIES

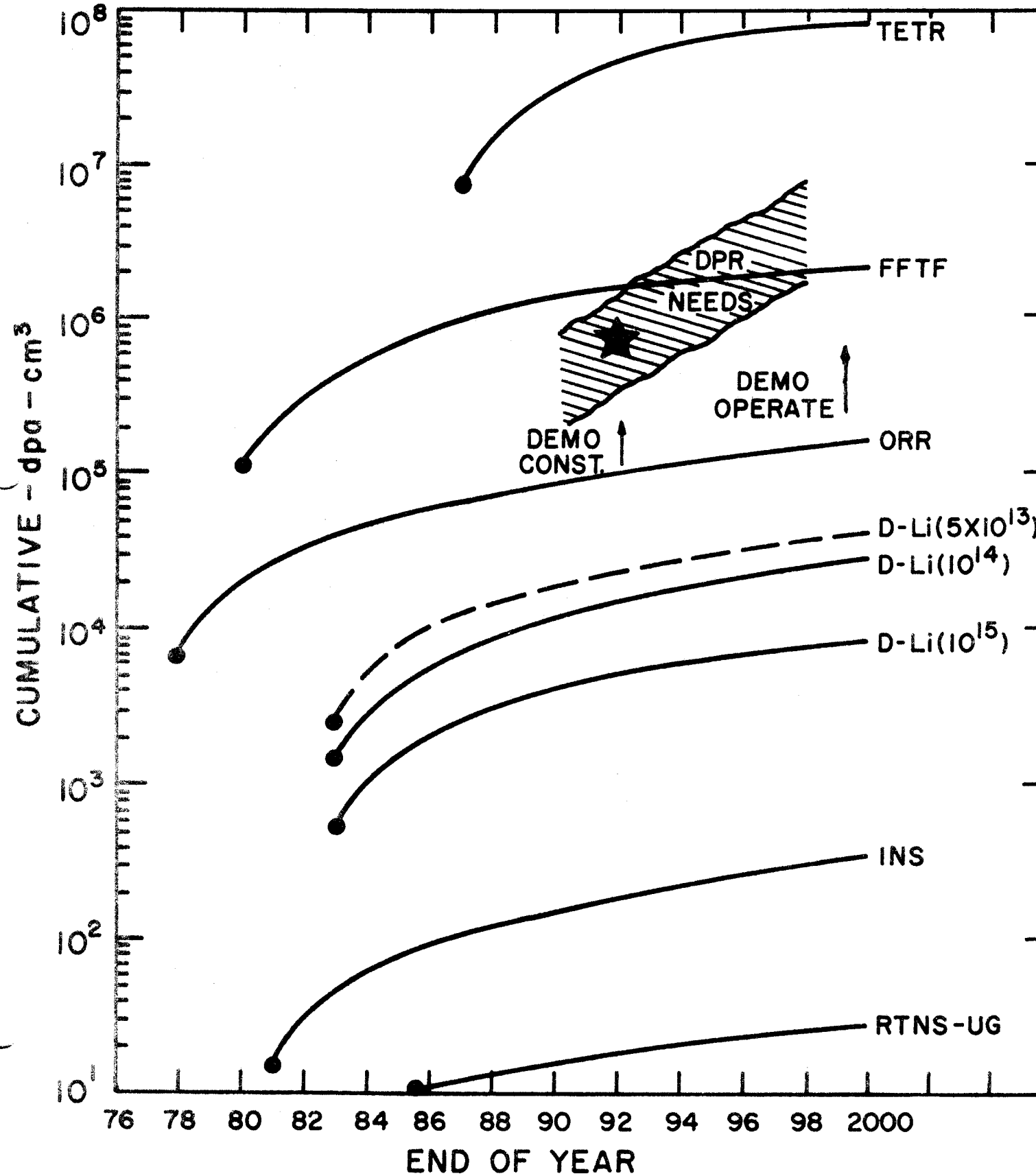

FIGURE II-D-4 CUMULATIVE DAMAGE TEST VOLUME THAT CAN BE PROVIDED BY POTENTIAL CTR INSTRUMENTED IRRADIATION FACILITIES

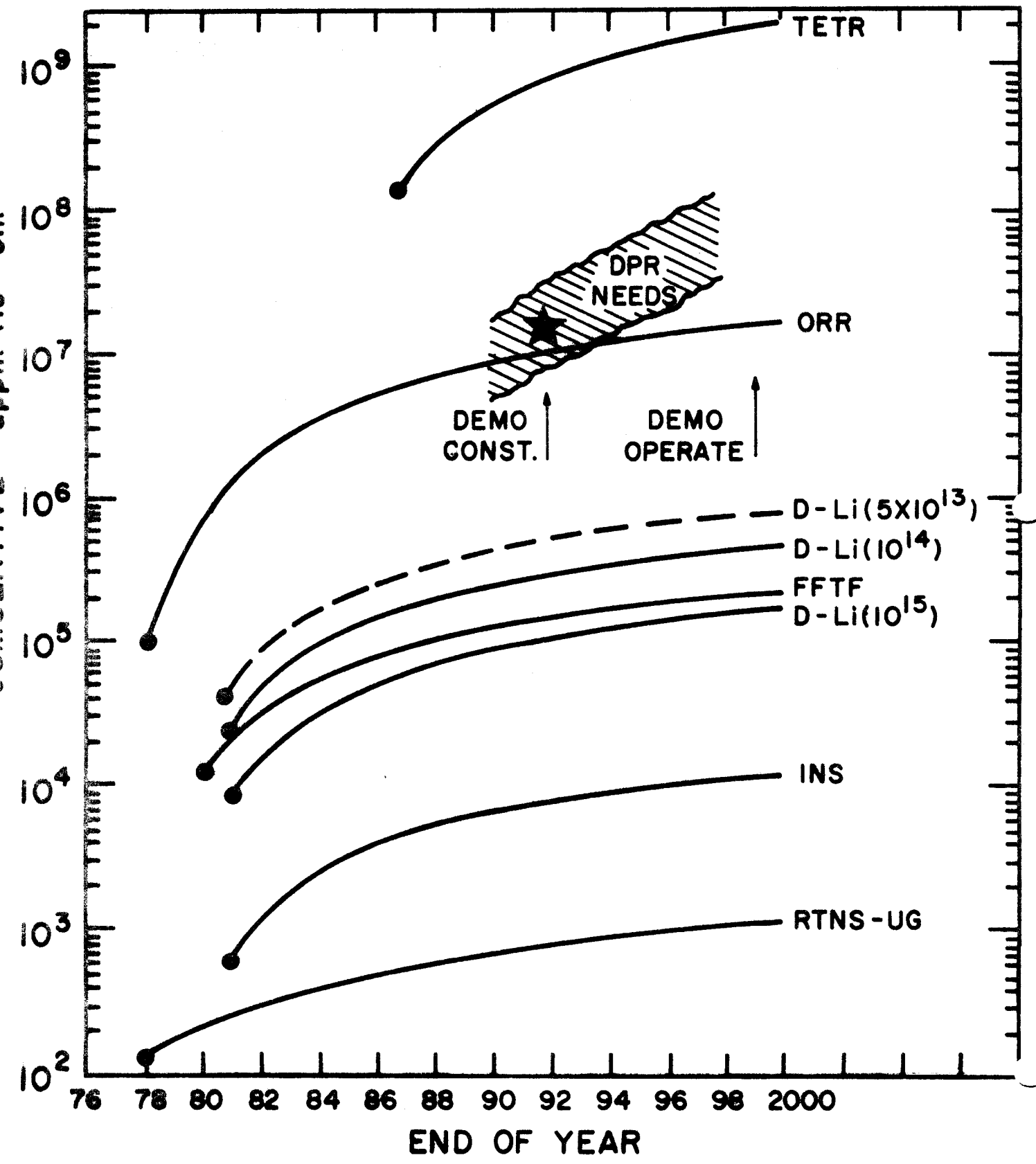

FFTF, can provide the necessary displacement damage test volume product but it produces helium at much too low a rate to be of significant use in the prediction of high temperature embrittlement.

The situation with respect to helium is much better and the thermal reactors can provide information close to that required (that is, if the samples are removed every few years after the appropriate dpa damage is accumulated).

The only facility that could provide more than enough displacement and helium accumulation information is a DT plasma device like the TETR which operates at an average 1 MW/m^2 over a year with a large testing volume. This is not to say that the other facilities should be neglected. They need to be used and supported to develop the necessary base of information that can be used by the mid 1980's to reduce the size of the test matrix to be addressed in TETR.

It needs to be emphasized that neither fast or thermal fission reactors can properly simulate the primary knock on atom spectra nor the production solid transmutation products. The latter effect can have profound effects on the behaviour of metals as 1000's to 10,000's of atomic parts per million of impurity elements can be produced in some metals over their anticipated lifetime in a DPR. Prior doping can give limited information at best and in fact may give wrong results if the elements exceed their solubility limits.

A final comment in this regard is the ability to test in all environments: vacuum, gaseous, liquid metals, water, etc. Such environmental tests in reactors require a great deal of auxillary tubing and equipment and could increase the test volume per sample by factors of 3 to 10. Obviously, such requirements would be extremely hard to handle in fission test facilities

with their small and limited cores. The safety problems of introducing high pressure and potentially explosive materials into current fission reactor cores must also be addressed and could limit the usefulness of fission reactors.

In summary, while current and proposed test facilities could produce a few specimens tested under realistic environments by the time the data is needed for a DPR, there is currently no facility except a large scale D-T reactor which can simultaneously provide the appropriate number of samples in the correct encironment of displacements, helium-solid transmutation product and coolant environments. Future investigations will better define what is required in terms of a test matrix and what is ultimately possible from proposed test devices. Therefore, continued up-dating of this information is necessary to provide the fusion community with more options to generate the necessary information.

References for Chapter II

1. "Fusion Power by Magnetic Confinement Program Plan", Energy Research and Development Administration, Division of Magnetic Fusion Energy, ERDA-76/110/1, July 1976.

2. B. Badger et al., "UWMAK-I - A Wisconsin Toroidal Fusion Reactor Design," UWFDM-68, 1973.

3. J. W. Davis and G. L. Kulcinski, "Assessment of Titanium For Use in the First Wall/Blanket Structure of Fusion Power Reactors" EPRI-ER-386, April 1977.

4. G. L. Kulcinski, "Materials Problems and Possible Solutions for Near Term Tokamak and Fusion Reactors", UWFDM-186, 1976.

5. W. M. Stacey, Jr., C. C. Baker and M. Roberts, "Tokamak Experimental Power Reactor Studies", Paper IAEA CN-35/I3-2 presented at the 6th Int. Conf. on Plasma Physics and Controlled Nuclear Fusion Research, Oct. 1976, Berchtesgaden, FRG.

6. G. L. Kulcinski, D. G. Doran, and M. A. Abdou, in Properties of Reactor Structural Alloys After Neutron Irradiation, ASTP-STP-570, Amer. Soc. for Testing and Materials, Philadelphia, 1975, p. 329.

7. G. L. Kulcinski, H. H. Barschall, J. C. Davis, and J. L. Straalsund, "A Plan for Obtaining Timely Neutron Radiation Damage Information for Experimental Fusion Reactors", UWFDM-131, 1975.

8. G. L. Kulcinski, "The Need for Neutron Radiation Damage Information From the Viewpoint of the Fusion Reactor Designs", p. 89 in Proc. of Int. Conf. on Radiation Test Facilities for the CTR Surface and Materials Program, ANL/CTR075-4, 1975.

III. Plasma Physics Analysis

III-A. Introduction

The design goals for achieving the stated purposes of an engineering test reactor are; (a) that the 14 MeV neutron wall loading should be about 1 MW/m^2 (to achieve the proper volumetric heating and bulk radiation damage); (b) that the surface heat load on the first wall be similar to that expected in Tokamak power reactors (to simulate first wall stresses and surface damage correctly); and (c) that sufficient space be available for blanket module design testing (such as the thermal hydraulics of particular blanket designs.) The test reactor should achieve these goals subject to the constraints that it be small, flexible, and as inexpensive as possible. It should also be a minimal extrapolation beyond the expected state of tokamak plasma physics experience soon after the operation of the Tokamak Fusion Test Reactor (TFTR).[1] This means a date like 1982.

In this chapter, we present the plasma physics analysis supporting the conceptual design of TETR. The original analysis for this device was given by Conn and Jassby[2] and we shall review in this section the general reasoning which led to the present design. In particular, we illustrate here why the system is designed to operate as a neutral beam driven two component tokamak rather than as an ignition machine and we also describe why such a device will require a divertor. This is followed by sections that present a more thorough analysis of the plasma physics of this device. In Section II-B, we describe the MHD equilibrium and stability studies that have been performed and the design of a double null poloidal divertor for TETR. The elongated plasma design described in Section III-B has a negative decay index such that

feedback stabilization of the plasma vertical position will be required. An analysis of the feedback requirements as well as a review of currently operating devices of similar design using feedback is given in Section III-C. Section III-Dcontains the analysis of plasma startup and the ohmic heating system design. In Section III-E, we discuss the plasma operating parameters and the space-time tokamak plasma modelling analysis. Profile effects are found to be very important and strongly influence the relationship between the particle confinement time, τ_p, and the energy containment time, τ_E. We also make clear why such a neutral beam driven device requires a divertor to maintain a high ratio of tritium to deuterium in the target plasma. Finally, in Section III-F, we present an analysis of the thermal stability of a beam driven two component plasma including space dependent effects.

The fusion core of an engineering test reactor should have the maximum possible fusion power density, P_f. Conn and Jassby[2] discussed the plasma conditions for maximizing P_f in a beam-driven tokamak reactor, and applied these results to determine suitable plasma parameters for such a reactor. In a two-energy-component tokamak (TCT)[3], the temperature of the tritium bulk plasma is maintained against transport and radiation losses by means of injected energetic deuterons, which undergo fusion reactions with the relatively cold tritons. The large beam-plasma fusion reactivity allows the TCT to attain a fusion energy gain, Q, approximately equal to 1 at values of $n\tau$ many times lower than that required for a Q = 1 thermonuclear reactor (where all reacting ions are thermalized). The fusion energy gain is defined as

$$Q = \frac{\text{Fusion power produced by the plasma in neutrons and alphas}}{\text{External beam power absorbed by the plasma}} \qquad (1)$$

No account is taken of any energy amplification by the blanket, so that the energy released per fusion reaction is 17.6 MeV. For driven tokamaks with the temperature maintained entirely by injected beams, we define

$$\bar{\Gamma} = (\text{fast-ion pressure/bulk-plasma pressure}) \simeq 0.5\ \tau_s/\tau_E, \qquad (2)$$

where τ_s is the fast-ion slowing-down time, and τ_E is the bulk-plasma energy confinement time. For Q-values larger than attainable in "pure" TCT operation, $n_e\tau_E$ must be increased so that the injected beam power can be reduced while the proportion of the fusion power output coming from thermal-plasma reactions increases. At the same time, P_f decreases because of the reduction in beam-plasma reactions.[4] Therefore, attaining large Q requires thermal-plasma operation with large $n_e\tau_E$, while producing the largest neutron flux demands TCT operation at low $n_e\tau_E$. The trade-off between Q and P_f for a given plasma pressure is shown in Fig.III-A-1, taken from Ref. (4). For a Tokamak engineering test reactor, a small-$n\tau$ plasma that delivers a large neutron flux at $Q \sim 1$ is desirable. As such, TCT operation is the optimal mode.

For given values of electron temperature, T_e, and injection energy, w_o, one can express P_f in terms of a single variable (for example, $\bar{\Gamma}$) which is then optimized to maximize P_f. The optimal values of $\bar{\Gamma}$ for w_o = 200 keV and the corresponding Q and P_f are shown in Fig. III-A-2, as well as the maximum P_f for a thermonuclear reactor of the same pressure. At the conditions giving Q approximately equal to one in a TCT, P_f is a factor of four larger than the maximum P_f attainable in a thermal plasma at any temperature, for the same total plasma pressure.

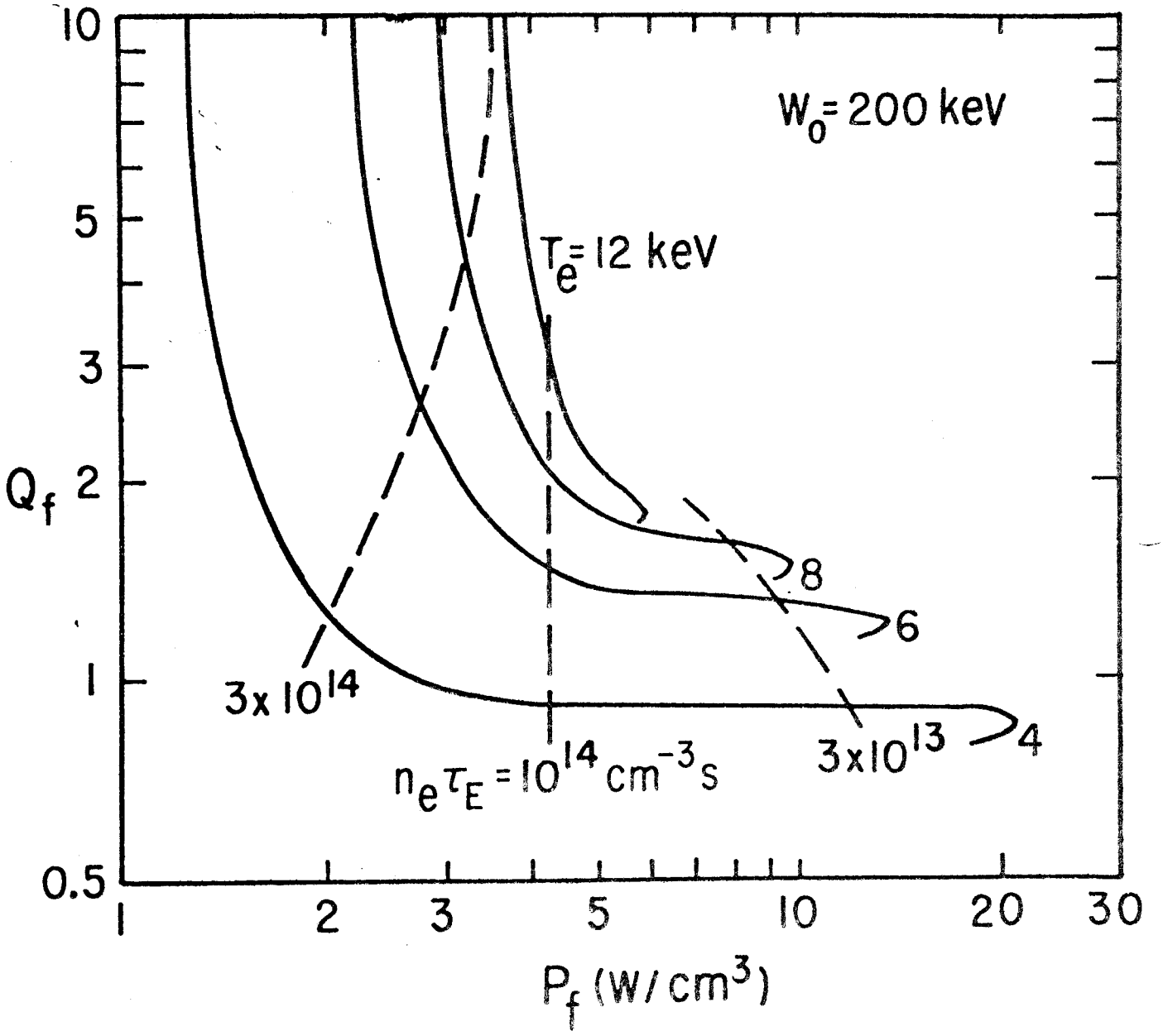

Figure III-A-1 - Fusion power gain Q_f vs power density P_f for a D-T plasma with $T_e = T_i$ heated by 200 keV D beams. For each $n_e\tau_E$, the D-T composition of the background plasma is adjusted for maximum Q_f. For each T_e there is a maximum in P_f, while Q_f increases nonotonically with $n_e\tau_E$. The dashed curves are contours of constant $n_e\tau_E$ ($cm^{-3}sec$). Total plasma pressure = 0.655 J/cm^3. (Taken from reference 4)

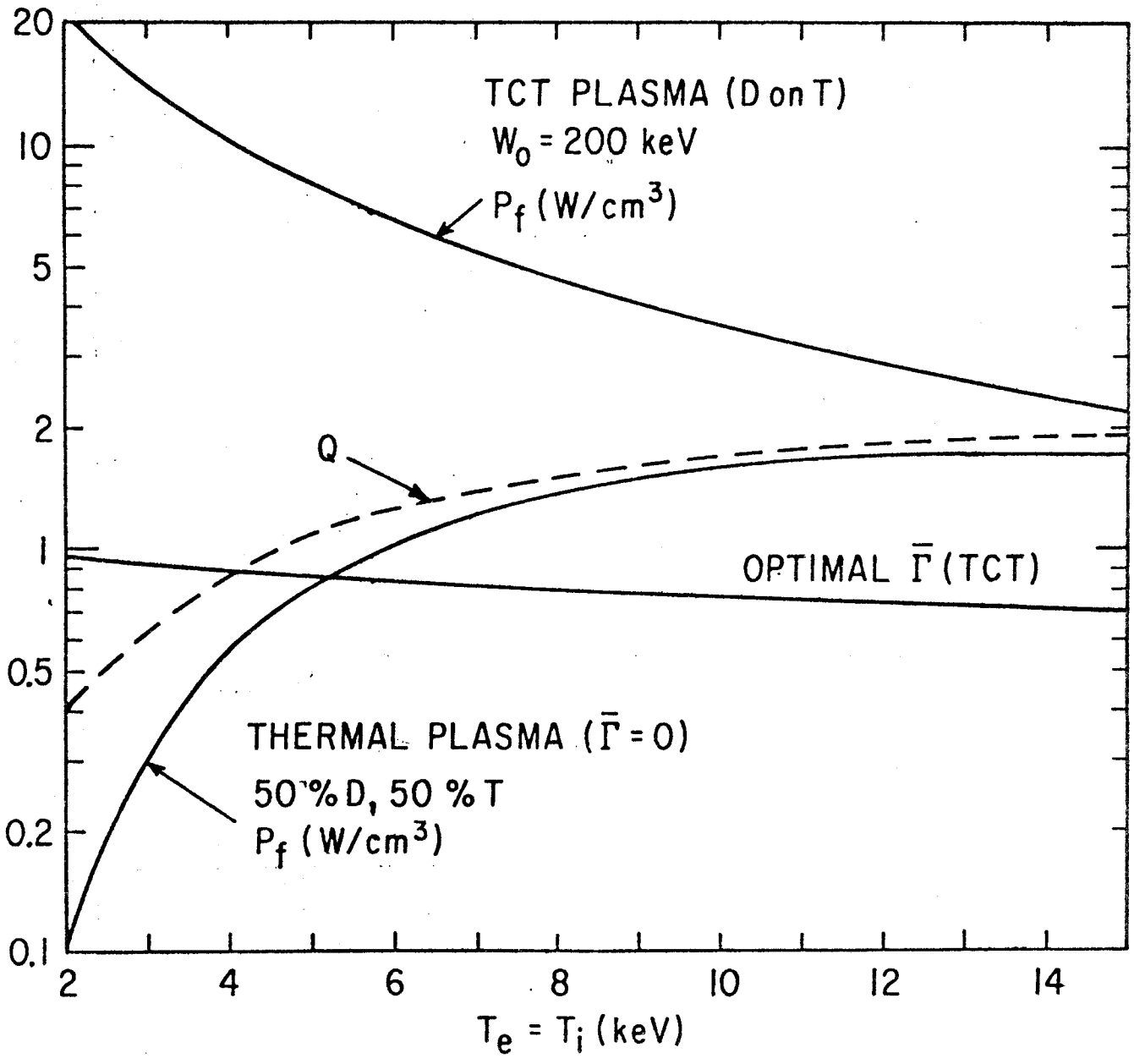

Figure III-A-2- Comparison of fusion power density P_f for a TCT plasma with optimal $\bar{\Gamma}$ and a thermal plasma with $\bar{\Gamma} = 0$. In each case, B_t = 50 kG, A = 3.5, β = 3.5, q = 2.5. Q is the fusion power gain of the TCT plasma. (Taken from reference 4.)

For plasmas of arbitrary q, A = R/a, $\beta_p < A$, and axial magnetic field, B_t (in kG), the maximum attainable P_f is

$$P_f = 7.7 \times 10^{-5} P_{fo} \left(\frac{B_t}{qA}\right)^4 \beta_p{}^2 S^4 \qquad (3)$$

where P_{fo} is the value given in Fig. III-A-2 and

$$S = (\text{Plasma circumference}/2\pi a) \ . \qquad (4)$$

The quantity, a, is the plasma half-width at the midplane (i.e. the plasma radius for a circular device). The average neutron wall loading for a circular plasma is given by $0.40\ P_f\ a_p{}^2/a_w$, where a_p is the plasma radius and a_w is the wall radius. Figure III-A-3 shows the wall loading for circular and rectangular cross-section plasmas, as a function of the maximum magnetic field, for an illustrative set of plasma parameters.

The parameters for a minimum size test reactor should be chosen to minimize power requirements and capital investment, consistent with the following criteria:

(a) Time-averaged neutron wall loading approximately 1 MW/m^2.

(b) Useful wall testing area of at least 10 m^2.

(c) Ease of access for replacement of blanket modules.

(d) Confinement of 150-200 keV beams, and attainment of the required bulk-plasma $n_e\tau_E$.

(e) Containment of fusion alpha particles, in order to minimize alpha-wall interactions.

The minimum major radius of the plasma is determined by the minimum core size, the thickness of the TF coil system, and the thickness of the inner

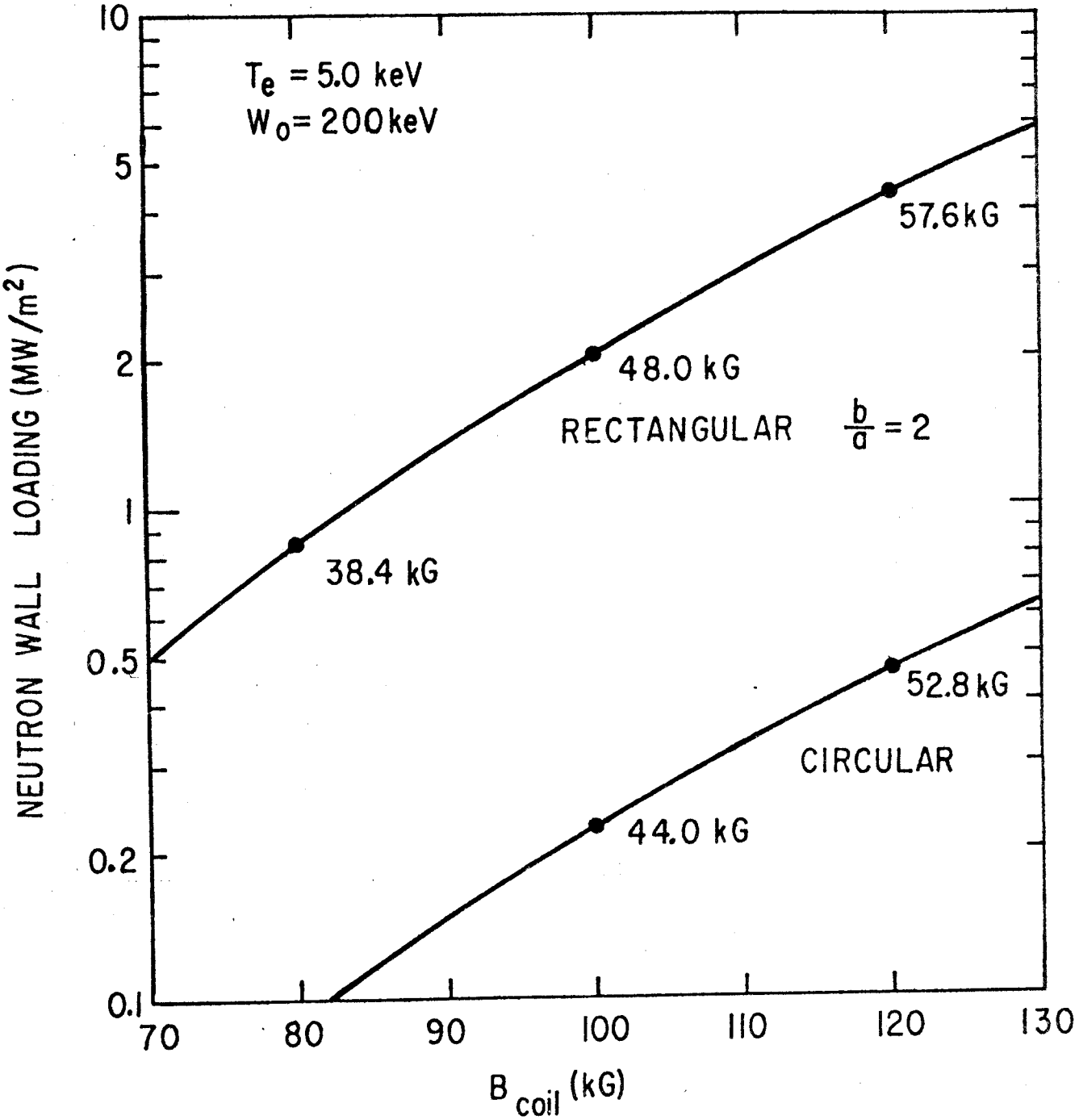

Figure III-A-3 - Neutron wall loading for circular and rectangular (b/a=2) TCT reactor plasmas. B_{coil} is the field at the TF inner wall, located at 1.45 m. The vacuum inner wall is at 2.3 m, and the thickness of the scrape-off layer is 20 cm. For the circular case, a=80 cm, A=4.1. For the rectangular case, a=50 cm, A=6.0. Both plasmas have the same cross-sectional area. In each case, β_p=0.5A, q=2.5. The fields at the magnetic axis are indicated. (From reference 2.)

shielding. Fig. III-A-4 in a preliminary study of the device shows a schematic layout of the machine. The dimensions shown were determined according to the following considerations.

The large time-averaged wall loading demands the use of superconducting coils. A reactor constructed in the next decade would probably have to utilize TiNb as the superconductor. Since P_f increases extremely rapidly with B_t (cf. Eq. 3), it is necessary to operate at the maximum possible field. For these illustrative considerations, we chose a maximum field of 80 kG at the coil with TiNb. The thickness of each coil and its supporting structure is 40 cm.

Suppose the design uses an air-core transformer. The diameter of the core is determined by the maximum flux-swing required to start up the plasma current ($\sim$2 MA) and to maintain this current for a period up to 50 s, subject to the limitation of 70 kG for the maximum field in the core. A suitable core diameter is 140 cm.

These general considerations result in the location of the inner wall at about 2.3 m. We note that the wall loading increases with plasma minor radius so that we first determine the radius at which criterion (a) is satisfied. The plasma size found in this way must be capable of carrying sufficient current, at $q \geq 2.5$, such that criteria (d) and (e) are satisfied. It is evident from Fig. III-A-3, that for relatively small plasmas and with the axial fields available using TiNb, somewhat elongated cross sections are essential to achieve large wall loadings. The minimum plasma radius that provides a neutron wall loading of 1 MW/m^2 is a = 55 cm, for a plasma elongation of 2:1. The plasma

PRELIMINARY SCHEMATIC LAYOUT OF IETR

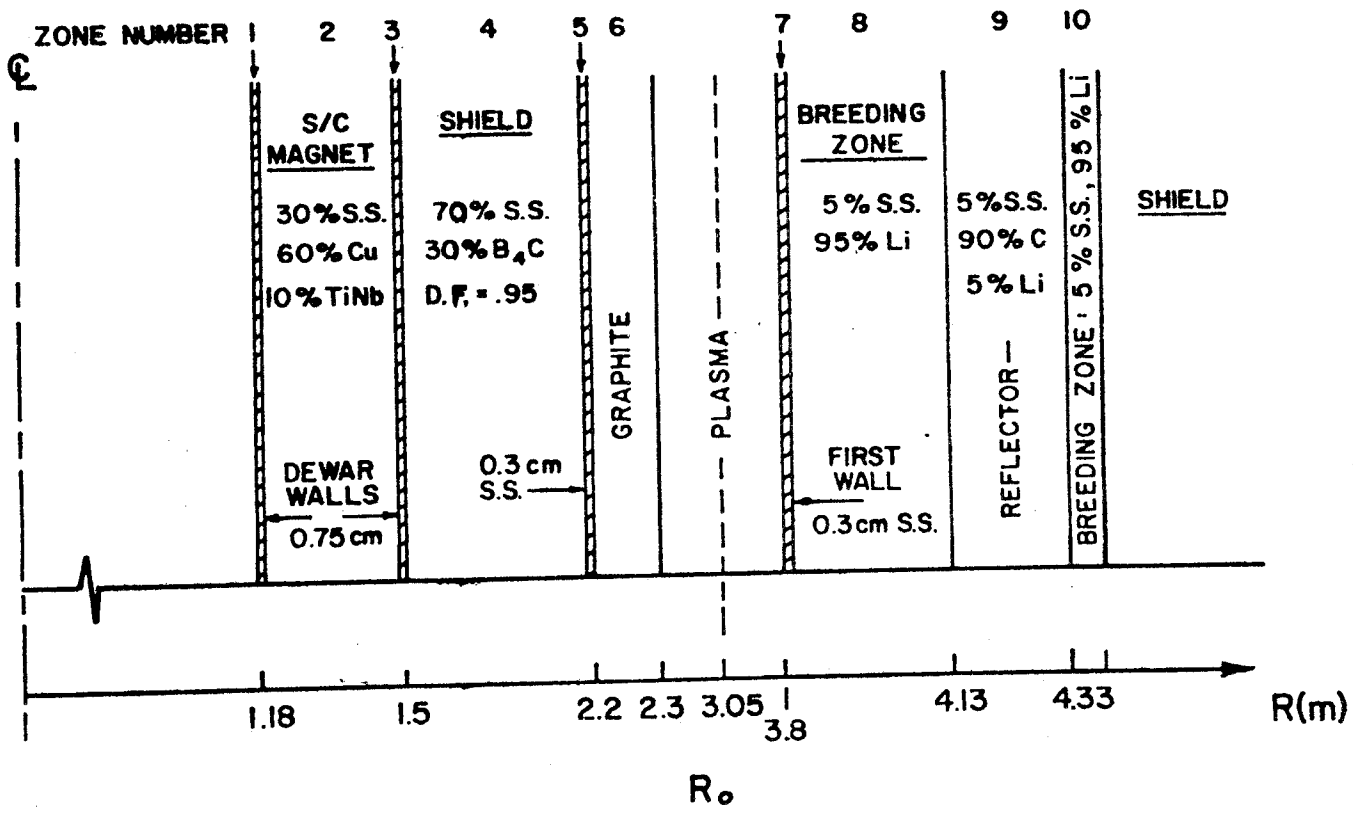

Figure III-A-4 - The graphite zone (6) protects the inner structural wall zone (5) from excessive radiation damage. The outer blanket contains Li if tritium production is necessary. Otherwise, zone (8) would be cooled with borated water and zones (9) and (10) would be replaced by normal shielding. (From reference 2)

current at q = 2.5 is then 2.4 MA, which is adequate for our confinement requirements at T_e = 5.0 keV. (Actually q = 3.0 operation, giving I_p = 2.0 MA, is probably adequate for confinement but leads to half the neutron flux).

Conn and Jassby chose a plasma cross section in the shape of a flattened "D" (S=1.78), because this shape has gross stability to vertical displacements as well as flutes.[5] Furthermore, the inside-D cross section lends itself well to the implementation of a double-null poloidal divertor[6,7] which is necessary for the removal of D and T ions, impurities, and alphas emerging from the discharge, thereby relieving the heat load on the wall. A scrape-off thickness of the order of 20 cm is required for adequate divertor performance.

From these general concerns, it is possible to determine plasma parameters and dimensions which can be made more specific by refined analysis. A list of such parameters are given in Table III-A-1. The choice of 5 keV for the spatially averaged plasma temperature is determined by the following considerations: (1) Q should be near unity, in order to minimize the investment in beam injectors, as well as the power demands; (2) Attaining maximum P_f at lower T_e requires an increase in n_e to values which make beam penetration difficult; (3) The required plasma $n_e\tau_E$ of 8×10^{12} cm^{-3} is well below the limitation set by trapped-ion instability diffusion.[8] The poloidal beta is chosen somewhat smaller than the MHD limiting value, and the value used here will actually be increased by about 10% due to the pressure of fusion alphas. While tokamak plasmas to date have operated in quasi-steady-state only at $\beta_p \lesssim 1 \ll R/a$, experiments have been performed[9,10] in which β_p was increased well above unity by an abrupt decrease in the plasma current, with apparently no adverse effect on the plasma equilibrium.

Table III-A-1

Preliminary Plasma Parameters of a Tokamak Engineering Test Reactor Based on General Plasma Engineering Considerations*

R_o	3.05 m
a	0.55 m
A	5.55
Elongation	2.0
Shape Factor	1.78 (flattened "D" shape)
Horizontal Wall Radius	0.75 m
Wall Area	149 m^2
Plasma Area	2.16 m^2
Axial B_t	38.0 kG
I_p	2.4 MA
q	2.5
$\bar{n}_e$	$1.2 \times 10^{14} cm^{-3}$
$\bar{T}_e = \bar{T}_i$	5.0 keV
$\bar{n}_e \tau_E$	$8 \times 10^{12} cm^{-3} s$
W_o	200 keV
P_{beam}	177 MW
I_{beam}	885 A
β_p	3.5
Q_b(ideal)	1.0
P_f(ideal)	4.3 W/cm^3
$\bar{\Gamma}$	0.85
Neutron Production	6.4×10^{19} n/s
Neutron Power	142 MW
Neutron Wall Loading	0.96 MW/m^2
Total Thermal Power	355 MW

* From the early paper of Conn and Jassby.[2] The final parameters are given later in Section II-E of this chapter.

At T_e = 5 keV, there is little variation in Q for w_o in the range 150-225 keV. The value of w_o should then be chosen to maximize the efficiency of producing the beam while assuring adequate beam penetration. With the development of suitable direct conversion techniques[11] of the use of negative ion beams, an efficiency of 65% (busbar to beam) can be expected at 200 keV. A total power of 200 MW of neutral beams would be needed (in the D^o component), rather than the 177 MW actually required (Table II-A-1), because a small fraction of the injected neutrals are not trapped by the plasma, and the extra power also provides us with a small reserve. The fraction of the wall area taken up by the beam apertures is less than 1%. All vacuum pumping can be carried out through the beam lines, and through the divertor channels.

The trapping profiles of tangentially injected 200 keV neutrals are shown in Figure III-A-5 for a plasma with Z_{eff} = 1. Penetration is acceptable, but would be unsatisfactory for 15 keV beams. The ionization cross section of high energy beams increases nearly proportionally to Z_{eff}, so that if $Z_{eff} > 1$, oblique injection must be used in order to maintain good penetration. Figure III-A-5 also shows the trapping profile for perpendicularly injected 200 keV beams in the case of Z_{eff} = 3. Apparently, if $Z_{eff} \gtrsim 4$, w_o must be raised above 200 keV, or n_e must be reduced. For Z = 1, the fraction of injected neutrals trapped in the plasma is 99% and 97% for parallel and anti-parallel injection, respectively, while for Z = 3 and perpendicular injection, 93% of the neutrals are trapped.

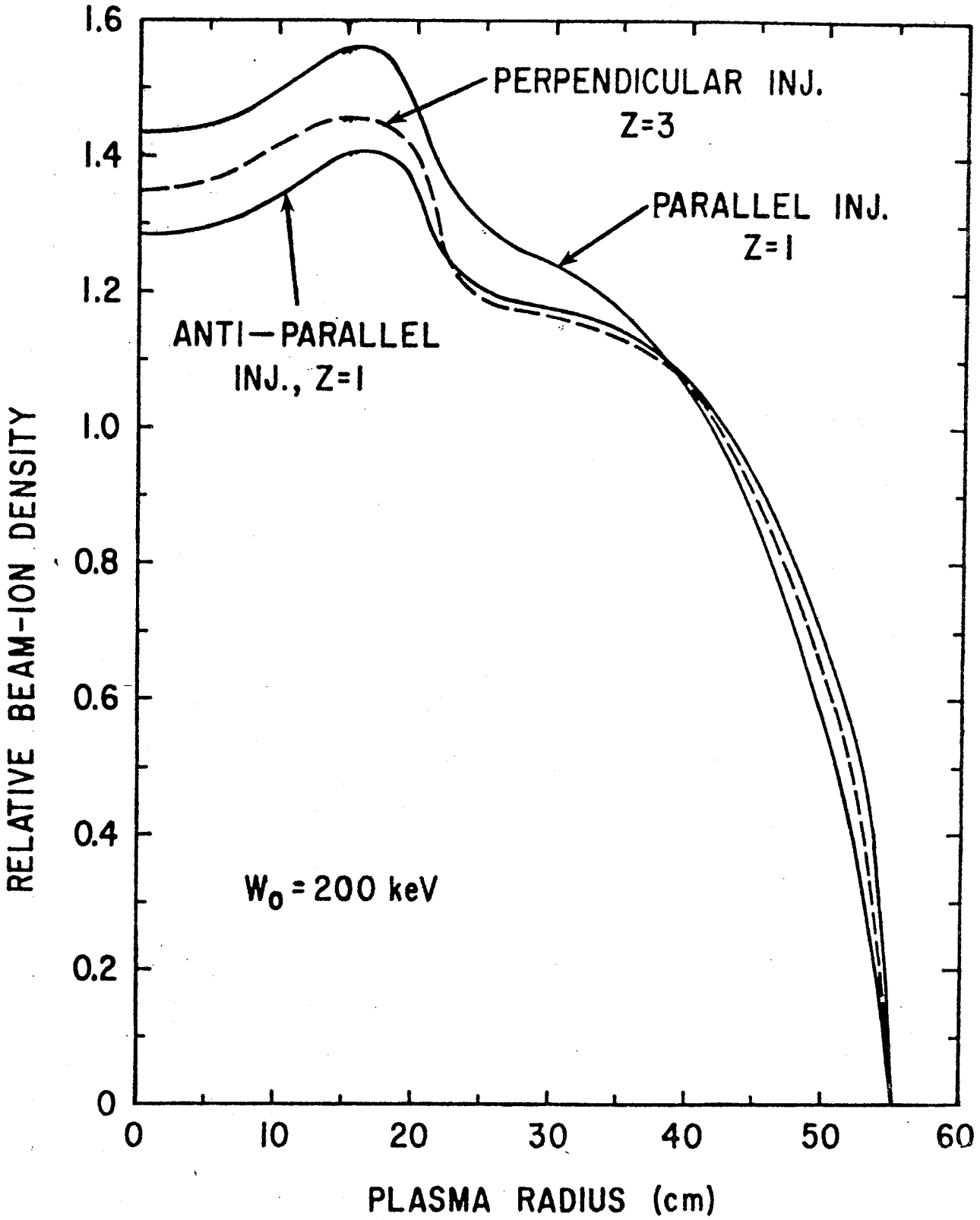

Figure III-A-5- Trapping profiles of 200-keV D neutrals injected into the test reactor plasma. The plasma density profile is shown in Figure II-A-5. (From reference 2)

The confinement of alpha-particles in tokamak plasmas has been discussed in Ref. 12. In this generalized test reactor, 92% of the alphas are confined at I_p = 2.4 MA (q = 2.5), and 87% at I_p = 2.0 MA (q = 3.0). This good confinement arises for a number of reasons: (1) The alpha source function is peaked; (2) the aspect ratio of 5.5 results in relatively small banana widths; (3) the scrapeoff layer of 20 cm effectively increases the plasma thickness; (4) the TF ripple at the plasma surface is only 1/4%.

Finally, we must consider the duty factor for such a reactor. The operating cycle of a TCT consists of (1) gas filling, (2) discharge current rise and **startup** of beam injectors, (3) operation at full injector power, (4) shutoff of injectors and reduction of current, and (5) vacuum system purge. The duty factor is the ratio of period (3) to the total cycle period and is determined by the maximum duration of the ohmic discharge, impurity buildup in the plasma, and refueling techniques.

In order to maintain the plasma current, the primary current of the air-core transformer must be increased linearly with time. For the dimensions of Figure III-A-4, the discharge period can be as long as 50 s. At least 10 s is required to reduce I_p, to purge the vacuum system and refill, and to bring I_p up to the maximum operating value of 2.4 MA. Thus, the duty factor could be as large as 0.83. High current neutral injectors are presently capable of 0.3 s pulses, and there appear to be no insuperable obstacles to steady-state injection. We assume that divertor technology, as developed in PDX[7] and other devices, will be effective in maintaining $Z_{eff} \lesssim 3$ in the case of heavy ions, or $Z_{eff} \lesssim 1.5$ in the case of carbon[13] for periods up to 50 s.

The lifetime of tritons in the plasma, τ_p, is expected to be long compared to τ_E which includes all transport and radiation losses. The lifetime of thermalized deuterons should be approximately τ_p-τ_s, since there is a gradual diffusion outward of fast deuterons during their slowing down. (That is, thermalized deuterons have a smaller diffusion scale length than do the tritons). At T_e = 5.0 keV, the proportion of tritons among the bulk-plasma ions is $f_T = (1 + 0.15\ (\tau_p/\tau - 1))^{-1}$. For the plasma conditions of Table III-A-1, τ_p should be of order 300 ms, for which f_T = 0.82. Taking into account bulk-plasma DT reactions, the neutron output will be reduced by about 15%.

The tritium composition must be maintained by injection of pellets.[14] Pellet injection into tokamak plasmas is a technology yet to be developed, but it appears to be feasible for a plasma of relatively small density-radius product, such as the present design. Penetration to the center of the plasma requires 1-mm diameter pellets, accelerated to 10 MV.[15] Maintaining f_T = 0.82 requires an injection rate of approximately 60 pellets per second. While it is possible to raise f_T by increasing the rate of pellet injection beyond 60 s^{-1}, T_e will be reduced if the beam input power is constant, so that the neutron output might not be increased.

The principal role of the poloidal divertor in the test reactor is to minimize the number of energetic particles striking the wall, and thereby reduce the impurity influx into the discharge. The plasma capture efficiency must be close to unity, so that the divertor entrance width should be at least 30 cm. Backflow of neutrals into the torus must be prevented (i.e. recycling coefficient $R_n \simeq 0$) in order to minimize charge-exchange loss of

fast ions, as well as charge-exchange neutral sputtering. The required cryogenic pumping surfaces can be readily accommodated inside the large TF coils. With this unload divertor, the plasma flow in the scrape-off region proceeds nearly at the speed of sound,[7] the density here is relatively low ($\sim 2 \times 10^{13}$ cm^{-3}), and the plasma temperature is high ($\sim$2 keV), as shown in Fig. III-A-6. These characteristics are favorable for a beam-injected reactor.

This general plasma engineering analysis gives the main features and dimensions a tokamak engineering test reactor will have. The final dimensions and anticipated plasma performance characteristics have been obtained from much more detailed specific studies presented in the sections to follow.

The main features include TCT operation, efficient ($\sim$50%) neutral beam injection, a divertor, relatively low $n\tau_E \sim 10^{13}$ cm^{-3}-s, noncircular plasma cross sections, cold pellet fueling, alpha particle containment, and reasonable duty factor. The magnetic field required is about 4T and the dimensions are: major radius ~3m; plasma radius ~0.5-0.6m; and plasma height-to-width ratio ~1.5-2.

An important criterion for the TETR design is that it should be based on plasma physics experience that can be verified in experiments up to and including those expected to run in 1982. Given the general features outlined, how does a TETR match up against this criterion? The plasma physics features of TETR related to large tokamak experience anticipated through 1982 is given on Table III-A-2. Essentially all the major features will have been tested on earlier experiments to some degree. The area receiving the least attention at this time is pellet fueling of a tokamak, but this can be part of the experimental program on any of the existing of forthcoming devices.

Table III-A-2

Features of TETR Related to Large Tokamak Experience

Feature	Implication	Relevant Preceeding Experiments†
High Neutron Flux and Small Size	TCT Operation	TFTR, JET
	Noncircular Plasma	D-III, JET PDX-UG
Low τ_p and Low Z_{eff}	Divertor	DITE, JFT-2a/DIVA PDX, ASDEX
Long Burn Time (~30-60s)	Pellet Fueling	ORMAK
Long Pulses at Reasonable Power Costs	Superconducting Toroidal Field Coils	T-7, T-10M Large Coil Project MFTF
High Power Neutral Beams	Efficiency ~50% at 150 keV	Beam Test Stands

† TFTR = Tokamak Fusion Test Reactor (PPPL)
JET = Joint European Torus (EEC)
D-III = Doublet-III (GA)
PDX-UG = Poloidal Divertor Experiment-Upgrade (PPPL)
DITE = Divertor Injected Tokamak Experiment (Culham)
JFT/2a = Japanese Tokamak with Divertor (JAERI)
PDX = Poloidal Divertor Experiment (PPPL)
ASDEX = Axisymmetric Divertor Experiment (MPI-Garching)
Ormak = Oak Ridge Tokamak (ORNL)
T-7, T-10M = Tokamak-7, 10 Modified (Kurchatov)
MFTF = Mirror Fusion Test Facility (LLL)

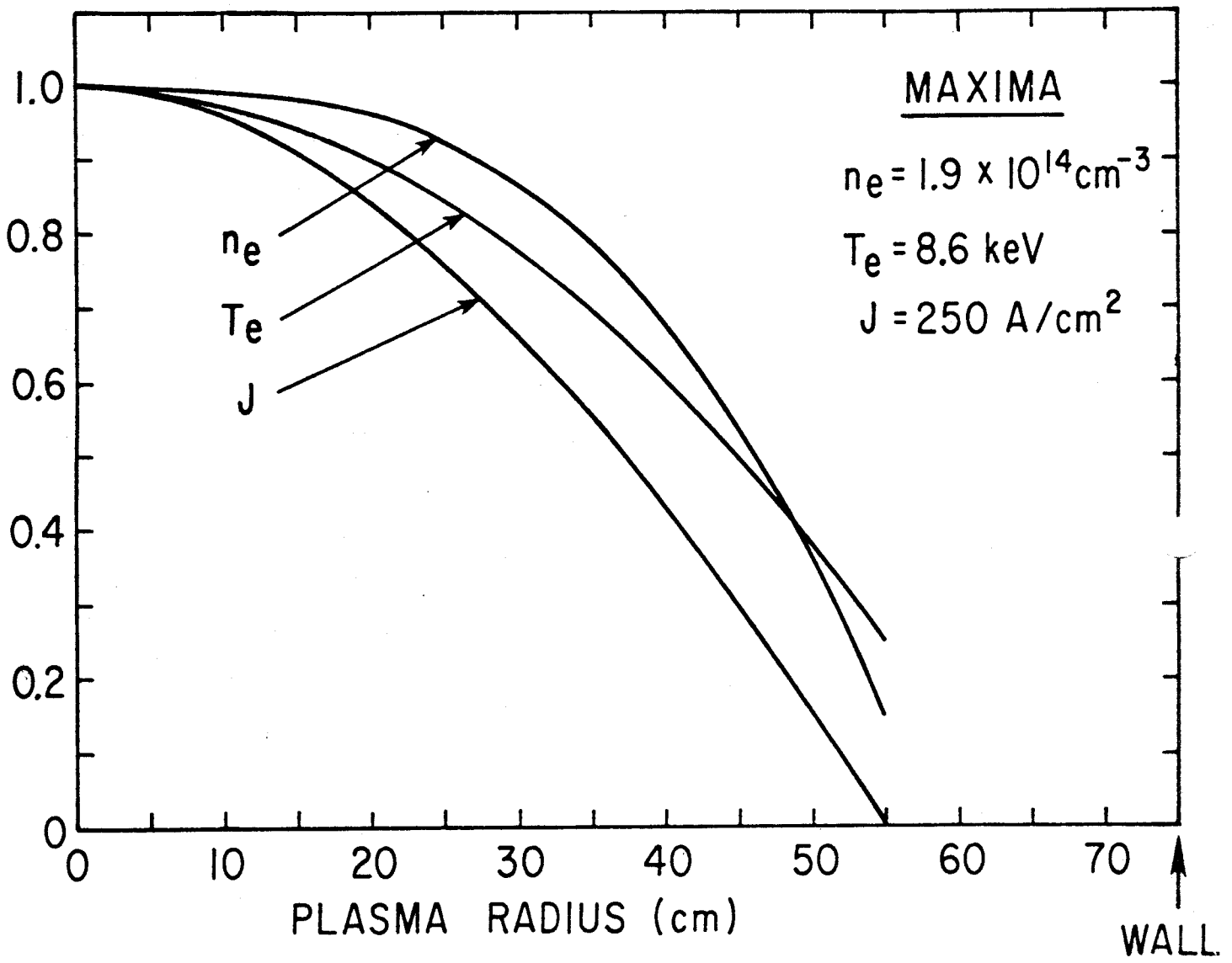

Figure III-A-6

Radial profiles in the plasma midplane. The discharge is confined to $r \leq 55$ cm. The scrape-off region lies between 55 and 75 cm. On-axis parameters are indicated (ref. 2).

References for Section III-A

1. "Tokamak Fusion Test Reactor: Final Conceptual Design Report," Princeton Plasma Physics Laboratory Report PPPL-1275, PH-R-001, Princeton University and Westinghouse Corp., Feb. 1976.

2. R. W. Conn, D. L. Jassby, "A Tokamak Engineering Test Reactor," in Proc. International Conf. on Radiation Test Facilities for the CTR Surface and Materials Program (ANL/CTR-75-4, Argonne National Lab., July 1975) p. 592. See also Nucl. Eng. Dept. Report, UWFDM-119, (April 1975) and Princeton Plasma Physics Lab. Report, MATT-1155 (Aug. 1975).

3. J. M. Dawson, H. P. Furth, F. H. Tenney, Phys. Rev. Lett., 26, 1156 (1971). See also H. P. Furth and D. L. Jassby, Phys. Rev. Lett., 32, 1176 (1974).

4. D. L. Jassby, "Optimzation of Fusion Power Density in the Two-Energy-Component Tokamak Reactor," Princeton Plasma Physics Lab. Report MATT-1072 (Oct. 1974); Nuclear Fusion 16, 15 (1976). See also D. L. Jassby, "Beam Driven Tokamak Fusion-Fission Hybrid Reactors," Princeton Plasma Physics Lab. Report MATT-1115 (March 1975), published in ERDA-4, S. L. Bogart, ed., pp. 221-245 (1975).

5. M. Okabayashi. G. Sheffield, Nucl. Fusion 14, 263 (1974).

6. G. A. Emmert, A. T. Mense, J. M. Donhowe, "A Poloidal Divertor for the UWMAK-I Tokamak Reactor," Proceedings 1st Top. Meet. on the Tech. of Cont. Nucl. Fusion, USAEC Conf.-740402-P1 (1974), p. 417.

7. D. M. Meade, et al., "The Effects of Impurities and Magnetic Divertors on High Temperature Tokamaks," Proc. 5th International Conf. on Plasma Physics and Cont. Nucl. Fus. Research, IAEA, Tokyo (1974). Vol. 1, p. 605.

8. S. O. Dean, et al., "Status and Objectives of Tokamak Systems for Fusion Research," USAEC Rep. WASH-1295 (July 1974).

9. S. V. Mirnov, JETP Lett. 12 64 (1970).

10. J. C. Hosea, Princeton Plasma Physics Lab. Report MATT-1128 (April 1975).

11. J. Hovingh, R. W. Moir, Nucl. Fusion 14, 629 (1974).

12. D. G. McAlees, "Alpha Particle Energetics and Neutral Beam Heating in Tokamak Plasmas," Ph.D. Thesis, University of Wisconsin (1974).

13. G. L. Kulcinski, R. W. Conn, G. Lang, Nucl. Fusion 15, 327 (1975).

14. S. Gralnick, Nucl. Fusion 13, 703 (1973).

15. M. S. Chance, et al., "Proceedings of 5th International Conf. on Plasma Physics and Cont. Nucl. Fus. Research, IAEA, Tokyo (1974) Vol. 1, p. 463.

III-B. MHD Equilibria for Plasmas in TETR

One key to the success in designing a tokamak engineering test reactor (TETR) lies in finding a MHD equilibrium configuration which can operate with parameters such that sufficient thermonuclear power is released to achieve the design goals. Three primary characteristics, high beta, elongated plasma cross sections, and high toroidal field, are found to be essential.[1] The achievement of a design producing the largest field on axis for a given maximum field at the coil and satisfying constraints posed by blanket and shield design and the desire (an apparent need) for a divertor adds to the difficulty of this problem. A further constraint we have placed on the TETR design is that it should be a reactor that one could conceive of building in the relatively near term, i.e., the mid-1980's. As such, the engineering of the toroidal and equilibrium field coils should be consistent with this constraint.

The operating mode which yields the highest neutron flux in a tokamak is the neutral beam driven two component approach.[2] This mode requires $n\tau_E$ values of $\sim 10^{13} cm^{-2}$-sec and typically involves values of both τ_p and τ_E on the order of several hundred milliseconds at most. Long burn times, pumping requirements, plasma protection from impurities, and first wall protection from excessive erosion imply that such devices will require a divertor.

The basic model chosen for this study is a "D" or triangularly shaped plasma that admits the inclusion of a double null poloidal divertor.[3] The reason is that this shape fills most optimally the available space inside the TF coils. A series of MHD calculations have been carried out, each time

iterating the results with plasma performance calculations based on space time fluid simulations and restrictions imposed by the problems associated with neutronics, toroidal field magnets, and access requirements for blanket modules and neutral beam injectors.

Three basic plasma designs were achieved and are classified as follows: (1) A highly elongated plasma equilibrium that is produced by a set of superconductive coils located outside the blanket and shield but inside the TF coils. The vertical field is such that the plasma is unstable to gross vertical motion. (2) A less elongated and vertically stable plasma with normal coils located inside the blanket. (3) A moderately elongated and mildly unstable plasma equilibrium with different coil arrangements. The results and reasons for our choice are discussed in detail in section III-B-2.

III-B-1. The Description of the MHD Code

The MHD equilibrium code developed by a group at the Princeton Plasma Physics Laboratory[4] was used for the equilibrium and local stability calculations. The original code has been modified in several ways, including an addition to calculate the general criteria for stability with respect to rigid motions. The MHD equilibrium for an axisymmetric system is determined by solving the usual equation for the flux function Ψ which satisfies

$$X \frac{\partial}{\partial X}\left(\frac{1}{X}\frac{\partial \Psi}{\partial X}\right) + \frac{\partial^2 \Psi}{\partial Z^2} = - X J_\phi \qquad (1)$$

where

$$J_\phi = X \frac{dp}{d\Psi} + \frac{R_o^2 B_o^2}{X} g \frac{dg}{d\Psi} . \qquad (2)$$

The magnetic field has been decomposed into poloidal and toroidal components using

$$\vec{B} = B_o[f(\psi)\ \vec{\nabla}\phi X \vec{\nabla}\psi + R_o g(\psi)\vec{\nabla}\phi]. \qquad (3)$$

The coordinates R, ϕ and Z are the axisymmetric coordinates, ϕ is the ignorable variable and X is the distance from the symmetric axis. ψ represents an arbitrary surface label and Ψ is the poloidal flux inside a magnetic surface. The nonlinear equation (1) is solved by prescribing the functions $p(\Psi)$ and $g(\Psi)$ in equation (2). The form employed for the functions $p(\Psi)$ and $g(\Psi)$, used in solving eqn. (1), can have a significant effect on the equilibrium and stability of the plasma. If we choose

$$P(\Psi) = P_o \left(\frac{\Psi_* - \Psi}{\Psi_* - \Psi_o}\right)^{\alpha_1} \tag{4}$$

and

$$g(\Psi) = \left[1 - g_p\left(\frac{\Psi_* - \Psi}{\Psi_* - \Psi_o}\right)^{\alpha_2}\right], \tag{5}$$

the plasma current, $J_\phi(\Psi)$, has the form

$$J_\phi(\Psi) = -\frac{XP_o\alpha_1}{\Delta\Psi}\left(\frac{\Psi_* - \Psi}{\Delta\Psi}\right)^{\alpha_1 - 1} + \frac{\alpha_2 R_o^2 B_o^2}{X\Delta\Psi} gp$$

$$\cdot \left(\frac{\Psi_* - \Psi}{\Delta\Psi}\right)^{\alpha_2 - 1} + \frac{\alpha_2 R_o^2 B_o^2}{X\Delta\Psi} g_p^2 \left(\frac{\Psi_* - \Psi}{\Delta\Psi}\right)^{2\alpha_2 - 1} \cdot \tag{6}$$

where $\Delta\Psi = \Psi_m - \Psi_*$, and Ψ_*, Ψ_m are the flux at the plasma surface and magnetic axis. The constant g_p is varied until Ψ converges. The current density distribution depends on the parameters, α_1 and α_2. The optimal values of α_1 and α_2 is in the neighborhood of 1.4[5] to give current profile consistent with present tokamak experiments. The plasma boundary is determined self consistently with the location of external coils. A square of arbitrary size is used as an outer boundary for the problem and the boundary conditions on this border are fixed by specifying the current in the external coils. As such, the procedure does not require the use of a

conducting external boundary. The plasma boundary can be fixed by a limiter or a separatrix. The program evaluates $q(\Psi)$, $\beta_\theta(\Psi)$ and $\overline{\beta_\theta}$ from the formulae[4,5,6]

$$q(\psi) = \frac{R_o g}{2\pi} \oint \frac{dl}{|\nabla\Psi| X} \quad , \tag{7}$$

$$\beta_\theta(\psi) = \frac{2\pi P}{< \frac{|\nabla\Psi|^2}{R^2} >} \quad , \tag{8}$$

and

$$\overline{\beta_\theta} = \frac{\int P \frac{dV}{d\Psi} \, d\Psi}{\int^\Psi P\frac{dV}{d\Psi} \, d\Psi - R_o^2 B_o^2 \int^\Psi Vg \frac{dg}{d\Psi} < \frac{1}{X^2} > \, d\Psi} \tag{9}$$

where V and $\frac{dV}{d\Psi}$ are the plasma volume and its derivative with respect to Ψ. The total β and average pressure defined respectively are as follows.

$$\beta_{total} \cong \frac{\int P \, dV}{\int \frac{B_t^2}{2\mu_o} dV} \tag{10}$$

$$\bar{p} = \frac{\int P \, dV}{\int dV} \tag{11}$$

The criteria for stability with respect to the localized modes are,[7,8] for idealized modes,

$$D_I = D + H - \frac{1}{4} < 0 \tag{12}$$

and for the resistive modes,

$$D_R + D + H^2 < 0. \tag{13}$$

The parameters D and H are defined by

$$D \equiv \frac{\langle B^2/|\nabla V|^2\rangle}{\Lambda^2}\left[J'\phi''-I'\Psi'' + \frac{\langle \sigma B^2\rangle}{\langle B^2\rangle}\right.$$

$$\left. + p'^2\left\langle\frac{1}{B^2}\right\rangle + \left\langle\frac{\sigma^2 B^2}{|\vec{\nabla} V|^2}\right\rangle - \frac{\langle \sigma B^2/|\vec{\nabla} V|^2\rangle^2}{\langle B^2/|\vec{\nabla} V|^2\rangle}\right] \tag{14}$$

$$H \equiv \frac{\langle B^2/|\vec{\nabla} V|^2\rangle}{\Lambda}\left[\frac{\langle \sigma B^2/|\vec{\nabla} V|^2\rangle}{\langle B^2/|\vec{\nabla} V|^2\rangle} - \frac{\langle \sigma B^2\rangle}{\langle B^2\rangle}\right] \tag{15}$$

where $\Lambda = \phi' \Psi'' - \Psi' \phi''$ and $\sigma = \vec{J}\cdot B/B^2$. ϕ and Ψ are the toroidal and poloidal field flux functions and J and I are the toroidal and poloidal current fluxes, respectively. Prime denotes derivatives with respect to the volume, V, and brackets denote field line averages.

A new routine has been written and included in this code to compute the general stability criteria related to quasi-rigid motions[5] (vertical and radial displacements and flippings). These modes have been observed experimentally and in many cases can be stabilized by a feedback system.[9] They are actually special kink modes and can be dangerous. In the past, the criterion for determining stability against vertical motion was that the decay index of the vacuum vertical field should be greater than zero.[10] However, this decay index criterion was derived for a circular plasma with uniform current density and large aspect ratio. A noncircular plasma with vertical elongation does not satisfy these restrictions. The general criteria of Rebhan[11] derived using an energy principle for general small rigid displacements will, therefore, be used in this study.

The sufficient criteria for horizontal displacement and flipping are, respectively,

$$C_h = \oint \frac{R\Psi_R}{|\nabla\Psi|} P_R^* d\ell \geq 0 \tag{16}$$

$$C_f = \oint \frac{R(R\Psi_z - z\Psi_R)}{|\nabla\Psi|} (Rp_z^* - zp_R^*) d\ell \geq 0. \tag{17}$$

The necessary and sufficient stability condition for vertical displacements is

$$C_v = \oint \{\frac{1}{R|\nabla\Psi|} [-\Psi_z\Psi_{RR} = \frac{\Psi_z\Psi_R}{R} + \Psi_R\Psi_{Rz}] + y\}x$$

$$\Psi_z d\ell \geq 0. \tag{18}$$

Here the antisymmetric part of y satisfies the integral function

$$\frac{1}{2\pi} \oint [K(\ell',\ell)y_a - K(\ell,\ell')y_a] d\ell'$$

$$= \frac{1}{2\pi} \oint [L(\ell,\ell')\sigma' - L(\ell',\ell)\sigma] d\ell'. \tag{19}$$

The functions $K(\ell,\ell')$ and $L(\ell,\ell')$ are defined as

$$K(\ell,\ell') = \frac{4R'}{|\nabla\Psi| r_o^3 (1 - k^2)} \{-R'\Psi_R E(k)$$

$$+ \frac{1}{k^2} [R\Psi_R + (z-z')\Psi_z]x$$

$$[(2 - k^2)E(k) - 2(1-k^2)K(k)]\} \tag{20}$$

and

$$L(\ell,\ell') = \frac{4}{|\nabla\Psi| r_o^3 (1-k)^2} \{[R\Psi_z - (z-z')\Psi_R]E(k)$$

$$- \frac{R'\Psi_z}{k^2}[(2-k^2)E(k) - 2(1-k^2)K(k)]\} \qquad (21)$$

where

$$\sigma = [\Psi_z\Psi_{xR} - \Psi_R\Psi_{zz}]/|\nabla\Psi|, \quad k = \{4RR'/[(R+R')^2$$

$$+ (z-z')^2]\} \text{ and } r_o = 2\sqrt{RR'}/k.$$

The functions E(k) and K(k) are complete elliptical integrals of the first and second kinds. The general criteria C_h, C_f and C_v have been evaluated numerically using as input the plasma pressure profile and shape generated by MHD equilibrium calculations.[5]

III-B-2. Calculational Results

The optimal size for TETR has been determined to be a machine with a major radius of about 3 m and a plasma half width of about 0.5 m.[1] The initial plasma current was chosen to be 2.4 MA. The other parameters were B_o = 4.0 T, β_θ = 3.0 and the shape factor, S, the ratio of the plasma circumference to the largest inscribed circle, about 1.8. These parameters will give sufficient power density and are simply estimated from the scaling law

$$P_{nw} \cong 6.15 \times 10^{-4} \left(\frac{B_T}{q_{max}}\right)^4 \beta_\theta^2 \left(\frac{V_p}{A_w}\right) \qquad (22)$$

where P_{nw} is the neutron wall loading, B_T is the toroidal field (kgauss), q_{max} is the safety factor at the edge, β_θ is the poloidal beta, V_p is the plasma volume and A_w is the first wall surface area. This formula was obtained

using the optimized values of Γ, the fast ion pressure/bulk plasma pressure, and the fusion power gain, Q, by assuming T_e is 5 keV and the neutral beam injection energy is 200 keV.[1] For convenience, we have replaced A_w by the area of the plasma in our survey calculation.

A general decision was made prior to performing any detailed calculations to place the EF coils inside the TF magnets. The reasons are that it is difficult to shape the plasma when the coils are too far away and the currents in these coils would be large, relative even to the plasma current. This would in turn influence the power requirements during start-up and shut-down.

We have investigated two extreme cases in an effort to understand the relationship between plasma MHD equilibrium and stability and various engineering constraints. In the first case, case A, superconducting EF coils are located outside the blanket region. The plasma is highly elongated at the cost of other problems, such as stability and unusual plasma current profiles. In the second case, case B, normal coils are located as close to the plasma as possible (even within the blanket region.) This provides the most highly elongated yet stable plasma with a reasonable current profile. A comparison of the coil arrangement and plasma shape for both cases is shown in Fig. III-B-1. The pressure and current density profiles are plotted as a function of major radius on the midplane in Fig. III-B-2 and the vacuum equilibrium field is shown in Fig. III-B-3. Table III-B-1 lists the plasma parameters and power output for both cases.

The criteria for obtaining the solutions are that $q(\Psi)$ should be greater than 1 and that the plasma should satisfy the local stability criteria. Stability with respect to rigid motion is ignored for the time being.

The plasma in case A provides the required neutron power density and wall

Fig. III-B-1 - Two MHD equilibria with different external coil locations. Case A uses coils far from the plasma and the plasma is highly elongated. Case B uses more external coils of lower current closer to the plasma.

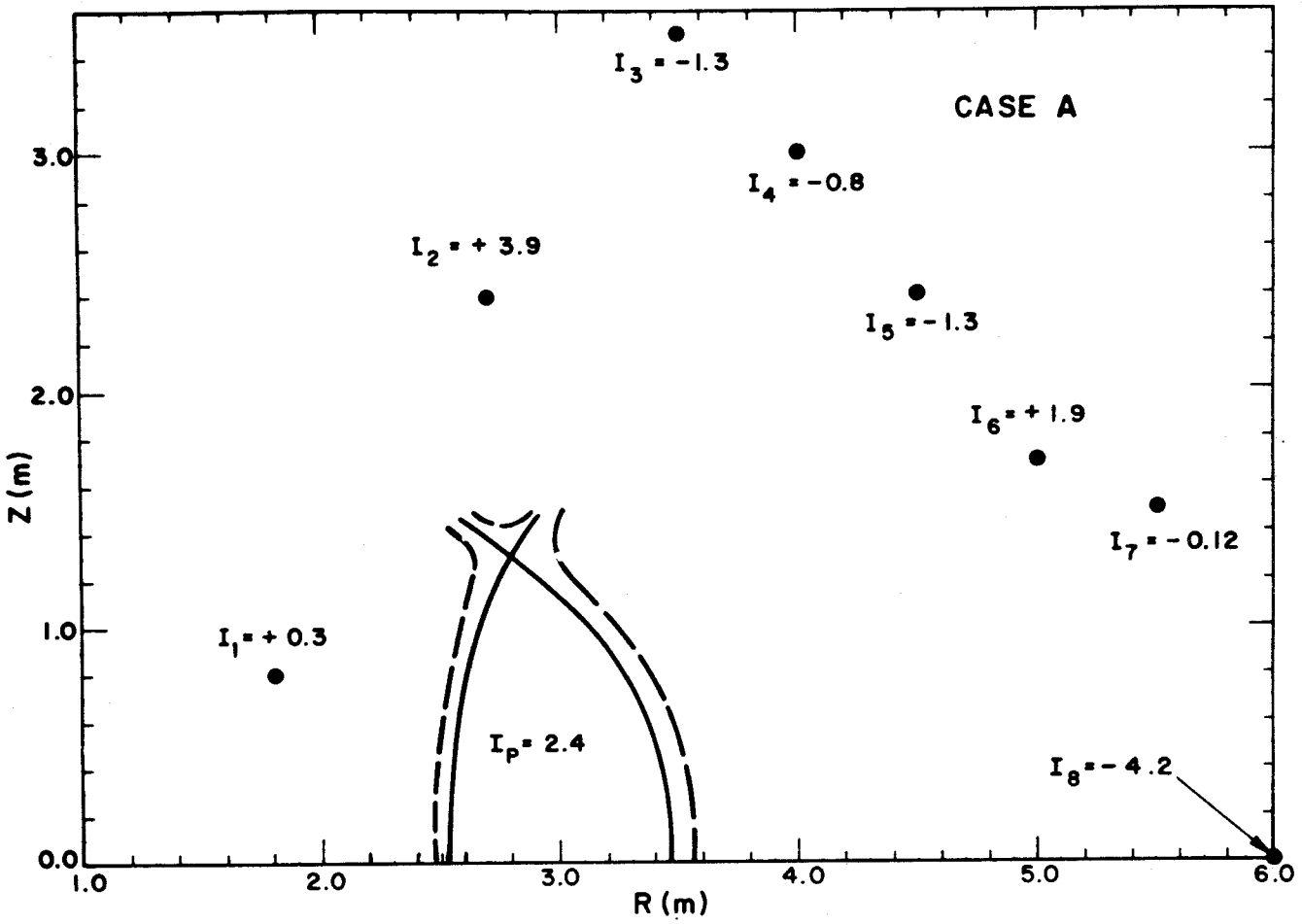

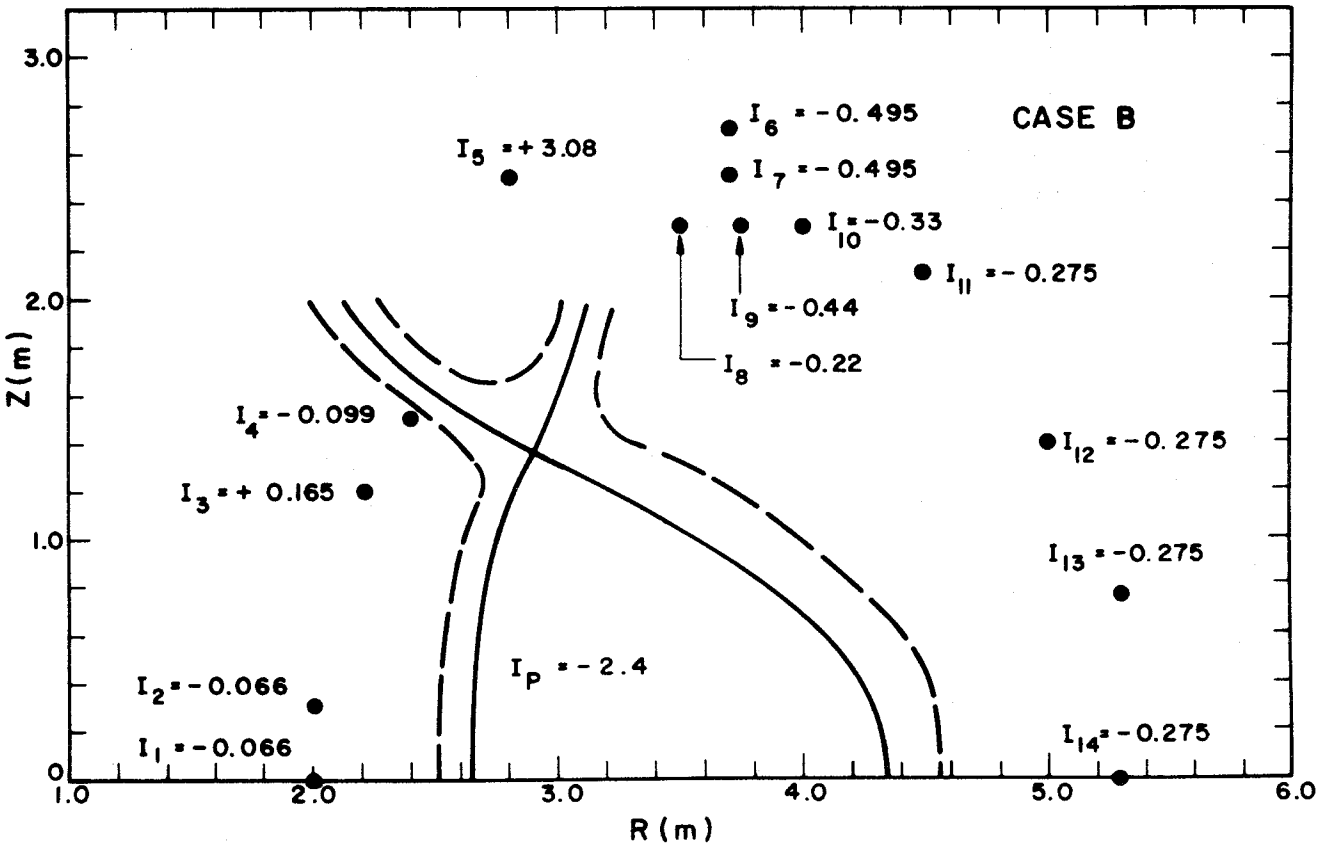

Figure III-B-2 - Plasma current and pressure profiles for the equilibria, cases A and B, described in the text.

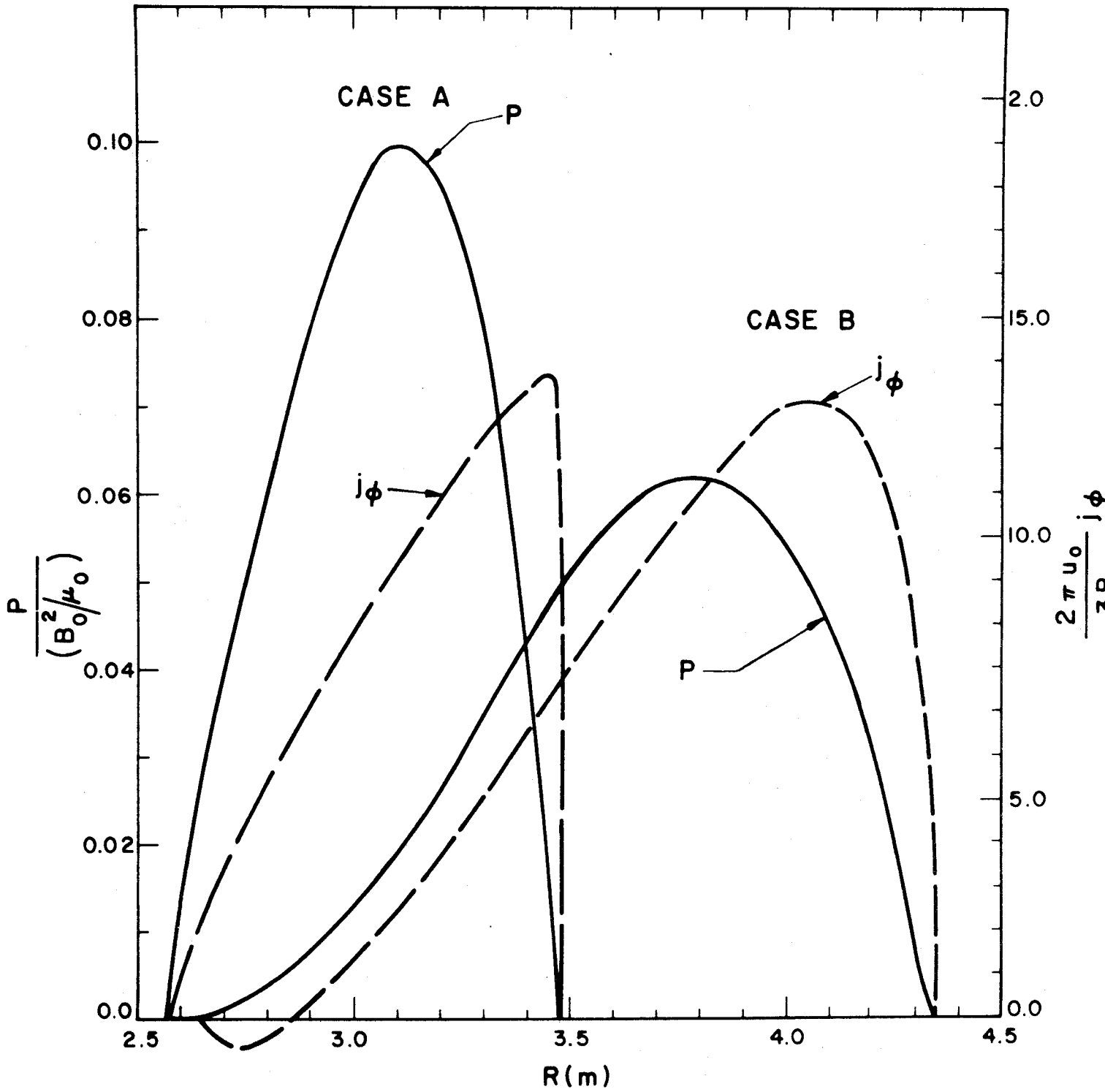

Figure III-B-3

Vacuum Vertical Fields for Cases A & B

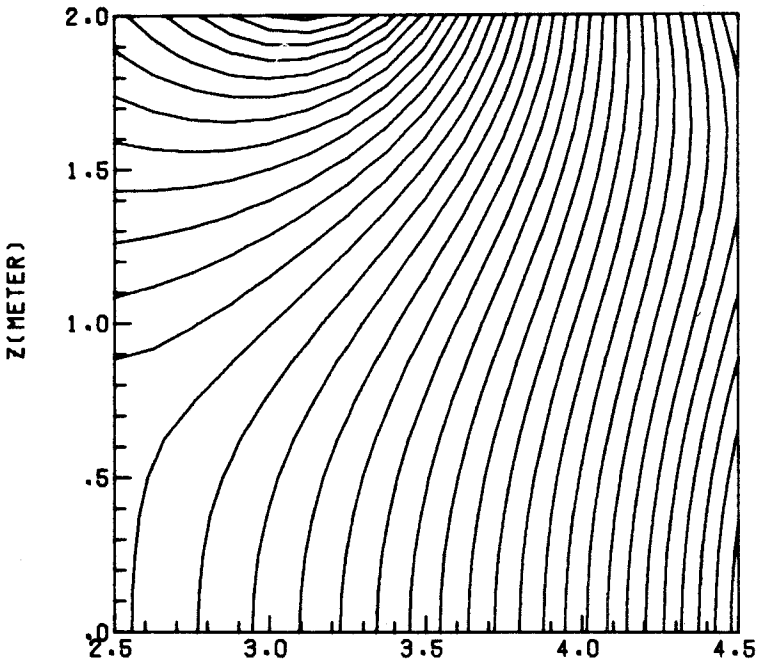

CASE A

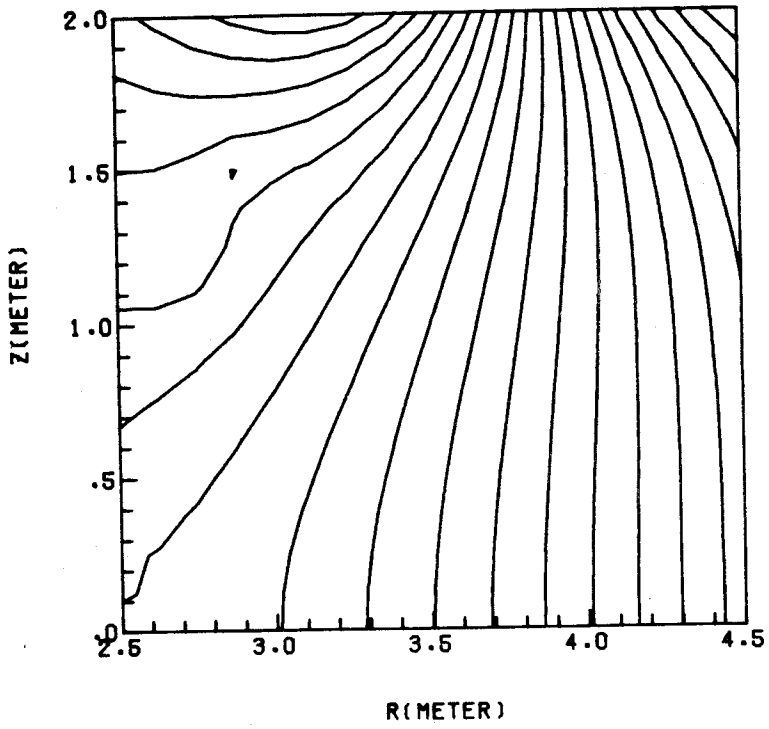

CASE B

Table III-B-1

Plasma Parameters for the MHD Equilibrium Cases A and B

	Case A	Case B
I_p(MA)	2.4	2.4
B_T(T)	4.0	4.0
B_{max}(T)	85.0	92.3
R_o(m)	3.0	3.46
R_m(m)	3.1	3.80
b/a	2.75	1.6
a(m)	0.46	0.86
A	6.5	4.1
β_θ	3.5	3.0
S	2.0	1.4
q_{max}	2.6	3.0
A_w(m^2)	109	135
V_p(m^3)	32	74
P_{nw}(MW/m^2)	1.13	0.60

loading ($\sim$1.1 MW/m^2). However, analysis shows this plasma to be highly unstable against the vertical motion and the currents in the superconducting EF coils are very large. Rapid pulsing of such magnets is probably not consistent with the constraint on the TETR design that technologies be reasonably available in the mid-1980's. (This does not imply steady state superconducting toroidal fields cannot be assumed. Indeed, these should be available given the present magnet development program plans).

In case B, the plasma elongation is less ($\frac{b}{a}$ = 1.6) and the major radius R_o, and the plasma width, a, are larger than in the previous case. Thus, the reactor is somewhat larger. The coil arrangement has been optimized to give the largest possible elongation consistent with the gross rigid motion stability. (This is possible because the coils are now much closer to the plasma). The currents in the external coils are relatively small (less than 0.5 MW) except for the null-defining coil which is about 3.1 MA. However, this design only produced about 0.5 MW/m^2 for the neutron wall loading, far from the design goal for this machine.

The results from these two extreme cases indicate that one should use normal EF coils and a plasma with intermediate elongation which, when combined with the variation of other parameters such as B_T, β_θ, A and I_p, will produce at least 1 MW/m^2 neutron wall loading.

One obvious possibility is to increase the size of the device to produce greater flexibility but this has the undesirable effects of increasing costs and increasing the volume of the plasma. In turn, this increases the beam power required to maintain the plasma temperature and, overall, is an undesirable solution. We have, therefore, taken the cue from several recent

experiments such as Rector and Versator[9] and studied the use of feedback stabilization of the plasma loop. Our analysis shows that plasmas which are mildly unstable against rigid motions can be stabilized with a reasonable feedback system. Thus, we have searched for a mildly unstable plasma equilibrium of smaller size which would nevertheless produce an acceptable neutron wall loading. (By mildly unstable, we mean plasma where the decay index of the vacuum vertical field, $n = -\frac{1}{B_\perp}\frac{dB_\perp}{dr}$, is between 0 and -2). Based on case B summarized in Fig. II-B-1 and Table II-B-1, we have obtained a series of MHD equilibria with different plasma parameters and coil arrangements. Five most typical cases are summarized in Table III-B-2. The plasma shapes for cases I and IV are similar and are shown by the solid curve in Fig. III-B-4. The plasma shape for cases II and III are also similar and are indicated by the dashed curve in the same figure. The shaded squares show the arrangement for the external EF coils in the case IV.

All these cases present one or another difficulty. For example, the plasma in case I has a large shape factor, S = 1.55, and a small but negative decay index, n = -0.85. However, because of the presence of EF coils near the midplane, accessibility is poor for beams and test modules. Space for beam and test modules are provided in case IV but to obtain a shape like that in case I, the external midplane coil had to be moved closer to the plasma which left only 85 cm for the blanket and shield. Nevertheless, the beam port can be placed immediately underneath the midplane clear of the coils and shield. The entire space above the midplane is available for test modules. These are shown by the drawing of the cross sectional view of the final design in Fig. III-B-5.

Table III-B-2

Plasma Parameters for the MHD Equilibrium Cases I to V

	I	II	III	IV	V
I_p(MA)	2.4	2.4	2.4	2.4	2.4
B_T(T)	4.68	4.68	4.68	4.68	4.68
B_{max}(t)	10.0	10.0	10.0	10.0	10.0
R_o(m)	3.20	3.22	3.22	3.22	3.2
R_m(m)	3.35	3.35	3.35	3.35	3.3
a	0.62	0.65	0.65	0.62	0.62
b/a	2.0	1.9	1.88	2.0	2.0
A	5.2	4.95	4.95	5.1	5.2
β_θ	3.0	3.0	3.0	3.0	3.06
S	1.55	1.40	1.40	1.55	1.55
q_{max}	3.27	3.3	3.28	3.28	2.4
A_w(m^2)	120	125	125	120	118
V_p(m^3)	42.5	45.5	45.5	43.0	42.5
n	-0.85	-0.9	-1.5	-2.0	-2.0
P_{nw}(MW/m^2)	0.6	0.5	0.5	0.7	2.2

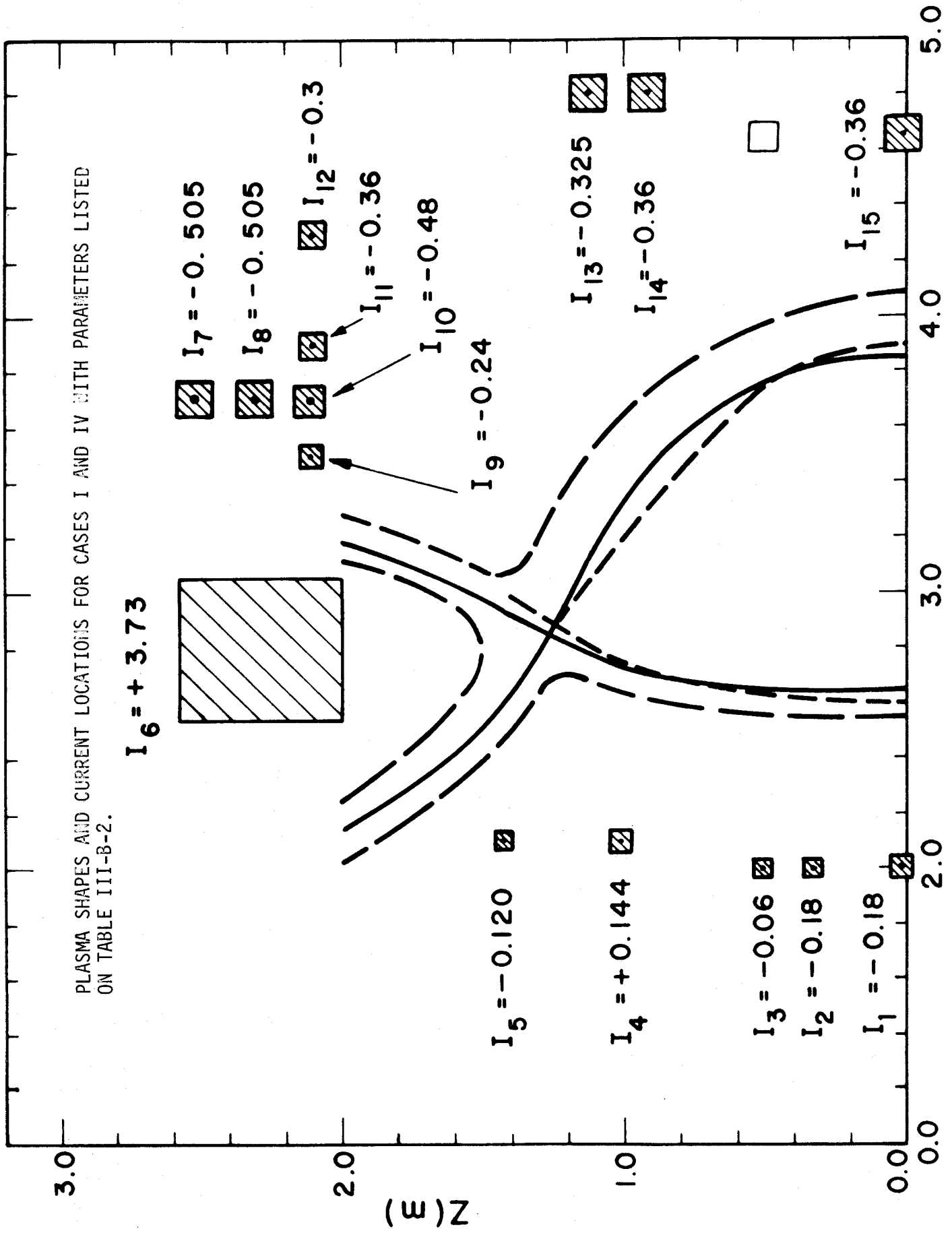

Figure III-B-4

Figure III-B-5 - Cross Sectional View of TETR

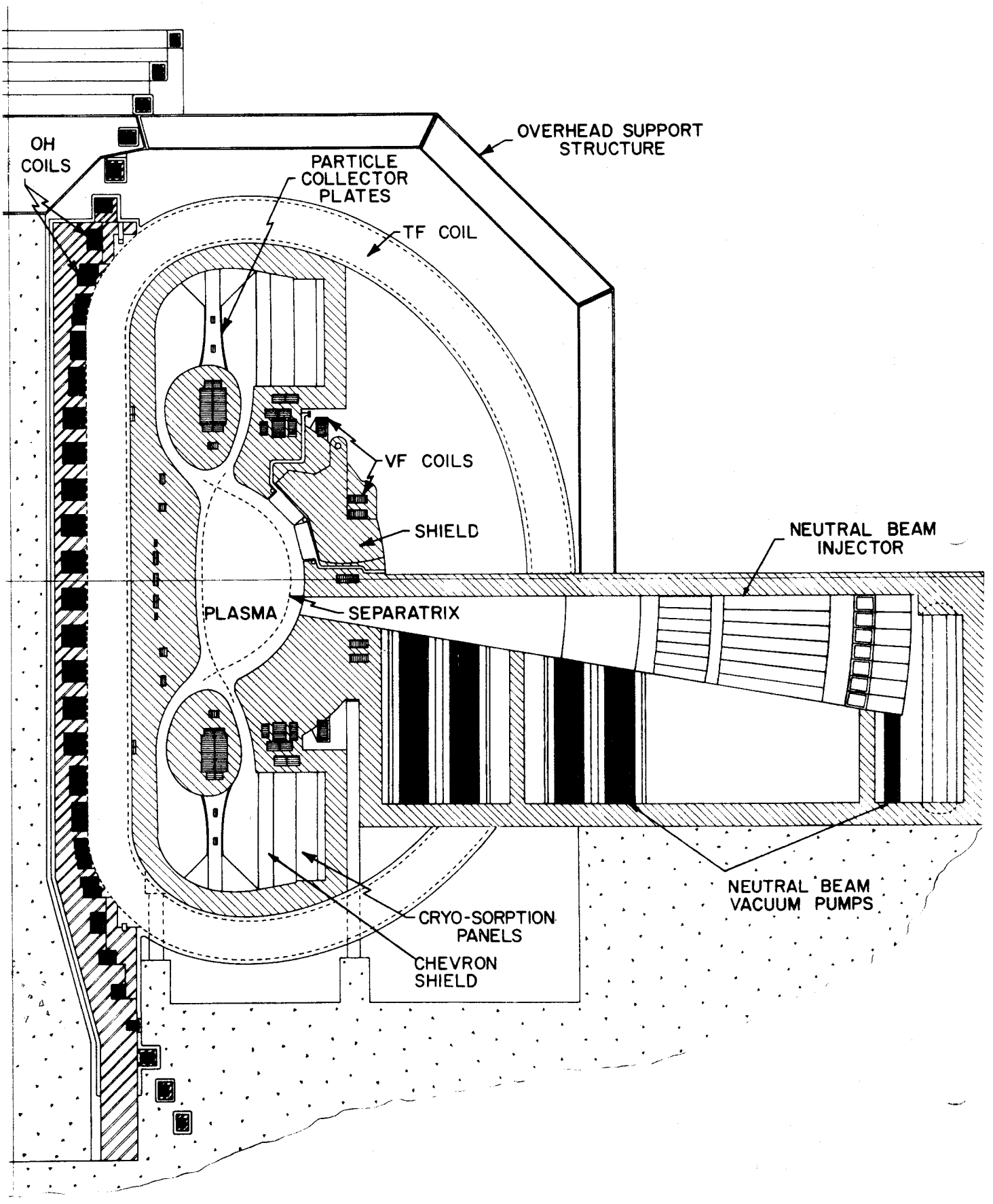

The plasma parameters for the four cases listed in Table III-B-2 are similar. The power density and neutron wall loading cannot be increased simply by increasing B_T and S because q and A will increase such that the ratio $(\frac{B_T}{q_{max}} \frac{S}{A})$ changes little.

In case V, the plasma current has been raised to 2.9 MA with $q_{max} = 2.4$. The wall loading is now 2.2 MW/m^2 while the EF coil arrangement is the same as for case IV except that the coils carry slightly different currents. Note that in all cases, the maximum field is 10 T and the on-axis field is 4.68 T.

Design number 5 in Table III-B-2 would meet the goal of the proposed TETR machine if the technology for building 10 T superconducting coil can be presumed for the mid-1980's. This may prove feasible and would ease the problems of developing a high neutron flux machine for either TETR or a tokamak hybrid application. We have taken as a base case the design of a device with a maximum toroidal field of 8.5 T. To meet this stringent constraint, the inner leg of the TF coil is moved outward 10 cm compared to the previous cases. Then with $B_{max} = 8.5$ T, B_T on axis is reasonably high, 4.2 T. In addition, I_p has been reduced while keeping q_{max} at about 2.5 to yield a higher β_θ. To compensate the loss of space, the distance between the first wall and the plasma on the inside is only 10 cm. The final value of β_θ is 3.8 and the total β is 0.066, quite reasonable values. There may be some local transport activity near the magnetic axis due to MHD effects because q is less than 1 there. However, the $n\tau_E$ requirement is not large in a two component device so low q operation should be acceptable. The final TETR plasma design is summarized in Table III-B-3 and Table III-B-4. They contain a list of the poloidal field coils. The plot

Table III-B-3

Final Plasma Parameters for TETR from MHD Analysis

R_o = 3.25 m

R_m = 3.37 m

R_{in} = 2.65 m

R_{out} = 3.85 m

a = 0.6

b = 1.20

b/a = 2.0

S = 1.53

A = 5.42

V_p = 41.6 m^3

A_w = 115 m^2

B_T = 41.9 Kgauss

B_{max} = 85 Kgauss (at R = 1.60 m)

β_θ = 3.8

q_o = 0.95

q_{max} = 2.5

I_p = 2.52 MA

n = -2.0

B_θ = 3.7 KGauss

$\bar{p}$ = 0.49 x 10^6 joules/m^3

β(total) = 0.066

Table III-B-4

Equilibrium Field Coil Arrangement

#	Z	R	I(MA)
D1	0.0	2.0	-0.165
D2	0.3	2.0	-0.165
D3	0.5	2.0	-0.165
D4	1.0	2.1	+0.132
D5	1.4	2.1	-0.110
D6	2.3	1.7	-0.132
†D7	3.2	2.8	+0.066
†D8	3.6	2.8	+0.066
*D9	1.85	2.8	+0.186
*D10	2.1	2.8	+0.477
*D11	2.2	2.8	+0.477
*D12	2.3	2.8	+0.477
*D13	2.4	2.8	+0.477
*D14	2.5	2.0	+0.477
*D15	2.6	2.9	+0.477
*D16	2.7	2.8	+0.239
D17	2.3	3.7	-0.462
D18	2.1	3.7	-0.440
D19	2.5	3.8	-0.473
D20	2.1	3.5	-0.220
D21	2.1	3.9	-0.330
D22	2.1	4.3	-0.275
D23	1.1	4.8	-0.297
D24	0.9	4.8	-0.330
D25	0.0	4.65	-0.330

of the surfaces on constant Ψ is shown by Fig. III-B-6. A perspective of the pressure and current profiles are presented in Figs. III-B-7 and III-B-8. respectively, while the vacuum vertical field is shown by Fig. III-B-9. Stabilization of the vertical instability by a feedback system is required and, as mentioned, experience on several experiments indicates this to be feasible. A detailed analysis of the feedback requirements for TETR is given in the next section, III-C. For construction reasons, the null-defining coil is split into six coils on top of one another, as indicated by asterisks in Table III-B-4. Three additional coils (indicated by a †) are added to spread the field lines near the separatrix at the top of the divertor to lower the particle power density and ease the particle collection problem in the divertor.

In summary, an optimized system of poloidal field coils has been developed for a small, high power density tokamak device which will produce elongated "D" shaped MHD equilibrium plasma with a current of 2.52 MA, an axial toroidal field of 4.2 T, a shape factor of 1.54 at a poloidal β of 3.8. The aspect ratio is 5.4. This system can produce sufficient power to generate neutron wall loadings above 1 MW/m^2 and has ready accessibility to meet the design goals of TETR. A feedback stabilization system based on the existing EF coils is required to provide overall vertical stability of the current loop and this is described in section III-C.

Figure III-B-6

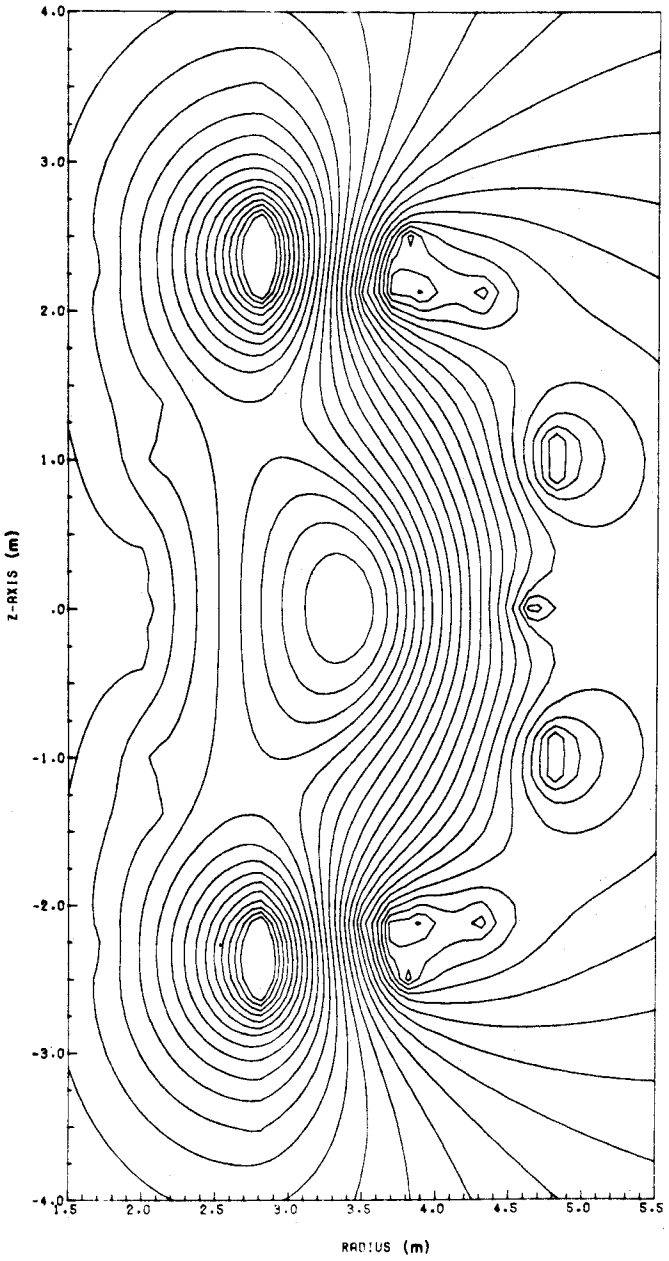

Flux Surfaces for the Final TETR Plasma Design

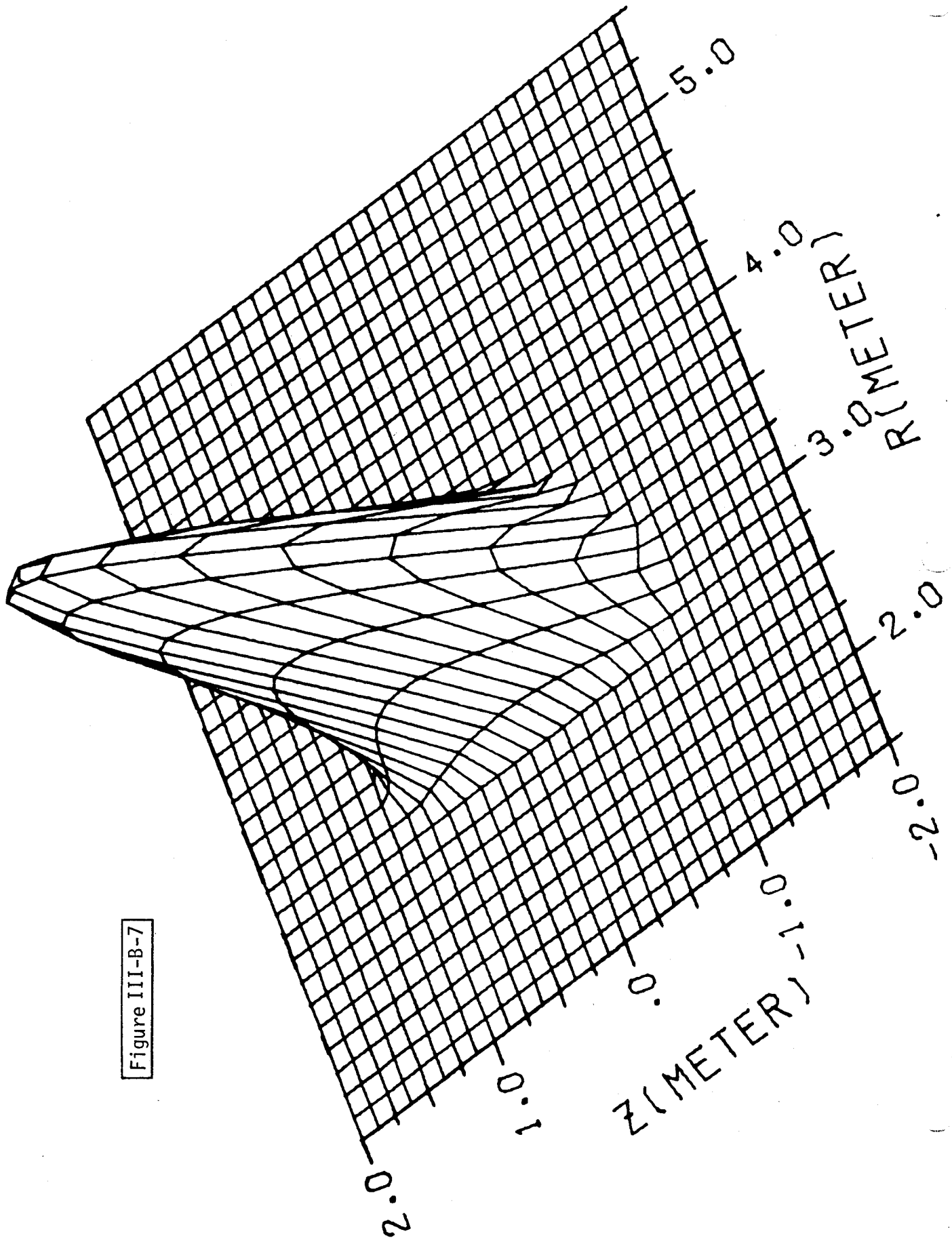

PLASMA PRESSURE PROFILE FOR THE FINAL TETR PLASMA DESIGN

Figure III-B-7

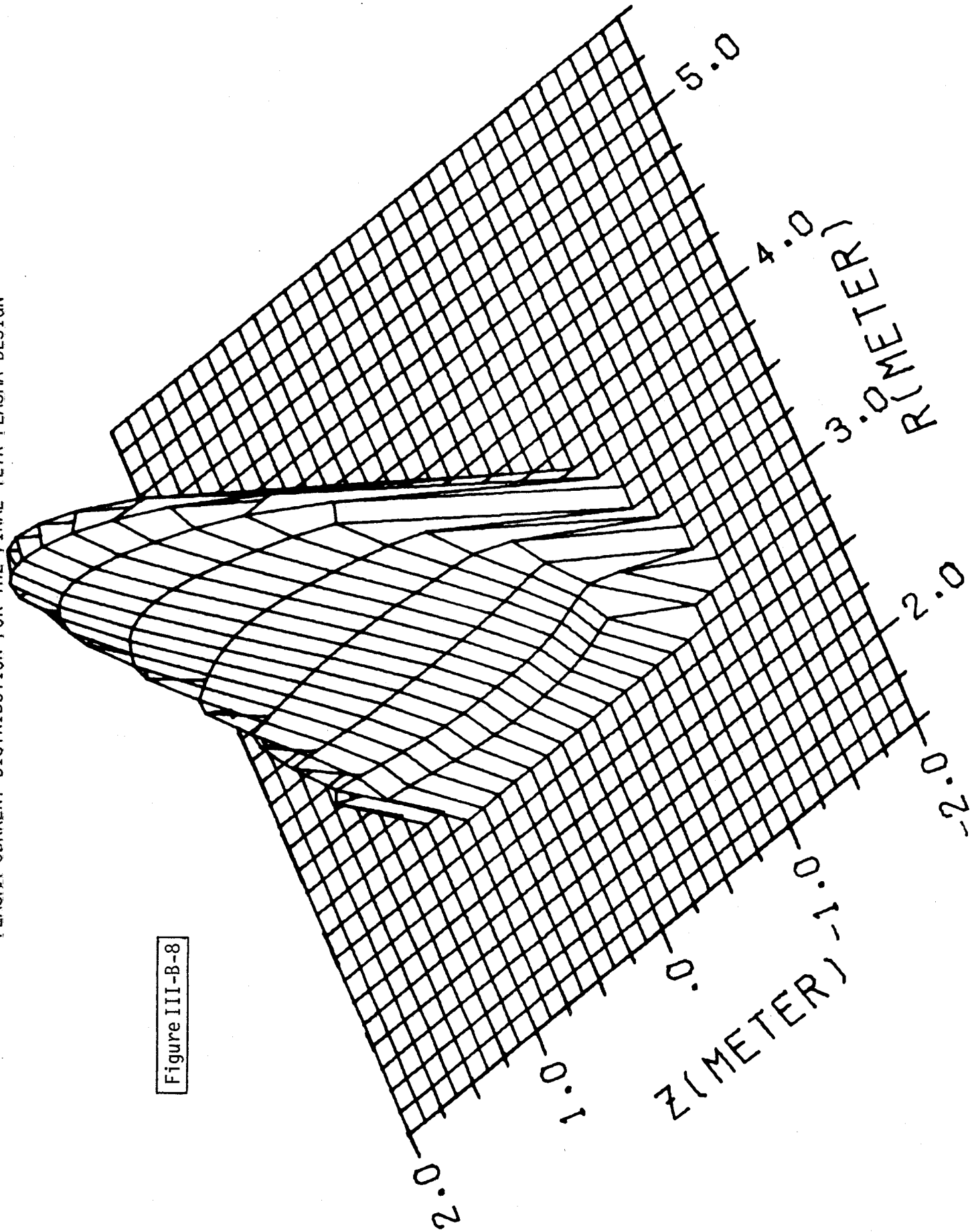

Figure III-B-8

PLASMA CURRENT DISTRIBUTION FOR THE FINAL TETR PLASMA DESIGN

VACUUM VERTICAL FIELD IN THE TETR DESIGN. THE DECAY INDEX IS NEGATIVE.

Figure III-B-9

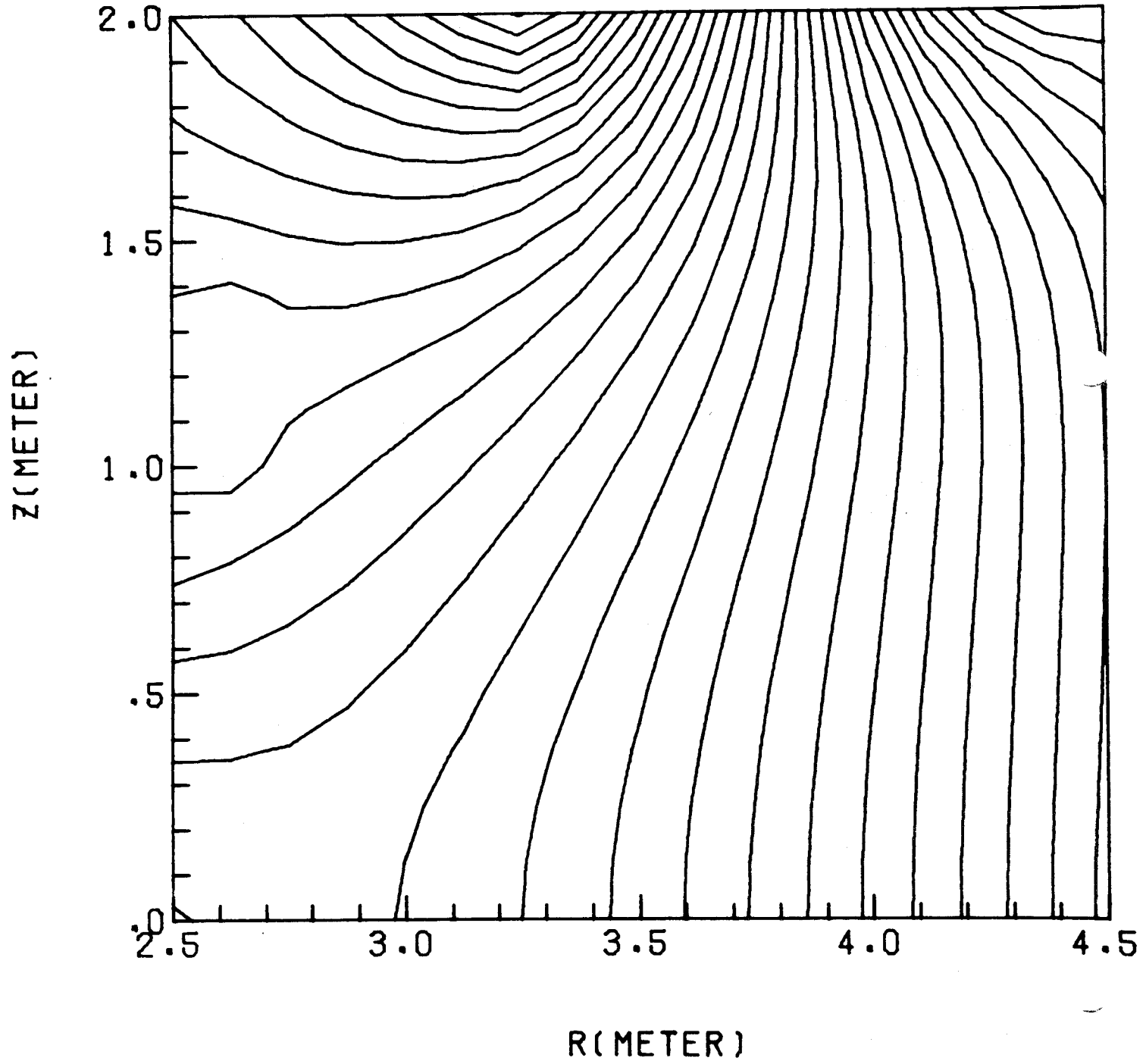

References for Section III-B

1. R. W. Conn and D. L. Jassby, "A Tokamak Engineering Test Reactor," in Proc. International Conf. on Radiation Test Facilities for the CTR Surface and Materials Program (Argonne National Laboratory, ANL/CTR-75-4, 1975) p. 592-624. Also UWFDM-119, University of Wisconsin and MATT-1155, Princeton Plasma Physics Laboratory Report (July 1975).

2. J. M. Dawson, H. P. Furth, F. H. Tenney, Phys. Rev. Lett., 26 1156 (1971). See also H. P. Furth and D. L. Jassby, Phys. Rev. Lett., 32, 1176 (1974).

3. B. Badger et al., "UWMAK-I , A Wisconsin Toroidal Fusion Reactor Design," UWFDM-68, Nuclear Engineering Department, Univ. of Wisconsin (Nov. 1973), Vol. 1.

4. M. S. Chance et al., Proc. 5th IAEA Conf. on Plasma Physics and Cont. Nucl. Fus. Research, 1974 (IAEA, Vienna, 1975) Vol. 1, p. 463.

5. T. F. Yang and R. W. Conn, "Computational Study of MHD Equilibrium on Non-Circular Tokamak Reactor Plasma," to be published in IEEE Trans. on Plasma Science.

6. L. E. Sakharov and V. D. Shafranov, Sov. Phys. Tech. Phys. 18, 151 (1973).

7. J. L. Johnson, J. M. Greene, Plasma Physics 9, 611 (1975).

8. A. H. Glasser, J. M. Greene, H. L. Johnson, Phys. Fluids 18, 875 (1975).

9. U. Ascoli-Bartoli, et al., 5th IAEA Conf. on Plasma Phys. and Cont. Nucl. Fus. Research, 1974 (IAEA, Vienna, 1975) Vol. I, p. 191.

10. S. Yoshikawa, Phys. Fluids 7, 278 (1964).

11. E. Rebhan, Nuclear Fusion 15, 277 (1975).

III-C. Feedback Stabilization System for TETR Plasma Position Control

The vertical magnetic field in TETR has the wrong curvature for vertical stability for reasons just discussed. The vertical position can, however, be feedback stabilized to keep the plasma properly centered. This has been accomplished for example, in the Versator experiment.[1] The plasma position is stable in the horizontal direction; variations in the plasma current or pressure may, however, cause the plasma to sit off-center horizontally. It is becoming common practice in present Tokamaks[2] to include a feedback loop to keep the plasma centered horizontally. This is technologically not very different from stabilization of the vertical position. In this section we present a linear stability analysis of the vertical position, including the effect of eddy currents in the conducting wall surrounding the plasma, and determine the necessary characteristics of the feedback system.

III-C-1. Dispersion Relation Without Feedback

Consider a plasma of major radius R carrying a toroidal current I and situated in an external transverse magnetic field which is slightly non-uniform. We assume the transverse field, coupled with the plasma current and toroidal field, produces the desired MHD equilibrium. We consider, for simplicity, a rigid displacement ε of the plasma along the Z-axis (symmetry axis). Because of the curvature of the magnetic field, the plasma experiences a radial component of B and hence a z-component of the Lorentz force:

$$F_z = 2\pi R\ I\ B_r(\varepsilon). \qquad (1)$$

We expand $B_r(\varepsilon)$ in a Taylor series about $\varepsilon = 0$, use $B_r(0) = 0$ and $\vec{\nabla} \times \vec{B} = 0$ to get

$$F_z = 2\pi R\ I \left.\frac{\partial B_z}{\partial r}\right|_0 \varepsilon, \qquad (2)$$

to the first order in ε. The equation of motion of the plasma is thus

$$\frac{d^2\varepsilon}{dt^2} + \omega_o^2 \varepsilon = 0, \tag{3}$$

where

$$\omega_o^2 = \frac{I B_z n_r}{\bar{n} m a R}, \tag{4}$$

and the decay index, n_r, is defined as

$$n_r = \frac{-R}{B_z} \frac{\partial B_z}{\partial r}\bigg|_o \tag{5}$$

$\bar{n}$ is the mean density of the ion species with mass m and a is the cross-sectional area of the plasma.

The plasma is vertically stable if $\omega_o^2 > 0$; this requires that the decay index n_r be positive. In TETR $n_r < 0$ so that $\omega_o^2 < 0$ and the plasma is unstable. The growth rate predicted by (4) ($\gamma_o = \sqrt{-\omega_o^2}$) is grossly incorrect because eddy currents in the conducting wall surrounding the plasma significantly slow down the plasma motion. Equation (4) predicts a growth rate of 7×10^5 sec $^{-1}$; we will see later that a 2 mm thick stainless steel wall reduces the growth rate to 1.3×10^3 sec $^{-1}$.

To develop the effect of eddy currents in the wall, we use a cylindrical model and neglect toroidal effects. The wall has a radius ρ_w and thickness δ, which is assumed to be much less than a skin depth for magnetic field penetration. This assumption is justified a posteriori. Let (ρ, θ, z) be cylindrical coordinates as shown in Fig III-C-1. For $\rho > \rho_o$, the plasma radius, the magnetic vector potential of the plasma is

$$A_z^{(o)} = \frac{-\mu_o I}{2\pi} \ln \rho$$

We displace the plasma a distance ε in the y direction; the vector potential then becomes

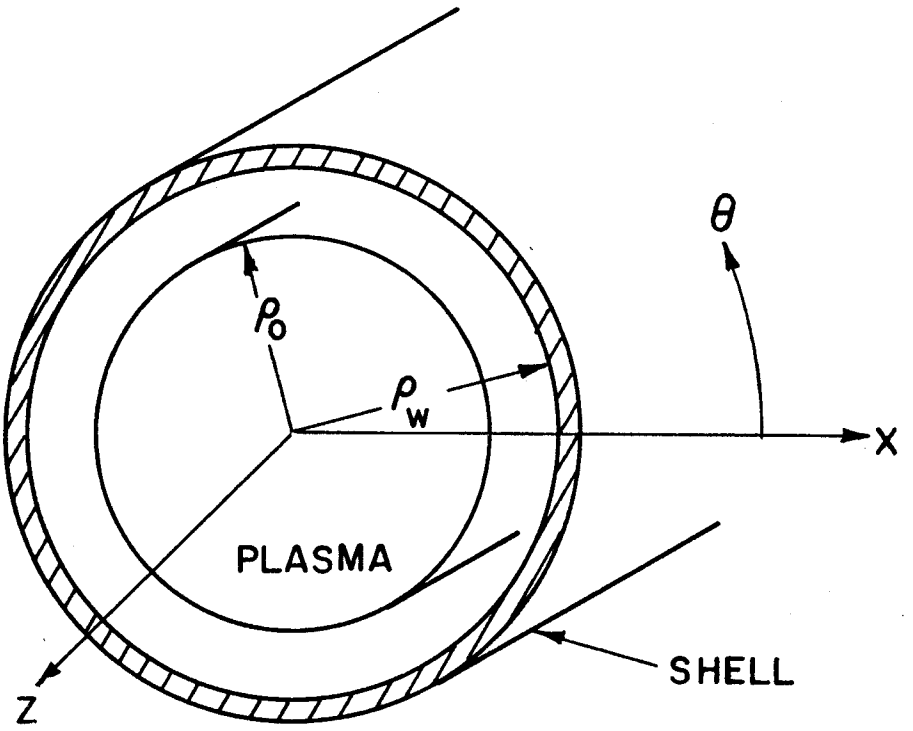

Figure III-C-1

GEOMETRY FOR FEEDBACK ANALYSIS

$$A_z \rightarrow A_z^{(1)} = \frac{-\mu_o I}{2\pi} \ell n(h),$$

where h is the distance from the new location of the plasma center. Now, by the law of cosines,

$$h^2 = \rho^2 + \varepsilon^2 - 2\rho\varepsilon \sin\theta,$$

so that

$$A_z^{(1)} = A_z^{(0)} + \frac{\mu_o I}{2\pi} \frac{\varepsilon}{\rho} \sin\theta \tag{6}$$

to first order in ε.

The electric field induced by the plasma motion is

$$E_z = - \frac{\partial A_z}{\partial t} = - \frac{\mu_o I}{2\pi\rho} \frac{d\varepsilon}{dt} \sin\theta \tag{7}$$

for $\rho > \rho_o$.

Since $E_z \sim \sin\theta$, the eddy currents in the wall will be of the form

$$J_z = J_o \sin\theta, \tag{8}$$

where J_o can be assumed to be uniform over the radial thickness of the shell since $\delta << \rho_w$ and $\delta <<$ skin depth. It is a standard E-M field theory problem to show that the current density profile in (8) produces a uniform B_x inside the shell ($\rho < \rho_w$),

$$B_x = \frac{\mu_o J_o \delta}{2}, \tag{9}$$

and a linear dipole field for $\rho > \rho_w$.

The next step is to develop a "circuit" equation for J_o that includes the self-inductance of the eddy currents. Consider the path shown in Fig.III-C-2. We apply the integral form of Faraday's law to this path

$$\int \vec{E} \cdot d\vec{l} = E_o = - \frac{d}{dt} \Phi$$

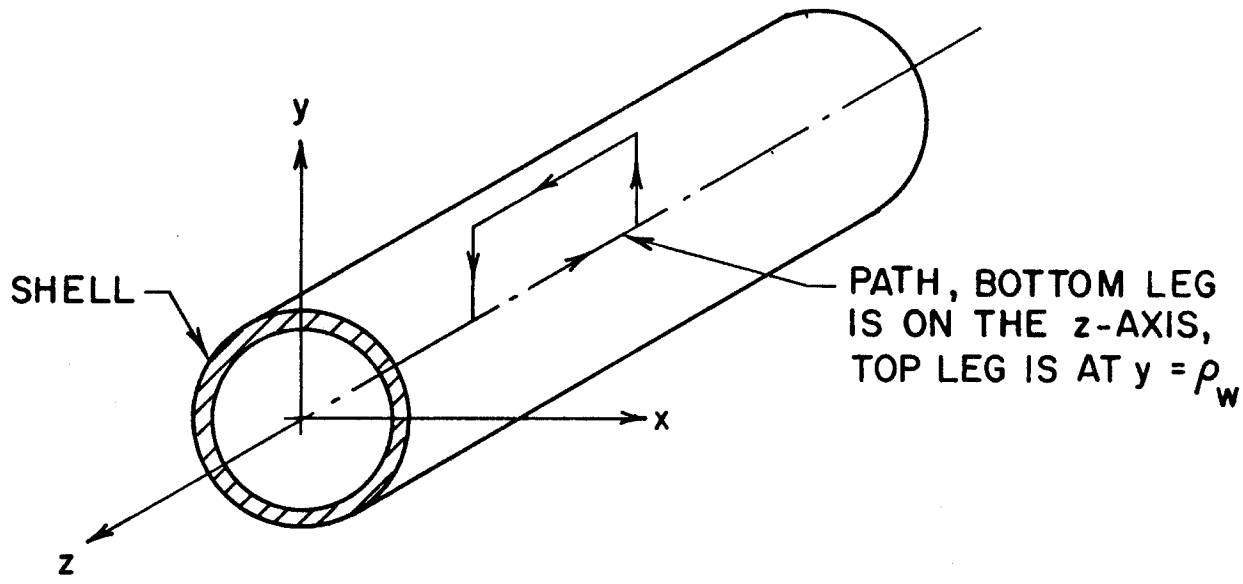

FigureIII-C-2

PATH FOR LINE INTEGRAL

where E_0 is magnitude of E_z at $\theta = \pi/2$ and Φ is the net magnetic flux enclosed by the path. Now

$$\Phi = \Phi \text{ (plasma)} + \Phi \text{ (shell)},$$

where $$\Phi \text{ (shell)} = \frac{\mu_o \delta}{2} J_o \rho_w$$

and $$-\frac{d\Phi}{dt} \text{ (plasma)} = \int \vec{E}(\text{pl}) \cdot d\vec{l} = -\frac{\mu_o I}{2\pi\rho_w} \frac{d\varepsilon}{dt}.$$

Also we use Ohm's law, $J_o = \sigma E_o$, for the shell, to get

$$\frac{J_o}{\sigma} + \frac{\mu_o I}{2} \rho_w \frac{dJ_o}{dt} = \frac{-\mu_o I}{2\pi\rho_w} \frac{d\varepsilon}{dt}. \tag{10}$$

This equation determines the time evolution of $J_o(t)$ given $\varepsilon(t)$. But $\varepsilon(t)$ is determined by

$$2\pi R \bar{n} m a \frac{d^2\varepsilon}{dt^2} = 2\pi\, RI \left(\frac{-n_r B_z}{R} \varepsilon + \frac{\mu_o J_o \delta}{2} \right).$$

The last term is the effect of the magnetic field produced by the eddy currents. We can rewrite this equation as:

$$\frac{d^2\varepsilon}{dt^2} + \omega_o^2 \varepsilon = \frac{\mu_o \delta I}{2 \bar{n} m a} J_o. \tag{11}$$

Equations (10) and (11) are the coupled set of equations that determine the growth rate of the vertical positional instability.

To get a dispersion relation from (10) and (11), it is sufficient to assume a time-dependence of the form $e^{-i\omega t}$. We eliminate J_o and ε to get the dispersion relation:

$$\omega^2 + \frac{i\alpha\omega}{1 - i\beta\omega} - \omega_o^2 = 0, \tag{12}$$

where ω_o is the same as before and

$$\alpha = \frac{\mu_o^2 I^2 \delta\sigma}{4\pi\rho_w \bar{n} m a}, \tag{13}$$

$$\beta = \frac{\mu_o \sigma \delta \rho_w}{2}. \tag{14}$$

Equation (12) is a cubic equation with three roots; it can be solved using standard formulas. The interesting root, however, occurs for $\omega \sim \omega_o^2/\alpha << \omega_o$. This suggests that we drop the ω^2 term to get

$$\omega = \frac{i \gamma_o^2}{\alpha(1 - \beta\frac{\gamma_o^2}{\alpha})} \tag{15}$$

where $\gamma_o^2 = -\omega_o^2$. One can show that the other two roots of (12) correspond to high frequency damped oscillations. If we assume a 2 mm thick stainless steel wall at $\sim 350^oC$, the growth rate predicted by (15) for TETR is 1.3×10^3 sec $^{-1}$ which is three orders of magnitude smaller than the growth rate without eddy currents. The eddy currents have a very strong effect on the motion of the plasma. The self-inductance of the shell is accounted for in the $1 - \frac{\beta \gamma_o^2}{\alpha}$ term in the denominator of (15); the effect of this term is to approximately triple the growth rate over what it would have been without the inductive effect included.

Equation (15) predicts a growth rate of 1.2×10^3 sec $^{-1}$ for Versator in the unstable configuration ($n_r = -1$). This growth rate is in reasonable agreement with the observed behavior in Versator and gives us some faith that our calculation is not totally incorrect.

The growth rate predicted for TETR is quite modest; it implies that a rise time of 0.3 msec of the feedback amplifiers ought to be sufficient. In comparison, the difficulty of the Scyllac[3] feedback system is that $\gamma \sim 10^6 \text{sec}^{-1}$ which requires an amplifier rise-time of less than 0.5 μsec. This is a much more difficult technological problem. On this basis, we are encouraged to incorporate a feedback loop in the TETR design to stabilize the vertical position.

III-C-2. Dispersion Relation with Feedback

We add a set of feedback coils outside the conducting shell. These coils are imagined to be equivalent to a surface current density proportional to $\sin\theta$ and thus produce a uniform B_r^{fb} feedback magnetic field. The equation of motion of the plasma becomes

$$2\pi R\, \bar{n} m a\, \frac{d^2\varepsilon}{dt^2} = 2\pi\, RI \left[-\frac{n_r B_z}{R}\,\varepsilon + \frac{\mu_o J_o \delta}{2} + B_r^{fb} \right] . \qquad (16)$$

The feedback coils also couple to the conducting shell and modify the eddy currents. The flux enclosed by the path in Fig. III-C-2 now includes a term due to B_r^{fb}. Thus

$$\Phi = \Phi\,(\text{plasma}) + \Phi\,(\text{shell}) + \Phi\,(\text{feedback}),$$

where $\frac{d}{dt}\,\Phi\,(\text{feedback}) = \rho_w \frac{dB_r^{fb}}{dt}$,

Thus, eqn. (10) is modified to become

$$\frac{J_o}{\sigma} + \frac{\mu_o \delta \rho_w}{2}\frac{dJ_o}{dt} = -\frac{\mu_o I}{2\pi\rho_w}\frac{d\varepsilon}{dt} - \rho_w \frac{dB_r^{fb}}{dt}. \qquad (17)$$

To close the feedback loop one specifies $B_r^{fb}(t)$ as a function of $\varepsilon(t)$. To keep the analysis general, we allow for the possibility of including velocity feedback as well as position feedback. Thus, we let

$$B_r^{fb}(t) = -G_1\ \varepsilon(t) - G_2\ \frac{d\varepsilon}{dt}, \tag{18}$$

where G_1 and G_2 are constants to be chosen.

We assume a time-dependence of the form e^{st} in (16), (17), (18) to get the dispersion relation

$$s^2-\gamma_o^2 + \frac{\alpha s}{1+\beta s}\ (1-g_1-g_2 s) + \eta g_1 + \eta g_2\ s = 0, \tag{19}$$

where
$$g_{1,2} = \frac{2\pi\rho_w^2}{\mu_o I}\ G_{1,2} \tag{20}$$

and
$$\eta = \frac{\mu_o I^2}{2\pi\bar{n}ma\rho_w^2} \tag{21}$$

We let $s = p/\beta$ and rewrite (19) as a polynomial

$$p^3 + p^2 + bp + c = 0, \tag{23}$$

where $b = \alpha\beta - \beta^2\gamma_o^2 + \beta g_2$

$$c = \beta^2(\eta g_1 - \gamma_o^2).$$

The Routh-Hurwitz array for the dispersion relation (23) is

p^3	1	b
p^2	1	c
p^1	c_1	o
p^o	c	

where $c_1 = b-c$. Stability ($R_e\ p < 0$) requires $c_1 > 0$ and $c > 0$. Thus we can feedback stabilize the plasma if

$$G_1 > \frac{(-n_r)\ B_z}{R}, \tag{24}$$

$$G_2 > \beta \left[G_1 - \frac{\mu_o I}{2\pi \rho_w^2} \right] \tag{25}$$

We see that for a given velocity feedback (G_2 = constant), there is an upper limit on G_1. To see the origin of this effect we consider the solution, to (23) when b and c are large ($\sim 10^6$ in our application). From Cardan's solution to the cubic equation, one can easily show that the roots are given approximately by

$$\begin{aligned} p_1 &= -\frac{c}{b} \\ p_{2,3} &= \frac{1}{2}\left(\frac{c}{b} - 1\right) \pm i\sqrt{b} \end{aligned} \tag{26}$$

The high-frequency roots are destabilized when c > b, which is the same as violating (25). When this occurs the feedback field reverses the direction of the eddy currents in the shell. This is destabilizing for the high frequency modes because they experience negative dissipation. The root p_1 is not destabilized because it is a purely damped mode (for c > 0) and the direct part of the feedback field is stronger than that produced by the eddy currents.

In TETR, the magnetic field diffusion time is 3×10^{-6} sec. The damping time of the low frequency root is $\sim 10^2 - 10^3$ sec $^{-1}$ and the frequency of the high frequency roots is 5×10^5 rad/sec. Consequently our assumption of the skin currents being uniform over the cross-section of the shell is valid (a posteriori justification) for the low-frequency root but questionable for the high frequency roots. These roots are probably more stable than indicated here because the shell contains the internal flux better (and excludes the feedback flux) at high frequency than we have supposed. Furthermore, one can avoid the coupling of the feedback loop to the high frequency motion (if it is a problem) by the insertion of a low-pass filter in the feedback loop. This

will have negligible effect on the low frequency behavior. Consequently, in the following analysis, we put $G_2 = 0$ and ignore the high frequency behavior of the plasma.

III-C-3. Effect of Time Delay in the Feedback Loop

We consider now the possibility that the feedback field is delayed from the instantaneous response. The primary source of such a time delay is the finite charging time of the feedback coils. For a voltage V(t) applied to a coil of resistance R and inductance L, the current is

$$I(t) = \frac{1}{L} \int_0^t V(t') \, e^{\frac{R}{L}(t'-t)} \, dt'. \tag{27}$$

If we apply a step current V at $t = o$, then the time to a given current I_o ($I_o \ll V/R$) is given by

$$\tau = \frac{I_o L}{V}, \tag{28}$$

and the rise is linear for $t < \tau$;

$$I = I_o \frac{t}{\tau} \tag{29}$$

Consequently one can shorten the rise time by increasing V for a given L and I_o. Technologically there are limits, however, on the voltage that can be applied. In this section we consider how short the time delay of the feedback loop must be in order to maintain stability.

Rather than consider a time delay characterized by (27) or (29), it is simpler (and conservative) to consider a pure time delay:

$$B_{fB}(t) = - G_1 \, \varepsilon \, (t - \tau_1) \tag{30}$$

where τ_1 is given by (28), or whatever else may be appropriate. We put this into eq. (16) and (17) to get

$$\frac{d^2\varepsilon(t)}{dt^2} - \gamma_o^2\varepsilon(t) + \frac{I}{\bar{n}ma} G_1\, \varepsilon(t - \tau_1) = \frac{\mu_o I\delta}{2\bar{n}ma} J_o(t)$$

$$J_o(t) + \beta \frac{dJ_o(t)}{dt} = -\frac{\mu_o I}{2\pi\rho_w} \frac{d\varepsilon(t)}{dt} + \rho_w G_1\, \varepsilon(t - \tau_1)$$

We use Laplace transforms to write these equations in the form

$$\tilde{J}_o\,(1 + \beta s) - \beta\, J_o(0) = -\frac{\mu_o I}{2\pi\rho_w}\,(s\,\tilde{\varepsilon} - \varepsilon(0)) + \rho_w\, G_1\, e^{-s\tau_1}\,[s\,\tilde{\varepsilon} - \varepsilon(0)]$$

$$s^2\,\tilde{\varepsilon} - \dot{\varepsilon}(0) - s\varepsilon(0) - \gamma_o^2\,\tilde{\varepsilon} + \frac{I}{\bar{n}ma}\, G_1\, e^{-s\tau_1}\,\tilde{\varepsilon} = \frac{\mu_o I\delta}{2\bar{n}ma}\,\tilde{J}_o,$$

where $\tilde{f}$ is the Laplace transform of $f(t)$.

The dispersion relation with time delay is thus

$$p^3 + p^2 + (\alpha\beta - \beta^2\,\gamma_o^2)p + \beta^2\,\eta g_1\, e^{-p\tau 2} - \beta^2\gamma_o^2 = 0$$

where $p = s\beta$, $\tau_2 = \tau_1/\beta$. All the other symbols are the same as before. Since we are interested only in the low-frequency behavior, we drop the p^3 and p^2 terms to get

$$p = p_o\,(1 - ae^{-p\tau 2}), \tag{31}$$

where

$$p_o = \frac{\beta\,\gamma_o^2}{\alpha(1 - \frac{\beta\,\gamma_o^2}{\alpha})}$$

$$a = \eta g_1/\gamma_o^2$$

To determine the conditions under which (32) possesses an unstable root, we use the method of Nyquist diagrams.

Lwt $x = p/p_o$, $\tau = p_o\tau_2$, and

$$F = x + ae^{-x\tau} - 1 \tag{32}$$

The dispersion relation is F = 0, and unstable modes correspond to Pe x > 0. Consider a mapping of the right half of the x-plane into the F-plane under the transformation (32), as shown in Fig. III-C-3a. For $|x| \to \infty$, $F(x) \to x$ when Re x > 0.

For x = iz, z real

$$\text{Re } F = -1 + a \cos z\tau$$

$$\text{Im } F = z - a \sin z\tau$$

Now Re F(0) = a - 1, Im F(0) = 0. Hence, Re F(z) oscillates between a - 1 and -(a + 1). The origin is enclosed, first of all, if a < 1 for any τ; this implies instability. Consequently, we need a > 1 as a necessary (but not sufficient) criteria for stability. This is our old result, eq. (24). If $a\tau < 1$, then Im F = 0 only at z = 0 and the Nyquist diagram is as shown in Fig. III-C-3b. For $a\tau > 1$, Im $F(z_o) = 0$ for $z_o \neq 0$ and the Nyquist diagram is as shown in Fig. III-C-3c. Stability is determined by Re $F(z_o) > 0$ so that the origin is not enclosed. Hence, for a given a > 1, the maximum τ is determined by Re $F(z_o) = 0$ where Im $F(z_o) = 0$ defines z_o.

This gives

$$\tau < \frac{1}{\sqrt{a^2-1}} \cos^{-1}\left(\frac{1}{a}\right),$$

as the limit on the time delay in order to maintain stability. Written in terms of more physical parameters, the result is

$$\gamma\tau_1 < \frac{1}{\sqrt{a^2-1}} \cos^{-1}\left(\frac{1}{a}\right), \tag{33}$$

where

$$a = \frac{RG_1}{(-n\gamma)B_z}, \tag{34}$$

and γ is the growth rate without feedback.

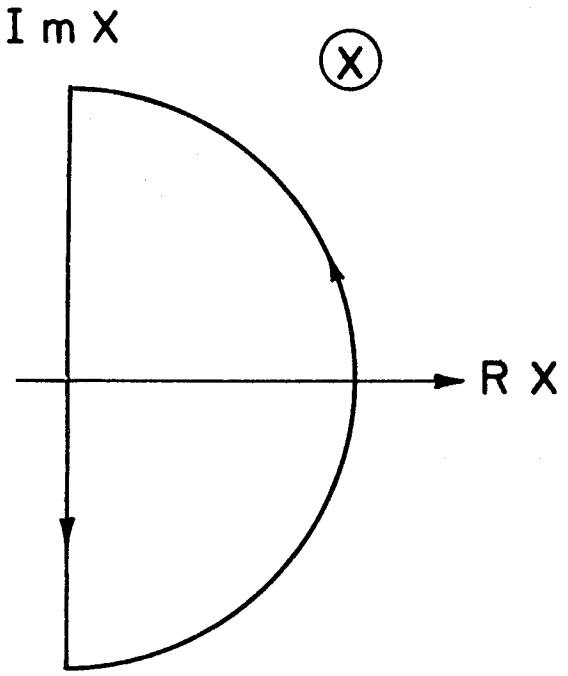

(a)

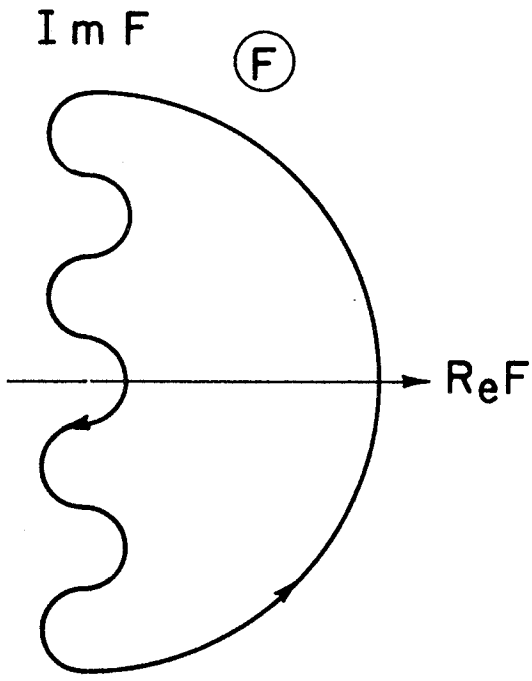

(b) $a>1$
$a\tau>1$

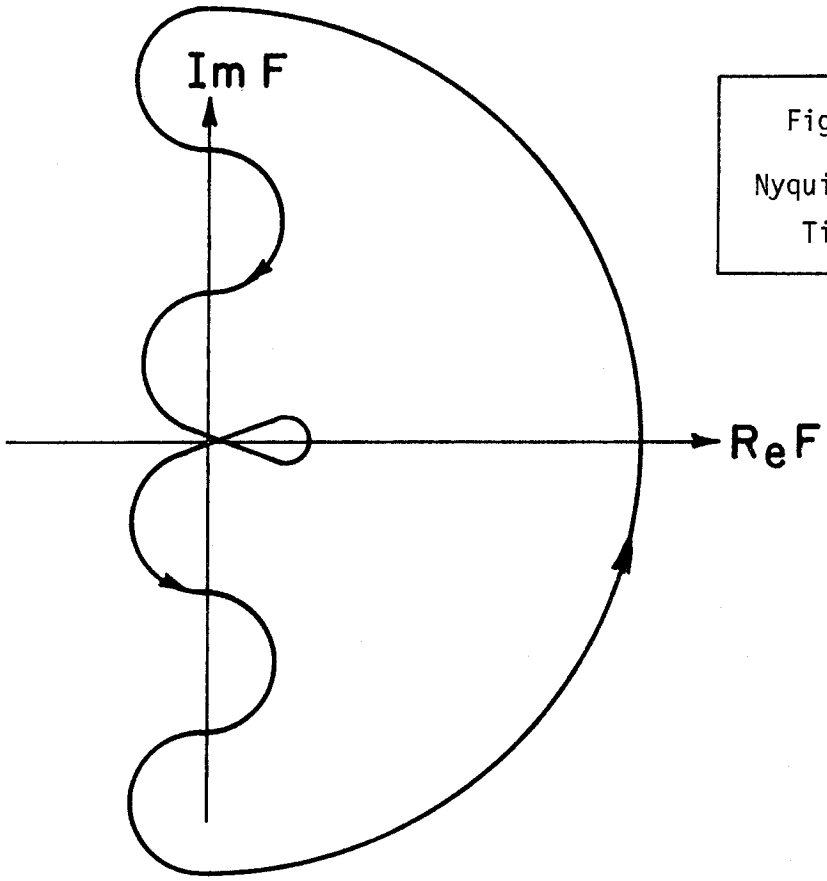

(c) $a>1$ $a\tau>1$

Figure III-C-3

Nyquist Diagrams for Time Delay

A second and more restrictive limit can be obtained by considering the transient response. Suppose the plasma is released at time t = 0 with an initial displacement $\varepsilon(o)$. The feedback system is "dead" until $t = \tau$, with a restoring force determined by $\varepsilon(0)$. Requiring that the restoring force be greater than the driving force on the plasma implies

$$G_1\, \varepsilon(0) > \left(\frac{-n_r B_z}{R}\right) \varepsilon(0)\, e^{\gamma\tau_1} ,$$

or

$$\gamma\tau_1 < \ln\ a \tag{35}$$

If this is satified, then the plasma motion is reversed at $t = \tau$ without further excursion from the equilibrium position. For τ between the limits defined by (33) and (35) the plasma experiences a greater excursing before eventually returning to the equilibrium position. The limit (35) needs to be treated with a certain degree of caution; it applies only if the motion is pure growth and decay. This ceases to be true when a is too large. In particular, (35) should not be used when it violates (33).

III-C-4. Minimization of the Required Power

We are now able to minimize the peak power demand on the feedback amplifier by appropriate choice of the gain and time delay. We again consider the transient response. The plasma is released at t = 0 from an initial displacement $\varepsilon(0)$ and the feedback system has a delay time τ_1. We assume that (35) applies. Thus, the behavior of $\varepsilon(t)$ and $B_{fB}(t)$ are as shown in Fig. 4. The maximum excursion occurs at $t = \tau_1$ but the maximum feedback field occurs at $t = 2\tau_1$. The jump in B at $t = \tau_1$ implies infinite power; this is unphysical. A better approximation for power calculations is to assume a straight line between t = o and $t = \tau_1$. The power peaks at $t = 2\tau_1$ and perhaps also at $t = T_1$.

FigureIII-C-4

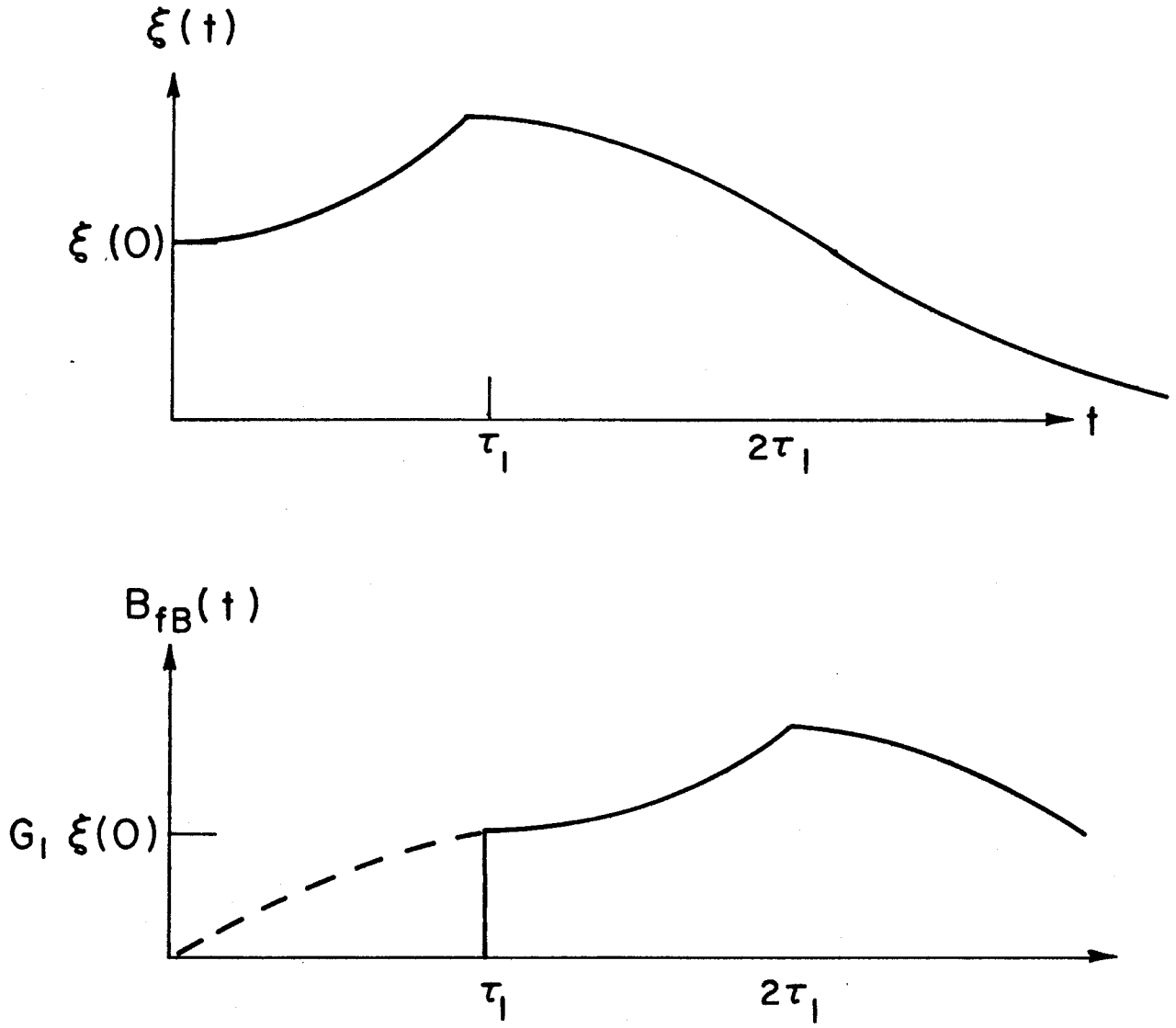

$\varepsilon(t)$ and $B_{fb}(t)$ during an excursion

$$P(2\tau_1) \propto \frac{d}{dt} B^2 \Big|_{t=2\tau_1} = 2\gamma G_1^2 \, \varepsilon^2(0) \, e^{2\gamma\tau}$$

$$P(\tau_1) \propto 2 \frac{G_1^2 \, \varepsilon^2(0)}{\tau_1}$$

Increasing τ_1 reduces $P(\tau_1)$ and increases $P(2\tau_1)$. Hence the optimum is obtained when they are equal. Thus

$$\gamma\tau_1 \; e^{2\gamma\tau_1} = 1$$

or
$$\gamma\tau_1 = .43 \tag{36}$$

Using (35) to determine a, we get

$$a \geq 1.537 \tag{37}$$

These values of $\gamma\tau_1$ and a satisfy (33) so that we are assured of a stable solution. The maximum excursion of the plasma during the transient is $1.54\varepsilon(0)$ and the peak power demand is

$$P = 4.7\gamma \, G_1^2 \, \varepsilon^2(0) \, K \tag{38}$$

where K is the stored magnetic energy per $(\text{gauss})^2$.

III-C-5. Application to TETR

The physical parameter for TETR, listed in Table III-C-1, are the values used in the feedback calculations. To provide the radial feedback field a small change in the current of eight of the divertor coils is made. For example, the ΔI values shown in Table III-C-2 produce a radial magnetic field of 50 gauss; this corresponds to a stored magnetic energy of 5 kJ for the feedback field. One might do better using a separate set of coils for the feedback system and placing them closer to the plasma. This system, however, is workable and sufficient to indicate the order of magnitude of the power requirements for the feedback amplifiers.

Table IIIC-1

TETR - Physical Parameters

Plasma current, I	2.5×10^6 A
Major radius, R	3.25 m
Cross-sectional area, a	2.04 m^2
Vertical field, B_z	3 kG
Decay index, n_r	-2
Average density, $\bar{n}$	1×10^{14} cm^{-3}
Ion mass	4.2×10^{-27} kg
Wall radius, ρ_w	1.4 m
Wall thickness, δ	2 mm
Wall conductivity	1.1×10^6 mho/m

Table III-C-2

Coil	I(nominal), MA	ΔI, amps
D 4 (top)	.132	2×10^3
D 4 (bottom)	.132	-2×10^3
D 5 (top)	-.110	5×10^3
D 5 (bottom)	-.110	-5×10^3
D 11 (top)	.477	10×10^3
D 11 (bottom)	.477	-10×10^3
D 17 (top)	-.220	10×10^3
D 17 (bottom)	-.220	-10×10^3

The rather complicated blanket and shield structure in TETR is modeled for these calculations by a 2 mm SS thick wall of radius 1.4 m. The 1.4 m radius corresponds to the half-height of the blanket. We have chosen this since the eddy currents have a $\sin\theta$ distribution and hence flow primarily at the top and bottom. The 2 mm thickness models the tubing comprising the blanket. This neglects eddy currents in the shield. The shield is composed primarily of stainless steel powder which because of contact resistance acts like an insulator. There will be some structure as well; by proper design this can be effectively segmented to minimize the effects of eddy currents in the structure.

The values of the relevant parameters for the feedback analysis are shown in Table III-C-3. We see that the growth time is indeed slower than the magnetic field diffusion time (skin time) as we assumed in the analysis. Hence the results are consistent with that assumption. The high frequency mode, however, has its period about equal to the skin time. Thus these modes may be artifacts of the analysis and not exist physically, as discussed above. If one assumes $\varepsilon(0)$ = 3 cm, then the plasma makes a maximum excursion of 5 cm, and the peak power required during the transient to return the plasma to its equilibrium position is 90 MW. The relevant $\varepsilon(0)$ is determined by the resolution of the sensor system. One ought to be able to do better than this; present Tokamaks with feedback control on the radial position (e.g. TFR, Ormak) are centered to less than 1 cm. However, a certain amount of reserve power is required for safety purposes. 90 MW is sufficient to insure that any initial displacement of up to 3 cm can be corrected. During the maximum design transient the plasma moves 5 cm; this is 25% of the distance between the plasma edge and the wall.

Table III-C-3

Feedback Parameters of TETR

Growth Rate - no shell, γ_o	7.3×10^5 sec^{-1}
Growth Rate with shell	1.3×10^3 sec^{-1}
Frequency of high frequency modes	5×10^5 sec^{-1}
β (L/R time of shell)	1.9×10^{-3} sec
Skin Time $(\frac{1}{2} \mu_o \sigma \delta^2)$	2.8×10^{-6} sec
Minimum gain for stabilization	18.5 Gauss/cm
Design Gain	28 Gauss/cm
Maximum allowable delay time	.74 msec.
Design delay time	.33 msec.
Required power @ $\varepsilon(0) = 3$ cm	90 MW
Maximum excursion for $\varepsilon(0) = 3$ cm	4.6 cm

References for Section III-C

1. U. Ascoli - Bartoli, 5th International Conference on Plasma Physics and Controlled Fusion, Tokyo 1974. Vol I, page 191.

2. F. Schneider, 9th Symposium on Fusion Technology, Garmisch-Partenkirchen, Germany, 1976; J. L. Anderson, et al. Nuclear Fusion 16,629 (1976); J. Fugita et al., 6th International Conference on Plasma Physics and Controlled Fusion, Berchtesgaden, Germany, 1976, paper CN-35/D-3; TFR Group, 6th European Conference in Controlled Fusion and Plasma Physics, Moscow, 1973, 2,20.

3. R. Gribble, Technology of Controlled Thermonuclear Fusion Experiments and the Engineering Aspects of Fusion Reactors, Austin, Texas, 1972, page 801; K. Kutac et al. 6th Symposium on Engineering Problems of Fusion Research, San Diego, 1975, page 705.

III-D. Plasma Startup Analysis for TETR

As in our previous design studies,[1-3] the transformer for TETR has an air core with the plasma current acting as a single turn secondary. Startup flux is provided by the combined effect of the transformer primary currents and divertor currents. Flux loss due to plasma resistance during burn will be provided by the transformer primary. The locus of the transformer coils is determined by generating a magnetic flux line suitably encircling the region occupied by the plasma. Current distributed continuously along this line according to

$$dI = Hds \tag{1}$$

will produce no net magnetic induction in the plasma region. Discretization of the current gives the location of the transformer primary coils and the relative magnitudes of their currents.

In our previous designs, the plasma is considered to be a purely inductive load during startup. In this analysis, plasma resistive effects during startup as well as the burn have been included in calculating the programming of the transformer currents. During startup, changing magnetic flux through the plasma major radius due to changing currents in the transformer and divertor coils will induce an EMF around the plasma ring. The plasma current is related to this EMF by

$$\varepsilon_{ext} = L_p \frac{dI}{dt} p + I_p R_p \ . \tag{2}$$

Here ε_{ext} is the induced EMF, L_p is the plasma self inductance, I_p is the plasma current, and R_p is the plasma resistance. This EMF is also related to the transformer and divertor currents by

$$\varepsilon_{ext} = - \sum_i M_{1i} \frac{dI}{dt} i \qquad (3)$$

where M_{1i} is the mutual inductance between the plasma and the $i^{\underline{th}}$ coil and the summation runs over all the transformer and divertor coils.

For this design, the rates of change of the currents in the plasma and divertor coils were taken to be constants; that is, the plasma and divertor currents rise linearly in time during startup. The right hand side of Eqn. 3 may then be written as a sum of two terms,

$$\sum_i M_{1i} \frac{dI_i}{dt} = \sum_i M_{1i} \frac{dI_i}{dt} \text{ (divertor)} + \sum_j M_{1j} \alpha_j \frac{dI_{Tj}}{dt} \qquad (4)$$

where $I_{Tj} = \alpha_j I_T$. (5)

In Eqn. 4, the first summation now runs only over the divertor coils and the entire sum is constant in time. The second sum runs over the transformer coils. Since the relative magnitudes of the currents in the transformer coils, α_j, are constants, the rate of change of the current in the first transformer coil T_1 is factored out and the remaining sum is a constant. Thus, Eqn. 3 may be written as

$$6.) \quad \varepsilon_{ext} = -C_1 - C_2 \frac{dI_{T1}}{dt}$$

which is solved for $\frac{dI_{T1}}{dt}$.

$$7.)\ \frac{dI_{T1}}{dt} = -(\varepsilon_{ext} + C_1)/C_2 \ .$$

The induced EMF is known at each time step by computing the plasma resistance given by

$$R_p(t) = R_{po}\left(\frac{T_o}{T}\right)^{3/2} = \frac{\bar{\sigma}_{po} 2R}{a_{eff}^2}\left(\frac{T_o}{T}\right)^{3/2} \ . \qquad (8)$$

Here $\bar{\sigma}_{po}$ is the neoclassically corrected Spitzer resistivity at temperature T_o, averaged over the cross section plasma, R is the major radius, and a_{eff} is the effective minor radius. The plasma temperature as a function of time during startup was computed using a space-time plasma transport code[4] taking account of pseudoclassical transport scaling and radiative losses. Eqn. (7) is then solved for $\frac{dI_{T1}}{dt}$ and the rate of change of the current in the $j^{\underline{th}}$ transformer coil is given by

$$\frac{dI_j}{dt} = \alpha_j \frac{dI_{T1}}{dt} \ . \qquad (9)$$

The currents are advanced in time giving the complete programming of the transformer currents, which is shown in Table III-D-1.

In computing the induced EMF by Eqn. (2), the plasma self inductance was taken to be a constant. This assumes that the plasma size, shape and current profile remain constant. A recent study[5] has shown that in the slow rise-time category, ($\sim 10^{-1}$ s) full current penetration can occur by classical toroidal transport alone, and the assumption of constant self-inductance seems to be reasonable. Also in this calculation, no account was taken of impurities, which might have a serious effect.

Table III-D-1

Transformer Programming

Coil	R	Z	Initial(MA)	Current (MA) End of Startup	End of Burn
T_1	.85	.25	3.00	0.0435	-1.01
T_2	.85	.75	2.98	0.0432	-1.003
T_3	.86	1.25	2.93	0.0425	-0.986
T_4	.87	1.75	2.86	0.0415	-0.963
T_5	.89	2.25	2.75	0.0399	-0.926
T_6	.91	2.75	2.61	0.0379	-0.879
T_7	.95	3.25	2.42	0.0351	-0.815
T_8	1.00	3.75	2.18	0.0316	-0.734
T_9	1.08	4.24	1.9	0.0276	-0.640
T_{10}	1.18	4.73	1.59	0.0231	-0.535
T_{11}	1.31	5.21	1.29	0.0187	-0.434
T_{12}	1.46	5.69	1.02	0.0148	-0.343
T_{13}	1.65	6.15	.68	0.0099	-0.229
T_{14}	1.85	6.60	.62	0.009	-0.209
T_{15}	2.07	7.06	.49	0.0071	-0.165
T_{16}	2.31	7.5	.39	0.0057	-0.131

During the one second startup, the single turn loop voltage around the plasma ring, shown in Fig. III-D-1, reaches a maximum of 25.3 volts at about 0.1 seconds. The average electron density for these calculations was taken to be 10^{13} cm^{-3}, less than the final density of 7.5×10^{13} cm^{-3} which will be achieved after the startup phase by gas injection. Recent calculations done for TFTR device[6] using parameters very similar to TETR indicate that the loop voltage attained may indeed be insufficient to properly form the discharge. Inclusion of impurity effects in the computational model would raise this voltage hopefully above the minimum critical voltage, although this calculation has not been carried out as yet. Assuming a thermal distribution for the electrons, the fraction of runaway electrons in this field is entirely negligible and, unless the discharge fails to form, runaway electrons are not anticipated to be a problem.

The initial temperature and current used in the calculations were 100 eV and 20 kA, respectively. Several calculations done for startup conditions[6,8] have shown the results to be relatively insensitive to the initial temperature. The choice of an initial current physically represents current due to preionization and soak of a skin effect current, if formed.[8] The results are also relatively insensitive to this choice. Based on the TFTR calculations and interpretation of TFR results,[7] it appears entirely possible that either one or both of preionization and supplementary heating will be necessary for discharge formation.

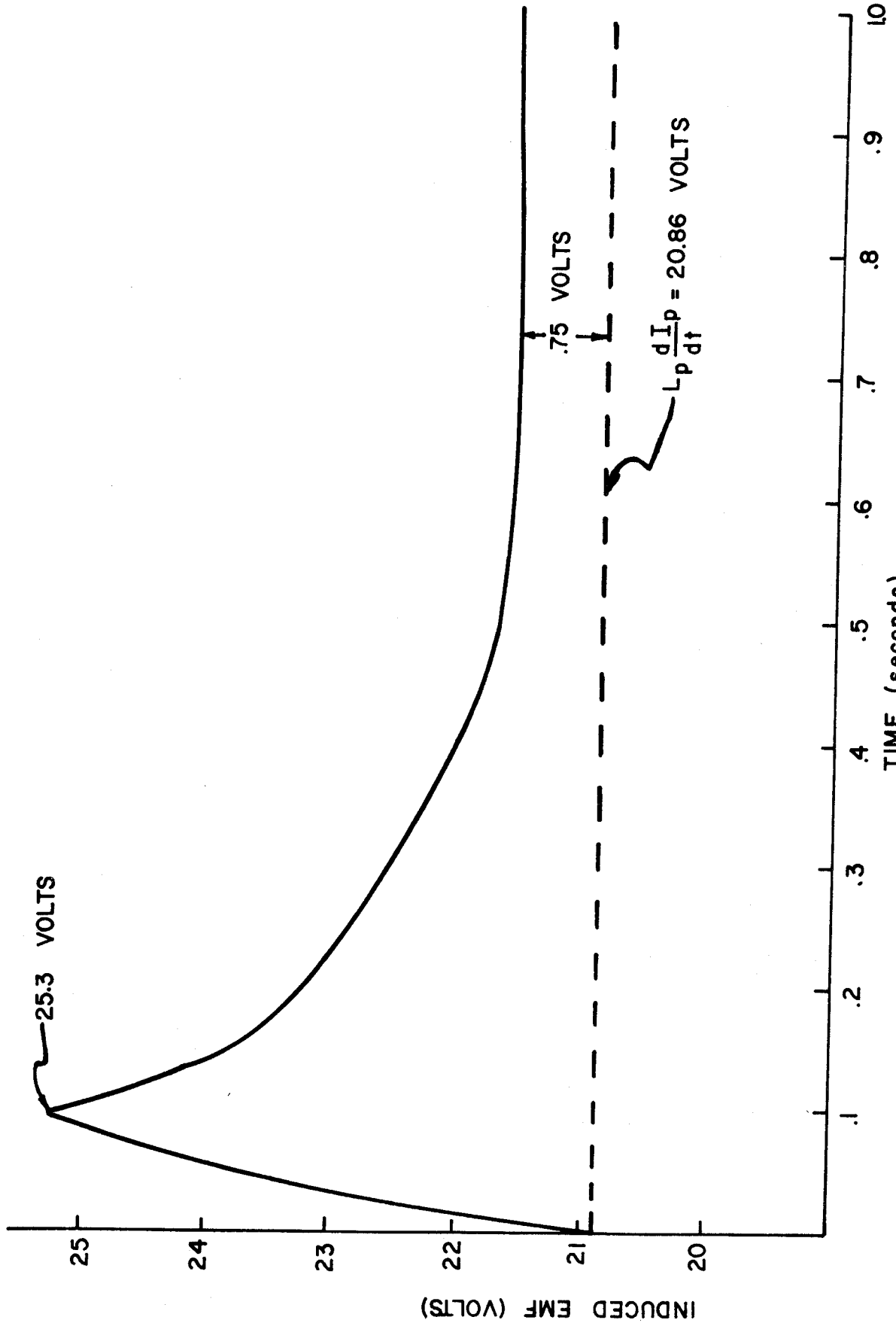
INDUCED EMF (VOLTS)
25
24
23
22
21
20
25.3 VOLTS
.75 VOLTS
$L_p \frac{dI_p}{dt}$ = 20.86 VOLTS
.1
.2
.3
.4
.5
.6
.7
.8
.9
1.0
TIME (seconds)

Fig III-D-1

The results of the calculation for the startup phase are shown in Figure II-D-2, the transformer current, and in Figure II-D-3, the power. Parameters used in the calculations and results are summarized in Table II-D-2. The rate of change of the transformer current taking account of plasma resistivity is, at maximum, approximately 1.4 times greater than for a non-resistive case. This accounts for the peaking of the power at about 0.1 seconds, when the change in the transformer current is maximum and before plasma resistivity has dropped very much. As the plasma heats up, the resistivity becomes a much less dominant factor, and the loop voltage and the rate of change of the transformer currents approach constant values. Transformer current programming for the entire operating cycle is shown in Fig. II-D-4. Power and the energy stored in the magnetic fields are shown in Fig. II-D-5. A detailed description of the operating is given in Table III-D-3. During the final, or recharge phase, neutral gas influx cools the plasma. Minimum time for this phase is dictated by mechanical pumping requirements, and is chosen to be 10 seconds. During this recharge phase, the transformer must be reset to its initial current for the beginning of a new cycle. The electric field generated will be approximately 0.3 mV/cm, which will induce a current in the chamber. If the pressure is low enough, an avalanche breakdown could occur. However, by having the divertor coils carry a nominal current, field lines can be diverted to intersect the walls, and the particles will be deposited on the walls. Maximum energy flux to the first wall during this period will be less than 1 Joule/m^2/sec, which is negligible.

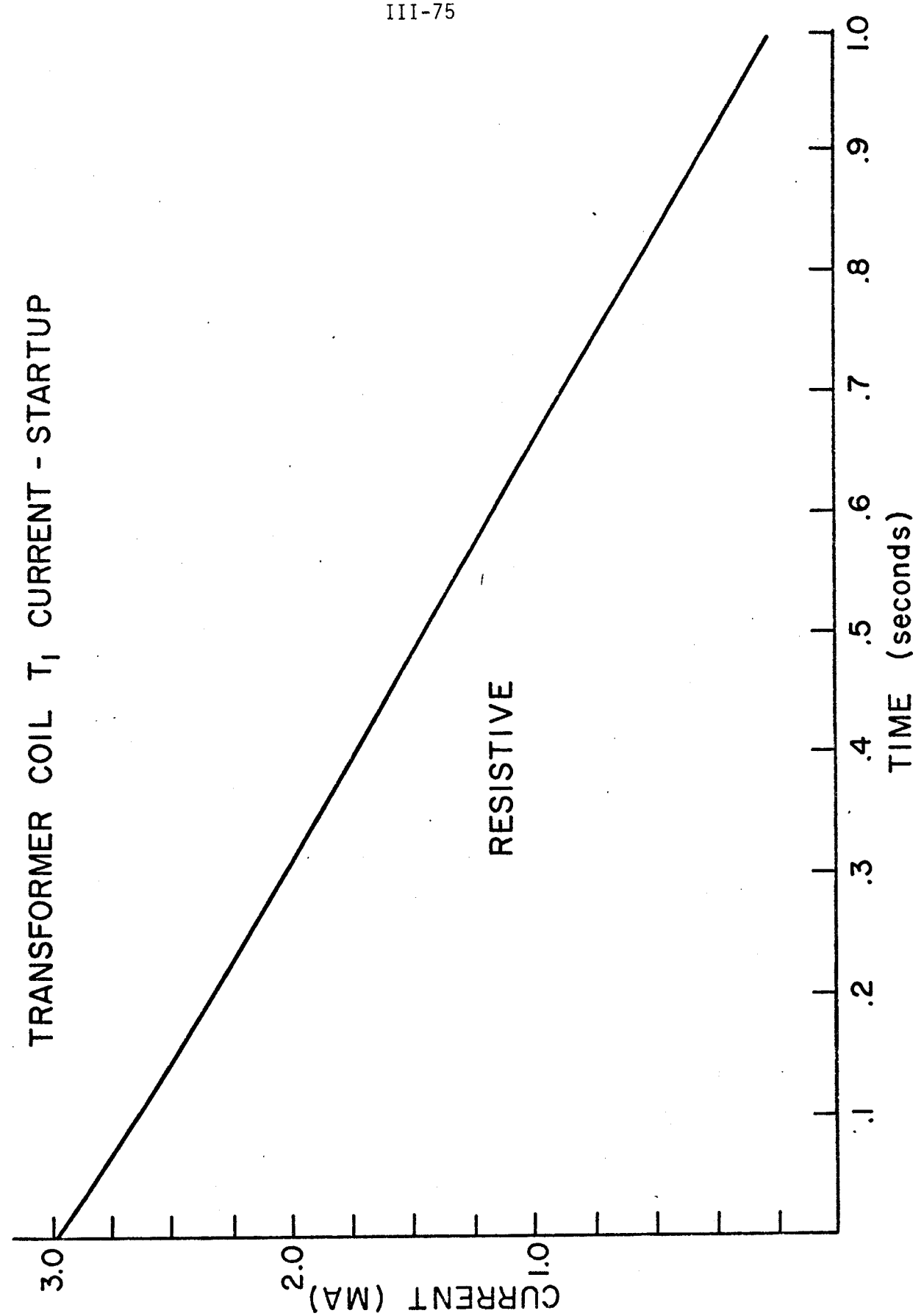

Figure III-D-2

Table III-D-2

Startup Transformer Characteristics for TETR

Max. current, coil T_1	3.0 MA
Max. net transformer current	59.4 MA
Max. power	890 MW
Max. stored energy in fields	4.608×10^8 J
Transformer flux swing total	20.6 V-sec.
: startup, total	15.2 V-sec.
: startup, resistive	1.4 V-sec.
: burn phase	5.4 V-sec.
Maximum single turn loop voltage	25.3 V
: inductive voltage	20.8 V
: resistive voltage	4.5 V
Integrated power, one cycle	1.613×10^8 J
Initial startup electron temp., T_o	100 eV
Saturation electron temp., ohmic heating	2.1 keV
Breakdown plasma toroidal current	20 kA
Final plasma toroidal current	2.52 MA
Startup time	1 sec.
Burn time	60 sec.
Shutdown time	1.5 sec.
Recharge time	10 sec.
Total cycle time	72.5 sec.
Duty factor	.828
Startup flux swing, transformer	15.2 V-sec. (68.7%)
Startup flux swing, divertor	7.05 V-sec. (31.3%)

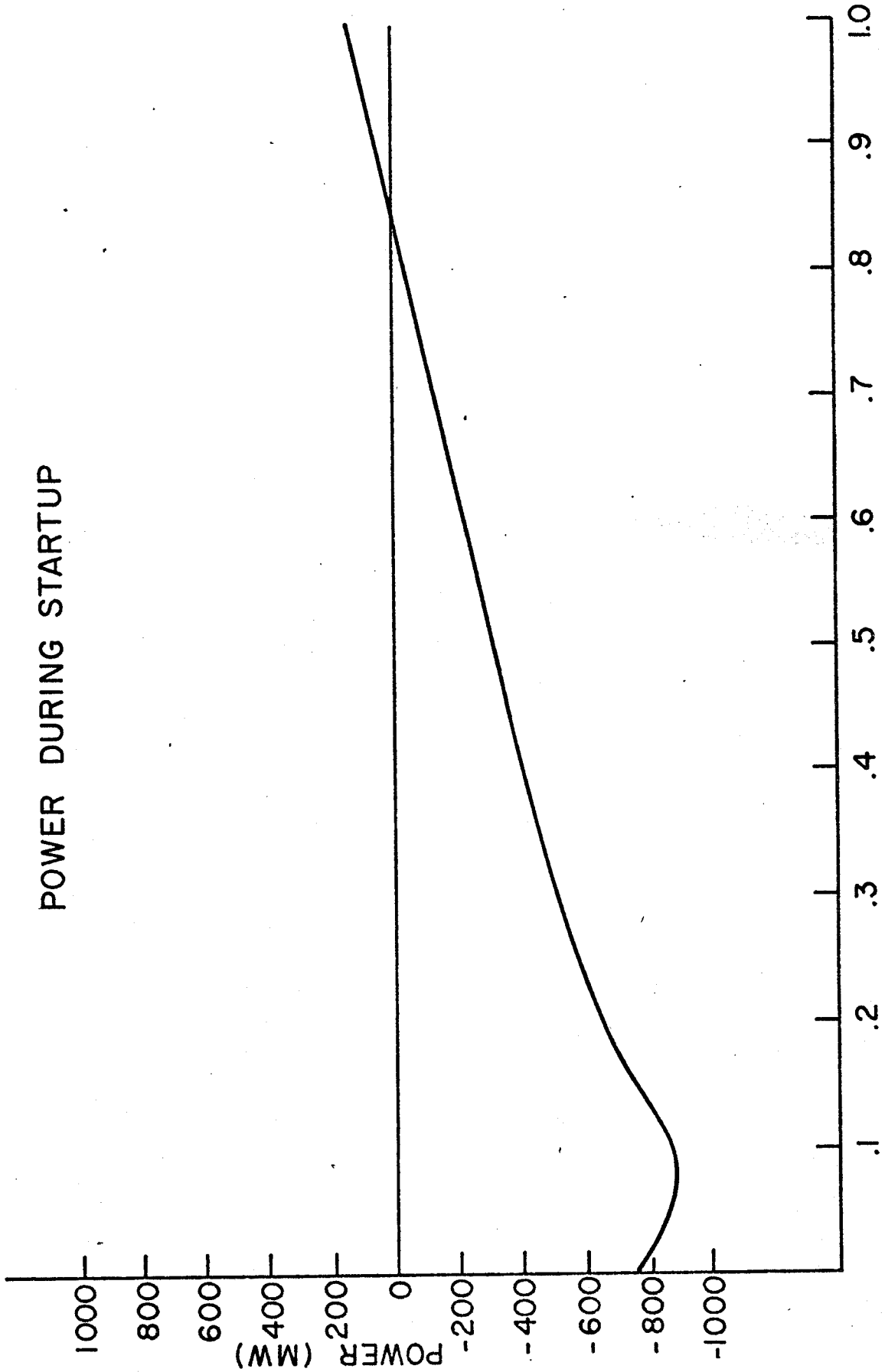

Figure III-D-3

Figure III-D-4

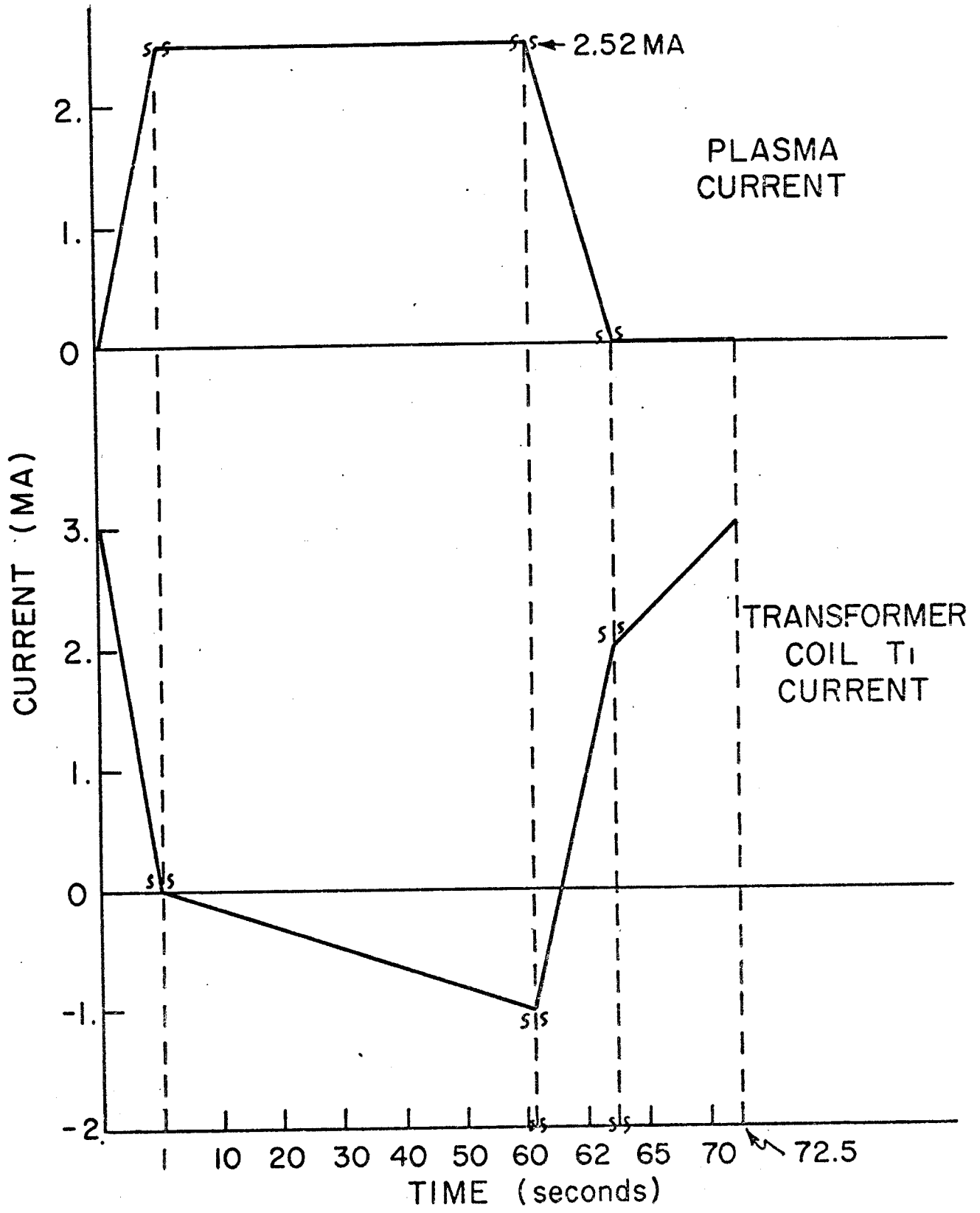

Figure III-D-5

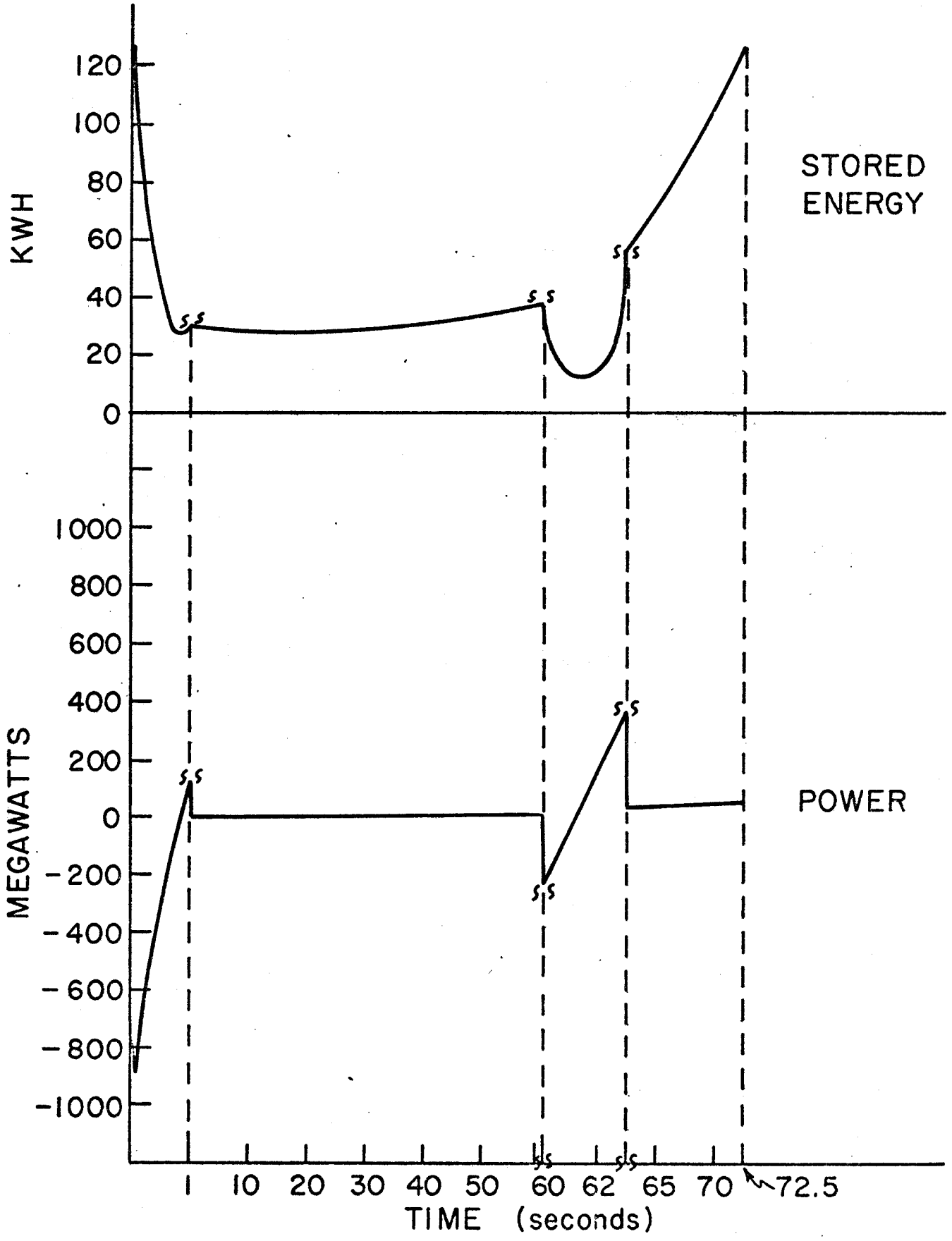

Table III-D-3

TETR Operating Cycle

Time (seconds)	Phase Description
0-1	Startup: plasma and divertor currents rise to full maximum; transformer currents begin to drop; plasma ohmically heats to T_e = 2.1 keV.
1-61	Burn: gas injection to full density; neutral beam injecti to maximum temperature; transformer currents drop to maximum negative values.
61-62.5	Shutdown: beam injection discontinued; current in transformer reversed; plasma and divertor currents drop to zero.
62.5-72.5	Recharge: plasma cool-down; residual gas pumped out; chamber refilled with fresh fuel; transformer currents reset to initial values.

In considering factors limiting the extent to which the presently designed burn time could be extended, it is felt that with the present transformer design, the burn time cannot be further extended. The reason for this is the sizing of the transformer coils, namely coil T7, where space is most limited. To extend the burn time will require a greater volt-second capacity from the transformer, and hence larger coils. To accommodate longer burn times, a complete redistribution of the transformer coil locations would be necessary.

It is assumed that power up to 500 MW can be supplied directly from line. Peak power demand of 130 MW occurs at the end of startup period, with a peak power demand of 350 MW at the end of shutdown. Therefore, the power for the poloidal field coil system is supplied from an ac/dc conversion bridge.

References for Section III-D

1, 2, & 3. B. Badger et al., "UWMAK-I, A Wisconsin Toroidal Fusion Reactor Design," UWFDM-68, Vol. 1; "UWMAK-II, A Conceptual Tokamak Reactor Design," UWFDM-112; "UWMAK-III," UWFDM-150, Department of Nuclear Engineering, University of Wisconsin.

4. W. A. Houlberg and R. W. Conn, "Fluid Simulation of Large Tokamak Plasmas Using a Variable Spatial Mesh, Variable Time Step Implicit Procedure," March 1977, Mathematics & Computations Division, ANS, Tucson, Arizona, March 28-30, 1977, to be published in those proceedings.

5. J. B. McBride, H. H. Klein, R. N. Byrne, N. A. Krall, "Current Penetration in Tokamak-Type Discharges," Nuclear Fusion 15, 393 (1975).

6. R. J. Hawryluk and J. A. Schmidt, "Effects of Low Z Impurities During the Startup Phase of a Large Tokamak," Plasma Physics Laboratory Report MATT-1201, Princeton University.

7. R. Papular, "The Genesis of Toroidal Discharges," Nuclear Fusion 16, 37 (1976).

8. J. C. Hosea, "Ohmic Heating of Tokamaks," Plasma Physics Laboratory Report MATT-1128, Princeton University.

III-E. Global and Space-Time Analysis of Plasma Operating Conditions

III-E-1. Introduction and General Considerations

A study has been made to better understand the scaling of very strongly driven two component tokamaks. The basic criteria and restrictions to be met are the following:

1. Produce above 1 MW/m^2 of average neutron wall loading. Given a plant factor of 70% this amounts to an instantaneous wall loading of 1.4 MW/m^2.

2. Be fairly consistent with MHD equilibrium calculations which determine the following parameters.

Poloidal beta (β_e) = 3.8

$\frac{\text{Separatrix Surface Area}}{\text{Inscribed Circular Area}} \equiv S = 1.55$

$\frac{\text{Volume of plasma}}{\text{Volume of inscribed circular torus}}$ = 1.64 which implies a plasma volume of 37.8 m^3.

Minor Radius (a) = 0.6 m, Plasma Height = 1.2 m.

Axial Toroidal field (B_T) = 4.18 Tesla (8.5 T at the Magnet)

Plasma Current (Ip) = 2.5 MA

3. Beam injection should require less than 150 MW of power and the beam energy should be greater than about 150 keV for adequate penetration and sufficiently high beam-plasma fusion probability.

4. The plasma should remain clean of impurities for reasonably long run times (~60 sec to obtain acceptable duty cycle). This implies an effective "screen" divertor.

A series of calculations were made using both a global balance[1] and a radially dependent tokamak transport code[2] to see if we can in fact produce a sufficiently high neutron loading. We will first discuss some of the problems that arise, and then present results of the parametric study.

a. Fraction of Tritium in Target

Ideally, the neutron flux is optimized by injecting deuterons into a pure tritium target plasma. At the high injection currents

needed, however, it is not possible to maintain a pure target.

A rough estimate of the fraction of tritium in the plasma (f_{TP}) is obtained by solving the following equations for the energetic and thermal deuterium components:

$$\frac{\partial}{\partial t} n_D^* = 0 = I_B - n_D^*/\tau_{SD} - n_D^*/\tau_p^* \tag{1}$$

$$\frac{\partial}{\partial t} n_D = 0 = n_D^*/\tau_{SD} - n_D/\tau_p \tag{2}$$

where τ_{SD} = slowing down time (sec), τ_p = thermal particle containment time (sec), τ_p^* = suprathermal particle contaiment time (sec), n_D^* = density of energetic deuterium (cm^{-3}), n_D = density of thermal deuterium (cm^{-3}) and I_B = injected current density (#/cm^3-sec).
In steady state,

$$n_D^* = I_B \frac{\tau_{SD}}{1 + \tau_{SD}/\tau_p^*} \tag{3}$$

and

$$n_D = I_B \tau_p/(1 + \tau_{SD}/\tau_p^*) \tag{4}$$

If the plasma density is taken as $n = n_D + n_T$ this gives

$$f_{TP} \equiv \frac{n_T}{n} = 1 - \frac{I_B}{n} \times \frac{\tau_p}{1 + \tau_{SD}/\tau_p^*} \tag{5}$$

In the above equations,

$$\tau_{SD} = 6.6 \times 10^{11} \frac{T_e^{3/2}(keV)}{n\ (cm^{-3})} \ln\left(1 + (W_B/E_c)^{1.5}\right) \tag{5a}$$

with

$$E_c = 18.7\ T_e \left[\frac{n_D}{n_e} + \frac{2}{3}\frac{n_T}{n_e}\right]^{2/3}$$

Here W_B is the injected beam energy and T_e is electron temperature (KeV).

Defining

$$\tau_E \equiv \overline{3nkT}/P_{inj} \tag{6}$$

where P_{inj} is the injected power gives

$$f_{TP} = 1 - 3\,(T/W_B)\,(\tau_p/\tau_E)\,\frac{1}{1 + \tau_{SD}/\tau_p^*} \tag{6a}$$

This indicates that as (τ_p/τ_E) gets large, there will be a buildup of tritium in a plasma of a given temperature. Substituting the tokamak parameters A (aspect ratio), q (a) (safety factor near the plasma separatrix), B_T (toroidal magnetic field G)), and β_θ (poloidal beta) yields

$$f_{TP} = 1 - 8 \times 10^{-11} \frac{I_B\, q^2\, A^2\, \overline{T}}{\beta_\theta\, B_T^{\,2}}\;\frac{\tau_p}{1 + \tau_{SD}/\tau_p^*} \tag{6b}$$

Notice that for high injection currents or large particle containment times, the tritium fraction drops. High β_θ and high toroidal field have favorable effects.

In present experiments τ_p/τ_E ~ 3 to 6. However, for divertor-like boundary conditions and trapped particle scaling τ_p/τ_E may be in the range of 0.2 to 0.5. Approximate estimates of τ_p/τ_E can be determined from the continuity and energy balance equations. The continuity equation may be written as:

$$\frac{\partial n}{\partial t} = \nabla\cdot nV + \quad = -\nabla\cdot D\,\frac{\partial n}{\partial r} + I_B \tag{7}$$

where n is electron density (cm^{-3}). Defining $\tau_p \equiv \bar{n}/I_B$ and integrating eqn. (7) over the plasma volume (for a circular cross-section plasma) gives in steady state

$$\tau_p = \frac{\bar{n}a}{2D\nabla n(a)} = \frac{a\bar{n}}{2n(a)}\,\frac{L_N}{D(a)} \tag{7a}$$

where a is the plasma minor radius, D(a) is the diffusion coefficient at the separatrix and $L_n \equiv n(a)/\frac{\partial n(a)}{\partial r}$ is the density gradient scale length. The barred quantities are volume averaged. The electron energy equation may be written as

$$\frac{\partial(\frac{3}{2} n\bar{T})}{\partial t} = S_e - \nabla\cdot\left(n\chi \frac{\partial T}{\partial r}\right) - \left(\frac{3}{2} D T \frac{\partial n}{\partial r}\right) - P_{rad} \qquad (8)$$

where S_e, the energy source will include ohmic heating as well as beam and RF auxiliary heating. We will in fact be interested in the situation where the auxiliary heat source is much larger than the ohmic source.

Defining $\tau_{E_e} \equiv \frac{3\overline{nT}}{2S_e}$ and averaging (2) over volume as before gives

$$\tau_{E_e}^{-1} = \frac{2n_e(a)\, T_e(a)}{a\, \overline{nT}} \left(\frac{2}{3}\frac{\chi_e}{L_{Te}} + \frac{D}{L_N}\right) + \frac{2}{3} \frac{P_{rad}}{\overline{nT}} \qquad (8a)$$

where $L_{T_e} \equiv T_e(a)/\frac{\partial Te}{\partial r}(a)$ is the temperature gradient scale length. The ion energy containment time may be defined similarly except that there is no radiation term. The total energy containment time ($\tau_E = \frac{3\overline{nT}}{S_e}$) may then be written as:

$$\tau_E^{-1} = \frac{2n(a)\, T(a)}{a\, \overline{nT}} \left(\frac{\chi_e}{3L_{Te}} + \frac{\chi_i}{3L_{Ti}} + \frac{D}{L_n}\right)_{r=a} + \frac{\overline{P_{rad}}}{3\overline{nT}} \qquad (9)$$

In the global balance model the energy confinement time is given by

$$\tau_{E_{e,i}}^{-1} = \frac{4}{a^2} \left(D(\bar{n}, \bar{T}) + \chi(\bar{n}, \bar{T})\right).$$

Clearly, the accuracy of this approximation is quite dependent on behavior at the plasma edge. In the above equations, we have set the ion and electron temperatures and densities equal. The ratio of particle energy to energy containment time is then:

$$\frac{\tau_p}{\tau_E} = \frac{\bar{n}\, T(a)}{3\, \overline{nT}} \left\{\left(\frac{\chi_e}{D}\right)\left(\frac{L_n}{L_{Te}}\right) + \left(\frac{\chi_i}{D}\right)\left(\frac{L_n}{L_T}\right) + 3\right\} + \frac{\overline{P_{rad}}}{6\, \overline{nT}} \frac{\bar{n}}{n(a)} \left.\frac{L_n}{D}\right|_{r=a} \qquad (10)$$

If the outer edge of the plasma is dominated by a convective mode such as the trapped particle mode we can set $D \approx \chi_e \tilde{\simeq} \chi_i$. Furthermore, we will show that under these conditions $L_{T_e}, L_{T_i} >> L_n$. Since, in this case transport energy losses will dominate over radiative losses, eqn. (10) simplifies to:

$$\tau_p/\tau_E = \frac{\bar{n}\, T(a)}{\overline{nT}} \approx \frac{T(a)}{\bar{T}}$$

and since $T(a)/\bar{T} \approx .2$ to $.5$, the particle containment time can be <u>significantly smaller</u> than the energy containment time.

It is interesting to note that for neoclassical scaling, we still have $L_n << L_{T_e}$ or L_{T_i} but now conduction may dominate over convection ($\chi_e >> D$). If $\chi_e > \chi_i$ and if we can ignore radiative losses, we find

$$\tau_p/\tau_E \sim \frac{T(a)}{3\,\bar{T}} \left(\frac{\chi e}{D} \frac{L_n}{L_{Te}} \right)_{r=a}$$

so in this case we may expect that $\tau_p > \tau_E$.

<u>b. Beam Pressure and Beta Considerations</u>

The ratio of beam to plasma pressure, Γ, is defined as

$$\Gamma = \frac{\text{Energy in energetic plasma component}}{\text{Energy in thermal plasma component}} = \frac{n_D^* \overline{E_b}}{3/2 \sum_j \overline{n_j\, T_j}} \qquad (11)$$

where $\bar{E}_b$ is the mean energy of the energetic particle as it slows down. Using eqns. (3) and (6) and approximating $\overline{E_b}$ as $W_b/2$ gives

$$\Gamma = 0.5 \left(\frac{\tau_{SD}}{\tau_E} \right) \frac{1}{1 + \tau_{SD}/\tau_p^*} \qquad (11a)$$

This equation indicates that the slowing down time (τ_{SD}) should not be larger than twice the energy containment time.

Combining this with eqns. (5a) and (6) gives

$$\Gamma = 6.9 \times 10^{26}\, T_e^{1/2}\, P_{inj}\, \ell n(1 + (10\, T_e)^{1.5})/(n_e^2\, V\, (1 + \tau_{SD}/\tau_p^*)). \qquad (11b)$$

For a plasma volume V and P_{inj} the injected power in watts. It is generally assumed that Γ should not be much larger than 1 for plasma stability.

The ratio of slowing down time to energy containment time appears in eqn. 11a, and is important in particle and energy balance considerations.

Since $\tau_E(\sim \Sigma nT/P_{inj})$ is proportional to density and τ_{SD} is inversely proportional to density the ratio τ_{SD}/τ_E scales inversely with density squared. For a given amount of injected power, say 150 MW, and for a plasma density of 7.5×10^{13} (cm^{-3}), the slowing down time will always be greater than the energy containment time when τ_E is less than about 250 ms. Fig.III-E-1 indicates to attain $\tau_{SD}/\tau_E \lesssim 2$ requires densities above $\sim 8 \times 10^{13} cm^{-3}$.

The values of β_θ, the plasma pressure to poloidal magnetic field pressure ratio, may be an important constraint in a tokamak. From its definition

$$\beta_\theta = \frac{4 \times 10^{11}}{B_p^2(\text{gauss})} \left(\sum_j N_j\, T_j + \frac{2}{3} P_B\right) \sim \frac{8 \times 10^{11}}{B_p^2}\, \bar{n}\, \bar{T}\, (1 + \Gamma) \qquad (13)$$

with P_B the beam pressure. This may be written as

$$\beta_\theta = 8 \times 10^{11}\, \frac{P_{inj}}{B_p^2}\, (\tau_E + .5\, \eta \tau_{SD}) \qquad (13a)$$

Here $\eta = \tau_p^*/(\tau_{SD} + \tau_p^*) \approx 1$. This indicates that as τ_{SD} and τ_E increase, the permissible power that can be injected drops.

II-E-2. Global Balance Calculations

A series of calculations were done to examine the variation in neutron production for a given amount of injected power. Fig.III-E-2 shows the neutron wall loading versus injector power for injection of pure D beams into a tritium fueled target. The fraction of tritium in the target appears to be around 80 to 85% for variation of injected power from 100 to 150 MW. In these calculations, β_θ is fixed and density is allowed to vary.

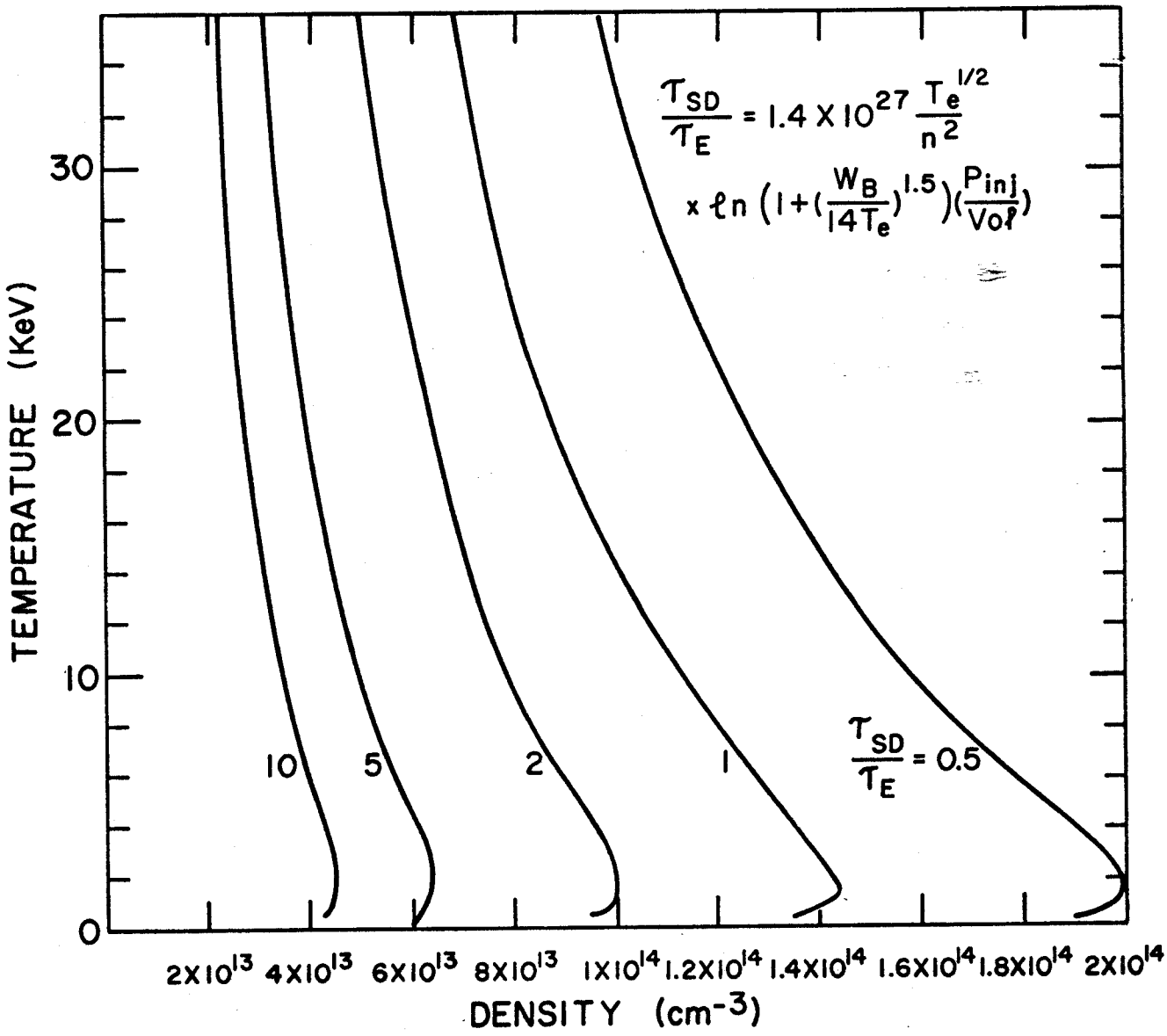

Figure III-E-1

τ_{SD}/τ_E Contours for 150 MW Injected at 150 keV into a Circular Cross Section Tokamak with Major Radius of 324 cm and Minor Radius of 75 cm.

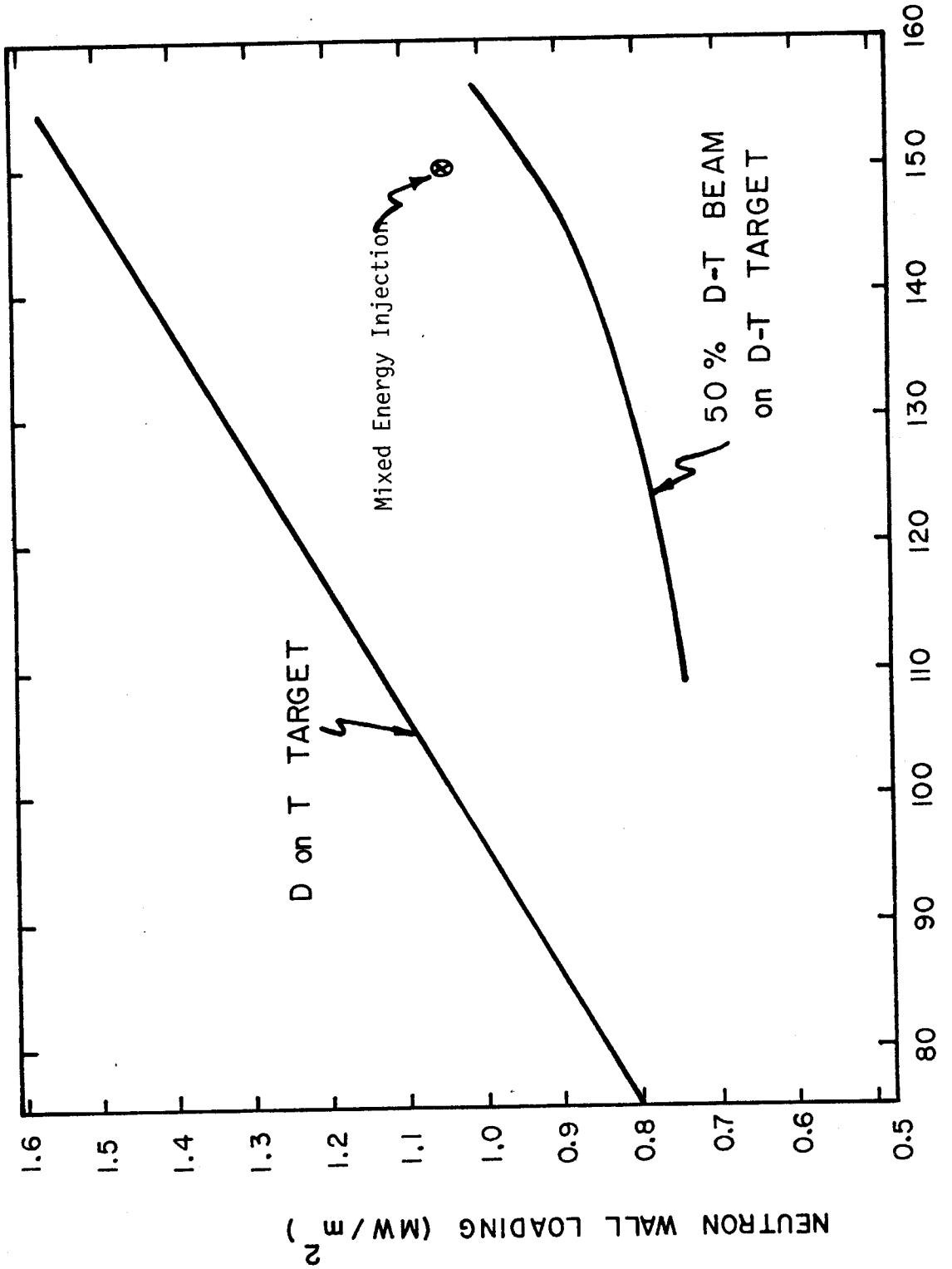

Figure III-E-2 - Neutron Wall Loading vs. Injected Power (a) 150 keV Deuterium Injected Into a Tritium Target (b) Mixed (50%) Deuterium-Tritium Beam Injected at 150 keV on a D-T Traget (c) Single Point Indicating Injection of a Deuterium Beam Made up of 60% Full Energy Component (150 keV), 24% Half Energy Component (75 keV) and 16% One-Third Energy Component (50 keV).

For injection power above ~ 125 MW, neutron wall loadings above 1.3 MW/M^2 are attainable. These calculations indicate that for τ_E between 120 and 150 ms ($n\tau_E$ = 9 x 10^{12} to 1.2 x $10^{13} cm^{-3}$-s) and τ_p between 150 and 175 ms ($n\tau_p \approx$ 1.1 x 10^{13} to 1.4 x $10^{13} cm^{-3}$-s), a sufficiently high wall loading is predicted by the global calculation.

If τ_p were larger for the same τ_E, eqn. (6) indicates that we would be forced to operate with 50-50 D-T beams injected into a 50-50 D-T target. Fig. III-E-2 indicates that this would significantly degrade the wall loading and probably not be acceptable. Some problems such as tritium recycle would be ameliorated however. This case is discussed in detail by Jassby.[4]

There is one point (circled) on Fig. III-E-2 for the case of injecting 150 MW of power made up of 60% @ 150 keV, 24% @ 75 keV and 16% @ 50 keV. This represents the case of positive ion beam injection in which the half and third energy components are not removed (using data for the Berkeley Sources developed at LBL.[5]) The neutron wall loading is about 1.03 MW/m^2 which is too low for our purposes. In this calculation the target is only 69% tritium so a significant contribution is coming from thermal D-T fusions.

A series of calculations were run in which we decreased the magnetic field on axis and varied β_θ between 3 and 4 while keeping q(a) constant. It was seen that the neutron production remained constant to within 12%. The effect of impurities was also examined and a summary of results are shown in Fig. III-E-3. It is seen that above 1% carbon or ~ 0.2% Fe the amplification (Q) and wall loading falls off significantly.

III-E-3. Spatially Dependent Transport Calculations

A series of transport calculations were made to study the temperature and density profiles in TETR and to help understand the impact that these profiles would have on the design of such a tokamak.

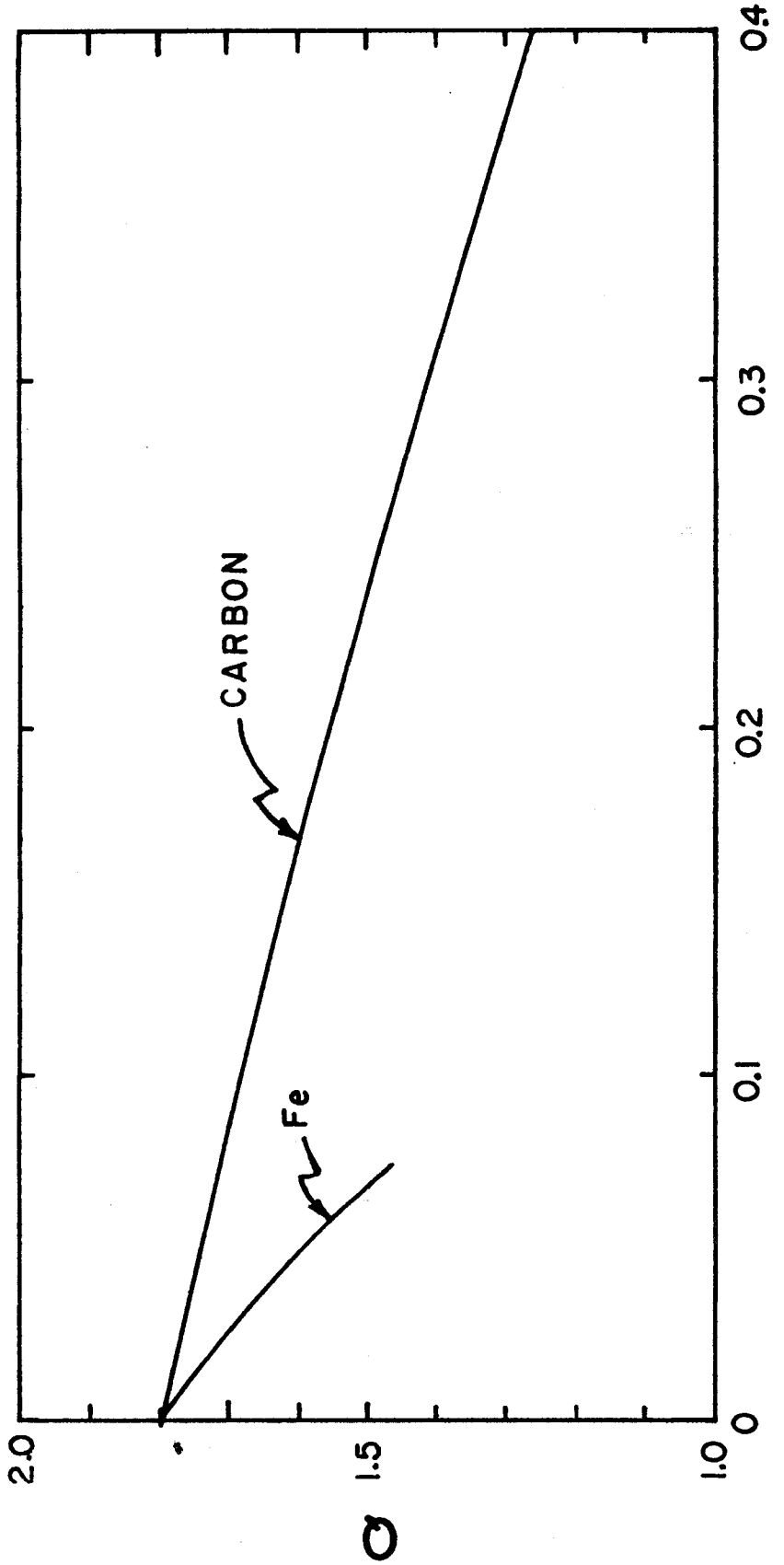

Figure III-E-3

Amplification Factor Q vs. Impurity Content

The transport code used in these calculations has been largely rewritten by Houlberg[2] and uses the same method for linearization and solution of the transport equations as has been developed at Oak Ridge[3]. Provision was made, however, for a varying degree of implicitness in the integration as well as a variable spacial mesh size. The transport coefficients are calculated following a multi-regime model under which, as the plasma becomes more collisionless, trapped particle driven turbulence is assumed to appear and to dominate transport causing the scaling to pass successively from neoclassical scaling[6] (pseudoclassical for electrons[7]), to trapped electron mode turbulent transport[8], trapped ion mode transport[9], and finally into the collisionless trapped particle interchange mode.[10] The transport coefficients are calculated in a more detailed manner than they had been in the previous version of the code. Neutral transport is handled using a slab model described in ref. (11). The noncircularity of the plasma is handled by choosing an equivalent minor radius in the calculation that gives the same plasma volume and incorporating non-circular effects into the beam penetration calculation and the calculation of transport coefficients.

Since the code assumed a circular plasma cross section, we have used in these calculations a minor radius of 75 cm which was chosen to give approximately the same plasma volume as determined by the MHD equilibrium calculation.

III-E-3-a. Calculation of a Plasma Bounded by a Divertor

In order to prevent a very high rate of sputtering of charged particles on the chamber walls, to remove impurities and helium from the plasma, to aid in pumping of the chamber and possibily to screen the plasma from impurities, we have assumed that a magnetic divertor will be needed.

For example, for an average particle containment time of 100 ms with a mean density of $\sim 10^{14}$, the first wall would sputter about 1 mm per year

(assuming an average sputtering coefficient of .01) for kilovolt range ions on either an iron or carbon liner. This would present a serious problem in designing the first wall and create a very "dirty" plasma which could not attain sufficient electron temperatures to insure the desired neutron production. Beam penetration would become very difficult if not impossible.

We have therefore attempted to model the plasma divertor boundary by a judicious choice of boundary conditions[12], which are determined as follows: At the plasma divertor boundary, the continuity equation is approximately $D\frac{\partial^2 n}{\partial r^2} = n/\tau_D$ where τ_D is the time an ion spends in the divertor ($\tau_D \approx q(a)aS/V_{th}$ where a is the plasma width, S is the shape factor and V_{th} is the ion thermal speed). This gives a characteristic length for density decay of $L_D \approx \sqrt{D(a)\tau_D}$. For 3 keV ions and a diffusion coefficient of 3×10^6 cm^2/sec (these values come from the calculations), we find $L_D \approx 5$ cm. This represents approximately two banana widths and so it would appear to be a reasonable guess for the rapid density drop that occurs in a divertor. To be consistent with previous divertor studies[12] we have chosen the electron temperature scale length somewhat larger (10 cm) and the ion temperature scale length an order of magnitude larger. Results do not appear to be sensitive to a factor of 2 variation in these boundary conditions. Furthermore, we will assume that the plasma in the divertor causes a burnout of neutral gas in the chamber.

The resulting temperature and density profiles are shown in Fig. III-E-4 and III-E- respectively. Note the very peaked density profiles typical of divertor boundary conditions in the presence of trapped particle scaling. The plasma separatrix (edge) density is quite low ($\sim 2 \times 10^{12}$ cm^{-3}) which indicates that the divertor may not be very useful as a screen to impurities.

Mean plasma parameters for the run are shown in Table III-E-1. The steady state neutron flux at the wall is $\sim$ 1.3 MW/m^2. The mean energy and particle

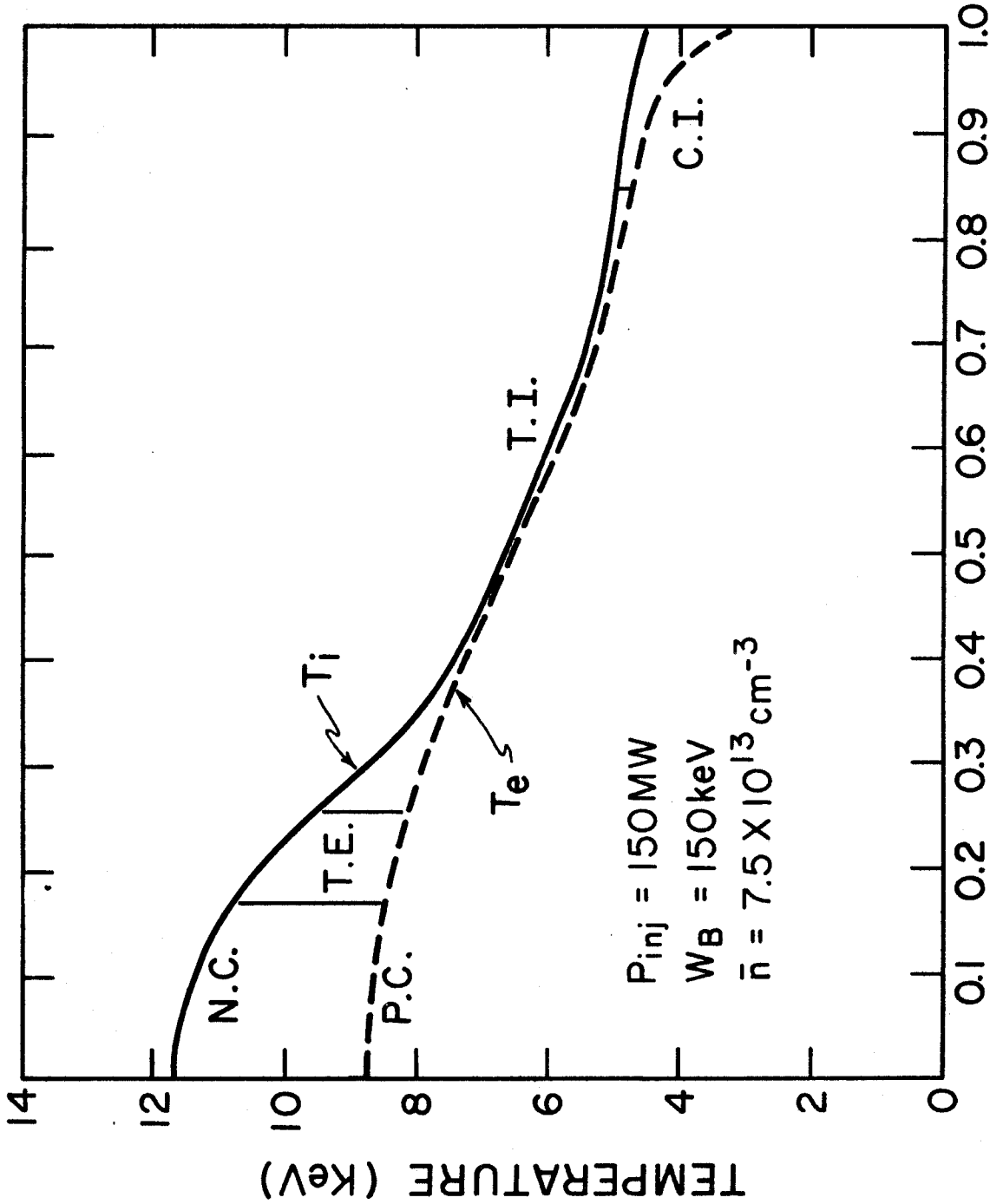

Figure III-E-4 - Equilibrium TETR Temperature Profiles for Ions and Electrons. Dominant Diffusion Mechanism in Various Regions are Indicated.

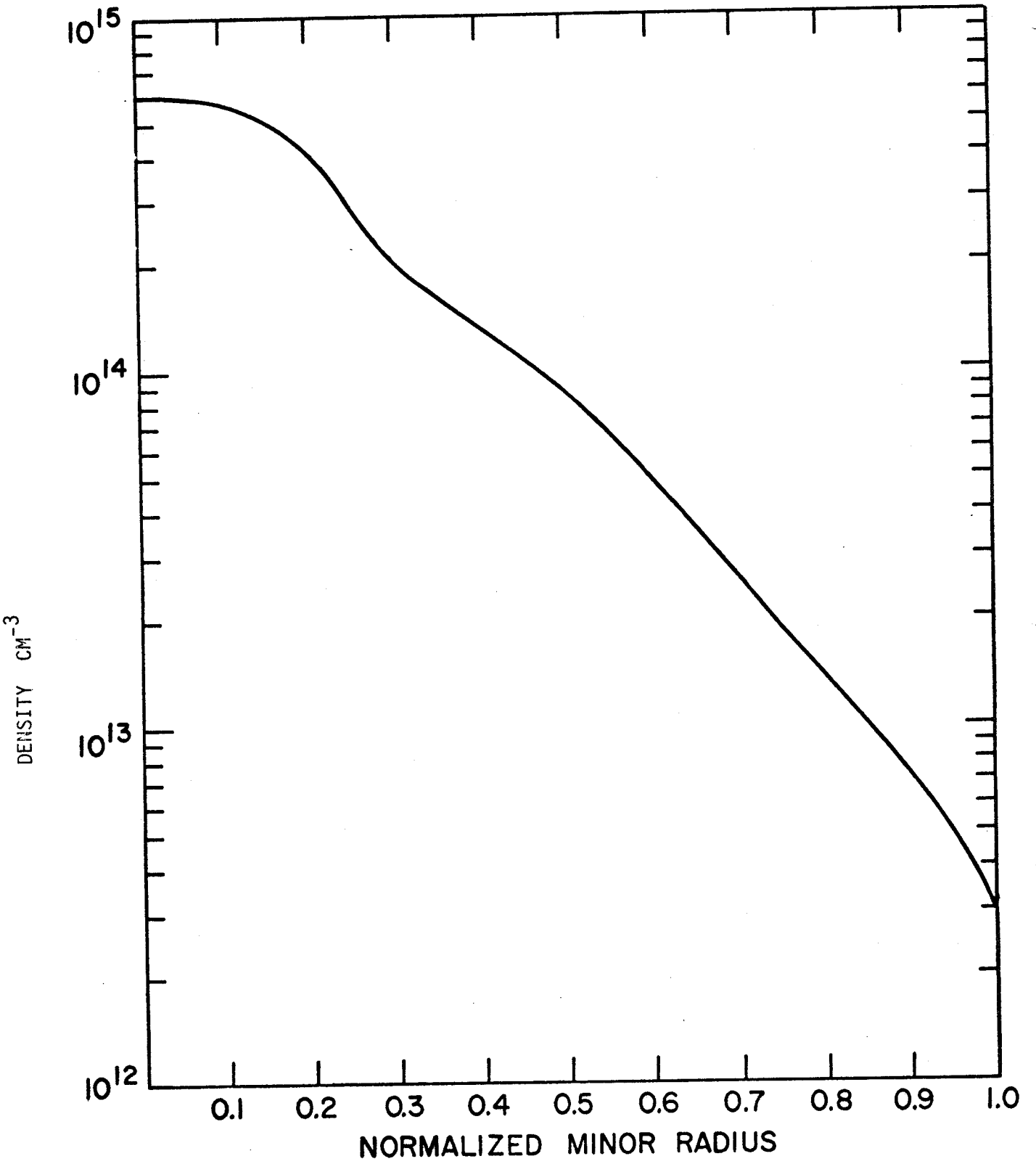

Figure III-E-5 - Equilibrium TETR Density Profile. The Sharp Density Decrease is Typical of Divertor Bounded Tokamak.

Table III-E-1

Final Plasma Parameters of TETR from Energy Balance Analysis

	Global Model	Space-Time Analysis
Major Radius (m)	3.24	3.24
Poloidal Beta	2.8	3.2
Toroidal Current (MA)	2.54	2.52
Volume (m^3)	37.8	36.
Toroidal Magnetic Field (kG)	41.8	41.9
q(a)	2.4	2.4
Plasma Circumference/Inscribed Circle	1.55	1
Half Width	0.60	0.75
Half Height	1.20	0.75
Electron Density (cm^{-3})	7.7×10^{13}	7.5×10^{13}
Mean Electron Temp. (keV)	11.3	7.4
Mean Ion Temp. (keV)	12.2	8.6
Amplification Factor - Q	1.78	1.62
Neutron Flux at Wall (MW/m^2)	1.44	1.31
Γ	.36	1.0
Energy Containment Time (ms)	80	52
Power to Divertor (MW)	203	190
$n\tau_E$	6.2×10^{12}	3.9×10^{12}
Beam Slowing Down Time (ms)	160	
Particle Containment Time (ms)		29
Pellet Source (#/cm^3-sec)		2.4×10^{15}
Injected Power (absorbed) (MW)	150	144
Injection Energy (keV)	150	150
Radiated Power (MW)		0.5

containment times are τ_E = 52 and τ_p = 31 ms respectively. These times are quite small if we consider that present tokamaks show energy containment times up to 50 ms although they are smaller in size. The reason for these short times is related to the rapid increase in transport coefficients predicted for the trapped ion mode at the high temperatures that are generated in this very strongly driven device. Less pessimistic scaling laws would predict a larger τ_E, considerably higher temperatures and therefore and enhanced TCT fusion probability. However, larger values of τ_E and mean temperature would drive up beta and the MHD determined beta limit would then necessitate a decrease in injected power. This indicates that we are near the peak in neutron energy density attainable in a fixed β tokamak system[13]. We may be helped here by the fact that the q profile is frozen into the plasma, as discussed in ref. 14, which will serve to raise the beta limitation. Furthermore, the fusion probability is also proportional to the fraction of tritium in the plasma which decreases approximately linearly with the particle containment time (see eqn. 5). It may be noted that as the fraction of tritium drops to near 50%, the thermal fusion contribution increases, but this will not make up for the decrease in beam plasma fusions. Therefore, we would like to increase τ_E somewhat while τ_p remains $\leq$ 100 ms. (From eqn. 5 for τ_p = 100 ms, the fraction of tritium in the plasma is 83%). The total poloidal beta of the beam and plasma is 3.2 which indicates a total beta of 4.6%).

As an alternative to the non-circular plasma, we could consider a circular plasma of higher poloidal beta, which implies utilization of the flux conservation as proposed by Oak Ridge.[14] This would have the advantage of simpler magnetic field design, lower plasma current and better vertical stability. Table III-E-2 shows the two designs in which the plasma current and volume are kept constant as well as the inner major radius (R-a) and the

Table III-E-2

Comparison of Circular and Non-Circular Plasma Parameters for a TETR Machine. Inner Major Radius, Plasma Volume and q(a) Kept Constant.

	Non-Circular Plasma	Equivalent Circular Plasma
Minor Radius (a)	0.60	0.75 (m)
Major Radius (R)	3.24	3.39 (m)
Plasma Current (Ip)	2.5	1.5 (MA)
Aspect Ratio	5.4	4.5
Poloidal β (β_θ)	3.8	
Total Beta	.054	

safety factor at the plasma edge. This plasma will bulge out an additional 30 cm at the outside but this would not be difficult to design around. A detailed MHD equilibrium study was not carried out for this case but it offers a promising alternative to the more non-circular lower β_θ design.

It may be noted that when electron temperatures are above 5 keV, the slowing down time of the beam is above 100 ms (for $n = 10^{14}$ cm^{-3}). The fact that the slowing down time is longer than the particle containment time is not expected to pose a problem however because the small particle containment time results from trapped particle driven turbulence and ref. 15 indicates that the nonthermal ions are not diffused by these waves to an appreciable degree.

A detailed survey of microinstability theory for two component tokamaks is presented by Berk et al.[15] and we will only mention some of the results of this analysis. Although the ratio of beam pressure to plasma pressure (Γ) in the calculations is about 1, other factors serve to eliminate the micro-instabilities looked at in this paper. Since we are interested in running for times that are long (~60 seconds) compared with the beam slowing down time (which is ~100 to 200 ms) we can expect the nonthermal component to have attained its equilibrium distribution function which appears to be stable to the microinstabilities looked at. Furthermore, for $n_i \lesssim 2.6 \times 10^{14}$cm^{-3} the energetic ion speed is below the Alfven speed and this is a sufficient condition for eliminating the waves at the cyclotron frequency and its harmonics that were analyzed. At the pressure peak where the density is above this level a number of instabilities could be excited, which could serve to flatten the injection profile in this region. Rosenbluth et al.[16] have shown that under some circumstances shear Alfven waves could be excited which would also lead to a flattening of the injection profile within the inner ~30 cm of the plasma. These effects, however, do not appear to present

serious difficulties. Experimental measurements of up to $\Gamma \sim 0.5$ been attained and serve to support optimism that a Γ of about 1 may be obtainable without suffering serious consequences in the plasma stability.

In summary, although the assumed (trapped particle) scaling laws predict a very short energy and particle containment time, the plasma will be sufficiently hot to produce the levels of neutron flux we require. Longer values of τ_E would enhance neutron production but would necessitate the need for high β equilibria. Longer particle containment times would cause a dilution of the tritium fraction in the target and thereby reduce neutron production. It would, however, have the advantage of lessening the fueling, tritium handling and pumping problems.

III-E-3-b. Neutral Recycle

The flux of energetic neutrals leaving the plasma has been considered. In these calculations we use a neutral transport slab model[11] which has been modified to take account of energetic neutral backscatter that takes place at the first wall.[17,18] Input into the code is the isotropic flux of neutrals crossing the separatrix and entering the plasma. These neutrals are given an energy of 5 eV, which assumes that the hydrogen molecules leaving the wall are ionized in the divertor zone by a Franck-Condon process. We also will assume that the energetic neutrals leaving the plasma will traverse the divertor zone with little attenuation or scattering.

The wall pressure was assumed to be 10^{-5} torr, and the results will scale linearly with this pressure. This pressure yielded an energetic neutral flux of $7.0 \times 10^{15}/cm^2$-sec at a mean temperature of about 3.8 keV. This would lead to a physical sputtering wall erosion rate of 0.7 mm/yr for carbon and 0.97 mm/yr for iron. The energy distribution function for the neutrals leaving the plasma is shown in Fig. III-E-6.

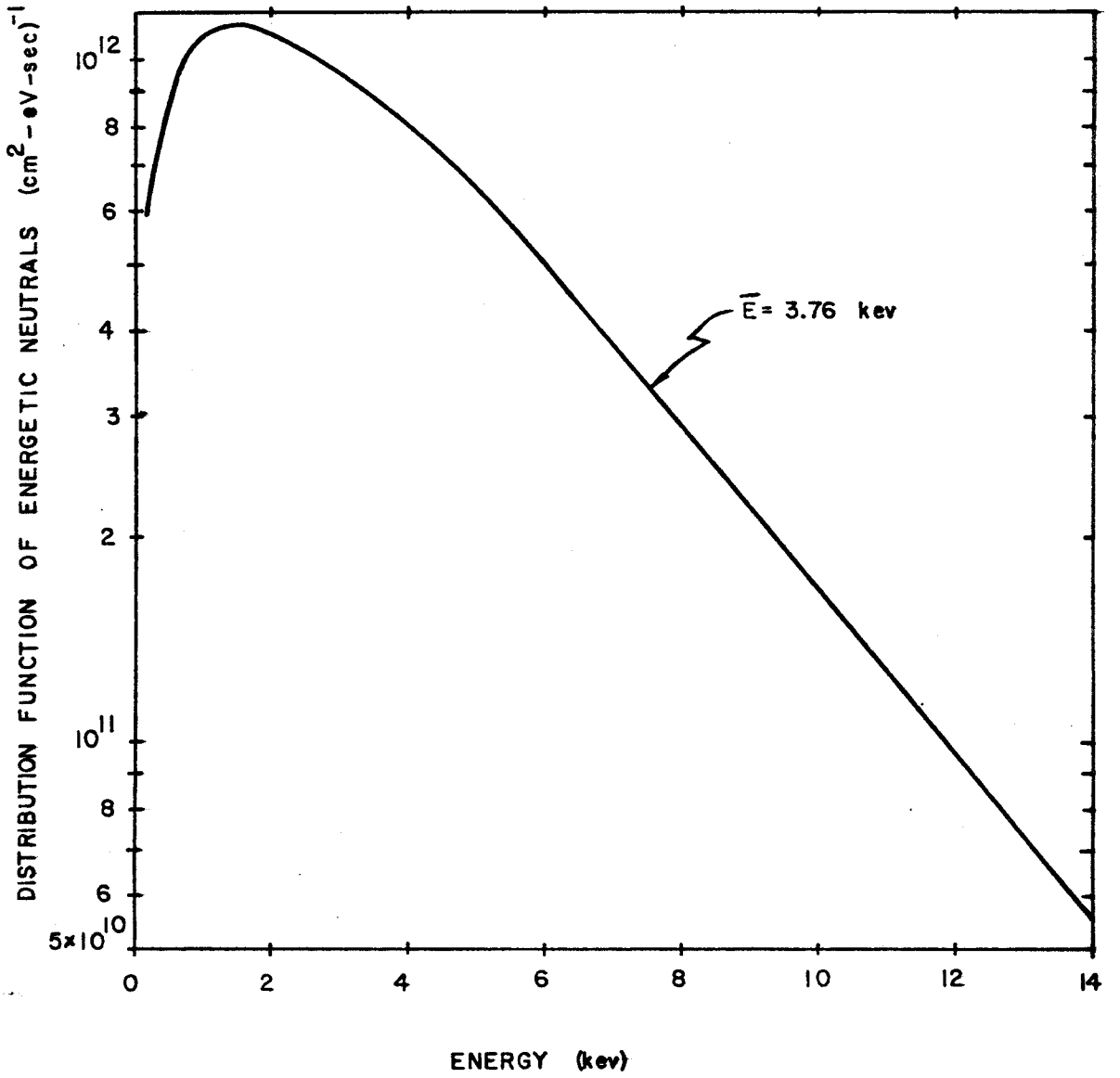

Figure III-E-6 - Neutral Particle Flux Spectrum to the Liner in TETR

It may be noted that the recycled neutrals tend to depress the ion temperature at the plasma edge below the value indicated on Fig. III-E-4, but the temperature profile in the bulk of the plasma is otherwise not significantly affected.

An accurate estimate of the vacuum chamber pressure would involve a calculation of the rate of backstreaming down the slots from the divertor chamber, where the pressure was calculated to be $\sim 10^{-4}$ torr, and this calculation was not attempted.

We have also looked into the possibility of increasing the energy containment time by means of puffing gas into the tokamak chamber. This would have the advantage of causing a good percentage of the ion energy leaving the plasma to be transported to the chamber walls via charge exchange thereby limiting the energy load to the divertor. Futhermore, it would eliminate the necessity for pellet fuelling which would be otherwise necessary.

Results of calculations indicate that at below about 4×10^{-4} torr, the source term is too small to cause any significant change in the equilibrium from the neutral burnup cases discussed previously. However, for a neutral pressure of above $\sim 6 \times 10^{-4}$ torr, the equilibrium switches markedly in character, giving rise to a flat density profile with a mean density value of above 2×10^{14} cm^{-3}. Some of the important parameters for this solution are displayed in Table III-E-3. For this solution, no source other than beams and recycle is needed to maintain the plasma density. This would eliminate the fueling problem, but it would necessitate that the beams be 50% tritium, 50% deuterium so as to avoid creating a 100% deuterium target.

At an external pressure of $\sim 5 \times 10^{-4}$ torr, the spacial equilibrium is unstable, with the equilibrium switching between the flat and peaked density solutions shown in Fig.III-E-7 with a frequency of 10 times/sec. Fig. III-E-8 displays the time history of the mean ion temperature, for the low, intermediate and high edge pressures. This transition in equilibrium appears to take place within a relatively small range of neutral pressure.

The reason for this behavior is as follows: the neutral flux entering at the plasma edge causes a plasma source that is peaked at the edge where

Table III-E-3

Comparison of Plasma Parameters for Two Cases of Divertor Operation

	Divertor With Neutral Burnout	Divertor With Gas Puffing
Density (cm^{-3})	1×10^{14}	2.1×10^{14}
Natural flux (cm^2-sec)	0	6×10^{14}
Electron temp (keV)	6.1	5.6
Ion temp (keV)	6.3	6.2
Fraction tritium	90%	50%
Q	1.36	.58
Flux at separatrix ϕ_s (MW/m^2)	1.37	.60
τ_E (ms)	72	140
τ_p (ms)	43	103
τ_p^* (containment time for beam injected ions)	43	1700
Pellet Source (#/sec)	7.8×10^{22}	0
$\beta_i + \beta_e$	1.66	2.8
β of Beam	1.66	.68
Γ	~ 1.0	.24

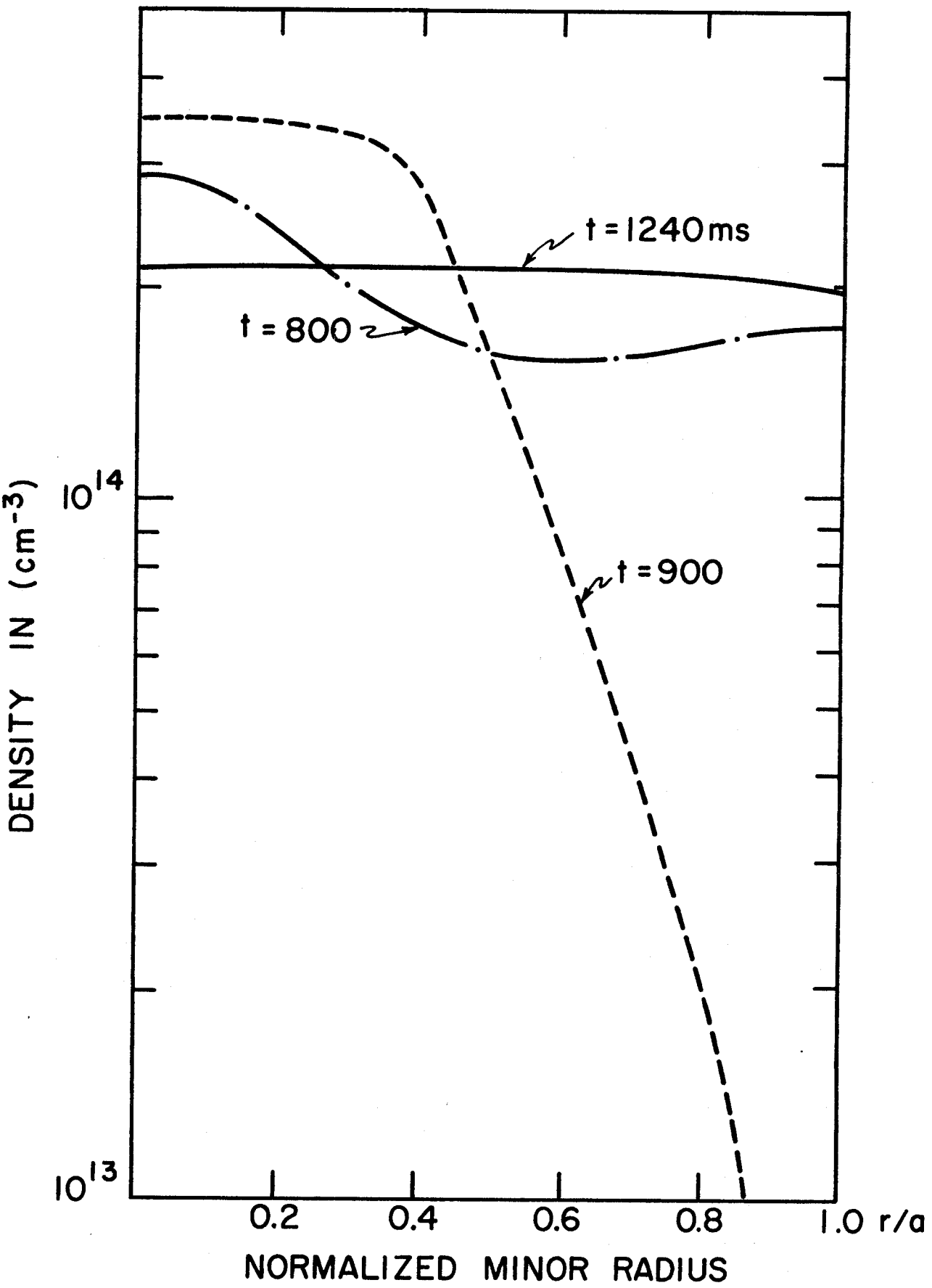

Figure III-E-7 - Unstable Density Profiles for TETR Plasma Surrounded by a Neutral Gas at 5 x 10-4 Torr.

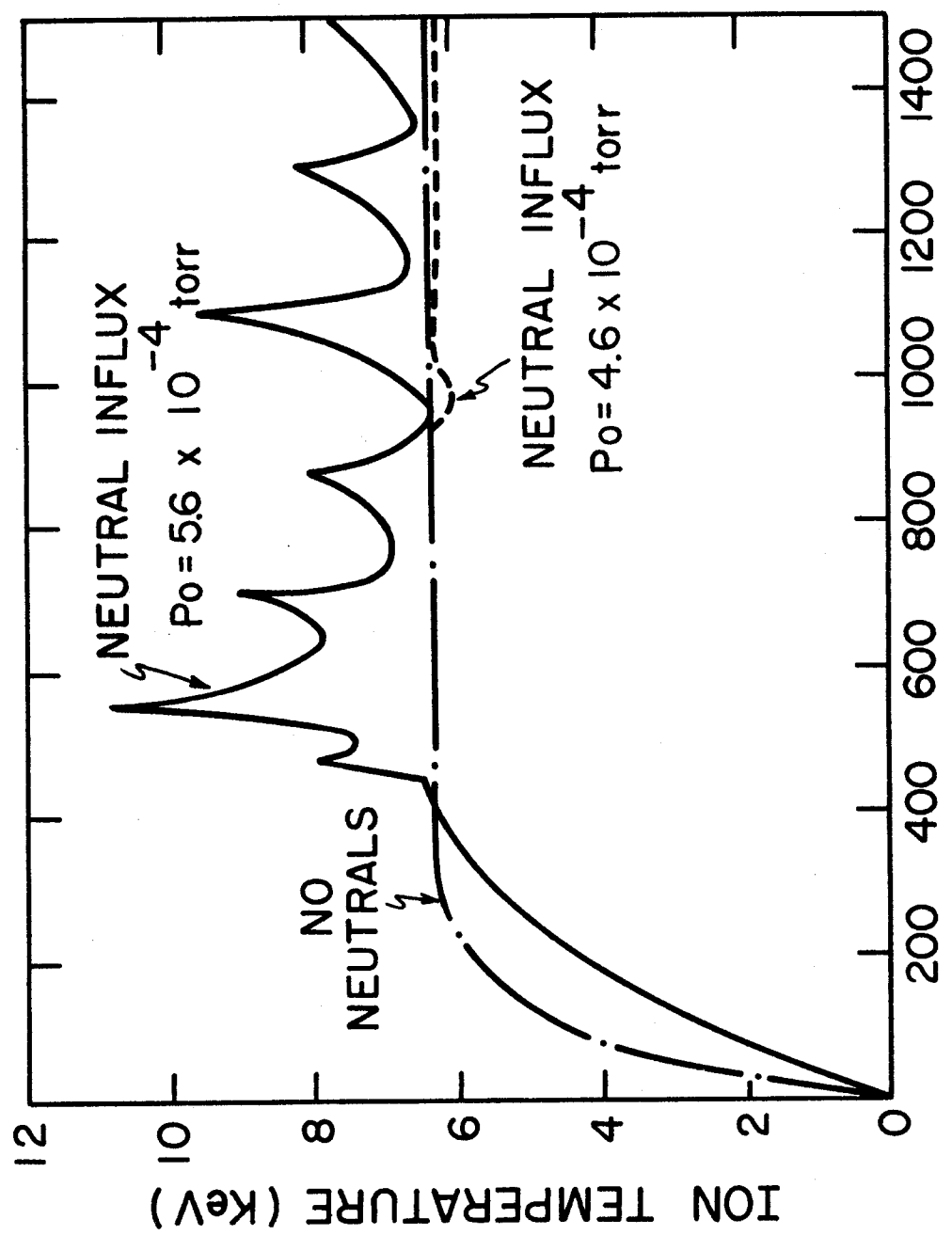

Figure III-E-8 - Ion Temperature Temporal Evolution for TETR Bounded by Neutral Gas of Pressure P_o: (a) $P_o = 0$, i.e. No Neutrals. (b) $P_o = 4.6 \times 10^{-4}$ torr Switched On At t = 900 ms. (c) $P_o = 5.6 \times 10^{-4}$ torr Plasma Becomes Thermally Unstable After 400 ms.

the diffusion coefficient is very large, and the rapid diffusion in this region prevents the density from rising very much. However, when the source becomes large enough to invert the profile at the edge the density will begin to rise, causing the diffusion coefficient at the plasma edge to pass from the collisionless interchange mode to the trapped ion mode and the density profile will begin to flatten. As the edge density increases, the diffusion coefficient decreases ($\frac{\partial D}{\partial n} < 0$ in trapped ion mode), causing a further increase in edge density. The edge density will continue to increase until the edge enters the trapped electron mode, (where $\frac{\partial D}{\partial n} > 0$). This results in a flat density profile if the edge recycle source is the dominant plasma source. The high and flat density profile, however, attenuates the beam in the outer portion of the plasma which heats the plasma edge and causes the plasma to become more collisionless. If the recycle source is not sufficient to maintain the plasma edge in the trapped electron mode, the plasma edge will re-enter the trapped ion mode where the unstable scaling will cause the edge density to decrease until it catches again on the collisionless trapped particle interchange mode (for which $\frac{\partial D}{\partial n} = 0$).

It is interesting to consider the consequence of providing a sufficient neutral source to maintain the flat density profile. This requires a neutral pressure of above 6×10^{-4} torr. As we have indicated, in this mode of operation the only fueling is edge recycle and the neutral beams, and this requires that the neutral beams be 50% deuterium, 50% tritium. In order to have a comparable fusion probability for the injected tritons as for the deuterons, we would require 50% higher trition injection energy (225 keV), which presents a technology problem. Even in this case, the neutron flux (ϕ_s) drops to about 0.6 MW/m^2 (at the separatrix) due to the beams being deposited closer to the plasma edge in a cooler region and a small decrease in the average

plasma electron temperature caused by an increase in electron density (this effect dominates over an observed increase in τ_E). In a similar calculation in which the same total power was injected but the tritium was injected at 150 keV, Q was found to drop to 0.42. Moreover, although the fact that a large amount of ion energy is transferred to the chamber walls via charge exchange thus decreasing the heat removal problems at the divertor, it causes an unacceptably high wall sputtering rate. For a sputtering coefficient of .01, 2 to 3 mm of wall material will sputter away per year. Therefore, we have concluded that the recycle fueled operating mode does not appear to be an acceptable mode of operation for TETR due to reduced neutron production and increased sputtering.

It is interesting to note that if scaling laws turned out to be less stringent than assumed such that the flat density-recycle fueling mode would lead to a lower mean density, and if the plasma edge could be made to be sufficiently cool so that the temperature remains below the sputtering threshold, both the beam penetration and sputtering problems would be ameliorated. This may be a reasonable mode of operation to consider.

III-E-4. Beam Penetration Calculations

A computer code has been developed which performs penetration and beam-plasma fusion calculations for a finite size beam injected into a circular or elliptically shaped plasma. The calculation entails a number of pencil beam calculations and can model either a rectangular or circular beam made up of parallel beamlets. (We do not take account of beam divergence). Furthermore, the beam is assumed to be injected parallel to the midplane of the plasma but at arbitrary angle in this plane.

Calculations were made for a rectangularly shaped beam 90 cm wide by 20 cm high as planned for TETR. Both parabolic and uniform beam intensity profiles

were considered but the results proved insensitive to the beam profile. The angle that the beam center makes with the plasma axis was varied and it was seen (Fig. III-E-9) that the beam absorption varies from 97 to 99.8% as the injection angle varies from perpendicular to 30° injection. An injection angle of 30° was chosen, because at this angle the outer beam edge is tangent to the centerline of the chamber, and absorption is very good. The beam deposition profile and neutron source profile are shown for this case on Fig. III-E-10.

Figure III-E-9 - Fraction of the Beam Absorbed by the Plasma as a Function of the Angle the Beam Center Makes with the Plasma Axis. Tangential Injection Corresponds to $\theta = 0$.

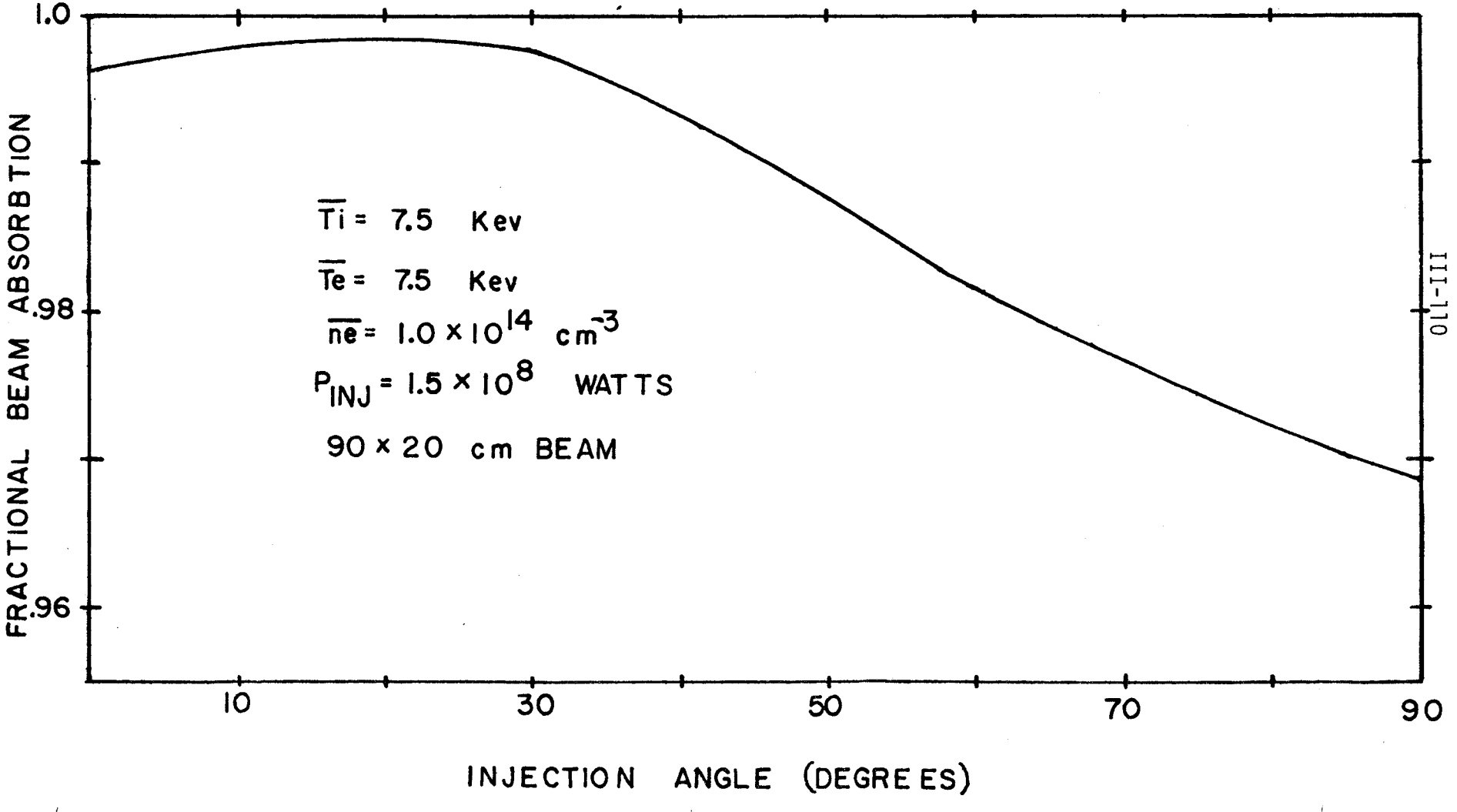

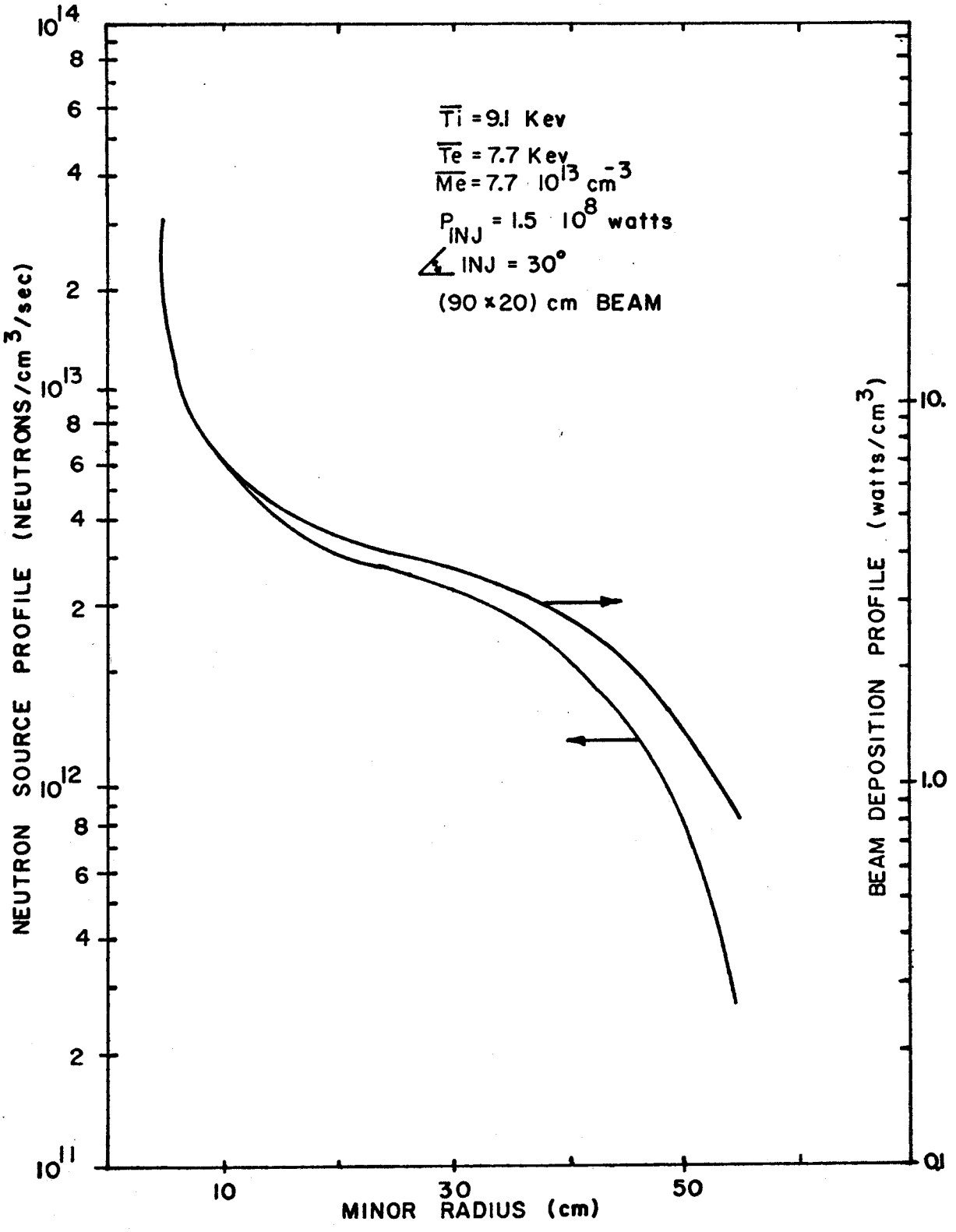

Figure III-E-10 - Beam Deposition and Neutron Production (Source) Profile for the Reference TETR Case of 30° Angle of Injection with the Magnetic Axis.

References for Section III-E

1) R. W. Conn and J. Kesner, Nuclear Fusion 15 (1975), 775. See also J. Kesner and R. W. Conn, Nuclear Fusion 16 (1976), 397.

2) W. A. Houlberg and R. W. Conn, Proceedings of ANS Topical Conference on Improved Methods for Analysis of Nuclear Systems (1977).

3) J. T. Hogan, Methods of Computational Physics, 16 (1976), 131.

4) D. L. Jassby and H. H. Towner, PPPL report MATT-1180 (1976).

5) K. H. Berkner, R. V. Pyle, J. W. Stearns, Nucl. Fus. 15 (1975) 249.

6) M. N. Rosenbluth, R. Hazeltine, F. L. Hinton, Phys. Flds. 15 (1972), 116.

7) L. A. Artsimovich, JETP Lett. 13, 70 (1971).

8) B. B. Kadomtsev and O. P. Pogutse, Sov. Phys. Dokl. 14, 470 (1969), and Nuc. Fus. 11, 67 (1971).

9) B. B. Kadomtsev and O. P. Pogutse, Sov. Phys. JETP Lett. 4 (1966), 10.

10) B. B. Kadomtsev and O. P. Pogutse, Sov. Phys. JETP 24 (1967), 1172.

11) R. W. Conn, M. Khelladi, J. Kesner, University of Wisc. report UWFDM-136 (1975).

12) A. T. Mense, G. A. Emmert, and J. D. Callen, Nuc. Fus. 15 (1975), 703. See also A. T. Mense, Ph.D. Thesis, University of Wisconsin (1977).

13) D. L. Jassby, Nuc. Fus. 15 (1975), 453.

14) R. A. Dory and Y-K. M. Peng, Nuc. Fus.

15) H. L. Berk, W. Horton, M. N. Rosenbluth, and P. H. Rutherford, Nuc. Fus. 15 (1975), 819.

16) M. N. Rosenbluth, P. H. Rutherford, Phys. Rev. Lett. 34 (1975), 1428.

17) R. Behrisch, W. Eckstein, P. Meischer, B. M. U. Scherzer, M. Verbeek, in Atomic Collision Phenomena in Solids, S. Datz et al., eds. (Plenum Pub. Corp., N.Y., 1975), 1, 315. Also W. Eckstein, M. Verbeek, P. Matsche, J. Nucl. Mat. 63, 1976.

18) R. W. Conn and J. Kesner, J. Nucl. Mat. 63 (1976), 1.

III-F. Analysis of Thermal Stability in TETR

III-F-1. Introduction and Global Analysis

The thermal stability of a tokamak is usually considered in terms of the fluid energy balance equations at constant plasma density. Stability against density perturbations however must also be examined. A technique is developed here to examine stability in temperature and density using a one-dimensional space-time analysis of the fluid equations applied with a trapped particle microinstability model for plasma transport in TETR. Finite alpha thermalization time is included to investigate the effect of this delay time on the stability.

At low temperatures, ohmic heating and external sources of energy such as high energy neutral beams and/or RF heating are needed to balance the diffusion, conduction and radiation losses in a tokamak. Ignition occurs when the energy input from fusion alphas is great enough to overcome these losses. The ignition point represents an unstable equilibrium in temperature since an increase in the temperature causes the plasma to cool. Once past ignition, the plasma heats to a second equilibrium where increased energy losses due to synchrotron radiation and perhaps enhanced diffusion and conduction losses from microinstabilities overcome the energy source from the fusion alphas. Fig. F-1 is a qualitative plot of the energy losses and fusion power as a function of temperature. In cases (a) and (b), the intersection of the energy loss and fusion energy curves at lower temperature represent the ignition point. The intersection at higher temperature gives a stable equilibrium in temperature. In case (c), the losses always exceed the fusion energy input and an external

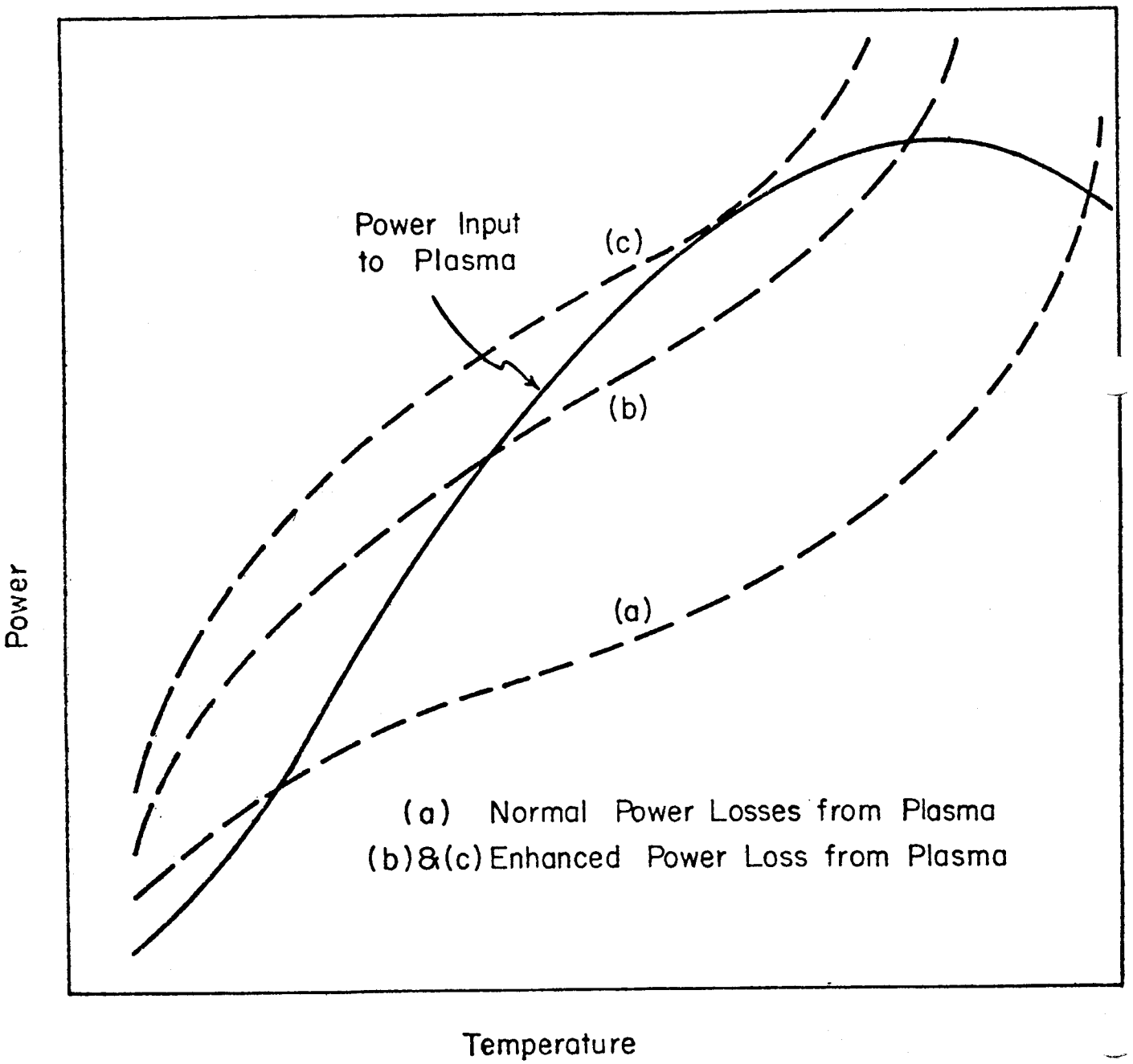

FIGURE III-F-1

source of energy would be required to maintain a thermal equilibrium. Case (c) could be a candidate for a beam driven device such as TETR. The energy input is from beams and beam-plasma fusions while the losses are basically the same as in an ignited plasma. Figure III-F-2 is a qualitative plot of the energy sources and losses as a function of temperature for the TCT mode of operation. The intersection of the loss and gain curves represent a stable equilibrium in temperature.

An external source of fueling is required in a large tokamak in addition to the source from high energy neutral beams if steady state or long pulse operation is to be attained. In order to maintain constant or slowly rising density during the startup phase, this source would have to be programmed to make up for the diffusion losses. This would require some type of feedback mechanism on the particle source. At equilibrium, the feedback can be turned off and a steady rate of fueling would maintain constant plasma density provided the plasma is stable against density perturbations. If unstable, a feedback on the particle source would be required during the entire lifetime of the plasma.

A simple global analysis of the plasma can be carried out to illustrate the conditions for stability in density at the stable equilibrium in temperature. The global density equation is written as:

$$\frac{dn}{dt} = -\frac{n}{\tau_p} - S_{fus} + S_b + S_p \qquad (1)$$

where n - average plasma density

τ_p - particle confinement time

S_{fus} - loss of ions due to fusion

S_b - source of ions from neutral beams

S_p - external source of ions (e.g., pellets)

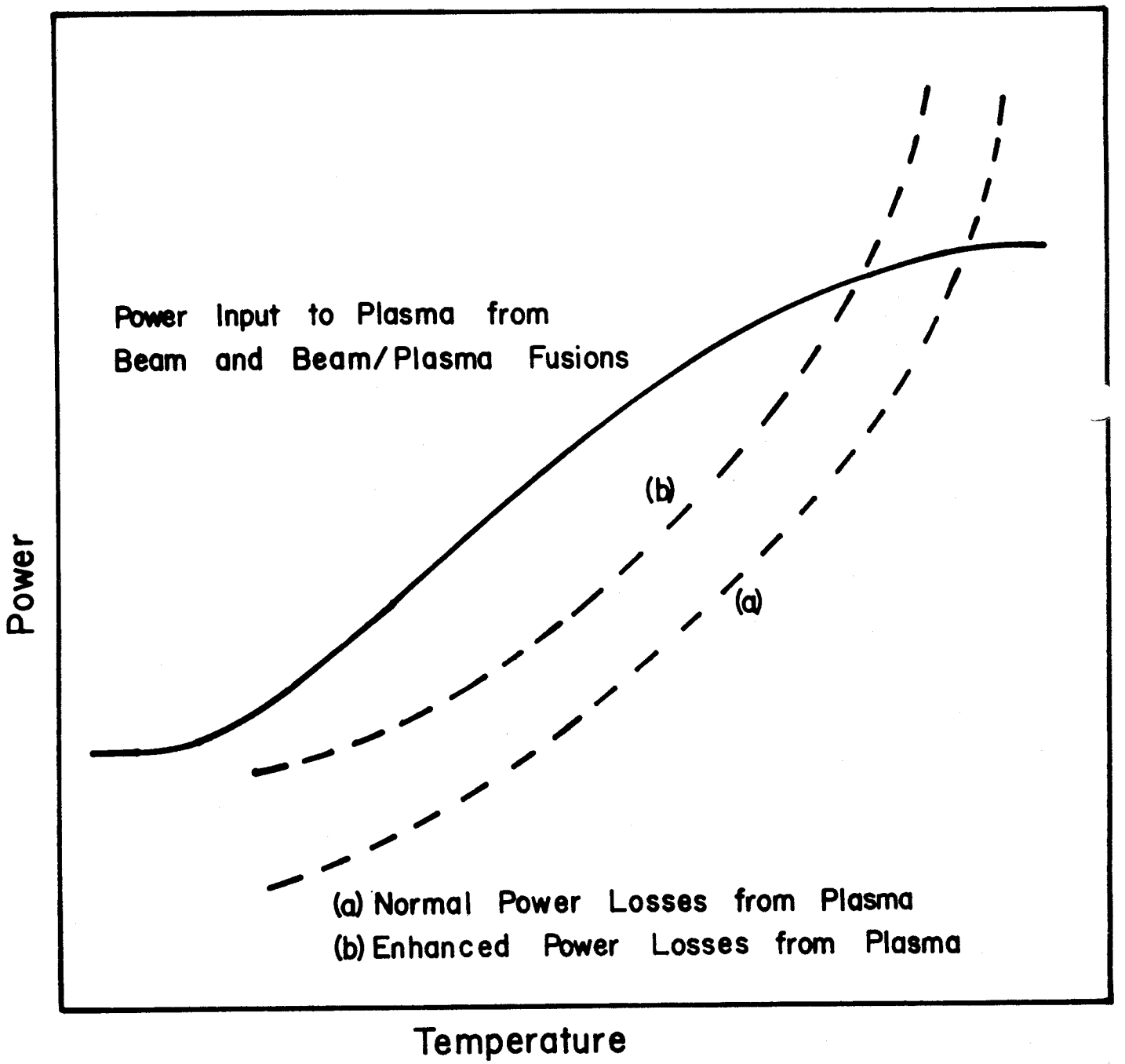

FIGURE III-F-2

Designate n_o, T_o, τ_{po}, S_{bo}, S_{po}, and S°_{fus} as equilibrium quantitites and expand about equilibrium:

$$n = n_o + \delta n$$

$$T = T_o + \delta T$$

Let

$$\tau_p = \left(\frac{n}{n_o}\right)^{\alpha} \left(\frac{T}{T_o}\right)^{\beta} \tau_{po}$$

For a constant beam source, the perturbed density satisfies the linearized time dependent equation

$$\frac{\partial \delta n}{\partial t} \cong \left[-(1-\alpha) \frac{\delta n}{n_o} + \beta \frac{\delta T}{T_o} \right] \frac{n_o}{\tau_{po}} - \left. \frac{\partial S_{fus}}{\partial n} \right|_o \delta n - \left. \frac{\partial S_{fus}}{\partial T} \right|_o \delta T$$

$$+ \left. \frac{\partial S_p}{\partial n} \right|_o \delta n + \left. \frac{\partial S_p}{\partial T} \right|_o \delta T \qquad (2)$$

The loss of ions due to fusion can be neglected in systems with small fractional burnup since the diffusion losses predominate. For an ignited plasma, this loss is a strong function of density and temperature because of the $n^2 \langle \sigma v \rangle$ dependence and should be incorporated in the stability analysis if large fractional burnup of the fuel is anticipated. For a beam driven device such as TETR, the fractional burnup should be small to prevent the buildup of deuterium in the predominantly tritium plasma. In addition, the density and temperature dependence of the fusion rate is very weak so the effect on the stability analysis is minimal. The density dependence of the particle source could enter through a feedback scheme. The possible temperature dependence of the particle source will be neglected here. With these simplifications, eqn. 2 becomes:

$$\frac{\partial \delta n}{\partial t} \simeq \left[-(1-\alpha) \frac{\delta n}{n_o} + \beta \frac{\delta T}{T_o} + \tau_{po} \left. \frac{\partial S_p}{\partial n} \right|_o \right] \frac{\delta n}{\tau_{po}} \qquad (3)$$

Stacey[1] used a perturbation analysis similar to that above for the global hydrogenic ion and fusion alpha density equations and the electron and ion energy balance equations. He considered stability both at the ignition point (unstable to pure temperature perturbations) and at the stable equilibrium in temperature for various scalings of the particle and energy confinement time. A more simplified global analysis is used here to examine conditions for stability against perturbations only at the stable equilibrium in temperature. Through the electron and ion energy balance equations, the temperature responds to a change in the density. Simplistically, let

$$\frac{\delta T}{T_o} \simeq \varepsilon \frac{\delta n}{n_o}$$

where ε is analogous to a temperature coefficient of reactivity in fission reactor analysis.

$$\frac{\partial \delta n}{\partial t} \simeq \left[-(1-\alpha) + \beta\varepsilon + \tau_{po} \left. \frac{\partial S_p}{\partial n} \right|_o \right] \frac{\delta n}{\tau_{po}} \qquad (4)$$

The stability requirement for density perturbations is given by:

$$\alpha - 1 + \beta\varepsilon + \tau_{po} \left. \frac{\partial S_p}{\partial n} \right|_o < 0 \qquad (5)$$

With the particle source feedback off and the temperature response to density perturbations turned off, the "pure density" stability analysis of Stacey[1] is obtained. This requires $\alpha < 1$ for stability. $\alpha = -1$ for classical, neoclassical and pseudoclassical scaling of the particle confinement time which exerts a strong stabilizing influence. Dissipative trapped ion mode scaling of the particle confinement time gives $\alpha \cong 1$ and neutral stability

against density perturbations is found. The temperature response to density perturbations then solely determines stability, i.e., $\beta\varepsilon < 0$. $\beta \simeq -7/2$ for the trapped ion mode which would require $\varepsilon > 0$ for stability without particle source feedback.

Table III-F-1 gives a summary of the temperature response of the various terms in the energy balance due to density perturbations. The only stabilizing terms are the Maxwellian fusion energy source and the synchrotron radiation loss ($n^{1/2}$ dependence). If the net response of the temperature yields an unstable equilibrium, a particle source feedback can be used to maintain the density at the desired level. The condition on the particle source for stability is then

$$\left.\frac{\partial S_p}{\partial n}\right|_o < \frac{1-\alpha-\beta\varepsilon}{\tau_{po}} \tag{6}$$

A linear feedback system on the particle source is used here. The source response is modelled as:

$$S_p = S_{po}\left(1 - G\,\frac{\delta n}{n_o}\right) \tag{7}$$

Where G represents the gain for the source response. For stability, the gain must satisfy:

$$G > -(1-\alpha-\beta\varepsilon)\,\frac{n_o}{\tau_{po} S_{po}} \tag{8}$$

A source response time can be defined in terms of the gain requirement as:

$$\tau_s \equiv \frac{\tau_{po}}{G} \tag{9}$$

which means that increases in the gain requirement decreases the time in which the source must respond to changes in density. At equilibrium:

TABLE III-F-1

Temperature Response of Density Perturbations in Energy Balance

TERM	ε
Maxwellian fusions	+
Beam-plasma fusions	-
Ohmic heating	-
Beam injection	-
Bremstrahlung, line, recombination radiation	-
Synchrotron radiation	+
Conduction, diffusion (trapped ion)	~ 0

$$\frac{n_o}{\tau_{po}} = S_{po} + S_{bo} - S^{\circ}_{fus} \cdot$$

Define the fractional burnup as

$$f_b \equiv \frac{S^{\circ}_{fus}}{S_{bo} + S_{po}} = \frac{S^{\circ}_{fus}}{S^{\circ}_{tot}} \qquad (10)$$

then

$$G > - (1-\alpha-\beta\varepsilon)(1 - f_b) \frac{S^{\circ}_{tot}}{S^{\circ}_{po}} \qquad (11)$$

Increasing the fractional burnup reduces the gain requirement. If the component of the total particle source being used for the feedback is a small component of the total source, the gain requirement can be significantly increased.

A global analysis has several inherent deficiencies. The stabilizing influences of Maxwellian fusions and synchrotron radiation (although weak) are strongly peaked in the central core of the plasma. The destabilizing terms such as radiation and diffusion and conduction losses (especially trapped ion mode) are strongest in the outer region of the plasma. A strong coupling between the central core and outer region may be required to give overall stability. Changes in the shape of density and temperature profiles may also play an important role especially for the trapped particle modes which are sensitive to gradients. Density increases in the central core tend to increase the average density gradient while increases at the plasma edge decrease the center and stabilizing in the average gradient. This gives ε a spatial component which is destabilizing at the outer region for transport due to the trapped ion mode.

III-F-2. One Dimensional Space-Time Analysis of Thermal Stability

Thermal stability in TETR is examined here using a one-dimensional space-time transport code for the ion density and the electron and ion energy fluid eqs.[2] The numerical techniques employed in the code are very stable against numerical oscillations and preserve particle and energy fluxes.[3] These two conditions are necessary to insure that an instability is physical and not numerically introduced. First, a run is made with feedback on the particle source until a stabilized equilibriu is reached at the desired average plasma density. A second run is then made and the feedback is turned off just before equilibrium is reached. This effectively introduces perturbations in both source intensity and densities and temperatures from the equilibrium values determined in the first run. The profiles are then allowed to evolve in time until a second equilibrium is reached or the plasma quenches. If a second equilibrium is reached which is close to the equilibrium found in the first run, the plasma is thermally stable against density, temperature and source perturbations. If not, the dominant mechanisms for the unstable behaviour can be determined from the time evolution of the plasma.

A simple feedback mechanism is used on the particle source. The source profile is assumed constant in time with a variable amplitude.

$$S_p(r,t) = S_p(t)\, f(r) \qquad (12)$$

This source may be provided by pellets and is in addition to the sources from beams and neutral gas recycle. The spatially averaged density, $\bar{n}$, is sensed at equally spaced time intervals τ_s and the source amplitude is readjusted to attain the desired density, $\bar{n}_o$, at time τ_s later.

$$t_i - \tau_s < t < t_i: \quad \frac{d\bar{n}}{dt} \simeq \frac{\bar{n}_i - \bar{n}_{i-1}}{\tau_s} = -\bar{L}_i + \bar{S}_{p,i} + \bar{S}_{b,i} + \bar{S}_{n,i}$$

$$t_i < t < t_i + \tau_s: \quad \frac{d\bar{n}}{dt} \simeq \frac{\bar{n}_o - \bar{n}_i}{\tau_s} = -\bar{L}_{i+1} + \bar{S}_{p,i+1} + \bar{S}_{b,i+1} + \bar{S}_{n,i+1}$$

where L - diffusion losses

S_b, S_n - beam and neutral gas recycle sources

To close the equations, assume the loss rates in time intervals i and i + 1 are approximately equal, $\bar{L}_{i+1} \simeq \bar{L}_i$, and the beam and neutral recycle sources are constant. Then solve for $\bar{S}_{p,i+1}$:

$$\bar{S}_{p,i+1} = \bar{S}_{p,i} + \frac{(\bar{n}_o - 2\bar{n}_i + \bar{n}_{i-1})}{\tau_s}$$

This type of feedback scheme has several limitations. The source response time must be short compared to the rate of change of the diffusion loss terms, i.e., a high gain is needed. Since the average density is being sensed, the feedback would be incapable of stabilizing perturbations which are primarily due to changes in the shape of the density profile. It has also been assumed in the model that the source deposition profile is insensitive to changes in the density and temperature profiles. Coupling between the source deposition profile and the density profile may have a stabilizing or destabilizing influence.

Several "clean" plasma cases are examined here for TETR in which there are no impurities and no neutral gas recycle. A multi-regime model for plasma transport is used in which the trapped ion mode is dominant over most of the plasma radius. In Figures III-F-3 and 4 the time histories of the average density and temperatures are plotted for two different source profiles. In Case I (Fig. III-F-3 the source profile is linearly decreasing in radius and in Case II (Fig. III-F-4) the source profile is flat. A source response time of τ_s = 4 msec gives stabilized equilibria in both cases at an average density of 7.5×10^{13} cm^{-3} with particle confinement times of $\tau_{po} \cong$ 37 msec and 27 msec respectively. When the source feedback is turned off at 200 msec, the plasma relaxes to a second equilibrium.

In both Cases I and II the plasma can be considered marginally stable. Table III-F-2 shows that when the source feedback is turned off at 200 msec, all the global plasma parameters were within a few percent of the equilibrium values. The new equilibrium values of the average density are much lower which indicates the sensitivity to the source strength. From the global analysis, the diffusion loss is roughly n/τ_p and $\tau_p \sim n$ for the trapped ion mode which dominates the diffusion. The temperature dependence of τ_p then dictates the new equilibrium density when the source is perturbed.

The global analysis with the trapped ion mode would indicate the plasma should be unstable, i.e., the net temperature response is $\varepsilon < 0$. In Figure III-F-5 the density profiles are shown for Case I at the stabilized equilibrium and at the second equilibrium after the source feedback is turned off. The differences in the shapes of the profiles are extremely small. The slight flattening of the profile reduces the losses but doesn't account for all of the stabilizing influence. Although the diffusion is dominated by the trapped ion mode, the other components of the diffusion have a stabilizing influence particularly the conversion of the trapped ion mode to the "collisionless" mode in which $D \sim n^{1/2}$. (4)

TETR CASE I

INSTANTANEOUS ALPHA THERMALIZATION

$S_p(r,t) = S_p(t)(1-r/a)$

--- FEEDBACK ON

—— FEEDBACK OFF AT 200 MSEC

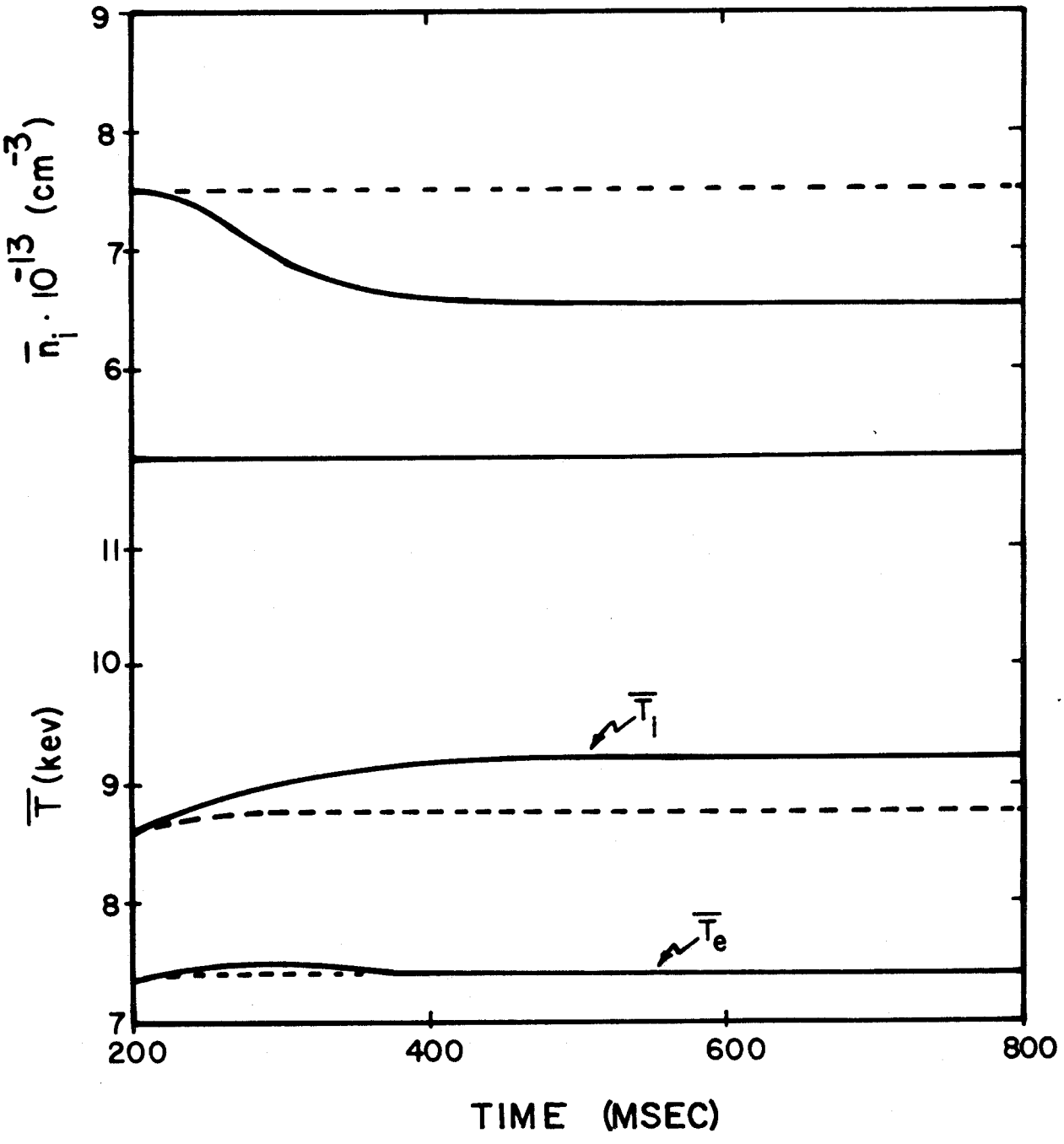

Fig. III-F-3

TETR CASE II

INSTANTANEOUS ALPHA THERMALIZATION

$S_p(r,t) = S_p(t)$

--- FEEDBACK ON

—— FEEDBACK OFF AT 200 MSEC

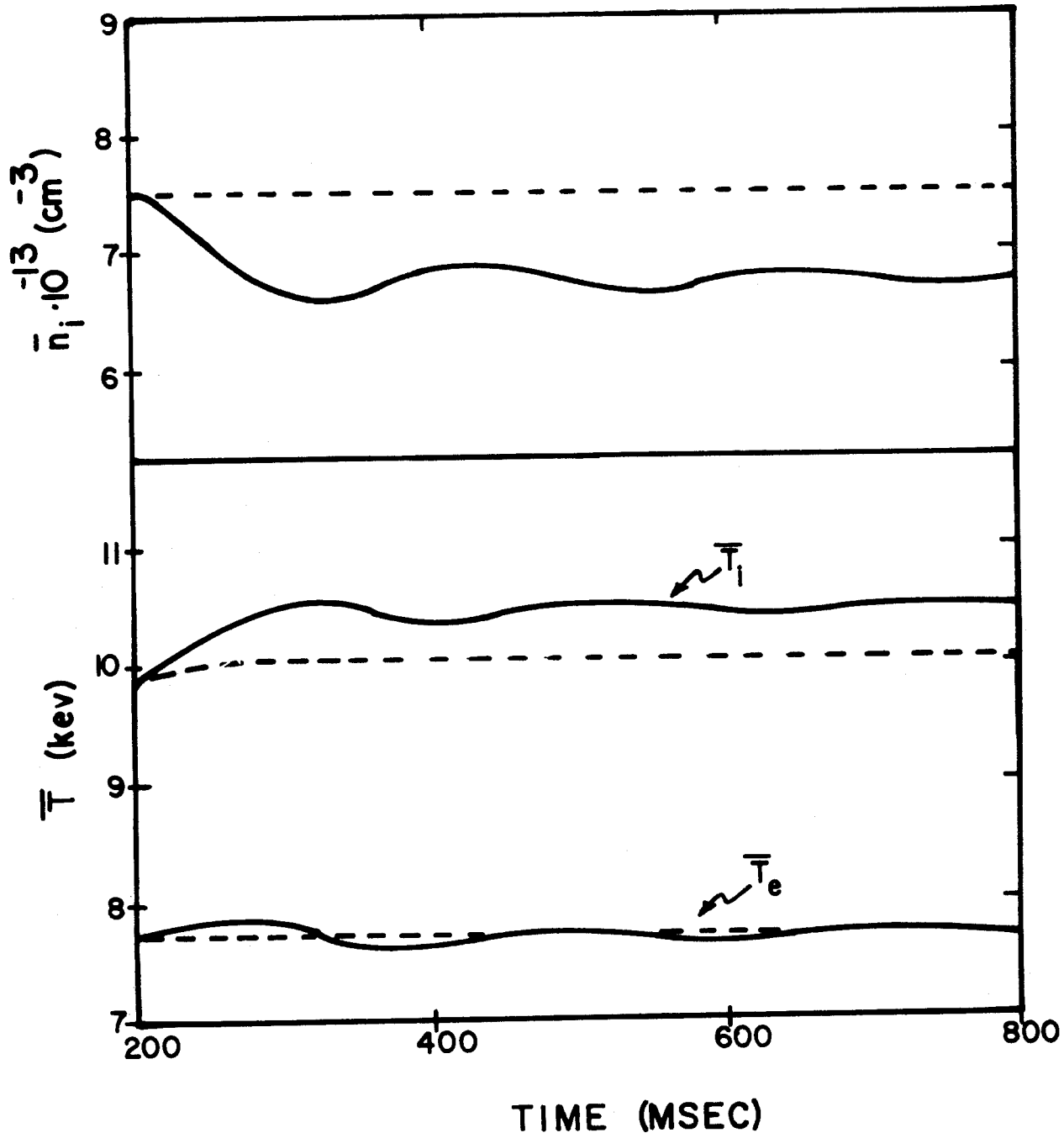

Fig. III-F-4

TABLE III-F-2

Parameter	CASE I		CASE II	
	At equilibrium	At 200 MSEC(%)	At equilibrium	At 200 MSEC(%)
$\bar{n}_i$ (cm^{-3})	7.500×10^{13}	7.498×10^{13}(-.27)	7.500×10^{13}	7.495×10^{13} (-.67
$\bar{T}_e$ (keV)	7.406	7.343(-.85)	7.730	7.734 (+.52
$\bar{T}_i$ (keV)	8.769	8.599(-1.94)	10.067	9.886 (-1.80
$\bar{S}_p$(cm^{-3} $msec^{-1}$)	1.879×10^{12}	1.834×10^{12}(-2.39)	2.645×10^{12}	2.586×10^{12}(-2.23
$\bar{S}_{tot}$($cm^{-3} msec^{-1}$)	2.032×10^{12}	1.986×10^{12}(-2.26)	2.797×10^{12}	2.738×10^{12} (2.11
τ_{po} (msec)	37.0	----	26.8	----
τ_s (msec)	4.0	----	4.0	----

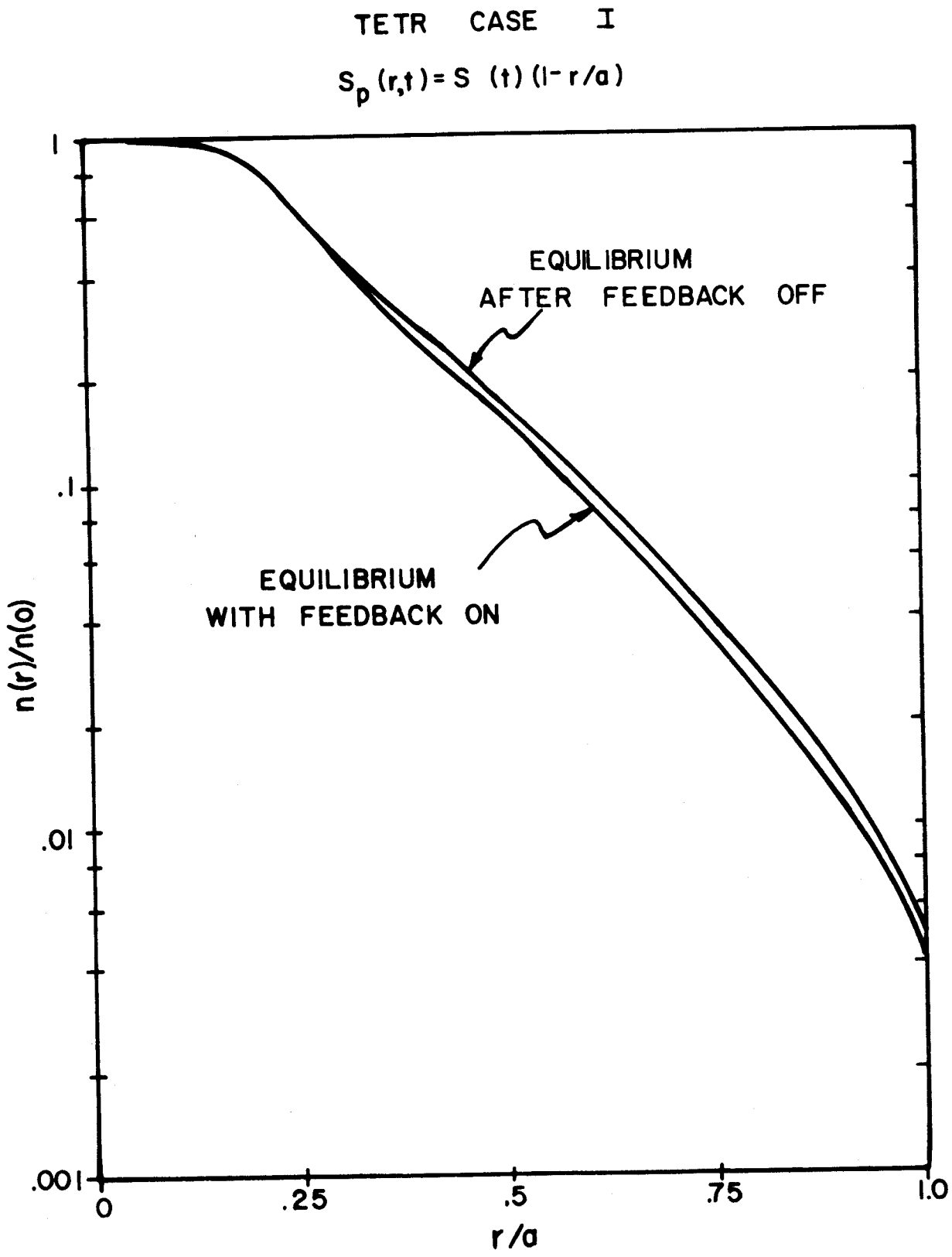
TETR CASE I
$S_p(r,t) = S(t)(1 - r/a)$
EQUILIBRIUM
AFTER FEEDBACK OFF
EQUILIBRIUM
WITH FEEDBACK ON
n(r)/n(o)
1
.1
.01
.001
0
.25
.5
.75
1.0
r/a

Fig. III-F-5

In Cases I and II the fusion alphas were assumed to thermalize instantaneously. Finite alpha thermalization time introduces a delay between the time of production of the alphas and the time in which their energy is given to the ions and electrons. In a beam driven device such as TETR, the rate of production of alphas is insensitive to the plasma density. In a 50-50 DT plasma the fusion rate is very sensitive to the density and a much stronger coupling between the density and the energy source from fusion is found. The alpha thermalization time is density dependent which introduces an additional effect in the coupling of the fusion energy source to the plasma.

The rate of energy loss of an energetic alpha particle in a Maxwellian plasma is given by:[5]

$$\frac{dE}{dt}^{3/2} = -\frac{1}{\tau}\left(E_c^{3/2} + E^{3/2}\right) \qquad (13)$$

E - mean energy of alpha particle

$$E_c \equiv 59.2\ T_e \left[\frac{1}{n_e \ln\Lambda_e} \sum_{\text{ions}} \frac{Z_j^2 n_j \ln\Lambda_j}{A_j}\right]^{2/3}$$

- critical energy

$$\tau^{-1} \equiv \frac{8\sqrt{2\pi}}{3}\left(\frac{e^2}{4\pi\varepsilon_o}\right)^2 \left(\frac{m_e}{m_p}\right)^{1/2} \frac{n_e \ln \Lambda_e}{(kT_e)^{3/2}}$$

- energy relaxation time

Equation (13) gives the rate of relaxation of the mean energy and neglects the spread in energy about the mean as the particles thermalize. This

expression can be used to find the rate of energy transfer to the plasma from alphas born at all past times. A time history of the production rate of alphas is maintained as a function of the radial position in the plasma. In each time interval, the rate of energy loss and the fraction of the energy given to each plasma specie are found. Radial diffusion of the alphas while thermalizing is neglected but may play an important role.[6]

Tsuji, et al.[5] used a similar model for the rate of alpha thermalization to evaluate the time dependent energy distribution for the alpha particles in a global analysis and the effects on plasma heating. Their analysis included velocity diffusion (spread about the mean energy) and an energy independent loss of the alpha particles from the plasma volume due to radial diffusion. The time dependence of the alpha thermalization produced an "inertial" effect on the transient response of the plasma. Decreases in plasma density and increases in temperature reduce the rate of energy transfer from the fast alpha distribution because of the reduction in collisionality. This density and temperature effect is in addition to the changes in the source strength of fusion alphas, $n^2 \langle \sigma v \rangle$. The heating efficiency of fast alphas is found to be dramatically reduced when the confinement time is comparable to or less than the thermalization time.

FiguresIII-F-6 and 7 show the effects of finite alpha thermalization on the time history of the average plasma density and temperatures. These cases are the same as Cases I and II except for the finite thermalization time. When the feedback is turned off,the plasma relaxes to a stable thermal equilibrium with the same qualitative behaviour as in Cases I and II. When the feedback is turned off at 200 msec the plasma is further from equilibrium than in the previous cases due to the slower heating rates of the alphas. This accounts for the greater difference in densities at the second equilibrium. When the feedback is turned off at 300 msec the plasma is closer to equilibrium and the drift in density is reduced.

TETR CASE III

FINITE ALPHA THERMALIZATION

$S_p(r,t) = S_p(t)(1 - r/a)$

--- FEEDBACK ON

—— FEEDBACK OFF AT 200, 300 MSEC

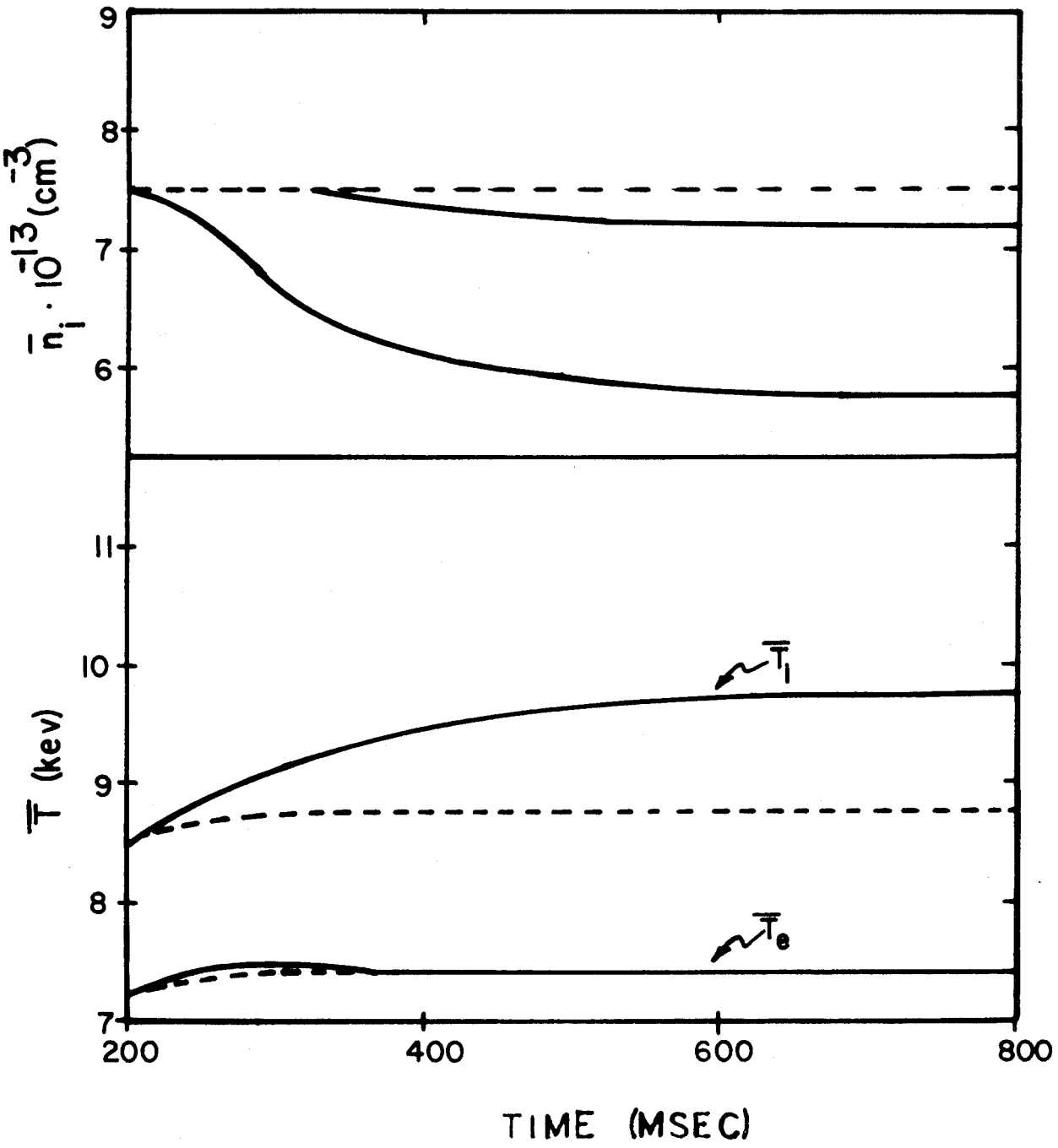

Fig. III-F-6

TETR CASE IV

FINITE ALPHA THERMALIZATION

$S_p(r,t) = S_p(t)$

– – – FEEDBACK ON

——— FEEDBACK OFF AT 200, 300 MSEC

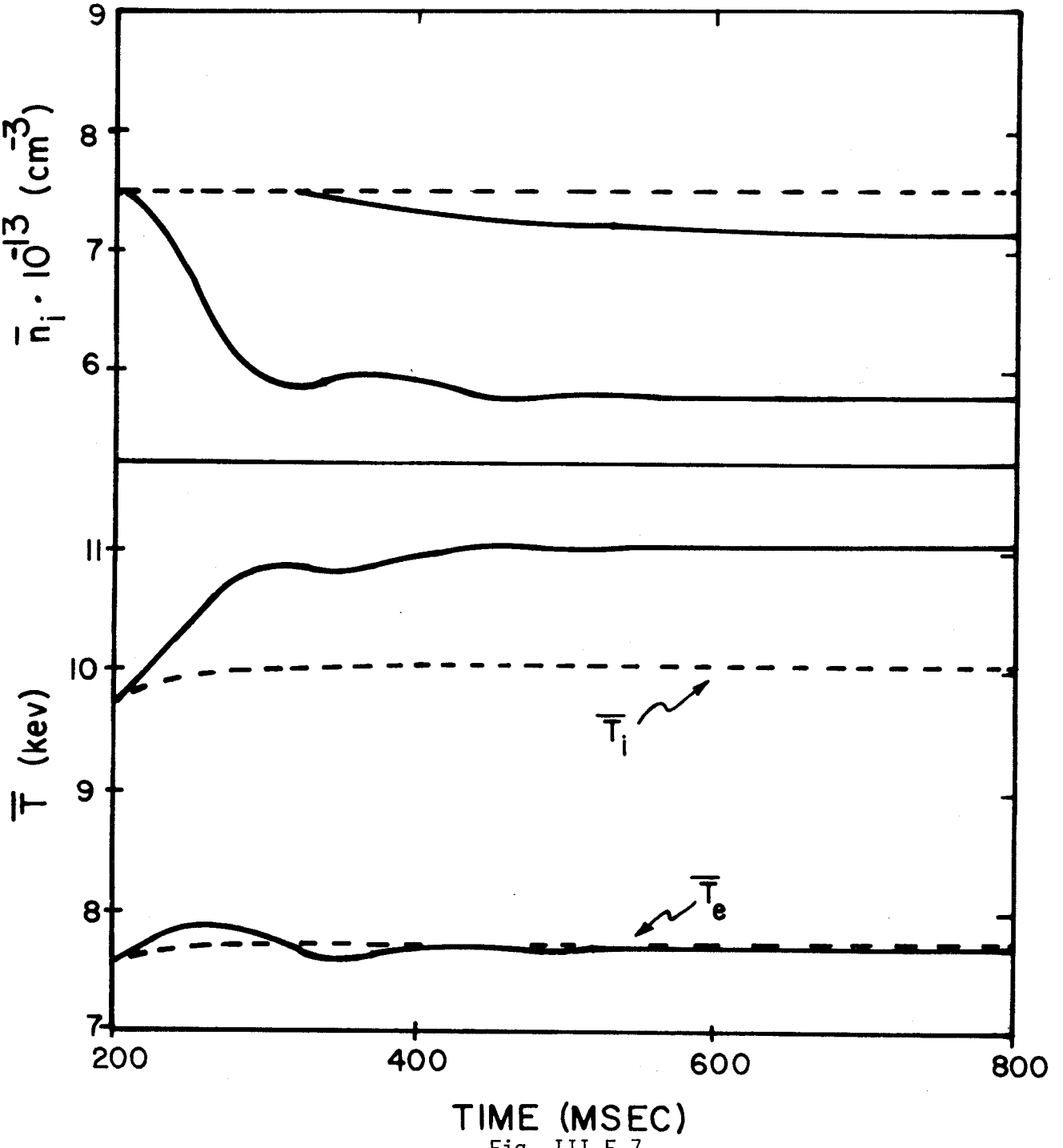

Fig. III-F-7

III-F-3. Summary

The sensitivity of the equilibrium density in TETR to the source level for the transport model used here indicates that the source should at least have a tuning capability if feedback is not used. The addition of impurities and coupling of the source deposition profile to the density would likely impose greater restrictions on the feedback system if the plasma is thermally unstable.

A built-in feedback system is provided in currently operating tokamaks since the system is closed. Ions lost from the plasma by diffusion are neutralized on limiter and can return to the plasma. The plasma density remains fairly constant during the discharge even though no external source of ions is provided. Even if unstable scaling of the diffusion losses exists it may be masked by the built-in feedback.

One dimensional space-time transport codes are widely available and can be used to examine the thermal stability of tokamaks. Important spatial dependent effects limit the applicability of global analyses but are automatically included in a space-time simulation. The physical model used here is greatly simplified and is meant to illustrate the general technique. The effects of impurities, neutral gas recycle and various transport mechanisms can easily be examined with existing models. Several other physical mechanisms may affect the stability analysis but would require some model development. The transport of fast alphas while thermalizing may have a significant impact on the heating profile in the plasma. Strong coupling between the particle source deposition profile and the density and temperature would add an additional space-dependent effect not examined here due to the lack of a specific fueling model.

References for Section III-F

(1) W. M. Stacey, Jr., Nuclear Fusion 15, 63 (1975).

(2) W. A. Houlberg, "Development of a One-Dimensional Fluid Transport Model and the Analysis of Thermal Stability in Large Tokamaks," Ph.D. Thesis, University of Wisconsin-Madison (1977).

(3) W. A. Houlberg and R. W. Conn, "Fluid Simulation of Large Tokamak Plasmas Using a Variable Spatial Mesh, Variable Time Step Implicit Procedure," ANS Topical Conference on Improved Methods for Analysis of Nuclear Systems, Tucson, Arizona (March 28-30, 1977).

(4) W. A. Houlberg, "Growth Rates and Transport Coefficients for the Trapped Ion/Collisionless Trapped Particle Instability," University of Wisconsin Fusion Design Memo, UWFDM-162 (June, 1976).

(5) W. A. Houlberg, "Thermalization of an Energetic Heavy Ion in a Multispecies Plasma," University of Wisconsin Fusion Design Memo, UWFDM-103 (May, 1974).

(6) H. Tsuji et al., Nuclear Fusion 16, 287 (1976).

III-G. Primary Vacuum System

III-G-1. General Description

The function of the primary vacuum system in a fusion reactor is to pump out the unburned fuel and the reaction products during the burn cycle, and to clean and condition the chamber surfaces during the down time between cycles.

Since the fractional burnup in a magnetically confined reactor of the Tokamak type is very low, the order of several percent, most of the fuel leaves the plasma in the form of charged particles, and, eventually, has to be pumped out as a gas. Moreover, each DT reaction produces an α particle which also leaves the plasma and is pumped out as helium.

The gas throughput in such reactors is extremely high requiring a very large capacity pumping system in a rather limited space. Furthermore, since the effluent is recycled for fuel recovery, it is important that it be uncontaminated with hydrocarbons or any other contaminants. This requirement severely limits the type of pumps that can be used.

Cryo-sorption pumps have been the leading candidates for use in fusion reactors. They fill the requirement of high capacity and lack of contamination admirably. They are generally trouble free and require almost no maintenance. This is an extremely important criterion, since any maintenance in such close proximity to the reactor will have to be done by remote control.

Cryo-sorption pumps operate on the principle of attracting and trapping molecules in a molecular sieve attached to a surface cooled with boiling liquid helium. Molecular sieve is nothing more than a synthetic zeolite in the form of a very porous sponge which has an enormous molecular effective surface area. Condensable gasses will liquify within it, depending on their partial pressure. Non-condensable molecules are attracted to the

very cold surface and are trapped within the pores of the molecular sieve. When the molecular sieve becomes saturated, the pump is valved off, the pumping surfaces heated and the evolved gasses pumped out. As soon as the molecular sieve is regenerated and recooled to 4.2 K, the pump is ready to go on line again.

In TETR, the charged particles leaving the plasma are guided along magnetic field lines into the divertor zone where they give up their energy by striking a sacrificial plate and are then pumped out in molecular form. A double null poloidal divertor system is used to guide the particles out of the plasma chamber.

The space available in the divertor zone is limited and the pumping capacity needed is very high. Furthermore, the pumps have to be shielded from secondary neutrons. This requires space and is an additional complication. In order to fit in as many pumps as possible in the available space, a new and innovative idea in pump design was conceived. The idea is to build two pumps back to back, such that while one is on line, the other can be regenerated. As soon as the pump on line is saturated, the pump pair is rotated 180^{o}, and a freshly regenerated pump is in place to start pumping. In this way nearly all the available space is used by pumps which are actively pumping, whereas in previous designs, only half of the pumps could be on line, while the other half is being regenerated. This idea was discussed with a pump manufacturer[1] who saw no reason why it could not be implemented. Some R & D will be required to establish the most practical way of sealing such a rotatable pump. The sealing problem, however, will have to be solved in any case, since the pumps have to be valved off for regeneration.

The design of the primary vacuum system is described in the next section.

III-G-2. System Design, Capacity and Base Pressure

The primary vacuum pumps in TETR are situated in the top and bottom divertor zones as shown in Fig. III-G-1.

There is a total of 66 pump pairs, 33 in each divertor zone. Thus a set of 66 pumps can be on line at any one time with an equal number being regenerated.

Each pump pair is built into a cylinder 66 cm in diameter and 162 cm high. The pumping surface with the bonded molecular sieve comprises one side of the liquid helium reservoir and is 58 x 150 cm^2. The frontal area through which the gasses have to flow is covered with liquid nitrogen cooled (80 K) chevron baffles and is 47 x 150 cm^2. Each side is completely sealed and superinsulated from the other. As conceived, the outer seal goes around the shafts which are used to rotate the pump pair and then goes down on each side of the cylinder as shown in Fig. III-G-2. The supply and return lines for the nitrogen and helium go through the shaft in flexible metal hoses.

The size of the pump was dictated by the available space for rotating it. A larger diameter pump would have made better utilization of the space. As it is, the pumping area constitutes 80% of the total circumferential space.

The back side of the pump array is a continuous plenum which is used for regenerating the cryo-sorption surfaces. Since regeneration takes place at a pressure several orders of magnitude higher than the chamber operating pressure, the pumps needed to evacuate the evolved gasses can have a much smaller capacity. Roots blowers and dry compressors which are relatively contamination free are good candidates for use in regenerating the cryo-sorption pumps. The effluent at about an atmosphere of pressure then goes to purification and separation columns.

Figure III-G-1

CROSS SECTION VIEW OF TETR

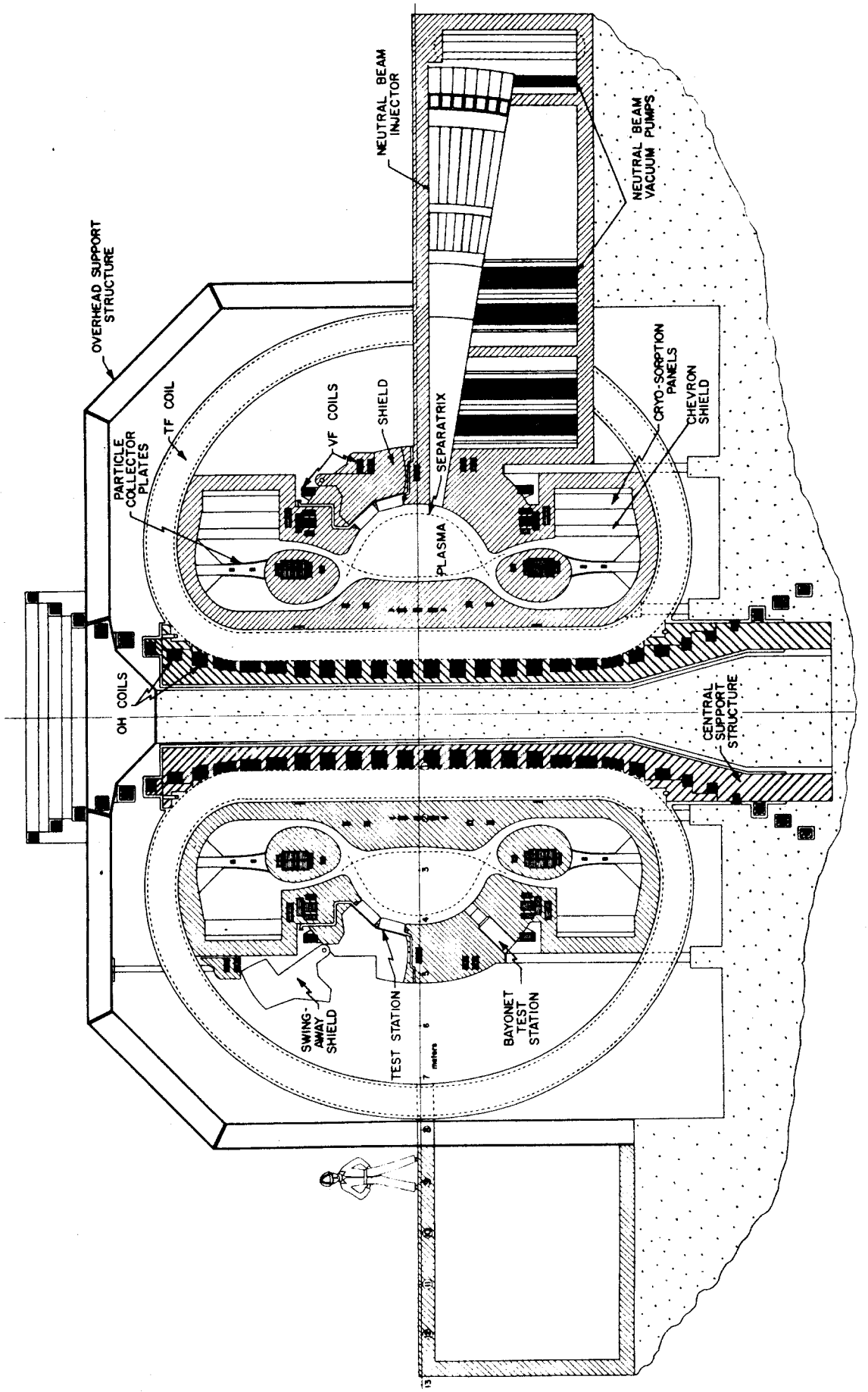

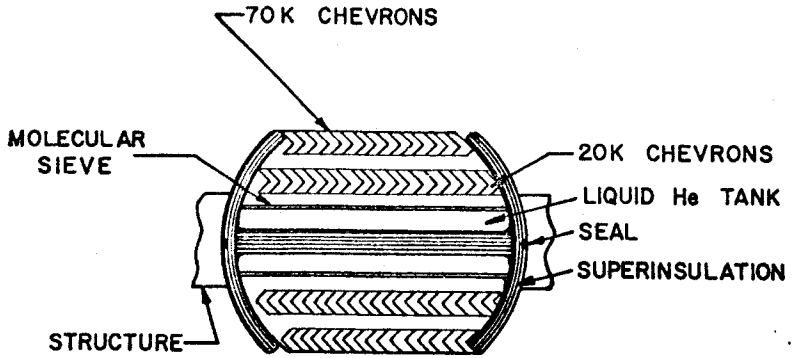

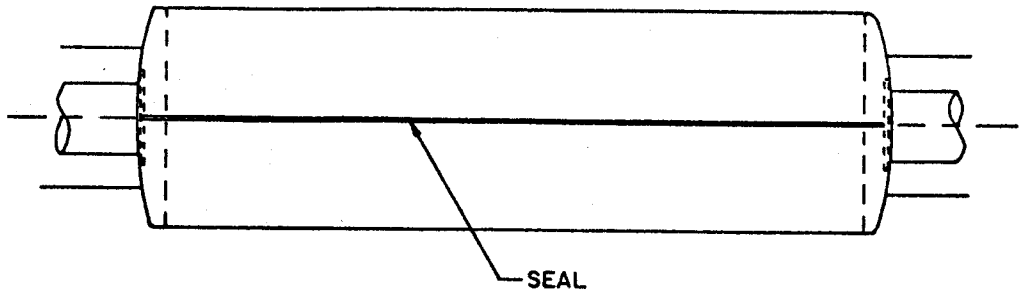

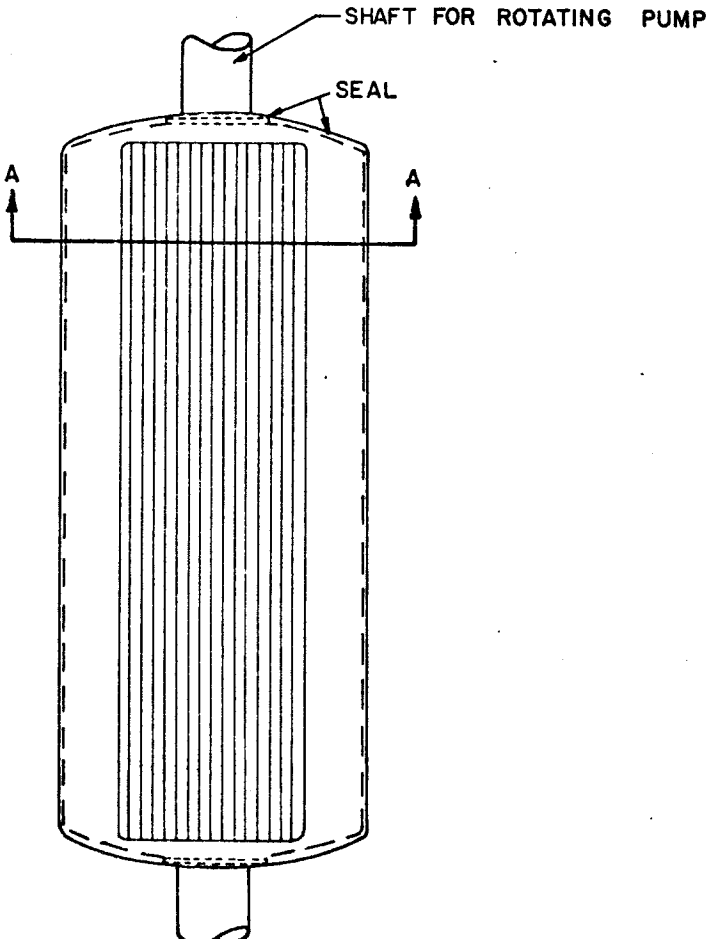

FIGURE III-G-2

Sketch of Proposed Rotatable Cryo-Sorption Pump

During initial evacuation of the chamber, the pumps are rotated 90° to allow the back up roots blower and dry compressors to pump the chamber down to ~1 x 10^{-3} torr. At this point the cryo-sorption pumps are rotated the rest of the way shutting off the pumpout plenum. Liquid helium and nitrogen is then supplied to the pumps facing the vacuum chamber and evacuation will proceed to ~1 x 10^{-7} torr. The chamber is then ready for initiation of burn.

In order to prevent secondary neutrons from striking the cryo-sorption pumps, a water cooled chevron shield was placed in the divertor zone. This shield, shown in Fig. III-G-3, is estimated to have a total conductance of 3.36 x 10^6 liters/sec for D_2 and T_2 at 500 K.

Experiments at ORNL with cryo-sorption pumping of deuterium gas indicate a pumping speed of 3.1 ℓ/sec. cm^2 between 10^{-8} - 10^{-4} torr, increasing to 5.6 ℓ/sec. cm^2 at 3 x 10^{-3} torr[2] [3]. This pump was definitely flow limited by the 6 inch diameter mounting flange. It is estimated that the speed would increase to 5 ℓ/sec. cm^2 if the mounting flange diameter was increased. The speed at 3 x 10^{-3} torr would then go up to ~8 ℓ/sec. cm^2. The pump used in the tests has two sets of chevron type thermal radiation shields similar to the design discussed above. It is readily admitted that the pumping speed could be increased by a factor of 2-3 if one set of chevrons can be eliminated.[3] Similarly, the pumping speed can be increased if the chevrons are not as closely packed. Pumping speeds of 8-15 ℓ/sec. cm^2 have been reported[4]. Eliminating chevrons and spacing them wider apart, while increasing the pumping capacity will also increase the cryogen requirement of the pumps.

Although the pumping of deuterium and tritium is primarily by cryo-condensation[3], pumping of helium gas is by cryo-sorption. Specific pumping speeds for helium are in the order of 1-2 ℓ/sec. cm^2 [3] [4].

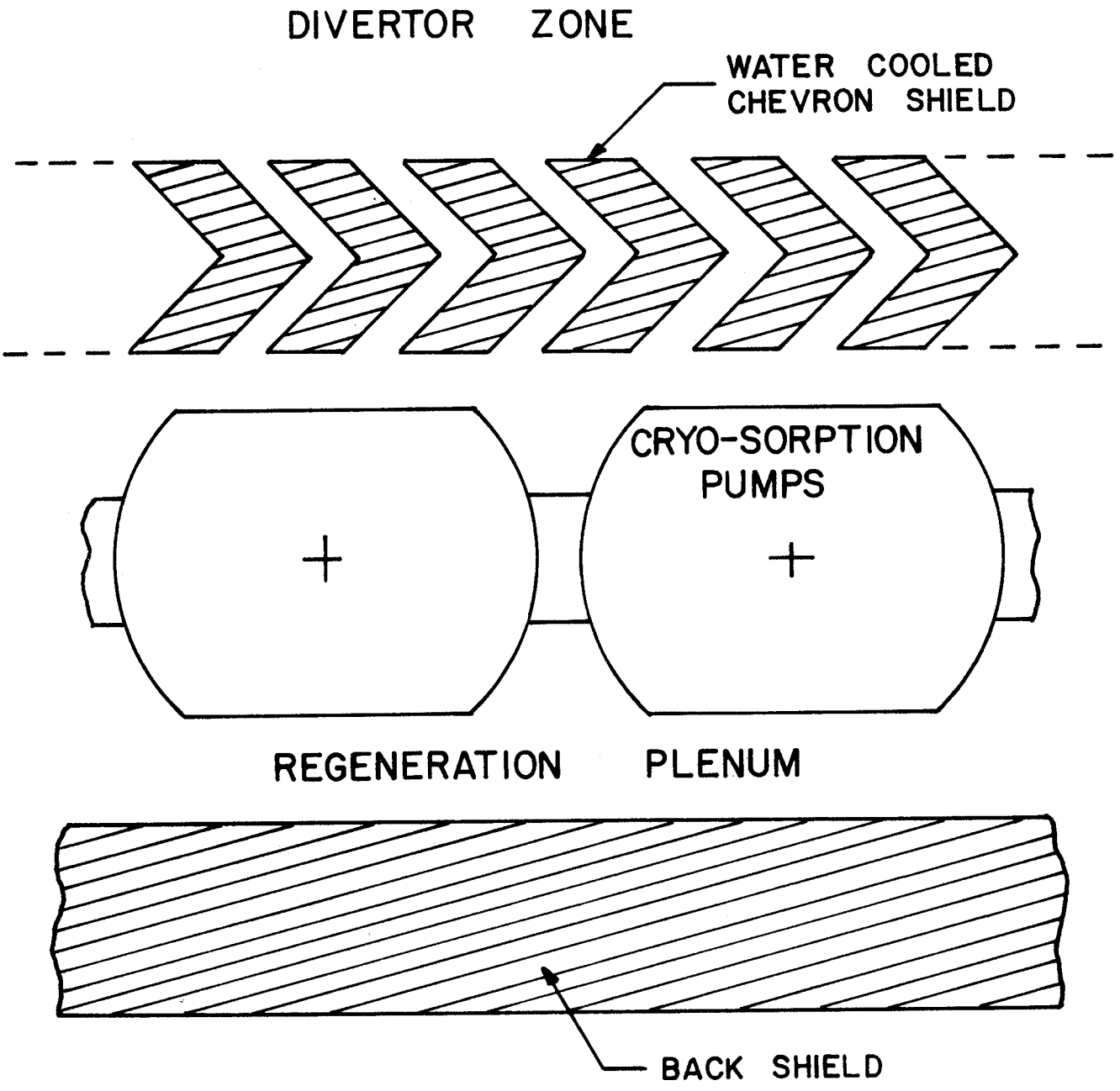

Figure III-G-3
View Showing the Relative Location of the Chevron Shield and the Cryo-Sorption Pumps.

The total pumping area in both divertor zones is equal to 57.4×10^4 cm^2. If we assume 8 ℓ/sec. cm^2 pumping speed for D and T, and 1 ℓ/s cm^2 for helium, then the capacity of the pumps will be

$$\overset{\circ}{S}_{D\&T} = 57.4 \times 10^4 \times 8 = 4.59 \times 10^6 \text{ ℓ/sec.}$$

$$\overset{\circ}{S}_{He} = 57.4 \times 10^4 \times 1 = 0.57 \times 10^6 \text{ ℓ/sec.}$$

If we now include the conductance of the chevron shield which was found to be 3.36×10^6 ℓ/sec, the pumping capacity of the system will be

$$\overset{\circ}{S}_{D\&T} = 1.94 \times 10^6 \text{ ℓ/sec.}$$

$$\overset{\circ}{S}_{He} = 0.48 \times 10^6 \text{ ℓ/sec.}$$

The particle flux in the divertor zones in TETR is 2.8×10^{22} ions/sec of D and T, and 9.5×10^{19} α/sec. If we assume that after recombination, the temperature of the gas will average out at somewhere between the temperature of the divertor walls and the chevron shield, about 500 K, the gas through put will be

$$\overset{\circ}{Q}_{(D,T)} = \left(\frac{2.8 \times 10^{22}}{2}\right) (1.03 \times 10^{-22}) (500) = 7.2 \times 10^2 \text{ torr liters/sec.}$$

$$\overset{\circ}{Q}_{(He)} = (9.5 \times 10^{19}) (1.03 \times 10^{-22}) (500) = 4.9 \text{ torr liters/sec.}$$

The expected base pressure in the divertor zone will be

$$\overset{\circ}{P}_{D\&T} = \frac{7.2 \times 10^2}{1.94 \times 10^6} = 3.7 \times 10^{-4} \text{ torr}$$

$$\overset{\circ}{P}_{He} = \frac{4.9}{0.48 \times 10^6} = 1 \times 10^{-5} \text{ torr}$$

and in front of the cryo-sorption pumps.

$$\overset{\circ}{P}_{D\&T} = \frac{7.2 \times 10^2}{4.59 \times 10^6} = 1.5 \times 10^{-4} \text{ torr}$$

$$\overset{\circ}{P}_{He} = \frac{4.9}{0.57 \times 10^{6}} = 8.6 \times 10^{-6} \text{ torr}$$

Between pulses the plasma chamber is back filled with D_2 to $\sim 1 \times 10^{-3}$ torr and then pumped down to $\sim 1 \times 10^{-7}$ torr in order to clean and condition the surfaces. The conductance of the divertor slots is estimated at $\sim 1.5 \times 10^{6}$ ℓ/sec making the pumping capacity of the divertor system during down time, $\overset{\circ}{S}_{D\&T} = 8.5 \times 10^{5}$ ℓ/sec. In addition, the neutral beam pumping system adds 2×10^{5} ℓ/sec after the conductance of the beam lines is accounted for. Thus, the total pumping capacity when the plasma is down is

$$\overset{\circ}{S}_{D\&T} = 10.5 \times 10^{5} \text{ ℓ/sec}$$

In a properly cleaned and baked stainless steel system the outgassing rate can be reduced to about 1×10^{-5} torr liters/sec. cm^2.[5] Since the walls of the chamber are essentially continuously baked and pumped, it can be assumed that they will stay relatively clean. The outgassing from the stainless steel is then negligible. We will also assume that leaks will add a negligible quantity of gas.

The graphite liner, however, will absorb gas during the back filling state. Experiments[6] have shown that for certain graphites during repeated absorption desorption cycles, the amount of gas absorbed decreases dramatically and is readily released upon pumping. We estimate that ~200 torr liters of D_2 will be absorbed by the graphite liner during the back filling stage of the cycle and will have to be subsequently pumped out. In addition, the vapor pressure of graphite at 2000 K is 1×10^{-7} torr and this then limits the pressure to which the chamber can be evacuated.

The time needed to evacuate the chamber from 1×10^{-3} torr to 1×10^{-7} torr is estimated to be ~5 seconds.

III-G-3. Regeneration and Cryogenic Requirement

It has been decided to regenerate the cryo-sorption pumps every two hours. This decision was based on the need to minimize the tritium hold-up in the pumps.

For a steady state duty cycle of 83%, the amount of D&T trapped in the pumps will be ~3400 ℓ (STP), of which half is tritium. This amounts to 375 gm of tritium or ~3.75 MCi.

There will be a total of 60 Kg of molecular sieve in each set of 66 cryo-sorption pumps. After two hours of pumping, 57 cm^3 (STP) of D&T and 0.4 cm^3 (STP) of He will have been absorbed per gram of molecular sieve. Experiments have shown that as much as 300 cm^3 (STP) of D&T can be adsorbed per gram of molecular sieve before there are indications of saturation.

The amount of cryogen used by a cryo-sorption pump is a strong function of the frequency of regeneration. If we extrapolate cryogen usage from presently operating pumps we find that 2250 liters of liquid helium are needed to recool 66 pumps of our design from 80 K to 5 K, whereas only 250 liters are used up in two hours of steady state pumping. If the pumps are regenerated twelve times in 24 hours, the total liquid helium consumption per day is 30 x 10^3 liters. Similarly 220 x 10^3 liters/day of liquid nitrogen will be needed for both precooling and steady state use. The refrigeration needed to provide this amount of cryogen is 3.4 kW at 4.2 K and 0.4 MW at 77 K. This amounts to ~2.75 MW of power at 300 K for 66 pumps.

Dry compressors will be used to regenerate the cryo-sorption pumps. A single 100 ℓ/sec compressor capable of pumping at an inlet pressure of 10 torr will regenerate the pumps in less than one hour.

III-G-4. Initial Pumpdown

The time it takes to pump down the chamber to operating pressure depends on the conditions to which the chamber has been exposed. If the chamber was

let up to an atmosphere of pressure with a dry gas, then the pump down period will be shorter. A bake out will be required if the chamber surfaces were exposed to moisture.

Evacuation of the chamber from atmospheric pressure commences with the turning on of the dry compressor. In approximately two hours the pressure will reach 10 torr at which point a 4000 ℓ/sec roots blower will be turned on with the dry compressor as its back up pump. Within 5-6 minutes the pressure in the chamber will reach 0.25 torr. At this point the cryo-sorption pumps are rotated 90° to seal off the pumpout plenum and liquid nitrogen is admitted to precool the chevrons and the molecular sieve. As soon as the pressure in the chamber stabilizes indicating that the condensable constituents have been removed, the liquid nitrogen is pumped out of the molecular sieve cooling vessel and is replaced with liquid helium. The remaining constituents of the gas in the chamber will be rapidly pumped out and the pressure will reach $\sim 1 \times 10^{-7}$ torr.

The time required to pump a system down below 1×10^{-3} depends on the amount of outgassing from the chamber surfaces. If the chamber was clean and dry to begin with, it will take a shorter time to pump it down. Assuming that the chamber was clean, the time required to pump it down from one atmosphere will be about three hours. This time can be substantially decreased by making the capacity of the dry compressor larger than that needed to regenerate the pumps in one hour.

References for Section III-G

1. Private Communication - Mr. H. Farrow, Excalibur Corp., Waltham, Mass.

2. P. W. Fisher, J. S. Watson (ORNL) "Cryosorption Vacuum Pumping of D_2, He and H_2 at 4.2K for Controlled Thermonuclear Reactor Application." ANS Translation, 1976 Winter Meeting, Vol. 24, p. 501.

3. J. S. Watson et al. (ORNL), "Current CTR Related Tritium Handling Studies at ORNL", Proceed. 2nd Topical Meeting on the Technology of Controlled Nuclear Fusion, Sept. 1976, Richland, Wash., Vol. III, p. 895.

4. V. B. Yuferov, et al., "Cryogenic Pumping of Fusion Reactors", Physical-Technical Institute of Ukrainian Academy of Sciences, Kharkov, USSR.

5. H. A. Steinherz, "Handbook of High Vacuum Engineering", Reinhold Publishing Corp.

6. B. Badger et al., UWMAK-III, A Noncircular Tokamak Power Reactor Design, UWFDM-150, Univ. of Wisconsin Fusion Tech. Program, Madison, WI, July 1976.

IV. Plasma Heating

IV-A. Introduction

The neutral beam system for TETR provides 150 MW of injected power in the form of 150 keV atomic deuterium (D^0). Since TETR operates in the beam driven two component mode, the beams must be on for the full 60 sec burn time.

Two basic systems have been considered for the neutral beam injectors. The choice of ion source type, positive or negative, is dictated by the injection energy. In Figure IV-A-1, we show the maximum neutralization efficiency versus beam energy calculated by Berkner et al.[1] for positive and negative ion beams. The neutralization efficiency for D^+ drops rapidly above 40 keV, while that for D^- remains large even at very high energy. For the TETR beams at 150 keV, tolerable net electrical efficiency can be obtained even with positive ions, provided that direct conversion is employed to recover most of the power in the unneutralized beam fraction.

The base case system for the TETR neutral beam injectors is a 1980's state of the art positive ion system. In order to obtain the required power at full energy, the molecular species D_2^+ and D_3^+ are removed magnetically from the beam before entering the neutralizer cells. In order to achieve reasonable electrical efficiency, the energy in the unneutralized fraction of the beam emerging from the neutralizer cell must be recovered by a direct conversion system. The positive ion system is described in Section IV-B.

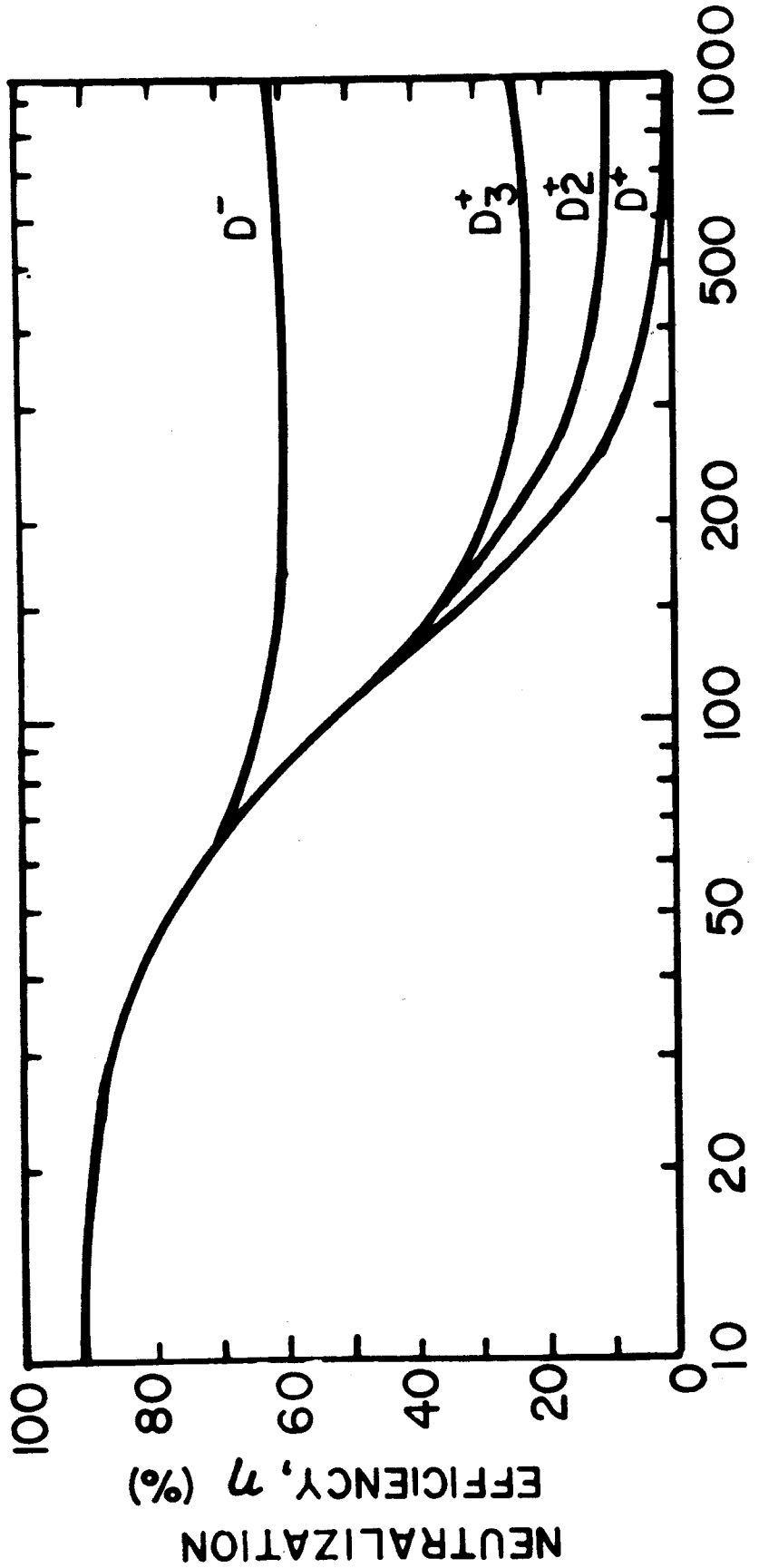

Figure IV-A-1

Maximum Neutralization Efficiency Calculated by Berkner et al., For Positive and Negative Ion Beams

An alternate system based on negative ion sources is also considered. Such a system would operate with a greater inherent efficiency, even at energies above 150 keV. The negative ion system is described in Section IV-C.

The principal features of both the positive ion and negative ion systems are summarized and compared in Section IV-D. Finally, the use of supplementary RF electron heating of the neutral beam heated plasma is described in Section IV-E.

References for Section IV-A

1. K. H. Berkner, R. V. Pyle, and J. W. Stearns, "Mixed Species in Intense Neutral Beams," Proc. 1st Topical Meeting on the Technology of Controlled Nuclear Fusion, ANS CONF-740402-P1 (1976).

IV-B. Positive Ion Source System

IV-B-1. Overview

A schematic diagram of the neutral beam system using positive ion sources is shown in Figure IV-B-1. Ion sources of the Berkeley type are used to generate positive deuterium ion beams at an energy of 150 keV. The extracted beam contains both atomic and molecular species. The molecular fraction, if left in the beam, would break up in the neutralizer cell giving birth to neutrals at one-half and one-third of the peak injection energy. These less energetic neutrals would not effectively penetrate the plasma, leading to enhanced wall loadings. They would also decrease the electrical efficiency of the injector system, and would constitute an additional source to drive the so-called Riviere "beam choking" effect.[1] Consequently, it is desirable to remove the molecular species from the beam before entering the neutralizer cell. This is accomplished by passing the beam through a transverse magnetic field. The heavier molecular ions (principally D_2^+ and D_3^+) experience a smaller deflection than the lighter atomic D^+ ions and are collected on direct converters. The atomic fraction is then passed through a decoupled gas cell neutralizer. The neutral fraction is then injected into the plasma. At 150 keV, the neutralization efficiency for positive ions is approximately 33%. Thus, in order to achieve tolerable electrical efficiency, the power in the un-neutralized fraction must be recovered in a direct converter. The base case design employs an in-line space-charge blowup type of direct converter.[2]

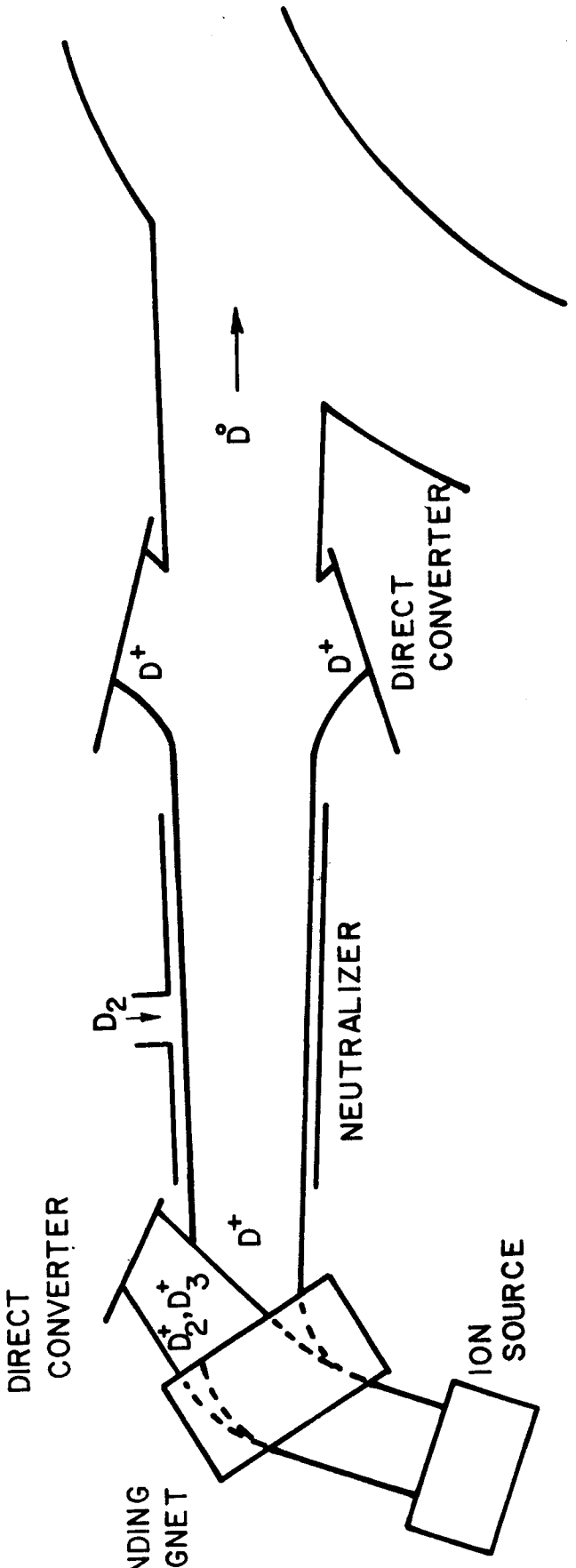

Figure IV-B-1
Schematic Diagram of the Neutral Beam
System Using Positive Ion Sources

IV-B-2. Ion Source Requirements

In order to provide 150 MW of power at 150 keV, the ion sources must produce 1000 A equivalent injected current. However, due to the species composition of the source, finite neutralization efficiency, and beam transport losses, the total source extraction current must be considerably greater than the injection current of 1000 A.

The current flow through the neutral beam system is shown schematically in Figure IV-B-2a. The species composition of a Berkeley type source is typically 75% D^+, 15% D_2^+, 10% D_3^+, and depends somewhat on source operating conditions. If the total extracted source current is I_e, we will denote by ε_a the atomic fraction of I_e. Due to the finite pressure in the bending magnet region, a fraction of the beam is lost due to premature neutralization by charge exchange. The pressure in the bending magnet region is chosen to limit this loss to 5% (see Section IV-B-4). Thus, the current I_a of atomic ions entering the neutralizer is reduced to

$$I_a = (0.95)\ \varepsilon_a\ I_e\ . \qquad \text{(IV-B-1)}$$

In the neutralizer, a fraction η_n is coverted to D^o. Before entering the plasma, a fraction of the neutral beam is lost to charge exchange in beam transport line. The pressure in this region is chosen to limit this loss to 5% (see Section IV-B-7). The final injected equivalent neutral current I_{inj} which reaches the plasma is thus

Figure IV-B-2a

Current Flow through the Neutral Beam System

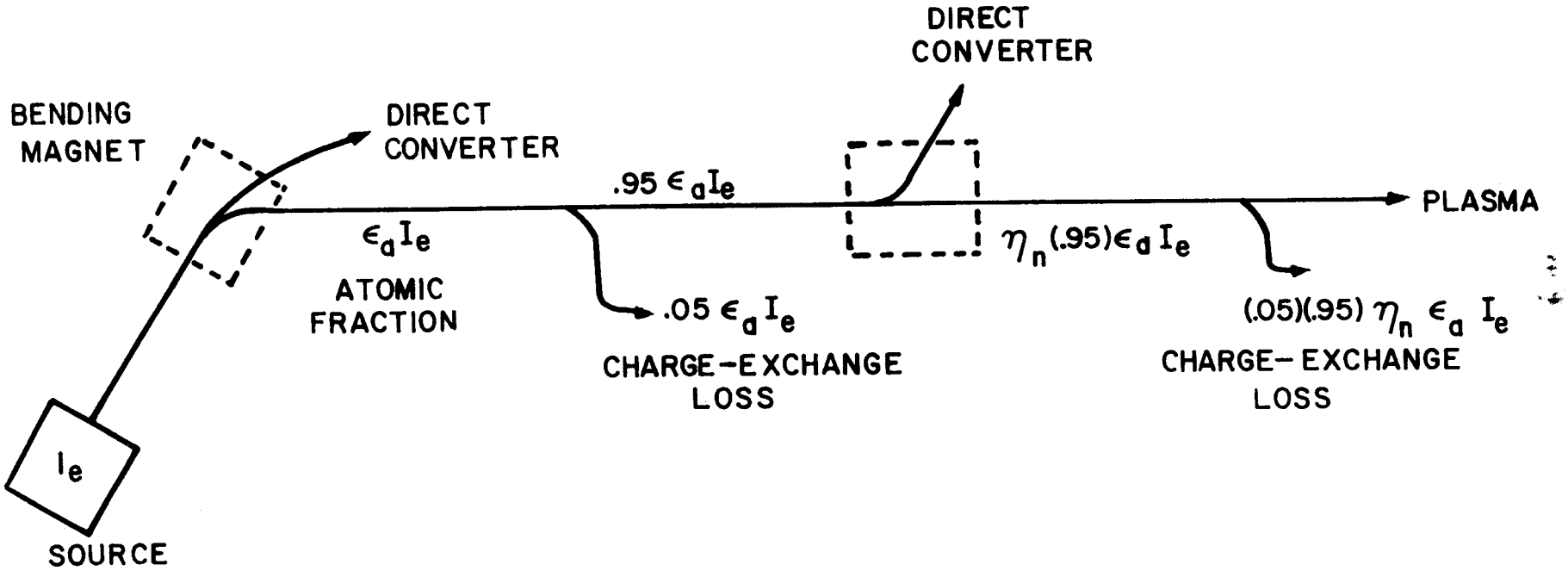

$$I_{inj} = (0.95)^2 \eta_n \varepsilon_a I_e$$

and thus

$$I_e = I_{inj}/(0.9025 \varepsilon_a \eta_n) \qquad \text{(IV-B-2)}$$

The neutralization efficiency calculated in Section IV-B-5 is 32.4% at 150 keV. Thus, to supply 1000 A of neutral current, a total of I_e = 4460 A (all species) must be extracted from the source, assuming ε_a = 0.75.

IV-B-3. Layout

The mechanical layout of the neutral beam injectors is shown in Figure IV-B-2b. The system consists of 12 beam lines, half of which are aimed in the clockwise direction, half in the counter clockwise direction in order to avoid imparting a net plasma momentum. Access between the toroidal field coils precludes exact tangential injection. The included angle (in the horizontal plane) between the beam line and the plasma axis is 26^{o}.

Each of the twelve beam lines contains 7 positive ion sources of the Berkeley type arranged in a vertical array, for a total of 84 sources. Since the cold gas flow from the sources is proportional to total source area, it is desirable to minimize the total number of sources in order to ease vacuum pumping requirements. For specified values of injection current and energy, there are basically two source limitations which determine the required number of sources. These two limitations are source current density and beam power density. Present available source current densities are typically 0.5 A/cm^2 for positive ion sources and 0.01 A/cm^2 for negative ion sources. Beam power density is limited by melting or warping of the electrodes in the high voltage accelerating structure. Steady state power densities of about 10 kW/cm^2 have been obtained with Berkeley sources, which have uncooled extraction grids. Significantly higher power densitites are possible if the extraction grids are water cooled, as in the ORNL sources. We will assume that water cooled grids on the TETR sources will allow beam power densitites of 20 kW/cm^2.

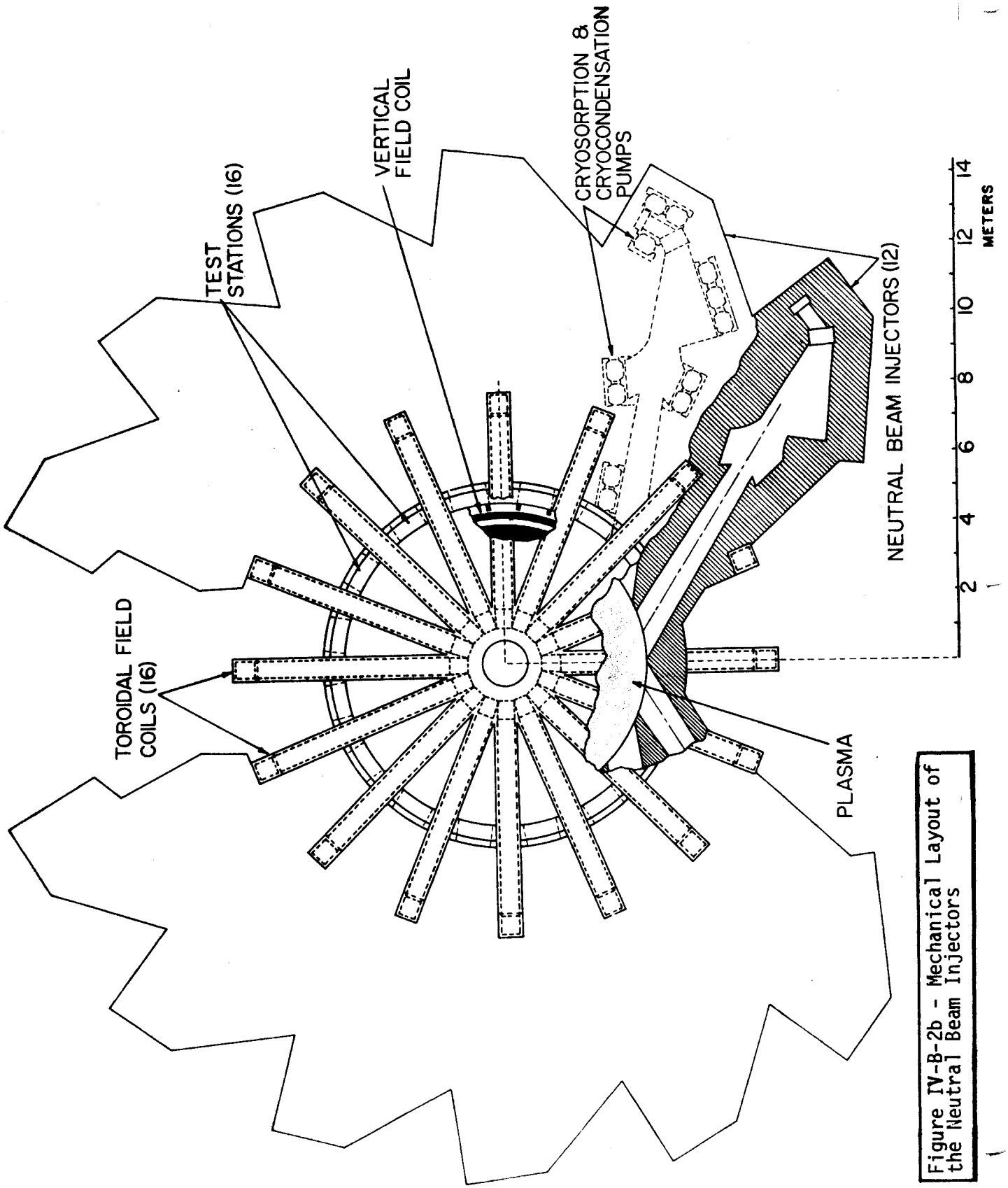

Figure IV-B-2b - Mechanical Layout of the Neutral Beam Injectors

Each of the 84 ion sources has an emitting area of 10 cm (vertical plane) x 40 cm (horizontal plane) = 400 cm^2. The single beamlet divergence of 20 keV Berkeley sources is $\pm$ 0.5^o parallel and $\pm$ 2.0^o perpendicular to the grid laterals. The inherent single beamlet divergence should be smaller at higher extraction energies. However, molecular species selection requires that the gas cell neutralizer be decoupled from the source. This may lead to additional beam divergence due to space charge blow up in the bending magnet region. To be conservative, we will assume single beamlet divergences 25% higher than those stated above. That is, we take the divergence to be $\pm$ 0.63^o parallel and $\pm$ 2.5^o perpendicular to the grid laterals. Using grid displacement and curvature, the sources will be aimed and focused at a single aperture in the blanket wall. The beam path is shown in Figure IV-B-3, where the curved portion of the path in the horizontal plane has been projected onto a straight line path. At the edge of the blanket, the neutral beams fill a window 24 cm (vertical plane) x 96 cm (horizontal plane) measured normal to the beam path.

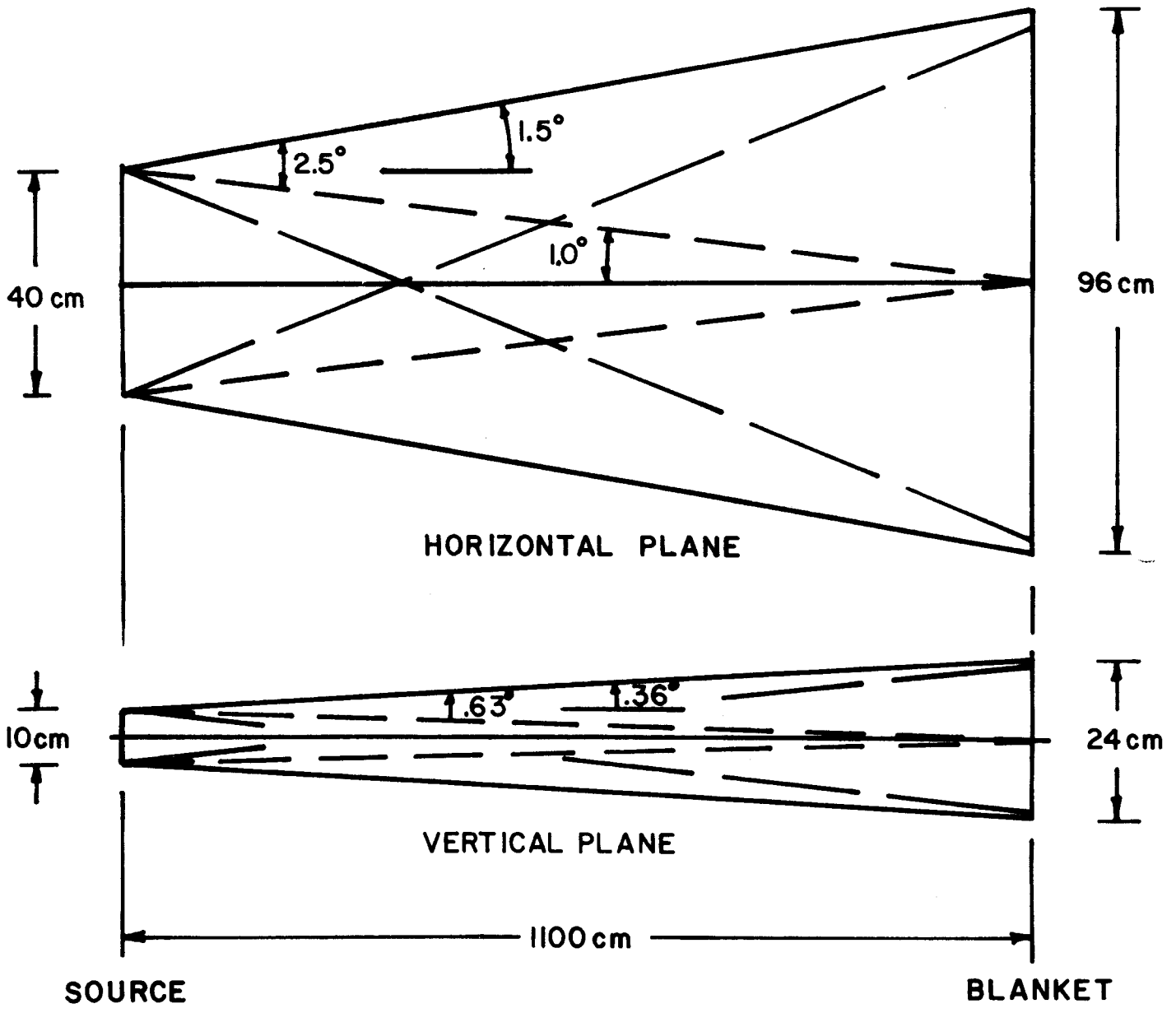

FIGURE IV-B-3
Neutral beam envelopes

IV-B-4. Molecular Species Removal

The orbit envelopes of the principal source species in the bending magnet region are shown in Figure IV-B-4. A transverse magnetic field of 1.9 kG provides a bending radius of 40 cm for 150 keV D^+ ions. The heavier molecular ions are collected on direct converter plates. Sufficient separation must be provided between the magnet and source in order to provide adequate magnetic shielding.

Due to the finite pressure in the bending magnet region, before reaching the neutralizer, a fraction of the ion beam is lost by premature charge exchange. In particular, the current I_{D^+} of D^+ ions decays according to

$$\frac{dI_{D^+}}{d\pi} = - \sigma_{10} I_{D^+} \qquad \text{(IV-B-3)}$$

where σ_{10} is the cross section for the production of D^0 from D^+ and

$$\pi = \int_{\ell} n \, dx \qquad \text{(IV-B-4)}$$

is the target line density of the background gas with density n along the path ℓ. Equation (IV-B-3) has the solution

$$I_{D^+} = I_o \exp (-\sigma_{10}\pi) ,$$

and if $\sigma_{10}\pi << 1$, we have

$$I_{D^+} = I_o (1-\sigma_{10}\pi) .$$

If we then specify a 5% neutralization loss as an upper bound, we find the maximum allowable average neutral density $\bar{n}_1$ in the bending magnet region

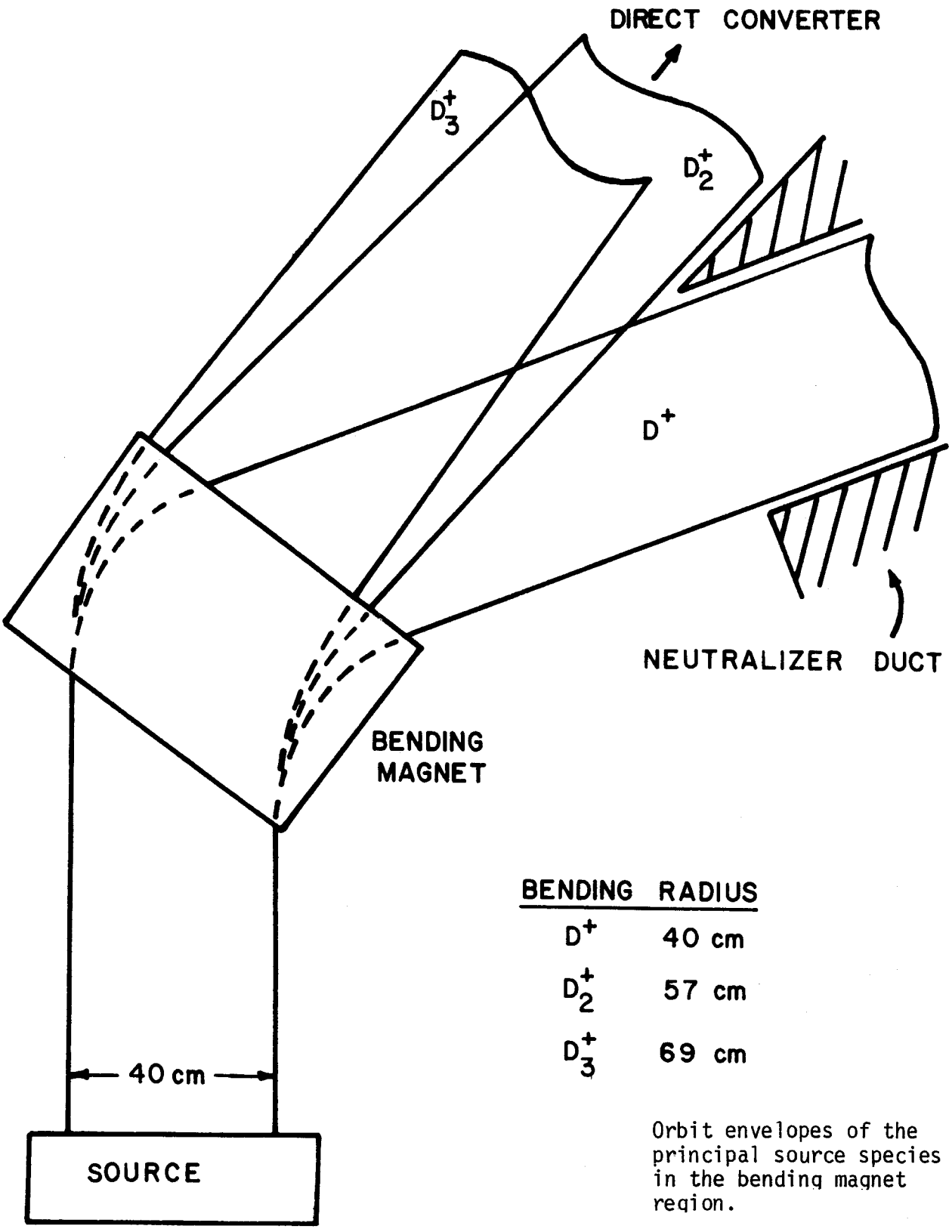

BENDING	RADIUS
D^+	40 cm
D_2^+	57 cm
D_3^+	69 cm

Orbit envelopes of the principal source species in the bending magnet region.

FIGURE IV-B-4

$$\bar{n}_1 = 0.05/(\sigma_{10} L_1) \ , \qquad \text{(IV-B-5)}$$

where L_1 is the average arc length from the source to the neutralizer cell. ($L_1 \sim 200$ cm in the base case design). At 150 keV, $\sigma_{10} = 6.2 \times 10^{-17}$ cm^2 and thus the allowed average neutral density in the bending magnet region is 4.0×10^{12} cm^{-3}. Assuming the neutral gas to be at 300°K, this density corresponds to an average pressure of 1.2×10^{-4} Torr.

IV-B-5. Neutralizer Cell and Direct Converter

Present day neutral beam injector systems employ gas cell neutralizers coupled directly to ion sources with gas efficiencies (defined in Section IV-B-6) of approximately 30-40%. The neutralizer cell is essentially a pumping impedance duct which concentrates the residual cold gas flow from the source. The resulting cold neutral gas target serves two purposes. First it serves to convert the energetic ion beam to an energetic neutral beam by charge exchange collisions. Secondly, ionizing collisions of the energetic ion beam with the target gas provide a source of space charge neutralizing electrons. In present day neutral beam systems the neutralizer cell is coupled directly to the ion source to minimize space charge blowup of the beam and to best utilize the cold gas flow from the source. With the neutralizer cell coupled directly to the source, both the atomic and molecular components of the beam are neutralized. For the TETR beams, removal of the molecular beam components necessitates a decoupled neutralizer cell with separate gas feed.

The variation of the neutralizer output species composition with target thickness π (defined in Eq. IV-B-4) is governed by

$$\frac{dD^0}{d\pi} = \sigma_{10}D^+ - \sigma_{01}D^0$$

$$\frac{dD^+}{d\pi} = -\sigma_{10}D^+ + \sigma_{01}D^0 \qquad \text{(IV-B-6)}$$

where D^0 and D^+ represent the fraction of neutral and ionized atomic deuterium ($D^0 + D^+ = 1$), and σ_{01} and σ_{10} are the cross sections for electron capture and loss respectively. The solution for the neutral fraction is

$$D^0 = D^0_\infty \{1 - \exp [-(\sigma_{01}+\sigma_{10})\pi]\} \qquad \text{(IV-B-7)}$$

where

$$D^0_\infty = \frac{\sigma_{10}}{\sigma_{01}+\sigma_{10}}$$

is the maximum neutral fraction obtained with an infinite cell thickness π. At 150 keV, $\sigma_{10} = 6.2 \times 10^{-17}$ cm^2 and $\sigma_{01} = 1.2 \times 10^{-16}$ cm^2 if the target gas is D_2. The maximum neutral fraction then is D^0_∞ 0.341 at 150 keV. In order to have a manageable cell length, we choose the target thickness in Eq. IV-B-6, such that $D^0 = 0.95\ D^0_\infty = 0.324$. We will refer to this value as the neutralization efficiency η_n. From Eq. IV-B-6, the required target thickness is $\pi = 1.66 \times 10^{16}$ molecules/cm^2. If we then specify a cell length L_3 of 200 cm, the required average neutral target density is $\bar{n}_0 = 8.5 \times 10^{13}$ molecules/cm^3. In order to decrease both the neutralizer gas load and associated pumping speeds, we assume that the target gas flow is cooled to liquid nitrogen temperature (77^{o}K). The required average neutralizer pressure is then 6.5×10^{-4} Torr.

Exiting the neutralizer cell, the beam enters a direct converter system in which the energy of the unneutralized fraction of the beam is recovered with efficiency η_{dc}. The direct converter is of the in-line, space charge controlled type,[2] which is simpler, smaller, and less expensive than converter systems employing a bending magnet to deflect the charged fraction out of the neutral beam path before conversion. Space charge controlled converters are also more amenable to high current density, steady state operation than are converters of the immersed grid type.

The performance of space charge controlled converters has been examined by Bender et al.[2] Using TETR beam parameters, Bender's results indicate that an efficiency of $\eta_{dc} = 0.9$ can be obtained with a direct converter approximately 50 cm in length.

Due to the finite pressure in the beam transport tubes, a fraction of the neutral beam exiting the neutralizer is re-ionized by charge exchange collisions before reaching the plasma. This ionized fraction will be deflected in the fringing magnetic field of the torus and strike the walls of the beam transport tubes. The background neutral pressure in the beam lines must be low enough to limit this loss mechanism. We choose to provide sufficient vacuum pumping to limit charge exchange losses to 5%. The maximum allowed average neutral density $\bar{n}_2$ in the beam lines can be obtained from Eq. (IV-B-5) if we replace σ_{10} by σ_{01}, and L_1 by L_2, the average distance from the neutralizer cell output to the blanket wall. Thus we have

$$\bar{n}_2 = 0.05/(\sigma_{01} L_2) \ . \qquad \text{(IV-B-8)}$$

At 150 keV, $\sigma_{01} = 1.2 \times 10^{-16}$ cm^2 for a D_2 target gas. With $L_2 = 700$ cm, we find $\bar{n}_2 = 6.0 \times 10^{11}$ cm^{-3}, which corresponds to an average neutral pressure of 1.8×10^{-5} Torr at a temperature of 300° K.

IV-B-6. Gas Flow and Vacuum Pumping

The neutral beam gas flow and vacuum pumping is shown schematically in Figure IV-B-5. Throughout this section, unless otherwise stated, all gas flows and conductances refer to one beam line containing seven sources.

IV-B-6-a. Gas Loads

The cold gas flow Q_{so} from the source into the first vacuum chamber is given by

$$Q_{so} = (1 - \eta_g)\, Q_{in} \qquad \text{(IV-B-9)}$$

where Q_{in} is the gas flow into the source, and η_g is the gas efficiency of the source. The gas efficiency is defined by

$$\eta_g = \frac{[\frac{1}{2} D^+ + D_2^+ + \frac{3}{2} D_3^+]}{eQ_{in}} \qquad \text{(IV-B-10)}$$

where D^+, D_2^+ and D_3^+ are the output currents of the three principal source species, Q_{in} is the number of neutral D_2 molecules per second which must be supplied to the source, and e is the charge of an electron. We will assume a source gas efficiency of $\eta_g = 0.4$, and a species composition of 75% D^+, 15% D_2^+ and 10% D_3^+. For a total extracted current of 370 A per beam line,

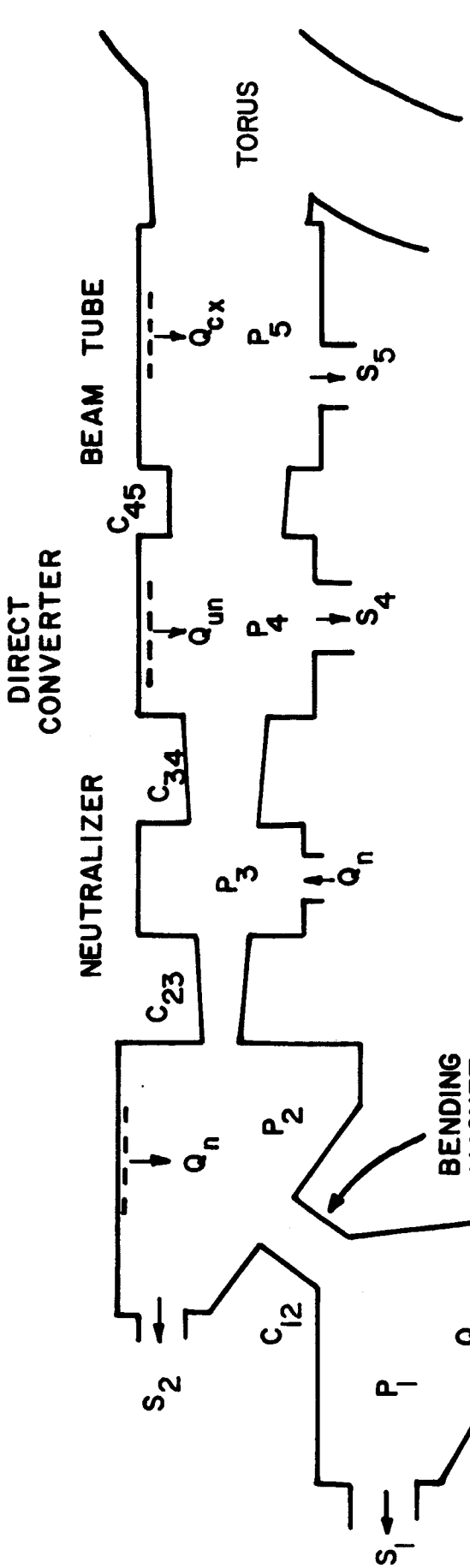

Figure IV-B-5
Schematic Diagram of the Neutral Beam System Gas Flow and Vacuum Pumping

the required flow of D_2 into the sources is then $Q_{in} = 3.90 \times 10^{21}$ molecules/sec per beam line. If this input gas is at 300°K, we have $Q_{in} = 118$ Torr-ℓ/sec. The cold gas flow out of the source Q_{so} is thus 70.8 Torr-ℓ/sec per beam line.

A gas load Q_m is generated in the second chamber due to the molecular components of the beam which are dumped there. This load is given by

$$Q_m = \frac{1}{e} [D_2^+ + \frac{3}{2} D_3^+] \text{ molecules/sec} . \qquad \text{(IV-B-11)}$$

For the base case parameters, $Q_m = 6.94 \times 10^{20}$ molecules/sec per beam line, or $Q_m = 21.0$ Torr-ℓ/sec.

Since the molecular species removal requires a decoupled gas cell, an additional gas load Q_n must be supplied to the neutralizer. The value of Q_n required to establish a near equilibrium cell thickness will be calculated in Section IV-B-6-d.

In chamber 4 a gas load Q_{un} is generated by the unneutralized fraction of the beam. From Figure IV-B-2, this gas load is given by

$$Q_{un} = (0.95)\ (1 - \eta_n)\ \varepsilon_a\ I_e/(2e) \qquad \text{(IV-B-12)}$$

where we have assumed that the unneutralized D^+ beam leaves the direct converter plates as molecular D_2. For the base case parameters $Q_{un} = 5.5 \times 10^{20}$ molecules/sec = 15.7 Torr-ℓ/sec (per beam line).

In chamber 5 a gas load Q_{cx} is generated by premature charge exchange in the beam tubes. Assuming that 5% of the neutral beam current is lost, we have

$$Q_{cx} = 0.05\ I_{inj}/(2e) \qquad \text{(IV-B-13)}$$

where we again assume that the gas is pumped as molecular D_2. For the base parameters $Q_{cx} = 1.3 \times 10^{19}$ molecules/sec = 0.37 Torr-ℓ/sec (per beam line).

IV-B-6-b. Pressure Profile

The pressure profile in the neutral beam line is shown in Figure IV-B-6. This pressure profile is dictated by charge exchange considerations (Secs. IV-B-4 and IV-B-5) and neutralizer cell considerations (Sec. IV-B-5).

The average pressure in the bending magnet region (chambers 1 and 2) must be low enough to limit charge exchange losses to 5%. The total neutral gas target thickness T_{12} (Torr-cm) for the dimensions noted on Figure IV-B-6 is

$$T_{12} = 80\ P_1 + 40\ \frac{P_1+P_2}{2} + 80\ P_2 = 100\ (P_1 + P_2)\ . \qquad \text{(IV-B-14)}$$

From Section IV-B-4 the maximum allowed target thickness τ_m is given by

$$\tau_m = \bar{n}_1\ kT\ L_1 \qquad \text{(IV-B-15)}$$

where k is the Boltzmann's constant and T is the neutral gas temperature. Combining Eqs. (IV-B-14) and (IV-B-15), we have

$$P_1 + P_2 = P_B \qquad \text{(IV-B-16)}$$

where for convenience we define

$$P_B = \tau_m/100\ . \qquad \text{(IV-B-17)}$$

FIGURE IV-B-6

Pressure profile in the neutral beam line

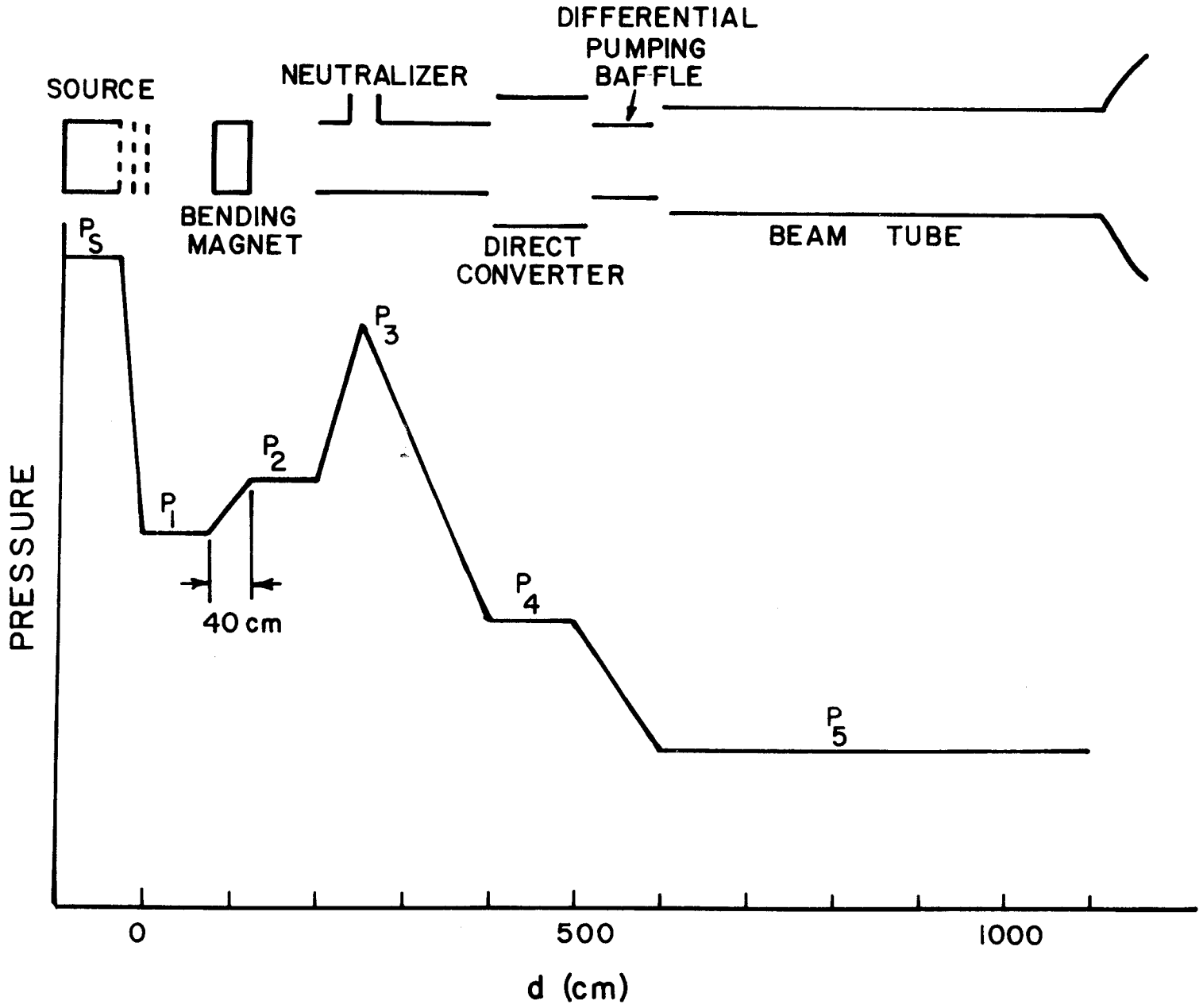

For the base case parameters $P_B = 2.4 \times 10^{-4}$ Torr.

The pressures in the direct converter and transport tube regions are determined in a similar fashion, based on the results of Sec. IV-B-5. We find

$$P_4 + 3.67\ P_5 = P_T \qquad \text{(IV-B-18)}$$

where we have defined

$$P_T = \bar{n}_2\ kTL_2/150\ . \qquad \text{(IV-B-19)}$$

For the base case parameters, $P_T = 8.7 \times 10^{-5}$ Torr.

The average pressure in the neutralizer cell is determined by the target thickness which was calculated in Sec. IV-B-5. Since the required pressure is an order of magnitude higher than that which must be maintained in chambers 2 and 4, we will take the average neutralizer pressure to be half the peak value P_3 (see Figure IV-B-6). From Sec. IV-B-5 then, we have

$$P_3 = 2\ \bar{n}_o\ kT\ . \qquad \text{(IV-B-20)}$$

For the base case parameters, $P_3 = 1.3 \times 10^{-3}$ Torr, assuming the target gas is cooled to 77^oK.

IV-B-6-c. Conductances

In order to determine the required pumping speeds, the conductances of the connecting ducts in Figure IV-B-5 must be determined. The location and

dimensions of these ducts are given in Figure IV-B-7. Since the amount of taper of the ducts is small, we will calculate the conductances using results for uniform rectangular ducts.

The molecular flow conductance of a long uniform rectangular duct for deuterium gas at 300°K is given by[3]

$$C_\ell = 84.0 \frac{a^2b^2}{(a+b)\ell} \text{ liters/sec} \qquad \text{(IV-B-21)}$$

where ℓ, a, and b are the length, width, and height expressed in cm and which holds provided that $\ell >> \max(a,b)$. To obtain the finite length correction, we note the conductance of an aperture of width a and height b is

$$C_a = 31.5\ ab \text{ liters/sec} . \qquad \text{(IV-B-22)}$$

The effective conductance C_{eff} of a short duct is thus given by

$$\frac{1}{C_{eff}} = \frac{1}{C_\ell} + \frac{1}{C_a} \qquad \text{(IV-B-23)}$$

so we find

$$C_{eff} = \frac{84.0\ a^2b^2}{2.67\ ab + (a+b)\ell} \text{ liters/sec} . \qquad \text{(IV-B-24)}$$

In calculating the conductances, we use values of a and b at the midplane of each duct. These dimensions and the resulting conductances are given in Table IV-B-1. Since each beam line consists of seven sources, the values of C given there represent the contribution of seven ducts in parallel.

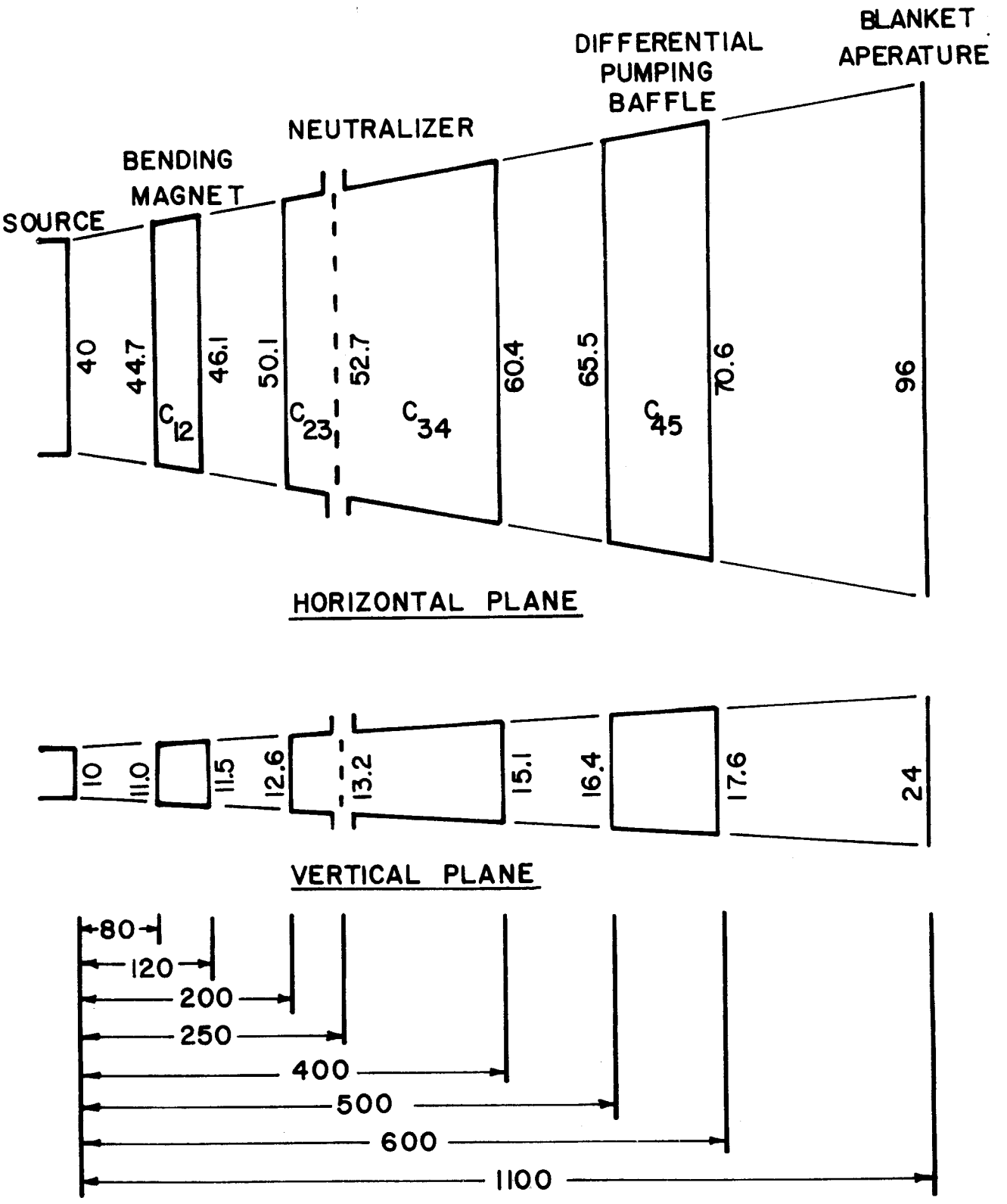

Location and dimensions of gas ducts in the neutral beam line

FIGURE IV-B-7

Table IV-B-1

Average Dimensions and Molecular Flow Conductances of Beam Line Vacuum Ducts

Duct	a (cm)	b (cm)	L (cm)	C_{total}* (ℓ/sec)
C_{12}	45.4	11.2	40	4.2×10^4
C_{23}	51.4	12.9	50	5.2×10^4
C_{34}	56.6	14.1	150	2.9×10^4
C_{45}	68.0	17.0	100	6.8×10^4

*C_{total} is the conductance of seven such ducts in parallel, i.e. $C_{total} = 7\ C_{eff}$ where C_{eff} is given by Equation IV-B-24.

IV-B-6-d. Flow Balance Equations

The flow balance equations for the neutral beam system are obtained with the aid of Figure IV-B-5. These equations are:

$$Q_{so} = S_1 P_1 + C_{12} (P_1 - P_2) \qquad \text{(IV-B-25)}$$

$$Q_m = S_2 P_2 + C_{12} (P_2 - P_1) + C_{23} (P_2 - P_3) \qquad \text{(IV-B-26)}$$

$$Q_n = C_{23} (P_3 - P_2) + C_{34} (P_3 - P_4) \qquad \text{(IV-B-27)}$$

$$Q_{un} = S_4 P_4 + C_{34} (P_4 - P_3) + C_{45} (P_4 - P_5) \qquad \text{(IV-B-28)}$$

$$Q_{cx} = S_5 P_5 + C_{45} (P_5 - P_4) \; . \qquad \text{(IV-B-29)}$$

In this set, S_1, S_2, S_4 and S_5 represent the conductance limited pumping speeds in their respective chambers. We neglect the gas flow from chamber 5 into the torus since the pressure difference between chamber 5 and the torus is small.

In order to optimize the pumping system, we determine P_1, P_2, P_4 and P_5 in such a way that

$$\frac{\partial}{\partial P_2} (S_1 + S_2) = \frac{\partial}{\partial P_5} (S_4 + S_5) = 0 \qquad \text{(IV-B-30)}$$

subject to the constraints on pressures given by Eqs. (IV-B-16) and (IV-B-18). This procedure leads to two quadratic equations for P_2 and P_5:

$$(Q_{so} - Q_m - C_{23} P_3) P_2^2 + 2 P_B (Q_m + C_{23} P_3 + C_{12} P_B) P_2 - P_B^2$$

$$(Q_m + C_{23} P_3 + C_{12} P_B) = 0$$

and

$$[C_{45} P_T + 3.67 (Q_{un} + C_{34} P_3) - 13.47 (Q_{cx} + C_{45} P_T)] P_5^2 + 7.34 P_T$$

$$(Q_{cx} + C_{45} P_T) P_5 - P_T^2 (Q_{cx} + C_{45} P_T) = 0 .$$

These equations are solved for P_2 and P_5 and then P_1 and P_4 are obtained from Equations IV-B-16 and IV-B-18. Finally, the pumping speeds S_1, S_2, S_4 and S_5 and the neutralizer gas load Q_n are obtained from Equations IV-B-25 through IV-B-29. The results of the vacuum system optimization are presented in Table IV-B-2 and Figure IV-B-8.

Table IV-B-2

Neutral Beam System Vacuum Parameters

Gas Loads* (Torr-ℓ/sec)

$Q_n = 97.0$

$Q_{so} = 70.8$

$Q_m = 21.0$

$Q_{un} = 15.7$

$Q_{cx} = 0.4$

Pressures (Torr)

$P_1 = 1.1 \times 10^{-4}$

$P_2 = 1.3 \times 10^{-4}$

$P_3 = 1.3 \times 10^{-3}$

$P_4 = 5.3 \times 10^{-5}$

$P_5 = 9.3 \times 10^{-6}$

Pumping Speeds* (ℓ/sec)

$S_1 = 6.5 \times 10^5$

$S_2 = 6.2 \times 10^5$

- - - - -

$S_4 = 9.2 \times 10^5$

$S_5 = 3.6 \times 10^5$

*Gas loads and pumping speeds per beam line, each beam line containing seven sources.

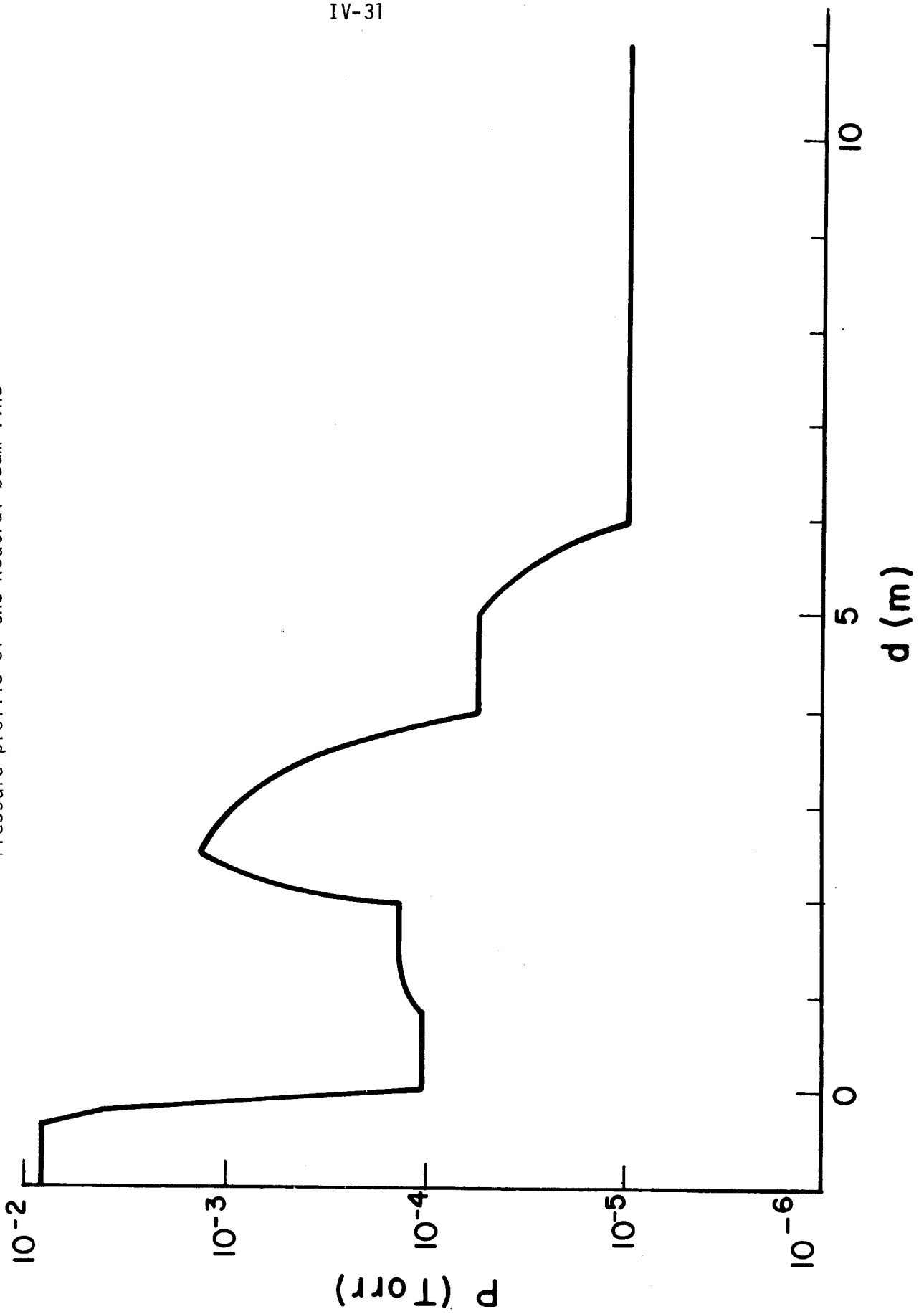

FIGURE IV-B-8

Pressure profile of the neutral beam line

IV-B-7. Power Flow

The power flow for the neutral beam system is shown schematically in Figure IV-B-9. We exclude from the power flow calculations the power consumed by the beam line vacuum pumping system and by the molecular species bending magnets.

The total power P_s required by the neutral beam system is given by

$$P_s = P_i + P_{dm} + P_{du} \qquad \text{(IV-B-31)}$$

where P_i is the net external input power while P_{dm} and P_{du} are the powers recovered by direct converters from the molecular and atomic ion species respectively. This total power P_s is distributed as

$$P_s = P_a + P_m + P_{ad} + P_{fa} \qquad \text{(IV-B-32)}$$

where P_a and P_m are the powers required to accelerate the atomic and molecular species of the beam, P_{ad} is the power loss in the accel-decel structures, and P_{fa} is the power consumed by the source filament and arc supplies. From Eq. IV-B-1, we have

$$P_a = \varepsilon_a I_e \phi_e$$

$$P_m = (1 - \varepsilon_a) I_e \phi_e \qquad \text{(IV-B-33)}$$

where ε_a is the atomic fraction of the source output, and I_e is the total extraction current and ϕ_e is the extraction potential (150 keV in the base case design). The accel-decel losses and filament-arc supply requirements are calculated using empirical results by Bender, et al.,[2] who find

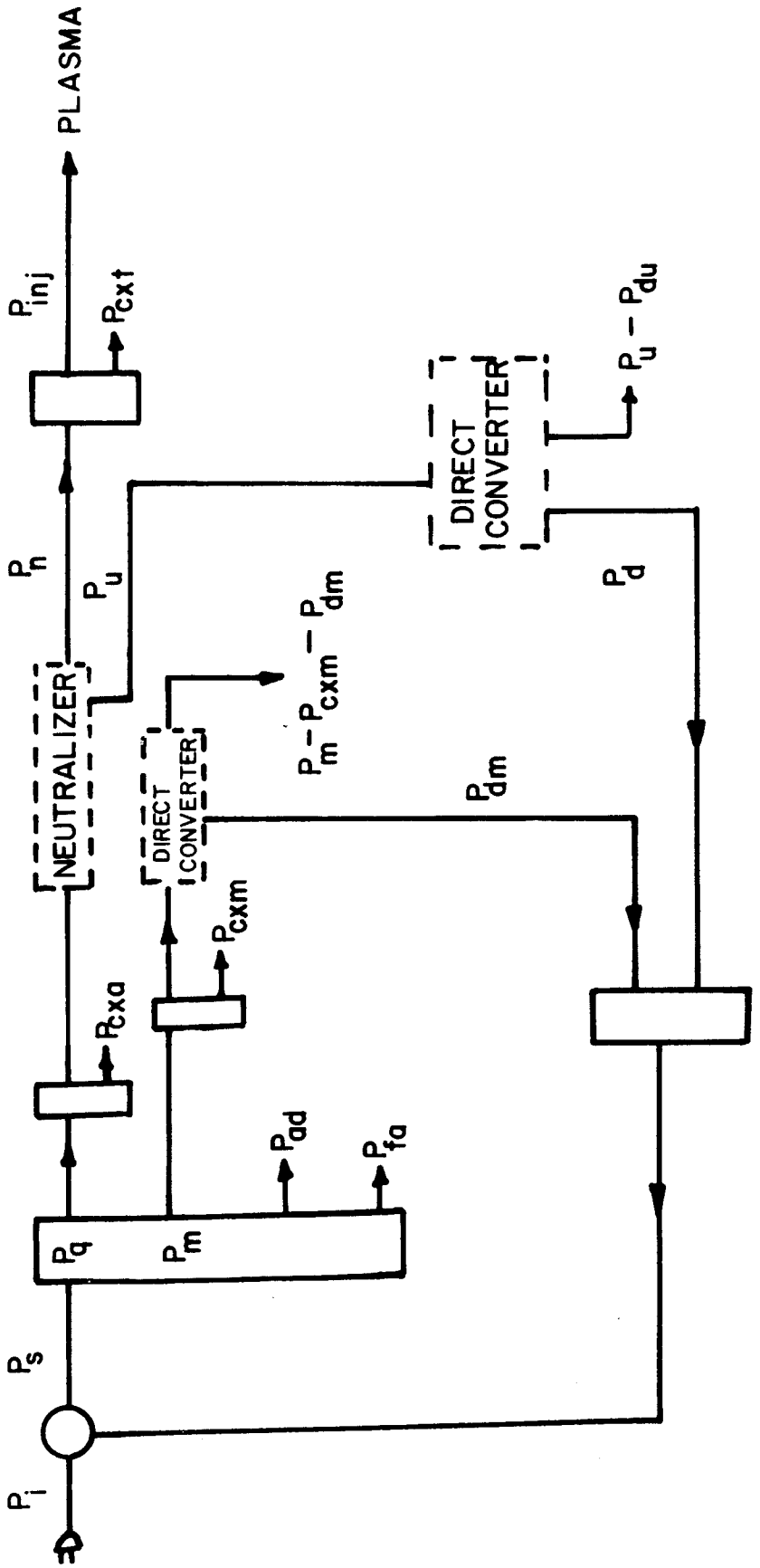

FIGURE IV-B-9

Power flow for the base case, positive ion neutral beam system

$$P_{ad} = 0.075\ I_e\ \phi_e$$

$$P_{fa} = 2500\ I_e \text{ (watts/ampere)} . \qquad \text{(IV-B-34)}$$

Before entering the neutralizer cell a fraction of the atomic ions are lost due to premature neutralization. The neutral pressure in the bending magnet chamber is chosen to limit the change exchange losses to 5% (see Section IV-B-4). Thus we have

$$P_{cxa} = 0.05\ P_a . \qquad \text{(IV-B-35)}$$

The atomic ion fraction of the beam minus charge exchange losses enters a neutralizer cell where a fraction P_n is converted to neutrals with an efficiency η_n, and the remaining fraction P_u is collected by a direct converter with electrical efficiency η_{dca}. Thus we have

$$P_n = \eta_n\ (P_a - P_{cxa}) ,$$

$$P_{du} = \eta_{dca}\ (1 - \eta_n)\ (P_a - P_{cxa}) . \qquad \text{(IV-B-36)}$$

In order to achieve reasonable overall electrical efficiency, the power associated with the molecular fraction of the beam must also be recovered in a direct converter system. Before entering the direct converter, the slower molecular ions experience larger charge exchange losses than do the faster atomic ions. With the pressure chosen to satisfy Eq. IV-B-35, the molecular charge exchange power losses are roughly twice as large, on a percentage basis; the exact amount depends on the ratio of D_2^+ to D_3^+ ions. We will assume that the molecular species charge exchange loss is given by

$$P_{cxm} = 0.10\ P_m\ . \qquad \text{(IV-B-37)}$$

The recovered molecular beam power P_{dm} is then given by

$$P_{dm} = \eta_{dcm}\ (P_m - P_{cxm})\ , \qquad \text{(IV-B-38)}$$

where η_{dcm} is the recovery efficiency for the molecular species.

Due to the finite pressure in the beam transport tubes, a fraction of the neutral beam exiting the neutralizer is re-ionized before reaching the plasma. This ionized fraction will be deflected in the fringing magnetic field of the torus. The final injected neutral beam power $P_{inj} = \phi_e\ I_{inj}$ is thus

$$P_{inj} = P_n - P_{cxt} \qquad \text{(IV-B-39)}$$

where P_{cxt} is the charge exchange loss in the beam transport lines. Sufficient pumping is provided in these lines to limit the charge exchange losses to 5%. (For details, see Section IV-B-5). We then have

$$P_{cxt} = 0.05\ P_{inj}\ . \qquad \text{(IV-B-40)}$$

Combining Eqs. (IV-B-2), (IV-B-31)-(IV-B-40), we find the net electrical power P_i to be given by

$$P_i = \{1.075 + 2500/\phi_e + 0.95\ \eta_{dca}\ \varepsilon_a\ (\eta_n - 1) + 0.9\ \eta_{dcm}\ (\varepsilon_a - 1)\}$$

$$\times\ P_{inj}/(0.9025\ \varepsilon_a\ \eta_n)\ . \qquad \text{(IV-B-41)}$$

The beam injector electrical efficiency which we define as $\eta_e = P_{inj}/P_i$ is thus

$$\eta_e = 0.9025\ \varepsilon_a\ \eta_n/\{1.075 + 2500/\phi_e + 0.95\ \eta_{dca}\ \varepsilon_a\ (\eta_n - 1)$$

$$+ 0.9\ \eta_{dcm}\ (\varepsilon_a - 1)\}\ . \qquad \text{(IV-B-42)}$$

For the base case parameters, and with $\varepsilon_a = 0.75$, $\eta_{dca} = \eta_{dcm} = 0.9$, we find $P_i = 311.7$ MW for an electrical efficiency of $\eta_e = 48\%$. A detailed breakdown of the base case power flow is shown in Table IV-B-3.

The variation of P_i and η_e with the source atomic species fraction ε_a is displayed in Figure IV-B-10. The incentive to recover the power in the molecular fraction is obvious. For the base case design ($\varepsilon_a = 0.75$), failure to recover the molecular beam power ($\eta_{dcm} = 0$) would result in a total neutral beam power consumption increase of 140 MW. The benefits to be derived from increasing the atomic fraction of the source output are also clear. For example, consider the effect of increasing the atomic fraction from 0.75 to 0.92. This would decrease the power consumption by 32 MW (for the case employing direct conversion of the molecular beam) for an operating cost reduction of 2 M$/year, assuming a plant factor of 70% and a power cost of 10 mills/kWh. Alternatively, an increase of ε_a to 0.92 would allow the system to operate with the same efficiency without molecular beam direct conversion, as is obtained in the base case with molecular beam direct conversion.

IV-B-8. Molecular Species Rejection at Low Energy

In this section we examine the increase in neutral beam injector efficiency which could be realized if the molecular species were removed from the beam at low energy (option 2) rather than at full injection energy

Table IV-B-3

Power Flow Values for Option 1 Positive Ion System

Symbol	Explanation	Power (MW)
P_s	Total power requirement	745.3
P_i	Net external input power	310.3
P_{dm}	Power recovered by direct converter from molecular species	138.5
P_{du}	Power recovered by direct converter from atomic species	296.5
P_a	Accel power for atomic species	513.0
P_m	Accel power for molecular species	171.0
P_{ad}	Accel-decel power loss	50.2
P_{fa}	Filament and arc supply power	11.2
P_{cxa}	Charge exchange power loss of atomic ions in bending magnet region	25.7
P_n	Neutral beam (D^o) power exiting neutralizer	157.9
P_u	Positive ion (D^+) beam power exiting neutralizer	329.4
P_{cxm}	Charge exchange power loss of molecular ions in bending magnet region	17.1
P_{cxt}	Charge exchange power loss in beam transport lines	7.9
P_{inj}	Injected neutral beam (D^o) power	150.0

Figure IV-B-10

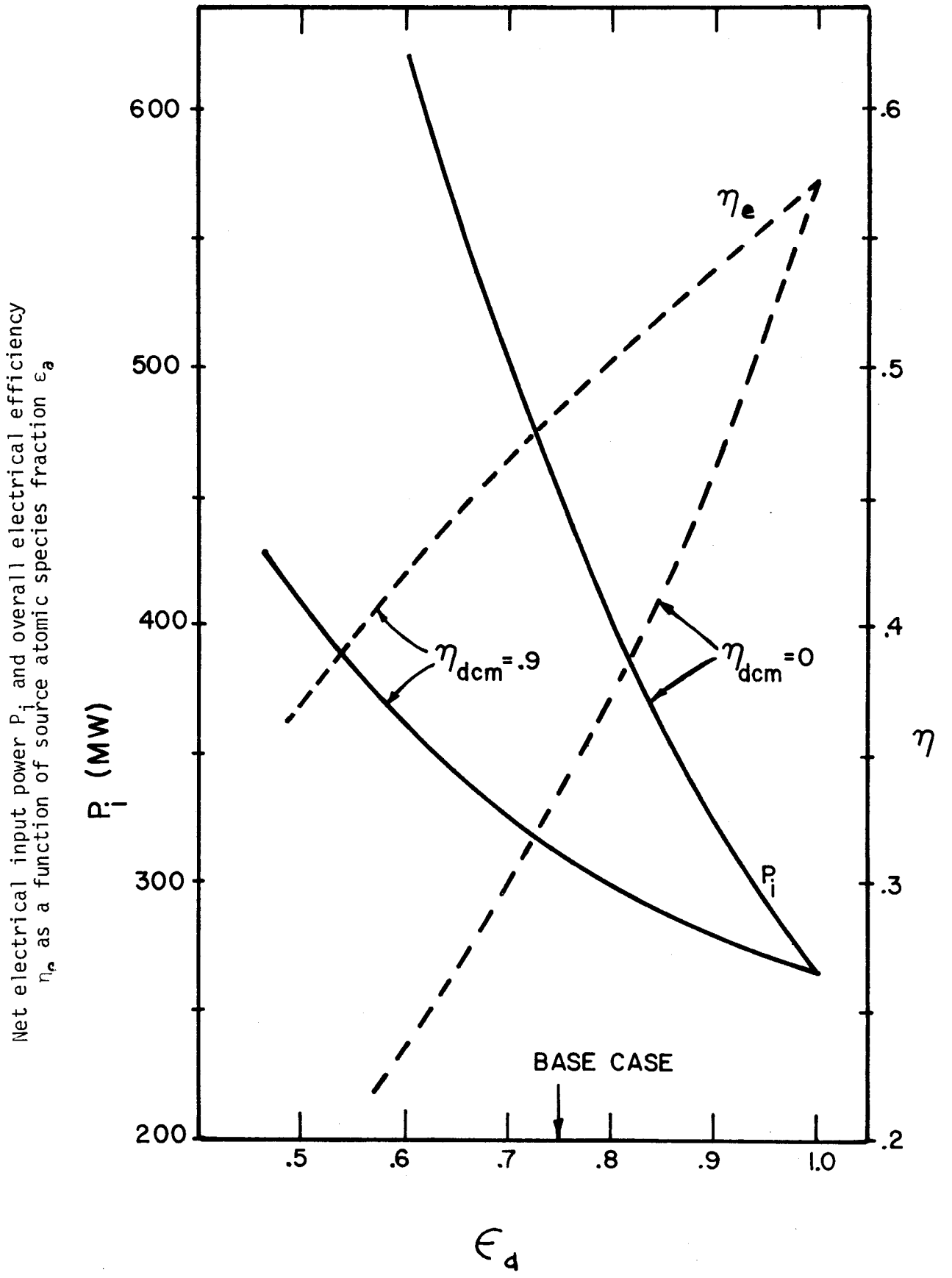

as in the base case design (option 1). The principal advantage of option 2 is that high efficiency can be obtained without the need to provide a direct recovery system for the molecular fraction of the beam. A major disadvantage of option 2 is that the final high voltage accelerator must be located in a position which is in direct line of sight for the fusion neutrons.

The power flow for the option 2 system is shown schematically in Figure IV-B-11. The total power P_s required by the neutral beam system is given by

$$P_s = P_i + P_{dco} \qquad \text{(IV-B-43)}$$

where P_i is the net external input power and P_{dco} is the power recovered from the unneutralized beam in the direct converter. This total system power P_s is distributed as

$$P_s = P_\ell + P_h \qquad \text{(IV-B-44)}$$

where P_ℓ and P_h are the powers delivered to the low voltage and high voltage sections of the beam system.

The power in the low voltage section of the system is given by

$$P_\ell = P_{\ell a} + P_{\ell m} + P_{fa} + P_{ad\ell} \qquad \text{(IV-B-45)}$$

where $P_{\ell a}$ ($P_{\ell m}$) is the power required to accelerate the atomic (molecular) fraction of the beam, P_{fa} is the power consumed by the source filament and arc supplies, and $P_{ad\ell}$ is the accel-decel power loss in the first stage accelerator. If ε_a is the atomic fraction of the source output have

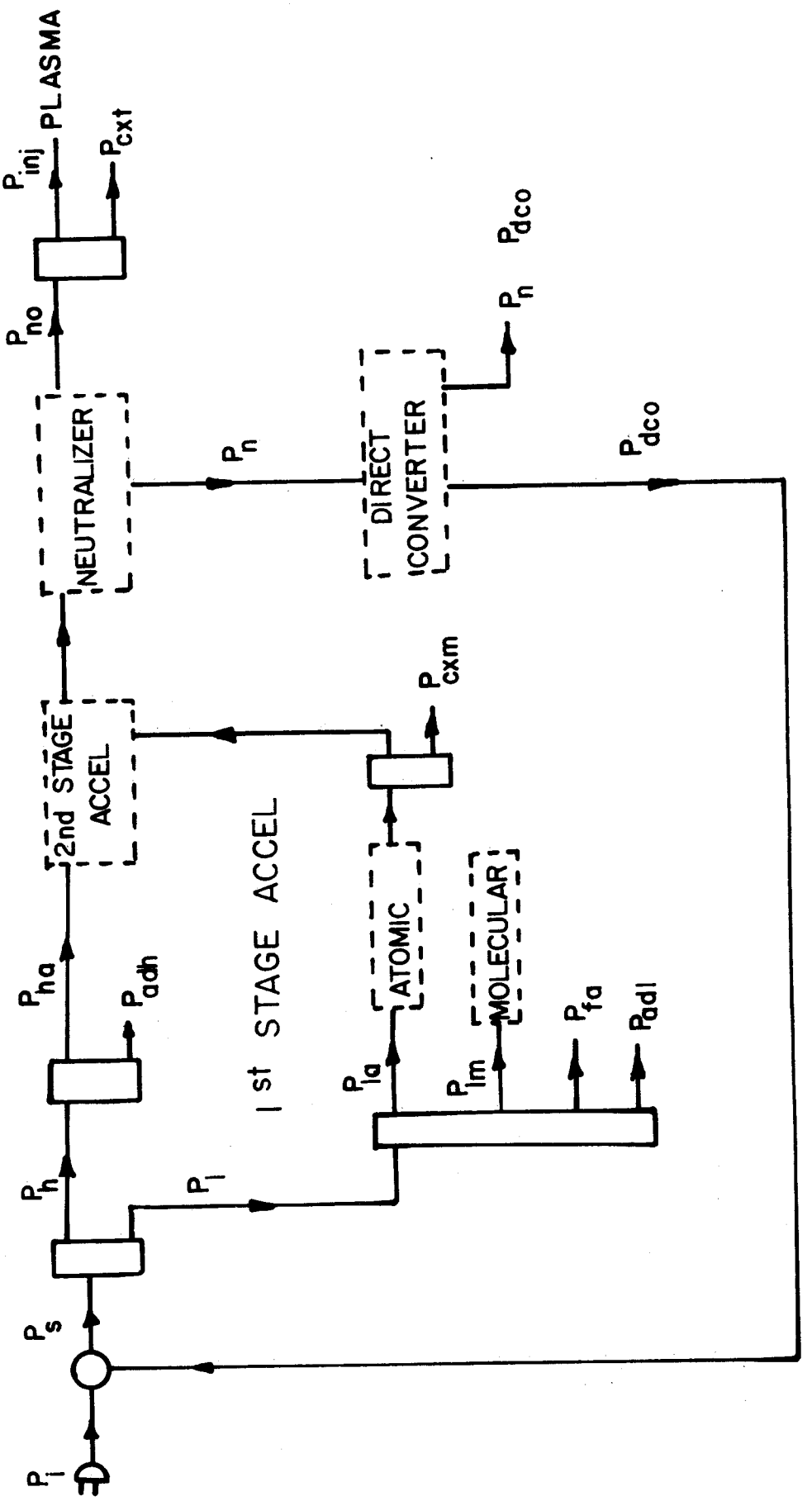

FIGURE IV-B-11
Power flow for the option 2, positive ion source neutral beam system

$$P_{\ell a} = \varepsilon_a \beta I_e \phi_e , \qquad \text{(IV-B-46)}$$

$$P_{\ell m} = (1 - \varepsilon_a) \beta I_e \phi_e \qquad \text{(IV-B-47)}$$

where $\beta\phi_e$ is the potential applied to the initial accelerator. The last two quantities in Eq. IV-B-45 are calculated as in Section IV-B-7. We take

$$P_{fa} = 2500 \, I_e \text{ (watts/ampere)} \qquad \text{(IV-B-48)}$$

$$P_{ad\ell} = 0.075 \, (P_{\ell a} + P_{\ell m}) . \qquad \text{(IV B-49)}$$

The power $P_{\ell m}$ in the molecular fraction of the beam is dumped on collector plates after passing through the separating magnets. If the first stage beam energy is much smaller than the final beam energy (β small), then $P_{\ell m}$ is small enough that recovery by an intermediate energy direct converter is unwarranted.

Charge exchange losses due to premature neutralization in the bending magnet region are determined by the neutral pressure in this region and by the energy of the first stage accelerator. The details of this problem are described in Section IV-B-4. We choose the pressure in the bending magnet region to limit the charge exchange losses to 5% of the power in the atomic fraction.

$$P_{cxm} = 0.05 \, P_{\ell a} . \qquad \text{(IV-B-50)}$$

We now consider the high voltage part of the system, where the bulk of power P_h flows. We have

$$P_h = P_{ha} + P_{adh} \qquad \text{(IV-B-51)}$$

where P_{ha} is the power delivered to the beam in the high voltage accelerator, and P_{adh} is the accel-decel power loss in the final accelerator.
Since the beam enters the high voltage acclerator with energy $\beta e\phi_e$ we have

$$P_{ha} = (1 - \beta)\, \phi_e\, I_a \qquad \text{(IV-B-52)}$$

where ϕ_e is the potential applied to the high voltage accelerator, and I_a is the atomic fraction of the source output which enters the accelerator. Allowing a 5% charge exchange loss in the bending magnet region, we have

$$I_a = 0.95\, \varepsilon_a\, I_e \,. \qquad \text{(IV-B-53)}$$

The accel-decel power loss is calculated as in Sec. IV-B-7. We take

$$P_{adh} = 0.075\ P_{ha} \,. \qquad \text{(IV-B-54)}$$

The beam of D^+ ions with power $P_{ha} + P_{\ell a} - P_{cxm}$ enters the neutralizer cell. The neutralization efficiency η_n is discussed in Section IV-B-5. The neutralized fraction of the beam exits the neutralizer cell with power P_{nt}, where

$$P_{n+} = \eta_n\, (P_{ha} + P_{\ell a} - P_{cxm}) \qquad \text{(IV-B-55)}$$

and the unneutralized fraction of the beam exits with power P_n, where

$$P_n = (1 - \eta_n)\, (P_{ha} + P_{\ell a} - P_{cxm}) \,. \qquad \text{(IV-B-56)}$$

Due to the finite pressure in the beam transport tubes, a fraction of the neutral beam power P_n is lost to charge exchange before entering the plasma. The final injected neutral beam power P_{inj} is thus

$$P_{inj} = P_n - P_{cxt} \qquad \text{(IV-B-57)}$$

where P_{cxt} is the charge exchange power loss in the beam transport lines. Sufficient pumping is provided in these lines to limit the charge exchange losses to 5%. (For details, see Section IV-B-5). We then have

$$P_{inj} = 0.95\ P_n \ . \qquad \text{(IV-B-58)}$$

The power P_{nt} in the unneutralized fraction of the beam is recovered with efficiency η_{dc}, so that the power

$$P_{dco} = \eta_{dc}\ P_n t \qquad \text{(IV-B-59)}$$

is available from the direct converter.

Combining Eqs. (IV-B-43) - (IV-B-59) with Eq. (IV-B-2), we find the net electrical power to be

$$P_i = \{1.075\ \beta + 2500/\phi_e + 1.02125\ \varepsilon_a\ (1 - \beta) + 0.95\ \varepsilon_a\ \eta_{dc}\ (\eta_n - 1)\}$$
$$\times\ P_{inj}/(0.9025\ \varepsilon_a\ \eta_n) \ . \qquad \text{(IV-B-60)}$$

We define the beam injector electrical efficiency as $\eta_e = P_{inj}/P_i$, as before. For the base case parameters and $\beta = 0.1$ (i.e. the species selection is done at 15 keV), we find $P_i = 260$ MW for an electrical efficiency of 57.7%. A detailed breakdown of the option 2 power flow is shown in Table IV-B-4.

Table IV-B-4

Power Flow Valves for Option 2 Positive Ion System

Symbol	Explanation	Power (MW)
P_s	Total power requirement	555.6
P_i	Net external input power	259.1
P_{dco}	Power recovered by direct converter	296.5
P_ℓ	Power required by low voltage stage	83.0
P_h	Power required by high voltage stage	472.6
$P_{\ell a}$	First stage accel power for atomic fraction	50.2
$P_{\ell m}$	First stage accel power for molecular fraction	16.7
P_{fa}	Filament and arc supply power	11.1
$P_{ad\ell}$	Accel-decel power loss in first stage	5.0
P_{cxm}	Charge exchange power loss in bending magnet region	2.5
P_{ha}	Second stage accel power	439.6
P_{adh}	Accel-decel power loss in second stage	33.0
P_n	Neutral beam (D^0) power exiting neutralizer	
P_{n+}	Positive ion beam (D^+) power exiting neutralizer	329.4
P_{cxt}	Charge exchange power loss in beam transport lines	7.9
P_{inj}	Injected neutral beam (D^0) power	150.0
P_{dco}	Power recovered by direct converter	296.5

In Figure IV-B-12, we show the variation of P_i and η_e with $e\phi_\ell$, the energy at which the molecular beam components are separated out. On the basis of net power consumption, there is clearly an advantage to do the magnetic preselection at low energy. However, it must be remembered that preselection at low energy requires that the high voltage accelerating structure be located in a region more vulnerable to radiation damage. In addition to this problem, it must also be remembered that the power flow model discussed here assumes a constant charge exchange loss fraction in the bending magnet region. In order to satisfy this assumption, the neutral gas pressure must decrease at lower values of ϕ_ℓ since σ_{10} increases as $e\phi_\ell$ decreases (see Section IV-B-4). Thus, in order to achieve greater electrical efficiency by rejecting the molecular species at low energy, increased vacuum pumping in the bending magnet region is necessary. We also show in Figure IV-B-12 the average pressure which must be maintained in this region to limit the charge exchange losses to 5%.

In Figure IV-B-13, we show the variation of input power P_i with the atomic species fraction ε_a for different values of ϕ_ℓ. For the sake of comparison, we also show the power requirement for option 1 calculated in Section IV-B-7.

FIGURE IV-B-12

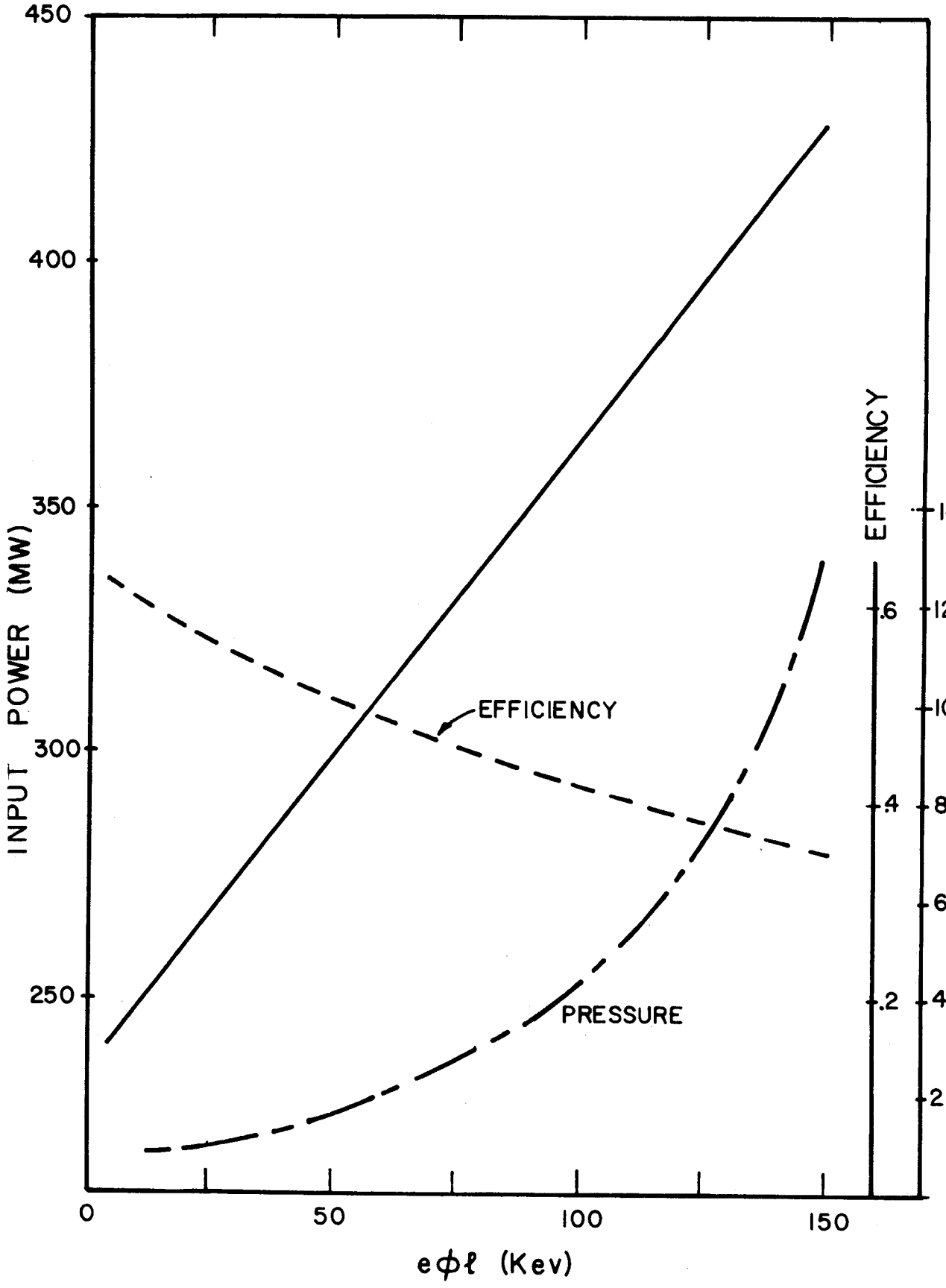

Variation of net electrical input power P_j, and overall electrical efficiency η_e with $e\phi_l$, the energy at which the molecular beam components are separated out. Also shown is the average pressure which must be maintained in the bending magnet region in order to limit charge exchange losses to 5%.

Figure IV-B-13

Variation of Input Power P_i with Atomic Species Fraction ε_a

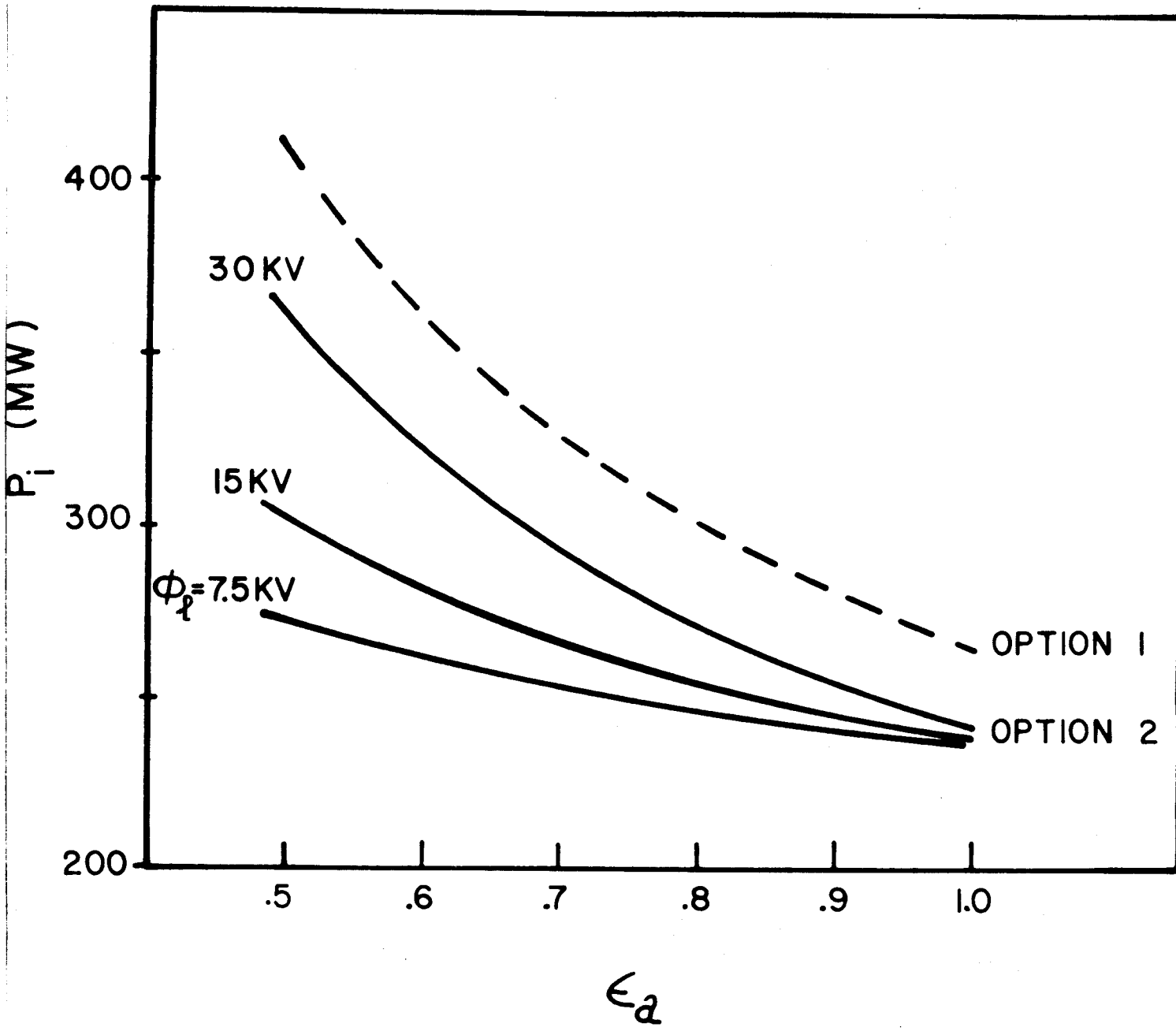

References for Section IV-B

1. A. C. Riviere and J. Sheffield, "Transfer Efficiency of Intense Neutral Beams," Nucl. Fusion 15, 944 (1975).

2. D. J. Bender, W. L. Barr, and R. W. Moir, "Performance Analysis of In-Line Direct Converters for Neutral Beam Sources," Proc. 1st Topical Meeting on the Technology of Controlled Nuclear Fusion, San Diego, California (1976).

3. S. Dushman and J. M. Lafferty, Scientific Foundations of Vacuum Technique, 2nd ed., pp. 87 - 97 (John Wiley and Sons, New York, 1962).

IV-C. Negative Ion Source System

On the basis of gas target neutralization efficiency, it is clear from Figure IV-A-1 that at energies in excess of 100 keV/deuteron, a negative ion source system will exhibit better performance than a positive ion system. Furthermore, at energies in excess of 200-300 keV/deuteron, it is virtually impossible to design a manageable intense neutral beam system based on positive ion sources.

It is unlikely that negative ion source technology will have progressed to the level required for TETR size beams by the mid 1980's. However, we will consider briefly a negative ion source system in order to demonstrate the potential advantages.

Several types of negative sources are currently under development, notably double charge exchange systems[1] employing a cesium cell, and direct extraction sources of the magnetron type.[2] The performance of these two types of sources has been reviewed recently by Fink, et al.[3] We will consider here a system based on a direct extraction negative ion source.

While the gas target neutralization efficiency for negative ions is relatively large (approximately 60%) at high energy, an even higher neutralization efficiency (approximately 90%) can be achieved by electron photodetachment.[3]

To obtain an estimate of the neutral beam power requirements for the negative ion system, we will make use of the power flow analysis of Section IV-B-7. In Equation IV-B-41, we take the atomic fraction $\varepsilon_a = 1$ to model the direct extraction negative ion source, and thus find the net external input power P_i to be given by

$$P_i = \{1.075 + 2500/\phi_e + 0.95\ \eta_{dca}\ (\eta_n - 1)\}\ P_{inj}/(0.9025\ \eta_n)\ . \quad \text{(IV-C-1)}$$

This model underestimates somewhat the filament, arc, and accel-decel power losses of present day direct extraction negative ion sources which suffer from high electron current loading of the extraction grid.[2]

For a gas target neutralization efficiency $\eta_n = 0.61$, and other parameters chosen as in the base case design, we obtain $P_i = 206.6$ MW for an efficiency $\eta_e = 73\%$. For the case of neutralization by photodetachment with $\eta_n = 0.90$, we find $P_i = 185.8$ MW and $\eta_e = 81\%$.

References for Section IV-C

1. J. E. Osher, "Formation of a D^- Beam for Efficient Production of D^0 at High Energies," Lawrence Livermore Laboratory, Rept. UCID-15893 (1971).

2. K. Prelec and Th. Sluyters, "Formation of Negative Hydrogen Ions in Direct Extraction Sources," Rev. Sci. Instr. 44, 1451 (1973).

3. J. H. Fink, W. L. Barr, and G. W. Hamilton, "A Study of Efficient High-Power, High-Energy Neutral Beams for the Reference Mirror Reactor," Lawrence Livermore Laboratory, Rept. UCRL-52173 (1976).

IV-D. Summary

The major design parameters for the positive ion system, Option 1, are summarized in Table IV-D-1. A summary and comparison of the power requirements for Options 1-3 is given in Table IV-D-2.

The use of negative ion sources would allow neutral beam injection at energies well above the base case value of 150 keV. For the sake of comparison, we plot in Figure IV-D-1 the overall electrical efficiency vs. injection energy for Options 1-3.

Table IV-D-1

Summary of Design Parameters for Positive Ion Source System, Option 1

Total injection power (D^0)	150 MW
Beam energy	150 keV
Total injected current	1000 A equivalent
Number of beam lines	12
Sources per beam line	7
Total number of sources	84
Total extracted current (all species)	4460 A
Extracted current per source	53.1 A
Source species composition:	
D^+	75%
D_2^+	15%
D_3^+	10%
Source extraction area	400 cm^2
Source current density	133 mA/cm^2
Source extraction power density	20 kW/cm^2
Beam dimensions at blanket:	
Vertical	24 cm
Horizontal	96 cm
Neutralizer type	D_2 gas target
Neutralizer target thickness	1.66×10^{16} molecules/cm^2
Neutralization efficiency	0.324
Source gas efficiency	0.4
Source gas input per beam line	188 Torr-ℓ/sec
Neutralizer gas input per beam line	97 Torr-ℓ/sec
Direct converter type	In-line, space charge controlled
Direct converter efficiency	0.9
Net electrical input power	312 MW
Net electrical efficiency	0.48

Table IV-D-2

Power Requirements for Options 1-3

Option	Ion Source Type	Neutralizer	Energy (keV) at Which Molecular Species are Removed	Neutralization Efficiency η_n	Net Input Power (MW)	Electrical Efficiency η_e
1	positive	gas target	150	0.324	312	0.48
2	positive	gas target	15	0.324	260	0.58
3a	negative	gas target	-	0.61	207	0.73
3b	negative	photodetachment	-	0.90	186	0.81

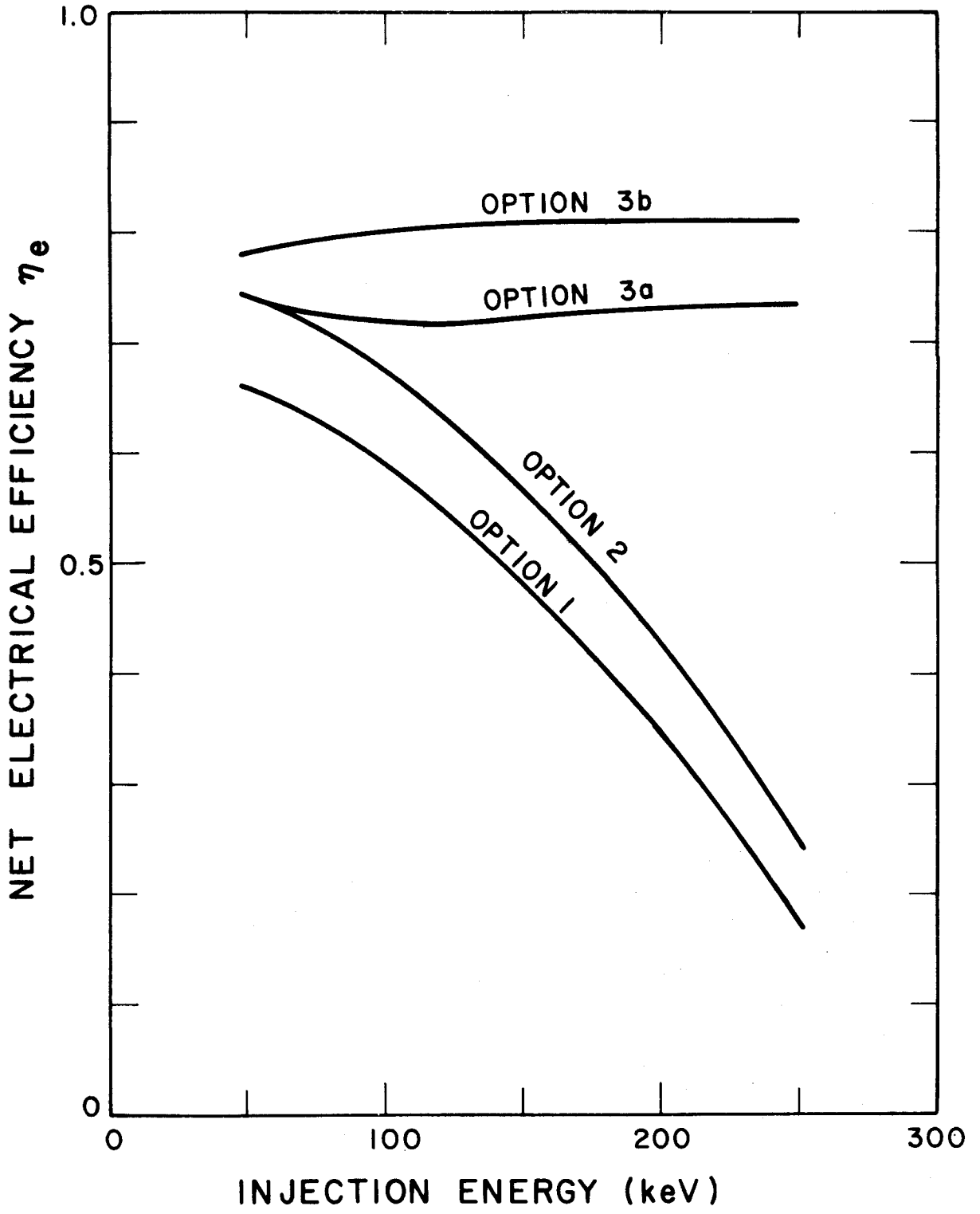

Overall electrical efficiency vs. injection energy for options 1-3.

Figure IV-D-1

IV-E. Supplementary RF Electron Heating of TETR Neutral Beam Heated Plasma

IV-E-1. Introduction

We first considered the alternative roles that radiofrequency (RF) heating of driven tokamaks such as TETR might play. They can be broken down into two major categories: (1) wave heating which provides direct ion heating without other supplementary heating such as neutral beams. (2) radiofrequency heating schemes to compliment primary neutral beam heating of driven tokamaks. We exclude wave heating which primarily heats electrons such as electron cyclotron resonance heating and fast low frequency Alfvén wave heating from the first category for TETR plasmas. This is because the objectives of high neutron yield and fusion Q require relatively short plasma density and energy confinement times which do not allow sufficient equilibration time for the heated electrons to heat the ions and produce copious amounts of fusion reactions.

The remaining wave heating schemes which fall under the first category are: (a) heating the tritium ions at the first cyclotron harmonic ($\omega = 2\omega_{CT}$) with the fast magnetosonic wave with a deuterium blanket;[1] (b) two-ion hybrid wave heating with a minority species of fundamental resonance;[2,3] (c) ion heating by means of lower hybrid waves. While some experimental experience exists for all three schemes in deuterium plasmas, these are still preliminary and further work on PLT and TFTR is required before they could be considered as the primary supplementary heating means for a TETR device.

In the area of radiofrequency heating techniques to compliment neutral beam heating, we have two major subcategories: (a) RF ion clamping neutral beam heated plasmas, and (b) supplementary electron heating of neutral beam heated plasmas. Possibilities of RF clamping of neutral beam generated

ions include lower hybrid wave heating at the fundamental or first harmonic of the ion cyclotron beam frequency. Much more theoretical and experimental work is required before these methods can be seriously considered for a TETR design. Lastly, we have supplementary electron heating of neutral beam heating plasmas. Both the low frequency compressional Alfvén wave and electron cyclotron resonance heating can be considered in this category.

Due to the assumed near term time frame of the TETR machine, we have decided to consider only radiofrequency heating techniques which complement primary neutral beam supplementary heating. The concept of RF clamping of neutral beam heated plasmas seems attractive, but the analysis is complex and no theoretical work on the subject has been published. We therefore decided to concentrate our work on a study of the effect of RF electron heating on the neutral beam heated plasma. Our initial rationale was that by heating the electrons to a sufficiently high temperature, one could improve the efficiency of beam plasma fusions. The beam would have a higher probability of slowing down on the tritium ions rather than the electrons.

The main wave heating modes which can achieve this are the electron Landau damping of the low frequency fast Alfvén wave[4] and electron cyclotron damping. Since the sources for the electron cyclotron resonance heating are gyrotrons which are in the development stage and are expected to have efficiencies $\eta \leq 30\%$ in the high frequency range required for a machine such as TETR, we rule out this technique for such a near term machine requiring up to 50 MW power levels. The fast Alfvén wave, however, would be launched at a low frequency ($f \sim 300$ kHz) so that multi-megawatt sources can be seriously considered. Stix[4] has provided a preliminary treatment of plasma heating by this mode. Among its advantages are the avoidance of impurity ion acceleration, the use of electron Landau damping as the absorption of a single eigenmode allowing wave enhancement in the

plasma zone and lessening arcing problems for a given power input at the antenna. This mode would require a set of poloidal coils made of short sections which are located just inside the torus wall and shielded by a magnetic or mechanical limiter.

IV-E-2. Fast Alfvén Wave Electron Heating of TETR Plasma

In this section we investigate the feasibility of heating TETR with a low frequency fast Alfvén wave, $\omega = 0.01\omega_{cd}$, corresponding to a frequency of 300 kHz in a 40 kG toroidal field. Mode conversion effects can be neglected since no hydrogen resonance occurs within the device. The electrons are heated by electron Landau and transit time magnetic damping. In the limit of weak damping, the power absorbed is given by

$$P = \omega \, \bar{E}^* \cdot (\bar{\bar{K}}^a \cdot \bar{E})/2 \ (\text{watts/cm}^3) \qquad (1)$$

where $\bar{\bar{K}}^a$ is the anti-Hermetian part of the dielectric tensor. For these low frequency waves, the displacement current can be neglected and Ampere's law can be written[5]

$$\nabla \times \bar{B} = 4\pi\bar{J}/c \ . \qquad (2)$$

$$P_e = \frac{\omega_{pe}^2 \omega^2 v_e |B_z|^2 e^{-(\omega/k_{\parallel} v_e)^2}}{8\pi^{1/2} \omega_{ce}^2 c^2 k_{\parallel}} \cdot (\text{watts/cm}^3) \qquad (3)$$

with

$$v_e = \left(\frac{2kT_e}{m_e}\right)^{1/2} \qquad \omega_{ce} = \frac{-eB_o}{m_e c} \qquad \omega_{pe} = \left(\frac{4\pi n_e e^2}{m_e}\right)^{1/2}$$

In order for an appreciable amount of power to be absorbed by the electrons, $k_{\parallel}$ was chosen to be 0.001 cm^{-1}. Since $k_{\parallel}$ is small, hot plasma effects can be neglected and one may use cold plasma theory in calculating $k_{\perp}$. For fast magnetosonic waves in an unbounded plasma we can write

$$k_{\perp} = [k_{\parallel}^4 - 2k_o^2 k_{\parallel}^2 + k_o^4 RL/S]^{1/2}/[k_o^2 - k_{\parallel}^2/S]^{1/2} \qquad (4)$$

with $k_o^2 = \omega^2/c^2$ and R, L, S defined by Stix.[5] We obtain $k_{\perp} = 0.003$ cm^{-1} for TETR with an average density of 7.5×10^{13} cm^{-3}.

The quality factor Q may be calculated in order to obtain an estimate of the absorption of the RF power in the walls. The Q of the walls is approximately given by

$$Q_w = a/\delta \qquad \text{where } \delta = (\pi f \mu \sigma)^{-1/2}$$

δ is the skin depth and σ is the electrical conductivity. At room temperature for 316 stainless steel $\sigma = 3.33 \times 10^6$ $(\Omega m)^{-1}$ and $Q_w = 1600$ while at 500°C $\sigma = 9.5 \times 10^5$ $(\text{ohm-m})^{-1}$ and the resultant $Q_w = 850$.

The Q of the plasma may be defined as

$$Q_p = \frac{\omega U}{P_e} = \frac{k_{\parallel}\omega_{ce}^2 c_e^2 (\omega/k_{\parallel} v_e)^2}{\pi^{1/2} v_e \omega \omega_{pe}^2}$$

where $U = |B_z|^2/8\pi$

At $T_e = 1$ keV, $Q_p = 3660$ while at 10 keV, Q_p drops to a value of 160. Q_p approaches a minimum value when $k_{\parallel} = .001$ cm^{-1} and $\omega = .01\ \omega_{cd}$. This minimum value does not change as long as $k_{\parallel}/\omega$ is constant. Q_p increases when either $k_{\parallel}$ or ω is changed. Q_p is relatively sensitive to changes in T_e as can be seen from the two values given above. On the other hand, Q_w

may be raised to an acceptable value by raising both the frequency and $k_{\parallel}$. Thus, due to the plasma volume to surface area and magnetic field intensities in TETR the use of low frequency fast Alfvén wave heating does not seem attractive. However, for larger devices and higher toroidal magnetic field strengths, this technique is more attractive.

The electron power absorption density given by Equation (3) was included in an explicit fluid model space-time code which solves both ion and electron energy balance equations as well as the particle balance equation. The ion and electron energy balance equations may be written as[6]

$$\frac{\partial n_i T_i}{\partial t} = -4.28 \times 10^{-11}\, n_i n_e \frac{(T_i - T_e)}{3/2} + \frac{1}{1.5r}\frac{\partial}{\partial r}\left(r n_i \chi_i \frac{\partial T_i}{\partial r}\right) - \frac{1}{r}\frac{\partial}{\partial r}(r n_i V_i T_i)$$

$$+4.17 \times 10^{15}\left\{n_D n_T \langle\sigma v\rangle_{DT} U_{\alpha i} + P_{inj}\left(U_{bi} + f\left(\frac{E_\alpha}{E_B}\right)U_{\alpha i}\right)\right\} \qquad (5)$$

and

$$\frac{\partial n_e T_e}{\partial t} = 4.28 \times 10^{-11} n_e n_i \frac{(T_i - T_e)}{T_e\ 3/2} + \frac{1}{1.5r}\frac{\partial}{\partial r}\left(r n_e \chi_e \frac{\partial T_e}{\partial r}\right) - \frac{1}{r}\frac{\partial}{\partial r}(r n_e V_e T_e)$$

$$+4.17 \times 10^{15}\left\{n_D n_T \langle\sigma v\rangle U_{\alpha e} + \underline{E}\cdot\underline{J} + P_{inj}\left(U_{be} + f\left(\frac{E_\alpha}{E_b}\right)U_{\alpha e}\right)\right. \qquad (6)$$

$$\left. - P_{RF} - P_B - P_S\right\} .$$

T_i,(e) is the ion (electron) temperature (eV), n_i,(e) is the ion (electron) density (cm^{-3}), V_i,(e) is the ion (electron) velocity (cm/ms), J is the toroidal current density (amp/cm^2), E is the toroidal electric field (volt/cm), r is the radius (cm), t_2 is time (ms), χ_i,(e) is the ion (electron) thermal diffusivity (cm^2/ms), U_{bi},(e) is the fraction of alpha energy going to ions

(electrons), and f is the fraction of deuterons in the neutral beam which undergo fusion as they slow down in a tritium target plasma. P_B and P_S represent bremsstrahlung and synchrotron radiation, respectively (watts), and P_{RF} is the injected RF power (watts).

In Equation (3), B_z was normalized so that $B_z = B_{zo}J_m(k_\perp r)$ where B_{zo} is a constant such that $B_{zo}^2 = P_{RF}/2\pi^2 R_o \int_o^a J_m^2(k_\perp r)rdr$ where R_o is the major radius, a is the minor radius and P_{RF} is the amount of injected RF power.

The initial temperature and density profiles were assumed parabolic with $T_e=T_i$ and taken to be 500 eV and 2×10^{19} cm^{-3} at the center and 135 eV and 1.9×10^{13} cm^{-3} at the edge. The diffusion coefficients were optimistically taken to be one-tenth the value of that obtained using trapped particle modes scaling.

We decided to first examine the m=1 mode which peaks the electron temperature and RF injected power near the edge as shown in Figures IV-E-1 and IV-E-2. It was thought that by heating the electrons near the edge, the neutral beam particles would impart their kinetic energy more efficiently to the ions resulting in more beam plasma fusions. Figures IV-E-2 and IV-E-3 display the electron and ion temperature profiles as they evolve in time when 50 MW of RF power was used to preheat the plasma for 500 ms before 150 MW of neutral beams were turned on. The electrons reached an average value of 5 keV with a peak near the edge of 12.5 keV after 500 ms. The ions, after the 500 ms, reached an average value of 2 keV with a peak near the center of 2.4 keV. However, as seen in Figures IV-E-2 and IV-E-3 within 300 ms after the neutral beams are turned on, the plasma reaches the same operating conditions as those obtained with neutral beams without an RF preheat. Similar results were obtained when 150 MW of RF was used to preheat the electrons for 500 ms. In this case the electrons reached a peak of 29.8 keV with an average value of 24.0 keV while the ion temperatures were 2.4 keV and 4.0 keV respectively.

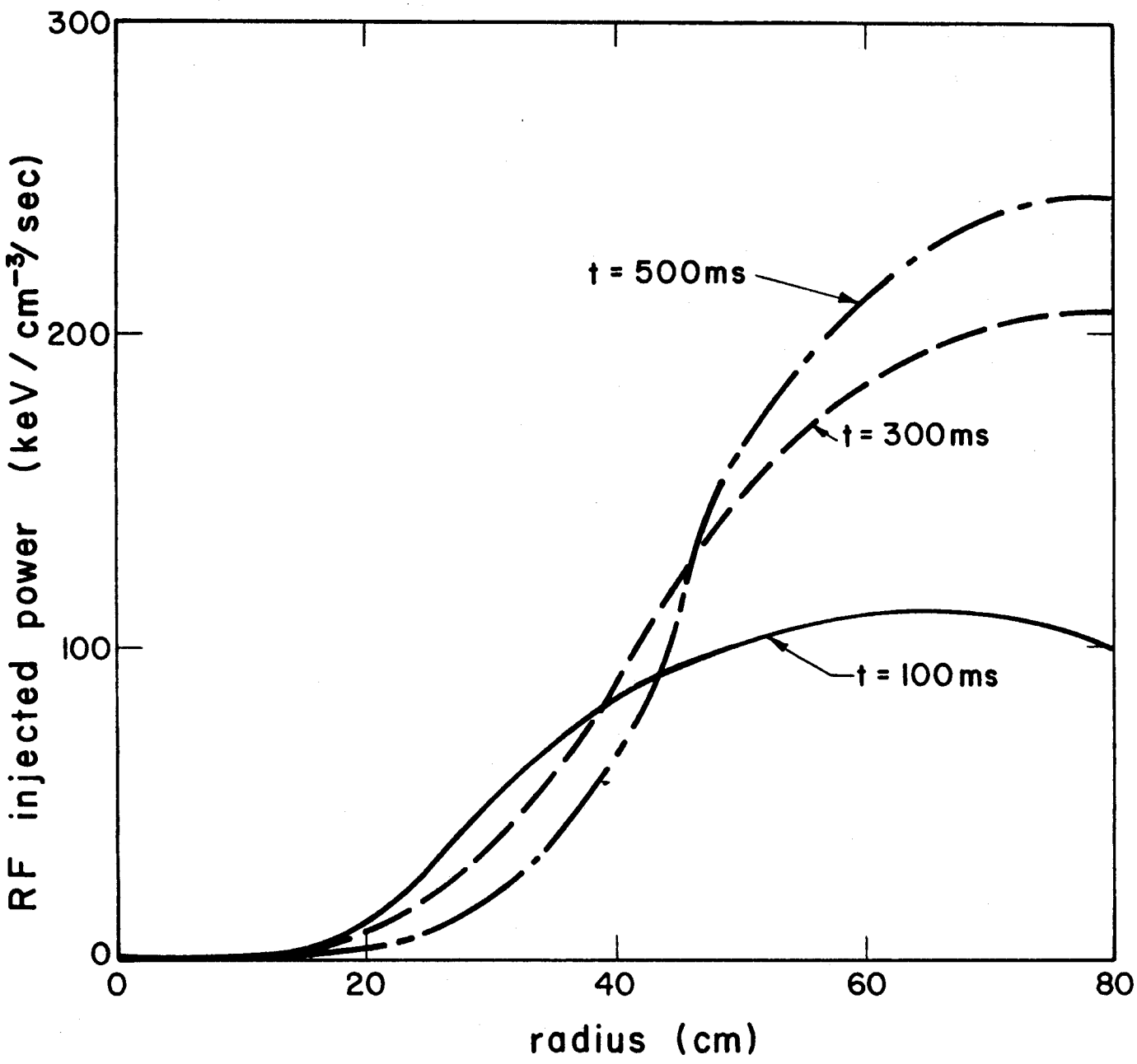

RF heating profile as a function of time with 50 MW supplied. In this case, $k_{||} = 10^{-3}cm^{-1}$, $\omega = 10^{-2}\omega_{CD}$ and the m=1 mode was assumed.

Figure IV-E-1

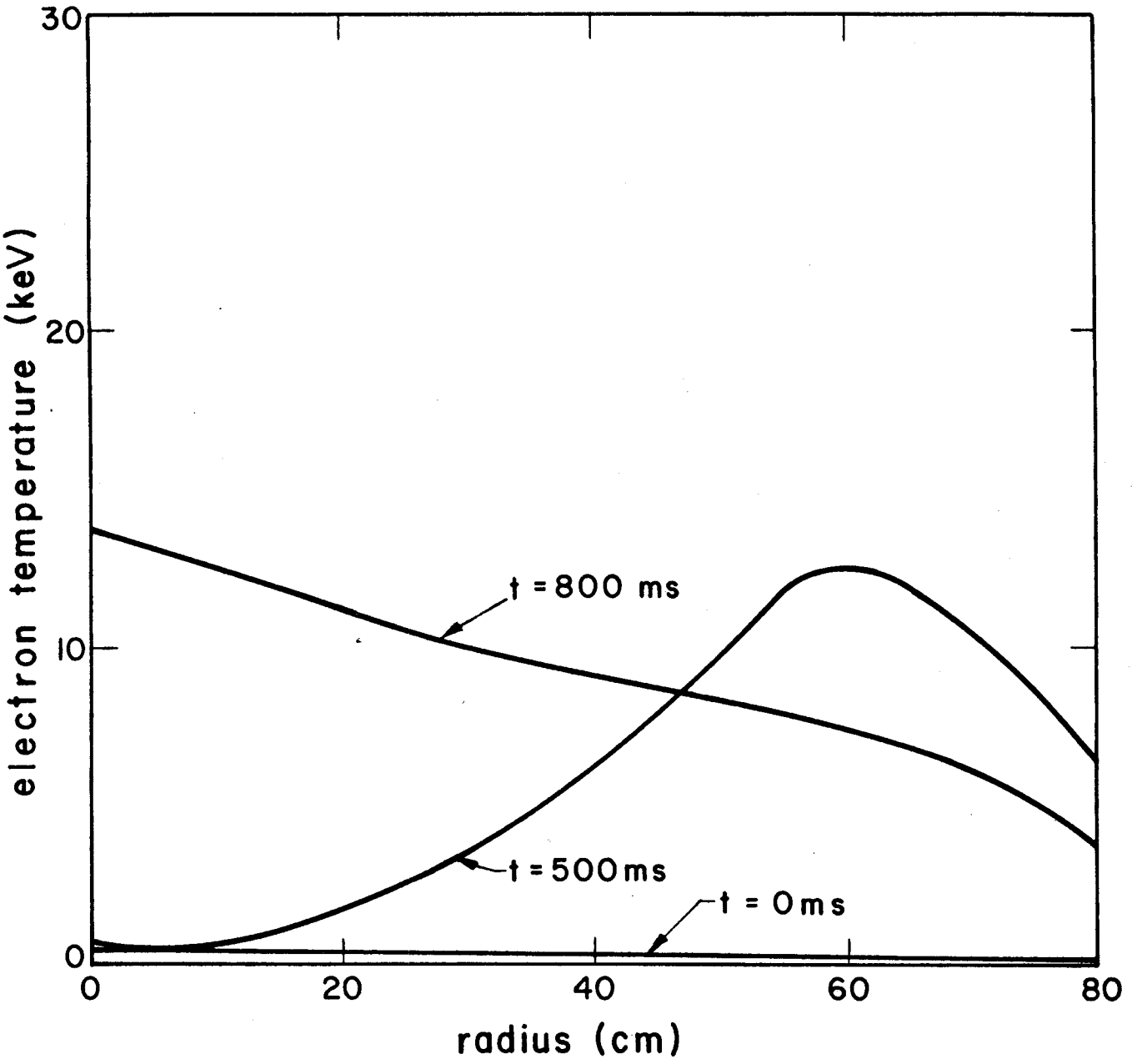

Electron temperature profile when 50 MW of RF power is supplied in the initial 500 ms of heating. After 500 ms, the RF is turned off and 150 MW of neutral beams are injected. In the RF phase $k_{\parallel} = 10^{-3} cm^{-1}$, $\omega = 10^{-2} \omega_{CD}$ and the m=1 mode was assumed.

Figure IV-E-2

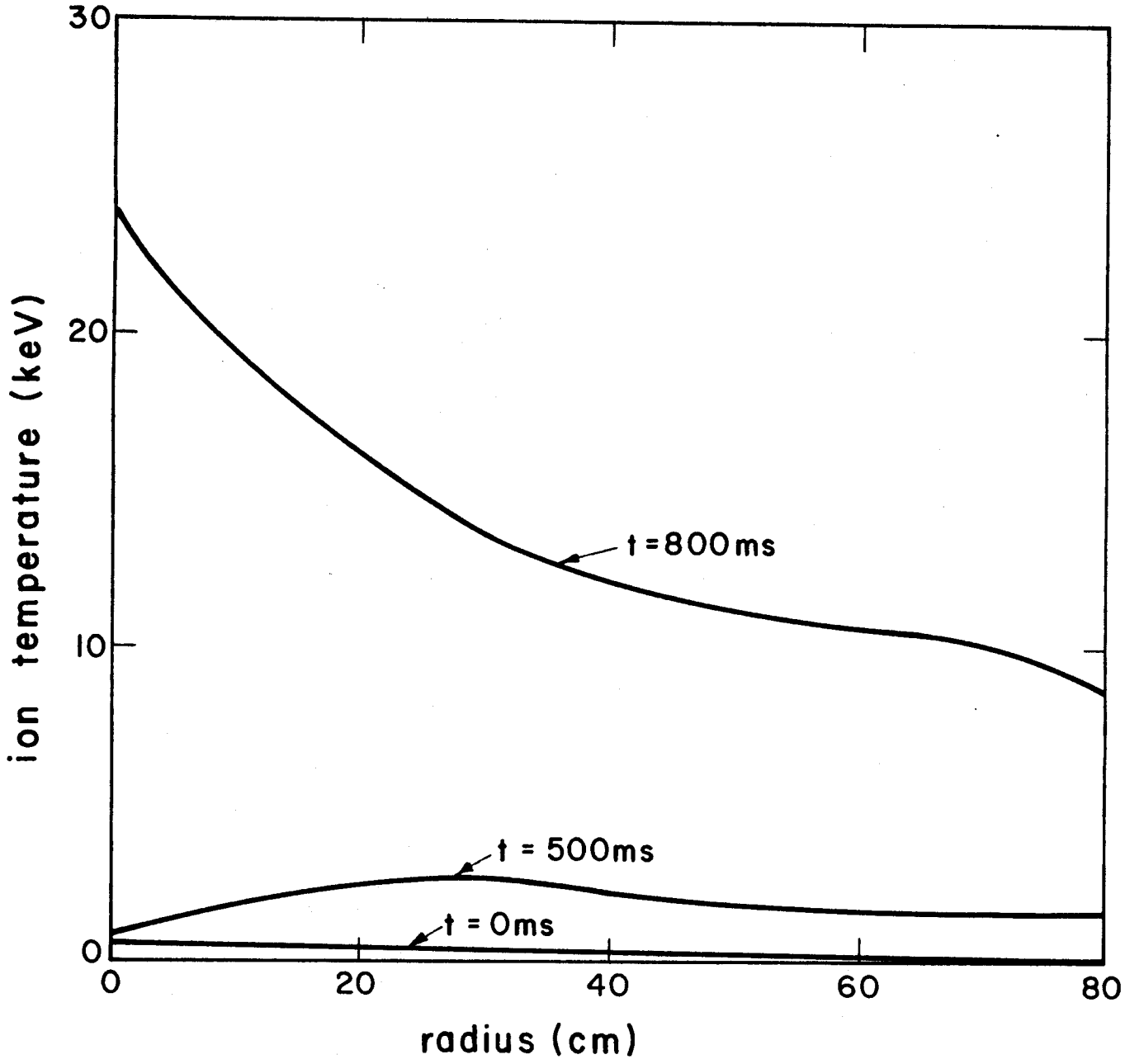

Ion temperature profile when 50 MW of RF power is supplied in the initial 500 ms of heating. After 500 ms, the RF is turned off and 150 MW of neutral beams are injected. In the RF phase, $k_{\parallel} = 10^{-3}cm^{-1}$, $\omega = 10^{-2}\omega_{CD}$ and the m=1 mode was assumed.

Figure IV-E-3

When the 150 MW of RF was used, the neutral beams produced more fusions in their initial 50 ms than without the RF preheat. However, the 150 MW of RF power produced less than 0.1 MW of fusion power in the preheat phase while the neutral beams would have produced over 50 MW of power in this same period. Therefore, any increase in the efficiency of the neutral beams was not great enough to offset the initial loss of fusion power. TETR reached the same operating parameters as those without an RF preheat within 300 ms because both τ_p and τ_E are of the order of 100 ms, τ_p and τ_E are purposely kept short in order that a high flux of neutrons can be obtained for the various engineering and materials tests.

We then proceeded to investigate the possibility of increasing the amount of alpha fusions by dividing 150 MW of injected power between the RF and neutral beams. Figure IV-E-4 is a plot of the power from the alpha fusions as the RF power varies from 0 to 50 MW while the total input power is kept constant. In Figure IV-E-5 we notice that the injected power to the ions, and consequently the ion temperature, drops as the proportion of RF power increases. In Figure IV-E-6 we see that though the injected power supplied to the electrons increases, P_B, the power supplied to the electrons from the neutral beams decreases, as does the beam power supplied to the ions. We also notice that as the amount of RF power increases, the power delivered to the electrons via alpha fusions and ion-electron collisions, as well as the diffusion power caused by colder electrons leaving an area rather than entering decreases. The net result of this is that as the RF power is increased, the ion temperature steadily drops from an average value of 13.4 keV to 10.0 keV while the electron temperature rises slightly from 9.2 keV to 9.4 keV. Therefore, there appears to be no advantage to using RF heating in this manner for the TETR tokamak.

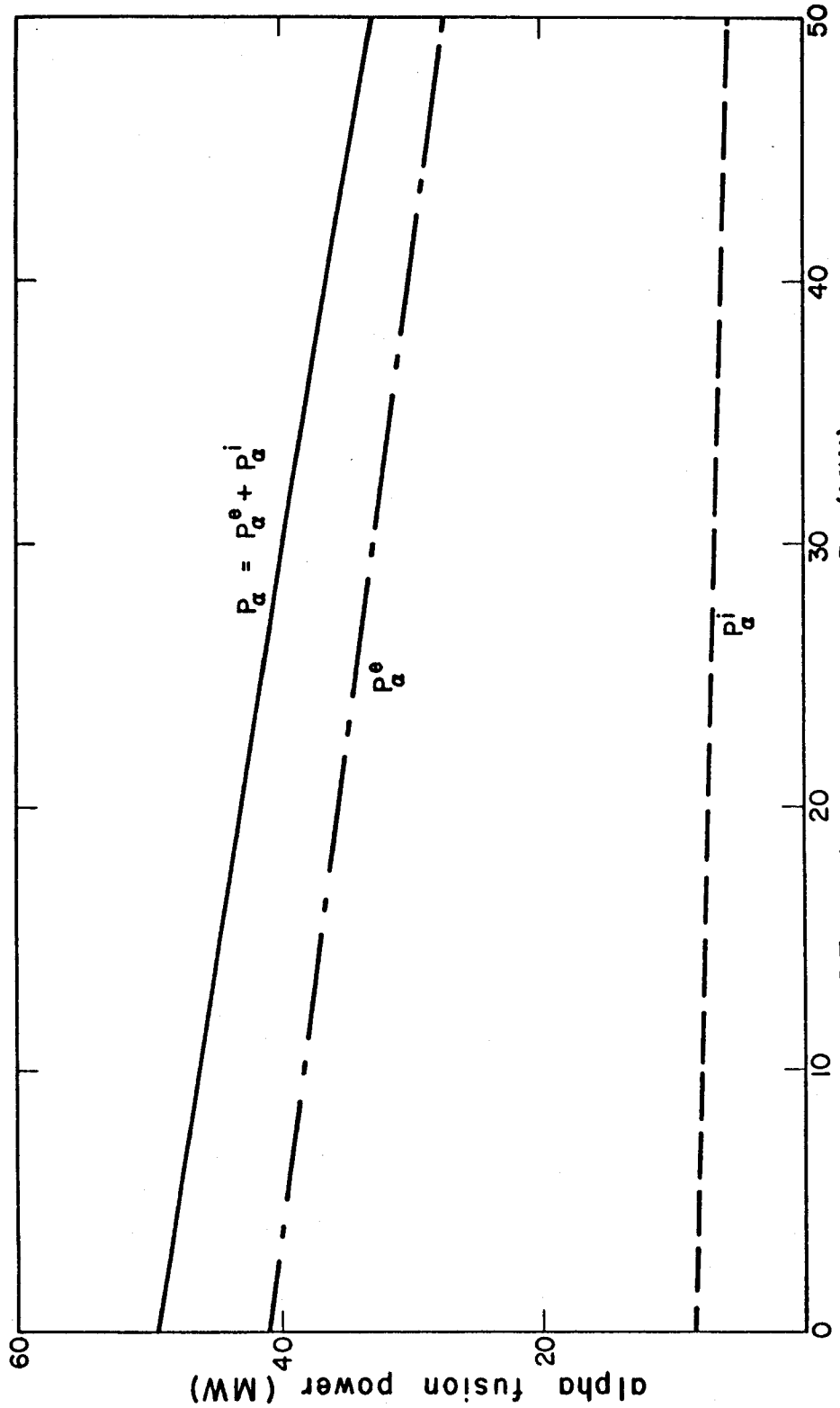

Alpha fusion power produced as a function of RF supplementary power. The total injected power is maintained at 150 MW. $\omega = 10\text{-}2\omega_{CD}$, $k_{//} = 10\text{-}3\text{cm}^{-1}$ and $t = 1.5$sec. In addition, an m=1 mode and the diffusion coefficients one-tenth those of trapped particle scaling were assumed.

Figure IV-E-4

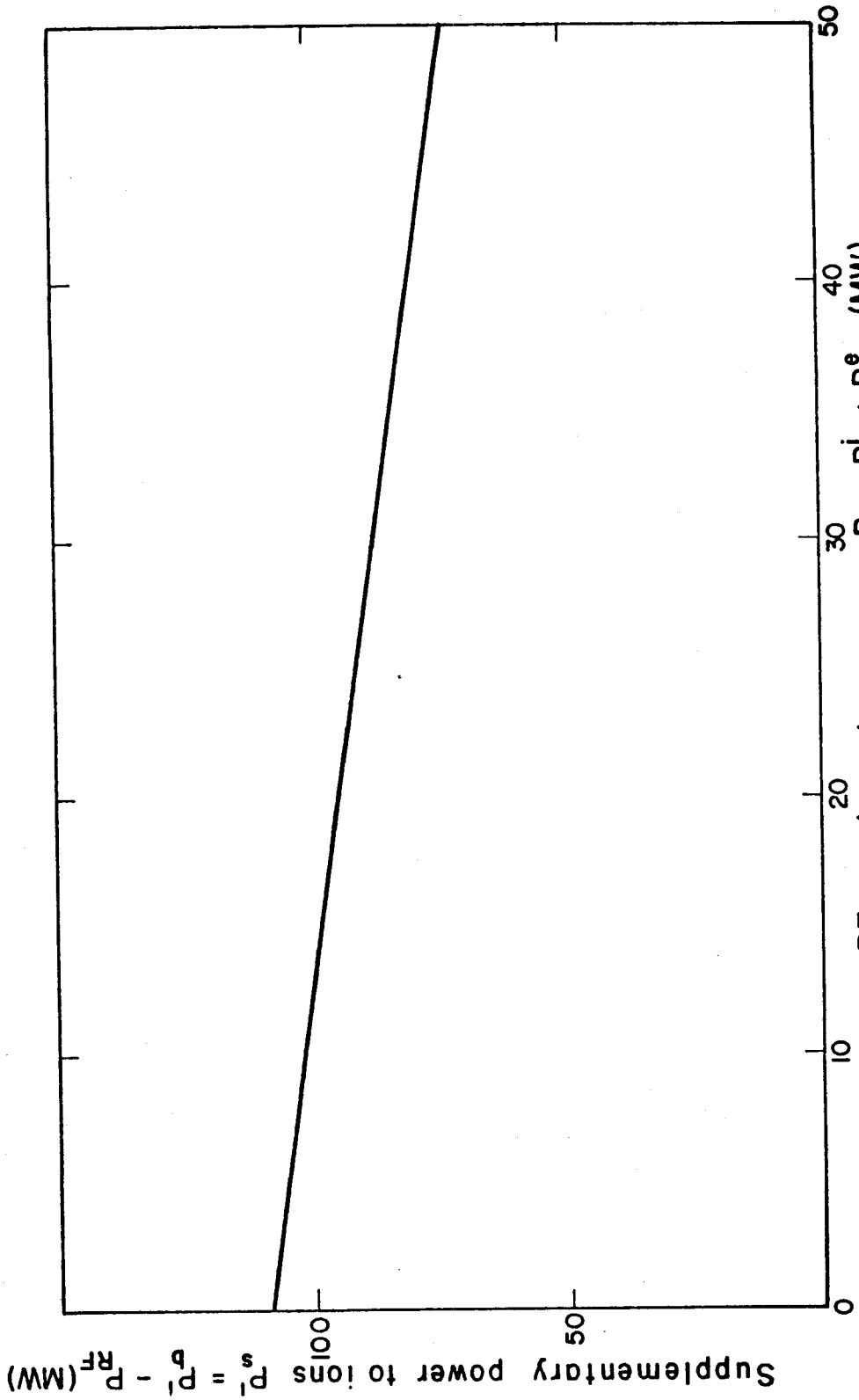

Power supplied to the ions from the neutral beams as the RF injected power varies from 0 to 50 MW. The total injected power remains constant at 150 MW. In this case, $\omega = 10^{-2}\omega_{CD}$, $k_{//} = 10^{-3}cm^{-1}$ and $t = 1.5$ sec. In addition, the m=1 mode and the diffusion coefficents one-tenth trapped particle scaling were assumed.

Figure IV-E-5

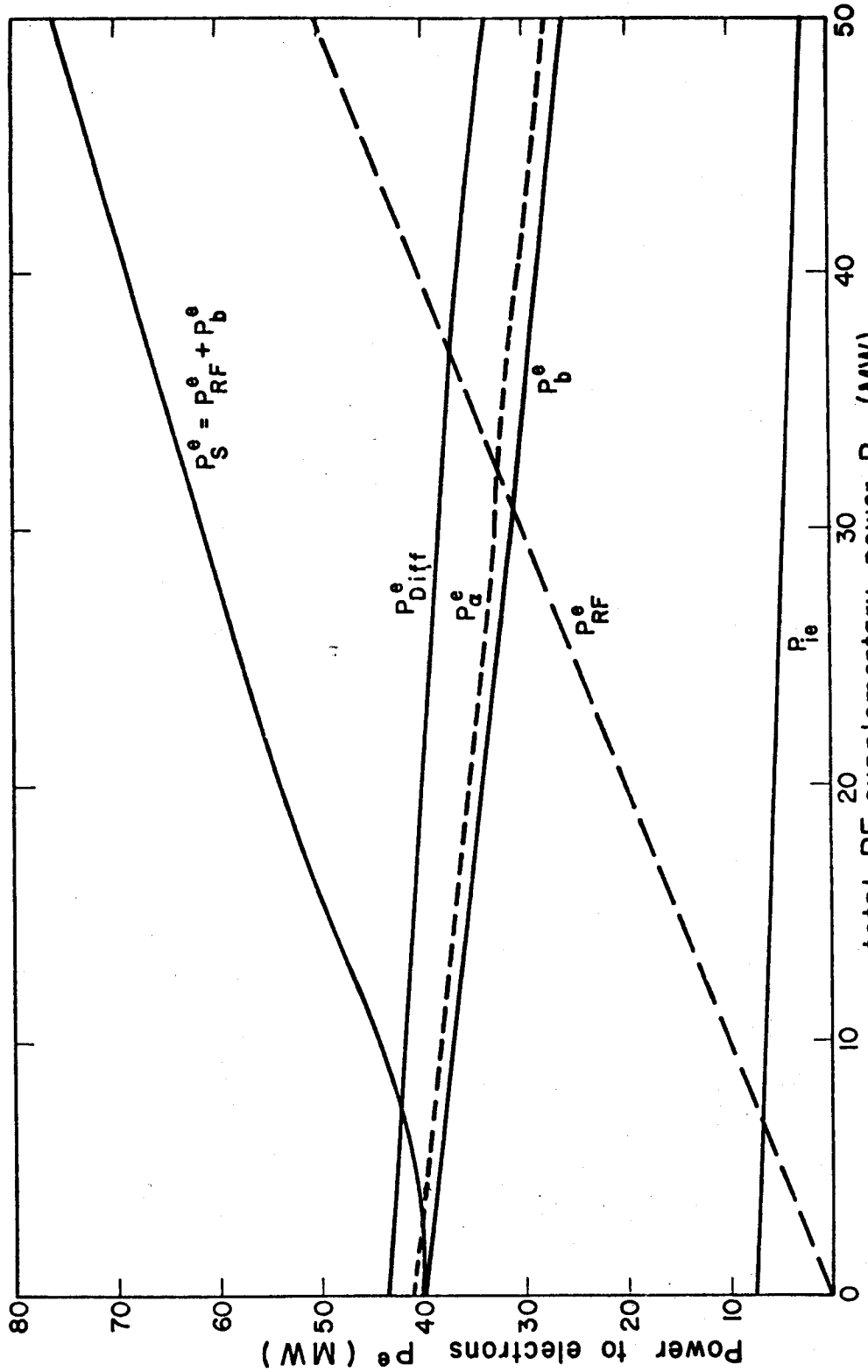

Power supplied to the electrons as the RF injected power varies from 0 to 50 MW. The total injected power remains constant at 150 MW. In this case, $\omega = 10^{-2}\omega_{CD}$, $k_{//} = 10^{-3}m^{-1}$ and $t = 1.5$ sec. In addition, the m=1 mode and the diffusion coefficient being one-tenth of the value in the trapped particle regimes were assumed.

Figure IV-E-6

Since τ_p and τ_E are short, the profile relaxation time is on the order of 300 ms as compared to a burn time of 60 s. Consequently, RF heating profile effects do not alter our results. However, transport scaling may be quite important. If different scaling is assumed so that the neutral beams could not heat the electron temperature past 8 keV, the RF power would make the beams more efficient in creating fusions. Above 8 keV, Q_F, the ratio between fusion output power and injected power only slightly increases as the electron temperature increases. However, when trapped particle scaling is assumed, the manner in which TETR operates essentially precludes RF efficient utilization of the fast Alfvén wave to heat the electrons and provide more fusion output power from the neutral beams.

References for Section IV-G

1. F. W. Perkins, Internal Princeton Report.

2. Stix, T. H., "Fast-Wave Heating of a Two-Component Plasma," Nuc. Fusion 15, (1975) pp. 737-754.

3. Scharer, J. E., McVey, B. D. and Mau, T. K., "Fast Wave Ion Cyclotron and First Harmonic Heating of Large Tokamaks," submitted to Nuclear Fusion.

4. Stix, T. H., "Report of the Ad Hoc Panel on RF Heating in Tokamaks," ERDA Report 76/115, pp. A.1-3 to A.1-12, July 1976.

5. Stix, T. H., Theory of Plasma Waves McGraw-Hill Book Co., New York (1962), pp. 10, 207.

6. B. Badger et al., "UWMAK-III, A Noncircular Tokamak Power Reactor Design," Nucl. Eng. Dept. Report UWFDM-150 (Univ. of Wisconsin-Madison; July 1976) p. II-D-2.

IV-F. Vacuum Pumps

There are four locations in each neutral beam line where vacuum pumps will be needed: at the ion source, immediately following the bending magnet, at the direct converter, and in the beam tube leading to the plasma chamber. The gas loads and the pressures as evaluated in the previous section in the order listed above are given in Table IV-F-1.

Table IV-F-1

Pump Location	Gas Load (ℓ/s)	Pressure (torr)
(1) Ion Source	0.65×10^{6}	1.1×10^{-4}
(2) Bending Magnet	0.62×10^{6}	1.3×10^{-4}
(3) Direct Converter	0.92×10^{6}	5.3×10^{-5}
(4) Beam Tube	0.36×10^{6}	9.3×10^{-5}

Except for the small amounts of He, D_2, T_2, DT and other species such as methane, deutero-methane, etc. that will back diffuse from the plasma chamber, the predominant gas load in the neutral beam lines will be deuterium. The extremely large gas loads shown in Table IV-F-1 make it difficult or impossible to contemplate the use of any mode of vacuum pumping other than the cryocondensation and cryosorption.

A cryocondensation pump operating at a temperature of ~15-16K will pump all gaseous species except helium. Experiments have shown that the pumping speed of a cryocondensation pump for hydrogen isotopes is a factor of two higher than an equally sized cryosorption pump.[1] An added benefit of cryocondensation is that instead of being trapped in a molecular sieve, the

condensate simply runs down the condensing surface and is collected and pumped out. Regeneration is only needed if contaminants cover the condensing surface and begin to impair heat transfer. Pumping speeds for hydrogen isotopes at 78 K are on the order of 15 ℓ/sec cm^2.(1)

Because of space limitation, we contemplate using the same type of rotatable pumps which were described in Section III-F but without the water cooled chevron shield. For the pressure range of 1×10^{-4} torr to 1×10^{-6} torr, a pumping speed of 8 ℓ/sec cm^2 for deuterium and 1 ℓ/sec cm^2 for helium was assumed for cryosorption pumps. The speed for a cryocondensation pump for deuterium is taken as 15 ℓ/sec cm^2.

Figure IV-F-1 is a top cutaway view of TETR showing the neutral beam tubes and the vacuum pump locations. Pump station number one has three cryocondensation pumps 2.5 m high for a total pumping area of $4.35 \times 10^4 cm^2$ and a pumping speed of $0.65 \times 10^6 \ell$/sec. Station number two has the same pump arrangement with the same pumping speed. The converter (No. 4) has a gas load of $0.92 \times 10^6 \ell$/sec and will require four cryocondensation pumps 2.65 m high with a total pumping surface of $6.15 \times 10^4 cm^2$. Space limitations have necessitated the placement of two pumps on each side of the beam tube at this location. The last pumping station (No. 5) which evacuates the beam tube leading to the plasma chamber will have a hybrid system of a single cryosorption pump 2.65 m high and a single cryocondensation pump of the same size. The combined pumping speed for D_2 will be 0.37×10^6 ℓ/sec and for He, $0.16 \times 10^5 \ell$/sec. Any helium gas diffusing back from the chamber will be pumped by the cryosorption pump. The pumping speed provided can take care of one-third of the helium gas generated by the reactor if we assume the chamber pressure to be on the order of 1×10^{-5} torr.

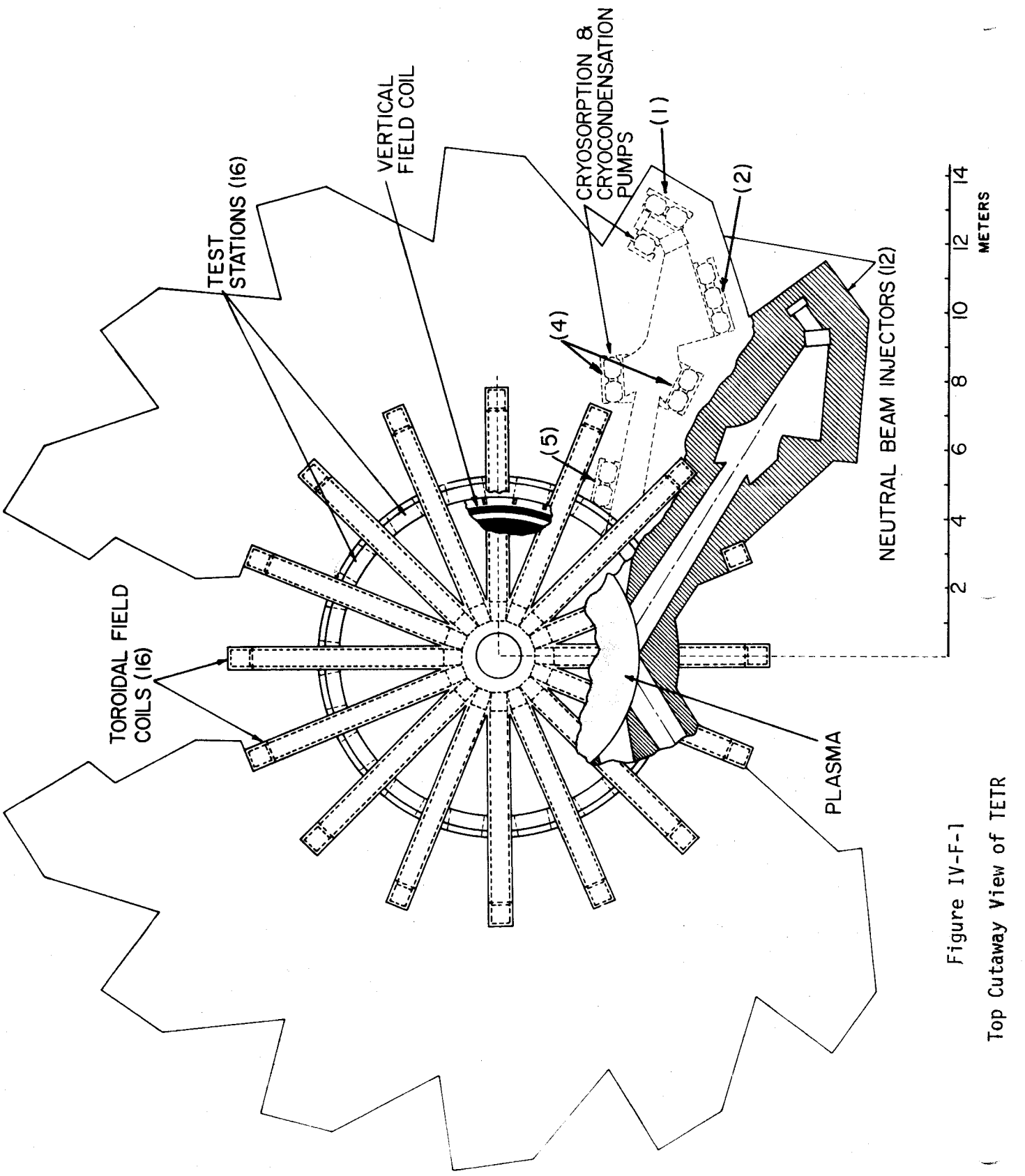

Figure IV-F-1
Top Cutaway View of TETR

The major power expenditure in the neutral beam system will be the provision of ~750 x 10^3 ℓ/day of liquid nitrogen which will require ~5.5 MW of power at 300 K. Approximately 1 kW of power at 4.2 K and 11.7 kW at 15 K will be needed to provide the cryocondensation and cryosorption surfaces with the needed refrigeration. The total amount of power needed at 300 K is 6.3 MW.

References for Section IV-F

1. V. B. Yuferov, et al., "Cryogenic Pumping of Fusion Reactors," Physical-Technical Institute of Ukranian Academy of Sciences, Kharkov, USSR.

V. Magnet System

V-A. Introduction and General Description of System

The design of the toroidal field (TF), ohmic heating (OH) and vertical field coils are described in this chapter. The basic design philosophy is very similar to that of UWMAK-I,[1] II[2] and III[3] with some changes due to the limited space and short rise time, especially in the ohmic heating and vertical field coils.

The TF magnets are composed of 16 cryogenically stable superconducting coils with NbTi filaments in OFHC copper stabilizer. The TF coils are pure constant tension "D" shape obtained from the analytical formulation by Moses[4]. This formulation corrects the magnetic forces for variations in field due to the discreteness of the finite number of coils and the shape of the cross section. As proposed for the magnets of the UWMAK-I, II and III studies, embedded conductors in structural discs are employed in order to hold the conductor rigidly within the supporting structure.

The ac losses in the conductors of the TF coils due to the pulsing fields of the VF coils and plasma are estimated. The TF coils are shielded from the pulsed field during the rapid rise of the plasma current.

The shell structure between toroidal field magnets is designed in conjunction with the magnet dewar to sustain the lateral loads due to pulsing fields from the VF coils and plasma current and the much larger loads produced if one adjacent magnet should lose current. These shells also provide for magneto electric stability of the toroidal field coils.

The limited space near the central core does not allow for provision of higher current than the design current. If all of the current is carried by the OFHC copper stabilizer then recovery to the superconducting state will take place. Safety protection is provided by a dumping resistor

applied to the 16 magnets in series, not just to the bad magnet. High purity aluminum has been considered as an alternative stabilizer which will provide a measure of extra current capacity.

To avoid the technological complexity of pulsing superconducting coils during the short 1 to 2 second rise time of the plasma current, the VF and OH coils are wound with normal metal conductors. The VF coils are water cooled OFHC copper operated at 64°C. The OH coils are high purity aluminum cryogenic coils operated at 4.2 K because the coils are located in the central support structure which is cooled to 4.2 K.

V-B. Toroidal Field Magnets

The design of the TF coils for TETR is quite similar to that used in the UWMAK-I[1], II[2] and III[3] designs. These designs utililze full cryogenic stability and reliably solid structures. The design choice is a pure constant tension "D" shaped toroid which produces a magnetic field of 4.19 tesla at the plasma's radius of 3.25 m.

Moses and Young[4] showed how to calculate the fields and forces for discrete toroid sector coils and developed the design equations for the position of maximum height, position B in Fig. IV-B-1, the top of the vertical inner leg of the magnet, position C, and the center of the outer leg of the magnet. The design equations for the TF magnet system of 16 coils are (see Fig. V-B-1 for dimensions).

$$R_1/R_2 = 1{,}000 - 2.253\,(\rho_2/R_2) + 2.440\,(\rho_2/R_2)^2 - 1.497\,(\rho_2/R_2) + 0.417\,(\rho_2/R_2)^4$$

$$H_{R_1}/R_2 = -0.200\,(\rho_2/R_2) + 2.57\,(\rho_2/R_2)^2 - 1.748\,(P_2/R_3)^3 + 0.560\,(\rho_2/R_2)^4$$

$$H_{max}/R_2 = 1.026\,(\rho_2/R_2) - 0.232\,(\rho_2/R_2)^2 + 0.053\,(\rho_2/R_2)^3 - 0.008\,(P_2/R_2)^4$$

$$R_{Hmax}/R_2 = 1.000 - 1.062\,(\rho_2/R_2) + 0.560\,(\rho_2/R_2) - 0.186\,(\rho_2/R_2)^3 + 0.033\,(\rho_2/R_2)^4 .$$

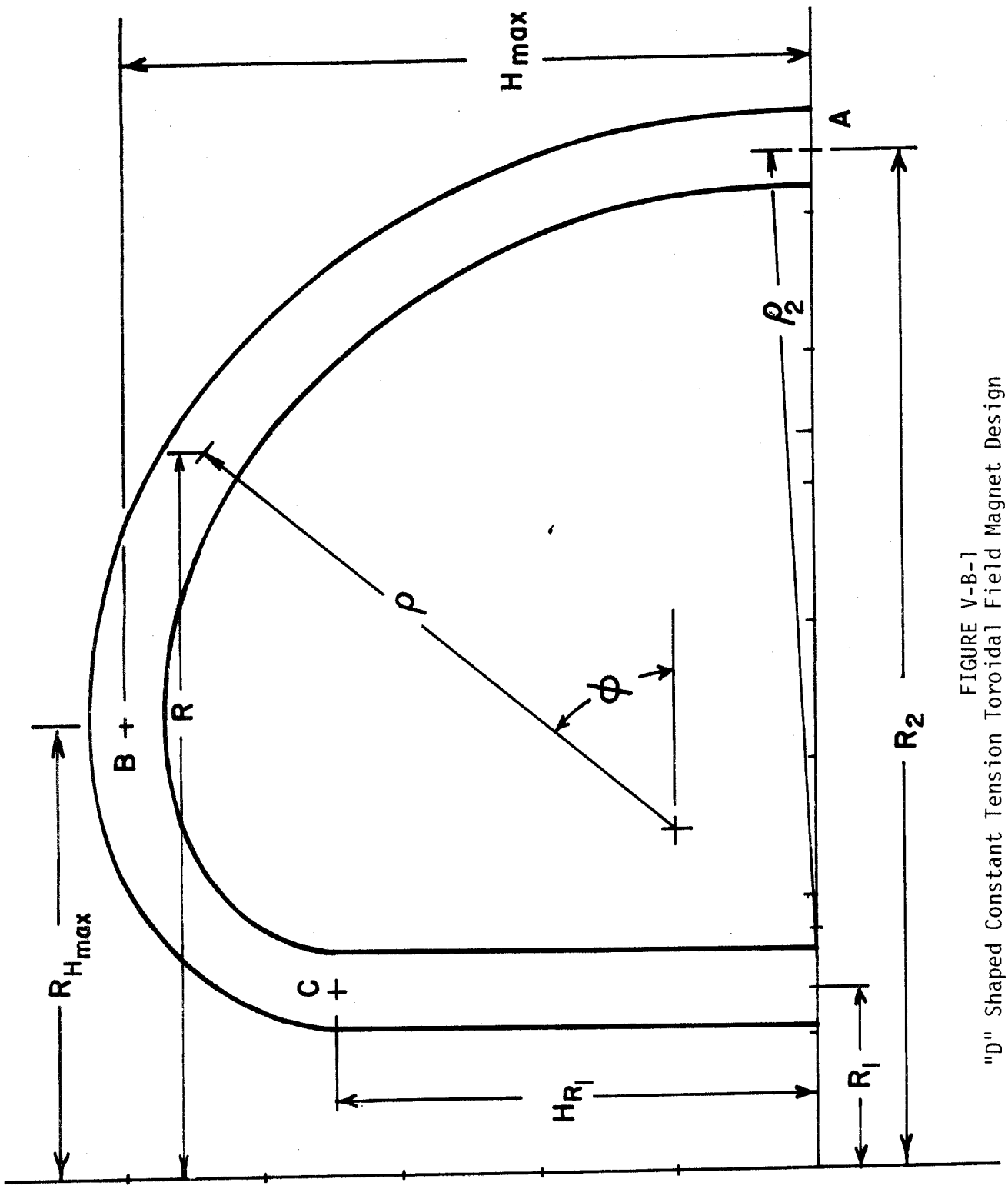

FIGURE V-B-1
"D" Shaped Constant Tension Toroidal Field Magnet Design

By determining the values of R_1 and H_{max} which are needed to allow space for blanket, shield removal, vacuum parts for divertor, etc., one can reasonably estimate R_2 and ρ_2 from the above design equations. These estimated values are used as the initial value of the computer iteration of the analytic expression[4] for the constant tension "D" shape for a magnet with a square cross section

$$\rho = \frac{R[k - \frac{1}{N} \ell n\ 2.276\ R/WN]}{1 + \cos\phi/N}$$

where k = a constant directly proportional to the design tensile force and inversely proportional to the square of the total current in a coil

R = distance from major toroid axis

N = number of discrete magnets in the toroidal system

ϕ = angle from midplane to normal vector

W = width of the magnet.

With OFHC copper stabilizer, the space available near the central core is just sufficient for cryogenic stability but not sufficient to permit having extra disks or turns. Extra turns and extra current capacity have been used in previous design for extra reliability. The crowding in this case is due to difficulties encountered in manufacturing and assembling the disks and conductors. As an alternative, the use of high purity aluminum as the stabilizer is considered as in UWMAK-III[3], since then excess current capacity would be available.

V-B-1. Materials

Even though considerable progress has been achieved in the development of multifilamentry Nb_3Sn for superconductors, the degradation of critical

current under relatively low strain is much more severe than for NbTi. Therefore, for a first option, NbTi is chosen as the superconductor in an OFHC copper stabilizer.

The magneto-resistance of OFHC copper at the temperature of liquid helium is $\rho_B \cong 10^{-8}$ (1 + 0.455 x B) ohm-cm with B in tesla. As applied to the disk design such copper provides 2600 A/cm^2 which is quite low for the limited space available.

High purity aluminum was the stabilizer in the magnet system in UWMAK-III. Based upon the experiments of Boom[5] and Segal[6] the resistivity of over-strained high purity aluminum does not increase excessively if elastically reinforced and restrained by high-strength aluminum. Figure V-B-2 is a sketch of the resistivity of high purity aluminum[7] after 1000 cycles of strain. In order to avoid a drastic increase in the resistivity, the maximum strains must be kept less than 0.003. For aluminum of RRR = 5000, the resistivity at a maximum strain of 0.2% is 1 x 10^{-9} ohm cm and with a magnetic field of B = 8 tesla, the extrapolated resistivity is about 3 x 10^{-9} ohm cm. An alternate design of the toroidal field magnets uses high purity aluminum at a conservative value of resistivity of ρ = 1 x 10^{-8} ohm cm. For thermal expansion compatibility between the conductor and structure 316 stainless steel was used as the structure for the OFHC copper stabilized conductor and 2219 aluminum alloy structure for the high purity aluminum stabilized conductor. Because of the lower resistivity of aluminum stabilizer the cross section of the conductor is smaller. The structural material quantities are determined by the need to segment and contain the conductors rather than by stress level. Thus, enough additional conductor turns equivalent to a redundancy of two discs per magnet are possible. If one also considers the

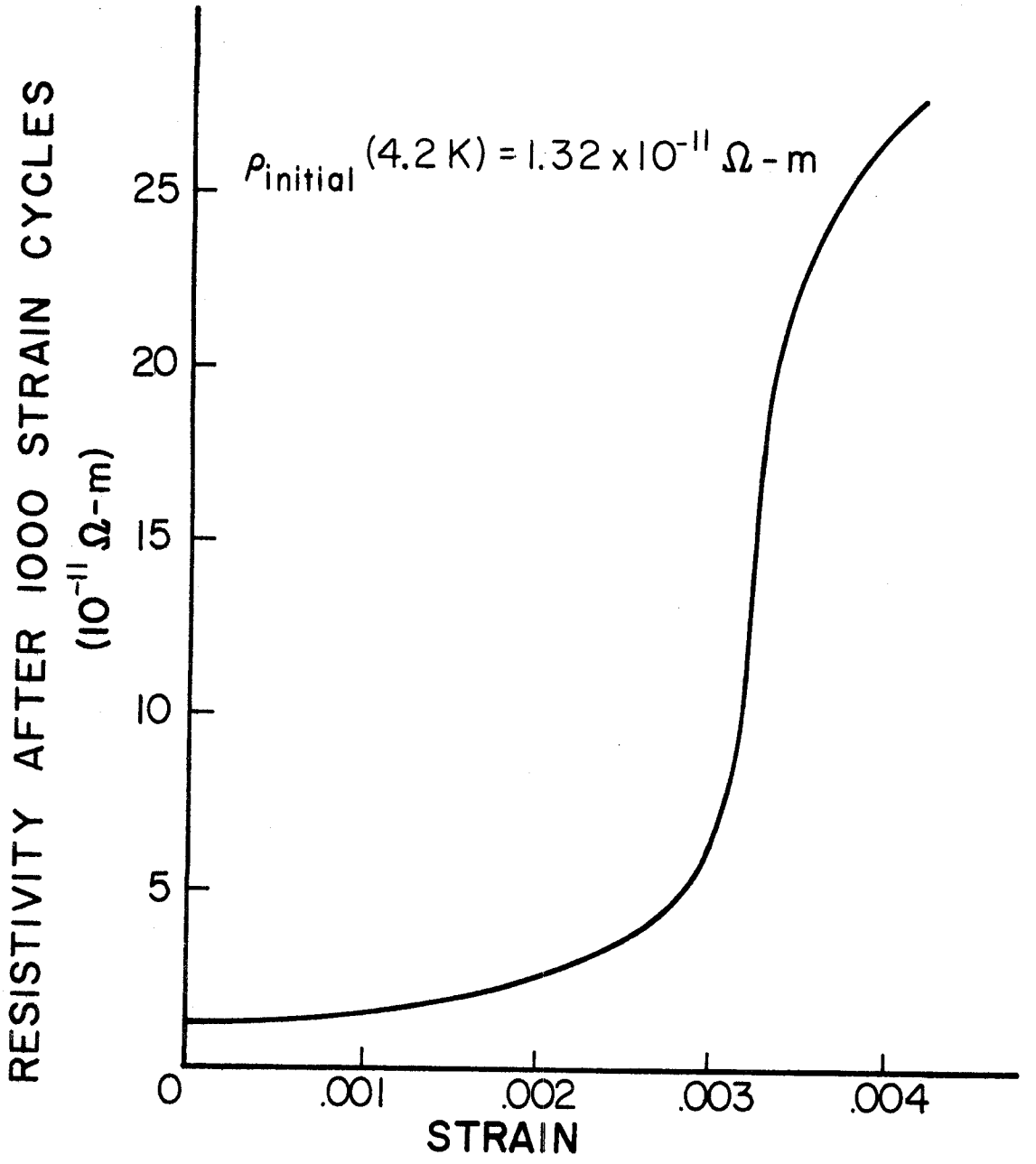

FIGURE V-B-2

Resistance and Strain at B = 0 for Reinforced High Purity Aluminum of RRR = 5000

lower value of actual resistivity of the aluminum a total redundancy of 30% can be obtained. This will handle the current rise in a coil due to the loss of current in an adjacent magnet. Considerable research and development is needed before one can accept aluminum stabilized conductors in such large magnets. The aluminum conductor cross section is smaller than the copper conductor and the aluminum structure cross section is larger than the steel structure. Thus, both magnets are of similar size. Further discussion will be limited to the copper stabilized magnets.

V-B-2. Specifications

Table V-B-1 is the list of specifications of the toroidal field magnets.

V-B-3. Construction Techniques

The construction techniques of TF magnets are similar to those of UWMAK-I and II for the copper-stainless steel magnet and UWMAK-III for the aluminum-aluminum alloy magnet.

The conductor is a composite strip containing 40 μm diameter NbTi filaments which have been co-drawn in a copper matrix and then soldered to additional OFHC copper stabilizer. As in the UWMAK-I design, the heat transfer coefficient is chosen to be 0.4 W/cm^2 and the design is such that the temperature of superconductor will not exceed 5.2 K. For such design, Hilal[8] found that the amount of superconductor which allows complete recovery to the superconducting state following a normal excursion should be sized at $T > 4.3$ K for use at 4.2 K. Thus, using J_c at 5.0 K allows for an extra amount of superconductor. The volume ratio of superconductor to copper in the composite strip is one to 2.5 and one to 100 in the stabilized conduction. The composite is twisted a full turn every 15 cm to minimize the ac loss in the conductor due to the pulsed poloidal field.

Table V-B-1

(a)	Field Specifications		
	On axis field	B_o = 4.19 tesla at R = 3.25 m	
	Maximum field at conductor	B_m = 8.5 tesla at R = 1.6 m	
	Total energy stored	6.3GJ = 1.75 MWh	
	Field ripple along the far edge of plasma	2%	
(b)	Magnet Components		
	Number of magnets	16	
	Number of disks per magnet	12	
	Superconductor	NbTi with filament diameter 40 μm and twist pitch 15 cm	
	Spacer between disks	0.5 cm micarta	
	Insulation between conductor and structure	0.1 cm epoxy fiberglass	
	Disk cross section	3.2 x 55 cm	
		Option I	Option II
	Stabilizer	OFHC copper	High purity Al
	Structure	316 SS	2219 Al
	Maximum structure design stress	1.03×10^8 N/m^2	1.5×10^8 N/m^2
	Maximum design strain	0.05%	0.19
	Conductor current (A)	9838	8050
	Number of turns/disk	36	44
	Conductor size	3.09 x 1.35 cm on inside turn, tapers to 1.40 x 1.35 cm on outer-most turn	1.41 x 1.25 cm
	Aluminum alloy bolts to fasten the discs together	375	375
	Lateral support between the magnet and dewar (reinforced epoxy struts each side cross section)	3000 cm^2	3000 cm^2
	Each magnet weight	45 Mtons	15.3 Mtons
(c)	Total Materials Required		
	NbTi superconductor	37.5 Mtons	37.5 Mtons
	Stabilizer	447 Mtons	110 Mtons
	Structure	230 Mtons	110 Mtons
	Insulation (epoxy)	15 Mtons	15.4 Mtons
	Micarta spacers	11.7 Mtons	11.7 Mtons
	Dewar (inner)	22 Mtons	22 Mtons
	Epoxy struts	1.2 Mtons	1.2 Mtons
	Aluminum alloy bolts	0.7 Mtons	0.7 Mtons
	Aluminum shielding	12.5 Mtons	12.5 Mtons
	Cryogenic Insulation	803 m^2	803 m^2

The cross section of the conductor is tapered as shown in Figure V-B-3 from 3.09 cm wide and 1.25 cm deep at the high field inner turn to 1.40 cm wide and 1.25 cm deep at the low field outer turn.

A full disk in the magnet is a large "D" shaped washer 3.2 cm thick and 55 cm wide weighing 3.6 Mtons. The 36 spiral grooves (18 on each side) on the surfaces will be forged or machined. The 960 m long conductor, shaped to the cross sections described above, is bonded into the grooves with fiber glass reinforced epoxy.

Each magnet consists of nine full discs with 36 conductor turns, two discs with 34 turns and four split discs with a total of 44 turns. The six partial discs are slanted and/or split to fit into the limited space near the central core as shown in Figure V-B-4. These six disks are equivalent to three disks having a total of 108 turns of conductor each carrying a current of 9838 amperes.

The complete disks are assembled with 0.5 cm micarta spacers between them by tightening 375 aluminum bolts which are about 20 cm apart from center to center in the circumferential direction. Three 55 cm bolts are used in the radial direction at each circumferential position except in the vertical leg portion near the central core where the magnets are space limited and only two larger diameter bolts are used.

Figs. V-B-4 and V-B-5 represent cross sections of the assembled magnet. Fig. V-B-4 is for the limited space region near the vertical inner leg and V-B-5 is for the region where more space is available. The inner dewar wall with high purity aluminum shield panels attached to it is assembled against micrata spacers to a tight fit around the magnet. A series of reinforced epoxy struts between inner and outer dewar walls provides lateral support to the magnet particularly in the case of a loss of current in an adjacent magnet which would distort the field and produce large lateral forces.

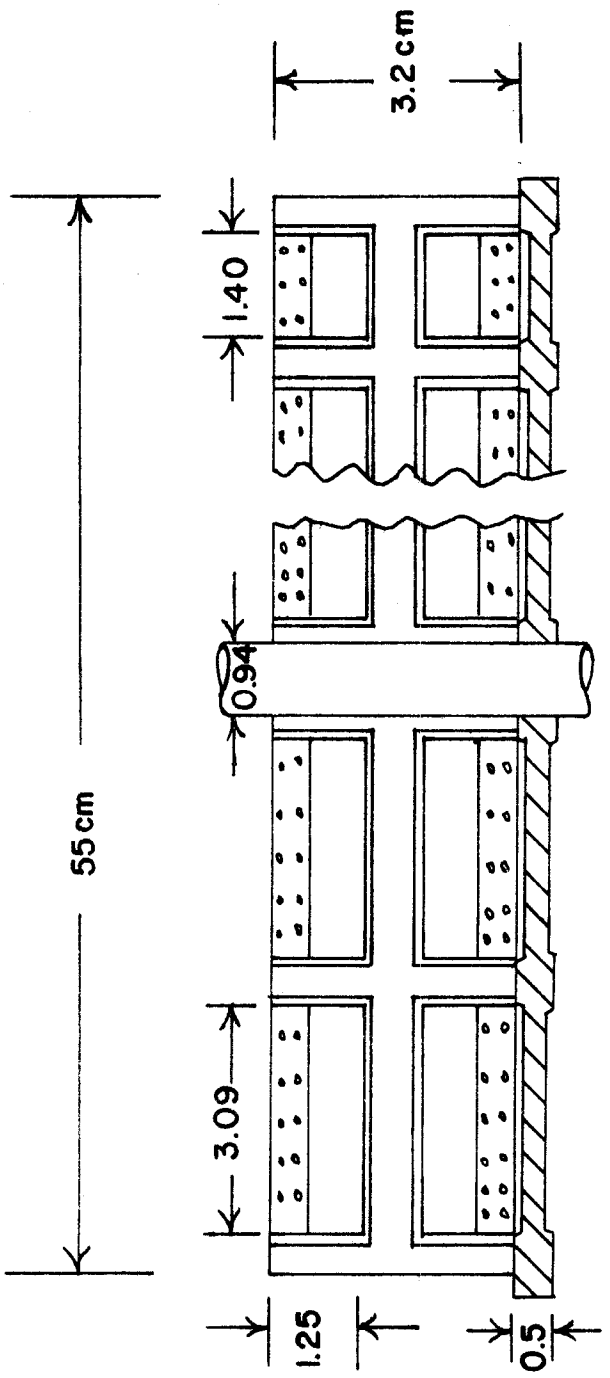

FIGURE V-B-3

Cross Section of Magnet Disk

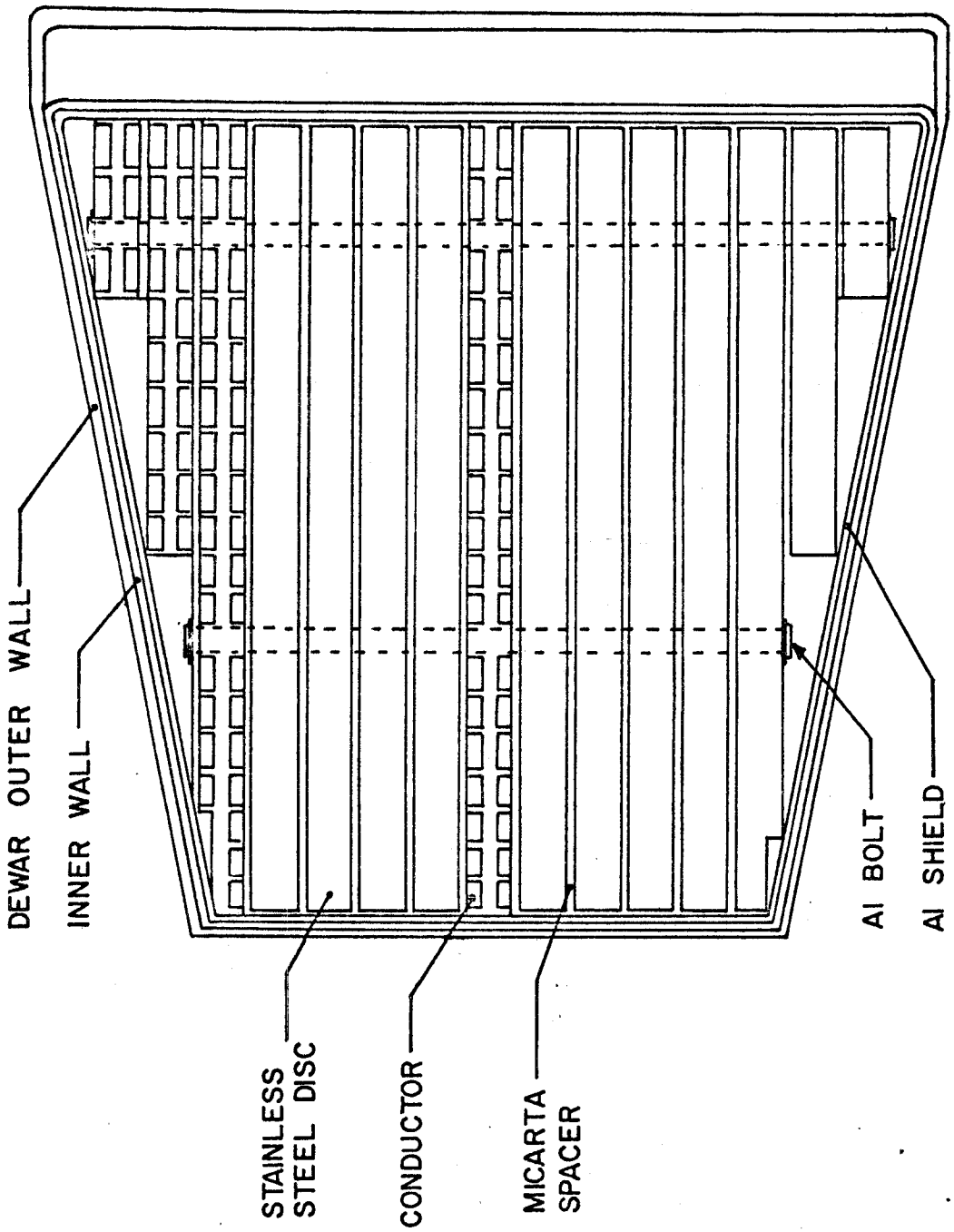

FIGURE V-B-4

Cross Section of TF Coil at Inner Leg

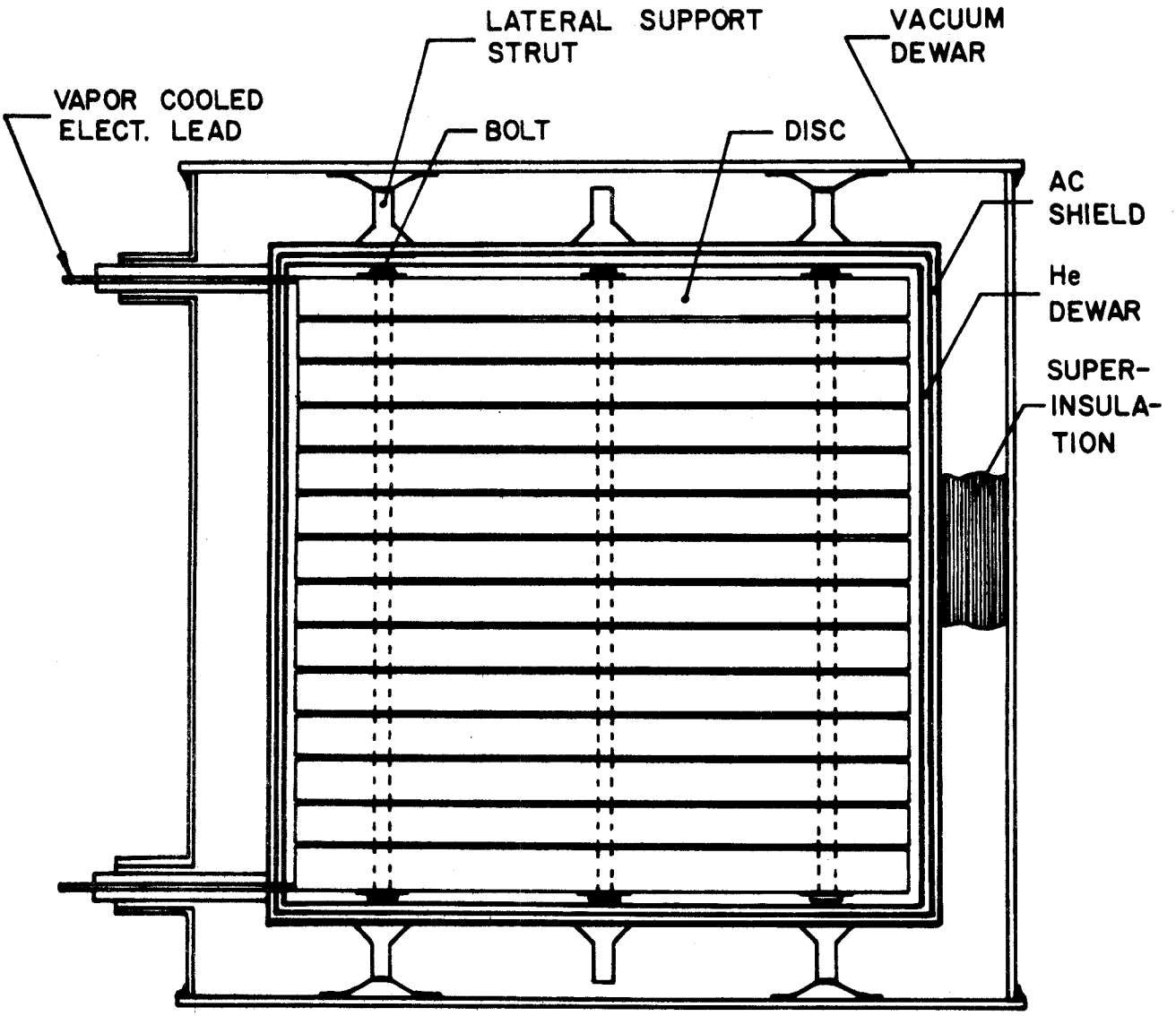

FIGURE V-B-5
Cross Section of TF Coil at Back Leg

V-B-4. Dewar Design

The TF magnet dewars in TETR are designed to be independent of the central support structure and of each other. This means that each magnet has its own liquid helium barrier and its own vacuum system.

The inner legs of the TF coils are crowded together such that all the dewar surfaces are in contact with each other. Since the central support structure is at the same temperature as the TF coils, there is no need to insulate at the point of contact between them.

The advantages of such a design are obvious. If one magnet loses current its effect on the others is minimized by isolation. Similarly, if one vacuum system fails, it would not contaminate the other vacuum systems. Another advantage, which is not immediately obvious, is the fact that a TF coil can be removed from the reactor without disturbing the remaining coils, which could remain cold.

In all other respects, the dewar design is similar to UWMAK-III. The liquid helium barrier is a 3 mm thick 304 stainless steel sheet which completely surrounds the coil. This container will be reinforced externally by a matrix of ribs in order to support a pressure of several atmospheres. The vacuum space between the inner dewar and the outer will be 5 cm on the inner leg facing the shield and 7 cm everywhere else. This space will be filled with superinsulation.

The vacuum dewar will be made of 2 cm thick 6061-T6 aluminum alloy, tapering down to 1 cm at the inner leg where it is in contact with the inner dewar wall. The vertical sides of the dewar will have fiberglass epoxy struts bridging the vacuum gap of which 10% are in permanent contact between the dewar walls. Then struts which align with holes cut out in the super-insulation are needed to provide lateral stability for the TF coils as discussed in section V-B-5.

The amount of materials in the dewars is 112 MT aluminum alloy and 32 MT stainless steel for the OFHC copper coils.

V-B-5. Lateral Support and Structural Safety

The UWMAK-II report described in detail the use of a vacuum tight shell to support the lateral loading between magnets on the occasion of a loss of current in one TF coil. The shell also supports the torsional loading on the TF magnets from the top to the bottom due to the interaction of the fields from the vertical field coils, the plasma and the currents in the TF magnets. However, the torsional loading is small compared to the lateral loading due to failure of a magnet. Therefore, the support structure designed for the failure mode is adequate for the torsional loading.

The support structure for TETR is quite similar to that described in the UWMAK-II report except that it is not required to provide a secondary vacuum as in UWMAK-II and III. It is a combination of shells and axially loaded struts. The neutral beam injection ports, cooling lines and the supports for the VF coils make it difficult to have a shell structure all around the TF magnets. The struts are used instead of shell structure at the locations where open spaces are necessary.

A decrease of current in one of the TF coils will induce a current increase in the remaining TF coils because of the inductive coupling between them. By using the measured mutual inductance values[9] of the "D" shaped coils as a function of angle, the ratios of the current changes in each of the several magnets to that in the failing magnet are found and listed in Table V-B-2. The relative magnitudes of the lateral forces, F_k/F_o, acting on each magnet caused by the distortion of the field and the summation of those forces, $\Sigma F_k/F_o$, which creates the shell stresses are also listed. The last column of data indicates the lateral motion in

Table V-B-2

Induced currents in the TF magnets, shell stresses and circumferential motions of the dewars due to the failure of magnet No. 1.

Magnet No.		$\Delta I_k/I_o$ *	F_k/F_o **	$\Sigma F_k/F_o$	Lateral Compression Stress, N/m^2	Lateral Dewar Motion, cm
1		-1	0			
				0	0	2.00
2	16	0.29	1.33			
				1.33	6980	1.77
3	15	0.16	0.24			
				1.57	8240	1.51
4	14	0.09	0.13			
				1.70	8922	1.22
5	13	0.06	0.06			
				1.76	9237	0.92
6	12	0.04	0.03			
				1.79	9394	0.61
7	11	0.03	0.01			
				1.80	9447	0.31
8	10	0.03	0.01			
				1.81	9500	0
9		0.03	0			

* $\Delta I_k/I_o$ is the ratio of the change in current during a fault to normal current

** F_k/F_o is the ratio of lateral forces to the normal repulsive force between two conductors carrying current I_o

centimeters of the outer leg of each dewar at the midplane of each magnet. F_o is the normal repulsive force between two parallel conductors, each of which is carrying I_o and separated by a distance S.

$$F_o = \frac{2x10^{-7} I_o^2}{S} \quad N/m$$

with $I_o = 3.774 \times 10^6$ amperes, the normal operating current of each toroidal magnet field. The current change in the failed magnet, ΔI, is taken to be $- I_o$.

As in the designs for UWMAK-II and III the lateral support structure is not allowed to carry tension since the tensile stresses could develop over a much shorter lateral span and therfore, would be much larger than the compressive stresses. To allow for the lateral dewar motion without developing tensile stresses in the shells or posts, a spring loaded slip joint is provided at the centerline of each shell and post. The shell panels between the outer legs of the upper part of the toroidal magnet are removable in order to gain access to the test modules.

The wall thickness of the shells and posts are designed to vary inversely as the radius in order to keep the compressive stress as constant as possible throughout the shell structure, i.e., to cause each radial plane of each magnet to remain essentially plane as it moves laterally. The inner wall of the shell is twice as thick as the outer wall because of the variation of loading on the side wall. The bending resistance of the side walls of the dewars is assisted by the ribbed radial edges of the shell panels. The total material required is 86 Mtons of aluminum alloy. The lateral magnetic forces on the TF coils are transmitted to the side walls of the dewar by the fiber-reinforced epoxy struts as in UWMAK-II and III. To prevent excessive thermal leaks the conical spring caps at the outer ends of 10% of the fiber-

glass epoxy struts are designed to support the transverse loading due to the pulsing of VF coils and plasma current. These conical caps also provide a necessary portion of the elastic stiffness necessary to prevent any magneto-elastic instabilities in the toroidal field magnet system.

V-B-6. AC Losses in TF Coils and Shielding

The toroidal field coils are subjected to the pulsed field from the plasma current and vertical field coils with a maximum variation $\Delta B \simeq 0.5$ tesla in 1 second. Filamentry superconductors in such pulsed field will dissipate heat and may become unstable. The power dissipation mechanisms are the eddy current loss in the normal metal, the multifilamentry coupling losses and the hysteresis losses in the superconducting filaments. In the environment of a time varying transverse magnetic field it is essential to twist superconducting filaments for stability. However, when transient longitudinal fields are considered, the twisting is responsible for the flux linkage[10] which creates coupling between filaments.

The ac losses in the conductors of the coils are estimated from the resultant fields computed along the coil centerline. It is assumed that the total loss is the sum of the separate losses of the transverse and longitudinal field components. The loss in the structural material is neglected.

The maximum field variation of the transverse components of the pulsed resultant field is $\Delta B_{\perp} \simeq 0.13$ tesla in one second during field increase and 1.5 seconds during field decrease per 72.5 second reactor cycle. This field is large enough to completely penetrate an individaul filament, but small enough so that only a small fraction of the wire, a thick outer layer, reaches current density saturation. The coupling loss in a unit volume of superconducting strand in a low frequency transverse field[11] is

$$\frac{Pe}{V} = \frac{B_{\perp}^2}{\rho_{\perp}} \left[\frac{L}{2\pi}\right]^2 \text{ watts/m}^3$$

where $\rho_{\perp}$ is the effective resistivity and L is the twist pitch length. The pitch length L = 15 cm is obtained by optimizing the total dissipated heat loss in the conductor. The sum of the average coupling losses of the filaments and the eddy current losses in the normal portion of the conductor, when averaged over the entire conductor length and integrated over a reactor cycle, is estimated to be 9.44×10^{-5} W/cm^3.

At saturation the hysteresis loss in the outer layer is small. The average hysteresis loss is approximately the same as the individual filament loss per unit volume, which is given as[12]

$$\frac{P_{\perp h}}{V} \simeq \frac{8}{3\pi} \lambda J_c d \frac{B_m}{\Delta T}$$

where λ is the superconducting volume fraction, J_c is the critical current density, d is the filament diameter, B_m is the maximum applied field and ΔT is the period of a cycle. With d = 40 μm the loss averaged for a cycle and over an entire conductor length is found to be 1.68×10^{-5} W/cm^3.

In a changing magnetic field parallel to the conductor the coupling losses in the superconducting filaments result from filament twisting. However, filament twisting is beneficial in reducing losses from a changing transverse field. Parallel field coupling can be reduced by periodic reversals of the twist[10]. However, it is not clear at the present stage of design that the reverse twisting of filaments can be easily manufactured. The ac losses of a superconducting conductor in a changing parallel field are again a combination of hysteresis and coupling losses. For infinitely long samples in a uniform parallel field for which the entire filaments

are saturated with current density J_c the loss in the filamentry conductor, excluding the eddy current losses in the normal metal, is given by

$$\frac{P_{11f}}{V} = B_{11}\lambda\, J_c R_o \quad \frac{\sqrt{1 + x_o^2} - 1}{4x_o}$$

where R_o = the composite radius and $x_o = 2\pi R_o/L$. With a transport current I_T through the conductor, the above loss should be modified by the factor $[1 + (\frac{I_T}{Ic})^2]$.

The coupling and hysteresis losses in the superconducting composite due to parallel field components is estimated to be 2.86×10^{-4} W/cm^3. The time averaged eddy current loss in the normal copper is 6.51×10^{-6} W/cm^3.

The total AC loss in the conductors of all TF magnets due to both the transverse and longitudinal pulsed fields from the plasma current and the divertor is 9.25 kW, which is small compared to 31.2 MW of available helium surface cooling power. However, during rapid field changes a local thermal instability may be possible near the vertical leg where the variation of field is large.

Shielding the TF coil from the pulsed external field with high purity aluminum sheet at low temperature has been proposed in the ANL-EPR[13] studies. As pointed out earlier, cyclic loading of high purity aluminum beyond its yield strength does not increase its resistivity excessively if the high purity aluminum is attached to an elastic structure. Aluminum shows low magneto-resistance. Therefore, in spite of its low yield strength it is quite reasonable to use high purity aluminum effectively at low temperature in the limited space of a Tokamak. Assuming that a residual resistivity ratio RRR of 5000 will be reduced to about 2000 by overstrain and also assuming a mean value of magnetic field over the inner wall of helium dewar

of about 4 tesla, one can estimate that the total resistivity of the aluminum is about $\rho = 4 \times 10^{-9}$ ohm cm including strain induced resistance and magneto resistance. The lack of space does not allow a shielding panel thick enough to shield out all of the Fourier components of the ramping field. The time constant of the pulsed field inside the shielding[14] is

$$\tau = \frac{\mu_o w t}{4\rho}$$

where w is the width of the square box and t is the thickness of the wall. The time constant is about 20 - 40 sec for a shield thickness of 0.5 to 1.0 cm. This aluminum shielding does not decrease the time averaged loss over the reactor cycle but does reduce the loss in the conductor during the rapid ramping phase.

High purity aluminum is sensitive to radiation. The radiation induced resistivity increase is about 1.3×10^{-9} Ω-cm at a damage level of 1×10^{-6} dpa. When added to the residual resistivity of 1.3×10^{-9} Ω-cm for 2000 RRR aluminum the total resistivity in zero field is 2.6×10^{-9} Ω-cm. The magneto resistance at 4 tesla increases ρ to 7×10^{-9} ohm cm which provides a 23 second time constant for a 1 cm thick wall. The highest radiation damage level in the shielding panel is about 7×10^{-6} dpa/year at the straight vertical leg near the divertor. In order to hold $\rho < 7 \times 10^{-9}$ Ω cm the magnet must be annealed at 77 K every two months. Since TETR has a large refrigeration power for the cryogenic ohmic heating coils it is possible to cool down a TF magnet in about a day.

A superconducting field shield might be a better option for high radiation damage levels but, as pointed out in an EPR[13] report, some technological uncertainty is involved.

V-B-7. Magnet Safety and Protection

In the UWMAK-III report a magnet safety and protection system was described for the case in which one or two adjacent coils develop a problem which requires that the current be discharged as soon as possible from a coil. As mentioned earlier, there is no space for extra OFHC copper in TETR so that cryogenic stability will be lost if the current in the conductor is higher than the normal operating current. Therefore, it is not desirable to discharge only the bad magnet since the current in a neighbouring magnet could increase inductively as much as 30%. There is enough extra superconductor to carry the increased current, but recovery for a normal region is not possible at increased current levels. Development of a normal region is quite possible due to flux jumps during a rapid shutdown of a bad coil.

Since stored energy and inductance of the magnet system under discussion is relatively small, it is possible to discharge all 16 magnets in series in a reasonably short time. The self inductance of the TF magnet system is L = 130 Henries. With a dump resistor of 0.5 ohm, the discharge time constant is $t_c = \frac{L}{R}$ = 260 sec and the maximum voltage is 5000 volts. For the worst case, consider that a normal region is heating up after losing all helium cooling. The maximum temperature can be obtained from

$$\int_0^{\infty} j^2 dt = \int_{4.2}^{T_{max.}} \gamma c/\rho \, dT$$

where j is current density, γ is density, c is specific heat and ρ is resistivity. Assume that the resistance of normal regions remains small compared with that of the external dump resistor. Using a numerical calculation of Maddock[15] for current density 3000 A/cm^2 and RRR = 100 copper, T_{max} is estimated to be 250 K.

References for Section V-B

1. B. Badger et al., UWMAK-I, A Wisconsin Toroidal Reactor Design, Nuclear Engineering Department Report UWFDM-68, Univ. of Wisconsin, 1974.

2. B. Badger et al., UWMAK-II, A Conceptual Tokamak Fusion Reactor Design, Nuclear Engineering Department Report UWFDM-112, Univ. of Wisconsin, October, 1975.

3. B. Badger et al., UWMAK-III, An Advanced Noncircular Tokamak Power Reactor Design, Nuclear Engineering Department Report UWFDM-150, Univ. of Wisconsin, 1976.

4. R. W. Moses, Jr. and W. C. Young, Analytic Expressions for Magnetic Force on Sectored Toroidal Coils, Proc. of the Sixth Symposium on Engineering Problems of Fusion Research, p. 917 (1975).

5. R. W. Boom, P. Brown and F. J. Worzala, Bull. Am. Phys. Soc. 17, p. 1195 (1972).

6. H. R. Segal and T. G. Richard, Low Temperature Resistance of Cyclically Strained Aluminum, Adv. in Cryogenic Engineering, Vol. 22, p. 486 (1975).

7. H. R. Segal, Reinforced Aluminum as a Superconducting Stabilizer, IEEE Trans. on Mag, MAG-13, p. 109 (1977).

8. M. A. Hilal and R. W. Boom, Cryogenically Stable Conductors for Toroidal Fusion Reactor Magnets, Proc. of the Sixth Symposium on Engineering Problems of Fusion Research, p. 111 (1975).

9. R. L. Willig, private communication.

10. W. J. Carr, Jr., Parallel Field Losses in Twisted Multi-filament Superconductor, Proc. of the Sixth Symposium on Engineering Problems of Fusion Research, p. 152 (1975).

    S. S. Shen and J. R. Miller, Transient Poloidal Field Effects in Twisted Multi-filamentry Superconductor for Toroidal Field Windings of Tokamaks, Proc. of the Sixth Symposium on Engineering Problems of Fusion Research, p. 145 (1975).

11. W. J. Carr, AC Loss in a Twisted Multi-filamentry Superconducting Wire I, J. of App. Phy. 45 p. 929 (1974).

12. J. H. Murphy, M. S. Walker and W. J. Carr, Jr., Theory of Alternating Field Losses in Cylindrical Twisted Multi-filamentry Superconductors, IEEE Trans. on Magnetics, MAG-10, p. 868 (1974).

13. S. T. Wang, et. al., A 10 Tesla Pure Tension Superconducting Toroidal Field Coil System Design, IEEE Trans. on Mag., MAG-13, p. 605 (1977).

14. K. Khalaf-Allah, Time Constant for Magnetic Field Diffusion Into A Hollow Cylindrical Conductor, CLM-R 141, Culham Laboratory Report (1974).

15. B. J. Maddock and G. B. James, Protection and Stabilization of Large Superconducting Magnets, Proc. IEEE 115 p. 543 (1968).

V-C. Vertical Field Coils

V-C-1. General Description

Conventional water-cooled copper conductors are planned for the vertical field coils which is consistent with guidelines adopted for a machine operating in the near term. The technology for such coils is well established, needs no extrapolation, and can be used to design rapidly pulsed coils without adverse effects. A major advantage is that copper conductors can be joined and repaired by conventional brazing techniques.

The VF system is not space limited and does not require high strength superinsulation because the VF coils are not near cryogenic structures.

The VF coils in TETR not only provide the poloidal field needed for plasma confinement and stability, but also provide the flux lines along which charged particles leaving the plasma are diverted to the particle collector plates, which substantially complicates the VF system. For example, there is a null driving coil in the central shield which is equal in size to the rest of the VF coils combined. The multipurpose nature of the VF coil system requires additional coils with more ampere turns than is usually required.

Figure V-C-1 is a cross section of TETR showing the location of the VF coils which are numbered 1-25. The large null driving coil in the central shield is divided into eight separate coils numbered 9-16. There are 48 coils altogether, ranging in current from 0.066 MA to 0.477 MA, see Table V-C-2. In all cases the conductor is in the form of a rectangular bar with multiple cooling holes. Table V-C-1 lists the characteristics of the three types of conductors. The coils can be wound either with the major dimension of the conductor parallel or perpendicular to the axis of the coil. The shape of the coil, its proximity to other coils, the forces, and the amount

Figure V-C-1

Cross Section of TETR with Numbered VF and OH Coils

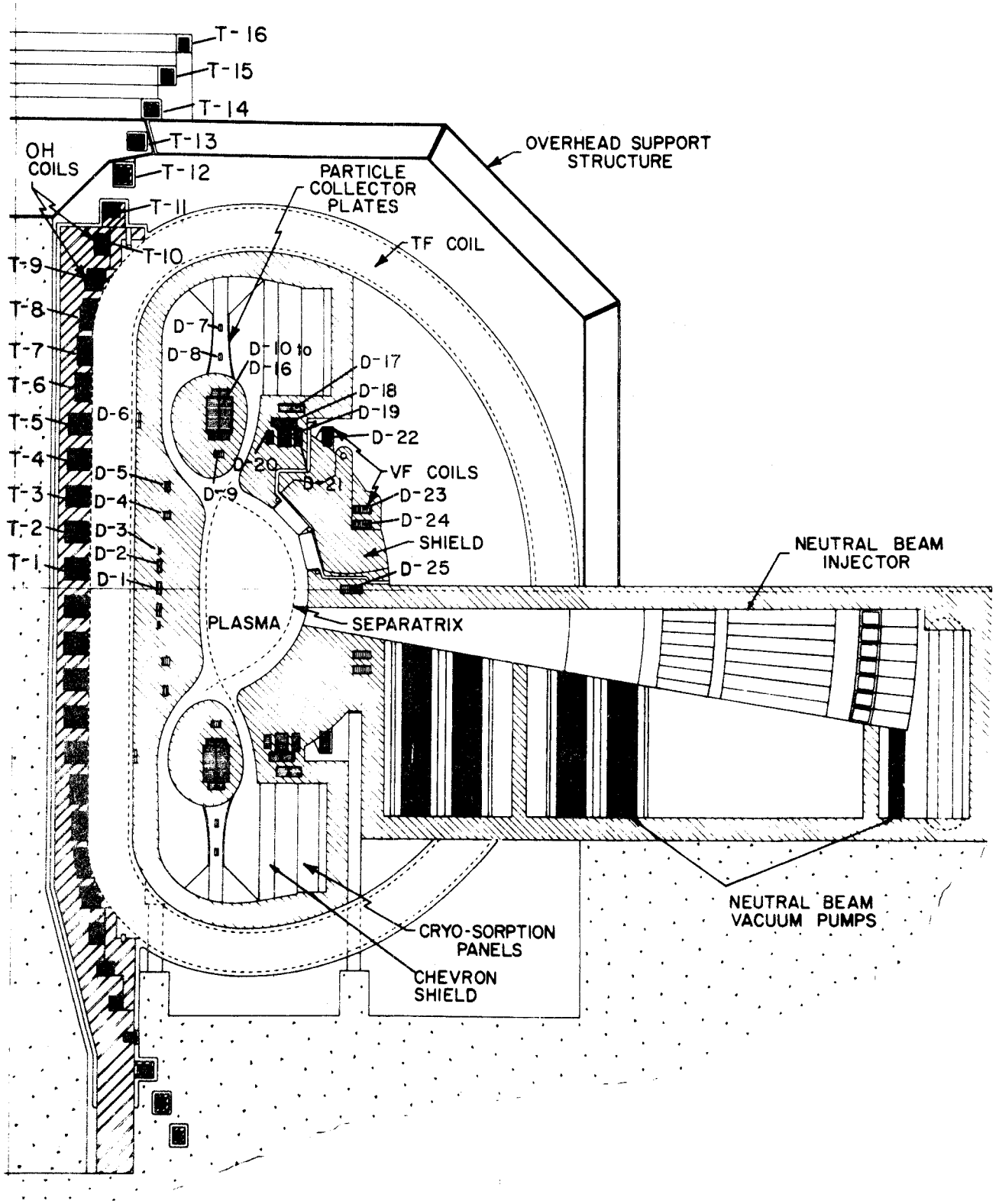

of shielding space available are some of the variables used to determine how to wind a coil. The large null driving coil, for instance, is wound with the major conductor dimension perpendicular to the coil axis. Cooling connections can be made on either side of the coil in this perpendicular configuration, whereas in the parallel configuration, the proximity of the adjacent coils would make cooling connection difficult to locate. Figure V-C-1 is a cross section of TETR showing the numbering sequence for the VF and OH coils.

Table V-C-1

Conductors in VF Coils

Conductor	Dimensions (cm)	Number of Cooling Holes	Effective Cond. Area, cm^2	Current Capacity, A
Type I	8.8 x 2.3	4	17.10	34,000
Type II	11 x 2.3	5	21.38	42,000
Type III	17.6 x 2.3	8	34.20	68,000

V-C-2. Coil Specifications

The conductor in the VF coils is made of extruded 10% cold worked OFHC copper. There are three different sizes, ranging in width from 8.8 cm to 17.6 cm, 2.3 cm thick, and with four, five, and eight cooling channels respectively. The current capacity ranges from 34 kA for type I to 68 kA for type III.

The conductors are wrapped with 1 mm thick silicate impregnated glass or mica tape during winding after which the whole coil is wrapped again with a double thickness of the same tape. Silicate impregnated glass or mica tape has a useful radiation limit of 10^{12} rads, which is equivalent to a fluence of 10^{21} neutrons/cm^2. In the worst case, this amounts to 10 years

of operation in TETR. The electrical breakdown of this tape is greater than 100 kV/mm.

Figure V-C-2 is a cross section of a typical VF coil consisting of five turns of type II conductor and a single cooling water connection. One manifold can supply cooling water to several turns of conductor, but of course each connection must have an insulated transition joint in order to avoid an electrical short circuit. Joints are made by brazing with a BAg filler. Induction brazing with low frequency RF can be used on conductors of this thickness. With proper preparation, the heat affected zone can be minimized. Copper inserts are used in the cooling channels to improve the sealing possibility at the joint. Figure V-C-3 shows a typical brazed joint.

Tables V-C-2 and V-C-3 list the physical and the electrical specifications for the VF coils respectively. The VF coils are cooled with water entering at 30 C and exiting at 70 C. Maximum temperature in the conductor is 77 C and the average temperature is 60 C, based on coils D-10 to D-15 which have the highest current density, 1743 A/cm^2. The resistance of OFHC copper averaged over this temperature range is 1.914×10^{-6} Ω cm. Values of coil resistance, ohmic heating and water flow rate given in Table V-C-3 are based on this resistance. The total time average power loss is 63 MW.

Supply water connections are made at every other turn with the return connections at the intervening turns so that the cooling water traverses a complete coil circumference before emerging into the return manifold. Each supply connection allows water to flow in both directions and each return connection collects water from both directions, which has the effect of counter current heat exchange to minimize temperature gradients. Figure V-C-4 is a schematic representation of how supply and return water connections are made to a typical four turn VF coil in TETR.

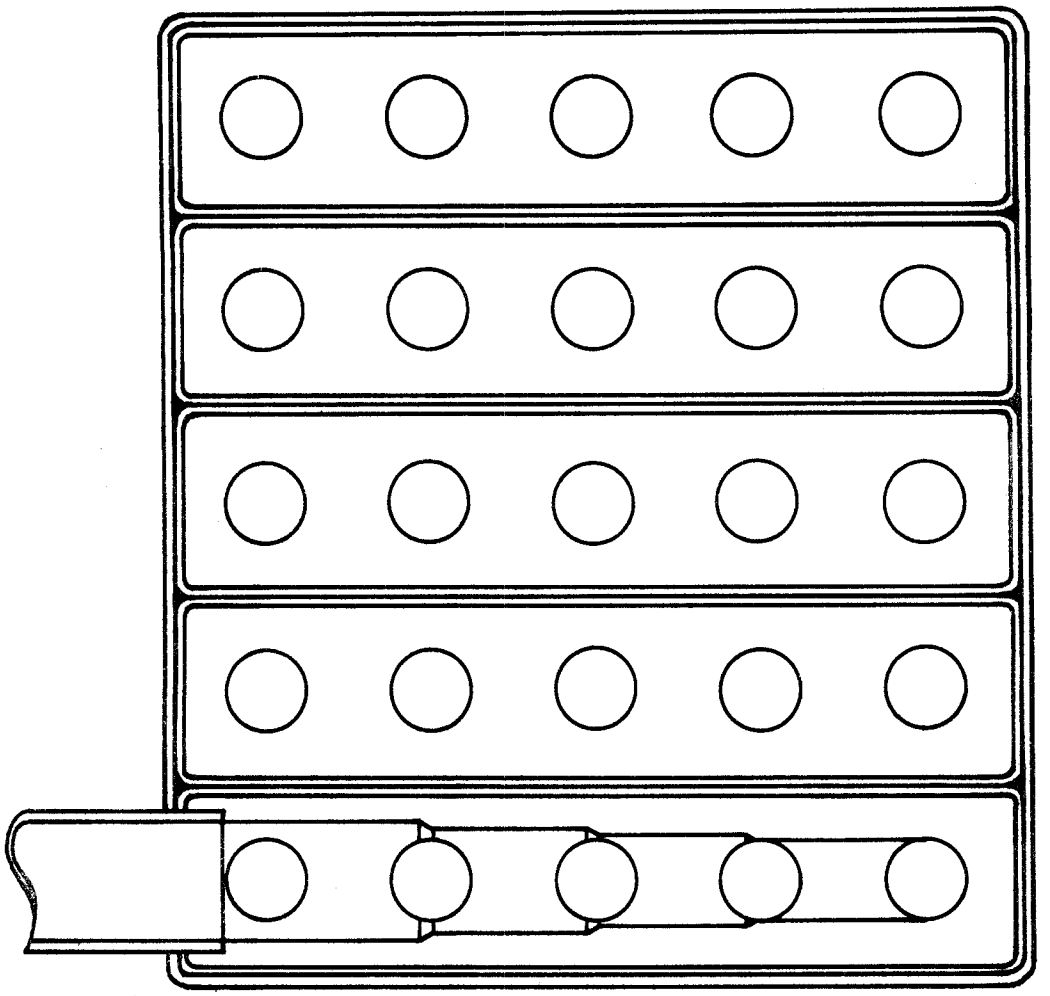

FIGURE V-C-2
Cross Section of a Typical VF Coil

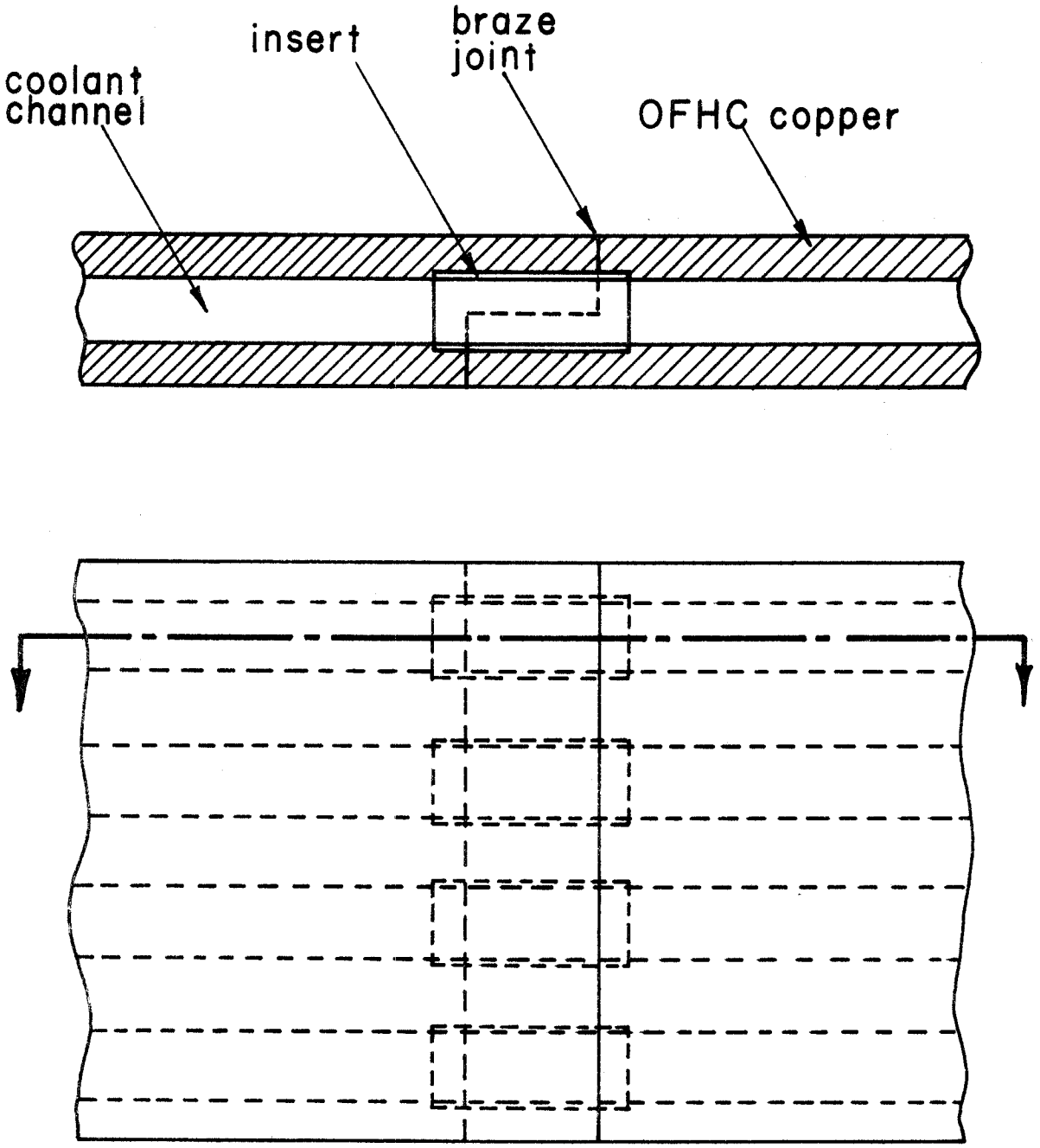

FIGURE V-C-3
TYPICAL BRAZED JOINT IN A VF COIL

Table V-C-2

Physical Characteristics of VF Coils

Coil	Coordinates Z(m)	Coordinates R(m)	Current I(MA)	Conductor Type	Number of Turns	Conductor Length (m)	Mass of Cu (kg)	Water Flow (liters/min)
D-1	0.00	2.00	-0.1650	I	6	75.40	1152.6	220
D-2	0.30	2.00	-0.1650	I	6	"	"	"
D-3	0.50	2.00	-0.055	I	2	25.13	384.2	74
D-4	1.00	2.10	+0.132	II	4	52.78	1008.8	177
D-5	1.40	2.10	-0.110	II	4	"	"	123
D-6	2.30	1.70	-0.132	II	4	42.72	816.5	144
D-7	3.20	2.80	+0.066	II	2	35.19	672.5	119
D-8	3.60	2.80	+0.066	II	2	"	"	119
D-9	1.85	2.80	+0.186	II	6	105.56	2017.6	339
D-10	2.10	2.80	+0.477	III	8	140.74	4303.3	967
D-11	2.20	2.80	"	III	8	"	"	"
D-12	2.30	2.80	"	III	8	"	"	"
D-13	2.40	2.80	"	III	8	"	"	"
D-14	2.50	2.80	"	III	8	"	"	"
D-15	2.50	2.60	"	III	8	"	"	"
D-16	2.70	2.80	+0.239	II	8	"	2690.2	392
D-17	2.5	3.80	+0.473	III	10	238.7	7300	1033
D-18	2.3	3.70	+0.462	III	10	232.5	7108.1	960
D-19	2.1	3.70	-0.440	III	10	"	"	870
D-20	2.1	3.50	-0.220	II	8	175.93	3362.7	411
D-21	2.1	3.90	-0.330	II	10	245.04	4683.7	825
D-22	2.1	4.30	-0.275	II	10	270.17	5164.2	632
D-23	1.1	4.80	-0.297	II	10	301.6	5764.6	822
D-24	0.9	4.80	-0.330	II	12	361.9	8069.9	845
D-25	0.0	4.65	-0.385	II	14	409	10163.0	956

Table V-C-3

Electrical Characteristics of VF Coils

Coil	Conductor Current (kA)	Coil Resistance (OHMS x 10^{-3})	Power Loss (MW)	Current Density (kA/cm^2)
D-1	27.5	0.8439	0.638	1608
D-2	27.5	"	"	"
D-3	27.5	0.2813	0.213	"
D-4	33.0	0.4725	0.514	1543
D-5	27.5	"	0.357	1286
D-6	33.0	0.3824	0.416	1543
D-7	"	0.3150	0.343	"
D-8	"	"	"	"
D-9	31.00	0.945	0.908	1450
D-10	59.63	0.7877	2.800	1743
D-11	"	"	"	"
D-12	"	"	"	"
D-13	"	"	"	"
D-14	"	"	"	"
D-15	"	"	"	"
D-16	29.87	1.260	1.124	1397
D-17	47.3	1.336	2.989	1383
D-18	46.2	1.301	2.777	1350
D-19	44	"	2.519	1286
D-20	27.5	1.575	1.191	"
D-21	33	2.194	2.389	1543
D-22	27.5	2.419	1.829	1286
D-23	29.7	2.700	2.381	1389
D-24	27.5	3.240	2.450	1286
D-25	27.5	3.662	2.769	"

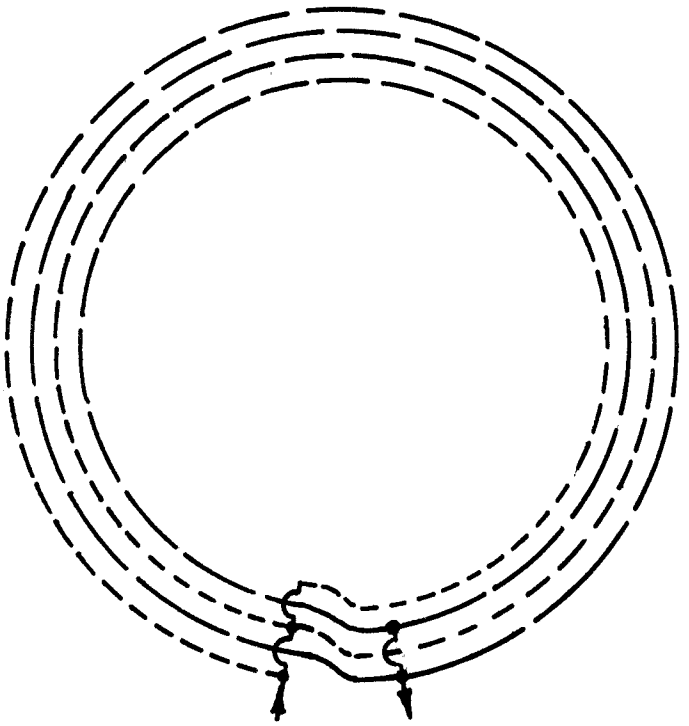

_____ inlet at 30°C

_____ outlet at 70°C

Figure V-C-4

SCHEMATIC REPRESENTATION OF WATER COOLING CONNECTIONS IN A VF COIL

V-C-3. Structural Consideration

The average and maximum values of the vertical and radial field components and the consequent forces on the VF coils are listed in Table V-C-4. Two design criteria are the maximum allowable stress to produce failure in 4.2×10^6 cycles of operation in TETR (15 years, 60% duty factor) and the creep rate produced by the average stress. The allowable stress range for 4.2×10^6 cycles of reversed flexure for 10% cold worked OFHC copper is $\pm 124 \times 10^6 N/m^2$ ($\pm 18{,}000$ psi).[1] Stress reversal occurs in two VF coils, D-17 and D-18, which unfortunately are the highest stressed coils in the VF system. These two coils experience a maximum compressive force of $11 \times 10^6 N$ and a maximum tensile force of about $7.5 \times 10^6 N$. If unreinforced, the stress range would be 447×10^6 N/m^2 (65,000 psi) with about 2/3 in compression and 1/3 in tension. The stresses are calculated on the basis of thick-walled pressure vessel theory. In order to reduce the cyclic stresses in D-17 and D-18, an effective thickness of 30 cm of stainless steel structure is used in the coil forms at the inner and outer radii. The resulting cyclic stress is -130×10^6 N/m^2 (18,900 psi) compressive and $+117.6 \times 10^6$ N/m^2 (17,000 psi) tensile.

The limiting stress to produce a creep rate of 0.01% in 1000 h in 10% cold worked OFHC copper at 70°C is 117×10^6 N/m^2 (17,000 psi).[1] The average compressive stress in D-17, which has the highest average stress, would be 62×10^6 N/m^2 (9000 psi) if unreinforced. Of the unreinforced coils, the highest average compressive stress is 81×10^6 N/m^2 (11,800 psi) in coil D-20. All other coils have lower stresses.

Joints will not have the full strength of 10% cold worked OFHC due to high temperature joining procedures. Induction brazing with low frequency

Table V-C-4

Magnetic Fields and Forces in VF Coils

	B_r(tesla)		B_z(tesla)		F_r(10^6N/m)		Hoop Force(10^6N)		ΣF_z(10^6N)	
	Avg.	Max.	Avg.	Max.	Avg.	Max.	Avg.	Max.	Avg.	Max.
D-1	3.9×10^{-10}	4.284×10^{-4} -0.043	-2.589×10^{-1}	-0.341	0.04013	0.05286	0.1035	0.1290	-7.5×10^{-10}	-0.0838
D-2	0.148	0.187	-0.302	-0.343	0.04681	0.05286	0.1169	0.130	-0.251	-0.377
D-3	0.347	0.394	-0.292	-0.317	0.01606	0.01744	0.0355	0.0382	-0.251	-0.274
D-4	0.163	0.170	-0.285	-0.292	-0.03762	-0.03854	-0.0967	-0.0986	0.283	0.296
D-5	2.75×10^{-2}	0.059	-0.354	-0.721	0.04673	0.09512	0.0964	0.1787	-0.0389	-0.083
D-6	0.220	0.255	-0.416	-0.452	0.04576	0.04972	0.1084	0.1667	-0.3193	-0.370
D-7	-0.595	-0.681	0.176	0.234	0.0162	0.01544	0.0374	0.0481	-0.691	-0.791
D-8	-0.341	-0.379	0.117	0.143	0.00772	0.00944	0.0265	0.0313	-0.396	0.441
D-9	1.242	1.518	0.329	0.642	0.0602	0.1175	0.7032	0.3636	3.999	4.887
D-10	1.801	2.932	0.380	1.846 -1.279	0.1813	0.8805 -0.6101	-0.7192	2.678 -1.920	15.11	24.60
D-11	0.995	2.843	0.359	2.239 -1.569	0.1712	1.068	0.6916	3.203	8.35	23.86
D-12	0.558	6.216 -4.394	0.306	5.980 -5.421	0.1460	1.414	0.6208	4.172	4.683	-36.87
D-13	-0.617	1.619 -2.001	0.325	2.319 -1.663	0.155	1.106	0.6462	3.309	-1.40	13.59 -16.79
D-14	-0.758	0.869 -2.605	0.311	2.255 -1.631	0.1483	1.076	0.6275	3.224	-6.361	7.292 -21.86
D-15	-1.504	-3.358	0.305	2.038 -1.439	0.1455	0.9722	0.6195	2.934	-12.62	-28.2
D-16	-2.602	-6.458	2.60×10^{-1}	2.555 -2.66	0.0621	0.6106	0.2313	1.767	-10.94	-27.15
D-17	-0.144	5.214 -5.471	1.037	6.377 -4.213	-0.4791	-2.946 1.946	-1.984	-10.69 7.413	1.547	58.76 -56.00
D-18	-0.025	5.247 -5.369	1.099	6.519 -4.168	-0.5097	-3.012 1.926	-1.668	-10.93 7.336	-11.8	-56.36 57.67
D-19	0.854	1.491	0.396	0.850	-0.1873	-0.4021	-0.4978	-1.314	-9.645	-16.84
D-20	-0.257	-0.610	2.073	2.323	-0.4561	-0.5111	-1.545	-1.738	1.243	2.951
D-21	-0.404	-0.739	-.1299	-0.329 0.106	0.0428	0.1086	0.2808	0.537	3.529	5.979
D-22	0.039	-0.145	-.172	-0.247	0.0473	0.06793	0.2838	0.3724	0.290	1.077
D-23	0.271	0.427	0.1639	0.436 -0.086	-0.0487	-0.1295	-0.138	-0.5259	-2.427	-3.825
D-24	0.061	0.117	0.231	0.317	-0.0762	-0.1046	-0.2478	-0.384	-0.607	-2.299
D-25	2.66×10^{-10}	0.026 -0.026	0.403	0.492	-0.1693	-0.2066	-0.5968	-0.771	-3.3×10^{-9}	-3.190 3.190

RF is selected since it is a very rapid process with small heat effected zones. A more advanced design of the VF coil system should also take into account stress concentration and reinforcement at cooling connections.

References for Section V-C

1. "Technical Survey OFHC Brand Copper," The American Metal Company Ltd.

V-D. Ohmic Heating Coils

V-D-1. General Considerations

Ohmic heating coils for TETR are non-superconducting normal metal coils in accordance with a mid-1980 operation schedule. It is unlikely that large pulsed superconducting coil technology will be available by then. The three main design options are conventional water-cooled copper or aluminum, liquid nitrogen cooled cryogenic coils, and liquid helium cooled cryogenic coils. The major design factors are power consumption, space availability and compatibility with the superconducting toroidal field coils.

Most of the OH coils are in the central core close to the TF coils. If the OH coils are not at 4.2 K then thermal insulation must be provided between the TF and OH coils. If the central support structure is not at 4.2 K then the insulation around the TF coils must withstand a large radial inward force and still provide thermal isolation.

Water cooled coils are large since the relatively high electrical resistivity corresponds to relatively low current densities. The consequent large cross-sectional area of the coils leads to space limitation problems. The need for thermal insulation between the OH and TF coils is an added complication. Liquid nitrogen cooled cryogenic coils have higher current densities but also need separate dewars and insulation. The power saved at 77 K is about equal to the power required to manufacture the liquid nitrogen. The saving in space does not seem to justify the use of 77 K coils.

The last option is the use of cryogenic coils at liquid helium temperature, either with copper or aluminum conductors. OFHC copper at 4.2 K may be assumed to have a resistivity of 1×10^{-8} Ω cm and in a

magnetic field obeys the empirical equation $\rho \approx 10^{-8}$ (1 + B/2) Ω cm, where B is in tesla. If we assume for the sake of comparison a time average magnetic field of 2T, then the resistivity of OFHC copper would be $\rho \approx 2 \times 10^{-8}$ Ω cm. High purity aluminum on the other hand which has been strained many cycles from zero to 0.1% strain in an elastic structure has a resistivity of less than 1.7×10^{-9} Ω cm.[1] Since the maximum strain in our designed conductor is only .029%, with small localized areas strained to .07%, it can be expected that the resistivity will be less than 1.7×10^{-9} Ω cm. We have taken $\rho \approx 1.5 \times 10^{-9}$ ohm cm, which is equivalent to a RRR (residual resistance ratio) of 1600. The magneto-resistance of aluminum at 2T is an additional 2.16×10^{-9} Ω cm[2]. The total resistivity is $\rho \approx 3.7 \times 10^{-9}$ Ω cm which is about one fifth that of OFHC copper.

High purity aluminum has a very low yield strength. Zone purified ultra-high purity aluminum with RRR > 5000 has a yield strength of about 6.9×10^{6} N/m^2 (1000 psi) at 4.2 K. The aluminum foil with RRR = 1370 used in a magnet built by Purcell and Payne[3] had a yield strength of 2.07×10^{7} N/m^2 (3000 psi) at room temperature. The yield strength is $1.73 - 2.07 \times 10^{7}$ N/m^2 (2500 - 3000 psi) at 4.2 K for 2000 RRR high purity aluminum.

The maximum stress in the highly loaded T-1 coils is 2.76×10^{7} N/m^2 (4000 psi) in small localized areas of the first few innermost turns where the magnetic pressure is the highest. The conductor will be degraded to a RRR $\approx$ 1600 in these localized areas only. Since resistivity ρ(B=0) = 1.5×10^{-9} Ω cm (RRR = 1600) is used for the conductor throughout the OH coil system, it is felt that the design is fairly conservative. A value of $\rho = 3.7 \times 10^{-9}$ Ω cm at 2T time average field is used to calculate I^2R heating in the OH coil system.

V-D-2. Coil Description

The primary consideration in designing a conductor with high purity aluminum is to ensure that the operating stresses and the consequent cyclic strains are low. Because of the low yield strength, the conductor must be encapsulated to present aluminum extrusion or creep. Figure V-D-1, which shows the cross section of coil T-14, is representative of all OH coils. The conductor consists of a stainless steel casing which encloses the five strips of high purity aluminum on three sides. The ribs of the casing are tapered to confine the conductor during field reversal.

The high purity aluminum conductor is 1.3 cm wide by 5.7 cm high for a cross-sectional area of 7.41 cm^2. Each conductor is divided into five strips to suppress eddy currents in the radial direction due to the rapid one second changes in the B_z field. An oxide layer on the conductor should be sufficient to prevent large eddy current loops. All five strips of the conductor are bonded together and insulated from the casing with 1 mm thick fiber glass epoxy insulation. The conductor is then rolled into the casing and the ribs swaged in a single step before curing the epoxy. The stainless steel casing is 6.5 cm by 1.8 cm with a 0.2 cm thick web. The ribs which are 0.3 cm thick at the base increasing to 0.4 cm are notched over 20% of the contact surface. The notches provide space for liquid helium entry and for vapor exit from the interstices of a coil. The coil pancakes are separated by 0.5 cm thick micarta spacers covering 50% of the contact area. Overall there is a 25% void fraction for helium within the coil cavity.

Ohmic heat from the conductor is transferred to the liquid helium bath through the uncovered surface. The maximum heat flux at the peak of the pulse is < 0.1 watts/cm^2 which is a very conservative operational choice. The conductor is sized to carry a maximum current of 32 kA which is a current

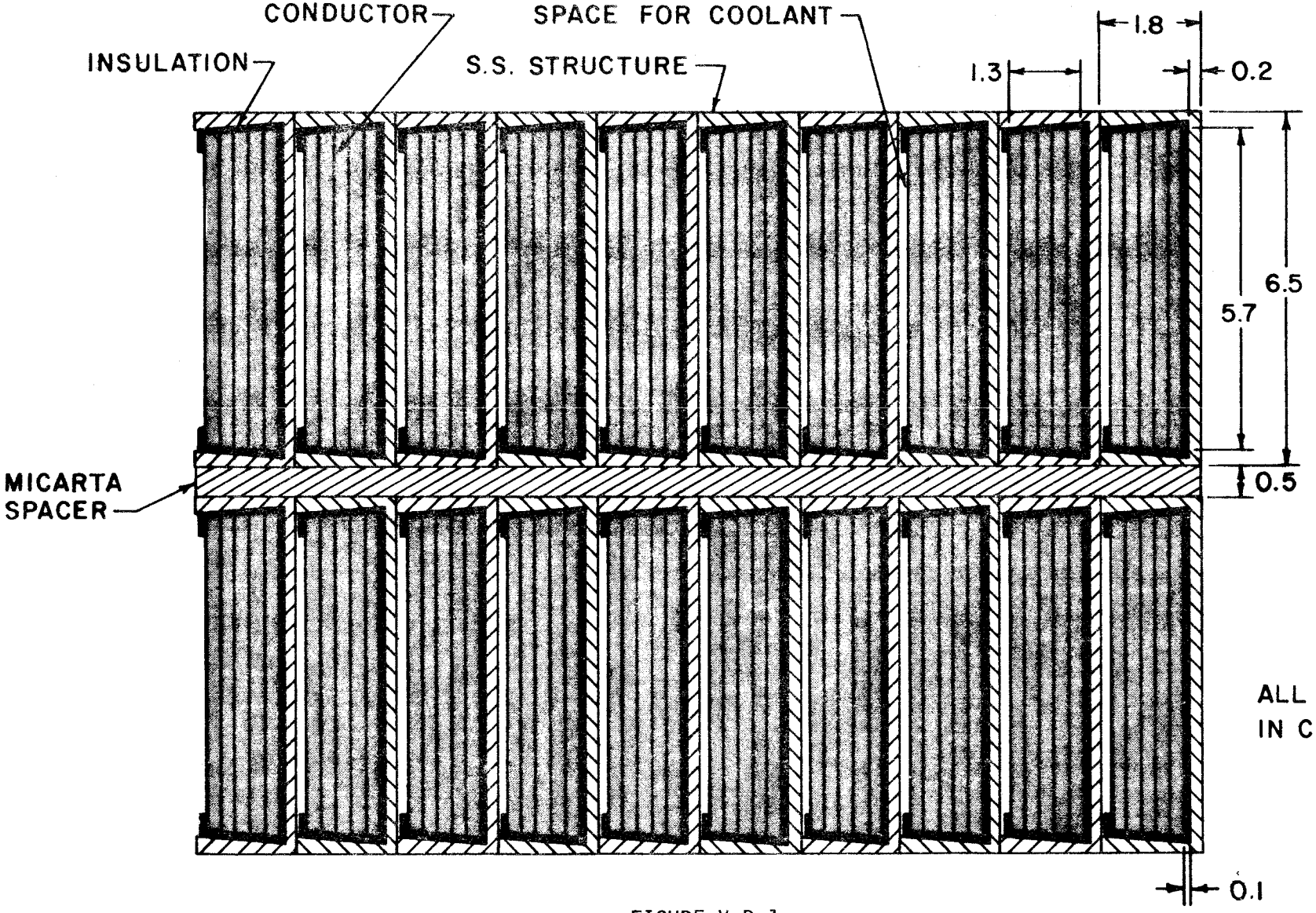

FIGURE V-D-1

Cross Section of OH Coil

density of 4250 A/cm^2. The same conductor is used in all the OH coils, with the largest coil having 100 turns and the smallest, 14 turns. The major physical characteristics of the OH coil system are listed in Table V-D-1.

D-3. Stress Analysis of OH Coils

Twenty of the 32 OH coils are completely contained within the central support structure. The centering radial force produced by the TF coils on the central support structure exceeds the maximum radial outward force on the central support structure exerted by the OH coils. These forces essentially cancel each other. Radial strain in the OH conductors is due to the compression of the ribs, which transmit the pressure on the conductors back to the central support structure.

Using T-1, the largest OH coil as an example, we calculate this effect. The average radial load plus the self load on T-1 at the peak of the pulse is 9.96×10^6 N/m seen in Table V-D-2. Divided among five pancakes with 20 turns each, the force on the last conductor in each pancake is 1.992×10^6 N/m. Such load produces a compressive stress of 3.32×10^8 n/m^2 (48,153 psi) at the base of the rib (3 mm thickness) and essentially the same value at the contact point (4 mm thickness) since 25% of the material is removed for helium passageways. This high stress in the ribs is of no concern since 10% cold worked 316 SS has a yield strength of $> 6.2 \times 10^8$ N/m^2 (90,000 psi) at 4.2 K. The compressive stress is highest in the outermost turn and goes to zero in the innermost. The integrated accumulated radial strain over the 36 cm of coil width is 0.025 cm which implies that there is a .029% strain and 2×10^7 N/m^2 (2900 psi) stress in the innermost conductor. The critical buckling load for the casing ribs is substantially higher than the existing load.

Table V-D-1

Physical Characteristics of OH Coils

	Coordinates R(m)	Z(m)	Max. Current (MA)	No. of Pancakes	No. of Turns	Max. Current in Cond. (kA)	Max. Current Density (kA/cm^2)	Mass of Structure (Kg)	Mass of Conductor (Kg)
T-1	0.85	0.25	3.000	5	100	30.00	4.048	1022.8	1069.2
T-2	0.85	0.75	2.98	5	100	29.80	4.021	1022.8	1069.2
T-3	0.86	1.25	2.93	5	100	29.30	3.954	1034.4	1081.2
T-4	0.87	1.75	2.86	5	100	28.60	3.860	1047.8	1095.2
T-5	0.89	2.25	2.75	5	95	28.947	3.907	1017.2	1063.3
T-6	0.91	2.75	2.61	5	90	29.00	3.914	986.1	1030.7
T-7	0.95	3.25	2.42	7	77	31.429	4.241	880.5	920.4
T-8	1.00	3.75	2.18	7	70	31.142	4.203	842.0	880.2
T-9	1.08	4.24	1.90	5	65	29.230	3.945	844.1	882.4
T-10	1.18	4.73	1.59	4	52	30.577	4.126	763.9	771.5
T-11	1.31	5.21	1.29	4	44	29.318	3.957	2106.4	725.0
T-12	1.46	5.69	1.02	3	33	31.212	4.212	1760.2	605.9
T-13	1.65	6.15	0.68	2	22	30.909	4.171	1325.8	456.3
T-14	1.85	6.60	0.62	2	20	31.000	4.184	1351.8	465.3
T-15	2.07	7.06	0.49	2	16	30.625	4.133	1209.9	416.4
T-16	2.31	7.50	0.39	2	14	27.857	3.759	1181.6	406.7

Table V-D-2

Magnetic Field & Forces in OH Coils

	Average Field Br (tesla)	Bz (tesla)	Max. Field Br (tesla)	Bz (tesla)	Self Field (tesla)	Vertical Forces (Fz) Avg. (10^6N/m)	Max. (10^6N/m)	Radial Force (Fr) Avg. (10^6N/m)	Max. (10^6N/m)	Self Force (10^6N/m)
T-1	0.032	2.34	1.436 -1.363	4.247	3.006	0.095	4.31 -4.09	7.02	12.74	2.94
T-2	0.796	2.30	1.494 -1.300	4.209	2.980	0.237	4.45 -3.87	6.85	12.54	2.90
T-3	0.103	2.17	1.515 -1.253	4.041	2.930	0.302	4.44 -3.67	6.30	11.84	2.78
T-4	0.133	2.07	1.507 -1.202	3.807	2.860	0.380	4.31 -5.18	5.92	10.90	2.63
T-5	0.124	1.93	1.483 -1.114	3.584	2.750	0.341	4.08 -3.06	5.31	9.86	2.40
T-6	0.145	1.877	1.847 -1.421	3.345	3.070	0.379	5.08 -3.91	4.90	8.73	2.25
T-7	0.158	1.741	1.758 -1.280	2.840	3.030	0.383	4.26 -3.10	4.21	6.87	1.92
T-8	0.194	1.655	1.780 -1.214	2.886	2.290	0.423	3.88 -2.65	3.61	6.29	1.42
T-9	-0.009	0.020	-0.129	-0.061	2.240	0.019	-0.247	-0.04	-0.12	1.06
T-10	0.411	1.428	1.284 -0.331	2.171	2.270	0.653	2.042 -0.53	2.27	3.45	0.74
T-11	0.342	0.943	0.945 -0.079	1.555	2.150	0.40	1.22 -0.10	1.22	2.01	0.47
T-12	0.408	0.759	0.884	1.192	1.850	0.42	0.90	0.77	1.22	0.28
T-13	0.369	0.563	0.713	0.863	1.510	0.25	0.48	0.38	0.59	0.12
T-14	0.408	0.380	0.650	0.501	1.380	0.25	0.40	0.24	0.31	0.09
T-15	0.398	0.202	0.589	0.316	1.230	0.19	0.29	0.10	0.16	0.05
T-16	0.407	0.202	0.589	0.316	0.980	0.16	0.23	0.08	0.12	0.03

Another source of stress on the conductor comes from the bending associated with the conductor support structure. Again, the innermost turns are subjected to the highest loading, which in T-1 is 2.75×10^6 N/m^2 (400 psi). This loading is the sum of the force exerted on the turns by other coils and the self-force. Since all the components of the conductor are epoxied together as described previously, the conductor resists the bending as a monolithic plate. If the ends are assumed to be simply supported, the maximum stress is in the center of the face of the conductor and is about 2.9×10^7 N/m^2 (4210 psi). If the ends are assumed fixed, however, the maximum stress is at the edge and is about 1.9×10^7 N/m^2 (2860 psi). Since the ribs carry the full pressure of the conductor, the ends will probably be semi-fixed and the maximum stress will have some intermediate value.

The high bending stresses affect small local areas of the conductor in the innermost turns. Local yielding occurs in these areas and could decrease the electrical conductivity somewhat although the overall effect on the whole coil is small.

Ohmic heating coils numbered T-11 through T-16 are not contained within the central support structure and will, therefore, need additional reinforcing against radial and vertical forces. The average radial and self force in T-11 for example, is 1.69×10^6 N/m. If equal volumes of structure and conductor are provided then the maximum stress in the conductor will be $< 1.69 \times 10^7$ N/m^2 (2500 psi) and in the stainless steel $< 5.17 \times 10^7$ N/m^2 (7500 psi). Since the same conductor is used for all the OH coils, those that need additional structure (T-11 to T-16) have the balance of the stainless steel distributed around three sides as shown in Fig. V-D-2. T-11 has a coil form 3.5 cm thick and the others will have progressively thinner coil forms, depending on the forces acting on them.

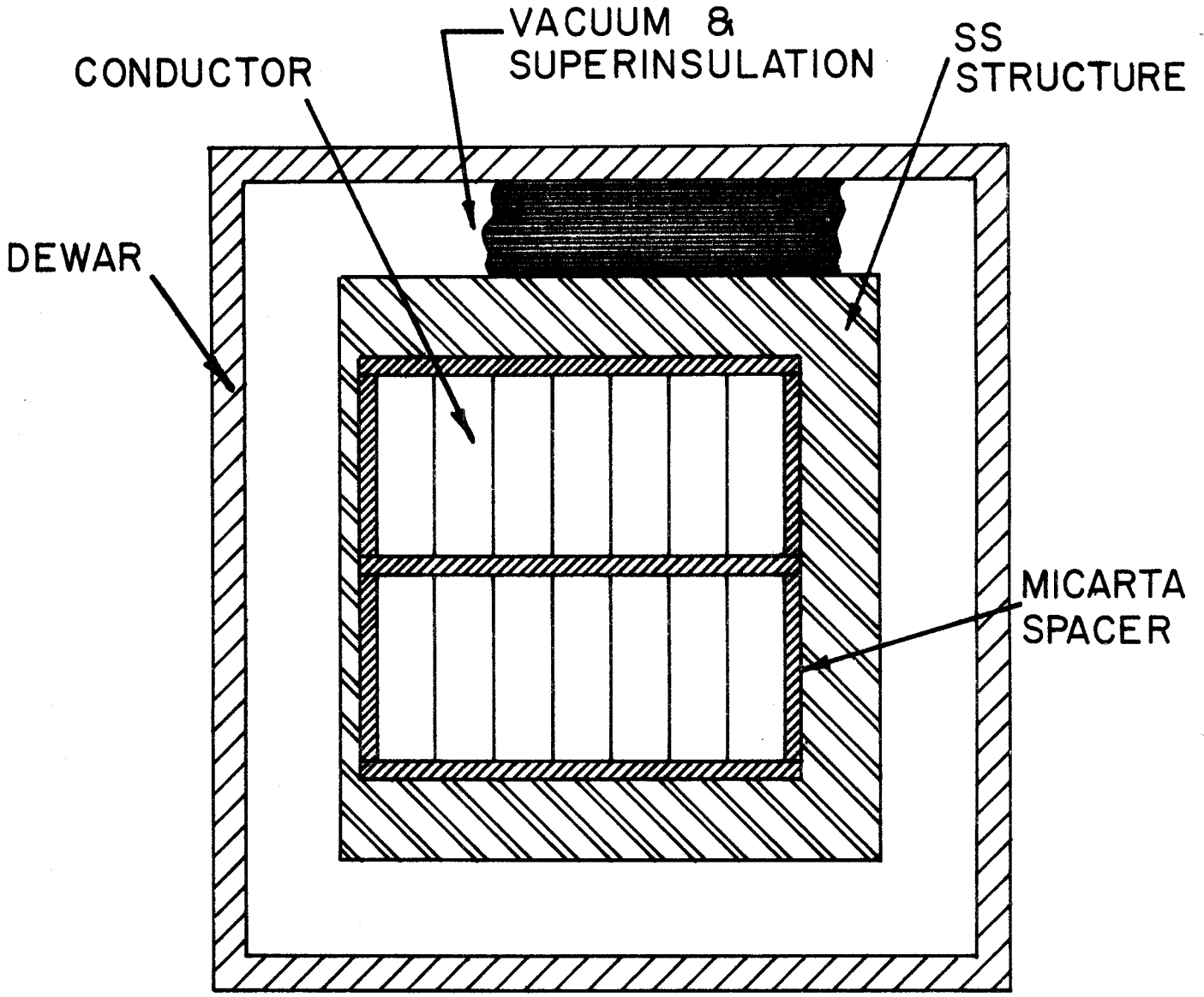

FIGURE V-D-2

Cross Section of OH Coil with External Structure

The maximum bending stresses in T-11 are 2% of those in T-1 because of smaller magnetic pressure. The maximum combined bending and tensile stress is 2.2×10^7 N/m^2 (3200 psi) in localized volumes on the innermost turns. Stresses in the remaining OH coils (T-12 to T-16) are progressively lower.

D-4. Cryogenic Considerations

The OH coils are cooled by pool boiling in liquid helium at 4.2 K. One side of the conductor is open for cooling and the maximum heat flux at the peak of the pulse is < 0.1 watts/cm^2.

The temperature drop through four epoxy interfaces is estimated to be no greater than 4 K which means that the part of the conductor farthest from the cooling surface may reach 9-10 K. This, however, does not affect the resistivity of the high purity aluminum, since the resistivity curve is flat to around 15 K.[4]

A 25% void fraction in T-1 provides an inventory of 130 liters of helium. Energy generated during a single cycle of current shut-down, recock, and rapid discharge cycle will boil off about 60 liters in 13.5 seconds. The vapor return lines are sized to handle this rapid vapor discharge and the liquid supply lines must be capable of keeping the coil cavity full of liquid at all times.

The OH coils which are contained within the central support structure do not need any insulation but each will have its own liquid helium container. The cavity within which the coil is housed can be sealed off to act as the containment for the coolant. Supply and return lines are mounted in the central support structure. Coils not enclosed within the central support structure need both liquid helium containment and a vacuum super-insulated space.

The vacuum space is 4 cm thick and filled with superinsulation. The outer vacuum dewar is reinforced aluminum alloy. Fiberglass-epoxy struts are used to transmit forces across the vacuum space.

The total radiant load from the twelve external OH coils and the central support structure is estimated at 20 watts. Conduction losses through the fiberglass epoxy struts and the base of the central support structure are about 1138 watts. These values are insignificant compared to the I^2R losses which are in excess of 80 KW as shown in the next section.

V-D-5. Losses

V-D-5-a. I^2R Losses

In Table V-D-3 are listed values of time average current, resistance and power loss in each of the OH coils. A resistivity of 3.7×10^{-9} Ω cm and a cross-sectional area of 7.41 cm^2 is assumed. The total time average power loss for all the coils is 82.65 kw.

V-D-5-b. AC Loss

As stated earlier the OH coils are cryogenic normal coils. The limited space in the central core requires high current density. AC losses due to rapid pulsing, as high as 8T/sec, might irreversibly quench a superconducting coil. For B parallel to the surface of a conductor of thickness t, the loss per unit surface area in the resistance limit is approximately

$$P = \frac{1}{3} \omega^2 \frac{1}{\rho} t^3 B_o^2 \quad \text{for } t << \delta = \text{skin depth}$$

ω is the angular frequency, ρ the resistivity and B_o the peak field. In the inductive limit the loss is

$$P = \frac{\rho}{\mu_o^2 \delta} B_o^2 \quad \text{for } t >> \delta.$$

Table V-D-3

Time Average Current & Power Dissipated in OH Coils

	Time Avg. Coil Current (MA)	Time Avg. Cond. Current (kA)	Conductor Length (m)	Coil Resistance ($\times 10^{-5}$ ohms)	I^2R Power Dissipated (kW)
T-1	1.114	11.14	534	2.6664	3.309
T-2	1.105	11.05	534	2.6664	3.254
T-3	1.092	10.92	540	2.6962	3.215
T-4	1.072	10.72	547	2.7300	3.138
T-5	1.035	10.89	531	2.6507	3.143
T-6	0.988	10.98	515	2.5714	3.100
T-7	0.917	11.91	460	2.2966	3.257
T-8	0.823	11.75	440	2.1969	3.032
T-9	0.695	10.68	440	2.1969	2.505
T-10	0.599	11.53	385	1.9213	2.555
T-11	0.528	12.00	362	1.8064	2.603
T-12	0.399	12.10	302	1.5078	2.210
T-13	0.265	12.05	228	1.1384	1.652
T-14	0.241	12.05	232	1.1583	1.682
T-15	0.190	11.88	208	1.0385	1.464
T-16	0.153	10.91	203	1.0136	1.205

The conductor is laminated vertically since the pulsed field is primarily a vertical field. The loss due to the vertical component is treated as in the resistance limit and the radial component loss is treated as in the inductive limit. The total time averaged ac loss in the OH coil system is estimated to be about 12 kW.

V-D-5-c. Thermal Radiation Losses

The surface area of the external OH coils and of the room temperature part of the central support structure is about 190 m^2. Assuming a 10 $\mu W/cm^2$ radiation loss rate, the total load amounts to 19 watts.

V-D-5-d. Conductive Losses

There is 1500 cm^2 of 4 cm long fiberglass epoxy struts conducting heat between 300 K and 4.2 K across the vacuum space. Assuming a conductivity of 5.74 mW/cmK, the heat load is 637 W. Another conductive loss occurs between the base of the central support structure and the helium region. Assume the case is grounded to a 77 K thermal sink 1 meter below the lowest liquid helium point. The area is 4.55 m^2 and the average thermal conductivity for 316 SS between 4.2 K and 77 K is 1.5 W/mK. The heat load is 500 W.

V-D-5-e. Resistive Losses in Power Leads

The highest time average current in the OH coil conductor is 12 kA. For a well designed vapor cooled lead, a loss of 5 mW/A may be used. The thirty-two pairs of leads with a total current of 768 kA have a total loss of 3840 W.

V-D-5-f. Nuclear Heating

The nuclear heating in the OH coils is so small compared to the I^2R losses that it will be completely neglected.

V-D-5-g. Total Losses

The total losses for the whole OH system are estimated to be 100 kW.

References for Section V-D

1. H. R. Segal and T. G. Richards, "Low Temperature Resistance Studies on Cyclically Strained Aluminum," Proceedings of the 1st International Cryogenic Materials Conference, July 22-25, 1975, Vol. 22, p. 486.

2. R. J. Corruccini, "The Electrical Properties of Aluminum for Cryogenic Electromagnets," Technical Note 218, August 30, 1964, National Bureau of Standards, Boulder, Colorado.

3. J. R. Purcell and E. G. Payne, Rev. Sci. Inst. 34 893 (1963).

4. Handbook on Materials for Superconducting Machinery - MCIC-HB-04-NBS, Boulder, Co. and Battelle Columbus Labs.

V-E. Refrigeration Requirements

The total refrigeration required for TETR is about 114.5 kW. This is primarily due to the enormous losses which exist in the cryogenic OH coils. The following is an estimate of the losses.

V-E-1. TF Coils

V-E-1-a. AC Losses

As discussed in Section V-B-6, the AC losses in the TF coils are 9.2 KW.

V-E-1-b. Radiation Losses

If we assume a radiant energy transfer of 5×10^{-5} $\mu W/cm^2$ through the superinsulation, then the total energy loss for the 16 magnets is 490 W.

V-E-1-c. Thermal Conductive Losses

As mentioned previously, 10% of the fiberglass epoxy struts make permanent contact between the inner and outer dewar walls and will be a source of conductive heat. If we assume a conductivity of 1700 mW cm/cm^2 between 300 K and 4.2 K, the total amount of heat conducted to the cold surface is 1630 W.

V-E-1-d. Resistive Losses at Conductor Joint

At the joints, the 1.4 cm wide conductors are made to overlap for 20 cm and are clamped tightly together. Assuming a 0.5 cm path length, the normal path resistance is $0.018 \times 10^{-8}\Omega$. In addition, a $10^{-8}\Omega$ contact resistance is expected. The total joint resistive power loss is 250 W.

V-E-1-e. Lead Losses

A properly designed vapor cooled current lead has a loss of 5 mW/A. The total lead losses are 1574 W.

V-E-2. Ohmic Heating Coil

As discussed in Section V-D-5, the total heat loss in the OH coil system is 100 kW.

V-E-3. Cryosorption Pump Requirements

As discussed in Section III-F-3, the power required to operate the pumps is 34 kW at 4.2 K.

V-F. Power Requirements

V-F-1. TF Coils

The total stored energy in the TF coils, obtained by integrating the energy density $B^2/2\mu_o$ over the volume of the toroid is found to be 6.3 x 10^9 joules (1.75 MWh). The self inductance L of the toroidal system is 130 henries. Assuming a 24 hour charging time, the voltage rating of the power supply is 15 volts. An ac/dc bridge rated at 147.6 kW is required for the TF coil power supply.

V-F-2. OH and VF Coils

The charge, discharge and power cycle curves for TETR are shown in Fig. V-F-1 and V-F-2. During the initial 1 sec startup period, the VF coils are charged while the OH coils are discharged. The maximum total stored energy in the poloidal system is 128 kW. Unlike UWMAK-I, II and III, the stored energy in the VF coils is small compared to the OH coils, and consequently a large amount of instantaneous power, 890 MW, is released from the poloidal field coils which could be sent back to the power grid. The maximum power required is 370 MW at the end of reset. Since it has been assumed that a maximum of 500 MW can be purchased directly from the electric utilities, a single 370 MW ac/dc bridge is needed. The time average resistive loss in the OH coil system is 82.7 kW and the peak value is 600 kW. The time average resistive loss in the VF coils is 63 MW while the maximum is 84 MW during the burn period.

The total amount of power required by the cryogeneration for both the magnet and the vacuum system is 118 kW at 4.2 K, or about 35.4 MW at 300 K. If we add to this all the other power requirements, then the total for TETR is about 410 MW at room temperature.

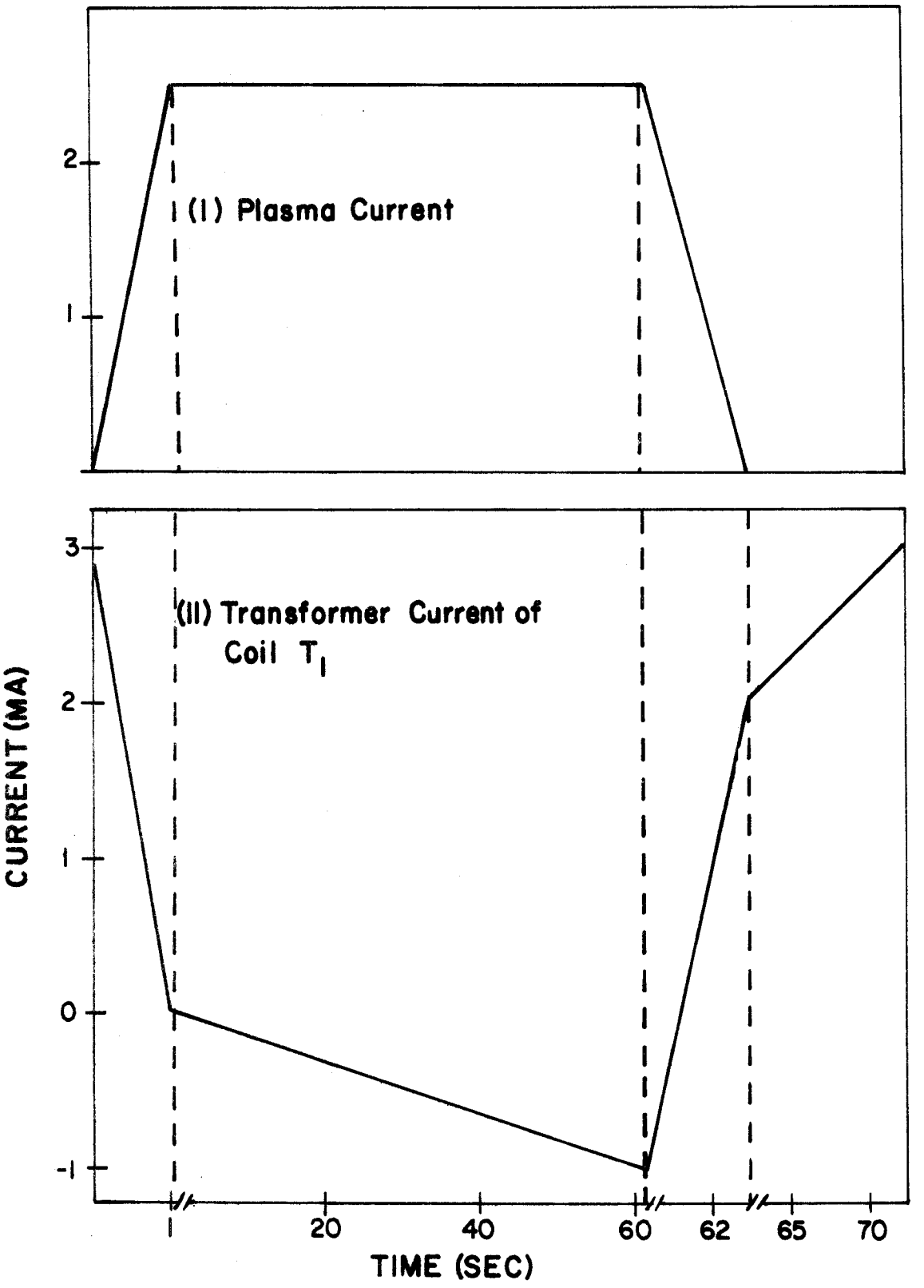

Figure II-F-1

Time Variation of Plasma Current and Representative Transformer Coil Current

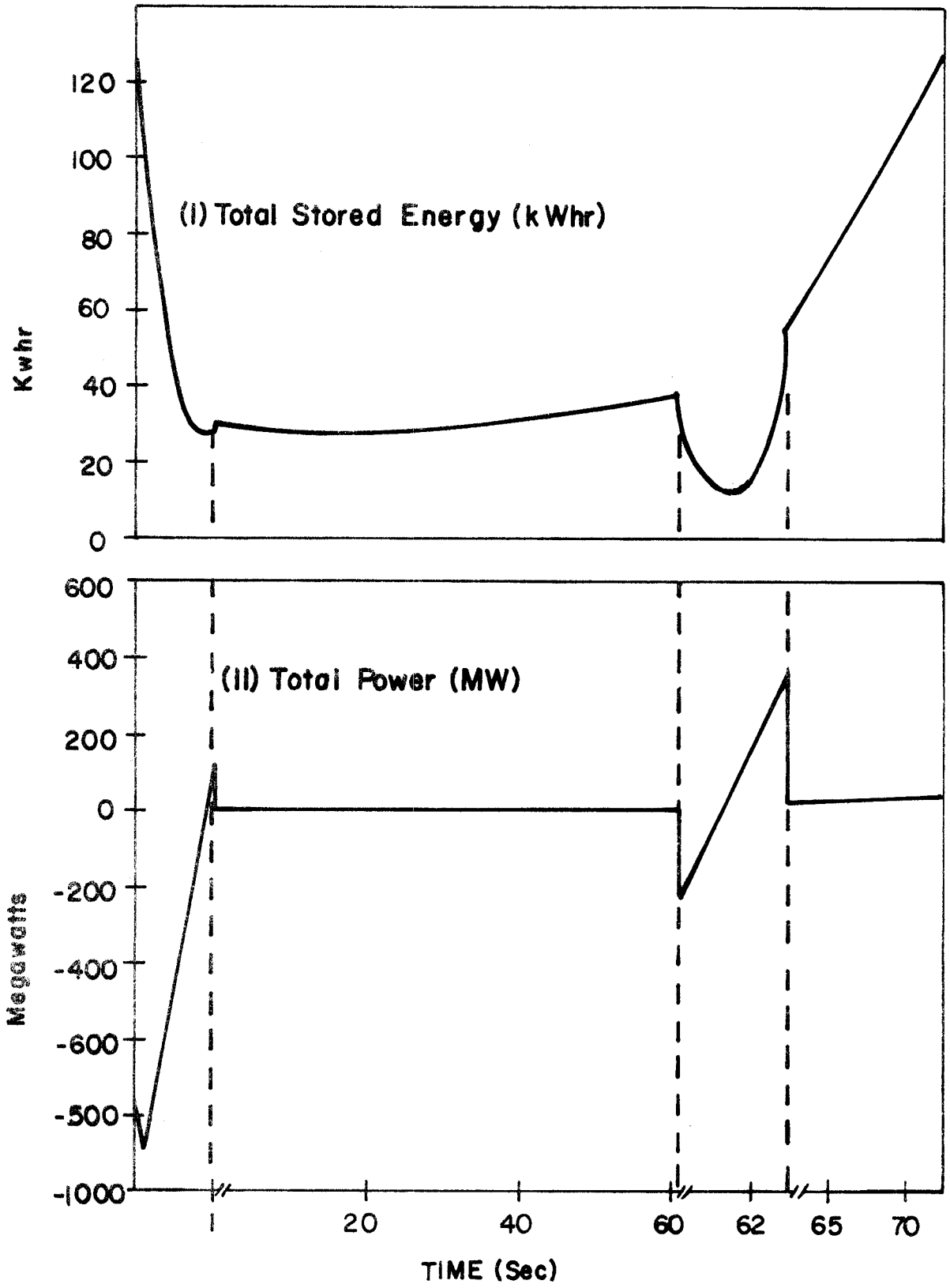
(i) Total Stored Energy (kWhr)
Kwhr
120
100
80
60
40
20
0
(ii) Total Power (MW)
Megawatts
600
400
200
0
-200
-400
-600
-500
-1000
1
20
40
60
62
65
70
TIME (Sec)

FIGURE V-F-2

VI. Blanket and Shield Design

VI-A. Introduction

TETR will not have an energy conversion system nor will it contain breeding material (except in the test stations) and therefore, in the strict sense of the word, it will not have a blanket. Instead, it will have a water cooled first wall which will be the primary vacuum barrier. With the exception of the test zone, the first wall will be immediately followed by the shield.

As an aid in identification, the first wall and shield will be divided into three zones. The area inside the inner divertor slots will be referred to as the inner zone, that between the inner and outer divertor slots as the central zone and that beyond the outer divertor slots as the outer zone.

Like the later UWMAK designs, TETR is equipped with a graphite liner which radiates energy to the cooled first wall. The liner is attached to the first wall with stainless steel studs.

The first wall itself consists of a bank of squashed stainless steel tubes attached to a heavier stainless steel sheet. The entire assembly is then covered with a thin corrugated stainless steel sheet which conforms to the shape of the tubes. This type of first wall covers all the chamber areas exposed to the plasma, including the divertor slots and part of the neutral beam tubes. It is supported on the shield structure by means of a mechanically actuated latch system. This provision makes the first wall capable of supporting an atmosphere of pressure and can therefore be used as the primary vacuum barrier.

The shield for TETR will be entirely supported on the floor foundation of the primary containment building. It will be constructed from a combination of

stainless steel box beams filled with shielding material and heavy ribs oriented radially to provide maximum rigidity. Cooling tubes within the shield will extract the large amount of nuclear heating generated in it.

The shield in the central region is needed to protect the large null driving vertical field coil. A capability of moving these shields into the divertor zone will make the divertor slots accessible for servicing. Access into the divertor zone for servicing particle collection plates and cryopumps will be provided through hatches in the shield between the TF magnets. These hatches will be equipped with mechanical seals at the back of the shield for quick opening and closing.

VI-B. General Description and Specifications

Since all the surface wall heating in TETR will be extracted by the first wall coolant, it is imperative that all the surfaces exposed to radiant energy from the graphite liner be adequately cooled. To accomplish this, approximately 300 m^2 of water cooled first wall has to be provided.

The geometry of a Tokamak plasma chamber would be very difficult to cover with a bank of constant diameter tubes running in the poloidal direction. A 30% variation in the tube diameter is needed in order to provide coverage with the same number of tubes from the narrowest circumferential distance at the outer divertor slot to the widest, at midplane. If the tubes are squashed to varying degrees, this 30% variation can be handily accomodated. Figure VI-B-1 is a full scale cross section of the first wall showing the tube shapes at the narrowest and the widest circumferences in the plasma chamber.

The tubes selected have an initial outer diameter of 1.2 cm and a wall thickness of 0.1 cm. The width of the squashed tubes varies from 1.3 cm to 1.7 cm.

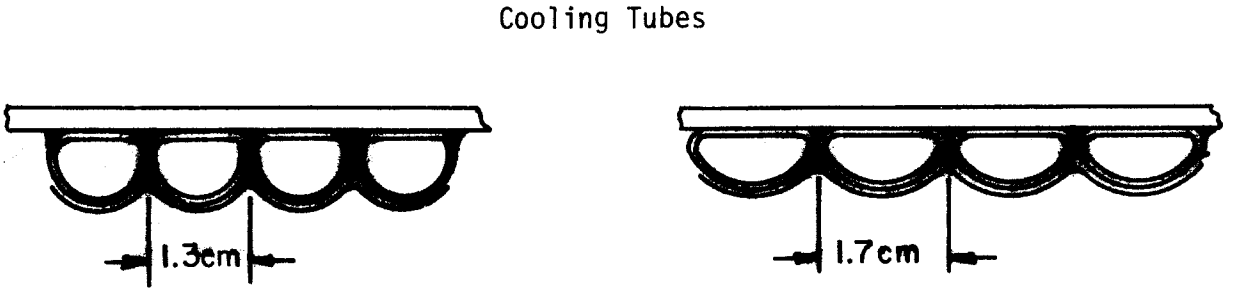

Fig. VI-B-1 Cross Section of First Wall Showing Variation in Tube Width

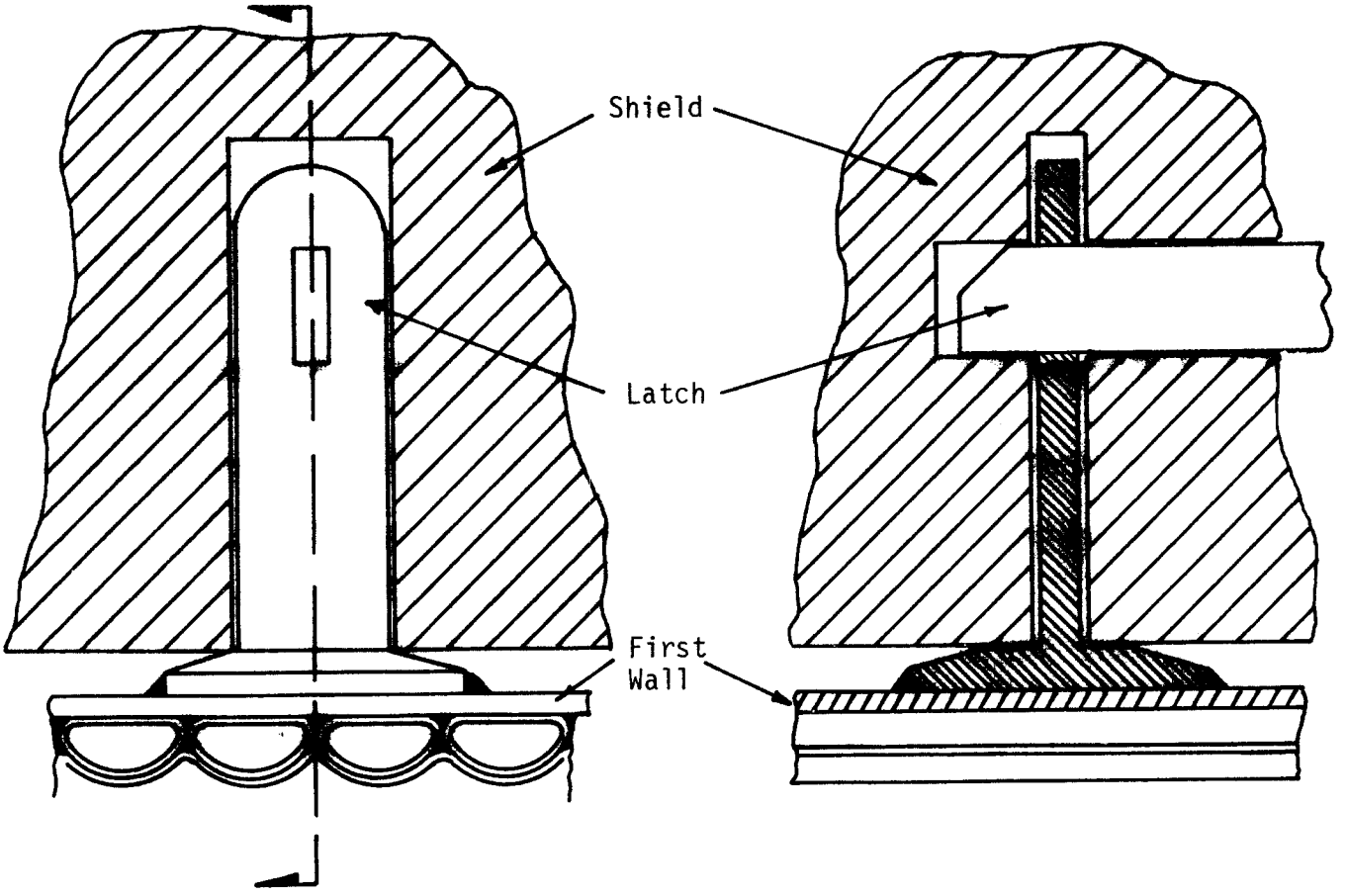

Fig. VI-B-2 Mechanical Latch System for Supporting the First Wall

A 0.4 cm thick sheet of stainless steel is used as the back up plate for the tubes. Electron beam welding will be used to attach the tubes to the back up plate. To provide additional stiffness in the direction parallel to the tubes and also a measure of redundancy against front wall leaks, a corrugated sheet of stainless steel, 0.1 cm thick,is electron beam welded to them as shown in Fig. VI-B-1. Obviously, this sheet has to be shaped to conform closely to the tubes and will vary from one location within the chamber to another.

Stainless steel pads with rectangular rods are welded to the back of the 0.4 cm sheet in a square matrix spaced 20 cm apart. These rods are used to engage with latches which support the first wall on the shield. A mechanical actuator will be used to engage the latches into the rods and anchor the first wall to the shield. Figure VI-B-2 shows how that is done.

Manifolds for cooling water will run in the toroidal direction. Figure VI-B-3 shows a set of adjacent water manifolds as well as the weld joint between sections of the first wall. These welds are made on the inside of the chamber.

The top half of the outer zone will contain the main test stations, of which there will be 16, one between each TF coil. Here the shield is made to swing open on hinges thus making the test station accessible. Before this can be done, the two VF coils which surround the outer shield just above mid-plane have to be lifted up. The first wall sections in front of the test stations are made to be taken out from the outside. Figure VI-B-4 shows toroidal and poloidal sections of a test station with the first wall attached to it. Note that the weld joint is made on the outside of the chamber. This feature provides ready access to the chamber interior for inspection or servicing.

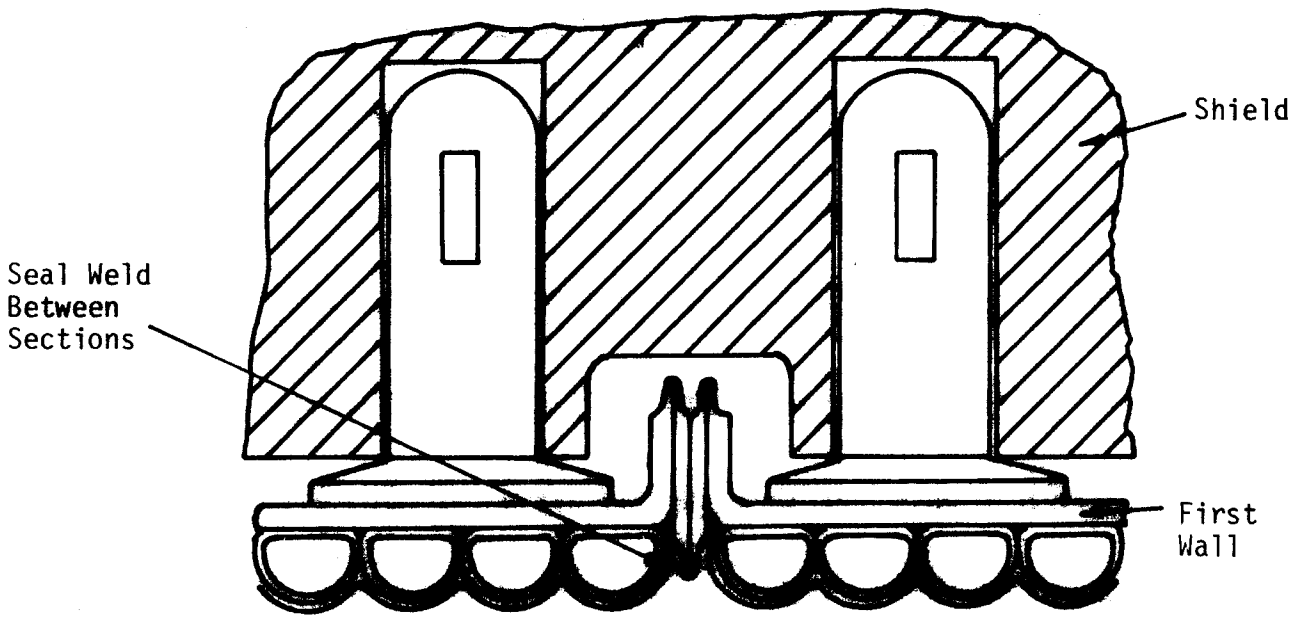

Poloidal View of a Joint Between First Wall Sections

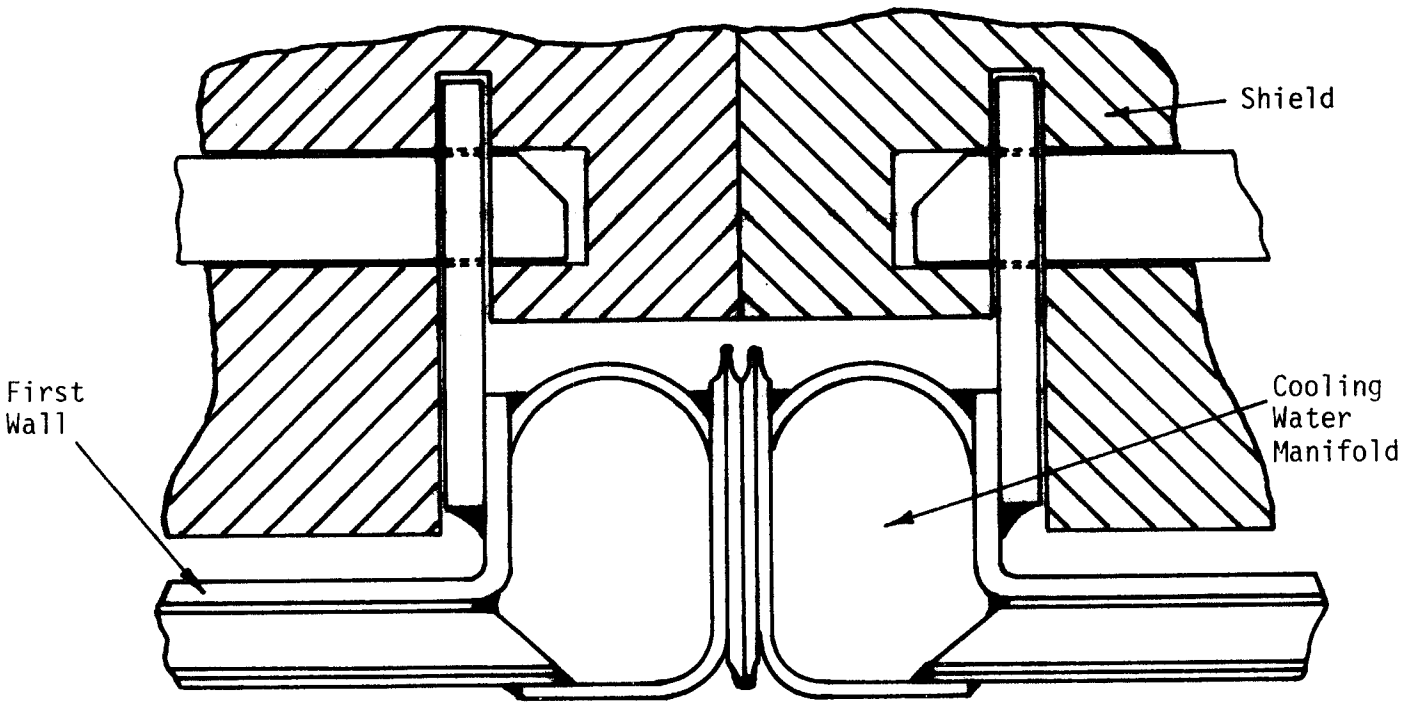

Toroidal View of a Joint Between First Wall Sections Showing
Cooling Water Manifolds

Figure VI-B-3

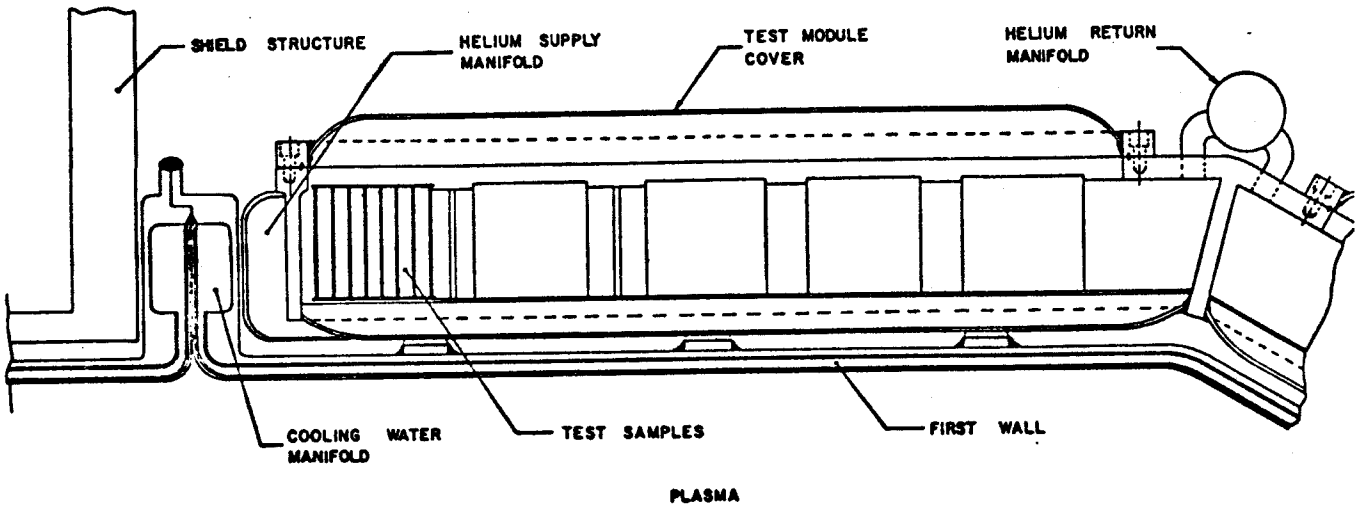

Toroidal View

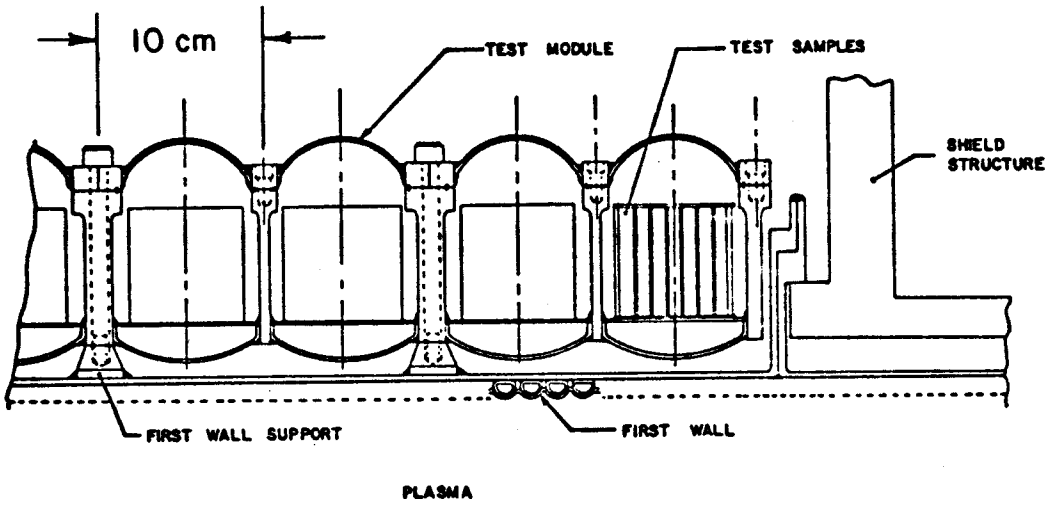

Poloidal View

Figure VI-B-4 Toroidal and Polidal Cross Sections of a Typical Test Module

For the inner zone, manifolds near the top of the divertor slot will supply cooling water to tubes which will run all the way down to the bottom divertor slot where the return manifolds will be located. In this zone, the connections between the manifolds and the supply lines will be made in place by brazing with resistance heaters since this region is not accessible from the back. Seals between adjacent sections will be made with welds on the inside of the chamber.

Sections of the first wall in the central zone will be made U-shaped to slip over the central shield. Seals between these sections need not be provided because they are contained within the vacuum chamber. Connections between the manifolds and the coolant supply and return lines are made in the same way as discussed above.

The woven graphite liner is attached to the first wall at the same locations as the rods which hold the first wall to the shield, but at greater intervals. The intervals between supports can be every 60 cm, or at every third rod. A specially shaped post is welded to the first wall as shown in Fig. VI-B-5 and the liner is then fixed to it by means of a graphite nut which fits over the post. This nut is designed to be attached to the post with a single 90% twist. A spacer is used to ensure that the liner is properly spaced from the first wall.

The outer shield is designed with a combination of box beams and ribs oriented in the radial direction. The box beams which are filled with shielding material are used to surround the plasma chamber circumferentially along the outer divertor slot. They provide the hoop strength needed to counteract the bending due to the shield overhang and the compressive forces due to the atmospheric loading on the chamber. Heavy radial ribs running in

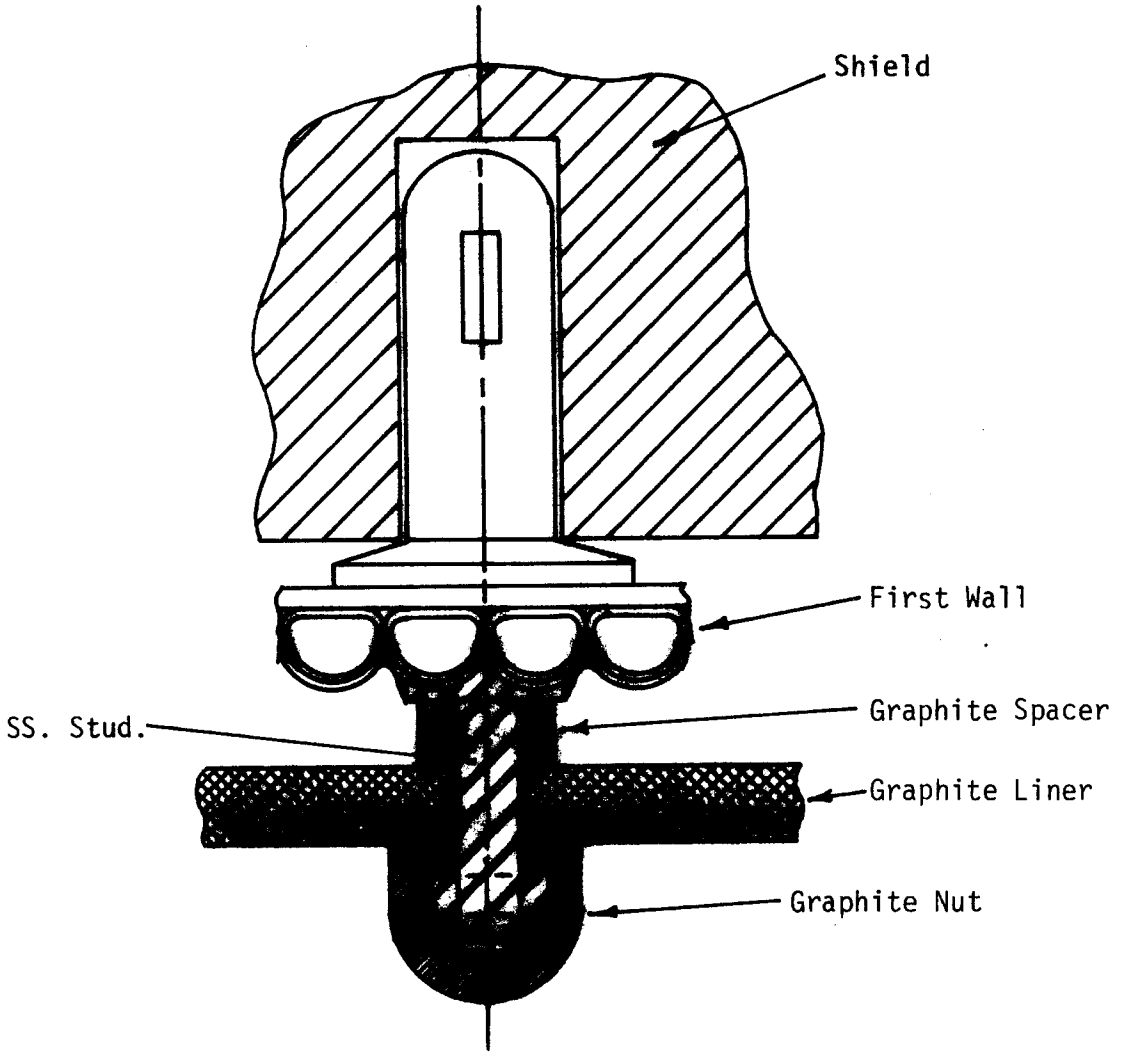

Fig. VI-B-5 Cross Section Showing the Method for Attaching Graphite Liner to the First Wall

the poloidal direction join the box beams together and provide the stiffness needed to make the shield self supporting. They are welded to plates which make up the inner boundary of the shield and which contains the needed penetrations.

The shield construction in the neutral beam ports area will have to depart from the usual. Here the neutral beam ports merge together almost slicing the chamber in half. Reinforced frames will be used to surround the neutral beam ducts. The radial shield structure will terminate in the top plate of the frame and continue again from the bottom plate. Structure will be needed between the neutral beam ducts to transfer the loads from the top half of the shield to the bottom half.

The central and the inner shields will be constructed in much the same way as the outer shield. Since there are no penetrations here, it will be simpler. Part of the structure in the central shield will be used to restrain it against the hoop forces which will be induced in it.

Most of the vertical field coils are essentially contained within the shield and are continuous. The shield itself, however, can be made in sections which are bolted together. This provides the flexibility of being able to dismantle it when the need arises.

Table VI-B-1 gives the specifications for the first wall and shield.

VI-C. First Wall Stresses

In order to be able to analyze the first wall stresses, an assumption has to be made that it behaves as a monolithic plate. This, of course, implies that all the parts of the first wall are sufficiently attached together to be able to transmit reactions and loads as if they were one piece.

Table VI-B-1

First Wall and Shield Specifications

Total surface area covered by first wall	300 m^2
Initial outer diameter of cooling tube	1.2 cm
Thickness of cooling tube wall	0.1 cm
Thickness of back-up sheet	0.4 cm
Thickness of front corrugated sheet	0.1 cm
Spacing between tubes:	
Maximum	1.7 cm
Minimum	1.3 cm
Maximum pressure in tubes	3.43×10^6 Pa (500 psi)
Maximum stress in first wall	
Spacing between first wall supports	20 cm
Spacing between graphite liner supports	60 cm
Thickness of graphite liner	1 cm
Weight of stainless steel in first wall	18.5 MT
Weight of graphite liner	3.4 MT
Maximum operating temperature of first wall	300°C
Maximum operating temperature of graphite liner	1100°C
Total weight of shield (including VF coils)	9081 MT
Mass of stainless steel in shield	792 MT
Mass of H_2O in shield	25 MT
Mass of W in shield	3310 MT
Mass of B_4C in shield	237 MT
Mass of Pb in shield	4560 MT
Mass of Cu in VF coils	157 MT

Although a brazed structure can be assumed to behave as a monolithic plate, a question remains as to whether such a condition can be achieved in a structure assembled with multiple pass electron beam welding.

The stresses in the first wall can be divided into four categories:

1. Thermal stresses
2. Pressure stresses
3. Mechanical support stresses
4. Cyclic stresses.

Each category will be discussed separately and the cumulative effect will be tabulated at the end of this section.

Thermal Stresses

Thermal stresses will exist in a plate as long as there is a temperature gradient in it and its boundary conditions impose a restraint on it. In the case of the first wall, since active cooling occurs within the tubes only, a temperature gradient will exist across the surface facing the graphite liner as well as the surface facing the shield. These gradients will produce thermal stresses in the first wall.

When steady state conditions are reached, the surface wall heating on the first wall is estimated at 3.4 W/cm^2 and the nuclear heating in it at 30 W/cm^3. The first wall surface facing the graphite liner will have both surface and nuclear heating while the surface facing the shield will have only nuclear heating.

The thermal stress in a plate which has a temperature gradient ΔT in it is given as

$$\sigma_{th} = \pm \frac{\alpha}{2} \frac{E}{(1-\nu)} \Delta T$$

where α is the coefficient of expansion, ν is Poisson's ratio and E the modulus of elasticity. The temperature gradient across a plate with both surface and bulk heating is expressed as

$$\Delta T = \frac{1}{k} \left(W_s + \frac{W_n t}{2}\right) t$$

where k is the thermal conductivity, W_s the surface heating, W_n the bulk heating (nuclear in this case) and t the plate thickness. Combining the two equations together, we obtain

$$\sigma_{th} = \pm \frac{\alpha}{2} \frac{E}{k(1-\nu)} \left(W_s + \frac{W_n t}{2}\right) t \ .$$

The following values were used for 316 stainless steel at 300°C:

$\alpha = 17.62 \times 10^{-6}$ cm/cmK

k = 18.3 W/mK

$E = 176 \times 10^{9}$ N/m^2 (25.6×10^{6} psi)

$\nu = 0.283$

$W_s = 3.4$ W/cm^2

$W_n = 30$ W/cm^3

$t_1 = 0.2$ cm (wall thickness facing graphite liner)

$t_2 = 0.4$ cm (wall thickness facing graphite shield).

Values of thermal stresses obtained were:

For t_1 $\sigma_{th} = \pm 15.1 \times 10^6$ N/m^2 ($\pm$ 2200 psi)

t_2 $\sigma_{th} = \pm 28.4 \times 10^6$ N/m^2 ($\pm$ 4124 psi).

Negative values are compressive and correspond to the hot surface of the first wall, while the positive values are tensile and are for the cooled surfaces inside the tubes.

Pressure Stresses

The pressure of the coolant produces hoop stresses in the tubes and in the attached sheets. Its effect on the heavy back up plate is negligible and will be ignored.

Hoop stresses in a thin walled tube are given by

$$\sigma_h = \frac{pr}{t}$$

where p is the pressure, r the radius and t the wall thickness. Taking the maximum coolant pressure as 3.4×10^6 N/m^2 (500 psi), the radius of curvature for the 1.7 cm wide tube as 1.0 cm and the composite wall thickness facing the graphite liner as 0.2 cm, the hoop stress is

$$\sigma_h = 17 \times 10^6 \text{ N/m}^2 \text{ (2500 psi)} .$$

For the narrower tubes, the radius of curvature is smaller and the stress is proportionately smaller.

Mechanical Support Stresses

As described in the previous section, the first wall is supported on the shield by means of rods located on a square matrix 20 cm apart. The stresses

due to atmospheric loading on the first wall were calculated from equations derived for uniformly loaded plates supported by rows of equidistant columns.

If the dimensions of the plate are large in comparison with the distance between supports and the lateral load is uniformly distributed, it can be concluded that the bending in all the panels which are not close to the boundary of the plate may be assumed to be identical, so that we can limit the problem to the bending of one panel only.

Figure VI-C-1 shows the distribution of supports on the first wall and the deflection curve in a single panel loaded from one side. There are two places where the bending moments in the panel are going to be high, at the support and in the center of the panel.

The bending moment in the center of the panel is given by

$$M_o = \beta q b^2$$

where β is a coefficient which depends on the location of supports, q is the load and b the distance between supports.

In the case of the first wall where the support matrix is square, the value of $\beta = 0.0331$.[1] Distance between supports b = 20 cm and the atmospheric loading $q = 1.01 \times 10^5$ N/m^2. The moment in the center of a panel is,

$$M_o = 1.337 \times 10^2 \text{ Nm/m} .$$

The bending stress is expressed as

$$\sigma_b = \frac{6M}{t^2}$$

where t is the panel thickness. The minimum thickness of the first wall panel perpendicular to the tubes is 0.85 cm and occurs in the crease between tubes. The bending stress based on this thickness is $\sigma_b = 11.1 \times 10^6$ N/m^2 (1615 psi). Bending stresses occurring parallel to the tubes are based on a thickness of 1.2 cm and are equal to $\sigma_b = 5.55 \times 10^6$ N/m (807 psi).

Bending moments at the supports are somewhat higher and depend on the concentration of the load at the support. A 4 cm diameter pad is used as the transition between the first wall and the support rod. This tends to distribute the loading and produces a smaller bending moment. The bending moment at the support is given by

$$M_{sup} = \frac{qb^2}{4\pi} [(1 + \nu) \text{ Ln } \frac{b}{c} - (\alpha + \alpha\nu)]$$

where c is the radius of the support pad (c = 2 cm) and α is a coefficient similar to β, which for this case is $\alpha = 0.811$.[1] The bending moment calculated is

$$M_{sup} = 6.15 \times 10^2 \text{ Nm/m} .$$

Again the bending stress perpendicular to the tubes is $\sigma_b = 51.1 \times 10^6$ N/m^2 (7432 psi) and parallel to them $\sigma_b = 25.6 \times 10^6$ N/m^2 (3430 psi).

Cyclic Stresses

Between burn cycles when the plasma is down, there is no nuclear heating except for residual activity which is negligible, and the only stresses effected are the thermal.

The graphite liner which operates at around 1100°C has a fair amount of thermal inertia and during the 12.5 sec down time cools approximately 30°C. The surface of the first wall facing the graphite liner will continue to receive a surface wall heating at roughly the same rate, but there will be no nuclear heating. Thermal stresses in it will relax to $\sim \pm 8.03 \times 10^6$ N/m^2 ($\pm$ 1169 psi). The back up sheet facing the shield, however, has very little thermal inertia. As nuclear heating ceases, it will rapidly reach isothermal conditions and its thermal stresses will go to zero.

All the calculated stresses are tabulated in Table VI-C-1 for several locations in the first wall as shown in Fig. VI-C-2. Thermal stress variations and their effect on the total stresses are also shown.

The highest compressive (negative) stress occurs during burn and is at a support in the crease between tubes at the surface facing the graphite liner (point E on Fig. VI-C-2). The highest tensile (positive) stress, however, occurs during down time also at a support, and is on the surface facing the shield (point D or Fig. VI-C-2).

Maximum stress cycling between burn and down time is equal to 28.4 x 10^6 N/m^2 (4124 psi). It occurs in the back up sheet (at points C, D, c & d on Figure VI-C-2) both at a support and in the center of a panel. It is important to note that the only place where stress reversal occurs during a complete cycle is in the center of a panel on the inner tube surface which is against the

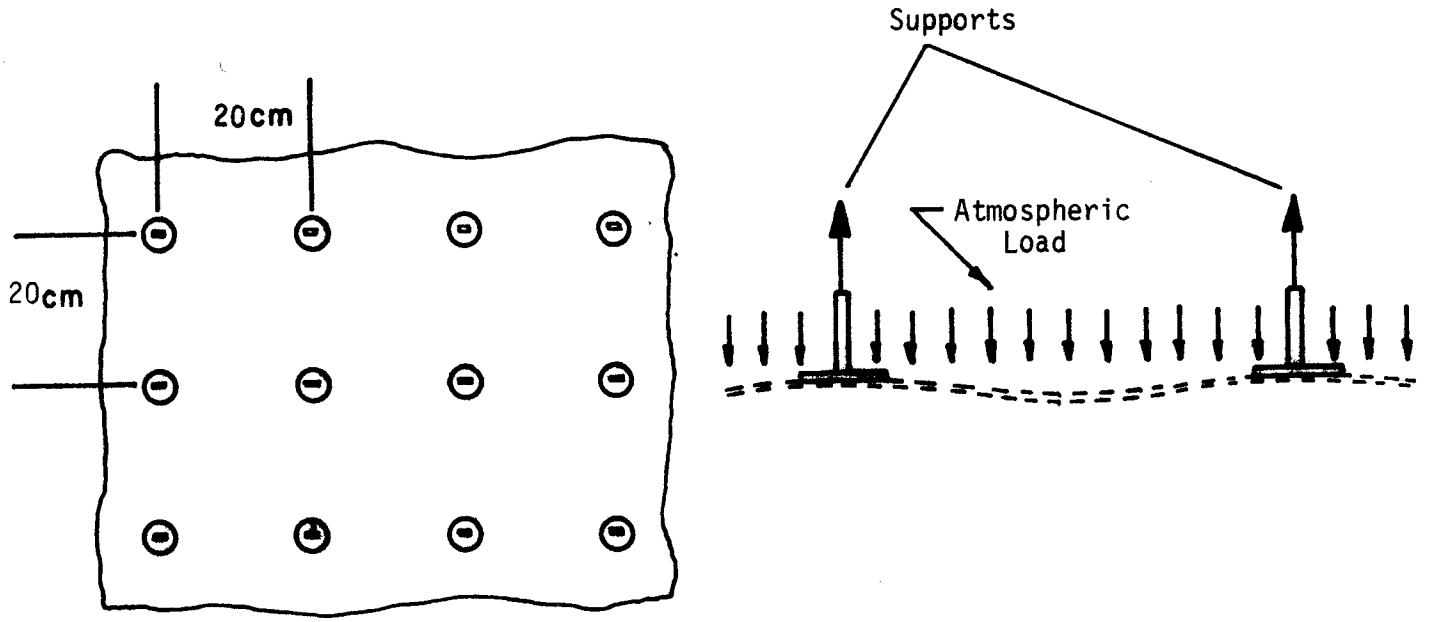

Fig. VI-C-1 First Wall Showing Support Matrix and Mode of Loading

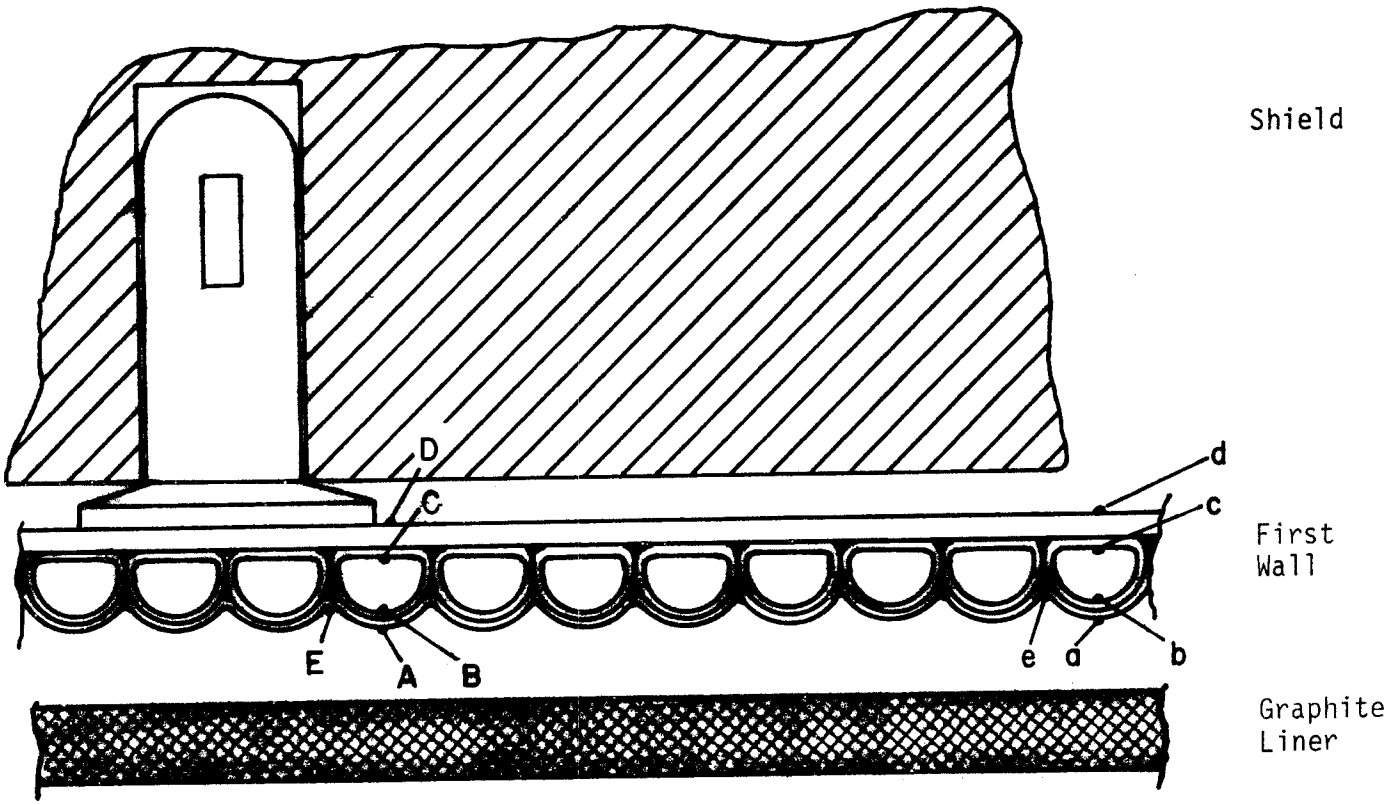

Fig. VI-C-2 Location on First Wall of Stresses Given in Table VI-C-1

Table VI-C-1

First Wall Stresses During a Complete Cycle[a]

Position[b]	Thermal σ (Burn)	Thermal σ (Down)	Atmospheric Pressure σ	Atmospheric Pressure σ	Total σ (Burn)	Total σ (Down)	Max. Δσ
A ($\times 10^6$ N/m^2)	-15.1	-8.03	-25.6	+17.2	-23.5	-16.5	7.09
(LBS/IN^2)	-2200	-1169	-3730	+2500	-3430	-2399	1031
B	+15.1	+8.03	-19.2	+17.2	+13.1	+6.00	7.09
	+2200	+1169	-2798	+2500	+1902	+871	1031
C	+28.4	0	+8.54	0	+36.9	+8.54	28.35
	+4124	0	+1243	0	+5367	+1243	4124
D	-28.4	0	+51.1	0	+22.7	+51.1	28.35
	-4124	0	+7432	0	+3308	+7432	4124
E	-15.1	-8.03	-51.1	+17.2	-49.0	-41.9	7.09
	-2200	-1169	-7432	+2500	-7132	-6101	1031
a	-15.1	-8.03	+5.55	+17.2	+7.61	+14.7	7.09
	-2200	-1169	+807	+2500	+1107	+2138	1031
b	+15.1	+8.03	+4.85	+17.2	+37.2	+30.1	7.09
	+2200	+1169	+706	+2500	+5406	+4375	1031
c	+28.4	0	-1.86	0	+26.5	-1.86	28.35
	+4124	0	-270	0	+3854	-270	4124
d	-28.4	0	-11.1	0	-39.4	-11.1	28.35
	-4124	0	-1615	0	-5739	-1615	4124
e	-15.1	-8.03	+11.1	+17.2	+13.2	+20.2	7.09
	-2200	-1169	+1615	+2500	+1915	+2946	1031

a) Compression is negative, tension positive
b) See Figure VI-C-2

heavy back up sheet (point c on Fig. VI-C-2). Here the stress reverses from a tensile condition during burn to a slightly compressive condition during down time. The maximum strain cycle is 0.016% based on a modulus of elasticity for 316 SS at 300^{o}C.

These favorable cyclic strain conditions in the first wall will prolong its useful life from the standpoint of the fatigue limit.

References for Section VI-C

1. Theory of Plates and Shells, "Timoshenko & Woinowsky Krieger, Second Edition McGraw-Hill, 1959.

VI-D. Disassembly and Maintenance

The need for easy accessibility to the test stations in TETR also facilitates accessibility for maintenance of the whole reactor blanket. Unfortunately, it was not possible to incorporate into the design of TETR a capability for quick removal of large segments of the blanket for servicing in a hot cell. However, small sections in all three zones of the blanket can be removed from inside the reactor with specially designed remote handling machines. These machines will have a large degree of accessibility through the test station apertures.

In order to gain access to the blanket region through a test station aperture, the following operations have to be performed:

1. VF coils Nos. 23 and 24 with their integral shield have to be raised as shown in Fig. VI-D-1.
2. The hinged shield behind the test station is swung open and secured.
3. Cooling supply and return lines are disconnected.
4. The peripheral weld which seals the first wall section immediately below the test module to the adjacent sections is machined off.
5. The test module is lifted out of the reactor with its first wall and graphite curtain sections attached to it.

Once access has been provided to the inside of the blanket, remotely controlled machines can be fitted to operate inside the toroid for in situ maintenance or for removal and replacement of first wall sections.

Visual inspection with optical instruments can be made through the bayonette test stations located on the lower half of the reactor. These

stations can be removed very quickly with a minimum amount of down time.

The first step in replacing first wall sections is to remove the graphite curtain. This is done by removing the graphite nuts which hold the curtain to the first wall and then lifting the curtain out. Simultaneously, the cooling connections have to be undone and removed. The next step is to machine off the peripheral welds and release the mechanical latch system described in Section VI-B. This will completely uncouple the first wall section from its supports on the shield. It can then be simply lifted out and removed from the toroid and a new replacement put in.

During periodic replacement, all the first wall sections from a whole quadrant or octant can be removed, new ones put in and attached with the mechanical latches and then all welded together in one operation. Finally, the cooling lines have to be reconnected and the graphite liner replaced and fixed to the first wall.

As mentioned in Section VI-A, provision is made to move the central shield section containing the null driving VF coil into the diverter zone. This will provide space for servicing the first wall sections in the diverter slots.

The procedure for closing the test station apertures is the reverse of that outlined earlier in this section.

Figure VI-D-1

CROSS SECTION VIEW OF TETR

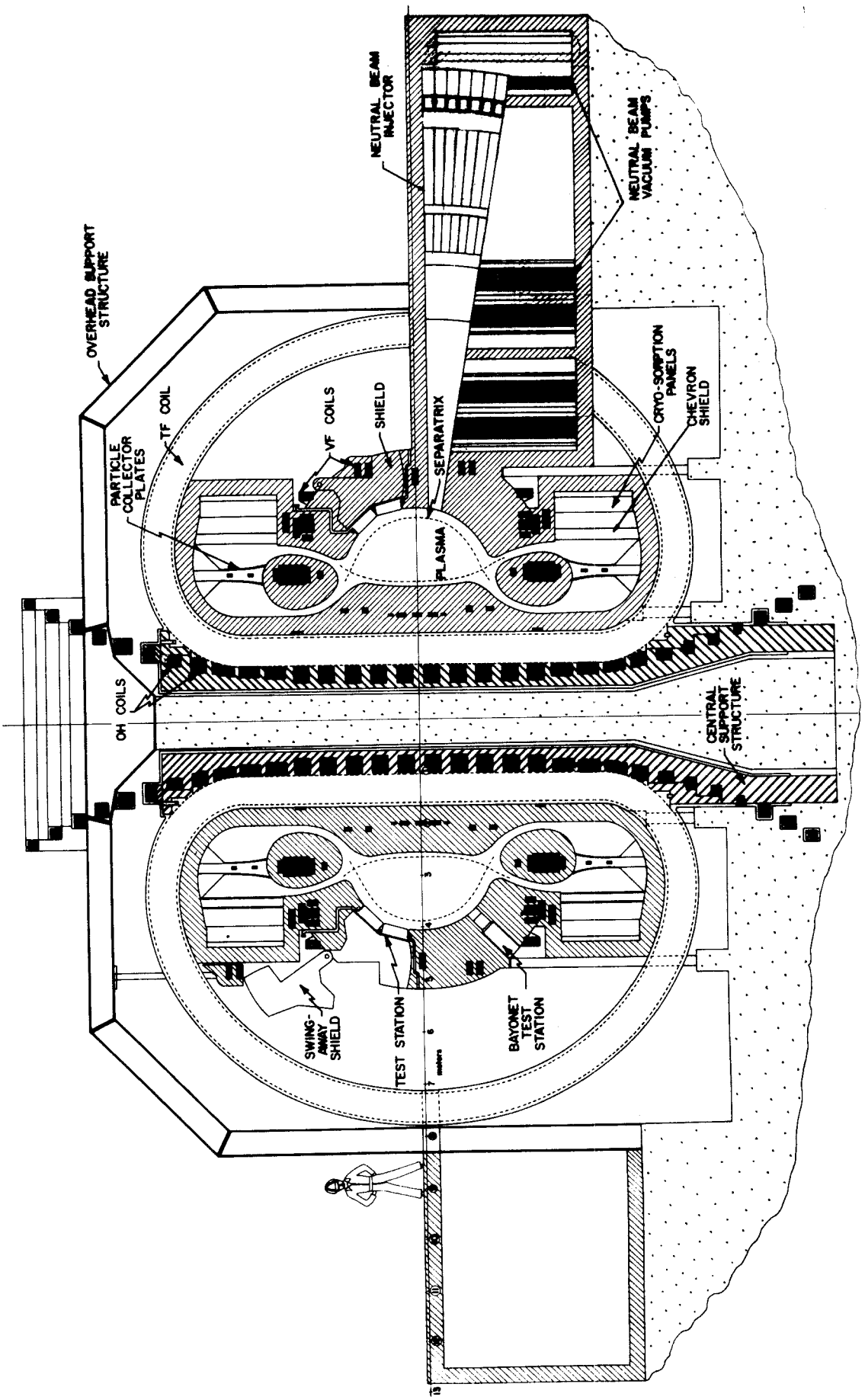

VII. Neutronics

VII-A. Introduction

The fundamental object of the TETR is to simulate a fusion power reactor environment for engineering materials and components testing. This is necessary to reduce the risk involved in the design and construction of a demonstration fusion reactor. Other simulations have been proposed which are generally less expensive. However, they either fail to provide a true simulation or provide test volumes falling short of those required for an adequate program. In addition, the operational experience with a large tokamak will be of great value in its own right.

Drawing on our previous studies of fusion reactors[1,2,3] and those of other groups[4] the simulation should employ a D-T fuel cycle, provide a temperature environment covering the approximate range from 300 to 1000°C, and a neutron flux corresponding to a first wall neutron wall loading of the order of one megawatt per square meter (design values range from about 0.5 to 5 MW/m^2) in order to obtain useful information on a reasonable time scale. The volume required is discussed in Chapter X, but a tokamak should give far greater test volumes than any other type of source. Further, the simulation is essentially exact and thus avoids the interpretations and extrapolations inherent in other test machines. The above discussion fixes the approximate wall loading. The questions raised of the neutronics part of the blanket and shield design are (1) will the reactor itself dominate the spectrum in sample regions, (2) does the reactor have to breed tritium, (3) can the temperature in the test regions be readily controlled and made independent of that of the first wall and other required reactor zones, (4) are there special shielding requirements?

The answer to the first can strongly affect the test volume available. The question of tritium breeding depends strongly on the availability and cost of tritium from other sources and on the tritium handling and containment problems posed. It was determined from discussions with ERDA contractors in the tritium area that it would be possible to obtain adequate supplies of tritium at an acceptable price. Since this eliminates one type of tritium handling problem and frees a great amount of high flux volume for experimental purposes, the decision was made not to require tritium breeding.

Preliminary neutronics calculations showed that in zones fairly close to the first wall, the spectra relax in a few centimeters in the transverse direction as one moves from a reactor region to a test region. Thus, the spectra seen by an experimental module is determined by the experimental module and not by the TETR itself. This will be discussed in detail in a later section of this chapter.

In a similar view, it is readily established that thermal isolation and control of test modules can be achieved and is a problem for the experiment designer, but should not influence the design of TETR. As no electrical power is to be generated it is unnecessary to operate the reactor at high temperatures. Thus, a low temperature water cooled wall is possible and this can be used to strongly influence the first wall life.

The remaining problems are dominated by shielding requirements, wall life questions, and activity production. The main toroidal magnets will be superconducting (NbTi); however, the near term (~1980) nature of the TETR makes the use of superconducting magnets in a time varying mode a poor risk. Thus, water cooled copper vertical field and transformer coils will be employed and size considerations will tend to push these coils toward the plasma creating special shielding problems. The timeframe also dictates a driven machine for which plasma physics extrapolations are as small as practicable. The relatively large beam requirements generate greater streaming problems in the radiation shields and shadow shields must be given attention.

In order to keep the duty factor high, the first wall should have a long life, ideally the life of the machine. Due to the time goals the design must rely primarily on current radiation performance data. This weights the decision toward stainless steel as the first wall material in spite of its mediocre performance from the activation point of view. Inspection of the radiation effects data for stainless steel indicate that operation of the first wall at around 250°C will allow the first wall life to approach that of the test facility itself, especially if operated at low pressure as well. This seems considerably more desirable than use of a ten centimeter carbon ISSEC which could also give the desired wall life. The low pressure requirement excludes helium as the coolant. An organic coolant was considered briefly, but was found to decompose in the fusion spectrum at an unacceptable rate. The coolant choice was water which at the temperature chosen is very effective and inexpensive.

The small size of the TETR results in a relatively large particle leakage. This in turn led to the use of a divertor for impurity control and particle pumping. The streaming of radiation through the divertor slots will influence the shielding design significantly. These main design features are summarized in Table VII-A-1.

Design constraints to meet the goals and design features from the radiation point of view were formulated. The desire for reactor and first wall lives to be equal results in an integrated load of 10 MW-yr/m^2 (based on a 10 year facility). The toroidal field magnets must last for the facility lifetime also. Several limits are imposed by this requirement. If the copper stabilizer must not have a greater than 50% resistivity increase over the five year interval between room temperature anneals, the atomic displacement rate limit in the magnet must be less than 4×10^{-5} dpa/year. The dose limit for the insulation should be 8×10^6 rads/year for mylar or 2×10^8 rads/year for epoxy assuming the

Table VII-A-1

Main Design Features of the TETR Conceptual Design, Neutronics and Photonics Considerations

(1) Superconducting toroidal field coils (NbTi)

(2) Neutron wall loading of 1 MW/m^2 average

(3) Divertor for impurity control

(4) Stainless steel structure

(5) Beam driven machine

(6) No Tritium breeding (except possibly in test modules)

(7) No net electrical power

(8) Normal vertical field and transformer coils

limitation is a 25% degradation of their mechanical properties. Further, the total nuclear heating to these magnets should be less than 60 KWth to keep the refrigeration power less than 18 MW_e. The nuclear heating in the vertical field coils must not unduly complicate their cooling. A nominal ohmic heating value in the copper is one watt per cubic centimeter. A very conservative requirement would limit nuclear heating to a tenth of this, i.e. to 0.1 watt/cm^3. Finally, to the extent possible, radioactivity and the dose level outside the shield after shutdown should be a minimum. These design constraints are listed for convenience in Table VII-A-2.

VII-B. Calculations

Neutrons and photonics calculations employed the ANISN program[5] for one-dimensional discrete ordinates results and DOT[6] for two-dimensional studies. The data base used 100 neutron and 21 gamma groups and was generated for EPR design by Plaster, et al.,[7] from ENDF/IV data. The neutron data was then collapsed to a 46 group set retaining the group structure of the original set above 2 MW as in previous work.[3]

The survey studies were based on a one-dimensional model resulting from a horizontal cut through the midplane as developed during the UWMAK-III design.[3] The reason for this choice can be seen by inspecting the TETR cross section shown in Figure VII-B-1. The vertical elongation of the plasma is necessary to achieve the required wall loading with reasonable capital costs, but the poloidal symmetry is destroyed and the usual one-dimensional model is not useful. This is made even more obvious by noting that the plasma and thus the neutron source distribution is shifted from the geometric center of the chamber. The neutron source distribution at the midplane obtained from the plasma calculations is shown in Figure VII-B-2. In addition, the vertical field coils on the inner and outer sides of the chamber are at different distances from the first wall and the torus is of very low aspect ratio. None of these features prevents the use of the horizontal cut model.

The parametric study involved a substantial number of potential designs. The discussion will be confined to six of these. A reference design is described by dimensions and compositions in Tables VII-B-1a & b. Similar descriptions of the other five designs are included in Tables VII-B-2 through 5. The basic design and designs A and B are water cooled while the remainder are helium cooled. The last three designs employ the ISSEC concept to protect the first wall. A carbon ISSEC is used in designs C and D and a tungsten ISSEC with a carbon curtain is employed in design E. The first three designs use only a carbon curtain which protects the plasma from the high Z structure.

Table VII-A-2

TETR Design Constraints for Neutronic and Photonic Considerations

(1) The first wall should last the lifetime of the reactor

(2) The atomic displacements in the toroidal field magnets should not exceed 4×10^{-5} dpa/year

(3) The total nuclear heating in the toroidal field magnets should not exceed 60 KW_{th}

(4) The maximum allowable dose for the insulating materials are 8×10^{6} Rad/year for Mylar, 2.05×10^{8} Rad/year for Epoxy and e.c.e.

(5) The maximum nuclear heating in the vertical field coils is 0.1 w/cm^3

(6) The induced radioactivity should be minimal

(7) The dose outside the reactor during and after the operation should be minimal

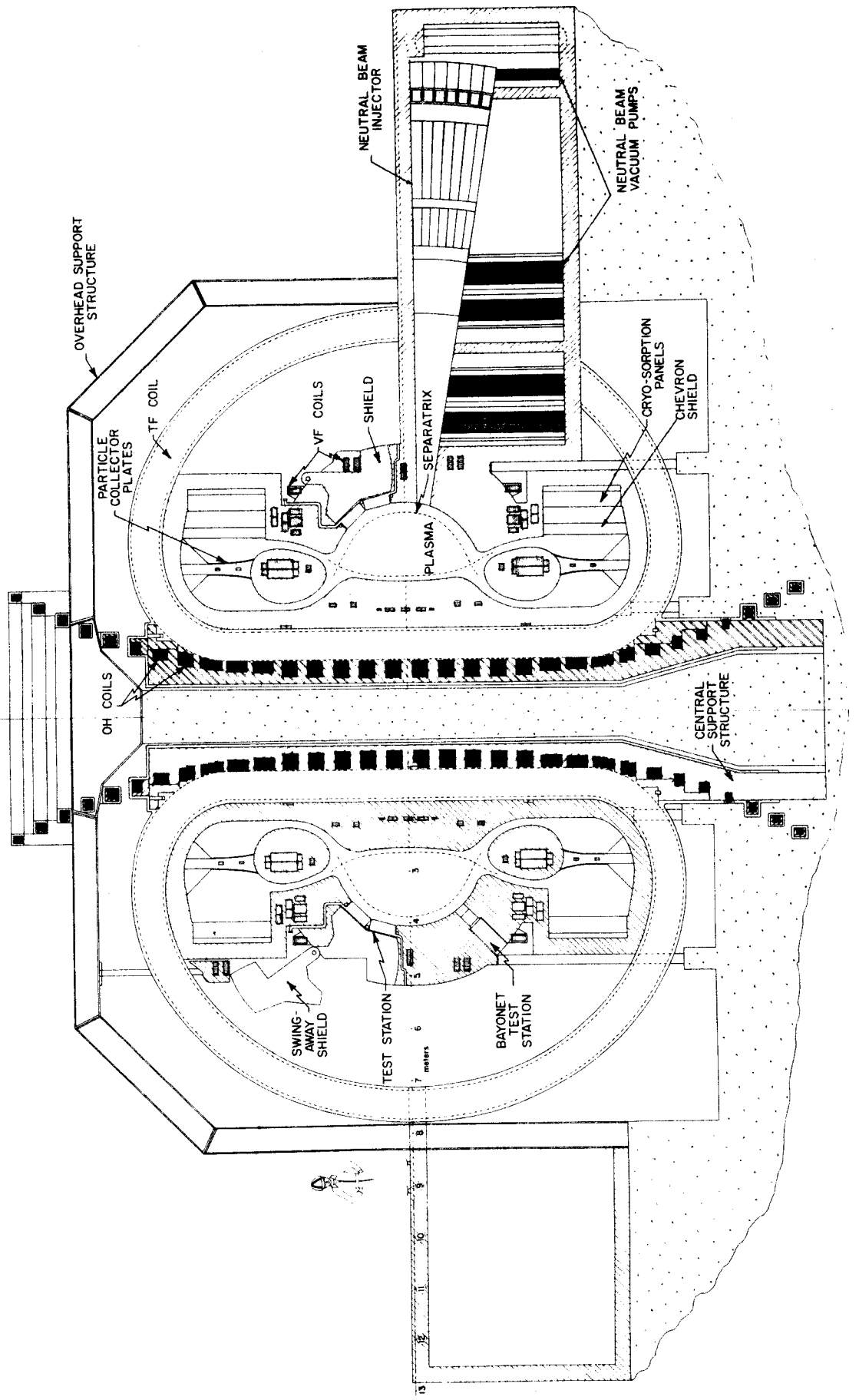

Figure VII-B-1

Figure VII-B-2

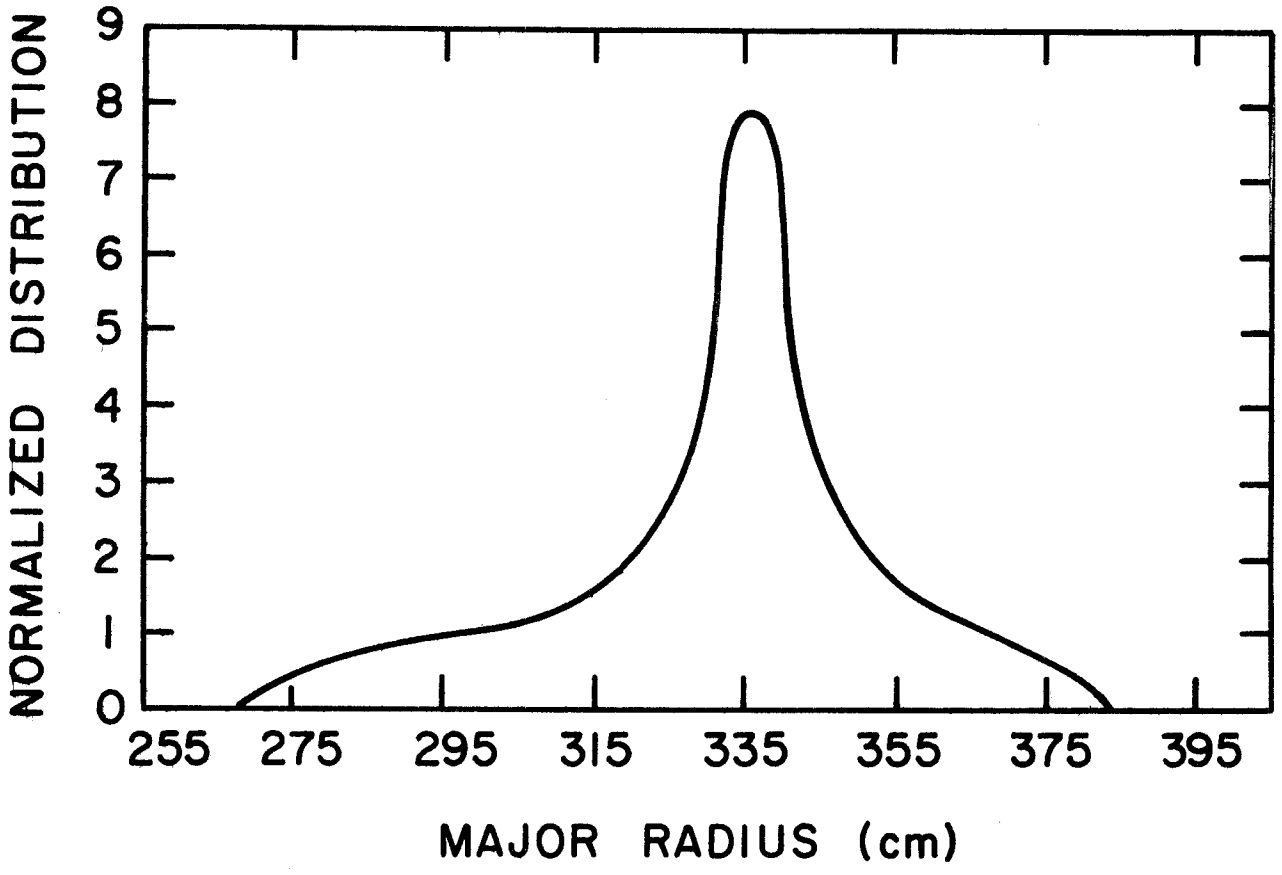

THE NEUTRON SOURCE DISTRIBUTION
AT MIDPLANE

Table VII-B-1a

Zone Compositions for the Basic TETR Design at the Midplane

Composition	Volume Present	Material
I	57.65	Cu
	30.65	St.St.
	10.11	NbTi
	1.59	Insulation
II	100	Al
III	5	Mylar ($Hg\ C_{10}\ O_4$)
IV	100	St.St.
V	87.4	B_4C
	4	St.St.
	4	H_2O
VI	92	Pb
	4	St.St.
	4	H_2O
VII	96	St.St.
	4	H_2O
VIII	75	Cu
	20	H_2O
	5	Insulation
IX	87.6	W
	4	St.St.
	4	H_2O
X	40	St.St.
	50	H_2O
XI	100	C
XII	100	Vacuum

Table VII-B-1b

Dimensions and Compositions per Zone for the Basic TETR Design at the Midplane

Zone Number	Radius (cm)		Thickness (cm)
	Inner	Outer	
1	105.0	160.0	55
2	160.0	161.0	1
3	161.0	164.0	3
4	164.0	165.0	1
5	165.0	170.0	5
6	170.0	175.0	5
7	175.0	186.5	11.5
8	186.5	191.5	5.0
9	191.5	196.5	5.0
10	196.5	203.5	7
11	203.5	211	7.5
12	211	218.5	7.5
13	218.5	253.0	34.0
14	253.0	254.5	1.5
15	254.5	255.0	0.5
16	255	405	150
17	405	405.5	0.5
18	405.5	407	1.5
19	407	435	28
20	435	442.5	7.5
21	442.5	450.0	7.5
22	450.0	480	30
23	480	485	5
24	485	490	5
25	490	505	15
26	505	510	5
27	510	515	5

Table VII-B-2

Dimensions and Compositions per Zone for Designs A and B Compared to the Basic TETR Design at the Midplane

Zone Number	Basic Design	A Design	B Design
1-6	All the same as the basic design		
7	11.5 cm, VII*	11.5 cm, IX	11.5 cm, VII
8-12	Identical to the basic design		
13	34 cm, IX	34 cm, IX	34 cm, VII
14-18	Identical to the basic design		
19	28 cm, IX	28 cm, IX	28 cm, VII
20-27	Identical to the basic design		

*Compositions from Table VII-B-1a

Table VII-B-3

DIMENSIONS AND COMPOSITION PER ZONE FOR DESIGN-C AT THE MIDPLANE

Zone	Radius (cm)	Thickness (cm)	Composition (Volume Percent)	Composition
1	106-161	55	NbTi superconductor 45 cu 45 st. st. 10 NbTi	I
2	161-162.5	1.5	Mylar	II
3	162.5-167.5	5	90 B_4C 5 st. st. 5 He	III
4	167.5-172.5	5	90 Pb 5 st. st. 5 He	IV
5	172.5-182.5	10	95 st. st. 5 He	V
6	182.5-190.0	7.5	90 Pb 5 st. st. 5 He	IV
7	190.0-197.5	7.5	90 B_4C 5 st. st. 5 He	III
8	197.5-204.5	7	75 Cu 25 H_2O	VI
9	204.5-212	7.5	90 B_4C 5 st. st. 5 He	III
10	212-219.5	7.5	90 Pb 5 st. st. 5 He	IV
11	219.5-224	4.5	95 st. st. 5 He	V
12	224-244	20	90 W 5 st. st. 5 He	VII

Table VII-B-3, Continued

Zone	Radius (cm)	Thickness (cm)	Composition (Volume Percent)	Composition
13	244-245	1	100 st. st.	VIII
14	245-255	10	100 C	IX
15	255-405	150	Vacuum	X
16	405-415	10	100 C	IX
17	415-416	1	100 st. st.	VIII
18	416-435	19	90 W 5 st. st. 5 He	VII
19	435-442.5	7.5	90 Pb 5 st. st. 5 He	IV
20	442.5-450	7.5	90 B_4C 5 st. st. 5 He	III
21	450-476	26	75 Cu 25 H_2O	VI
22	476-483.5	7.5	90 B_4C 5 st. st. 5 He	III
23	483.5-491	7.5	90 Pb 5 st. st. 5 He	IV
24	491-506	15	95 st. st. 5 He	V
25	506-511	5	90 B_4C 5 st. st. 5 He	III
26	511-518.5	7.5	90 Pb 5 st. st. 5 He	IV
			100%	XI

Table VII-B-4

DIMENSIONS AND COMPOSITION PER ZONE FOR DESIGN-D AT THE MIDPLANE

Zone	Radius	Thickness	Composition	
1	105 - 160	55	NbTi superconductor 45 cu 45 st. st. 10 NbTi	I
2	161 - 162.5	1.5	Mylar	II
3	162.5 - 167.5	5	90 B_4C 5 st. st. 5 He	III
4	167.5 - 172.5	5	90 Pb 5 st. st. 5 He	IV
5	172.5 - 182.5	10	95 st. st. 5 He	V
6	182.5 - 190.0	7.5	90 Pb 5 st. st. 5 He	IV
7	190.0 - 197.5	7.5	90 B_4C 5 st. st. 5 He	III
8	197.5 - 204.5	7	75 cu 25 H_2O	VI
9	204.5 - 212	7.5	90 B_4C 5 st. st. 5 He	III
10	212 - 218.5	6.5	90 Pb 5 st. st. 5 He	IV
11	218.5 - 233.5	15	90 W 5 st. st. 5 He	VII
12	233.5 - 234.5	1	100 st. st.	VIII

Table VII-B-4, Continued

Zone	Radius	Thickness	Composition	
13	234.5 - 225	19.5	100 C	IX
14	225 - 405	150	Vacuum	X
15	405 - 427.5	22.5	100 C	IX
16	427.5 - 428.5	1	100 st. st.	VIII
17	428.5 - 443.5	15	90 W 5 st. st. 5 He	VII
18	443.5 - 448.5	5	90 Pb 5 st. st. 5 He	IV
19 z	448.5 - 456	7.5	90 B_4C 5 st. st. 5 He	III
20	456 - 470	14	75 cu 25 H_2O	VI
21	470 - 477.5	7.5	90 B_4C 5 st. st. 5 He	III
22	477.5 - 485	7.5	90 Pb 5 st. st. 5 He	IV
23	485 - 500	15	95 st. st. 5 He	V
24	500 - 505	5	90 B_4C 5 st. st. 5 He	III
25	505 - 512.5	7.5	90 Pb 5 st. st. 5 He	IV

Table VII-B-5

DIMENSIONS AND COMPOSITION PER ZONE FOR DESIGN-E AT THE MIDPLANE

Zone	Radius	Thickness	Composition	
1 - 9	- - - The same as Design-D - - -			
10	212.0 - 219.5	7.5	90 Pb 5 st. st. 5 He	IV
11	219.5 - 234.5	15	st. st.	
12	234.5 - 246.5	12	90 W 5 st. st. 5 He	VII
13	246.5 - 247.5	1	100 st. st.	VIII
14	247.5 - 255	7.5	100 W	XI
15	255 - 405	150	Vacuum	X
16	405 - 415	10	100 W	XI
17	415 - 416	1	100 st. st.	VIII
18	416 - 431	15	90 W 5 st. st. 5 He	VII
19	431 - 441	10	95 st. st. 5 He	V
20	441 - 448.5	7.5	90 Pb 5 st. st. 5 He	IV
21	448.5 - 456	7.5	90 B_4C 5 st. st. 5 He	III
22	456 - 470	14	75 Cu 25 H_2O	VI
23	470 - 477.5	7.5	90 B_4C 5 st. st. 5 He	III

Table VII-B-5, Continued

Zone	Radius	Thickness	Composition	
24	477.5 - 485	7.5	90 Pb 5 st. st. 5 He	IV
25	485 - 500	15	95 st. st. 5 He	V
26	500 - 505	5	90 B_4C 5 st. st. 5 He	III
27	505 - 512.5	7.5	90 Pb 5 st. st. 5 He	IV

The neutronics and photonics results for the first three designs are compared in Table VII-B-6 to the design requirements given earlier. The first three comparisons relate to the toroidal magnets. Only design B fails significantly here (maximum dose to Mylar criteria). All three designs fail, in that the fiberglass insulation in the vertical field coils receives too high a dose. This is by a factor of over three. There are two approaches to resolving this problem. First, more radiation resistant insulation may be possible. Silicate impregnated fiberglass is considered better in this regard. Second, the design basis was for the coil to last the entire lifetime of the reactor. Thus, if the coil is changed three times during the reactor's life, the requirements will be met. Since the coils in question are on the outside of the torus, access is not a major problem, nor is the cost prohibitive. This will be our solution to the problem even though it will increase operating costs somewhat. Actually, a close inspection of these results will show design A is generally comparable to the basic design, but will cost more. Designs which would cost less unfortunately perform at a significantly lower level as can be seen from Table VII-B-6. The cost differences are related primarily to the extra cost of tungsten relative to stainless steel and the composition differences on which the cost comparison is based are brought out in Table VII-B-2. Table VII-B-7 shows the main results for the last three designs. Design D gives good protection to the first wall compared to all other designs but then fails to adequately protect the toroidal field magnets, vertical field coils, and the insulation. In addition, the carbon ISSEC surface would exceed the maximum allowable operating temperature of 2000°C. Design C meets operating temperature requirements for the ISSEC but gives less first wall protection and also fails to adequately protect the magnets in the same general way as design D. Design E more or less satisfies the design requirements from the nuclear radiation point of view, but exceeds the surface temperature limit for the tungsten ISSEC. This results from the very high energy generation in the tungsten which for a ten centimeter ISSEC averages 20 watt/cm^3 which may be compared to 4 watt/cm^3 in a graphite ISSEC of the same thickness. Cooling of the ISSEC is by radiation to the 250° first wall.

VII-C. Blanket and Shield Performance

The details of the analysis for the first three designs is given in this section. Figures VII-C-1 to VII-C-27 show the main responses as a function of the major radius at the midplane for these designs. The responses are neutron heating, gamma heating, total heating, atomic displacement, helium production, hydrogen production and dose rate.

Table VII-B-6 shows the total heating, atomic displacement, helium production and hydrogen production rates in the first wall are about the same for the three designs. The tungsten in the first two designs has a negligible effect on the first wall as expected, since the 14 MeV neutron damage represents about 50-80% of the total damage in the first wall.

Table VII-B-6

THE NEUTRONICS AND PHOTONICS RESULTS COMPARED TO THE DESIGN REQUIREMENTS FOR THE BASIC DESIGN AND DESIGNS A AND B

		Design Requirement	Basic Design	Design A	Design B
Max. atomic displacement in the toroidal field magnet DPA/year		5.7×10^{-5}	1.2×10^{-5}	6.5×10^{-6}	4.5×10^{-5}
Max. nuclear heating in the toroidal field magnet W/cm^3		1.5×10^{-3}	4.7×10^{-5}	2.8×10^{-5}	2.2×10^{-4}
Max. dose for Mylar Rad/year		1.1×10^{7}	1.3×10^{7}	8.4×10^{6}	6.7×10^{7}
Max. nuclear heating in the vertical field coil W/cm^3	(Inner)	0.1	0.01	0.01	0.09
	(Outer)	0.1	0.05	0.05	0.13
Max. dose for fiber glass Rad/year	(Inner)	2.9×10^{8}	2.5×10^{8}	2.5×10^{8}	2.3×10^{9}
	(Outer)	2.7×10^{8}	9.6×10^{8}	9.6×10^{8}	5.6×10^{9}
Total heating in the first wall W/cm^3	(Inner)	-----	10.7	10.7	11.3
	(Outer)	-----	12.5	12.5	13.2
Atomic displacement in the first wall DPA/year	(Inner)	-----	8.3	8.3	8.4
	(Outer)	-----	10	10	10
He production in the first wall APPM/year	(Inner)	-----	189	189	194
	(Outer)	-----	240	240	234
H production in the first wall APPM/year	(Inner)	-----	369	369	378
	(Outer)	-----	467	467	475

Table VII-B-7

THE NEUTRONICS AND PHOTONICS RESULTS COMPARED TO THE DESIGN REQUIREMENTS FOR THE LAST THREE DESIGNS (C, D, AND E)

	Design Requirement	Design C	Design D	Design E
Max. atomic displacement in the toroidal field magnet dPa/year	$5.7X10^{-5}$	$7.1X10^{-5}$	$1.9X10^{-4}$	$3.2X10^{-6}$
Max. nuclear heating in the toroidal field magnet W/cm^3	$1.5X10^{-3}$	$1.49X10^{-4}$	$3.9X10^{-4}$	$7.4X10^{-5}$
Max. dose for Mylar Rad/year	$1.1X10^{7}$	$1.06X10^{8}$	$2.8X10^{8}$	$4.9X10^{7}$*
Max. nuclear heating in the vertical field coils W/cm^3	0.1 0.1	0.05 0.11	1.1 1.34	0.05* 0.04*
Total heating in the first wall W/cm^3	----- -----	5.85 7.05	4.6 4.9	1.74* 1.52*
Atomic displacement in the first wall dPa/year	----- -----	4.1 5.2	2.1 2.3	3.0 2.6

*Does not account for gamma production from tungsten

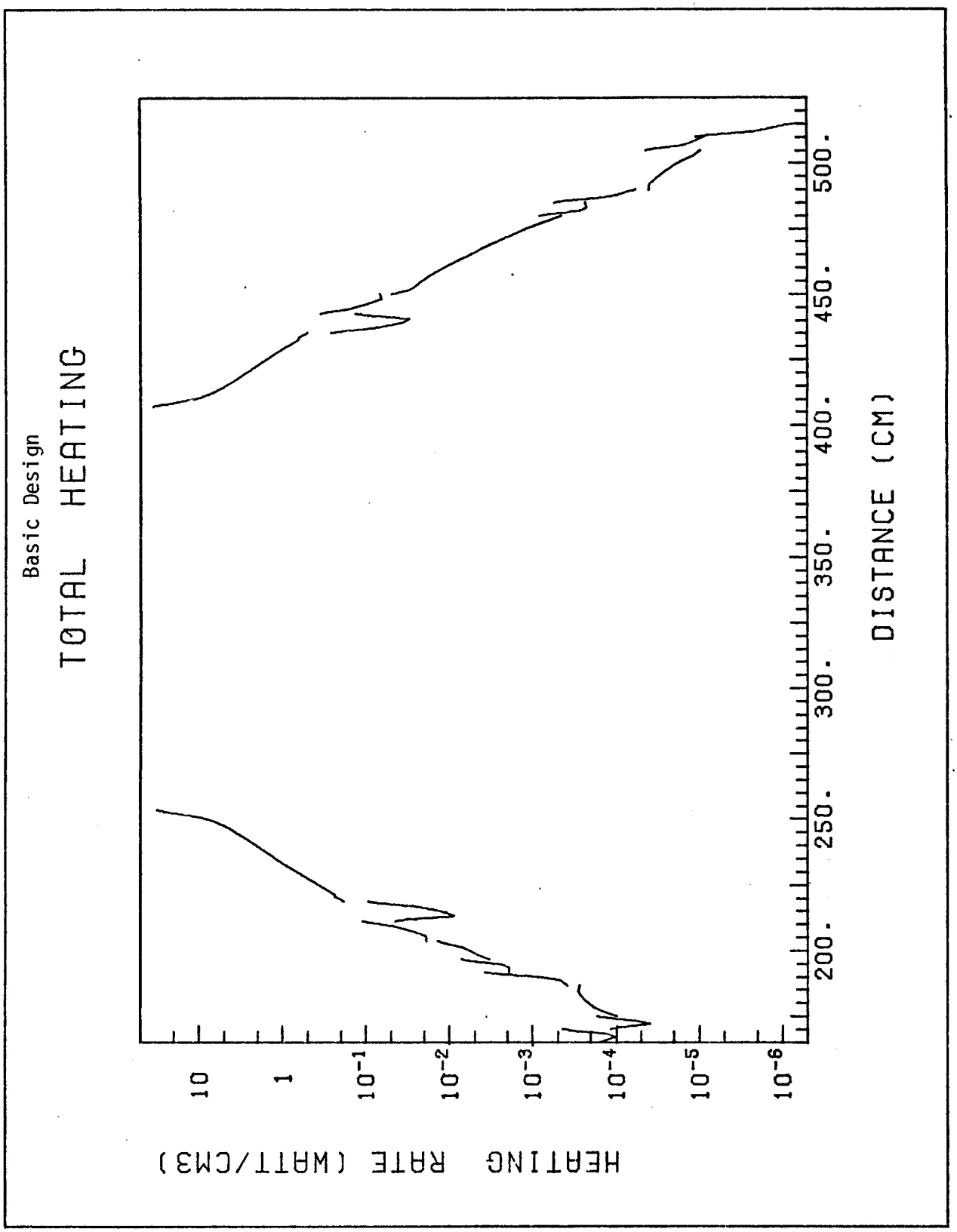

Figure VII-C-1

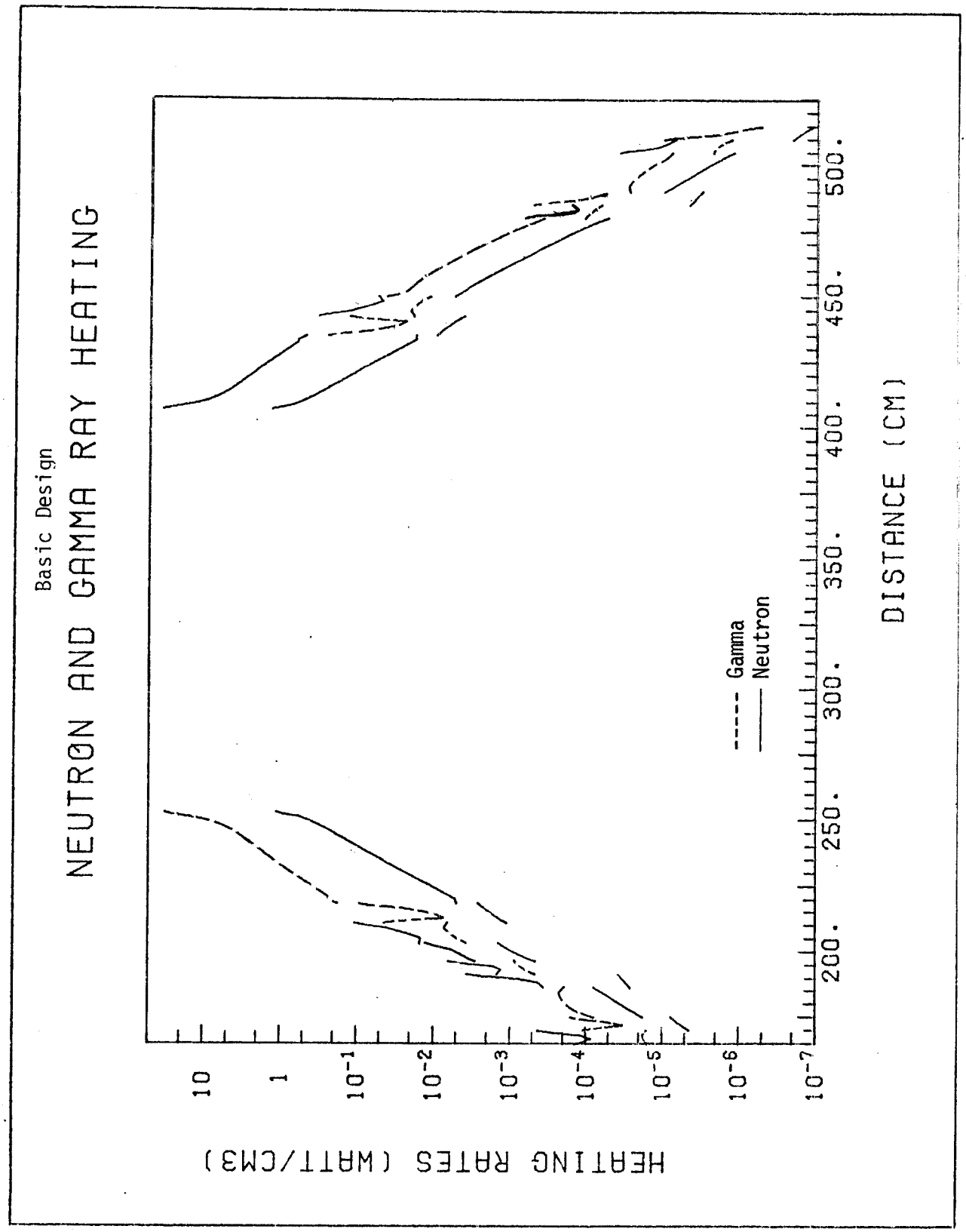

Figure VII-C-2

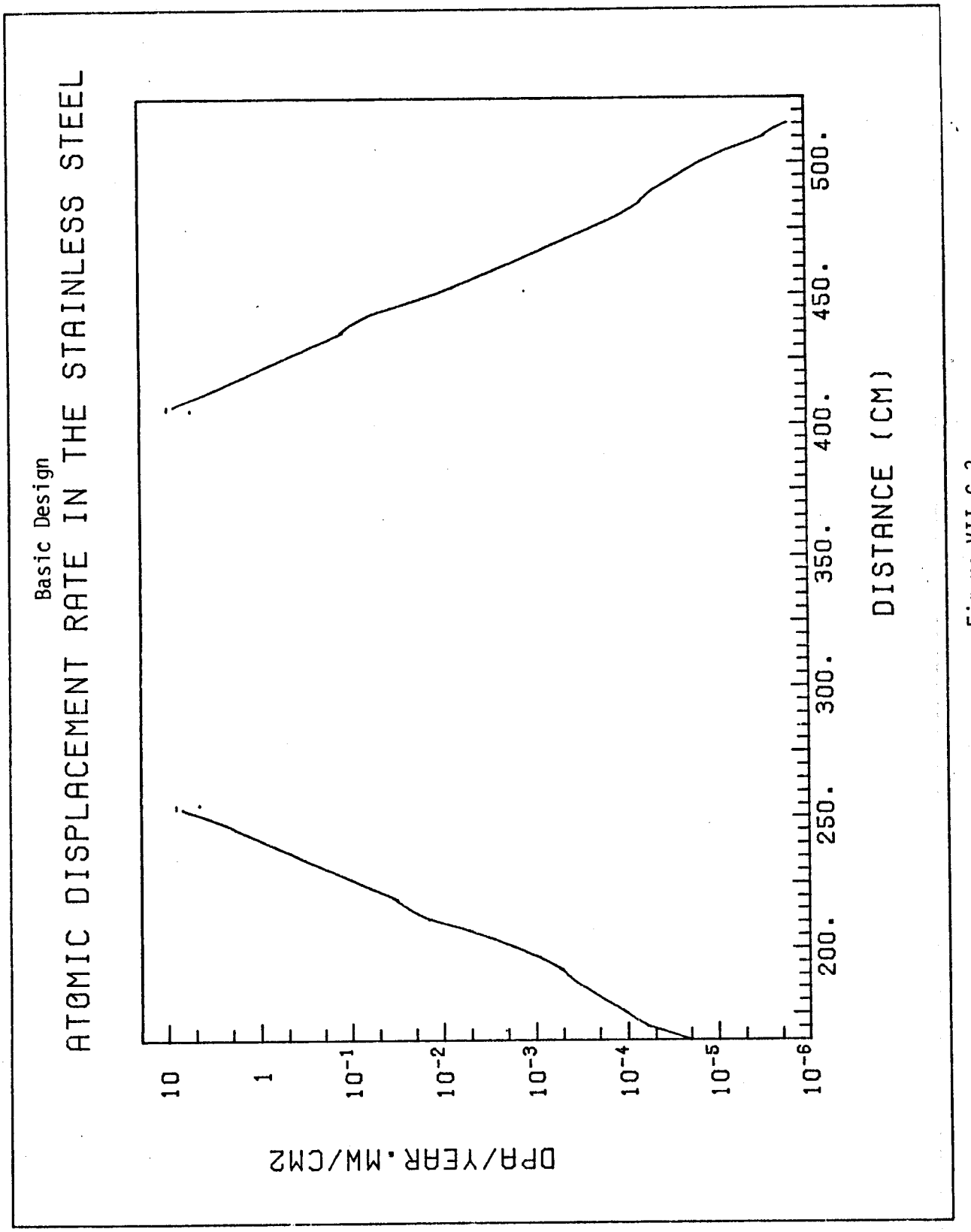

Figure VII-C-3

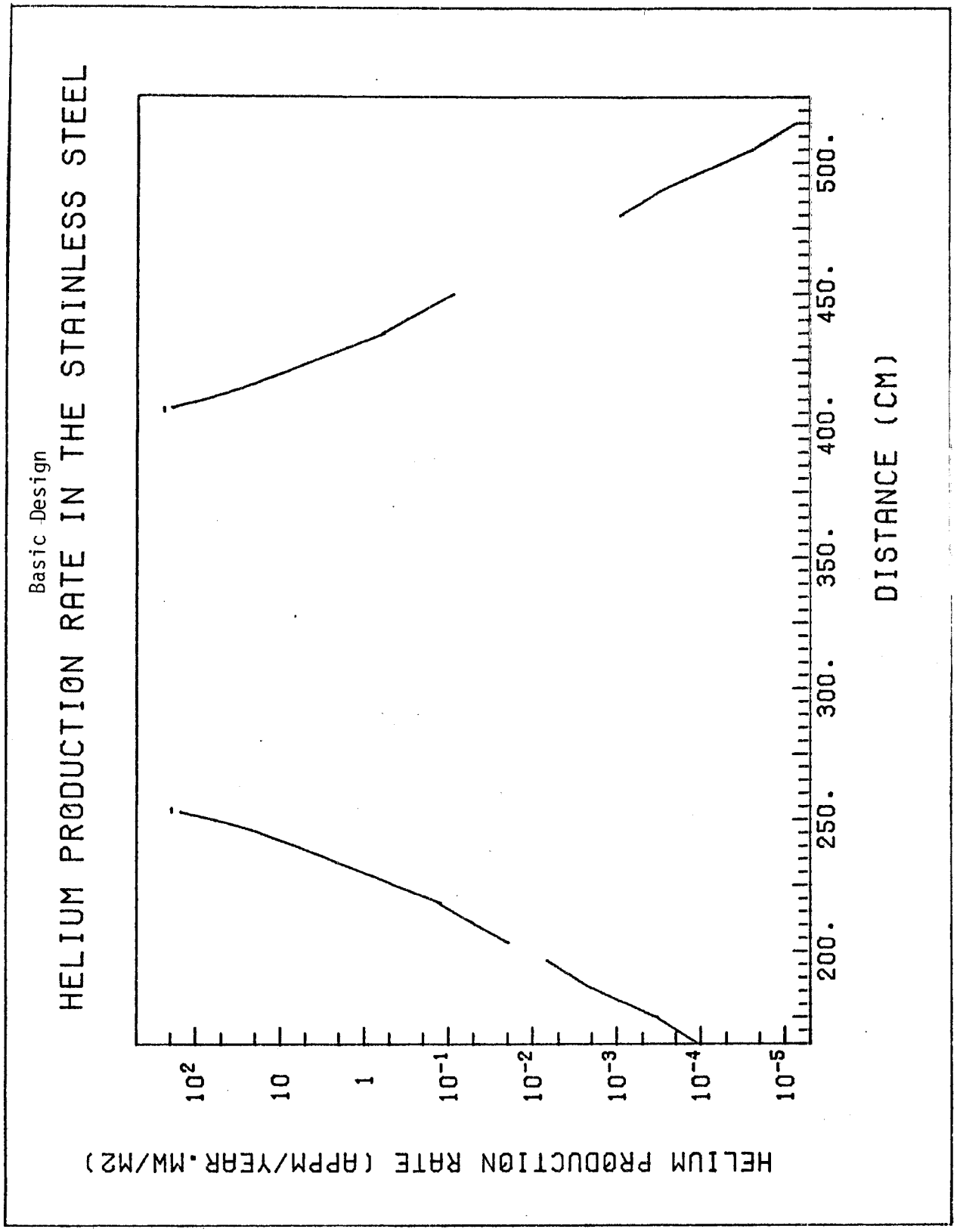

Figure VII-C-4

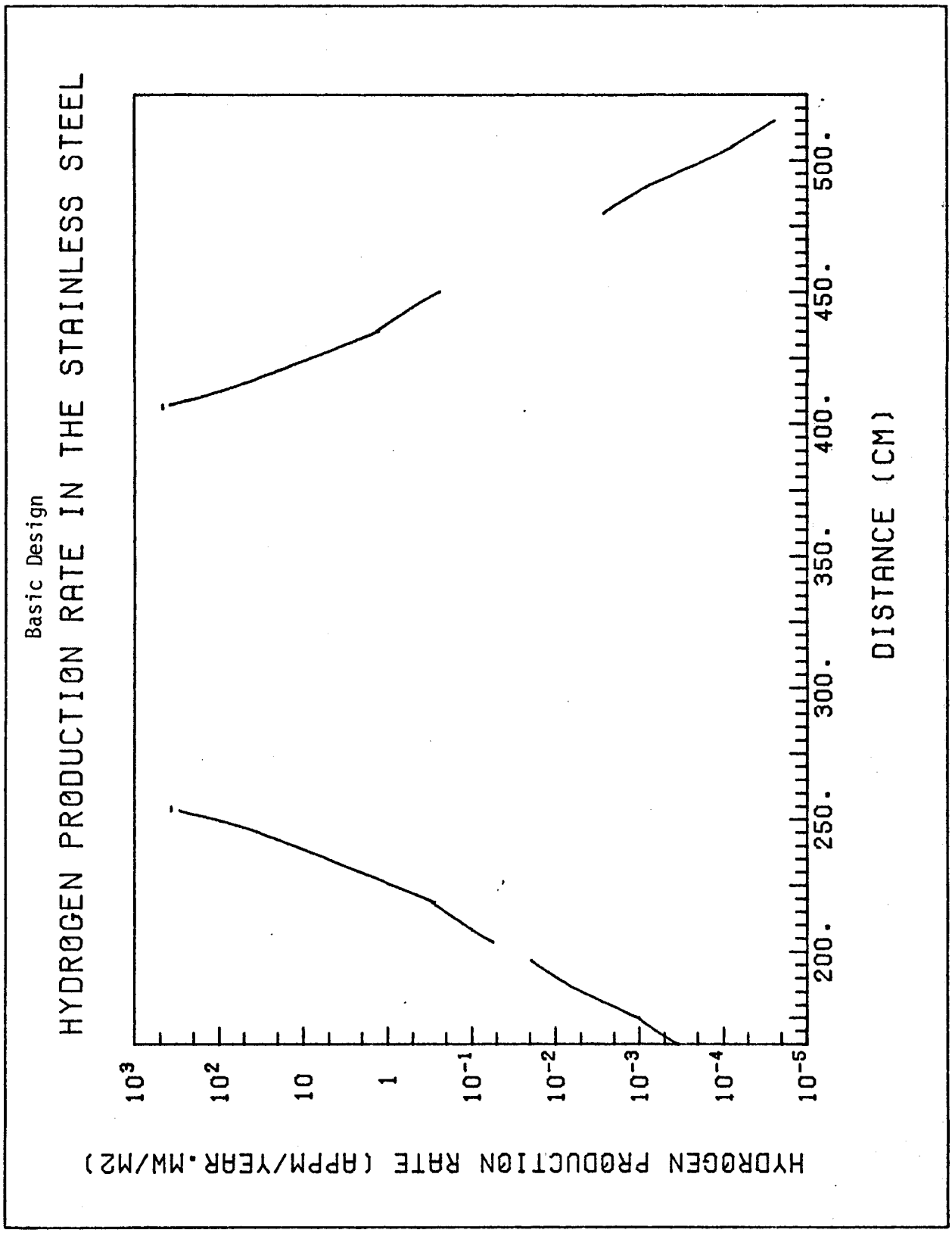

Figure VII-C-5

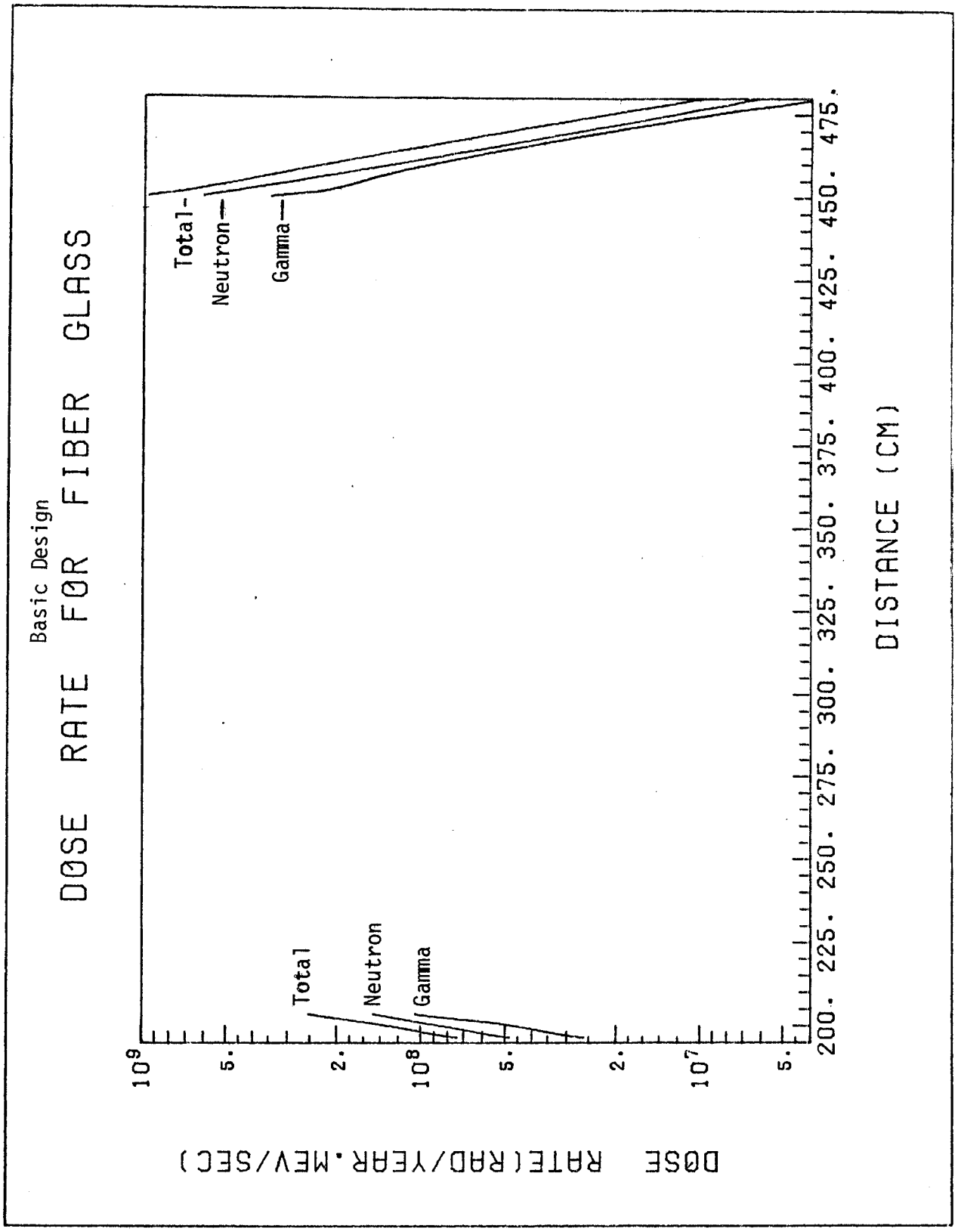

Figure VII-C-6

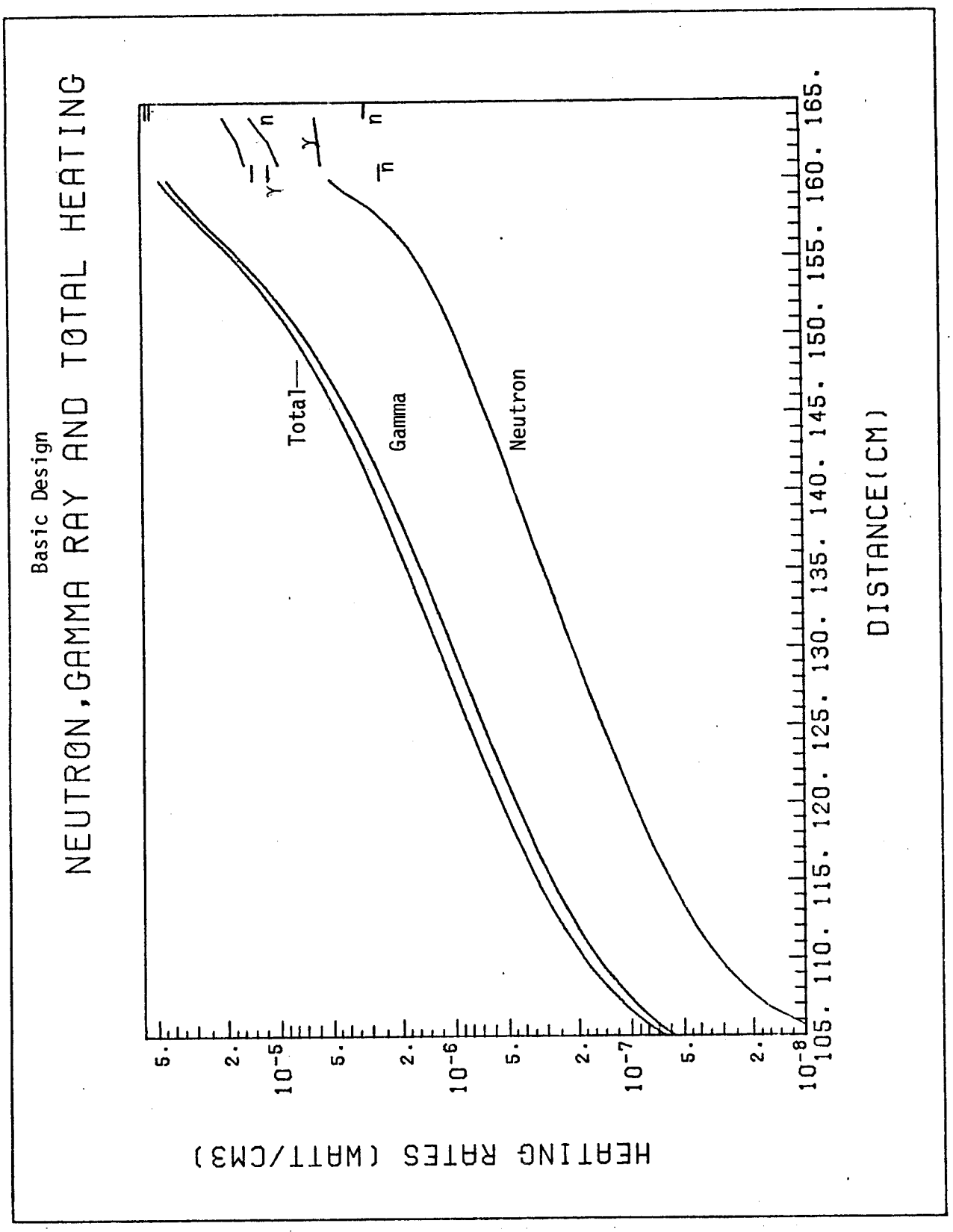

Figure VII-C-7

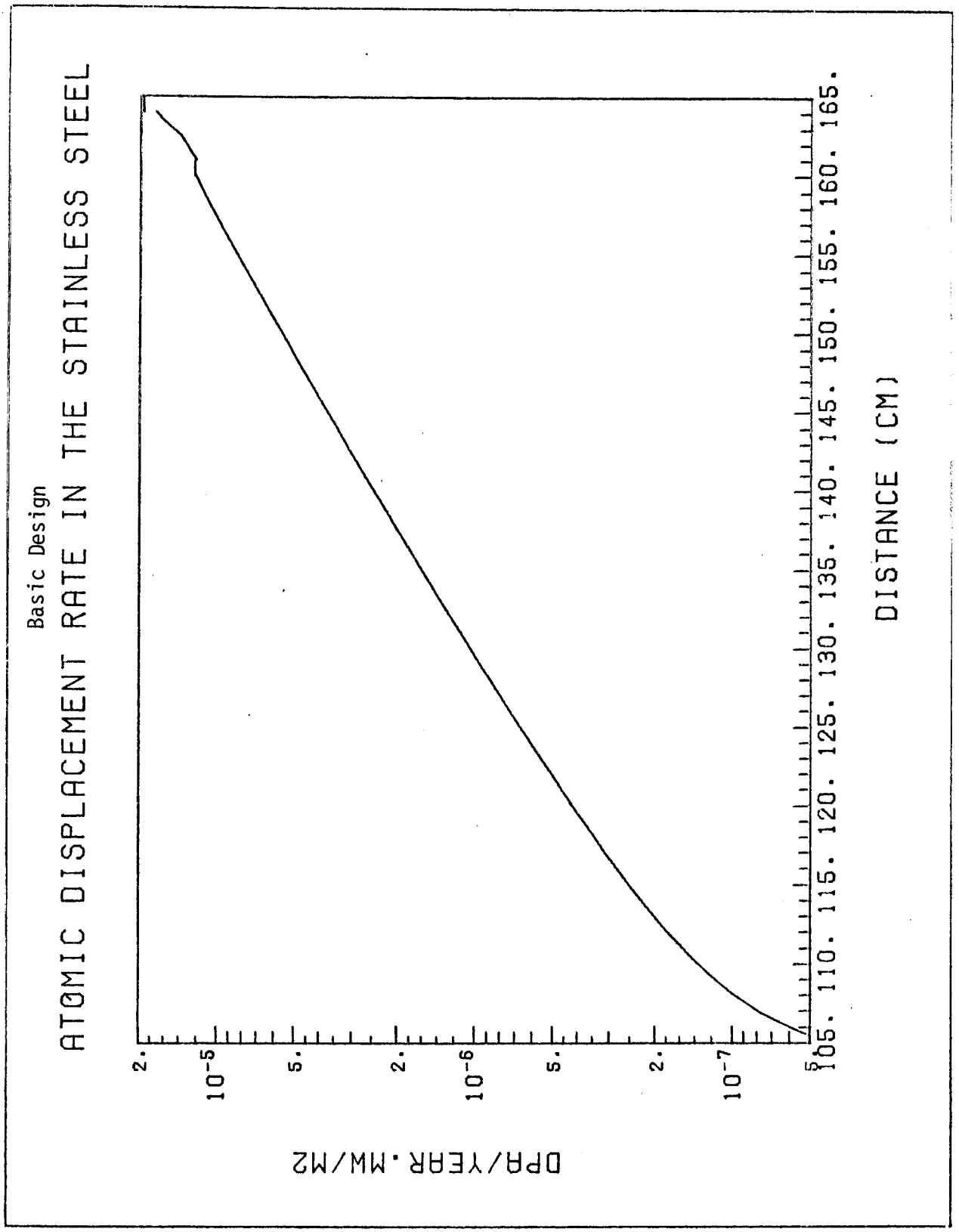

Figure VII-C-8

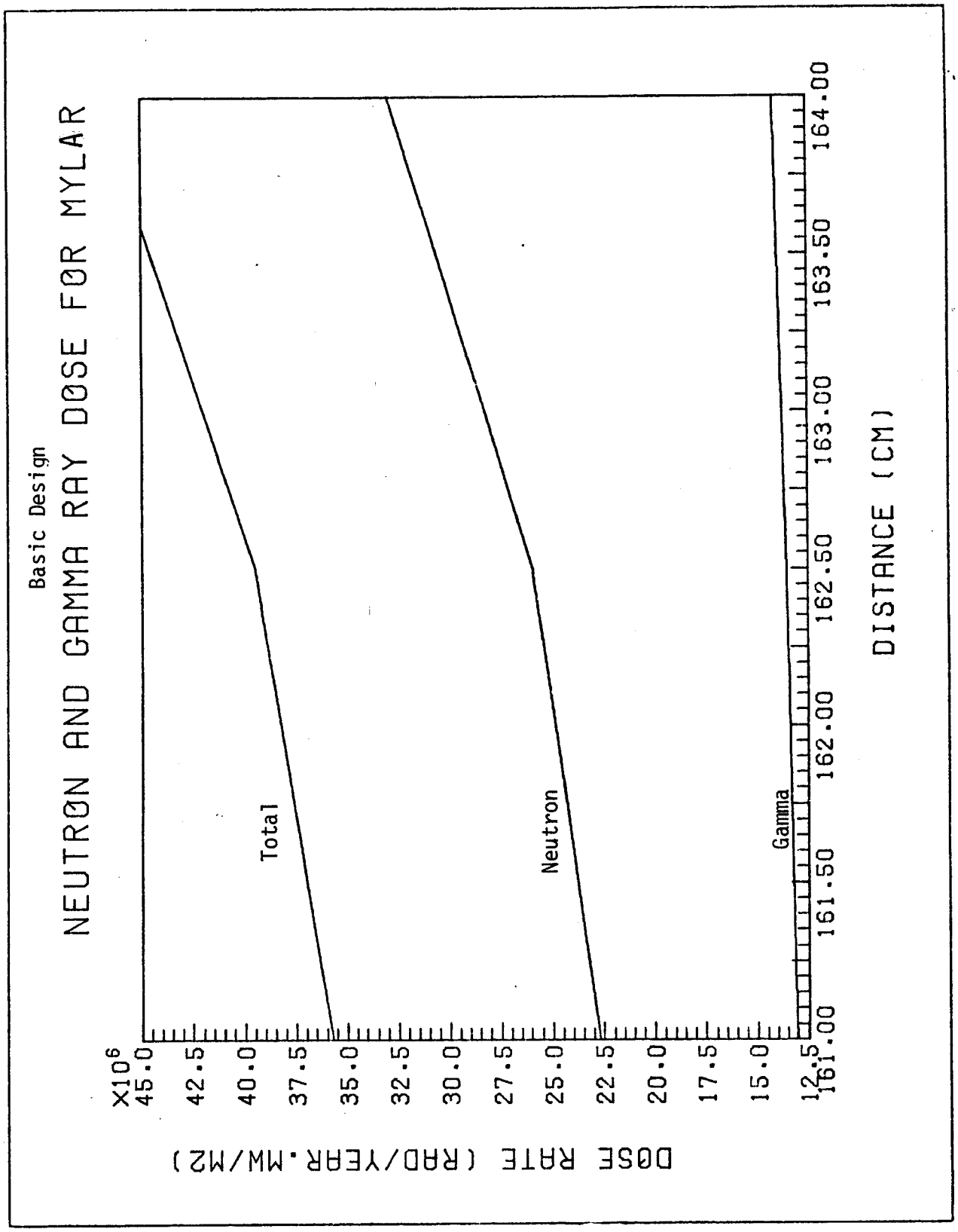

Figure VII-C-9

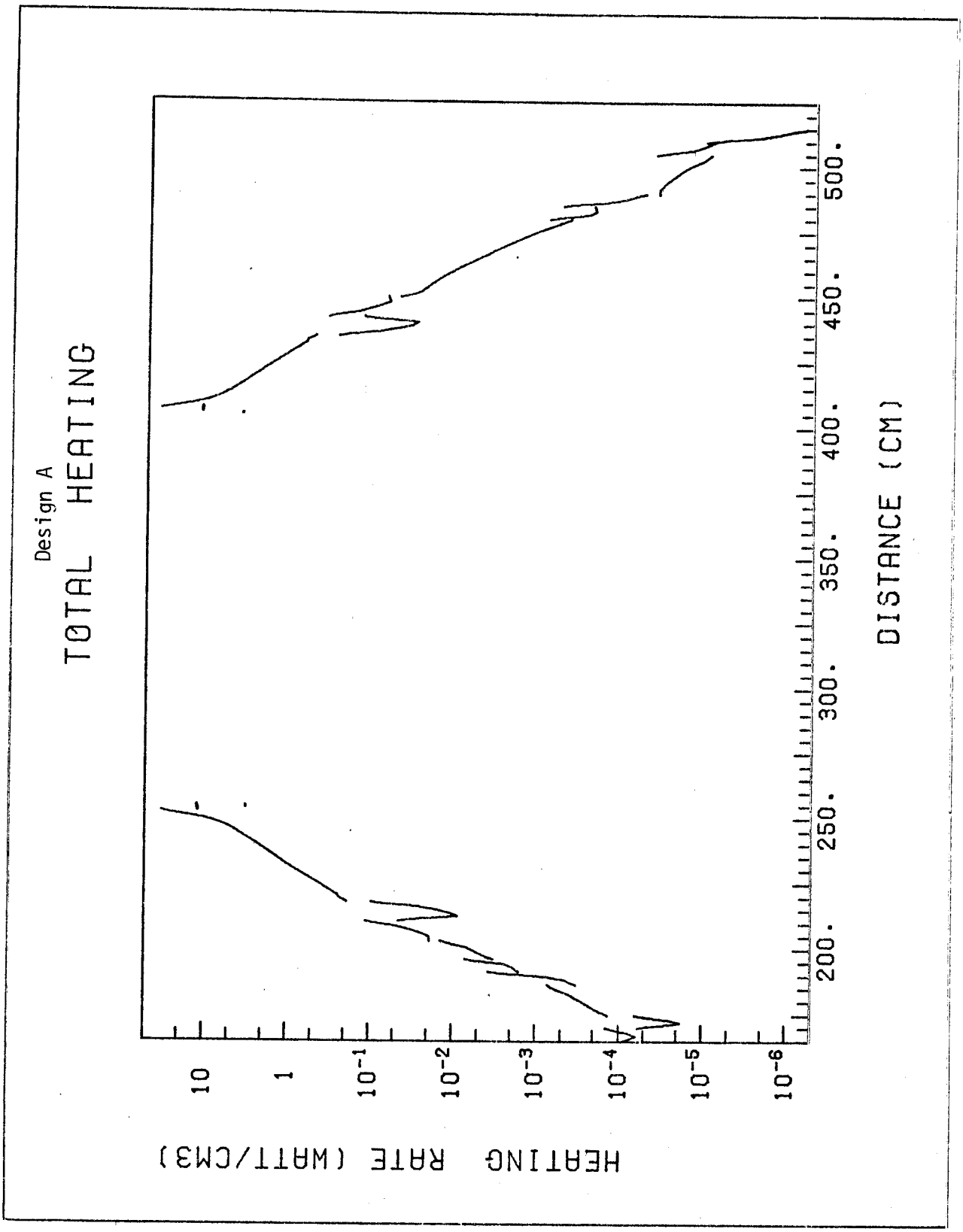

Figure VII-C-10

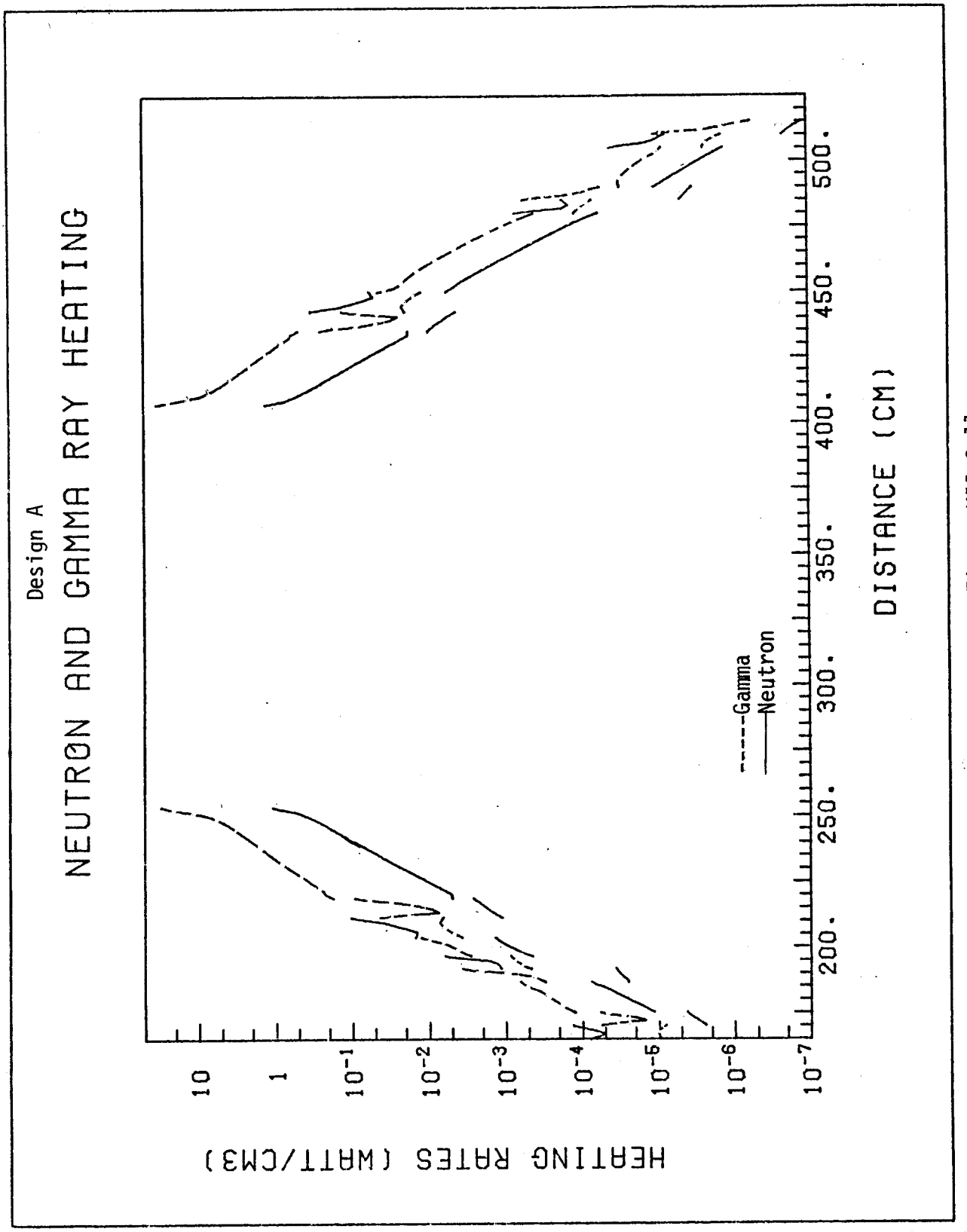

Figure VII-C-11

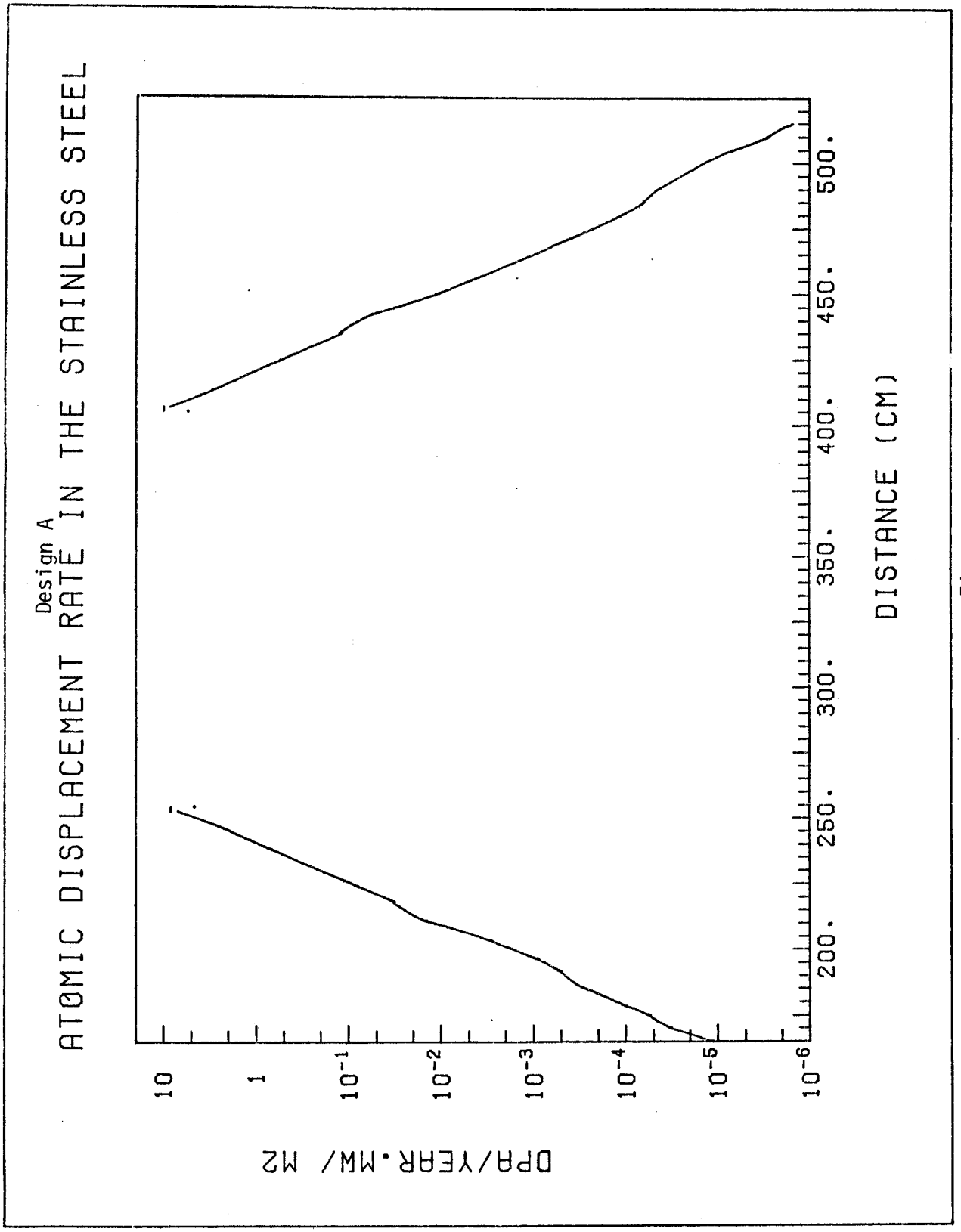

Figure VII-C-12

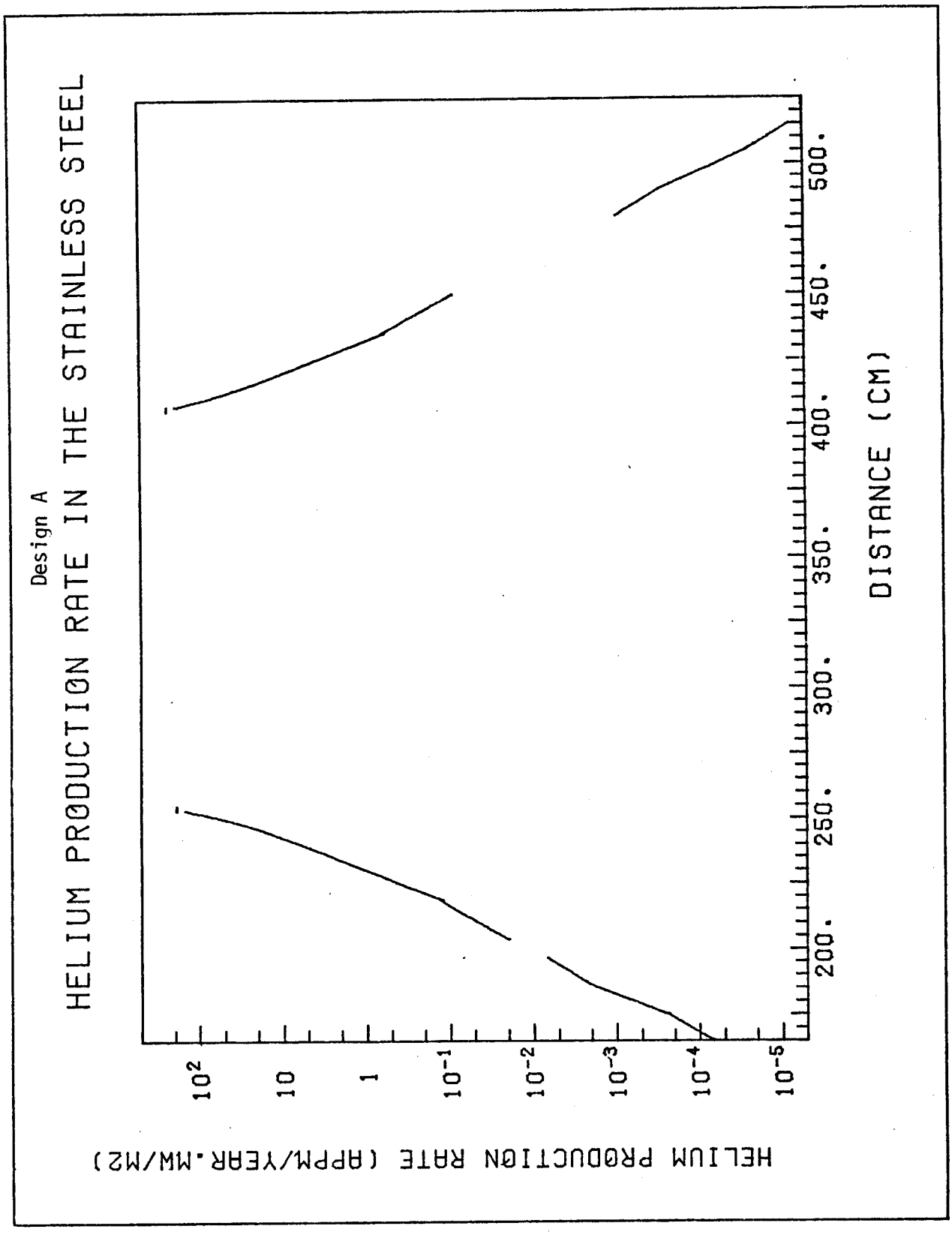

Figure VII-C-13

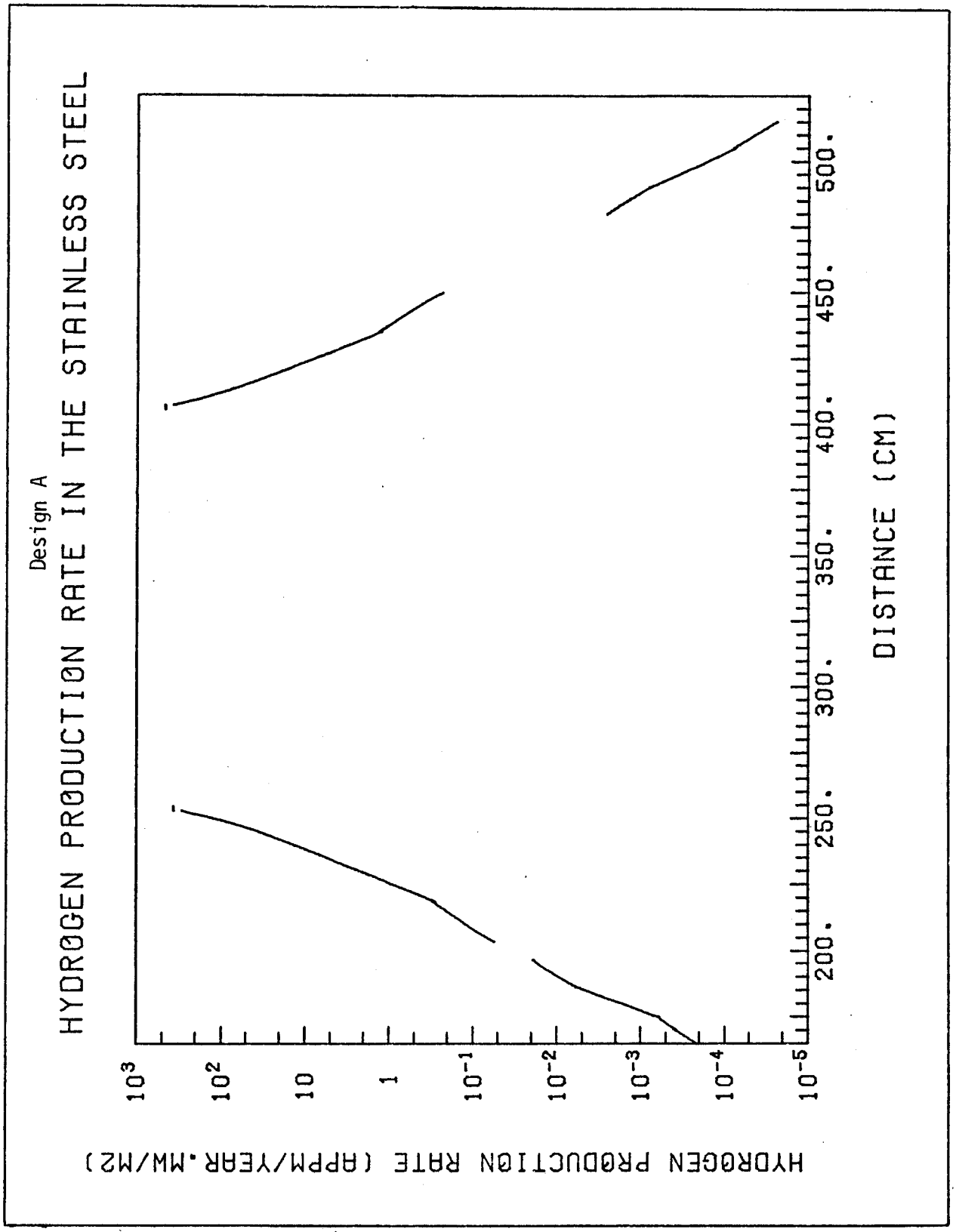

Figure VII-C-14

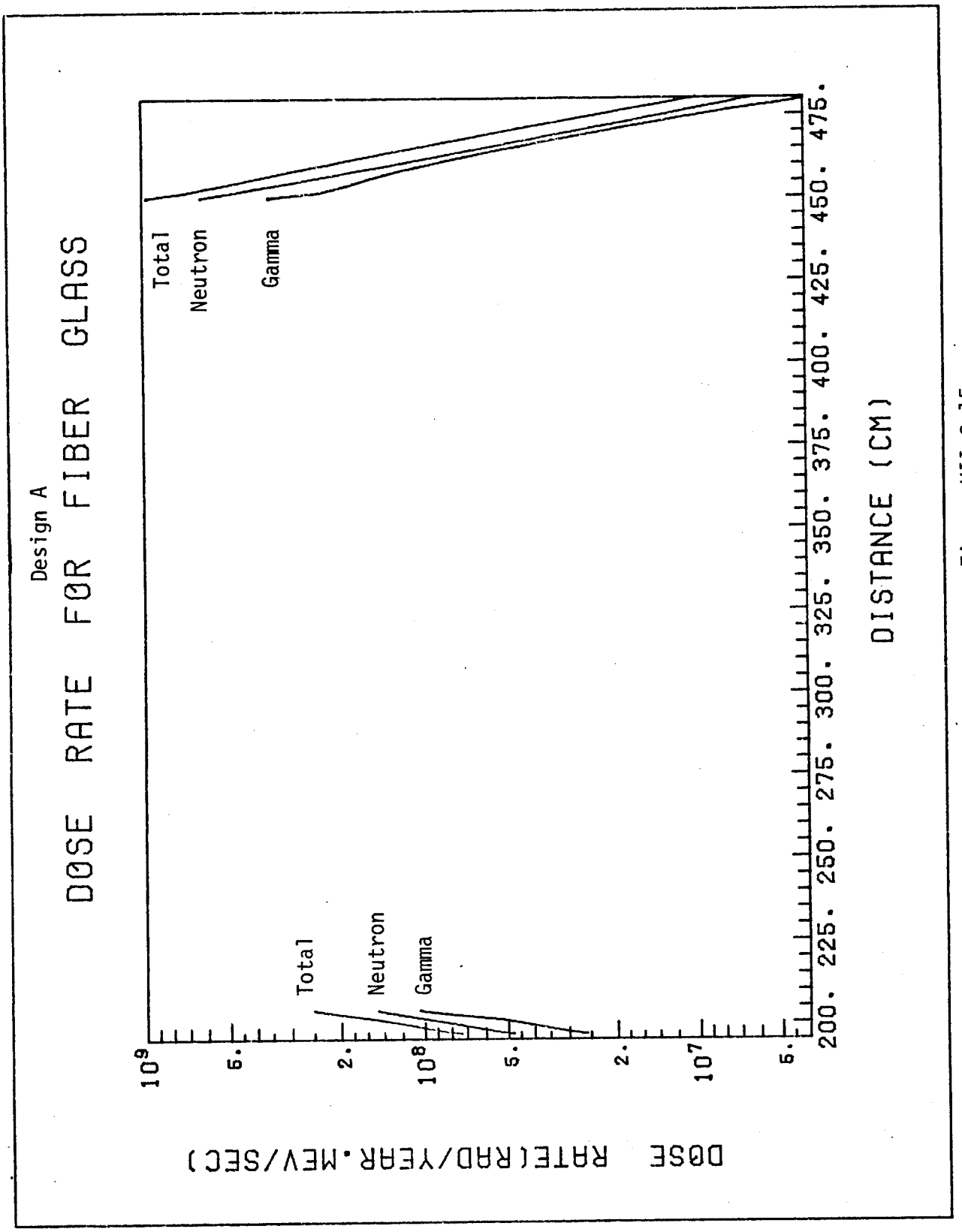

Figure VII-C-15

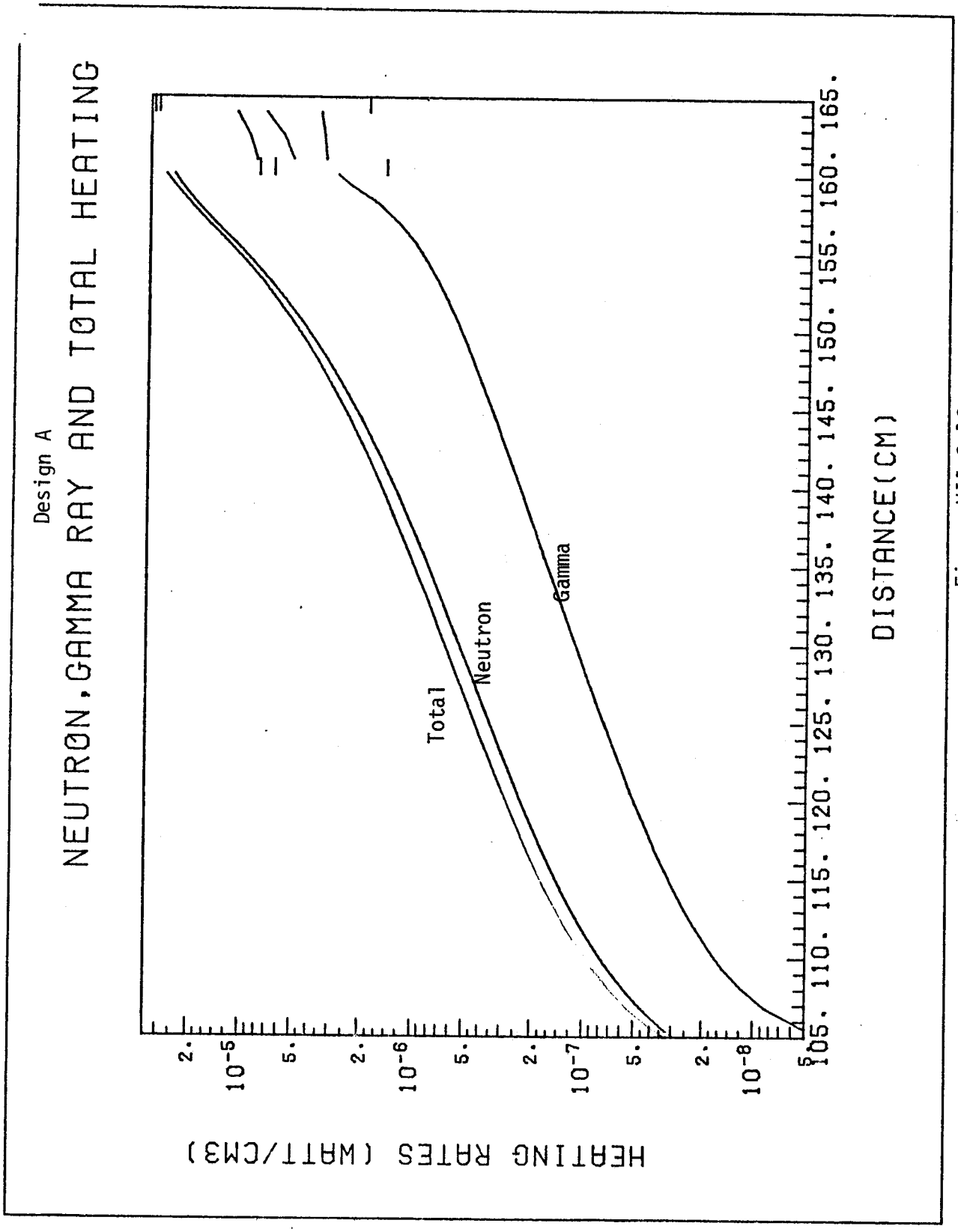

Figure VII-C-16

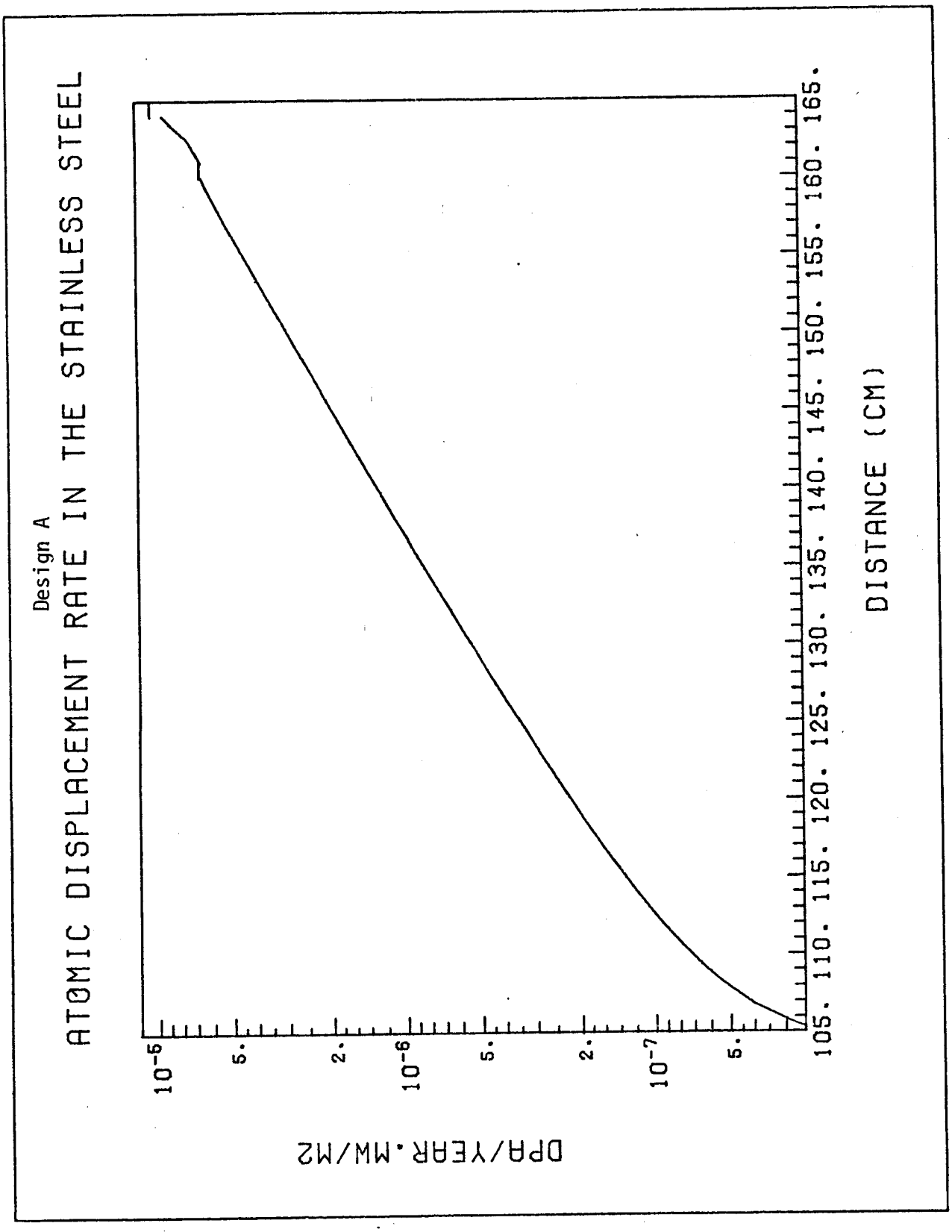

Figure VII-C-17

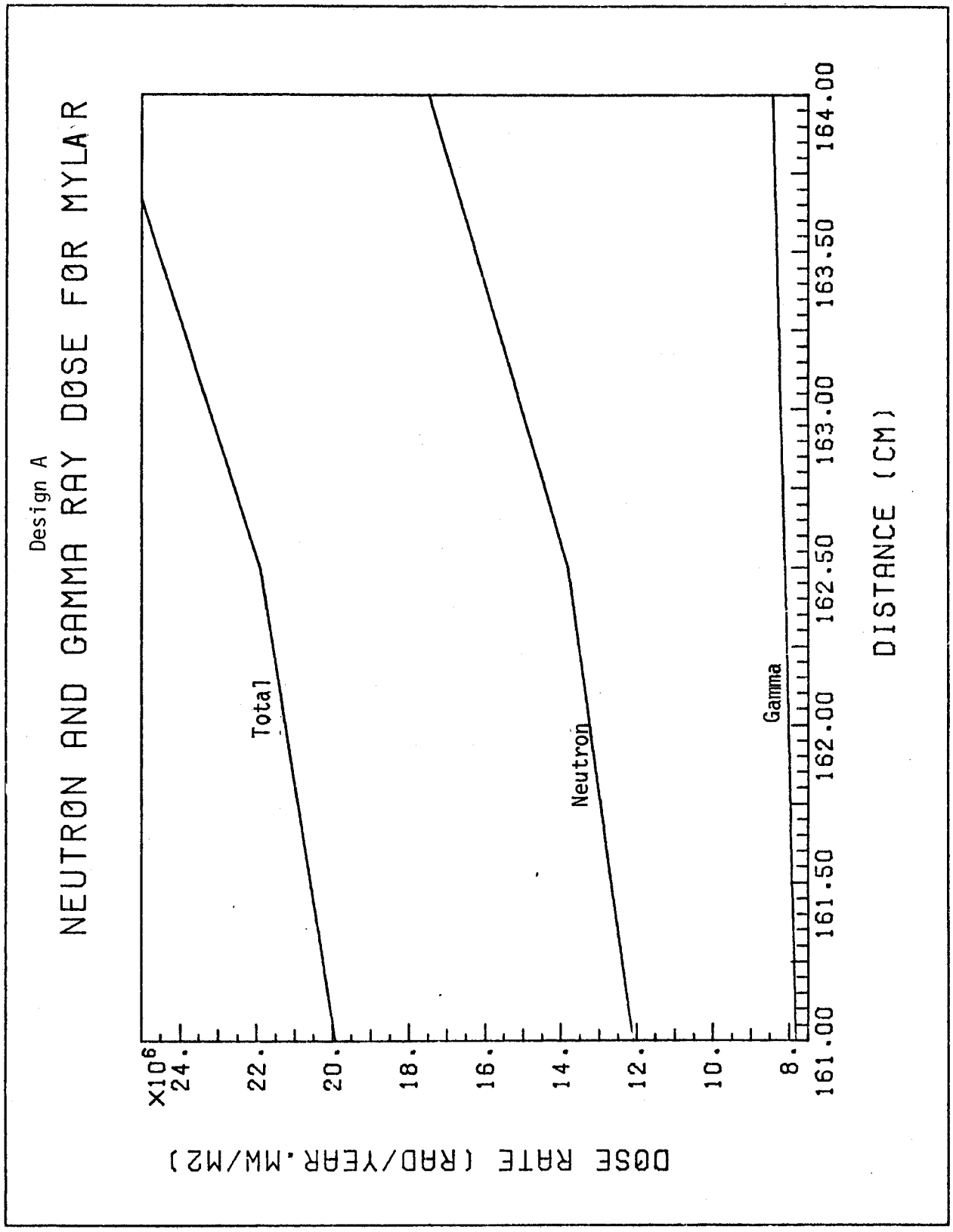

Figure VII-C-18

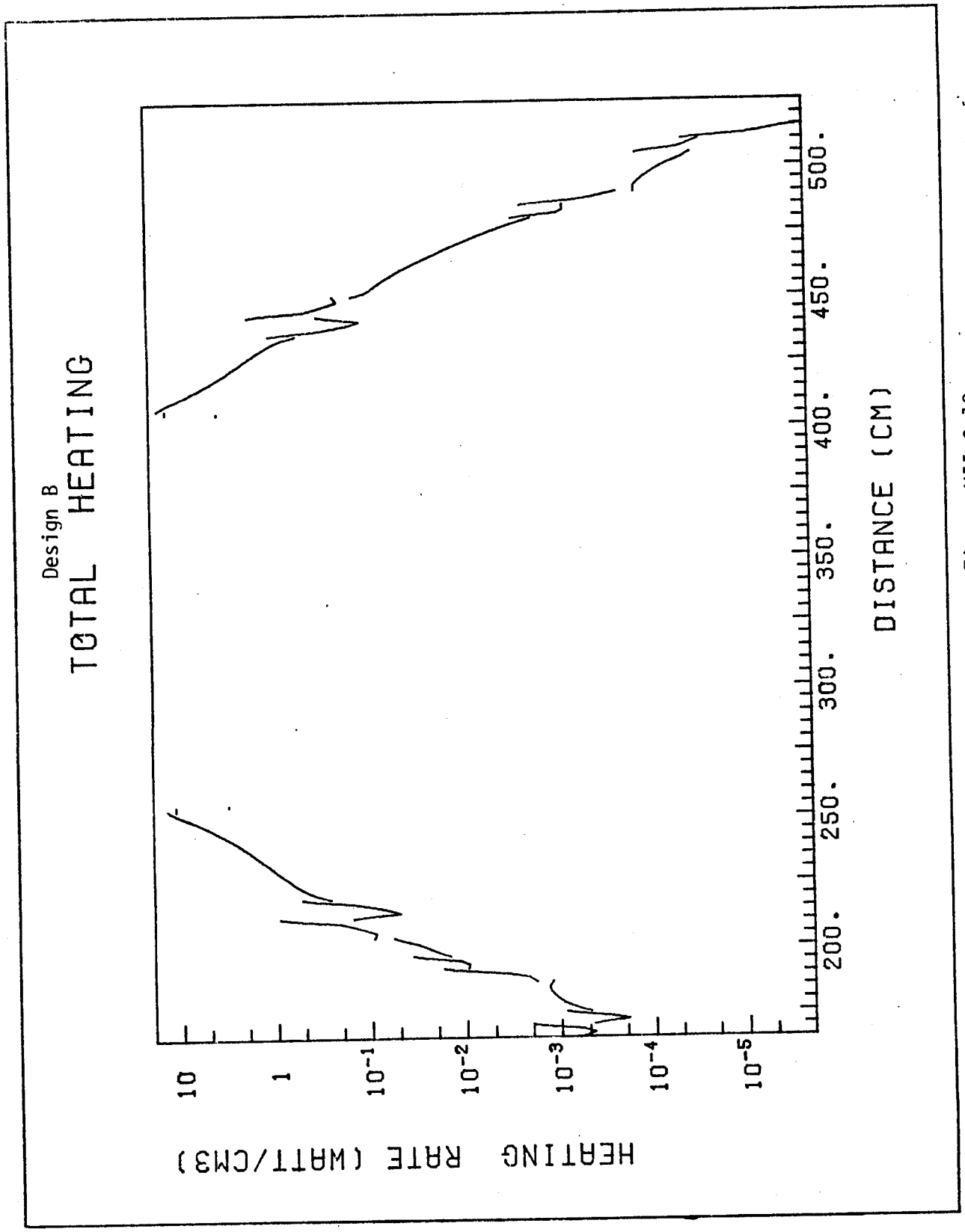

Figure VII-C-19

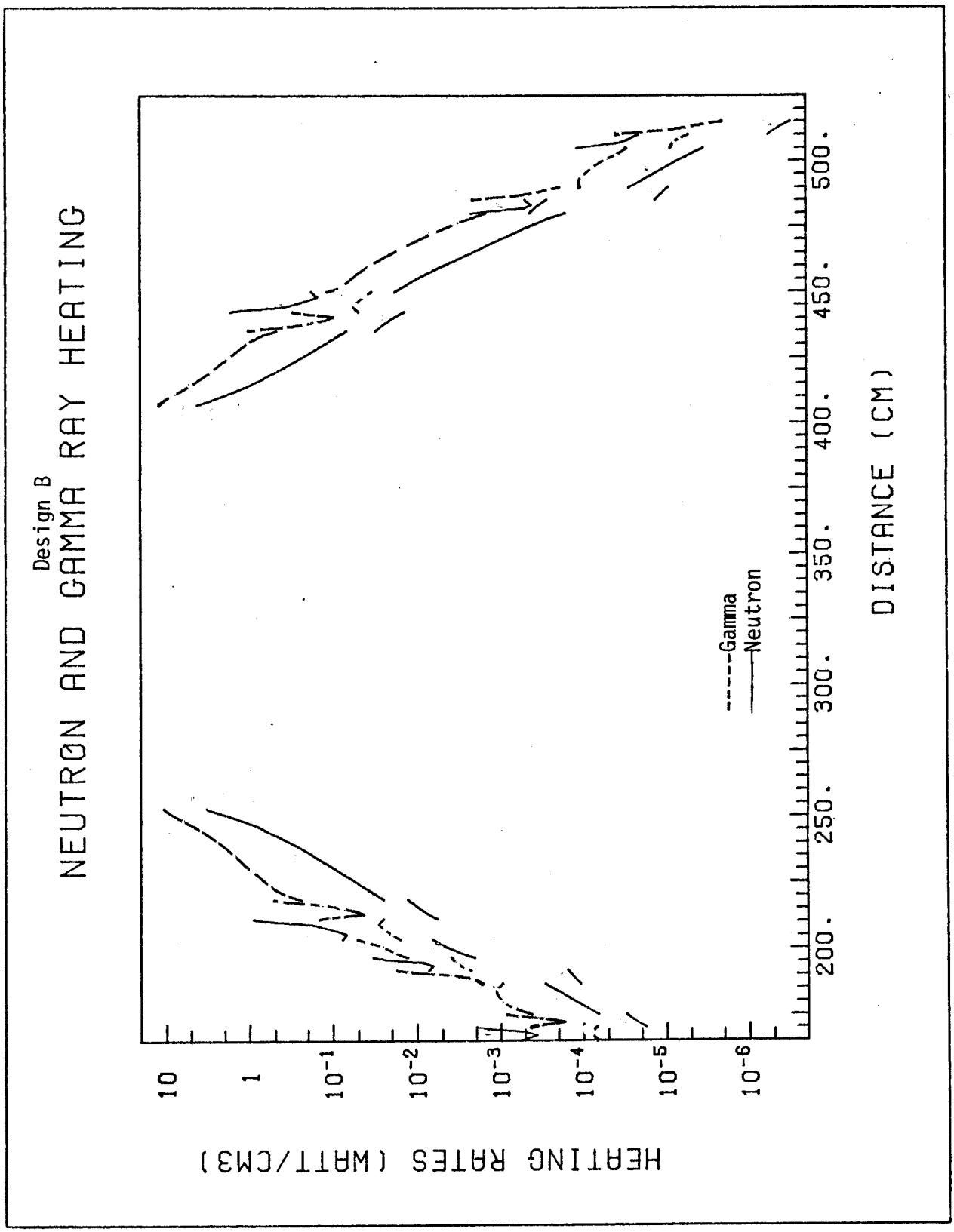

Figure VII-C-20

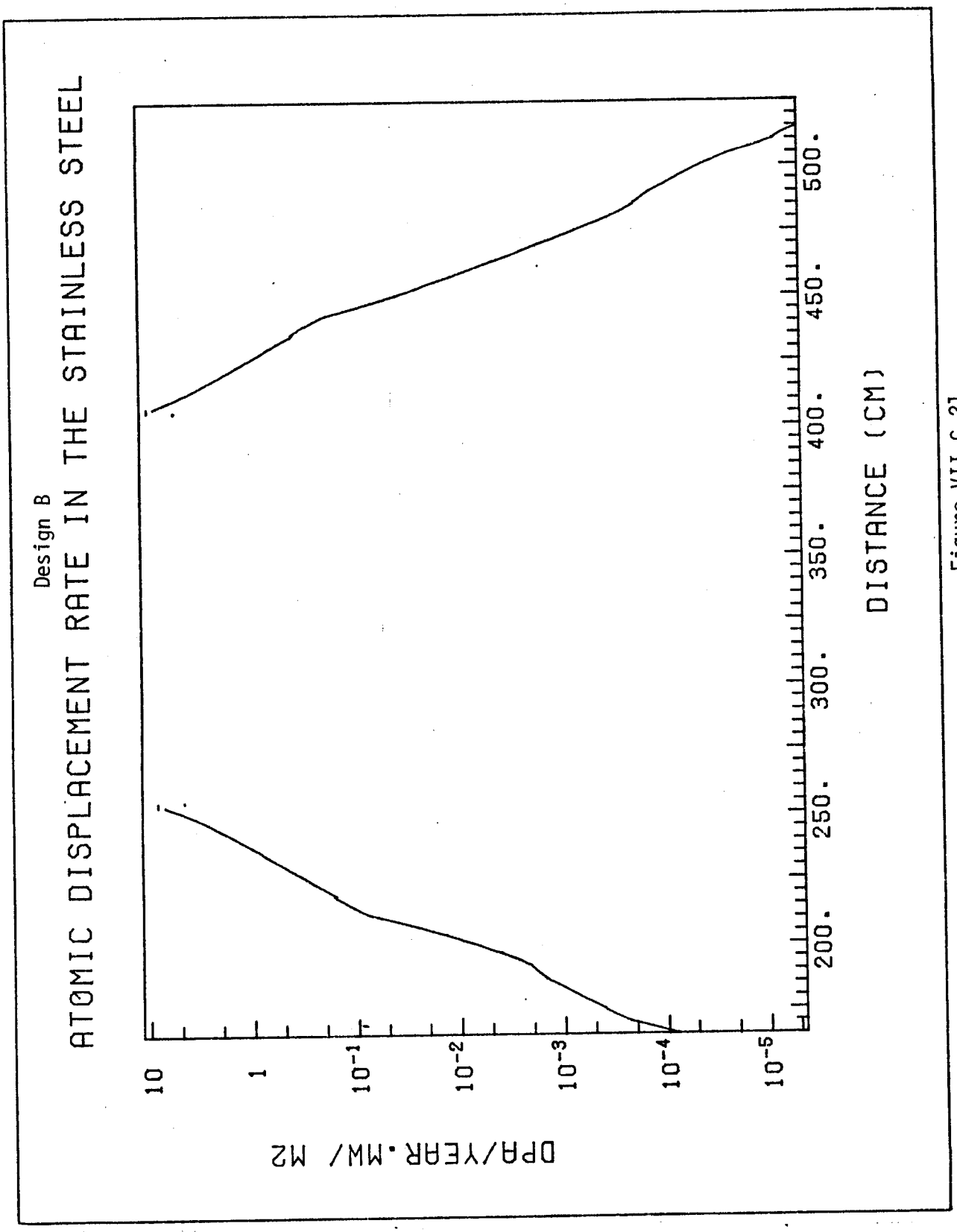

Figure VII-C-21

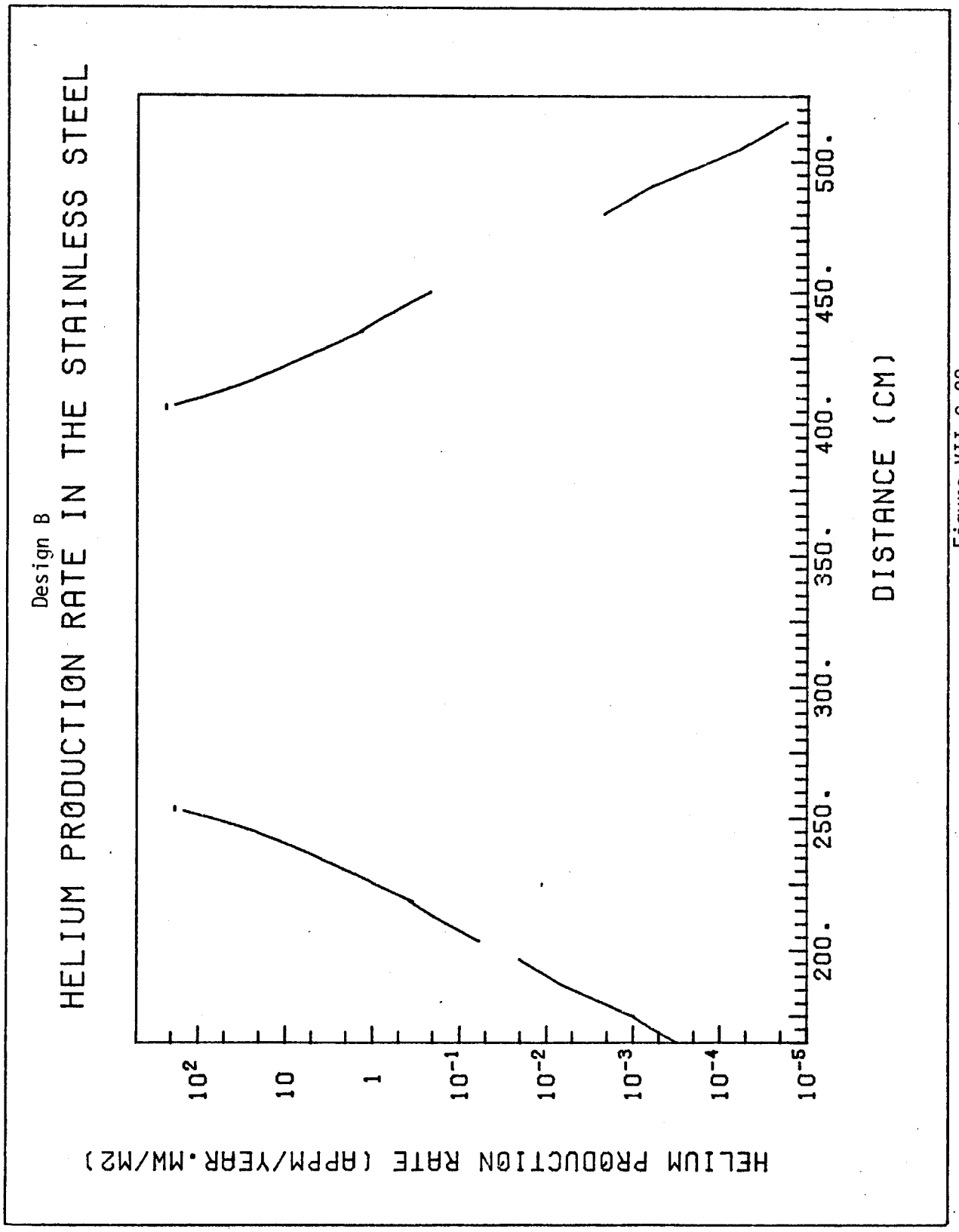

Figure VII-C-22

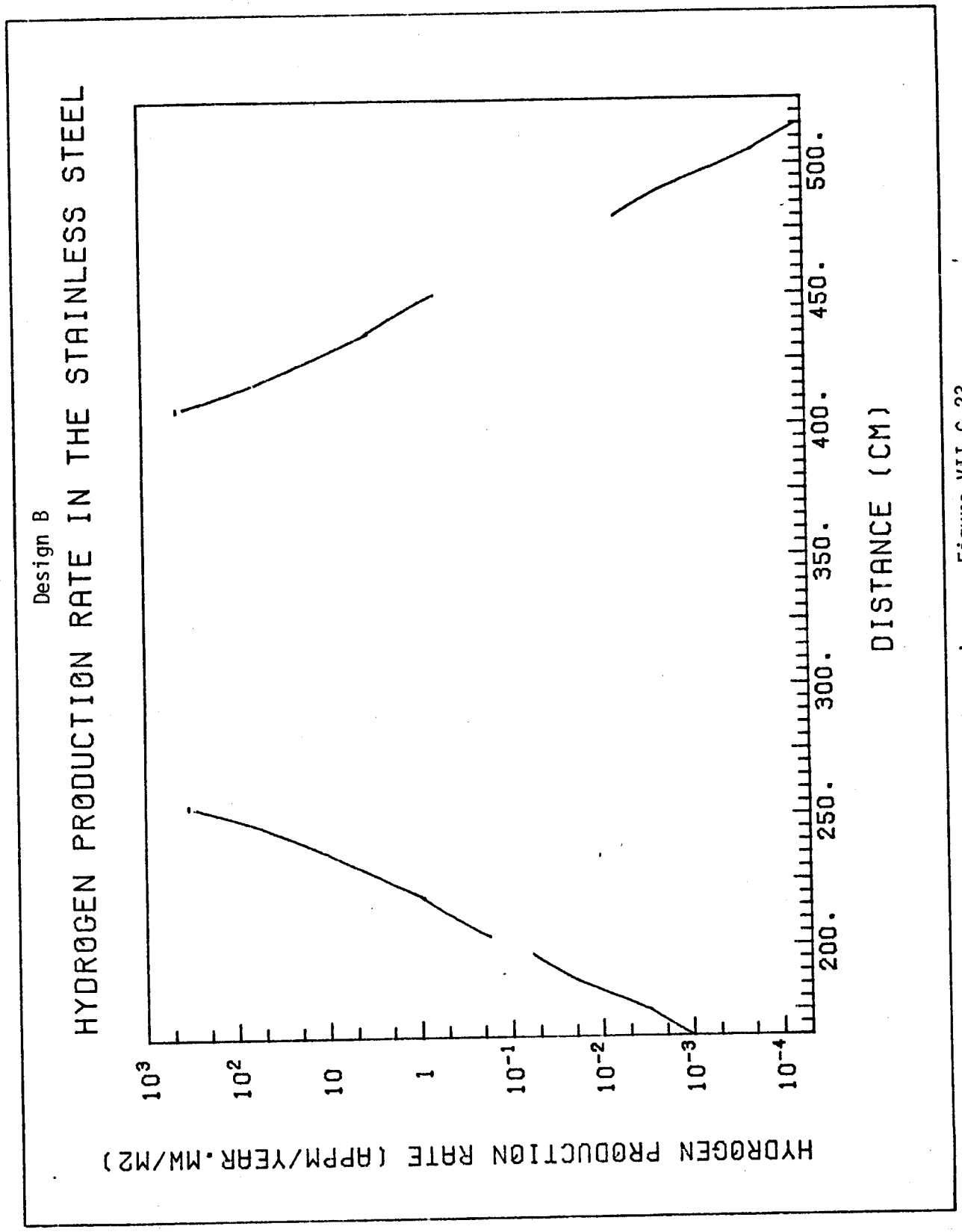

Figure VII-C-23

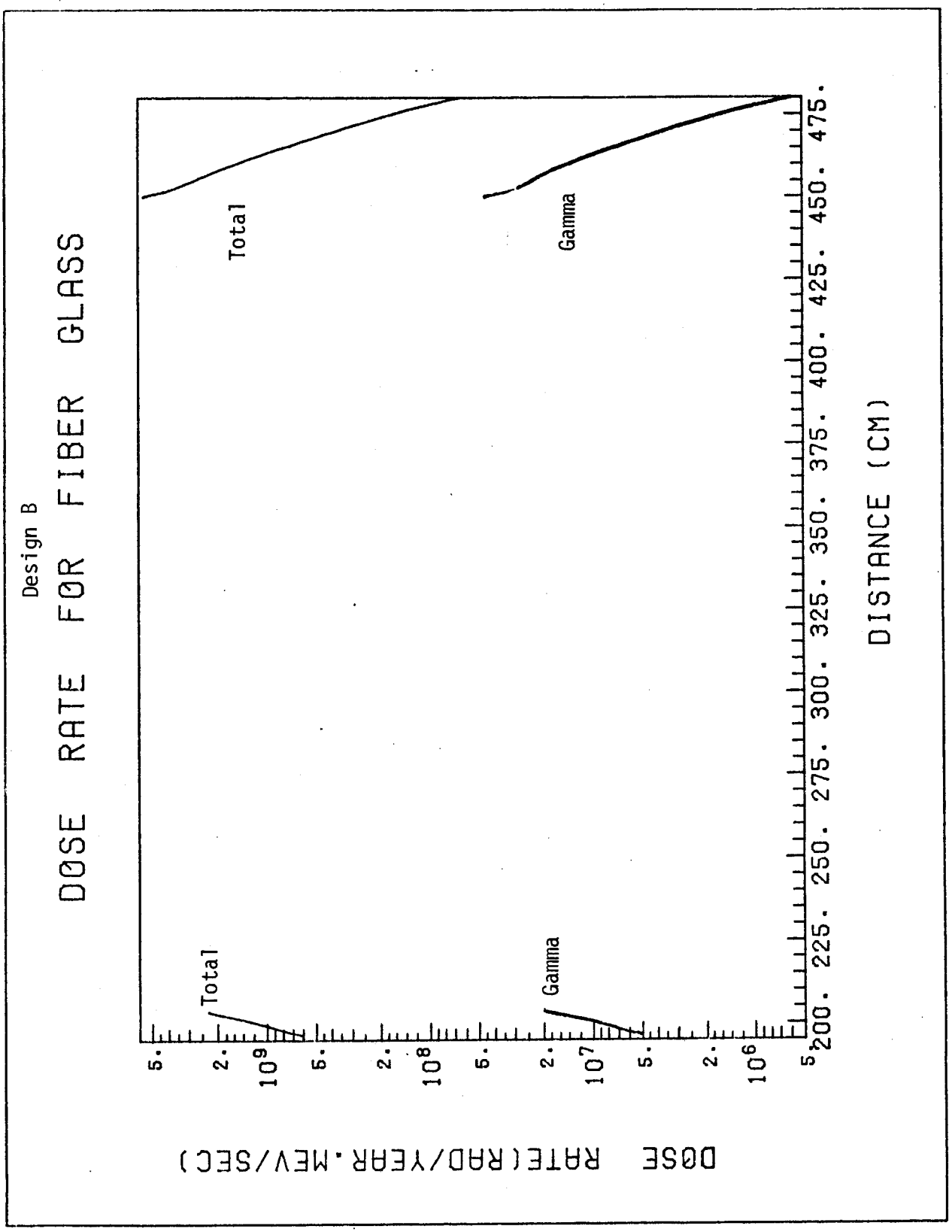

Figure VII-C-24

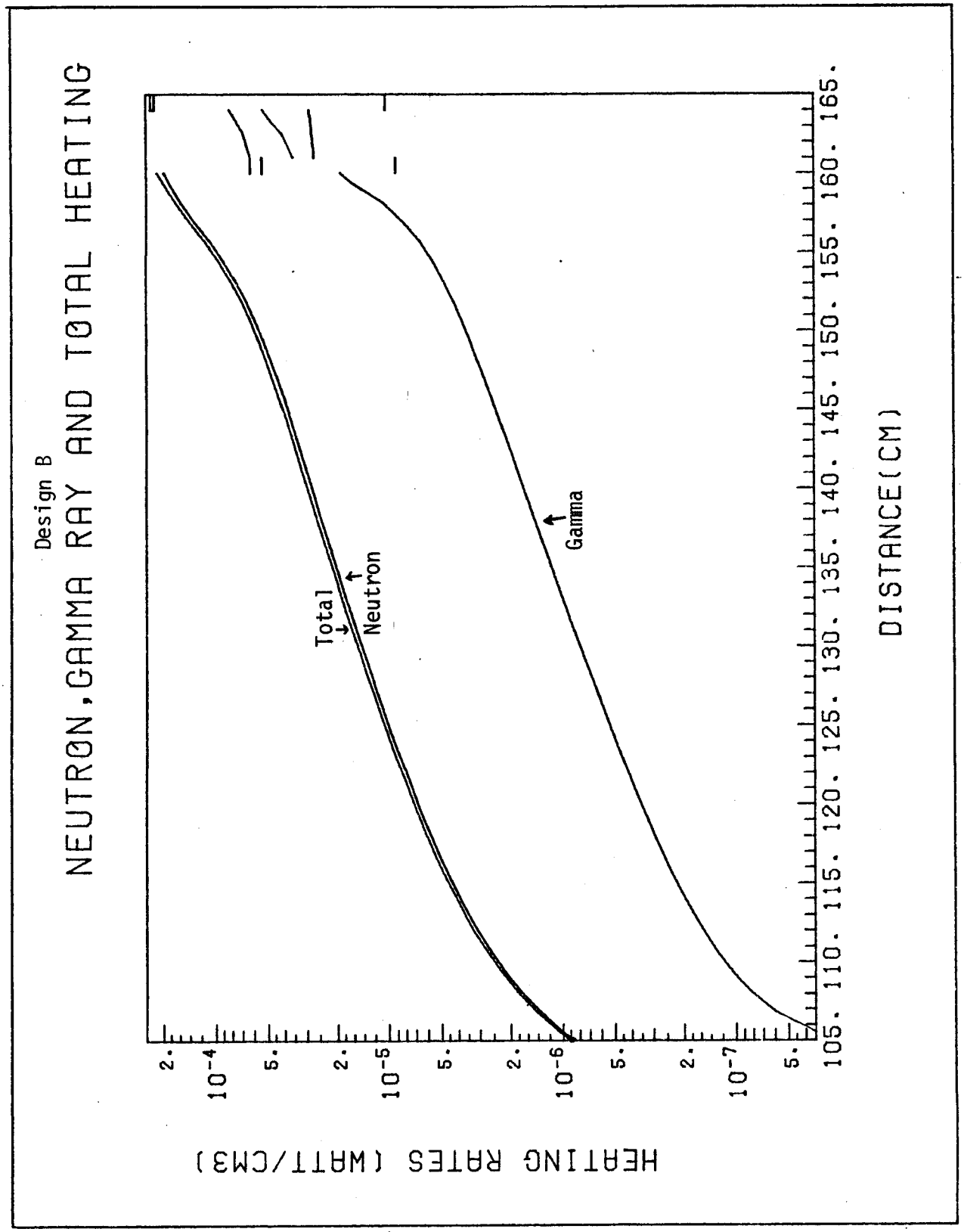

Figure VII-C-25

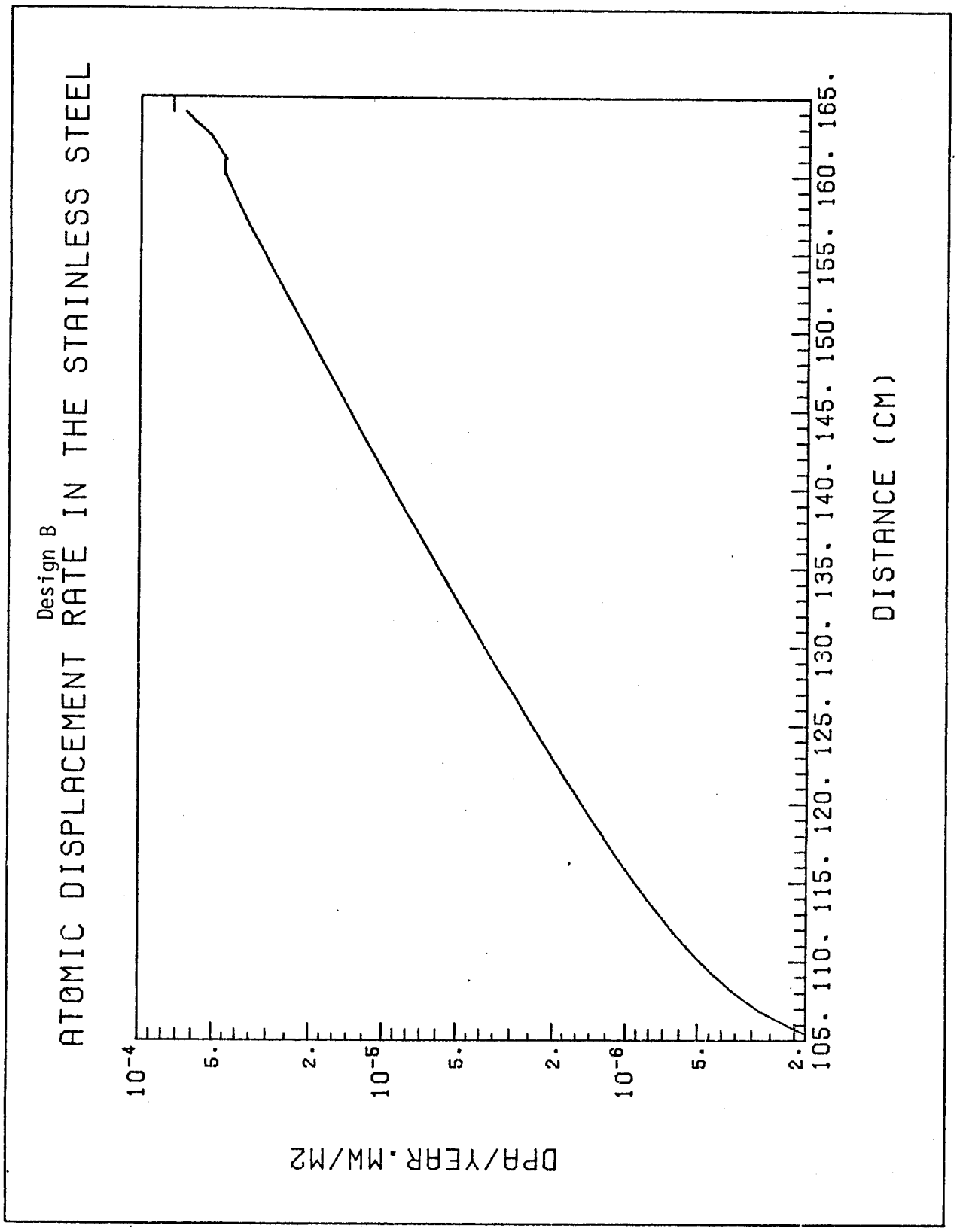

Figure VII-C-26

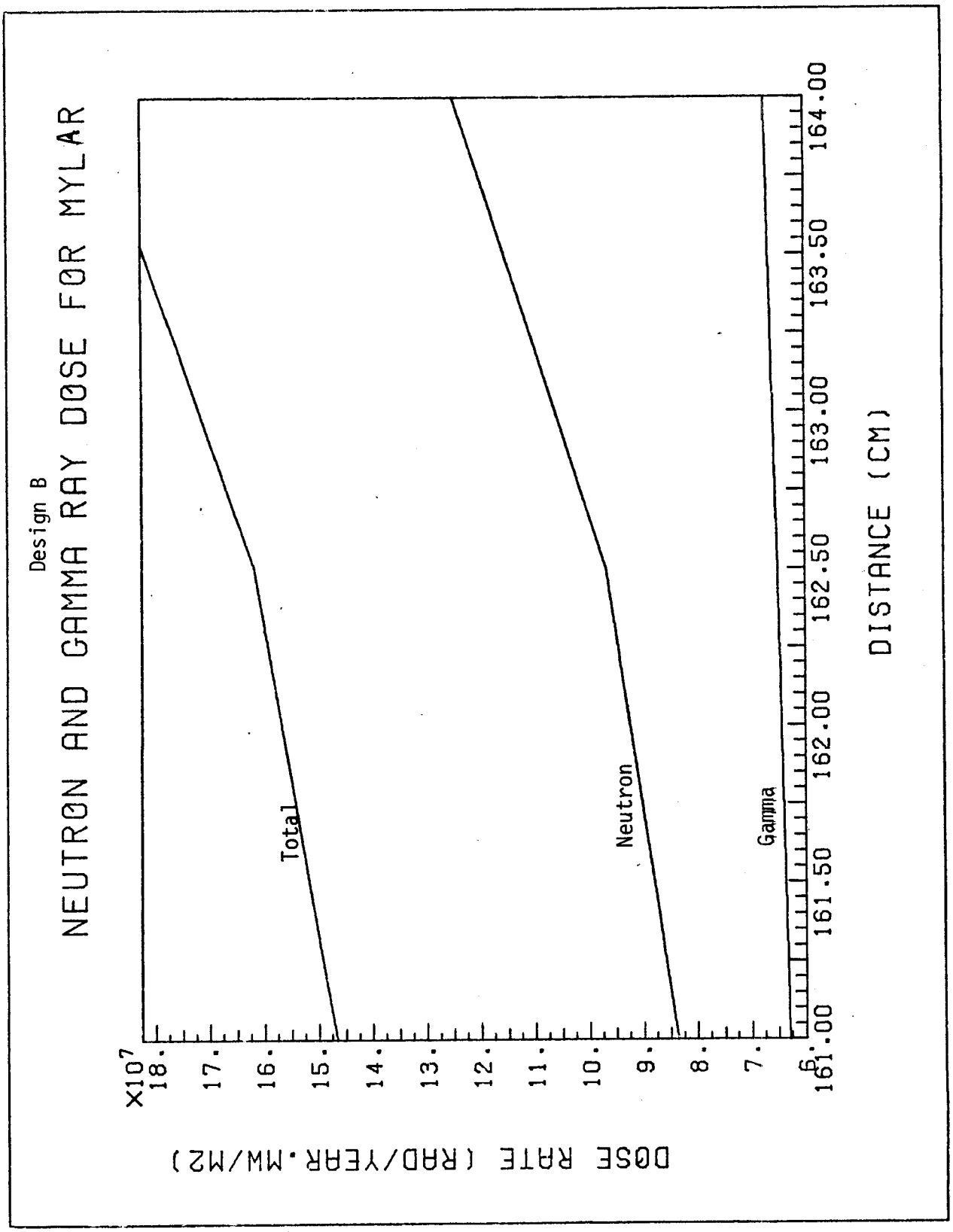

Figure VII-C-27

The total heating rate in the first wall of design B is a little higher than for the first two designs. The difference in the heating rates is related to the gamma energy production and attenuation. The stainless steel generates more gamma energy and attenuates it less when compared to tungsten, thus allowing a larger gamma energy source for the first wall. On the other hand, the high percentage of water in the first wall minimizes the effect of the gamma heating. Figures VII-C-1, 2, 10, 11, 19, and 20 show the total heating as a function of the major radius. The total heating rates in the first few centimeters behind the first wall for the basis design and design A are larger than the correponding value for design B due to the high gamma attenuation of the tungsten.

The total heating in the vertical field coils is minimized by using two zones of lead and boron carbide around each coil. The lead is used to reduce the gamma source from the heavy materials which reaches the coils. The boron is required to absorb the low energy neutrons since the neutron kerma factor in copper is very high at low neutron energy.

Figures VII-C-3, 4, 5, 12, 13, 14, 21, 22, and 23 show the atomic displacement, helium production and hydrogen production rates for the stainless steel structure. The comparison between these three designs shows the effect of the tungsten is to reduce the nuclear damage in the structural material by a factor of 2 to 10. This is required to increase the lifetime of the structure and reduce the radioactivity level in the magnet structure. Figures VII-C-6, 9, 15, 18, 24 and 27 show the dose rate for the insulators used for the toroidal field magnet and the vertical field coils. The tungsten has the effect of lowering the dose by one order of magnitude compared to stainless steel in design B. Figures VII-C-7, 16 and 25 show the total heating in the toroidal field magnet. The refrigeration power required for the basic design is about one order less than the requirement for design B which represents a saving in the cost and operating power of the cryogenic system.

VII-D. Two-Dimensional Analysis

Greater attention was given to two-dimensional studies than in our earlier work to check the effects of blanket and shield penetrations and flux distributions in experimental zones. The calculations were carried out with a modified version of the DOT III program using the same data as in the ANISN calculations for the one-dimensional models and the S_6-P_3 approximation.

The calculations are done for only a part of the reactor at a time to retain reasonable geometric detail with manageable memory and computing requirements. There are five regions which overlap to relate them in the different calculations which are all carried out in R-Z geometry. Calculations labeled "A" cover a region from the midplane to two meters above the plane and from a major radius 2.05 meters to 4.65 meters. The zone

map for this calculation is shown by Figure VII-D-1. The upper and lower halves of the reactor are not identical but the differences are not expected to prevent the horizontal midplane from being a reflecting boundary to a very good approximation. Thus the base plane of the figure is treated as a reflecting boundary. The remaining boundaries are handled with albedo conditions, these having been obtained from an earlier calculation covering more of the reactor but using a cruder representation of it. The central region of Figure VII-D-1, i.e., below the fifth and sixth lines emerging vertically from the base is the plasma region. The first wall is outlined by the fourth and seventh lines starting vertically from the midplane. Other zones can be recognized by comparing this Figure with Figure VII-A-1. The region behind the first wall on the right from about 0.2 meters is the test section and is of great importance to potential users. It was treated as containing stainless steel with a density factor of 0.4 as roughly approximating an experimenters samples and apparatus.

Calculations denoted as zone B extend over the same radial interval and from the midplane to two meters below it, shown as a mirror image in Figure VII-D-2. The beam port is at the lower right side. The boundary conditions employed are similar to those employed in part A.

Part C overlaps with but extends above part A and the computer model of the geometry is shown in Figure VII-D-3. Radially the same interval as in the previous two parts is covered, but vertically it extends from 1.33 meters to about 3 meters above the midplane. The top three boundaries are treated using albedo conditions obtained as in the earlier calculations. The lower boundary uses a surface source condition based on the angular flux at that value of the Z coordinate in the calculations for part A. Part CM covers the same reactor region as C but for modified divertor slots. The location of the modified slots is shown on Figure VII-D-4 and the computer model for this case appears in Figure VII-D-5. Above part C, part D covers the interval from 2.7 meters to about 5 meters above the midplane for the same radial interval as shown in Figure VII-D-6. The lower boundary surface source condition is obtained from the angular flux results for part C. The remaining boundaries are again treated by albedo factors.

Finally, the radiation streaming down the neutral beam port is based on an R-Z geometry calculation with the Z-axis along the axis of the port. The radial variable moves first through the vacuum zone, then through the port shield and finally into another void region outside the shield. The radiation enters from the reaction chamber at Z=0 into the port and a surface source is used to impose this while using a reflecting condition on this boundary. This does not properly represent the blanket and shield contribution outside the shield but the attenuation of the flux by the main blanket and shield is so great, (energy flux attentuated 10^{-8}) that this represents the flux outside of and down the beam port.

The results of the calculations include the flux above 13.5 Mev, 0.12 Mev, and 0 Mev, i.e., essentially the uncollided, the fast, and the total fluxes. The number of displacements per atom per year (dpa rate), and the helium and hydrogen production rates (appm/yr) were also calculated. These contour plots are presented in Figures VII-D-7 through VII-D-33.

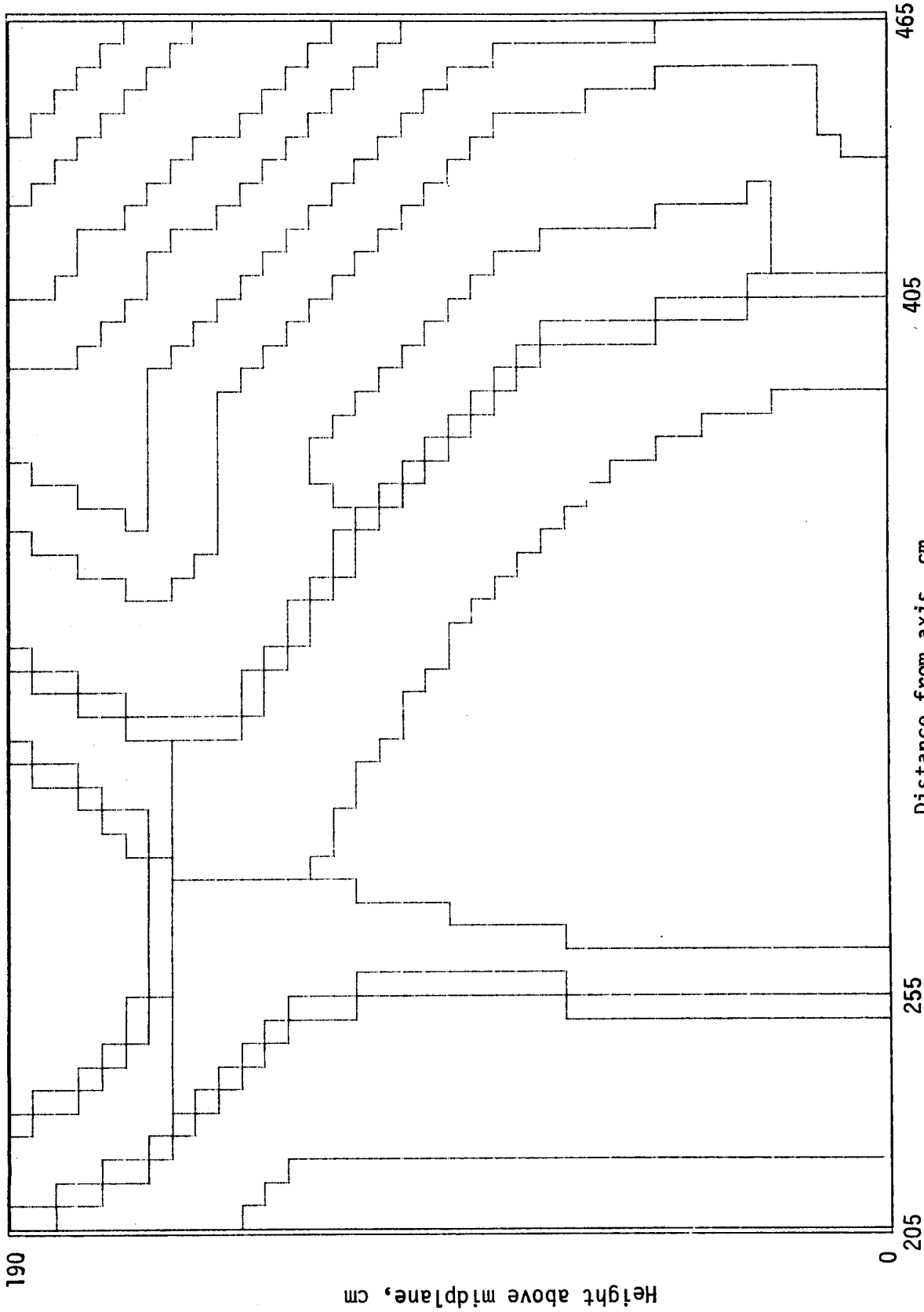

Figure VII-D-1

Computer Model for Reactor Part A

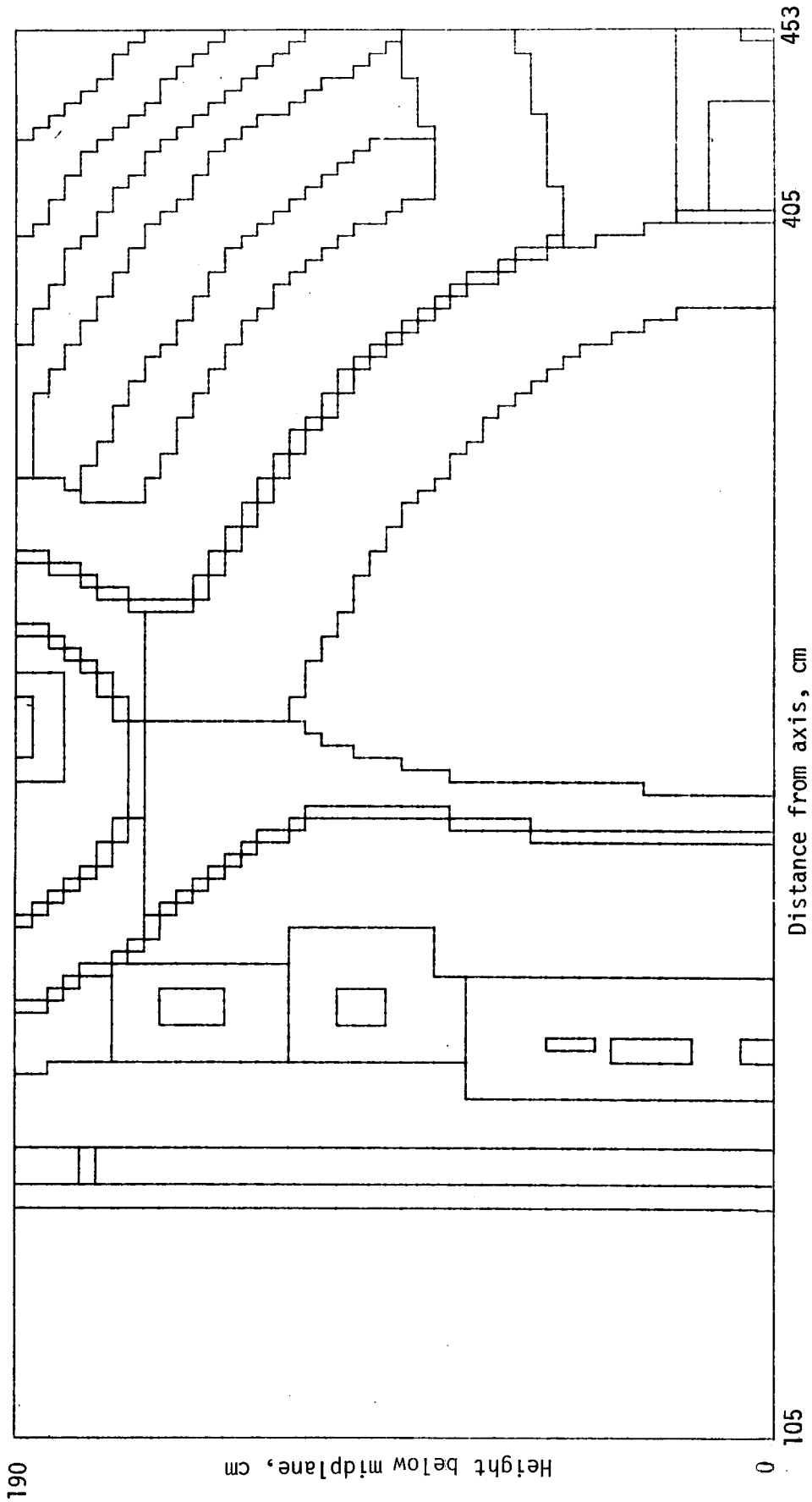

Figure VII-D-2
Reflection in the Horizontal Midplane
of the Computer Model of Reactor Part B

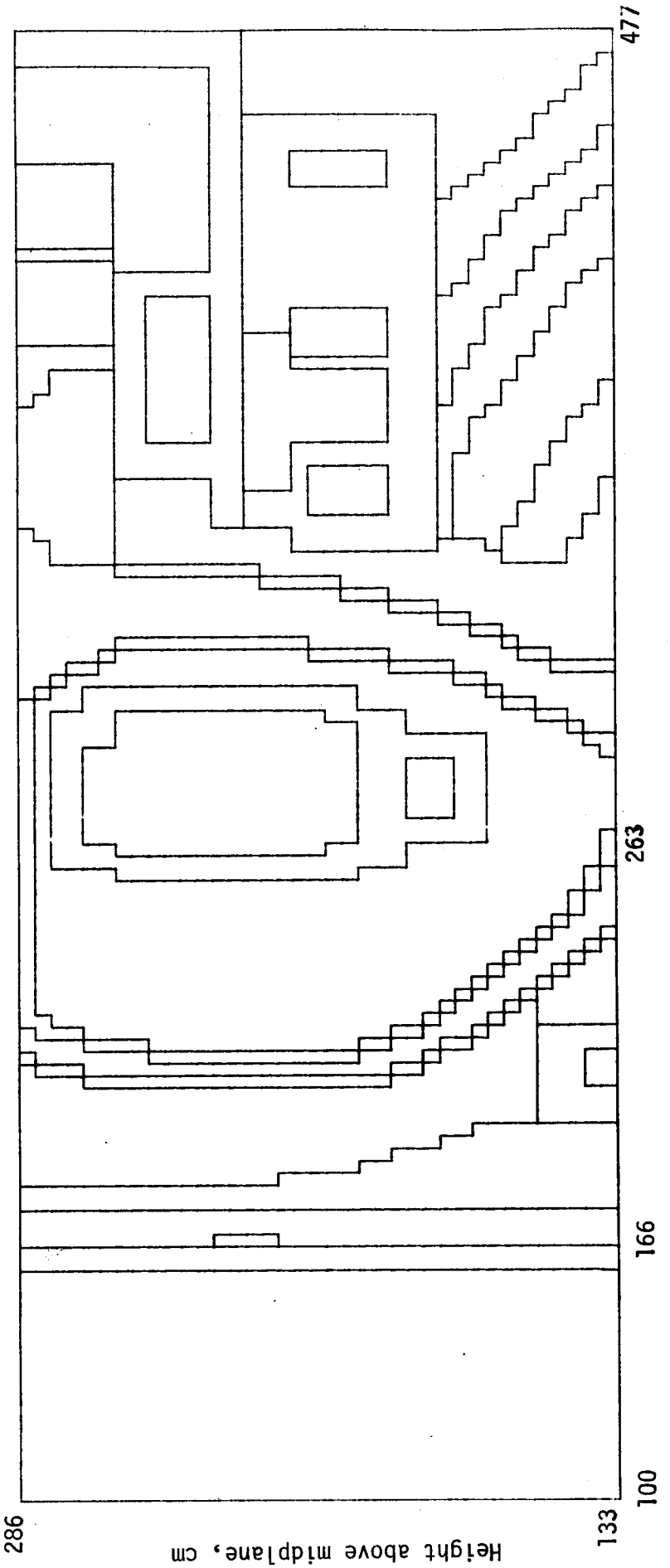

Figure VII-D-3
Calculational Model of Part C Located
Above and Overlapping with Part A

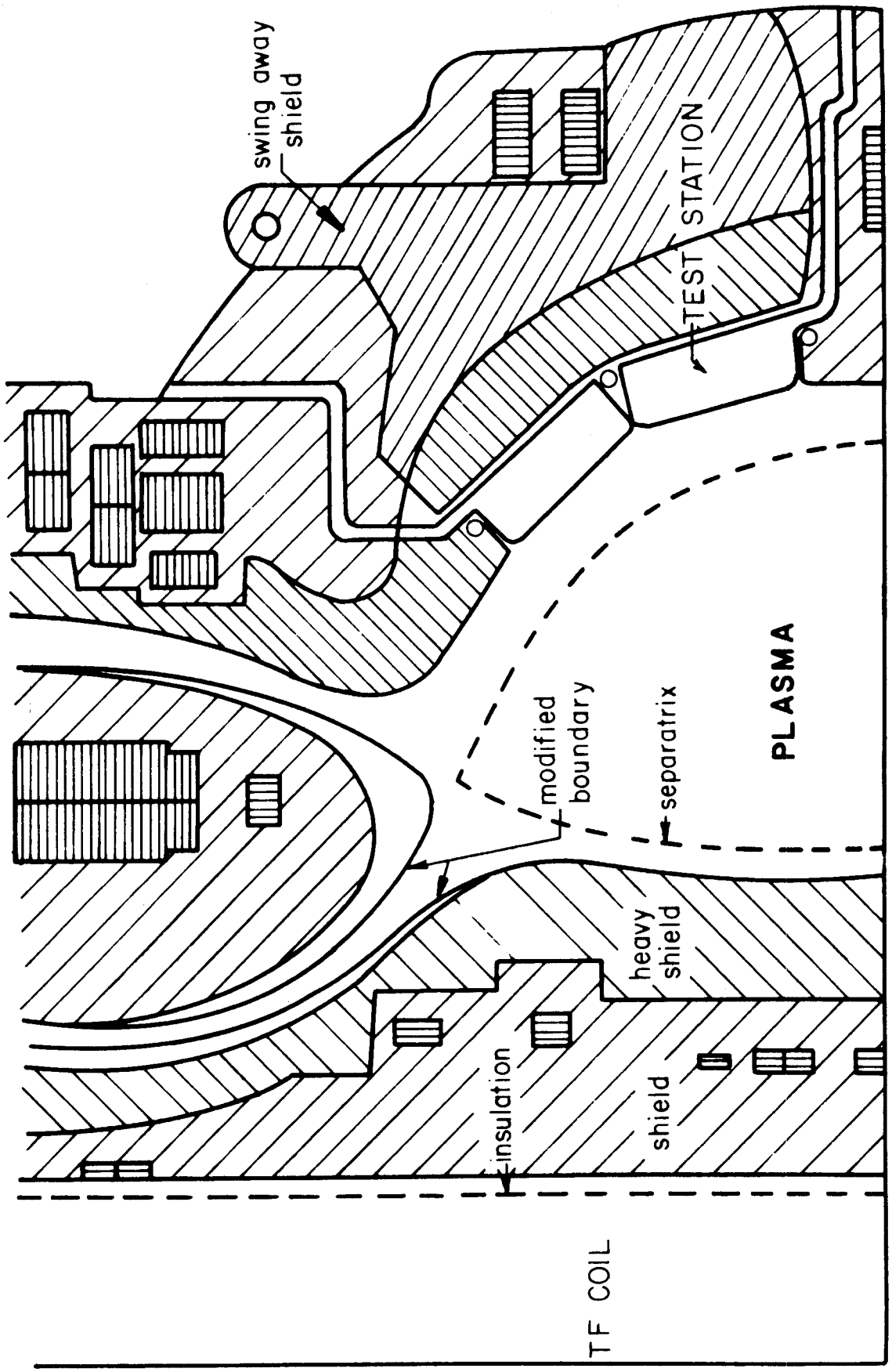

Fig VII-D-4 A schematic diagram of TETR showing modified divertor slots

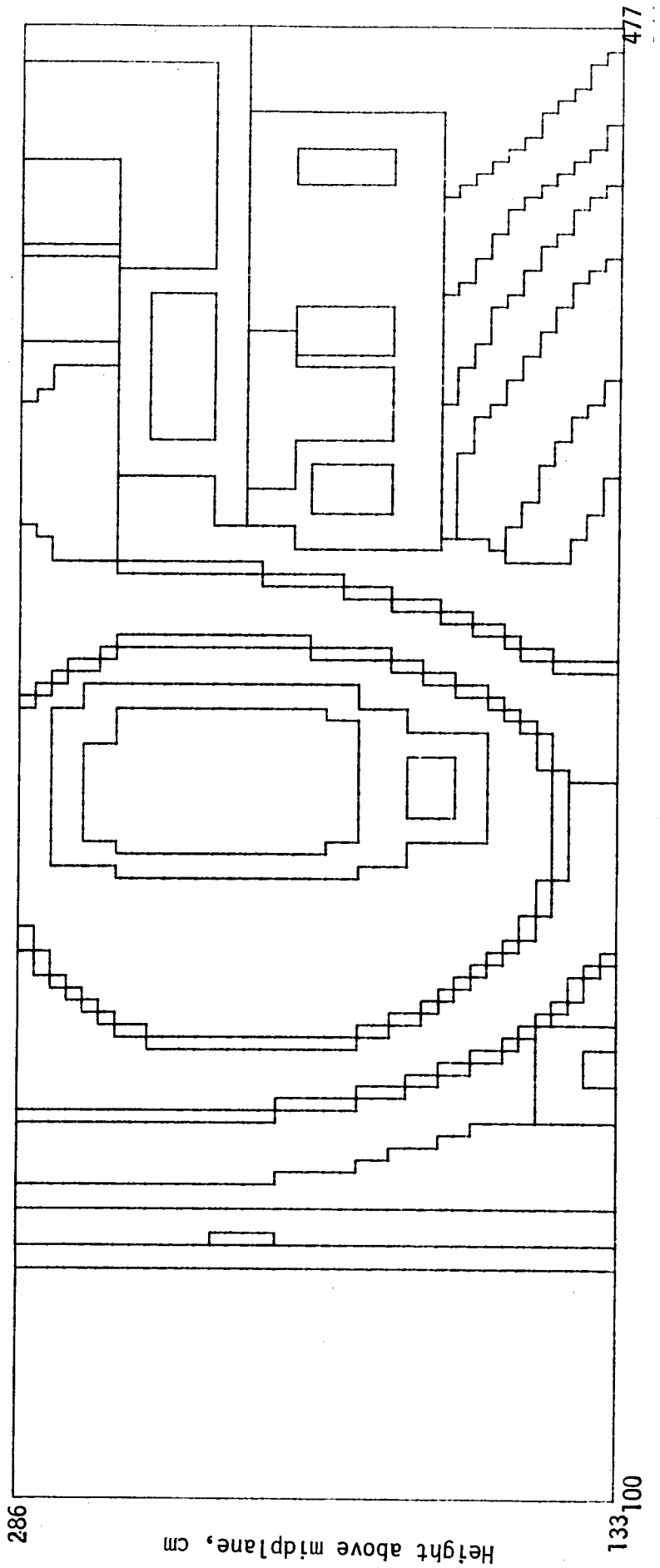

Figure VII-D-5
Calculational Model for Part CM

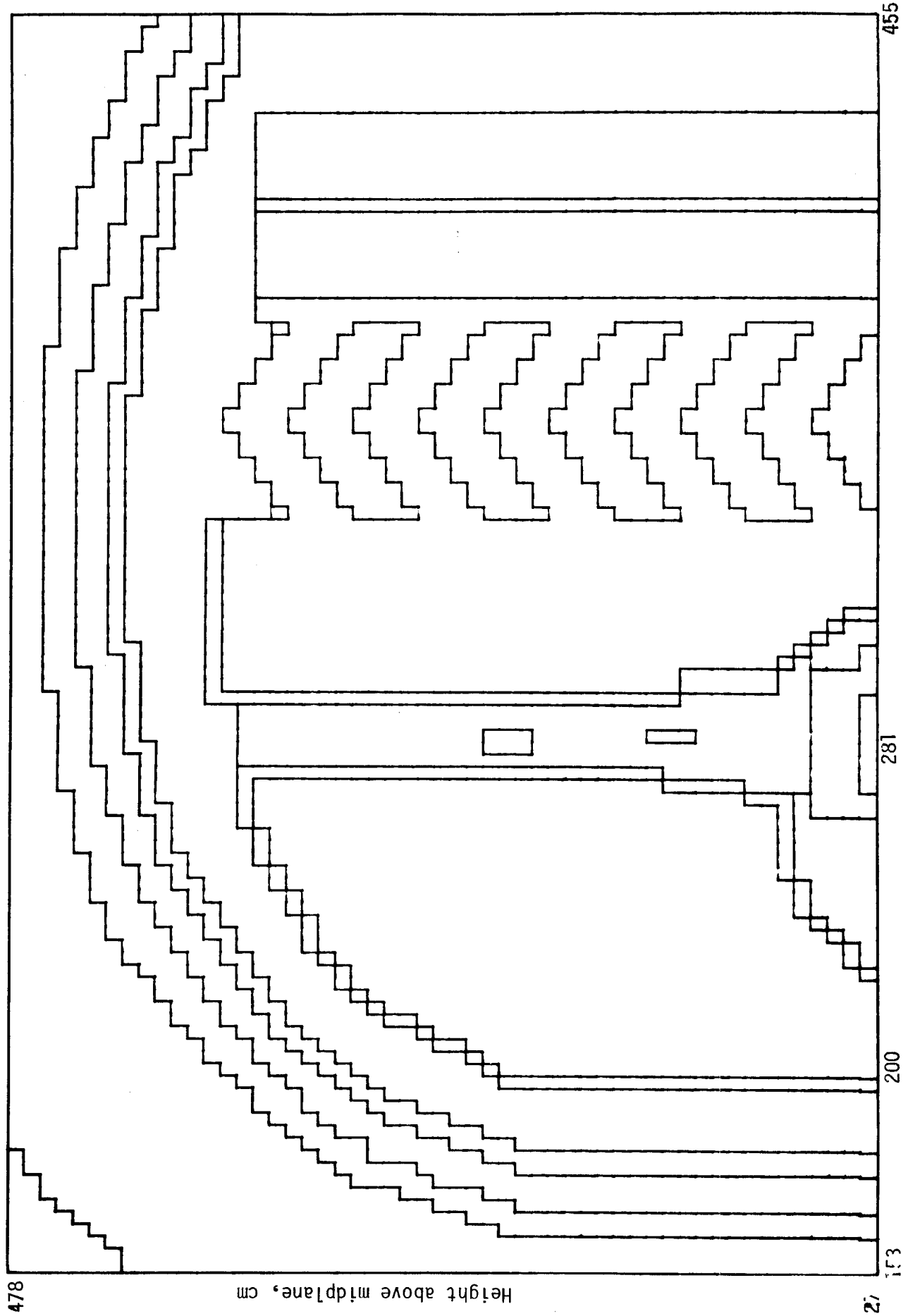

Figure VII-D-6
Calculational Model of Region Above Part C Referred to as Part D.

TETR NEUTRON FLUX PART A (E>13.5 MEV)

Figure VII-D-7

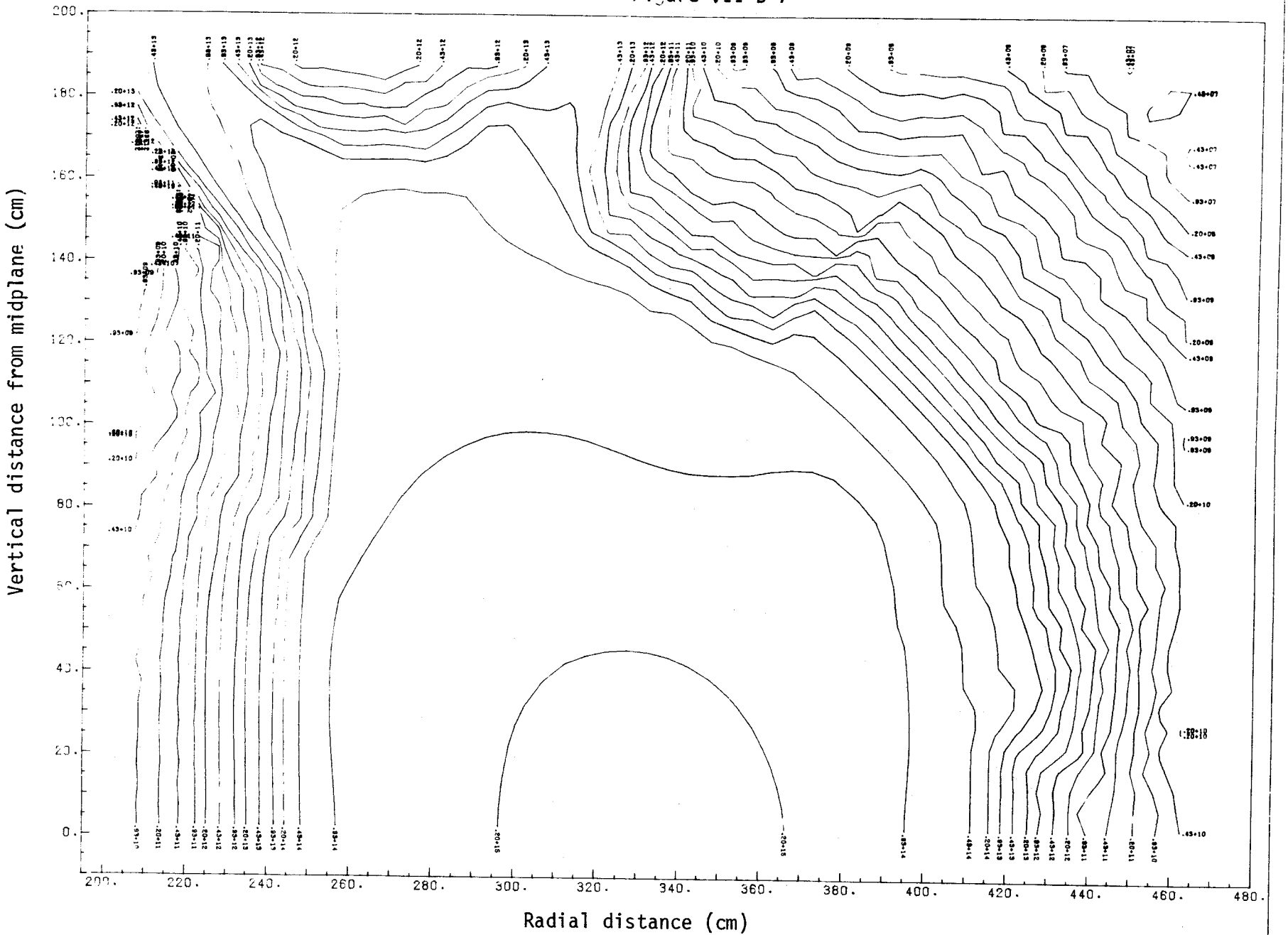

Figure VII-D-8

TETR NEUTRON FLUX PART A (E>0.12 MEV)

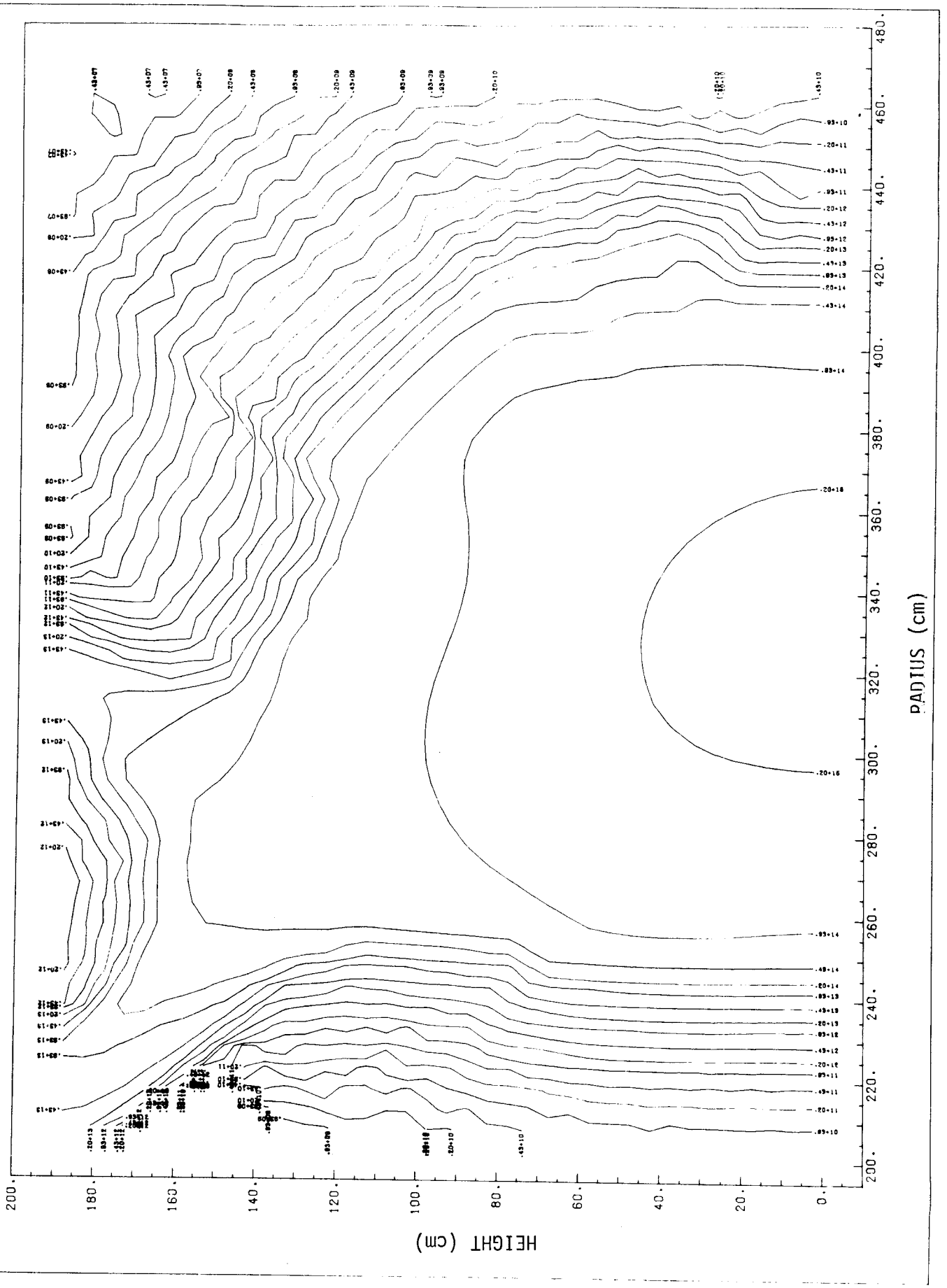

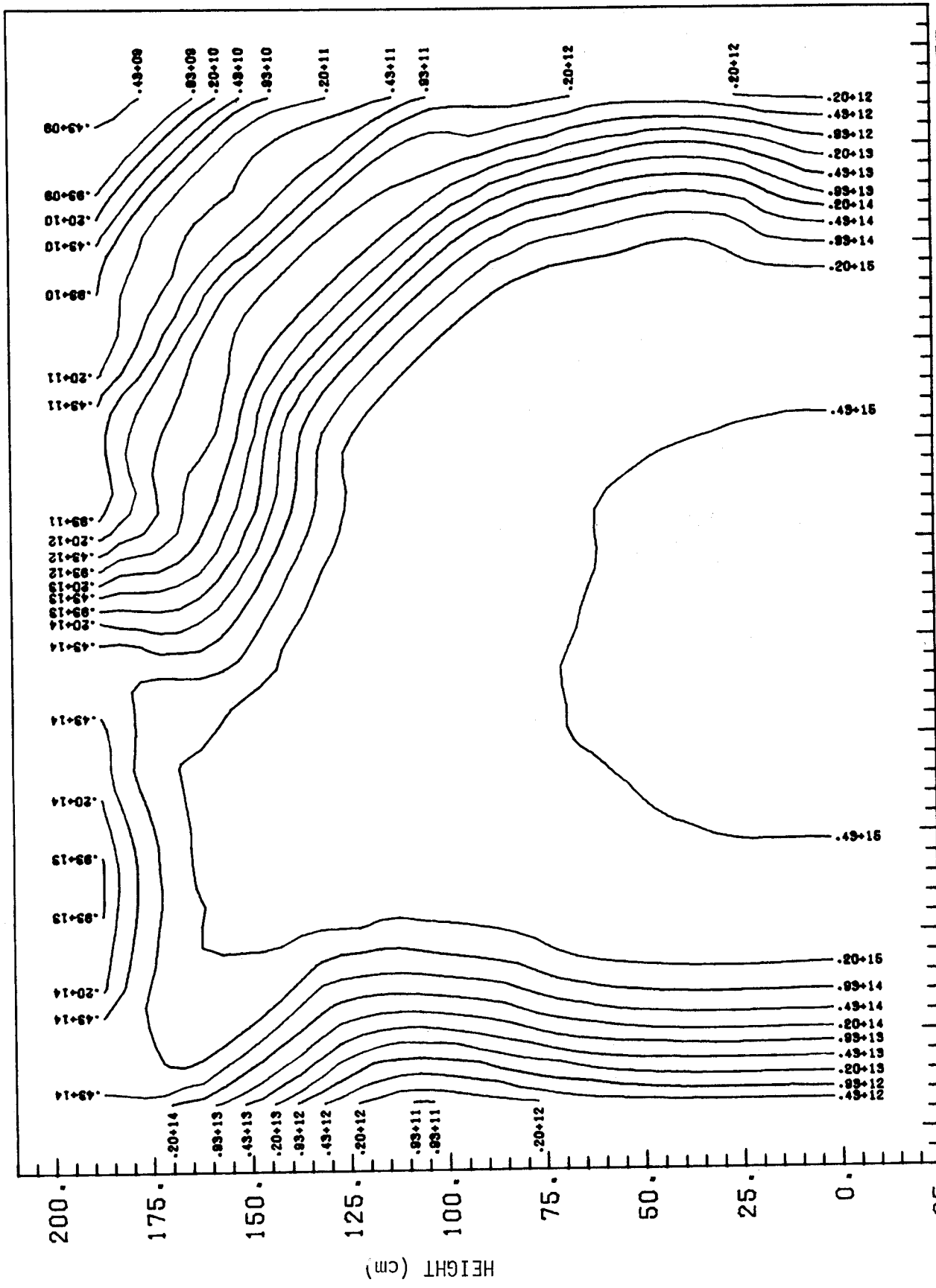

Figure VII-D-9 TETR NEUTRON FLUX PART A (E>0.0 MEV)

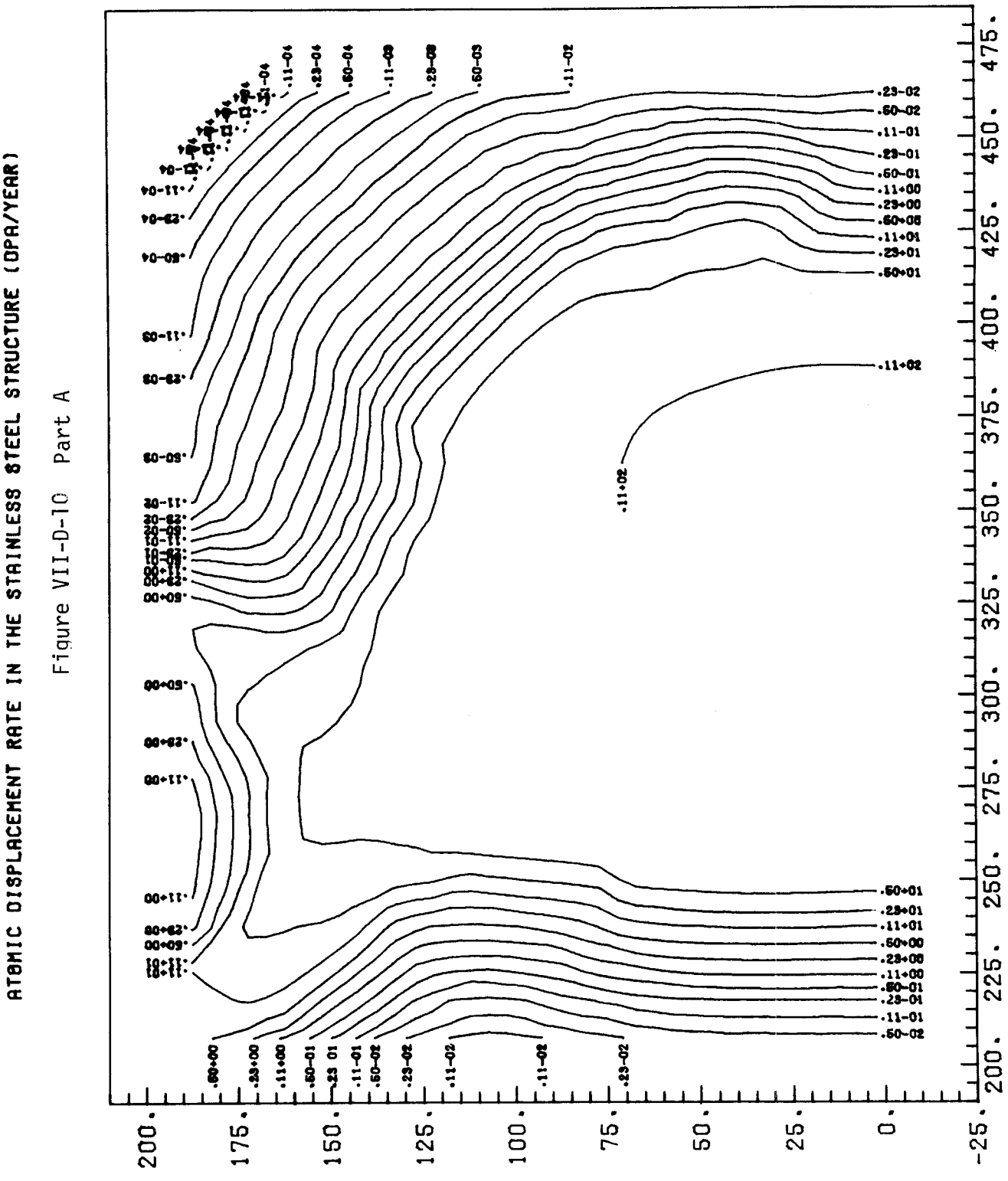

Figure VII-D-10 Part A

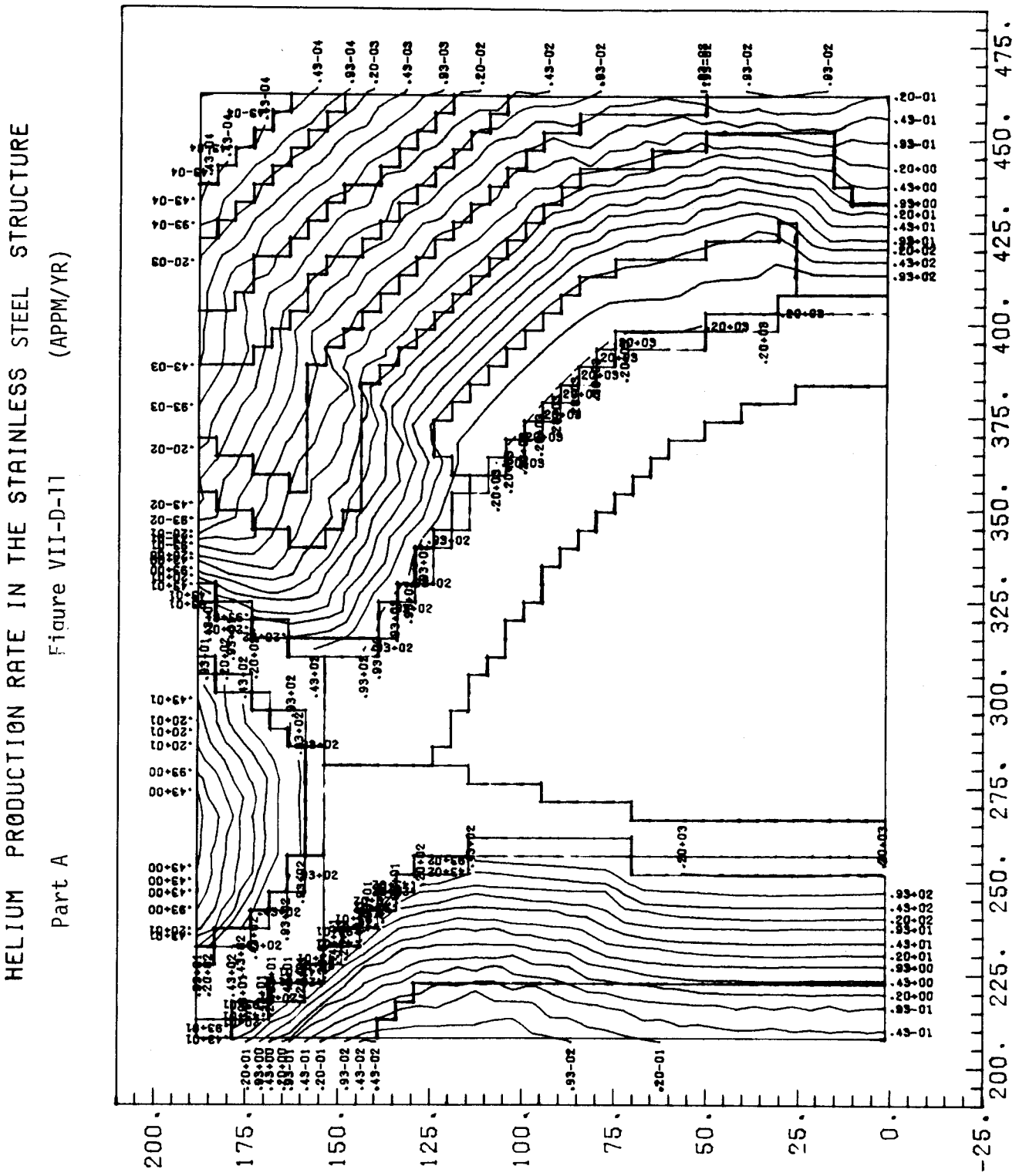
HELIUM PRODUCTION RATE IN THE STAINLESS STEEL STRUCTURE
Part A
Figure VII-D-11
(APPM/YR)
HEIGHT (CM)
RADIUS (CM)
200.
175.
150.
125.
100.
75.
50.
25.
0.
-25.
200.
225.
250.
275.
300.
325.
350.
375.
400.
425.
450.
475.

TETR NEUTRON FLUX PART B (E>13.5 MEV)

Figure VII-D-12

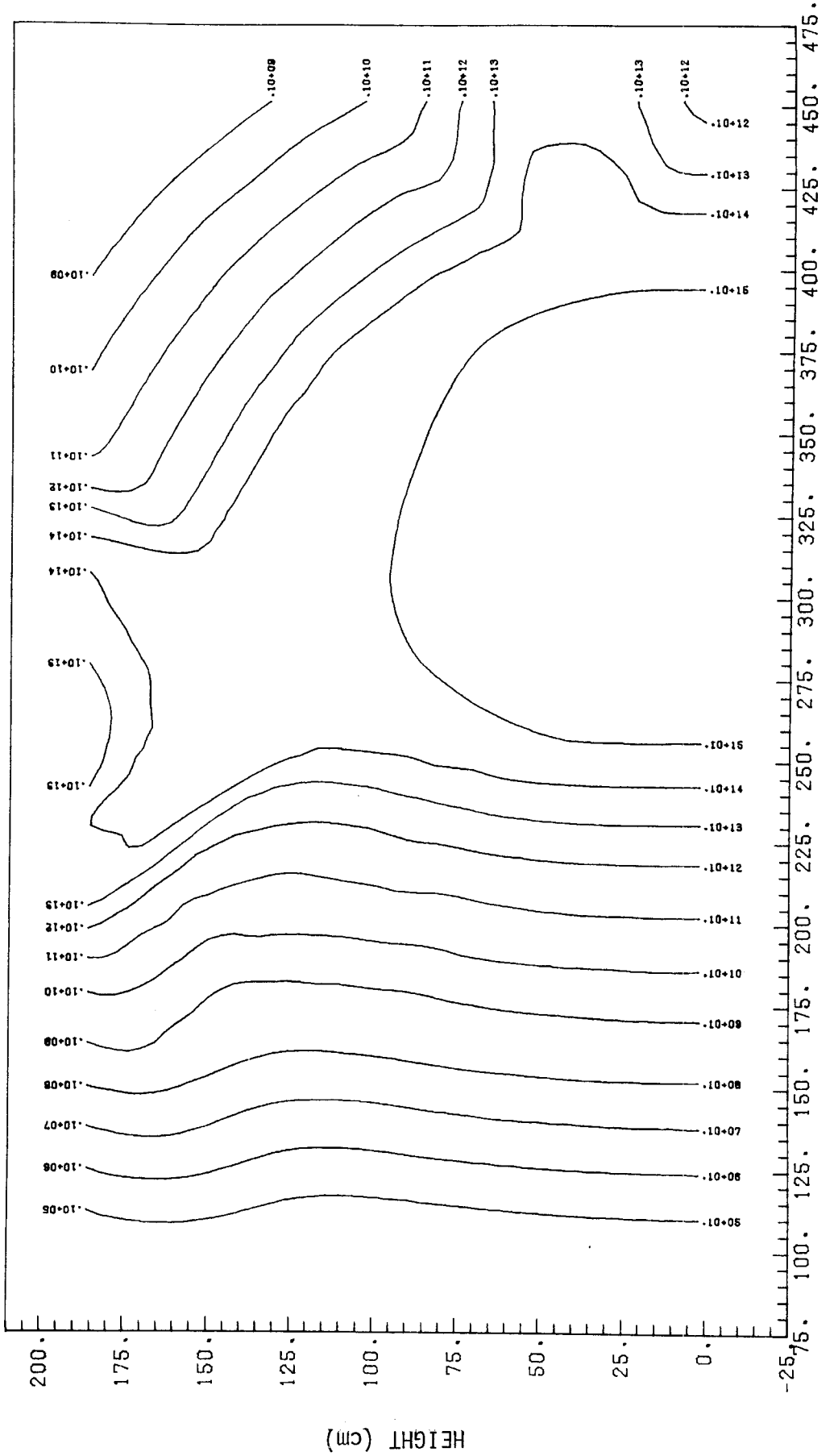

TETR NEUTRON FLUX PART B (E>0.12 MEV)

Figure VII-D-13

TETR NEUTRON FLUX PART B (E>0.0 MEV)

Figure VII-D-14

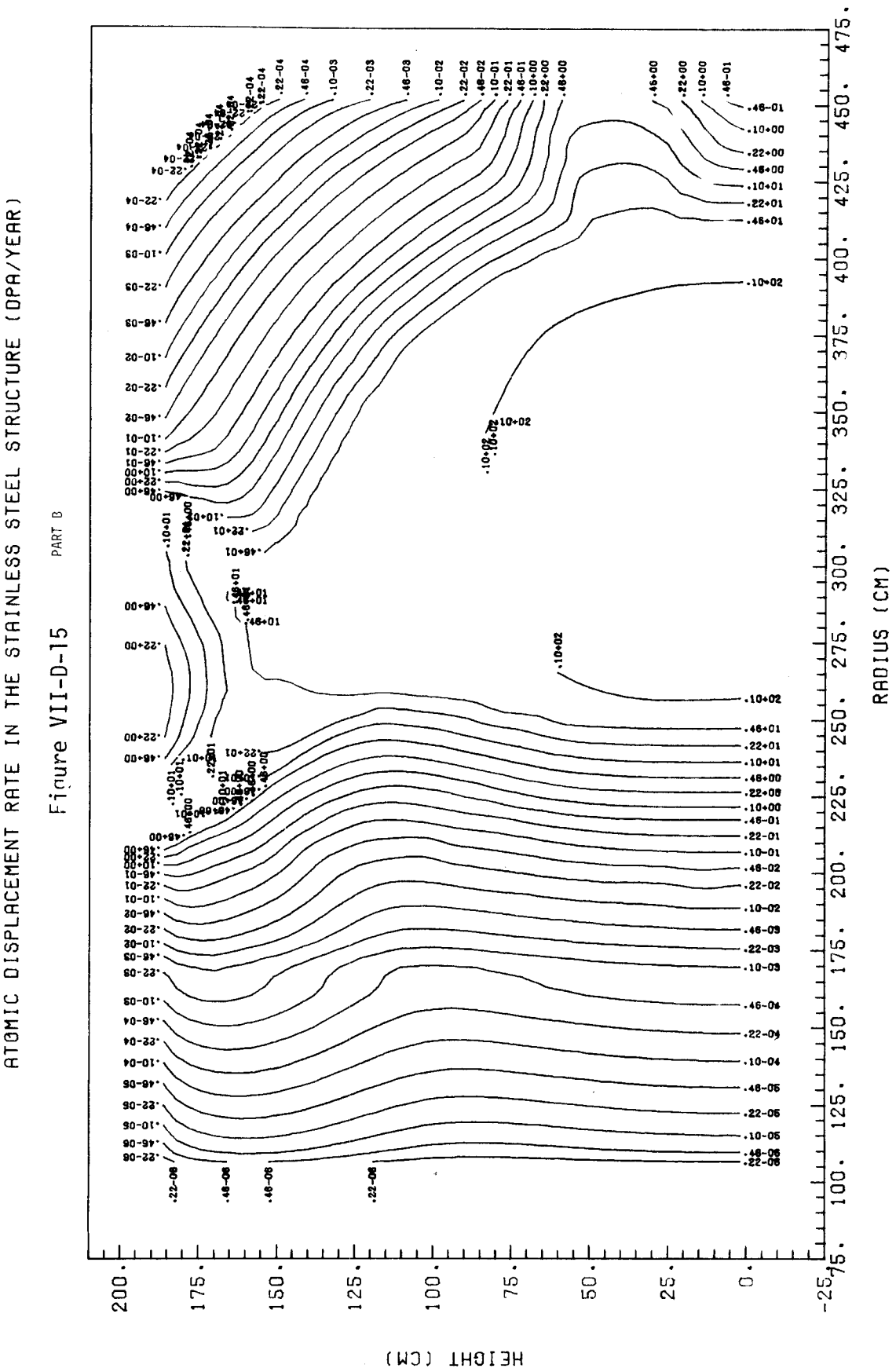

Figure VII-D-15 PART B

TETR NEUTRON FLUX PART C (E>13.5 MEV)

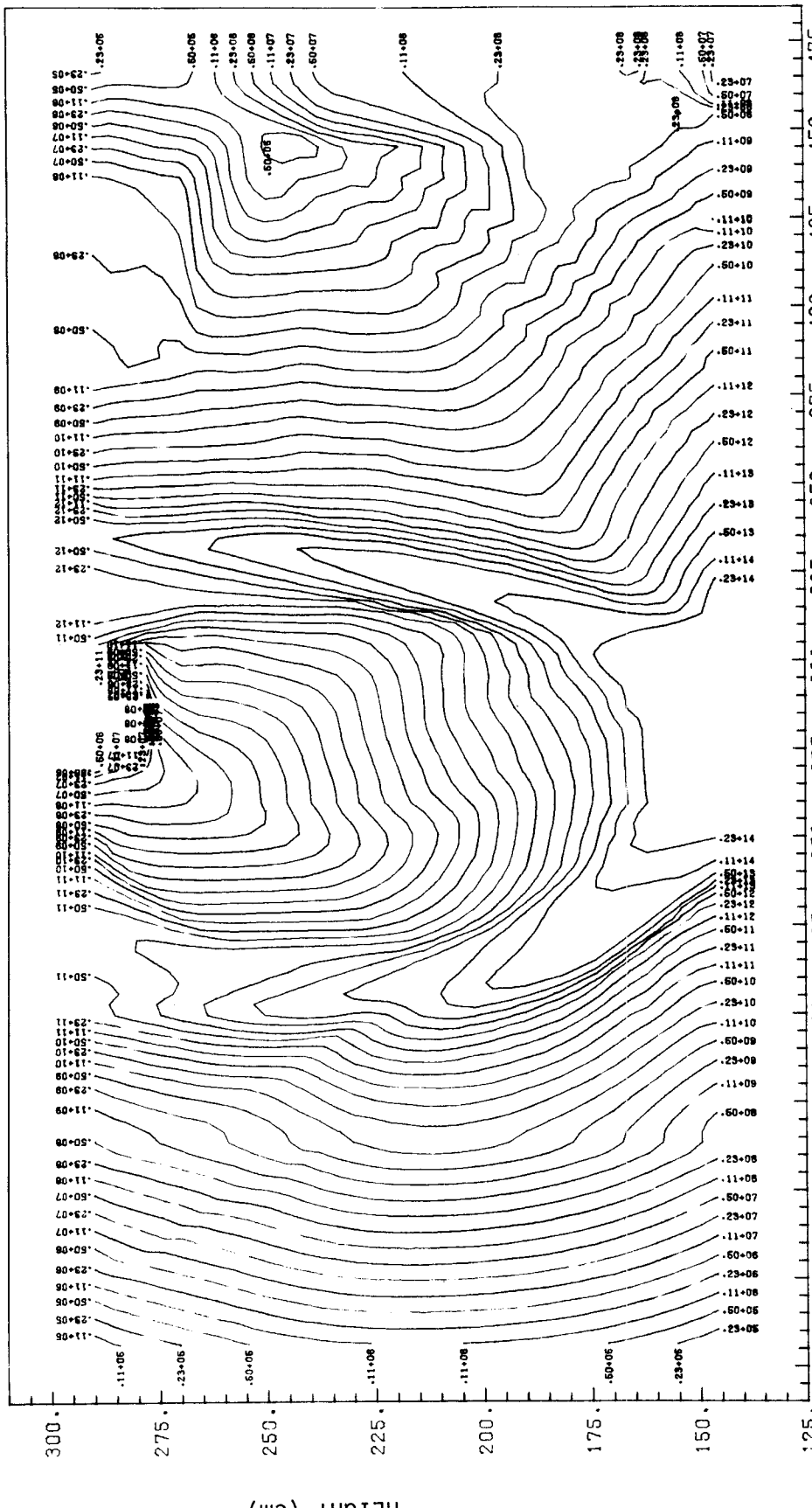

Figure VII-D-16

TETR NEUTRON FLUX PART C (E>0.12 MEV)

Figure VII-D-17

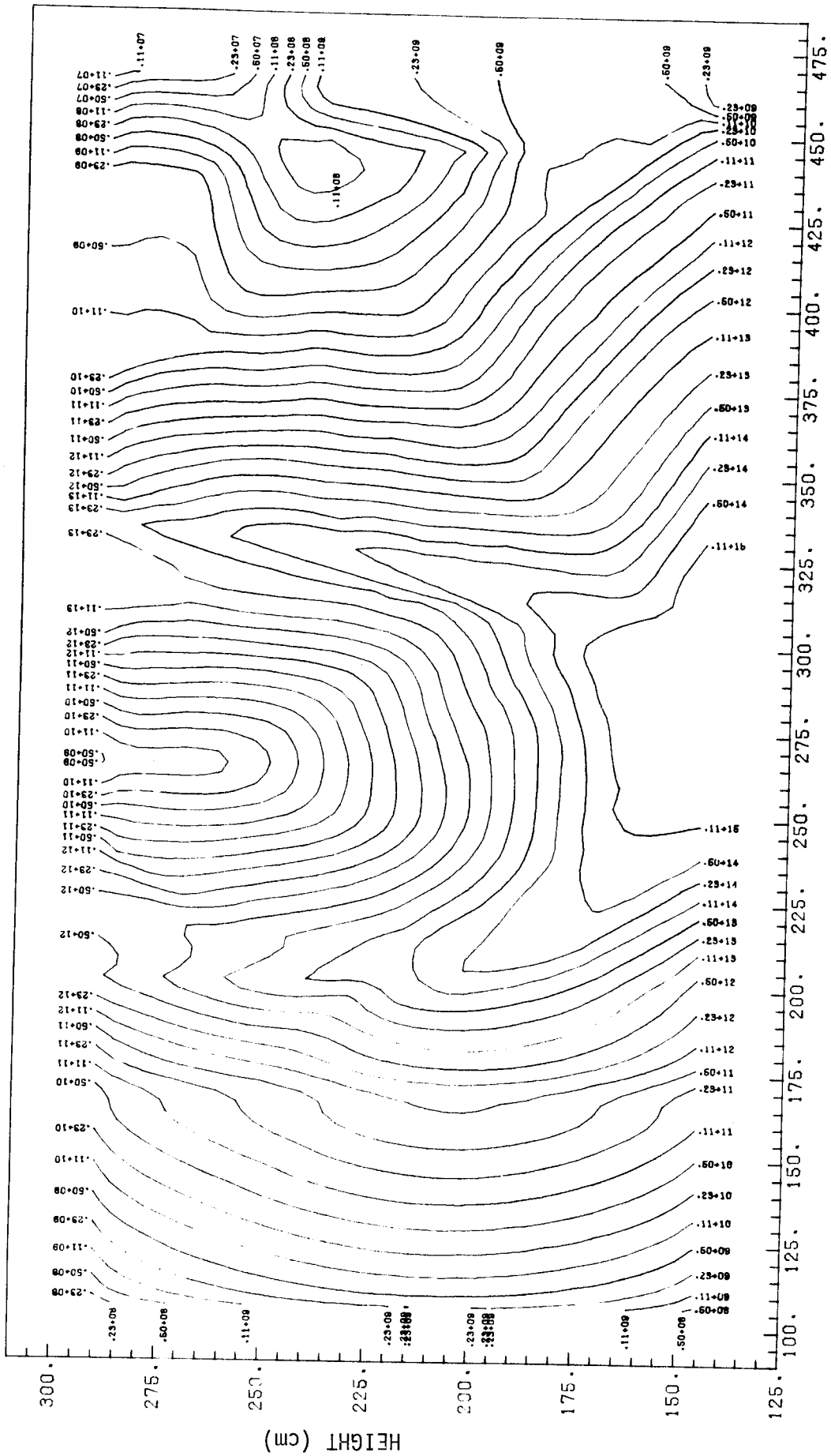

TETR NEUTRON FLUX PART C (E>0.0 MEV)

Figure VII-D-18

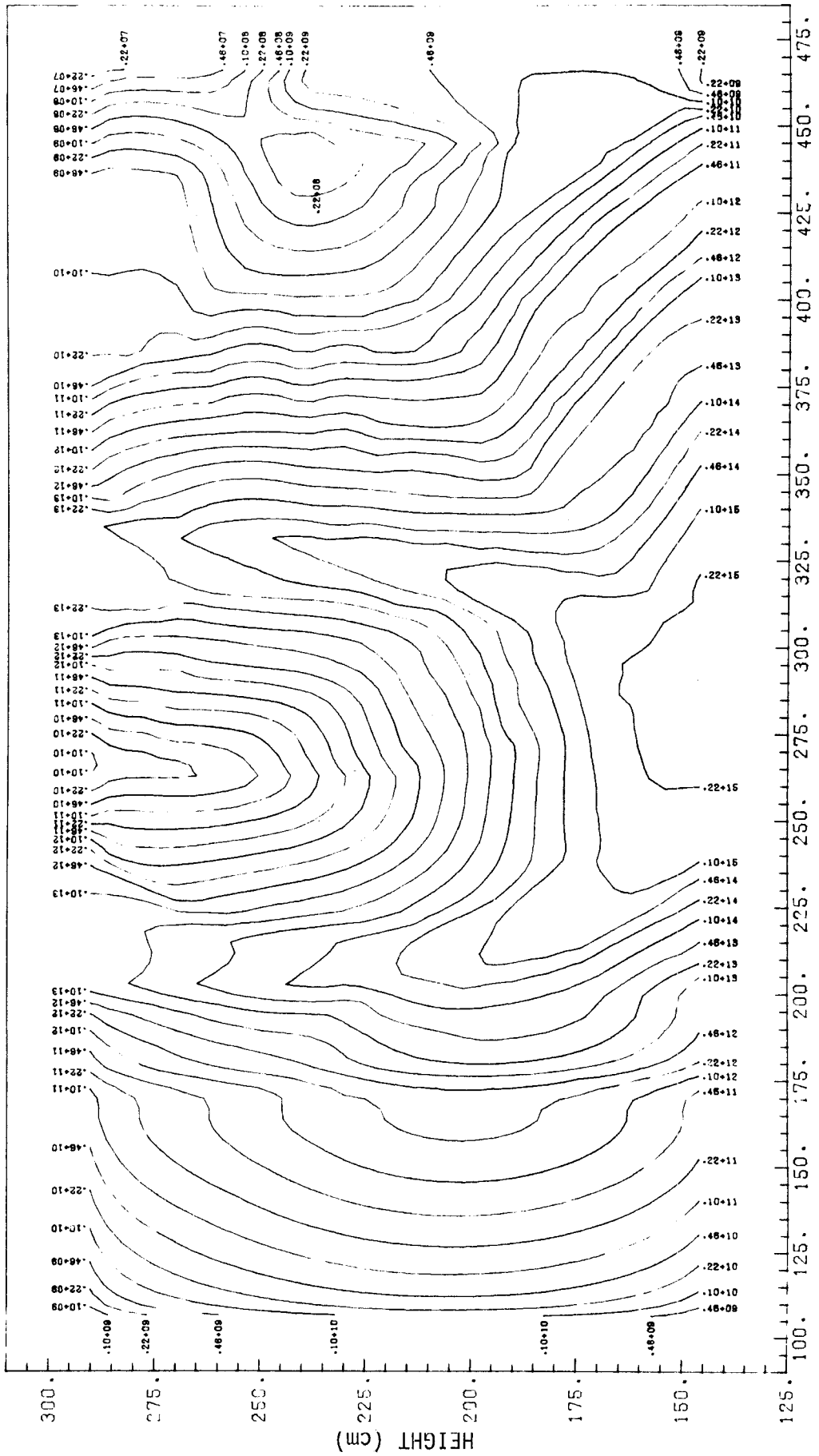

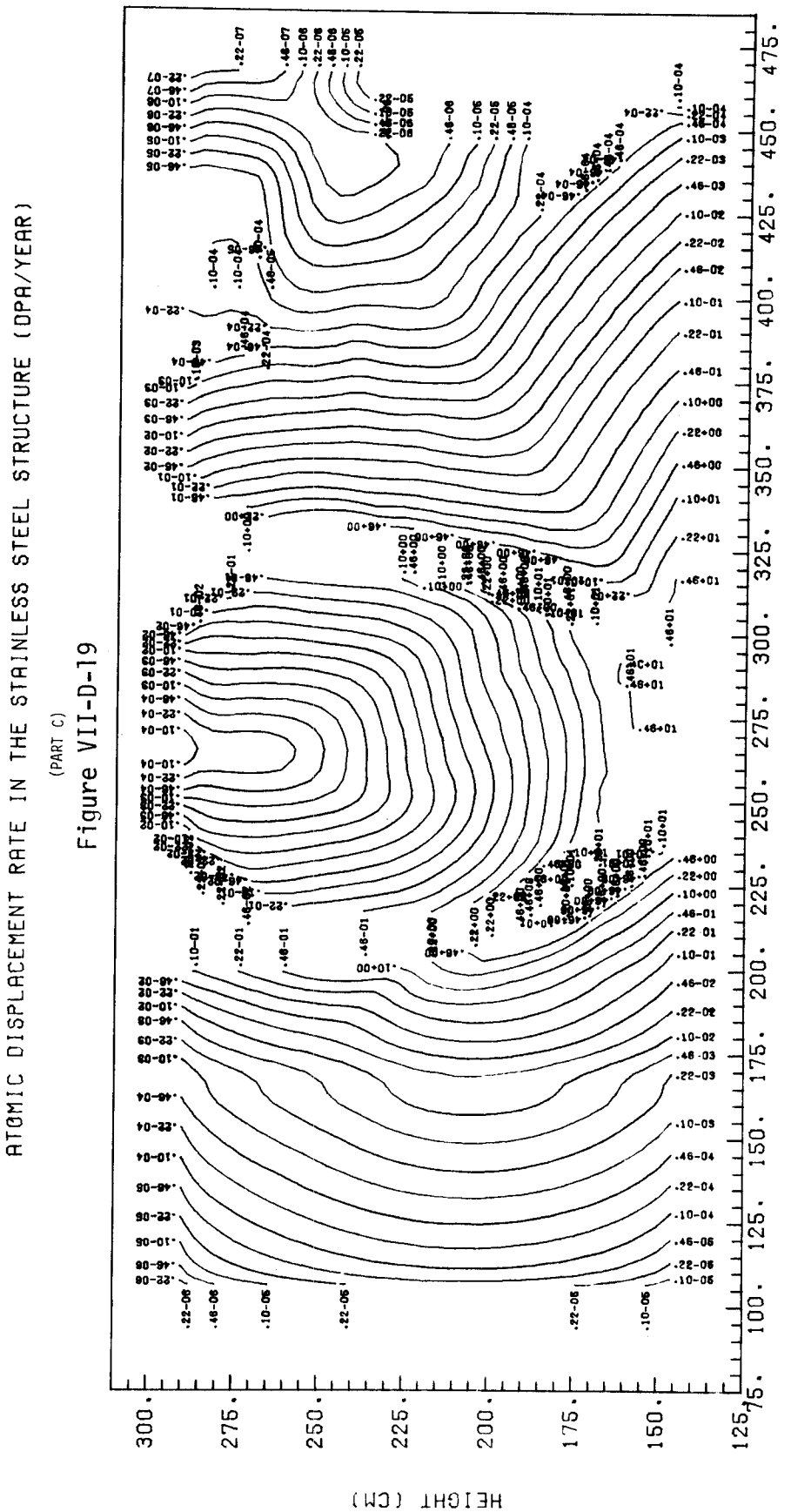

(PART C)

Figure VII-D-19

TETR NEUTRON FLUX PART CM (E>13.5 MEV)

Figure VII-D-20

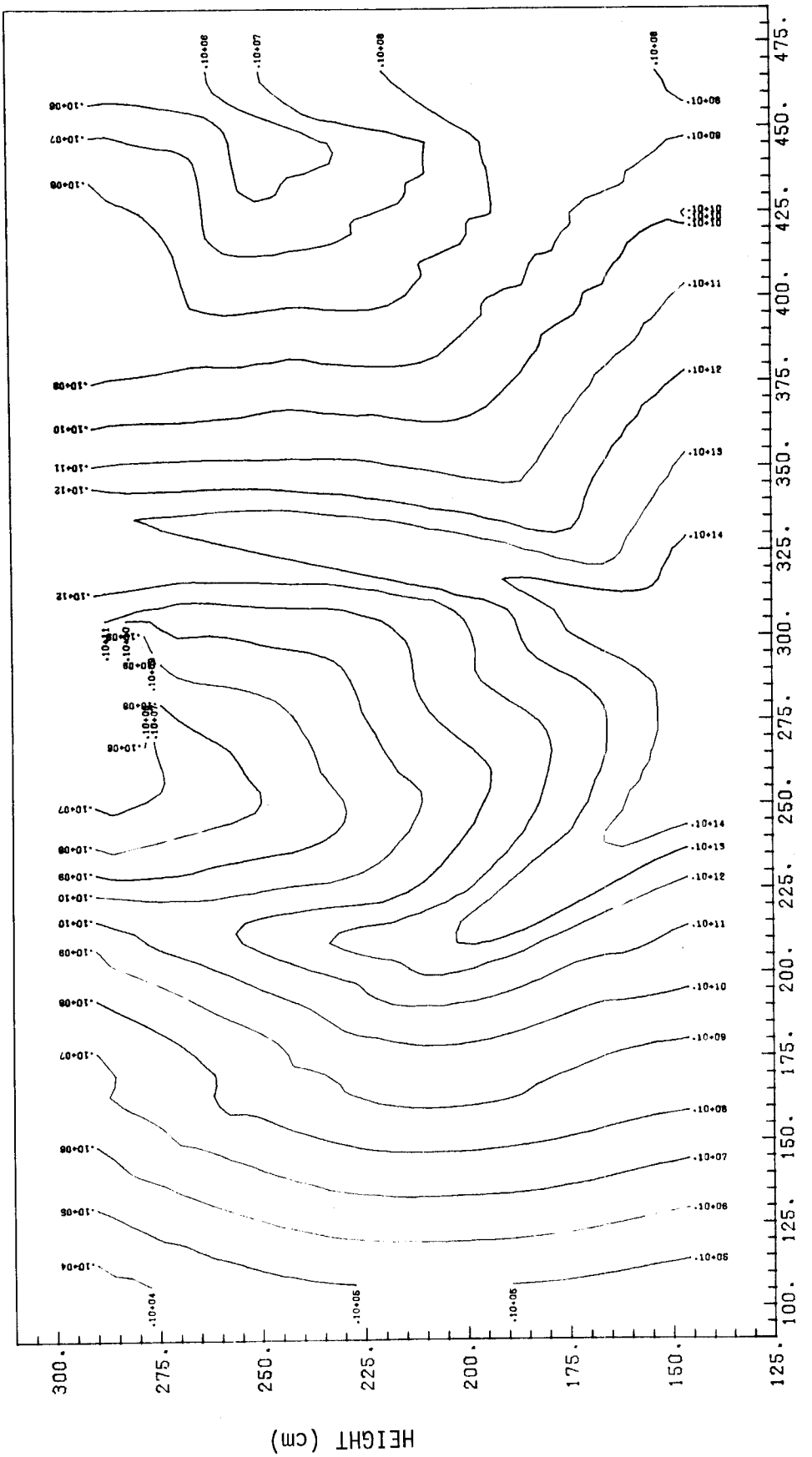

TETR NEUTRON FLUX PART CM (E>0.12 MEV)

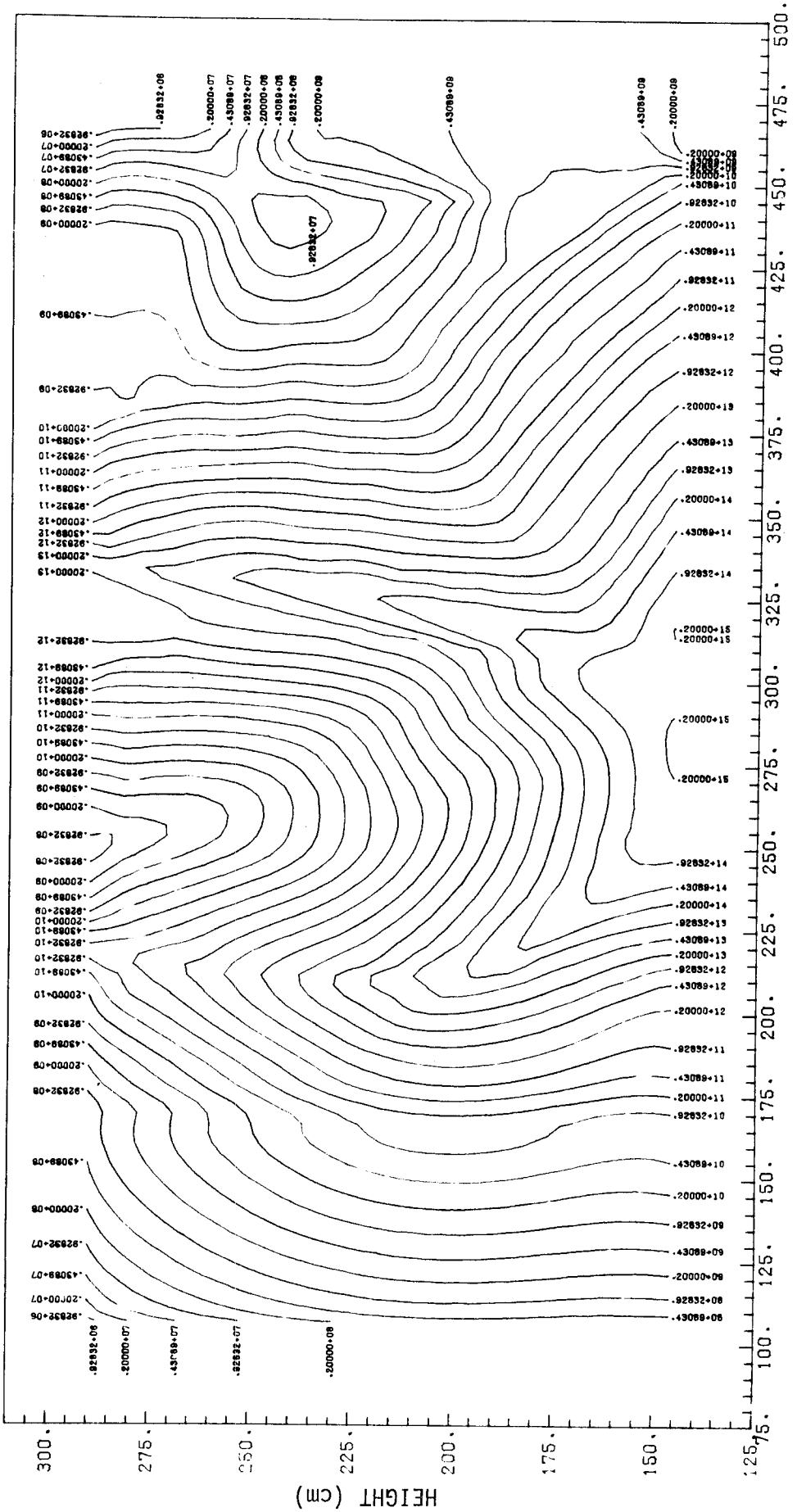

Figure VII-D-21

TETR NEUTRON FLUX PART CM (E>0.0 MEV)

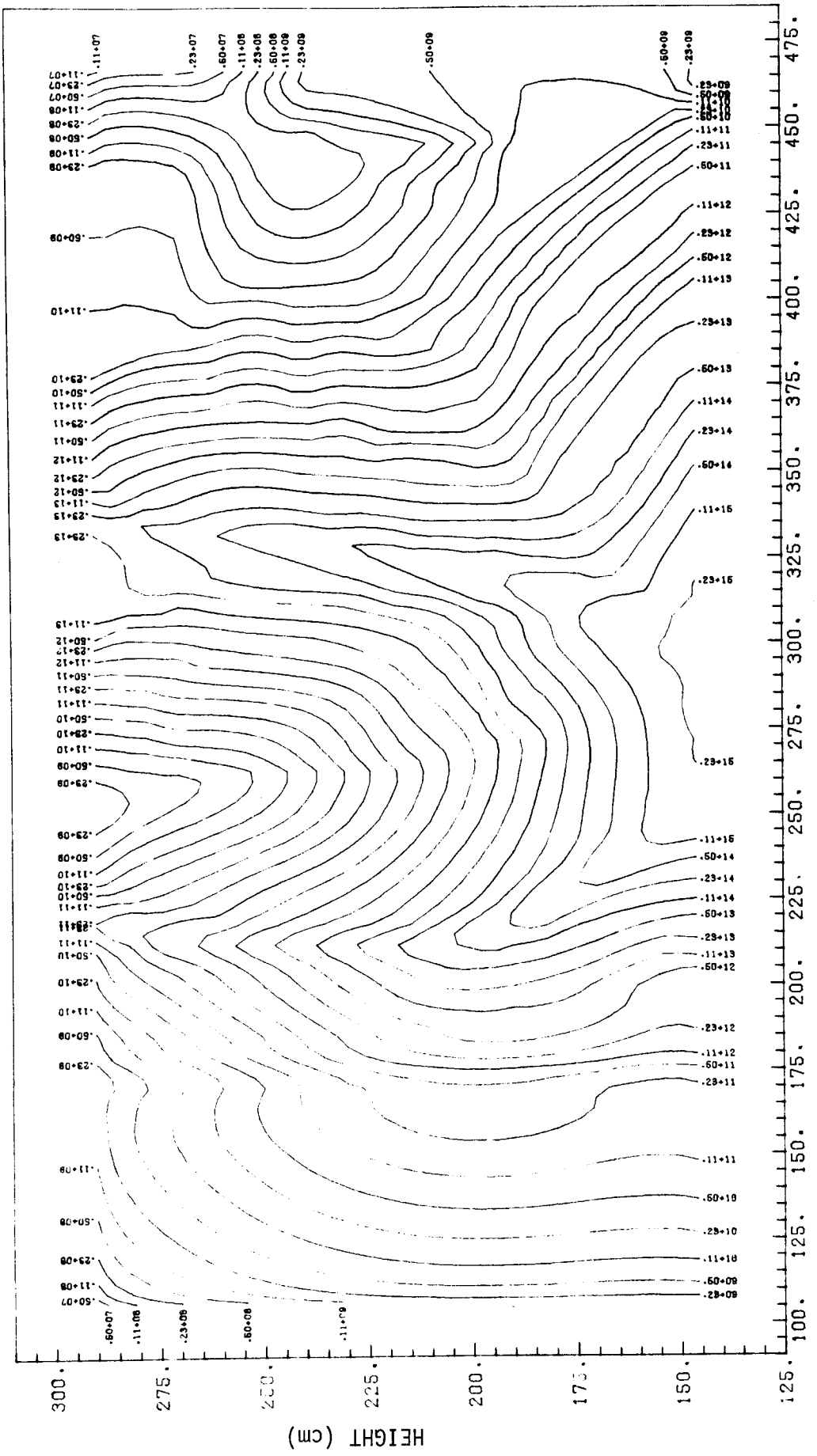

Figure VII-D-22

ATOMIC DISPLACEMENT RATE IN THE STAINLESS STEEL STRUCTURE (DPA/YEAR)

PART CM

Figure VII-D-23

TETR NEUTRON FLUX PART D (E>13.5 MEV)

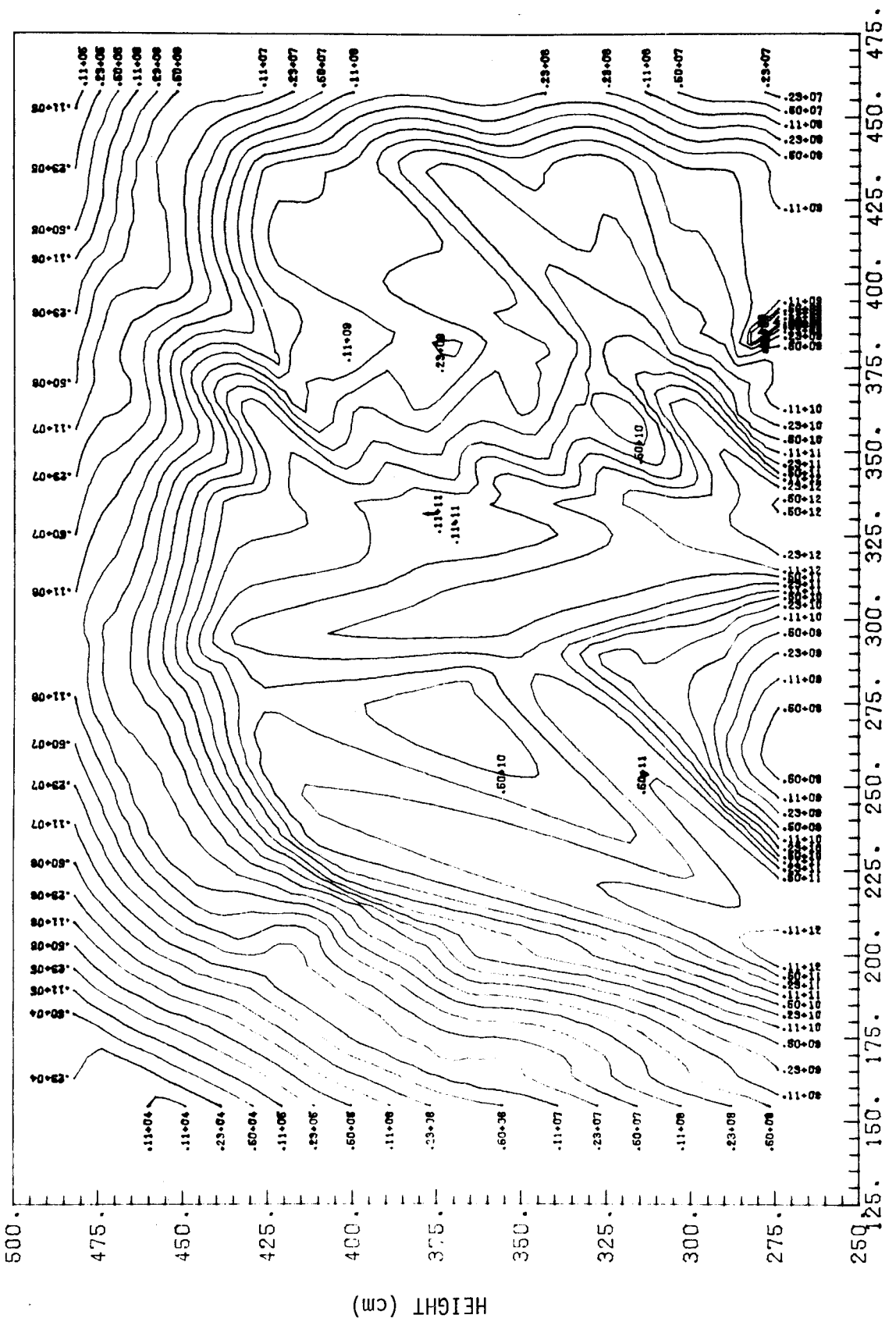

Figure VII-D-24

TETR NEUTRON FLUX PART D (E>0.12 MEV)

Figure VII-D-25

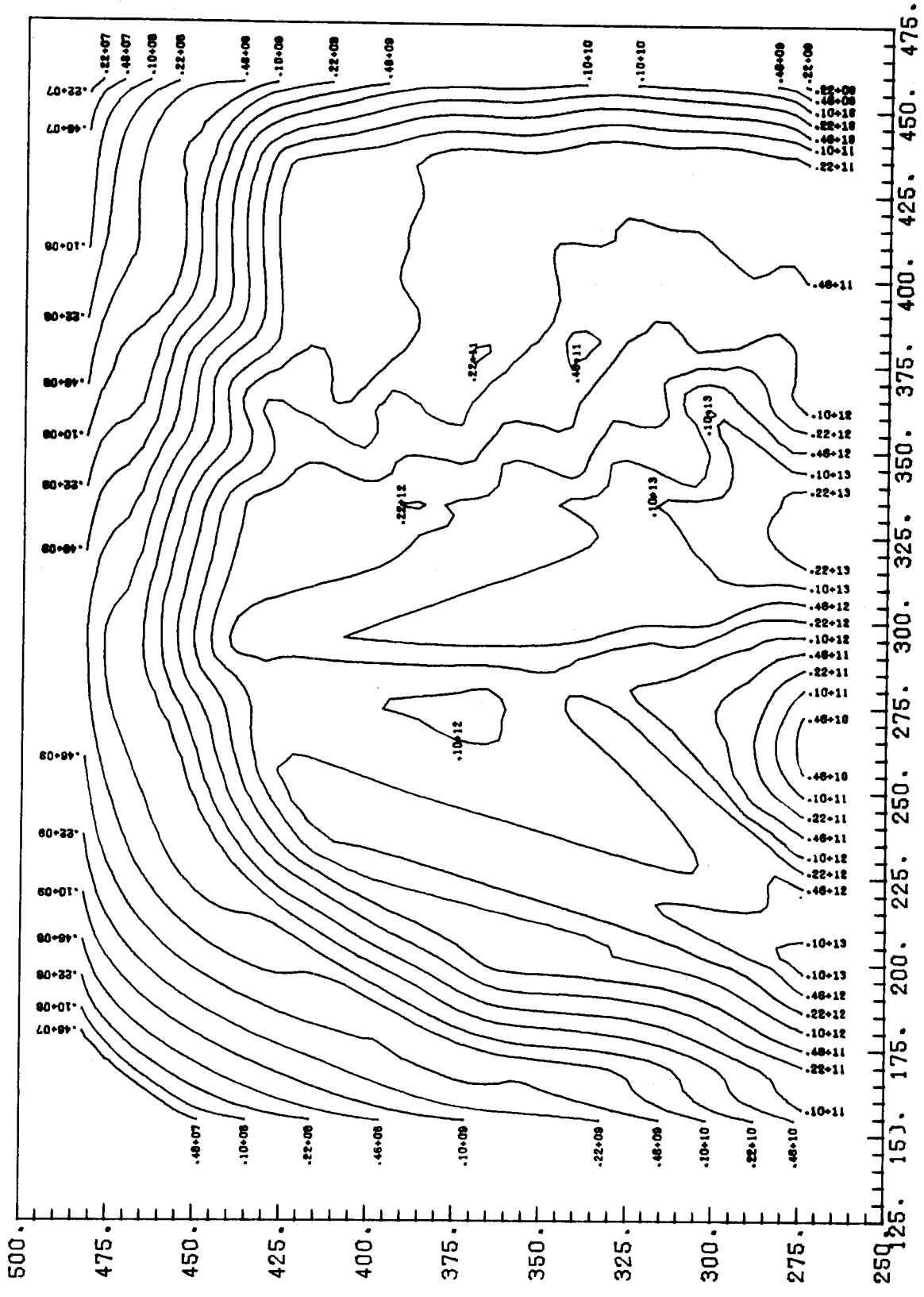

TETR NEUTRON FLUX PART D (E>0.0 MEV)

Figure VII-D-26

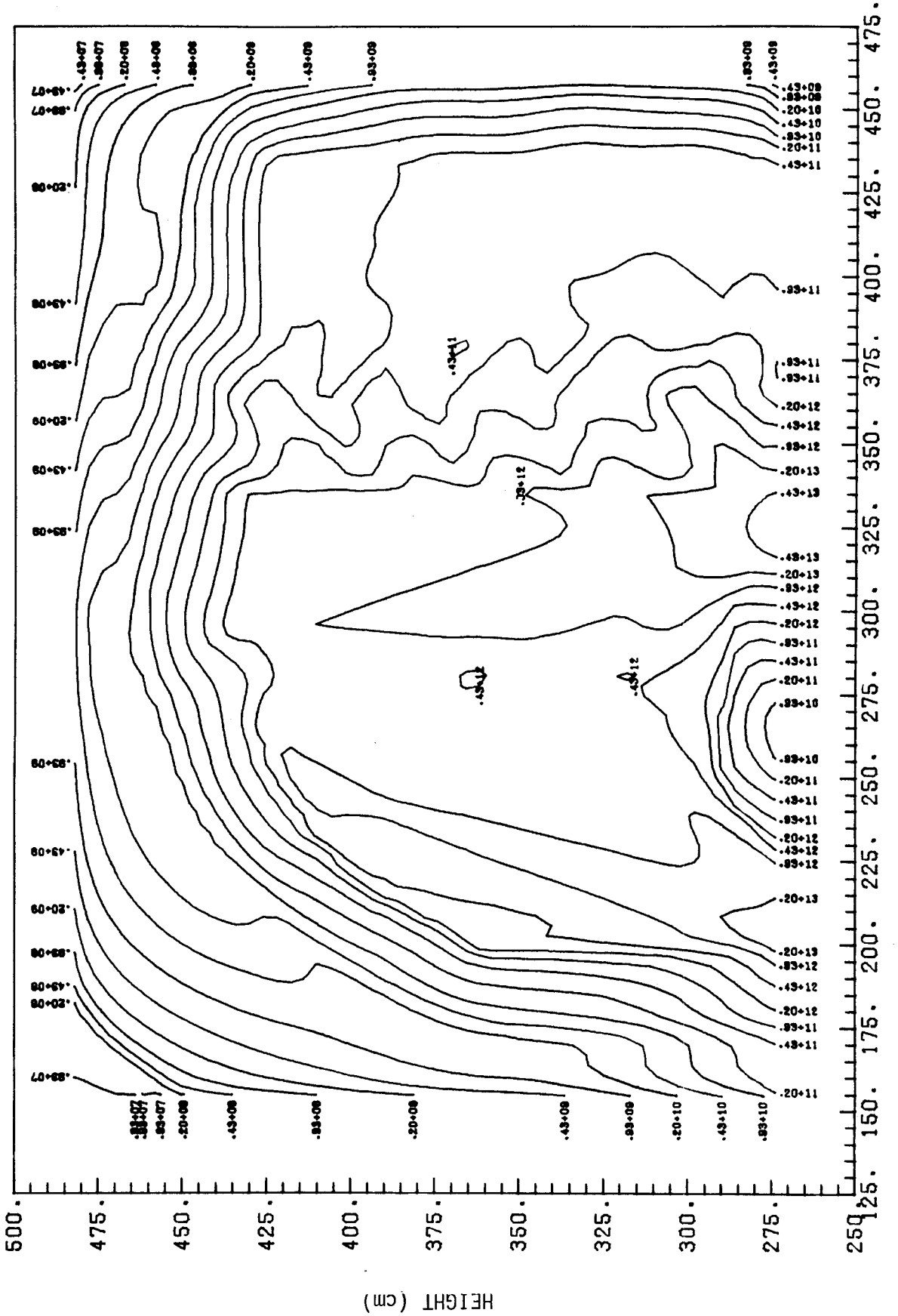

ATOMIC DISPLACEMENT RATE IN THE STAINLESS STEEL STRUCTURE (DPA/YEAR)

PART D

Figure VII-D-27

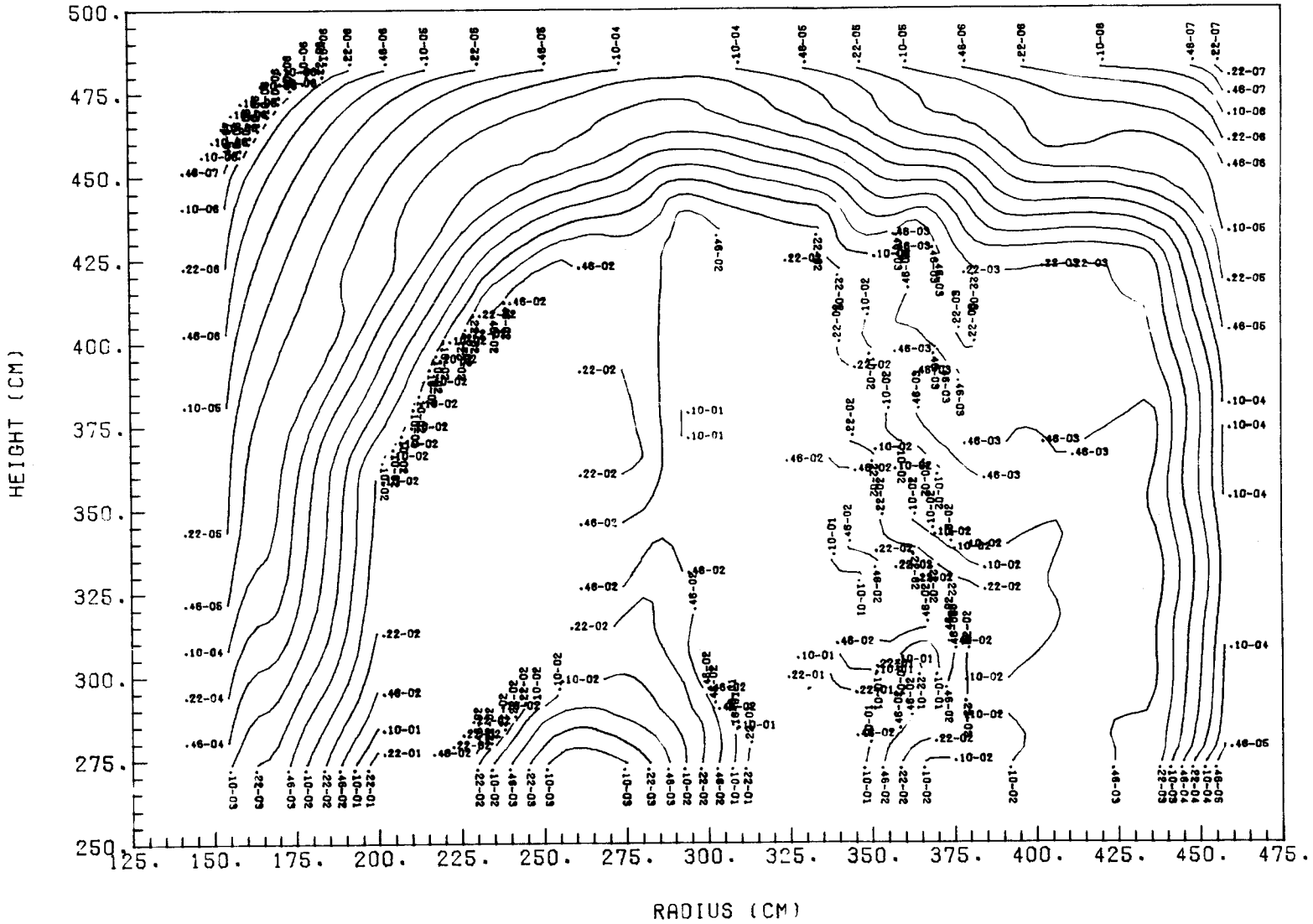

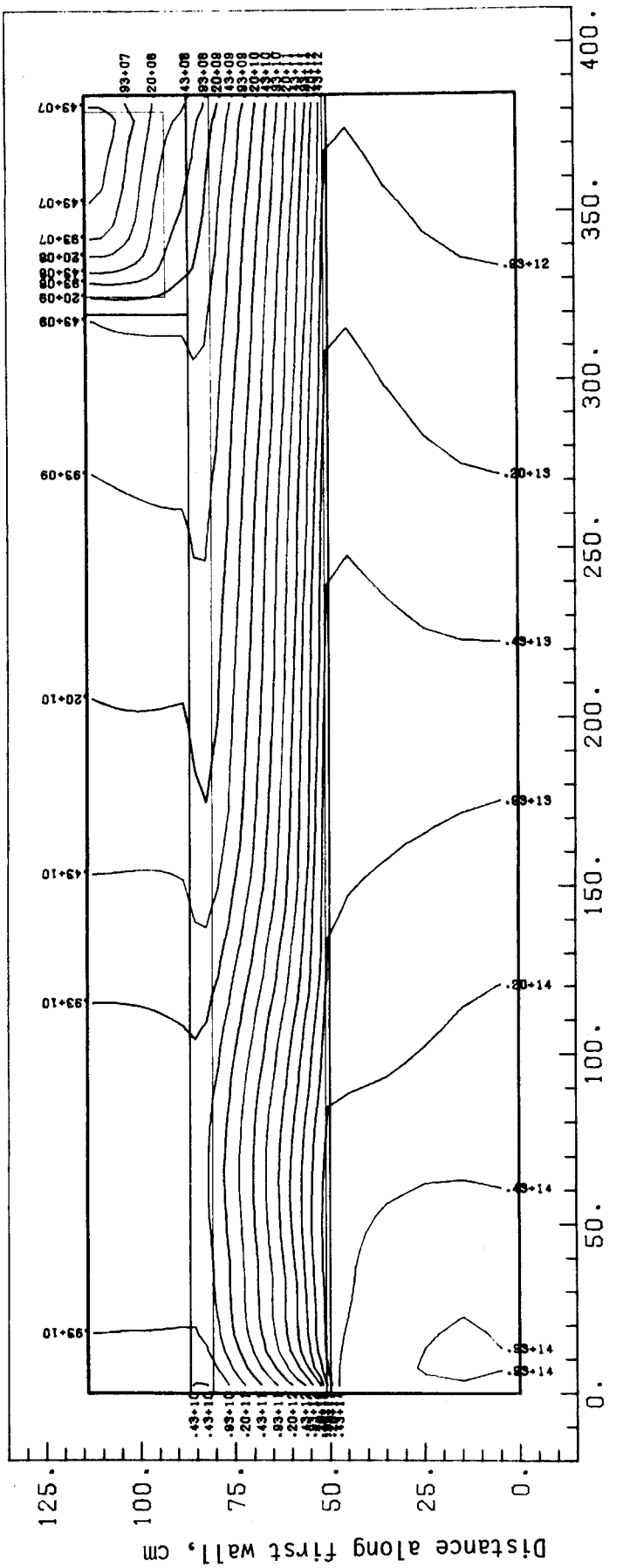

Figure VII-D-28 NEUTRON FLUX IN TETR NEUTRAL BEAM INJECTOR (E>13.5 MEV)

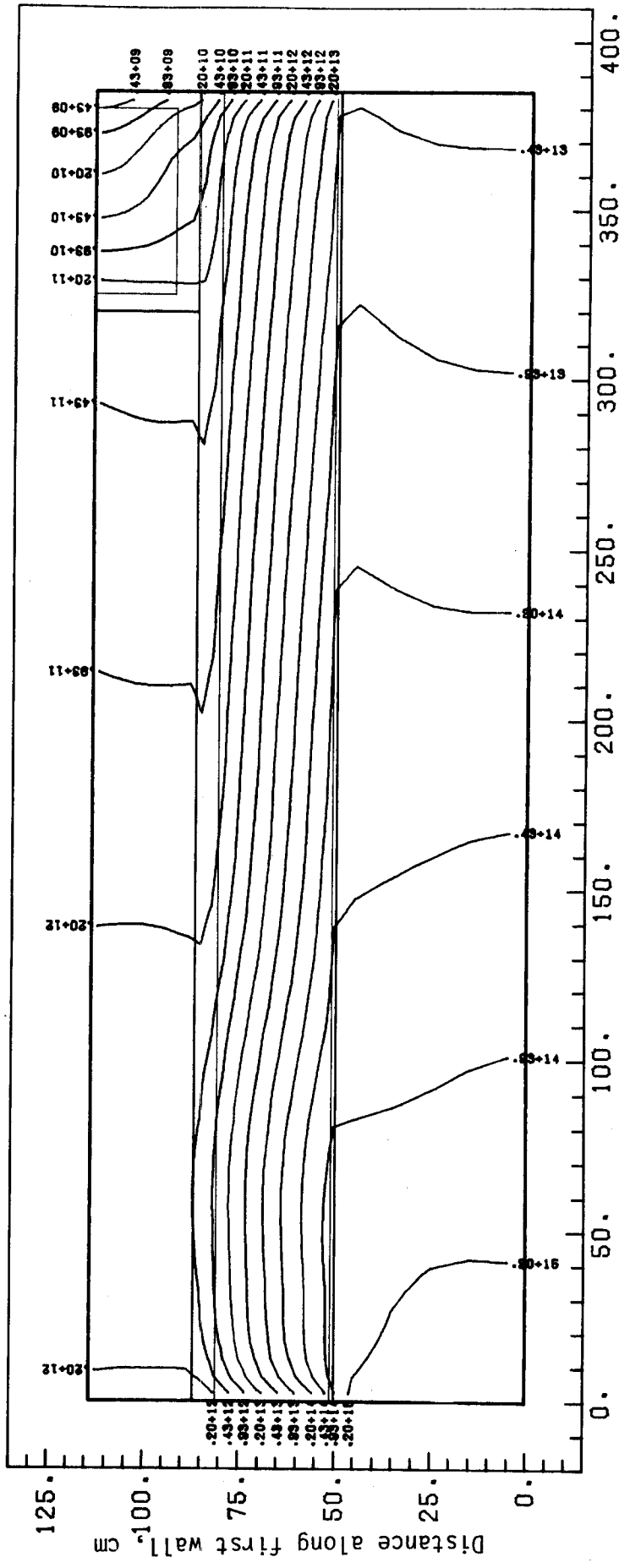

Figure VII-D-29 NEUTRON FLUX IN TETR NEUTRAL BEAM INJECTOR (E>0.12 MEV)

Figure VII-D-30 NEUTRON FLUX IN TETR NEUTRAL BEAM INJECTOR (E 0.0 MEV)

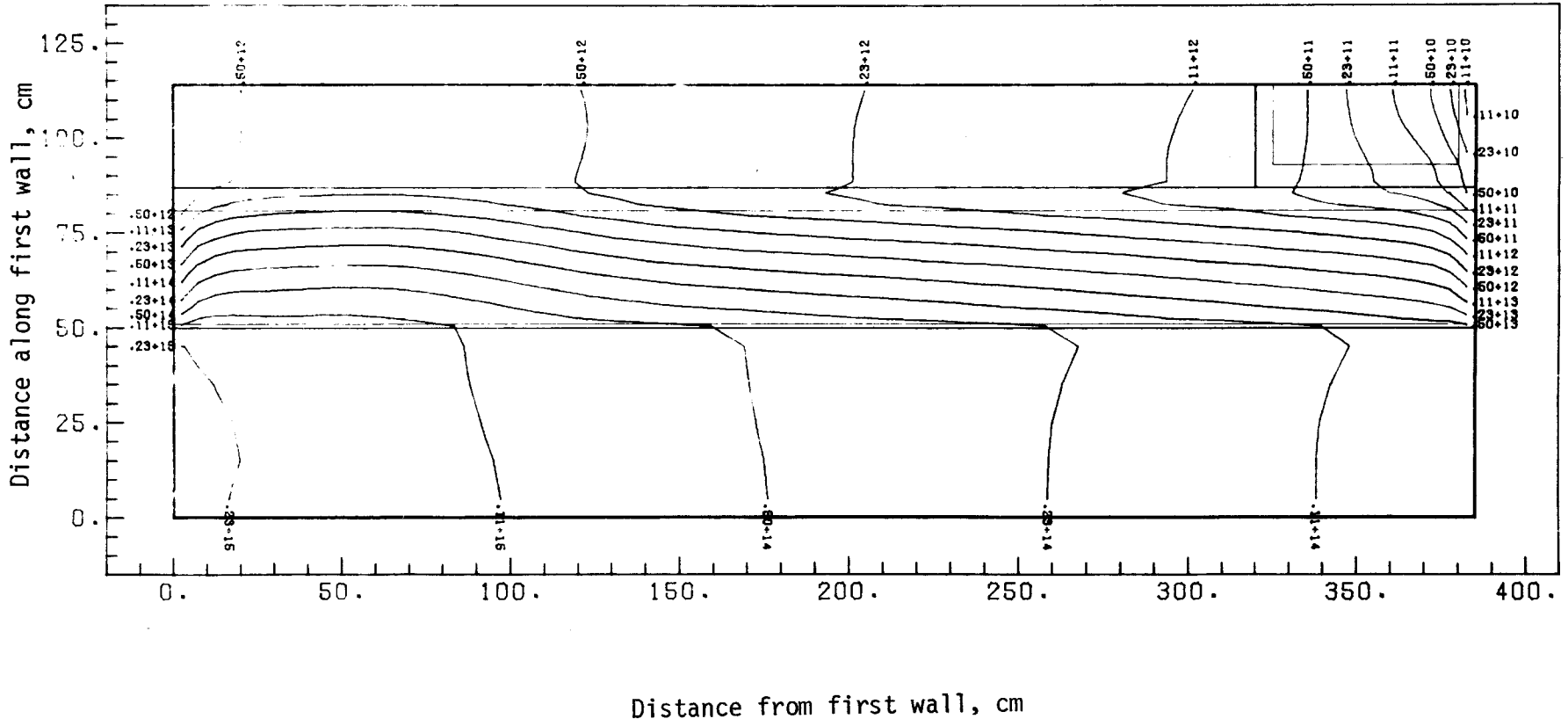

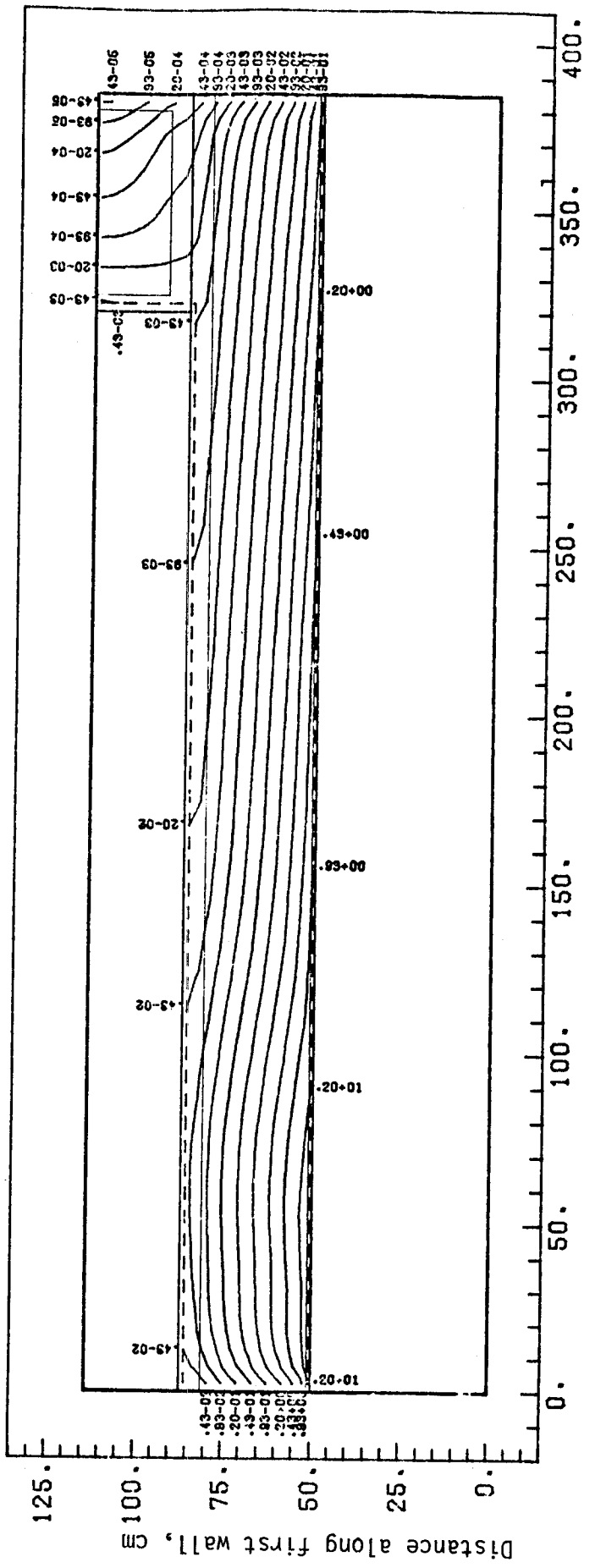

Figure VII-D-31 ATOMIC DISPLACEMENT IN THE STAINLESS STEEL STRUCTURE (DPA/YEAR)

HELIUM PRODUCTION RATES IN THE STAINLESS STEEL STRUCTURE (APPM/YEAR)

Figure VII-D-32

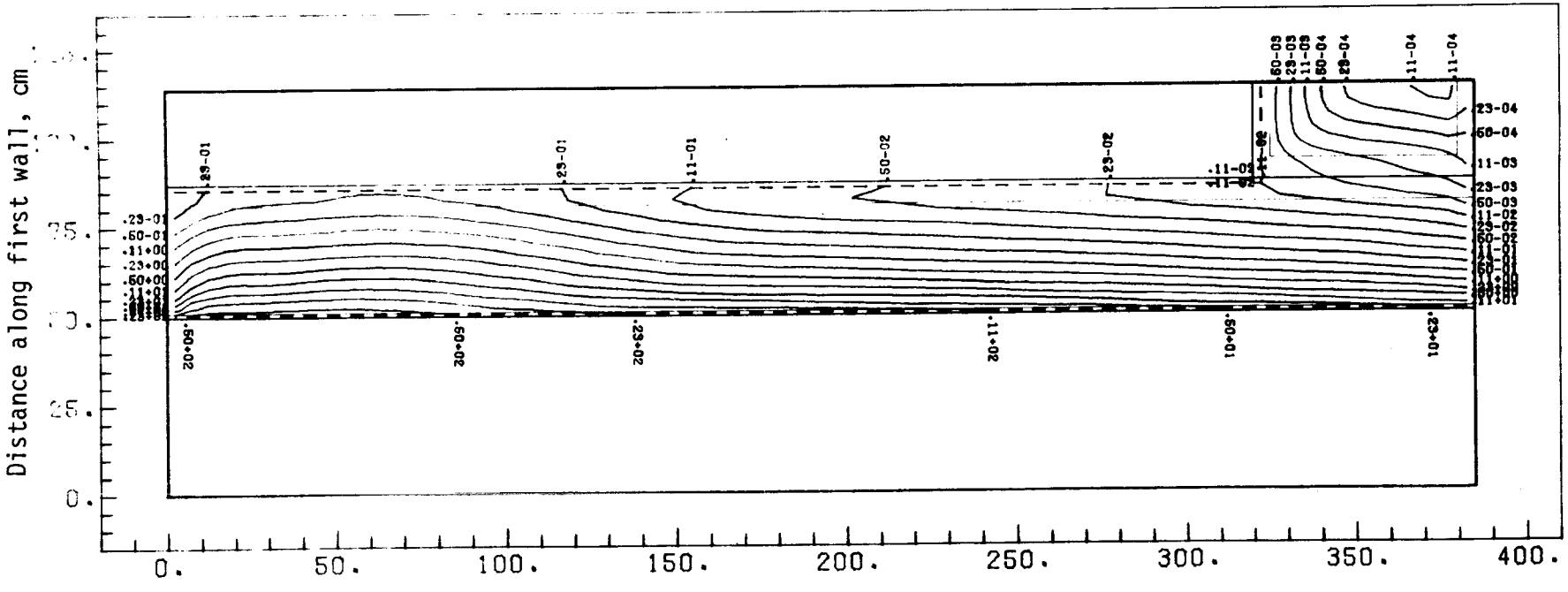

HYDROGEN PRODUCTION IN THE STAINLESS STEEL STRUCTURE
(APPM/YEAR)

Figure VII-D-33

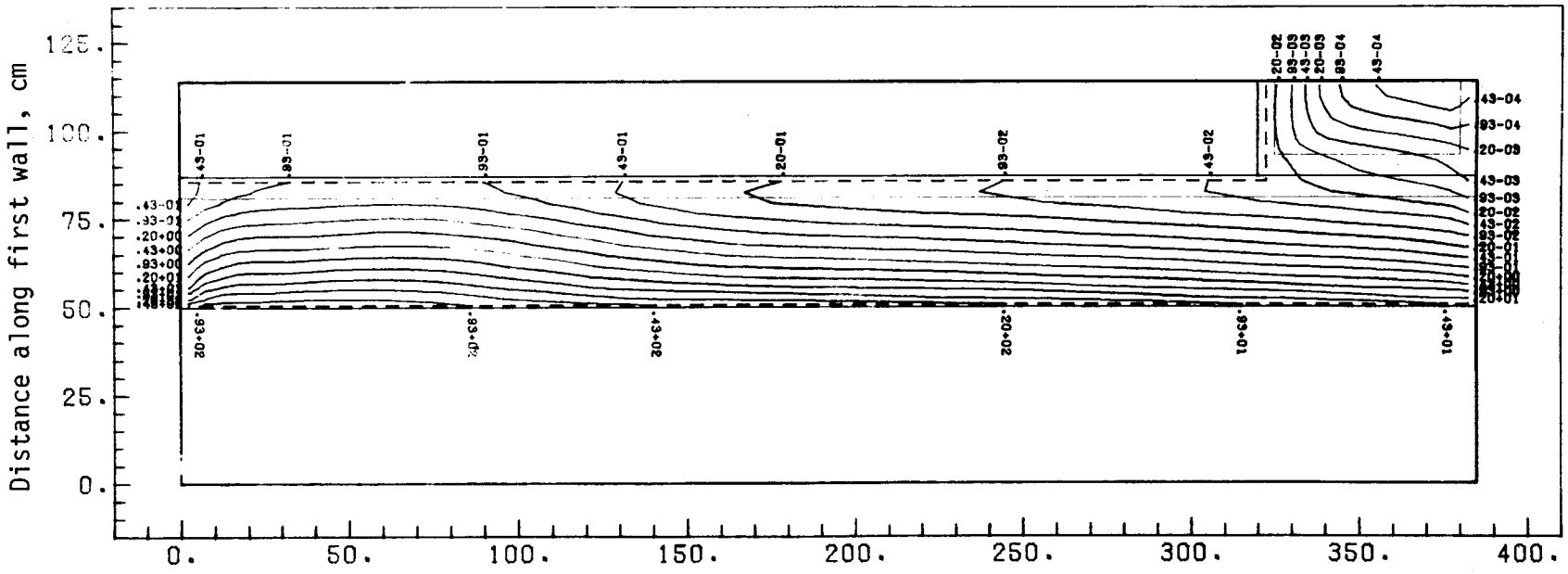

The design requirements can be checked by inspection from the contour plots. For example inspection of the dpa rate at the toroidal magnet (R = 1.6 m) in Figures VII-C-3, Figures VII-D-15, 19, and 23 allows Table VII-D-1 to be presented. The one-dimensional calculation implied a midplane result that is low by a factor of 5. Further the maximum rate is not at the midplane, but 2 meters above this plane. At this point the displacement rate is 1.3×10^{-3} dpa/yr -MW/m^2. The slight modification of the divertor slots to part CM reduces this to 1.6×10^{-4} or by essentially an order of magnitude. The reduction at other points is even greater in most cases.

Inspection of Figures VII-D-18 to 33 illustrates the shielding problems posed by the beam ports. For example, four meters from the plasma chamber, the total flux is only between one to two orders of magnitude less than its value at the port entrance. The .35 m radial shield achieves a reduction of only three orders of magnitude. This means the neutral beam system must be surrounded by a further shadow shield. The implications of the intense flux down the port is that the insulators for the ion sources and the insulation in the deflection and focusing coils will be subjected to very high radiation levels. However, as these components are outside the reactor and normally have a life expectancy of only about one year, the influence of the radiation may not appreciably increase the replacement rate.

Table VII-D-1

DISPLACEMENT RATE IN TOROIDAL FIELD MAGNET

(dpa/yr-MW/m^2)

Distance from the Midplane	Design C	Design CM
0	5.9 E-5	5.8 E-5
0	(1.2 E-5 I-D)	(1.2 E-5 I-D)
150	2.1 E-4	7.3 E-5
158	3.3 E-4	7.5 E-5
166	4.9 E-4	8.6 E-5
174	6.9 E-4	1.1 E-4
182	9.2 E-4	1.3 E-4
190	1.1 E-3	1.5 E-4
198	1.3 E-3	1.6 E-4
206	1.3 E-3	1.6 E-4
214	1.3 E-3	1.4 E-4
222	1.1 E-3	1.2 E-4
230	8.2 E-4	8.1 E-5
238	5.9 E-4	5.3 E-5
246	4.3 E-4	3.2 E-5
254	3.1 E-4	1.9 E-5
262	2.3 E-4	1.1 E-5
270	1.6 E-4	5.8 E-6
278	1.1 E-4	3.0 E-6
286	6.4 E-5	1.4 E-6

References

1. Badger, B., et al.,"A Wisconsin Toroidal Fusion Reactor Design, UWMAK-I," University of Wisconsin, UWFDM-68 (1974).

2. Badger, B., et al.,"A Conceptual Tokamak Reactor Design, UWMAK-II," University of Wisconsin, UWFDM-112 (1975).

3. Conn, R.W., et al.,"UWMAK-III, A Noncircular Tokamak Power Reactor Design," University of Wisconsin, UWFDM-150 (1976).

4. Stacey, W.M., Jr., et al.,"Tokamak Experimental Power Reactor Conceptual Design," Argonne National Laboratory, ANL/CTR-76-3 (1976).

5. Engle, W.W., Jr.,"A User Manual for ANISN," L-1973, Oak Ridge National Laboratory.

6. Mynatt, F.R., et al.,"The DOT-III Two-Dimensional Discrete Ordinates Transport Code," ORNL-TM-4280 (1973).

7. Plaster, D.M., Sentoro, R.T., and Ford, W.E. III,"Coupled 100 Group Neutron and 21 Group Gamma Ray Cross Sections for EPR Calculations," ORNL-TM-4872 (1975).

VIII. Heat Transfer and Cooling

VIII-A. Introduction

The function of the blanket for a testing reactor is completely different from that of a power reactor. While the blanket is a power converter and tritium breeder for a power reactor, it is basically a shield for a testing reactor. Both tritium breeding and high temperature operating are not required except in the testing zone. A testing reactor is a near term reactor so that a minimum extension of state of art technology should be used. An extensive life of the first wall and the reliable operating of the reactor are the most important considerations of the blanket design.

Since the function of the blanket is for shielding, the composition of the blanket is dominated by neutronics and is discussed in Chapter VII. A coolant has to be introduced to control the temperature of the blanket and removal of the heat. The coolant should be inert, compatible with structure, and have a low pressure. A high temperature operating capability is not required.

To support the blanket, contain the coolant, and ensure reliable operation; a structural material must be chosen which must be compatible with the coolant and must maintain its mechanical integrity in an extreme severe radiation environment. The blanket structure must be easily fabricated and meet strict construction requirements. Radiation damage data should be available so that a reasonable structure behavior in the fusion environment can be forecasted.

A number of coolants have been considered which includes He, organics and water. Organics was rejected because of the lack of data of its stability under 14 MeV neutrons. Helium is neutronically stable, but offers no particular advantage with a low temperature operation. The boiling water system is used because of the abundancy of operating experiments. The additional advantage with a boiling system is to reduce the temperature fluctuation in the structural due to the cyclic behavior of the plasma operation. The reliability of the blanket structure can be enhanced with the reduction of thermal fatigue.

The first choice of the structural material is clearly 316 stainless steel. It has a qualified industry with decades of experience of fabrication and welding. It has more data on radiation damage than any other metal. It has a reasonable long life expectancy in a fusion environment, especially if the blanket is designed such that the structure is at the optimum temperature.

The temperature in the testing section may vary from 200°C to 1000°C.* This temperature range extends far beyond the cooling range of boiling water. Pressurized helium is chosen for the coolant for the testing zone. The helium is at a moderately high pressure of 210 MN/m^2 (300 psi). The testing coupon cells have to be individually designed so that different temperatures can be maintained at various testing coupons cooled by the same stream of coolant. Temperature control and thermal analysis for some typical testing coupons will be included later in this chapter.

---

*Refractory metal components will be needed in some parts of the testing cells, but the bulk of the test cell will be 316 SS at much lower temperatures.

The first wall is protected from the plasma by a carbon curtain. The main purpose of the carbon curtain is for impurity control of the plasma. Important side effects of the curtain are to protect the first wall from a plasma dump and from accidents caused by neutral beam impingent on the first wall. The thermal inertia of the curtain can also minimize the charge of the thermal load to the first wall during plasma cycling.

The problems associated with the collector plate design are very complicated. This is caused by the extremely high peak thermal load of ~60 MW/m^2 on the plate. This peak thermal load results a high surface temperature if lithium film is used as the coolant as suggested by UWMAK-I.[1] A solid target is a possible candidate for the collect plate. The most serious problem is the thermal stress caused by the high thermal load. Ta-10 W was picked to be the structural material for the collect plate due to its excellent material properties.[2] The coolant for the collector plate is water operating at a temperature and pressure just below the sub-cooled boiling regime. The sputtering problem will probably limit the life of the plate to a few months.

References:

1. B. Badger, et al., "A Wisconsin Tokamak Reactor Design, UWMAK-I," UWFDM-68, Nuclear Engineering Department, University of Wisconsin, (November, 1973).

2. M. A. Hoffman and R. H. Werner, "Heat Flux Limitations on First Wall Wall Shields For Early Fusion Machines," Proceedings of the First Topical Meeting on the Technology of Controlled Nuclear Fusion, San Diego, (April, 1974).

VIII-B. Thermal Hydraulic Design and Calculations for the Blanket

The design philosophy of TETR is minimum extrapolation of today's (1980) technology and reliability. Therefore, the structure is 316 SS. The coolant is low temperature, moderate-pressured boiling water. Boiling water is picked to minimize the effort of thermal fatigue. The blanket is protected from the plasma by 1 cm thick carbon curtain. The shield is cooled by low temperature water. The heating rate in the blanket is furnished by neutronic calculations, and is shown on Fig. VIII-B-1. The heating rate near first wall is 30 W/cm^3, which is very high comparing to UWMAK-I[1] at 6 W/cm^3. The high heating rate results from the W in the shield near the first wall. The surface heating rate from the plasma is 3.4 W/cm^2 and the curtain temperature is 1000°C.

VIII-B-1. Temperature Range

The saturation pressure of water increases rapidly with temperature. For a conservative blanket design, a maximum coolant pressure of 345 $\frac{MN}{m^2}$ (500 psi) is chosen. This limits the coolant boiling temperature to 240°C. The operating temperature and pressure are almost identical to that of the Experimental Boiling Water Reactor (EBWR) (2). Therefore, operating experience is available and reliability can be ensured. The coolant enters the reactor at 220°C, and exits as a slightly superheated steam at 260°C. The maximum structure temperature change due to the cyclic behavior of the plasma is, therefore, only 40°C, comparing to ~ 200°C if helium is used as the coolant. This low temperature fluctuation will greatly reduce the effect of thermal fatigue.

VIII-B-2. Burnout Considerations

A typical curve of heat flux, q, versus a temperature ΔT between the surface and the bulk liquid temperature is shown in Fig. VIII-B-2. Detail description

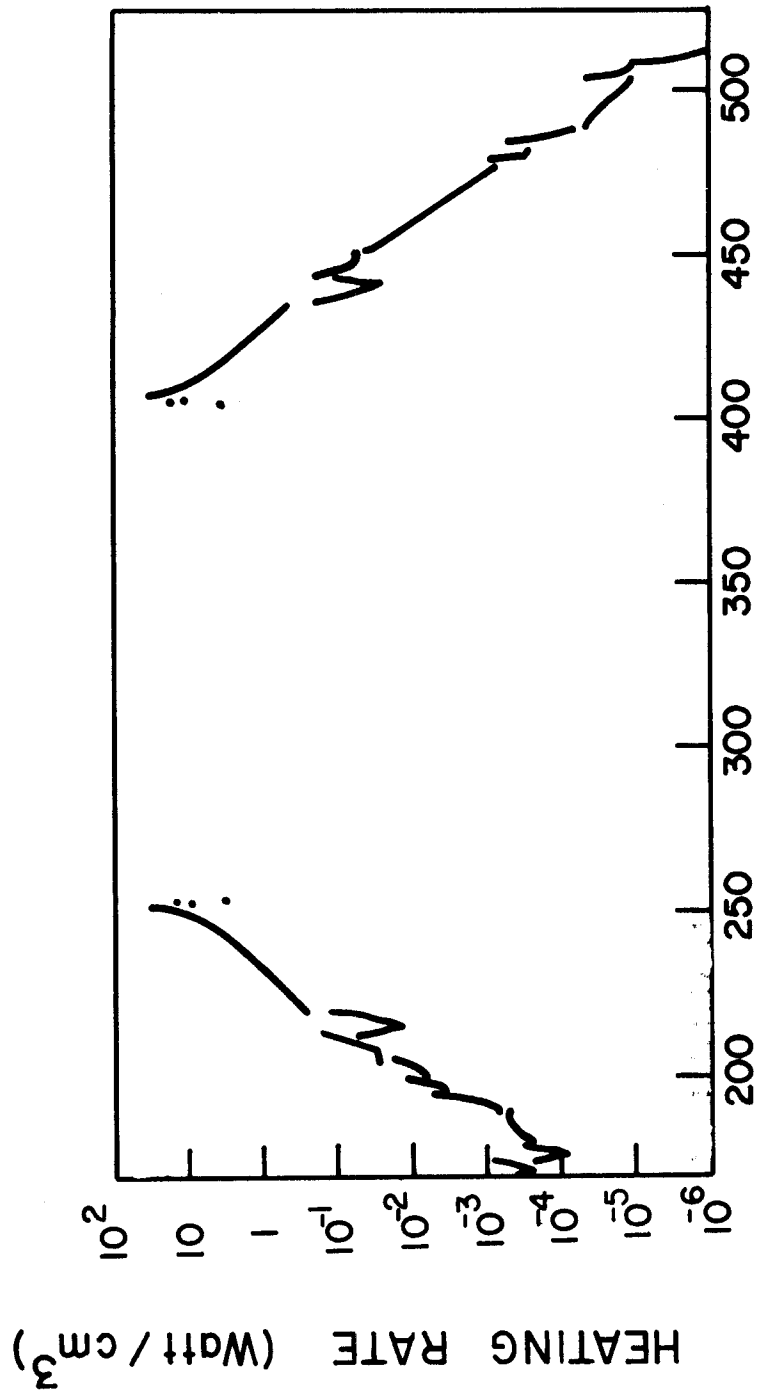

NEUTRON, GAMMA RAY HEATING AND TOTAL HEATING

Fig. VIII-B-1

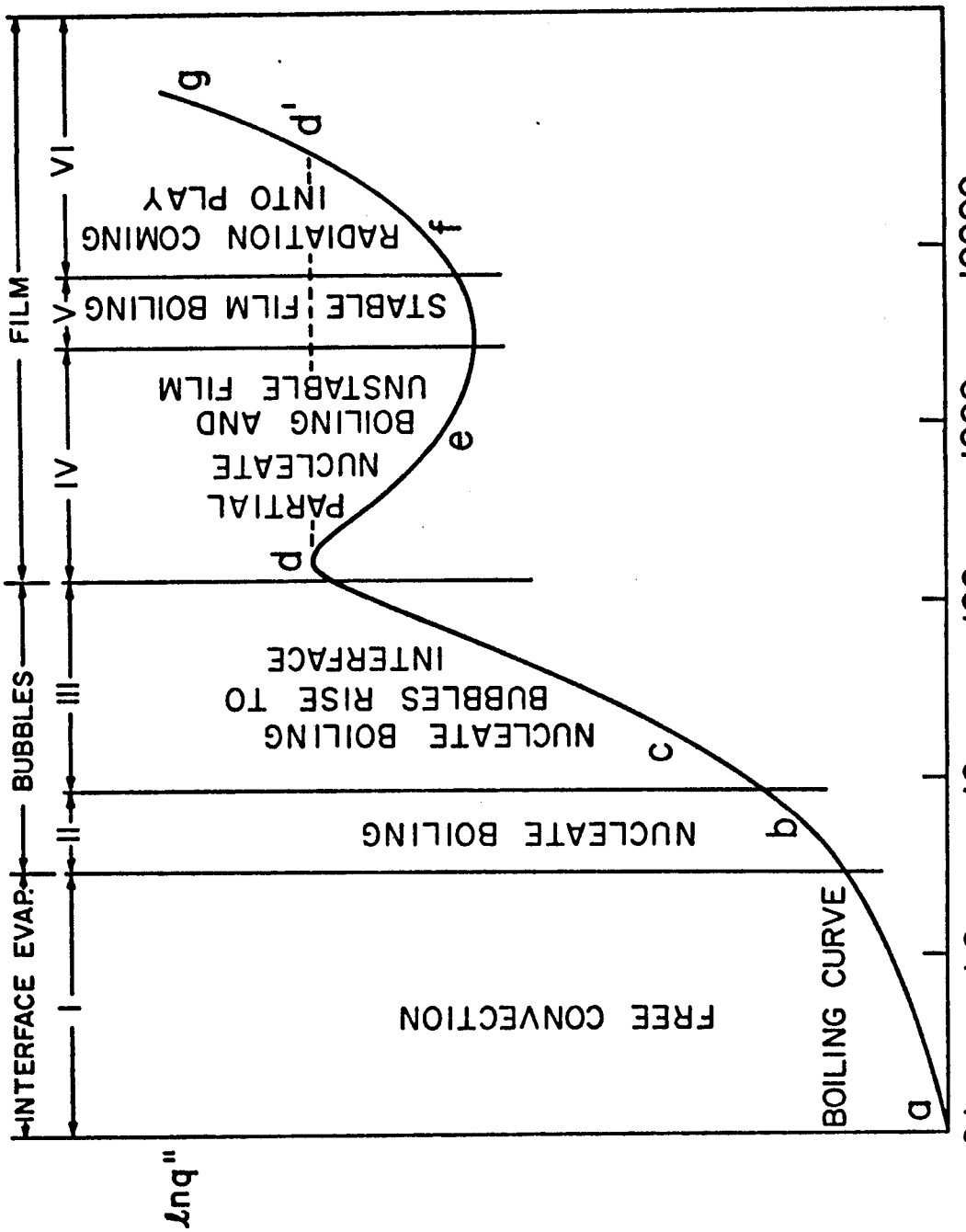

Fig. VIII-B-2 TYPICAL POOL BOILING DATA.

of this curve can be found in heat transfer books (3) and will not be repeated here. If the heat flux is increased beyond d, the heating surface temperature will suddenly jumped from d to d'. The temperature at d' is so high that it mostly likely exceeds the safe limits of the heating surface. The surface in such is said to be burnout. The thermal flux at d is called burnout heat flux.

In the reactor design, the maximum heat flux should be sufficiently below the burnout heat flux. A factor of safety, equal to the ratio of burnout heat flux and the design heat flux, is usually used in the design. A safety factor of 3 is a conservative value. The burnout heat flux for water can be calculated with reasonable accuracy, and it is important a proper maximum design heat flux is used.

The burnout heat flux of light water boiling in tubes under forced-flow conditions were experimentally investigated,(4) and those results can be summarized by:

$$q_c'' = 0.28 \times 10^6 \left(\frac{h_c}{1000}\right)^{-2.5} \left(1 + \frac{G}{10^7}\right)^2 e^{-0.0012\ L/D} \qquad \text{(VIII-B-1)}$$

in which q_c'' = burnout heat flux

G = water mass flow rate

h_c = water bulk enthalpy

L/D = tube length to diameter ratio

Assuming tube is 1 cm diameter with 2 m length, and heat flux of 10 watts/cm of tube, the burnout heat flux is 400 w/cm^2. This far exceeds the possible maximum design flux and burnout is not a problem.

VIII-B-3. Coolant Flow Arrangement

The cross-section of the blanket is shown on Fig. VIII-B-3. The first wall is a bank of tubes, with I.D. = 1 cm and wall thickness = 2 mm. The 2 mm tube

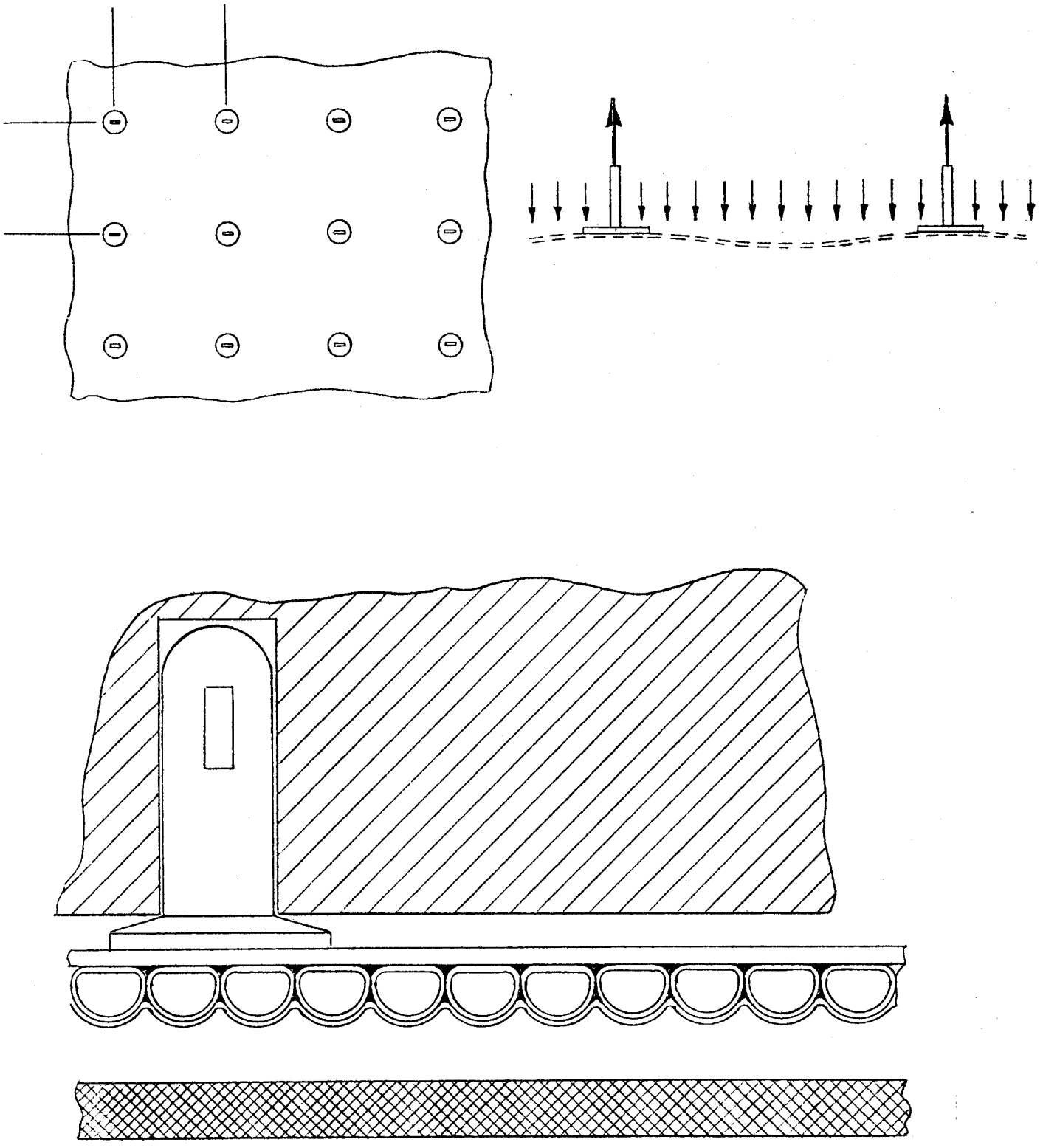

FIG. VIII - B - 3. CROSS-SECTION OF BLANKET

wall is in two layers, of 1 mm thick each, to provide redundancy. The first wall is protected from the plasma by a carbon curtain 1 cm thick. The carbon curtain has a large thermal inertia so that the surface wall loading to the first wall varies only by 4% from the plasma burn period to plasma down period. Therefore, the temperature profile across the first wall remains unchanged despite the cyclic operation of the plasma. The coolant temperature rise is 40°C, which is also the variation temperature level of the first wall. This temperature variation is small comparing to a He cooled system so that thermal fatigue effects are minimized.

The density of the coolant tube distribution within the blanket is inversely proportional to the heat generation ratio. The heat generation rate, as can be seen from Fig. VIII-B-1, decreases rapidly with distance from the plasma, and so does the coolant tube density. The average heat flux to the coolant tube is only 5 watts/cm^2 which is well within the cooling capacity of the boiling water so that heat transfer is no problem.

Since the coolant has a large heat transfer coefficient ($\sim 2 \frac{watt}{cm^2\text{-}°C}$) and a very small heat flux ($\sim 5 \frac{watt}{cm^2}$), the coolant tube temperature is essentially same as the coolant temperature, i.e., 220 to 260°C. This low structural temperature may not be optimum from radiation damage point of view, but is limited by the choice of using boiling water as the coolant.

References

1. B. Badger et al., "A Wisconsin Tokamak Reactor Design, UWMAK-I," UWFDM-68, Nuclear Engineering Department, University of Wisconsin, (November, 1973).

2. "EBWR, The Experimental Boiling Water Reactor," U.S. Atomic Energy Commission, Nuclear Technol. Ser. Rept. ANL-5607, Argonne National Lab, May, 1957.

3. W. M. Rohsenivow and H. Choi, "Heat, Mass and Momentum Transfer," Prentice-Hall, 1961.

4. R. A. DeBortoli, "Forced Convection Heat Transfer Burnout Studies for Water in Rectangular Channels and Round Tubes at Pressures Above 500 psia," U.S. Atomic Energy Commission Report, WAPD-188, October, 1958.

VIII-C. Annealing Requirements

The first wall of TETR operates around 250°C. This low temperature reduces swelling and extends first wall life. However, the ductility of the structure will be reduced due to the formation of dislocation loops in the lattice structure. One way to remedy the loss of ductility is to anneal the structure periodically. When annealing is required, the cooling water will bypass the heat exchanger and be electrically super-heated to 400°C. This super-heated steam passes through the blanket and the blanket is heated up to 400°C. By such an annealing process, it is expected that the displacement damage can be tolerated.

VIII-D. First Wall Protection by Curtain to a Plasma Dump

The plasma dump to the first wall of a fusion reactor is a possible and maybe unavoidable accident. This type of difficulty was encountered in the early tokamak works both in the United States and abroad.[1] For a reactor with a feedback controlled plasma, the likelihood of plasma dump is even higher. In addition, there is the possibility that the neutral beam injector is on without starting the plasma proceeding a thermal load of $\sim 10^3$ W/cm^2 on the first wall. If the first wall is made of stainless steel at 300°C and 2 mm thick, the first wall can be melted through within a fraction of a second. The frequency of such accidents cannot be assessed at this stage. The first wall design, however, should be able to absorb this order of thermal input unless it can be positively proved this type of accident will not occur.

Some of the recent designs (2,3) inserted a low-Z curtain between the plasma and the first wall. This curtain is to protect the plasma from the high Z impurities and, if the divertor does not function perfectly, to protect the first wall from particle sputtering. This low-Z curtain can be made of graphite, which has a melting temperature of 3600°C. The low-Z curtain is usually radiatively cooled and has a normal operating temperature of 1200°C. This large difference between the melting temperature and operating temperature provides large thermal inertia and results a large damping effect to a sudden large thermal output to the first wall. Therefore, if a relatively thick curtain is used, the rate of temperature change of the metallic first wall becomes

much slower and corrective action can be taken before permanent damage to the structure can happen. The low-Z curtain is not a vacuum retaining wall and it is not catastrophic if the curtain is melted through.

Two types of accident are assumed. The first type of accident assumes the plasma expands uniformly to the first wall. The input onto the first wall suddenly increase to a high value, and the temperature response of the first wall is calculated. The low-Z curtain provides only a damping effect. The second type of accident assumes a localized plasma damping. Only a small area receives the high energy flux. As the first wall of the low-Z curtain is getting hot, it starts to radiate energy to other parts of the blanket. The first wall is being cooled by a coolant at 250°C with a heat transfer coefficiency of $2 \frac{\text{watt}}{\text{cm}^2\text{-°C}} \left(3000 \frac{\text{BTU}}{\text{hr-ft}^2\text{°F}}\right)$.

VIII-D-1. Mathematical Formulation

The governing equations of the two types of accidents are identical and have the following form:

$$\frac{\partial T_c}{\partial t} = \alpha \frac{\partial^2 T_c}{\partial x^2} \qquad \text{VIII-D-1}$$

$$mc_p \frac{dT_{E.W.}}{dt} = \sigma\varepsilon_1 \left(T_c^4 - T_{F.W.}^4\right) - h \left(T_{F.W.} - T_o\right). \qquad \text{VIII-D-2}$$

The boundary conditions are different. For the first type of accident, i.e., a uniformed plasma dump, the boundary conditions are:

$$\frac{\partial T_c}{\partial x} = - \frac{q}{K} \text{ at } x = 0 \qquad \text{VIII-D-3}$$

$$\frac{\partial T_c}{\partial x} = \frac{\sigma \varepsilon_1}{K} (T_c^4 - T_{F.W.}^4) \text{ at } x = \ell. \qquad \text{VIII-D-4}$$

For the second type of accident, i.e., a localized plasma dump, or a neutron beam accident, the boundary conditions are:

$$\frac{\partial T_c}{\partial x} = - \frac{q}{K} + \frac{\sigma \varepsilon_2}{K} (T_c^4 - T_c^{o4}) \text{ at } x = 0 \qquad \text{VIII-D-5}$$

$$\frac{\partial T_c}{\partial x} = \frac{\sigma \varepsilon_1}{K} (T_c^4 - T_{F.W.}^4) \text{ at } x = \ell. \qquad \text{VIII-D-6}$$

T_c is temperature of the curtain

t is time

α is thermal diffusivity of the curtain material

mc_p is thermal inertia of the first wall per unit area

$T_{F.W.}$ is temperature at the first wall

σ is Stefan-Boltzmann constant

ε_1 is the total exchange factor between the curtain and the first wall

h is the heat transfer coefficient of the coolant

T_o is the temperature of the coolant

x is the distance in the curtain from the front wall

ℓ is the thickness of the curtain

K is the thermal conductivity of the curtain material

ε_2 is the total exchange factor between the front of the curtain that receives the energy and the rest of the curtain.

T_c^o is the original curtain temperature.

Since the boundary conditions are non-linear, the exact solution of the temperature response cannot be obtained. A finite difference form of Eq. VIII-D-1, VIII-D-2 can easily be written and the solution obtainable numerically. The temperature response of the first wall and the curtain are thus obtainable as a function of surface heating value, curtain thickness, etc.

VIII-D-2. Results and Discussion

The first wall of TETR is 2 mm thick and operating at 250°C. This first wall is cooled by boiling water which has a heat transfer coefficient of $2 \frac{\text{watt}}{\text{cm}^2\text{-°C}}$ ($3000 \frac{\text{BTU}}{\text{hr-ft}^2\text{-°F}}$). The temperature responses of such a first wall without protection are shown in Fig. VIII-D-1. It is obvious that within a second or less, after the accident occurs the first wall will be melted through. To detect and control an accident within such a short period of time is very difficult. Therefore, it can be concluded that if a plasma dump type of accident is a possibility, the first wall of a fusion reactor has to be protected. If the first wall is a simple metallic wall, a melt through can happen before the accident can be detected and stopped. This will result in reactor shutdown and require costly and time consuming repairing work.

However, if a curtain, of 1 cm thick, is inserted between the plasma and the first wall, the temperature rise of the first wall due to a plasma dump is much slower compared to the case of bare metallic first wall.

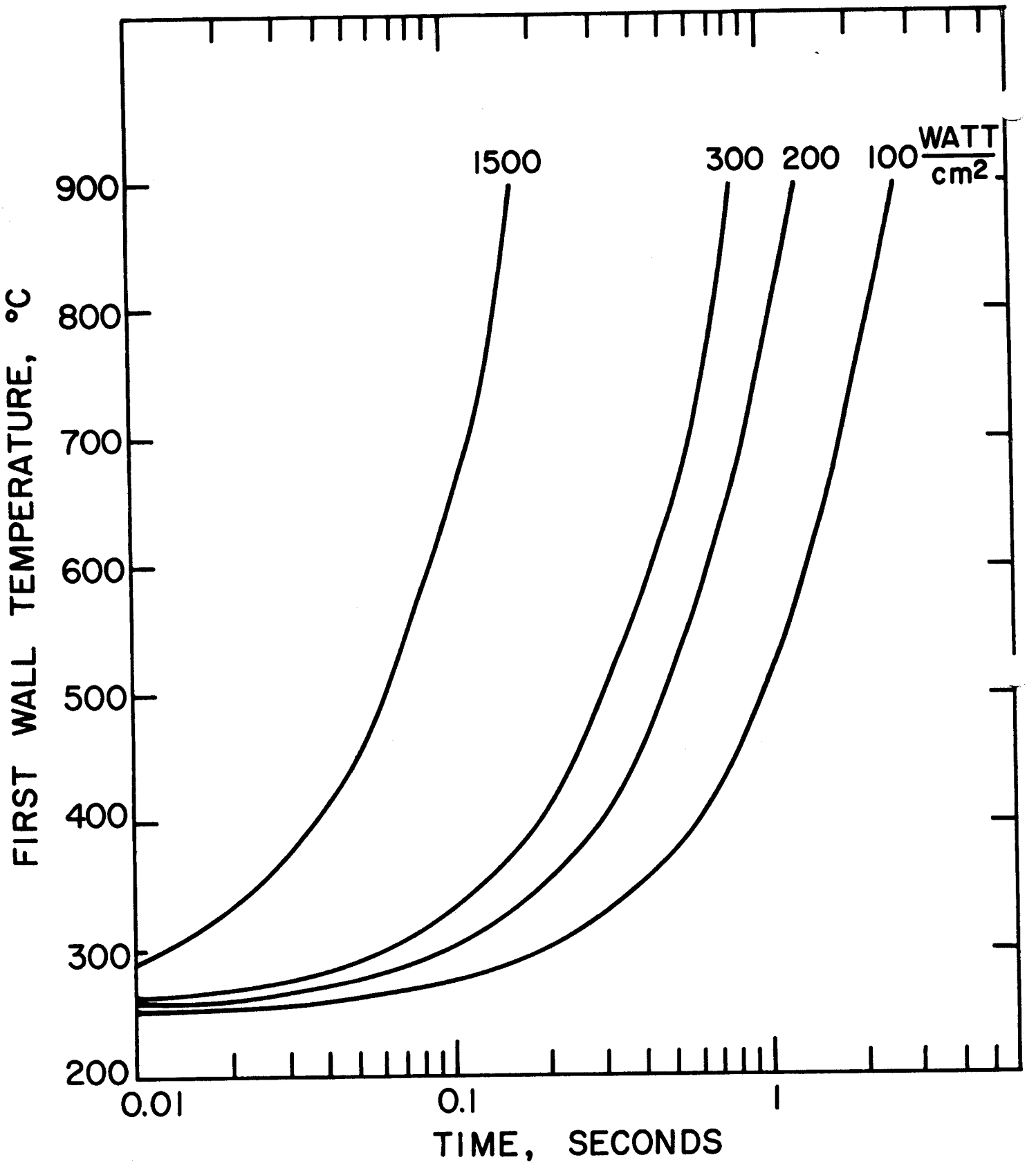

Fig VIII-D-1

Temperature Response of Unprotected First-wall

Figure VIII-D-2 and 3 show the temperature response of the first wall and front surface of the curtain, respectively, due to an uniformed plasma dump. Fig. VIII-D-4 and 5 show the same results due to a localized plasma dump; or an accident due to the neutron beam impinged onto the curtain.

The results thus calculated showed that the time for a first wall melt through becomes a few seconds, comparing to a few tenths of a second for an unprotected metallic wall. If the accident can be brought under control within 2 or 3 seconds, no permanent damage will occur to the first wall. The temperature of the curtain will be very high, but if the accident can be brought under control within a few seconds, no permanent damage to the curtain can occur.

If the curtain can be made even thicker, or with a graphite having a lower thermal conductivity, the protecting effect to the first wall will even be better. Figs. VIII-D-6, 7, 8 and 9 show the temperatures of the first wall and front wall of the curtain, for a uniformed plasma dump and localized plasma dump, respectively for a thicker (3 cm) graphite curtain. The first wall can now stand ~ 20 seconds before a permanent damage to the structure will occur. The graphite curtain, on the other hand, will become so hot and excessive vaporization, or even melting, will happen. The purpose of the thick curtain is for the sacrificial wall so the damage to the curtain is accpetable.

Conclusions

The effects of first wall protection provided by a relatively thick carbon curtain have been calculated. If a plasma dump type accident cannot be avoided in a fusion reactor, a metallic first wall will require frequency repairment to make reliable operation of a power plant or testing reactor impossible.

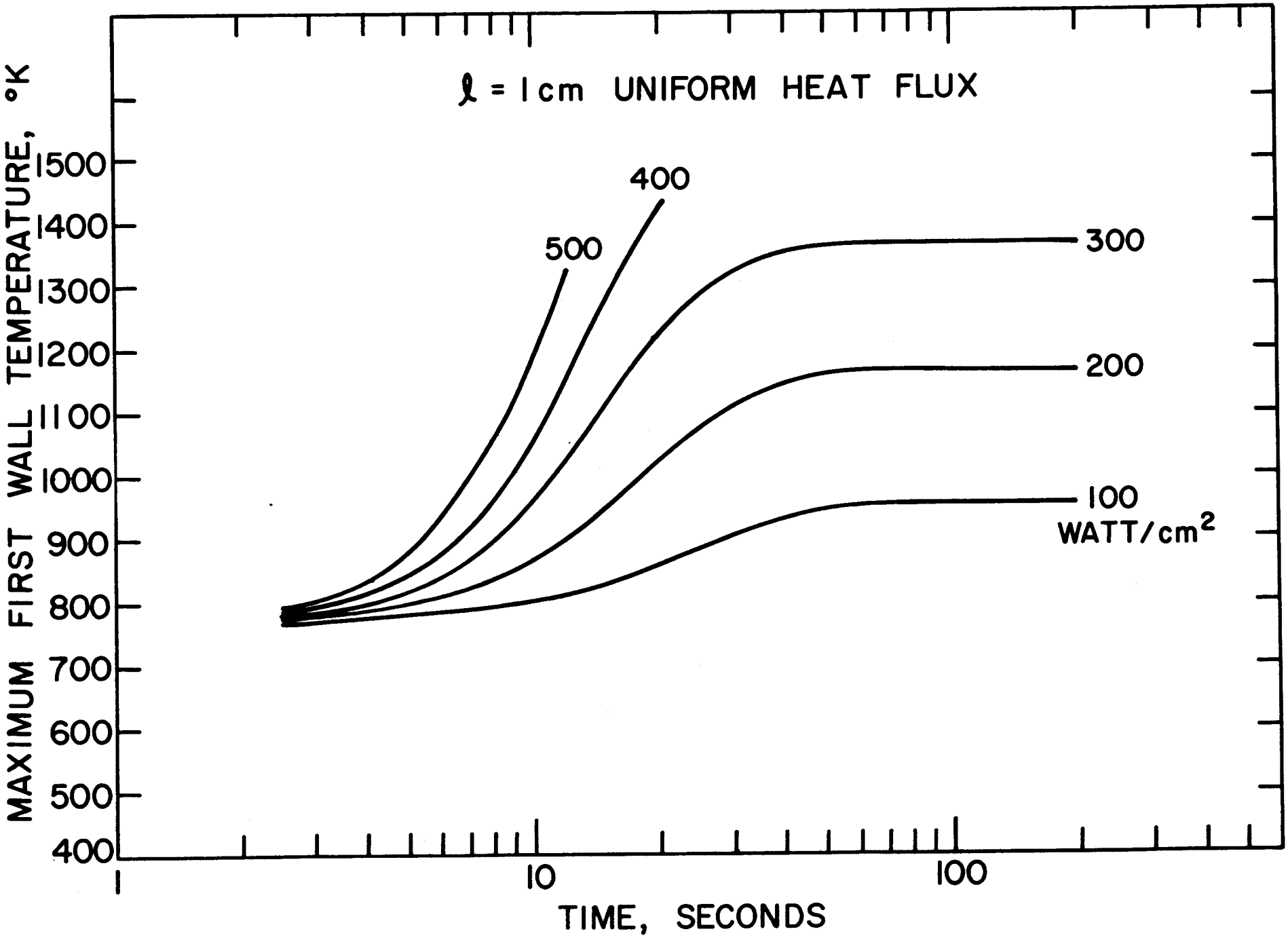

Fig VIII-D-2

Temperature of First Wall, Protected by 1 cm Thick Curtain

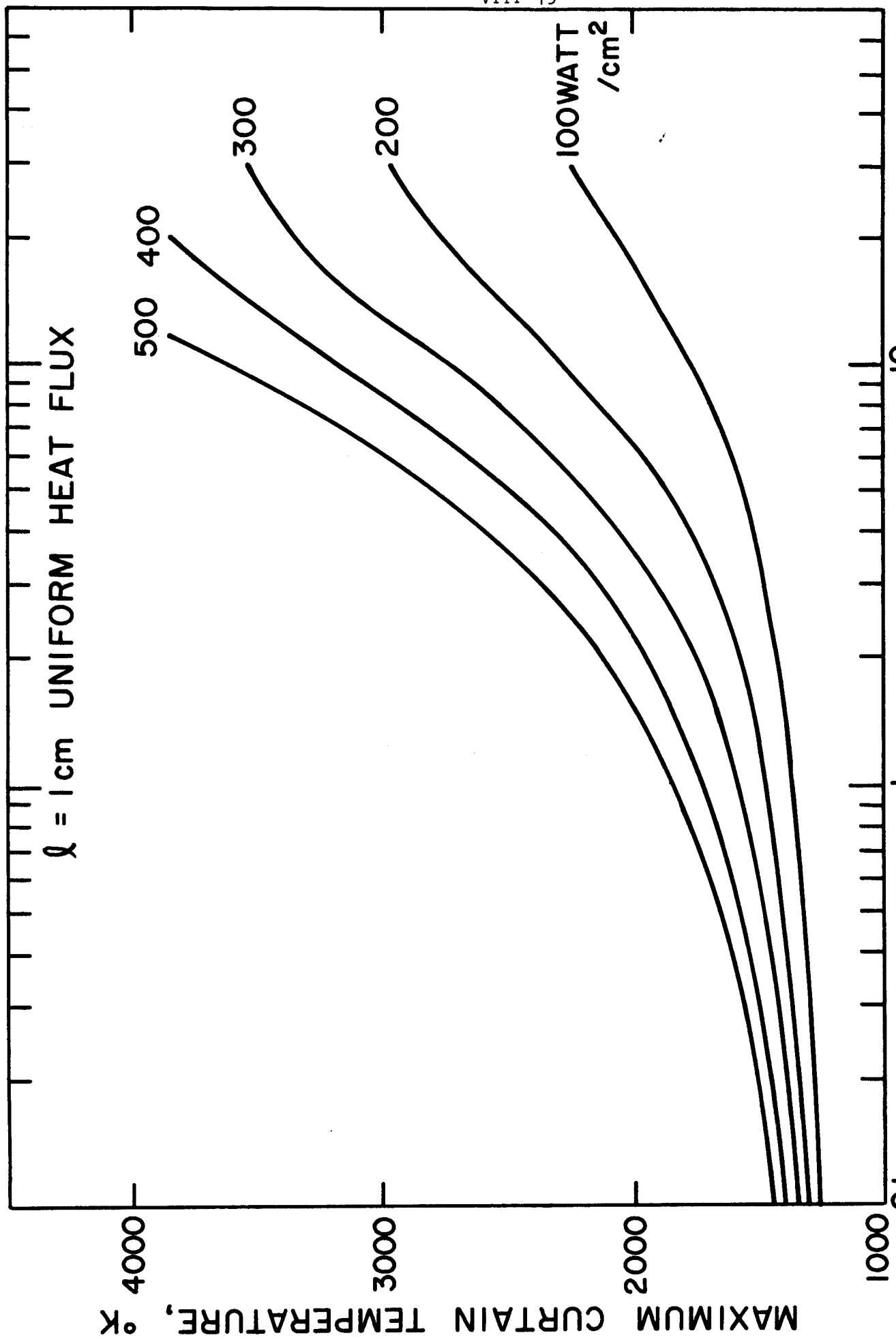

Fig. VIII-D-3
Temperature Response of the 1cm Thick Curtain

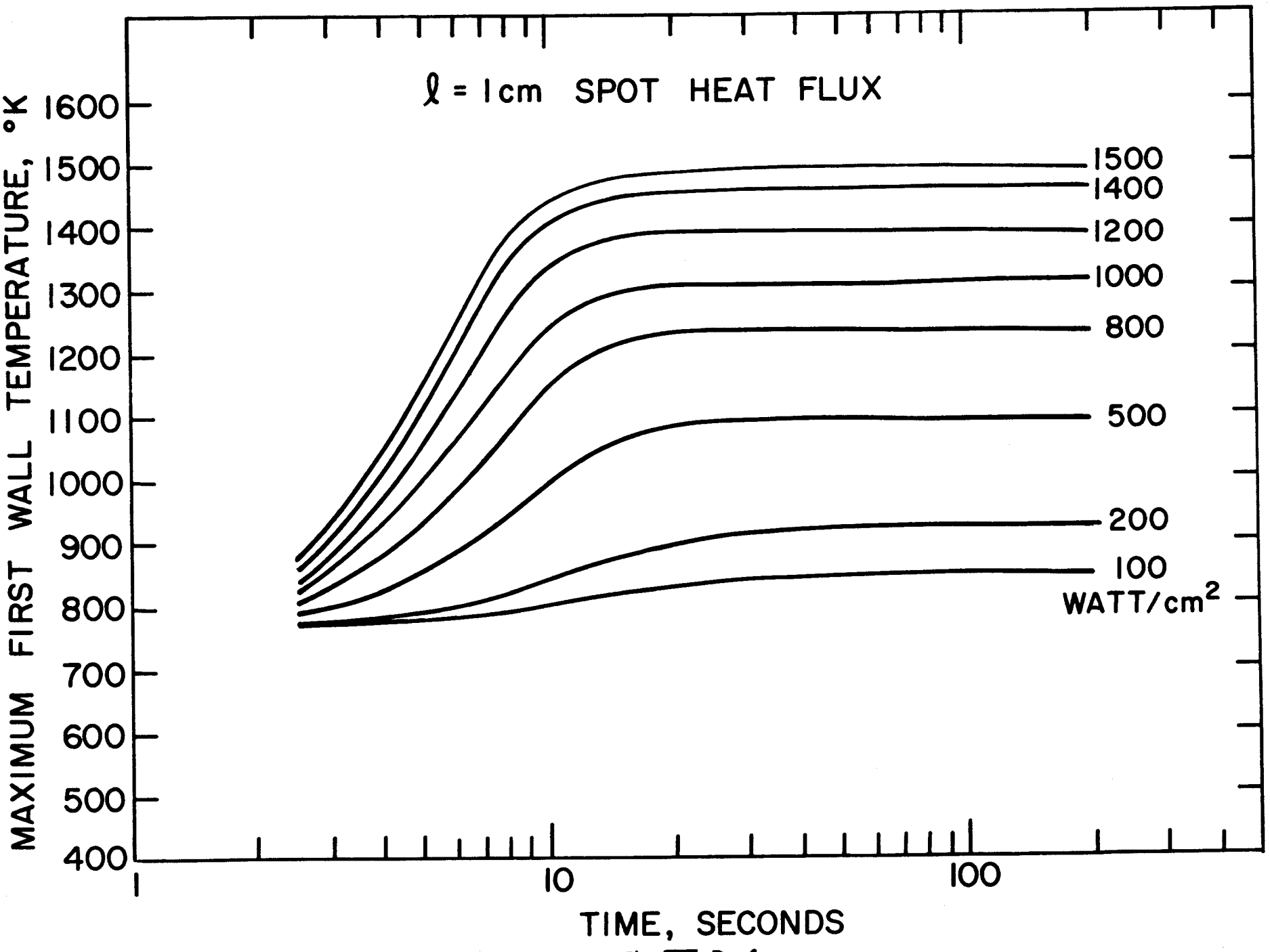

Fig VII-D-4

Temperature Response of First Wall Protected by a 1 cm Thick Curtain

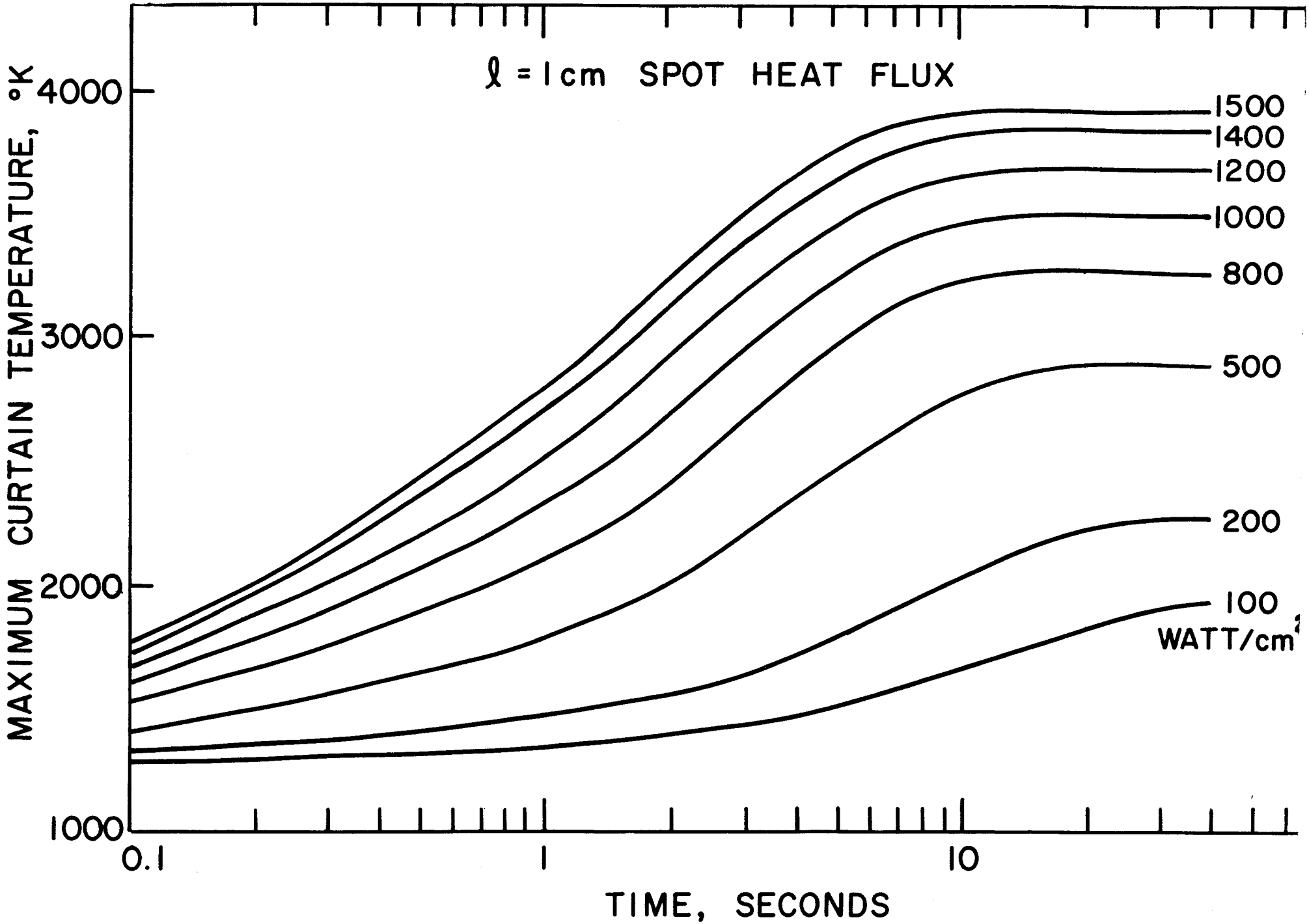

Fig VIII-D-5

Temperature Response of 1 cm Thick Curtain

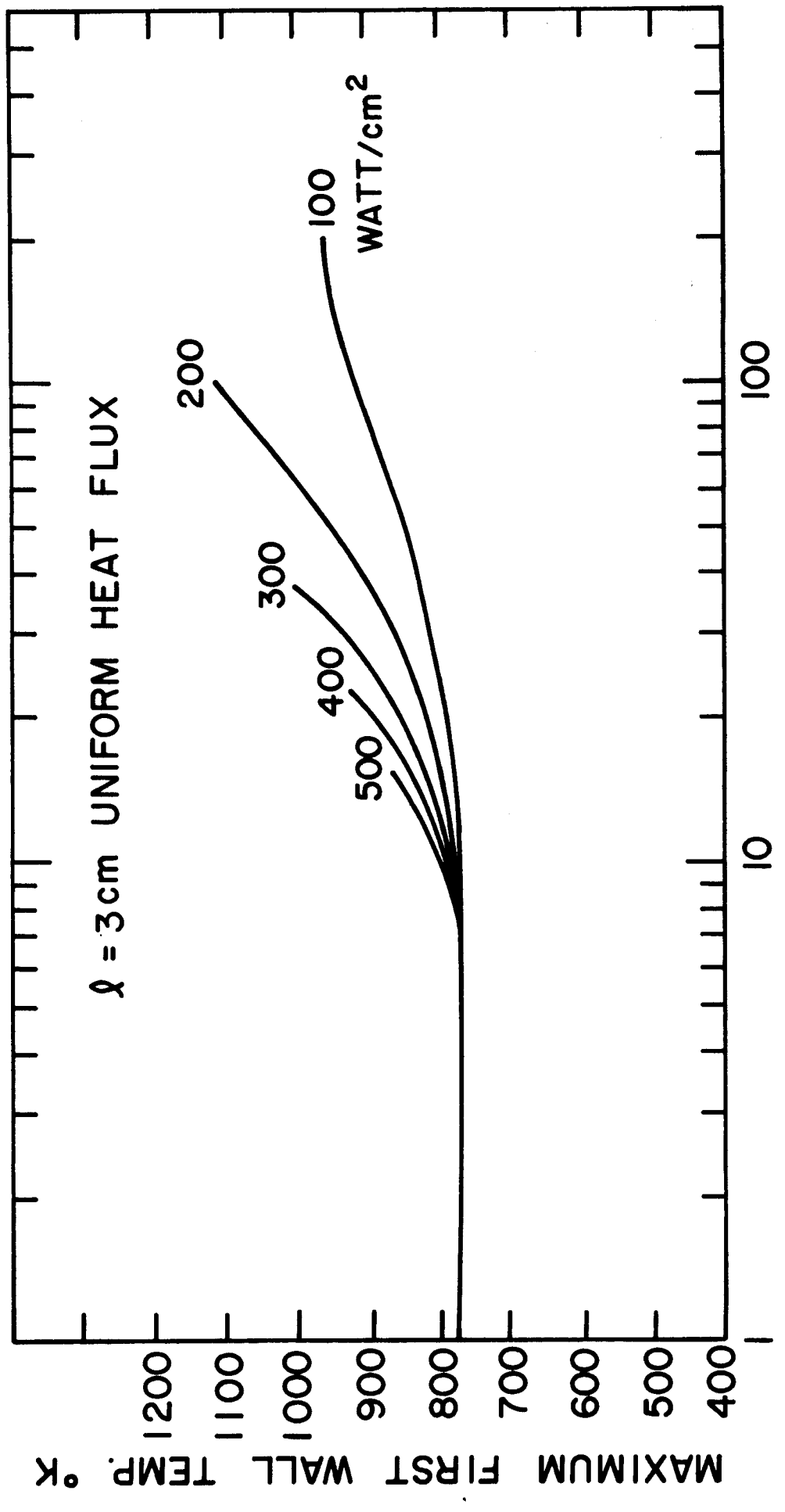

Fig VIII-D-6
Temperature Response of First Wall Protected by a 3 cm Thick Curtain

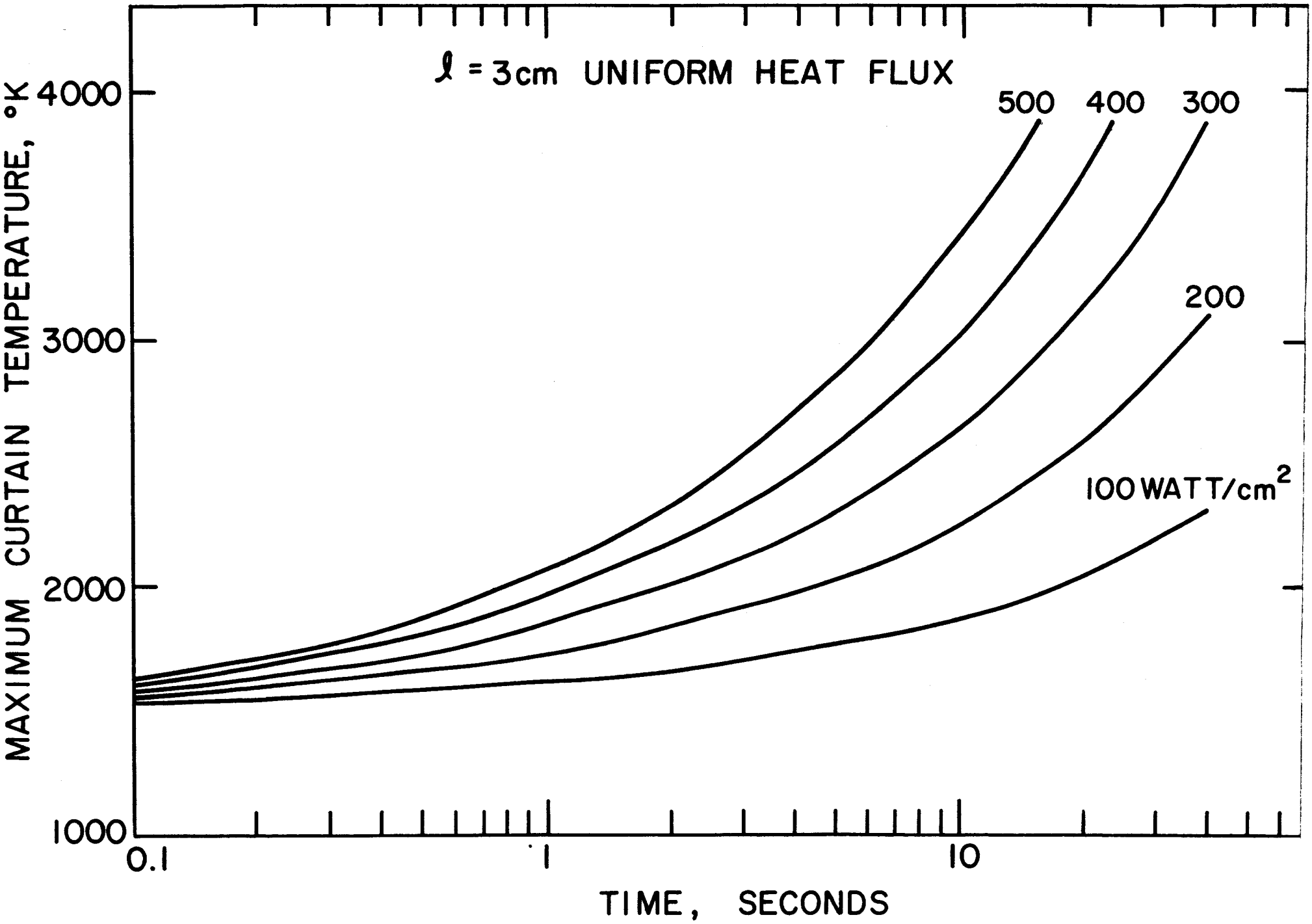

Fig VIII-D-7

Temperature Response of the Curtain

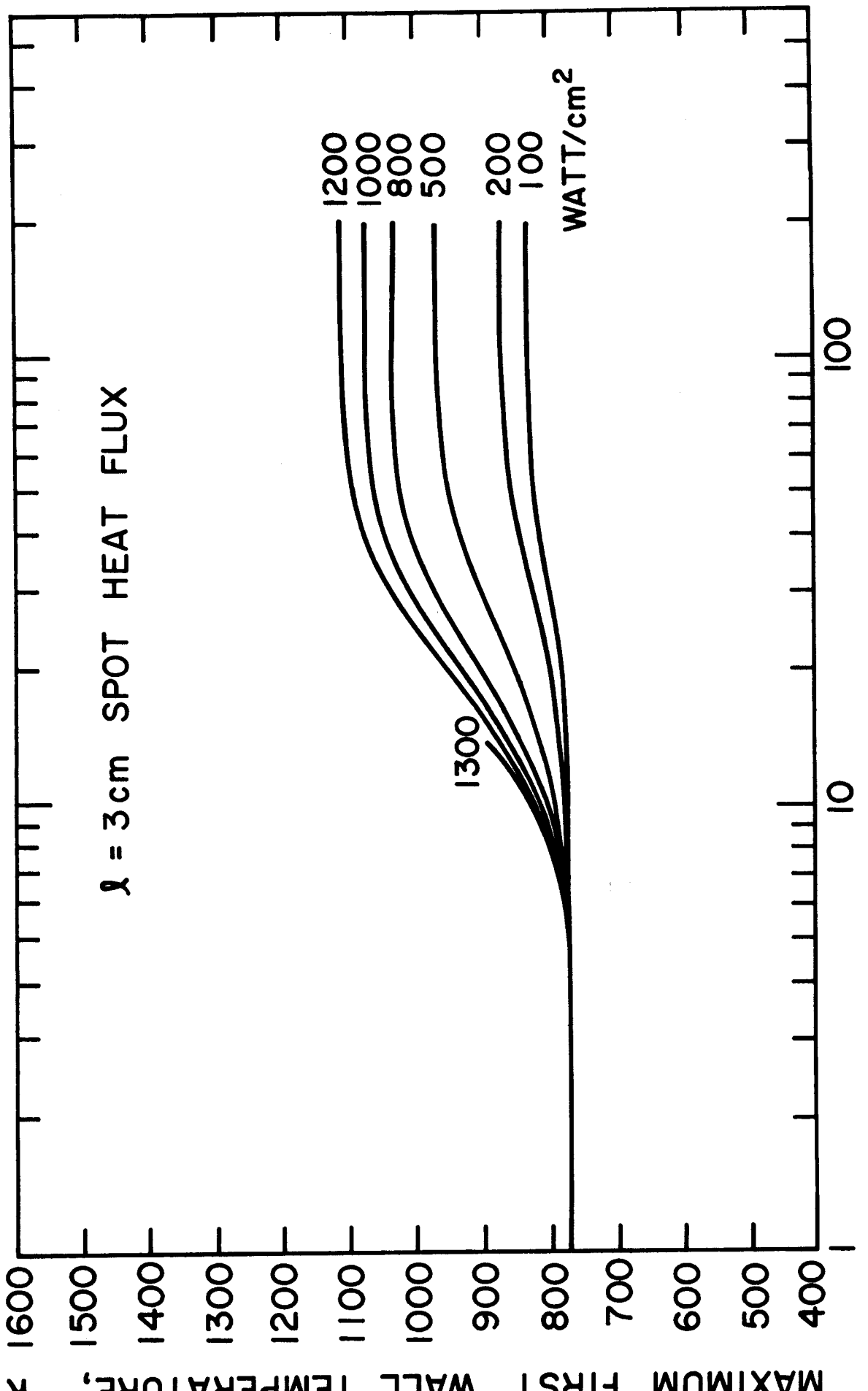

Fig VIII-D-8
Temperature Response of First Wall Protected by a 3 cm Curtain

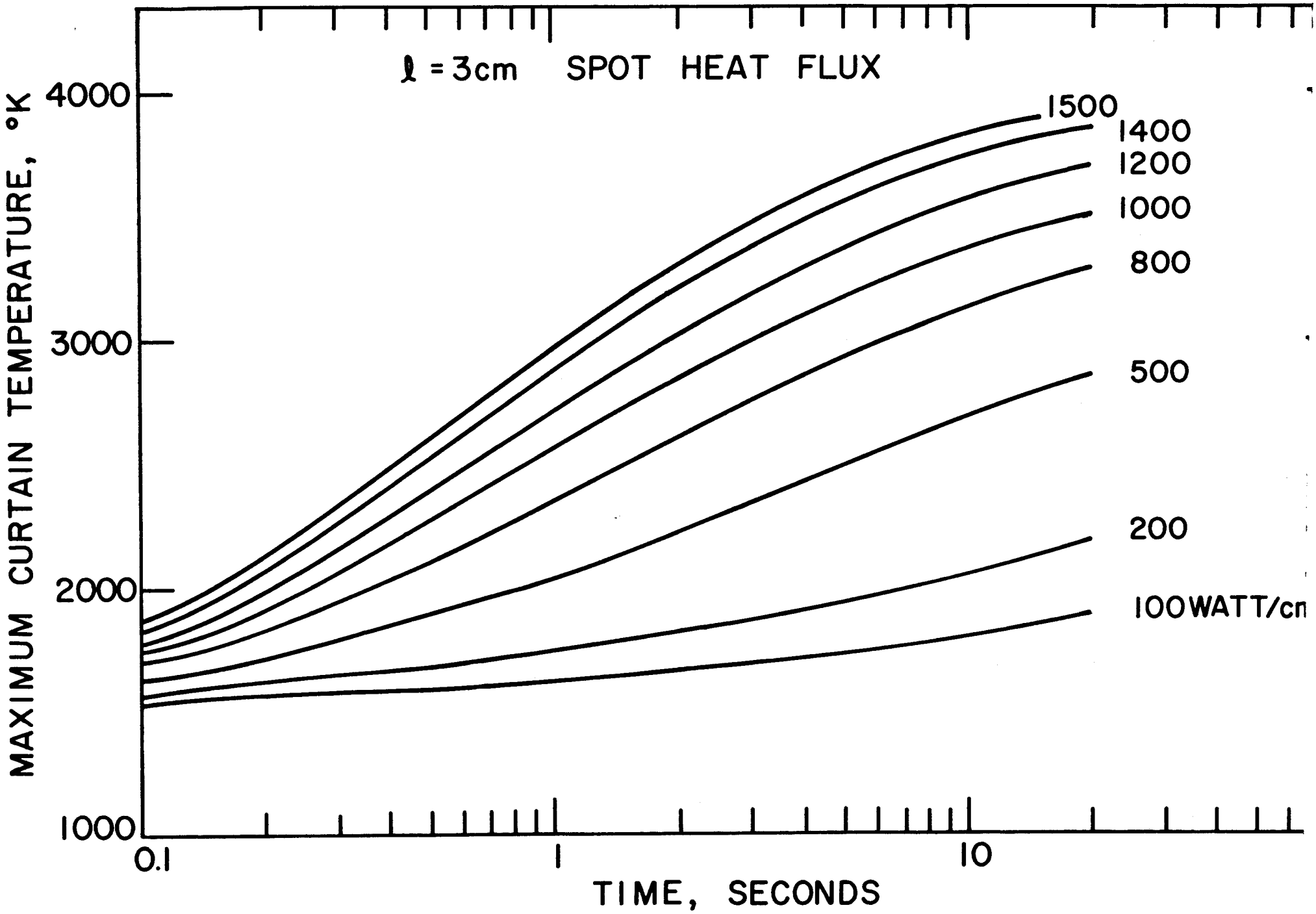

Fig VIII-D-9

TEMPERATURE RESPONSE OF CURTAIN

A thick carbon curtain will increase the thermal response time from a fraction of a second to ~ 20 seconds. This great increase in time will alleviate the control problems.

The carbon curtain so employed will be subjected to extremely high temperatures. Excessive evaporation of the graphite is possible. But the curtain is neither a load bearing structure, nor a vacuum containing wall. Therefore, it will be much easier to replace the curtain than the first wall. Even in case the curtain is melted through, the curtein can still function with a number of small holes.

References

1. TFR, ALCATOR Experiments.

2. The University of Wisconsin Fusion Technology Program, "UWMAK-II, A Conceptual Tokamak Reactor Design," UWFDM-112.

3. Baker, C. C. et al., "General Atomic Company Experimental Power Reactor Conceptual Design," Second Topical Meeting on the Technology of Controlled Nuclear Fusion, Richland, Washington, 1976.

VIII-E Heat Rejection System

There are three separated coolant loops for the TETR. The first wall and blanket are cooled by boiling water ~ 250°C. Boiling water is used to minimize the effect of thermal cycling. The testing module requires an inert coolant at a moderately high temperature so high purity helium is used. The coolant for the collector plates has to handle a large thermal flux, while keeping the plate structure at a moderate temperature. High velocity water is used as the coolant for this region. The cooling regimes, the coolant and their temperature ranges are shown on Table VIII-E-1.

Table VIII-E-1

Summaries Of Blanket Cooling

Regime	Coolant	Temperature	Thermal Energy
First Wall and Blanket	Boiling Water	220 to 260°C	275 MW
Testing Module	He (300 psi)	250 to 300°C	40 MW
Collector Plate	Water	66 to 71°C	200 MW

The temperature rise of the coolant from the collector plate is very small due to the high velocity required. To facilitate the heat exchanger design, only a fraction of the coolant is directed to the heat exchanger and cooled to 45°C. The return stream will be united to the hot stream and the resultant temperature is 66°C. This is then fed to the collector plate.

Power generation is not the primary function of this reactor so that a power conversion system is not included. The coolant of the blanket is high enough, however, that a low pressure steam turbine may be included to demonstrate the power conversion from fusion reaction. The heat exchangers have been designed kept this in mind so that the water from the heat exchangers is hot enough

for power conversion with a thermal efficiency about 20%. In the normal operations, the thermal energy will be dumped to a cooling towel.

A summary of the heat exchanger designs are shown on Table VIII-E-2. All three designs are point designs and no optimization were attempted. The fourth column is for the magnet coolant. No intermediate coolant is required for this loop. Three different cooling towers are required for the blanket and testing section, for the collector plate, and for the magnet, respectively.

Table VIII-E-2

Summary For The Heat Exchanger Designs

	Main Blanket	Testing Section	Collector	Magnets
Q, MW	275	40	200	70
Coolant	Steam	He (300 psi)	Water	Water
Tin, °C	220	250	45	30
Tout, °C	260	300	71	65
Flow Rate, $\frac{kg}{hr}$	7500	5.56×10^5	6.6×10^6	2×10^6
Secondary Coolant	H_2O	H_2O	H_2O	None
T, °C	100 to 200	100 to 200	35 to 60	---
Flow Rate, $\frac{kg}{hr}$	2.4×10^6	3.4×10^5	6.9×10^6	---
U $\frac{watt}{cm^2\text{-}°C}$	.78	.37	.90	---
ΔTm, °C	80	125	10.5	---
Area, m^2	440	90	2200	---
ID, HX m	2.0	1.0	3.65	---
Length, HX m	4.4	3.6	6	---
Weight, kg	25,000	6000	110,000	
Cost@ $30/kg	$.75 \times 10^6$	$.18 \times 10^6$	3.3×10^6	

Total Cost 4.23×10^6

VIII-F. Design Considerations for Collector Plates

The collector plate design is always one of the most difficult problems associated with fusion technology. To protect the first wall, the problems associated with a large area are concentrated to a much smaller area. Therefore, the problems encountered by the collector plates become orders of magnitude higher than what would be encountered by the first wall. The problems facing the collector plates and their possible solutions are:

1. Particle collection: lithium film or vacuum pumping.
2. Tritium recovery: compatible with particle collection.
3. Thermal stress: lithium film or high stress solid target.
4. Sputtering: lithium film or frequent change.
5. Energy removal: lithium film; water or direct conversion.

A lithium film appears to be a very attractive candidate for the collector plate.[1] The drawback of a lithium film is the low velocity and the small operating temperature range. The high thermal flux will overheat the surface of the lithium film and the vapor pressure of lithium will be too high. The lithium film is capable of handling up to $\sim$ 1 MW/m^2 thermal loading. The possible maximum loading in the TETR collector plate is $\sim$ 60 MW/m^2 which is far beyond what a lithium film is able to handle.

The design proposed here uses a solid target to collect the kinetic energy of particles. The particles. upon the release of its energy, will be vacuum pumped out of the reactor. Ta-10 W is picked as the structural material of the collector plate for its low modulus of elasticity and water is used as the coolant for the plates. Because of the sputtering problem, the collector plates have

to be replaced periodically. Tritium recovery from the vacuum pump system and tritium leakage through the collector plate to the cooling water are also considered and are discussed in Chapters III and XII.

VIII-F-1. Thermal Input

The total thermal energy impinged on the collector plates is 200 MW. This energy is highly concentrated on the edge of the plate and the energy flux is reduced by a factor of 10 for every 10 cm of distance from this edge. The energy distribution can be represented by the following equation:

$$Q = 66.7\ \bar{e}^{.23\kappa}\ MW/m^2 \qquad \text{(VIII-F-1)}$$

where κ is distance from the edge in cm. The peak flux here is about 20 times higher than the maximum thermal flux encountered in today's power plant. This very large flux generates problems in both heat transfer, thermal stress and material sputtering.

If the direction of the collector plate is not perpendicular to the incoming thermal flux, the energy received by the plate can be reduced by a factor of $\cos\theta$. Therefore, by the geometry of the plate, it will be possible to change the thermal flux to

$$Q = 6.67\ MW/m^2 \qquad -39\ cm < \kappa < 0$$

$$Q = 6.67\ \bar{e}^{.23\kappa} \qquad 0 < \kappa < \infty\ . \qquad \text{(VIII-F-2)}$$

That is, for the first 39 cm, the plate will be at an angle to the trajectory of the particle which spreads the thermal energy to a uniform

6.67 MW/m^2. The angle between the leading edge of the plate and the particle trajectory is about 6^0.

The 6.67 MW/m^2 is the maximum thermal load under the normal operating condition. However, it is possible for a short period of time for the thermal energy to stream to only one plate instead of all four. The maximum thermal load for a short period of time can be as high as 20 MW/m^2. Therefore, for a time dependent process, like sputtering, the average thermal loading is 6.67 MW/m^2. However, for thermal stress a thermal loading of 20 MW/m^2 must be considered.

VIII-F-2. Structural Material

The most important property in picking the structure material for the collector plates is to be able to withstand high thermal stress or to minimize the thermal stress. The thermal stress on a flat plate heated on one side by a uniform thermal load is:

$$\sigma_{th} = \pm \frac{\alpha}{2} \frac{E}{k(1-\nu)} qt \qquad \text{(VIII-F-3)}$$

in which α is the coefficient of expansion

E is modulus of elasticity

ν is Poisson's ratio

q is thermal input

t is plate thickness.

The ratio of yield stress, σ_y, and thermal stress, σ_{th}, can be termed as a safety factor,[2] or

$$S.F. \equiv \sigma_y/\sigma_{th} = \pm \left[2\left(\frac{\sigma_y\, k(1-\nu)}{\alpha E}\right)\left(\frac{1}{qt}\right)\right] \qquad \text{VIII-F-4}$$

The first term is material properties dependent, while the second term is operating conditions dependent. Therefore, to pick the material with the minimum effect by the thermal stress, the first term of the right side of the equation must be large. Figure (VIII-F-1) shows the value of $\frac{2\sigma_y k(1-\nu)}{\alpha E}$ of various materials. It is obvious Ta-10 W is the material to use. (Note the change of the scale). The mechanical and thermal properties of Ta-10 W, TZM and 316 SS are listed in Table VIII-F-1.

The collector plate is made of a bank of tubes, 1 cm I.D. with 1 mm thick wall. The maximum thermal load is ~ 20 MW/m^2. The thermal stress on the Ta-10 W structural is 13800 MN/m^2 (20,000 psi), which is one-sixth of the yield stress. Therefore, the thermal stress is well under the limit. Later calculation will show that the sputtering is the most critical problem.

VIII-F-3. Cooling Scheme

Water is one of the best coolants, and certainly is the coolant we know most about. It appears that high velocity water is well capable of handling a thermal flux as high as 10^4 W/cm^2. A typical temperature and thermal flux relation for water flowing within a tube at constant velocity is shown in Fig. VIII-F-2. At low thermal flux regions, heat transfer is by forced convection, and the relation is

$$\frac{hD}{k} = 0.023\left(\frac{Dv\rho}{\mu}\right)^{0.8}\left(\frac{C_p\mu}{k}\right)^{0.4} \qquad \text{VIII-F-5}$$

and $q = h\Delta T$ in which h is heat transfer coefficient

D is diameter of the tube

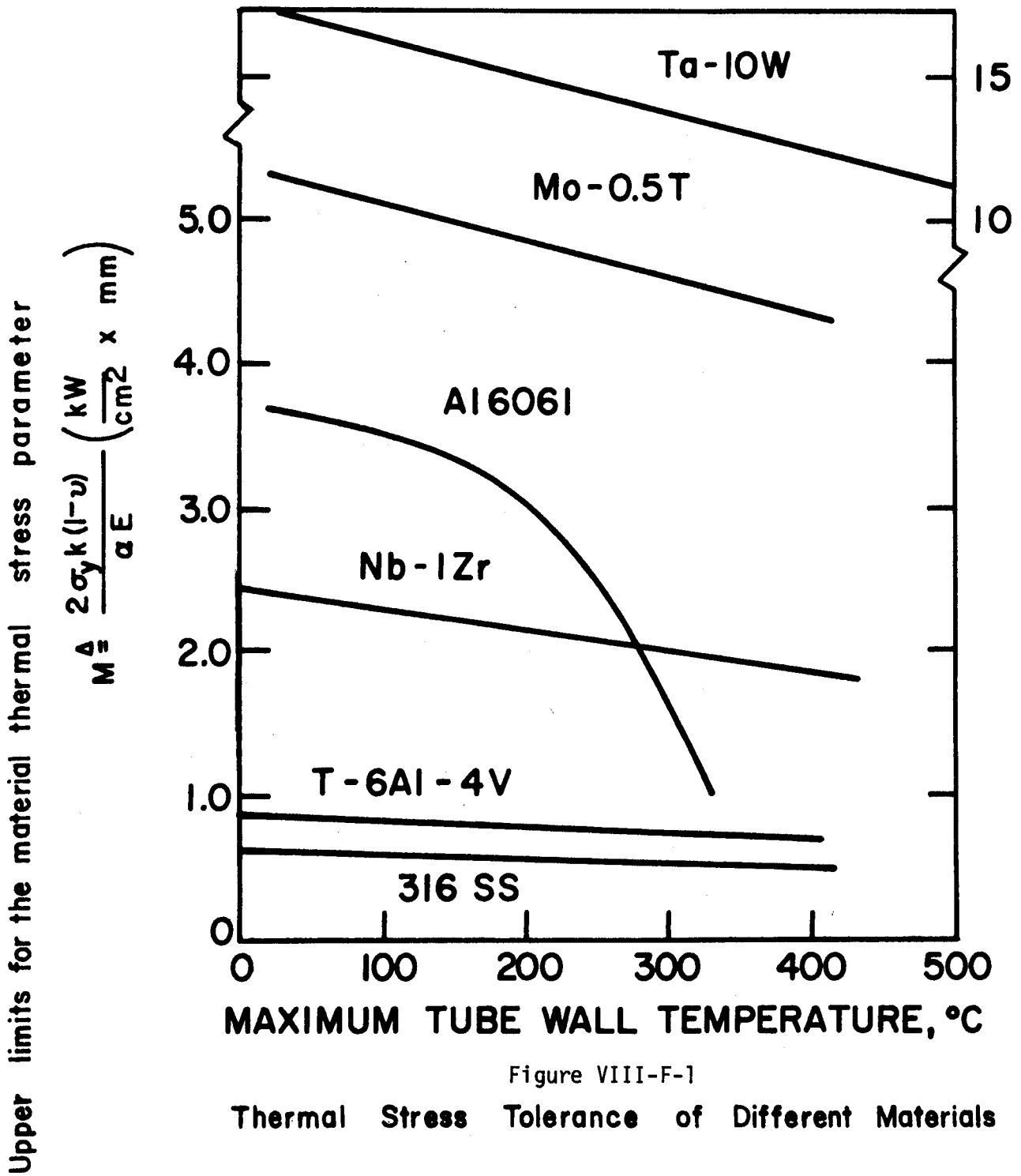

Figure VIII-F-1

Thermal Stress Tolerance of Different Materials

Table VIII-F-1

Thermal and Mechanical Properties of Some
Possible Structure Materials for the Collector Plate

	316 SS	Invar	TZM	Ta-10 W
Modulus of Elasticity, E, psi	23×10^6	21×10^6	44×10^6	10×10^6
Yield Stress, σ, psi	67,500	50,000	80,000	120,000
Thermal Expansion Coefficient, α, $\times 10^{-7}/°C$	180	10	54	50
Thermal Conductivity, k, $\frac{watt}{cm-°C}$	.2	.11	1.4	.5
Poisson's Ratio, ν	.3	.32	.32	.32
$\frac{2\sigma_y k\,(1-\nu)}{\alpha E}$	50	356	641	1600

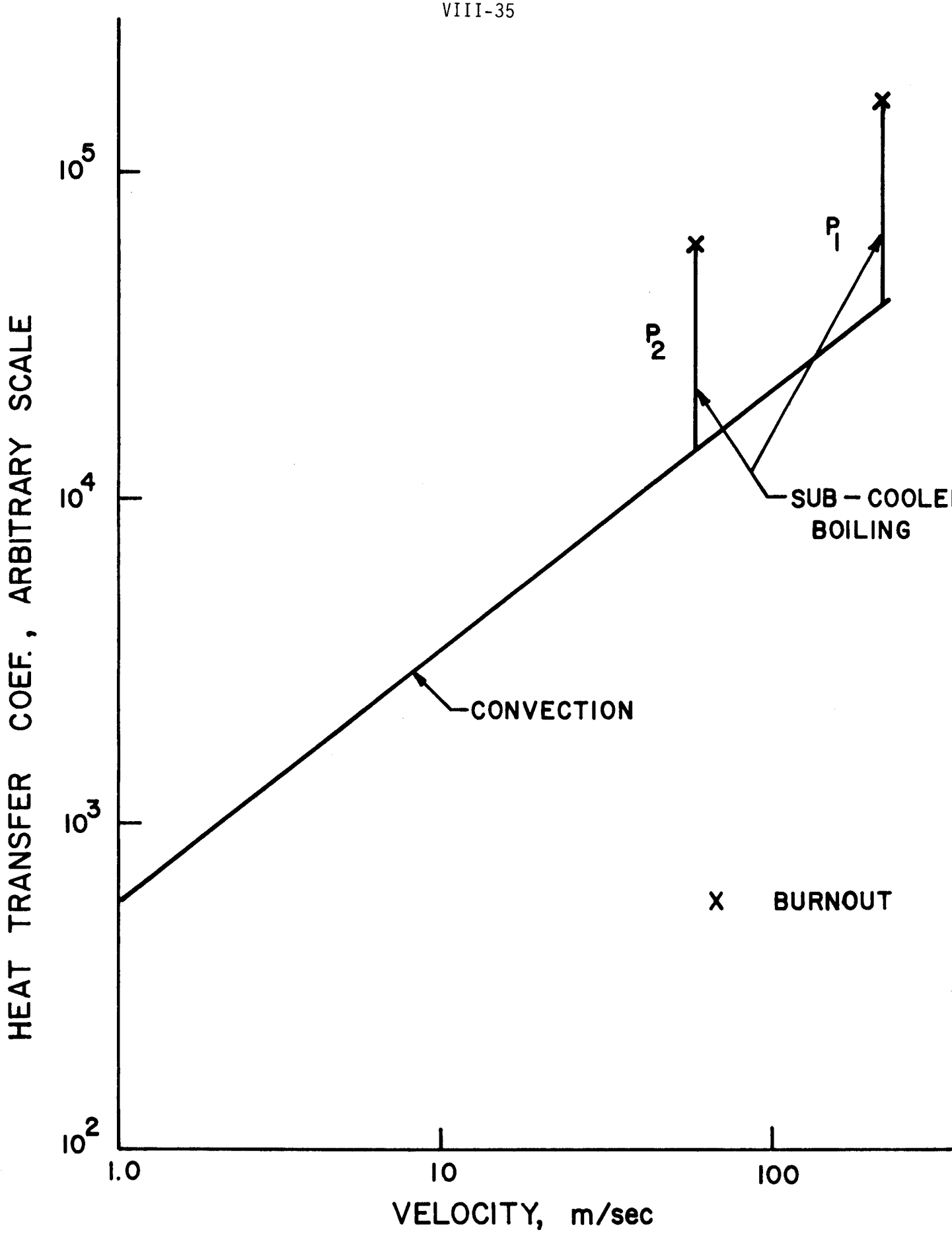

Figure VIII-F-2

Typical curve of heat transfer correlations

K is coolant thermal conductivity

v is coolant velocity

ρ is coolant density

μ is coolant viscosity

C_p is coolant specific heat

ΔT is film temperature drop

As q (and ΔT) increases the coolant temperature near the wall exceeds the saturation temperature, while the rest of the coolant is still under saturated. This leads to the sub-cooled boiling region. This is the vertical region of Fig. VIII-F-2. If the thermal flux is decreased further, burnout may occur.

Since the normal maximum thermal flux is 6.67 MW/m^2, while the abnormal maximum can be as high as 20 MW/m^2, the best operating point of the coolant is just below the sub-cooled boiling point. Therefore, the cooling is by forced convection at the normal operating condition. As the thermal load to the plate increases, the heat transfer mode changes to sub-cooled boiling with a significantly larger heat transfer coefficient. The plate structure will not be overheated despite the 3 fold larger thermal load.

To maintain a reasonable structure temperature, a very high heat transfer coefficient is needed which requires a high coolant velocity. A large pressure drop will be caused by the high velocity. So that to ensure a proper cooling of the plate, the following requirements have to be fulfilled for a thermal input of 6.67 MW/m^2:

1. A heat transfer coefficient $\geq 10 \frac{W}{cm^2\text{-}^oC}$
2. A film temperature drop $\leq 50^oC$
3. A coolant pressure drop $\leq 70 \frac{MN}{m^2}$ (10^2 psi)

The important relations are

$$\frac{hD}{k} = 0.023 \left(\frac{Dv\rho}{\mu}\right)^{0.8} \left(\frac{C_p\mu}{k}\right)^{0.4}$$

$$Q = h\Delta T \qquad \text{(VIII-G-5)}$$

$$\Delta p = \frac{2fv^2L\rho}{g_c D}$$

$$f = 0.0014 + 0.125 \left(\frac{Dv\rho}{\mu}\right)^{-0.32}$$

in which f is the friction factor

g_c is gravitational constant

Assuming L = 100 cm, D = 1 cm, with $Q = 6.67 \frac{MW}{m^2}$ the relation between h, Δp, ΔT and v are shown in Fig. VIII-F-3. At velocity of 30 m/sec, all the prementioned requirements seem to be satisfied. Therefore, this is the coolant operating point. A summary of the coolant operating conditions are listed on Table VIII-F-2. It should be noted that the high velocity required for cooling results in an unusually small coolant temperature rise of only 5°C.

VIII-F-4. Sputtering Considerations

The erosion rate due to physical sputtering by many types of species may be calculated by:

$$d(t) = \sum_{\mu} S_\mu \phi_\mu \frac{tAw}{N_o \rho} \qquad \text{(VIII-F-6)}$$

where S_μ is the sputtering yield in atoms per particle for a particular bombarding particle μ.

ϕ_μ is the flux of the bombarding particle μ.

A_w is the atomic weight of the material.

t is the irradiation time.

N_o is Avagadro's number.

ρ is the density of the wall material.

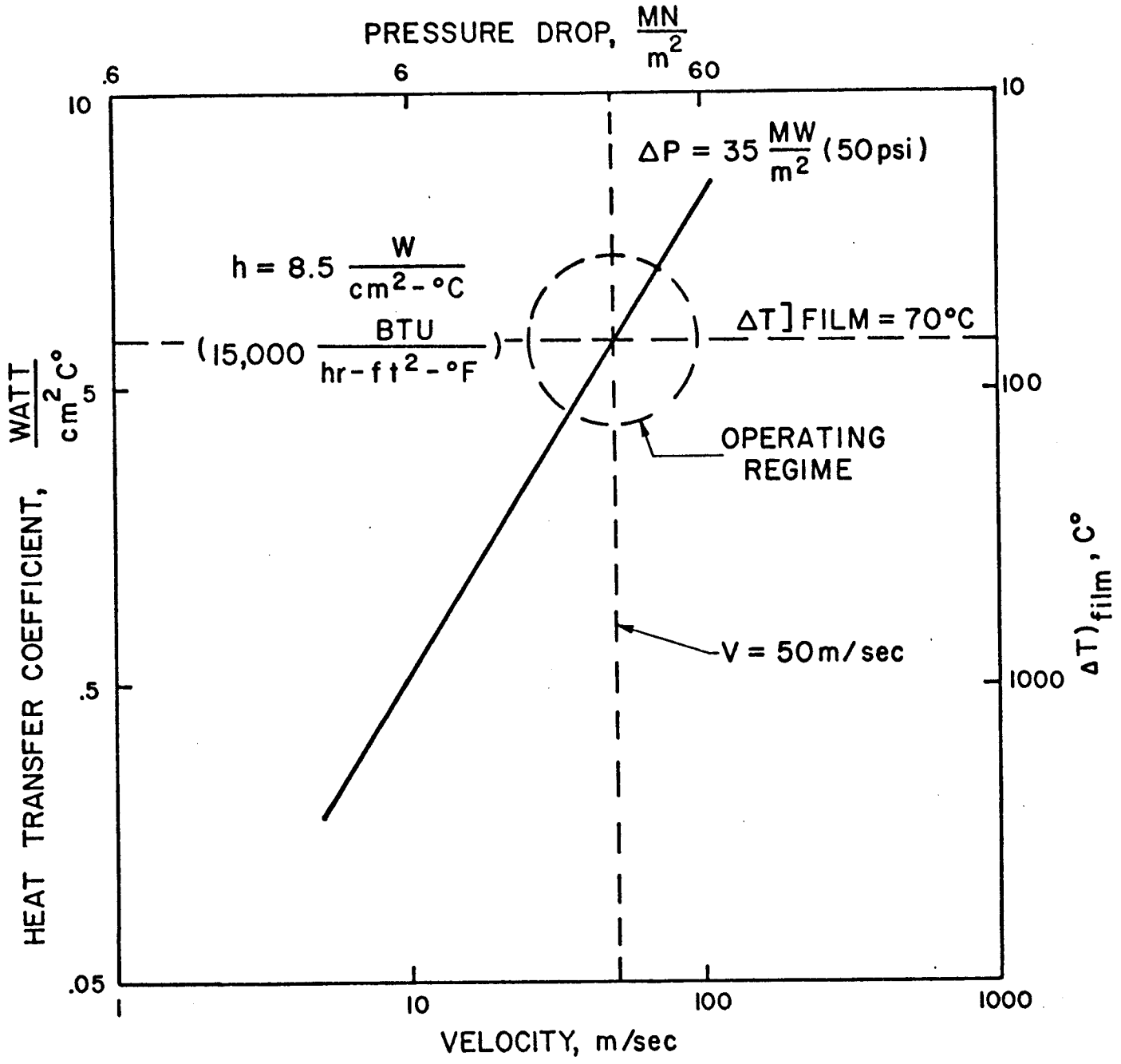

Fig VIII-F-3
Coolant operation point for the collector plate

Table VIII-F-2

Summary of Collector Plate Design

Material	Ta-10 W
Coolant	H_2O
Coolant Pressure	140 $\frac{MN}{m^2}$ (200 psi)
Coolant Velocity	30 m/sec
Coolant Inlet Temperature	65°C
Coolant Exit Temperature	71°C
Maximum Film ΔT	70°C
Maximum Structure Temperature	295°C
Coolant Pressure Drop	35 $\frac{MN}{m^2}$ (50 psi)
Coolant Tube I. D.	1 cm
Coolant Tube Wall Thickness	1 mm
Maximum Stress	14,000 $\frac{MN}{m^2}$ (20,000 psi)
Safety Factor	6
Plate Life	~ 1 month at S = 0.005

The sputtering yield of plasma ions on Ta-10W is unknown but a reasonable estimate is ~0.005. Assuming the coolant wall thickness is 1 mm and that 50% of it can be sputtered away before replacement is required, the wall life is 0.5 months.

VIII-F-5. Conclusions

A possible collector plate design for a near term system is presented. This design is summarized on Table VIII-F-2. The problems associated with collector plates and there solutions are :

1. Particle collection : by vacuum pump.
2. Energy removal : by high velocity, low temperature water.
3. Thermal stress : by proper material choice.
4. Sputtering : by frequent plate change.

While this design appears feasible to a test reactor, it may not be applicable to a power reactor. The thermal energy released to low temperature water will reduce the thermal efficiency. The frequent replacement of the plate will have a major impact of plant availability.

References for VIII-F

1. B. Badger, et al., "A Wisconsin Tokamak Reactor Design, UWMAK-I," UWFDM-68, Nuclear Engineering Department, University of Wisconsin (November 1973).
2. M. A. Hoffman and R. H. Werner, "Heat Flux Limitations on First Wall Shields for Early Fusion Machines," Proceedings of the First Topical Meeting on the Technology of Controlled Nuclear Fusion, San Diego, (April 1974).

IX. Radiation Damage Considerations

IX-A. Introduction and Perspective

Since one of the primary goals of the TETR is to provide a suitable test bed for long-term testing of materials, it is extremely important to insure that the reactor has a high reliability factor. Obviously, the bulk of the reactor will experience the same damage environment as present in the short time tests, but we do have the variables of temperature and stress at our disposal to extend the useful lifetime of the structure.

The object of this chapter is two-fold. First, the nature of the damage environment is described in great detail with respect to spatial distribution of displacement and transmutation effects. We have tried to give the reader a feeling for the combination of temperatures, damage rates and total damage levels so that he might be better able to assess the ultimate response of the structure to the reactor environment. Secondly, the effects of neutron and charged particle bombardment on carbon, steel, and superconducting materials is then reviewed in advance of satisfying the second goal of this chapter, namely an estimate as to how the normal TETR components will respond to long-term irradiation. This latter area is by its very nature speculative because of the lack of hard experimental data and the incompleteness of theoretical approaches to the problem. Nevertheless, it is important to document why we think we can build a reactor which will last the 10-15 MW-yrs/m^2 of first wall loading without excessive failure rates. The reader should carefully distinguish between the damage to the long-lived components and that to test specimens under a more severe environment.

IX-B. Radiation Environment

The object of this section is to restructure the information given in Chapter VII so as to make it more meaningful to the materials scientist. In many cases the information is taken directly from Chapter VII but it is felt that this overlap is necessary to develop a complete picture of the damage conditions.

IX-B-1. Neutron Flux and Energy Spectra

IX-B-1-a. Poloidal Variation

It is important to recognize that there is a considerable difference between neutron wall loading (which is a measure of neutron current) and neutron flux (which is a measure of the damage and transmutation rates) in noncircular tokamak reactors. It has been shown in previous studies[1] that the poloidal variation in wall loading and neutron flux may be drastically different and that the peak damage rate does not occur at the peak neutron wall loading. We will quote both parameters in the present work but the damage rate is better described by the neutron flux. The neutron wall loading has been calculated from a S_8P_3, R-Z shifted source, toroidal geometry model with the DOT Code. Figure IX-B-1 shows the geometry of the TETR used for this work where $\theta = 0$ corresponds to the outside midplane point and $\theta = 180°$ corresponds to the inner midplane point. The homogenized blanket and shield composition used for the 1-D neutronic calculations is shown in Figure IX-B-2 and Table IX-B-1 (see Chapter VII for a description of the 2-D models used).

LOCATION OF POLOIDAL COORDINATES FOR TETR NEUTRONICS CALCULATIONS

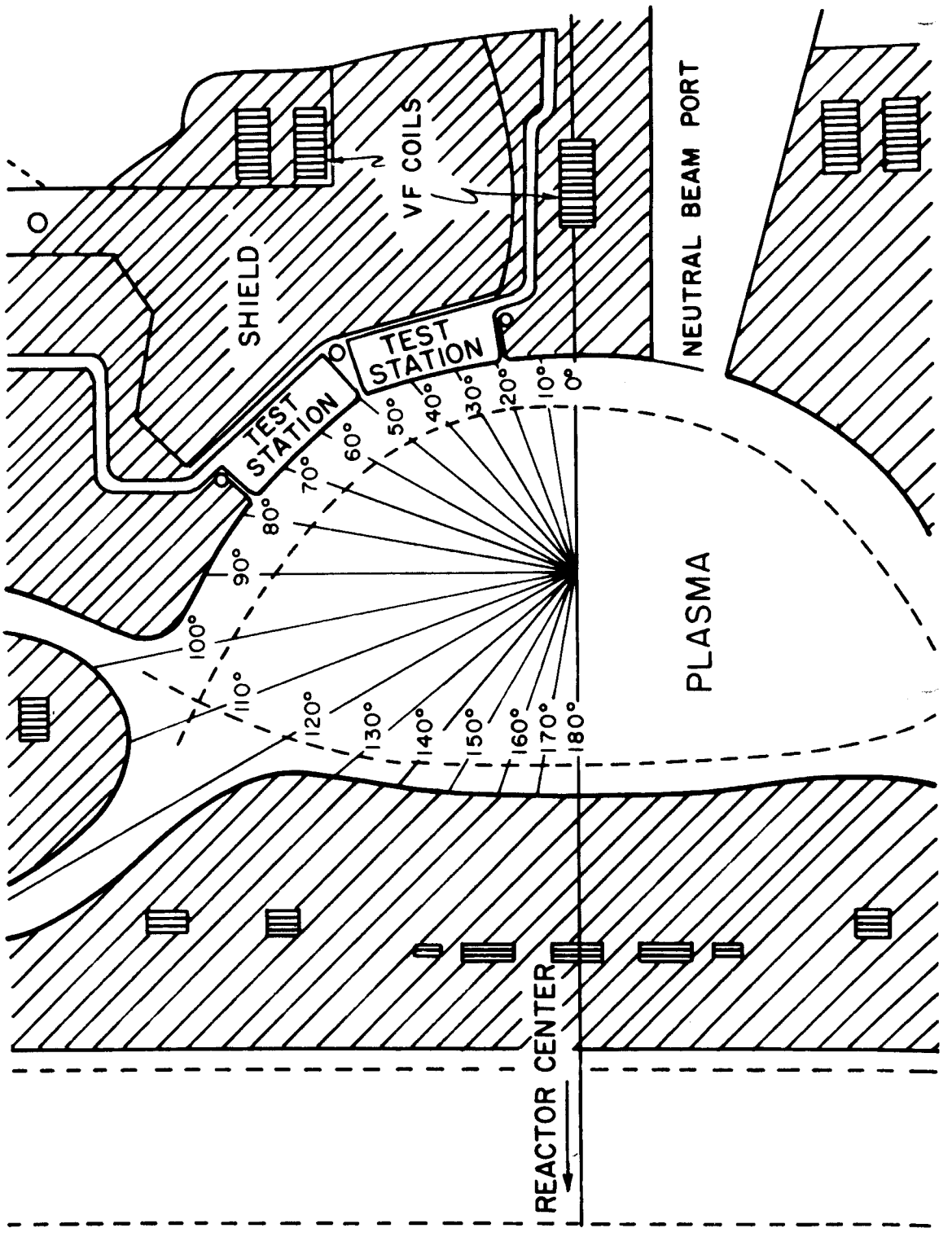

Figure IX-B-1

Figure IX-B-2

Schematic of Blanket and Shield Design-TETR

Inner Blanket (midplane)

Composition	I	II	III	IV	V	VI	VII	VI	V	VIII	V	VI	IX	VII	XI
Thickness -cm	55	1	3	1	5	5	11.5	5	5	7	7.5	7.5	34.5	1.5	0.5
Zone	1	2	3	4	5	6	7	8	9	10	11	12	13	14	15

Plasm

150 cm

Outer Blanket (Midplane)

	XI	VII	IX	VI	V	VIII	V	VI	VII	V	VI	
Plasma →	0.5	1.5	28	7.5	7.5	30	5	5	15	5	5	
	17	18	19	20	21	22	23	24	25	26	27	

110 cm

C-VI-1

Key for Figure IX-B-2

Zone Compositions for the Basic TETR Design at the Midplane

Composition*	Volume Percent	Material
I	57.65	Cu
	30.65	St.St.
	10.11	NbTi
	1.59	Insulation
II	100	Al
III	5	Mylar (H_9 C_{10} O_4)
IV	100	St.St.
V	87.4	B_4C
	4	St.St.
	4	H_2O
VI	92	Pb
	4	St.St.
	4	H_2O
VII	96	St.St.
	4	H_2O
VIII	75	Cu
	20	H_2O
	5	Insulation
IX	87.6	W
	4	St.St.
	4	H_2O
X	40	St.St.
	50	H_2O
XI	100	C
XII	100	Vacuum

*St.St. = 316 Stainless Steel

Table IX-B-1

Dimensions per Zone for the Basic TETR Design of the Midplane

Zone Number	Radius (cm)		Thickness (cm)
	Inner	Outer	
1	105.0	160.0	55
2	160.0	161.0	1
3	161.0	164.0	3
4	164.0	165.0	1
5	165.0	170.0	5
6	170.0	175.0	5
7	175.0	186.5	11.5
8	186.5	191.5	5.0
9	191.5	196.5	5.0
10	196.5	203.5	7
11	203.5	211	7.5
12	211	218.5	7.5
13	218.5	253.0	34.0
14	253.0	254.5	1.5
15	254.5	255.0	0.5
16	255	405	150
17	405	405.5	0.5
18	405.5	407	1.5
19	407	435	28
20	435	442.5	7.5
21	442.5	450.0	7.5
22	450.0	480	30
23	480	485	5
24	485	490	5
25	490	505	15
26	505	510	5
27	510	515	5

The poloidal variation in wall loading is shown in Figure IX-B-3. The neutron wall loading is 0.9 MW/m^2 at $\theta = 0°$, it drops until it reaches 0.85 MW/m^2 at 30° after which it increases to 1.0 MW/m^2 at 60°. As one moves towards the top of the reactor the wall loading drops off quickly until it reaches a minimum somewhere around 100-110°. Progressing toward the inside of the reactor one finds that the wall loading rises to a value of 1.2 MW/m^2 at 180°. The ratio of the maximum wall loading at 180° to that at 0° and 60° is 1.4 and 1.3 respectively.

The neutron flux is given in Figure IX-B-4 for three different lower energy limits; $E_n > 13.5$ MeV, $E_n > 0.1$ MeV, and $E_n > 0$ MeV. The poloidal variation in the neutron flux is much less than the wall loading and qualitatively different as well. For example, the maximum neutron flux occurs at $\theta = 60°$ (compared to $\theta = 180°$ for the wall loading) and the peak to average value is < 1.1 for the total flux ($E_n > 0.1$ MeV). The flux values are also essentially constant for the inner blanket from 130 to 180°. A detailed examination of the neutron energy spectra at $\theta = 0°$, 60°, and 180° shows that the spectrum is noticeably harder (as measured by the ratio of flux to current) at $\theta = 60°$ than at the inner or outer midplane. This is exactly what is desired because we want to "concentrate" the damage in the test zone while at the same time minimizing the damage in the rest of the reactor. This also explains why the test stations are off the midplane between $\theta = 20°$ and 75°.

IX-B-1-b. Variation Through Blanket and Shield

As one moves away from the first solid surfaces that intercept the neutrons from the TETR plasma, the neutron flux level drops and the spectrum softens. Figures IX-B-5 to IX-B-8 show how the neutron flux varies in two dimensions over the blanket, shield and test cell area. (See Chapter VII for the details of the 2-D calculations.)

The spatial profiles in these figures and others which are not shown, show several interesting points:

(1) The attenuation of the high energy (>13.5 MeV) neutron flux at the reactor midplane is rather uniform showing a decade drop every 10 to 25 cm.

(2) There is a slight distortion of the first neutron group flux around the test cells but nothing that should present problems.

(3) There is a significant leakage of high energy neutrons up the divertor slots which means that damage rates in those areas must be closely examined.

(4) The flux gradient for the damaging neutrons (>0.12 MeV) also drops off rather gradually at the midplane; reductions of an order or magnitude require 10 to 20 cm.

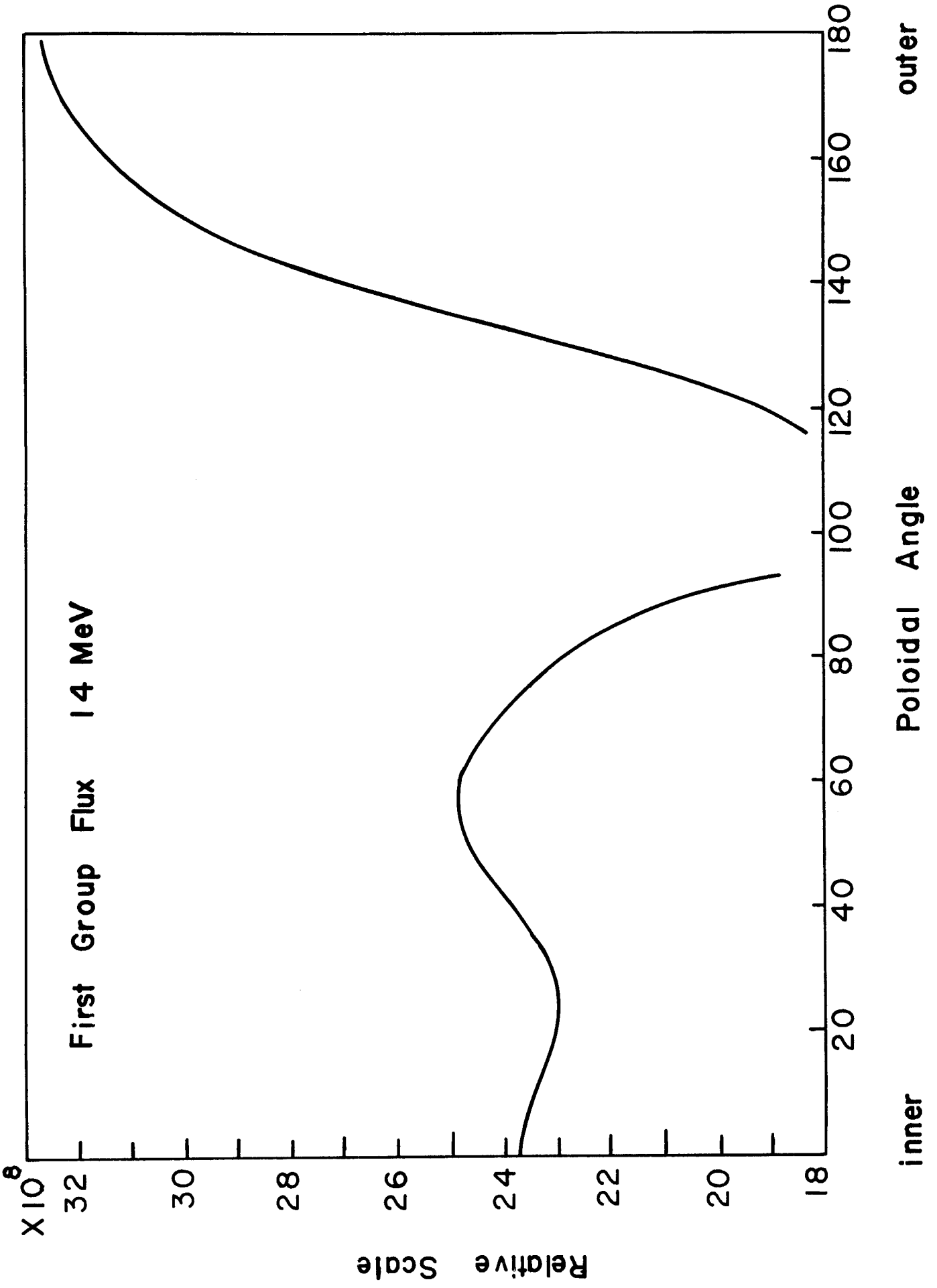

FIGURE IX-B-3 Poloidal Variation of Neutron Wall Loading in TETR (Uncollided ~99% of 1st Group)

NEUTRON FLUX VALUES IN TETR

Figure IX-B-4

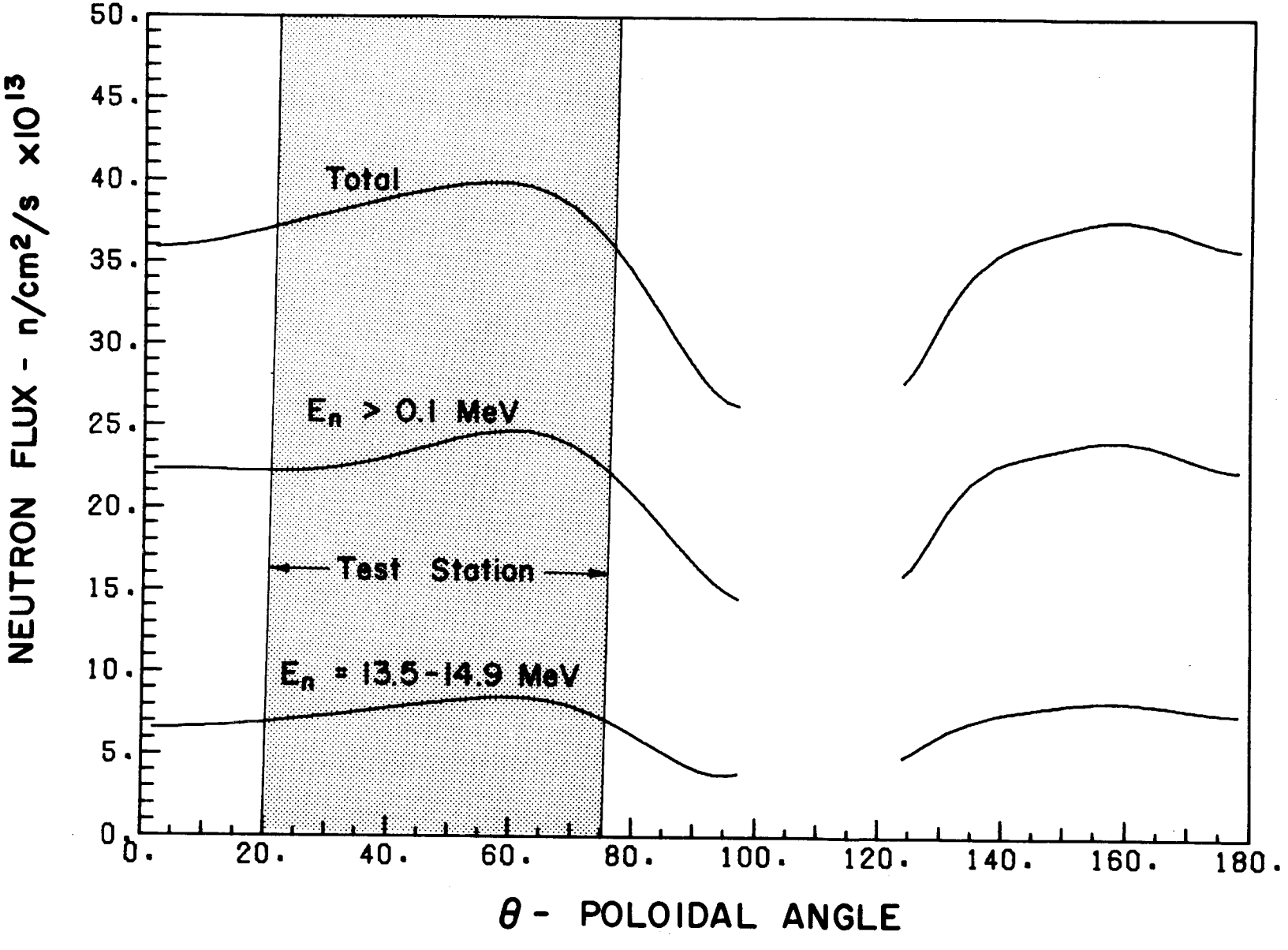

FIGURE IX-B-5 SCHEMATIC OF TETR USED FOR NEUTRONICS CALCULATIONS

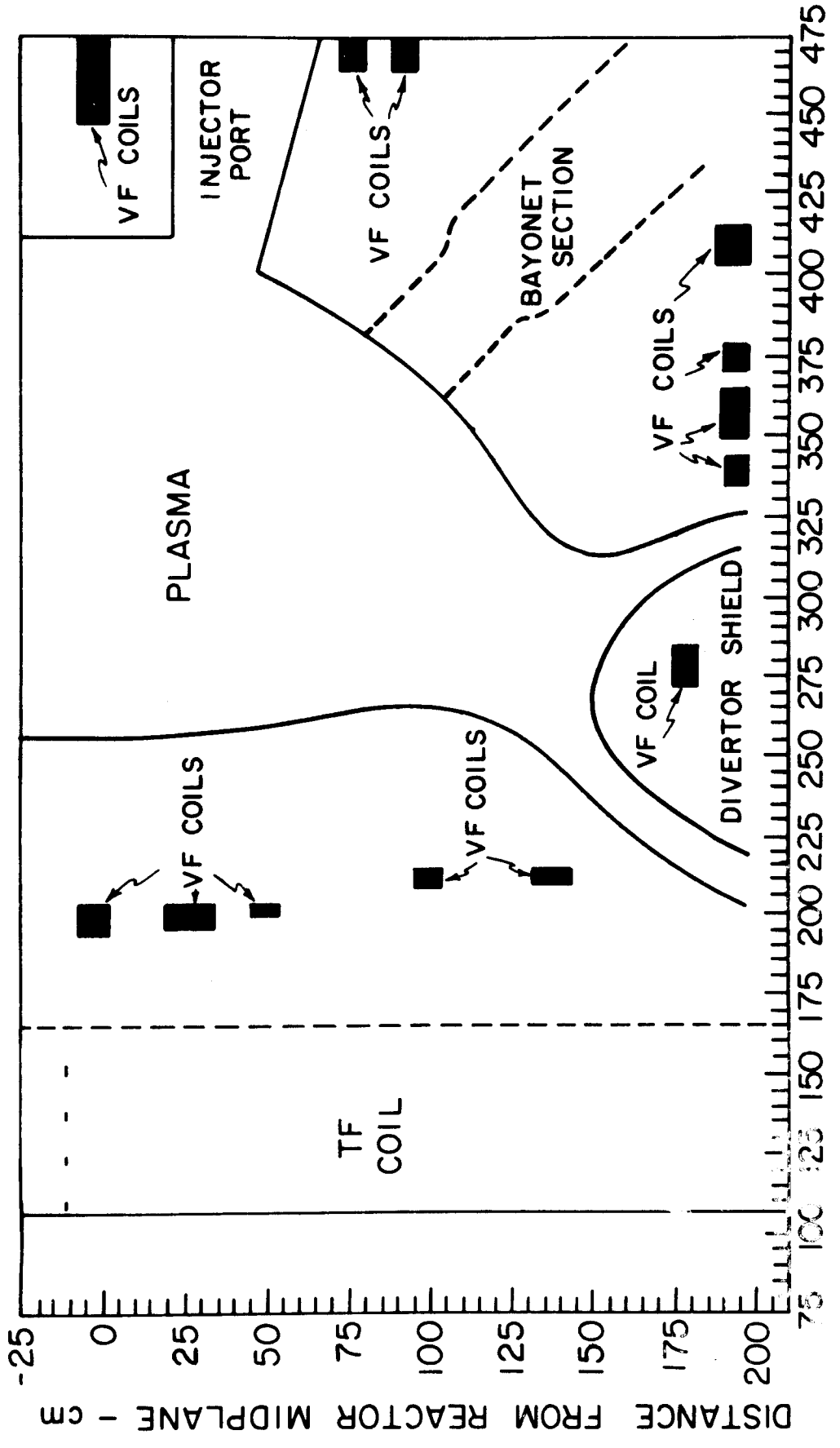

FIGURE IX-B-6 NEUTRON FLUX IN LOWER HALF OF TETR
(E > 0.12 MEV)

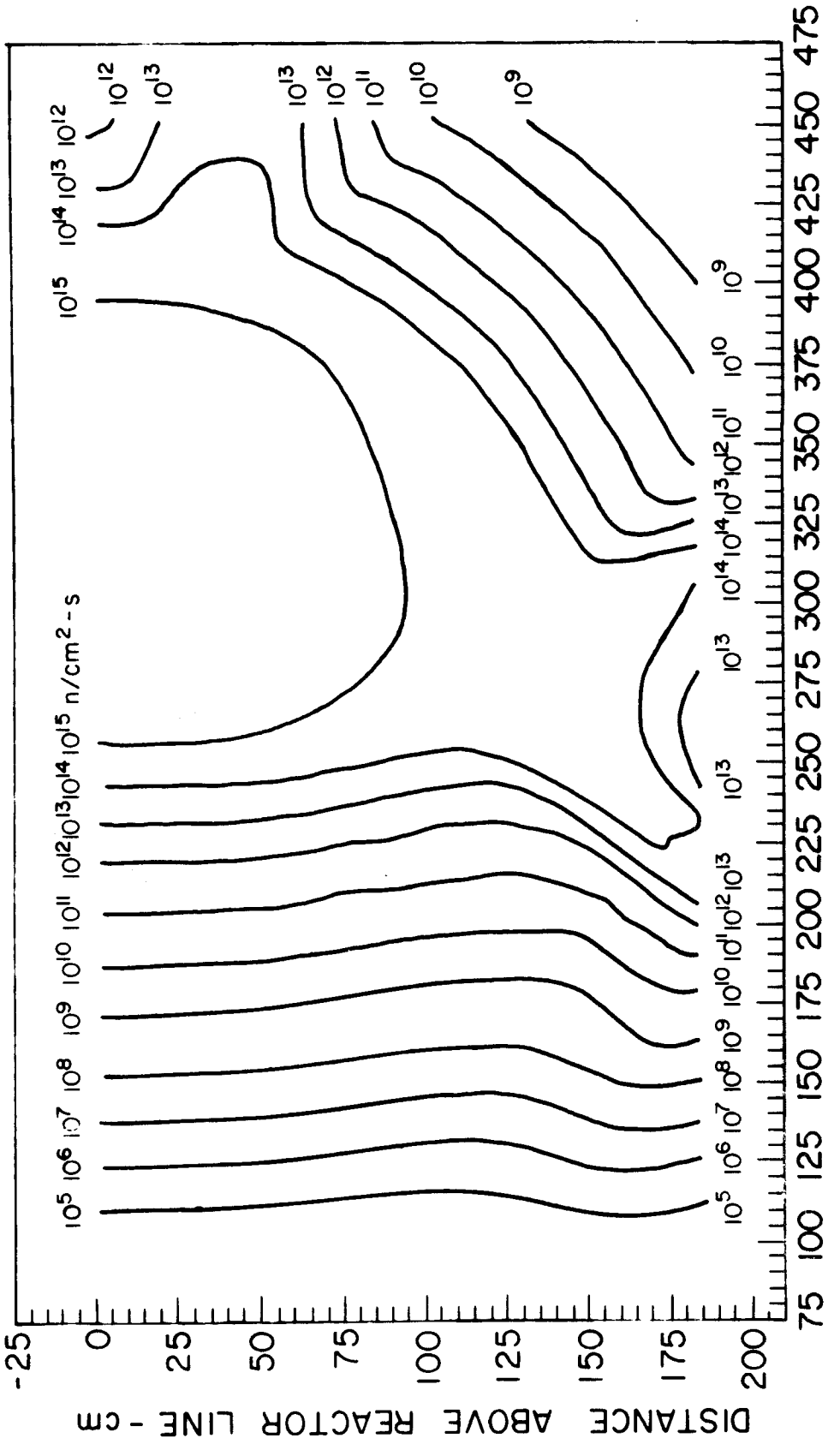

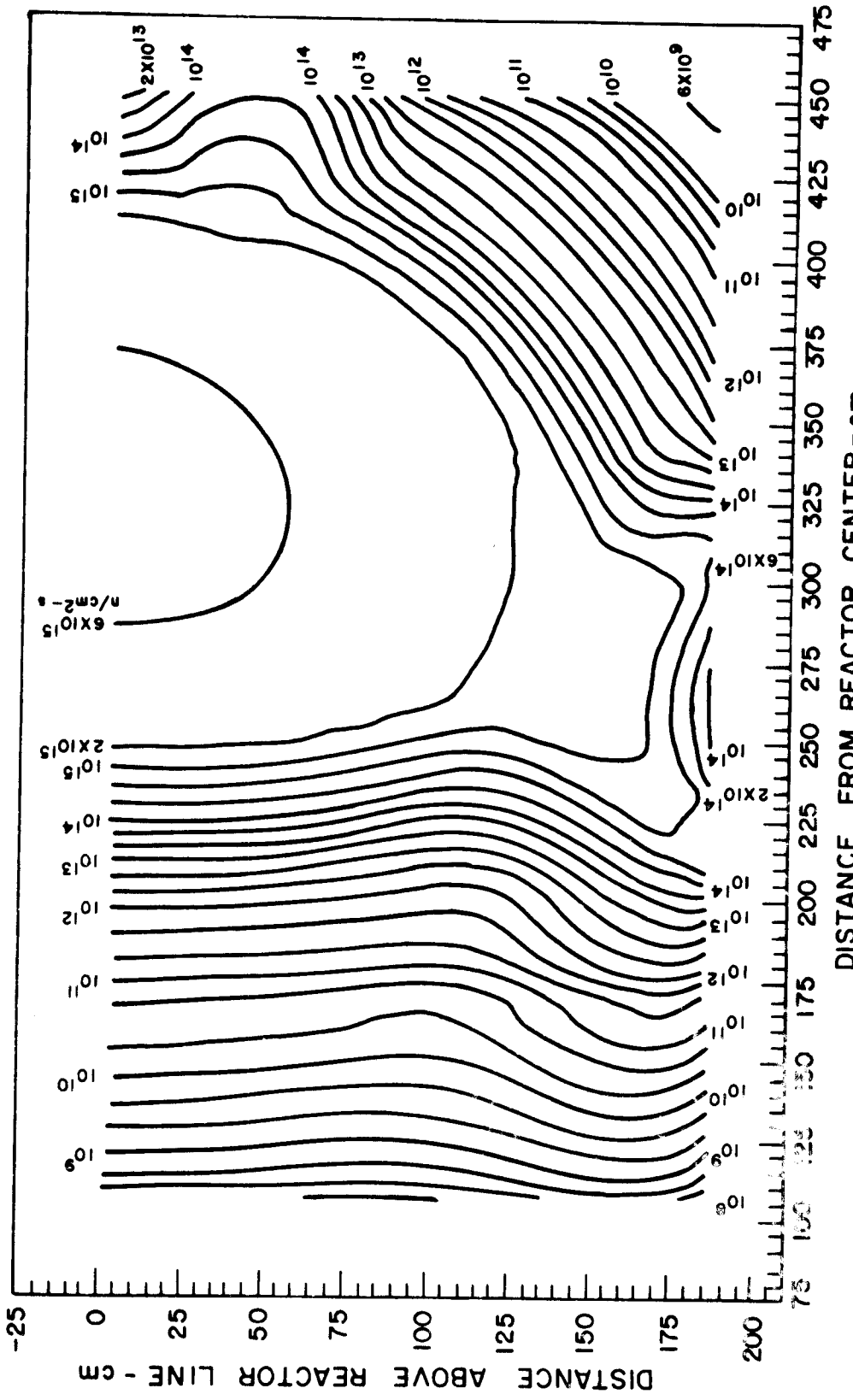

FIGURE IX-B-7 NEUTRON FLUX IN LOWER HALF OF TETR (E>0.12 MEV)

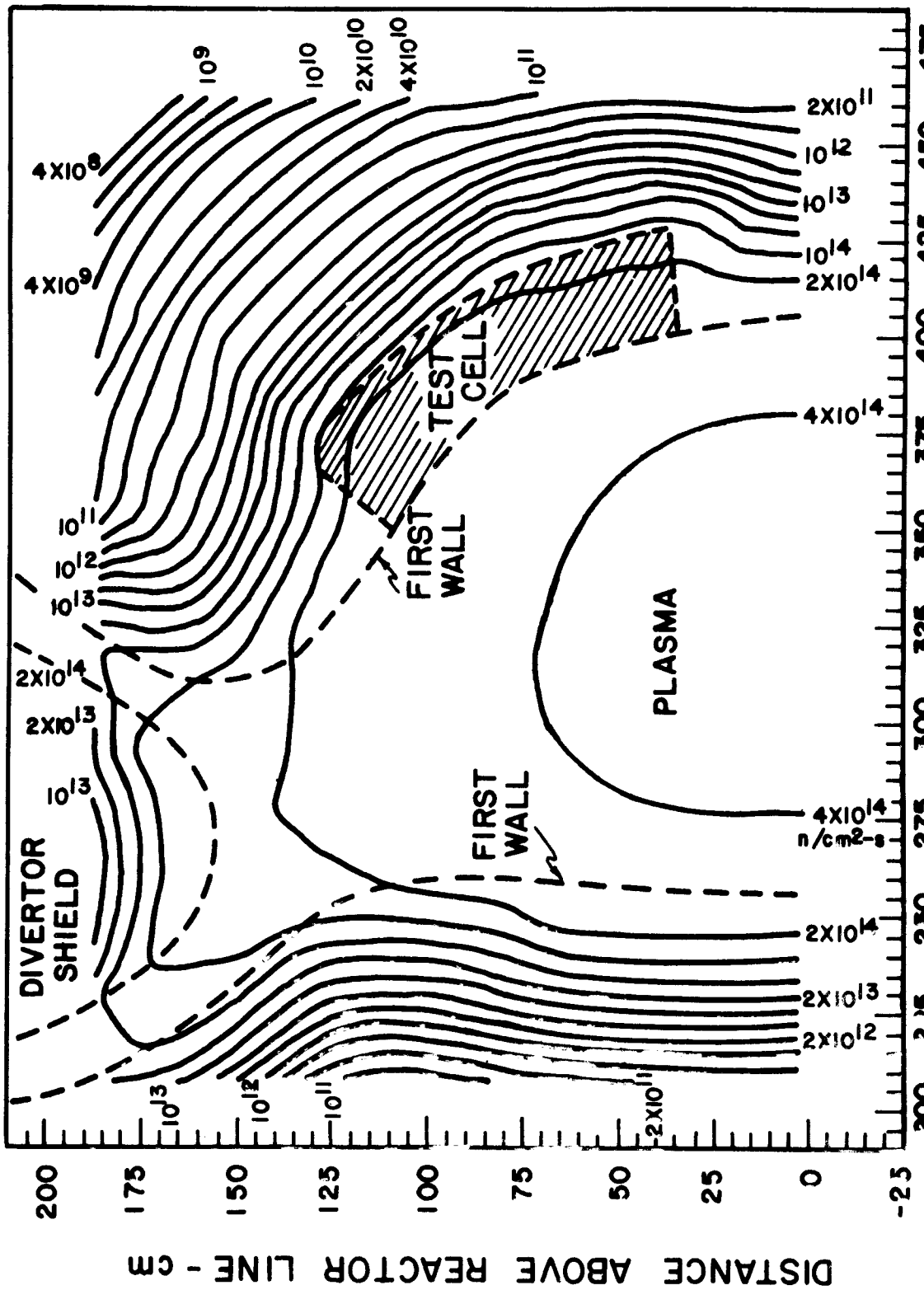

FIGURE IX-B-8 TETR. NEUTRON FLUX (E>0.12 MEV)

(5) The damaging flux in the 10 cm thick test cell area drops by less than a factor of 3 from front to back.

(6) The leakage of damaging neutrons up the divertor slots is even more pronounced than in the case of the uncollided flux.

(7) The total neutron flux (>0.0 MeV) also requires a 15 to 20 cm thickness to be attenuated by an order of magnitude.

(8) The maximum flux of neutrons at the inner TF coil surface closest to the plasma is approximately

	n/cm^2-s	
	Maximum (Divertor Slots)	Midplane
(>13.5 MeV)	1×10^8	2×10^7
(>0.12 MeV)	2×10^{10}	5×10^9
(>0.0 MeV)	9×10^{10}	9×10^9

IX-B-1-c. Neutron Flux Variations in Neutral Beam Injector Port and Shield

A two-dimensional plot of the high energy neutron flux resulting from neutrons leaking down the neutral beam injector port is given in Figures IX-B-9 and 10. The important points to note with respect to radiation damage considerations are:

(1) The damage flux (E>0.12 MeV) is high at the front surface ($10^{14} n/cm^2$-s) and it does not drop to $10^{13} n/cm^2$-s in the injector port liner until ~300 cm from the front surface.

(2) Where as one-dimensional shielding calculations would predict that the back side of the TF coil would receive a factor of ~100 less neutron damage than the front surface of the coil, leakage of neutrons down the port can reduce that ratio to ~10.

(3) The leakage of neutrons down the neutral beam port and through the neutral beam shield can increase the neutron flux a factor of 100 more than predicted by one-dimensional calculations through the TETR blanket and shield alone.

Examination of Figures IX-B-5 to 8 shows that similar statements could be made about the VF coils in the proximity of the divertor slots.

IX-B-2. Particle Flux to Solid Surfaces

IX-B-2-a. Flux to Carbon Curtain

There are basically three classes of particles that strike the carbon curtain in TETR:

FIGURE IX-B-9 ADDITIONAL NEUTRON FLUX IN TETR NEUTRAL BEAM INJECTOR (E > 0.12 MEV)

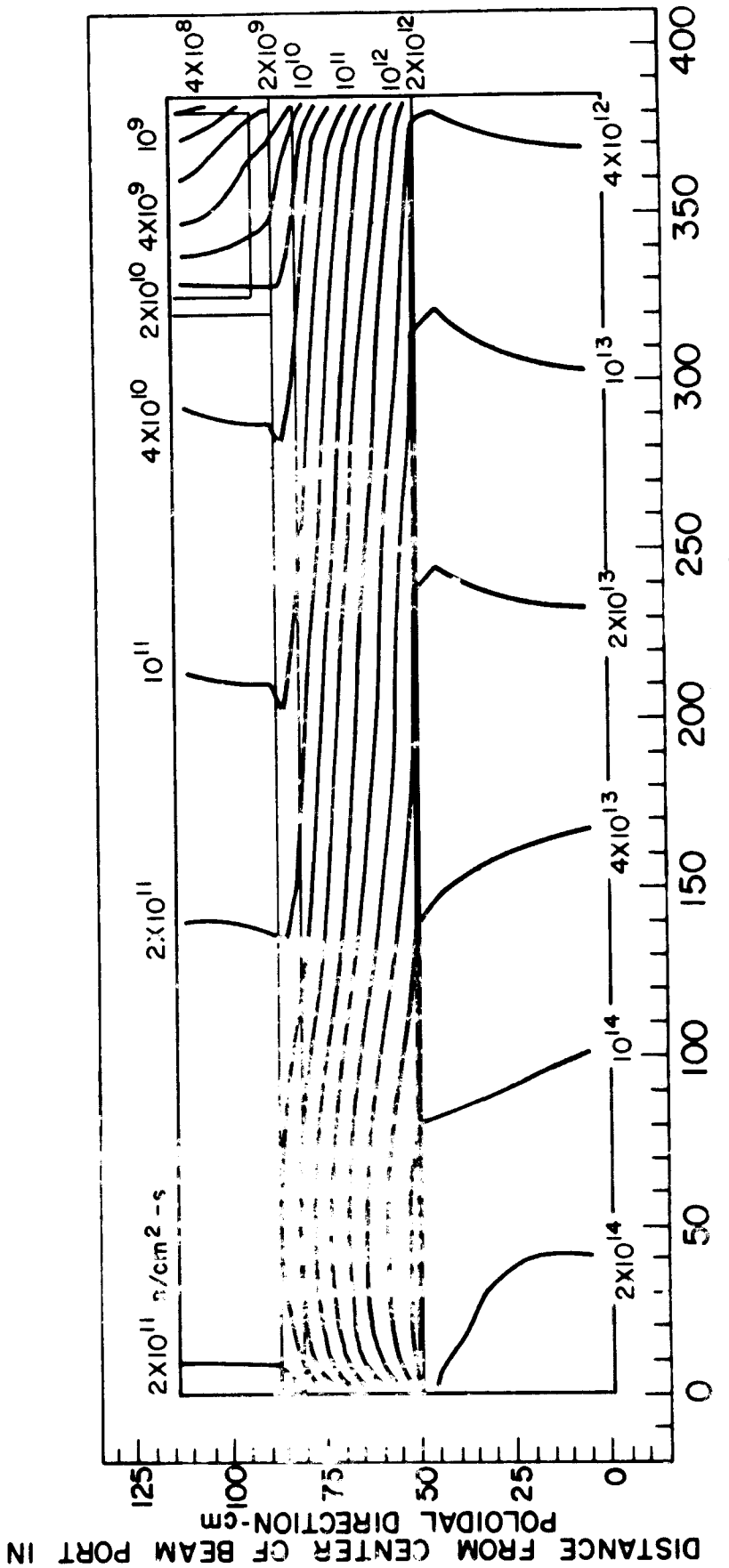

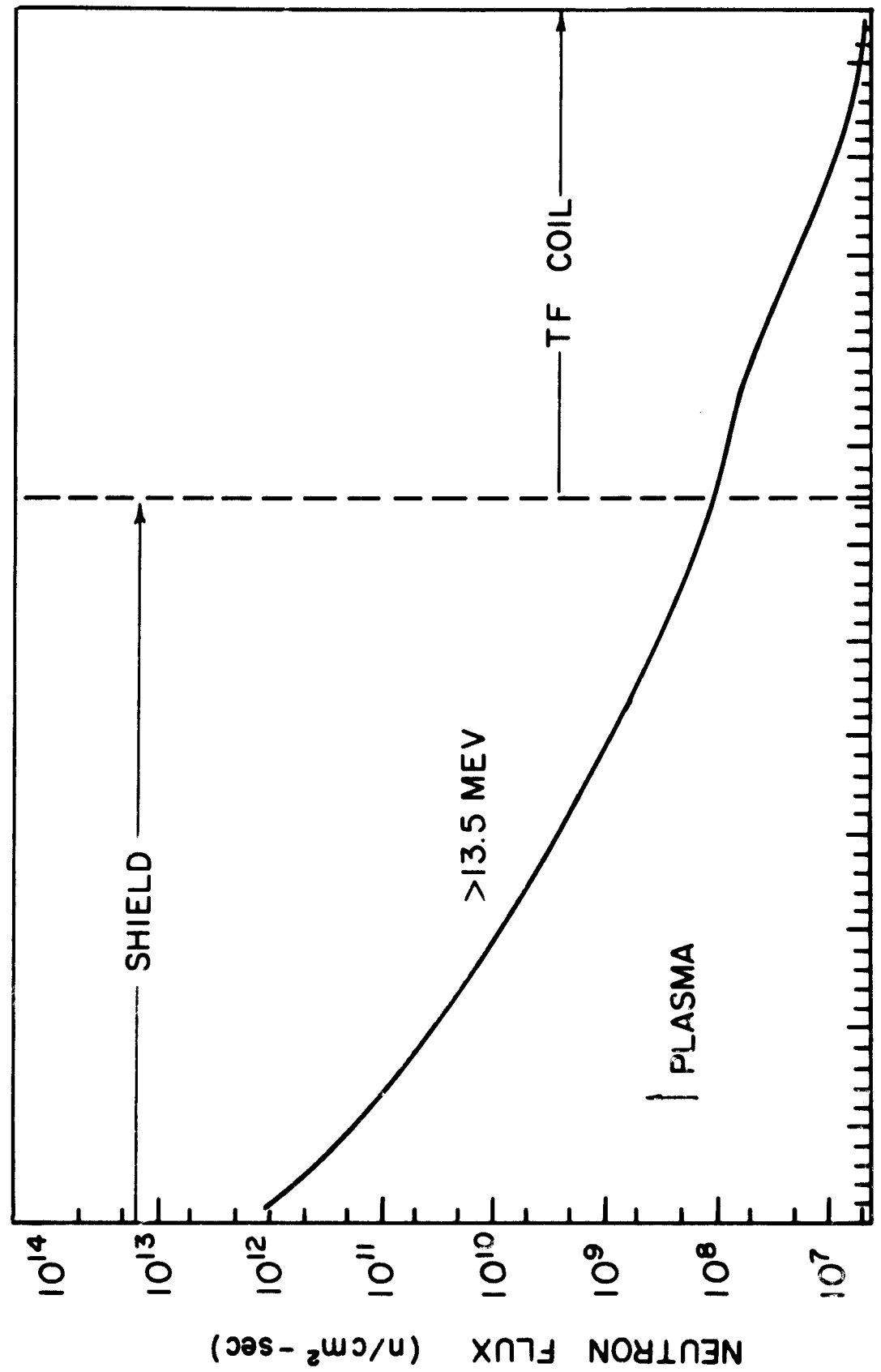

FIGURE IX-B-10 NEUTRON FLUX AT THE CENTER LINE OF TOROIDAL FIELD COIL PERPENDICULAR TO THE NEUTRON BEAM INJECTOR

(1) Thermalized and ionized D^+, T^+, and He^{++} leaking from the plasma.

(2) Nonthermalized helium from DT reaction.

(3) Charge exchange neutrals.

The absolute flux levels in the above categories depend on the efficiency of the divertor, the temperature of the plasma at the edge, and the vacuum at the edge of the plasma among other things. Much of this has been discussed previously in Chapter III and we will only quote the most pertinent information for materials here.

The plasma analysis has shown that the flux of charged particles leaving the plasma to strike the curtain should be very small and the energy of the particles should be very low (<10 eV). Hence such particles should not be of concern to physical sputtering. It was also shown that practically all of the 3.5 MeV alpha particles are thermalized in the plasma and there should be relatively few nonthermalized particles available for sputtering of the carbon liner.

However, there is a substantial flux of charge exchange neutrals. With the plasma parameters in Chapter III and a background pressure of 10^{-5} torr, the energetic neutral flux is 7×10^{15} particles per sec per cm^2 at a mean temperature of 3.8 keV.* The energy spectrum is repeated in Figure IX-B-11 and it reveals that the flux of high energy particles (>10 keV) is on the order of $\sim 3 \times 10^{14}$ particles/cm^2-s

IX-B-2-b. Flux to Divertor Surface

As outlined in Chapter III there is ~190 MW of charged particle energy incident on the Ta-10W collector plate and ~10 MW of charge exchange neutrals to the carbon curtain.

The specific information on the particle flux and energy used for the present work is given in Table IX-B-2. The maximum flux to the plates was calculated assuming the conditions given in section VIII-F-1 where the maximum heat flux is 6.67 MW/m^2 (5.0 MW/m^2 particle heat flux).

IX-C. Response Rates in TETR Materials

IX-C-1. Displacement Rate

IX-C-1-a. Stainless Steel

IX-C-1-a-i. Poloidal Variation

The neutron fluxes from Figures IX-B-6 thru 8 were coupled with stainless steel displacement cross sections given in Table IX-C-1 to yield the poloidal variation of displacement rates in the first wall. The results are displayed

*The plasma edge temperature is 1.7 keV

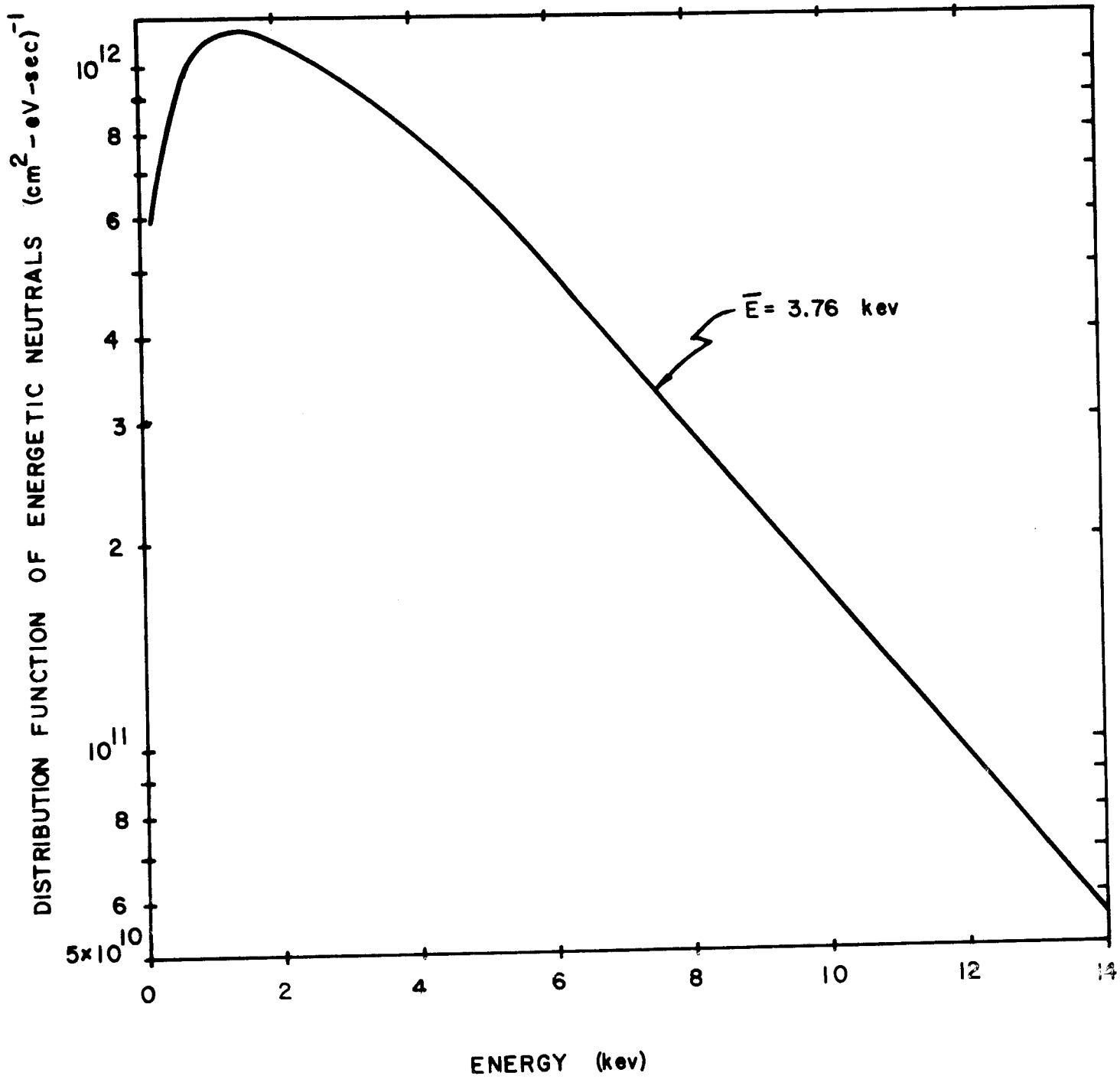

Figure IX-B-11 Neutral Particle Flux Spectrum to the Liner in TETR

Table IX-B-2

Summary of Particle Fluxes to Divertor Collector Plates[a]

Particle	Total Flux Particles/sec	Maximum Particle Flux, $cm^{-2}s^{-1}$	Average Particle Energy keV	Power MW_{ions}
D	0.625×10^{22}	2.37×10^{16}	9.8	10
T	8.6×10^{22}	3.27×10^{17}	9.8	136
He	8.6×10^{19}	3.27×10^{14}	13.3	0.15
Elec.	9.3×10^{22}	3.56×10^{17}	2	44
			Total	190 MW

[a] assuming particle confinement times of 0.03 sec.

---

graphically in Figure IX-C-1. It can be seen that the dpa levels vary from a minimum of ~7.7 per year (at 70% plant factor) to a maximum of ~9.5 per year over the majority of the first wall. The dpa rate drops to much lower values (4-7 dpa/year) near the divertor slots.

Table IX-C-1

Displacement Cross Sections Used for TETR

2/14/77

Energy Group	Upper Energy - eV	Al	Fe	Ni	Cr	316 SS	Ta	W	Ti	Cu	Nb
1	1.4918(+7)	2605.	3058.	3245.	2773.	3029.	1043	898.2	3676.	3788.	1871.
2	1.3499(+7)	2526.	2884.	3094.	2706.	2877.	968.4	848.4	3536.	3653.	1736.
3	1.2214(+7)	2455.	2753.	2939.	2582.	2745.	907.2	804.0	3524.	3530.	1657.
4	1.1052(+7)	2315.	2606.	2794.	2441.	2599.	874.2	757.8	3324.	3402.	1603.
5	1.0000(+7)	2224.	2469.	2630.	2309.	2460.	810.	713.4	3224.	3223.	1537.
6	9.0484(+6)	2161.	2329.	2392.	2216.	2316.	742.8	661.2	3189.	3041.	1467.
7	8.1873(+6)	2174.	2203.	2247.	2146.	2198.	708.6	630.6	3126.	2861.	1409.
8	7.4082(+6)	2143.	2080.	2140.	2075.	2086.	654.6	601.8	3052.	2702.	1339.
9	6.7032(+6)	2099.	1960.	2045.	2005.	1978.	610.8	563.0	2962.	2578.	1249.
10	6.0653(+6)	2068.	1859.	1978.	1933.	1887.	573.6	528.1	2860.	2438.	1166.
11	5.4881(+6)	2039.	1772.	1844.	1877.	1800.	543.	492.7	2752.	2314.	1103.
12	4.9659(+6)	1956.	1691.	1689.	1814.	1713.	505.5	460.1	2593.	2194.	1037.
13	4.4933(+6)	1919.	1594.	1585.	1666.	1606.	464.4	430.3	2409.	2018.	957.0
14	4.0657(+6)	1948.	1509.	1472.	1599.	1521.	433.6	403.5	2264.	1847.	877.2
15	3.6788(+6)	1940.	1388.	1382.	1525.	1412.	414.7	379.6	2165.	1684.	814.2
16	3.3237(+6)	1860.	1372.	1234.	1476.	1374.	393.5	355.9	2058.	1545.	764.4
17	3.0119(+6)	1847.	1280.	1217.	1423.	1298.	372.3	335.0	1935.	1415.	710.4
18	2.7253(+6)	1951.	1286.	1084.	1383.	1279.	351.6	315.9	1795.	1292.	669.0
19	2.4660(+6)	1732.	1035.	904.5	1134.	1037.	306.7	278.5	1460.	1107.	600.9
20	1.8268(+6)	1543.	793.8	752.6	978.0	822.0	250.2	226.9	1236.	907.4	481.7
21	1.3534(+6)	1342.	557.6	668.3	677.4	592.4	189.2	194.2	888.4	832.4	419.6
22	1.0026(+6)	1316.	442.1	512.4	551.1	470.2	145.5	156.0	750.9	725.8	398.7
23	7.4274(+5)	1069.	317.5	391.0	454.5	351.0	116.6	119.2	561.8	619.0	364.4
24	5.5023(+5)	1059.	362.3	387.9	405.7	373.2	91.9	92.20	400.2	520.0	318.8
25	4.0762(+5)	713.8	288.2	349.6	227.4	284.6	74.06	72.96	255.4	421.7	273.7
26	3.0197(+5)	562.8	182.3	356.8	231.7	212.1	62.22	59.26	251.8	367.1	223.6
27	2.2371(+5)	575.8	217.5	299.2	230.8	229.7	50.92	49.07	175.0	295.9	176.6
28	1.6573(+5)	697.6	159.6	226.3	278.6	189.0	38.91	41.07	92.19	242.9	137.0
29	1.2277(+5)	449.4	122.9	147.5	169.3	134.2	29.85	32.36	127.8	185.0	71.20
30	6.7379(+4)	225.9	73.06	106.3	78.25	77.98	18.22	21.33	252.6	118.6	36.14
31	3.1828(+4)	18.53	88.48	168.6	22.42	86.20	9.78	12.98	536.3	103.6	18.61
32	1.5034(+4)	10.88	21.67	80.85	32.82	30.78	6.56	8.337	171.7	71.94	10.06
33	7.1017(+3)	8.075	11.00	31.30	40.88	18.81	5.11	6.152	24.70	19.91	7.684
34	3.3546(+3)	2.802	5.415	11.81	6.395	6.359	3.33	1.831	9.718	20.19	6.196
35	1.5846(+3)	1.381	4.901	6.457	1.371	4.452	5.37	1.901	2.542	2.209	6.121
36	7.4852(+2)	.7241	2.003	3.073	.1276	1.794	8.41	2.761	1.550	13.58	2.187
37	3.5358(+2)	.4371	.1214	.2373	.0	.1135	16.12	5.887	.6125	1.802	5.982
38	1.6702(+2)	.2193	.1536	.3381	.0	.1481	21.61	4.756	.5313	.4623	4.039
39	7.8893(+1)	.2302	.2218	.4884	.0	.2139	30.26	9.406	.7138	.5816	.3691
40	3.7267(+1)	.2598	.3210	.7076	.0	.3096	47.68	138.7	.9834	.7612	.6013
41	1.7603(+1)	.3026	.4677	1.027	.0	.4506	64.03	5.284	1.353	1.021	.1183
42	8.3153(+0)	.3666	.6831	1.492	.0	.6572	349.8	69.05	1.899	1.376	.1711
43	3.9279(+0)	.4596	.9890	2.181	.0	.9540	11.84	3.604	2.687	1.918	.2477
44	1.8554(+0)	.5948	1.445	3.171	.0	1.392	2.89	1.668	3.844	2.707	.3580
45	8.7643(-1)	.7922	2.119	4.615	.0	2.037	3.09	2.159	5.562	3.829	.5192
46	4.1399(-1)	2.613	8.100	18.01	.0	7.831	10.06	7.776	21.33	14.21	1.978

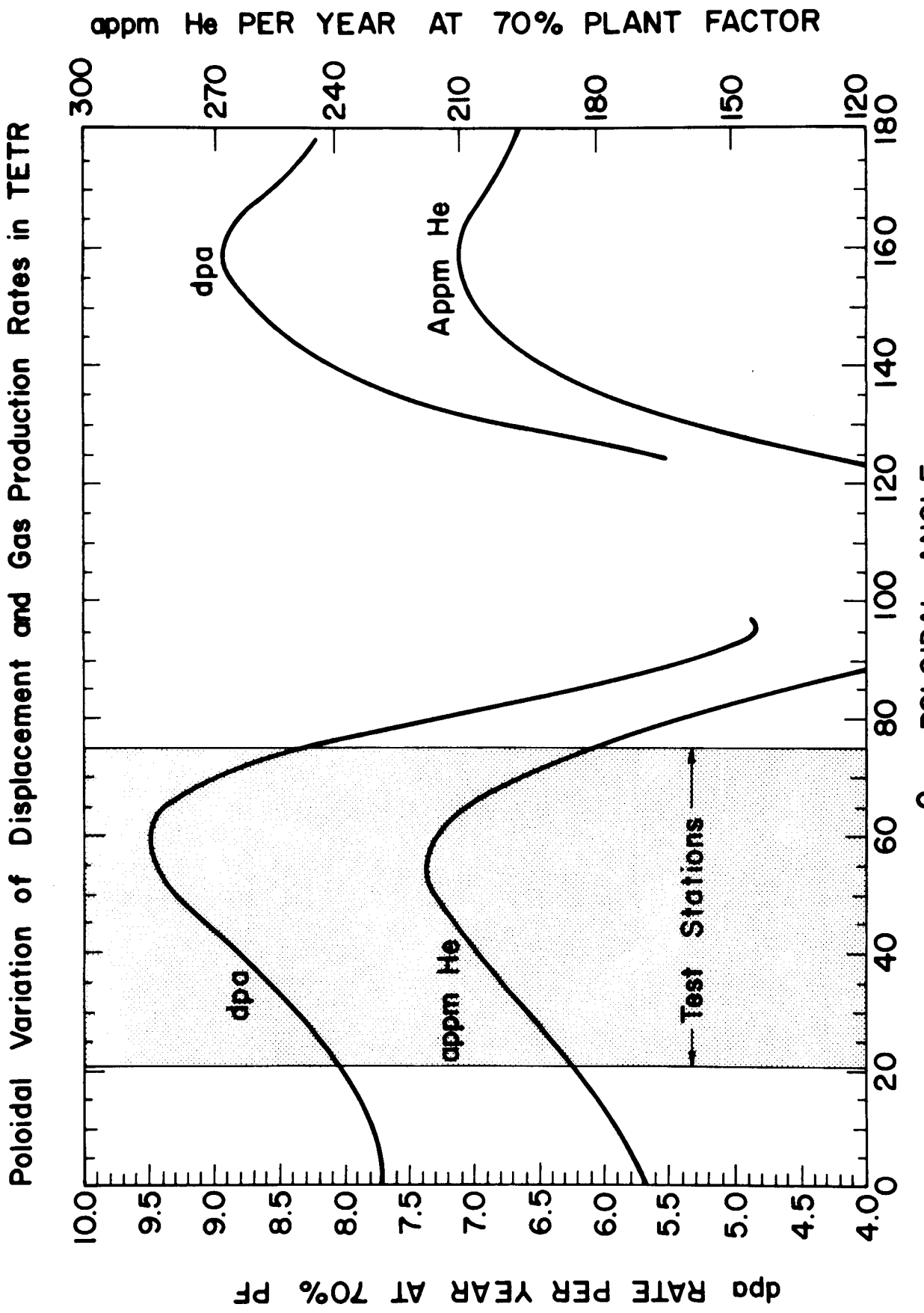
Poloidal Variation of Displacement and Gas Production Rates in TETR
dpa RATE PER YEAR AT 70% PF
appm He PER YEAR AT 70% PLANT FACTOR
θ - POLOIDAL ANGLE
dpa
appm He
Test Stations
dpa
Appm He
10.0
9.5
9.0
8.5
8.0
7.5
7.0
6.5
6.0
5.5
5.0
4.5
4.0
300
270
240
210
180
150
120
0
20
40
60
80
100
120
140
160
180

Figure IX-C-1

IX-C-1-a-ii. Two-Dimensional Variation

Figures IX-C-2a and 2b show how the displacement rates vary throughout the upper and lower half of the blanket and shield of TETR. These dpa rates are calculated for a year of operation at the 70% plant factor. The notable features of these figures are:

(1) The variation of dpa rate at the reactor midplane is very well behaved, dropping from ~11 dpa/year at the first wall to 5×10^{-3} dpa/year at the inside surface of the inside divertor coil and 0.1 dpa/year at the inside surface of the outer vertical field coil.

(2) The gradient in dpa rate is slightly steeper on the inner blanket than the outer blanket. For the inner blanket it takes 27 cm to drop the dpa rate by a factor of 100 while it takes ~30 cm to accomplish the same thing in the outer blanket.

(3) The test cells have only a minimal perturbation on the damage rate compared to the rest of the blanket and shield. The dpa contours only deviate by ~5 cm at most through the test cell region.

(4) The dpa gradient in the test cell region is such that there is only a factor of 2 variation between the first wall and the back of the 10 cm thick test section. The poloidal variations are also less than a factor of two. Hence maximum damage gradients are ~0.2 dpa/cm.

(5) The leakage of neutrons up the divertor slots results in higher dpa rates in the TF coils than would normally be calculated.

(6) Figure IX-C-2b shows that the maximum dpa rates on the TF coil occur at the midplane and ~175 cm from the midplane at $\sim 10^{-4}$ dpa per year.

(7) The maximum dpa rate on the inner divertor coils is $\sim 4 \times 10^{-3}$ dpa/year at the midplane.

(8) The maximum dpa rates on the outer VF coil on the midplane is $\sim 1 \times 10^{-2}$ dpa/year and the VF coils near the outer divertor slots experience 10^{-2} to 1 dpa/year.

(9) The neutron damage to the steel in Ta-10W particle collector area ~ 0.01 to 0.02 dpa/year.

(10) The neutron damage levels to the SS in the cryogenic pump area is from 0.001 to 0.01 dpa/year.

There is a great deal of information contained in Figures IX-C-2a & 2b and the reader is urged to study them at his leisure.

FIGURE IX-C-2a ATOMIC DISPLACEMENT RATES IN STAINLESS STEEL STRUCTURE (DPA/YEAR) – UPPER HALF OF TETR

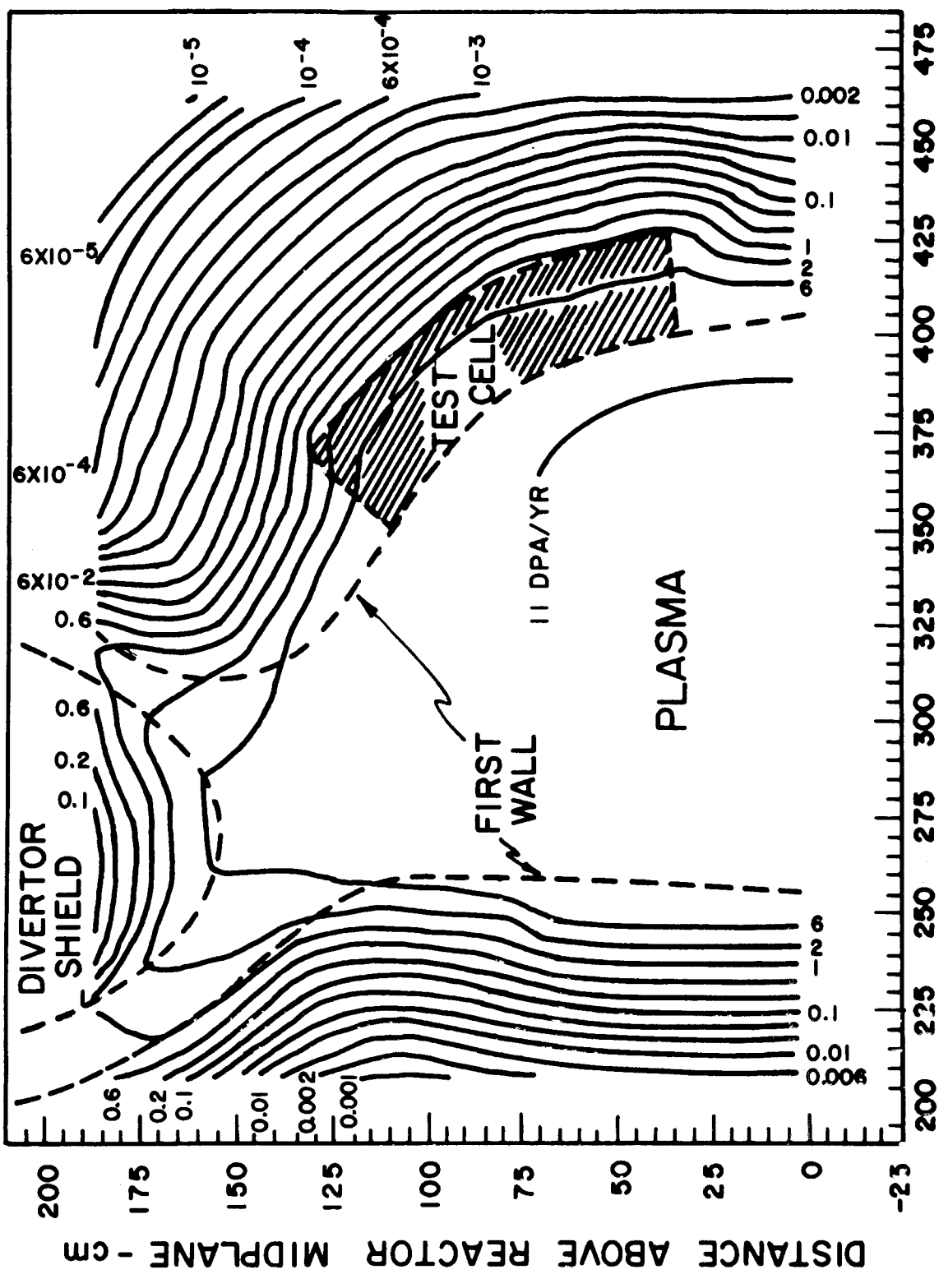

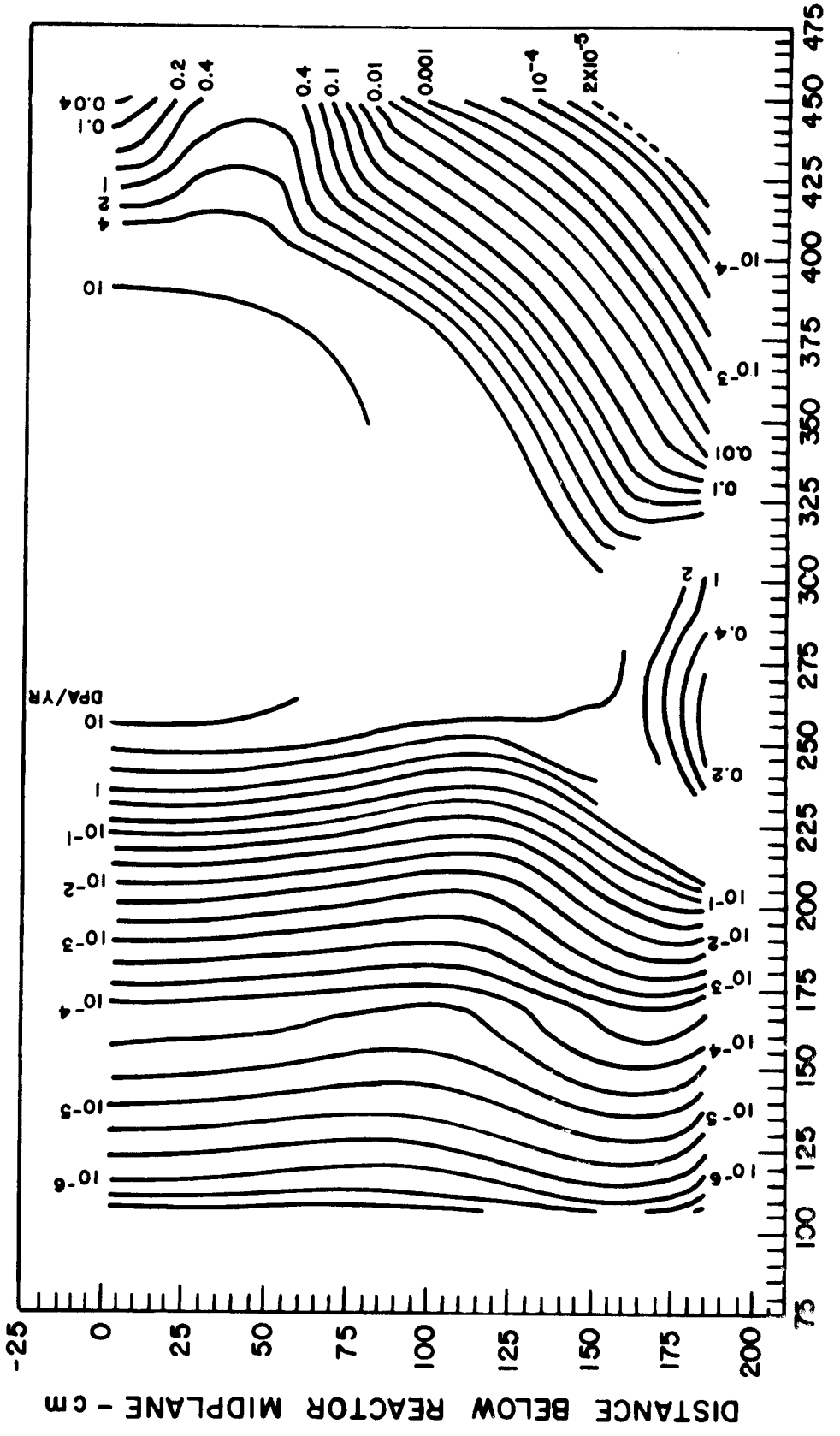

FIGURE IX-C-2b ATOMIC DISPLACEMENT RATES IN THE STAINLESS STEEL STRUCTURE (DPA/YEAR) - BOTTOM HALF OF TETR

IX-C-1-a-iii. Displacement Variation Along Neutral Beam Ports

Figure IX-C-3 shows how the displacement rate varies from the front surface of the beam port to the TF coil on the outside. It is important to note that the values here are in addition to those determined by 1-D analysis of the blanket and shield structure. The first point to note that is the dpa rate along the wall of the neutral beam penetration port only drops from ~10 dpa/year at the front wall to 1 dpa/year at ~120 cm from the first wall. This is in contrast to ~10^{-4} dpa/year rate in the normal blanket and shield without penetrations. In fact the damage rate in the SS liner of the neutral beam port is still ~0.1 dpa/year outside the reactor and parallel with the TF coil.

There is ~85 cm of shield between the neutral beam port and the TF coil. This shield drops the damage rate from neutron leakage by a factor of ~300 to 3000 so that the maximum dpa rate is ~3 x 10^{-4} dpa/year in the TF coil. This rate is 10 times higher than the damage rate predicted by 1-D analysis for the outer coil.

IX-C-2. Gas Production Rates

The 2-D description of the helium and hydrogen production rates in the steel is given in Chapter VII. Since the helium damage is currently envisioned to be the most critical we will only address that area here.

IX-C-2-a. Poloidal Variation

The helium production rate varies from a maximum of 210 appm/year in the first wall of the test zone to ~160 appm/year at the midplane of outside of the reactor (see Figure IX-C-1). These values illustrate again the necessity to place the test cells off of the midplane of the reactor to receive the highest damage rate.

IX-C-2-b. Two-Dimensional Variation of Helium Gas Production

The neutron fluxes described in section IX-B were folded into ENDF-IV cross sections to obtain the helium production rates in the TETR blanket and test section. A summary of the results is given in Figure IX-C-4. Important features of this display are:

(1) The helium production rate varies by ~5 appm/cm for the first 10 cm from the first wall and less than 1 appm/cm in the poloidal direction in the same zone.

(2) The helium production rate is still 0.1 appm/yr at the surface of the outer VF coil on the midplane.

(3) Significant streaming of the neutrons up the divertor slots causes helium production rates of up to 10 appm/year for more than 25 cm along the slots.

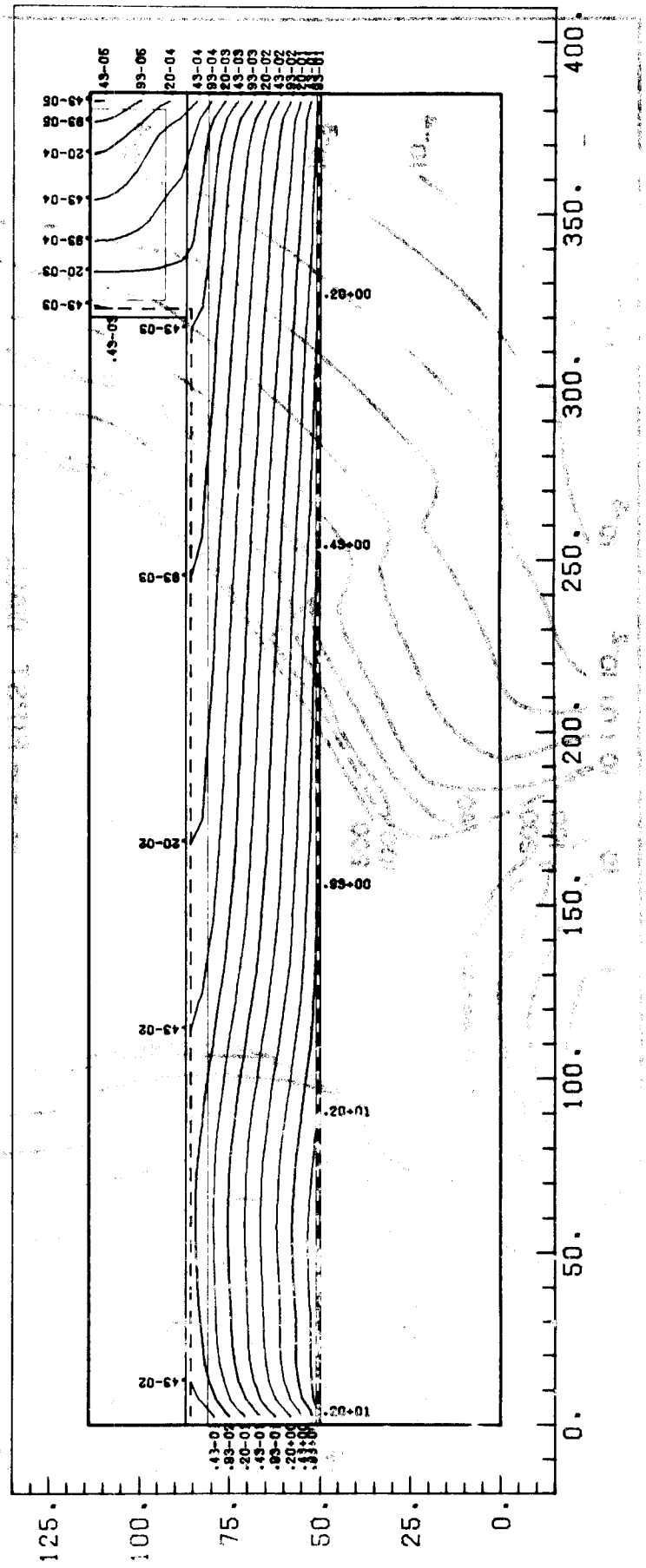

FIG. IX-C-3 ATOMIC DISPLACEMENT IN THE STAINLESS STEEL STRUCTURE (DPA/YEAR)

FIGURE K-C-4 HELIUM GAS PRODUCTION CONTOURS IN TETR

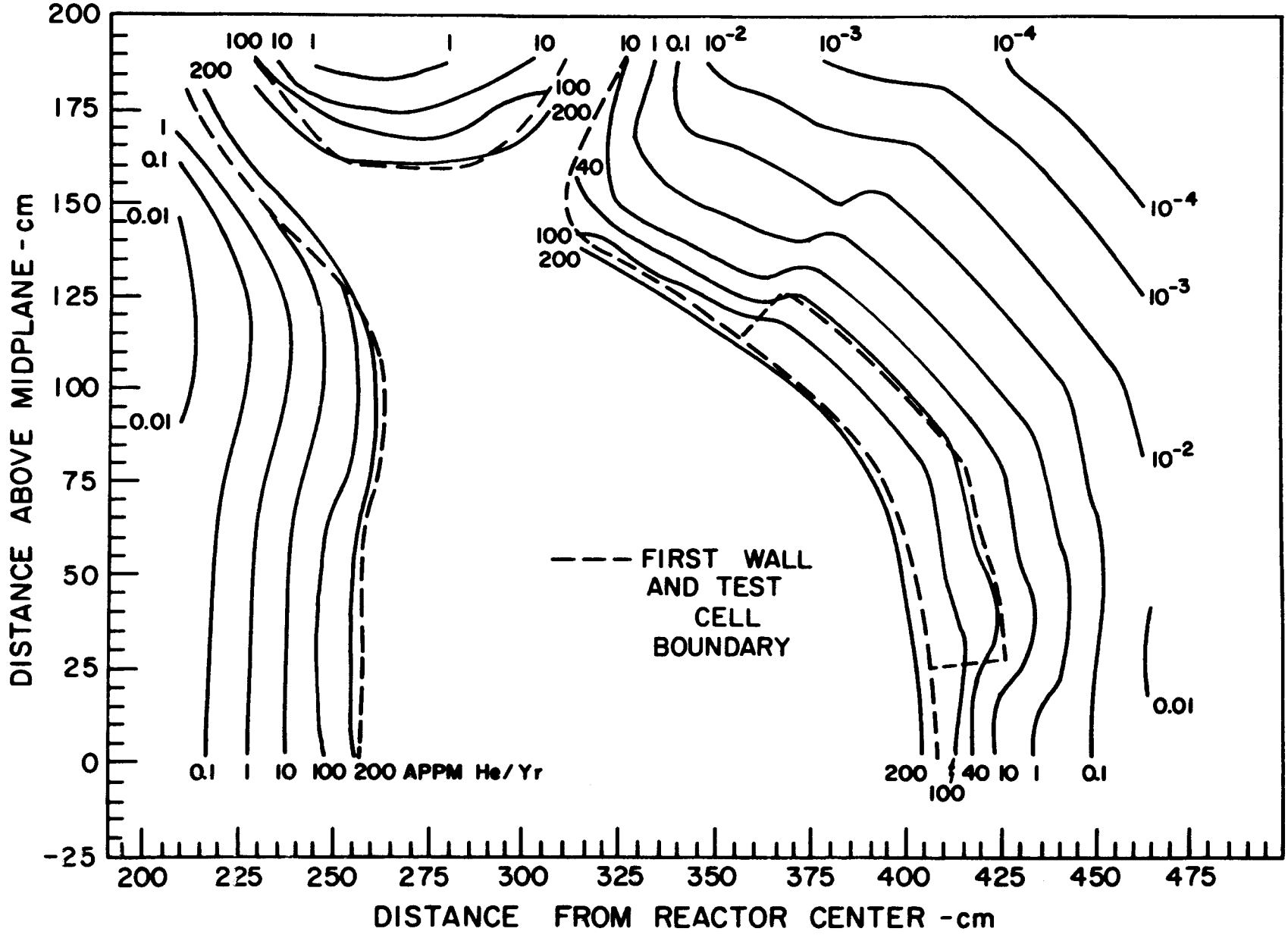

IX-C-3. Parametric Representation of the Damage Environment

IX-C-3-a. He/dpa Ratio

It has become traditional to characterize the irradiation environment by the ratio of gas to displacement damage. This parameter is valuable because it is an indication of how close the damage is to more traditional irradiation environments. It is also important to know this quantity to predict void nucleation and growth rates at various temperatures.

Analysis of the figures in section IX-C-1 and IX-C-2 reveals that the He/dpa ratio in the test zone area is ~20. As one progresses farther into the blanket this ratio drops to as low as 6 near the back. One should contrast this to values of ~1 or less in fast fission reactors. It then becomes apparent why such fast fission facilities are not suitable for simulation of fusion reactor damage even in the components which are damaged by a so-called "softened" spectra.

IX-C-3-b. Temperature Plots

A schematic representation of the temperature in the blanket, shield, and magnet components is given in Figure IX-C-5 (excluding the testing station). We have chosen the midplane for comparison purposes but a choice at other poloidal positions would yield similar results.

The carbon curtains are the hottest component in TETR, operating at ~1200°C. The first wall temperature has been maintained at 300°C by the boiling water coolants while the tungsten and B_4C may approach 350°C. The temperature drops to 100°C in the final Pb shield. The temperature then rapidly plunges to 77°K at the front of the TF coil and finally to 4.2°K in the TF coil itself.

IX-C-3-c. Stress

The nominal stress levels (in the unirradiated condition) are listed in Table IX-C-2. These levels should be used as rough indicators of the minimum stresses that might be present. Further finite element analysis of the exact shape and external constraints needs to be done for more precise values.

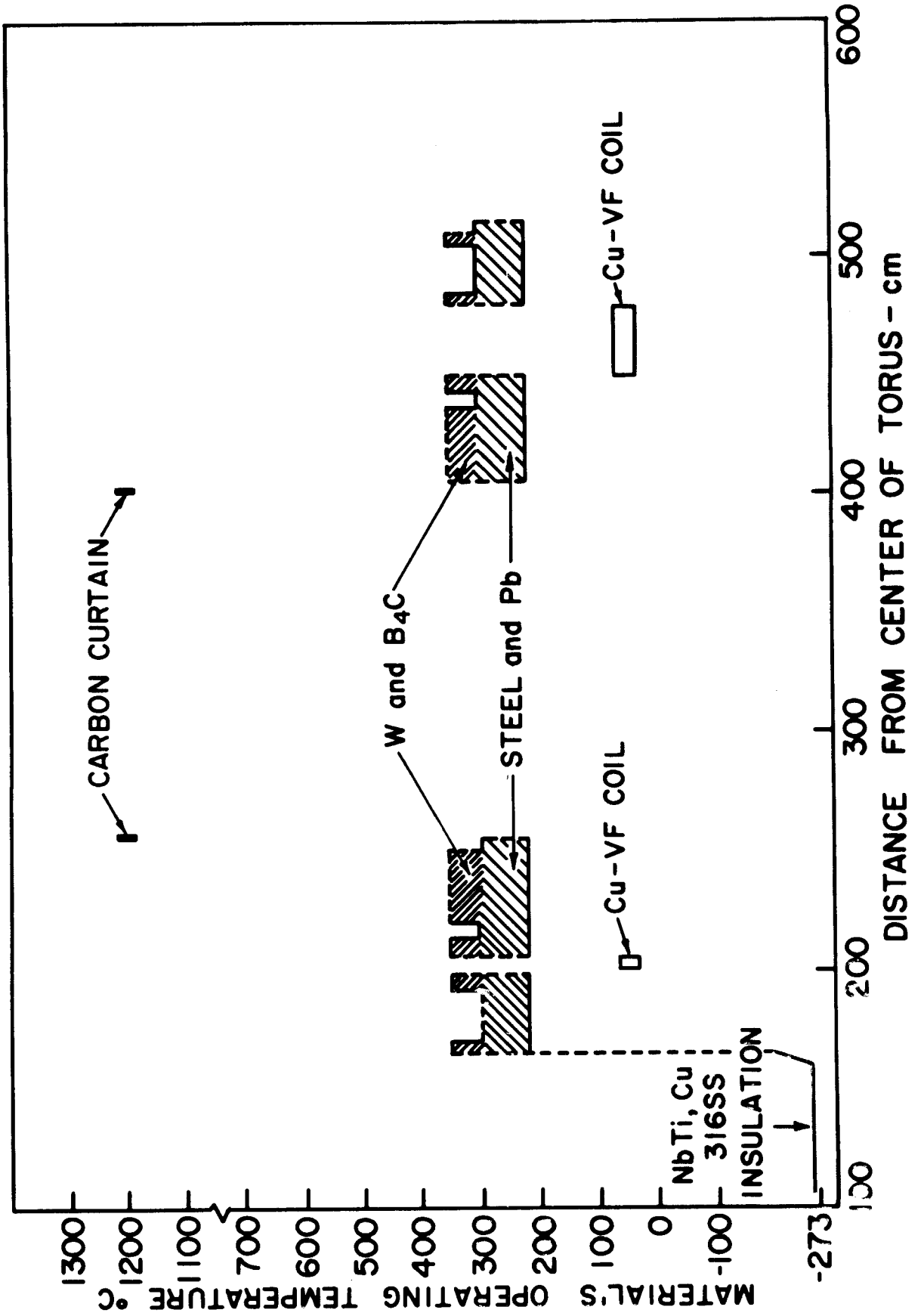

FIGURE IX-C-5 TEMPERATURE PROFILES IN TETR

Table IX-C-2

Nominal Stress Levels in TETR

Material	T °C	Max Stress-MPa Tension	Compression
3/6 SS First Wall Coolant Tubes	300	39	51
Cu-SS VH Coil	100	118	130
Cu-SS-OH Coil	100	---	332
Cu-SS-TF coil	-269	100	---

IX-C-4. Transmutation Rate in 316 Stainless Steel First Walls

Long-term irradiation of the 316 SS structural components can produce a significant amount of transmutations, both gaseous and solid elements. These isotopes are either produced directly, or result from the decay of radioactive species (see Chapter XIII). The objective of this section is to document the chemical changes in the TETR blanket at three different depths for $\theta = 0°$; the first 316 SS wall, the tungsten shield material closest to the plasma (~ 2 cm from the first wall) and the copper in the VF coil at the outer midplane roughly 45 cm from the first wall.

The data will be reported in terms of appm of impurity per year at a 70% plant factor and the following convention followed for a determination of which isotopes to count.

If $t_{1/2} < 10$ years, count final product only

If $t_{1/2} > 10$ years, count long-lived isotope only

Table IX-C-3 lists the original composition of the materials considered and the production rate (in appm per year at 70% PF) of new isotopes is given in Table IX-C-4.

Many of the isotopes of 316 SS are transmuted into stable isotopes of the original elements. Therefore, one must tabulate both the production and destruction rates to determine the net effect of the irradiation. This is done in Table IX-C-5.

The data in Table IX-C-4 and 5 shows that the major effect in the 316 SS after 10 years of irradiation at 70% plant factor is the buildup of almost 0.2% V, 0.14% Co, and the increase in the Mn content by 33% from 2.01% to 2.67%. The addition of these elements to the steel will not decrease the austenite phase and small amounts of Ti may actually be beneficial to the irradiation stability of the alloy. The other trace elements or slight change in existing elements would not seem to pose any major problems.

The impurity production in the copper VF coil is quite low (total of <5 ppm per year) and such impurities may slightly (but not significantly) increase the resistivity of the coil after long-term irradiation. On the other hand, the transmutation of W into Ta and Re is at a rather high rate, producing 0.83% Ta-181 after 10 years at 70% P.F. and over 1% of Re-187 and 1.5% of Re-185. The Re is known to promote ductilization and the Ta may cause changes in the mechanical response of W. Induced radioactivity is also of importance now because of the production of Ta-182 and the associated high energy gamma rays.

In summary, no serious harmful effects are expected in the 316 SS or Cu coil material but significant transmutation effects in the W shield material are expected with possible deleterious effects on long-term radioactivity.

Table IX-C-3

Summary of Initial Material Compositions Used for Transmutation Reactions

Element	Isotope Number	Assumed Isotopic Abundance %	Atomic % in Alloy
		316 Stainless Steel	
C	12	100	0.37
P	31	100	0.008
S	32	100	0.005
Si	28	92.2	1.82
	29	4.71	0.093
	30	3.12	0.062
Cr			(18.07)*
	50	4.3	0.78
	52	83.8	15.14
	53	9.6	1.73
	54	2.4	0.43
Mn	55		2.01
Fe			(64.70)*
	54	5.8	3.75
	56	91.7	59.33
	57	2.2	1.42
	58	0.3	0.19
Ni			(11.30)*
	58	67.8	7.66
	60	26.2	2.96
	61	1.3	0.15
	62	3.7	0.42
	64	1.2	0.14

* represents sum of given element in alloy.

Table IX-C-3 - Continued

Element	Isotope Number	Assumed Isotopic Abundance %	Atomic % in Alloy
		316 Stainless Steel	
Mo			
	92	15.86	0.23
	94	9.12	0.13
	95	15.70	0.23
	96	16.50	0.24
	97	9.45	0.14
	98	23.75	0.34
	100	9.62	0.14
		W Shield	
W			(100)*
	82	24.7	24.7
	83	13.5	13.5
	84	28.6	28.6
	86	26.5	26.5
		Cu Coil	
Cu			(100)*
	63	69.1	69.1
	65	30.9	30.9

Table IX-C-4

Production of New Isotopes in TETR Blanket Materials (only solid elements considered)

Transmutation Product to New Elements	Isotope Number	From	Production Rate appm/year at 70% PF, $\theta = 0^o$
	316 Stainless Steel First Wall		
Mg	25	Si-28	1.65
Ti			(18.33)*
	46	Cr-50	0.06
	47	Cr-50	2.28
	48	Cr-50,52	0.001
	49	Cr-50	2.1
		Cr-52	12.5
		Cr-53	0.27
	50	Cr-53	1.12
		Cr-54	0.003
V			(175.03)*
	50	Cr-50	6.4
	51	Cr-50	39.37
		Cr-52	116.95
		Cr-53	0.36
		Cr-54	0.11
		Mn-55	0.02
		Fe-54	11.82
Co			(140.92)*
	59	Ni-58	110.53
		Ni-60	30.23
		Ni-62	0.16
Sr	88	Mo-92	0.004
Y	89	Mo-92	0.17
Zr			(1.94)*
	90	Mo-92	0.002
	91	Mo-92	1.88
		Mo-95	0.06
	92	Mo-95	0.09
		Mo-96	0.003
	93	Mo-96	0.006
	94	Mo-98	0.002
Nb			(0.44)*
	92	Mo-92	0.38
	93	Mo-95	0.02
	94	Mo-95	0.04
Tc	99	Mo-98	3.96

* represents total production rate for given element

Table IX-C-4 - Continued

Transmutation Product to New Elements	Isotope Number	From	Production Rate appm/year at 70% PF, $\theta = 0^{o}$
	W Shield (First Interval)		
Hf			(0.72)*
	179	W-182	0.46
	180	W-183	0.26
Ta			(826)*
	181	W-182	825
		W-184	0.54
Re			(2472)*
	185	W-184	524
		W-186	922
	187	W-186	1026
	Copper VF Coil (First Interval)		
Ni			(2.09)*
	60	Cu-63	0.02
	64	Cu-63	1.97
		Cu-65	0.10
Zn			(1.6)*
	64	Cu-63	1.21
		Cu-65	0.06
	66	Cu-65	0.33

Table IX-C-5

Summary of Net Effects of Transmutations in Selected TETR Blanket Materials

Element	Initial Atom %	appm/year Production	Destruction	Net	Final Atom %-10 years[a]
		316 SS First Wall			
C	0.37	-	-	-	0.37
Mg	-	1.65		+1.65	1.65-03
Si	1.97		1.67	-1.67	1.83-02
Ti	-	18.33	-	+18.33	1.83-02
V	-	175.03	-	+175.03	0.175
Cr	18.07	155.25	180.16	-24.9	18.04
Mn	2.01	692.10	37.47	+655.04	2.67
Fe	64.70	140.78	740.32	-599.54	64.10
Co	-	140.92	-	-140.92	0.141
Ni	11.30	-	281.17	-281.17	11.02
Y	-	0.17	-	+0.17	0.17-03
Zr	-	1.94	-	+1.94	1.94-03
Nb	-	0.44	-	0.44	0.44-03
Mo	1.44	-	7.56	-7.56	1.43
Tc	-	3.96	-	3.96	3.96-03
		Copper Coil Zone (1st Interval)			
Ni	-	2.09	-	+2.09	2.09-03
Cu	100	-	3.66	-3.66	99.996
Zn	-	1.60	-	+1.60	1.6-03
		Tungsten Shield			
Hf	-	0.72	-	+0.72	0.72-03
Ta	-	826	-	+826	0.83
W	100	-	3307	-3307	96.72
Re	-	2472	-	+2472	2.48

(a) 70% Plant Factor

IX-D. Effect of Irradiation on TETR 316 SS Components

IX-D-1. Introduction

An assessment of the data base for neutron irradiated steel reveals that most of the high fluence (high dpa) information has been obtained from sodium cooled fast reactors. This means that all of the data has been obtained at temperatures above the coolant input temperature, which is 350-370°C. On the other hand what low temperature data that is available has been obtained from light water cooled thermal reactors which tend to produce large amounts of helium through the Ni-59 (n, α) reaction. Unfortunately, most of this data is generated at temperatures of 250°C and lower leaving the region between 250-350°C rather devoid of data. Therefore, we will have to rely on extrapolation of data available at different temperatures and from different irradiation facilities to estimate the behavior of the steel structure in TETR.

IX-D-2. Swelling Due to Void Formation

The situation with respect to void induced swelling in 316 SS has been the subject of much study for the LMFBR program and has been reviewed in previous UWMAK reports[1-3] and elsewhere[4,5]. These summaries will not be included here and only that information which we think is relevant to TETR will be discussed.

The fluence and temperature dependence of swelling in cold worked 316 SS has been described as follows:

$$\text{(IX-D-1)} \quad \frac{\Delta V}{V_o} = R(T) \left\{ \phi + \frac{1}{\alpha} \ell n \left[\frac{1+\exp[\alpha(\tau-\phi)]}{1+\exp(\alpha\tau)} \right] \right\}$$

where

R(T) is the temperature dependent slope
α is a constant
ϕ is the fluence
τ is an incubation parameter dependent on temperature.

The functional dependence is shown schematically in Figure IX-D-1.

Use of equation IX-D-1 yields the predicted swelling shown in Figure IX-D-2 for displacement levels of 56-94 dpa in EBR-II. The higher damage level is close to a 10 MW-yr/m^2 exposure level (i.e., ~110 dpa). From Figure IX-D-2 one could surmise that the swelling at 300°C will be less than 5% after a 10 MW-yr/m^2.

The next question to ask is how much will the ~200 appm of helium gas atoms generated per year change the swelling in 316 SS. Recent results at ORNL[6], shown in Figure IX-D-3, have revealed that as much as 4000 appm He

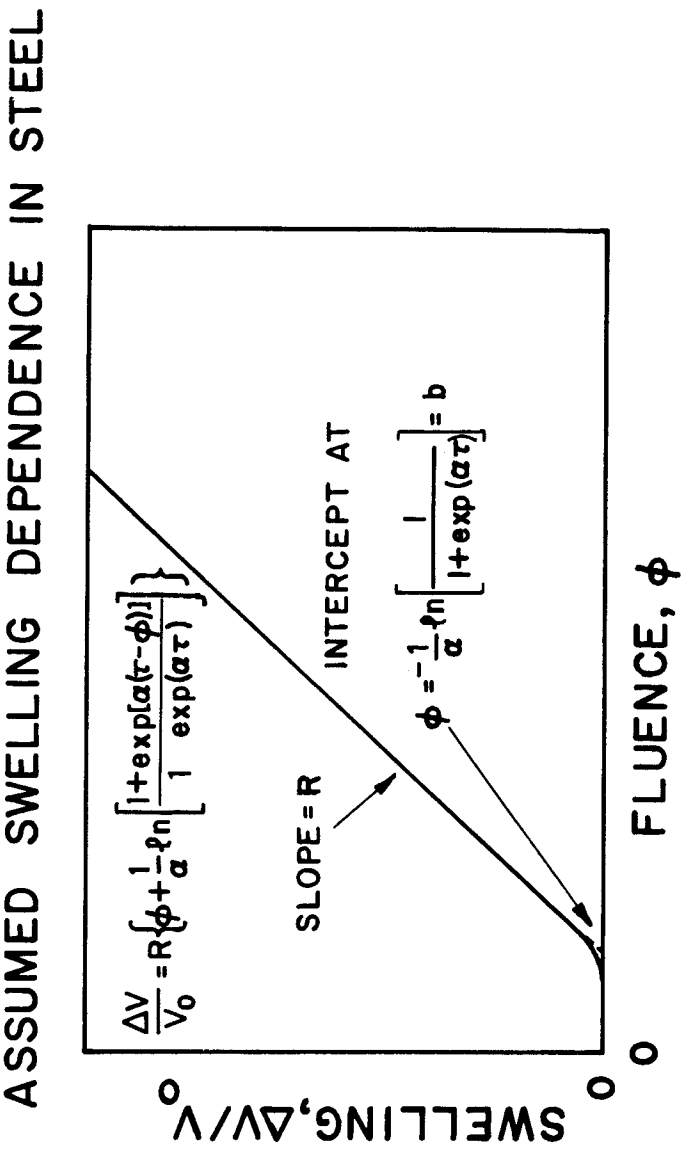
ASSUMED SWELLING DEPENDENCE IN STEEL
SWELLING, ΔV/V
FLUENCE, φ
0
0
$\frac{\Delta V}{V_0} = R\left\{\phi + \frac{1}{\alpha} \ln\left[\frac{1+\exp[\alpha(\tau-\phi)]}{1+\exp(\alpha\tau)}\right]\right\}$
SLOPE = R
INTERCEPT AT
$\phi = -\frac{1}{\alpha} \ln\left[\frac{1}{1+\exp(\alpha\tau)}\right] = b$

FIGURE - IX - D - 1

FIGURE IX -D-2

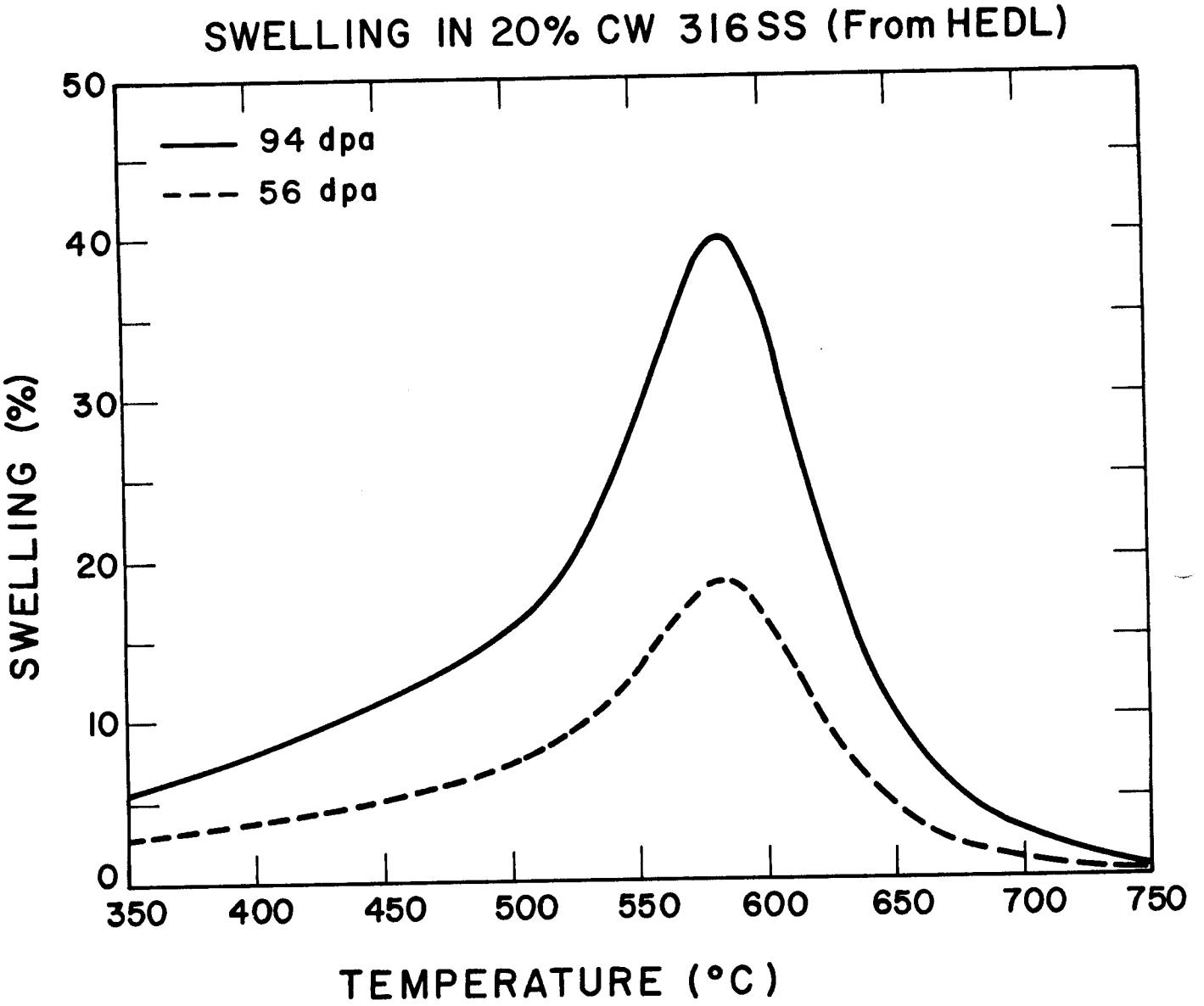

62937-C-2

FIG. IX-D-3

EFFECTS OF HIGH DAMAGE LEVELS ON SWELLING AND DUCTILITY IN 316SS-ORNL

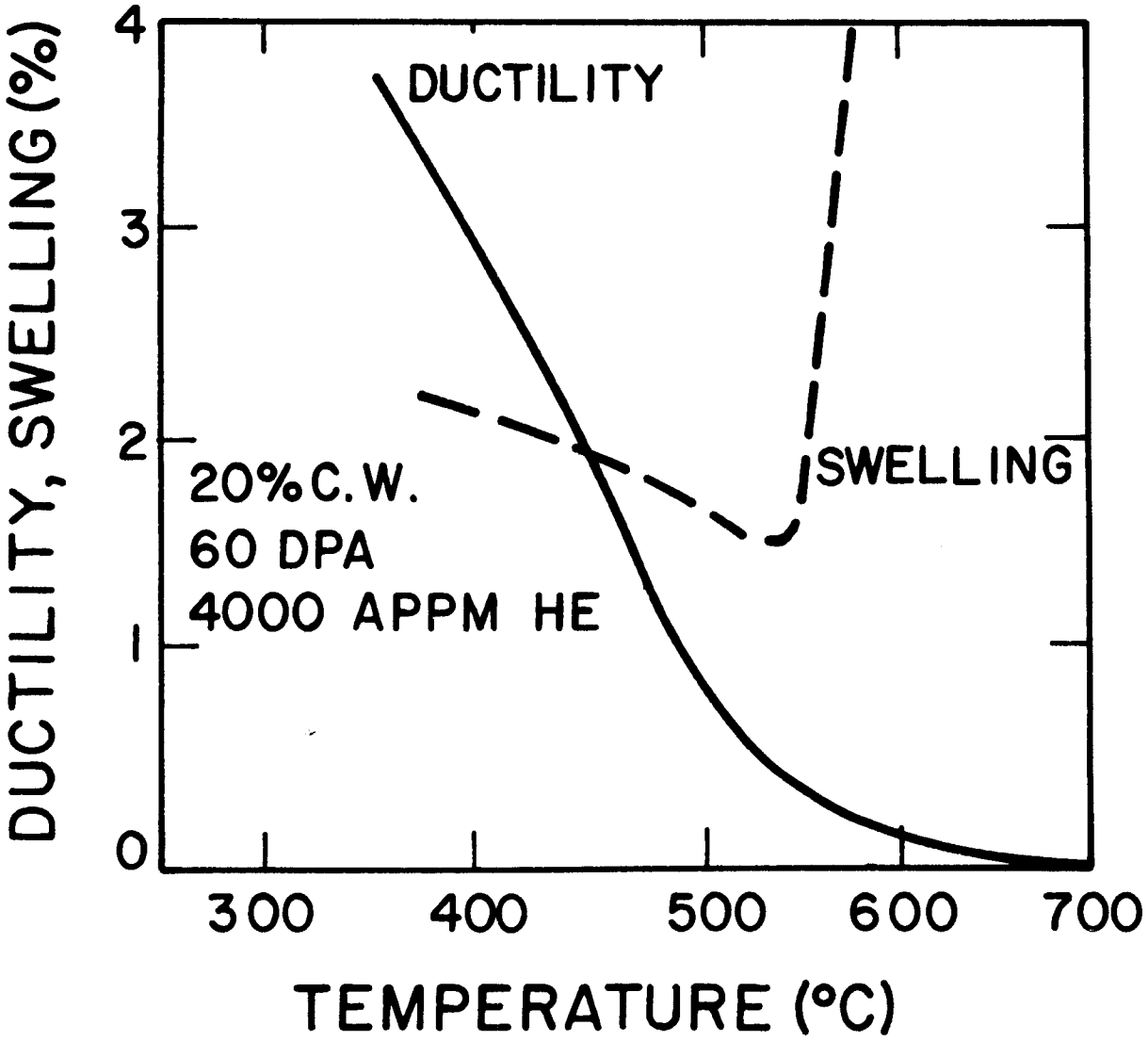

(~ twice that which would be accumulated at 10 MW-yrs/m^2) has little effect on swelling below 500°C. Above that temperature, helium driven growth will produce dramatic increases in swelling over that experienced in a fast reactor. If we again extrapolate the data to 300°C, one would conclude that less than 5% swelling would occur after a 10 MW-yr/m^2 exposure.

If such levels of swelling are not tolerable, one could also rely on the Ti produced by the transmutation reactions (see section IX-C-4) to reduce swelling. Bloom et al.,[7] have shown that as little as 0.2 wt % of Ti can drastically reduce the swelling in 316 stainless steel at low temperatures (Figure IX-D-4). This amount of Ti is close to what will be produced after a 10 MW-yr/m^2 exposure (see Table IX-C-5).

Therefore, we conclude that swelling in the permanent first wall structure of TETR is not a severe problem. A useful lifetime, based on swelling alone, of 10 MW-yr/m^2 at 300°C is a reasonable value to expect at this time.

IX-D-3. Fatigue Life

The relatively short burn cycle (60 sec) and the 12.5 second down time between cycles means that there are a potential of 300,000 stress-strain cycles per year. If we wish to have the blanket structure last for 10 years, then we must insure that the components can withstand some 3 x 10^6 cycles over the lifetime of the plant. From Table VI-C-1 we see that the maximum $\Delta\sigma$ is ~4100 psi in the first wall coolant tubes, producing a maximum strain per cycle of 0.016%.

There is very little irradiated material data to compare the above conditions with so we are forced to considerable extrapolations. The fatigue properties of both unirradiated and irradiated 304 stainless steel continuously fatigued in are shown in Figure IX-D-5.[8] This data shows that at the maximum stress level we are still an order of magnitude away from the failure life after a million cycles. Futhermore, if the tests were conducted in a vacuum, the trend is usually toward even longer lifetimes. Finally, a more complete finite element analysis of the specific geometry of the TETR first walls should be conducted with special attention paid to the effect of hold time on the fatigue resistance.

IX-D-4. Tensile Properties

It is very difficult to obtain high fluence, low temperature data as was indicated previously. Rather than analyze a great deal of low fluence data (<10^{21}n/cm^2, E > 0.1 MeV) we will simply quote some results from recent studies at ORNL in HFIF and ORR where the fluence exceeded 10^{22}n cm^{-2} (E > 0.1 MeV). This corresponds to 4.7 dpa.

There are basically two sets of data that are of interest, that from 316 SS irradiated in the range of 350°C and above[9] and that from CW 316 SS irradiated at 55°C[10]. A summary of the first set of data is given in Figure IX-D-6 where the yield stress, ultimate tensile stress, and total elongation values are given for 20% CW and annealed 316 SS irradiated to

FIGURE IX-D-4

SWELLING IN ANNEALED STAINLESS STEEL IRRADIATED IN HFIR (3000-4000appm He,40-60dpa)

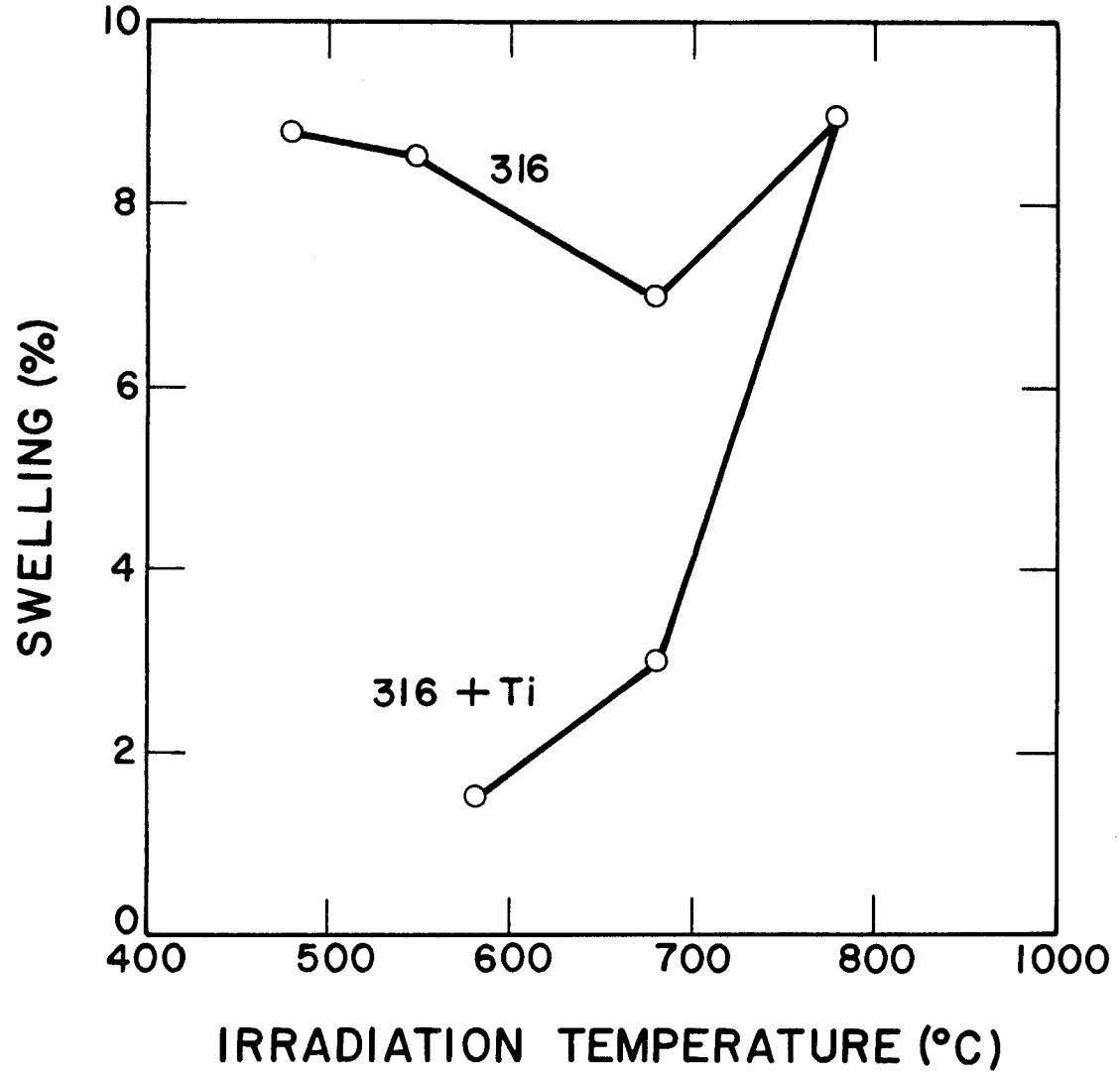

Data from E. Bloom, ORNL

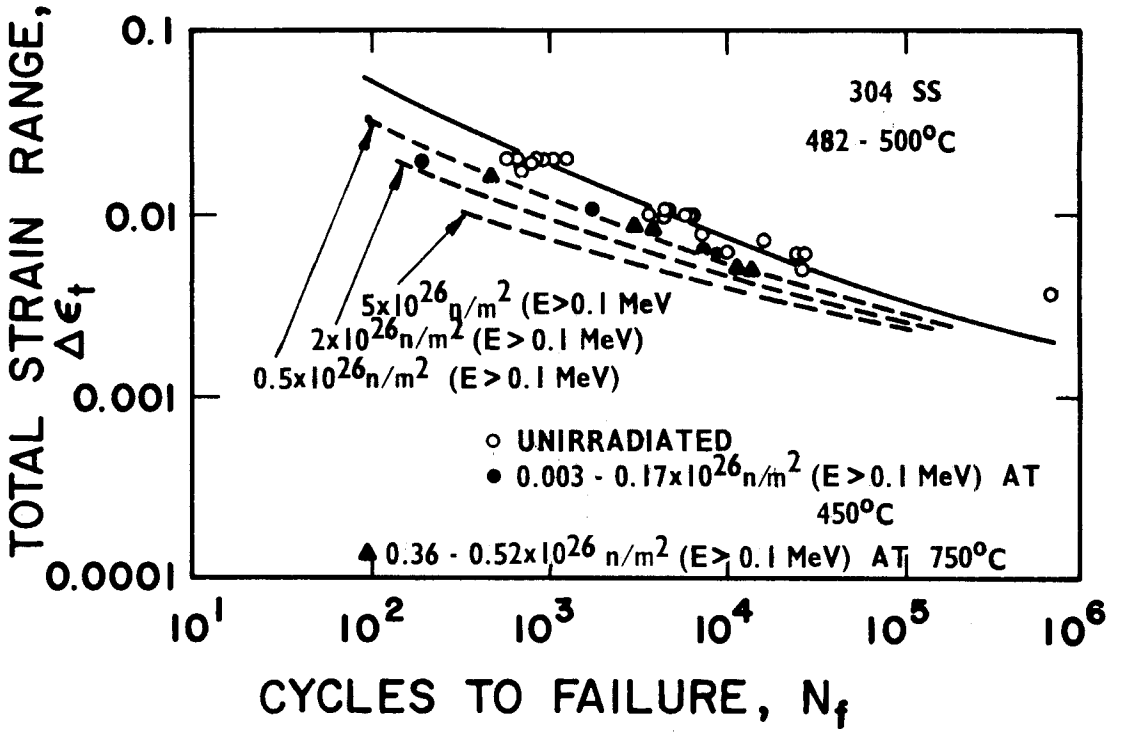

FIGURE IX - D - 5 FATIGUE LIFE OF IRRADIATED 304 SS AT 482 - 500°C (AFTER BLACKBURN AND KNECHT)

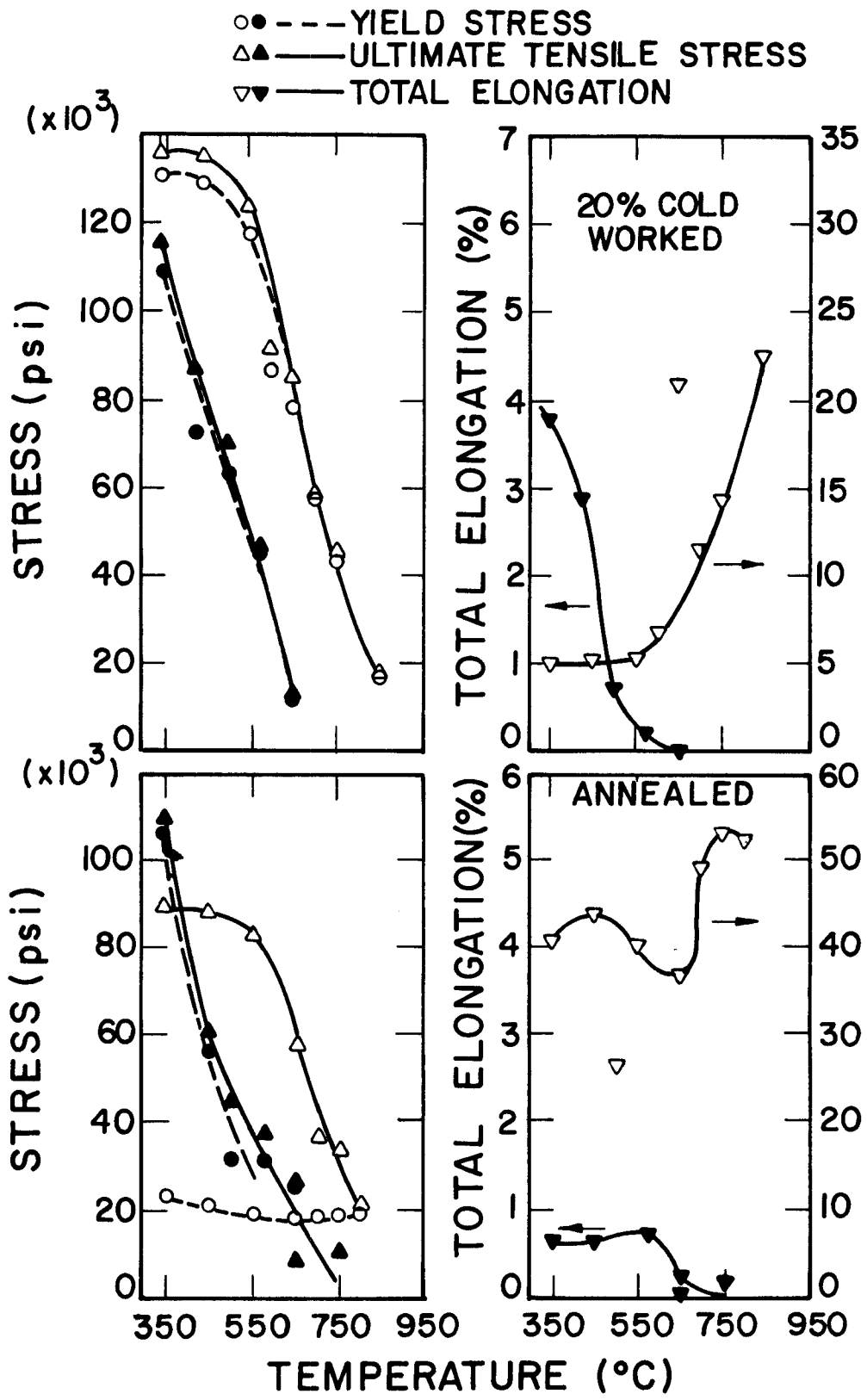

FIGURE IX - D - 6 TENSILE PROPERTIES OF 20% COLD-WORKED (UPPER FIGURES) AND ANNEALED (LOWER FIGURES) TYPE 316 STAINLESS STEEL. OPEN SYMBOLS ARE FOR UNIRRADIATED MATERIAL AND FILLED SYMBOLS ARE FOR HFIR - IRRADIATED SAMPLES (5.6 TO 8.7 x 10^{26} n/m^2). SAMPLES WERE IRRADIATED NEAR THE TEST TEMPERATURE TO 40 TO 60 dpa AND 3000 TO 4300 appm. HELIUM. (Ref. 9)

40-60 dpa at 3000-4300 appm He. It can be seen that at the low temperature end, this irradiation causes a slight (~20%) reduction in the tensile properties for the CW 316 SS and it causes ~20% increase in the tensile properties of the annealed material. The tensile strengths both end up in the 110 ksi range after the 4-6 MW-y/m^2 exposure.

The total elongation of the cold worked material is only lowered about 20% at 350°C but it is dropped by a factor of ~80 in the case of the annealed material. The absolute level in the later case is roughly 0.5%, a level which is very worrisome. The message here seems to be that one must avoid all fabrication procedures (e.g., welding) which might cause the cold working to anneal.

The conclusion from the data in Figure IX-D-6 is that no serious problems are anticipated in material irradiated to 4-6 MW-y/m^2 at 350°C and one should retain total elongation values of >1% after 10 MW-y/m^2 of equivalent damage.

A more recent set of data has been obtained at 0.5 to 1 MW-y/m^2 from 55°C irradiations.[10] At these low temperatures there should be no voids formed and helium content should be 150 to 500 appm which should not cause any serious dimensional changes. The data from this test is shown in Figure IX-D-7. The effect of irradiation is to cause a slight increase (~15%) in the tensile strength and a 10% decrease in the total elongation. However, the uniform elongation is dropped to very low levels (<1%). This low uniform ductility was present until post irradiation anneals of 400°C were performed. On the basis of this data one might expect that irradiation at a higher temperature (i.e., 250-350°C) would result in less property degradation (as indicated by Figure IX-D-6) but such a hypothesis certainly needs to be substantiated. Nevertheless, such information does serve as a warning that we must not allow the structure temperature to drop too low during the operation or we might enter into this severly embrittling condition.

IX-D-5. Creep-Rupture Life

Because of the low irradiation temperature and the low swelling rate expected, the creep-rupture life is expected to be very long and no indepth analysis was attempted. However, for comparison purposes we calculate from the Larson Miller parameter (see Figure IX-D-8)[11] that the rupture life at 300°C and 4 ksi is >>10^{10} year!

IX-D-6. Crack Growth Rates

Because of the many cycles envisioned for TETR per year, it is important to estimate the order of magnitude crack growth rates that might be possible. To do this we will use the relationships developed for the crack growth rate da/dn and the stress intensity factor, K. The latter term is defined as,

(IX-D-2) $$K = \frac{\sigma\sqrt{\pi\alpha}\ \lambda}{\sqrt{Q}}$$

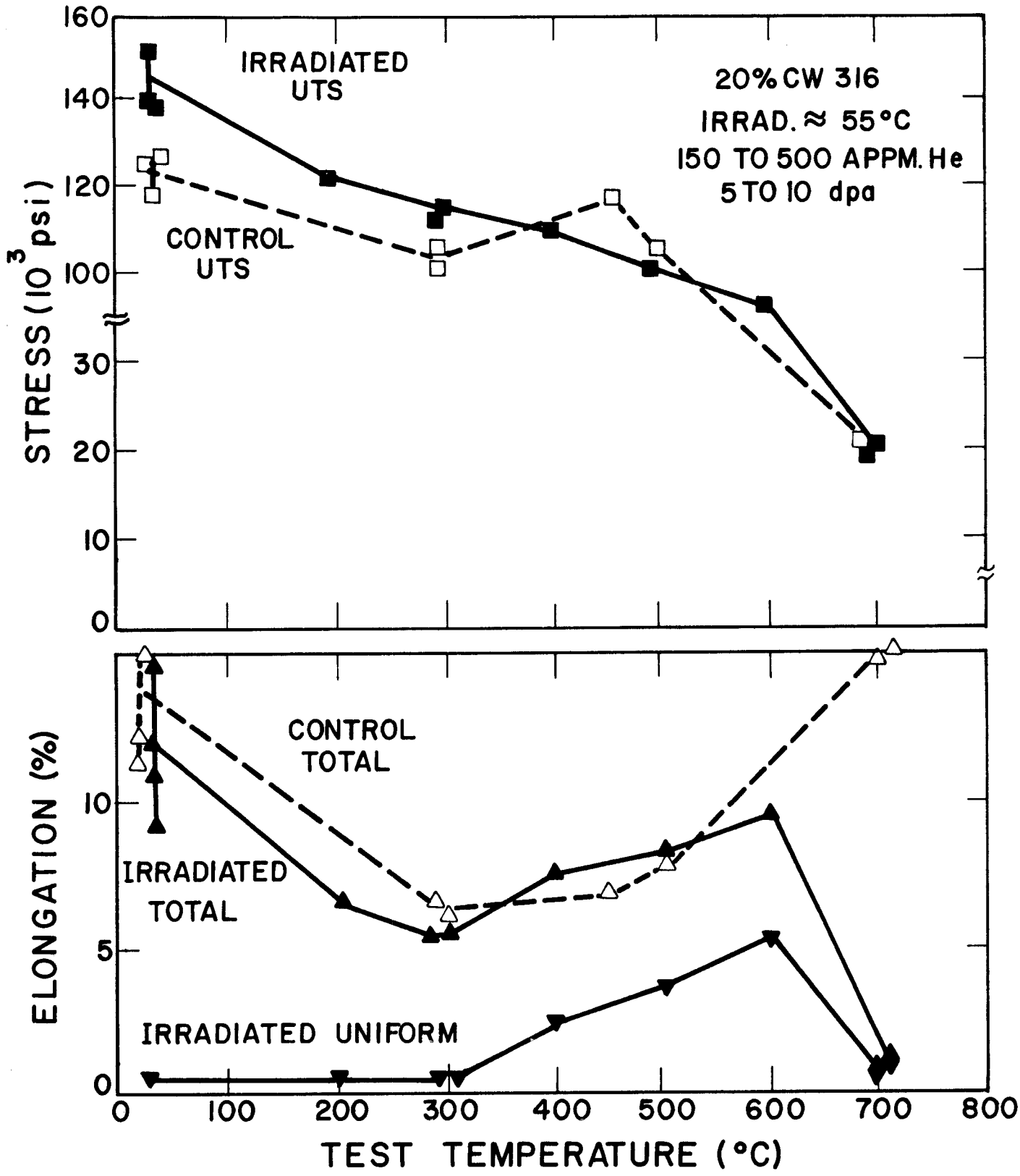

FIGURE IX - D - 7 TENSILE TESTS OF 20% CW 316 IRRADIATED AT 55°C TO PRODUCE 150 TO 500 APPM. He SHOW ADEQUATE PROPERTIES ARE RETAINED IN TESTS UP TO 600°C. HOLD TIME AT TEST TEMPERATURE WAS 30 MINUTES. (ORNL - DATA).

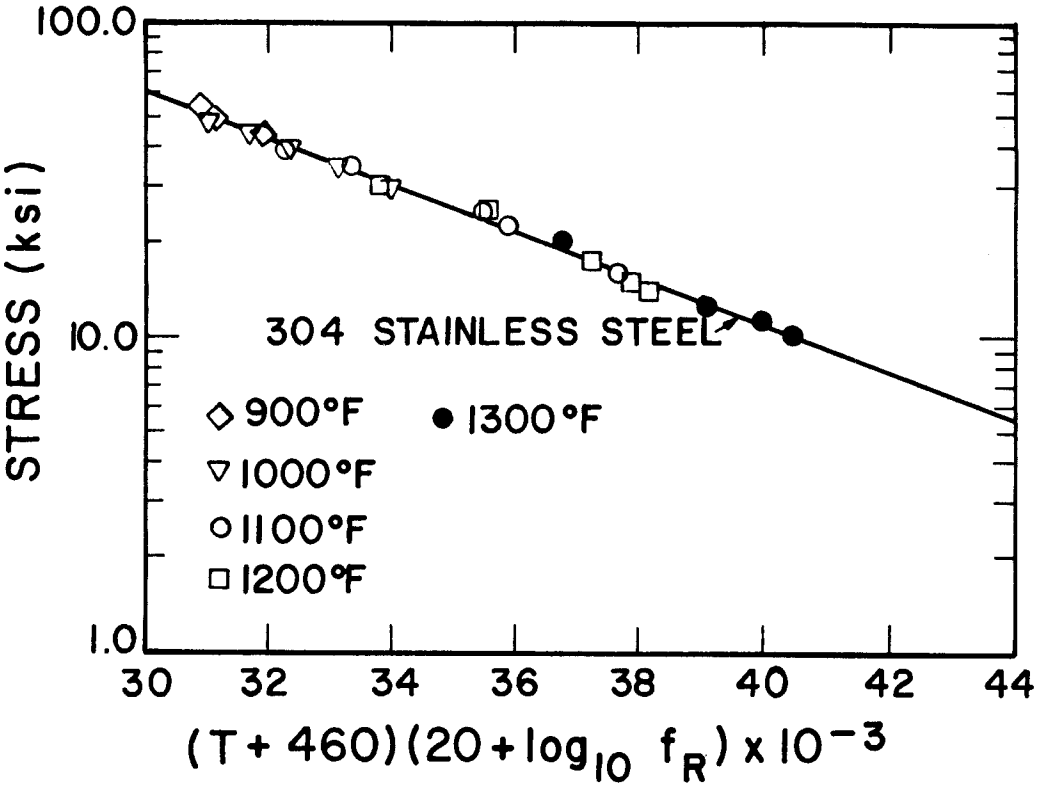

FIGURE IX - D - 8 STRESS RUPTURE PROPERTIES OF ANNEALED STAINLESS STEEL. (ANL/FPP/TM-99)

where

α is the crack depth
Q is the flow shape parameter
λ is a correction factor which accounts for finite boundaries, variations in crack geometry and variations in type of loading

The relation between the stress intensity factor and crack growth rate in steel is shown in Figure IX-D-9. Using a crack depth of 0.64 mm (0.025 inch) and a stress cycle of 4100 psi one finds ΔK on the order of a 1000. Since this value indicates crack growth rates of $<<10^{-5}$ cm/cycle, we conclude that we would have only a stationary crack and hence no particular problem.

IX-D-7. Conclusions

The most serious threat to a 10 MW-yr/m^2 lifetime appears to be the drop in uniform elongation after a few years of irradiation at 300°C. However, an analysis of the fracture characteristic reveals that sufficient toughness should remain to accommodate the rather low stresses in TETR. Void swelling and tensile property changes do not appear to be very serious under the proposed operating conditions and the low temperature and stress levels should allow a very long creep rupture life to be achieved.

Fig. IX-D-9

PROPERTY CODE 2431 PAGE 1.0

NUCLEAR SYSTEMS MATERIALS HANDBOOK

VOL 1 - DESIGN DATA

PART I - STRUCTURAL MATERIALS	GROUP 1 - HIGH ALLOY STEELS	SECTION 2 - 304 SS, ANNEALED
REVISION: 0, 11-30-76 PREVIOUS REVISION:	FATIGUE-CRACK GROWTH BEHAVIOR, EFFECT OF TEMPERATURE IN AIR	

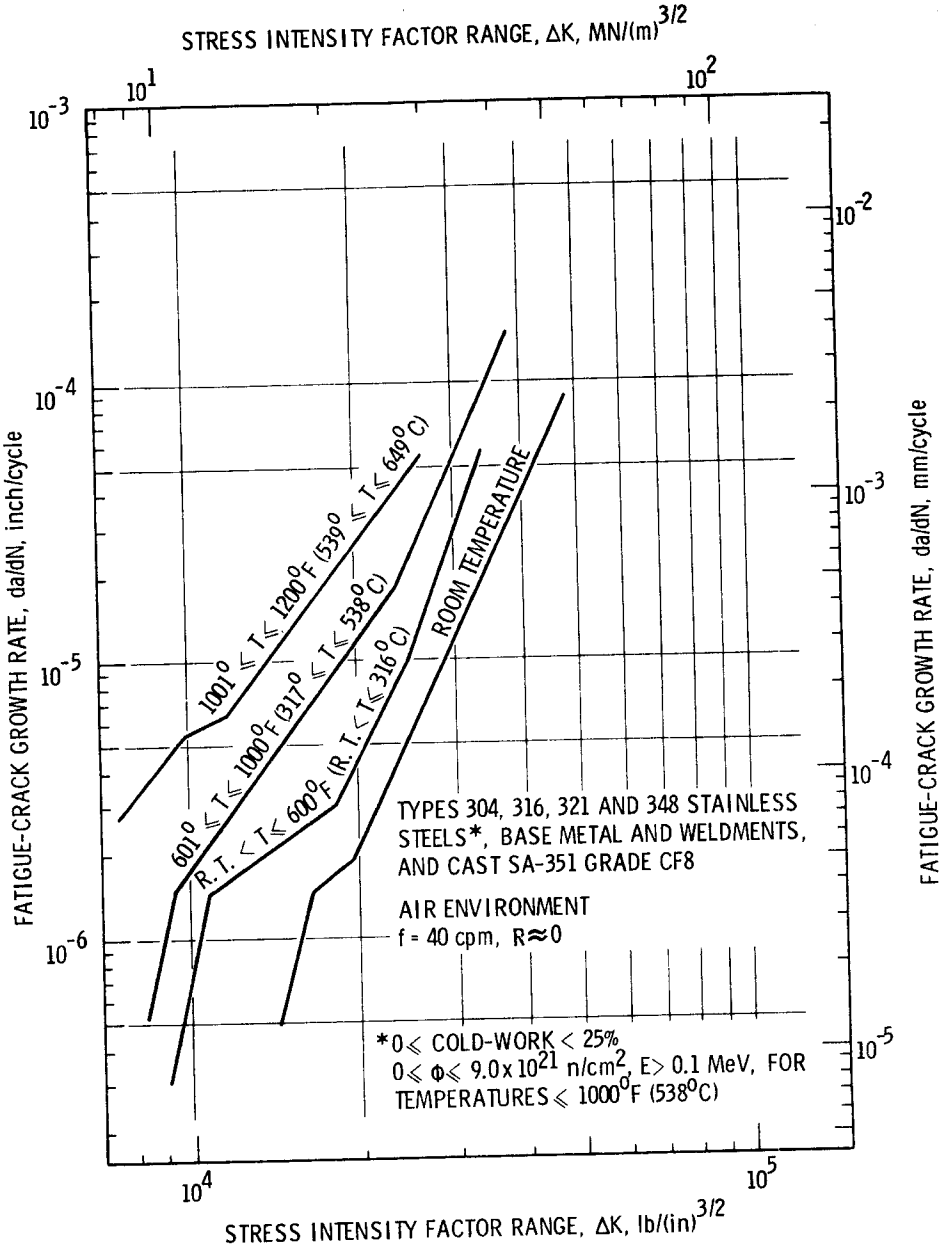

APPLICABLE PRODUCT FORMS: All product forms.
NOTES: Extrapolation of these curves is not recommended. For frequency correction see page 2.0. For mean stress correction see page 3.0.

IX-E. Effect of Irradiation on Non-Structural Components of TETR

IX-E-1. Introduction

Aside from the basic structure of the TETR blanket and shield there will be irradiation damage in the carbon curtain, tungsten and boron carbide neutron shield material, the Ta-10W collector plates, and in the magnet components. It is quite probable that there will be other specialized materials such as ceramics, thermocouples, chevrons for the cryopumps, and neutral beam injector materials which will also be affected by the radiation. However, we will not cover the latter class of materials here. No attempt will be made to make an exhaustive study of the other non-structural materials other than to indicate where problems may arise.

IX-E-2. Carbon Curtain

The effects of neutron and charged particle irradiation on carbon at high temperatures has been summarized elsewhere[1-3,12-15] and we will use the results of that work to assess the response of carbon to the TETR irradiation. The problem for the curtain lies in three areas.

(1) The effect of high temperature neutron damage on the dimensional stability of the carbon.

(2) The effect of the neutral particle flux on the thinning of the carbon curtain.

(3) Chemical sputtering by the hydrogenic species on the hot carbon fibers.

The good vacuum properties of the weaver have been demonstrated previously[16] as have the techniques that might be used to fabricate and deploy the curtain.[15]

IX-E-2-a. Neutron Effects in Carbon at High Temperatures

We will assume that the average operating temperature of the carbon curtain is 1200°C (Chapter VIII) and at a 1 MW-yr/m^2 wall loading the displacement rate is 6.7 dpa/y (for comparison purposes we will use a conversion factor of 5 dpa/10^{22} n cm^{-2} (E > 0.1 MeV)). The dimensional changes in graphite irradiated with fission neutrons between 1000 and 1600°C are shown in Figure IX-E-1 and the final growth rates (after the carbon returns to its original volume) have been determined by Wolfer[14] and are displayed in Figure IX-E-2. From this data we see that it is possible for the carbon to shrink by ~7 to 8% after 1 MW-y/m^2 and return to its original volume after ~4 MW-yr/m^2. The volume increase after the next 6 MW-y/m^2 would cause the carbon to expand by ~34%.

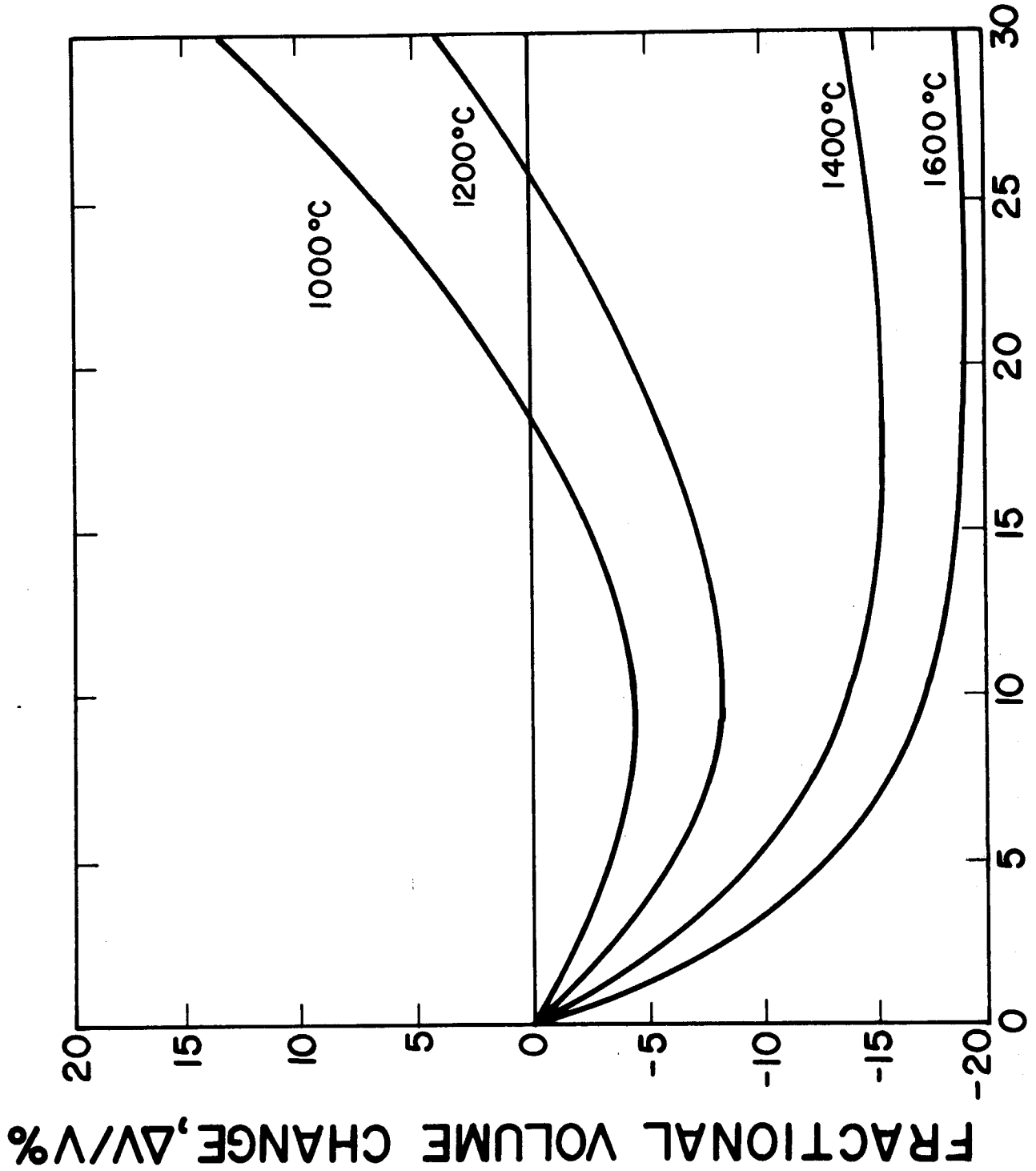

Fig. IX-E-1 Volume Change of Graphite with 20 % Initial Porosity Irradiated at Temperatures between 1000°C and 1600°C

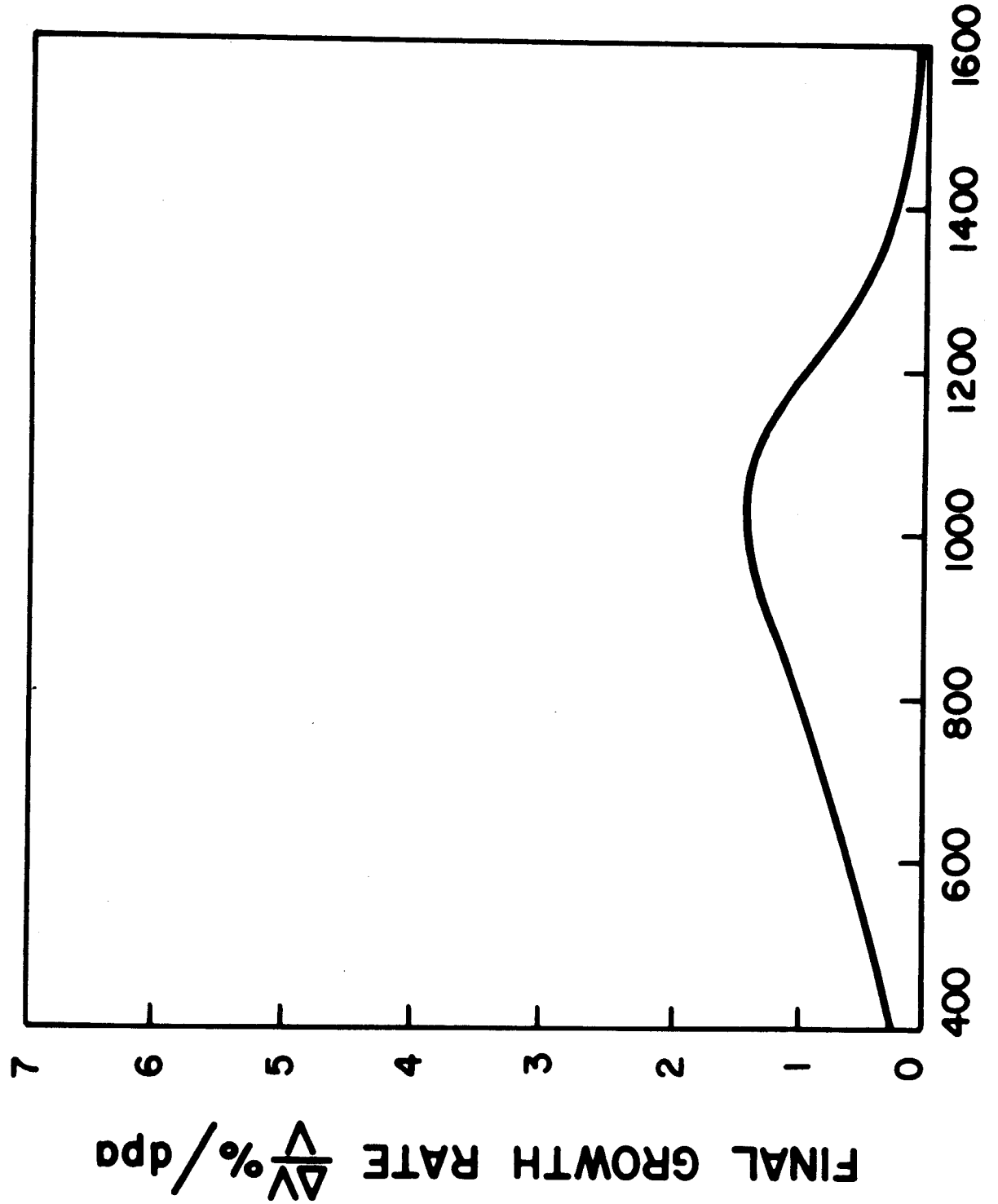

Fig. IX-E-2 Final Volumetric Growth Rate in Carbon (Reference 14)

Since the carbon is used as a non-structural component, the initial shrinkage is easily accommodated as was demonstrated by Gray[17] in lower temperature irradiated carbon cloths. The expansion is much larger but some "sagging" of the curtain should not be too serious and it is quite possible that we will be able to get a 10 MW-yr/m^2 performance from the carbon curtain. Obviously confirmatory experiments need to be performed.

IX-E-2-b. Physical Sputtering of the Carbon Curtain

The flux of neutral particles to the carbon curtain was determined earlier to be 7×10^{15} $cm^{-2}s^{-1}$ with an average energy of 3.8 keV. The sputtering coefficients for various plasma particles (assumed to be all D and T) are shown in Figure IX-E-3.[18] We have assumed the sputtering curve for T lies between that for D and He.

The average sputtering coefficients for the 3.8 keV D & T are 4×10^{-3} and 8×10^{-3} respectively. Combining that with the fact that 80% of the particles leaving the plasma are deuterium and 20% are tritium yields an average sputtering coefficient of 4.8×10^{-3} atom/ion. This in turn predicts a surface atom sputtering rate of 3.4×10^{13} atoms/cm^2-s or a thinning rate of $\sim 10^{-2}$ cm/year or ~1mm in ten years. Since the original thickness of the curtain can be several mm's, this should be tolerable from the thickness standpoint. (However, the problems with the vacuum system may be another matter!)

IX-E-3. Chemical Sputtering of Carbon in a DT Environment

The interaction between hydrogenic species and carbon at high temperature has been discussed previously[1] and it was shown that at 1200°C and above the main cause of chemical erosion would be the formation of acetylene.[19] The Balooch and Olander model[19] would predict reaction rates at ~1500°C of ~10^{-3} for low energy hydrogenic ions and Guseva[20] has measured a yield of 0.03 at 1400°C for a 10 keV H^+ ion on carbon cloth. Since the physical sputtering at that energy is only ~ 5 to 10×10^{-4}, the increase could be due to C_2H_2 formation. Using an upper limit of 0.03 atom/ion at 1200°C means that the thinning rate due to charge exchange D & T neutrals would be ~0.6 mm/year. This could be much more serious than physical sputtering and it may shorten the useful lifetime to less than 10 years. However, the assumed chemical sputtering value of 0.03 is probably too pessimistic and if it was as low as 0.01, the problem would be manageable.

FIG. IX-E-3 PLOT OF CALCULATED ENERGY-DEPENDENT PHYSICAL SPUTTER YIELD CURVES FOR CARBON (GRAPHITE) SHOWING COMPARISON WITH AVAILABLE EXPERIMENTAL DATA (AFTER ANL/FPP/TM-91, 1977)

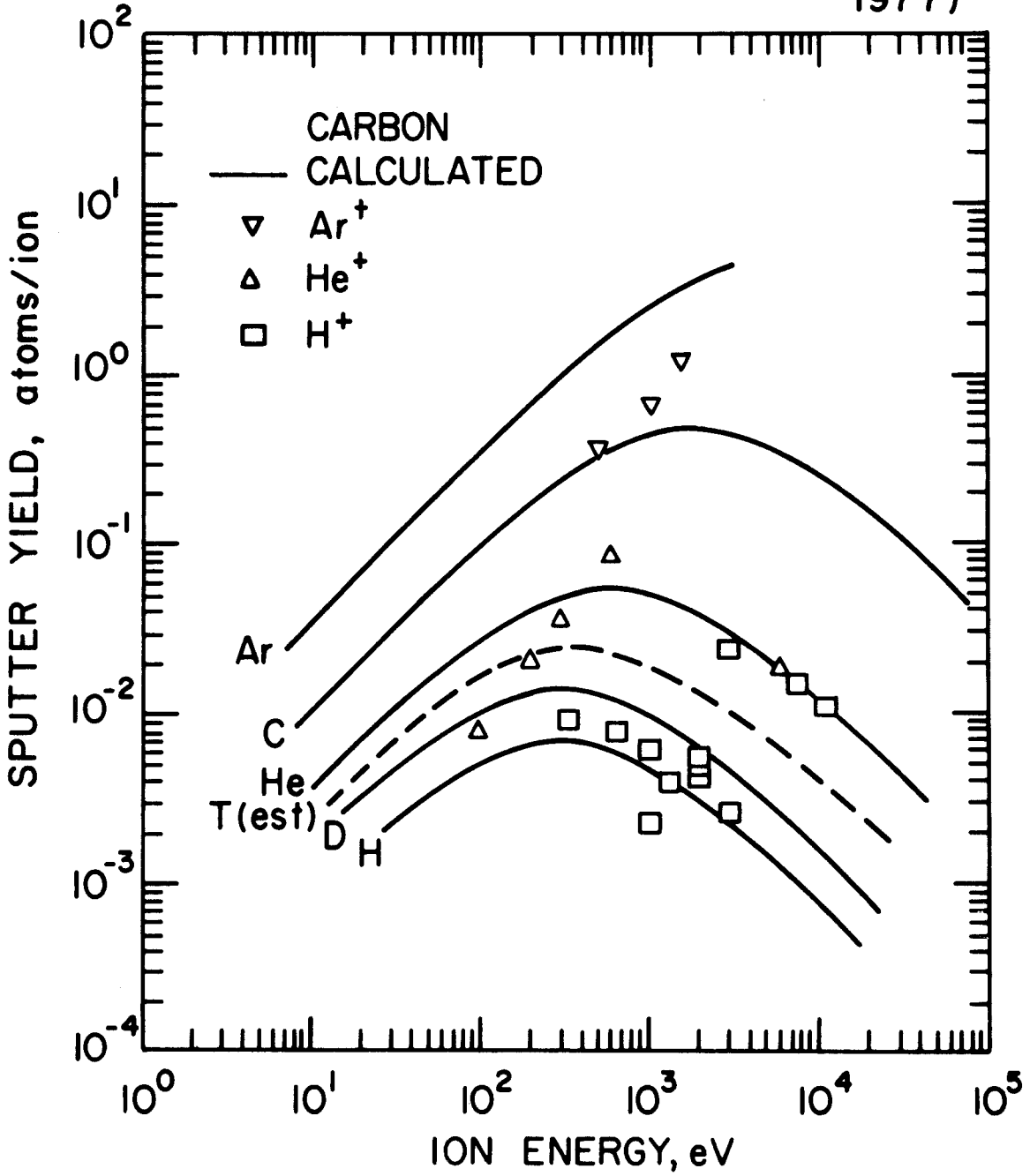

IX-E-4. Sputtering Damage to the Particle Collector Plates in the Divertor

The maximum particle flux to the Ta-10W collector plates was given in Table IX-B-2 and the sputtering coefficients for those particles are given in Figure IX-E-4.[18] We have approximated the Ta-10W sputtering coefficient with that from W. At 10 keV the sputtering coefficient for D is 5×10^{-3} and that for T is 10^{-2}. The value for He is $\sim 3 \times 10^{-2}$ atom/ion. Combining the maximum fluxes in Table IX-B-2 with the average sputtering coefficients above we find that the thinning rate is ~0.8 cm/year at a 70% plant factor. This means that if we must change the tubes after 50% of the thickness has been eroded away (0.5 mm) the expected lifetime will be ~1-2 weeks. Such replacement times require extremely rapid turn around times and represents one of the most severe limitations of the TETR design.

IX-E-5. Radiation Damage to the Tungsten Shield Material

Since the W shield material plays no structural role in the reactor, there is very little concern for radiation effects on its mechanical properties. Furthermore, the operating temperature of 350°C is only 16% of the melting point and far below the temperature for void formation. Helium accumulation over the ten year operating life will be less that a few hundred appm so no gas bubble swelling is expected.

In conclusion, there appears to be no immediate concern over the radiation damage response of the tungsten in the shield area.

IX-E-6. Radiation Damage in the Boron Carbide Neutron Absorber Material

The production of helium gas in the B_4C is probably the most severe problem that material will face. This gas (and other reaction products) can cause the material to change volume and generate large stresses in the blanket area. An idea of how much swelling could occur is shown in Figure IX-E-5. Since the maximum B-10 burnup (helium production rate) is $< 10^{20}$ cm^{-3} y^{-1} very little dimensional change is to be expected.

FIG. IX-E-4 PLOT OF CALCULATED ENERGY-DEPENDENT PHYSICAL SPUTTER YIELD CURVES FOR TUNGSTEN SHOWING COMPARISON WITH AVAILABLE EXPERIMENTAL DATA (AFTER ANL/FPP/TM-91, 1977)

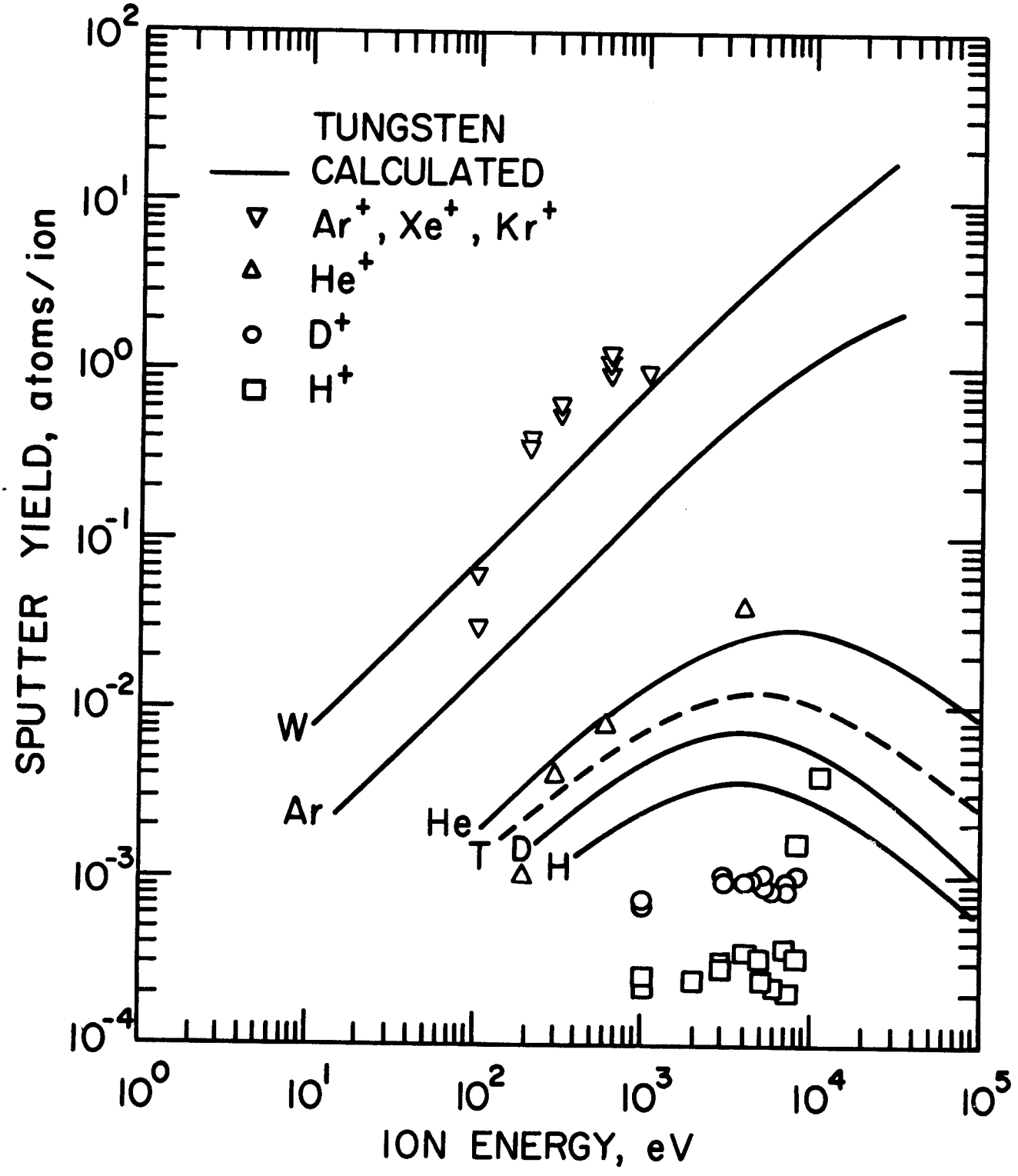

Figure IX-E-5

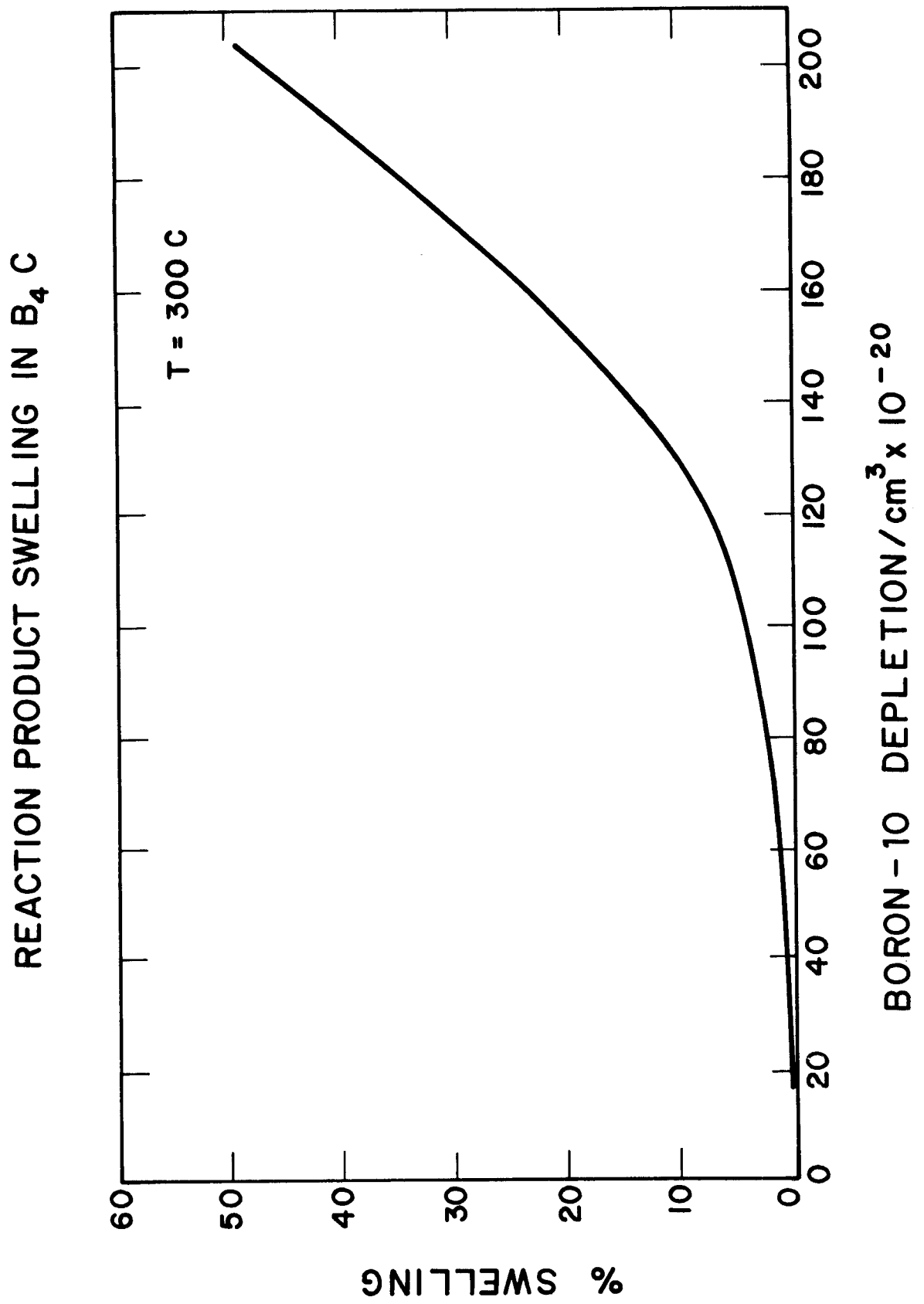
REACTION PRODUCT SWELLING IN B_4C
T = 300 C
% SWELLING
0
10
20
30
40
50
60
BORON-10 DEPLETION/cm^3 x 10^{-20}
0
20
40
60
80
100
120
140
160
180
200

IX-E-7. Radiation Effects to Magnet Materials

There are five areas which need attention in the TETR magnet system,

- Displacement damage in the OFHC copper of the TF coil at 4.2°K
- Displacement damage in the NbTi superconductor in the TF coil at 4.2°K
- Radiation exposure to the Mylar Thermal Insulation in the TF coil at 4.2°K
- Radiation exposure to the epoxy fiberglass insulator of the TF and OH coil at 4.2°K, and the VF coils at 70°C
- Displacement damage in OFHC copper of the VF coils at ~70°C

A review of the pertinent exposure information is given in Table IX-E-1.

IX-E-7-a. Damage in Cu Stabilizer

The damage rate of 4×10^{-5} to 2×10^{-4} dpa per year in the OFHC copper stabilizer will tend to increase the electrical resistance according to the rate depicted in Figure IX-E-7. From this information it can be seen that, at the midplane, the resistivity of the copper in the TF coil will be doubled in one year of operation. It is also seen that the resistivity after one year of operation at the highest damage rate (that due to neutron streaming down the divertor ports) will be ~6 times the residual value at 4.2°K.

It has been shown earlier[1-3] that a large fraction of the damage (~90%) can be removed by periodic annealing at room temperature. This means that it will be necessary to raise the TF magnet at least once a year to room temperature during normal maintenance procedures.

The high damage rate at ± 175 cm from the midplane also raises the possibility that cryogenic stability criteria may be violated. This could be avoided by making the thickness of the copper stabilizer greater on the side of the TF coil facing the plasma as was done in the UWMAK-I design.

IX-E-7-b. Radiation Effects in the NbTi Superconductor

The effects of neutron irradiation at cryogenic temperatures on NbTi superconductor are shown in Figure IX-E-8.[21] At a 4×10^{-5} dpa/yr rate we see that even after 10 years the critical current density should be degraded by less than 5%. However, at the maximum damage rate of 2×10^{-4} dpa/yr there could be significant degradation of the critical current density (e.g., >20%). Because of the need to periodically raise the TF coil to room temperature to anneal the damage in the copper it is possible that there could be some recovery of the damage in NbTi but that remains to be proven by experiments.

Table IX-E-1

Summary of the Radiation Damage Environment in the TETR Magnets

Component	Temperature ^{o}K	Exposure Rate
1) OFHC Cu Stabilizer	4.2	4×10^{-5}(a) 3×10^{-4}(b)(c)
2) NbTi Superconductor	4.2	4×10^{-5}(a) 3×10^{-4}(b)(c)
3) Epoxy Fiberglass Insulator - TF Coil	4.2	2×10^{7} rad/yr(a) $\sim 10^{8}$ rad/yr(b)(c)
4) Mylar Thermal Insulation - TF Coil	4.2	2×10^{7} rad/yr(a) $\sim 10^{8}$ rad/yr(b)(c)
5) Epoxy Fiberglass Insulator - VF Coil	343	10^{9} rad/yr, D-1(b) 2×10^{11} rad/yr, D-9(b)
6) OFHC Copper VF Coil	343	4×10^{-3} dpa/yr, D-1(b) 1 dpa/yr D-9(b)

a) Midplane

b) See Figure IX-E-6 for coil designation from 2D calculations

c) 175 cm above and below midplane

Figure IX-E-6

Cross Section of TETR with Numbered VF and OH Coils

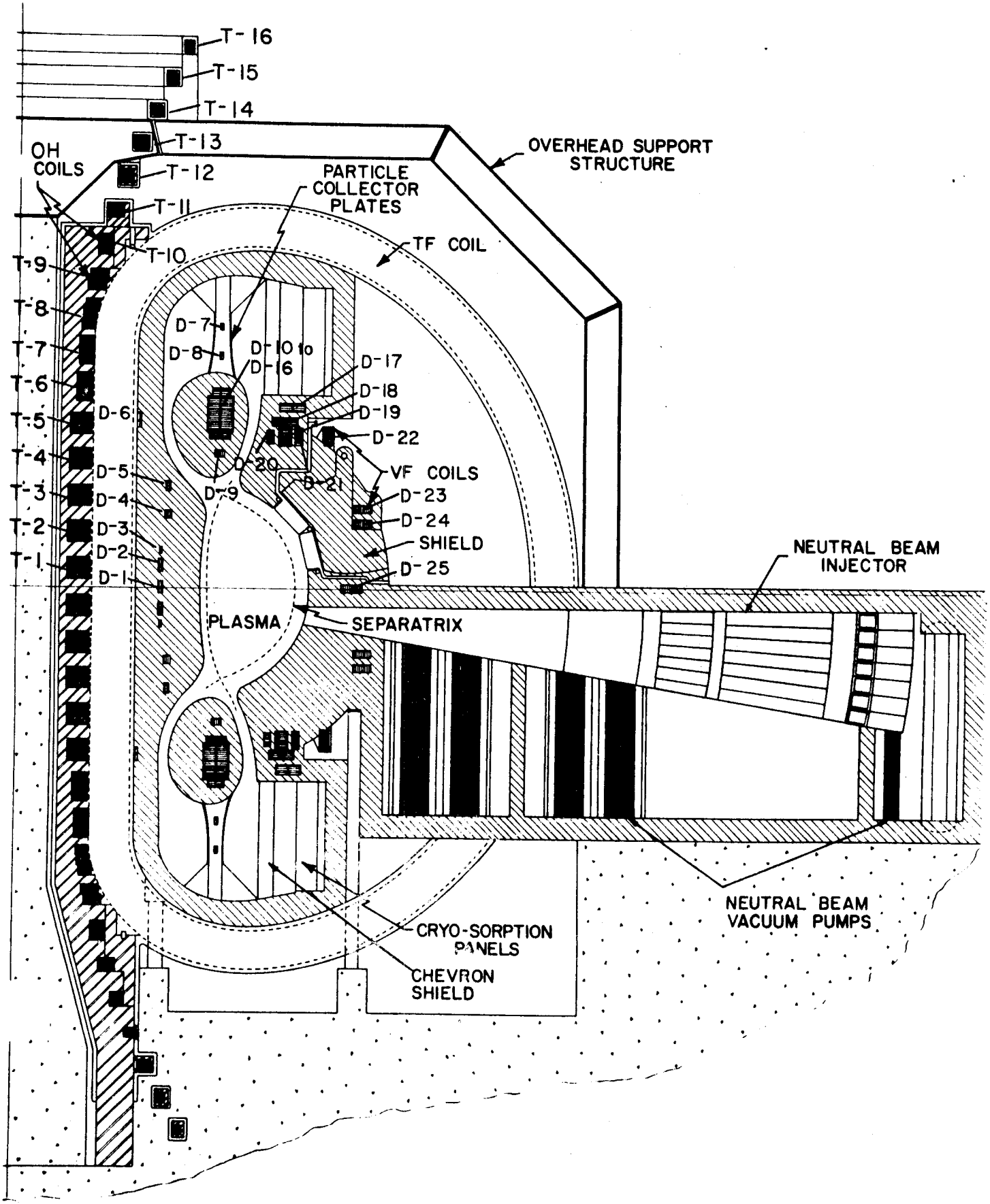

Figure IX-E-7

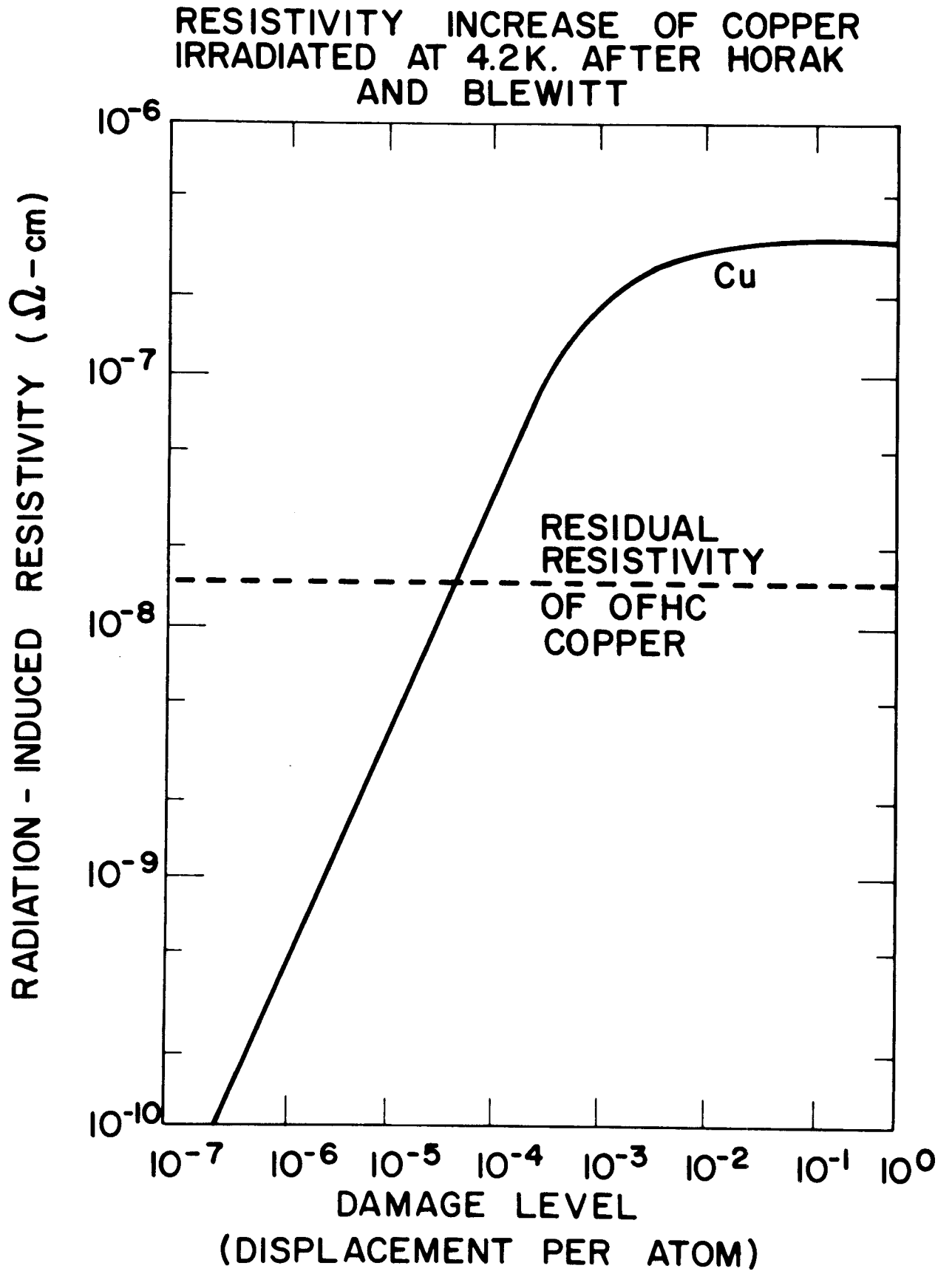
RESISTIVITY INCREASE OF COPPER IRRADIATED AT 4.2K. AFTER HORAK AND BLEWITT
RADIATION - INDUCED RESISTIVITY (Ω-cm)
10-6
10-7
10-8
10-9
10-10
Cu
RESIDUAL RESISTIVITY OF OFHC COPPER
10-7 10-6 10-5 10-4 10-3 10-2 10-1 100
DAMAGE LEVEL
(DISPLACEMENT PER ATOM)

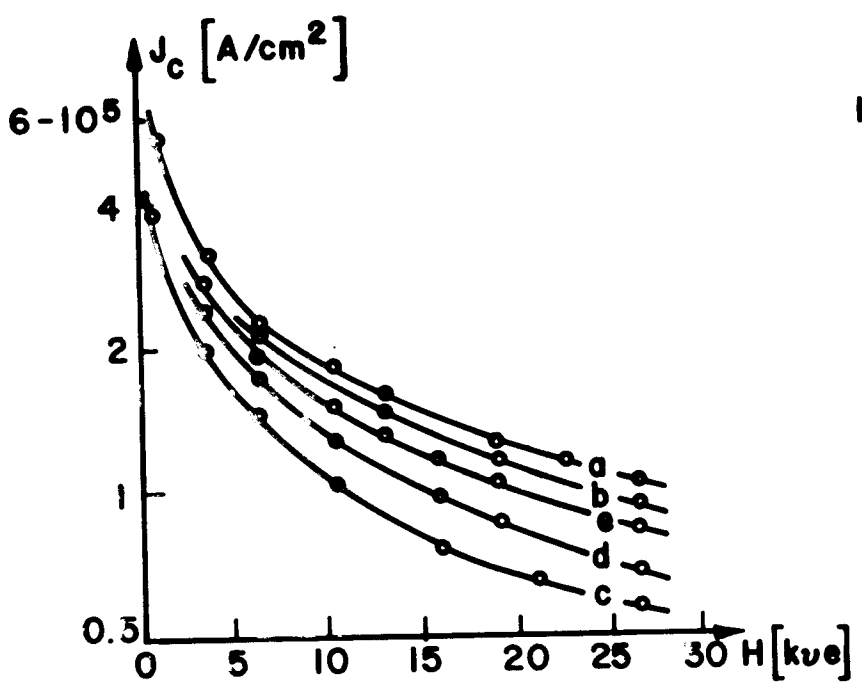

Critical current density j_c versus applied transverse magnetic field H for Nb-50wt% Ti at 5.3K. Curve a unirradiated, b irradiated with 3.2×10^{18} neutrons/cm^2 (E > 0.1 MeV), c irradiated with 7.5×10^{18} n/cm^2, d annealed at 100 K, e annealed at 270 K (after Soell)

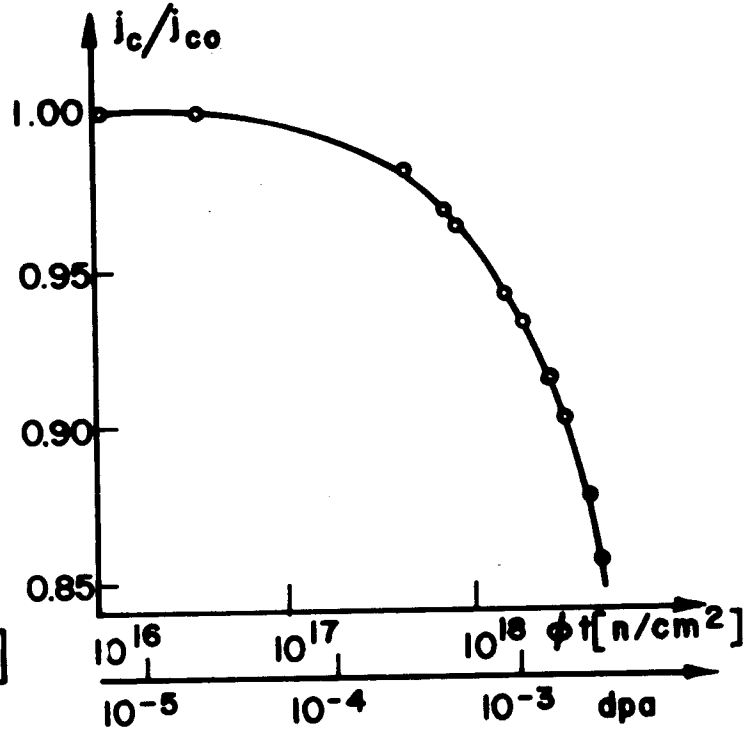

Relative change of the critical current density j_c of a Nb-50wt% Ti sample at zero field (H=0) as a function of the neutron dose $\phi \cdot t$. j_{co} is the current density before the irradiation (after Soell)

Figure IX-E-8

The effect of the fast neutron irradiation at cryogenic temperature on the critical current of Nb-50 w/o Ti. The conversion to dpa was made using a typical thermal reactor spectrum.

The conclusion of this analysis is that the damage in the NbTi is not as limiting as that in the Cu stabilizer and therefore does not tend to limit the useful lifetime of the TF coil.

IX-E-7-c. Radiation Damage to the Mylar Thermal Insulation

Previous[1-3] discussions have shown that the threshold for loss of tensile strength in mylar is ~ 3×10^7 rad (~1.5 year of exposure at the midplane). By 1.2×10^8 rads, the mylar is expected to lose ~25% of its strength and by 2×10^8 rads it may lose up to 50% of that property. While such degradation as described above may be tolerable, it is certain that exposure to 10^9 rads will cause severe problems. Therefore, more radiation damage resistant thermal insulators may have to be developed for selected hot spots in a reactor like TETR.

IX-E-7-d. Radiation Damage to the Electrical Insulator Material in the TF Coil

The exposure level to the epoxy fiberglass of the TF coil is found to range from 2×10^7 to 10^8 rad per year. The effect of radiation on a specific epoxy (epikote-828) at 77°K is shown in Figure IX-E-9.[22] It is seen that the ultimate flexural strength is unaffected up to ~10^9 rad and then it starts to drop. Since a 10 year exposure corresponds to ~10^9 rad we feel that the epoxy fiberglass insulation will perform satisfactorily with respect to strength. The information available on the insulating properties (discussed in references 2,3) reveals that the epoxy will suffer a 25% reduction in resistivity by 5×10^{10} rads. Since this is more than an order of magnitude higher than anticipated in TETR, we foresee no particular problem in this area.

IX-E-7-e. Radiation Damage to the Electrical Insulation in the VF Coil

As can be seen from Table IX-E-1, the exposure levels to the VF coils are much higher than to the TF coils. The 10^9 rad/yr exposure to the VF coil D-1 and ~ 2×10^{11} rad/yr exposure to the D-9 coil represent very severe environments. It is expected that the higher operating temperature will help to alleviate some of the damage so that it is possible that the D-1 coil will operate satisfactorily. However, not even the high temperature operation is expected to help the epoxy in the D-9 coil. Both the mechanical properties and insulating ability will suffer severe degradation.

No obvious solution to this problem exists at this time and it may be necessary to use ceramic electrical insulators. The overall requirement of ~ 2×10^{12} rad lifetime will undoubtedly be a very difficult criterion to meet.

IX-E-7-f. Radiation Damage to the OFHC Copper in the VF Coil

The damage rate in the VF coils ranges from 4×10^{-3} dpa/yr to ~ 1 dpa/yr. The main problem will be the production of impurities and the increase in electrical resistance due to the introduction of point defects.

FIG. IX-E-9 THE ULTIMATE FLEXURAL STRENGTH OF EPOXY RESIN EPIKOTE 828 AS FUNCTION OF RADIATION DOSE AT 77K (22)

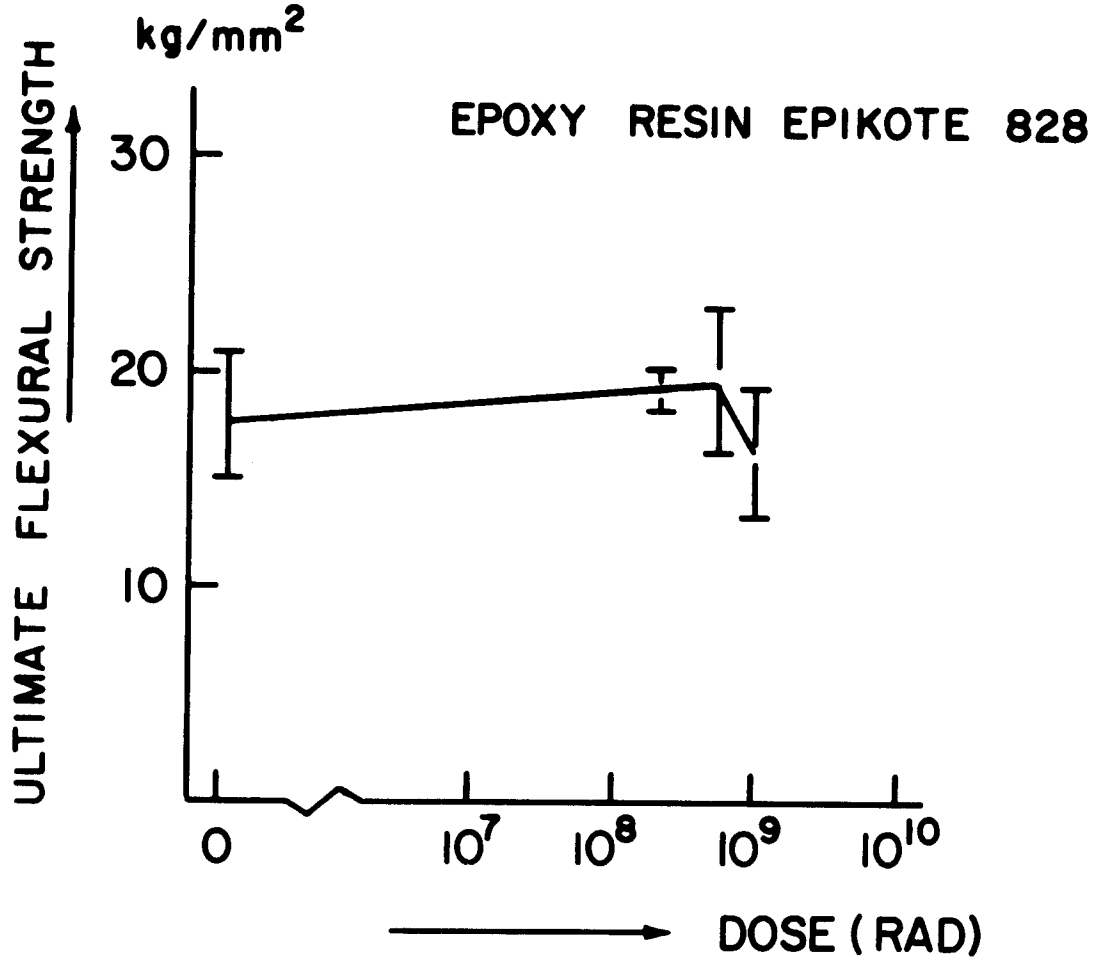

One way of estimating the problems with the electrical resistance increase would be to calculate the residual resistivity increase at 4.2°K and then assume that 90% of the anneals by 70°C according to previous isochronel annealing results. This will probably result in an overestimate of the residual damage.

The resistivity of copper at 70°C is ~1.7 micro-ohm-cm. Using a saturation value of ~0.5 micro-ohm-cm after ~10^{-3} dpa we see that the resistivity of the VF coils will very quickly reach that value. Thermal annealing would then indicate that the resistivity at 70°C might be increased by <5%.

The transmutation rate in the VF coil amounts to 2 appm/yr of Ni, 2 appm/yr of Zn. The total introduction of impurities is 4 appm/yr which is estimated[23] to contribute <1% to the resistivity after a 10 year exposure. Therefore, we conclude that transmutation product induced resistivity increases are not a severe problem for the VF coils.

IX-F. Summary of Radiation Damage Problems in the Non Test Cell Area of TETR

The previous analysis reveals that the most severe problems in TETR appear to be associated with the electrical insulating material of the VF coils, thermal insulators for some places in the TF coils, and the Ta-10W collector surface. We have no clear cut solutions for those areas at the present time and further research is clearly required.

We are also concerned about the degradation of mechanical properties in the 316 SS first walls of the blanket and the increase in resistivity of the copper stabilizer in the TF coil. The latter problem can be alleviated by design modifications, but a more detailed stress analysis is required before a definitive fatigue-crack analysis can be attempted in the 316 SS.

Finally, we see some potential problems in the high erosion rates of the carbon curtain, and the possibility that there may be some helium assisted void formation in the first wall which will induce stresses over and above those already analyzed.

References

1) B. Badger, et al., UWMAK-III, UWFDM-150, 1976.

2) B. Badger, et al., UWMAK-I, UWFDM-68, 1974.

3) B. Badger, et al., UWMAK-II, UWFDM-112, 1975.

4) Consultants Symposium on "The Physics of Irradiation Produced Voids", AERE-R7934, 1975.

5) "Radiation-Induced Voids in Metals", Ed. J.W. Corbett and L.C. Ianniello, AEC Symposium Series-26, 1972.

6) P.J. Mazlasz, F.W. Wiffen, and E.E. Bloom, ORNL-TM-5396, May 1976.

7) E.E. Bloom, to be published.

8) L.D. Blackburn and R. Knecht, to be published.

9) E.E. Bloom and F.W. Wiffen, ORNL-TM-4861, 1975.

10) E.E. Bloom and F.W. Wiffen, Private communication.

11) M. Abdou, et al., ANL/FPP/TM-99, Nov. 1977.

12) W.C. Morgan, E.M. Woodruff, and W.J. Gray, P. 189 in "Proc. 2nd Topical Meeting on the Technology of Controlled Nuclear Fusion", ed. G.L. Kulcinski, USERDA, Conf-760935.

13) J.H. Cox and J.W. Helm, Carbon, 7, 319, 1969.

14) W. Wolfer in UWFDM-220, 1978.

15) H. Avci, et al., To be published Nuclear Design and Engineering, 1978.

16) G.P. Lang and V.L. Holmes, Nucl. Fusion, 16, 162, 1976.

17) W.J. Gray, BNWL-2390, 1977.

18) W.M. Stacey, et al., ANL/FPP/TM-91, Aug. 1977.

19) M. Balooch and D.R. Orlander, J. Chem. Phys., 63, No. 11, Dec. 1975.

20) M.I. Guseva, Private communication.

21) M. Soell, Thesis, Technical University, Munich, FRG.

22) M.H. Van de Voorde, CERN-MA/72-14 (1972).

23) N.F. Mott and H. Jones, "The Theory of the Properties of Metals and Alloys", Oxford University Press, Oxford, England, 1936, P. 293.

Chapter X. Test Modules for Structural Materials.

X.A. Introduction

Current preliminary design work for the fusion demonstration power reactor is severely hampered by the lack of data for the behavior of materials in the unique fusion environment. The combination of severe radiation damage and high helium formation rates characteristic of a fusion first wall are expected to produce major dimensional changes and embrittlement. However, it is not yet possible to quantify such changes because no test chamber is available which provides the appropriate flux of 14 MeV neutrons.

In the near future it is expected that neutron sources will become available[1] but even then the volume available for materials testing will be far too small for a substantial test program of principal alloy candidates for first wall materials (see chapter II).

To cope with this difficulty it is currently being proposed that the DMFE program should provide design data by means of a simulation program testing theoretical predictions by a small number of tests in a neutron source. The simulation facility most favored at this time is a mixed flux reactor with the flux 'tailored' to give the correct ratio of damage to helium production. The main disadvantage of this approach (apart from the lack of a 'correct' PKA spectrum) is that it is specific to nickel alloys. The high He production from nickel under first wall conditions however is an undesirable feature of such alloys. Under these circumstances there is a danger that the alloy could be chosen on the ground that it can be tested in available reactors and hence data will be available rather than that it is the best alloy for the actual environment.

Other simulation techniques all suffer from the major disadvantage of uncertainty in their predictions. They are useful for developing a fundamental understanding of damage processes and for alloy development. They cannot themselves provide design data.

It is the purpose of this study to develop a design for a materials test reactor which would substantially solve this dilemma. The test volume provided by this design is extraordinarily large, larger than that available in the equivalent reactor in the LMFBR program. It is therefore possible to select a large number of test materials and to conduct tests on specimens large enough for realistic mechanical property testing. Most such tests could be conducted in the actual neutron flux from a fusion plasma with the appropriate duty cycles. With such a machine, the design program would have available reliable data of precise materials behavior under realistic reactor conditions.

X-B. The Test Requirements

X-B-1. Wall and Blanket Materials

The environment in the first wall and blanket will differ from that in a fast fission reactor in many different ways. As a result different materials properties may be limiting the material lifetime. The damage rates are not excessively high by fast reactor standards, but the high helium production rate is a complicating factor. The major concern is therefore the effect of helium and displacement damage together on the mechanical properties.

The stress conditions which wall and blanket must carry are in some ways less severe than in the fast reactor. In the latter practically all of the heat produced flows through the clad into the coolant whereas in

a fusion reactor using a lithium coolant, much of the heat is produced in the coolant itself as it flows through the first wall tubes and the blanket. There are therefore no very high temperatures like those existing in LMFBR fuel rods (e.g., 2500-2800°C) and consequently much smaller temperature gradients.

On the other hand the gradients that do exist occur in somewhat thicker metallic structural members rather than passive fuel rods. Furthermore these structural members support a much larger and heavier structure than in the fast reactor case. The most sensitive area from the stress point of view is however the pressurized coolant tubing in the first wall facing the plasma and blanket and here conditions of stress will be comparable with the fast reactor. Tests designed for the tubes will therefore also include stress conditions appropriate for much thicker structural support members.

A unique problem for the wall and blanket materials lies in the inherent pulsing prevalent in most fusion devices. The pulse length varies greatly but it is to be expected that the first wall and blanket will experience a neutron flux that will frequently stop abruptly and often be generated entirely in pulses that may vary from tens of seconds to minutes in tokamaks.

Design features such as internal spectral shifters or curtains,[2] will smooth out some of these fluctuations and the inherently large mass of the cooled blanket will also help. Nevertheless oscillating temperatures will occur in the first wall and blanket and will give rise to oscillatory stresses. The mechanical properties of importance therefore include fatigue behavior.

Because the source of heat in a fusion device is inherently less stable than in the fission case, an additional problem is rapid heat loss. Normally, operating at high temperature causes the stresses during irradiation to relax by creep but sharp decreases in temperature will cause relatively sudden stresses to occur. This transient behavior coupled with radiation embrittlement is a major concern and a mechanical property testing program must include tests of brittle failure resistance fracture toughness. This property is dependent on specimen geometry so that tests must use the actual thicknesses for tubes and sheet materials as well as the larger cross sections for structural members.

One area of crucial importance in the first wall and blanket as in fission reactors is creep. The provision of creep rate data for several materials under a wide range of stress and temperature conditions is a major part of the testing program. Since radiation has such a powerful effect on creep rates it is essential that these creep tests be in-situ. The large test volume in TETR facilitates a real advance over the fast breeder creep test approach since most creep tests can be conducted entirely in the fusion reactor with full instrumentation and good temperature definition. This is particularly important here because of microstructural changes occurring as helium accumulates which will modify creep rates and alter the conditions for the onset of creep failure. It is essential that these changes during the life of the wall and blanket are taken account of in the design data and hence in the test program.

Since small structural flaws or microcracks are present in all welded fabrications it is essential to know whether the cracks will propagate under service conditions. Since so much of the wall/blanket region consists

of sheet fabrications the propagation of through-cracks is the primary but not exclusive interest. Crack propagation rates in-situ are likely to be different from those ex-reactor because of radiation creep relaxation. This could well be a beneficial result which may have a good effect on wall lifetimes. Crack propagation studies have advanced in recent years through improved measurement techniques. Such advanced modern techniques are capable of providing reliable and meaningful test data.

In summary the important tests for fusion materials in the wall/blanket are

i) fatigue
ii) creep
iii) biaxial stress loading
iv) crack propagation

all in-reactor, and post irradiation tests such as

iv) fracture toughness
v) tensile
vi) swelling
vii) residual stress
viii) Li corrosion

X-C. Materials Choice

A final commitment to a first choice of alloy in advance of testing would be a mistake. Rather the choice should be regarded as somewhat provisional and there is a real possibility that early in the testing program a backup alloy may be promoted to first choice if the early results are clearly superior (such was infact the case in the fast breeder program for 316 SS). The requirements of fabricability, availability and a pre-existent data base under irradiation dictate the current choice of austenitic stainless steel as the principal alloy.

A possible choice for a backup alloy is a Fe-Ni-Cr superalloy. This is because increased nickel contents decrease the void swelling and increase high temperature mechanical properties. The high concentration of nickel in both these alloy types however implies high production rates for helium.

If the helium problem turns out under testing to be severe or if swelling or embrittlement turn out to be catastrophic it will be necessary to turn to less conventional alloy systems. The refractory metals niobium, molybdenum and vanadium are possible basic metals which have the advantage of lower helium production rates. Several alloys based on these metals have been reported to have low or zero swelling in the broad temperature range of possible fusion conditions (~ 300-700°C).* These include V-Ti alloys[3] for example. The major disadvantages of these materials are the susceptibilities to small amounts of impurities, the absence of engineering experience in fabrication of large structures from them and the lack of a readily available, large-quantity, supply in the U.S.

A further possibility is the use of a titanium base alloy.[3] This material appears to resist swelling and there is considerable fabrication experience

*However, it is not certain that the lack of void nucleation will persist in the presence of high helium gas concentrations.

in the aircraft industry. Furthermore its availability is not in doubt. However there has as yet been little experience in radiation damage and the effect of helium is unknown.

It will be assumed here that a prudent testing program will include a wide range of these alloys in preliminary testing to assess possible replacement candidates for the principal and backup alloys.

X-D. Test Matrix Philosophy

The planning of a test matrix should capitalize on experience gained in the LMFBR alloy development program. The major difference for fusion is that the greater uncertainty involved for the fusion environment (e.g., neutron flux, spectrum, stress history, etc.) requires a rather broader approach.

Prime emphasis here is on the in-reactor instrumented fatigue, creep and biaxial tests, and a smaller number of crack propagation measurements, since these will take up most space. The material variables as usual involve a large part of the duplication. Experience has shown that heat to heat variations can often be important in the steels while for the more unusual materials, alloy compositions are not yet determined. In consequence we have selected for each material a duplication factor of three or four and a back-up material redundancy factor of two or three. For the chosen test therefore six to sixteen duplicates will be available for redundancy alloy variation and heat variations. Since welds will probably be a sensitive area both base and weld metal tests are projected. This total combination may be broken down in various ways depending on alloy type but it represents a reasonably generous test program overall.

The test variables themselves, stress and temperature require further duplication. The temperature for appropriate fusion materials testing is strongly dependent on the actual design chosen for the EPR. It is by no means clear that high coolant temperatures are mandatory for power requirements. So demanding are first wall conditions that low coolant temperatures may be acceptable if this proves useful in extending first wall life. A rather wide temperature range 200-500°C has therefore been chosen at 100°C intervals except for an additional 450°C test temperature in the crucial range. The stress requirements are also strongly machine dependent but we estimate that a wide enough range for fatigue testing will be covered in five tests with fewer still for creep and biaxial tests. A large number of tensile tests and fracture toughness will be conducted ex-reactor on irradiated samples. These obviously require much less room than the instrumented rigs. These specimens will require similar temperature ranges to the in-reactor tests. The increased number of samples will however allow for many more variations of test conditions than are possible in-reactor testing.

The environments appropriate to the testing program are vacuum (facing the plasma), helium and liquid lithium. However the danger of a leak into the plasma chambers shutting down the machine precludes much testing in the plasma vacuum. The bayonet fittings (see figure VI-D-1) and two test stations will be available for such exposure of samples to be post-irradiation tested to determine the effect of sputtering and other surface changes. For most tests on non-refractory metals it is felt that there should be no practical difference between commercial purity helium and vacuum environments, only one of these has therefore been chosen.

The effect of liquid lithium on metals during irradiation and stressing is clearly a basic part of the testing program and approximately one third of the test program is planned under this environment.

X-E. Test Matrix Details

X-E-1. Test Facilities

There are sixteen test stations in TETR each consisting of a $(1\ m)^2$ area facing the plasma (see chapter VI for a more detailed description). Each station is hinged so that it can be pulled back for test renewals and each is sealed by its own walls to provide a vacuum tight enclosure for the internal environment.* The planned use of the sixteen test stations is shown in table X-1.

Apart from the mechanical property tests stations (1-6, 13-16) there are two stations open to the plasma. One of these is intended to house first wall alloys (mainly the primary and backup alloys) as test plates for microscopic surface examination, fatigue and fracture toughness testing. Approximately five hundred plates could be irradiated in this way at one time. The second open test station will be used for testing curtain or ISSEC materials which may be used to even out temperature fluctuations, shift the neutron spectrum and protect the first wall from sputtering erosion. Carbon is the most important candidate and we assume one station will be needed to test the behavior of this material in the plasma environment.

The two further test stations (#'s 9 + 11) will be used to test coolant behavior. One will be used as a lithium corrosion cell mainly testing stainless steel for corrosion in varied dynamic and stagnant lithium

* Two test stations however will be open to the plasma to study plasma/material interactions.(#'s 7 and 16.)

Table X-1

TETR Test Station Usage

Station #	Material Tested	In Situ Study	Post Irradiation
1-6	Primary Alloy	Mech. Props.	Swelling & Mech. Props.
7	Primary Alloy	Surface Effects	Swelling & Mech. Props.
8	Carbon	Plasma Int.	Swelling & Mech. Props.
9	Steel-Li	Leakage	Corrosion
10		Dynamic Testing of Defected Blanket Designs	
11		Non-Li Coolants	
12		T_2 Breeder & n-multipliers	
13,14	Backup Alloy		
15,16	Refractory & Reactive Metals & Other Advanced Materials	Mech. Props.	Corrosion

environments. The main tests in these capsules is described in chapter 11. The other will be available for studying other coolants, including powders, liquids and gases.

Test station twelve is a neutron multiplier and tritium breeding test facility as shown in the table. No specific program has been developed for this station at the present time.

Station eleven is reserved as a testing site for engineering design of in-situ repair facilities. The exact details of this cell were not available at the time of this printing but the ability to detect and repair leaks by remote control equipment in the radioactive environment will be critical in controlling the economics of reactors.

X-E-2. Test Volume Requirements

Within the 1 m x 1 m area facing the plasma the tests are arranged in rows of test modules. Each module is a box 10 cm x 10 cm x 10 cm (fig. VI-B-4) and may contain one or more tests. From the individual test designs discussed later, the number of tests per module are as shown in table X-2.

Table X-2

Number of Tests Per Module

Test Type	# Per Module	
Creep	5	
Fatigue	3	
Biaxial		
10% with instrumented pressure line	2	mean 4.7
90% without instrumented pressure line	5	
Crack Propagation		
Fully instrumented - in-situ tests	1	
Ex Reactor Tests		
Specimen irradiation only	5	

Averaging the estimated volume of test material, supports, etc. over the various tests gave a solid volume of 58% of the total volume. We have assumed that the mechanical test volume will be divided between the four major mechanical tests approximately:

creep	1/3
fatigue	1/3
biaxial	1/6
crack propagation and ex reactor testing	1/6

This division of the volume and the number of different tests per module (table X-2) gives total test numbers (per year) as shown in table X-3.

X-E-3. Data Extrapolation and Optimization

The basic dose for testing will be one year at the 1 MW/m^2 wall loading of the reactor. Once the test stations are in place it will be very undesirable to require access to them in shorter times since removal will involve shutdown and remote handling. Some specimens can of course be left in place for further exposures. The entire mechanical property test program therefore over the five years' of testing before design data is required for the EPR, assuming a one year dose is sufficient will be:

Creep Tests	6000
Fatigue Tests	6000
Biaxial Tests	2435
Crack Propagation	125
Ex Reactor Tests	12840

The annual dose in stainless steel appropriate to these conditions is 11 dpa. For most design considerations this is sufficient. However a few longer term tests running for the full five years to measure creep, swelling

Table X-3

Use Of Mechanical Property Test Stations

Alloy	# of Test Stations	# In He	# In Li	# of Modules	# of Creep Modules	# of Creep Tests	# of Fatigue Modules	# of Fatigue Tests	# of Biaxial Modules	# of Biaxial Tests	# of Crack Propgn. Modules	# of Crack Propgn. Tests	# of Ex Reactor Test Modules	# Ex Reactor Test Specimens
Primary	6	4	2	600	144	720	240	720	62	291*	15	15+	139	1112
Backup	2	$1\frac{2}{3}$	$\frac{1}{3}$	200	48	240	80	240	21	98*	5	5+	91	728
Refractory Metals & Adv. Matls.	2	$1\frac{1}{3}$	$\frac{2}{3}$	200	48	240	80	240	21	98*	5	5+	91	728
	---	---	---	---	---	---	---	---	---	---	---	---	---	---
Totals	10	11	5	1000	304	1200	400	1200	104	487	25	25	321	2568

*10% of these tests with instrumented pressure lines for leak testing.

+These tests instrumented for crack opening measurements in-situ.

Total of simultaneously irradiated mech. props specimens = 5480

Total in-situ simultaneous tests = 2912

and fatigue limits will be desirable to confirm that linear extrapolation from the 11 dpa dose is reasonable.

One of the principal variables of CTR design is the first wall and blanket temperature range. Past experience in power production has shown that materials problems in turbines and associated plant make it undesirable to go to temperatures greater than ~600°C in spite of increased efficiency. In fusion reactors the loss of efficiency may be more than compensated for by longer wall life and having a higher plant factor. Given this uncertainty we have chosen a wide temperature range of 200-500°C for testing with five temperatures being chosen in this range. Finally, since stress varies widely depending on design (as well as swelling) five stress values have also been chosen for creep and fatigue testing.

X-E-4. The Test Matrix For Environmental Variables

The test matrix obtained from the considerations of the last two sections is shown in table X-4. The totals conform to the previous tables and can be obtained by multiplying the factors in the horizontal rows. Fractional values are explained in the footnotes.

The redundancy and alloy variations combined give a factor of 5-10, a redundancy of 2 has been used throughout to test reproductibility and to allow for failures. For ex reactor testing there are no variations of stress since the specimens will not be stressed in reactor. The redundancy factor in these cases allows for wide variations in test conditions ex reactor.

X-F. Individual Test Facilities

X-F-1. Creep Tests

It is not the purpose of this section to describe all of the test modules down to the 'last nut and bolt'. Rather we will briefly describe

Table X-4

Test Matrix At The Base Fluence of 1 MW-Yr/m^2

Material & Test		Environment	Base Metal + Weld	Alloy Variation and Heats	Stress Ranges	Temp. Ranges	Redundancy	Totals
Primary Alloy	creep	1.5(a)	2	4.8(c)	5	5	2	720
	fatigue	1.5	2	4.8	5	5	2	720
	biaxial	1.5	2	4.85	2	5	2	291
	cracking	1.5	2	1	2.5	2	1	15
	ex reactor	1.5	2	5	1	5	14(g)	1112
Backup Alloy	creep	1.2(d)	2	$3\frac{1}{8}$(f)	4	4	2	240
	fatigue	1.2	2	$3\frac{1}{8}$(f)	4	4	2	240
	biaxial	1.2	2	3.4	2	3	2	98
	cracking	1.2	2	3.4	2	3		5
	ex reactor	1.2	2	$3\frac{1}{8}$	1	5	19.4(g)	728
Refractories Metals & Advanced Materials	creep	1.5(a)	2	2.5	4	4	2	240
	fatigue	1.5	2	2.5	4	4	2	240
	biaxial	1.5	2	2.72	2	3	2	93
	cracking	1.5	2	2.72	2	3	2	5
	ex reactor	1.5	2	2.5	1	5	19.4(g)	728

a) Helium and liquid lithium, with twice as many in He.

b) 500°C, 450°C, 400°C, 300°C, 200°C.

c) For example 5 variants tested in ratio 5:5:5:5:4. (giving 4.80 average)

d) Tests' ratio 5 in He to 1 in Li.

e) Tests' ratio 2 in He to 1 in Li.

f) Tests' ratio for 4 alloy variants 3.5:3:3:3.

g) This redundancy allows for different tests; tensile, fracture toughness, etc.

Total number of simultaneous tests 2912

The total for each horizontal line is obtained by multiplying all the factors in the line.

a few of the ideas that could be used to test small specimens in the hostile irradiation environment of TETR. There will undoubtedly be more ideas in the future and we full expect that the ultimate test modules could be drastically different from those proposed here.

The problems involved in applying varying stresses to 100 test modules in a 1 m^2 area are severe if the loads are to be applied externally by a hydraulic system. The requirement of constant stress over a large stroke or specimen strain can however be satisfied by spring mechanisms. Since the force applied by a compressed spring depends on the elastic properties and these are little affected by irradiation, the force will remain constant during the dose.

Conical or 'Belleville' washers are particularly suitable for applying creep loads because by combining them rather large creep strains can be accomodated without difficulty.[4] A typical creep rig is shown in figure X-1. Four spring washers are compressed to produce the tensile load on the specimen. The compression is achieved by screwing down the upper compression ring. The center cylinder which carries the screw thread for the compression ring is attached to the base only through the specimen. However it is prevented from rotating by two or more spigots on the base which permit it to move up and down only. The compression ring is marked and the whole system precalibrated using a load cell. Alternatively the washers can be precompressed on a hydraulic press and the compression ring then tightened up. In any event actual calibrations of creep measurements at temperature on well studied materials would be necessary to insure complete calibration. The specimen temperature will be maintained by flow of coolant (helium of lithium) around it, through the holes in the cylinder.

Fig. X-1

BELLEVILLE SPRING WASHER CREEP RIG

MATERIAL: Ti ALLOY

SCALE:
APPROX. 2 X FULL SIZE

OVERALL HEIGHT 2'-4"
O.D. 1 1/8"

LOADING NOTE-
LOAD APPLIED BY SEPARATE TOOL TO SPRING WASHERS AND UPPER COMPRESSION RING SCREWED DOWN INTO PLACE. THE LOAD IS THEN RELEASED & TAKEN UP BY RING PUTTING SPECIMEN IN TENSION

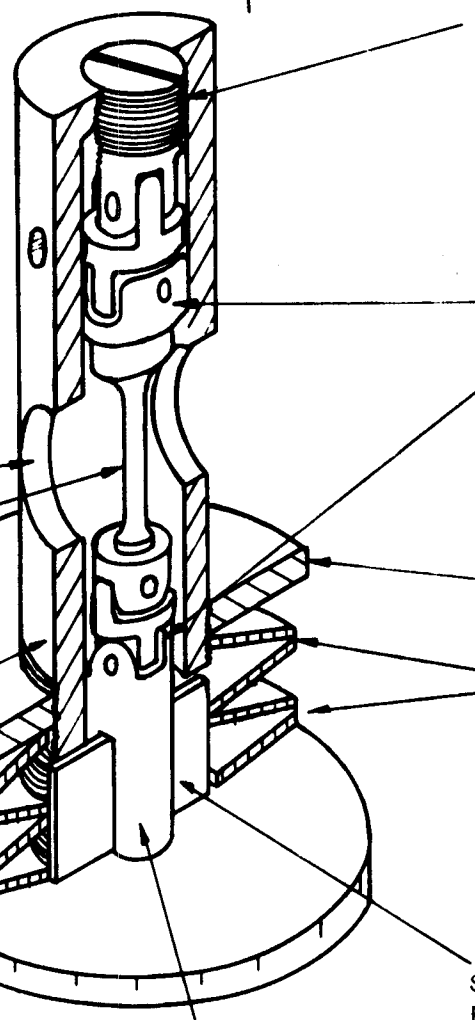

UPWARD FORCE FROM WASHERS

SCREW TO ADJUST LENGTH OF OUTER CYLINDER TO WASHER SPRING GAUGE MUST BE SET BEFORE APPLYING LOAD

SHACKLES TO INSURE AXIAL SPECIMEN LOADING

COOLANT GAS HOLES & EXITS FOR STRAIN LEADS

SPECIMEN ~ 1/16" dia. 3/8" GAUGE LENGTH

UPPER COMPRESSION RING

FOUR BELLEVILLE WASHERS, 1-1" O.D. 0.49" I.D. MAX LOAD VARIES

OUTER SLEEVE FREE TO SLIDE UP AND DOWN ON PEDESTAL SHAFT & SPIGOTS

SPIGOT INTEGRAL WITH BASE PEDESTAL TO INSURE NO TWIST ON SPECIMEN WHEN APPLYING LOAD NOTE - SLOTS IN OUTER CYLINDER LOCATE ON THESE TO MAINTAIN AXIAL CENTERING AS OUTER SLEEVE SLIDES ON PEDESTAL SHAFT

BASE PEDESTAL WITH COMPRESSION REF MARKS

PEDESTAL SHAFT

The only leads required for the measurement of creep data are therefore those from a strain cell and thermocouple. For measuring strain, the devices developed for in-reactor testing in the LMFBR program would be used for helium atmospheres. For the liquid metal environment however encapsulation of strain gauges in electrical insulating groups will be required and techniques for this will have to be developed.

The extremely compact nature of this device permits close packing of the creep tests (fig. X-2) giving five tests in each $(10\ cm)^2$ module in the wall.

X-F-2. Biaxial Creep Testing

The biaxial creep test using pressurized tubes has been fully developed for the breeder materials program [5] and no further design is attempted here.

It is assumed that tubes can be packed in a similar way to the creep tests described above giving five specimens per module. Temperature control will once again be affected by coolant temperature control and once again we note that the measurement of strain in a liquid lithium environment will require encapsulation.

In a few cases it may be desirable to test tubes under a maintained pressure up to failure, to determine failure modes. In particular it will be important to know whether catastrophic shear occurs at once or whether a slow leak develops first. Materials which fail in the latter mode are clearly desirable since it may be possible in a reactor to shut off a few individual coolant tubes which develop leaks without closing the machine down. A few tests of this kind would no doubt be included in a program such as this.

Fig. X-2

STACKING OF CREEP TESTS RINGS

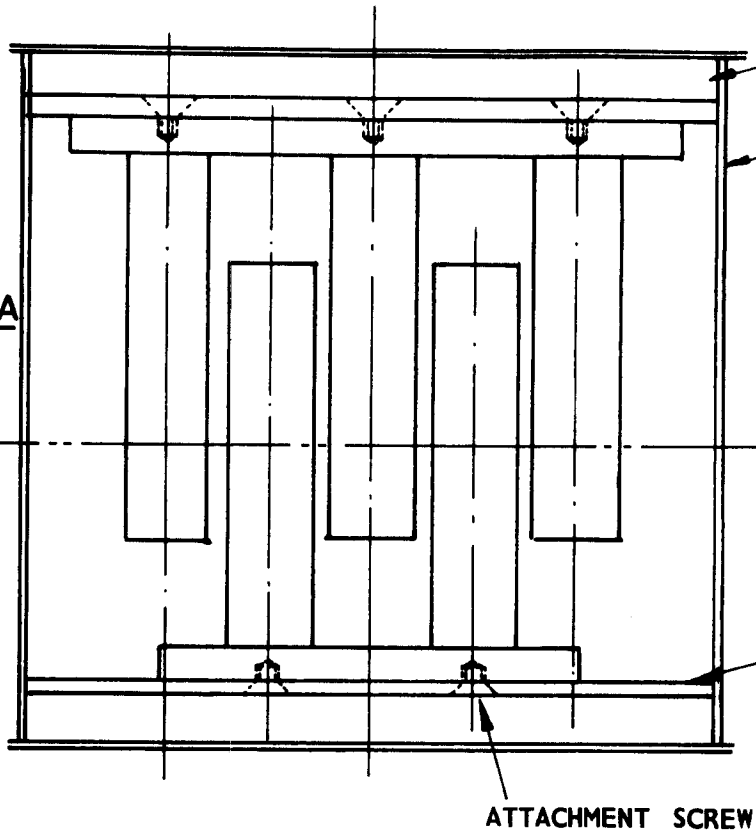

VIEW FACING PLASMA

5 TESTS EXPOSED ON FIRST ROW

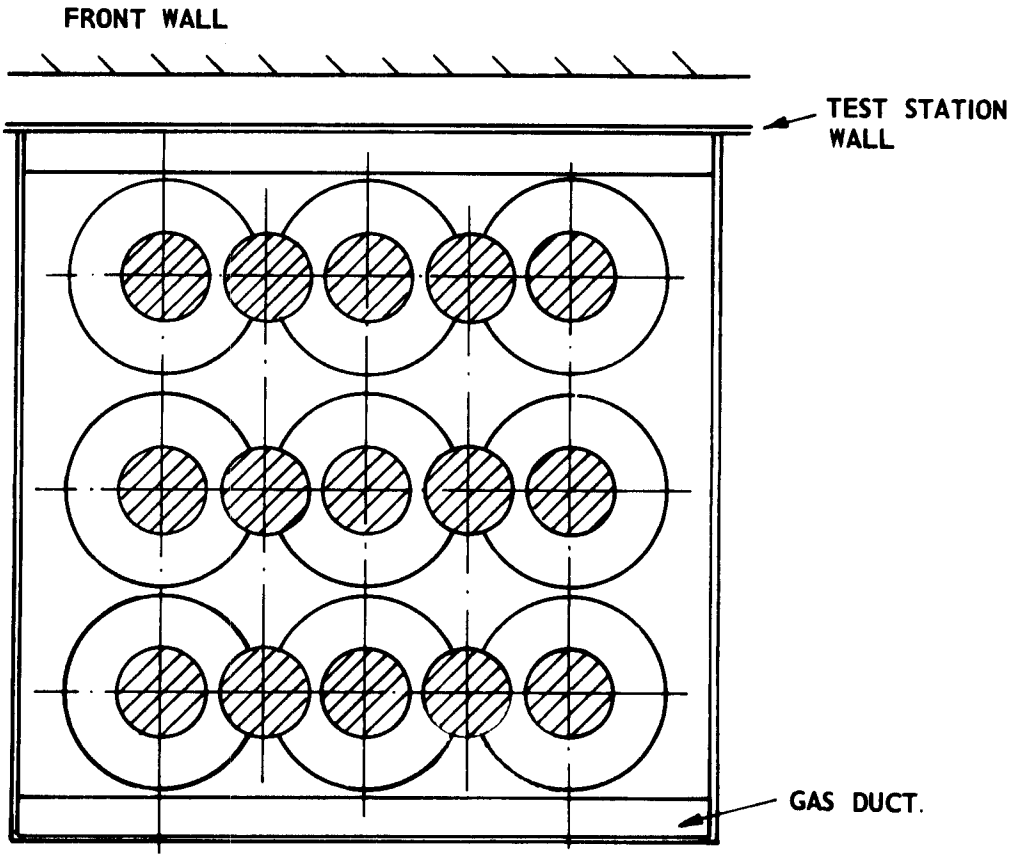

SECTION AA

15 CREEP RINGS IN c/s. IN 3 ROWS NO INTERNAL DETAILS SHOWN.

However, since all that is required is a hydraulic loading system to a closed tube no difficulty is envisaged in adding these to the sealed tube experiments described in this section.

X-F-3. Fatigue Tests

The continual thermal cycling involved in the running of a fusion power reactor makes good fatigue properties a prime requirement for first wall materials. However, fatigue tests on this scale have never been attempted in reactor.

Ideally one should be able to apply any stress cycle about any mean stress level and on any time scale. There are several possibilities for methods of stressing.

a) Wöhler type, rotating specimen with an applied weight. The difficulty would be to mount motors and shafts in the test environment. Also the stress conditions are complicated.

b) Sheet specimen stressed back and forth electromagnetically. Frequency here is specimen dependent but the main difficulty is finding a mechanism which will work in the field of the plasma control magnets. If these vary slowly relative to the frequency of specimen stressing this may not be a problem. This method has the great advantage of not requiring pressurized leads to each specimen. Furthermore the simplicity of such a system for testing sheet materials is very attractive given the severe environment. Finally testing in a liquid lithium environment would once again require encapsulation of strain measurement devices. However this may be irrelevant since the liquid metal will probably prevent the magnetic device from applying sufficient stress in any case. When the method can be used (in the helium environment) we estimate that three magnetic drivers and specimens can be accomodated in one $(10\ cm)^3$ module facing the plasma.

c) Hydraulic (bellows) force application in tension or bending. This is in principle the best method since the stress cycle is controllable. For example an oscillation of stress about some mean positive value can be arranged by balancing the bellows force against spring loading. However, the requirement of an external pressure line for each test limits the number of tests and also makes them bulky since to avoid bellows failure they will have to be much larger than the specimen. In spite of this, testing under liquid lithium will require this method of stress application.

The simplest form of this test is the tubular specimen connected to a gas pressure line to apply the load. Since this closely simulates the situation for first wall materials it is to be preferred over bending or tensile systems in spite of the biaxial loading. In addition the same test then permits the monitoring of leakage of gas (and hence crack development) during the test. This method also has the possibility of monitoring volume changes (i.e., strain) externally, without electrical leads and encapsulated strain sensors.

X-F-4. Crack Propagation Tests

Most crack propagation and fracture toughness testing will be done on pre-irradiated samples because the effect of irradiation creep in relaxing stresses at crack tips will probably reduce crack propagation rates in-reactor. The worst case will then be when the irradiation ceases and stresses remain. The testing of pre-irradiated samples outside the reactor simulates this situation accurately and is in fact the most severe case.

From a design point of view however it is important to know whether this idea is in fact justified and a small number of crack opening displacement tests would be desirable. Such tests should simulate the thin wall geometry

of a reactor to insure that stress intensity factors measured are indeed appropriate. Various stress modes would be desirable but all will require pre-cracked specimens in which the cracks are propagating at a slow, known rate.

The tests are then similar to creep tests with the crack opening displacement devices replacing the overall strain gauges. The instrumentation of a device of this type under liquid lithium is currently an unsolved problem which calls for development.

We assume that these tests will take up similar space to the creep tests for the tensile case and to the fatigue tests for the bending case. For the tubular case the specimen will be identical to the biaxial tests except for being precracked, with crack opening instrumentation on the crack.

X-F-5. Specimens For Post Irradiation Study

There is considerable space in the modules designated for irradiation only, because of the absence of stress requirements and instrumentation. Only temperature measurement and control facilities are needed. In both He and liquid lithium we estimate that eight flat specimens could be easily accomodated placed edgewise to the plasma. If smaller samples were used larger numbers would be available.

As usual in irradiation programs, all the specimens discussed above, after testing is complete, can be used for microscopic examination. Unstressed regions of the specimens can be used as reference datum points to establish stress-free swelling and microstructures. The stressed and fractured regions can be compared with these.

In addition there is ample space around specimen areas for large numbers of TEM samples so that microstructural information can be gained

on a wider variety of alloy variations than can be covered by mechanical testing.

X-F-6. Temperature Control

See chapter VIII.

X-F-7. Instrumentation

A) Temperature

The use of thermocouples in a reactor environment is well established and this experience can be applied to tests in TETR. The additional features of higher transmutation and helium production rates will require that thermocouples be calibrated both before and after irradiation. Readings can then be back corrected to allow for induced changes in thermo-power. Further work is also required on the influence of the strong and varying magnetic fields on thermocouple behavior.

B) Strain

Similar remarks apply to strain gauges as to thermocouples. The difficulty of using such devices under liquid lithium has already been referred to and methods of encapsulation clearly require more study.

C) Stress

Stress can be monitored externally when it is applied hydraulically. It is determined before installation in reactor for the spring loading case.

X-F-8. Shield and Leakage Containment

Each test station is contained in its own wall so that leakage in one does not affect others. Since rows of specimens loaded hydraulically share a single header tube, a leak in one will of necessity affect the others in its row. There is an optimum between individual pressure pipes to each test specimen which produces impossible pipe configurations, and putting

large numbers of specimens on a single header pipe. Such an optimum will evolve when more detailed analysis of the test cells has been performed.

X-F-9. Test Access Requirements

We have assumed that each test station stays in place for one year so that an annual removal will be all that is necessary as a routine. Any specimens failing in less time than this will stay in place (with pressure lines disconnected for hydraulic tests).

X-G. Summary

We have shown in this chapter that there is ample testing space in TETR to provide solid experimental data from which to design the DPR in the early 1990's. More specifically, the current design of TETR provides more than 16 m^2 of high flux test area directly facing the plasma. These test stations also provide approximately 2 m^3 of high flux test volume which can be instrumented and closely controlled with respect to temperature, environment, and stress. The specific test matrix for primary DPR and backup DPR alloys reveals that more than 3000 in situ mechanical property tests can be conducted simultaneously. In addition, at least 2000 additional post irradiation samples can be irradiated at the same time. Finally, it is important to emphasize that the specimens in TETR are being tested in the "proper" radiation environment with the characteristic transmutation, damage, and microstructural cascade features. In contrast to all other currently proposed test facilities, no "simulation" is involved with the TETR test program.

References for Chapter X

1.) Proc. Int. Conf. Radiation Test Facilities for the CTR Surface and Materials Program - ANL/CTR-75-4, July 1975.

2.) H. I. Avci, et al., to be published. See also UWFDM's 115, 127, 128, 135, 205 and 208.

3.) J. W. Davis and G. L. Kulcinski, "Assessment of Titanium For Use in the 1st Wall/Blanket Structure of Fusion Power Reactors", EPRI ER-386, April 1977.

4.) G. L. Kulcinski, BNWL-613, May, 1968.

5.) A. J. Lovell and R. W. Barker, "Irradiation Effects on Structural Alloys for Nuclear Reactor Applications", ASTM-STP-484, p. 471, 1970.

XI. Engineering Test Modules for Liquid Breeders and Heat Transfer Fluids

XI-A. Introduction

The central function of TETR is that of a materials testing facility incorporating experimentation applicable to future fusion reactor designs. In this chapter, we will describe modular tests involving structural and heat transfer materials of interest in CTR design. Our experimental focus is limited to a few important materials, but the experimental design and the methods employed therein will be applicable to many materials. We will examine liquids and solids which function as coolants and as breeding materials.

The operation of a fusion power reactor is dependent on a readily available supply of tritium. As tritium is present in nature only at very low levels it is necessary to breed tritium for fueling. Lithium compounds are useful for this purpose owing to the $^{6}Li(n,\alpha)T$ and $^{7}Li(n,n'\alpha)T$ reactions. The thermal neutron cross section of ^{6}Li (950 barns) is much greater than that of ^{7}Li (.036 barns), while the natural abundance of ^{6}Li (7.42%) is smaller than that of ^{7}Li (92.58%). In practice, the optimum $^{6}Li/^{7}Li$ mole ratio is that which gives breeding ratios of just over 1.0 (1;13 therein). In general, lithium species are required in CTR designs because of the necessity of breeding tritium.

Lithium species to be considerd may be divided into four classes: the pure metal, salts, intermetallic compounds and oxide-bearing ceramics. In practice, only lithium metal and its salts are low-melting enough to be used as liquids in a stainless steel structure. All of the ceramics and intermetallic compounds of lithium and aluminum, bismuth, silicon, tin and lead are high-melting (> 600°C) and are used as solids[2]. Liquid breeding materials have the advantage of doubling as heat transfer agents.

Their primary disadvantage is the resulting corrosive action on materials of containment. Solid breeding materials are generally immobile and do not corrode containment materials. However, at high temperatures, sintering and phase changes due to lithium depletion are troublesome. Because solid and liquid breeding materials embody different problems with respect to their use, modular experimentation will be divided into two areas. In module I, we will investigate the interaction of liquid lithium with various structural materials in a radiation environment. In module II, we will investigate the diffusion of tritium produced in solid lithium compounds. Table XI-A-1 lists some solid breeding materials of current interest and properties related to use in CTR's[7]. We will examine lithium metal in section XI-B.

XI-B. Module I: Liquid Lithium

XI-B-1. Review of Lithium Corrosion Studies

The properties of lithium metal which make it attractive in CTR design have been reviewed elsewhere[1]. In looking at the literature on liquid lithium corrosion, several facts stand out. In the first place, recent studies have shown that lithium corrosion rates are more sensitive to experimental parameter than had been appreciated by previous investigators. Secondly, corrosion mechanisms presently proposed suffer a lack of predictive value due in part to inconsistencies in the solubility data for metals in liquid lithium. Finally, the term 'solubility' in lithium solubility studies is used loosely to describe only the weight of material which is removed from a solid sample in lithium at a given temperature. It may also refer to the gross concentration of an element in lithium regardless of the chemical composition of the species containing the element of interest. The solubility values reported not only express the levels of solvated

Table XI-A-1. Characteristics of Solid Lithium Compounds for Tritium Breeding (7)

LITHIUM ALLOY OR COMPOUND	M.P. ^{0}C	TRITIUM RETENTIVITY AT OPERATING CONDITIONS	NEUTRON MULTIPLIER NEEDED FOR BR > 1	LOW RESIDUAL RADIOACTIVITY	REACTS WITH AIR	SINTERING PROBLEMS	CHEMICALLY STABLE	RESOURCE LIMITATIONS
$LiAl$ (5)	718	VERY LOW	YES	YES	SLOWLY	MAYBE	YES	NO
$LiAlO_2$ (6)	1900-2000	VERY LOW	YES	YES	NO	PROBABLY NOT	YES	NO
Li_2SiO_3 (6)	1204	VERY LOW	YES	YES	NO	PROBABLY NOT	YES	NO
$Li_2Be_2O_3$ (7)	1150	UNKNOWN	NO	YES	NO	UNKNOWN	YES	Be(?)
Li_7Pb_2 (5,8)	726	VERY LOW	NO	YES	SLOWLY	UNKNOWN	YES	NO
Li_3Bi (5)	1145	UNKNOWN	NO	SOME Po^{210}	PROBABLY SLOWLY	UNKNOWN	YES	Bi
Li_4Si (8)	635	UNKNOWN	NO	YES	PROBABLY SLOWLY	UNKNOWN	PROBABLY	NO
Li_3N (9)	~800	UNKNOWN	NO	YES	PROBABLY SLOWLY	UNKNOWN	PROBABLY REQUIRES N_2 GAS	NO
Li_4Sn (5)	765	UNKNOWN	NO	NO	PROBABLY SLOWLY	UNKNOWN	PROBABLY	NO
$Li_2B_4O_7$ (6)	930	UNKNOWN	YES	YES	PROBABLY NOT	UNKNOWN	YES	REQUIRES SEPARATED B^{11}

solute species but also include the levels of oxides, nitrides, and carbides and other compounds of the solute both dissolved and suspended in lithium. The term 'solubility' is used imprecisely, thus confusing the interpretation of the data reported.

Interest in the corrosive properties of liquid lithium began when investigators became interested in materials suitable for use in the synthesis of lithium compounds. Efforts were directed towards the study of corrosion by liquid lithium in both static and convective experiments. The effect of temperature, temperature gradients, flow rates, impurity levels, concentration gradients and other conditions were studied at this time. Important features of the mechanism of lithium corrosion first recognized were[3]:

(1) The effect of a temperature gradient on the transport of metals in lithium, and

(2) The role of carbide formation on the rate of corrosion of low-alloy steels.

Additionally, radiation did not appear to affect the corrosion of iron. The types of liquid lithium attack observed and reported include (quoting ref. 4)

I. Pure Metals

1. Solution of the solid metal with the liquid metal

a. Uniform simple solution

b. Intergranular solution or penetration of the liquid metal grain boundaries because of surface tension phenomena

c. Development of crystalline facets caused by different solubility rates in various crystal directions.

2. Diffusion of liquid metal atoms uniformly or intergranularly into the solid metal lattice which may or may not result in a phase transformation.

3. Formation of an intermetallic layer on the solid metal surface.

4. Mass transfer of three types:

   a. Isothermal mass transfer caused by concentration gradients.

   b. Thermal gradient mass transfer.

   c. Mass transfer by energy gradient; that is, a reorientation of the contour to one of lower energy state.

II Alloys

5. Leaching of one or more alloy constituents from the surface of the alloy because of selective solution which can result in phase transformation and/or subsurface voids within the grains or along grain boundaries.

6. Subsurface precipitation of an intermetallic compound as the result of inward diffusion of liquid metal atoms and interaction with alloy components.

III Impurities

7. Impurities forming simple or complex substances on the metal surface or beneath it which can stimulate or supress interaction. Examples are formation of oxides and nitrides.

Liquid metal corrosion rates were found to be sensitive to many variables, all of which can be difficult to control over a series of experiments. Some of these variables are[3]

(1) temperature and temperature gradients
(2) cyclic temperature fluctuations
(3) surface area-to-volume ratio
(4) purity of liquid metal
(5) flow velocity
(6) surface and internal conditions of container material
(7) number of materials in contact with the liquid metal

Efforts have been made to alter the corrosion rates of a material by the use of layers of corrosion resistant materials and by alloying with tungsten and niobium, which were found to be very corrosion-resistant. Carbon, nitrogen and oxygen were identified as impurities whose concentrations in the metal greatly affected corrosion rates. This phenomenon occurs when the oxide, carbide, or nitride of the metal under study is less stable than the corresponding lithium compound. The lithium compound forms in the metal, wedges the metal grains apart and allows further penetration of liquid lithium into the metal interior.

The main thrust of recent work has been to understand underlying mechanisms of corrosion by lithium. The results of this work, mainly on steels, have clarified the role of impurities in corrosion. Among the conclusions reached are:

(1) Carbon, nitrogen and oxygen in the structural material accelerate corrosion by lithium (3, ref 60, 67, 81)
(2) A stressed material corrodes more quickly than an unstressed material (3, ref 68, 69, 78)
(3) High carbon steels are subject to cracking due to the formation of the lower density Li_2C_2. (3, ref 58, 59, 64)
(4) Stainless steels are depleted in chromium due to the formation of $Cr_{23}C_6$ and nickel is dissolved. (3, ref 65, 76)

(5) Flowing lithium is slightly more corrosive than static lithium; the resultant corrosion reduces the mechanical properties of the material (3, ref 63, 66, 67, 68)

(6) Corrosion resistance in steels is increased by low carbon content or by alloying with chromium. In stainless steels, alloying with molybdenum or aluminum increases corrosion resistance (3, ref 65, 73, 75, 76)

For reactor designs that run at higher temperatures with more efficient thermal cycles, the scope of lithium corrosion study has broadened to include refractory metals and their alloys. Austenitic stainless steels are, for all practical purposes, limited to about 500°C in contact with liquid lithium[3]. The elements of groups IVB, VB, VIB, and VIIB are of interest in reactor designs as structural materials and fortunately show good corrosion resistance.

The group IVB elements, titanium, zirconium and hafnium show good corrosion resistance up to 1000°C. The oxides, nitrides and carbides of these elements are more stable than the corresponding lithium compounds, contributing to the corrosion resistance of these metals in the presence of high nitrogen, oxygen and carbon levels. This property makes these metals useful as getters for these elements.

Since niobium and tantalum are more easily fabricable than the group IVB metals, lithium corrosion studies of these metals are more widely performed. Group VB metals form less stable oxides than lithium oxide, but the metal carbides and nitrides are more stable than the corresponding lithium compounds. With an oxygen getter, these metals are found to be very corrosion resistant.

Group VI-B metals show good corrosion resistance at high temperatures (> 1000°C) and for extended periods of time (> 1000 hrs.). While not as

extensively investigated as the VB metals, the same general corrosion behavior is exhibited. Chromium, molybdenum and tungsten alloyed with a metal which is an oxygen getter show an increased corrosion resistance.

Of the group VIIB metals, only rhenium has been studied for its lithium corrosion resistance. While its corrosion resistance is high, it is too expensive to be used except as an alloying agent[1]. An alloy of rhenium with molybdenum or tungsten shows improved corrosion resistance over that of pure rhenium. The solubility of the alloy constituents in lithium is an indication of the probable extent of corrosion. Solubility studies suffer from the same irregularities as do corrosion studies. Lack of controlled lithium impurity levels confuse the data on the solubility of the refractory metals. Because of the stability of the refractory metal nitrides, a high nitrogen level in lithium will increase the solubility of the metal. The most reliable solubility data specify the nitrogen levels of the test. Figure XI-B-1 summarizes solubility data on several metals of interest in CTR design (4, see also ref. 1). As with corrosion rates, there is wide scatter in the data. Reliability may be judged by the control exerted over the lithium impurity levels. Solubilities of tungsten, rhenium and hafnium have been carefully determined and are given in table XI-B-1 (1, ref 100), but solubility data on other metals are not widely available or reliable.

Table XI-B-1

Solubility of W, Re, Hf in liquid Li

Solute	Temperature (°C)	Solubility (atom %)
W	1200 - 1600	3×10^{-4}
Re	1200 - 1600	$.2 - 6 \times 10^{-4}$
Hf	1200 - 1400	6×10^{-4}

The solubility of these metals is of the same order of magnitude as niobium.

FIGURE XI - B - I

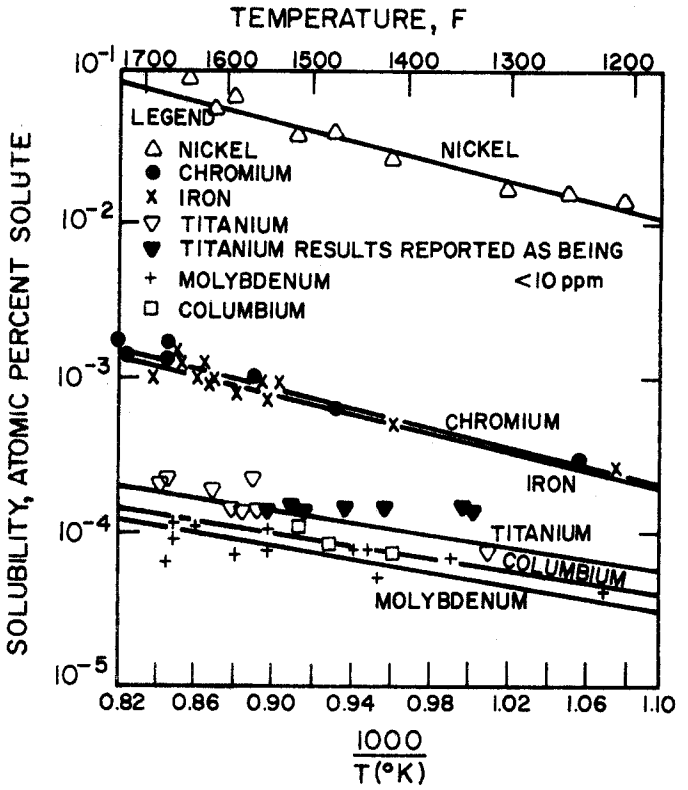

SOLUBILITY OF SOME METALS IN LITHIUM.
NITROGEN CONTAMINATION 25 TO 150 ppm.

Corrosion resistance generally increases as the solubility of the material in lithium decreases. Alloys of low solubility materials show good corrosion resistance and the addition of a less soluble material to one which is subject to corrosion will tend to increase its resistance. These trends are demonstrated by the data given in Table XI-B-2. The table shows that there are some alloys with very good resistance to corrosion by lithium at high temperatures for periods of time over a year. Experimental parameters of interest are also recorded with the results.

The primary function of module I is to examine the interaction of radiation damage and corrosion damage. It has been asserted that the damage caused by high energy particles in the structural material should enhance the corrosive effects of liquid lithium in spite of the fact that some of the proposed corrosion mechanisms contradict this assertion[8,11].

Sisman and Parkinson[9] observed no enhancement of corrosion effects due to the presence of radiation. These experiments involved the irradiation of liquid lithium and sodium in type 316 and Inconel steels. In the lithium loop at 1000°C, the total thermal neutron dose was 7×10^{16} neutrons/cm^2 with 3×10^{16} having energies > 0.5 MeV. An isothermal condition was maintained with a combination of resistance heating, insulation and water cooling. Since then, few experiments of this nature have been reported for lithium in the open literature. This may be due to the intricacy of the experimental apparatus, the lack of access to a radiation source significantly different than Parkinson's, or the difficulty of handling liquid metals. Any or all of these factors pose problems for the investigator. While much effort has been given to the study of lithium corrosion, comparatively little has been done on the subject of long-term

Table XI-B-2

Lithium Corrosion Data

Sample	Temperature °C	Other Conditions	Results	Reference*
Fe	816	108-138 hr, forced convection	2.0-4.5 mil decrease in wall thickness no penetration	(4; 196)
Ti	1000	400 hr, capsule	slight attack	(1; 104)
Zr	1000	400 hr, capsule	nil attack	(1; 104)
V	817	1194 hr, convection	nil attack	(1; 103)
Nb	816°-1093	8233 hr, convection	nil attack	(1; 106)
Ta	816-982	100 hr, convection	nil attack	(1; 106)
Cr	816	100 hr, capsule	1 mil dissolution	(1; 59)
Mo	1370	1000 hr, capsule	little attack	(1; 105)
W	1370	1000 hr, capsule	no attack	(1; 105)
Re	1370	1000 hr, capsule	no attack	(1;105)
Nr-1Zr	1150	6000 hr, capsule	slight attack	(1; 107)
Nb-10W-1Zr-.1C	1205	9437 hr, capsule	no corrosion	(1; 107)
Mo-.5Ti	816	694 hr, convection	nil attack	(1; 106)
95 Ni-4.5 Mn	816	100 hr, static	2 mil depth of attack, mass transfer occurs	(4; 197)
94 Ni-4.5 Al	816	100 hr, static	complete intergranular penetration of 55 mil wall	(4; 197)
Nichrome (80 Ni-20 Cr)	816	100 hr, static	1 mil intergranular attack, .2 mil of crystals attached to surface	(4; 197)

Sample	Temperature °C	Other Conditions	Results	Reference*
80 W-14 Cr-6 Fe	816	100 hr, static	1 mil intergranular attack, .5 ml of crystals	(4; 197)
65 Ni-14 Cr-10 Fe-6 Mo	816	100 hr, static	attacked to depth of .25 mil	(4; 197)
310 Stainless Steel	649	100 hr,	4 mil penetration	(4; 195)
316 Stainless Steel	816	52-155 hrs,	1-4.5 mil intergranular attack & 3.9-8.5 mil decrease in wall thickness	(4; 196)

*(reference in this work; reference therein)

radiation-enhanced corrosion. This is surprising since all of the liquid lithium work points to CTR applications. Nevertheless, with what is already known about lithium corrosion for a foundation, it should be possible to determine the degree of interaction between radiation and corrosion damage.

XI-B-2. Proposal for the Study of Lithium Corrosion

The operational lifetime of fusion power reactors will be limited by the amount of damage which may be sustained by the structural materials. It is with this in mind that we propose to investigate the effects of high energy radiation on the corrosive action of liquid lithium. A series of experiments in this area will yield useful information and experience on a number of fronts. These advances in expertise could include:

(1) A definitive look at corrosion rates, being fully aware of the need for rigid control over experimental parameters such as impurity levels, temperature and flow rates.

(2) Experience in handling liquid metals as part of a working subunit (on a reduced scale in the module) of a fusion reactor.

(3) Opportunity to test instrumentation for monitoring the behavior of a lithium-bearing structure in a reactor environment.

The radiation environment of the TETR will be more energetic than those used in previous lithium loop tests. The mean neutron energy in Parkinson's study[9] was approximately 0.5MeV. In the TETR environment, the mean neutron energy will be about 2.0 MeV in the lithium test module, therefore the damage rates in the material of containment will be higher. It will be seen in Section XI-B-3-b, that any significant disruption of the microstructure of a material is likely to affect the penetration of lithium into that material and, therefore, affect the corrosion rate.

XI-B-3. Structural Materials for a Liquid Lithium Test Module

XI-B-3-a. Modular Design

The amount of space alloted for a liquid lithium module within the shield surrounding the reactor is a 1m x 1m square facing the plasma with a depth of about 10 cm between the shield and the water-cooled first wall. Obviously, there will not be space in this area for the required experimental instrumentation. The in-reactor portion of the module will contain the stainless steel test tubing with a thermocouple to monitor the in-reactor temperature. This tubing will be surrounded by pressurized flowing helium to help control the in-reactor temperature. The test tubing will be welded to piping containing the lithium flowing into and out of the reactor. This piping will run alongside the swing-away shield and out of the reactor. With part of the module in the reactor and part out, the design of the module must take several features into consideration:

(1) Lithium bearing piping must be of sufficient thickness to minimize tritium permeation.

(2) Adequate shielding of the piping must be provided to protect personnel from any radiation hazard due to the accumulation of tritium and activation products in the lithium.

(3) Piping must be protected from accidental rupture in the out-of-reactor areas.

(4) To preserve the desired temperature conditions, the lithium-bearing piping ought to be surrounded by an insulating medium. This effect may be provided by the shielding medium. In any event, the system must be capable of maintaining either isothermal conditions or any desired temperature gradient. (See Section XI-B-4).

(5) As stated in (2), the radiation hazard that the lithium bearing lines present to personnel is not known. It may be possible (or desirable) to monitor an annulus for tritium leakage between the lithium-bearing lines and the shielding/insulation. This system might be similar to that used in the primary tritium containment system. (see Section XII-C-3).

(6) The system must provide for the replacement of lithium removed from the system for sampling purposes. In practice, this small amount can be replaced from a surge tank system. The precise quantitites of lithium involved in the system cannot be estimated at this point. (see Section XI-B-5).

(7) A simple design will facilitate the replacement of piping for each new run.

The last point suggests that the desire to minimize mass transport complexities by minimizing the number of different materials in contact with lithium may be incompatible with the desire to maintain a simple design. While the in-reactor specimen can simply be welded to the piping and the shield swung into place, the rest of the module may involve a fairly complex apparatus. It would be preferable to reduce mass transport complexities by having ductwork, welds, and specimens of the same material. The apparatus, however, may be too complex for this. If it is, then the ductwork out of the reactor ought to be of a material which is fairly inert to liquid lithium. The cost of the apparatus and the timescale of the experiment must be taken into consideration, too, in deciding whether to design and build a permanent or replaceable out-of-reactor syst

The lithium used in the experiment will be purified at the beginning of each run. During the run, tritium and activation products will build up in the lithium. No provision is made for continuous tritium removal during the run. Tritium buildup may be monitored by the level of tritium in samples taken at regular intervals. Tritium will be removed from the lithium at the end of each run. It may be stored and used for other experimental programs. Activation products will be removed by precipitation and filtration at the end of the run. The lithium may be recycled for further use if the levels of impurities can be reduced to their initial values.

The design problems of the loop are formidable. We will not attempt a design more detailed than block diagrams of components required for a complete examination of corrosion rates, consistent with safe modular operation in a reactor environment. Modular components will be described more fully in later sections of this chapter, but, at this point, a block diagram may provide a useful frame of reference (Fig. XI-B-2). The design of the liquid lithium test module will also involve complex shielding problems arising from the accumulation of activation products and from the generation of tritium. Remote handling equipment may lessen this complexity by reducing the amount of hands-on involvement with the loop. Providing adequate shielding may conflict with the desire to maintain simplicity of design.

FIGURE XI-B-2 LITHIUM LOOP BLOCK DIAGRAM

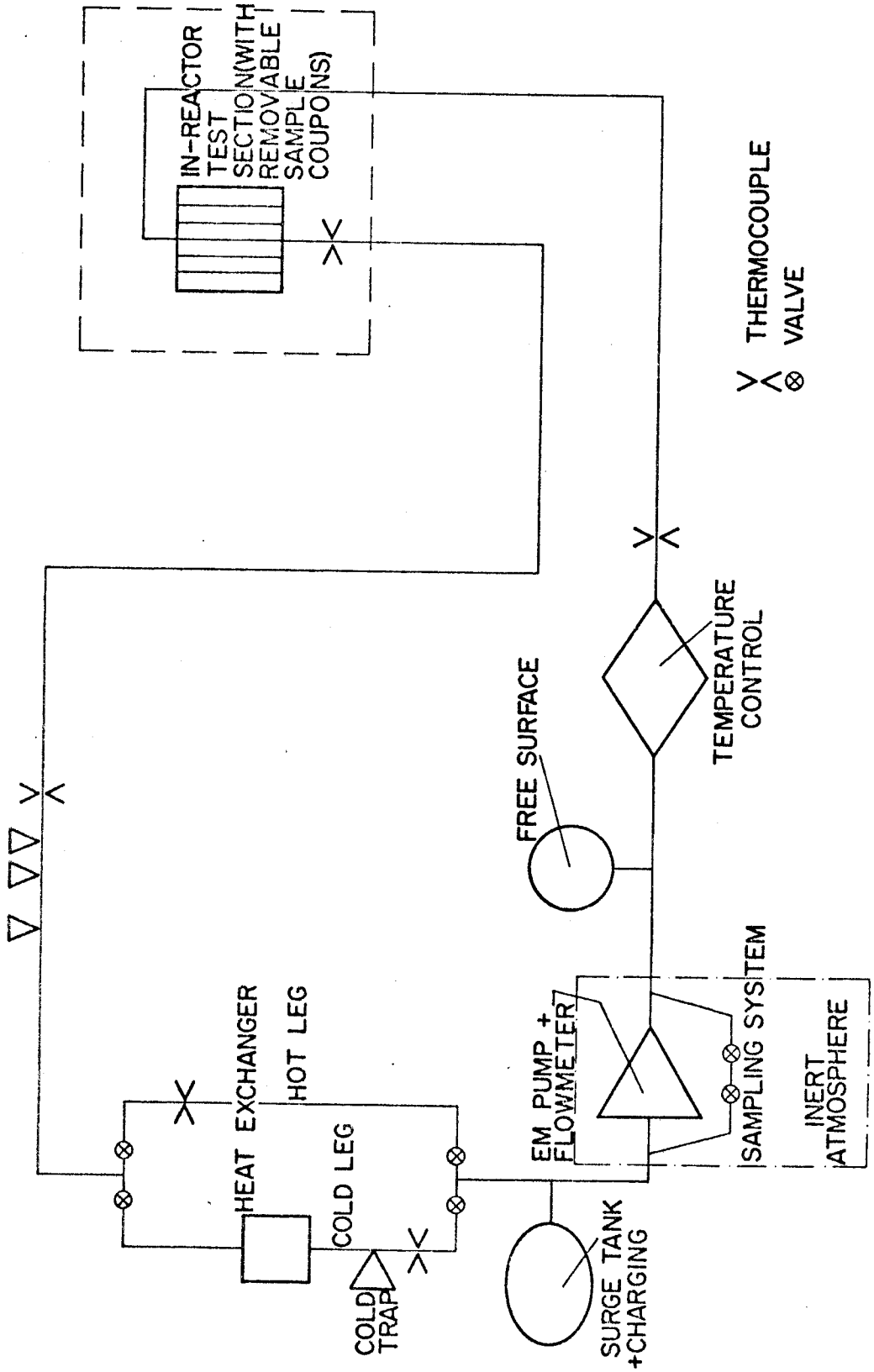

XI-B-3-b. Structural Materials for Module Specimens

In choosing structural materials for testing as containment materials for liquid lithium in the presence of radiation, it is desirable to select those materials which will be of greatest interest in CTR design. UWMAK-I[10] is a near-term Tokamak fusion reactor (5000 MW_{th}) using lithium as a breeder/heat transfer material. In this study, the first choice for a structural alloy is 316 type stainless steel. Three other alloys, Nb-1Zr, V-20Ti, and TZM, were also considered. We will summarize the considerations made in choosing 316 stainless steel for UWMAK-I since it represents a useful line of thought for choosing a structural material.

The first consideration was the existence of a well-developed industry for the alloy. This includes well developed design codes and fabrication procedures. The existence of such an industry implies that a product of uniform properties is available time and again.

Fabricability of the alloy was the second consideration. The size and complexity of fusion reactors requires that the structural materials be easy to weld simply and reliably. The alloy also must be capable of producing vacuum-tight welds. Ease of handling becomes an important property of the structural material when the amount of remote handling involved in fusion reactors is taken into account.

Susceptibility of the alloy to radiation damage was a third important consideration in the choice of a structural material. The amount of afterheat produced by the alloy was also under consideration here. The impact of high energy particles on the alloy produces four types of damage; embrittlement,

swelling, sputtering and blistering, and interstitial embrittlement. These forms of damage occur in addition to simple activation of the isotopic constituents of the alloy.

The structural material must also be compatible with other facets of the reactor environment. The structural material may limit the temperature range of the power cycle. It may limit the breeding ratio achievable, and finally, it may limit the safe operation of the reactor by its tritium permeation property.

All of the foregoing properties affect the operation of the reactor. Whether or not the reactor is built is dependent upon the availability of the elemental components of the alloy of choice and the cost of its fabrication. These considerations were the last made in the UWMAK-I study.

Table XI-B-3 (10) lists the foregoing considerations in order of importance to the UWMAK-I designers. Tabulated are the first and second choice of alloys - 316 SS, Nb-1Zr, V-20Ti, or TZM - for each property considered. Because 316 stainless steel was a first or second choice in almost every case and because of the existence of an already well developed industry, important for a near term device, the structural alloy of choice for UWMAK-I was 316 stainless steel. It is important to note that titanium alloys were not considered in early reactor designs, but now have the subject of intense investigation and show much promise (J. W. Davis and G. L. Kulcinski - MDC-E1655, 1977).

In much of the development of the liquid breeder/heat transfer test module, we wil use the UWMAK-I study as a guide for the liquid metal handling techniques which must b developed in order to build a fusion power reactor in the near term. For this reason, we will first examine liquid lithium compatibility with 316 stainless steel in a radiation environment. In a later section we will examine the possibility of performing similar studies with Nb-1Zr, V-20Ti, and TZM.

Table XI-B-3

Choice of CTR Blanket Material for Near Term Power Plant with Lithium Coolant[a][10]

Increasing Importance ↑

Property	First Choice	Second Choice
Qualified Metal Industry	316 SS	?
Fabricability, Weldability	316 SS	Nb-1Zr
Radiation Damage Embrittlement[c]		
Swelling Resistance	V-20Ti	316 SS
Sputtering and Blistering	Nb-1Zr	TZM
Interstitial Embrittlement	316 SS	TZM
Allowable Operating Temp.	TZM	Nb-1Zr
Effect on Breeding Ratio[b]	V-20Ti	316 SS
Induced Activity & Afterheat	V-20Ti	316 SS
T_2 Permeation	TZM	316 SS
Fabricated Costs	316 SS	Nb-1Zr
Long Term Availability to U.S.	TZM	316 SS

mportant

(a) Only the following non-magnetic alloys were considered - 316 SS, TZM Nb-1Zr, V-20Ti.

(b) All the alloys allow breeding, the question here is the value of the doubling time.

(c) No single alloy supersedes the others in this case.

We would now like to review some properties of 316 stainless steel which affect its use both as a containment material for liquid lithium and as a structural material in a radiation environment. 316 stainless steel is an alloy composed primarily of iron, chromium, nickel, manganese, molybdenum and other trace elements. Table XI-B-4 lists the composition of 316 stainless steel by element for a representative sample of 316 SS used in the radiation damage studies for UWMAK-I.

Studies of liquid lithium corrosion effects on 316 SS conclude that its limiting useful temperature is about 500°C. This may be pushed to approximately 590°C if the temperature gradients in the system are small.[14] The austenitic stainless steels are based on the non-ferromagnetic γ-iron structure formed at temperatures between approximately 900°C and 1400°C, stabilized with manganese, carbon and nickel and quenched to preserve the austenite structure.[16] The corrosive action of liquid lithium involves the conversion from the austenite structure to the ferromagnetic ferrite structure. 316 stainless steel is susceptible to lithium attack primarily because of the high solubility of nickel in lithium. Nickel dissolves out of the alloy and reduces the level of austenitic-stabilizing elements. This leaves the alloy more porous, reduces the ductility[13] and enhances the conversion from the austenite to the ferrite structure. A second conversion-enhancing mechanism is the formation of a chromium carbide phase at the grain boundaries which reduces the level of carbon in the steel and furthers the conversion fo the ferrite structure.

Corrosion rates increase slightly with flow rate, but the rate increase is not as large as that which results from changes in other parameters, such as temperature. Gill et al.[14] determined solution rate-constants from 510° to 612°C and the corresponding liquid phase mass transfer coefficients. The

Table XI-B-4

Typical Chemical Analyses of Commercial 316 Stainless Steel

Primary Elemental Constituents	% by Weight in 316 Stainless Steel
Fe	63
Cr	18
Ni	14
Mn	2
Mo	2
Si	0.7
Trace Elemental Constituents	**Ppm by Weight in 316 Stainless Steel**
Al	500
As	300
B	10
Co	500
Cu	1000
Nb	500
P	200
S	100
Ta	200
Ti	100
V	2000
C	600
H	?
N	100
O	<200

Table XI-B-5

Corrosion Rates for Stainless Steel in Lithium[10,ref. 29]

	Corrosion Rate	
Temperature °C	$\frac{mg}{cm^2 \cdot mo}$	$\frac{micron}{yr.}$
300 (extrapolated)	.01	.15
400	.11	1.6
500	1	15
550	3	45
600	6	90

resulting solution rate constants were on the order of 10^3 smaller than the liquid phase mass transfer coefficients. It appears, then, that the mass transfer process from the solid phase to the liquid phase is controlled by diffusion in the solid itself. The transfer of material from the interface to the bulk of the solution is fast by comparison. Therefore, as the flow rate would have little affect the diffusion process in the solid, the flow rate should not greatly affect corrosion rates.

The corrosion of an alloy occurs by processes which are rate controlled. The loss of alloy constituents is controlled by diffusion in the solid. The deposition of materials from solution in portions of the system at lower temperatures is also rate controlled. Here, the driving force is the difference in concentration between the bulk solution and the boundary layer at the interface. Part of the irregularity in corrosion rate data may very well be due to not taking into account the kinetic nature of the corrosion process. The data of Gill et al., for lithium corrosion of 316 stainless steel can be considered reliable since these studies take into account the rate controlled nature of the corrosion process. Gill's data, as summarized in UWMAK-I (Table XI-B-5) reflects the large temperature dependence of the corrosion rate. Since the corrosion rate is also dependent on the concentration profile of the prospective solute in the solid, any process which disrupts this profile can be expected to affect the corrosion rate. The presence of high energy particles affects the properties of the structural material in a number of ways. Upon impact with the structural material, high energy neutrons are capable of causing transmutation reactions with the isotopes of the constituents of the alloy.

The question of interest in a study of lithium corrosion of an irradiated alloy is the degree to which the chemical process of dissolution is affected by radiation damage occuring in the material. Brodzinski et al.,[15] have estimated the magnitude of the chemical and radiation effects in removing activity from the first wall of a fusion reactor. Fig. XI-B-3[15] graphs the equilibrium amount of activity in the coolant versus wall-loading values in MW/m^2. The corrosion damage effects are taken from (15) ref. 13. The radiation damage effects are plotted for the recoil atom sputtering ratios, S_r, and the lattice dynamic neutron sputtering, S_n. In this graph, two values of S_n are quoted for completeness of presentation; $S_n = .25$ and $S_n = 5 \times 10^{-5}$. The authors feel that an S_n of .25 is too high, however, and for an S_n of 5×10^{-5}, the erosive effects of radiation are two to three orders of magnitude lower than chemical corrrosion effects at wall loadings of 1 to 5 MW/m^2 and less than two orders of magnitude lower at wall loadings above 5 MW/m^2. Extrapolation of the plot beyond 10 MW/m^2 finds the difference between two effects decreasing further. For TETR, however, the wall loading is 1-2 MW/m^2 and so we are examining the interaction of two phenomenon roughly two orders of magnitude apart.

In summary, radiation damage effects are expected to contribute about 1% of the total damage due to both radiation damage and chemical corrosion effects. In the following sections, we will discuss the design of a module to examine this problem.

Those reactions of 316 stainless steel considered important in TETR are given in Table XI-B-6. For the length of the experimental run planned for the lithium loop (~1 year), it may be necessary to consider more of the reactions producing shorter-lived isotopes than those in Table IX-B-6 from the standpoint

FIGURE XI-B-3 ACTIVITY REMOVED FROM 316 SS FIRST WALL

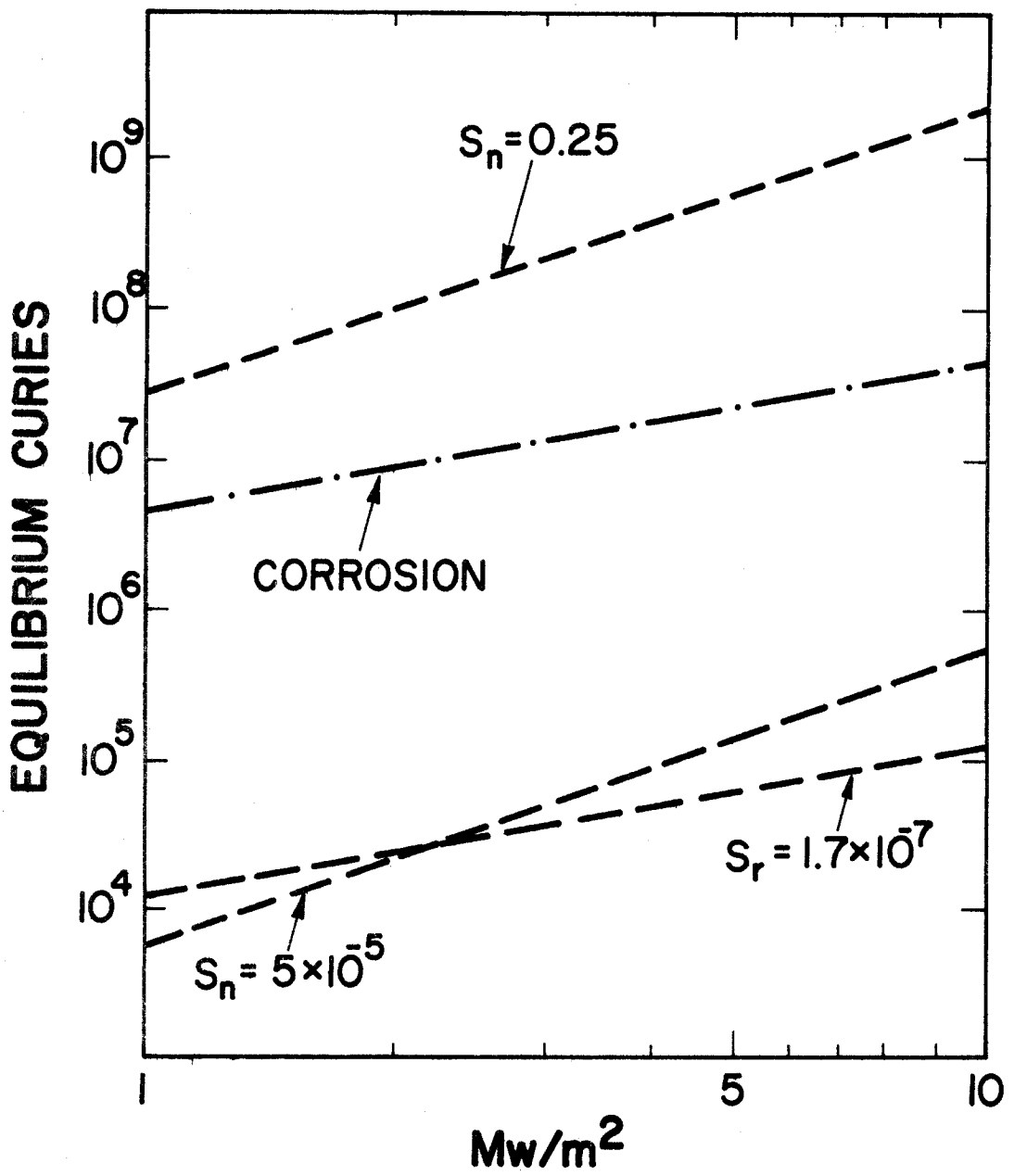

S_r = RECOIL ATOM SPUTTERING RATIO

S_n = LATTICE DYNAMIC NEUTRON SPUTTERING RATIO

of danger to the personnel handling the loop rather than from a materials damage standpoint. In general, transmutation effects can be expected to subtly change the composition of the alloy with time. Alteration of the ion and manganese content can be expected to affect the concentration profile of nickel, especially at the surface and thus affect the corrosion rate.

Table XI-B-6 Linear Decay Chains in TETR

1.1	^{10}B (n,p)	^{10}Be ⟶	
1.2.1	^{10}B (n,α)	^{7}Li (n,n'p)	^{6}He ⟶
1.2.2	^{10}B (n,α)	^{7}Li (n,γ)	^{8}Li ⟶
2.1	^{11}B (n,α)	^{8}Li ⟶	
3.1.1	^{12}C (n,α)	^{9}Be (n,α)	^{6}He ⟶
3.1.2	^{12}C (n,α)	^{9}Be (n,p)	^{9}Li ⟶
3.1.3	^{12}C (n,α)	^{9}Be (n,γ)	^{10}Be ⟶
4.1	^{13}C (n,γ)	^{14}C ⟶	
5.1	^{16}O (n,p)	^{16}N ⟶	
5.2.1	^{16}O (n,α)	^{13}C (n,γ)	^{14}C ⟶
6.1	^{28}Si (n,p)	^{28}Al ⟶	
7.1	^{50}Cr (n,d)	^{49}V ⟶	
7.2	^{50}Cr (n,γ)	^{51}Cr ⟶	
7.3.1	^{50}Cr (n,2n)	^{49}Cr ⟶	^{49}V ⟶
8.1	^{52}Cr (n,p)	^{52}V ⟶	
8.2	^{52}Cr (n,2n)	^{51}Cr ⟶	
9.1	^{53}Cr (n,d)	^{52}V ⟶	
10.1	^{54}Cr (n,α)	^{51}Ti ⟶	
10.2	^{54}Cr (n,γ)	^{55}Cr ⟶	

11.1	^{55}Mn (n,α)	^{52}V ⟶	
11.2	^{55}Mn (n,p)	^{55}Cr ⟶	
11.3	^{55}Mn (n,2n)	^{54}Mn ⟶	
11.4	^{55}Mn (n,γ)	^{56}Mn ⟶	
12.1	^{54}Fe (n,n'α)	^{51}Cr ⟶	
12.2	^{54}Fe (n,d)	^{53}Mn ⟶	
12.3	^{54}Fe (n,p)	^{54}Mn ⟶	
12.4	^{54}Fe (n,γ)	^{55}Fe ⟶	
12.5.1	^{54}Fe (n,2n)	^{53}Fe ⟶	^{53}Mn ⟶
13.1	^{56}Fe (n,t)	^{54}Mn ⟶	
13.2	^{56}Fe (n,p)	^{56}Mn ⟶	
13.3	^{56}Fe (n,2n)	^{55}Fe ⟶	
13.4.1	^{56}Fe (n,γ)	^{57}Fe (n,d)	^{56}Mn ⟶
13.4.2	^{56}Fe (n,γ)	^{57}Fe (n,p)	^{57}Mn ⟶
14.1	^{57}Fe (n,d)	^{56}Mn ⟶	
14.2	^{57}Fe (n,p)	^{57}Mn ⟶	
15.1	^{58}Fe (n,α)	^{55}Cr ⟶	
15.2	^{58}Fe (n,t)	^{56}Mn ⟶	
15.3	^{58}Fe (n,d)	^{57}Mn ⟶	
15.4	^{58}Fe (n,γ)	^{59}Fe ⟶	

16.1	^{58}Ni (n,α)	^{55}Fe ⟶	
16.2	^{58}Ni (n,d)	^{57}Co ⟶	
16.3	^{58}Ni (n,p)	^{58}Co ⟶	
16.4	^{58}Ni (n,γ)	^{59}Ni ⟶	
16.5.1	^{58}Ni (n,2n)	^{57}Ni ⟶	^{57}Co ⟶
17.1	^{60}Ni (n,t)	^{58}Co ⟶	
17.2	^{60}Ni (n,p)	^{60}Co ⟶	
17.3	^{60}Ni (n,2n)	^{59}Ni ⟶	
17.4.1	^{60}Ni (n,p)*	^{60m}Co ⟶	⟶
17.5.1	^{60}Ni (n,α)	^{57}Fe (n,d)	^{56}Mn ⟶
17.5.2	^{60}Ni (n,α)	^{57}Fe (n,p)	^{57}Mn ⟶
17.6.1	^{60}Ni (n,γ)	^{61}Ni (n,d)	^{60}Co ⟶
18.1	^{61}Ni (n,d)	^{60}Co ⟶	
18.2	^{61}Ni (n,p)	^{61}Co ⟶	
19.1	^{62}Ni (n,α)	^{59}Fe ⟶	
19.2	^{62}Ni (n,t)	^{60}Co ⟶	
19.3	^{62}Ni (n,d)	^{61}Co ⟶	
19.4	^{62}Ni (n,γ)	^{63}Ni ⟶	
20.1	^{64}Ni (n,2n)	^{63}Ni ⟶	
20.2	^{64}Ni (n,γ)	^{65}Ni ⟶	
21.1	^{63}Cu (n,α)	^{60}Co ⟶	
21.2	^{63}Cu (n,γ)	^{64}Cu ⟶	
22.1	^{65}Cu (n,2n)	^{64}Cu ⟶	
22.2	^{65}Cu (n,γ)	^{66}Cu ⟶	

23.1	^{92}Mo (n,n'α)	^{88}Zr ⟶		
23.2	^{92}Mo (n,α)	^{89}Zr ⟶		
23.3	^{92}Mo (n,p)	^{92m}Nb ⟶		
23.4	^{92}Mo (m,2n)	^{91}Mo ⟶		
23.5.1	^{92}Mo (n,γ)	^{93}Mo ⟶	^{93m}Nb ⟶	
24.1	^{94}Mo (n,p)	^{94}Nb ⟶		
24.2.1	^{94}Mo (n,2n)	^{93}Mo ⟶	^{93m}Nb ⟶	
25.1	^{95}Mo (n,d)	^{94}Nb ⟶		
25.2	^{95}Mo (n,p)	^{95}Nb ⟶		
25.3.1	^{95}Mo (n,p)	^{95m}Nb ⟶	^{95}Nb ⟶	
26.1	^{96}Mo (n,t)	^{94}Nb ⟶		
26.2	^{96}Mo (n,d)	^{95}Nb ⟶		
26.3	^{96}Mo (n,p)	^{96}Nb ⟶		
27.1	^{97}Mo (n,t)	^{95}Nb ⟶		
27.2	^{97}Mo (n,d)	^{96}Nb ⟶		
27.3	^{97}Mo (n,p)	^{97}Nb ⟶		
27.4.1	^{97}Mo (n,p)	^{97m}Nb ⟶	^{97}Nb ⟶	
28.1	^{98}Mo (n,t)	^{96}Nb ⟶		
28.2	^{98}Mo (n,d)	^{97}Nb ⟶		
28.3	^{98}Mo (n,p)	^{98}Nb ⟶		
28.4.1	^{98}Mo (n,α)	^{95}Zr ⟶	^{95}Nb ⟶	
28.5.1.1	^{98}Mo (n,γ)	^{99}Mo ⟶	^{99m}Tc ⟶	^{99}Tc ⟶

29.1	^{100}Mo (n,t)	^{98}Nb ⟶		
29.2	^{100}Mo (n,p)	^{100}Nb ⟶		
29.3.1	^{100}Mo (n,α)	^{97}Zr ⟶	^{97}Nb ⟶	
29.4.1	^{100}Mo (n,γ)	^{101}Mo ⟶	^{101}Tc ⟶	
29.5.1.1	^{100}Mo (n,2n)	^{99}Mo ⟶	^{99m}Tc ⟶	^{99}Tc ⟶
30.1	^{182}W (n,p)	^{182}Ta ⟶		
30.2	^{182}W (n,2n)	^{181}W ⟶		
30.3.1	^{182}W (n,γ)	^{183}W (n,d)	^{182}Ta ⟶	
30.3.2	^{182}W (n,γ)	^{183}W (n,p)	^{183}Ta ⟶	
31.1	^{183}W (n,d)	^{182}Ta ⟶		
31.2	^{183}W (n,p)	^{183}Ta ⟶		
31.3.1	^{183}W (n,γ)	^{184}W (n,α)	^{182}Hf ⟶	
31.3.2	^{183}W (n,γ)	^{184}W (n,d)	^{183}Ta ⟶	
31.3.3	^{183}W (n,γ)	^{184}W (n,p)	^{184}Ta ⟶	
31.3.4	^{183}W (n,γ)	^{184}W (n,γ)	^{185}W ⟶	
32.1	^{184}W (n,α)	^{181}Hf ⟶		
32.2	^{184}W (n,d)	^{183}Ta ⟶		
32.3	^{184}W (n,p)	^{184}Ta ⟶		
32.4	^{184}W (n,γ)	^{185}W ⟶		
32.5.1	^{184}W (n,2n)	^{183}W (n,d)	^{182}Ta ⟶	
32.5.2	^{184}W (n,2n)	^{183}W (n,p)	^{183}Ta ⟶	

33.1	^{186}W (n,p)	^{186}Ta ⟶		
33.2	^{186}W (n,2n)	^{185}W ⟶		
33.3	^{186}W (n,γ)	^{187}W ⟶		
33.4.1	^{186}W (n,α)	^{183}Hf ⟶	^{183}Ta ⟶	
33.5.1	^{186}W (n,d)	^{185}Ta ⟶	^{185}W ⟶	
34.1	^{204}Pb (n,p)	^{204}Tl ⟶		
34.2	^{204}Pb (n,2n)	^{203}Pb ⟶		
35.1	^{206}Pb (n,α)	^{203}Hg ⟶		
35.2	^{206}Pb (n,t)	^{204}Tl ⟶		
35.3	^{206}Pb (n,2n)	^{205}Pb ⟶		
36.1	^{207}Pb (n,n'α)	^{203}Hg ⟶		
36.2.1	^{207}Pb (n,2n)	^{206}Pb (n,t)	^{204}Tl ⟶	
36.3.1	^{207}Pb (n,2n)	^{206}Pb (n,2n)	^{205}Pb ⟶	
37.1	^{208}Pb (n,α)	^{205}Hg ⟶		
37.2.1	^{208}Pb (n,2n)	^{207}Pb (n,n'α)	^{203}Hg ⟶	

XI-B-4. Temperature Control of the Module

It is desirable to maintain as much control as possible over the temperature within the liquid lithium loop. The capacity to maintain isothermal conditions is necessary as it may be desirable to limit the amount of mass transfer which will occur in a thermal gradient. While the reactor is running, energy will be deposited in the loop specimen. However, the discontinuity of the reactor's operating cycle will cause some level of temperature fluctuation in the loop. How this is dealt with is dependent on the timescale of the fluctuation with respect to the timescale of the experiment. Assuming that some temperature fluctuation will occur in the loop specimen, feedback control between the thermocouples and heating elements thoroughout the system will be useful and should be utilized in every run for the overall maintenance of the desired experimental temperatures.

The temperature control system of the lithium loop consists of two segments, that controlling the in-reactor temperature and that controlling the out-of-reactor loop temperature. In the out-of-reactor portion of the loop, electrical heating will be provided by an element surrounding the lithium-containing pipe and contained within the shielding/insulation medium (Fig. XI-B-4). Clamshell-type furnaces will provide even heating over the pipe surface. Allowances must be made in the insulation and heating elements for thermocouple wells.

Within the reactor, the heating requirements are different due to the fact that reactor operation heats this portion of the module. The reactor first wall is designed to run at 300°C, so if temperatures below this are desired, some cooling must be provided. This is achieved by the helium cooling designed for the modular areas. Along with helium cooling, a

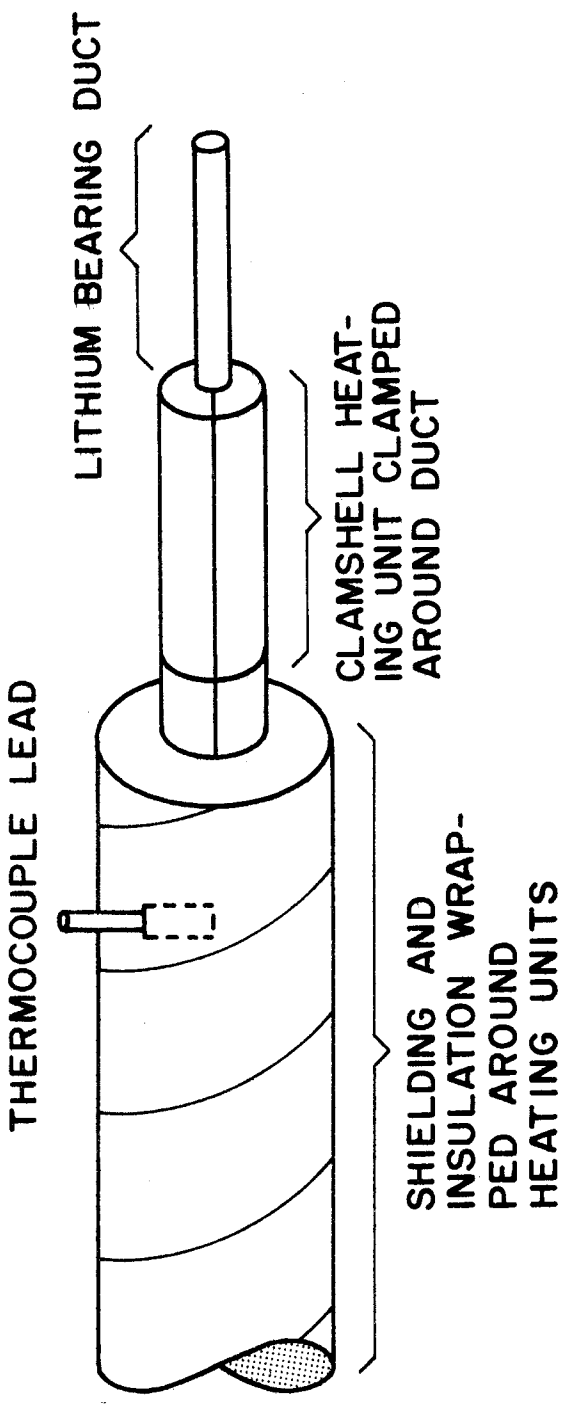

XI-B-4 OUT-OF-REACTOR LITHIUM-BEARING DUCT (NOT TO SCALE)

thermocouple for the in-reactor specimen must be provided. Since the temperature of the system is more responsive to a heating element than to a gas cooling system, helium over-cooling with the addition of a small amount of electrical heating is a more sensitive temperature control mechanism.

The loop lithium will be circulated, providing some measure of heat transport out of the specimen, depending on the ability of the temperature control system to match in- and out-of-reactor temperatures. Heat removed by the helium will be dumped. Although a thermal gradient will result, provision should be made for a heat exchanger in the loop. It may be desirable to run the loop with hot and cold legs at some point and a heat exchanger would be required for this. Additionally, as one purpose of the loop is to simulate as closely as possible the operation of a lithium loop in a power reactor, a heat exchanger becomes a necessary part of this simulation.

Temperature measurement is achieved by recording thermocouple responses throughout the system. The temperature of the system is recorded continuously, and this information is fed back to the heating element controls.

XI-B-5. Sampling System

XI-B-5-a. Isolation of In-Run Samples

During an experimental run, lithium will be flowing slowly (<100 cm/sec) through the loop and corrosion products and tritium will be accumulating therein. In a solute/solvent system experiment such as this, one may examine the solute and/or the solvent to obtain experimental data. In this case, since the source of dissolved material is the container, the majority of samples taken during a run will be of liquid lithium. A separate procedure will also make samples of 316 stainless steel available during the run, but these will not be cut out of the container itself.

It is possible to place a flexible strip of 316 stainless steel segments in the irradiated portion of the loop. These samples are removed during scheduled reactor shutdowns. During a shutdown, the lithium is pumped away from the irradiated segment of the loop and then pumping is stopped. The shield is swung open and the desired sample "coupons" are pulled out through an opening in the top of the loop segment, which is normally capped when lithium is being pumped. It is necessary to perform the removal operation while the reactor is down because exposure of the loop to radiation while the pumping is stopped would cause a hot spot in the loop.

The solid samples will be analyzed in the same manner as post-run samples. This will be discussed in Section XI-B-6. The methods by which the lithium samples are analyzed will be discussed in Section XI-B-6-a. In this section, we will discuss the main features of a sampling system capable of withdrawing an aliquot of lithium from the module during an experimental run.

There are two approaches to the design of the sample holder. The sample holder may be made of 316 stainless steel, as is the rest of the module.

The holder may then be considered a part of the loop. Lithium could flow through the sample holder as part of the loop until the sample is taken. A second approach would be to design the sampler of some alloy especially inert to lithium to avoid contamination of the lithium on contact with a fresh surface. Both of these approaches will be evaluated.

The sampler itself will consist of an evacuated sidearm bridging the electromagnetic pump (Figure XI-B-5). In this fashion, use is made of the pressure drop across the pump to fill the sample holder. There will be valves to open and close off the sampler to the lithium flow where the sidearm joins the main lithium duct. A simple cylindrical container is included in the sidearm. A valve is attached to this container if liquid samples are to be taken. The sample is then divided up volumetrically for the different analytical procedures planned. In operation, the valves are opened and the sample holder is allowed to fill with lithium. If the holder has been treated as part of the loop and has already had lithium flowing through it, the valves are simply closed when a sample is to be taken. In either case, after the holder is filled, the sample may be isolated as either a solid or a liquid. For a solid sample, the sidearm is cooled and the tubes on each side of the sample holder are constricted. The sample holder is then removed from the line. If a liquid sample is desired, the tubes may be constricted while hot. The sample holder must then remain heated during removal. If gamma counting is to be performed, it should be accomplished as soon as possible after the sample is removed from the main lithium line. Solid sample isolation is accomplished by cutting open and peeling away the container material. The resulting sample is a cylindrical block of solid lithium.

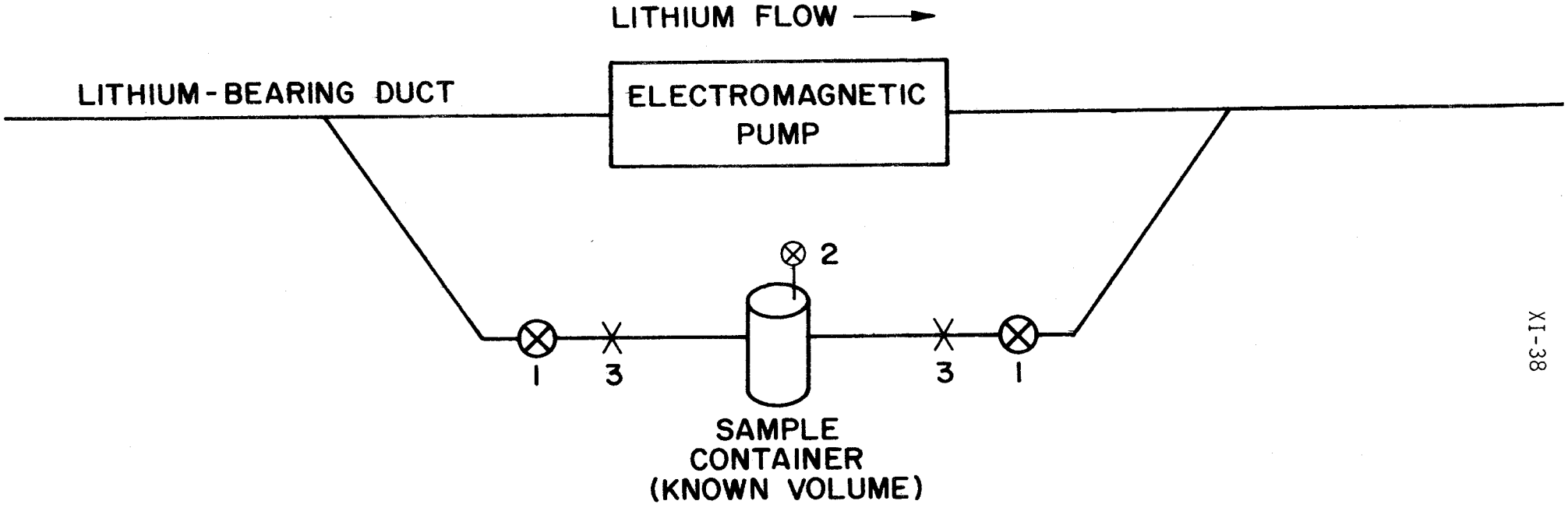

1) Li FLOW CONTROL VALVES
2) VALVE SYSTEM FOR VOLUMETRIC MEASUREMENT OF Li ALIQUOTS
3) TUBE CONSTRICTION POINTS

XI - B - 5 LITHIUM SAMPLING SYSTEM

The effect on solution homogeneity of the containment material and of freezing and redissolving an aliquot of lithium must be considered when choosing the sampling system material. It is not known whether freezing and redissolving a lithium sample will alter its composition due to the adsorption of sought-for impurities on container walls. The simplest approach towards avoiding this problem is either to first divide the sample into the sizes required for chemical analysis before recording the gamma spectrum (which requires a solid sample) or to withdraw two separate samples; one for counting and one for other analytical procedures. If one liquid sample is to be taken for gamma counting and other analytical procedures and the holder is not to be treated as part of the loop, the sample holder may be made of some alloy inert to lithium since the residence time of liquid lithium in it is greater than if a sample were isolated and solidified immediately. The sample material would be a refractory alloy which requires special handling procedures but the lithium sample could be maintained as a liquid for longer periods of time without risking an alteration of the impurity content of the lithium by the holder.

Since the gamma spectrum is best taken on an exposed sample, and must be recorded at liquid nitrogen temperatures, the simplest approach to sample taking would be to isolate one sample in a 316 stainless steel holder, solidify it, cut off cross sectional pieces of the cylinder and count one thin section as a solid. The stainless steel can be peeled away and the investigator is left with solid samples of lithium for other analytical procedures. In this case, allowing lithium to flow through the sample holder will equilibrate the lithium with the stainless steel so that, on isolation, there would not be a new interaction between the container and the lithium due to the contacting of liquid lithium with a fresh metal surface.

Although the aliquot of lithium taken is small, a large number of samples will deplete the lithium level in the module significantly. Provision must be made to replace lost lithium. A free surface of lithium maintains a constant pressure of lithium in the system. Placing a reservoir downstream from the lithium sampling system and overcharging the module with lithium at the start of the experiment will leave an excess of lithium in the reservoir. Exerting a positive pressure on the surface of this lithium forces lithium back into the module whenever an aliquot is removed elsewhere. It should be noted that while chemical corrosion rates do not vary greatly with flow rates, the quantity of lithium in the reservoir of possibly significant size compared to the entire module's inventory will be accumulating chemical corrosion products more slowly as a stagnant lithium pool than the rest of the module. Additionally, it will not be building up activation products at all except as they deposit in the reservoir due to a concentration gradient between the reservoir and the main line. In practice, the aliquot taken will be small with respect to the rest of the system. If the samples are not taken too frequently, the dilution effect should be negligible.

To maintain the integrity of samples taken and to insure the safety of personnel, the sampling system and gamma detector should be enclosed in an inert atmosphere box. This will be especially necessary if the sample must be exposed for counting. The inert atmosphere will also protect the detector from atmospheric attack. Shielding must also be provided for the detector to prevent the counting of stray radiation. The use of an inert atmosphere around both sampler and gamma detector will minimize the amount of handling and number of transfers in the atmosphere when preparing the sample

for analysis since the sample will be isolated, removed from the line, and counted in the same glovebox.

In summary, the module sampling system will consist of the in-reactor remote handling equipment necessary to remove solid samples of containment material from the loop and a sidearm bridging the pumping system for lithium samples. The sidearm contains a cylindrical sample holder which is filled and sealed off from the line by constricting the tubes connecting it to the sidearm. The size and shape of the sample holder is reproducible. A free surface of lithium will replace lithium taken from the system. The lithium sampler and gamma detector will be enclosed in a single inert atmosphere box. The counting equipment will be shielded.

XI-B-5-b. Post-Run Sample Isolation

The isolation of samples at the end of the run is a much simpler matter than sample isolation during a run primarily because because the reactor will be down for this procedure and there will be no handling of liquid metals involved. At the end of the run, the lithium will be drained from the module at temperature to prevent precipitation of solubilized substances. This procedure will be described in Section XI-B-7. When the lithium is drained, the in-reactor specimen can be cut away from its ductwork and removed to an appropriately shielded enclosure. Once removed, the specimen can be cut into as many pieces as are required for chemical, metallographic and radiochemical examination. If the ductwork in the module is to be replaced, used sections of it may be cut away for examination too. The amount of material needed for these analyses should be a consideration in designing the size of the test sections. Disposal of ductwork and specimens after examination will be discussed in Section XI-B-7.

XI-B-6. Sample Analysis

XI-B-6-a. Analysis of Samples Taken During a Run

XI-B-6-a-1. Analysis of Volatile Nonmetallics

Samples taken from the lithium module during an experimental run will consist of liquid lithium aliquots and, possibly, samples of 316 stainless steel which are inserted into the portion of the module to be irradiated. All samples of stainless steel will be analyzed in the same fashion whether taken during or after the run. This analysis will be discussed in Section XI-B-6-b.

Lithium aliquots are easily taken from the module (Section XI-B-5). They will contain tritium and metallic and nonmetallic materials as impurities resulting from chemical corrosion. Some of the materials will be activated by fast neutrons. The analytical techniques used must take into account all of the different types of substances to be determined; volatile, nonvolatile, metallic, and nonmetallic. The purpose of analyzing lithium samples during the run is to obtain a profile of the accumulation of tritium and corrosion products with time. To obtain meaningful data on the corrosion of 316 stainless steel, it is necessary to analyze not only the fate of the metallic constituents in the loop, but also the levels of those nonmetallic elements whose presence promotes alternative mechanisms to corrosion in addition to the fundamental solution process. We will, therefore, discuss the analysis of nonmetallics such as oxygen and nitrogen as well as the determination of the primary metallic constituents of stainless steel. The timing of sample taking, the impurities to be determined and the methods of analysis must be evaluated. We will discuss sampling intervals in Section XI-B-7.

In this section, we shall examine some of the analytical procedures applicable to lithium samples taken from the test module. There are three types of analysis which may be considered for the module. The first is continuous monitoring of gaseous constituents. There are currently under development meters for the continuous monitoring of oxygen,[17] tritium[1] and hydrogen[18] in sodium. To measure the level of oxygen in sodium, the emf of a concentration cell between dissolved oxygen in sodium and oxygen in air is calibrated with known sodium solutions. The probe, which consists of a barrier material and allo ance for the passage of air, is then inserted in solutions of unknown concentrations of oxygen. The barrier material is a mixture of ThO_2 and Y_2O_3 of very high purity. High purity components are required to achieve resistance to sodium corrosion. The resistance of this barrier material to lithium corrosion is not known, but should it or any other ceramic permeable to oxygen prove lithium resistant, the development of a reliable oxygen meter will be worth pursuing. A more cumbersome, but more sensitive oxygen monitoring technique is the vanadium wire equilibration method.[19] This technique is capable of determining very low levels of oxygen in sodium. A 30 to 50 mg sample of high purity

vanadium wire is equilibrated with sodium at a known temperature. Oxygen distributes between vanadium and sodium, described by the equilibrium distribution coefficient at that temperature. Equilibration requires about four hours. The oxygen in the wire is determined by inert gas fusion methods and is related to the concentration of oxygen in sodium by the distribution coefficient. Oxygen may be accurately determined in sodium in the 0.003 to 16 ppm range. For application to the lithium system, equilibrium distribution coefficients are required for oxygen in a vanadium (or other suitable metal)/ lithium system at temperatures applicable to the test loop. These data are known.[26] The use of distribution coefficients for oxygen in a metal/lithium system at the loop temperature would not necessitate the isolation and heating of a lithium sample in order to determine oxygen. The application of this technique to a lithium system should be studied.

Hydrogen in sodium is determined by the diffusion of hydrogen from sodium through a nickel membrane to an evacuated chamber where it is detected by an ion pump.[18] The pump current is a measure of hydrogen flux through the membrane. In lithium,[1] a pure, low-carbon, iron diaphragm, resistant to lithium corrosion may be used. In this fashion, the hydrogen meter should be capable of detecting hydrogen pressures of 10^{-7} to 10^{-8} torr. While oxygen is an active participant in the acceleration of corrosion rates, hydrogen is not. The necessity of monitoring hydrogen closely is questionable. The inclusion of a hydrogen meter might more usefully be set aside in favor of an occasional check through a chemical test.

The concentration of tritium is an important parameter of the loop. The increase in the tritium concentration in the loop and its subsequent behavior is an important portion of the experiment. Continuous monitoring of tritium in liquid metals is also the least-developed technique of the monitoring methods we will discuss. It is possible that the design for the hydrogen meter can be modified tritium detection.[1] In the modified form, the tritium diffusing through the iron membrane is mixed with a counting gas and passed to a proportional counter rather than to an ionization chamber. The detection limits of such a device are presently unknown. It is desirable that such a monitor be developed if liquid lithium is to be used as a breeder/coolant in future fusion reactor designs.

Of the three monitoring devices described, the two most useful for the lithium loop are the oxygen and tritium monitors. The tritium monitor provides a simple method of following the rise in concentration of tritium in the loop. Although low-carbon iron is fairly resistant to lithium corrosion, it would not be desirable to allow the membrane to remain in the lithium continuously. Dissolved iron can bias the determination of the iron release rate from stainless steel. The operation of the tritium monitor should involve the insertion of the probe into the flow by remote handling and removal after measurement. It should be located in a portion of the loop of moderate temperature compared to the high and low extremes to avoid biasing based on localized, non-representative temperatures. This is also true for the oxygen monitor. The probe should not remain in the lithium flow for

extended periods of time and it, too, should be placed in an intermediate temperature zone. Instrumentation for the monitors may be located in the same shielded area as that containing the sampling system and gamma detectors. It would be interesting to place the tritium probe in the reactor portion of the loop. However, the effect of a high fast neutron flux on the operation of such a probe is unknown. The activation of the iron membrane may cause a gradual deterioration of its ability to diffuse tritium. Similarly, other forms of radiation damage to the iron may affect its behavior towards the permeation of tritium. On line monitoring of oxygen, tritium has the advantage of being a simple method for the determination of these elements that does not require sample isolation. The determination may be performed remotely, eliminating sample handling.

XI-B-6-a-2. Analysis of Activated Corrosion Products

The analysis of activated corrosion products is adapable to remote handling techniques. A quantitative determination of the level of activated corrosion products can be made from the gamma spectrum if good resolution is routinely achieved. There are numerous transmutation reactions possible for

316 stainless steel in a fast neutron flux. Many will result in insoluble products or in very short-lived isotopes. The isotopes that will be suitable for analysis will be dependent upon the timescale of the sample isolation procedure. The activity of isotopes with short half-lives with respect to the isolation procedure will have begun to decay significantly by the time the spectrum is recorded on the lithium sample. Insoluble isotopes will not exist to any large extent in the lithium. However, the more soluble isotopes with comparable, or long, half-lives with respect to the isolation procedure are likely to be seen in the lithium.

The three major constituents of 316 stainless steel; iron, chromium and nickel, are also the most soluble. The level of radioactive products in the lithium resulting from the reaction of these elements with neutrons is indicative of the release of these elements due to corrosion. Table XI-B-7 lists some moderately short-lived isotopes resulting from neutron activation of iron, nickel and chromium.

The direct conversion of the concentration of activated products to the release rate of an element from 316 stainless steel cannot be made for two reasons. The first concerns material transfer effects. It has been noted that different isotopes tend to migrate to different temperature zones in a sodium loop.[20] In irradiated flowing sodium loops contained by stainless steel, ^{54}Mn tends to migrate to colder zones and ^{60}Co tends to migrate to hotter zones. Thus, not only does the temperature zone containing the sampling system affect to a certain extent the level of isotopes found,

Table XI-B-7

Short-Lived Isotopes Resulting from Neutron Irradiation of 316 SS

316 SS Component	% Abundance	Reaction	Product	(MeV) Energy of Gammas	Half-Life of Product
(a) ^{50}Cr	4.31	(n,γ)	^{51}Cr	.32	27.8 d
^{50}Cr	4.31	(n,2n)	^{49}Cr	.06, .09, .15	42 m
^{53}Cr	9.55	(n,p)	^{53}V	1.01	2.0 m
^{54}Fe	5.82	(n,p)	^{54}Mn	.84	312 d
^{56}Fe	91.66	(n,p)	^{56}Mn	.845, 1.81, 2.11	2.58 hr
^{58}Fe	.33	(n,γ)	^{59}Fe	.19, 1.10, 1.29	45 d
^{58}Ni	67.86	(n,p)	^{58}Co	.81, 1.65	71 d
^{60}Ni	26.23	(n,p)	^{60}Co	1.17, 1.33	5.24 y
^{62}Ni	3.66	(n,p)	^{62}Co	1.17, 1.97, 1.79 2.03	13.9 m

but the deposition of these materials out of solution in their favored temperature zone prevents their ever being mixed homogeneously in the lithium flow. In other words, while a homogeneous sample of lithium may be taken, the level of activated products will not be directly representative of the total release of these isotopes because of this effect.

A second unknown parameter of the loop chemistry is the relationship between the level of activated products and the level of chemical corrosion products. Even though the lithium is circulated through the loop, chemical corrosion will occur in nonirradiated portions of the loop carrying stable materials into the lithium flow. Depending on the fast neutron cross section of these materials and their solubility, the level of all activated corrosion products will be less than the level of all chemical corrosion products. However, by performing both radiometric and chemical analysis, the relationship between activated corrosion products and chemical corrosion products may be determined. Additionally, gamma spectra taken of sections of the loop piping will reveal the distribution of activated material deposited in the loop.

Additionally, an important function of gamma spectroscopy will be to measure long term accumulations of activity due to isotopes whose half-lives are long with respect to the experiment. These isotopes will not reach an equilibrium concentration due to equivalent rates of generation and decay as do shorter-lived isotopes, assuming that the interruptions due to reactor shutdowns are small. For long-lived isotopes, the release rate at long experimental times will be higher than at short experimental times as the same quantity of stainless steel dissolved will contain higher levels of activity due to these isotopes. The gamma spectroscopic data will be useful in determining

which isotopes reach equilibrium concentrations and which do not over the course of a long-term experiment.

Once the lithium sample is isolated in the shielded inert atmosphere area, the lithium requirements for other analytical procedures may be removed and the remaining weighed portion of lithium counted for gamma activity. From Table XI-B-7, it can be seen that there are several gamma energies possible from the nine isotopes derived from iron, nickel and chromium. These energies are spread out over a range of .06 MeV to 2.11 MeV. A moderate resolution capable of distinguishing peaks 2 keV apart should be sufficient to resolve these peaks. For larger numbers of isotopes, higher resolution may be required. A resolution capable of distinguishing peaks 2 keV apart is well within the capabilities of current detectors and multichannel analyzers.

Gamma spectroscopic techniques are well known. A commonly used detector is the lithium drifted germanium diode. Although not as efficient as some of the available detectors, it is somewhat more chemically stable in air than others. The germanium diode is saturated with lithium and to prevent precipitation of the lithium, the detector is kept at liquid nitrogen temperatures. Although a molten lithium sample may be drawn, the relationship of counting efficiency and counting geometry demands that the lithium sample be placed near the detector. As such, it will probably be necessary to count the lithium sample as a solid, since maintaining a molten state might overheat the detector diode and cause precipitation as described above. Although we have only considered counting the lithium sample in the elemental state, it is possible to dissolve the sample in water and count an aqueous solution. We have not considered this because (1) an extra handling step is required, and (2) although the quantity of

lithium involved is small, it may be desirable to recycle these samples for another experiment or for further analytical work. The lithium sample ought to be exposed to the dete tor as a very thin layer for counting. A small "pie-pan" type of sample holder of reproducible dimensions could be used for counting, with a known volume of lithium poured into it and solidified. A fresh holder should be used for each new counting sample.

It will be important to determine the levels of activity both in the lithium and deposited in the ductwork. The use of two detectors - one movable and one stationary - can perform both requirements. The fixed detector will remain in the inert atmosphere area. It will be used for gamma counting on lithium samples and may be calibrated with samples of isotopes expected in the lithium. The shielding may be more comprehensive as this detector will not be moved for counting purposes. On the other hand, a Ge(Li) detector mounted on a fork lift has been used to measure activity deposited on the ductwork of a sodium loop.[17] It is capable of measuring the gamma spectrum of piping, whose insulation and shielding has been removed, at a distance of 0.65m. It is calibrated with a standard suspended in the empty piping and all measurments are made after the sodium has been drained from that section of the loop. The movable detector can traverse the length of a pipe to determine the deposition profile along the length of the pipe and be moved to many different sites to analyze deposition of activity throughout the loop. There is no reason why this system cannot be applied to the lithium loop. These maneuvers can be handled remotely and the dual gamma detectors represent a useful system for the determination of the distribution of activity in a liquid metal loop.

XI-B-6-a-3. Analysis of Chemical Corrosion Products

A complete analysis of the impurity levels in the lithium sample will be made through chemical techniques. Over the course of the experiment, detectable levels of metallic and monmetallic impurities will build up in the lithium

flow. We have already discussed the determination of three important nonmetals: oxygen, hydrogen and tritium, by on-line monitoring of the lithium during the experimental run. Carbon and nitrogen are important nonmetallic impurities whose role in the corrosion process has been defined. The determination of these elements will be discussed in depth. Sulfur and phosphorous are two nonmetallic impurities whose role in the corrosion process is not thought to be as active as that of carbon and nitrogen. Therefore, although their determination is similar to that of carbon, we will not examine these analyses as closely.

Metallic impurities of importance in the lithium are iron, nickel, chromium, manganese and molybdenum. Trace constituents of stainless steel are also likely to appear as suspended solids. Some of these trace elements are aluminum, cobalt, copper, tantalum, titanium, vanadium, niobium and silicon. Emission techniques exist which are capable of handling the analyses of the major elements and some of the trace elements. We will discuss the analysis of the major constituents of stainless steel since their release rates are most indicative of the fate of stainless steel in a lithium environment over long periods of time.

Carbon is most reliably determined by the combustion technique.[1] In it, a lithium sample is ignited in a stream of oxygen at 900°C. The lithium sample is mixed with boric acid as an oxidizing flux. On heating, all of the carbon is converted to carbon dioxide. The carbon dioxide is then determined gas chromatographically. Since the experimentation in the lithium loop is not expected to exceed 600°C, this method is preferable to the acetylene evolution method. In it, lithium is mixed with water and the carbon is converted to acetylene and determined. The method depends for accuracy on the fact that all of the carbon is the form of a carbide. This is known to be true only for carbon heated in lithium to temperatures greater than 600°C.[1] While the detection

limit for the combustion method is higher than that of the acetylene evolution method (25 ppm vs 0.5 ppm), it will ultimately be more reliable for the type of lithium sample found in the loop. The maximum safe sample size for the combustion method is about 0.4g and the analysis is obviously destructive of the sample. It should be possible to perform accurate analysis with ~ 0.1g of lithium. The mimimum amount of carbon which may be determined is about 10 micrograms, which, at the detection limit, corresponds to a sample size of 0.4g. For 5 m^2 of stainless steel (including in- and out-of-reactor ductwork) contacted with lithium at 400°C for one year, the corrosion rate of about 0.11 $mg/cm^2 \cdot mo$[14] of stainless steel (about 0.06% carbon) would result in the removal of about 35 mg of carbon removed from the austenite structure. If all of the carbon remains in the lithium, the maximum amount of lithium into which this carbon could dissolve, and still be determined at the detection limit of the combustion technique, is 1.5 kg. It is expected that the module will contain between 1.2 and 1.5 kg of lithium, so, by the combusion technique, it may be difficult to determine quantities of carbon above the initial concentration in the lithium. If this is true, it may be necessary to heat the samples to convert the carbon to carbide and then perform the more sensitive acetylene evolution analysis.

The most frequently used analytical technique for nitrogen is the Kjeldahl method.[24] In this procedure, a sample of lithium is dissolved in water and the nitride nitrogen is converted to ammonia, distilled off, and determined quantitatively. An average nitrogen content of 0.01% in steel will result in a release of about 5 mg of nitrogen over a year at 400°C from 5 m^2

of surface area. Again, not all of the nitrogen released will exist as lithium nitride. However, 5 mg of nitrogen in a modular lithium inventory of 12.5 kg results in a nitrogen concentration equivalent to the detection limit of this technique. This hypothetical inventory is far more than the system is expected to contain, so the levels of nitrogen in the lithium should be determinable by this technique. Although this technique is suitable for the detection of 0.5 ppm of nitrogen in lithium,[1] the recovery levels determined on 1 g samples of lithium indicate that a minimum detection limit is about 10 ppm (Table XI-B-8).[24] The Kjeldahl technique requires up to 1 g of sample.

Table XI-B-8

Recovery Levels for Nitrogen in Lithium Determined by the Kjeldahl Method[24]

Concentration of Nitrogen (as nitride) (ppm)	Recovery Level (%)
10	81
20	89.5
100	97.0
200	99.3

Sulfur and phosphorus are present in 316 stainless steel to the extent of about 0.01%. A combustion method for sulfur exists which is similar to that for carbon.[22] Similarly, phosphorus may be determined as phosphorus pentoxide converted to an aqueous solution of phosphate,[23] but the analysis is not as essential as others in profiling corrosion rates.

The lithium samples will contain trace levels of most of the metallic elements in stainless steel. The more soluble elements will contribute detectable levels of dissolved species. The less soluble elements will be present as suspended particles, dislodged from the surface of the steel by lithium flow turbulence. It is desirable to determine as many elements as possible qualitatively and the five major constituents of stainless steel quantitatively. At the same time, it is desirable to perform such analyses with as small a sample of lithium as possible. The technique most applicable to these analytical requirements is emission spectroscopy employing spark excitation.

Quantitative analysis is performed by two methods. The common technique is the use of an internal standard. However, most of the commonly used standard elements are sought-for substances in this system. Photographic detection and preparation of working curves for elements of interest is the second quantitative method.[25] The photographic emulsion is calibrated in the wavelength region of interest and curves are made relating line density to line intensity. Then standards covering the concentration region of interest are measured and a working curve drawn up. The same instrumental conditions must prevail in the measurement of standards and samples. Apart from the use of a working curve, the sample may be bracketed by two solutions whose concentrations are just above and just below the unknown concentration. The unknown concentration may be interpolated from the line intensities of the three solutions and the concentrations of the two known solutions.

The solubility of nickel is on the order of 10^{-2} atom % and that of iron and chromium in on the order of 10^{-4} atom %.[4] Molybdenum is an order of magnitude lower yet[4] and the solubility of manganese is not known. These solubilities hold when the nitrogen content is between 25 ppm and 150 ppm. At most, the levels of these metals in lithium will be in the 1 to 100 ppm range. Thus, the analysis should emphasize sensitivity in the determination of these elements.

While the techniques described above for the analysis of elements of interest are standard ones for those elements, it must be noted that, in modular experimentation, the samples to be analyzed are radioactive. We have described a fairly simple sample isolation procedure (Section XI-B-5-a). which may be automated, but it may be necessary to expand the amount of remote handling involved to include the preparation of samples for analysis. Similarly, provision must be made for the disposal of radioactive residues from the procedures. For instance, the residue of a lithium sample which is vaporized in the emission analysis of trace metal levels is radioactive. After running many samples, there is the probability of a buildup of these materials in the spark chamber if the chamber is not adequately ventilated and provision is made for the trapping of activity removed. The analyses used will involve a large degree of instrumentation. In the design of the analytical facility, attention must be given to the protection of instrumentation and personnel from exposure to the radioactivity involved in preparing and executing analyses of loop samples.

To help parametrize the loop as a whole, it will be useful to evaluate the material requirements of the loop. It is possible at this time to estimate the surface area of the loop. By evaluating the sample size required for testing and making certain assumptions, the lithium inventory of the loop and the loop surface area can be estimated. Table XI-B-9 summarizes the sample size requirements for the analyses planned for the lithium. These are based either on recommended sample sizes or on extrapolation of the capabilities of the technique to the probable sample size requirements.

Table XI-B-9

Sample Size Requirements for Analyses of Lithium Samples

Analysis	Approximate Sample Weight	Approximate Sample Volume
Oxygen	Sampled on Line	Sampled on Line
Hydrogen	Sampled on Line	Sampled on Line
Tritium	Sampled on Line	Sampled on Line
Carbon	.1 g	.83 ml
Nitrogen	.5 g	4.17 ml
Metallic Substances	.5 g	4.17 ml
Activated Substances	.4 g	3.33 ml
Nonmetallic Impurities (S,P)	Performed infrequently; can replace an occasional N determination.	
TOTAL	1.5 g	12.50 ml

If it is assumed that 100 samples are taken over the course of a 12 month test run, then the total mass of samples taken is 150 g. If it is further assumed that this will not represent more than 10% of the total lithium inventory, then the required lithium inventory of the loop is 1.5 kg or 12.5 ℓ. Assuming an average inner diameter of 2 cm for all cylindrical ductwork, the surface area contacted by lithium is about 2.5 m^2. If 1% of this is test area, the loop contains 250 cm^2 of stainless steel under irradiation (not including removable samples and contacted with lithium. This area will be of primary interest in the post-run examination of samples.

XI-B-6-b. Post-Run Sample Analysis (316 Stainless Steel Analysis)

In this section, we will discuss the analysis of samples of the material of containment. Samples of 316 stainless steel will be available to the investigator during the experimental run (Section XI-B-5). However, the larger fraction of stainless steel samples are tied up as apparatus until the run is over. The analysis of damage sustained by the containment material includes three determinations:

(1) Analysis of the distribution of activity in the loop after the run.

(2) Analysis of structural changes in the stainless steel.

(3) Analysis of chemical changes in the outermost layers of the stainless steel.

The purpose of these analyses is to complete the history of radiation damage and chemical corrosion products in the long term operation of a lithium loop in a radiation field.

Stainless steel samples are removed and prepared for analysis at different points in the experimental run. When the reactor is shut down for scheduled maintenance, removable samples are carefully withdrawn (to avoid disturbing the surface structures) to a sample preparation area. At the end of the experiment, when the loop has been drained of lithium and scanned for activity deposition, in-reactor specimens are cut from the loop to serve as a source of samples.

The distribution of activity in the loop is determined by the gamma spectrum in various parts of the loop. The analysis is made on the loop as a whole and should be performed as soon as the loop is shut down and drained of lithium so that the existence of short-lived isotopes is recorded. The analysis is

performed with the movable gamma detector described in Section XI-B-6-a-2. Pumping equipment, valves, regions of turbulent and stagnant flow and temperature zones should all be scanned for a gamma spectrum of the activity deposited therein. Taken together, these spectra provide a profile of the migration of activity in the long term operation of a lithium loop. These spectra may be taken before or after the in-reactor specimen has been removed. However, if they are taken before the in-reactor specimen is removed, the spectra are recorded closer to the shutdown time of the loop and the reactor shielding (left in place) can prevent the detection of stray radiation. The level of activity of the in-reactor specimen will be very high compared to the rest of the loop since it has been itself activated. A gamma spectrum of it would not be indicative of the deposition of activity circulating in the loop. If scanning is to be performed with the shield swung open, the detector must be more rigorously protected from stray radiation from the activated structure. In general, shielding the detector from stray radiation will be difficult depending on the physical arrangement of the loop segment to be scanned. To lessen the severity of this problem, only the shielding and insulation of the loop segment of interest should be removed during the scan. After the scan is completed, it should be replaced and the next segment exposed and scanned, and so on, until the activity is recorded in all segments of interest in the loop.

After the gamma spectrum of the loop is recorded, the loop is dismantled. Shielding is required for the protection of personnel handling the loop segments. The stainless steel samples cut from irradiated and nonirradiated portions of the loop may be handled in the air, if all macroscopic traces of lithium

are removed, but should be protected to prevent disturbance of surface deposits and structures used to compare damage between irradiated and non-irradiated portions. Structural changes in the loop are indicative of the nature of the corrosion process. A number of techniques currently available, which are both destructive and nondestructive of the sample, are capable of determining surface and internal structural changes. Techniques such as optical microscopy, scanning electron microscopy, X-ray diffraction and spectroscopy, electron microprobe analysis, and auger spectroscopy sample surface or exposed layers of atoms. The capabilities of these and other techniques are described elsewhere.[27] We will not discuss the methods involved in these techniques, but will focus on sample preparation and handling for structural analysis by these techniques of removable specimens and samples of loop containment material.

In the analysis of surface structures, care must be taken to preserve the surface in its original condition. A typical sample preparation has at its aim the preservation of microstructural, macrostructural and compositional conditions.[27] The preparation of the sample for examination involves:

(1) Cutting a sample away from the original material.

(2) Cleaning the sample in such a way as to not disturb the surface.

(3) Preserving the sample for analysis. This may include protecting the sample from the destructive effects of water, oxygen and atmospheric particulates.

It may be desirable to make a replica of the surface at this point. This is also useful in studying the surface by optical spectroscopy.[27]

Subsurface structural examination requires a more involved sample preparation technique in order to expose a representative internal surface free of surface damage. After the plane of interest is chosen and a surface exposed along this plane, the surface is ground, polished, and etched before examination. For thin section microscopy, the sample is mounted on a slide. Figure XI-B-6 and XI-B-7 show the flowchart of operations in the preparation of a surface for internal and surface structural determination, respectively.[27] At appropriate points in the preparation, the analytical techniques applicable are listed.

Overall dimensional changes in the sample are indicative of the corrosion rate if the attack is heavy and uniform.[5] Changes in weight and physical dimensions can be measured directly for the samples removed during the run. In the case of samples cut out of the in-reactor specimen, the change in thickness can be measured taking into account radiation induced swelling. By knowing the change in thickness, density of the material and percent swelling, the change in weight per unit area of material can be calculated.

The profile of radiation damage as a function of the depth of attack is obtained by layer analysis of samples of the loop containment material. Electropolishing techniques have been developed which are capable of analyzing layers of material from rods, sheets, cubes, and other simple shapes resulting in uniform layer removal and no pitting. The method described by Brehm et al.,[17] includes the calculation of the release rates of isotopes from the body of the sample based on material loss rates. It is to be noted that the release of an activated product is not determined simply by the product of the weight loss and the fractional composition of the material.

Figure XI-B-6

SAMPLE PREPARATION FOR THE EXAMINATION OF INTERNAL STRUCTURE

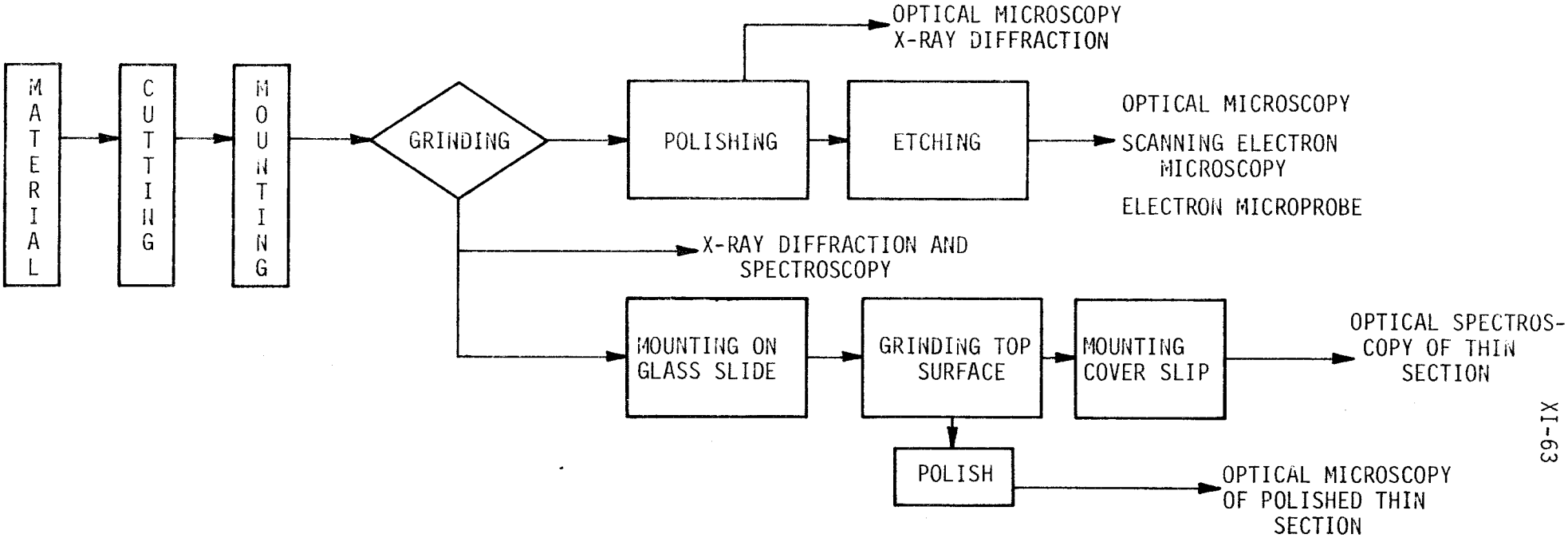

Figure XI-B-7

SAMPLE PREPARATION FOR THE EXAMINATION OF SURFACE STRUCTURE

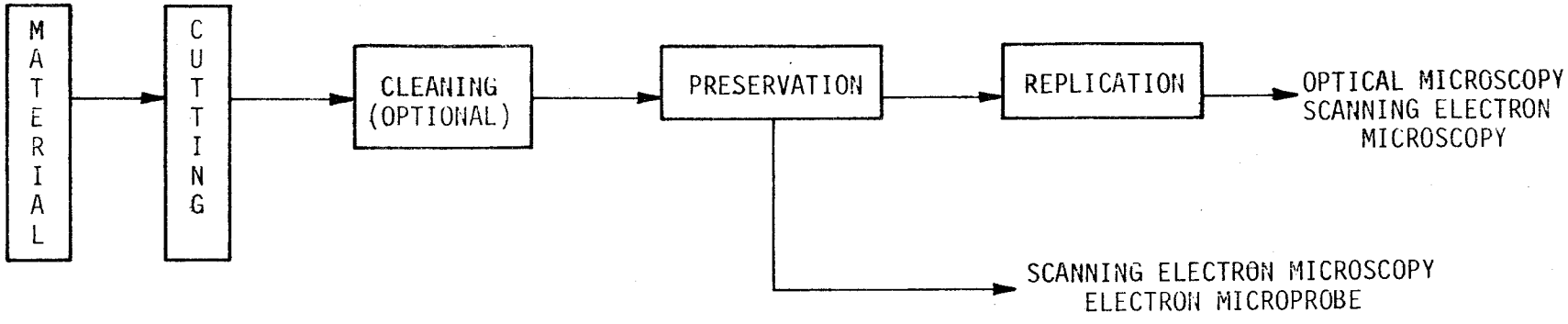

It is dependent on the solubility of the element and the tendency of the element to form compounds retained in the structure or on the surface of stainless steel. The calculational methods in (17) derive release rates from experimental quantities such as concentration and activity in the layers of the stainless steel sample.

The sample sizes required in the stainless steel analysis are small. The main consideration in the microscopic technique will be ease of handling. For layer analysis, an area of about 1 cm^2 is required. The thickness of the sample is determined by the probable corrosion rate over the course of the experiment. At a temperature of 400°C, the approximate corrosion rate is 1.6 microns/yr.[10] A useful sample thickness for the wall of the loop would be 1 mm which would suffer a 0.16% loss due to corrosion. To make the samples flexible enough to remove from the reactor easily, the thickness of the removable sample may be 0.1 mm to 0.4 mm. These samples would still suffer less than one percent loss due to corrosion. As chemical etching will alter the composition of the outermost layers of the sample, different samples should be used for surface, subsurface and layer analysis.

XI-B-6-c. Summary; Sample Examination Techniques

Figure XI-B-8 summarizes the operation performed on the samples available from the liquid lithium loop. In a closed system such as this, it should be possible to determine sources and repositories of the elements subject to

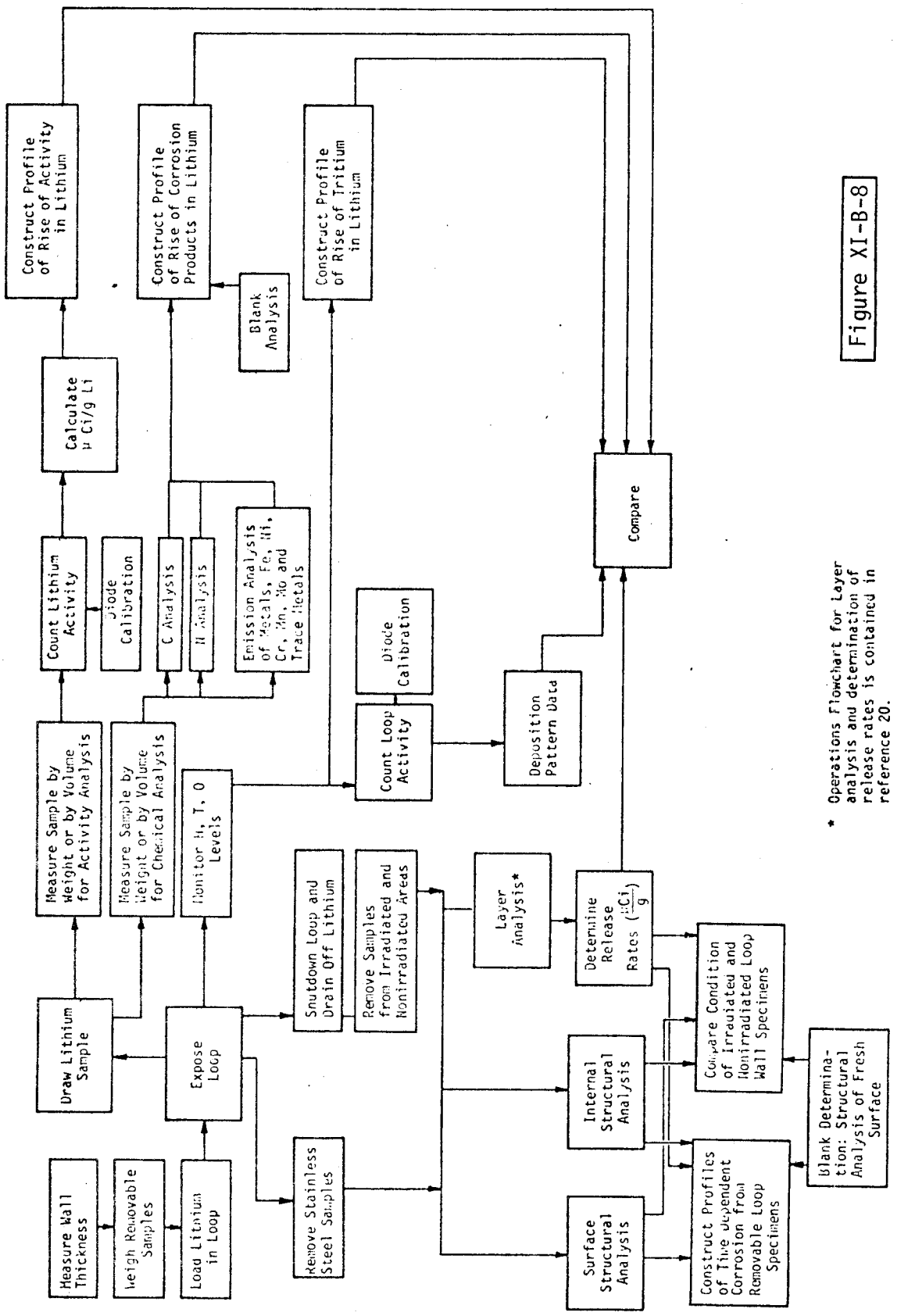

Figure XI-B-8

* Operations Flowchart for Layer analysis and determination of release rates is contained in reference 20.

liquid lithium corrosion. By comparing the release rates of elements from the stainless steel, the deposition patterns of activity in the loop and the levels of impurities in the lithium itself over a long period of time, it should be possible to more completely predict the condition of a lithium breeder/coolant system over long term operation in a fusion reactor.

XI-B-7. Lithium Loop Procedures

XI-B-7-a. Startup Procedures in the Lithium Loop

In this section, we will summarize the procedures involved in the startup of an experiment in the liquid lithium loop. Many of the procedures have been outlined in conjunction with various subsystems of the loop such as temperature control or sample taking. In this section, we will review these procedures and give an overview of an experimental run.

When loop construction reaches the point where the apparatus includes electromagnetic pumping and flowmeter equipment, temperature control apparatus (both in and out of the reactor), heat exchanger, monitoring equipment for hydrogen, tritium and oxygen, the sampling system, the inert atmosphere box containing the sampling system and the fixed gamma detector, and the shielding and heating elements are in place, the loop is ready to function as an experimental apparatus for the study of long term liquid lithium corrosion. It is assumed that at this point the necessary instrumentation has been tested and all required calibration procedures have been performed for the counting and temperature control systems.

All of the loop surfaces which will contact lithium, especially those which will act as test specimens, must be clean. The loop must be free of

contamination, especially air. The inner surfaces of the ductwork may be chemically cleaned and polished before fabrication into the loop. The removable test specimens are also cleaned and polished and initial weight and dimensional data recorded before insertion into the in-reactor section of the loop. The loop must be leak tight. The loop may either be pressurized with inert gas or evacuated to detect leaks. The loop may then be flushed extensively with an inert gas to purge the system of atmospheric oxygen and nitrogen. After leak testing and purging, the sealed loop is ready for charging with lithium and the shield to the reactor may then be swung back into place.

Commercially obtainable lithium contains many elemental impurities. In the UWMAK-I study,[10] lithium cleanup procedures consist of filtration at 205°C (M.P. of lithium: 180°C) followed by hot trapping at 870°C. Impurity levels are reduced as listed in Table XI-B-10. A purification procedure of this type should be performed on the loop lithium followed by a precise elemental analysis to determine baseline impurity levels.

Finally, the loop is flushed with purified lithium for several hours at the operating temperature and drained as a cleanup of the inner surfaces of the loop which will contact lithium in the experiment. The cleanup lithium may be stored for purification and recycle. The loop is then charged with lithium, brought to temperature and circulated before the reactor is brought up.

XI-B-7-b. In-Run Procedures

The experimental procedures during a run consist of those associated with temperature control and sample taking and have been described previously (Sections

Table XI-B-10

Influence of Purification Techniques on Lithium Purity[10]

(wt ppm of impurity)

IDENTITY	N	O	C	Ag	Al	B	Be	Ca	Cb	Co	Cr	Cu	Fe	Mg	Mn	Mo	Na	Ni	Pb	Si	Sn	Ti	V	Zr
LITHIUM AS-RECEIVED[a]	835	130	149	<5	<5	-	<5	135	<25	<5	<5	<5	<5	5	<5	<5	55	<5	<25	5	<25	<5	<25	<5
LITHIUM AS-RECEIVED AFTER FILTRATION	791	155	99	<5	<5	-	<5	55	<25	<5	<5	<5	5	<5	<5	5	<135	<5	<25	5	<25	<5	<25	<5
LITHIUM AFTER HOT TRAPPING 280 HOURS AT 1500°F	<10	-	25	<5	<5	<55	<5	5	<25	<5	<5	55	5	5	<25	<5	55	5	<25	5	<25	5	<25	<25

(a) American Producers: Foote Mineral
Lithium Corp.
Maywood Chemical

XI-B-4 and XI-B-5). Periodically, the levels of hydrogen and oxygen should be recorded. Over the course of a twelve month experiment, one to two readings per month should suffice to indicate conditions in the loop. The rise of tritium should be monitored frequently. If it is convenient, in the initial stages of the experiment, readings should be taken every 100 hours (about 4 days) and may be taken less frequently later in the experiment.

With an estimated minimum sample size requirement of 1.5 g of lithium and an estimated 150 g of lithium allowed for all analyses throughout the experiment, as many as 100 samples of lithium may be taken. If an additional 0.5 g is allowed for procedural error, the total number of samples which may be taken over a twelve month experiment is reduced to 75. A sampling schedule may be constructed as described in Table XI-B-11. Of 75 samples, the first twenty are taken every two days that the reactor is running, the second twenty are taken every four days, the third twenty are taken every six days and the final 15 are taken every eight days. This schedule represents a 360 day experiment. The schedule may be adjusted as desired for longer or shorter experiments. In the schedule of analyses to be performed is allowance for a regular determination of inactive nonmetals such as sulfur and phosphorus. The experimental design allows a fairly generous amount of lithium for analysis, so the length of the experiment is flexible depending on the actual amount of lithium required for each analysis and the desired sampling interval.

Table XI-B-11

Proposed Sampling Schedule for a 360 Day Experiment

Sample Number	Days Into The Experiment	Activated Products	Analysis to be Performed: Metals	Nitrogen	Carbon	Sulfur	Phosphoru
Unit I: Sample Taken Every Two Days							
1-4	0-8	X	X	X	X		
5	10	X	X			X	X
6-9	12-18	X	X	X	X		
10	20	X	X			X	X
11-14	22-28	X	X	X	X		
15	30	X	X			X	X
16-19	32-38	X	X	X	X		
20	40	X	X			X	X
Unit II: Sample Taken Every Four Days							
21-24	44-56	X	X	X	X		
25	60	X	X			X	X
26-29	64-76	X	X	X	X		
30	80	X	X			X	X
31-34	84-96	X	X	X	X		
35	100	X	X			X	X
36-39	104-116	X	X	X	X		
40	120	X	X			X	X
Unit III: Sample Taken Every Six Days							
41-44	124-144	X	X	X	X		
45	150	X	X			X	X
46-49	156-174	X	X	X	X		
50	180	X	X			X	X
51-54	186-204	X	X	X	X		
55	210	X	X			X	X
56-59	216-234	X	X	X	X		
60	240	X	X			X	X
Unit IV: Sample Taken Every Eight Days							
61-64	244-272	X	X	X	X		
65	280	X	X			X	X
66-69	288-312	X	X	X	X		
70	320	X	X			X	X
71-74	328-352	X	X	X	X		
75	360	X	X			X	X

The disadvantage of long term experimentation is that, by definition, such experimentation does not yield data at an efficient rate. In the interest of attaining the highest efficiency possible in running long term experiments of this type, it is suggested that the operation of one experiment and the construction of the apparatus for a second overlap. The second experiment may involve running stainless steel at an alternative temperature or running an alternative alloy altogether. Putting this procedure into effect, of course, will be dependent on the availability of personnel for the experiment.

XI-B-7-c. Loop Shutdown Procedures

The shutdown of the lithium loop will involve the handling of activated material either in irradiated stainless steel or in the lithium inventory of the loop. In all shutdown procedures, care must be taken to shield personnel involved with the experiment from such activity. The lithium is drained, at temperature, into a holding tank after shutdown of pumping. It should be drained at temperature to avoid precipitation of impuritites on areas of stainless steel which may be used for analysis, thus biasing the results of solid sample studies. Tritium accumulated in the lithium should be extracted by gettering with yttrium as the first step in lithium recycle. The tritium thus obtained may be put to other uses. As yttrium carbide and yttrium oxide are both more stable than the corresponding lithium compounds, there may be some interference due to carbon and oxygen gettering by the yttrium. The tritium remaining in the lithium may be determined by the level

of characteristic β activity. However, with an excess of yttrium, there should be little difficulty in removing the tritium from the lithium. The lithium inventory may then be subjected to the same filtration/hot trapping purification sequence described earlier with extra attention given to the disposal of filtering and hot trapping materials. The level of activity in the lithium should be reduced to background in this process. If it is not, more rigorous purification techniques (such as distillation) may be required.

After the loop is drained and the ductwork has been scanned for a gamma spectrum, the loop may be dismantled. The irradiated stainless steel specimen is first cut from the in-reactor ductwork and removed to a shielded area. Steel samples for analysis may then be cut from the irradiated specimens. Much of this step may be handled remotely.

The rest of the loop is dismantled and the functioning subsystems cleaned and examined for damage and activity levels. Equipment contacting lithium such as heat exchanger surfaces, pumping equipment, flowmeter, and impurity monitor membranes is to be retained for reuse but cleaned and checked for lithium damage and deposited activity. Damage to tritium, hydrogen and oxygen monitor membranes is assessed and they are examined to see if they are to receive continued use. The surfaces which are to contact lithium may require polishing to remove damage.

The remaining portion of the loop apparatus is stainless steel ductwork. It may be desirable to retain some of the ductwork for analysis of nonirradiated samples. But, in the main, these materials must be disposed of according to the level of activity in the steel. The ductwork which passes through the blanket and shield and behind the first wall may be expected to have a fairly high activity. The ductwork which lies outside of the reactor may be only slightly activated and contain only the activity deposited there by the lithium. Some of this activity may be cleaned away and disposed of in a liquid form. The steel left behind may then be sufficiently deactivated to be disposed of without special precautions. The irradiated steel, however, must be packaged for burial as an activated material.

Finally, a profile of lithium corrosion effects is constructed from the data.

XI-B-8. Alternative Studies in the Liquid Lithium Loop

We have discussed the design of an experiment to examine long term radiation effects on the operation of a liquid lithium loop in stainless steel. However, the basic concept of the test module is flexibility. It is desirable to have a module capable of testing corrosion effects on many different materials. The elements of the module described in this section are not constrained by the fact that stainless steel is the material of fabrication. Stainless steel was chosen for other reasons, primarily its importance to CTR design in general. The elements of the module were chosen so as to maintain simplicity of design. This simplicity permits the use of other, less easily fabricated materials as test specimens in the module. 316 stainless steel will be of great importance in near-term CTR design. However, since 316 stainless steel will not withstand structural temperatures greater than 500°C and since 316 stainless steel suffers from a high level of induced radioactivity other structural alloys should be investigated as materials of construction.

After stainless steel, three other alloys to be considered in a lithium corrosion study are TZM, V-20Ti and Nb-1Zr, the three alternative materials considered initially for this study. The temperature range may be greatly broadened as may the duration of the experiment. The use of TZM or Nb-1Zr in CTR design permits the use of higher operating temperatures and, while known to be resistant to lithium corrosion, radiation damage effects may be found to affect their suitability for use in a liquid lithium environment.

A second group of materials which may be considered for lithium corrosion studies are those which will not become highly alleviated in a CTR environment.

Alloys containing little or no nickel or molybdenum will have lower levels of activity than does stainless steel. Titanium-vanadium-aluminum alloys also produce less long-lived radioisotopes than stainless steel and should be examined for their long term compatibility with liquid lithium.

There are many alloys worth investigating which have the advantage over stainless steel either of higher allowable temperatures or lower afterheat. A complete program of investigation of lithium corrosion/radiation damage properties of these materials would be a useful adjunct to the study of the interaction of radiation effects with liquid lithium corrosion of stainless steel.

XI-C Solid Lithium Compounds: Modular Experimentation

XI-C-1) Introduction

Solid lithium compounds offer an alternative to breeding tritium in liquid lithium. Certain solid lithium compounds such as the oxide-bearing ceramics, intermetallics and salts have begun to be investigated as possible tritium breeding species. In this section, we will examine the use of various solid lithium compounds as tritium breeding materials. We will consider those properties which favor certain compounds over others and the properties of tritium diffusion in these materials. Finally we will examine the possible chemical consequences of the removal of a significant fraction of lithium atoms from these materials due to reactions with neutrons.

The primary advantage of the use of solid lithium compounds over the use of liquid lithium in CTR blanket design is the elimination of the danger of handling liquid metals. To be useful, however, the breeding material must be chemically stable for prolonged periods at elevated temperatures. The properties of tritium permeation must not change over time, as well. This is to say that the material cannot sinter noticably. In addition, the lithium atom density must be high enough to ensure a breeding ratio greater than one with a neutron multiplier, if one is needed.

A. B. Johnson, et al.,[28] have summarized extensive studies of the suitability of various lithium compounds for use as solid breeding materials in the Hanford Coproduct Program. The compounds considered have melting points above 250°C and lithium atom densities greater than

0.1 g/cc. In this program, the use of a neutron multiplier was not considered and the compounds chosen for use had melting points above 1000°C as the maximum transient temperature of the reactor was around 830°C. Organic compounds were excluded for lack of stability under irradiation and intermetallics, with the exception of Li_3Sb and Li_3Bi, were excluded for lack of fundamental information.

Tables XI-C-1, XI-C-2 and XI-C-3[28] summarize the fundamental physical properties of the twenty-eight compounds considered for use in the Hanford Coproduct Program. Many were eliminated for further consideration in this program on the basis of fundamental material properties: high aqueous solubility, vapor pressure, dangerous side reactions or companion atoms in the compound with high neutron cross sections. The compounds eliminated at this stage may not necessarily be unsuitable for any use in CTR blanket design but were only judged unsuitable for use in the N reactor involved in this study. Table XI-C-4 summarizes the compounds eliminated and the reasons for their unsuitability. Most of those eliminated suffered from undesirable side reactions or high vapor pressures. The remaining compounds, which were found to be suitable, included lithium oxide and the lithium aluminates, silicates, and aluminosilicates.

Table XI-C-1 - Lithium Compounds[28]

Compound	ρ g/cc	ρ Li^6 g/cc	ρ Li g/cc	Structure	mol. wt.
LiCl	2.068	0.0218	0.340	Cubic (NaCl)	42.40
LiBr	3.464	0.0178	0.277	Cubic (NaCl)	86.86
LiF	2.601	0.0447	0.696	Cubic (NaCl)	25.94
LiI	4.061	0.0136	0.212	Cubic (NaCl)	133.86
$LiNO_3$	2.38	0.0152	0.237		68.95
Li_2CO_3	2.111	0.0256	0.398		73.89
Li_3N	1.30	0.0498	0.775	Hexagonal	34.83
Li_2O	2.013	0.0599	0.931	FCC	29.88
$LiAlO_2$	2.55	0.0172	0.268	Rhombohedral (LT) Tetragonal (HT)	65.91
$LiAl_5O_8$	3.61	0.00605	0.094	Cubic (LT) Spinel (HT)	269.54
Li_2SiO_3	2.52	0.0229	0.356		89.94
Li_2TiO_3	~2.6	0.0212	0.330	Cubic (NaCl)	109.8
$Li_2O \cdot Al_2O_3 \cdot 4SiO_2$	~2.5	0.00714	0.111	Derivative quartz	372.3
$Li_2O \cdot Al_2O_3 \cdot 2SiO_2$	~2.5	0.00894	0.139	High quartz	252.1
$Li_2O \cdot 2SiO_2$	~2.5	0.0150	0.233		150.1
$2Li_2O \cdot SiO_2$	2.33	0.0347	0.540		119.90
$Li_2O \cdot B_2O_3$ ($LiBO_2$)	~2.2	0.0197	0.307		49.75
Li_2SO_4	2.22	0.0180	0.280		109.94
Li_2C_2	1.65	0.0452	0.0392		37.9
$LiSO_3F$	2.3 (?)	0.0113	0.00977		106
$LiGaN_2$	3.35	0.0168	0.0145		118.36
LiH	0.78	0.0508	0.0441		7.95
Li_2MoO_4	2.3 (?)	0.01035- 0.01556	0.161- 0.242	Tetragonal prisms	173.83
Li_2WO_4	(?)	(?)	(?)	Trigonal	261.8
Li_2GeO_3	3.53	0.0118	0.184	Monoclinic	134.48
LiOH	1.43	0.0269	0.418	Tetragonal	23.95
Li_3PO_4	2.54	0.0296	0.46	Rhombohedral	115.80
$Li_3Na_3(AlF^6)$	2.80	0.0102	0.158	Cubic	371.75

Table XI-C-2 - Lithium Compounds[28]

Compound	MP, °C	BP, °C	C cal/mole°C	Solubility
LiCl	614	1352	12.20	v soluble hygroscopic
LiBr	552	1310	-	v soluble
LiF	840	1681	2.59	insoluble
LiI	440	1171	-	v soluble
$LiNO_3$	254	-	26.65 (210°C)	v soluble
Li_2CO_3	735	d 1200	23.28	moderately soluble
Li_3N	856	-	-	decomposes
Li_2O	1427	1527	24 (25°C) 8,892 (200°C) 2,497 (100°C)	hygroscopic soluble
$LiAlO_2$	1610	-	-	insoluble
$LiAl_5O_8$	1950	-	-	prob. insoluble
Li_2SiO_3	1201	-	-	decomposes in hot H_2O
Li_2TiO_3	1520-1564	-	-	unknown
$Li_2O \cdot Al_2O_3 \cdot 4SiO_2$	~1420	-	-	prob. less soluble than Li_2SiO_3
$Li_2O \cdot Al_2O_3 \cdot 2SiO_2$	~1390	-	-	prob. much less soluble than Li_2SiO_3
$Li_2O \cdot 2SiO_2$	~1033	-	-	prob. decomposes
$2Li_2O \cdot SiO_2$	1250	-	-	hot H_2O decomposes
$LiBO_2$	846	d 1200	-	possibly decomposes
Li_2SO_4	859	-	-	v soluble
Li_2C_2	decomposes		-	reacts
$LiSO_3F$	360	-	-	very soluble
LiGaN2	800	-	-	decomposes
LiH	688		8,200 at 0°C 13,500 at 527°C	decomposes to LiOH + H_2(g)
Li_2MoO_4	705	-	-	hygroscopic
Li_2WO_4	742	-	-	very soluble
Li_2GeO_3	1239	-	-	slightly soluble
LiOH	450	925	1900	soluble
Li_3PO_4	837	-	-	slightly soluble
$Li_3Na_3(AlF_6)_2$	710	-	-	slightly soluble

Table XI-C-3 - Lithium Compounds[28]

Compound	Coeff. of linear Ex. α cm/cm	k	From the elements ΔH°,K cal/mole	ΔG or S°
LiCl	-	-	-97.70	-91.9 (ΔG°) (25°C) 13.9 (ΔS°)
LiBr	-	-	-87.40	-80.7 (27°C) (ΔG°)
LiF	-	-	-145.6	(ΔS°) 8.5 (25°C) (ΔG°) -138.7 (25°C)
LiI	-	-	-65.0 or -72.5	(ΔG°) -66.8 (25°C)
$LiNO_3$	-	-	115.28	-
Li_2CO_3	-	-	-290.54	21.60 (ΔS°)
Li_3N	-	-	-47.5	-
Li_2O	-	-	-142.4	(25°C) 9.06 (ΔS°) (25°C)-133.8
$LiAlO_2$	12.4×10^{-6} (25-1000°C)	-	-284.33	-269.49 (ΔG°)
$LiAl_5O_8$	8.2×10^{-6} (25-1000°C)	-	-	-
Li_2SiO_3	-	-	376.7	-
Li_2TiO_3	-	-	-399.2 (300°K) -396.1 (1500°K)	(ΔG°)-377.7 (300°K) -288.3 (1500°K)
$LiO{\cdot}Al_2O_3 {\cdot}4SiO_2$	0.9×10^{-6} (0-1000°C)	-	-	-
$Li_2O{\cdot}Al_2O_3 {\cdot}2SiO_2$	-6.5×10^{-6} (0-1000°C) -8.6×10^{-6} (0-600°C)	-	-	-
$Li_2O{\cdot}2SiO_2$	-	-	-	-
$2Li_2O{\cdot}SiO_2$	-	-	-	-
$LiBO_2$	-	-	-	-
Li_2SO_4	-	-	342.8	-
Li_2C_2	-	-	-	-
$LiSO_3F$	-	-	-	-
$LiGaN_2$	-	-	-	-
LiH	-	-	21.34	(ΔS°) 5.9 cal/mole°C at 25°C
Li_2MoO_4	-	-	-	-
Li_2WO_4	-	-	-	-
Li_2GeO_3	-	-	-	-
LiOH	-	-	105.13	(ΔS°)12.8 cal/mole°C)
Li_3PO_4	-	-	-	-
$Li_3Na_3 (A_2F_6)_2$	-	-	-	-

Table XI-C-4

Lithium Compounds Unsuitable for Use in the Hanford Coproduct Program[28]

Compound	Reason Rejected
LiCl	High vapor pressure and aqueous solubility, low melting point
LiBr	High vapor pressure and aqueous solubility, low melting point
LiI	High vapor pressure and aqueous solubility, low melting point
LiF	Presence of fluoride creates the danger of rapid chemical reaction or corrosion, also rejected for same reasons as LiCl.
$LiNO_3$	Unstable - decomposes with the liberation of O_2 and NO_x at operating temperatures.
Li_2CO_3	Oxidizes Al at operating temperatures, decomposes past the melting point (735°C) to Li_2O and CO_2.
Li_2SO_4	High aqueous solubility and unknown vapor pressures
Li_3N	Decomposes, reacts violently with H_2O
Li_2C_2	Dissociates to graphite and lithium on heating, reacts with H_2O.
$LiSO_3F$	Low m.p., high aqueous solubility, contains fluorine
$LiGaN_2$	Decomposes at 800°C, high neutron absorption cross section for gallium (30 barns)
LiH	Decomposes at 850°C and reacts with H_2O
$LiMoO_4$,Li_2WO_4	Low m.p., high aqueous solubility, high nuclear cross section due to Mo and W.
Li_2GeO_3	Ge has a high neutron cross section and is very expensive.

Compound	Reason Rejected
LiOH	Corrosive at high temperatures, low melting point. decomposes to Li_2O and H_2O near 1000°C.
Li_3PO_4	Molten at 837°C, somewhat below the maximum transient temperature for the N reactor. Otherwise suitable
$Li_3Na_3(AlF_6)_2$	Low m.p., presence of fluorine.
Li_2TiO_3	High neutron cross section of titanium (5.8 Barns) compared to Al or Si high material cost for Ti.
$LiBO_2$	High neutron cross section for boron (755 barns)

The lithium aluminates have been studied extensively in the Hanford and other programs[27] as breeding materials. The lithium aluminate, $LiAlO_2$, may be viewed as the addition compound resulting from one mole of lithium oxide and one mole of aluminum oxide. The lithium aluminate, $LiAl_5O_8$, is the result of the addition of two moles of aluminum oxide to one mole of the lower aluminate, $LiAlO_2$. The Li_2O-Al_2O_3 phase diagram (Figure XI-C-1)[28] shows that both aluminates coexist up to 80 mole % of aluminum oxide and that both undergo transformation reactions. The order-disorder reaction of $LiAl_5O_8$ takes place at 1300°C and is of no real importance since it takes place at temperatures far above those expected in practical use and since the reaction involves volume changes of less than 1% between the two forms of $LiAl_5O_8$. The phase transformation between the α and γ forms of $LiAlO_2$ involves a molar volume change of about 30% ($V_m(\alpha)$ = 32.205 $\mathring{A}^3$, $V_m(\gamma)$ = 42.775 $\mathring{A}^3$).[28] Fortunately, the correct Angstro- units transformation is effected essentially irreversibly at 900°C. Thus, if $LiAlO_2$ is synthesized at temperatures greater than 900°C before use in a reactor, this reaction should not subsequently occur and no expansion problems should result. The coefficients of thermal expansion of the two aluminates are of the same order of magnitude, with that of $LiAl_5O_8$ being about 30% lower than that of $LiAlO_2$ (see Table XI-C-3). Allowances for thermal expansion should be made in the design of containers for these materials. The tritium retention properties of the two aluminates should be similar and on the order of that of aluminium oxide (~10^{-7} to 5 x 10^{-9} cm^2/sec at 900° C).[28] The retention time for tritium in the aluminates should be correspondingly low. The major drawback to the

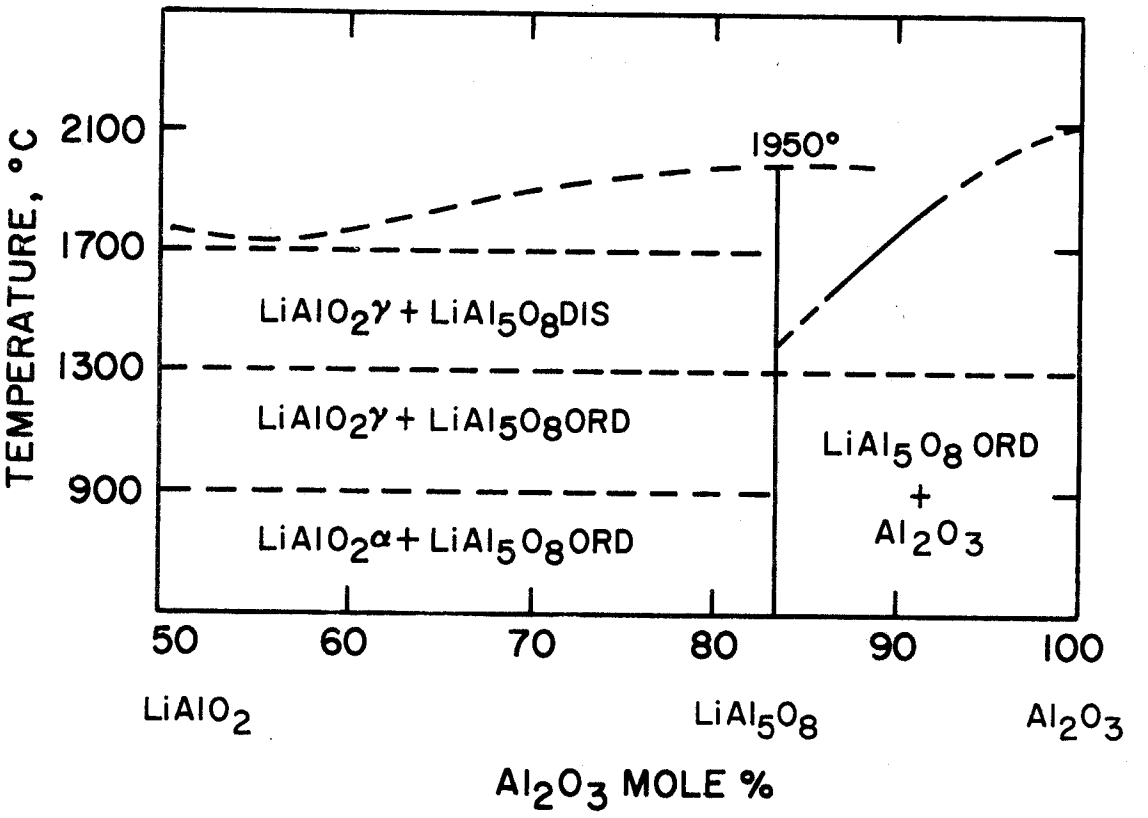

FIGURE XI-C-1. $LiAlO_2 - Al_2O_3$ PHASE DIAGRAM

use of $LiAl_5O_8$ is its low (0.094 g/cc) lithium density compared to that of $LiAlO_2$ (0.268 g/cc).

The lithium silicates have high lithium densities, but, on the whole, possess properties which render them less suitable than the aluminates for use as breeding materials. The melting point of Li_2SiO_3 is lower than that of $LiAlO_2$, suggesting that the vapor pressure of the silicate is probably less than that of the aluminate. The phase diagram [28] (Figure XI-C-2) indicates the existence of a low silicate compound ($2\ Li_2O{\cdot}SiO_2$ or Li_4SiO_4) and a high silicate compound ($Li_2O{\cdot}2SiO_2$ or $Li_2Si_2O_5$). Both of these are likely to decompose in water because the compound of intermediate composition ($Li_2O{\cdot}SiO_2$ or Li_2SiO_3) and Li_2O itself react with water. Additionally, the silicates are thought to be corrosive at high temperatures. (>1000°C)

The two lithium aluminosilicate compounds of interest are of composition $Li_2O{\cdot}Al_2O_3{\cdot}2SiO_2$ and $Li_2O{\cdot}Al_2O_5{\cdot}4SiO_2$. Their melting points, vapor pressures and aqueous solubilities would be expected to be intermediate to those of the aluminates and silicates and lie closest to the properties of the compound which the aluminosilicate resembles more closely in composition. The unusual feature of the aluminosilicate, $Li_2O{\cdot}Al_2O_3{\cdot}2SiO_2$ is its negative coefficient of thermal expansion ($-6.5 \times 10^{-6}{}^{\circ}C^{-1}$)[28]. The compound of composition $Li_2O{\cdot}Al_2O_3{\cdot}3SiO_2$, which exists in the solid solution region between the 1:1:2 and 1:1:4 compositions has a coefficient of thermal expansion of $-0.9 \times 10^{-6}{}^{\circ}C^{-1}$. For use as a breeding material, the amounts of $Li_2O{\cdot}Al_2O_3{\cdot}2\ SiO_2$ and $Li_2O{\cdot}Al_2O_3{\cdot}4SiO_2$ can be varied to control thermal expansion in the material.

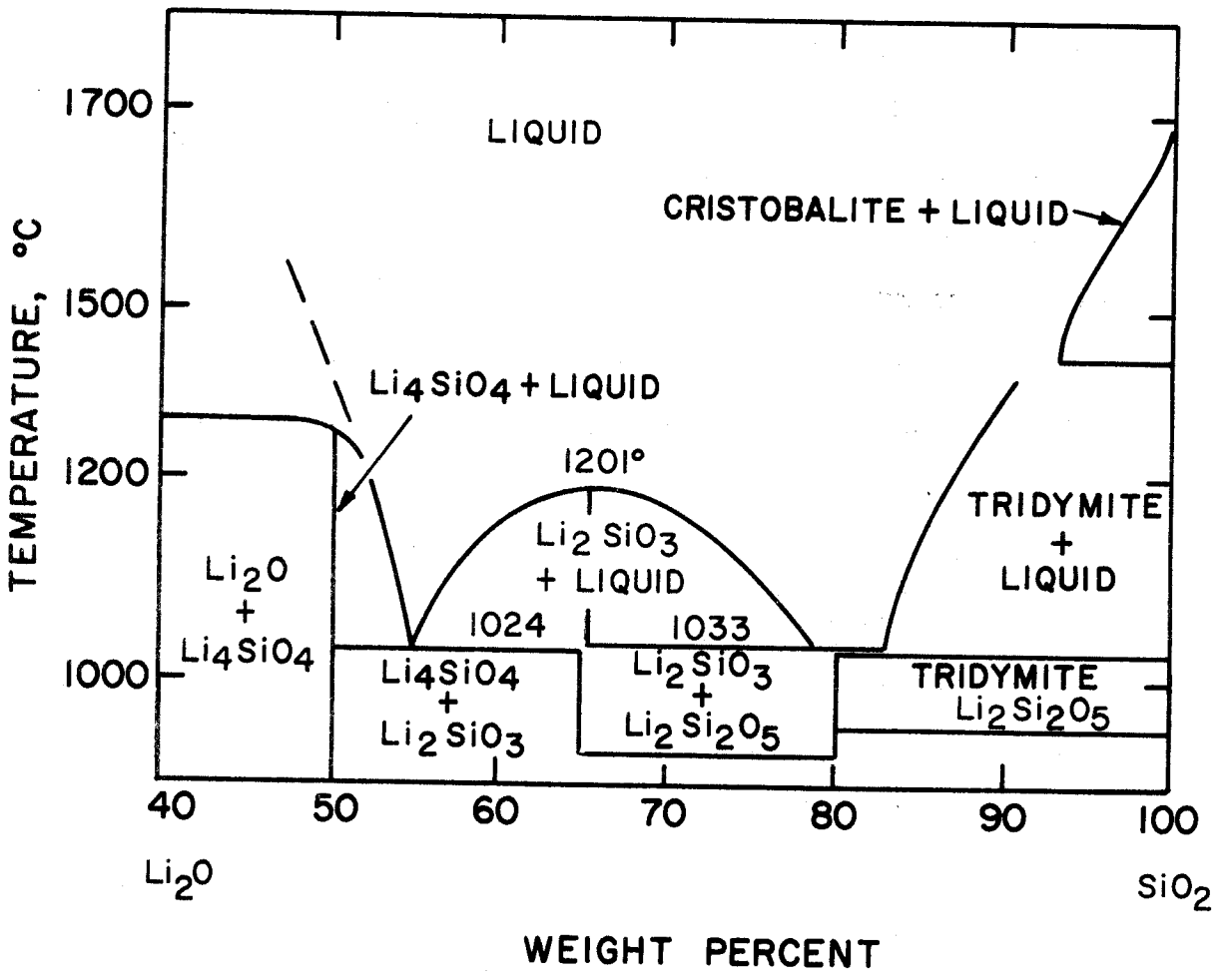

FIGURE XI-C-2. $SiO_2 - 2Li_2O \cdot SiO_2$ PHASE DIAGRAM

The two aluminosilicates have low lithium densities (ρLi = 0.139 g/cc for $Li_2O \cdot Al_2O_3 \cdot 2SiO_2$ and ρLi = 0.11 g/cc for $Li_2O \cdot Al_2O_3 \cdot 4SiO_2$.

Lithium oxide has a very high lithium denisty, 0.931 g/cc, and is very refractory and thermally stable. The melting point lies in the 1427°C to 1827°C range and the boiling point, subject to disagreement, has been reported as 1527°C and 2600°C. Sublimation occurs in the 800°C to 1000°C range. Finely divided lithium oxide is very soluble in water, but the rates of solution observed are variable depending on the state of subdivision and level of impurities. It is doubtful that pure lithium oxide, uncontaminated by lithium hydroxide, the product of the reaction of lithium oxide and water, has ever been prepared. Lithium hydroxide has a higher vapor pressure than lithium oxide, so the presence of any water will enhance the apparent vapor pressure of the oxide due to the presence of lithium hydroxide vapor. Herein lies the probable source of the ambiguity in the fundamental physical properties of lithium oxide. Figure XI-C-3 shows the vapor pressure of lithium oxide species in the presence of water. These curves were calculated from the thermo chemical data of the JANAF tables.[29] At high temperatures (>1000°C), lithium oxide is corrosive, attacking metals and oxides, including aluminum. Aluminum reduces lithium oxide at these temperatures. At lower operating temperatures, however, these reactions can be controlled such that lithium oxide should prove suitable for use as a breeding material.

A group of compounds not considered for the Hanford Coproduct Program are the intermetallic compounds lithium lead; Li_7Pb_2 (m.p. 726°C) lithium tin; Li_4Sn (m.p. 765°C), lithium silicon; Li_4Si (m.p. 635°C), and lithium

Figure XI-C-3

Vapor Pressure of Li_2O Containing .1% H_2O

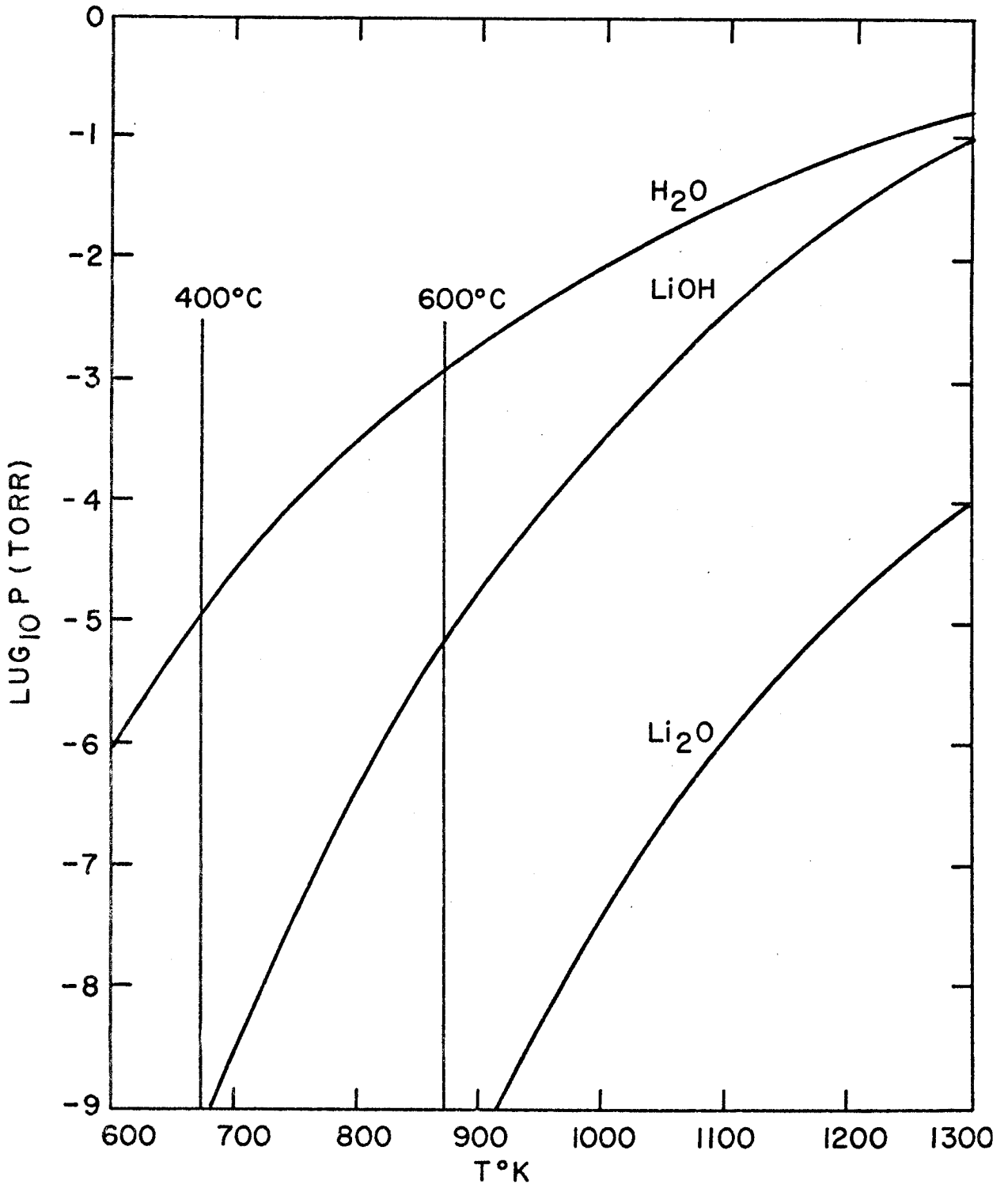

aluminum; LiAl (m.p. 718°C).[28] Little is known of these compounds with respect to vapor pressures, tritium retentivity, sintering, or tendency to decompose. All react slowly with air. One advantage of Li_7Pb_2 and Li_3Bi, mentioned earlier, is that they carry, in Pb and Bi, internal neutron multipliers. However, with little else known of these compounds, it is difficult to judge their suitability for use in a fusion reactor design.

The foregoing is intended as a brief review of the range of lithium compounds considered for solid breeding materials. Most can be eliminated on the basis of undesirable physical properties such as high vapor pressures or high aqueous solubilities or due to the existence of undesirable side reactions. The most promising materials are the lithium aluminates, silicates and aluminosilicates, and lithium oxide. If any of these are to be considered further, the properties of these materials in an irradiated blanket environment must be considered: tritium production and consequent evolution from the material, the chemical form of the tritium species evolved, the need for neutron multipliers, the effect of the particular breeder on tritium inventories, the effect of the containment material on the tritium species evolved, and possible consequences of extensive lithium burnup on the properties of the breeder.

Tritium is produced by the $^6Li(n,\alpha)T$ and $^7Li\ (n,n'\alpha)T$ reactions. In a solid lithium compound, T^+ ions are produced. Two release modes must be considered for tritium produced from irradiated solids; thermal diffusions and recoil ejection.[28] Tritium released by recoil ejection is likely to result in the release of HT or T_2 species (with accompanying O_2) depending on the level of water impurities. Tritium released from oxide-bearing ceramics

by thermal diffusion is likely to evolve as T_2O or HTO. Tritium release may be controlled either by diffusion in the solid or by the equilibrium between the concentration of tritium in the solid and the partial pressure of tritium over the solid. In this case, diffusion in the solid is assumed to be fast by comparison to exchange of tritium in the solid to tritium vapor resulting in a zero concentration gradient in the solid. Experiments have been performed [7, 30] which indicate that diffusion in the solid is the rate controlling step in the release of tritium from lithium aluminate and silicate. For diffusion controlled release, the holdup time is related to the particle size and the diffusion coefficient as follows:

$$\tau_T = \frac{r_p^2}{15\ D} \text{ (sec)}$$

Where τ_T = tritium retention time (sec)

r_p = particle radius (cm)

D = diffusion coefficient (cm^2/sec)

For use as breeding materials, the oxide-bearing ceramics of lithium must be capable of sustaining breeding ratios greater than one. Studies have shown [7] that the lithium content of these ceramics is not high enough in the aluminates, silicates and aluminosilicates to achieve sustaining breeding ratios without a neutron multiplier. Lithium oxide should not require a neutron multiplier due to its very high lithium content. Neutron multipliers may be refractory compounds of beryllium (BeO or Be_2C), lead (PbO or PbS), or bismuth (BiS or Bi_2O_3). Should beryllium prove to be resource limited, lead or bismuth compounds would be the materials of choice, although the long term radioactivity of these compounds may be an undesirable side effect.

If good breeding can be achieved through the use of either lithium oxide alone or one of the other ceramics and a neutron multiplier, it is expected that the tritium inventory of such a ceramic blanket would be low due to the low tritium retentivity of the ceramics. The tritium inventory is related to the holdup time by the following:[7]

$$I_T = 3 \times 10^4 \tau_t \frac{P_o(BR)}{Q N_o}$$

where I_T = inventory of tritium (curies)

τ_T = holdup time (sec)

P_o = reactor power (watts)

BR = breeding ratio (T atoms in blanket/ T atoms burnt)

Q = total energy per DT fusion (joules)

N_o = Avogadro's number

For a 2500 $MW_{(th)}$ reactor with a breeding ratio of 1.0 and 20 MeV DT fusions, holdup time of less than one hour can result in tritium inventories of less than 15g (Figure XI-C-4).[7] If the release rates of tritium in solid lithium compounds are controlled by equilibrium processes, higher blanket inventories (~0.2 kg of tritium) can result if natural lithium is used and if Sieverts' constant for the material is low (~10^4 torr/atom fraction). However, equilibrium controlled release seems to hold primarily for lithium intermetallics, for which the Sieverts' constants tend to be orders of magnitude higher. Thus even with solid intermetallics, where tritium release tends to be equilibrium controlled, small blanket inventories can be achieved.

We have said that tritium released from the solid ceramic breeding material may be in the form of either the condensible HTO or T_2O, or the noncondensible HT or T_2 depending on the release mechanism described.

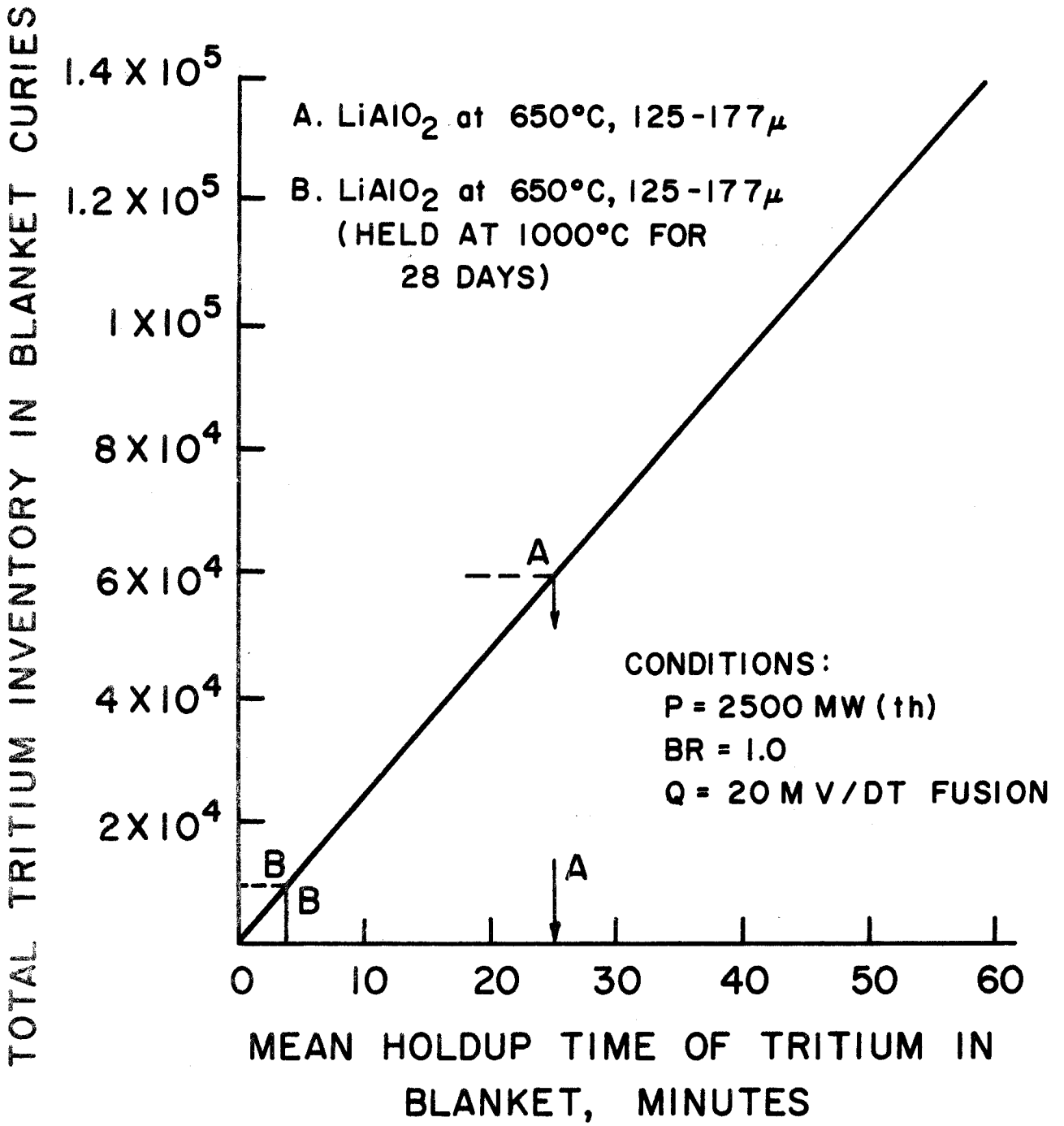

FIGURE XI-C-4 TRITIUM INVENTORY IN CTR BLANKETS AS A FUNCTION OF MEAN TRITIUM HOLDUP TIME

It is worthwhile to note here that while both mechanisms described earlier occur simultaneously, the fractions of condensible and noncondensible species obtained may depend on other factors. In the Hanford Coproduct Program [28] it was found that tritium thermal extractions run in all glass systems at 800°C resulted in high fractions (>85%) of condensible species. On the other hand, those run in stainless steel resulted in substantially lower fractions of condensibles extracted. One possible explanation for this is that condensible species were capable of being reduced on the metal walls of the container. If this is true, it may be possible to tailor containment materials and extraction temperatures to control the fractions of condensible and noncondensible tritium species obtained in breeding. This could greatly simplify the separation and purification of tritium species from the carrying gas and gaseous impurities in the system.

Finally, we wish to address the question concerning the effects of extensive lithium burnup on the chemical and mechanical properties of the breeder. The conceptual design, UWMAK-II[2], is designed to operate at a lithium burnup of 1.4% per year. After 10 years of operation 14% of the lithium atoms of the breeding material $LiAlO_2$ will have been removed. To maintain electroneutrality in the structure of $LiAlO_2$, every two T^+ ions formed and removed require the removal of one oxide ion, $O^=$. Every two lithium atoms burned, in effect, removes one Li_2O formula unit as T_2O. After 10 years, then, it can be considered that 7% of the original number of $LiAlO_2$ formula units will have reverted to Al_2O_3. Thus, in the use of oxide-bearing ceramics which are composites of Li_2O and another oxide as breeding materials, it would be interesting to know the effect of this continuous alteration of composition of a relatively pure

material. Speculation can touch upon the nature of the mixture generated (solid, homogeneous solution or heterogeneous mixture), the changes in physical properties (vapor pressure, melting point) and changes in chemical properties. The last is of particular interest since a 7% change in the fractions of Li_2O and Al_2O_3 represents a significant change along the composition axis of the phase diagram. The property of tritium permeation may be affected with time. Whether or not the mechanical properties are greatly affected and whether this is of importance depends on the physical form of the breeder material used and the reliance of the design on the maintenance of this form.

Without making a decision on the materials most suitable for study in modular experimentation, we have briefly reveiwed the fundamental properties of interest in examining a solid lithium compound for prospective use as a breeder. In section XI-C-2, we will formulate a plan for the study of suitable breeding materials of interest and of importance to future CTR blanket designs in modular experimentation.

XI-C-2. Proposal for the Examination of Solid Breeders in Modular Testing

In this section we will briefly describe the types of experiments to be performed in the solid breeder module. In the solid breeder module, we wish to propose a design for an experiment to examine solid breeder behavior over long periods of irradiation and the separation and purification techniques necessary to produce tritium of purity appropriate to CTR fueling requirements. The experiment will examine the characteristics not only of static breeder designs but also of a mobile blanket design involving flowing breeder particles in a carrying gas. Rather than an examination of the interaction of loop materials with the breeding material as in section XI - B, our main concern in the modular design is the

generation of tritium and the demands that this generation, as well as the separation and purification of the tritium generated, places on blanket design.

Apart from the quantitative results of the experiments, there is some expertise to be gained from the operation of such a module in TETR. In this module, tritium generated in the breeder will be examined as it is produced. There will be no removal of breeding material samples which are then heated to extract the tritium trapped in the solid . This makes the experimental design more complicated since provisions must be made for:

1. the sampling of the carrying gas in the module, with subsequent composition analysis.
2. the continuous removal of the tritium generated to prevent a buildup that may alter the mechanism of its release from the breeder.
3. a mechanism for the removal of heat generated in the module during the operation of the reactor.
4. an appropriate shielding and containment structure to prevent the leakage of tritium out of the module and the exposure of any personnel involved to radiation.

The modular design which will be described will revolve around the use of lithium aluminate and lithium oxide as breeding materials. This is not to say that the module is specifically designed for their use; the flexibility of the module will allow further experimentation with other materials. Lithium aluminate and lithium oxide satisfy the criteria of stability, high lithium density and low tritium holdup and will be used as sample materials in this module.

Lithium aluminate will require a neutron multiplier for use in an operating CTR blanket; lithium oxide will not. This fact will justify experimentation involving a neutron multiplier in the static lithium aluminate studies. The module will operate as a small scale breeding blanket and will include most of the components necessary to such a design. Operating such a module will result in experience and expertise in a number of different areas, including:

1. Design and operation of a system for the containment of gaseous tritium species generated in the breeding material.
2. Separation and purification (on a reduced scale) of the tritium species produced from impurity gases.
3. Characterization of the effects of long term irradiation on the breeding properties of lithium aluminate or lithium oxide (or other breeder)
4. Characterization of the effect of the containment material on the species of tritium produced.

The results of such a series of experiments will characterize a number of facets of solid breeder blanket operation. The major area of interest is the nature of tritium generation and release in the breeder. Short term and long term release rates (which may not necessarily be identical), the fractions of condensible and noncondensible tritium species produced, along with impurities, and the capabilities of the separation and purification system are data which will be available during the course of the experiment and after.

In later sections we will describe the main features of a module to study static solid breeders and one to study mobile solid breeders. Static system tests will be described for both lithium aluminate and lithium oxide while mobile system tests will be described only for lithium oxide. We will cover sample preparation and containment, temperature control and collection and

determination of the tritium species produced for each type of test, as well as covering those types of studies particular to each system, sintering studies in the case of static system tests and abrasion effects in the case of mobile system tests.

XI-C-3) Static Sample Experimentation

XI-C-3-a) Sample Preparation

The preparation of lithium oxide and lithium aluminate samples for modular experimentation involves determining the required purity of materials, percent of theoretical density, physical form of the sample, use of a neutron multiplier, and quantities of the ceramics to achieve a significant burnup over a one year experiment. There is little information available on lithium oxide fabrication for tritium extraction experimentation. We will, therefore, discuss a lithium aluminate fabrication procedure[28] and the appropriateness of each step in the procedure for lithium oxide.

Lithium ceramics are available commercially from the Lithium Corporation of America. At this time, such ceramics tend to be specialty items and the impurity levels vary. Lithium aluminate is produced from the reaction of lithium carbonate and aluminum oxide at 750° to 1000° C. The product can contain as much as 3% lithium carbonate and 7% water by weight. Detectable levels of fluorine and boron may be present. Lithium oxide is formed from the high temperature decomposition of the carbonate and can contain ~ 5% lithium hydroxide. As modular test samples, it is desirable that the ceramics used be as free of water and other impurities as possible. The fabrication procedure will require the introduction of some impurities, but these may be minimized.

Lithium aluminate may be purified by heating the crude material with the required amount of aluminum oxide to complete the conversion of carbonate to aluminate. Small residues of aluminum oxide may result, but as this material is more refractory than lithium carbonate, is a decomposition product of lithium aluminate and will accumulate as lithium is burned, its presence should not be harmful. An additional effect of heating will be the

conversion of any lithium hydroxide present to the oxide. This may then react with any excess aluminum oxide present to form the aluminate. Lithium oxide may be freed of carbonate and hydroxide impurities by strong heating (up to 1000° C). If this is insufficient to efficiently convert the carbonate to oxide, for the purposes of small scale experimentation, the crude oxide may be dissolved in water, precipitated as the peroxide and then decomposed by heating.

Both the aluminate and the oxide should be greater than 96% pure at this stage in fabrication. Impurity and lithium isotope levels should be determined at this point. Isotopic enrichment of lithium is achieved by addition of lithium hydroxide monohydrate enriched in ^{6}Li, which is converted to oxide, and then to aluminate.

The steps in sample fabrication following the initial purification steps are mechanical operations resulting in a dense solid of a shape appropriate to the experiment. In the static sample tests, we would like to fabricate the sample, with a large surface-to-volume ratio, that will, in use, face onto the plasma. This is accomplished by fabricating either plates or a series of rods which will be placed next to each other forming a corrugated surface on the plasma. Figure XI-C-5 describes the series of steps in the fabrication of samples for the Hanford Coproduct Program.[28] This series of steps was applied to the fabrication of lithium aluminate samples and we will describe their application to lithium oxide as well as to the aluminate.

There are four methods of fabricating solid ceramic forms: a straightforward pressing operation, fusion casting, sintering, and swaging. The most economical of these is pressing, but high theoretical densities are not achievable. A combination of pressing and sintering achieves high

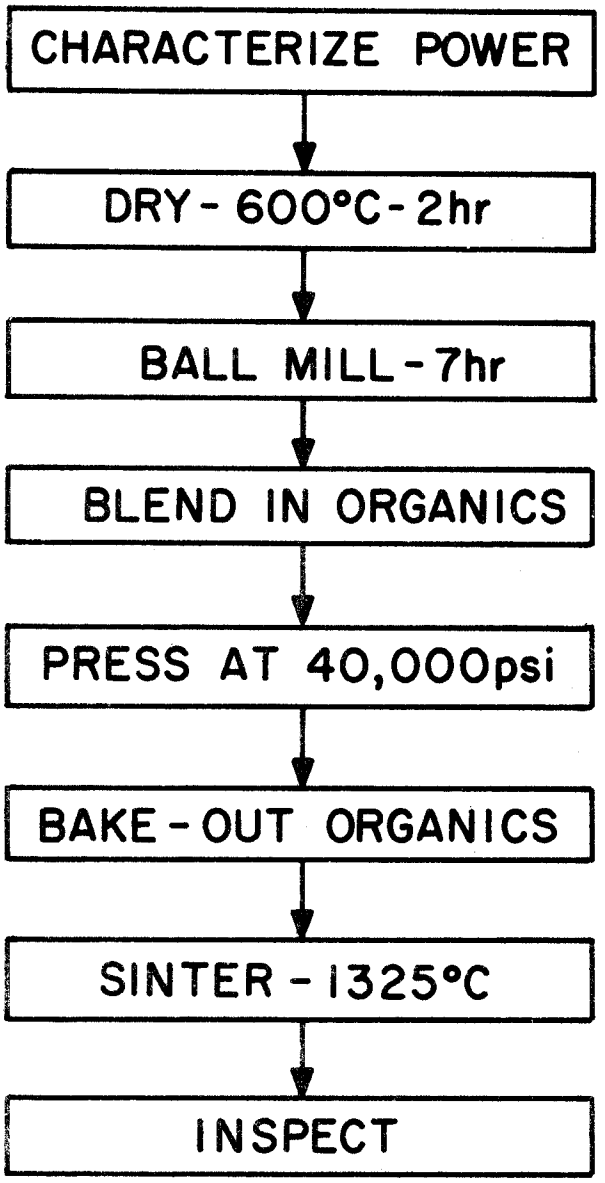

FIGURE XI-C-5. ALUMINATE PELLET PROCESS[28]

theoretical densities and is economical. Vibrational compaction followed by sintering is also applicable.[28] After samples of both materials are characterized as to impurity and isotope levels, dried and ball milled to the required particle size (operations in which both materials behave similarly) an organic lubricant and a binder are blended into the powder. The lubricant smooths the flow of particles during pressing, minimizes internal stresses in an unsintered pellet, and reduces pellet ejection forces after pressing.[28]

The lubricant used in (28) is 1 weight % lithium stearate ($LiC_{18}H_{35}O_2$). While containing 18 moles of carbon per mole of lubricant, 1 weight % will introduce only ~4 mole % of carbon per mole of ceramic. In the lithium aluminate samples, the subsequent bakeout procedure should not result in a stocchiometric conversion of the carbon to carbon dioxide, although some oxidation will occur. It has been found [31] that in lithium aluminate pellets pressed with the use of this lubricant, only 51 ppm of carbon were left in the final product. Any oxidation of the stearate which occurs in the bakeout of lithium oxide samples is likely to result in the formation of lithium carbonate to the same extent as the oxidation occurs, since lithium oxide is easily converted to carbonate. In the worst case, a complete oxidation of the stearic acid present (from the action of the binder, 1 weight % H_2O, on the lubricant, to produce stearic acid and lithium hydroxide) will introduce ~4 mole % of lithium carbonate into the oxide. This possibility has not been evaluated.

Following addition of the lubricant and binder, the powder is pressed, heated to bake out the binder and the lubricant, and sintered. The density of the sample is determined at this point. There are three methods available for this:

(1) determination of the bulk density, where density is equal to (weight of sample/volume of sample),

(2) determination of density by mercury displacement and is equal to (weight of sample/volume of mercury displaced),

(3) determination of density by water displacement where a sample is coated with Krylon first and then placed in water. Here, density is equal to (weight of sample/volume of water displaced).

Figure XI-C-6 shows the resulting percent of theoretical density of lithium aluminate obtained for varying fabrication pressures as determined by the three methods described above. It is seen that there is some disagreement among the methods, but that densities close to the theoretical value are obtainable. Depending on the size of the samples used in experimentation, the density of the samples should be between 85% and 99% of theoretical so that the neutronics necessary to achieve a 5% burnup per year is favored.

Alternatively, a plate of tubes filled with powdered sample can be fabricated and thus avoids the necessity of pressing samples altogether. This arrangement would simulate the UWMAK-II breeding blanket. In it, powdered breeding material is placed in a metal tube capped with a porous metal frit, which allows tritium, but not the "fines" generated in the breeder, to permeate out or with a gas plenum. A mixture of spheres of varying diameters (65% are 30μ spheres, 24% are 4μ and 11% are 1μ spheres) results in a 90% theoretical density. This mode of sample fabrication is applicable to both lithium oxide and lithium aluminate.

To estimate the quantities of lithium oxide and lithium aluminate needed, the parameters of the UWMAK-II[(2)] breeding blanket may be scaled down. The tritium generation rate is 10^{-2} g/sec or 3.15×10^{5} g/yr.

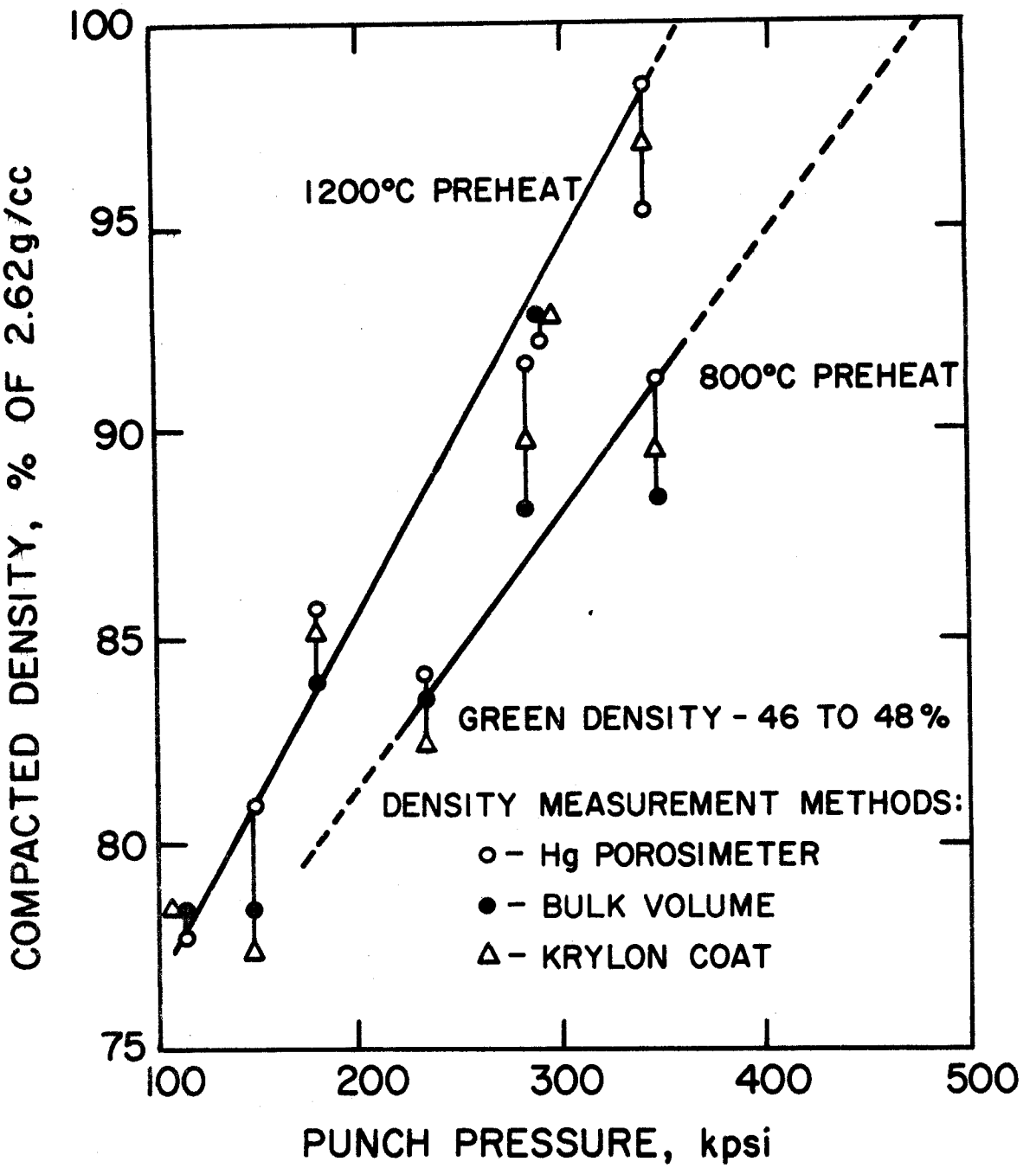

FIGURE XI-C-6.

PUNCH PRESSURE VERSUS COMPACTED DENSITY (28)

The inventory of lithium is 9 X 10^7 g as lithium aluminate and the burnup rate of all lithium isotopes is ~1.4%/yr. For a 5% burnup rate, the tritium generation rate must be ~3.6 X 10^{-2} g/sec. If the module is scaled down by a factor of 10^5 of a UWMAK-II breeding blanket with a 5% burnup rate, then the tritium generation rate in the module should be ~3.6 X 10^{-7} g/sec. If an overall burnup rate of 5% /yr. for all lithium isotopes is assumed (enriched to 90% ^{6}Li), 73.6 moles of lithium are required either in the form of 73.6 moles of lithium aluminate or 36.8 moles of lithium oxide. The required volume of lithium aluminate (for a sample of 85% of the theoretical density of 2.62 g/cm^3) is ~1850 cm^3. The sample may be fabricated as four 25 X 25 X 1 cm plates appropriately spaced to allow the escape of tritium and the passage of coolant. The required volume of lithium oxide (85% of theoretical density, density = 2.01 g/cm^3) is ~550 cm^3, and can be fabricated as three 15 X 15 X 1 cm plates, again appropriately spaced.

We will not address the question of the neutronics and associated design requirements (moderators, reflectors, etc.) of the module in this discussion. It is to be noted that the values given above are order of magnitude estimates. The module must be designed not only with the proper quantities of breeding materials, but also in accordance with the neutronics necessary to achieve a 5% burnup over a year. This should not be impossible, but it is left to a more detailed design description than will be presented here. Additionally, the use of a neutron multiplier such as beryllium should be considered for the lithium aluminate experiment. In a full scale breeding blanket, the lithium density of the aluminate is insufficient to achieve breeding ratios over 1.0, and the use of a neutron multiplier would be required. Therefore, in the interest of simulating a breeding blanket environment as closely as possible, a neutron multiplier should be considered where one would normally be used in CTR design. In fact, it may be necessary to use one in

the aluminate experiment to achieve 5% burnup in a year long experiment. A neutron multiplier should not be necessary in the lithium oxide experiment as the lithium atom density is sufficiently high to ensure a high level of tritium production and associated lithium burnup.

In summary, straightforward pressing and sintering techniques are applied to both lithium aluminate and lithium oxide in fabricating sample plates appropriate to tritium generation experimentation. The lithium oxide may require higher sintering temperatures and longer times than the aluminate as it is more refractory, but, in general, the two ceramics should fabricate in a similar fashion. The quantities of materials required, assuming that a 5% burnup can be achieved and that tritium can be generated at a rate of 3.6×10^{-7} g/sec., have been estimated and are found to be fabricable in convenient sizes. The use of a neutron multiplier is suggested for the aluminate experiments and is not for the oxide experiments based on the proposed manner of usage of the materials in a full scale breeding blanket.

XI-C-3-b) Containment in Static Sample Experimentation

In previous studies of tritium evolution from irradiated ceramic targets, [28, 31, 32] the material of containment was limited to those materials which were easily fabricated in ampoules, allowed easy extraction of tritium and which did not activate to any large extent over the irradiation period. Materials of choice have been stainless steel (in the interest of simulating CTR designs in the near term), aluminum, pyrex, or vycor. In the design of fusion reactor breeding blankets, the choice of structural materials is not made solely on the basis either of chemical compatibility with the breeding material or of the effect on the species of tritium produced in breeding. Design criteria with a greater impact on the operation of the reactor than the above are the deciding factors in choosing structural materials (see Section XI-B-3-b).

In this section, we would like to select a group of materials to act as experimental containment. These materials will not only be of interest in both near and long term CTR design, but also be of a broad enough range of composition to study the effect of containment on the chemical species of tritium produced in breeding. It has been observed[33] that the tritium released from ceramic breeding materials at ~100°C during irradiation was 95% to 99% T_2 and HT. The level of HT was dependent on the degree of moisture control. This tritium constituted 5% to 30% of all the tritium generated in the sample. On the other hand, the remaining 95% to 70% of the tritium, when extracted by heating at temperatures of up to 1300°C, was evolved as condensible HTO or T_2O. Finally, high temperature, in-reactor extractions result in mixtures of condensible and noncondensible tritium species. Clearly, the species evolved is dependent on the mode of extraction;

low temperature evolution under irradiation or high temperature thermal extraction. It is unclear whether:

(1) Tritium is evolved as the oxide in-reactor and is reduced by contact with the wall material, or

(2) Tritium is evolved in elemental form with concomitant oxygen release and is then oxidized during high temperature extraction.

The first mechanism is possible and evidence of it is provided by the fact that the level of condensibles produced is significantly lower in experiments using stainless steel containment than in those with glass containment [28, 33]. The second mechanism is not supported by thermodynamics since the dissociation of water is promoted by high temperatures, not the formation of it. It should be possible to study the effects described above by the use of a variety of containment materials in the static sample experiments.

The design of the loop will separate the tritium-bearing lines from the coolant lines. Cooling will be provided by pressurized helium (see Section XI-C-3-c) and the cooling lines may act as a secondary containment system for tritium since the primary containment, the alloy or metal under study, may be permeable to tritium. Thus the loop design will consist of a permanent apparatus consisting of the out-of-reactor tritium lines and cooling lines, and the in-reactor cooling lines which form a shell about the replaceable experimental containment and breeder. The tritium species will be passed through the cold leg of the loop to the detection, separation, and purification equipment. Extraction into lines through the cold leg should minimize any high temperature reactions between evolution in-reactor and detection.

The permanent loop apparatus should be designed for a material which is capable of withstanding temperatures up to ~700° C. While the temperature in the breeder will be higher and the permanent apparatus will be cooled,

the coolant temperature will determine the temperature in the breeder and thus the extraction temperature. It will be necessary for the structural material to be operable over a broad temperature range. A refractory alloy such as TZM is impermeable to tritium, suffers moderate radiation damage, and is functional in a blanket design up to ~900°C. Nb-1Zr would be an alternative material for which to design the permanent apparatus.

It is possible that tritium oxide species evolved from the breeding material are reduced on the surface of the containment material and a group which ranges from those alloys or metals which are inert to oxidation by steam to those easily oxidized by steam form a good basis of study. In general, if the alloy of choice has only a few elemental constituents, the analysis of its effect on the tritium species evolved will be simplified. The oxides of most metals are formed exothermically. However, if the oxide is to be formed as a result of the action of water on the metal, the formation of the oxide may not be exothermic enough to drive the reaction forward.

The group VI B metal oxides (Cr_2O_3, MoO_3, WO_3) are all formed exothermically from the elements. In water, Cr_2O_3 is formed exothermically, MoO_3 formation is favored only by a few kcal/mole, and WO_3 reduces water in a reaction which is about 10 kcal/mole exothermic. The group VB oxides ($V_2O_{3,4,5}$, Nb_2O_5, Ta_2O_5) and the group IVB oxides (TiO_2, ZrO_2, HfO_2) are all formed exothermically in reaction with oxygen and water. The oxides of other metals of importance such as iron, manganese, and aluminum are formed exothermically as well. Nickel is one of the few metals of interest which will not reduce water, however. The foregoing suggests that most of the alloys of interest in CTR design should be capable of reducing tritium oxide. However, we have not evaluated the kinetics of these reactions and it is possible that, at the low pressures of tritium species in the module and short reaction

times available, that a broad range of behavior will be observed for alloys of the metals used as experimental containment. Some of the alloys will undoubtedly produce mixtures of reduced and oxidized species. This will be of concern in the design of the separation and purification scheme of the module and will be discussed in section XI-C-3-d.

Four materials of interest to CTR design in the near and long term and as experimental containment for solid breeding materials are 316 stainless steel, Tenalon, a titanium-vanadium-aluminum alloy and Nb-1Zr. 316 stainless steel is of importance in near term CTR design and its properties are well characterized. Tenalon is a stainless steel containing no nickel or molybdenum (67% Fe, 14.5 % Mn, 17% Cr) and will have lower levels of induced radioactivity than other steels in a fusion blanket design. It, or a similarly designed steel will be important in future designs and should be investigated. Titanium-vanadium-aluminum alloys also have reduced levels of activity. They may be rather permeable to tritium, but, at low temperatures, this may be minimized. Nb-1Zr is refractory and nominally unstable to steam. It may prove to be a reducing medium for tritium oxide species, but it should be examined primarily because it will allow the study of high temperature extraction of tritium. All of the material choices should be fabricable and over a series of 1 year experiments, will provide an extensive program of study on solid breeder containment choices.

XI-C-3-c) Temperature Control in the Static Breeder Module

The temperature profile throughout the module as a whole will be complex and will require a complete heat transfer analysis to describe these profiles. This will not be attempted here. We have already suggested that the tritium-bearing lines and the in-reactor breeding segment be enclosed in a secondary containment system made of an alloy impermeable to tritium. To control the module's temperature profile, then, pressurized helium can be flowed through the annulus between the primary and seondary containment and to a heat exchanger, where the heat produced in the module is dumped. The temperature profile is determined by the flow rates and pressures applied to the helium. No electrical heating is required and temperature changes during the experiment may be made by altering the helium flow rates, if such changes are required.

The separation and purification of the tritium species produced in the module will require a system of heating and cooling appropriate to the methods employed. This will be provided separately and will not involve the cooling system of the module. The power levels involved should be small and should require only a very small fraction of the power output of TETR as a whole.

The highest temperatures in the module will be found in the breeding material. This is the temperature at which the tritium species will be said to be extracted. The tritium will pass into the lines leading to the detection system and then to the separation and purification system. As previously stated, this segment of the tritium line will pass through the cold leg of the heat exchanger. The coolant will be monitored for tritium content, since some permeation will occur through some of the alloys used experimentally, with the titanium-vanadium-aluminum alloys being potentially the most permeable to tritium.

Leakage out of the system should be small considering the low levels of tritium being handled, and the material planned for use as a secondary containment. We will not parameterize leakage in this discussion as we are limiting ourselves to a generalized design discussion.

XI-C-3-d) Determination and Purification of Product Gases

XI-C-3-d-1) Determination of Product Gases

A number of gaseous species are expected to be present along with the tritiated species and helium released from the solid breeder during irradiation. These species may arise either from air contamination of the sample or from contaminants in the fabrication procedure for the samples. Tritium will be present either as T_2 or T_2O along with helium generated from α particles, coproducts with tritium in the reaction of lithium with neutrons. Depending on the moisture content of the breeding material, some tritium may be present as HT and HTO, as well. Additionally, a certain amount of oxygen, equivalent to half of the tritium lost from the lithium ceramic lattice by recoil ejection, will be produced. Oxygen is lost to chemically compensate for the loss of lithium. In thermal evolution of tritium, oxygen is lost as T_2O.

The primary class of impurity gases are those resulting from the presence of carbon in the sample. Carbon dioxide and carbon monoxide result from lithium carbonate impurities. This can be controlled by reducing the level of carbonate impurities incurred in the sample preparation procedure. Carbonate impurities arise in the aluminate from incomplete conversion of the carbonate to the aluminate and in the oxide by air contamination and oxidation of the organic lubricant in the bakeout procedure. Atmospheric contamination of lithium oxide can be controlled by avoiding the exposure of finely divided oxide to the air or, in the extreme, by the use of an inert atmosphere in the sample preparation procedure. Some lower hydrocarbons, CH_4, C_2H_Z, C_XH_Y (X = 3, 4), may also result from traces of lubricant left in the sample.

A secondary class of contaminants results from trace levels of impurities in the sample. Nitrogen contaminants of the gaseous products result mainly from air contamination of the sample. Nitrogen will probably be present as NO. Some SO_2 may be present if the sample is exposed to a drying agent containing calcium sulfate. Particulate calcium sulfate can become incorporated into the sample and produce SO_2 on heating. The use of teflon fixtures in the preparation procedure has been known to result in the presence of low levels of fluoride contamination[33]. Hydrogen fluoride may be produced on contact with moisture.

To determine the fractional composition of the product gases in the loop, the gas stream may be sampled and analyzed mass spectroscopically. Table XI-C-5 lists the expected product gases and impurities of the loop along with the mass-to-charge ratio for the singly ionized species. The important peaks are easily differentiated and quantitative analysis can be used to distinguish overlapping peaks. It should be possible to place sampling ports in the tritium lines both near the core of the in-reactor samples and at the point in the apparatus where the product gases cease contact with the sample containment material and begin contact with the permanent apparatus. Thus, any changes in the composition of the product gases in transit to the separation and purification system through the sample containment material are detected mass spectroscopically. In practice, reliable detection of such changes is dependent on obtaining a sample of product gases which is representative of the product gases released as a whole. Additionally, it must be assumed that the composition determined for the product gases at any point in the apparatus is a relatively constant quantity. If equilibrium between the gases produced and those pumped out of the sample is not established, or if the production

Table XI-C-5

Product Gases in the Static Sample Loop

Species	Charge-to-Mass Ratio*
H_2	2
HT	4
He	4
T_2	6
HTO	20
T_2O	22
O_2	32
CO	28
CO_2	44
N_2	28
NO	30
CH_4	16
C_2H_Z	24+Z
C_XH_Y (X = 3, 4)	36+Y, 48+Y
SO_2	64
HF	20

*Singly ionized species based on the most abundant isotopes of the constituent atoms; ^{12}C, ^{14}N, ^{16}O, ^{19}F, ^{32}S.

of a gas is, for any reason, not constant, then assigning meaning to the variations in the product gas composition will be difficult. In general, mass spectroscopy will provide the most straightforward route to the determination of the composition of the gases produced in the irradiated sample.

XI-C-3-d-2) Separation and Purification of the Product Gases

The system designed for the collection of tritium-bearing species produced from the irradiation of an oxide-bearing ceramic of lithium in a full scale breeding blanket must take into consideration the removal of enough tritium to supply the fueling requirements of the reactor, the power required to run the system and the efficiency of removal. It is desirable to maximize the first and the third while minimizing the second. In practice, the mixture of oxidized and reduced tritium species would be either entirely oxidized or entirely reduced and the separation and purification system would be dependent upon this choice. The oxidized stream could be frozen out on molecular sieves or dessicants and the reduced stream collected over a metal hydrogen getter, such as yttrium.

However, since the amount of tritium to be collected in any period of time in the loop is small, and since we are interested in the fraction of oxidized and reduced tritium species produced, for the solid breeder loop, we would propose not to completely oxidize or reduce the tritium stream and, instead, collect the species as they are produced. In the collection and purification system, then, a large fraction of the product stream (due to the small quantities involved, up to 10% to 20%, or ~10 times the fraction normally expected to be processed in a full scale operating blanket) is diverted through a temperature regenerator to low temperature freezers or diverted to a dessicant. A dual bed system would be employed to allow regeneration of one while the other is in use. Some contamination of the product T_2O (or HTO) or poisoning of the dessicant bed is expected by the higher hydrocarbons, but the quantities involved are small and may be separated during bed regeneration and reduction of the tritium products.

The resulting stream, depleted in oxidized tritium species, may be sampled mass spectroscopically once more and then passed to a Pd-Ag diffuser through which only HT, T_2 and He will pass. T_2 and HT may be frozen out from the helium at cryogenic temperatures or trapped on a metal hydride absorbtion bed. All waste gases from the product stream, which include those gases not passing the Pd-Ag diffuser and the waste helium, must be monitored for their tritium content before disposal. Temperature regenerators may be used to conserve power in the heating and cooling legs. Figure XI-C-7 describes the separation and purification system for the test module.

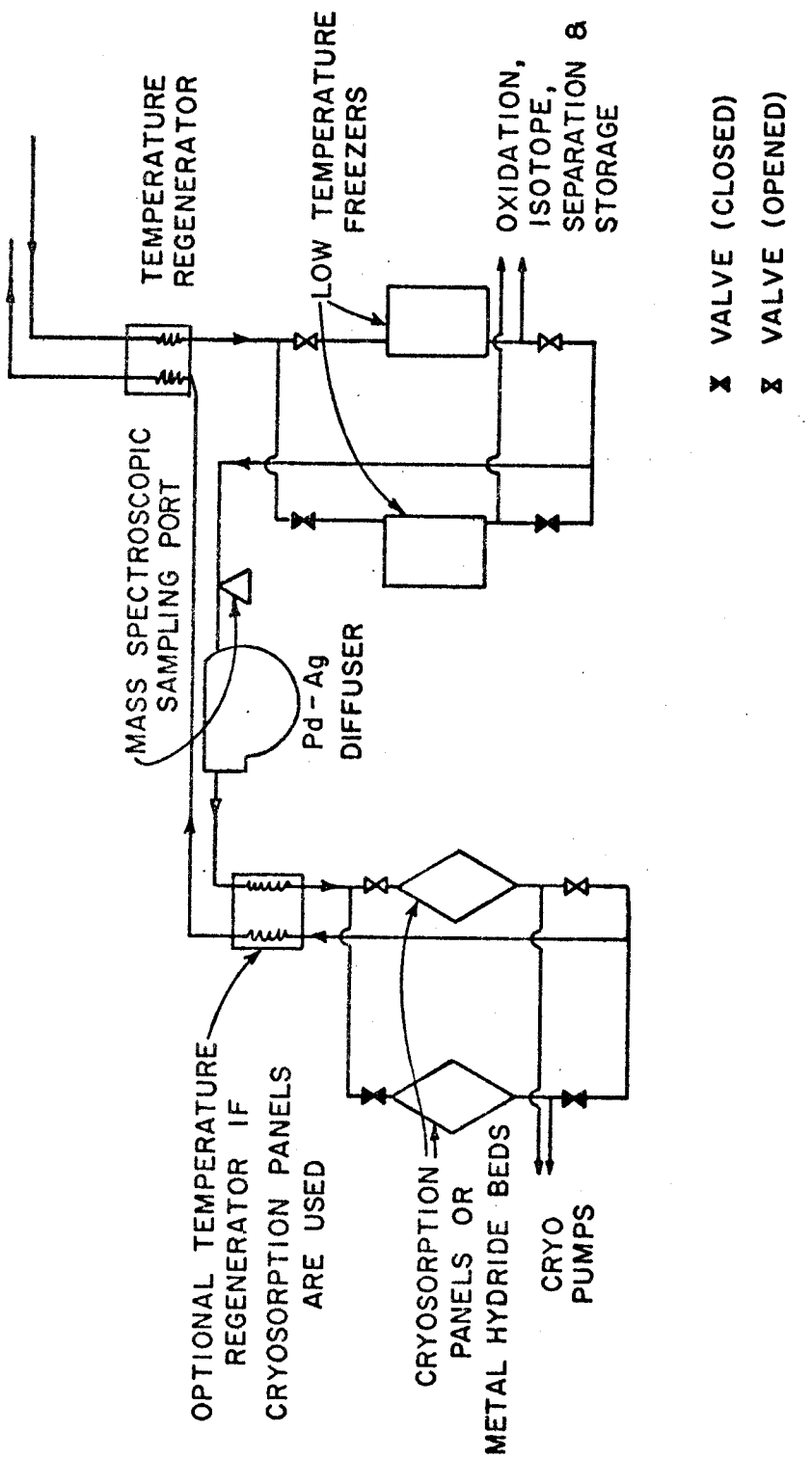

FIGURE XI-C-7 SEPARATION AND PURIFICATION SYSTEM FOR SOLID BREEDER LOOP

XI-C-3-e. Static Sample Loop Experiments

Figure XI-C-8 shows a block diagram of the experimental loop as a whole, but it does not include such elements as shielding, isotope separation and storage, and the required instrumentation for mass spectral analysis. We have also excluded instrumentation required to gather other data from the loop experiments. Nevertheless, in this section we will describe some of the experiments which may be performed and the questions to which the loop experimentation might address itself. The raw data produced in any given experiment consists of the values describing the fractional composition of the product gas stream and those describing the tritium production rate and its variations (if any) with time. Loop parameters subject to variation are temperature of extraction, percent of theoretical density of the sample, containment, and fabrication technique used (i.e., swaging, pressing, sintering, fusion or packed microspheres). Any of these parameters may be varied to study the effect of any given parameter on a tritium breeding blanket.

It has been anticipated that sintering will be a problem in the use of some solid ceramic breeding materials. Therefore, it is of primary importance that loop experimentation study this phenomenon since a large degree of sintering can greatly affect the tritium release properties of a ceramic. Tritium release is favored at high temperature although sintering is also promoted. Sintering is detected in pressed solids by increases in the bulk percent theoretical density and in packed spheres both by changes in percent theoretical density and by a visible agglomeration of particles. In general, however, sintering studies are made by examining changes desnity with temperature over a fixed time interval.

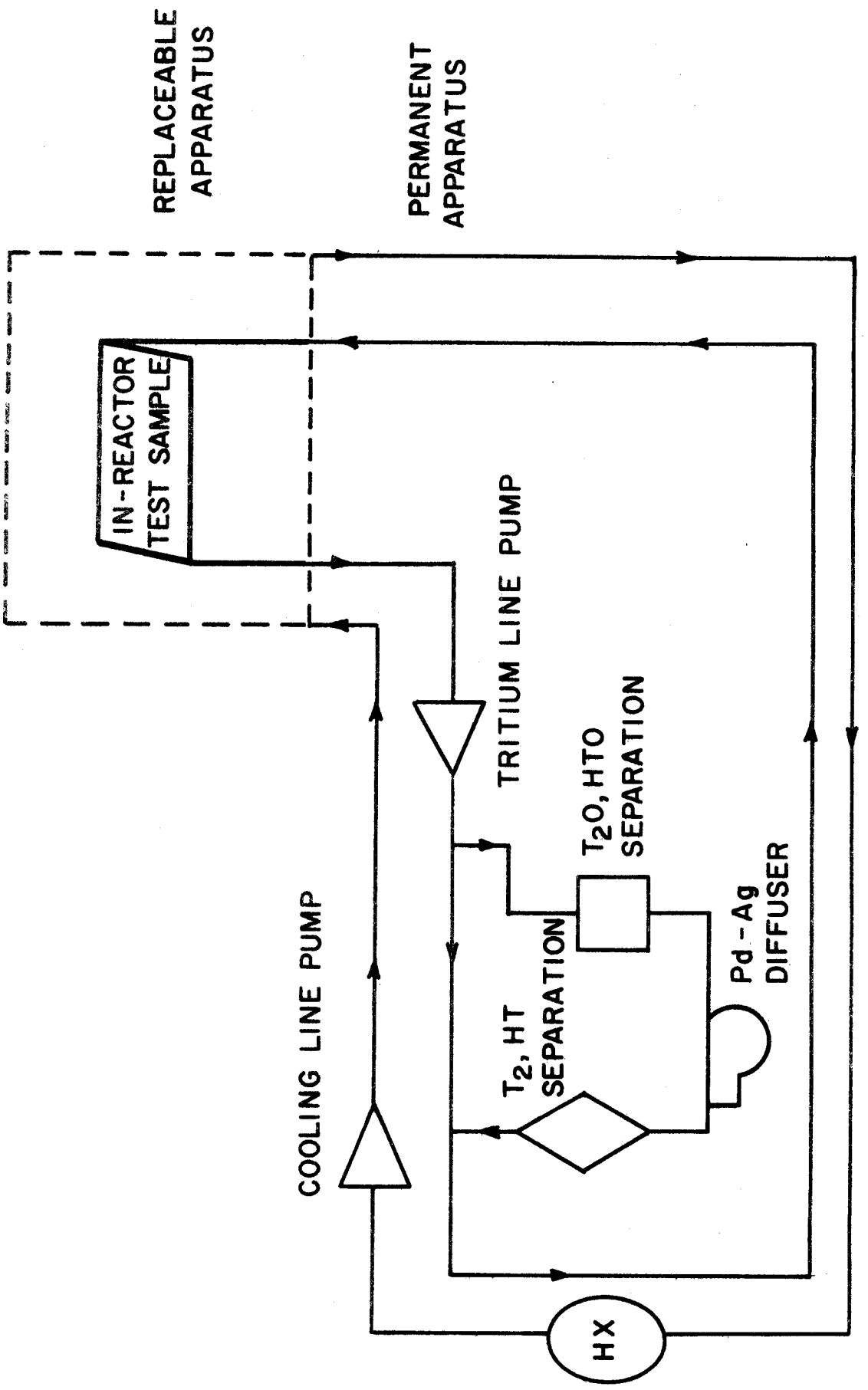

FIGURE XI-C-8 STATIC SAMPLE EXPERIMENTAL LOOP

In the solid breeder, lithium is "burned" in reaction with neutrons to produce tritium. At a burnup rate of 5% per year for all lithium isotopes, and with the loss of both lithium and oxygen from the lattice of the ceramic, some changes in the properties of the breeder are to be expected. These changes may be manifested in the mechanical properties, the chemical composition or the tritium production rate of the breeder. As lithium oxide undergoes reaction with neutrons, both lithium and oxygen atoms are lost from the lattice. Over the course of a year long experiment, 2.5% of the lithium oxide formula units are lost. This will probably result in an increase in porosity and a decrease in percent theoretical density of the bulk material. The increased porosity may result in an increased tritium production rate over time at a given temperature since the gaseous tritium species escape more readily from a porous structure. As lithium aluminate reacts with neutrons, lithium oxide formula units are removed, leaving behind one aluminum oxide formula unit for every two lithium atoms burned. This will result primarily in a change in the aluminum oxide/lithium oxide ratio, and an increase in the porosity of the breeder. The increase in the tritium evolution rate favored by increased porosity will be slightly offset by the reduction in the lithium atom density resulting fron the increase in the aluminum oxide/lithium oxide ratio. The burnup of lithium has the effect of "diluting" the lithium atom concentration in the breeder slightly which may slightly reduce the number of nuclear reactions taking place per unit time. Lithium burnup effects ought to be traceable through changes in the chemical composition of the breeder, the mechanical properties of a pressed solid, and, to a lesser extent, in the tritium evolution rate.

We have discussed the possible effects of the containment material on the species of tritium produced and a method by which to determine such effects (see Section XI-C-3-d-1). In such studies, it is assumed that the temperature of extraction is constant so as not to alter the proportions of tritium produced by recoil ejection and by thermal diffusion, and not to alter the kinetics of the reaction, if any, of the product gas stream with the containment walls. However, temperature studies may be performed to observe such effects on the reaction between the sample alloy and the product stream. It is possible that high temperatures may accelerate the reaction of containment with gaseous products. Variations in the product stream composition with temperature may be indicative of such surface reactions, although this may not necessarily be determined unambiguously. Competing with a faster reduction rate at the alloy surface at higher temperatures is the higher production rate of oxidized species due to faster thermal diffusion of such species. In spite of the possible ambiguity of interpretation, such temperature studies will provide useful fundamental data on the behavior of a solid breeder system.

Modular experimentation should be utilized to examine as many of the fundamental aspects of a breeding blanket using solid lithium breeders as is feasible in a reduced scale experiment. It is important to note, however, that the experiments must be designed carefully to derive unambiguous results. The purpose of the breeding blanket, which is to say, the production of tritium, is affected by a number of aspects of the blanket design. It is the main purpose of solid breeder modular experimentation to sort out the effects of these design features in order to promote efficiency of breeding in future blanket designs.

XI-C-4. Mobile Sample Loop Experimentation

This section will be included in a later edition of the report.

References For Chapter XI

1. V. A. Maroni, E. J. Cairns, F. A. Cafasso, "A Review of the Chemical, Physical and Thermal Properties of Lithium That are Related to its Use in Fusion Reactors", USAEC Report ANL - 8001 (March 1973).

2. B. Badger, et. al., "UWMAK - II, A Conceptual Tokamak Reactor Design", UWFDM - 112 (October 1975).

3. J. H. De Van, J. E. Selle, A. E. Morris, "Review of Lithium Iron-Base Alloy Corrosion Studies" ORNL/TM - 4927 (January 1976).

4. Warren E. Berry, Corrosion in Nuclear Applications, John Wiley and Sons, Inc., New York (1971).

5. E. E. Hoffman, "Corrosion of Materials by Lithium at Elevated Temperatures", ORNL - 2674 (October, 1959).

6. Gerrit De Uries "The Corrosion of Metals by Liquid Lithium", Corrosion by Liquid Metals, Ch. 7, J. E. Praley, J. R. Weeks, eds., Plenum Press, New York, (1970).

7. J. R. Powell "Tritium Recovery from Fusion Blankets Using Solid Lithium Compounds - I: Design and Minimization of Tritium Inventory", Proceedings of the International Conference on Radiation Effects & Tritium Technology for Fusion Reactors, Gatlinburg, Tenn. (1976).

8. Leo F. Epstein "Radiation Effects", Proceedings of the NASA - AEC Liquid Metals Corrosion Meeting, Vol 1, Oct. 2-3, 1967, Lewis Research Center, Cleveland, Ohio, NASA-SP-41.

9. O. Sisman & W. W. Parkinson "Liquid Metal Loops Irradiated in the ORNL Graphite Reactor and the LITR" ORNL-2630 (Oak Ridge, Tennessee, June 1, 1959).

10. B. Badger, et. al., "UWMAK-I, A Wisconsin Toroidal Fusion Reactor Design", UWFDM-68, (Nov. 20, 1973).

11. M. T. Thomas, O. K. Harling, R. L. Brodzinski & L. A. Rancitelli "Fusion Neutron Induced Radioactive Emissions From Surfaces", International Conference on Surface Effects in Controlled Fusion Devices, San Francisco, Feb. 16-20, 1976.

12. Leo F. Epstein, "Downstream Effect", Proceedings of the NASA-AEC Liquid Metals Corrosion Meeting, Vol. 1, Oct. 2-3, 1963. Lewis Research Center, Cleveland, Ohio. NASA-SP-41.

13. N. M. Beskorovainyi, V. K. Ivanov, and U.V. Petrashko. "Corrosion of Stainless Chromium - Nickel Steel in Molten Lithium." High Purity Metals and Alloys - Fabrication Testing and Properties, English translation by Consultants Bureau, New York (1967), pp. 131-138.

14. W. N. Gill, et al., "Mass Transfer in Liquid Lithium Systems" A.I.Ch.E. Journal 6(1) 139, (1960).

15. R. L. Brodzinski, et al., "Fusion Neutron Induced Nuclear Recoil Emission Probabilities" Battelle Memorial Institute, Richland WA, to be published.

16. A. F. Wells, Structural Inorganic Chemistry, pp. 1026-1028 (Oxford University Press, London, 1962).

17. W. P. Brehm, et al., "Technique for Studying Corrosion and Deposition of Radioactive Materials in Sodium Loops", HEDL-SA-986 (Sept. 1975).

18. W. E. Ruther, et al., "Investigation of Possible Line Length Effects in the Measurement of Oxygen and Hydrogen Impurities in Sodium", ANL-7893 (March 1972).

19. D. L. Smith and R. H. Lee, "Characterization of the Vanadium Wire Equilibration Method for Measurement of Oxygen Activity in Liquid Sodium", ANL - 7891 (Jan. 1972).

20. W. P. Brehm, et al., "Mass Transport of Radioactive Materials in Flowing Sodium" HEDL-SA-658 (1973).

21. J. R. Potts and W. E. Hobart, "The Determination of Carbon in Lithium", USAEC Report TID-7606 (1960).

22. R. F. Bunshah, ed., Modern Analytical Techniques for Metals and Alloys, Vol. III, Part 1, Wiley Interscience (1970).

23. W. Wagner and C.J. Hull, Inorganic Titrimetric Analysis, Marcel Dekker, Inc. (1971).

24. N. I. Sax, N. Y. Chu, R. H. Miles, R. W. Miles "Determination of Nitrogen in Lithium" (June 14, 1957) USAEC Report Number NDA-38.

25. Howard A. Strobel, Chemical Instrumentation, pp. 380-385 (Addison-Wesley Publishing Company, Reading, Massachusetts 1973).

26. D. L. Smith, K. Natesan, "Influence of Nonmetallic Impurity Elements on the Compatibility of Liquid Lithium with Potential CTR Containment Materials" Nuclear Technology Vol. 22, 392-404, (1974).

27. James H. Richardson, "Specimen Preparation Methods for Microstructural Analysis," p. 23-44, Microstructural Analysis; Tools and Techniques, James L. McCall, ed., Plenum Press, New York, 1973.

28. A. B. Johnson, Jr., et al., "Tritium Production from Ceramic Targets: A Summary of the Hanford Co-product Program," BNWL-2098 (August 1976).

XII.-The Tritium Cycle

XII-A-1. Introduction

TETR is to be operated according to the simplest and most reliable design concepts possible. As this is to be a materials testing facility and not a facility in which to further the technology of tritium breeding or recovery, unless as specified in a test module, tritium will not be bred in a blanket and no attempt will be made to recover tritium from the blanket or the cooling system.

In Chapter XI of this report we examined tritium removal methods from solid breeding materials in test module experimentation. The test modules investigated liquid lithium corrosion over extended periods of time in a radiation environment, radiation effects on liquid and solid breeding materials and tritium removal from solid materials.

In the routine operation of the reactor, tritium will be found in many subunits of the reactor design. TETR has a stainless steel structure, one heat removal loop, water as coolant in the non-module areas and, with a water-cooled front wall, He as coolant in the module areas. The presence of tritium must be evaluated in:

(1) the fueling cycle

(2) the cryopumps

(3) storage

(4) the reactor coolant

(5) the module coolant

(6) the divertor coolant

(7) emergency containment systems

(1) and (2) will be discussed in Section XII-B and (3) through (7) will be discussed in Section XII-C.

XII-A-2. Parameters Governing the Fuel Cycle

During the normal operation of the reactor, a large fraction of the fuel remains unburned and must be recovered and separated into the pure fueling components, deuterium and tritium. We will now consider tritium flow regulation in the fuel cycle by first looking at those parameters which determine the amounts and the flow rates of tritium and deuterium which must be dealt with by the fuel system.

TETR is fueled by the injection of pure tritium pellets into a stream of neutral deuterium particles. The gases exhausted from the plasma chamber after the burn contain primarily the hydrogen isotopes and small amounts of helium, hydrocarbons (mostly methane), nitrogen and oxygen. Solids knocked from the chamber walls may also be exhausted with these gases. The hydrogen isotopes must be separated from these impurities before passing to the separation system where they are separated by distillation into pure tritium and deuterium streams and then recycled to the fueling system. The operating parameters of TETR governing the required flows of tritium and deuterium to the fueling systems are given in Table XII-A-1.

XII-A-3. Fuel Flow Rates

In designing the TETR fuel cycle, the first step is to determine the rates of fuel flow and the required isotopic concentrations of deuterium and tritium.

The flow rates and isotopic concentrations in the fuel cycle are determined in the following way. The neutral beam power input to the plasma during the burn is 150 MW at 150 KeV, so that a beam current equivalent of 10^3 Amps is required. With a beam injector efficiency of 60%, the required flow of material into the injectors is 1.73×10^{-2} g-atoms/sec. This assumes that

Table XII-A-1

Operating Parameters Governing Tritium and Deuterium Flow*

Fractional Burnup	.33%
Power Thermonuclear Output (Total)	346 $MW_{(th)}$
Burn Time	60 sec
Down Time	12.5 sec
Neutral Beam Efficiency	60%
Neutral Beam Injector Energy	150 KeV
Beam Power	150 MW
Number of Beams	12
Q	1.78
n	$7.7 \times 10^{13} cm^{-3}$
τ_e	92 msec
Plasma Volume	41.6 m^3

*Base case numbers, some variation may occur with final plasma assumptions.

all the injected neutrals are monatomic. Because the plasma is principally tritium, a high deuterium concentration is desired in the injected beam to maximize the number of fusion reactions from the injected neutrals. A value of 95 atom percent deuterium is chosen for the beam.

The background tritium plasma is introduced by means of a "pellet maker" or other cold fueling device. This device supplies fuel, in addition to the beam, at a rate sufficient to balance plasma losses from diffusion. This rate is 4.72×10^{-2} g-atoms/sec which is calculated from plasma particle density, total particle input and particle input from the beams. A purity of 95 atom % T is considered sufficient. Because the burn time is 60 sec and the down time is 12.5 sec, the average flow rates through the fuel processors will be only 83% of the values calculated for full power operation. Thus, the required flow rates are

$$T = (4.72 \times 10^{-2} \times .95 + 1.04 \times 10^{-2} \times .05) \times .83$$
$$= 3.765 \times 10^{-2} \text{ g-atom/sec}$$

$$D = (4.72 \times 10^{-2} \times .05 + 1.04 \times 10^{-2} \times .95) \times .83$$
$$= 1.016 \times 10^{-2} \text{ g-atom/sec}$$

Dividing by 2 to get the molar flow rate, we have a total of 2.39×10^{-2} mol/sec of hydrogen isotopes with a tritium fraction of 78.8% and a deuterium fraction of 21.2%.

It is calculated from the power output requirements that approximately 0.33% of the tritium is lost via fusion reactions in each burn cycle. An equal number of deuterium and tritium nuclei are consumed, so that ~1.2% of the deuterium is burned. This corresponds to an average burnup of 1.3×10^{-4} mol/sec of fuel. This fuel must be made up from external deuterium and tritium supplies.

It is also assumed that the plasma exhaust contains ~1% hydrogen, principally as a result of back permeation through the reactor vacuum walls. The fuel purification includes the recovery and removal of 50% of this hydrogen. Thus, there will be 0.5% hydrogen impurity in the fuel supply. Some deuterium is discarded in the isotope separation process, so the deuterium makeup rates will be somewhat larger than that of tritium.

The neutral beam injectors are assumed not to be isotopically selective; that is, the isotopic composition of the neutral beam is the same as that of the material that supplies the injector. Cold gas from the plasma is assumed to back stream into the injector at a rate of ~5% of the injected flow. This gas, which has the isotopic composition of the plasma, is added to the 40% of the injector feed material which is not injected. This material must be returned to the isotope separator to remove the tritium that would otherwise accumulate.

For the purposes of parameterizing the isotope separation system, the cyclic operation of the reactor is reconciled with the continuous operation of the separation system by averaging the fuel flow rate during the burn over the entire burn cycle. For a 60 sec burn followed by a 12.5 sec shutdown, the fuel flow rate during the burn is reduced by a factor of 60/72.5, or 0.83, to represent the fuel flow rate averaged over the burn cycle. In practice the reactor as a whole will be subject to periodic shutdowns for maintenance and repairs, as well as the shutdowns inherent in the burn cycle, and so, averaged over a year's time, the reactor will be burning fuel at an overall rate of only 20% of that during the burn. The calculations which describe the isotope separation system

(section XII-B) and which determine tritium inventories (section XII-C) are based on fuel flow rates averaged over the burn cycle (83% burn cycle duty factor) rather than averaged over the operating time of the plant as a whole (70% plant duty factor). At a 70% plant factor, the tritium flow rate is 3.175×10^{-2} g-atom/sec (reduced from 3.765×10^{-2} g atom/sec by a factor of 70/83) and, at a burnup rate of .33%, 9912 g of tritium are burned per year. At 5000/g, the cost of the tritium burnup per year is 49.6 million dollars.

XII-B. Tritium-Deuterium Separation

XII-B-1. The Fuel Separation System

From the assumptions made in Section XII-A, it is possible to construct a preliminary isotopic flow diagram for the fuel cycle. This is shown in Fig. XII-B-1. Note that components not related to isotopic processing are not included. The flow rates and compositions are approximate, and are intended only to permit one to estimate the nature of the feed material for the isotope separator.

In addition to the unburned fuel which exhausts from the plasma, there will be a number of impurities. These are pricipally helium, carbon (as methane), oxygen, and nitrogen in the gaseous state; and solid debris such as carbon or steel resulting from the deterioration of surfaces exposed to the plasma. The fuel processing equipment will be required to remove these impurities from the hydrogen isotope mixture before the mixture can be separated.

The above characteristics of the TETR fuel system largely determine the nature of the TETR fuel processing system. In addition, the fuel processing system has been divided into four identical loops, one for each quadrant of the TETR torus. This division not only provides a measure of redundancy which permits continued fuel processing in the event of a component failure in one quadrant, it also partitions the tritium inventory so that no more than 25% of the inventory is contained in one loop. Thus, if there is a leak in one quadrant, the potential tritium release is reduced and the recovery process is simplified. We shall describe one fuel processing quadrant. Fig. XII-B-2 shows the principal components of one such quadrant. Each quadrant will have a number of cryosorption pumps to evacuate the vacuum

PRELIMINARY FUEL FLOW DIAGRAM

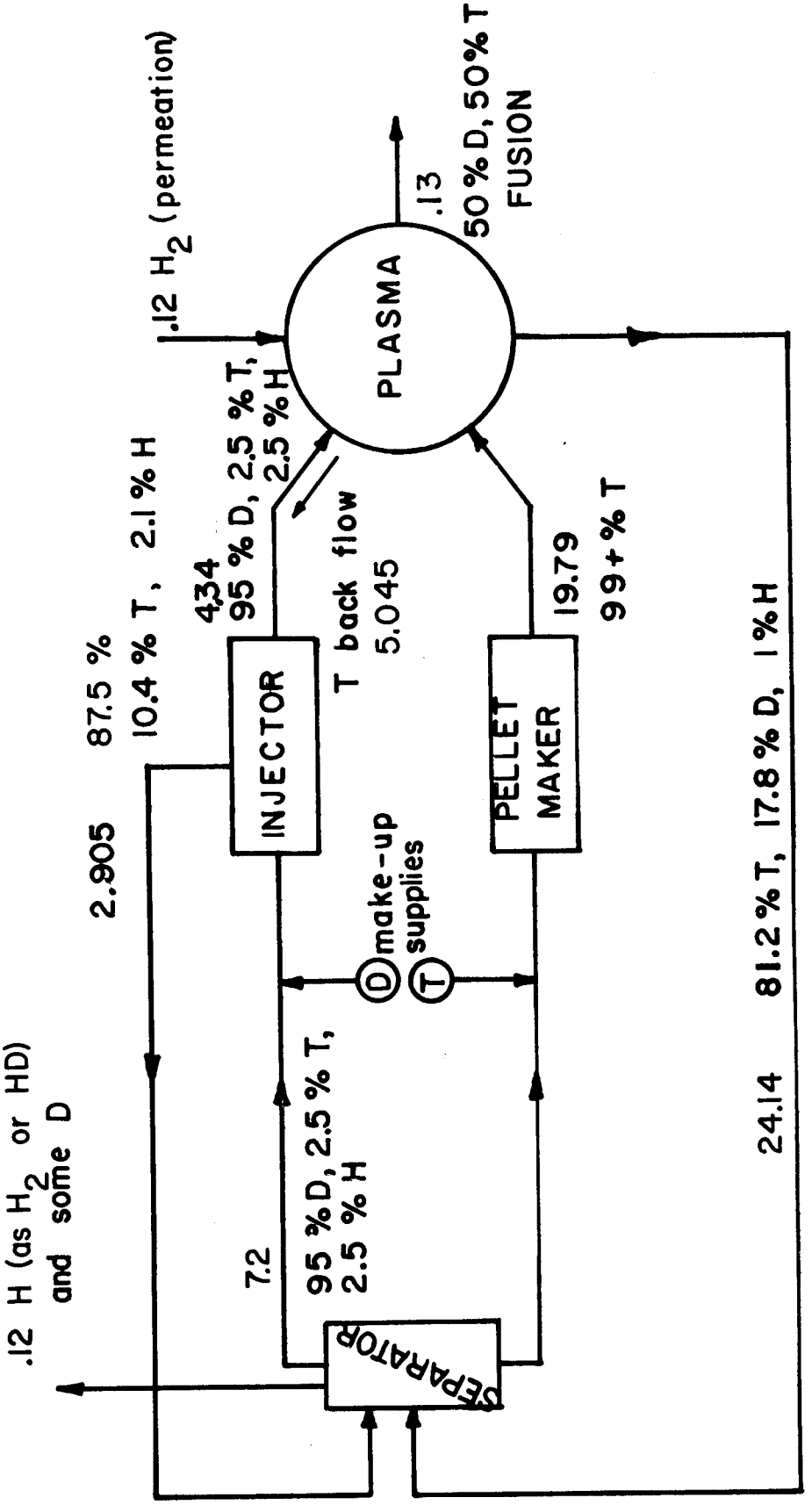

FIGURE XII-B-1

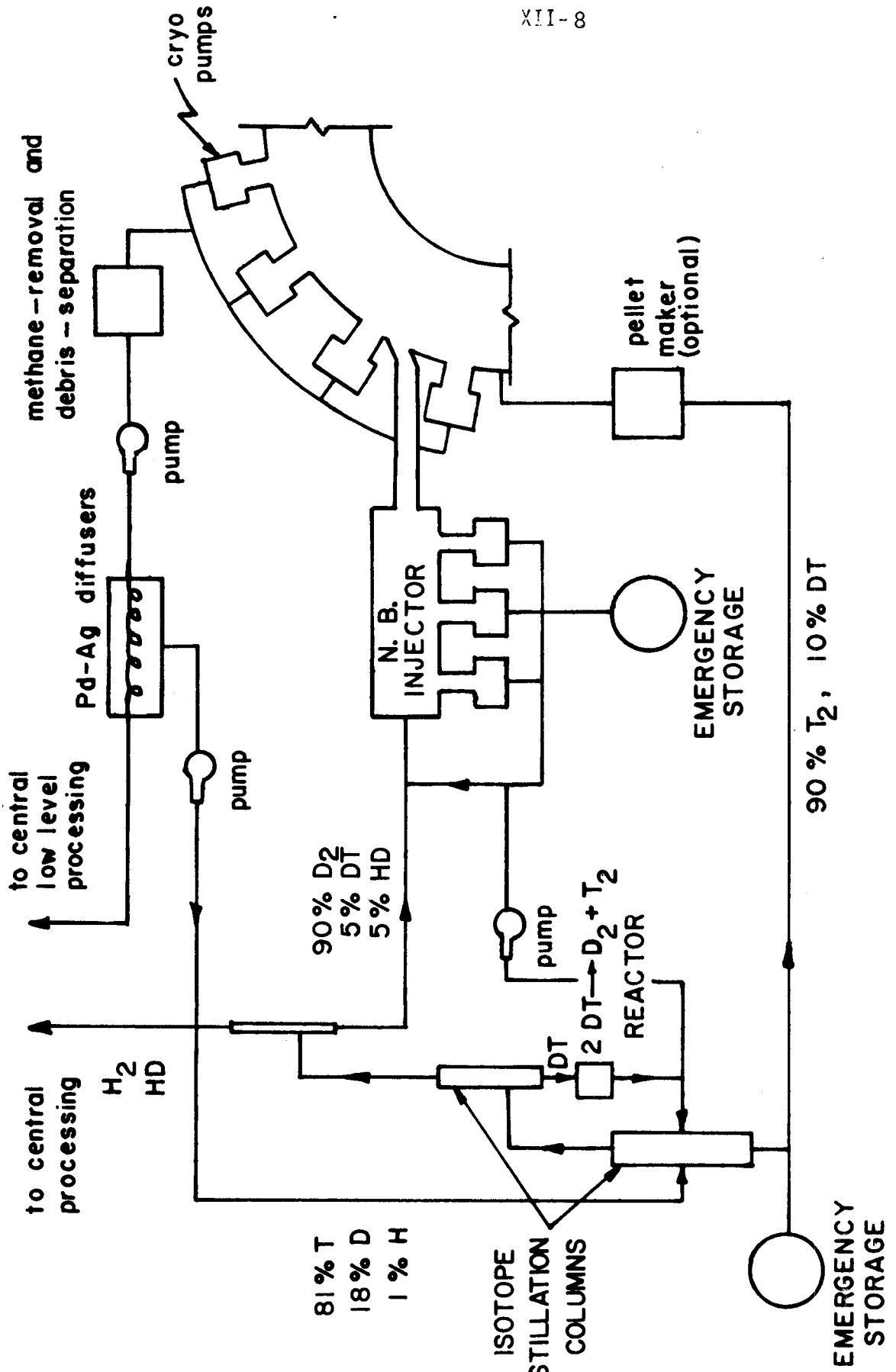

FIGURE XII-B-2

FUEL PROCESSING SYSTEM FOR ONE QUADRANT OF TETR

chamber after a burn, and in addition, divertors may be employed during the burn to remove impurities. The pumps will be phased so that some are pumping while others are regenerating. For the purpose of describing the fuel processing equipment, it is sufficient to assume that all the plasma exhaust is handled by the cryosorption pumps and that these pumps are in the pumping and regeneration modes for equal lengths of time. The pump cycles are very long compared to a burn time, so that an average fuel flow may be used to size the system.

With a 50% duty cycle, if regeneration occurs at a constant rate, the total pump inventory is constant, with a value equal to the circulation rate multiplied by half the cycle length. With a cycle length of 8 hours and a recirculation rate of 0.006 mol/sec, the main pump inventory is about 86 moles. This is approximately 78% tritium, so that the total tritium inventory is 3.8×10^6 Ci per quadrant.

There are also neutral beam injectors in each quadrant. These have cryosorption pumps which collect fuel which does not get injected into the plasma. If the injectors operate at 60% efficiency, and the only pumping required is to remove the non-injected 40%, the injector pump inventory is 7.3 moles at a 7.6% tritium concentration for a total of 3.2×10^4 Ci per quadrant.

The injector pump inventory is considerably less certain than that of the main vacuum pumps, because of unknown injector efficiencies. However, because of the small tritium concentration in the injector circuit and the small fraction of the total pump capacity devoted to the injectors, a very large error in this estimate will not affect the total TETR tritium inventory significantly.

The output of the cryosorption pumps will probably be at a pressure of a few torr or less, hence booster pumps will be required between the cryosorption pumps and the fuel processor. It is assumed that these pumps will have a small holdup compared with the cryosorption pumps. This may be accomplished with continuous mechanical pumps or with short cycle time sorption pumps.

Because of the intense neutron and particle flux at the first wall, there will be a steady flow of debris in the plasma exhaust. Much of this debris will be entrained in the spent fuel stream and will probably be separated downstream of the cryosorption pumps. Any upstream separator will create an intolerable flow impedance. This separator cannot yet be specified, but it may be a cyclone separator or even a simple porous metal filter if it can be put in at a point where the pressure drop can be tolerated. The particulate material that is separated will undoubtedly be radioactive and so will be further processed for proper disposal. Such processing may include a high temperature bake-out to drive off adsorbed tritium.

After particulate impurities are separated, the spent fuel will be passed through a high temperature cracker to break down organic impurities (principally methane) and then through a palladium silver diffuser to remove all non-hydrogenic impurities. The gas stream, which now contains only the three hydrogen isotopes, is cooled to about 25°K, mixed with a stream of gas from the injectors, and admitted to the isotope separation system.

The isotopic separation is accomplished by means of cryogenic distillation, with columns operating slightly above atmospheric pressure. This system was chosen for its compactness, simplicity, and low power consumption. Operation at positive gage pressure is a precaution against leakage of impurities

into the fuel. Such leakage could cause a solid plug to form in a narrow process line at low temperatures, shutting down the system. With positive gage pressure, a leak will result in a release of tritium to the secondary container. Tritium monitors there can detect the presence of tritium and signal a leak much sooner than would be possible if the leak flow were reversed.

The separated isotopes are either stored or transferred to the fueling devices. Makeup deuterium and tritium supplies are required to replenish fuel which is burned or discarded. Storage can be provided either by means of hydride beds or in gas cylinders.

The small quantity of hydrogen which is removed from the fuel stream and the helium collected in the diffusers will contain tritium impurities. Each of these waste streams will be collected in a storage vessel and monitored for tritium content to determine whether it can be discarded, fixed for burial, or processed further.

An emergency storage container is required for each processing loop, so in each loop, there will be an evacuated tank with a volume of 2×10^3 l. Such a tank will accomodate more than 85 moles of gas at NTP. A smaller tank of ~250 l volume is available for the injector system. These are connected to the operating system through lines sealed with rupture disks.

If hydrides are available which will adsorb the necessary quantities of gas rapidly enough without generating excessive heat, this too could be a satisfactory emergency storage system.

XII-B-2. The Isotope Separation Strategy

It was initially hoped to make a simple distillation separation of the plasma exhaust into T_2-rich, D_2-rich, and waste streams. Although the separation is possible, it is complex. This may be understood

as follows: In a mixed D/T stream coming from a hot plasma, the D and T will combine into D_2, DT, or T_2 molecules in proportions determined by the D and T atomic fractions. At high temperatures, a good approximation is that the concentration of a homonuclear molecule (i.e., D_2, T_2), equals the square of the corresponding atomic (D,T) fraction, whereas the heteronuclear molecules (DT) are formed in a concentration equal to twice the product of the separate atomic concentrations. For example, in a 50-50 mixture of D and T, 50% of the molecules will be DT and the remaining 50% will be evenly divided between the two homonuclear species D_2 and T_2.

To separate a DT mixture by distillation into D_2 and T_2, it is first necessary to separate the mixture into its three components, D_2, DT, and T_2. The D_2 and T_2 may be used immediately, but the remaining DT contains both D and T, thus it cannot be used until it is converted into D_2 and T_2. If the DT is heated and passed over a catalyst, a new mixture of D_2, T_2 and DT is created. This new mixture is now used as feedstock for the separator and the entire process is repeated until all the DT has been changed into T_2 and D_2 and separated. In practice, this is done continuously using two distillation columns and an equilibrator, as shown in Fig. XII-B-3.

The addition of a third isotope to the mixture further complicates the problem, as there are now six possible molecular variations, H_2, HD, HT, D_2, DT, and T_2, here listed in order of decreasing volatility. The molecular proportions are still given by the previous approximation; thus, if the mixture contains 1% H, 21% D and 78% T as does the plasma exhaust, one can see that almost all the hydrogen occurs in the form of either HD or HT; only about 10^{-2}% of the entire mixture is H_2. If this mixture is put into the two

column separator of Fig. XII-B-3 and if the T_2 and DT streams are pure, the top stream will necessarily contain not only D_2, but all the HT, HD and H_2 as well. A third column is now required to remove the H_2, HD and HT from the D_2 (Fig. XII-B-4).

This still doesn't solve the problem, however, for the HT is radioactive and cannot be discarded; yet there is too much HT to leave in the fuel. Two more columns are required to separate the tritium from the waste. These latter columns are small in relation to the rest of the system, but the control of so many columns adds to the complexity of the system.

There is a more straightforward solution, however, which also addresses the problem of processing the neutral beam injector exhaust to remove tritium buildup resulting from back-streaming. By mixing the plasma exhaust and the injector recycle stream before introducing them to the first column of the separator, a much higher D/T ratio (~1/2.5) is achieved than exists in the plasma exhaust (~1/4). As a result, the proportions of the six molecular species are shifted in a way which simplifies removal of the hydrogen from the fuel without tritium contamination of the waste. The entire separation cascade is shown in Fig. XII-B-5.

The flow rates and the concentrations in the distillation system have been calculated using a computer simulation of a multi-component, multi-stage distillation column. The values determined in the simulation can now be used to complete the specification of flow rates and concentrations in the entire fuel cycle. These are shown in Fig. XII-B-6. Note that the flow rates, as those in Fig. XII-B-1 are for all four quadrants combined. The concentrations of the hydrogen isotope mixtures at various points in the distillation system are shown in Table XII-B-1.

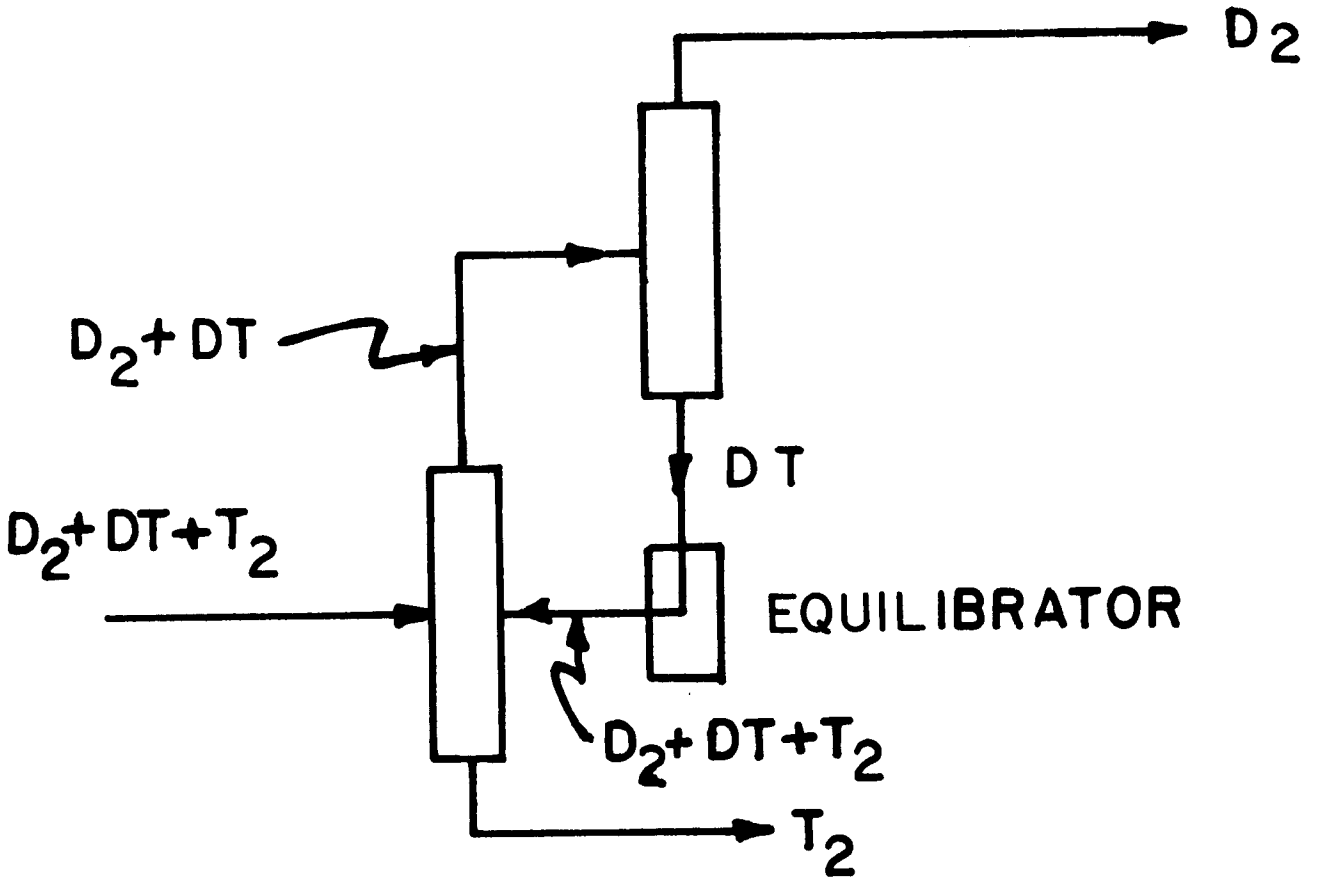

TWO-COMPONENT SEPARATION SCHEME FOR A MIXTURE OF D AND T

FIGURE XII-B-3

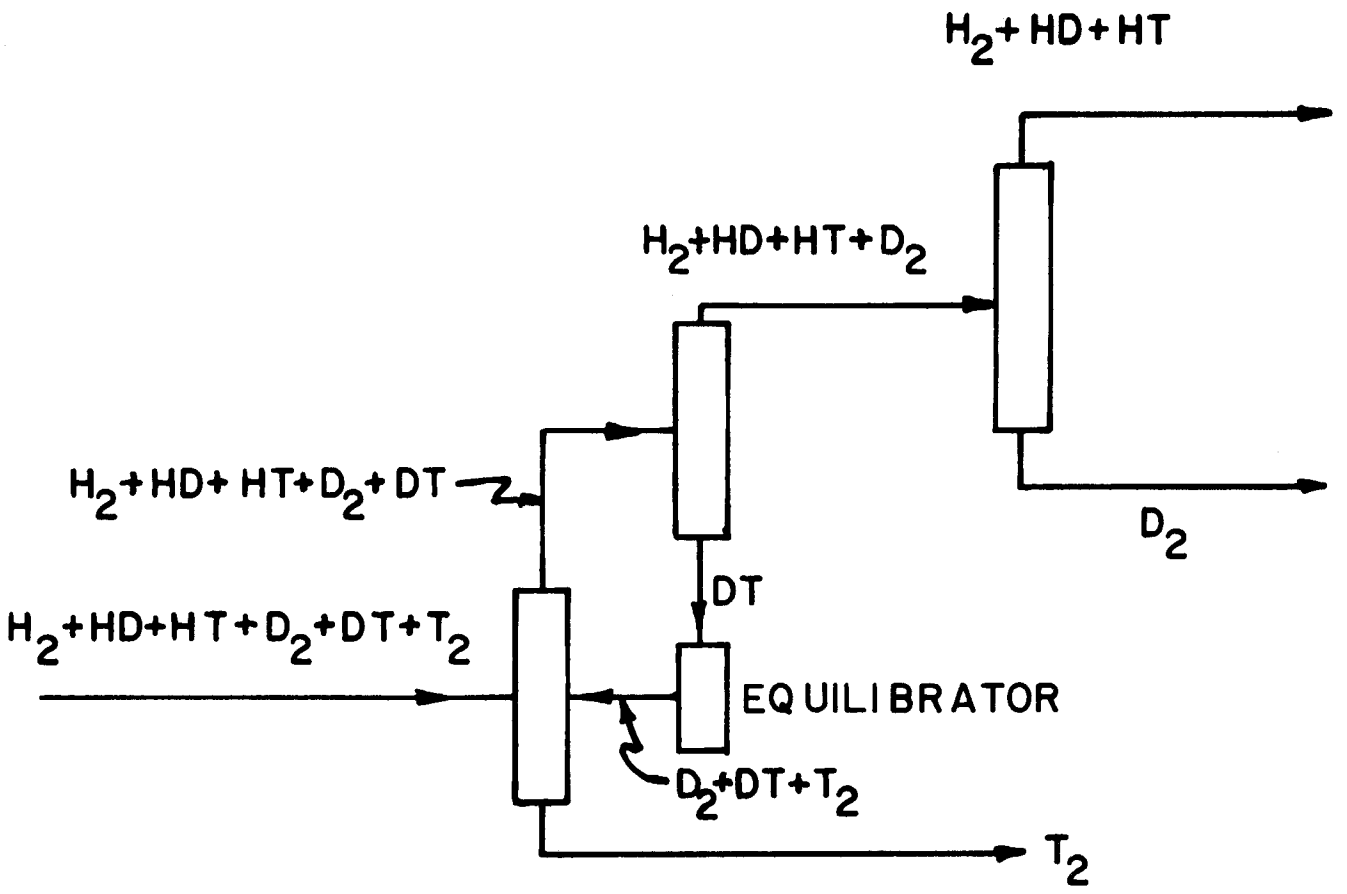

THREE COMPONENT SEPARATION SCHEME FOR A MIXTURE OF D AND T

FIGURE XII-B-4

TETR FUEL ISOTOPE SEPARATOR

Figure XII-B-5

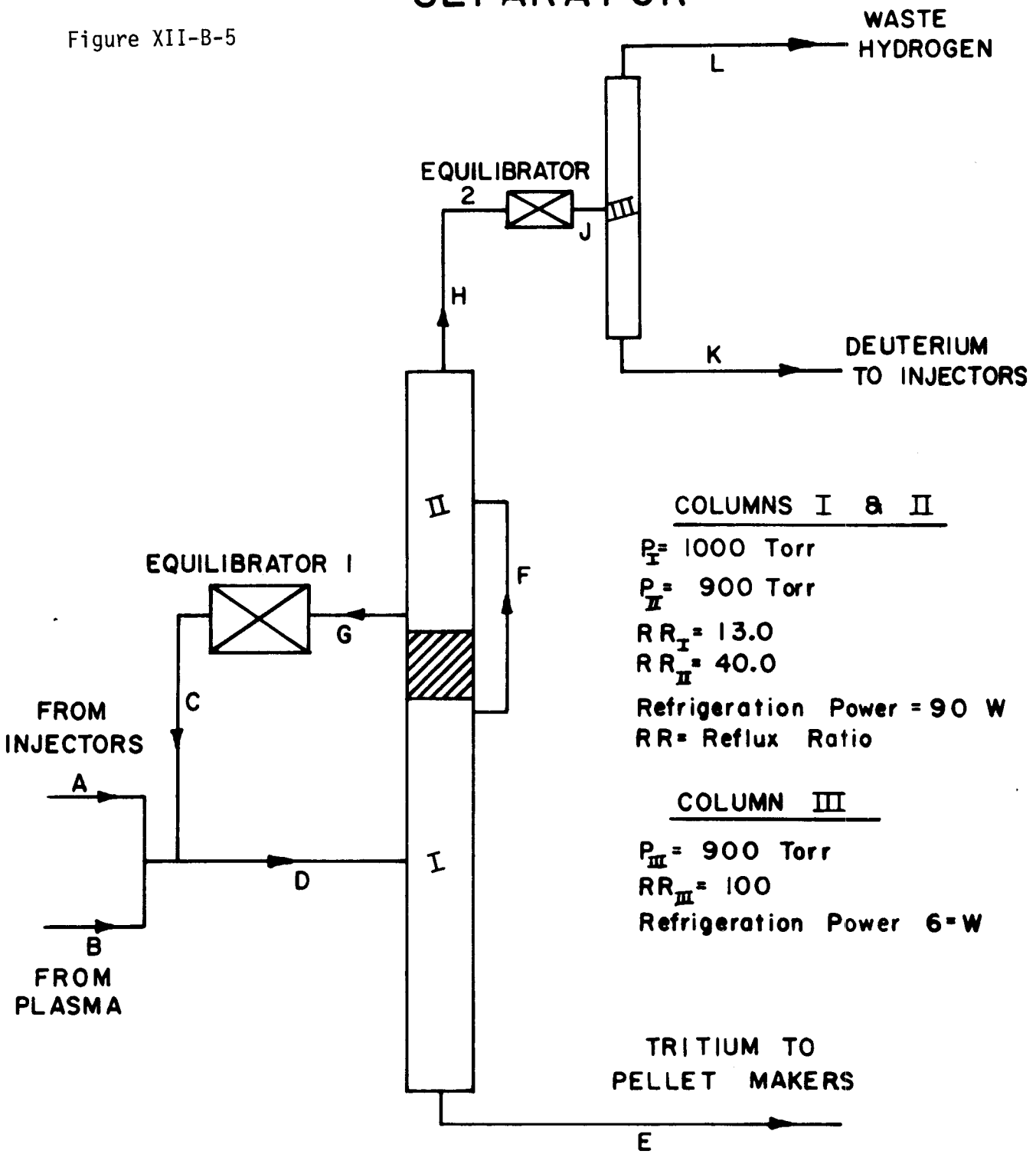

COLUMNS I & II

P_I = 1000 Torr

P_{II} = 900 Torr

RR_I = 13.0

RR_{II} = 40.0

Refrigeration Power = 90 W

RR = Reflux Ratio

COLUMN III

P_{III} = 900 Torr

RR_{III} = 100

Refrigeration Power 6 = W

POWER VALUES ARE FOR ONE FOURTH OF THE FUEL FLOW. FOUR COLUMNS, EACH OPERATING WITH 25 % OF THE FULL LOAD, ARE RECOMMENDED.

TETR FUEL CYCLE

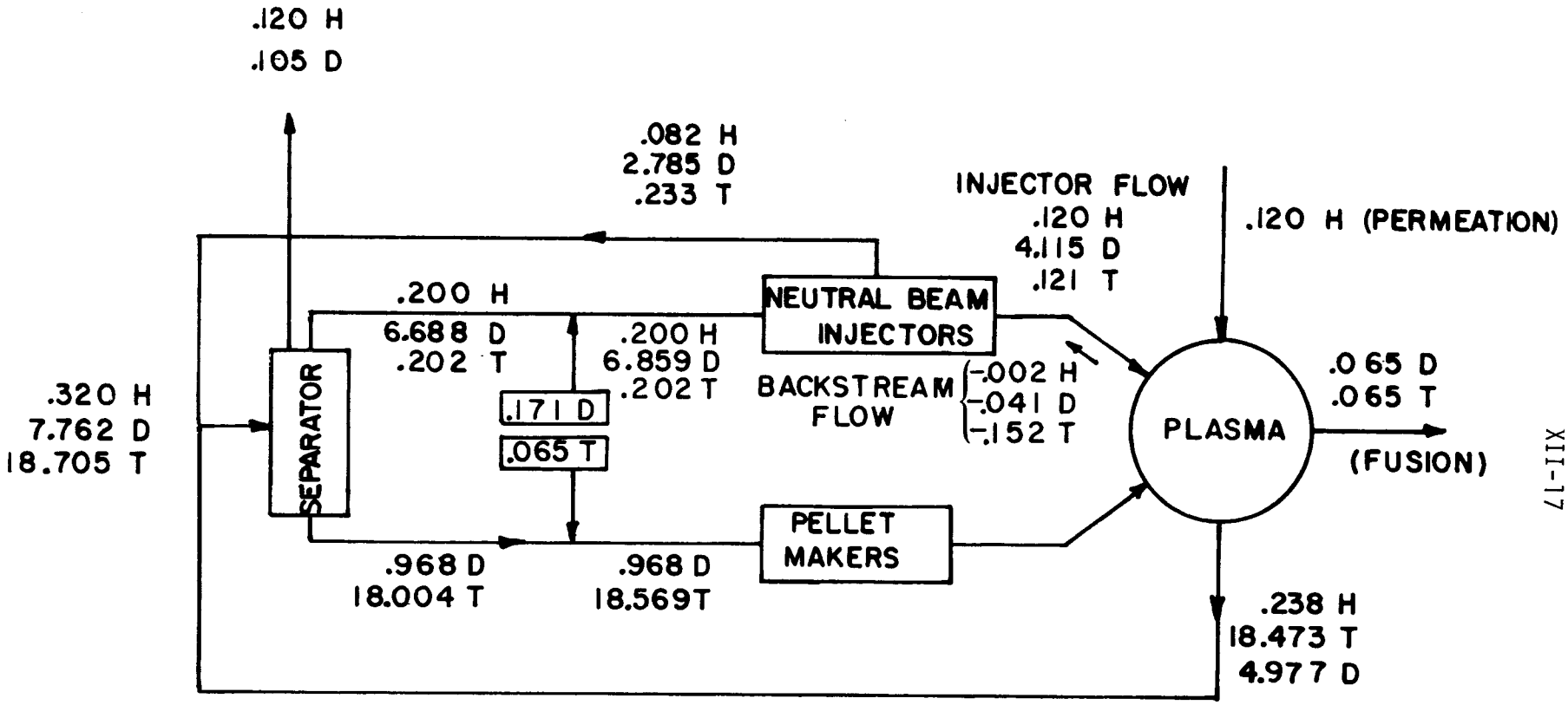

ALL FLOWS ARE IN m-mol/sec
PURITY OF EACH FUEL STREAM ~ 95 %

FIGURE XII-B-6

Table XII-B-1

Concentrations in the TETR Isotope Separator

	Flow Rate* 10^{-3}mol/sec	H_2	HD	HT	D_2	DT	T_2
			Concentrations (%)				
A	3.093	0.07	4.76	0.40	80.67	13.53	0.57
B	23.688	0.01	0.42	1.56	4.41	32.77	60.82
C	13.693	0	0	0	25	50	25
D	40.474	0.01	0.61	0.95	17.21	37.13	44.09
E	19.472	0	0	0	0	10.0	90.0
F	21.002	0.02	1.18	1.82	33.10	62.30	1.58
G	13.693	0	0	0	2.05	95.51	2.43
H	7.0309	0.06	3.38	5.23	91.06	0.28	0.0
J	7.0309	0.19	8.11	0.24	86.28	5.11	0.08
K	7.089	0.0	5.38	0.25	89.02	5.28	0.08
L	.226	6.17	93.93	0.0008	0.0	0.0	0.0

*Flow Rates are for a total of four quadrants. Divide by four for one quadrant.

The plasma exhaust and the injector recycle are mixed at low temperature (to prevent equilibration and thus creation of DT which would have to be reconverted to D_2 and T_2) and introduced to column 1. This column operates at a pressure of 1000 torr with a condenser temperature of 25.1 K. This is a packed column, 50 stages long with a reflux ratio of 13, requiring a reboiler power of 90 W. The bottom product is tritium of 95 atom % purity.

The overhead product of column 1 is fed to a second column. Columns 1 and 2 are connected end to end to form a single long tube. The reboiler of the second column is heated by the condenser of the first. Because of the lower flow rate in the second column, the effective reflux ratio is 40. The two columns are cooled by a single refrigerator at the top of the upper column.

The bottom product of the upper column is 95% DT. The upper product of the second column is >91% D_2 with small amounts of HD and HT. The DT mixture is catalyzed to molecular equilibrium and fed to column 1 as described earlier. It is now 50% DT with 25% each D_2 and T_2.

The overhead mixture is also equilibrated before further distillation occurs. In this step, because of the large D/T ratio, almost all (>90%) the hydrogen in this mixture combines with deuterium to form HD and almost all the tritium forms DT; very little HT remains. As the HD can be safely discarded as long as it is not contaminated by tritium, removing hydrogen from the fuel is now quite simple. A third, small distillation column separates enough HD and H_2 from the deuterium-rich mixture to provide 50% recovery of hydrogen. The remaining material which is 95% D, with ~2.5% each H and T, is used as feed to the injectors. The tritium content of the hydrogen waste is only 5.1×10^{-5}% and results in the loss of only 37 curies per year. A summary

of the characteristics of the three columns is given in Table XII-B-2.

The distillation system tritium inventories are estimated as follows: The column diameters are chosen to result in a 10 cm/sec superficial vapor velocity which is estimated to be below the flooding limit of a packed column containing hydrogen. The liquid hold-up is estimated to be 18% of the packed volume, and the molar volume is estimated at 25 cm^3. The HETP is estimated to be 2 cm in the larger columns and 1.6 cm in the smaller one.

With a total of 110 stages in columns 1 and 2, the overall length of the first two columns is about 2.2 meters. Because the column diameter is only 4 cm, the diameter of refrigerators, dewars and controls will probably dominate the overall physical dimensions of the system. Enclosing the entire initial part of the system in a dewar 1/2 meter in diameter and 4 meters long seems quite possible. The third column is estimated to be 96 cm long and 1 cm in diameter, so a dewar 25 cm diameter and 1.5 meters long will probably accomodate the necessary equipment.

Removing a stream of DT to a room temperature (or hotter) equilibrator and returning it to the cryostills requires heat exchangers to minimize refrigeration loads. A scale-up of existing heat exchangers indicates that adequate exchangers of 95+% efficiency can easily be accommodated in the dewars just described. With high efficiency heat exchangers, the refrigeration load will not be significantly increased.

A system to separate the fuel into 99.5% T and 95% D streams was also investigated. This was done on the assumption that the isotopic composition of the plasma determined that of the fuel streams, rather than the converse. That is, if the

Table XII-B-2

TETR Isotope Separator Characteristics

	Column I	Column II	Column III	
Bottom Product	95% T, 5% D	50% T, 50% D	94% D, 3% T, 3% H	
Top Product	36% T, 63% D, 1% H	94% D, 3% T, 3% H	53% H, 47% D	
Power/Quadrant	90	90	6.25	watts
Power (Refrigeration)*	360	360	25	watts
Diameter	3.9	4	1	cm
# Stages	50	60	60	
Length	100	120	96	cm
HETP (Height Equivalent to a Theoretical Plate)	2	2	1.6	cm
Total Volume	4700	6000	326	cm^3
T Fraction	0.68	0.23	0.07	
T/Quadrant	3.3×10^5	1.4×10^5	425	Ci
T Total	1.3×10^6	5.7×10^5	1700	Ci

* It is probably possible to cool columns I and II with a single refrigerator by using the heat of condensation in the column I condensor to warm the reboiler of column II.

neutral beam purity and the plasma concentrations are fixed, then the tritium beam purity is also fixed; the present calculations assume fuel stream purities, from which the plasma concentration is determined.

Increasing the T stream purity to 99.5% resulted in a net refrigeration power increase of 5% to 95 watts in the first two columns, and a 60% increase of the first column length to 80 stages. The average tritium content of the first column was 76%. No other changes were required. The total tritium inventory in the separation system was increased from 4.7×10^5 Ci/quadrant to 7.2×10^5 Ci/quadrant. This increase is about 10% of the entire TETR tritium inventory.

Some of the costs involved in the fuel separation system are shown in Table XII-B-3.

Table XII-B-3

TETR Costs for Fuel Separation

400 W of refrigeration at 20 K for column I and 4 refrigerators at 100 W	$280 K
4 double distillation columns with monitors and controls	200 K
Debris Separation Palladium diffuser systems including furnaces	20 K
4 systems with 3 diffusers in each	96 K
Methane cracking units	40 K
4 glove boxes	500 K
4 control systems	120 K
Emergency storage for stills	20 K
Total	1276 K

XII-C Tritium Control System for UWTETR

XII-C-1 Introduction

The total tritium inventory in the TETR facility represents over 10^8 Ci (0.37 EBq), most of which is constantly being recirculated through the plasma fuel and exhaust cycle. The designers and operating personnel must employ conservative and well-developed tritium control systems to assure that the escape of tritium from the facility is within acceptable levels.

In order to quantify the probable frequency and magnitude of possible tritium releases, it is necessary to identify the location of the tritium and the pathways for its escape. During operation of the facility, the potential sources of tritium release are components of the plasma fuel and exhaust system, the storage vault, the water used to cool the divertor and the water used to cool the first wall. Each of these potential sources for tritium release are examined separately. Some tritium contamination may exist on the irradiated specimens transferred to the hot-cell but this will be an insignificant part of the radiation emitted from these specimens.

XII-C-2 Plasma Fuel and Exhaust System

A large number of components interconnected with multipile pipes and valves comprise the plasma fuel and exhaust system. The fueling system consists of neutral beam injectors, and pellet fabrication equipment while the exhaust system consists of vacuum pumps for removal of unburned fuel from the plasma chamber and from the injector system. A fuel reprocessing system is required which will chemically purify the fuel and isotopically separate the hydrogen isotopes so that clean fuel is available for reinjection into the plasma. Many of these components contain large fuel inventories, and have the potential for release of significant quantities of tritium under off-normal operation.

A three-level barrier containment system, shown diagrammically in Figure XII-C-1, for control of gaseous tritium is provided, therefore, to ensure minimal tritium releases to the environment.[1] The rationale for this design is to prevent the dilution of tritium within each barrier system so that it can be recovered before it penetrates to the next barrier. These barrier systems are described next.

XII-C-3 Primary Containment System

The primary containment system consists of the components and pipes which enclose the tritium-bearing materials. These components must demonstrate high integrity for the containment of tritium and be assembled to ensure low tritium leakage. All connections must be welded, therefore, wherever possible. The complete assembly must be leak checked with helium prior to the introduction of tritium.

The impact of the release of tritium from one of the components is reduced further by subdividing the fuel system into at least four quadrants. The tritium inventory in any quadrant, Table XII-C-2, is therefore ~3.0 kg.

XII-C-4 Secondary Containment System

Most of the primary components are enclosed in a secondary containment system. Large pieces of equipment that may require adjustment or maintenance are enclosed in gloveboxes. These gloveboxes contain a circulating inert gas which is monitored for tritium. Preliminary estimates indicate that approximately 1% of the building volume is enclosed by the gloveboxes, Table XII-C-2.

The primary system pipes outside of the gloveboxes are enclosed within larger diameter pipes. The annulus between these pipes is filled with slowly flowing inert gas which is monitored for tritium.

It should not be necessary to enclose the plasma chamber in a glovebox. The shield which surrounds the blanket can serve as a secondary container if

TRITIUM EFFLUENT SYSTEM DESIGN FOR TETR

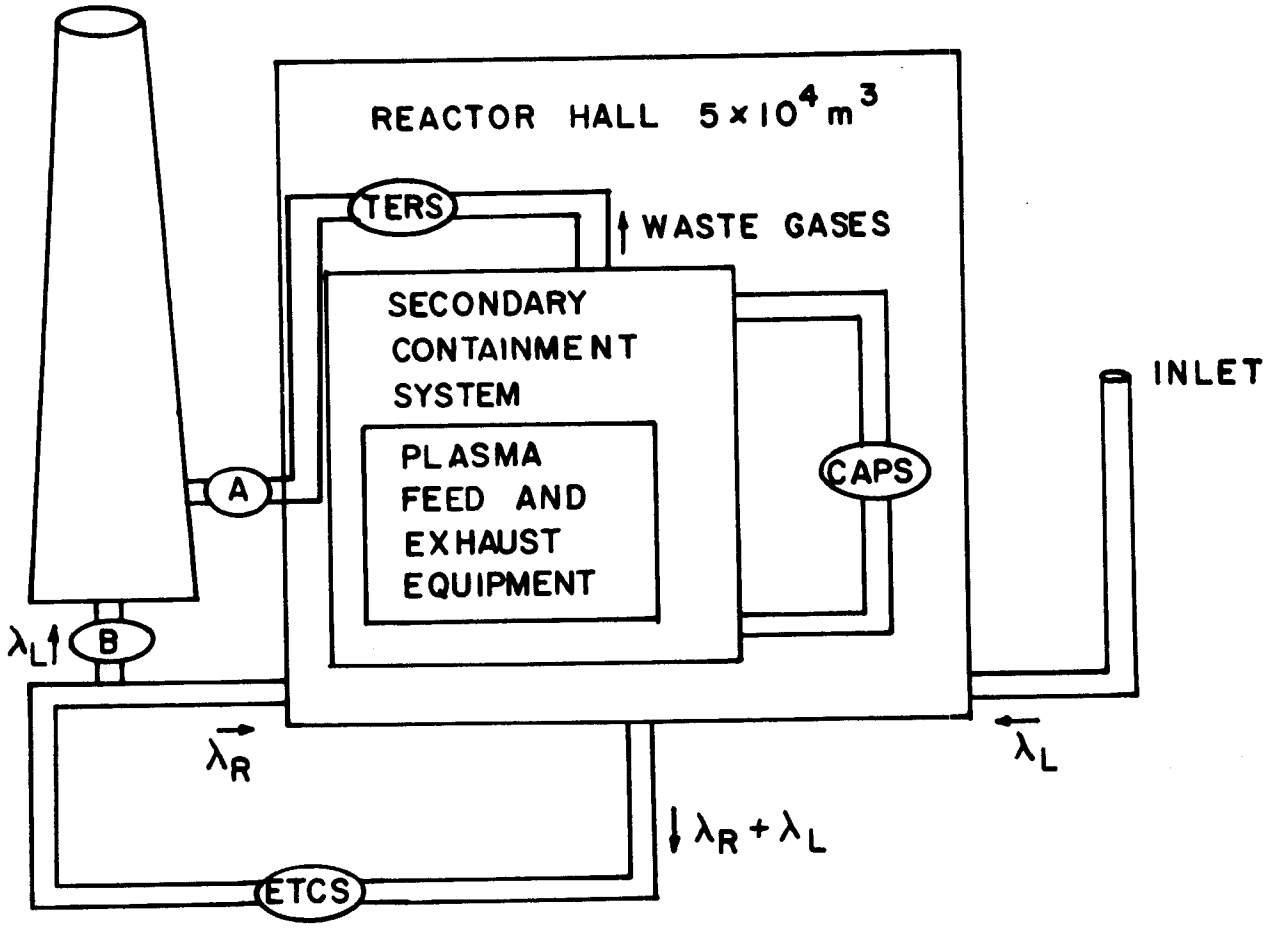

LEGEND:

CAPS = CONTAINMENT ATMOSPHERE PURIFICATION SYSTEM

TERS = TRITIUM EFFLUENT REMOVAL SYSTEM

ETCS = EMERGENCY TRITIUM CONTAINMENT SYSTEM

λ_R = FRACTIONAL AIR RECYCLE, SEC^{-1}

λ_L = FRACTIONAL AIR LEAK RATE, SEC^{-1}

Fig XII-C-1

it is gas-tight and a space is provided to circulate an inert gas between the blanket and the shield.

The secondary containment system is designed to capture any tritium leaking from the primary system. The tritium accumulating in the glovebox atmosphere must be removed, therefore, before it can escape into the reactor building. Two options are available for the operation of the Containment Atmosphere Purification System (CAPS); either continuous detritiation or detritiation only as required. Before the detritiation scheme can be specified an estimate is required of the permissible tritium concentration in the glovebox atmosphere.

Tritium escape from the gloveboxes can occur by either gas leakage or permeation. Gas leakage should be insignificant because the gloveboxes are fabricated and maintained in a leak-tight condition. Also, they are operated below atmospheric pressure so that in the event of a leak the inward velocity of air flow is greater than the outward diffusion of tritium.

Permeation of tritium through the gloves has been shown[2] to be the most probable path for tritium escape from the glovebox. This is expected because the gloves are the thinnest barrier and have the highest permeability of any of the construction materials of the glovebox.

The permeation of hydrogen isotopes has been measured for several rubber films used to make gloves[3,4,5,6]. These data have been combined, Figure XII-C-2, and expressed as the permeation rate for tritium (μ Ci/day) through one pair of gloves (1 m^2) for a one ppm difference in concentration as a function of various thicknesses. As noted, the permeation rate for tritiated water is 20-100 times faster through a particular rubber than the permeation rate for the dry, molecular gas HT. Also, the permeation rate of tritiated water is the slowest through butyl rubber, which should be used for fabrication of the gloves.

FIGURE XII-C-2

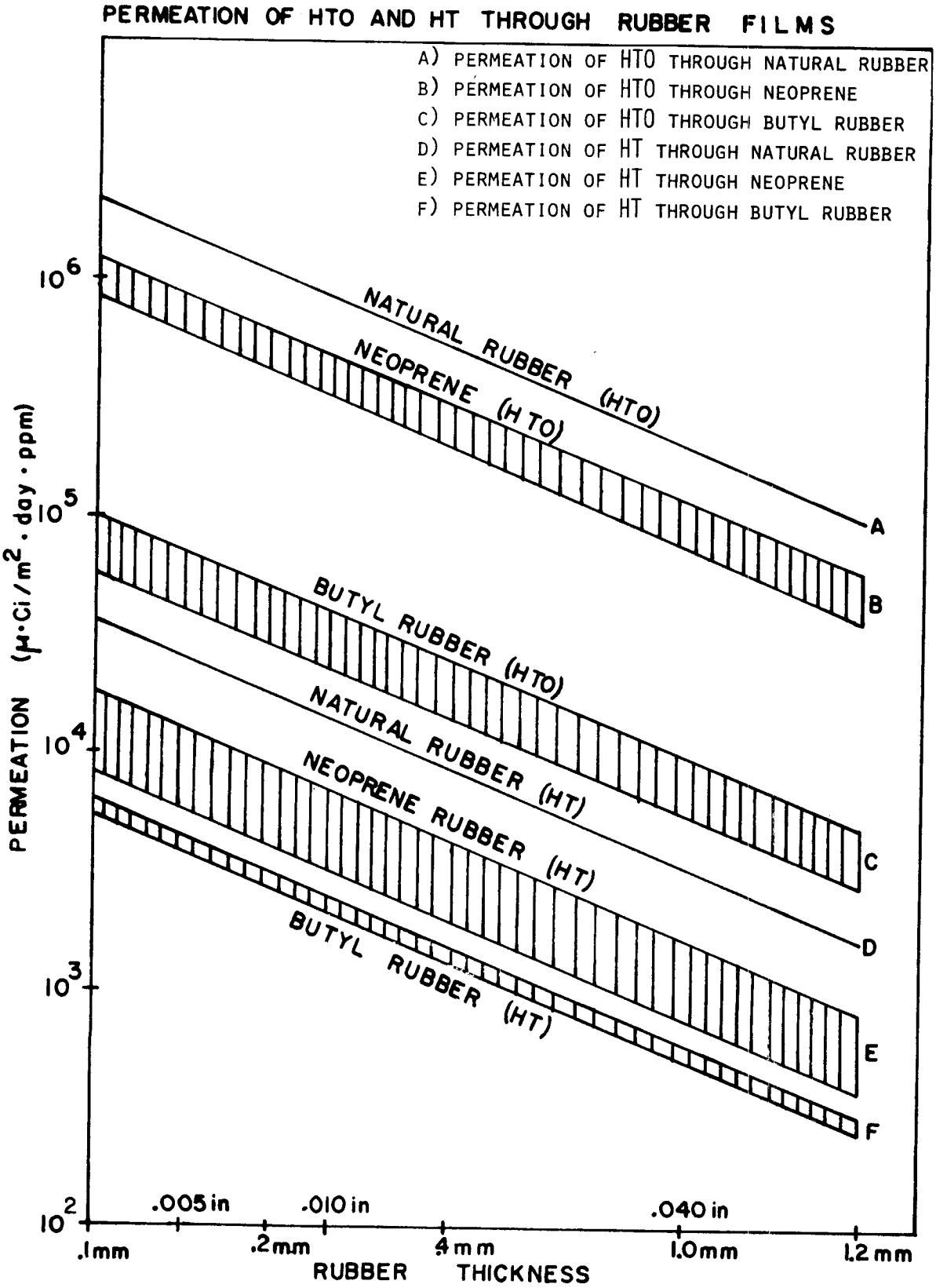

Because of the poor abrasion resistance of butyl rubber, a laminated glove comprised of 0.51 mm of butyl rubber and 0.25 mm of neoprene rubber is commercially available for this use.

The permeation data indicate that in order to reduce the permeation of tritium,it is important to prevent the formation of tritiated water, which occurs principally by chemical exchange with water and secondarily by direct oxidation. The formation of tritiated water in the glovebox can be controlled therefore, by continuously removing water vapor and oxygen from the glovebox atmosphere by use of the Containment Atmosphere Purification System.

The concentration of water in a glovebox atmosphere dried by molecular sieves operating at ambient temperature is typically 1 ppm (10^{-6} atm). The oxygen content is controlled at approximately 10 ppm by the use of Dow Q-1 reactant. At 50% relative humidity and 20°C in the room air, about 0.72 cm^3/sec of water vapor will permeate into the gloveboxes. In order to keep the glovebox atmosphere below 1 ppm water, the glovebox atmosphere is circulated through the desiccant at the rate of 0.72 m^3/sec.

Estimates can now be made of the permissible concentrations of HTO and HT within the gloveboxes and the subsequent permeation of each species through the gloves. The rate of HTO formation, S^{HTO}, is dependent upon the chemical conversion of part of the tritium that leaks from the primary system into the glovebox. Water vapor (H_2O) permeates through the gloves at the rate, S^{H_2O}, of 0.72 cm^3/sec. This water vapor mixes with the HTO in the glovebox and is captured on the desiccant in the ratio of the source terms, i.e.,

$$\frac{S^{HTO}}{S^{H_2O} + S^{HTO}} \left(\begin{matrix}\text{vap. press. } H_2O \\ \text{over mol. sieve}\end{matrix}\right) = \begin{matrix}\text{partial} \\ \text{press. HTO}\end{matrix}$$

By use of this relationship, it is possible to calculate HTO partial pressure and its permeation rate through the gloves into the room (see Table XII-C-1) for several values of S^{HTO}.

This calculation indicates that no more than 8400 Ci/day of HTO may be generated within the gloveboxes before the permeation rate exceeds one Ci/day. Experience with dry (1 ppm H_2O) glovebox atmospheres indicates that only 1% of the tritium is converted to HTO when the HT content is in the 1-10 ppm range. Based upon this ratio, nearly 8.5×10^5 Ci/day (85.0 g) of tritium could leak from the primary system to the glovebox without causing the permeation of HTO through the gloves to exceed 1 Ci/day.

Such a large leak rate from the primary system could not be tolerated, however, because the permeation of T_2 (or HT) through the gloves would become significant and because of the risk of a large release of HTO if the secondary containment should fail. Based upon the estimated permeability of molecular HT through the butyl gloves, a concentration of 1 ppm HT (10^{-6} atm) in all the gloveboxes will cause a permeation release of only 0.47 Ci/day. A concentration of 1 ppm HT will be reached in the 500 m^3 glovebox system in one day if 0.065 g/day T_2 leaks from the primary system to the gloveboxes. This corresponds to 650 Ci for the entire glovebox system. These estimates indicate that, by use of the continuously circulated and dried glovebox atmosphere system, the combined permeation of HT and HTO through the gloves is less than 1 Ci/day.

When a tritium monitor in a glovebox indicates the tritium concentration is above 2 ppm, that glovebox atmosphere is diverted to a Tritium Effluent Removal System and clean gas is supplied to the glovebox.

Parts of the primary system may leak at a rate which would cause the glovebox atmosphere to regularly exceed 1 ppm HT. These parts of the system

TABLE XII-C-1 Permeation Rate Through Gloves for Several Pressures of HTO in Glovebox

P_{HTO} ppm	$S^{HTO(a)}$ Ci/day	Permeation (HTO) Ci/day
1	8.4×10^{4}	7.3
10^{-1}	8.4×10^{3}	0.73
10^{-2}	8.4×10^{2}	0.073

(a) S^{HTO} = Production rate of HTO in glovebox.

are separated from the other gloveboxes and are serviced by a continuously operating detritiation system. This system may utilize cryogenic adsorption or hydrogen gettering in order to simplify later recovery of the tritium. Continuous detritiation is much more expensive than detritiation on demand, hence it is used only where the increased leakage rate requires it.

Another advantage in using a dry glovebox atmosphere accrues because of the reduced biological hazard of molecular tritium, which is not as readily absorbed by the body as is tritiated water vapor. The occupational Radiation Concentration Guideline[7] (RCG) for tritiated water in air, 5 $\mu Ci/m^3$, is 400 times less than the occupational RCG for molecular tritium, 2000 $\mu Ci/m^3$. By using room air monitors that distinguish between molecular tritium and tritiated water vapor, workers may remain in a room where tritium levels exceed 5 $\mu Ci/m^3$ if the HTO portion is small. This is an advantage, particularly if a large spill occurs within a glovebox containing a dry atmosphere because the permeation of HTO will be small.

XII-C-5 Tertiary Containment System

The tertiary tritium containment system consists of the reactor hall, rooms containing tritium processing equipment, the reactor building, an Emergency Tritium Containment System (ETCS) and a Tritium Effluent Removal System (TERS). As with the primary and secondary containment systems, the reactor building is subdivided so that no room or work area has a volume of more than 20% of the building volume. The reactor hall is assumed to have a volume of 5×10^4 m^3 (Table XII-C-2) and is divided radially into quadrants. Such a division is expected to offer the least possible impediment to maintenance of the vacuum chamber, the blankets and the magnets.

The reactor building atmosphere is maintained at a pressure of 1.23×10^{-3} atm below the external atmospheric pressure. Air flows through the building and

out a 30 m stack at a rate of approximately 20% of the building volume per day. This air flow enters the building through nonradioactive work areas and passes through areas of increasing radioactive hazard before being released. Under normal operation this exhaust would contain < 1 Ci/day. Because neutron leakage from the reactor will make the reactor hall uninhabitable during reactor operation and will create short-lived isotopes (e.g., ^{13}N, ^{16}N and ^{41}Ar), the main reactor hall may not be ventilated routinely.

Exhaust gases from vacuum pumps which are used to evacuate tritium equipment and purge gases are processed by the Tritium Effluent Removal System before being released to the atmosphere. The TERS converts tritiated gaseous waste (HT, tritiated hydrocarbons, etc.) to tritiated water which is collected. This water and other liquid or solid tritiated waste materials are then fixed in a solid matrix such as concrete, packaged in double, sealed drums, and buried.

The ETCS consists of a heated catalyst (170°C) which helps oxidize airborne HT (or T_2) to HTO (T_2O), a series of alumina adsorbent beds which are presaturated with H_2O at 100% relative humidity, and the required air handling equipment. If a simultaneous failure of both the primary and secondary containment systems should occur in one of the work areas, the ETCS is activated, and the building air flow is redirected so that the affected area is recirculated through the ETCS, and some fresh air leaks into the contaminated area from surrounding areas, ~ 0.1%/day of the building volume. In order to reduce the risk of releasing contaminated building air through the stack, building inlet dampers are shut during the cleanup, reducing the stack air flow to account for only the in leakage of air.

Because the ETCS is only used during emergencies, but represents a large capital investment, an assessment must be made of its flow rate requirements.

The time required to detritiate the reactor building atmosphere following a tritium spill is a function of the air flow rate (capacity) of the ETCS. Figure XII-C-3 shows the time required to decontaminate the air to the RCG level (5 $\mu Ci/m^3$) as a function of the flow rate of the ETCS for spills from 1 to 10^3 g into the reactor building (5×10^4 m^3). As noted, the time depends only slightly upon the quantity of tritium released.

Several factors need to be considered regarding the optimum time required to detritiate the building atmosphere. For instance, it may be desirable to return to the reactor building as soon as possible, in order to repair the cause of the tritium spill, and return the reactor facility to full service; however, the cost of the ETCS is high for this type of operation. Because the TETR is an experimental materials facility, rapid return to normal operation is probably not necessary. On the other hand, a long clean-up time may not be desirable because it could permit some tritium to be adsorbed on surfaces within the reactor hall. This absorbed tritium may require, then, an extended period of time to be desorbed.

The utilization of a 2.5 m^3/s ETCS provides reasonable detritiation in four days following a one 1kg tritium spill, or 2.5 days following a one g spill, to return the concentration of tritium in the building to the RCG value for HTO. There are several reasons for not considering detritiation to the RCG value, however. First; the detritiation efficiency may decrease as tritium concentrations fall; secondly, tritium will be adsorbed on walls, floors, and other surfaces and finally, it is quite possible to exercise several options and reenter the building long before tritium concentrations (as HTO) reach 5 $\mu Ci/m^3$.

One option is to detritiate the atmosphere to only 1000 $\mu Ci/m^3$, instead of 5 $\mu Ci/m^3$. At this concentration, the entire building atmosphere contains only

FIGURE XII-C-3

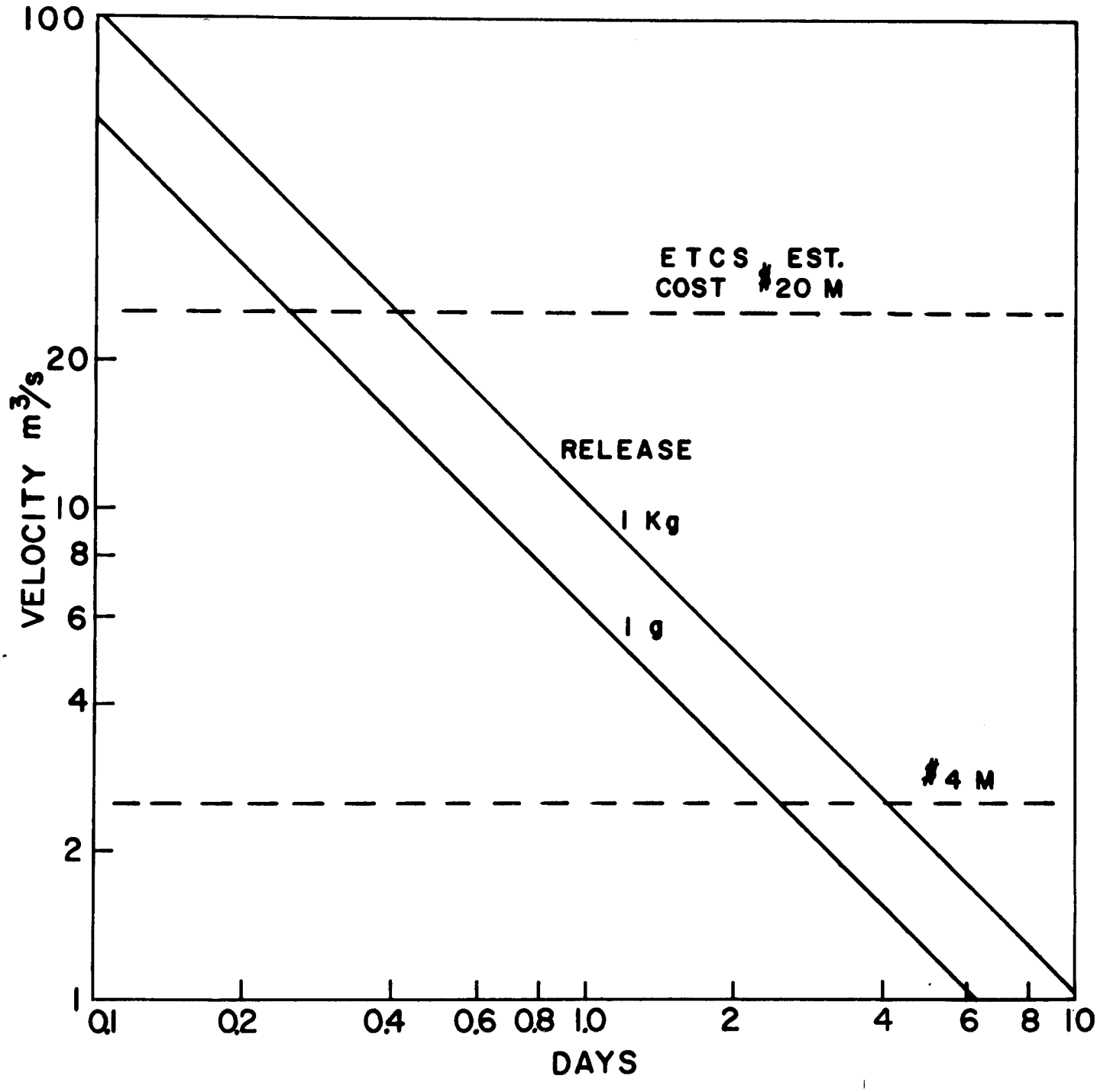

TIME REQUIRED TO REDUCE BUILDING ATMOSPHERE TO RCG FOLLOWING TRITIUM RELEASE AS A FUNCTION OF THE VELOCITY OF EMERGENCY TRITIUM CONTAINMENT SYSTEM

50 Ci which could be ventilated from the building with a small radiation hazard to the public. Detritiation to the 1000 $\mu Ci/m^3$ concentration requires only 2.85 days following a one kg spill compared with the 4 days required for detritiation to the 5 $\mu Ci/m^3$ concentration. Another 23 Ci will be released through the stack during the cleanup because of incomplete air detritiation. In the process of detritiating the contaminated air, 6.2×10^5 m^3 of air will pass through the ETCS. If a temperature of 20°C and 50% relative humidity are assumed, 5.7×10^3 liters of tritiated water at an average concentration of 1756 Ci/liter will be captured on the adsorbent. The adsorbent is regenerated by purging air through it and collecting the water. The tritium in the water could be recovered for reuse.

Another means of gaining early access to the contaminated reactor building following a tritium spill is to utilize a worker who is protected by a bubble suit[8,9] with a fresh air supply so that he will assimilate only one mCi of HTO while working for as long as 8 hours in an atmosphere of HTO at a concentration of 20,000 $\mu Ci/m^3$. This tritium uptake will result in a body level of approximately 25 μCi/liter, less than the 29 μCi/liter level which is the permissible limit for employees. If the airborne tritium after a release is less than 10% HTO, it will be possible to begin maintenance operations as soon as the total tritium reaches 2×10^5 $\mu Ci/m^3$, or about 39 hours after the one kg release. Smaller HTO fractions would permit even earlier access. Cleanup of the building atmosphere could continue as necessary.

XII-C-6 Tritium Permeation Into Cooling Water

The first-wall of the reactor is water-cooled stainless steel resulting in a maximum temperature of 200°C.* On the plasma side of the first wall is a carbon ISSEC which protects the first wall from energetic ions. This carbon shield is not gas tight; consequently, the first wall will be subjected to the

*This calculation was done before the final coolant temperature was decided. The conclusions are essentially unaltered at 260°C.

same tritium pressure as the gas pressure outside of the separatrix of the plasma. This gas pressure will cause tritium to permeate through the stainless steel first wall into the cooling water. An assessment of this tritium permeation is necessary.

Tritium permeation through a steel membrane can be estimated by the relationship,[14]

$$V = \frac{C°A}{\sqrt{3}x} (P_1^{1/2} - P_2^{1/2})\ e^{-Q/RT} \times 10^{-5}$$

where V = leak rate (cc (STP)/sec)

C° = temperature independent diffusion coefficient

$$(\frac{cc\ (STP)\ \ mm}{hr\ atm^{1/2}\ cm^2})$$

A = Area of diffusing medium (cm^2)

X = Thickness of diffusing medium (mm)

P_1 = downstream pressure (mm Hg)

P_2 = upstream pressure (mm Hg)

R = gas constant cal/°K mole

T = temperature (°K)

Q = activation energy of diffusion (cal/mole)

When $C° = 850\ (\frac{cc\ (STP)\ mm}{m\ atm^{1/2}\ cm^2})$

$A = 2.21 \times 10^6\ cm^2$

X = 1.5 cm = 15 mm

$P_1 = 10^{-5}$ mm Hg

$P_2 = 0$

Q = 16100 cal/mole

R = 1.98 cal/°K mole

T = 473°K = 200°C

duty factor = .83

$$1 \times 10^{-5} = \frac{\text{hr atm}^{1/2}}{\text{sec (mm Hg}^{1/2})}$$

The leak rate, V, is equal to

$$7.80 \times 10^{-8} \frac{\text{cc (STP)}}{\text{sec}}$$

or .015 Ci/day

Once the tritium is absorbed into the water, the following chemical change occurs, $T_2 + 2H_2O = 2HTO + H_2$. This reaction has a large equilibrium constant at 200°C and with the large excess of H_2O, essentially, all the tritium appears as tritiated water. Although the quantity of tritium is small, some consideration must be given as to its concentration in the water. An estimate of the volume of water required to cool the first wall can be obtained from the relationship,

$$P_d = \Delta T \times Cp \times V$$

where P_d = Power dissipated

ΔT = temperature change in coolant

V = Volume of water required per unit time

Cp = heat capacity of coolant

When P_d = 157 MW

ΔT = 75°C

Cp = 1 cal/g°K or 4.184 J/cm^3 °K

then $V = 5.00 \times 10^5$ cm^3/sec

$= 500$ l/sec

$= 4.32 \times 10^7$ l/day

The concentration of tritium in the water will be:

$$C_T = \frac{.015 \text{ Ci/day}}{4.32 \times 10^7 \text{ l/day}} = 3.47 \times 10^{-10} \text{ Ci/l}$$

While this conc. is small, the proposed[11] EPA quality for tritium drinking water is 20 nCi/l, which is about 60 times the concentration in the coolant water which passes only once through the reactor. The coolant water coming from the reactor would qualify for drinking, therefore, if it were recirculated, but 1/60 of it replenished with clean water on each pass through the reactor. The quantity of clean water required would be,

$$\frac{1}{60}\ (4.32 \times 10^7\ \text{l/day}) = 7.20 \times 10^5\ \text{l/day or about 200,000}\ \frac{\text{gal}}{\text{day}}$$

The expense of providing clean, deionized water at the rate of 200,000 gallons/day must be considered.

If the continuous replenishing technique is not practiced, as previously described, then a captive cooling water system must be considered. If a moderate recycle time of the water is assumed to be ~ 200 s, for the flow rate requirement of 500 l/s, then the system would require 10^5 l, which would continuously increase in tritium concentration by about .015 Ci/day. If the useful life of the facility is five years of full service, then the tritium conc. of the water will be,

$$\frac{5\ \text{yr} \times 0.015\ \text{Ci/day}}{10^5\ \text{l}} = \frac{27.4\ \text{Ci}}{10^5\ \text{l}} = 2.74 \times 10^{-4}\ \text{Ci/l}$$

This tritiated water might be disposed of by dilution to 5×10^9 l (5×10^6 m^3) with fresh water so that the combined quality is acceptable for drinking water standards. Alternatively, the water could be packaged for burial. The present cost for such an operation is estimated at $100 for a package containing 25 l of water. At this rate, it would cost $400,000 to dispose of this tritiated water. Some techniques are being investigated, however, which may be able to detritiate this water, and at a lower cost.[12]

Another possibility arises from the periodic clean out of the cooling system planned for TETR. At the end of a two month period, the concentration of tritium in the water is:

$$\frac{60 \text{ days } (.015 \text{ Ci/day})}{10^5 \text{ l}} = \frac{.90 \text{ Ci}}{10^5 \text{ l}}$$

$$= 9.0 \times 10^{-6} \text{ Ci/l}$$

This would require dilution to 10^8 ℓ with fresh water to render it drinkable.

The captive cooling water for the first wall must be subsequently cooled by a suitable heat reservoir by use of a heat exchanger. Permeation of tritium through this heat exchanger is a possibility but the tritium pressure causing the permeation is very small. For example, the tritium pressure is described by the formation of tritiated water, namely,

$$T_2 + 2\ H_2O = 2\ HTO + H_2 \ ,$$

for which the equilibrium constant is defined as,

$$K = \frac{(P_{HTO})^2\ (P_{H_2})}{(P_{H_2O})^2\ (P_{T_2})}$$

The partial pressure of T_2 is found by rearrangement of terms to be,

$$P_{T_2} = \frac{(P_{HTO})^2\ (P_{H_2})}{(P_{H_2O})^2\ K}$$

The pressure of tritium can be estimated as follows:

The partial pressure of HTO is defined as follows:

$$P_{HTO} = \frac{\text{moles HTO}}{\text{moles } H_2O}\ P_{H_2O}$$

At the end of five years, the previous calculations indicate the accumulation of 27.4 Ci of tritiated water in 10^5 l of H_2O. The P_{HTO} would be, therefore

$$P_{HTO} = \frac{9.13 \times 10^{-4} \text{ moles HTO}}{5.5 \times 10^{6} \text{ moles } H_2O} P_{H_2O} = 1.66 \times 10^{-10} P_{H_2O}$$

The P_{H_2} would be approximately the dissociation pressure for water at 200°; i.e.

$$P_{H_2} = 2 \times 10^{-15} \text{ torr}$$

The value[10] of K = 23.5 at 200°C.

Therefore:

$$P_{T_2} = \frac{[1.66 \times 10^{-10} P_{H_2O}]^2 [2 \times 10^{-15} \text{torr}]}{23.5 \times [P_{H_2O}]^2}$$

$$P_{T_2} = 1 \times 10^{-36} \text{ torr}$$

The conclusion is that any tritium permeation through the heat exchanger would be insignificant at such a low tritium driving pressure.

XII-C-7 Tritium Permeation Into Modular Coolant

Tritium leakage through stainless steel is described as before by the equation:

$$V = \frac{C^\circ A}{\sqrt{3}x} (P_1^{1/2} - P_2^{1/2}) \; e^{-Q/RT} \times 10^{-5} \qquad (14)$$

where V = leak rate in cc/sec

C° = permeation constant for stainless steel

A = area of diffusing medium (cm^2)

X = thickness of diffusing medium (mm)

P_1 = downstream pressure (mm Hg)

P_2 = upstream pressure (mm Hg)

Q = activation energy of diffusion for stainless steel $(\frac{cal}{mole})$

R = gas constant cal/°K mole

T = temperature of diffusing medium (°K)

$$10^{-5} = \frac{hr \cdot atm^{1/2}}{sec \cdot (mm\ Hg)^{1/2}}$$

When

$$C° = 850 \frac{cc\ (STP)\ mm}{hr \cdot atm^{1/2} \cdot cm^2}$$

$A = 16\ m^2 = 1 \times 10^4\ cm^2$

$X = 1.0\ cm = 10\ mm$

$P_1 = 10^{-5}$ torr

$P_2 = 0$

$Q = 16100$ cal/mole

$R = 1.98$ cal/°K mole

$T = 200°C = 473°K$ duty factor = .83

then $V = 7.04 \times 10^{-10} \frac{cc\ (STP)}{sec}$

$= 1.35 \times 10^{-4}$ Ci/day

It is seen that 1.35×10^{-4} Ci/day of tritium leaks into the water coolant of wall in front of the test modules. Over a five year operation period, the amount of tritium accumulating in the coolant is:

$$1.35 \times 10^{-4}\ \text{Ci/day}\ (\frac{365\ days}{yr})\ (5\ yrs) = .25\ Ci$$

This amount is insignificant with respect to consideration of leakage out of the coolant through the heat exchanger. Due to the high equilibrium constant for the conversion of T_2 to HTO tritium leakage out of the water to the modules themselves should be slight.

XII-C-8 Tritium Permeation Into The Divertor Coolant

The divertor plate design consists of tubes of thickness 1 mm and inner diameter 1 cm. The material used in construction is Ta - 10 W (10% tungsten, 90% tantalum) and the surface of the plate is corrugated in appearance. Water will be used to cool the plate. Because the coolant is water and because the volume of water involved is large (16,000 l), it is important

to know how much tritium may be expected to collect in the water due to leakage through the plate.

Data on tritium diffusion through Ta-10W are scarce. As a first approximation, let us assume that the plate material behaves towards the diffusion of tritium in the same fashion as pure tantalum does towards the diffusion of hydrogen. We may then make use of data given in (15) to calculate the permeation constant for hydrogen in tantalum.

The diffusion coefficient of hydrogen in tantalum is:

$$D = 7.5 \times 10^{-3} \exp - \left[\frac{10380}{RT}\right] \frac{cm^2}{sec} \qquad (15)$$

Sieverts' constant, K, is given as $3.033 \times 10^4 \exp - [4170/T] \frac{\text{torr}^{1/2}}{\text{(mole fraction H)}}$ (15) and is inversely related to the solubility of hydrogen in tantalum. The solubility, S, of hydrogen in tantalum may then be calculated:

$$S = \frac{1}{K} = \frac{1}{3.033 \times 10^4 \exp - [4170/T] \frac{\text{torr}^{1/2}}{\text{(mole fraction of H)}}}$$

$$3.29 \times 10^{-5} \exp \left[\frac{4170}{T}\right] \frac{\text{mole fraction H}}{\text{torr}^{1/2}}$$

Extracting the gas constant, R, from the exponential term leaves:

$$S = 3.29 \times 10^{-5} \exp [8300/RT] \frac{\text{mole fraction H}}{\text{torr}^{1/2}}$$

The mole fraction of hydrogen in tantalum is expressed as $\left(\frac{\text{moles H atoms}}{\text{moles Ta}}\right)$. If we convert this to an expression for the mole fraction of hydrogen in tantalum in terms of the number of moles of hydrogen gas, H_2, which has dissolved into

the metal as H atoms and the number of moles of metal, then the new mole fraction expression is:

$$1/2\ n_H = n_{H_2} \quad n_x = \text{mole fraction of species x in the tantalum}$$

We may convert the expression for the solubility of hydrogen in the tantalum metal to:

$$S' = 1/2\ (3.29 \times 10^{-5} \exp\ [8300/RT]\ \frac{\text{mole fraction } H_2 \text{ in Ta}}{\text{torr}^{1/2}}$$

$$= 1.64 \times 10^{-5} \exp\ [8300/RT]\ \frac{\text{mole fraction } H_2 \text{ in Ta}}{\text{torr}^{1/2}}$$

Permeability, C, is expressed as the product of solubility and diffusivity. Using S' and P, the temperature dependent permeation constant may be calculated:

$$C = S' \times D$$

$$= (1.64 \times 10^{-5} \exp\ [8300/RT])\ (7.5 \times 10^{-3} \exp$$

$$-[10400/RT])\ \left(\frac{\text{cm}^2 \text{ moles } H_2}{\text{sec torr}^{1/2} \text{ moles Ta}}\right)$$

(I) $$C = 1.23 \times 10^{-7} \exp\ [-2100/RT]\ \frac{\text{cm}^2 \text{ moles } H_2}{\text{sec torr}^{1/2} \text{ moles Ta}}$$

The molar volume of tantalum at 500°K is:

$$V_{500°K,\ 1\ \text{mole Ta}} = \frac{\text{At. Wt. of Ta}}{D_{\text{Ta, 298°}} \left(\frac{1}{3\alpha t + 1}\right)} \qquad (16)$$

where V = molar volume of tantalum at new temperature

D = density of tantalum

α = linear coefficient of thermal expansion

t = change in temperature

when $D = 16.6\ g/cm^3$

$\alpha = 6.7 \times 10^{-6}$

$t = 202^oK = (500^oK - 298^oK)$

then $V_{500°K,} = 10.94\ cm^3$

By the ideal gas law, one mole of hydrogen at STP occupies 22.4 l, or 22,400 cm^3.

A unit conversion on expression (I) results in:

$$C = 2.52 \times 10^{-4}\ e^{-2100\ RT}\ \frac{cm^2 \cdot cc\ (STP)}{sec\ torr^{1/2}\ cm^3}$$

or $$C = 2.52 \times 10^{-3}\ e^{-2100\ RT}\ \frac{mm \cdot cc\ (STP)}{sec\ torr^{1/2}\ cm^2}$$

The leak rate, V, of hydrogen through tantalum is expressed as:

$$V = \frac{CA}{x\sqrt{3}} (P_1^{1/2} - P_2^{1/2}) \qquad (14)$$

where V = leak rate in $\frac{cc\ (STP)}{sec}$

C = temperature dependent permeation constant

A = area of diffusing medium (cm^2)

x = thickness of diffusing medium (mm)

P_1 = downstream pressure (mm Hg)

P_2 = upstream pressure (mm Hg)

Before calculating the leak rate of hydrogen through tantalum, the temperature of the diffusing medium must be ascertained. The temperature of the Ta-10W tube is a complex function taking into consideration both the curvature of the surface and the extremes of temperature on the outer and inner surfaces. For a series of tubes laid next to each other, the, the temperature varies with θ, the angle describing the radial deviation of any point on the tube from perpendicularity with the plane of the plate and with the distance of the point from the outer surface of the tube.

As a worst case approximation, let us ignore the radial temperature dependence, look at the highest temperature profile across the tube thickness (θ=0), and assume a linear drop in temperature over the thickness of the tube. The temperature differential across the thickness of the tube and at the point on the tube where θ=0 is 165°C (the maximum temperature of the front wall is 315°C and the temperature of coolant is 150°C). The temperature of the diffusing medium may be chosen at the average value of 232°C.

For a plate of area 76.3 m^2, thickness 1 mm on a plasma with a tritium pressure of 10^{-5} mm Hg at 232°C (505°K), the leak rate, V, is:

$$V = 4.28 \times 10^{-1} \frac{cc\ (STP)\ T_2}{sec}$$

$$= 1.91 \times 10^{-5} \text{ moles } T_2/sec$$

$$= 8.23 \text{ g } T_2/day \text{ (@ 83\% duty factor)}$$

If the assumptions:

(1) Tritium diffusion is similar to hydrogen diffusion

(2) Diffusion through Ta-10 W is similar to diffusion through pure Ta

(3) The divertor plate as designed may be treated as a flat plate of uniform temperature

are valid, the expected tritium leak rate will be very large, on the order of 10 g/day, and provision must be made to remove the tritium.

However, two factors which will not be considered, but which may significantly reduce the level of tritium leakage are:

(1) The formation of an oxide layer on the coolant side of the plate

(2) The effect of the presence of 10% W, a material of low permeability, in the tantalum.

Additionally, we can attempt to evaluate more explicitly the temperature profile in the divertor plate. However, this treatment will only define the tritium leakage more exactly. The leak rate through tantalum at the lowest temperature to be found in the plate, 150°C, at the coolant surface is still about 5 g/day. Therefore, about 10^4 - 10^5 Ci/day can be expected to leak into the divertor coolant. This will significantly increase the inventory of tritium in the reactor. Also, as the equilibrium constant for the reaction:

$$H_2O + T_2 \rightarrow HTO + HT$$

is large at 150 °C, almost all of the tritium will be converted to HTO, reducing the danger of tritium leaking <u>out</u> of the system, but increasing the hazards of a spill of the coolant.

XII-C-9. Removal of Tritium from the Divertor Coolant

The previous estimates indicate that as much as 10 g/day of tritium may permeate through the divertor plates into its coolant water. This tritium will rapidly exchange with the water to form HTO so that the radioactivity of the water will increase at the rate of 6.26 Ci/ℓ per day. This water will be recirculated through an external heat exchanger operating between 150°C and nearly ambient temperature. The tritium partial pressure of this recirculating water is low and, additionally, its permeation rate through the steel heat exchangerat such a low temperature is extremely small; consequently, the tritium concentration of the water would continuously increase. A high tritium water concentration aggrevates, however, the radiolytic decomposition of water, and could lead to widespread contamination in the event of a leak.

For these reasons, the total tritium concentration in the water (volume of water is 16,000 ℓ) is limited to approximately 100 g, i.e. 60 Ci/ℓ (40×10^{-6} mole HTO/mole H_2O). When the concentration of tritium reaches this limit, after approximately 10 days of full-time operation, the water is processed continuously to remove tritium at the same rate that it is permeating into the water. The proposed concentration of tritiated water (40 ppm) is of the same magnitude as that of "heavy water" in natural water, i.e., 150 ppm; therefore, most of the processes used for the production of "heavy water" could probably be adapted for this detritiation process. A processing technique which has a large separation factor, and potentially a low operating cost has been chosen for the water detritiation system.[12]

One of the largest isotopic separation factors for tritium occurs in the chemical reaction,

$$HT + H_2O \rightleftarrows HTO + H_2,$$

in which the equilibrium constant, Table XII-C-5, increases with decreasing temperature.[17] Near 25°C where the equilibrium constant is large, the rate of exchange is extremely slow; therefore, a catalyst must be utilized. Most catalysts operate efficiently only in the gas phase and become flooded with water of used near ambient temperature. Hydrophobic catalysts which can be used in mixed gas-liquid phases are being developed and tested for this process. These catalysts, supported on ceramic beads approximately 5 mm in diameter, are utilized in packed columns for the process, Fig. XII-C-4.

The detritiation process[18] is operated in a recycle mode in which a side-stream of the coolant is continuously removed, detritiated and returned to the main flow stream. An optimization study of the number of decontamination stages and flow rates required would include considerations of both operating and capital equipment costs. Additionally, the optimum concentration of tritiated water in the bottom draw-off from the reflux column needs to be determined. In the absence of firm experimental information, this concentration was set at 30 Ci/mℓ which should result in minimum radiation damage to the electrolysis cell. A cursory examination of these factors indicated that 90% removal of tritiated water yielded approximately the lowest cost. This decontamination factor can be accomplished with a column containing seven theoretical stages.

In this process, the dilute HT in hydrogen rises through the column while water flows downward countercurrently. The divertor coolant water feeds into the column at the rate of 1.0232 ℓ/min (at approximately the stage corresponding to its steady-state composition) and flows to the bottom of the column. At this point, all of the feed water plus the reflux water circulating in the column

Table XII-C-5

Equilibrium Constant for the Reaction $HT + H_2O \rightleftharpoons H_2 + HTO$

Temperature °C	Equilibrium Constant
303	2.17
217	2.64
158	3.10
80	4.37
56	5.05
20	6.47

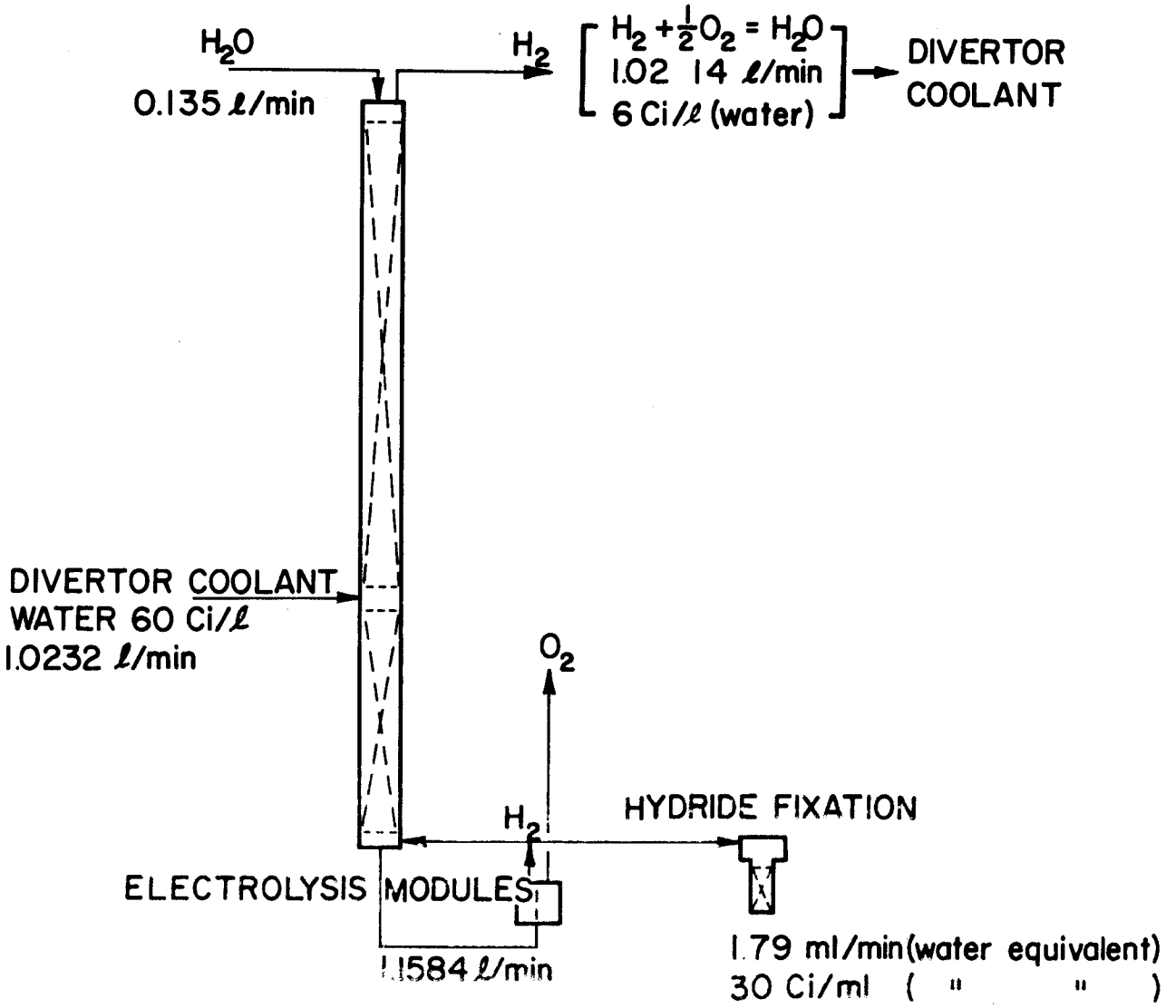

FIGURE XII-C-4 CATALYTIC EXCHANGE COLUMN

is electrolyzed at the rate of 1.1584 ℓ/min and the hydrogen and HT is introduced into the botton of the column. A small side-stream of this HT and hydrogen is removed and may be stored on a hydride bed. When sufficient tritium has been accumulated, this gas is desorbed and may be introduced into the cryogenic distillation system for isotopic enrichment and recovery of the tritium, if economical.

This type of detritiation system is well-suited for TETR operation because electrical power for the electrolysis cells is the only continuing operation requirement. The electrolysis of water requires 5.67 kWhr/ℓ of water and this process requires the electrolysis of 1.16 ℓ/min of water. At an assumed electrical cost of $0.06/kWhr the electrical cost/min would be,

$$\frac{5.67 \text{ kWhr}}{\ell} \times \frac{1.16 \ \ell}{\text{min}} \times \frac{\$.06}{\text{kWhr}} = \$0.40/\text{min}.$$

During this time, 1.79 mℓ/min of water is removed at a concentration of 30 Ci/mℓ for a total of 53.7 Ci/ℓ. The unit cost for tritium decontamination is, therefore, a modest $0.0074/Ci. If the process were operated full time, the electrical cost would be only $208,000/year.

The equipment for this process is composed chiefly of the electrolysis cells and the reflux column filled with catalyst. Near term commercial availability of this equipment is expected. Estimated costs of this equipment for this applicator are estimated as follows:

Electrolysis Cells	$207,800
Reflex Column w/Catalyst	97,000
Associated Equipment	749,800
	$1,054,600

The life-time of the catalysts and the electrolysis cells operating in intimate contact with the radioactive tritiated water is unknown but can be conservatively set at five years of full-time service.

XII-C-10 Tritium Storage Room

The repository for excess tritium should be a high integrity structure, such as a vault, which is hemetically sealed. The atmosphere for this vault would have a small volume and should probably be an inert gas, such as helium, to prevent explosive oxidation. This atmosphere is circulated through a cryogenically cooled adsorption column[13] which would remove any tritium as molecular T_2, together with water and other gaseous impurities. The tritium can be removed preferentially from this column by a chromatographic technique. One of these columns is proposed for stand-by use in the event of a large spill into a glovebox. This column could be used also to service this storage vault.

XII-C-11 Summary

In summary, a three-level atmospheric tritium control system is used to prevent the release of tritium to the atmosphere from the TETR facility. The first level consists of the major tritium processing systems. Rigorous standards for materials and construction ensure adequate routine tritium containment. A secondary containment system consisting of sealed enclosures, gloveboxes and secondary jackets for tritium containing pipes ensures that personnel are not endangered by tritium which may escape from the primary system. The secondary system further simplifies the recovery of such tritium by preventing its dilution with building air. The reactor building serves as a tertiary containment and is provided with an emergency detritiation system capable of reducing airborne tritium to the occupationa RCG value for HTO within 4 days following a 10^7 Ci release. Gaseous wastes containing tritium are detritiated by oxidation and drying and the resultant waste liquids are disposed of by burial. Routine releases of tritium to the environment are less than 1 Ci/day and less than 75 Ci escape following a postulated 10^7 Ci

release within the building. The tritium permeation from the plasma to the cooling water for the first-wall will increase at the rate of 0.015 Ci/day. Clean water must pass through this system at the rate of 4×10^5 l/day in order to have the discharge water be acceptable for drinking water standards. Alternatively, the use of a captive water system of 10^5 l for the life of the reactor, five years, would cost approximately $400,000 to dispose of the water.

The cost of some of the described equipment follows, Table XII-C-4 and Table XII-C-5 summarizes the tritium inventory for TETR. It is found that, including the storage requirements, there are ~ 12-13 kg of tritium in TETR.

Table XII-C-2

Parameters of Tritium Effluent Control System

Primary System	
Tritium Inventories (four quadrants)	
Cryopumps	1520 g ($\frac{380\ g}{quadrant}$)
Injector Pumps	12 g ($\frac{3\ g}{quadrant}$)
Distillation Columns I, II, III	188 g ($\frac{47\ g}{quadrant}$)
Storage (1 day's supply T) (.03765 mol/sec total T flow rate)	9760 g
Storage (1 day's replacement supply for T burned @ 1.3×10^{-4} mol/sec)	67 g
Divertor Coolant (steady state)	100 g
Reactor Coolant	~ 0
Module Coolant	~ 0
Total	11647 g
Secondary System	
Volume of Gloveboxes	500 m^3
Pressure in Gloveboxes	2.5×10^{-3} atm
Number of Gloves	500
Surface Area/Glove	.5 m^2
Flow Rate of Glovebox Atmosphere (per quadrant)	.25 m^3/sec
Tertiary System	
Volume of Reactor Building	5×10^4 m^3
Pressure in Reactor Building	1.23×10^{-3} atm
Maximum Volume of Any Room	1×10^4 m^3
Building Leak Rate (in leakage)	< 0.1%/day
Emergency Tritium Containment System Flow Rate	2.5 m^3/sec

Table XII-C-3

Cost Summary of Containment Systems for TETR

Item	Cost 10^6
Gloveboxes 500 m^3 @ \$9500/m^3	4.72
Containment Atmosphere Purification System	
1) Dryer and Oxygen Removal Flow Rate: 1 m^3/sec	1.5
2) Cryogenic Absorption Column Flow Rate: 0.5 m^3/sec	1.0
Tritium Effluent Removal System Flow Rate: .06 m^3/sec	6.0
Emergency Tritium Containment System Capacity: 2.5 m^3/sec	4.0
Divertor Coolant Tritium Removal	1.0
Total	18.22

Table XII-C-4

Tritium Inventories

Main Pumps	1520 g ($\frac{380\ g}{quadrant}$)
Injector Pump	~ 12 g ($\frac{3\ g}{quadrant}$)
1 Day's Supply of T (to replace T burned) [1.3×10^{-4} mol/sec burned]	~ 67 g
1 Day's Supply of T (for total fuel flow) [.03765 mol/sec T flow into plasma]	9760 g
Distillation Columns I, II, III	188 g ($\frac{47\ g}{quadrant}$)
Total	11547 g
Divertor Coolant	.1 kg
Total I_T	~ 12 kg

Chapter XII Section C References

1. L. J. Wittenberg, W. R. Wilkes and C. J. Kershner, "Environmental Control of the Tritium Inventory in a Fusion Reactor Facility", Second Fusion Tech. Conf., Richland, Washington, Sept. 21-23, 1976.

2. L. J. Wittenberg, Mound Laboratory, internal report.

3. R. H. Steinmeyer and J. D. Braun, "Hydrogen Isotope Permeation in Elastomeric Materials", Rad. Effects and Tritium Tech. Fusion Reactors, Vol. IV, CONF-750989 (March 1976).

4. R. Hughes, "The Permeability of Neoprene and PVC to Hydrogen, Deuterium and Tritium", AWRE-O-17/62, Atomic Weapons Research Establishment, Aldermaston, England (1962).

5. J. Crank and G. S. Park, Eds., Diffusion in Polymers, Academic Press, London, 1968, pp. 274-276.

6. E. V. Townsend, Charleston Products, private communication.

7. U.S. Nuclear Regulatory Commission, Title 10, Chapter 1, Part 20, 1975.

8. G. L. Phillabaum and P. C. Adams, "The Development of the Mound Laboratory Supplied-Air Bubble Suit", MLM-2008 (February 1973).

9. W. R. Bush, "Assessing and Controlling the Hazard from Tritiated Water", AECL-4150, Atomic Energy of Canada Ltd.

10. N. A. Maroni, "An Analysis of Tritium Distribution and Leakage Characteristics for Two Fusion Reactors Reference Designs", Argonne National Laboratory, CEN/CTR/TM-9 (1974).

11. Federal Register, Vol. 40, p. 34, 324, August 14. 1975.

12. J. C. Bexel, B. W. Hartzell and W. K. Park, "Experimental Determination of Reaction Rates of Water-Hydrogen Exchange of Tritium with Hydrophobic Catalysts", 14th ERDA Air Cleaning Conference, 1976.

13. C. J. Kershner and J. C. Bexel, "Tritium Effluent Control Laboratory", Proc. 13th AEC Air Cleaning Conf., pp. 948-970, USAEC, CONF-74087 (March 1975).

14. B. Badger et al., UWMAK-I, A Wisconsin Toroidal Fusion Reactor Design, UWFDM-68 (November 20, 1973).

15. G. L. Hollech, "Hydrogen Diffusion through (Palladium-Silver) - Tantalum - (Palladium-Silver) Composites", Journal of Physical Chemistry, Vo. 74, p. 1957 (1970).

16. Handbook of Chemistry and Physics 53rd Ed. R. C. Weast Ed. The Chemical Rubber Company, Cleveland, Ohio (1972-1973)

References for Section XII (cont.)

17. D. G. Jacobs, "Sources of Tritium and Its Behavior Upon Release to the Atmosphere", USAEC Document, TID-24635 (1968) pp. 8 and 9.

18. M. L. Rogers and T. K. Mills, Mound Laboratory, private communication.

XIII. Radioactivity and Safety

XIII-A. Introduction

XIII-A-1. Method of Calculation

The calculation of residual radioactivity and related quantities such as afterheat, biological hazard potential (BHP), and dose rates in TETR is similar to that of previous designs, i.e., UWMAK I,[1] II[2] and III.[3] The major differences include the use of the code DKR [4-5] in which the linear chains for calculation of activities are established automatically and all subsidiary calculations are performed within the DKR system and the additions of several new materials to the data library. The data is based primarily on ENDFB-IV supplemented by cross sections generated by the THRESH code when data for an isotope is not available in ENDFB-IV. A complete description of the details of the calculation method and the code is given elsewhere.[4,5] The linear chains which were used in the calculations are given in Table XIII-1. To simplify the calculation the reactor is primarily treated as one dimensional, i.e., calculations are basically performed along the midplane of the system. In addition, the reactor is broken up into a number of regions with the average fluxes taken from the neutronics calculations being used to calculate neutron rates in each of these regions. The decay heat from beta decay is taken as being generated at the point of the decay while the decay energy from gamma rays is either taken as being deposited at the point of decay which is adequate for determining heating rates or is used in a gamma transport problem as would be necessary in calculating dose rates.

Table XIII-1 Linear Decay Chains in TETR

1.1	^{10}B (n,p)	^{10}Be ⟶		
1.2.1	^{10}B (n,α)	^{7}Li (n,n'p)	^{6}He ⟶	
1.2.2	^{10}B (n,α)	^{7}Li (n,γ)	^{8}Li ⟶	
2.1	^{11}B (n,α)	^{8}Li ⟶		
3.1.1	^{12}C (n,α)	^{9}Be (n,α)	^{6}He ⟶	
3.1.2	^{12}C (n,α)	^{9}Be (n,p)	^{9}Li ⟶	
3.1.3	^{12}C (n,α)	^{9}Be (n,γ)	^{10}Be ⟶	
4.1	^{13}C (n,γ)	^{14}C ⟶		
5.1	^{16}O (n,p)	^{16}N ⟶		
5.2.1	^{16}O (n,α)	^{13}C (n,γ)	^{14}C ⟶	
6.1	^{28}Si (n,p)	^{28}Al ⟶		
7.1	^{50}Cr (n,d)	^{49}V ⟶		
7.2	^{50}Cr (n,γ)	^{51}Cr ⟶		
7.3.1	^{50}Cr (n,2n)	^{49}Cr ⟶	^{49}V ⟶	
8.1	^{52}Cr (n,p)	^{52}V ⟶		
8.2	^{52}Cr (n,2n)	^{51}Cr ⟶		
9.1	^{53}Cr (n,d)	^{52}V ⟶		
10.1	^{54}Cr (n,α)	^{51}Ti ⟶		
10.2	^{54}Cr (n,γ)	^{55}Cr ⟶		

Table XIII-1 (Cont.)

11.1	^{55}Mn (n,α)	^{52}V ⟶	
11.2	^{55}Mn (n,p)	^{55}Cr ⟶	
11.3	^{55}Mn (n,2n)	^{54}Mn ⟶	
11.4	^{55}Mn (n,γ)	^{56}Mn ⟶	
12.1	^{54}Fe (n,n'α)	^{51}Cr ⟶	
12.2	^{54}Fe (n,d)	^{53}Mn ⟶	
12.3	^{54}Fe (n,p)	^{54}Mn ⟶	
12.4	^{54}Fe (n,γ)	^{55}Fe ⟶	
12.5.1	^{54}Fe (n,2n)	^{53}Fe ⟶	^{53}Mn ⟶
13.1	^{56}Fe (n,t)	^{54}Mn ⟶	
13.2	^{56}Fe (n,p)	^{56}Mn ⟶	
13.3	^{56}Fe (n,2n)	^{55}Fe ⟶	
13.4.1	^{56}Fe (n,γ)	^{57}Fe (n,d)	^{56}Mn ⟶
13.4.2	^{56}Fe (n,γ)	^{57}Fe (n,p)	^{57}Mn ⟶
14.1	^{57}Fe (n,d)	^{56}Mn ⟶	
14.2	^{57}Fe (n,p)	^{57}Mn ⟶	
15.1	^{58}Fe (n,α)	^{55}Cr ⟶	
15.2	^{58}Fe (n,t)	^{56}Mn ⟶	
15.3	^{58}Fe (n,d)	^{57}Mn ⟶	
15.4	^{58}Fe (n,γ)	^{59}Fe ⟶	

Table XIII-1 (Cont.)

16.1	^{58}Ni (n,α)	^{55}Fe ⟶		
16.2	^{58}Ni (n,d)	^{57}Co ⟶		
16.3	^{58}Ni (n,p)	^{58}Co ⟶		
16.4	^{58}Ni (n,γ)	^{59}Ni ⟶		
16.5.1	^{58}Ni (n,2n)	^{57}Ni ⟶	^{57}Co ⟶	
17.1	^{60}Ni (n,t)	^{58}Co ⟶		
17.2	^{60}Ni (n,p)	^{60}Co ⟶		
17.3	^{60}Ni (n,2n)	^{59}Ni ⟶		
17.4.1	^{60}Ni (n,p)*	^{60m}Co ⟶	⟶	
17.5.1	^{60}Ni (n,α)	^{57}Fe (n,d)	^{56}Mn ⟶	
17.5.2	^{60}Ni (n,α)	^{57}Fe (n,p)	^{57}Mn ⟶	
17.6.1	^{60}Ni (n,γ)	^{61}Ni (n,d)	^{60}Co ⟶	
18.1	^{61}Ni (n,d)	^{60}Co ⟶		
18.2	^{61}Ni (n,p)	^{61}Co ⟶		
19.1	^{62}Ni (n,α)	^{59}Fe ⟶		
19.2	^{62}Ni (n,t)	^{60}Co ⟶		
19.3	^{62}Ni (n,d)	^{61}Co ⟶		
19.4	^{62}Ni (n,γ)	^{63}Ni ⟶		
20.1	^{64}Ni (n,2n)	^{63}Ni ⟶		
20.2	^{64}Ni (n,γ)	^{65}Ni ⟶		
21.1	^{63}Cu (n,α)	^{60}Co ⟶		
21.2	^{63}Cu (n,γ)	^{64}Cu ⟶		
22.1	^{65}Cu (n,2n)	^{64}Cu ⟶		
22.2	^{65}Cu (n,γ)	^{66}Cu ⟶		

Table XIII-1 (Cont.)

23.1	^{92}Mo (n,n'α)	^{88}Zr ⟶		
23.2	^{92}Mo (n,α)	^{89}Zr ⟶		
23.3	^{92}Mo (n,p)	^{92m}Nb ⟶		
23.4	^{92}Mo (m,2n)	^{91}Mo ⟶		
23.5.1	^{92}Mo (n,γ)	^{93}Mo ⟶	^{93m}Nb ⟶	
24.1	^{94}Mo (n,p)	^{94}Nb ⟶		
24.2.1	^{94}Mo (n,2n)	^{93}Mo ⟶	^{93m}Nb ⟶	
25.1	^{95}Mo (n,d)	^{94}Nb ⟶		
25.2	^{95}Mo (n,p)	^{95}Nb ⟶		
25.3.1	^{95}Mo (n,p)	^{95m}Nb ⟶	^{95}Nb ⟶	
26.1	^{96}Mo (n,t)	^{94}Nb ⟶		
26.2	^{96}Mo (n,d)	^{95}Nb ⟶		
26.3	^{96}Mo (n,p)	^{96}Nb ⟶		
27.1	^{97}Mo (n,t)	^{95}Nb ⟶		
27.2	^{97}Mo (n,d)	^{96}Nb ⟶		
27.3	^{97}Mo (n,p)	^{97}Nb ⟶		
27.4.1	^{97}Mo (n,p)	^{97m}Nb ⟶	^{97}Nb ⟶	
28.1	^{98}Mo (n,t)	^{96}Nb ⟶		
28.2	^{98}Mo (n,d)	^{97}Nb ⟶		
28.3	^{98}Mo (n,p)	^{98}Nb ⟶		
28.4.1	^{98}Mo (n,α)	^{95}Zr ⟶	^{95}Nb ⟶	
28.5.1.1	^{98}Mo (n,γ)	^{99}Mo ⟶	^{99m}Tc ⟶	^{99}Tc ⟶

Table XIII-1 (Cont.)

29.1	^{100}Mo (n,t)	$^{98}Nb \longrightarrow$			
29.2	^{100}Mo (n,p)	$^{100}Nb \longrightarrow$			
29.3.1	^{100}Mo (n,α)	$^{97}Zr \longrightarrow$	$^{97}Nb \longrightarrow$		
29.4.1	^{100}Mo (n,γ)	$^{101}Mo \longrightarrow$	$^{101}Tc \longrightarrow$		
29.5.1.1	^{100}Mo (n,2n)	$^{99}Mo \longrightarrow$	$^{99m}Tc \longrightarrow$	$^{99}Tc \longrightarrow$	
30.1	^{182}W (n,p)	$^{182}Ta \longrightarrow$			
30.2	^{182}W (n,2n)	$^{181}W \longrightarrow$			
30.3.1	^{182}W (n,γ)	^{183}W (n,d)	$^{182}Ta \longrightarrow$		
30.3.2	^{182}W (n,γ)	^{183}W (n,p)	$^{183}Ta \longrightarrow$		
31.1	^{183}W (n,d)	$^{182}Ta \longrightarrow$			
31.2	^{183}W (n,p)	$^{183}Ta \longrightarrow$			
31.3.1	^{183}W (n,γ)	^{184}W (n,α)	$^{182}Hf \longrightarrow$		
31.3.2	^{183}W (n,γ)	^{184}W (n,d)	$^{183}Ta \longrightarrow$		
31.3.3	^{183}W (n,γ)	^{184}W (n,p)	$^{184}Ta \longrightarrow$		
31.3.4	^{183}W (n,γ)	^{184}W (n,γ)	$^{185}W \longrightarrow$		
32.1	^{184}W (n,α)	$^{181}Hf \longrightarrow$			
32.2	^{184}W (n,d)	$^{183}Ta \longrightarrow$			
32.3	^{184}W (n,p)	$^{184}Ta \longrightarrow$			
32.4	^{184}W (n,γ)	$^{185}W \longrightarrow$			
32.5.1	^{184}W (n,2n)	^{183}W (n,d)	$^{182}Ta \longrightarrow$		
32.5.2	^{184}W (n,2n)	^{183}W (n,p)	$^{183}Ta \longrightarrow$		

Table XIII-1 (Cont.)

33.1	^{186}W (n,p)	^{186}Ta ⟶		
33.2	^{186}W (n,2n)	^{185}W ⟶		
33.3	^{186}W (n,γ)	^{187}W ⟶		
33.4.1	^{186}W (n,α)	^{183}Hf ⟶	^{183}Ta ⟶	
33.5.1	^{186}W (n,d)	^{185}Ta ⟶	^{185}W ⟶	
34.1	^{204}Pb (n,p)	^{204}Tl ⟶		
34.2	^{204}Pb (n,2n)	^{203}Pb ⟶		
35.1	^{206}Pb (n,α)	^{203}Hg ⟶		
35.2	^{206}Pb (n,t)	^{204}Tl ⟶		
35.3	^{206}Pb (n,2n)	^{205}Pb ⟶		
36.1	^{207}Pb (n,n'α)	^{203}Hg ⟶		
36.2.1	^{207}Pb (n,2n)	^{206}Pb (n,t)	^{204}Tl ⟶	
36.3.1	^{207}Pb (n,2n)	^{206}Pb (n,2n)	^{205}Pb ⟶	
37.1	^{208}Pb (n,α)	^{205}Hg ⟶		
37.2.1	^{208}Pb (n,2n)	^{207}Pb (n,n'α)	^{203}Hg ⟶	

XIII-A-2. Geometry of the System and Material Composition

A problem that arises in the reporting of the results for TETR stems from the fact that the design of the blanket and shield for TETR has gone through several modifications and changes in concept. Chief among these is the question as to whether a carbon ISSEC is to be used. In the final design it was established that the carbon ISSEC was not necessary and that an 18 cm essentially tungsten zone behind the first wall would be adequate for this application. However, since the radioactivity calculations must follow the neutronics calculations and the final decision on the blanket design occurred rather late in the design scheme, most of the detailed calculations and analysis have been performed on the carbon ISSEC design. This design which will henceforth be denoted as TETR-A does, however, have many similarities to the final design, particularly with respect to some of the relative contributions of particular isotopes and to the activities expected in the toroidal field magnets. Calculations using the final design have been restricted to the outer blanket and shield and to the calculations of particular non-one-dimensional effects. Thus, while results will often be presented for both designs, the results using TETR-A should only be taken as representative of the final design and not as the expected values.

Figures XIII-1 and XIII-2 show the one-dimensional models used in the TETR-A and final design calculations. These geometries are representative of a midplane cut through the reactor and should produce acitivties typical of those expected in the non-testing section parts of the blanket. There will undoubtedly be changes because of the two-dimensional nature of certain sections such as the vertical field coils, but these should not be great. In addition to the

Figure XIII-1

1-D Schematic of TETR-A Blanket and Shield

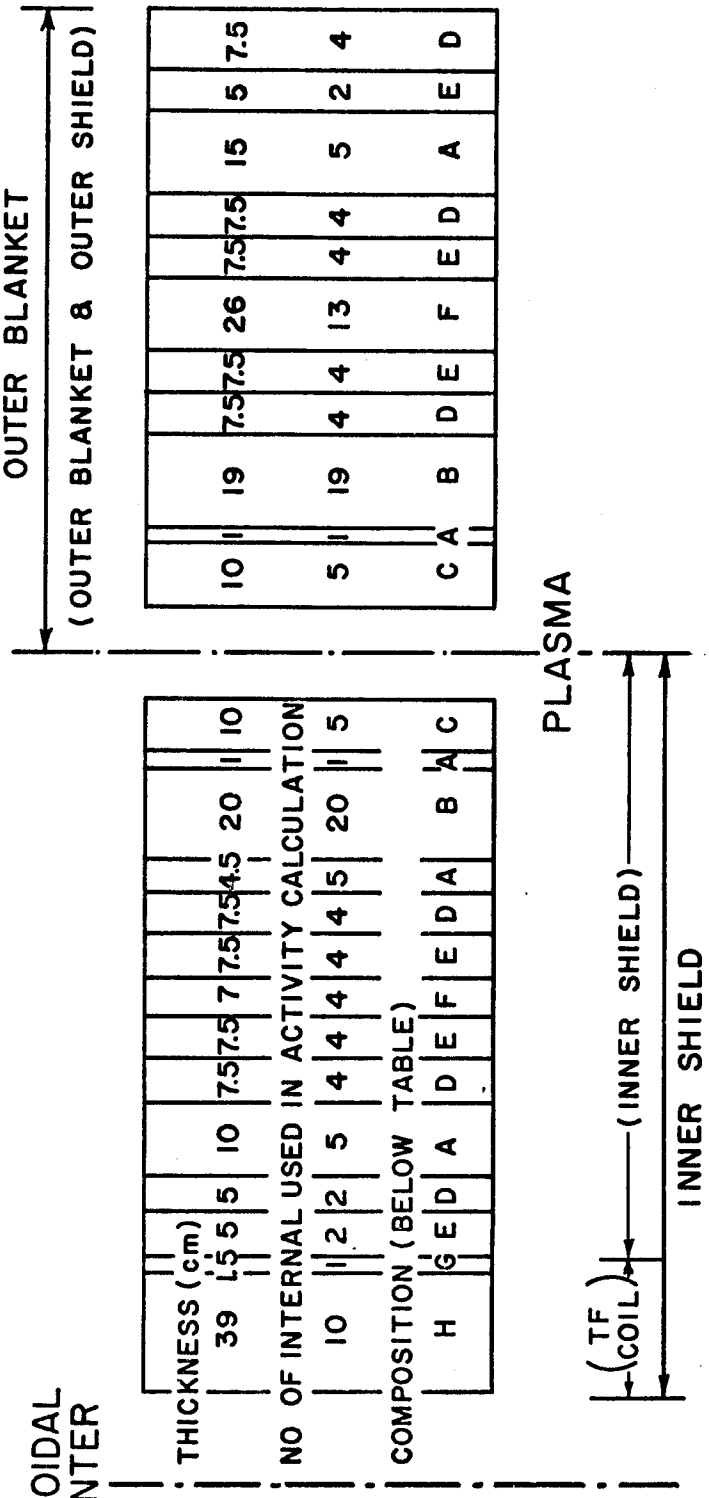

Composition Table (Volume %)

A. 100% 316 SS
B. 90% W + 5% 316 SS
C. 100% C (ISSEC)
D. 90% Pb + 5% 316 SS
E. 90% B_4C + 5% 316 SS
F. 75% Cu + 25% H_2O
G. Mylar
H. 45% Cu + 45% 316 SS

Figure XIII-2

1-D Schematic Diagram of TETR Outer Blanket

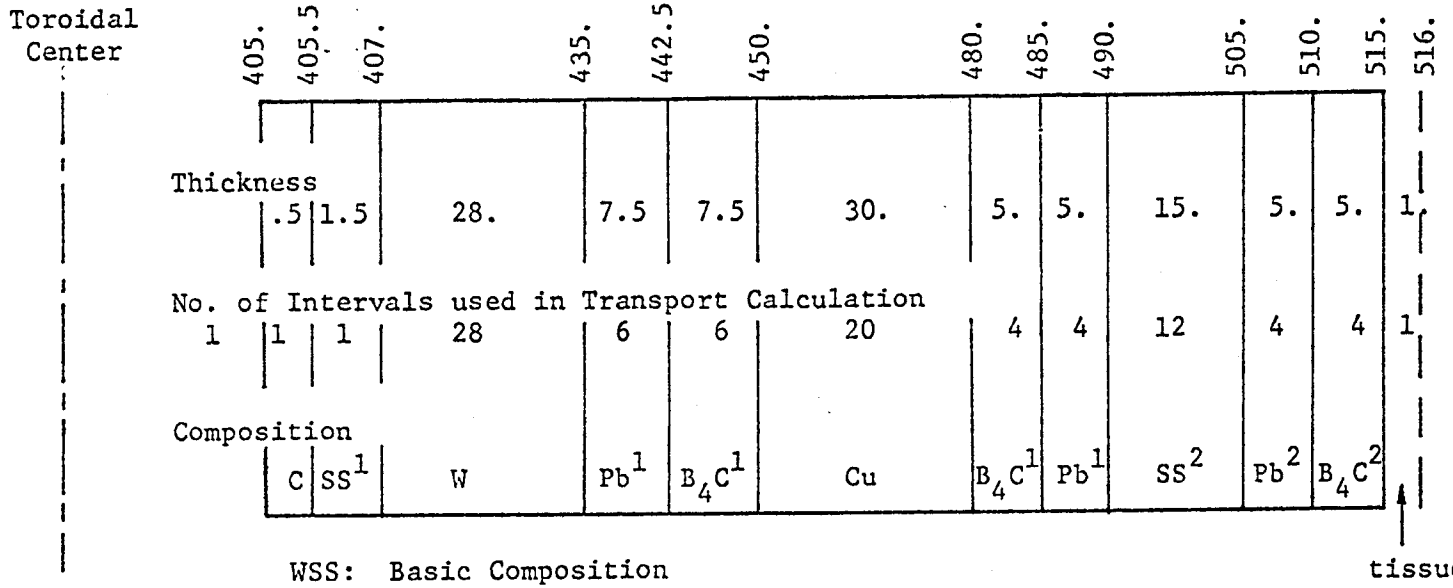

WSS: Basic Composition

SS^1	40 % 316 SS + 50 % H_2O
SS^2	96 % 316 SS + 4 % H_2O
W	4 % 316 SS + 4 % H_2O + 92 % W*
Pb^1, Pb^2	4 % 316 SS + 4 % H_2O + 92 % Pb
B_4C^1, B_4C^2	4 % 316 SS + 4 % H_2O + 92 % B_4C*
Cu	75 % Cu + 20 % H_2O + 5 % Insulator

*Density Factor

0.95 for W and B_4C

SSS: Alternative A - Same as basic case except

W	96 % 316 SS + 4 % H_2O

WAL: Alternative B - Same as basic case except

Pb^2	4 % Al + 4 % H_2O + 92 % Pb
B_4C^2	4 % Al + 4 % H_2O + 92 % B_4C*

basic final design shown in Figure XIII-2 and denoted as WSS, two variations have been studied. The first consists of replacing the 18 cm tungsten - stainless steel zone with stainless steel. This variation will be denoted as SSS. The second variation consists of replacing the stainless steel structure in the last two regions of the shield with aluminum. This variation is denoted as WAL.

Since the calculations are one-dimensional, some care must be taken in their presentation and interpretation. The data are presented as curies per watt in the case of radioactivity, percent of operating power for afterheat or km^3/kW_{th} for BHP (BHP is the volume of air required to dilute the isotopes in question to maximum permissible concentration per unit of power). Since these are one-dimensional calculations, what is meant is, in the case of radioactivity for example, activity per unit area normal to the midplane of the region or regions in question per unit of power produced in the blanket and shield in the volume associated with that area while the reactor is operating. Similar considerations apply to the other quantities.

The calculations also showed that there is little difference between the inner blanket and shield and the outer blanket and shield when compared and described as above. This is because the regions near the plasma dominate and they are very similar in this design. Consequently, results will be presented for the outer blanket only. An exception is made for the toroidal field coils. In this case the inner leg of the magnet will be used as it may well have the highest exposure.

XIII-B. Buildup of Activity in TETR-A

The overall behavior of the buildup and decay of the radioactivity in TETR-A is shown in Figure XIII-3(a). The activity builds up fairly rapidly such

Figure XIII-3. TETR-A Outer Blanket Activity Buildup

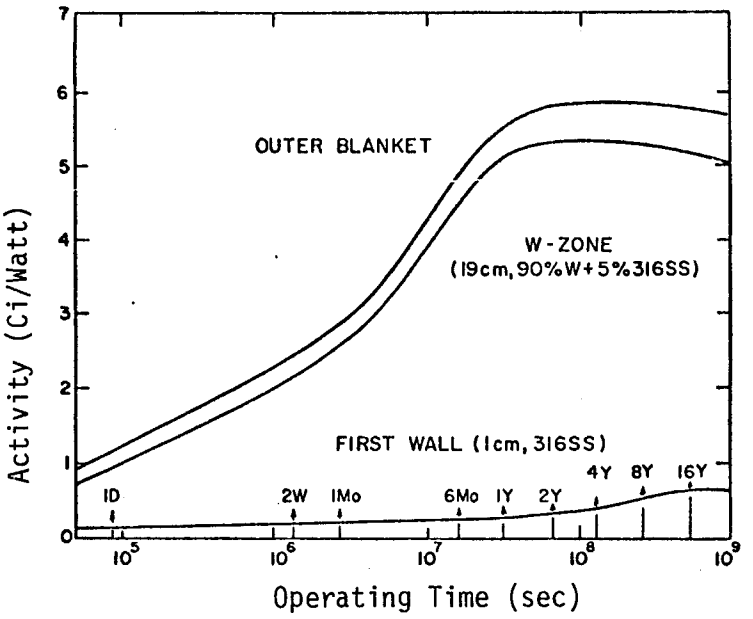

(a) Radioactivity

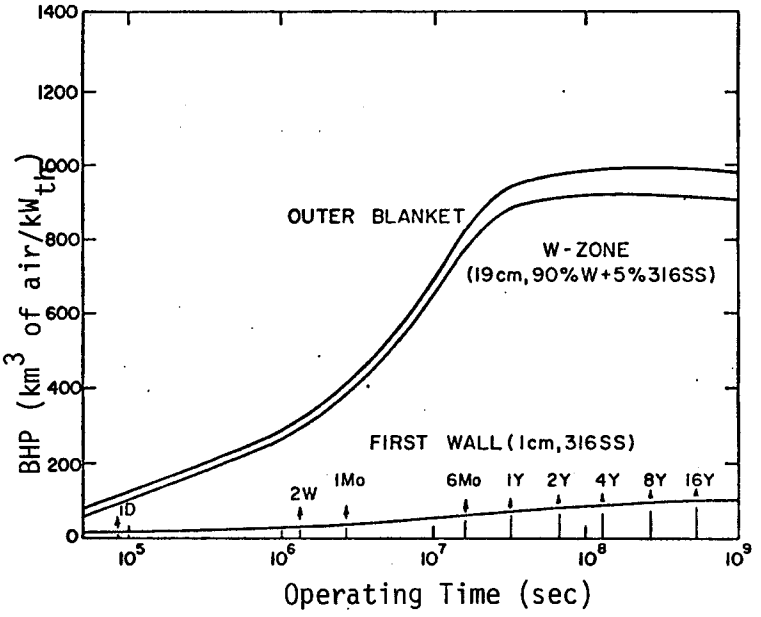

(b) BHP

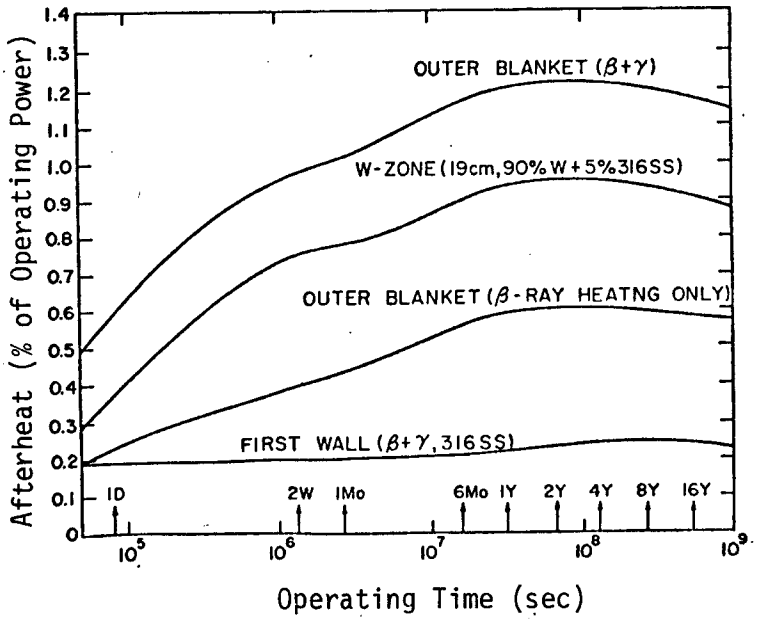

(c) Afterheat

that after one day of operation, it has attained about 15% of its maximum value. Subsequently, the long lived isotopes build in and start to saturate and the buildup is less rapid reaching a maximum value after about two years of operation. It then falls off slowly as the stable nuclei are gradually burned out. The levels of activity are of the same order of magnitude as calculated in previous studies. Note that the bulk of the activity comes from the tungsten zone and that the first wall plus the tungsten account for almost all of the activity in the system. It may also be noted that whereas the tungsten activity has saturated after 1-2 years, the first wall activity (stainless steel) is still increasing. This implies the tungsten activity should decay away faster than that of 316 stainless steel and this indeed will be shown later. Furthermore, part of the activity of the tungsten zone is due to the stainless steel structure. The BHP buildup of TETR-A is shown in Figure XIII-3(b). The curve is qualitatively similar in shape to that of the activity. The BHP values are somewhat higher (~ a factor of two) than those calculated for UWMAK-I using stainless steel. Again, the largest contribution is that of the tungsten zone.

The afterheat buildup of TETR-A is shown in Figure XIII-3(c). The buildup of afterheat is somewhat more rapid than the buildup of the activity. Also the contribution of the first wall is relatively greater. The maximum value of afterheat is quite comparable to that observed in previous studies. In addition, the split in the afterheat between beta and gamma heating is about 50-50 at saturation.

XIII-C. Activity Following Shutdown in TETR-A

The activity following shutdown is shown in Figure XIII-4 for TETR-A following two years of operation. Note the similarity between the inner shield and outer blanket, thus confirming that for the purposes of this report, it is only necessary to consider the outer region. The activity falls off relatively slowly requiring about one year to be reduced by a factor of ten. For the first ten years or so the activity is dominated by the tungsten and stainless steel in the large tungsten zone. After ten years the first wall is the major contributor. At first glance, the behavior of the activity in TETR-A appears very similar to that of previous designs incorporating 316 stainless steel. However, there are some significant differences that will become apparent as the regions are studied in more detail.

Figure XIII-5 shows the total activity of the first wall in TETR-A as well as the activity of each isotope. Immediately following shutdown the activity is dominated by Mn^{56} ($t_{1/2}$=2.6 hrs) which decays away fairly rapidly so that after one hour Fe^{55} and to a lesser extent Cr^{51} are the largest contributors and this dominance persists for the first few years. Subsequently, the activity is dominated by first Ni^{63} and at long times by Mo^{93} and $Nb^{93\,m}$ while at very long times Ni^{59} survives to be the limiting very long term radioactivity.

It is of perhaps more interest from the point of new of tailoring an alloy to minimize activity related quantities to determine what fraction of the activity originates with a particular element. The percent contribution to the activity originating in the constituents of the 316 stainless steel of the first wall of TETR-A is shown in Table XIII-2 for various times following two years of operation. Initially most of the activity originates in the iron with chromium

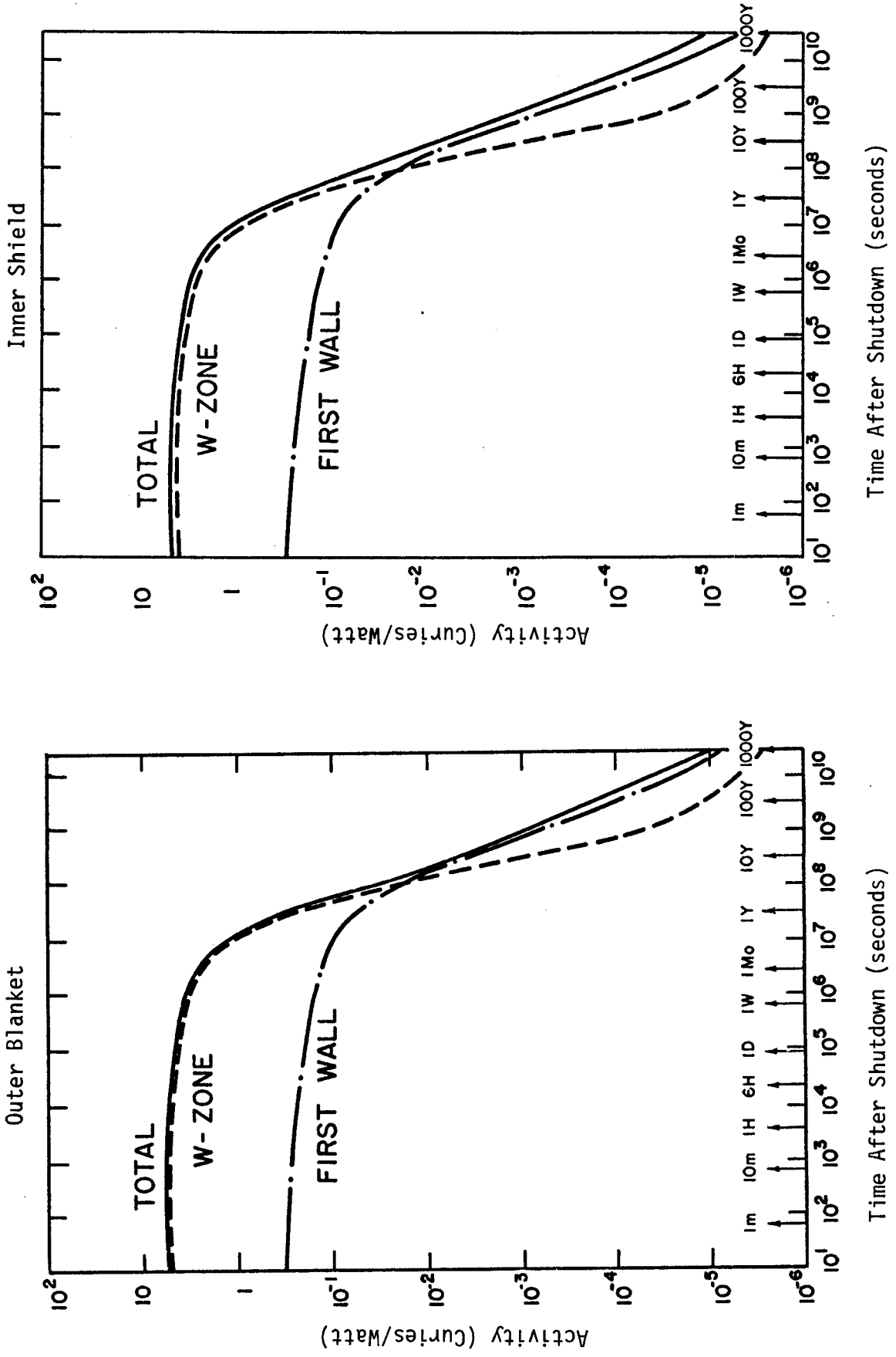

Figure XIII-4

Decay of Activity in TETR-A After Two Years of Operation

Figure XIII-5

Activity of the First Wall In TETR-A Following
After Two Years of Operation

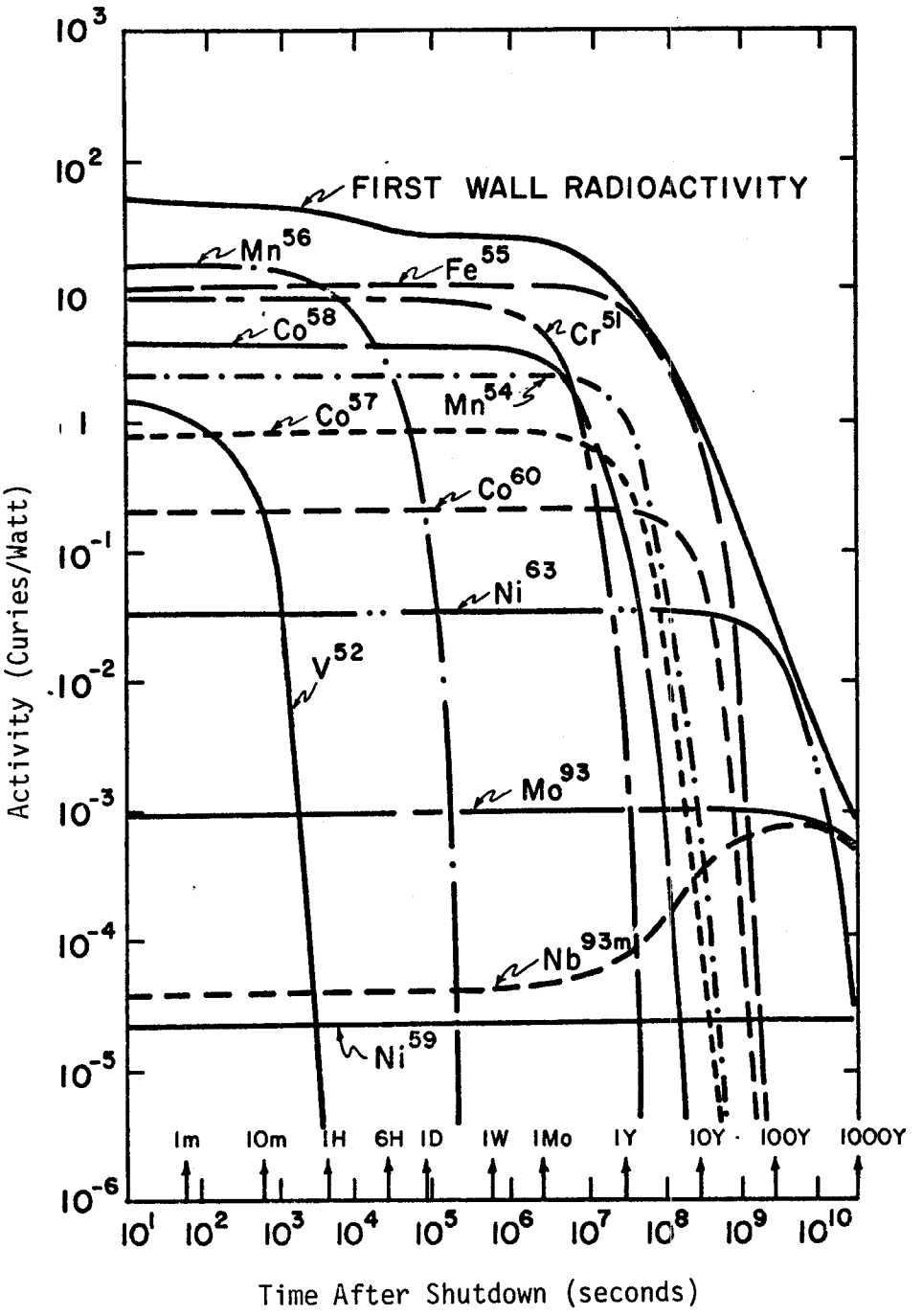

Table XIII-2. Contribution of Each Element in 316 SS to the First Wall Activity†

		Time After Shutdown										
		0	1 m	1 Hr	6 Hr	1 D	1 W	1 Mo	1 Yr	10 Yr	100 Yr	1000 Yr
Specific Activity (Ci/cm^3)		43.36	42.82	36.80	28.19	24.84	22.51	18.35	8.629	7.254-1*	1.691-2	9.000-4
Element, wt %						% Contribution						
Si	1.	1.34	0.99	-	-	-	-	-	-	-	-	-
Cr	17.	20.20	19.91	20.01	25.97	28.92	27.51	18.90	0.26	-	-	-
Mn	2.	22.11	22.25	20.15	9.02	3.42	3.65	4.26	4.19	0.03	-	-
Ni	12.	13.10	13.20	14.21	18.27	20.41	21.20	21.96	11.00	15.52	90.58	4.47
Mo	2.5	4.21	4.23	3.95	4.80	4.62	1.20	0.01	0.01	0.17	9.42	95.53
Fe	65.3	39.04	39.42	41.68	41.94	42.61	46.44	54.87	84.54	84.28	-	-
Specific BHP (km^3 of air/ $kW-cm^3$)		2.355-2*	2.351-2	2.279-2	2.116-2	1.948-2	1.622-2	1.439-2	5.933-3	5.910-4	2.230-5	3.253-7
Element, wt %						% Contribution						
Si	1.	0.23	0.17	-	-	-	-	-	-	-	-	-
Cr	17.	1.18	1.17	1.15	1.04	1.30	1.35	0.85	-	-	-	-
Mn	2.	15.37	15.36	14.57	12.42	12.23	14.47	15.24	17.32	0.09	-	-
Ni	12.	57.01	57.08	58.37	61.01	60.41	55.36	52.26	45.27	89.55	97.56	8.54
Mo	2.5	2.67	2.67	2.57	2.58	2.25	0.66	0.08	0.01	0.42	2.40	89.56
Fe	65.3	23.55	23.54	23.34	22.95	23.81	28.16	31.57	37.40	9.94	0.04	1.90
Specific Afterheat ($Watt/cm^3$)		3.069-1*	2.993-1	2.177-1	9.046-2	4.554-2	4.113-2	3.500-2	1.118-2	1.064-3	2.031-6	1.373-7
Element, wt %						% Contribution						
Si	1.	3.23	2.45	-	-	-	-	-	-	-	-	-
Cr	17.	6.94	6.00	0.63	1.44	2.80	2.69	1.82	0.21	-	-	-
Mn	2.	43.85	44.70	47.18	32.87	9.53	9.94	11.06	16.00	0.9	-	-
Ni	12.	9.45	9.68	13.05	30.44	57.84	60.27	58.46	34.17	75.92	91.74	33.50
Mo	2.5	2.31	2.32	1.47	2.94	4.85	1.31	0.11	0.01	0.02	8.26	66.50
Fe	65.3	34.22	34.85	37.63	32.31	24.98	25.79	28.55	49.61	23.97	-	-

† TETR-A Outer Blanket, 2 years operation

* $a \pm n$ should be read as $a \times 10^{\pm n}$

and manganese contributions about equal at a fraction about half that of iron. As the activity generated from manganese dies away, the percentage of the activity generated from the iron increases until the one to ten year period when about 85% of the activity comes from iron. For long term radioactivity only nickel and molybdenum are contributors. It is apparent, therefore, that eliminating nickel and molybdenum would have a significant effect on the long term activity if the object were to reduce it as low as possible regardless of whether it was significant or not.

It should also be noted that while the activity from the tungsten zone is the largest contributor to the activity for the first ten years after shutdown, the residual activity from this region after this time is due to the stainless steel structure. This is illustrated in Figure XIII-6(a) which shows the activity due to the tungsten and stainless steel in the tungsten zone along with the activity of the first wall. It is seen that the tungsten does indeed dominate at short times. The longest lived isotope produced is W^{185}. As it has a half life of 75 days the tungsten activity soon becomes negligible. This means that all aspects of tungsten activity should exhibit good long term effects.

Another measure of activity is the BHP, i.e., the amount of air required to reduce an isotope to maximum permissible concentration per unit power. The BHP of the inner and outer sections of the blanket are shown in Figure XIII-7. Again, the tungsten zone dominates. The contributors of various isotope to the BHP of the first wall is shown in Figure XIII-8. Note that now Mn^{54} is the dominant activity for almost the first year. However, at very long times $Nb^{93\ m}$ is still the major contributor. The percent contribution to BHP generated by activation of the various constituents of the first wall is shown in Table XIII-2.

Figure XIII-6

Activity Contributions of Tungsten and Stainless Steel in the Tungsten Zone of TETR-A Following Two Years of Operation

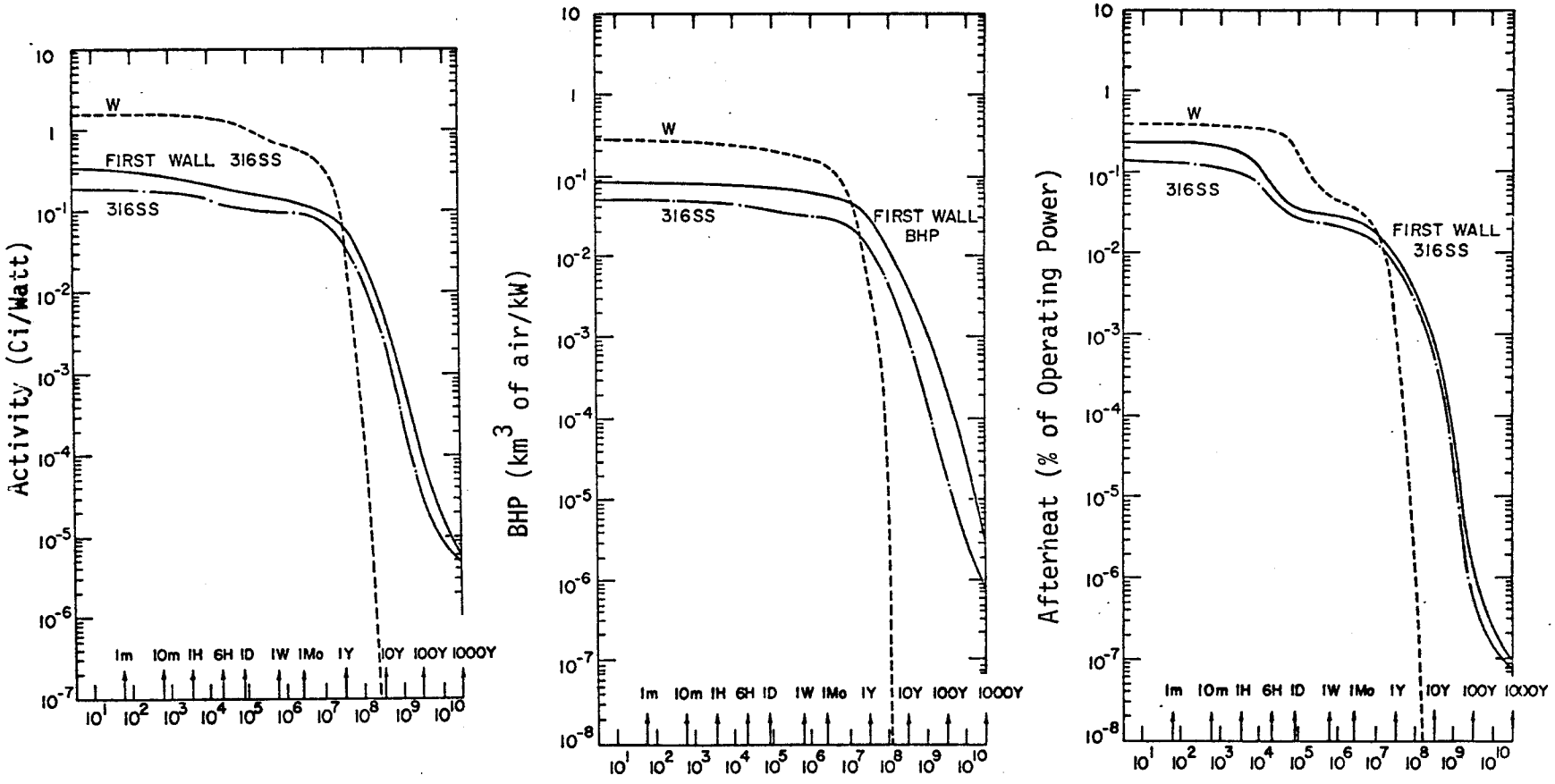

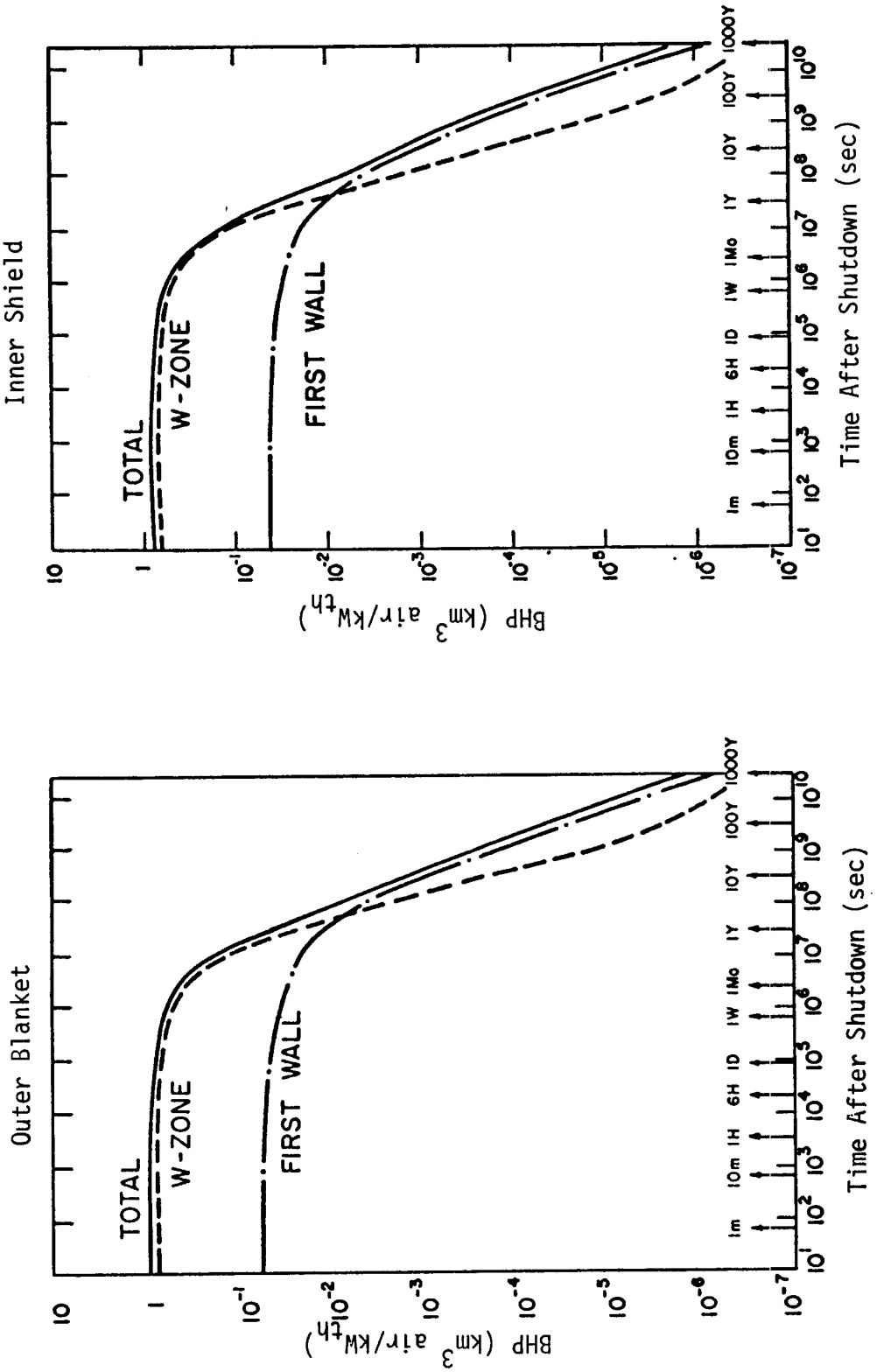

Figure XIII-7

Decay of BHP in TETR-A After Two Years of Operation

Figure XIII-8

BHP of TETR-A First Wall Following Shutdown

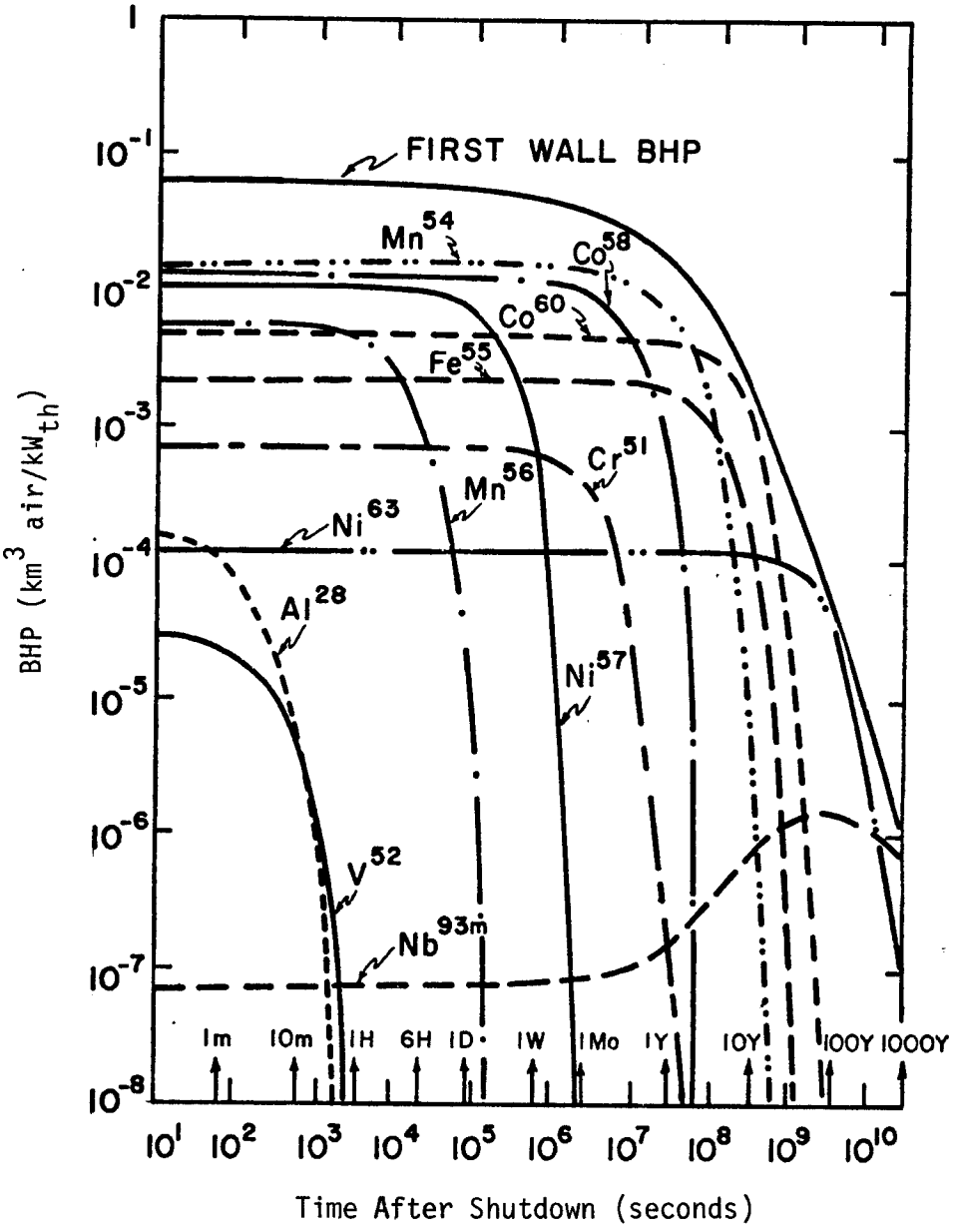

In this case, the nickel is the biggest contributor to the BHP initially and for the first ~200 years. At long times molybdenum is the source of the $Nb^{93\ m}$ activity again illustrating that a significant reduction in BHP at all times could be achieved if these two elements were not present in the first wall. In the tungsten zone, the BHP at shutdown is largely due to the tungsten, but as in the case of the radioactivity for times longer than ~2 years the BHP of the tungsten zone is due to the stainless steel structure as shown in Figure XIII-6(b). The point is perhaps better illustrated in Figure XII-9 in which the contributions of the various isotopes are shown. In the case of BHP W^{185} is the dominant isotope prpduced from tungsten at all times and, therefore, the decay of BHP is characterized essentially by a 75 day half life. This again emphasizes that significant reductions in long term BHP could be obtained with suitable changes in structural material.

Figure XIII-10 shows the afterheat of the inner shield and outer blanket of TETR-A. Again, the curves are quite similar and not too unlike in magnitude as shutdown similar calculations in previous studies. The tungsten zone dominates the afterheat as it does the radioactivity and BHP. As shown in Fig. XIII-11, the major contributor to the afterheat at shutdown is Mn^{56} followed by Cr^{58}. At long times the afterheat (which is reduced by six orders of magnitude) is again due to isotopes of nickel and niobium. The contribution of the alloying elements of 316 SS to the afterheat of the first wall is shown in Table XIII-2. Here at shutdown the major contributor is manganese producing 44% of the afterheat although present to only 2 w/o. As the isotopes produced from manganese decay away, nickel and iron become more important finally reaching the situation at very long times where once again nickel and molybdenum dominate.

Figure XIII-9

BHP of TETR-A Following Two Years of Operation

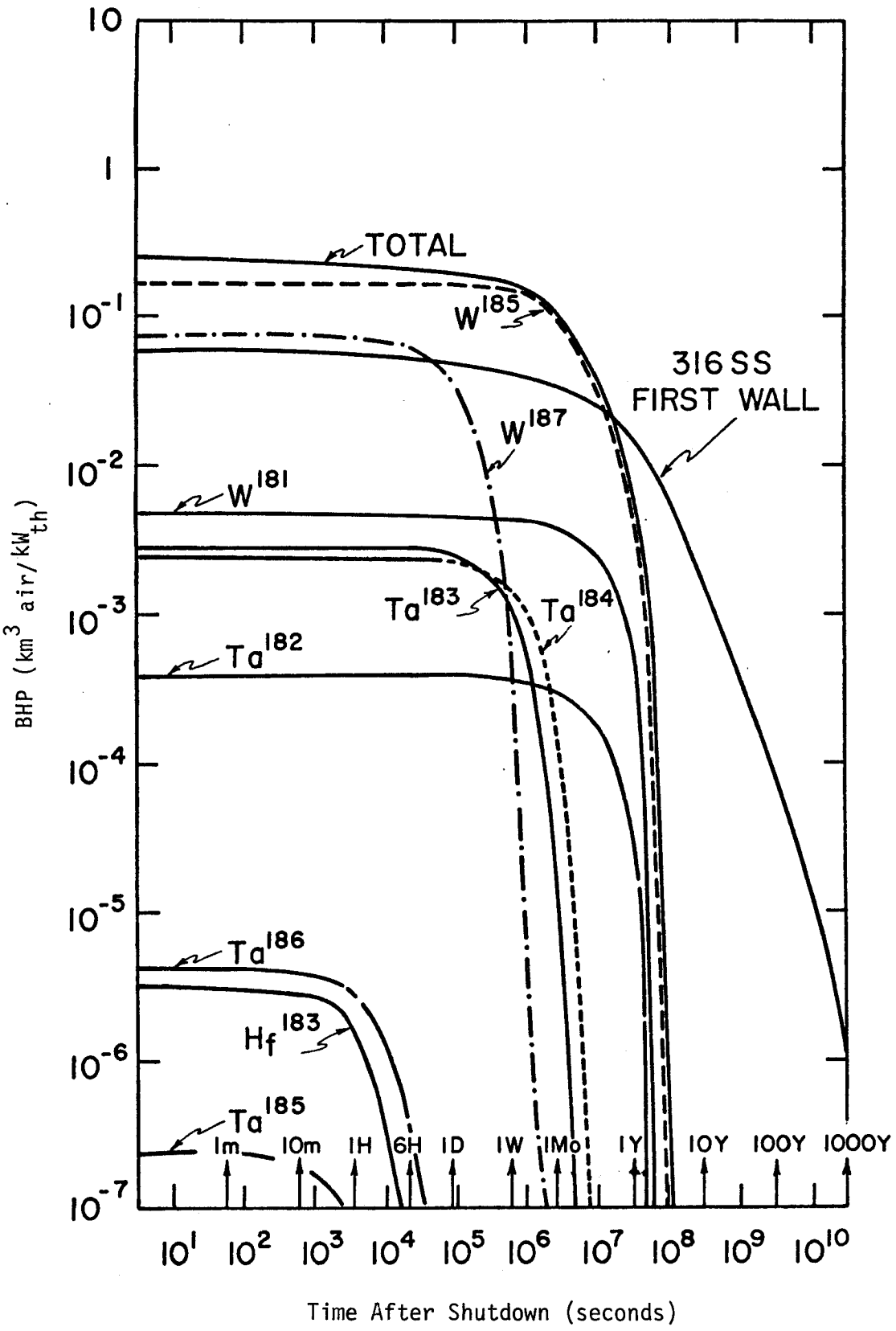

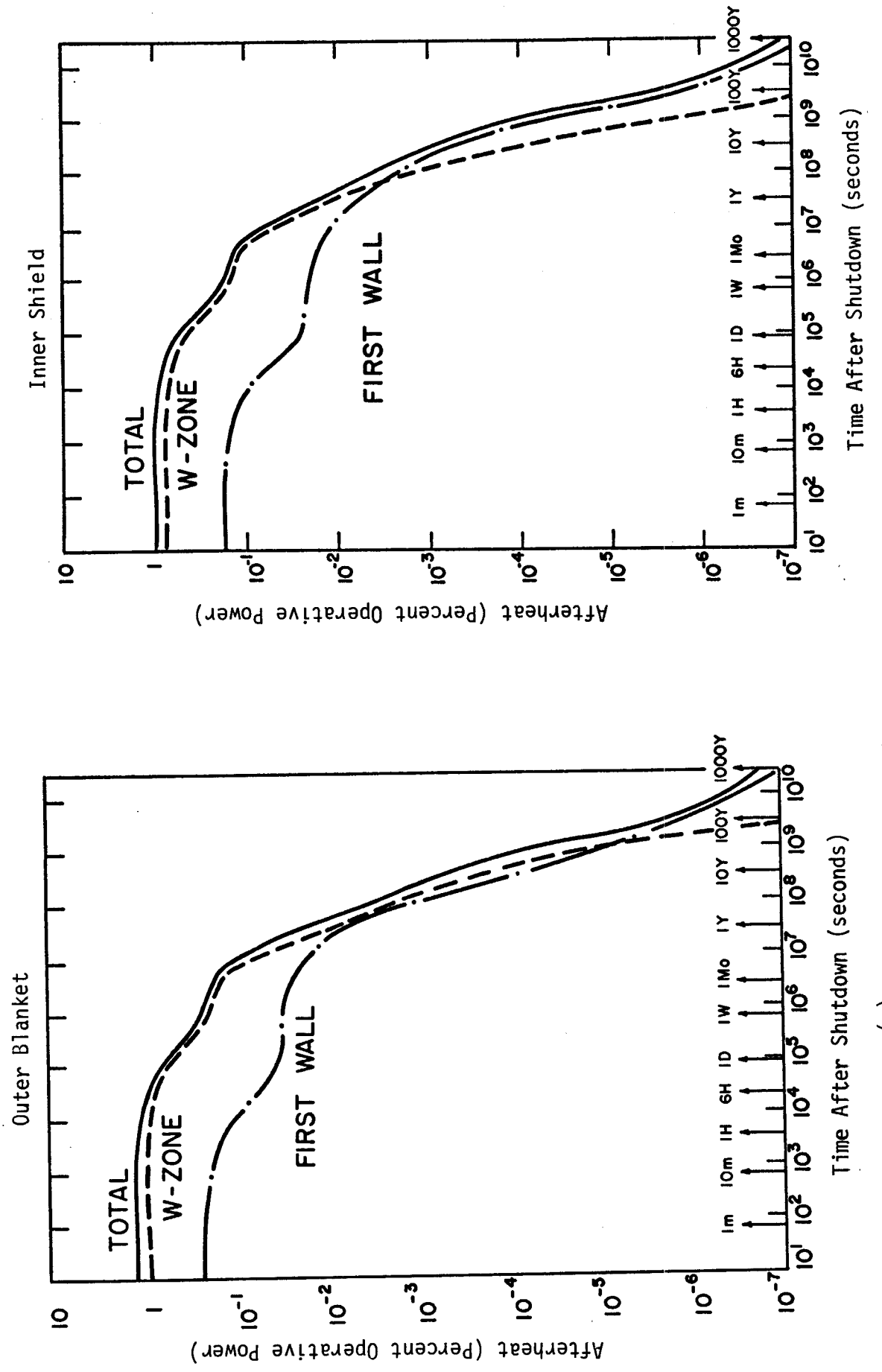

Figure XIII-10

Decay of Afterheat in TETR-A After Two Years of Operation

Figure XIII-11

TETR-A First Wall Afterheat Following Two Years of Operation

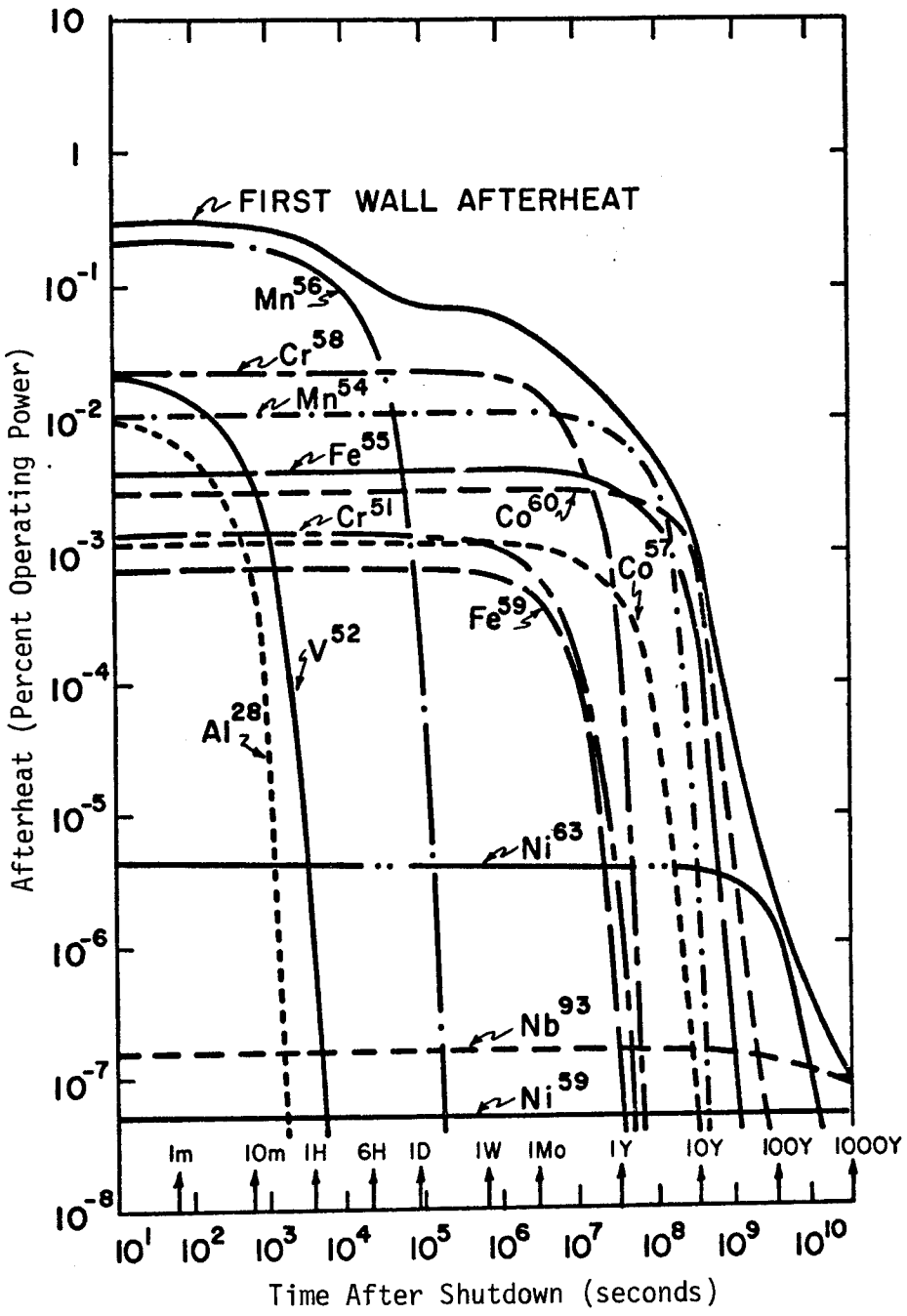

These data for the contributions originating in the alloying elements illustrate that if one could tailor an alloy, the elements or isotopes that one would choose to eliminate may depend on what end result is desired. For example, if the desire is to reduce the BHP at shutdown, then nickel should be removed. On the other hand, if it is the afterheat that is the problem, then the manganese should be removed. If one considers long term effects, then both nickel and molybdenum should be removed for all cases.

The final item of interest in the activity calculations is the dose outside the reactor shield. The dose ratios calculated for TETR-A are shown in Table XIII-3. For comparison purposes, the dose expected outside the shield of UWMAK-I is also shown. Both cases are done for two year operating times. It is clear that while the radiation levels are not insignificant at shutdown, the shield of TETR-A is superior to that of UWMAK-I by a factor of about five. This is not too surprising in view of the fact that large amounts of tungsten are present in TETR-A and the shield of TETR-A has no breeding requirements to fulfill. At the dose rate calculated, it would appear that significant hands on maintenance could be started about a day after the reactor is shut down, but that full shift work would not be possible except after an extended shutdown.

Activity of Toridal Field Magnets

The radioactivity, BHP, and afterheat of the magnets is shown in Figure XIII-12. Compared to the estimates of the blanket and shield structure, the activity of the magnets is quite low. It is initially dominated by the copper in the coils which, however, dies away after the first month leaning the contribution due to the steel structure. Replacement of the steel in the magnets by aluminum should reduce the long term activities significantly.

TABLE XIII-3. Calculated Dose Rate Outside the Shield

	TETR-A	UWMAK-I
Neutron Wall Loading	1.10 MW/m^2	1.25 MW/m^2
Time After Shutdown	Dose Rate, mrem/hr.	
0	790.0	4,072.0
1 min.	766.0	
10 min	675.0	
1 hr.	530.0	3,068.0
6 hr.	153.0	
1 day	21.7	1,165.0
1 week	17.9	1,084.0
1 month	15.8	870.2
1 yr.	6.8	167.2
10 yr.	1.3	
100 yr.	1.3×10^{-5}	
1000 yr.	2.2×10^{-6}	

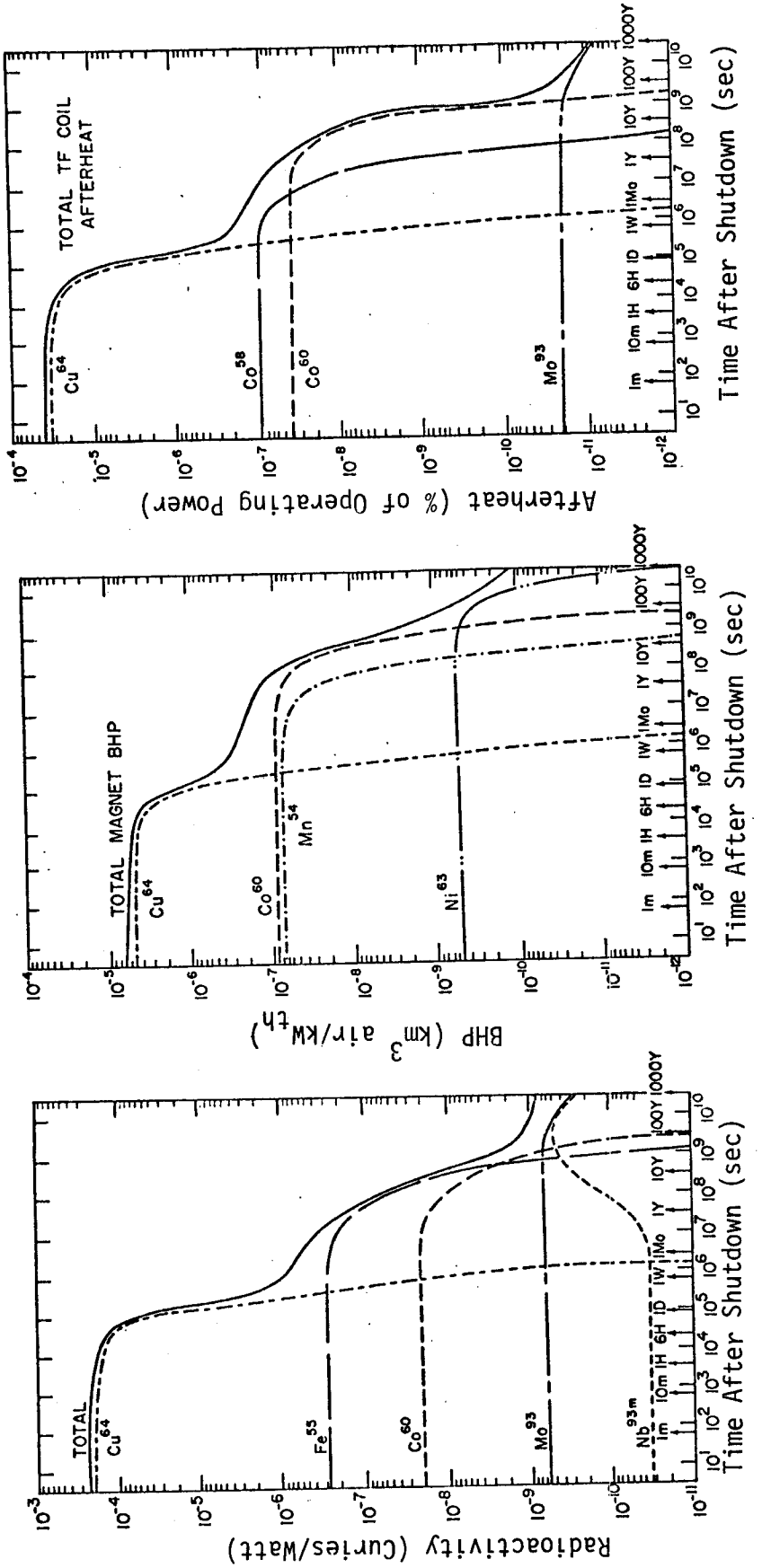

Figure XIII-12

Activity of Toroidal Field Magnets

XIII-D. Activity Following Shutdown in Final Design

The activity following shutdown was recalculated for the final design (WSS) shown in Figure XIII-2. In addition to the basic final design, two alternates were calculated, one in which the tungsten is replaced by 316 stainless steel (SSS) and one in which the structure in the two outer zones is replaced by aluminum (WAL). Figure XIII-13 shows the radioactivity following shutdown for the two cases WSS and SSS. The activity in the WSS case is quite similar in shape and magnitude to that of TETR-A. Again, the major contributor to the activity is the tungsten zone. The comments concerning the contribution of the different isotopes and elements made for TETR-A hold here also. In an effort to reduce the activity, the calculations were repeated substituting 316 stainless for tungsten. As is seen in Figure XIII-13, this indeed does result in a reduction in the activity at shutdown by about a factor of two. However, because of the longer lived isotopes generated in 316 stainless steel, the long term radioactivity is increased in the SSS case by about a factor of ten. The specific radioactivity for all three cases at shutdown is shown in Figure XIII-14. The BHP and afterheat following shutdown are shown in Figures XIII-15 and XIII-16. Again, the curves are similar to those of TETR-A. The SSS case again shows a slight improvement in BHP over the WSS case for early times at the expense of a much larger penalty in BHP at long times. On the other hand, the afterheat of the SSS case is always greater than that of the basic WSS case, except for the period between about six hours and one month.

The dose rate outside the outer blanket has also been calculated and the results are shown in Table XIII-4. For the WSS case, the results are quite comparable to TETR being slightly lower at early times after shutdown. The

Figure XIII-13

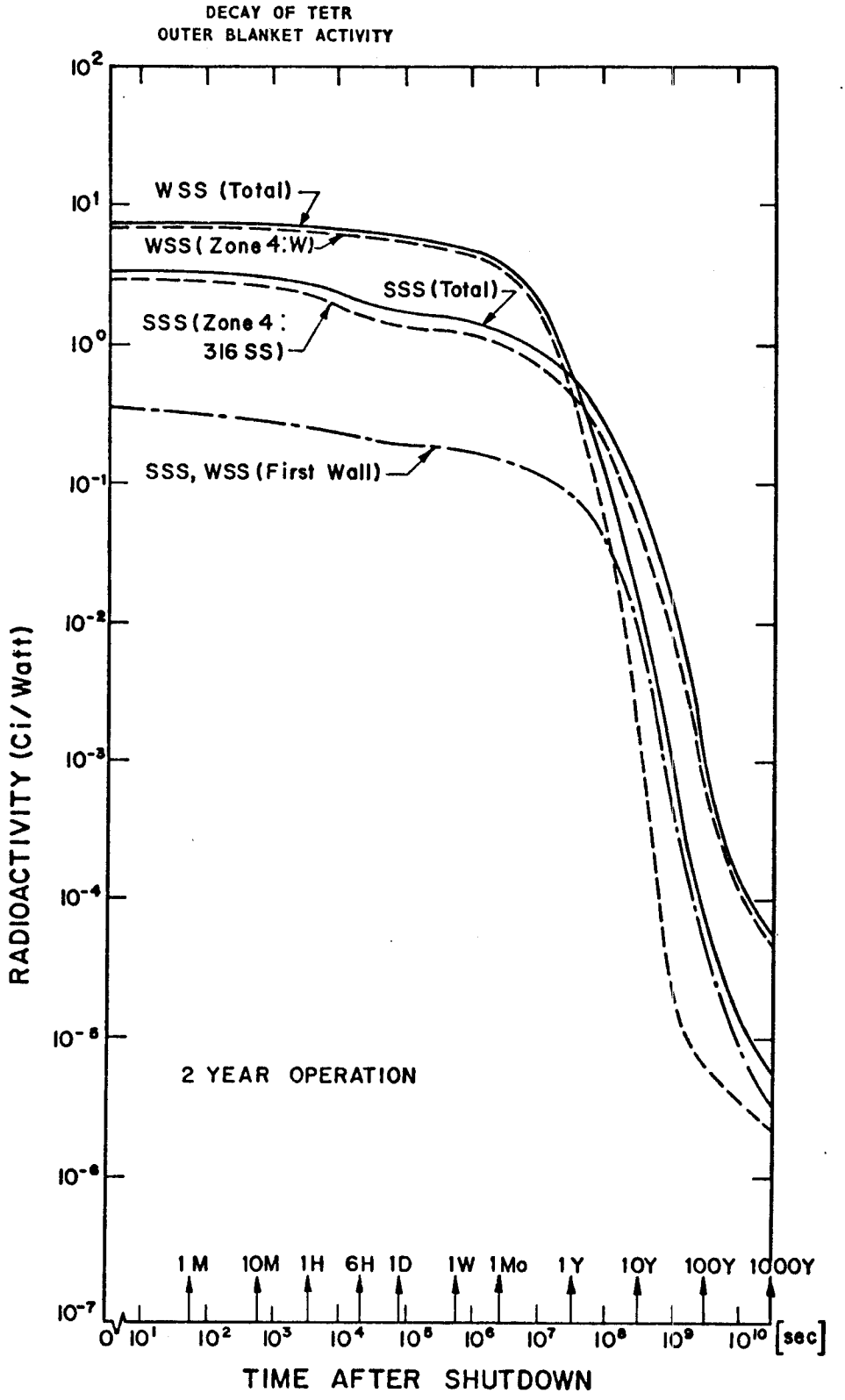

Figure XIII-14

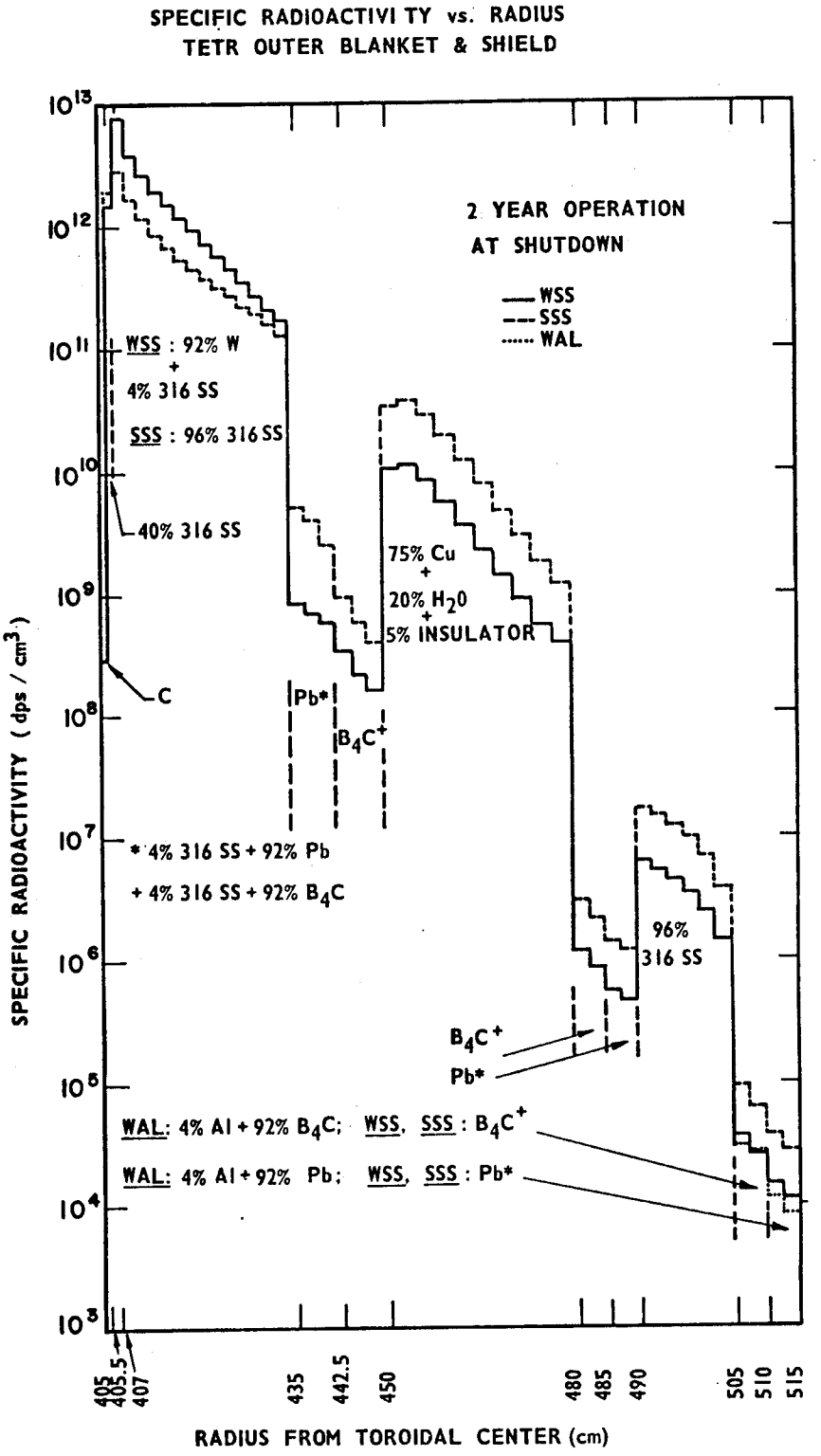

Figure XIII-15

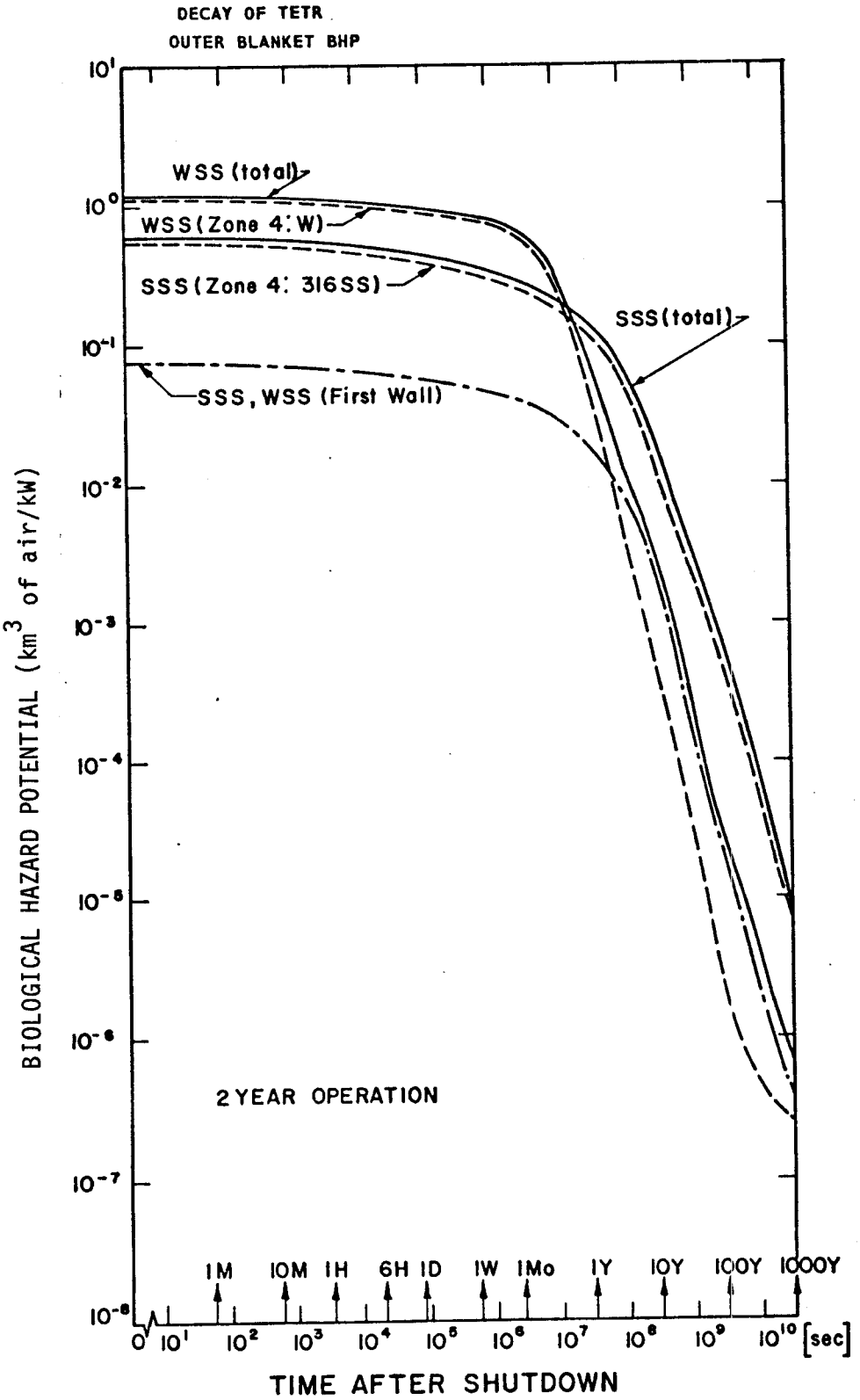

Figure XIII-16

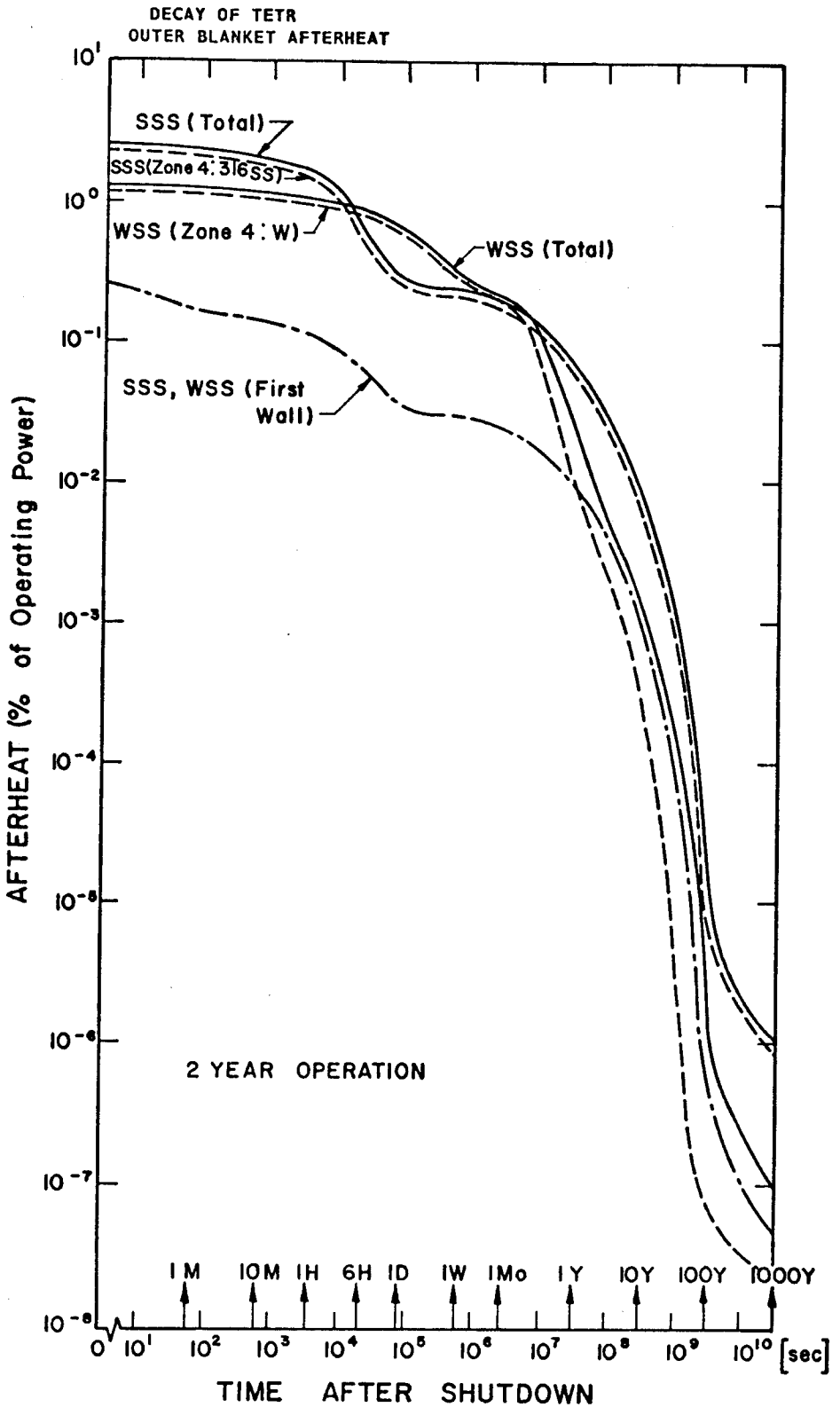

Table XII-4

Calculated Dose Rate Outside the Shield

Neutron Wall Loading	WSS	SSS	WAL
Time After Shutdown		1.10 MW/m^2	
		Dose Rate, mrem/hr	
0	683.2	1,875.1	826.9
1 min.	666.7	1,829.3	758.0
10 min.	598.3	1,625.9	551.8
1 hr.	474.2	1,311.6	438.6
6 hr.	143.5	390.6	181.9
1 day	27.9	69.3	46.9
1 week	24.0	59.8	3.5
1 month	21.0	51.9	3.1
1 yr.	7.7	18.7	1.5
10 yr.	1.3	3.1	1.5
100 yr.	7.8×10^{-5}	2.1×10^{-4}	3.3×10^{-1}
1000 yr.	2.9×10^{-5}	8.1×10^{-5}	3.7×10^{-5}

dose rates for the SSS case are, however, significantly higher than the base WSS case due to the reduced shielding properties of stainless steel compared to tungsten. The idea of such a substitution does not seem to be worthwhile from this aspect. The motivation for introducing the WAL case arose from the observations in earlier studies that most of the dose originates from activity in the outer part of the blanket-shield. Consequently, the substitution of a low residual activity structure in this region seems worth investigating. The results of the substitution on the dose outside the blanket is shown in the third column of Table XIII-4. For the first day or so the WAL case shows no particular improvement and over most of this interval even shows an increase. After the 15 hour Na^{24} decays away, there is a significant improvement such that after one week the dose is reduced by a factor of 27 to the point where shift maintenance is almost possible. This reduction is even more remarkable since the total amount of structural material in the last two zones of the blanket is equivalent to a thickness of 4 mm. It is very possible that a replacement of all or a portion of the 15 cm stainless steel zone (denoted as SS2 in Fig. XIII-2) with a lower activity material would result in a further reduction of the dose after shutdown. It must be noted, however, that these doses are calculated by the main shielding sections. When account is taken of the penetrations for the neutral beams, the shielding problem is much more difficult and could well prove to be the factor determining the limiting dose rate outside the reactor.

XIII-D-1. Two-Dimensional Effects

No attempt was made to perform a complete two-dimensional analysis of TETR for reasons of cost and time. However, several calculations were performed at selected locations in order to provide a feel for the levels of activity, afterheat and BHP. The points selected were in the region above the plasma near the collectors, VF and TF magnets and parts of the vacuum system. Figure XIII-D-17 shows the points selected along with the composition at each point. The activity, afterheat, and BHP are shown in Figures XIII-D-18, XIII-D-19 and XIII-D-20 at shutdown and 1 week and 100 years following shutdown. In order to provide a more meaningful comparison, the same quantities are plotted versus time after shutdown for four of the points along with the average values for the first wall in Figures XIII-D-21, XIII-D-22 and XIII-D-23. The points were selected on the basis of being representative of the different materials used in e.g. point 4 is 75% Cu, 20% H_2) and 5% glass while point 1 is 40% 316 SS and 50% H_2). It can be seen from the Figures that as suspected the activities are considerably smaller than that of the first wall. The only exception to this remark is the BHP for point 4 (mostly copper) which is a factor of five higher than the 1st wall BHP for the first day (on a specific BHP basis). When the relative volumes of materials are taken into account, the activity in regions of TETR other than the primary blanket and shield appears to be of much less consequence than that of the primary blanket and shield. An exception to the point might occur in the regions around the neutron beam ports and ducts. Unfortunately, fluxes were not available to check on this point.

Figure XIII-17

TETR TWO-DIMENSIONAL SPECIFIC RADIOACTIVITY POSITIONS -UPPER COLLECTOR PLATE CRYOPUMP REGION-

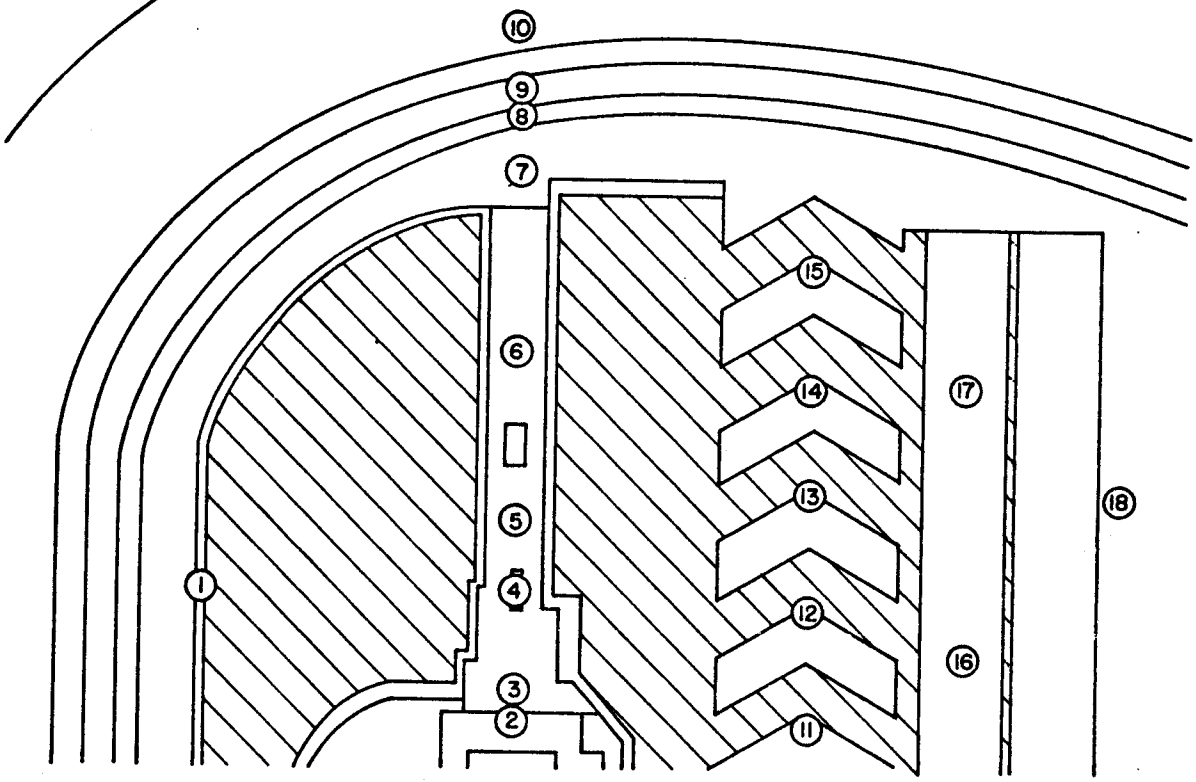

POSITIONS	COMPOSITION
1	40% 316 SS, 50% H_2O
2,9	92% Pb, 4% H_2O, 4% 316 SS
3,5,6	15% 316 SS, 15% H_2O
4	75% Cu, 20% H_2O, 5% glass
7,18	92% W, 4% H_2O, 4% 316 SS
8	96% 316 SS, 4% H_2O
10	30.65% 316 SS, 57.65% Cu, 1.59% mylar
11,12,13,14,15	5% H_2O, 40% W, 25% Pb, 25% B_4C, 5% Al
16, 17	10% Al

Figure XIII-18

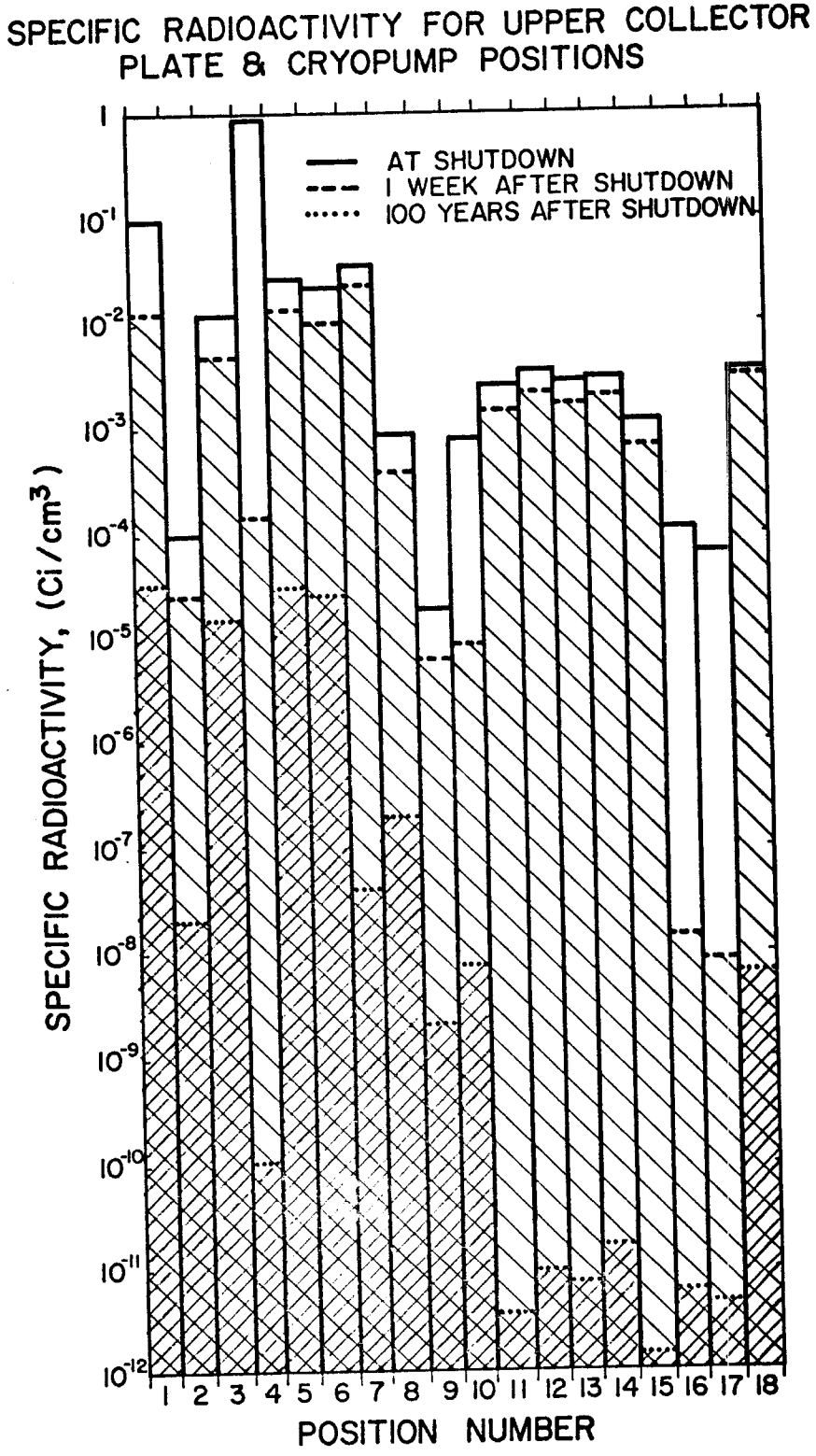

Figure XIII-19

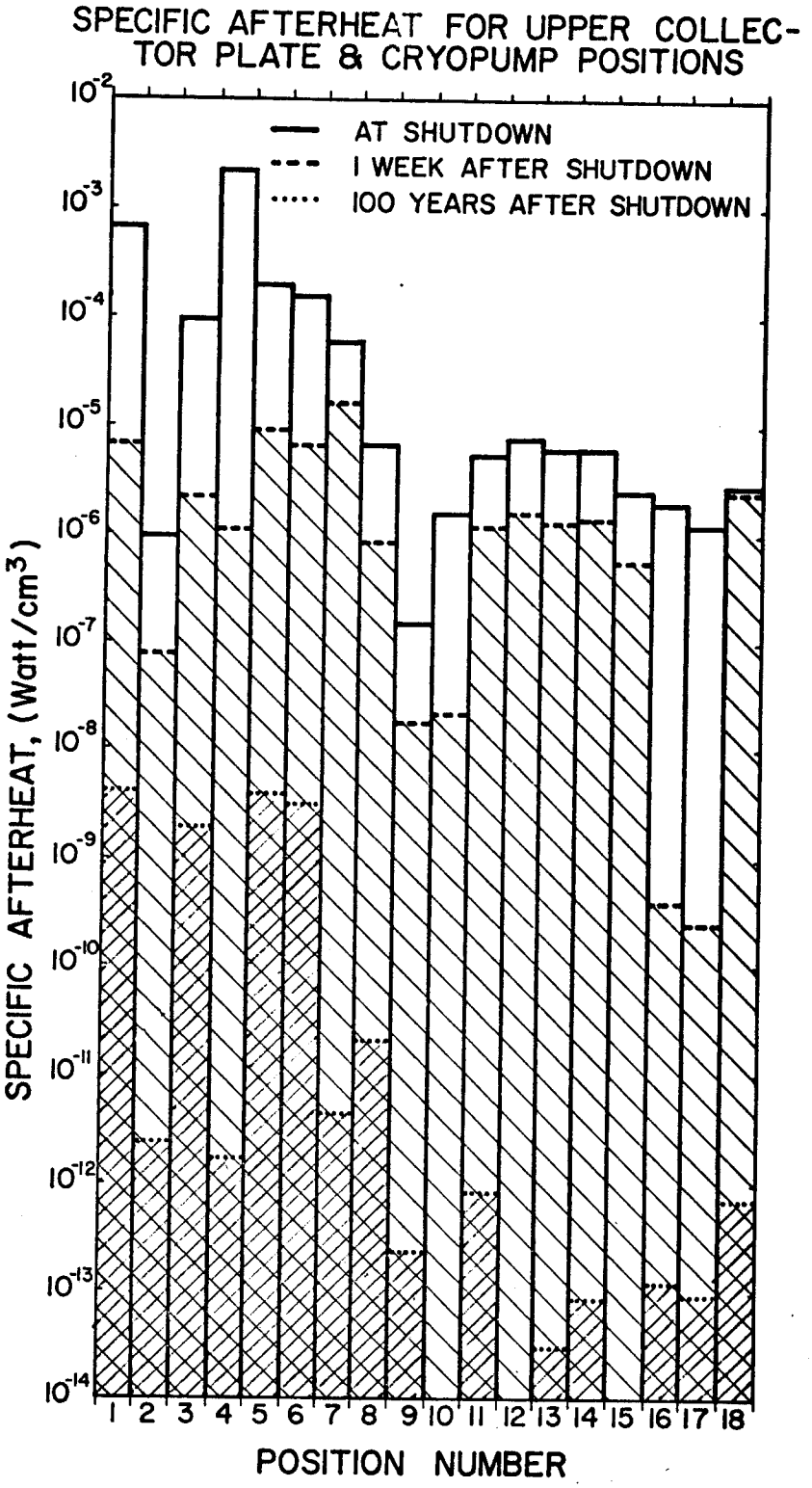

Figure XIII-20

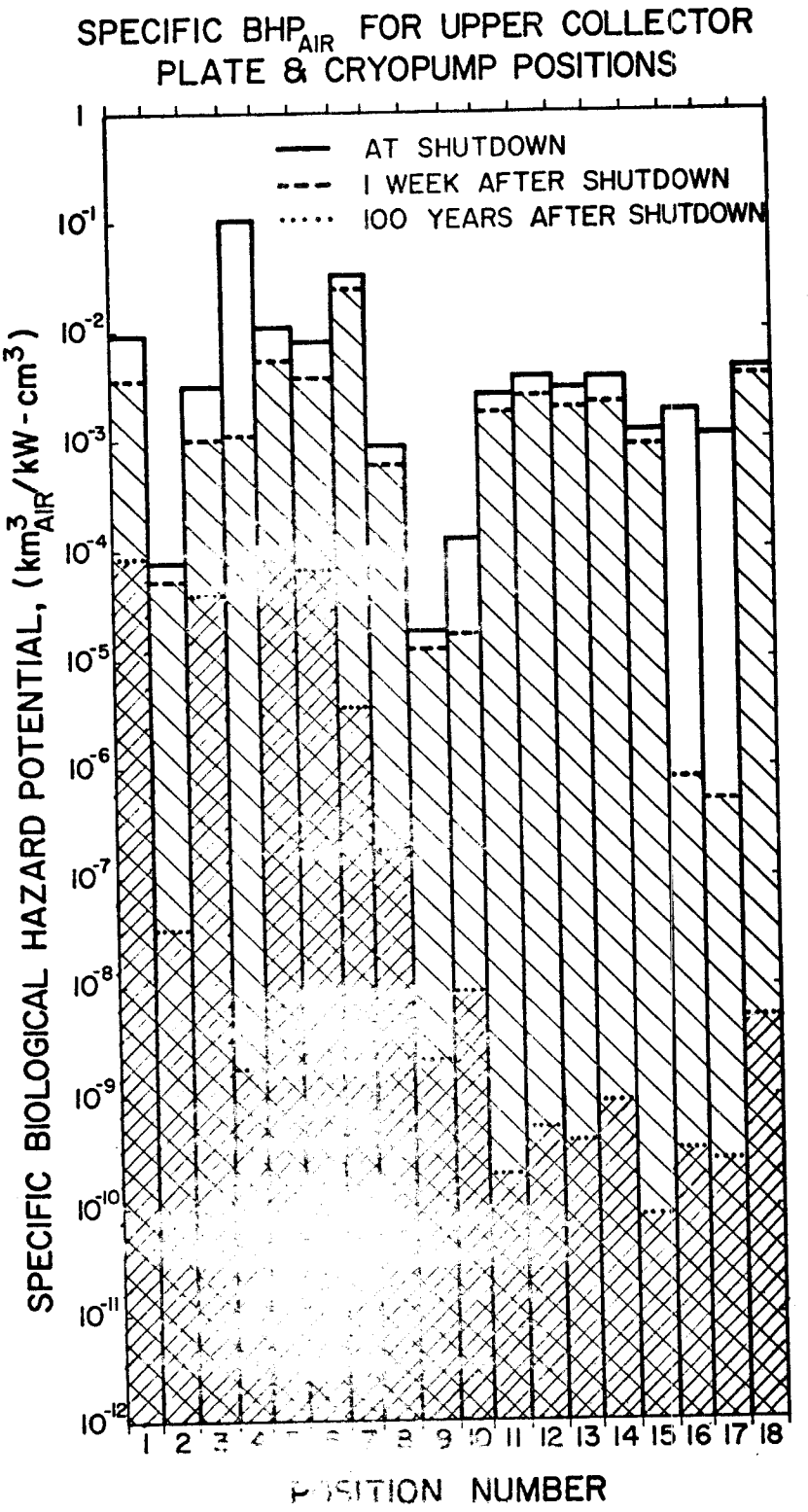

Figure XIII-21

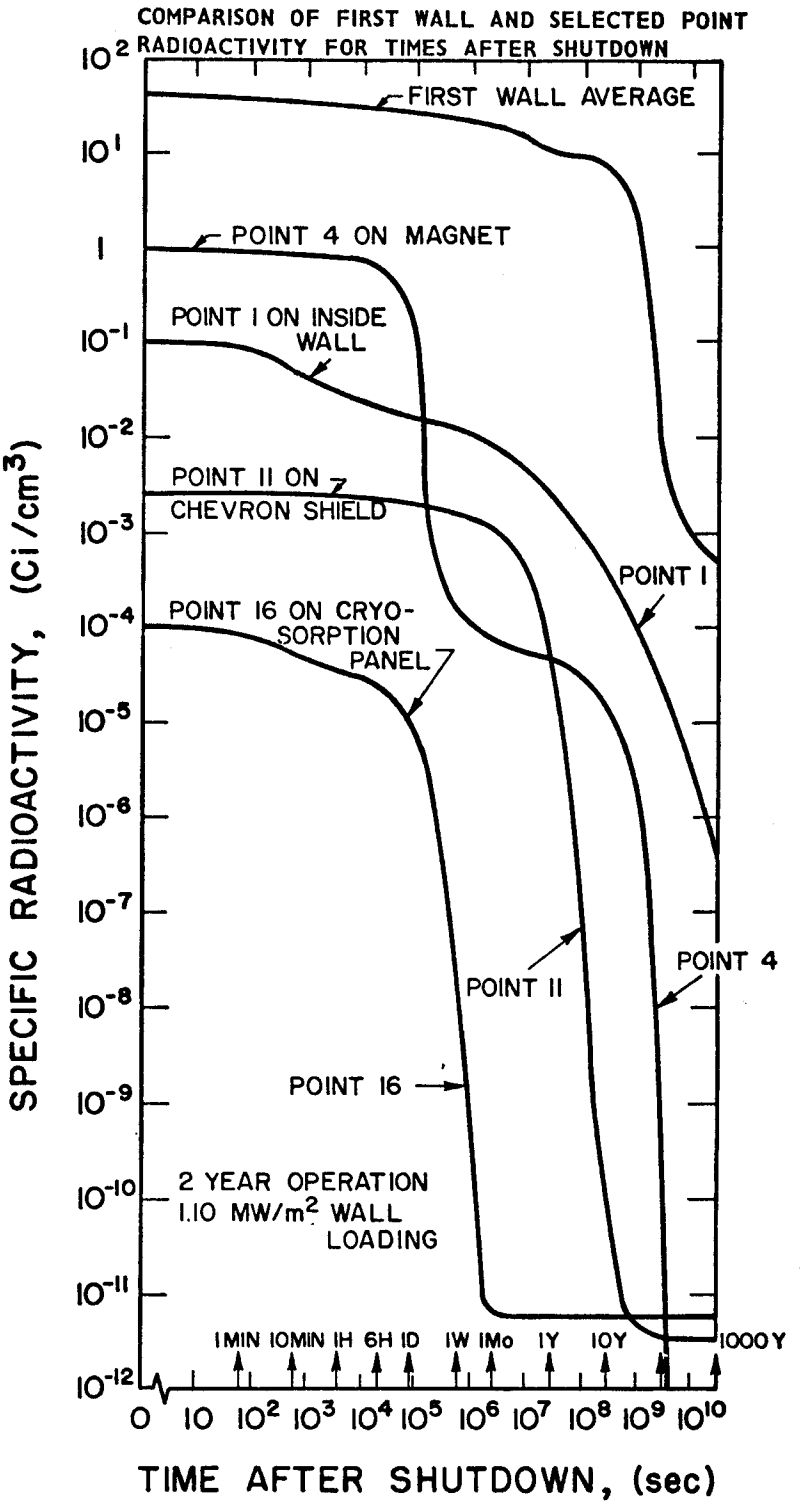

Figure XIII-22

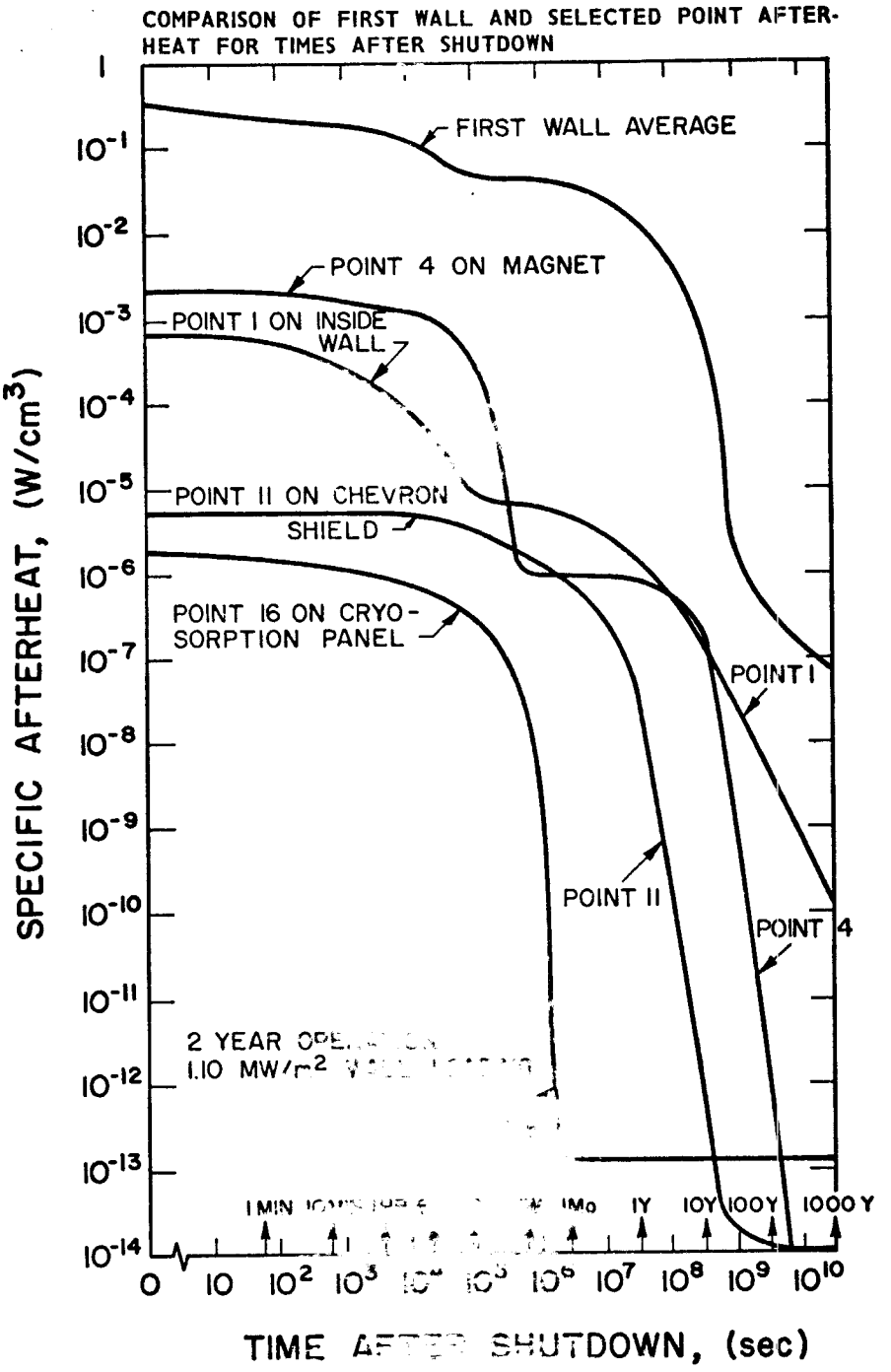

Figure XIII-23

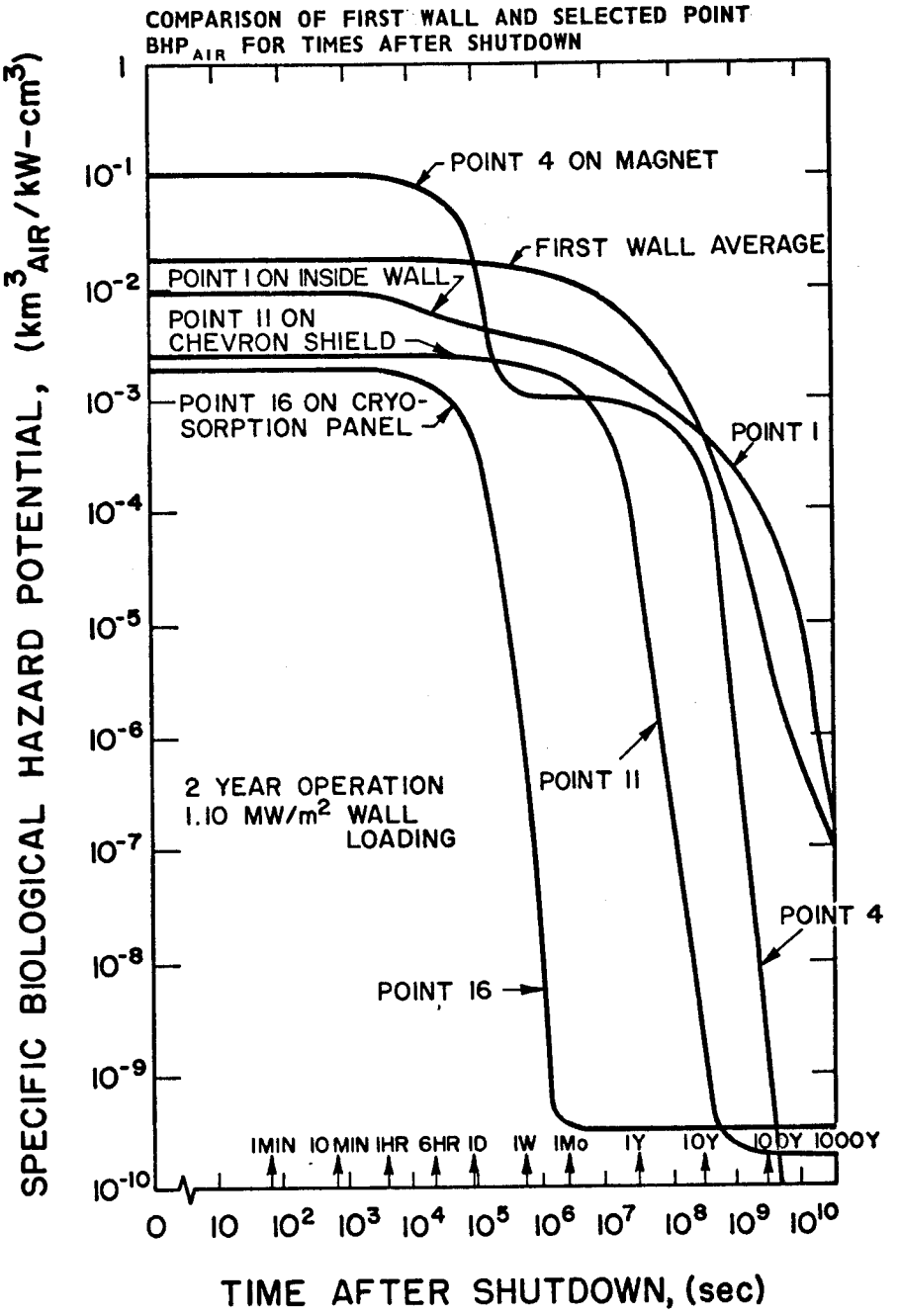

References for Section XIII

1. B. Badger et al., "UWMAK-I, A Wisconsin Toroidal Fusion Reactor Design", University of Wisconsin Report, UWFDM-68, 1974.

2. B. Badger et al., "UWMAK-II, A Conceptual Tokamak Power Reactor Design", University of Wisconsin Report, UWFDM-112, 1975.

3. B. Badger et al., "A Non-circular Tokamak Power Reactor Design, UWMAK-III", University of Wisconsin Report, UWFDM-150, 1976.

4. T. Y. Sung and W. F. Vogelsang, "DKR: A Radioactivity Calculation Code for Fusion Reactors", University of Wisconsin Report, UWFDM-170, 1976.

5. T. Y. Sung and W. F. Vogelsang, "Decay Chain Data Library for Radioactivity Calculations", University of Wisconsin Report, UWFDM-171, 1976.

XIV. Plant Layout

XIV-A. Introduction

This chapter should be considered as an interim report until a suitable Architect Engineer can be selected. The basic philosophy behind the siting of TETR is that it is, first of all, a one-of-a-kind facility so that it does not have to meet generic design criteria. It is also assumed that the TETR can be located inside of a government laboratory site such as Hanford, Oak Ridge, Los Alamos, Idaho Falls, etc. This latter criterion means that the construction time could be shorter than normally incurred for a "public" site due to reduced time for public hearings. Finally, we have decided that underground siting would be desirable to reduce the consequences of an accidental release of tritium.

The reader should recognize that this chapter will lack the normal detailed layout that we have made for the UWMAK series of reactors. This will be remedied as soon as possible and an updated chapter will be mailed to the holder of this report.

XIV-B. General Building Plot Plan

Figure XIV-B-1 shows a top view of a possible plot plan for TETR and Fig. XIV-B-2 shows a cut away. It is presumed that the reactor would be located near a source of cooling water adequate to provide the 40,000 gallons per minute required for operation. The administration, maintenance and control operations were all combined into one large (20 meters x 90 meters x 7 meters) building. This building should not contain any radioactive materials and should be far enough away from the reactor such that the magnetic field leakage does not interfere with the control operations. A schematic of the amount of

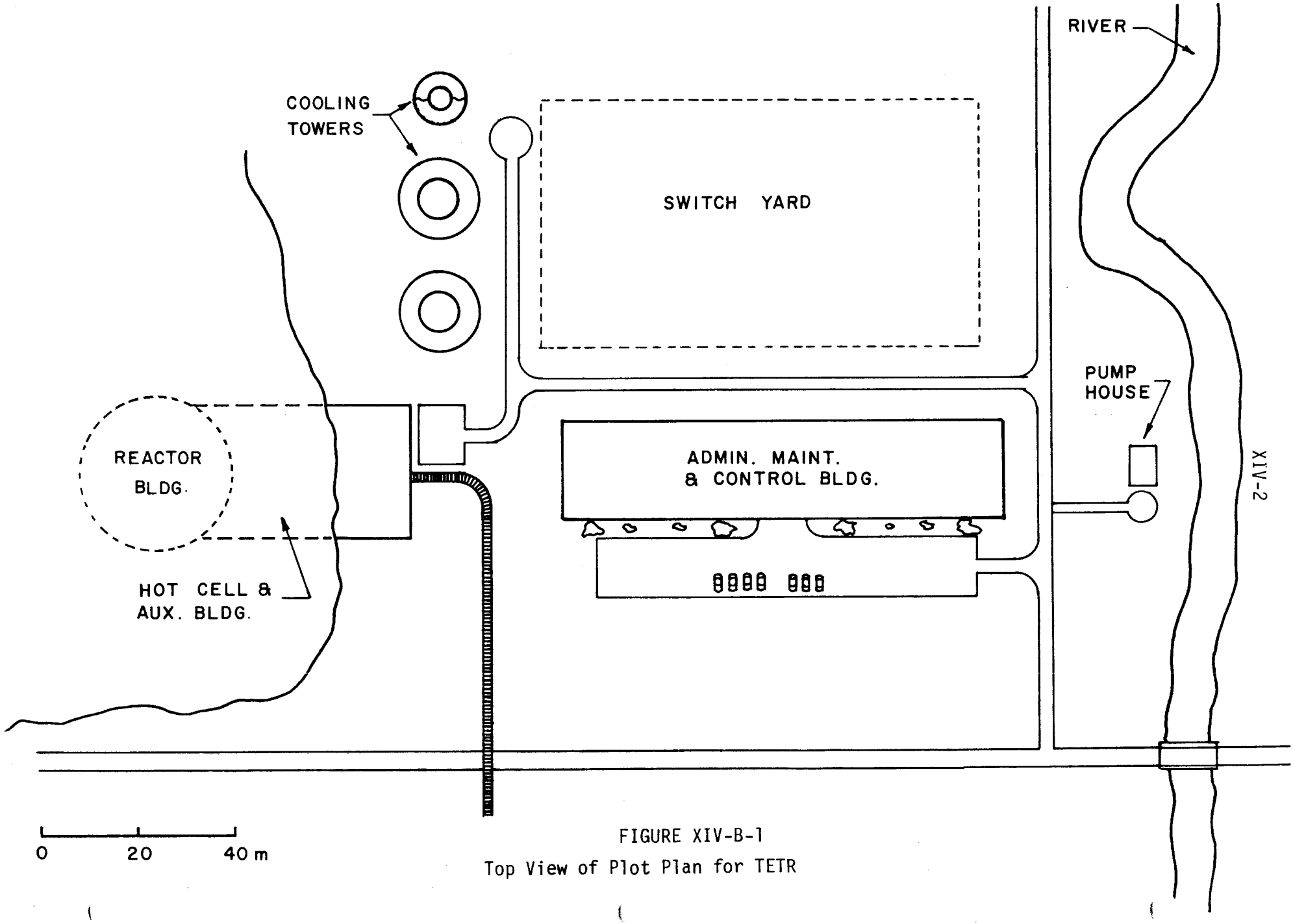

FIGURE XIV-B-1

Top View of Plot Plan for TETR

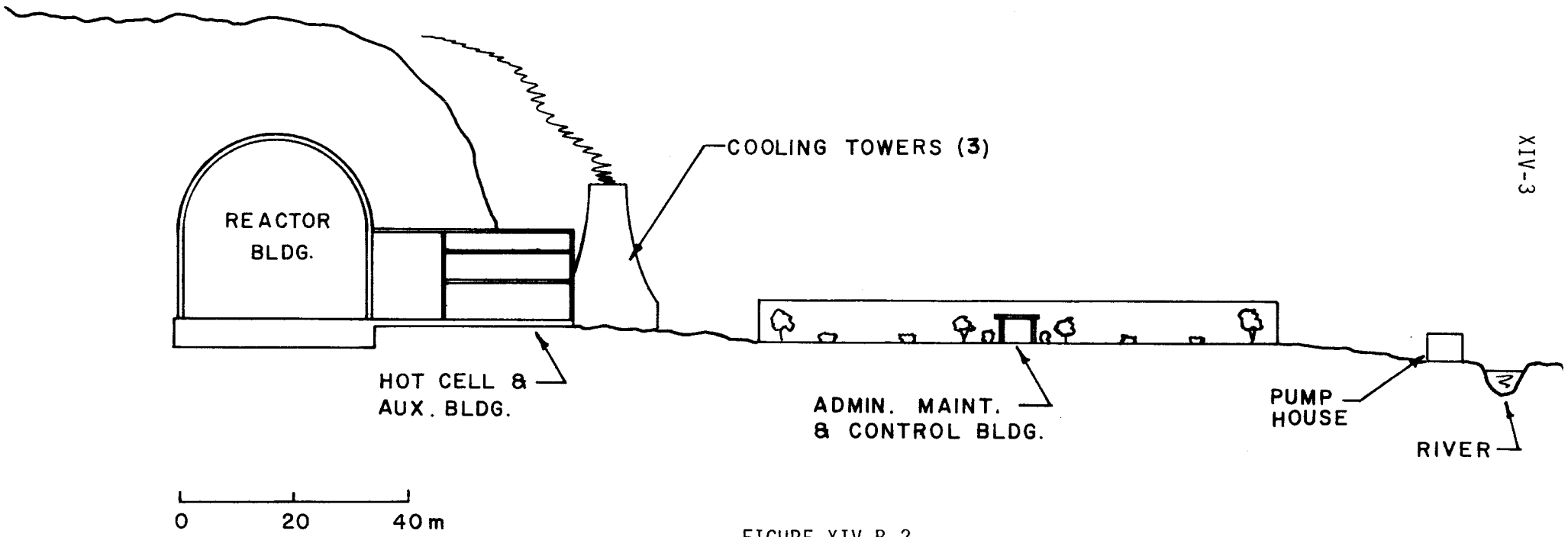

FIGURE XIV-B-2

Side View of Plot Plan for TETR

space alloted to each of the above functions is shown in Fig. XIV-B-3. The floor area and volume of space allowed is shown below.

Function	Floor Area-m^2	Volume-m^3
Administration (2 fl)	1200	4200
Maintenance	800	5600
Reactor Control	200	1400
Experiment Control	200	1400
TOTAL	2,400	12,600

It is important to note that all control of the experiments will be conducted well away from the radiation environment and in close proximity of the reactor control room.

The switchyard used to handle the 450 MW_e (peak) from the outside lines is 90 meters by 50 meters and takes up the largest fraction of the plant area.

We require two cooling towers to dispose of the approximately 500 MW_t of heat during the plasma operation and these are located close to the reactor building but on the level area outside the underground site.

Finally, the reactor building itself is buried under at least 20 meters of earth in all directions. The reactor building will be described in the next section. Attached to the 32 meter diameter domed reactor building is a 15 meter high, 42 meter long and 27 meter wide hot cell and auxiliary equipment building. About two-thirds of this building will also be underground and the last one-third protrudes from the hillside. A railroad track will run through this building into the reactor hall for removal and/or installation of large components. The railroad can also be used to transport highly radioactive

Figure XIV-B-3

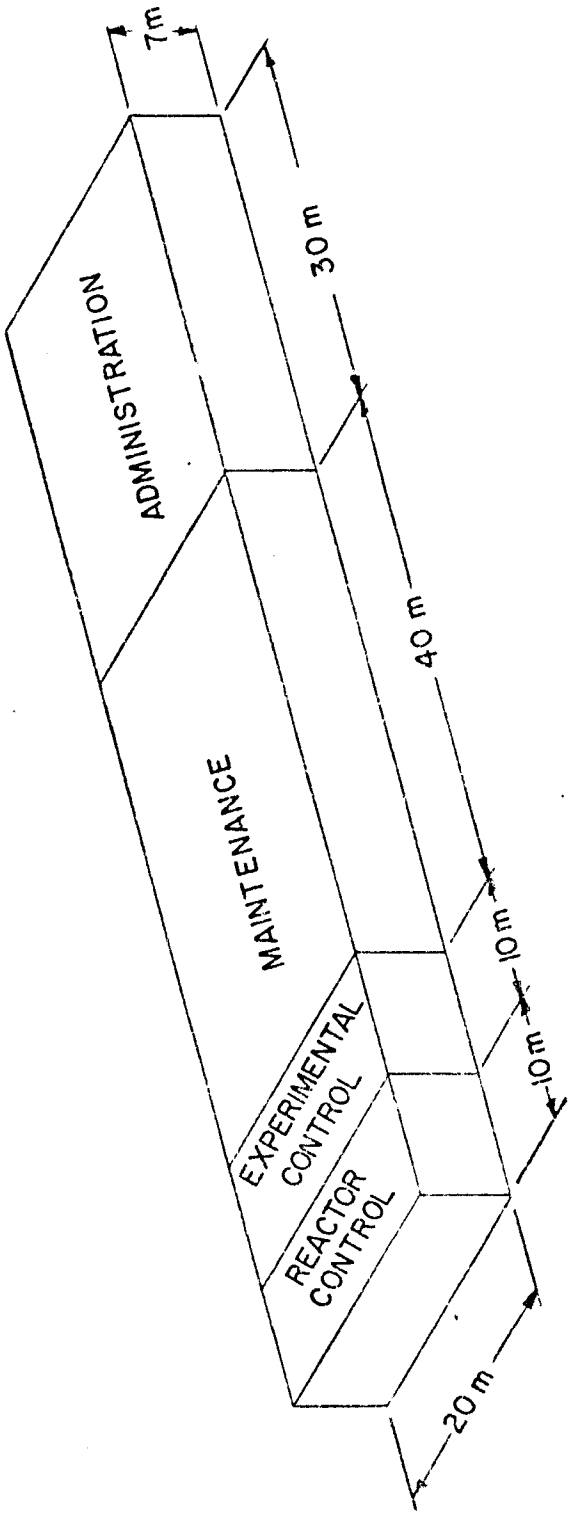

ADMINISTRATION AND CONTROL BUILDING

components out of the rad waste areas to appropriate storage areas.

It is anticipated that the total reactor site will be 500 acres, typical of current light water reactor sites.

XIV-C. Reactor and Auxiliary Buildings

TETR itself will be housed in a 31 meter high domed building as shown in Fig. XIV-C-1. Because of the fact that it is surrounded by at least 20 meters of earth the exterior walls need only be approximately 1 meter thick rather than the roughly 2 meters required in the UWMAK reactors to reduce the neutron flux to acceptable levels. The building is 32 meters in diameter which is sufficient to provide for 3-4 meters of clear space outside of the injector and 7 to 8 meters of space outside the TF coils. A 5 meter concrete foundation pad is required to support the roughly 10,000 tonnes of the nuclear island.

A cross sectional view of the reactor hall and its attached auxiliary building is shown in Figs. XIV-C-2 to 4. The auxiliary building has a 5 meter wide corridor down the center through which equipment can be withdrawn on a railroad bed. The first floor contains two hot cell areas, a rad waste disposal area, a room for maintenance and storage of slightly contaminated reactor equipment and a spare room which could contain a small turbine-generator unit.

The hot cell area for experiments is 11 x 13 x 7 meters in size and contains the necessary facilities for disassembly of test cells after they have been removed from the reactor. The reactor hot cell is 12 meters long by 9 meters wide and 15 meters high. It is designed to take one complete TF coil or smaller reactor components that would need minor repairs. Both the reactor

Figure XIV-C-1

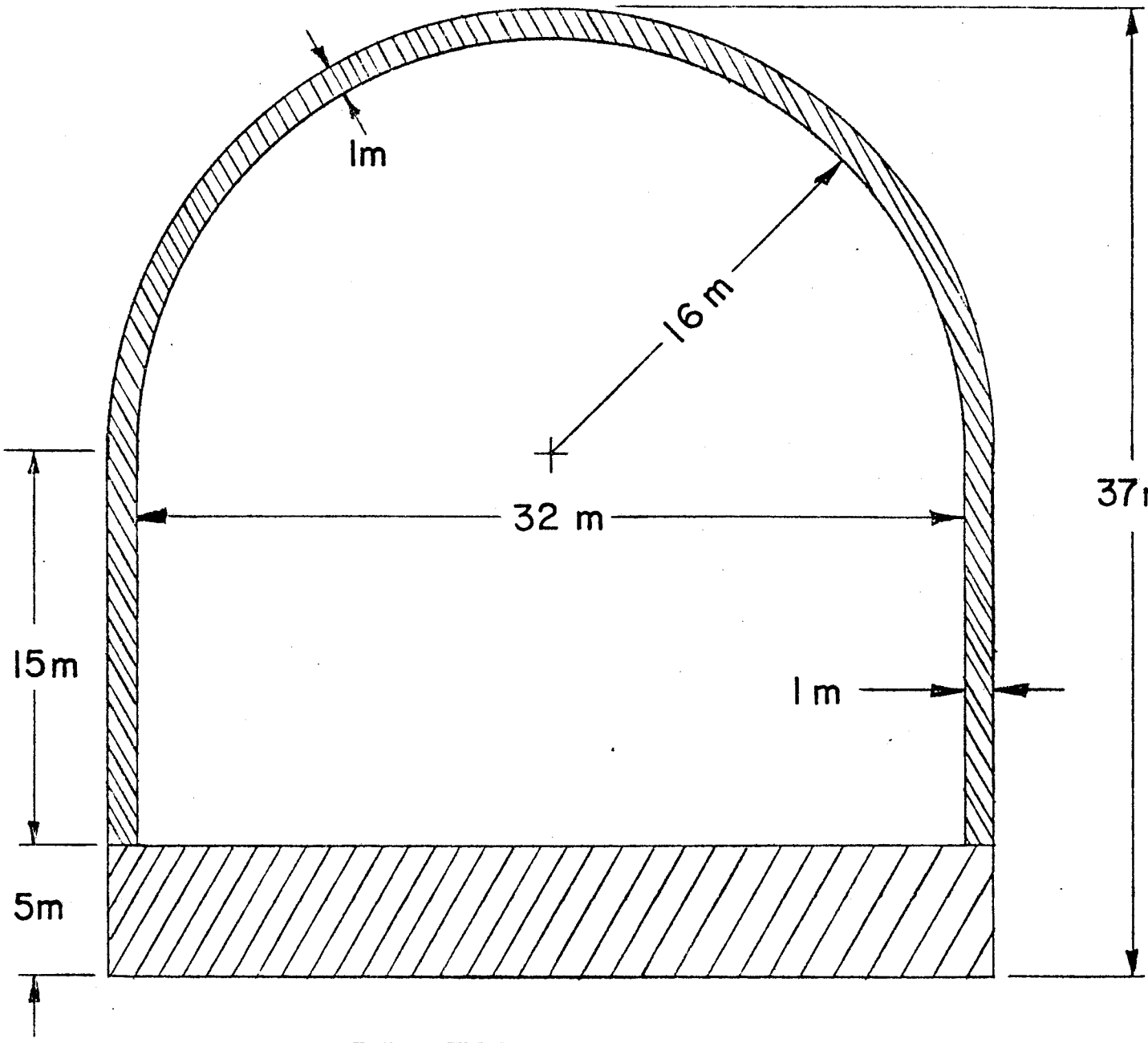

REACTOR HALL DESIGN

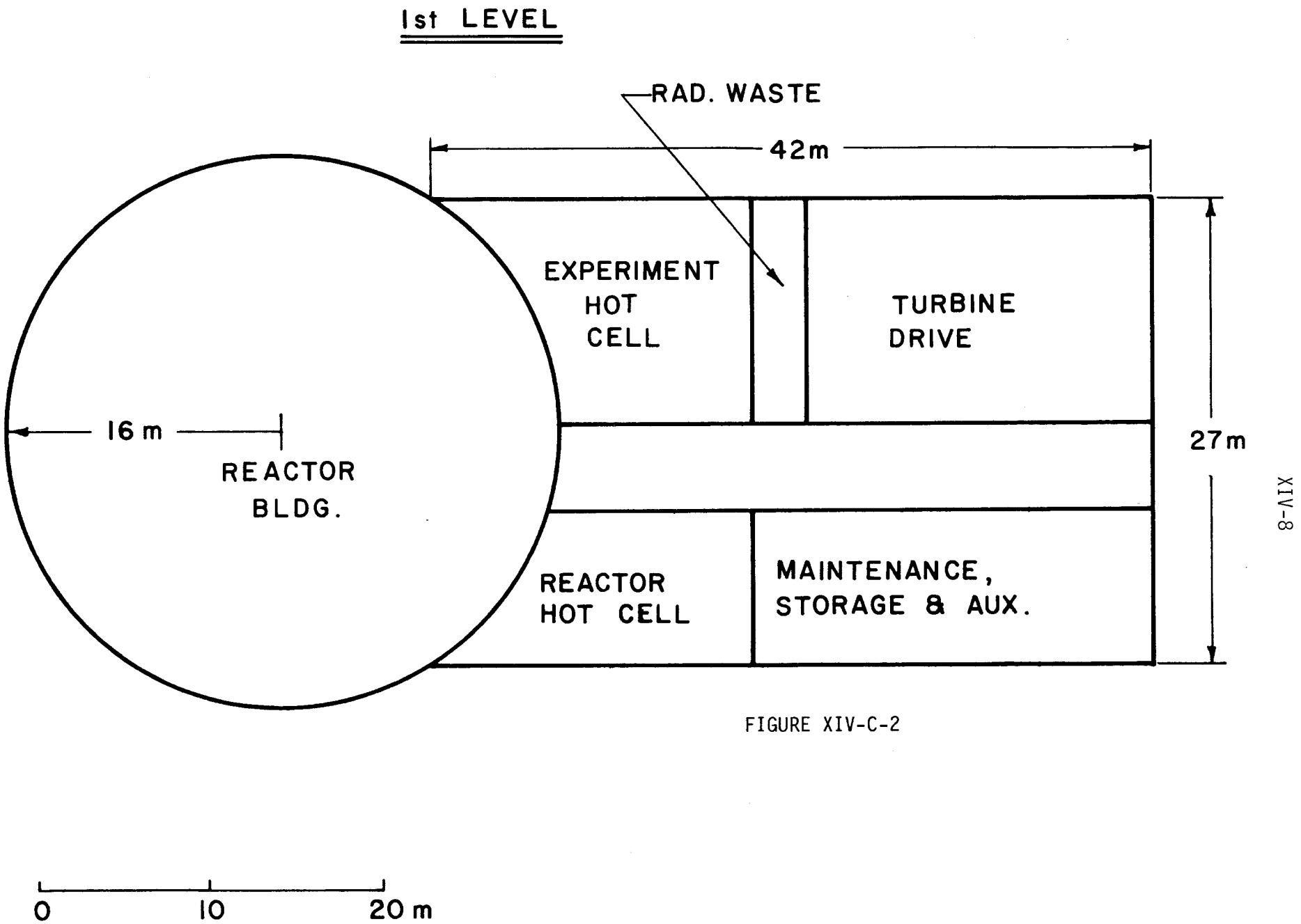

FIGURE XIV-C-2

2nd LEVEL (7 m above 1st level)

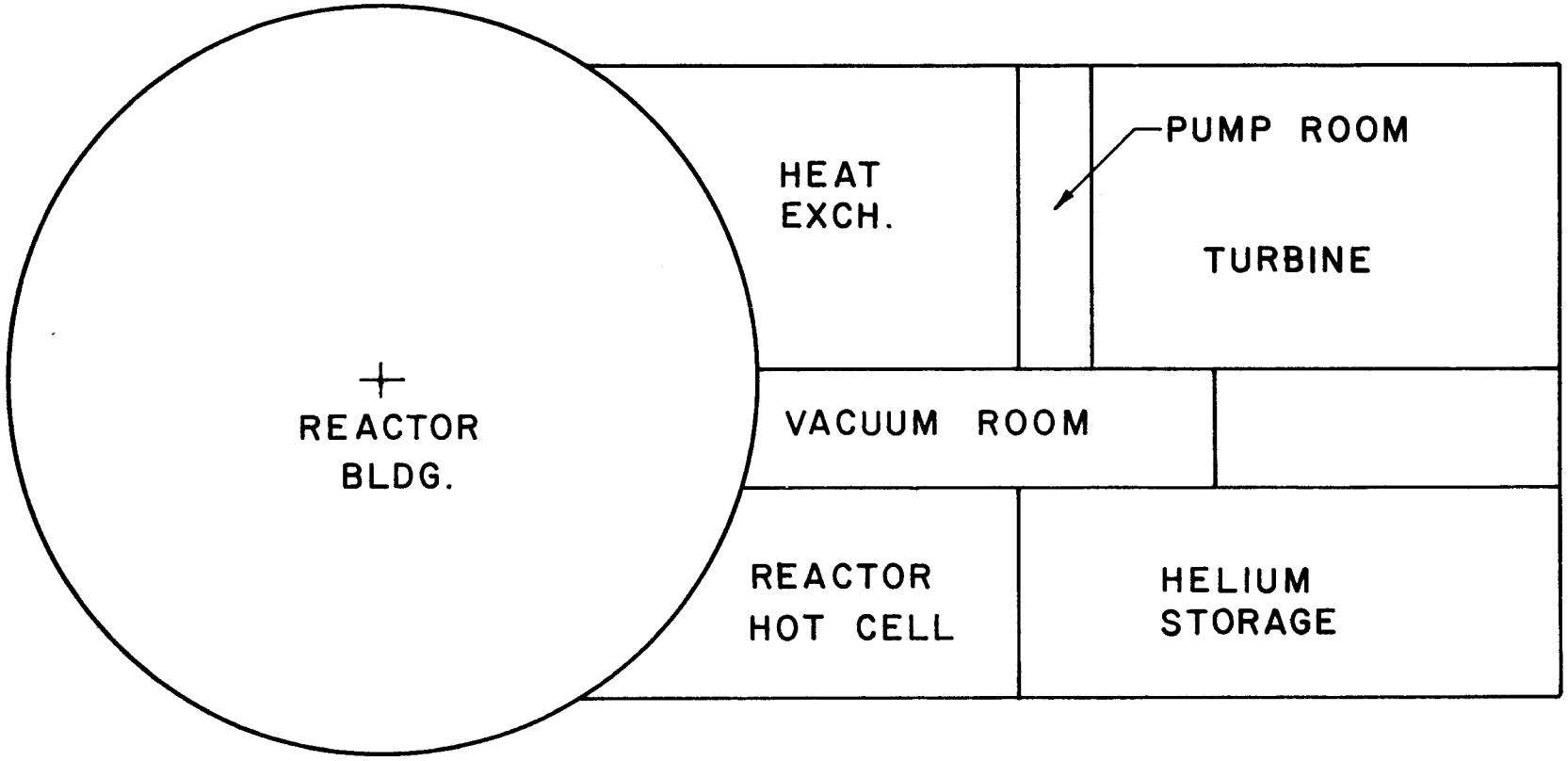

FIGURE XIV-C-3

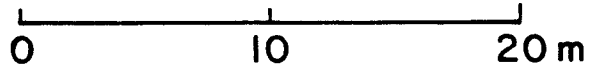

3rd LEVEL (5 m above 2nd level)

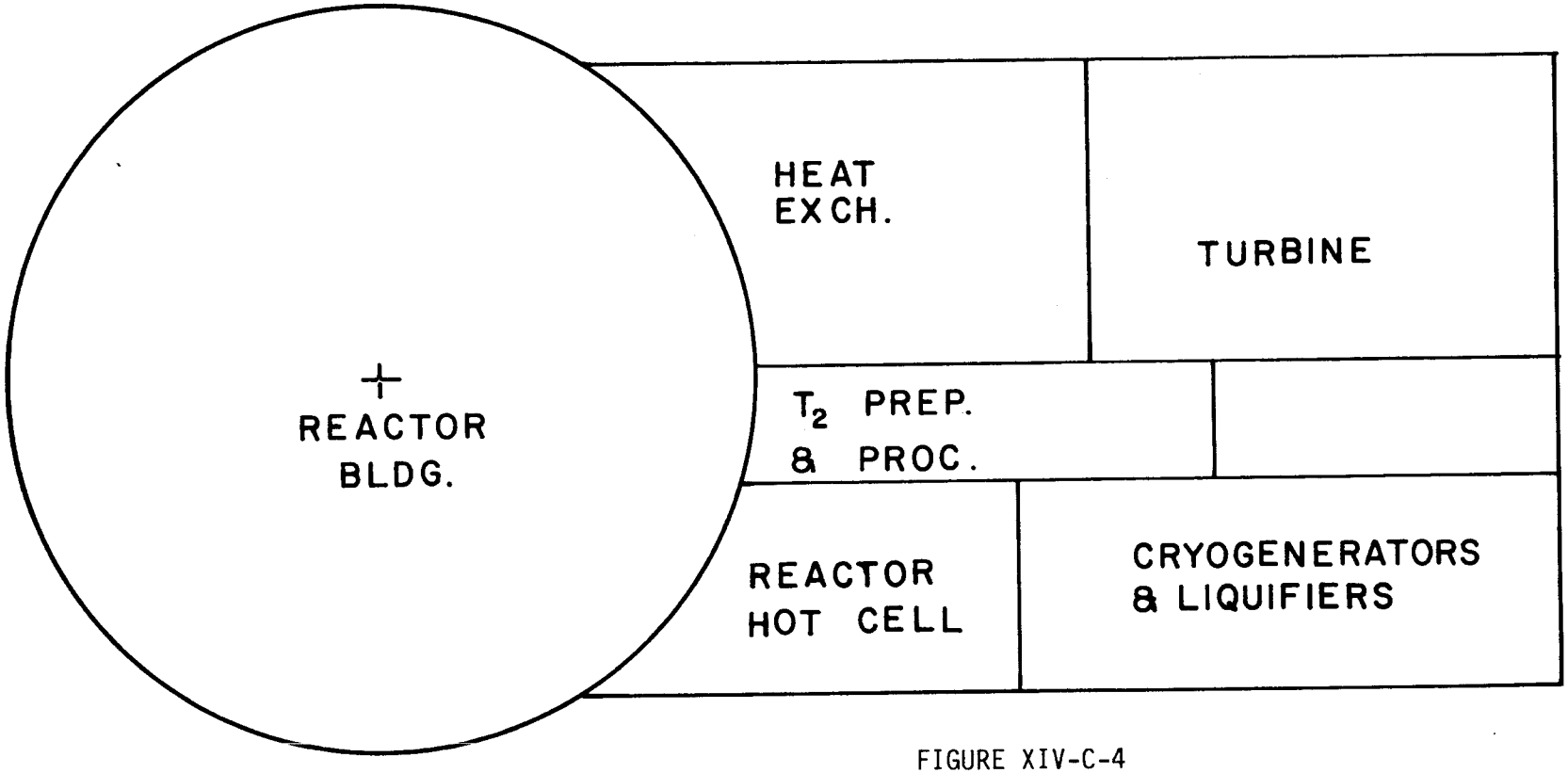

FIGURE XIV-C-4

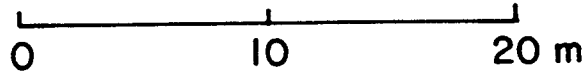

hot cell and experimental hot cell areas will have direct access to the reactor hall through properly designed double lock doors.

Immediately behind the experimental hot cell area is a 3 x 13 meter rad waste area which is 7 meters high. It is designed to accept waste from both hot cell areas and concentrate them for packaging and shipment to a final storage area.

The maintenance and storage area is 23 meters long, 9 meters wide and 7 meters in height. It will be used to store spare reactor components or to repair slightly contaminated equipment. Finally, the turbine bay has been included in the event that one would eventually want to generate electricity from the 260°C steam emanating from TETR. It is estimated that roughly 80 MW_e of electricity could be generated from the 275 MW_{th} generated in the blanket. The turbine-generator bay area is 20 meters long by 13 meters wide and 7 meters high.

The second floor of the auxiliary building (7 meters above the ground floor) contains the heat exchangers, coolant pump room, vacuum equipment and helium storage areas in addition to the reactor hot cell and turbine bays. The heat exchanger room will have to be designed to withstand a leak from the primary coolant circuit which could contain significant amounts of corrosion products. The background radiation levels in the heat exchangers, pumps and cleanup systems will probably be too high to allow access without special shielding and the equipment will have to be designed to be easily replaceable.

The vacuum equipment room will be adjoining the reactor hall and will contain large amounts of tritium in the cryopumps. The design of this room will have to take into account the possibility of kg level tritium spills and methods for

preventing such tritium from reaching the environment will have to be derived In fact, this room probably represents the most critical area of the safety analysis.

Finally, the third floor, which is 5 meters above the second floor, contains the tritium preparation room and the helium cryogenerator units. The tritium preparation unit is in close proximity to the vacuum equipment room to reduce the length over which large amounts of tritium need to be transported. The T_2 preparation room contains such equipment as distillation columns, cleanup systems, fuel preparation components and facilities to extract tritium from storage containers. This room will probably contain 10's to hundreds of grams of T_2 at any time and will be subject to the same design restrictions as the vacuum pumping room.

The storage of the reserve T_2 will be accomplished in a building physically removed from the reactor hall and auxiliary building. This storage facility, which may contain approximately 10 Kg T_2, will have to be protected from external attack since it may present a tempting target for a terrorist group.

Chapter XV - Resources and Cost

XV-A. Introduction

The fact that TETR is a "one of a kind" reactor means that materials resources do not have quite the same importance as in a generic design for a power reactor. Nevertheless, the cost of the reactor is closely aligned with the amount, form and type of materials used to make up the nuclear island as well as in auxiliary areas. Therefore, it is important to establish a clear inventory of those materials so that analyses can determine the effect of design modifications.

We will first detail only the materials required for the nuclear island because the balance of plant in this reactor design is rather standard (e.g. there is no steam conversion system). The bulk of this chapter will deal with the cost estimate for TETR and some comments about how it relates to current fission test facilities.

XV-B. Materials Inventory for the Nuclear Island of TETR

Table XV-1 contains the materials inventory for the TETR Nuclear Island (blanket, shield, test modules, magnets, neutral beam injectors, vacuum pumps, etc.). There are 6 features of this table which are worth noting;

1. The largest single demand for any element is for Pb (4560 tonnes).
2. The amount of W required is 3310 tonnes.
3. The shield accounts for more than 90% of the mass of the nuclear island.
4. Over 1300 tonnes of stainless steel are required.
5. The requirement for boron carbide is over 200 tonnes.
6. The total nuclear island material requirement is over 10,000 tonnes.

Table XV-B-1

Element	Blanket				Shield	Magnets			Central Support Structure	N. Beam Injectors	Vacuum System	Total (Tonnes)	Tonnes / MW_t
	Inner	Central	Outer	Test Stations	Supports	TF & Dewars	OH & Dewars	VF					
Al	0.05	0.025	0.07	0.03		144.31	26.34		1.7	0.28	0.65	173.455	0.337
B					185							185	0.359
C	0.46	0.22	0.60	0.27	52							53.55	0.104
Cr	0.97	0.46	1.26	0.56	158.4	45.72	7.89	2.66	30.6	5	11.7	265.22	0.515
Nb						25						25	0.049
Cu	0.05	0.025	0.07	0.03		450	0.44	159.52	1.7	0.28	0.65	612.77	1.19
He						1.5	0.4				2.75	4.65	0.009
Fe	3.35	1.59	4.34	1.93	522.7	156.2	27.19	8.78	105.4	17.2	40.3	888.98	1.726
Pb					4560							4560	8.854
Mn	0.11	0.05	0.14	0.06	15.8	5	0.88	0.27	3.4	0.55	1.3	27.56	0.054
Mo	0.11	0.05	0.14	0.06		5	0.88		3.4	0.55	1.3	11.49	0.022
Ni	0.76	0.36	0.98	0.44	95	35.28	6.13	1.50	23.8	3.88	9.1	177.33	0.344
Ti						12						12	0.023
W					3310							3310	6.427
Mg						0.56						0.56	0.001
Total	5.86	2.78	7.6	3.38	8898.9	880.57	70.15	172.83	170	27.74	67.75	10,307	20.014
Components													
316 SS	5.4	2.56	7.0	3.11		252	43.82		170	27.76	65	576.65	
304 SS					792			13.3				805.3	
B_4C					237							237	
Graphite	0.46	0.22	0.6	0.27								1.55	
NbTi						37.5						37.5	
Al (6061)T-6						121.2						121.2	
High Purity Al						25.4	25.9					51.3	
OFHC Copper						447		159.52				606.52	
Pb (Shield)					4560							4560	
W (Shield)					3310							3310	
												10,307	

None of the requirements will place a great strain on the US mining or mill capacity. Even the W requirement is only 1% of the US production in 1970.[1] Therefore, we conclude that resources will not be a problem for one TETR.

XV-C. Capital Costs of TETR

We have chosen to follow the approach of J. R. Young in determining the capital costs for TETR. The suggested format of "Economic Information Requirements - Fusion Reactor Design Studies," by J. R. Young, will be followed unless specifically stated to the contrary. A table of pertinent costs for common material in TETR is given in Table XV-C-1.

We have tried to use current (June 1977) costs for the materials in UWMAK-III and we have used rather liberal installation costs. For example, the cost of high quality stainless steel tubing for the LMFBR program is now estimated to be 20-30 $/kg and we expect that the cost for the complex first wall structure will not be less. On the other hand stainless steel support structure is costed at 10-20 $/kg depending on the function because of the simplier shapes and thicker sections.

It can be seen from Table XV-C-2 that the major direct cost item in TETR is the reactor plant equipment. It constitutes 86% of all the direct costs. Investigating this category in more detail, we find the following contributing factors to Account 22. (For more detail see Table XV-C-3 and Appendix A.)

Table XV-C-1
Standard Material Unit Costs[a]

Material	Purchase Cost	Installed Cost
Deuterium	$1070[c]/kg	
Helium	$2.5/liter	
Lithium	$10/kg	
Nitrogen	$0.25/ℓ	
Tritium[b]	$5000/g	
Stainless Steel	$3/kg	
Sheet or Bulk Usage	-	$10/kg
Support for Magnets	-	$10-20/kg
Special Shapes, First Wall	-	$30/kg
Lead	-	$0.60/kg
Concrete (reinforced)	-	$400-500 m^{-3}
Nb-Ti	$33/kg	
OFHC Cu Stabilizer	$3.30/kg	$10/kg
Nb-Ti and Cu Stabilizer	-	$15/kg
Al Conductor & Shield	-	$10/kg
Al Structural Support	-	$44
Tungsten (powder pressed & sintered)	-	$35/kg
B_4C	-	$13/kg
Micarta Insulators	-	$10/kg
Superinsulation	-	$90/$m^2$
Carbon Liner		$30/$m^2$

(a) June 1, 1977 dollars

(b) Cost applies only to that T_2 used or that which decays

(c) Nuclear News p. 138, April 1977.

Table XV-C-2

Summary of Costs for TETR

(June 1, 1977 dollars)

Account Number	Title	$
	Direct Costs	
20	Land	1,000,000
26	Spec. Mat.	1,020,000
21	Structure and Site	16,847,000
22	Reactor Plant Equip.	377,856,000
23	Heat Disposal Equip.	9,510,000
24	Electric Plant Equip.	30,820,000
25	Miscellaneous Equip.	3,120,000
	Sub Total Direct	440,173,000
	Indirect Costs (Based on Direct Minus W)	
91	Construction Facilities (15%)	48,648,000
92	Engr. & Const. Maint. (20%)	64,865,000
93	Other Cost (8%)	25,946,000
	Sub Total Indirect	139,459,000
	Total Reactor	579,632,000
	Contingency (15% of Direct)	48,648,000
	Total Cost Incl. Cont.	628,280,000

Table IV-C-3

Detailed Capital Cost Data for TETR*

Account Number	Account Title	Total
20	Land and Land Rights	
201	Land and Privilege Acquisition	1,000,000
202	Relocation of Buildings, Utilities, Etc.	0
	TOTAL - ACCOUNT 20	
21	Structure and Site Facilities	50,000,000
211	Site Improvements and Facilities	
.1	General Yard Improvements	
.11	Grading, General Excavation and/or Fill and Landscaping	
.12	Roads, Sidewalks and Parking Areas	
.13	Retaining Walls	
.14	Fences, Railings, and Gateways	
.15	Sanitary Sewer System:	
.151	Connection to Existing System	
.152	Septic Tank	
.153	Distribution Box	
.154	Tile Field (Drainage)	
.155	Piping, Conduits, and Manholes	
.16	Yard Drainage and Storm Sewer System:	
.161	Connection to Existing System	
.162	Manholes, Catch Basins and Inlets	
.163	Outfall Structure	
.164	Piping, Conduits, and Open Ditches	
.17	Roadway and General Yard Lighting	
.18	Cathodic Protection	
.2	Waterfront Improvements	
.21	Revetments	
.22	Levees	
.23	Breakwaters	

*Prices are present day and based on a 40-hour work week.

Account Number	Account Title	Total
21	Structures and Site Facilities (Continued)	
211	Site Improvements and Facilities (Continued)	
.3	Transportation Access	
.31	Highway Access	
.311	Grading	
.312	Surfacing	
.313	Culverts	
.314	Bridges, Trestles, and Causeways	
.315	Guards and Signs	
.316	Lighting	
.32	Railway Access	
.321	Grading	
.322	Bridges, Trestles, and Causeways	
.323	Ballast, Ties, Rails and Accessories	
.324	Signals and Interlocks	
.325	Switches, Crossovers and Bumpers	
.33	Waterway Access Facilities	
.331	Dredging	
.332	Piers, Barge Docks, Etc.	
	TOTAL ACCOUNT 211	50,000,000
212	Reactor Building Including Radwaste and Fuel Handling Areas	
.1	Basic Building Structures	
.11	Earth Work Including Dewatering, Walers Steel Sheeting	
.12	Substructure up to Grade Including Concrete, Reinforcing, Forms	
.13	Superstructure	
.131	Concrete Work Including Floors, Exterior Walls, Interior Walls Piers, Columns Reactor Area Concrete, Etc.	
.132	Structural and Gallery Steel	

Account Number	Account Title	Total
21	Structures and Site Facilities (Continued)	
212	Reactor Building Including Radwaste and Fuel Handling Areas (Continued)	
.1	Basic Building Structures (Continued)	
.13	Superstructure (Continued)	
.133	Exterior Metal Siding Walls	
.134	Roof Slabs, Roofing, Flashing, Etc.	
.135	Doors and Windows and Wall Louvers	
.136	Floor Finishes	
.137	Painting Including Special Coating	
.14	Structural Steel Stack	
	TOTAL ACCOUNT 212.1	
.2	Building Services	
.21	Plumbing Below and Above Grade	
.22	Heating, Ventilation, Air Conditioning	
.23	Fire Protection System	
.24	Electrical and Lighting	
.25	Elevator	
	TOTAL ACCOUNT 212.2	
.3	Containment Structures	
.31	Primary Containment Liners at Reactor Area	
.32	Secondary Liner Plant Work for Walls, Floors, Roof	
.33	Penetrations (Mechanical and Electrical)	
	TOTAL ACCOUNT 212.3	
	TOTAL ACCOUNT 212	$5,100,000

Account Number	Account Title	Total
21	Structures and Site Facilities (Continued)	
213	Turbine Building Including Control Room, Heater Bay, Diesel Generator Area	
.1	Basic Building Structures	
.11	Earth Work	
.12	Substructure	
.13	Substructure Including Structural and Gallery Steel	
.2	Building Services	
.21	Plumbing	
.22	Heating, Ventilation Air Conditioning	
.23	Fire Protection System	
.24	Electrical and Lighting	
.25	Elevator	
	TOTAL ACCOUNT 213	0
214	Cooling System Structures	
.1	Intake Structures	
.11	Earth Work	
.111	Supply Pipe, Excavation, Backfill, Disposal and Dewatering	
.12	Supply Pump House	
.121	Dredging and Forebay Construction	450,000
.122	Substructure	
.123	Superstructure	
.124	Structural Steel	
.125	Building Services	
.2	Discharge Structures	
.21	Earth Work	
.211	Discharge Pipe Excavation, Backfill, Disposal and Dewatering	50,000

Account Number	Account Title	Total
21	Structures and Site Facilities (Continued)	
214	Cooling System Structures (Continued)	
.3	Unpressurized Intake and Discharge Conduits	0
.31	Discharge Tunnel	
.32	Discharge Canal	
.33	De-icing Pump Pit	
.4	Recirculating Structures	
.41	Earth Work	
.411	Circulating Water Pipe Excavation, Backfill, Disposal and Dewatering	Incl. Acct. 232
.412	Pumphouse Excavation	
.42	Recirculating Pump House	
.421	Substructure	250,000
.422	Superstructure	
.423	Structural Steel	
.424	Building Services	
.43	Protective Relief Slabs for Circulating Pipe Lines	90,000
.5	Cooling Tower Systems	
.51	Earth Work	Incl. Acct. 232
.511	Foundation Excavation	
	TOTAL ACCOUNT 214	890,000
215	Reactor Auxiliaries Building Including Switchgear Bay	
.1	Basic Building Structures	
.11	Earth Work	
.12	Substructure	
.13	Superstructure Including Gallery Steel	
.2	Building Services	
.21	Plumbing	
.22	Heating Ventilation and Air Conditioning	
.23	Fire Protection System	
.24	Electrical and Lighting	
.25	Elevator	
	TOTAL ACCOUNT 215	1,280,000

Account Number	Account Title	Total
21	Structures and Site Facilities (Continued)	
216	Radioactive Waste Building	Incl. Acct. 215
.1	Basic Building Structures	
.2	Building Services	
	TOTAL ACCOUNT 216	---
217	Fuel Storage Building	
.1	Basic Building Structures	
.2	Building Services	12,000
	TOTAL ACCOUNT 217	12,000
218	Miscellaneous Buildings	
A	Control Room Building	
.1	Basic Building Structures	
.11	Earth Work	
.12	Substructure	
.13	Superstructure Including Structural Steel	
.2	Building Services	
.21	Plumbing	
.22	Heating, Ventilation and Air Conditioning	
.23	Fire Protection System	
.24	Electrical and Lighting	
.25	Elevators	
	TOTAL ACCOUNT 218-A	1,330,000
B	Diesel Generator Building	
.1	Basic Building Structures	
.11	Earth Work	
.12	Substructure	
.2	Services	
.21	Plumbing	
.22	Heating, Ventilation and Air Conditioning	
.23	Fire Protection System	
.24	Electrical and Lighting	
	TOTAL ACOUNT 218-B	160,000

Account Number	Account Title	Total
21	Structures and Site Facilities (Continued)	
218	Miscellaneous Buildings (Continued)	
C	Administration Building	
.1	Basic Structures	
.11	Earth Work	
.12	Substructure	
.13	Superstructure	420,000
.2	Services	
.21	Plumbing	
.22	Heating, Ventilation, and Air Conditioning	
.23	Fire Protection System	
.24	Electrical and Lighting	
	TOTAL ACCOUNT 218-C	420,000
D	Service Building	
.1	Basic Building Structures	
.11	Earth Work	
.12	Substructure	
.13	Superstructure Including Structural Steel	
.2	Building Services	1,500,000
.21	Plumbing	
.22	Heating, Ventilation and Air Conditioning	
.23	Fire Protection System	
.24	Electrical and Lighting	
	TOTAL ACOUNT 218-D	1,500,000
E	Helium Storage Building	
.1	Basic Building Structures	
.11	Earth Work	10,000
.12	Substructures	80,000
.13	Superstructure Including Structural Steel	0

Account Number	Account Title	Total
21	Structures and Site Facilities (Continued)	
218	Miscellaneous Buildings (Continued)	
E	Helium Storage Building (Continued)	
.2	Building Services	
.21	Plumbing	0
.22	Heating, Ventilation and Air Conditioning	0
.23	Fire Protection System	0
.24	Electrical and Lighting	10,000
	TOTAL ACCOUNT 218-E	100,000
F	Miscellaneous Structures and Building Work	
.1	Gate House (Permanent)	25,000
.2	Visitor Center Building	0
.3	Electrical Yard Foundations and Structures	Incl. Acct. 24
.4	Heating Boiler House	100,000
.5	Hypochlorination Solution Tank Foundation	5,000
.6	Oil Separator Underground Vault	Incl. Acct. 24
.7	Foundation for Tanks (Water Storage)	90,000
.8	Berm and Foundation for Oil Storage Tanks	10,000
.9	Test Borings	200,000
.10	Casino	0
.11	Laboratory Material Testing and Structural Steel Inspection (Not Including Quality Control and Assurance)	25,000
.12	Temporary Construction Buildings, Field Office Building, Toilet and Wash Building for Construction Employees	Incl. Acct. 91
.13	Maintenance and Services for Various Contractors Scope of Work	
.131	Maintenance of Roads and Track	
.132	Maintenance and Servicing of Sewage Plant and Lift Station	
.133	Maintenance and Servicing Construction Employees Wash and Toilet Building	

Account Number	Account Title	Total
21	Structures and Site Facilities (Continued)	
218	Miscellaneous Buildings (Continued)	
F	Miscellaneous Structures and Building Work (Continued)	
.13	Maintenance and Services for Various Contractors Scope of Work (Continued)	Incl. Acct. 91
.134	Snow and Ice Removal Maintenance	
.135	Guards Service	
.136	Switching and Handling of Railroad Cars on Station Property Including Necessary Yard Mobile Switching Equipment	
.137	Traffic Flagman	
.138	Miscellaneous Other Provisions	
.14	Miscellaneous Yard Structures and Building Work	100,000
	TOTAL ACCOUNT 218-F	555,000
	TOTAL ACCOUNT 218	4,065,000
219	Ventilation Stack	500,000
	TOTAL ACCOUNTS 21	16,847,000
22	Reactor Plant Equipment	
221	Reactor Equipment	
.1	Blanket	552,000
.2	Shield	133,547,000
.3	Magnets	30,565,000
.4	Neutral Beam Injectors	60,000,000
.5	Test Modules (including controls)	17,639,000
.6	Control Devices	18,000,000
	TOTAL ACOUNT 221	260,303,000

Account Number	Account Title	Total
22	Reactor Plant Equipment (Continued)	
222	Main Heat Transfer and Transport Systems	
.1	Primary Coolant System	
.11	Pumps and Motor Drives Modular and Nonmodular	210,000
.12	Piping (6c 400 apm + 1000 psi)	180,000
.13	Heat Exchangers (allowance)	750,000
.14	Tanks	
.141	Dump Tanks	30,000
.142	Make-Up Tanks	25,000
.143	Clean-up Tanks	20,000
.15	Clean-Up System (Tanks Included in 14)	
.17	Tritium Extraction	
.2	Divertor System	
.21	Pumping (9c 3600 apm + 100 psi)	230,000
.22	Piping	540,000
.23	Heat Exchangers	3,300,000
.24	Tanks	80,000
.25	Clean-Up	50,000
.26	Tritium Extraction	4,000,000
.3	Magnet Water Cooling System	102,000
.31	Pumps and Motor Drives (4c 3600 + 100 psi)	160,000
.32	Piping	
	TOTAL ACCOUNT 222	9,677,000

Account Number	Account Title	Total
22	Reactor Plant Equipment (Continued)	
223	Auxiliary Cooling Systems	
.1	Test System Cooling	
.11	Pumping (Same as UWMAK-II)	470,000
.12	Piping	270,000
.13	Heat Exchangers	180,000
.14	Purification	45,000
.2	Cryogenic Cooling System	
.21	Cryogenic System	58,125,000
.22	Piping	7,500,000
.23	Transport System	0
.24	Tanks	1,700,000
	TOTAL ACCOUNT 223	67,325,000
224	Radioactive Waste Treatment and Disposal	
.1	Liquid Waste Processing and Equipment	80,000
.2	Gaseous Wastes and Off-Gas Processing System	0
.3	Solid Wastes Processing Equipment	40,000
	TOTAL ACCOUNT 224	120,000
225	Fuel Handling and Storage Systems (Fuel Injection)	
.1	Fuel Handling Equipment and Systems	
.11	Fuel Purification Systems	1,276,000
.13	Fuel Fabrication	60,000
.14	Fuel Injection	1,500,000
.2	Remote Viewing Equipment	180,000
.3	Service Platforms	90,000
.4	Fuel Storage	50,000
	TOTAL ACCOUNT 225	3,156,000

Account Number	Account Title	Total
22	Reactor Plant Equipment (Continued)	
226	Other Reactor Plant Equipment	
.1	Gas Systems	200,000
.2	Ventilation Air Purification	17,200,000
.3	Coolant Receiving, Storage and Make-Up Systems	0
.4	Coolant Charge, Volume Control, Relief, Etc.	120,000
.5	Coolant Purification and Chemical Treatment	240,000
.6	Fluid Leak Detection Systems	40,000
.7	Auxiliary Cooling Systems	760,000
.8	Maintenance Equipment	800,000
.9	Miscellaneous Suspense Items	100,000
.10	Building Vacuum Systems	160,000
.11	Neutral Beam Systems	8,003,000
.12	Core Vacuum Systems	3,872,000
.13	Miscellaneous Systems	760,000
	TOTAL ACCOUNT 226	32,255,000
227	Instrumentation and Control	
.1	Reactor and Process I&C Equipment	
.2	Automatic Monitoring and Computation Equipment	
.3	Radiation Monitoring Systems	
.4	Isolated Indicating and Recording Gauges, Etc.	
.5	Control and Instrument Piping, Tubing and Wiring	
	TOTAL ACCOUNT 227	3,744,000
	TOTAL ACCOUNT 22	377,856,000

		Total
23	Heat Disposal Equipment	
231	Heat Rejection Systems	
.1	Water Intake Common Facilities	
.11	Traveling Screens	
.12	Screen Wash Pumps	90,000
.13	Piping	
.14	Chlorination	
23	Turbine Plant Equipment (Continued)	
231	Heat Rejection Systems (Continued)	
.2	Circulating Water Systems	
.21	Circulating Water Pumps and Motor Drives	510,000
.22	Circulating Water Piping, Valves and Fittings from Pumps to Condensers and to the Towers	4,730,000
.3	Cooling Towers	
.31	Foundation and Basins	290,000
.311	Towers	
.32	Primary Cooling Towers	1,480,000
.4	Blow Tank	400,000
	TOTAL ACCOUNT 231	7,300,000

Account Number	Account Title	Total
23	Turbine Plant Equipment (Continued)	
232	Water Treatment Equipment	
.1	Chemical Treatment and Condensate Purification Systems	
.11	Filtration Equipment, Including Sand Filters, Aerators, Retention Tanks, Pumps, Etc.	
.12	Demineralizing Equipment, Including Anion and Cation Units, Decarbonator, Mixed Bed Units, Pump Regeneration Units	2,210,000
.13	Chemical Feed Equipment Including Polishers Anion and Cation Regeneration Equipment, Resin Mixing and Storage Vessels, Pumps, Tanks, Instruments, Controls	
.14	Chemical Feed Equipment Including Mixing Tanks, Pumps	
	TOTAL ACCOUNT 232	2,210,000
	TOTAL ACCOUNT 23	9,510,000
24	Electric Plant Equipment	
241	Switchgear	
.2	Station Service	1,700,000
	TOTAL ACCOUNT 241	1,700,000
242	Station Service Equipment	
.1	Station Service and Startup Transformers	247,000
.2	Low Voltage Unit Substation and Lighting Transformers	560,000
.3	Diesel Engine Generators (202,000 kW)	2,940,000
.4	Diesel Auxiliaries (Fuel Tanks + Fire Drot.)	110,000
	TOTAL ACCOUNT 242	3,857,000

Account Number	Account Title	Total
243	Switchboards	
	TOTAL ACCOUNT 243	1,250,000
244	Protective Equipment	
	TOTAL ACCOUNT 244	43,000
245	Electrical Structures and Wire Containers	
	TOTAL ACCOUNT 245	520,000
246	Power and Control Wiring	
	TOTAL ACCOUNT 246	3,570,000
247	Electric Installation	
.1	Contractor Furnished Materials-Conduits, Lighting Fixtures, Etc.	
.2	Construction and Erection Labor	
	TOTAL ACCOUNT 247	
248	DC Converter System	
	TOTAL ACCOUNT 248	16,000,000
	TOTAL ACCOUNT 24	30,820,000
25	Miscellaneous Plant Equipment	
251	Transportation and Lifting Equipment	
.1	Cranes, Hoists, Monorails and Conveyors	
.11	Hot Cell Crane (50 tons)	100,000
.12	Miscellaneous Hoists, Cranes, Jibs and Trolleys for Equipment Maintenance	200,000
.13	Reactor Hall Crane	500,000
.2 to .6	Railway and Roadway Equipment, Watercraft, Aircraft and Vehicle Maintenance Equipment	50,000
	TOTAL ACCOUNT 251	850,000

252	Air and Water Service Systems	
.1	Air Systems	
.11	Service Air Compressor and Motor Drives	
.12	Service Air Receivers	
.13	Instrument Air Compressors and Motor Drives	150,000
.14	Instrument Air Receivers	
.15	Instrument Air Dryers	
.2	Water Systems	1,130,000
.3	Auxiliary Heating Boilers	600,000
	TOTAL ACCOUNT 252	1,880,000
25	Miscellaneous Plant Equipment (Continued)	
253	Communications Equipment	
.1	Local Communications Systems	110,000
.2	Signal Systems	40,000
	TOTAL ACCOUNT 253	150,000
254	Furnishing and Fixtures	
.1	Safety Equipment	
.2	Shop, Laboratory, and Test Equipment	
.3	Office Equipment and Furnishings	
.4	Change Room Equipment	
.5	Environmental Monitoring Equipment	
.6	Dining Facilities	
	TOTAL ACCOUNT 254	240,000
	TOTAL ACCOUNT 25	3,120,000
26	Special Materials	
261	Helium	1,000,000
	TOTAL ACCOUNT 26	1,000,000
91	Construction Facilities, Equipment and Services	
911	Temporary Facilities	
912	Construction Equipment	
913	Construction Services	
	TOTAL	
	Contingency	
	TOTAL ACCOUNT 91	

Account Number	Account Title	Total
92	Engineering and Construction Management Services	
921	Engineering Services	
922	Construction Management Services	
	TOTAL ACCOUNT 92	
93	Other Costs	
931	Taxes and Insurance	
932	Staff Training and Plant Startup	
933	Owner's G&A	
	TOTAL ACCOUNT 93	
94	Interest During Construction	
941	Physical Plant and Associated Indirect Costs	
942	Land and Land Rights	
943	Special Materials	
	TOTAL ACCOUNT 94	

NOTES:

1. The cost of construction labor included in the estimate is based on the following:

   a. Current Labor rates and fringe benefits as now apply in the state.

   b. Manhours and efficiency of work as has occurred in similar work areas.

   c. Manhour costs - as required to attract labor to man the job.

2. Prices for equipment and materials are present day and 40-hour week.

3. Allowances for future escalation of materials and construction labor are not included.

Account	Item	Million of Dollars	%
221	Reactor Equipment	260.303	69
222	Main Heat Transfer & Transport System	9.677	3
223	Auxiliary Cooling Systems	67.325	18
224	Radioactive Waste Treatment and Disposal	0.120	-
225	Fuel Handling and Storage Systems	3.156	1
226	Other Reactor Plant Equipment	32.255	9
227	Instrumentation and Control	3.744	1
		377.856	

Aside from the reactor plant equipment, we see that a major cost item is the cryogenic cooling systems for the OH coils ($58,125,000). This cost arises from the I^2R loss in the cryogenic Al coils and could be reduced by going to superconducting coils. The increase cost of the S/C coils would be minimal (< a few million dollars) so that our conservative assumptions that pulsed superconducting coils would not be available for TETR contributes approximately 13% to the overall cost of the reactor.

Another major cost item of the Reactor Plant Equipment is the ventilation and cleanup system used to protect against large T_2 leaks. This cleanup system amounts to $17,200,00 or 4% of the total plant costs.

Within the reactor equipment we find the following breakdown of costs.

Account	Item	Million of Dollars	%
221.1	Blanket	0.552	0.2
221.2	Shield	133.547	51
221.3	Magnets	30.565	12
221.4	Neutral Beam Injection	60.00	23
221.5	Test Modules	17.639	7
221.6	Control Devices	18.000	7
		260.303	

The surprising thing about the above table is that the shield is the dominant cost item (51%) and it is 4 times the cost of the magnets. Even the 150 MW of neutral beams (at 40¢/watt) is twice as expensive as the magnets. Hence, it is apparent that the magnets do not pace the total cost of the reactor as is normally assumed by most people.

Some background on our decision to use 40¢/watt for the neutral beams is given in Table XV-C-4. The beams for the mirror program devices such as MX and FERF were estimated to cost, in 1974-1975 dollars, 1.03 to 1.17 dollars/watt. Higher energy beams for TFTR were estimated to cost, in 1975 dollars, 0.81 to 1.09 dollars per watt. More recent (1976) estimates of 150 keV beams for the mirror program are in the 40 to 60¢/watt level. Hence, we assume that with another 5 years of research that the 40¢/watt value for 150 KeV positive or negative ion beams is not unreasonable.

Turning back to the costs of the shield, we see that they are divided as follows.

Shield Component	Millions of Dollars	%
304 SS	11,880	9
Tungsten	115,850	87
B_4C	3.081	2
Pb	2.736	2
	133.547	

The data above reveals that over 87% of the shield costs stems from our use of W as a shield material. This choice is necessary to protect the magnets from damage. The tungsten could be replaced with lead and more than 100 million dollars could be saved on the direct costs or approximately 16%.

Table XV-C-4

Estimated Neutral Beam Capital Costs

Design	ε_{INJ}	P_{EXT}	P_{INJ}	ηe†		Year For Dollar Evaluation	$\frac{Cost}{P_{EXT}}$	$\frac{Cost}{P_{INJ}}$	Ref.
	(Kev)	(MW)	(MW)		(M$)		($/WATT)	($/WATT)	
MX	80	60	23	0.38	27.0	1975	0.45	1.17	2
FERF	65	59	27.5						
	100	33.6	15.7	0.30	44.3	1974	0.48	1.03	3
	TOTALS	92.6	43.2						
TFTR (ORNL)	120	79.2	28	0.35	22.6	1975	0.29	0.81	4
TFTR (LBL/LLL)	120	80	28	0.35	30.5	1975	0.38	1.09	5
REF. MIRROR REACTOR	~150	-	-	0.81	-	1976	-	0.40*	6
"	"	-	-	0.71	-	"	-	0.60**	6

†$\eta e \equiv P_{INJ}/P_{EXT}$

*Neutralization by Photodetachment

**Neutralization by Stripping Cell

of the total costs of the reactor. However, replacing the W with Pb in the inner shield and along the divertor slots would not be acceptable from a radiation damage standpoint to the insulators. This obviously points out a fruitful area of research, namely, the development of a more radiation damage resistant insulator material. The other option is to build a much bigger device to allow more room in the inner shield for neutron attenuation. This would tend to increase the cost of the rest of the reactor and the exact optimum has not yet been determined.

It is instructive to rank the major cost items in TETR so as to understand what is contributing to the total costs. This is done in Table XV-C-5. This table again shows that the most costly item in TETR is the shield (30%) followed by the neutral beams (14%), cryogenic cooling for OH coils (13%), DC convertors (7%), magnets (7%), control (4%), test modules (4%), air purification (4%) and vacuum equipment (3%). This table again points out the great cost that is incurred by having to use W to protect the electrical insulator in the TF coils.

The indirect cost factors are based on utility industry estimates as compiled by McDonnell-Douglas.[7] We have used 15% of the direct costs (minus the W costs) for the construction facilities. We chose not to include the W in the value of the direct cost to which the 15% was applied because indirect costs are normally only figured on the conventional cost items. If we had used Pb and periodically replaced the damaged components, this approach would give the same value (however, the O & M costs would be greater).

Table XV-C-5

Summary of Major Cost Items - TETR

Item	Millions of Dollars	% of Direct
Shield & Blanket	133.1	31
(304SS)	(11.88	(3)
(W)	(115.850)	(26)
(B_4C)	(3.081)	(1)
(Pb)	(2.736)	(1)
Neutral Beams	60.00	14
Cryogenic Cooling	58.125	13
DC Converters	30.82	7
Magnets	30.565	7
Control	18.0	4
Test Modules	17.64	4
Air Purification	17.2	4
Vacuum Equipment	12.035	3

The Engineering Services and Construction Management costs were estimated at 20% of the adjusted direct costs and other costs such as insurance, taxes, staff training and owners G & A were set at 8%. No interest on capital was assumed because TETR is envisioned to be a government project.

The total indirect costs came to $139,459,000 which brings the reactor costs to $579,632,000. We added a 15% contingency allowance to bring the total reactor cost to roughly 630 million dollars. A prespective on this value can be obtained by noting that up through the completion date of the FFTF is 540 million dollars.[8] It should be noted that the true cost of FFTF in 1977 dollars would be much higher than 540 million when adjusted for inflation (FFTF started in the mid-1960's). Hence, one might say that TETR which in many ways plays the same key testing role in fusion as FFTF did in the fission industry.

Another perspective on the cost of TETR can be made by considering the recent EPR designs by ANL[9] and GA.[10]

The total estimated cost and the breakdown between direct and indirect costs are given below.

		Total Est.		% Costs	
Reactor	MW_t	Costx$10^6$$	$/Watt	Direct	Indirect
GA-EPR	410	696	1.7	66	34
ANL-EPR	638	868	1.36	67	33
TETR	515*(365)	628	1.22(1.72)	69	31

*includes 150MW of neutral beam power

Even though the reactor functions and designs are much different, the cost per thermonuclear watt is quite similar for the GA and TETR designs and these are only 25% higher than the ANL value. The EPR designs require much more advanced technologies and therefore have a greater potential for cost escalation and they do not serve a materials testing function. On the other hand, they do produce electrical power.

It is interesting to note that we could produce electricity with TETR quite easily by adding a 40 million dollar turbine generator in the reactor auxiliary building (see Chapter XIV). The 275 MW_{th} of 260°C heat could be converted to approximately 60-70 MW_e without increasing the TETR cost to over $700 million dollars. Such an attractive feature should be investigated further.

XV-D. Operating and Maintenance Costs for TETR

The operations and maintenance (O & M) costs consist of the routine day-to-day expenditures for salaries, supplies, chemicals, etc. We will assume these costs are constant from year to year.

The components of the O & M costs used for TETR are[11]

1) Salaries of power plant personnel.
2) Miscellaneous supplies and equipment.
3) Outside support services.
4) General and administrative costs.
5) Coolant makeup.
6) Miscellaneous costs.
7) Electricity costs for the plant.

We will have a few brief comments about the above categories and then summarize the O & M costs at the end of the chapter.

XV-D-1—SALARIES

The size of the operating crew depends on many factors, such as the number of test reactors per site, the degree of automation, and so forth. We used the following assumptions to arrive at the crew size indicated in Table XV-D-1.

a) There is only one test reactor at the site.
b) The technology is mature so that only routine technical assistance is needed.
c) The plant operates as much as possible, hopefully achieving a 70% plant factor.
d) The plant force does not include employees needed for major maintenance or modifications, such as first wall replacements.

Table XV-D-1—TETR OPERATING FORCE

Superintendent's Office	
Superintendent	1
Assistant Superintendent	1
Secretary	1
Operations	
Supervisors	1
Shift Supervisors	5
Senior Control Room Operators	5
Central Room Operators	10
Equipment Operators	5
Maintenance	
Supervisor	1
Mechanical Foreman	1
Electrical Foreman	1
Instrument Foreman	1
Mechanics	5
Electricians	5
Instrumentmen	5
Mechanical Helper	5
Instrument Helper	5
Electrician Helper	5
Welders	2
Machinists	2
Technical	
Supervisor	1
Plant Engineer	1
Instrument Engineer	1
Nuclear Engineer	1
Health Physicist	1
Chemist	1
Technicians	2
Clerical and Services	
Supervisor	1
Typist	2
Storekeeper	1
Clerks	2
Yardman	1
Janitor	2
Messenger and Handyman	1
Guards	5
	90

Cost C 16,000 each (a) = $1,440,000

a) 54 @ 15,000 = 810,000
20 @ 11,000 = 220,000
16 @ 25,000 = 400,000
1,430,000

e) The plant force does not include the personnel required to run the experiments.

f) Specialty services such as nonroutine analyses, film badge processing, etc. are contracted outside.

We have used an average salary per person of $16,000 per year (as detailed in Table XV-D-1) and multiplying that times the 90 people required yields an annual operating salary cost of $1,440,000.

XV-D-2—MISCELLANEOUS SUPPLIES AND EQUIPMENT

These costs include such items as ion-exchange chemicals, biocides for fouling progection, gases, routine maintenance materials (e.g., tools), waste containers, etc. These costs were scaled from UWMAK-I to yield an $800,000/year expenditure.

XV-D-3—OUTSIDE SUPPORT SERVICES

The major cost item here is for radioactive waste disposal, laundry, and film badge processing. These numbers were scaled from UWMAK-I and amount to $180,000/year.

XD-D-4—MISCELLANEOUS COSTS

These are all routine operating costs not included in the above categories. These were scaled from UWMAK-I to be $120,000/year.

XV-D-5—GENERAL AND ADMINISTRATIVE COSTS

These costs include charges for activities such as fringe benefits, administrators, purchasing, and division level management. The total G & A is figured as 20% of the total cost of Salaries, Miscellaneous Supplies and Equipment, Outside Support Services and Miscellaneous Costs. The G & A costs came to $500,000/year.

XV-D-6—COOLANT MAKEUP

The initial coolant inventory (cryogenic as well as high temperature) is included in the plant capital costs. This category should only include losses due to leakage, transimulations, cleaning operations, etc.

We have assumed that we will require a makeup of 20% of the Helium inventory per year. This amounts to $250,000/year for TETR.

XV-D-7—COST OF ELECTRICAL POWER

Since TETR does not produce electricity, the electrical power consumption has to appear as a separate item and not buried in the 'net' electrical output numbers. The first thing to establish is the integrated power required over one burn (72.5 sec) cycle. The instantaneous power required and the time over which it is required is given in Table XV-D-2.

Table XV-D-2

INTEGRATED POWER REQUIRED FOR TETR

Running Time-Sec	Δt-sec	Ave. MW_e Power Required	Total MW_e-sec
0 to 0.75	0.75	67	50
1.0	0.25	207	52
61	60	449	26,940
62.5	1.5	222	333
72.5	10	67	670
			28,045

Total Cycle Time = 72.5 sec.

Averaged Power Required Over Complete Cycle ≅ 387 MW_e

Averaged Power Required Over Burn Cycle = 467 MW_e

The power requirements include a constant 35 MW_e for refrigeration of the OH coils, 9 MW_e for vacuum equipment and 2.5 MW_e for the divertor coils. In addition to these constant loads, approximately 20.5 MW_e are required for 0.25 sec to charge the OH and VF coils, and another 70 MW_e for VF coil charging and 90 MW_e in I^2R loss in the VF coils is required for the next 0.25 seconds. During the burn there is approximately 90 MW_e required for the I^2R loss in the VF coils in addition to the 312.5 MW_e for the neutral beams. An average of 175 MW_e is required to recharge the VF coils for 2.5 seconds after the burn and another 20 MW_e is required to charge the OH coils during the 10 second pump out phase.

The total energy required over one complete cycle is 28,045 MW_e-sec. This amounts to 467 MW_e over the 60-second burn and 387 MW_e over the complete cycle. Adding another 13 MW_e for auxiliary systems, we will assume the average power over the burn is 480 MW_e. The annual cost of electricity is determined by using a 70% plant factor (47 days for maintenance and repair) and 10 mills/KWh for the electricity costs. This latter number is a reasonable value considering the 1976 rates at various points within the United States (D. Nygren, HEDL).

Hanford Washington	3.3 Mills/KWh
California	6.6 Mills/KWh
TVA (Tennessee)	13.2 Mills/KWh
Long Island	26.4 Mills/KWh

The annual electricity costs for TETR would then be $29,434,000.

XV-D-8--UNUSUAL MAINTENANCE ITEMS

This category includes replacement parts and labor for the first wall and shield. Even though the bulk of the reactor is designed to last the full reactor lifetime, there will be failures due to 'conventional' causes. It is estimated that these costs could run as high as $1,000,000 per year.

XV-D-9—TOTAL O AND M COSTS

A summary of all the O & M costs is given in Table XV-D-3. The annual requirement is $33,734,000, which is dominated by the cost of electricity (85%). It is important to note that the major contributor to the cost of electricity is the operation of the neutral beams which constitute 69% of the electrical requirements and 57% of the total O and M costs.

Table XV-D-3

SUMMARIZED O AND M COSTS

Cost Item		Annual Cost
Salaries		$ 1,440,000
Miscellaneous Supplies and Equipment		800,000
Outside Support Services		180,000
Miscellaneous Costs		120,000
	Sub-Total	$ 2,540,000
General and Administrative (20%)		510,000
Electricity (460 MW, 70% plant factor)		29,434,000
Coolant Makeup (20% He per year)		250,000
Unusual Maintenance Items		1,000,000
	Total	$33,734,000

Note: This does not include the labor and material costs for preparing test assemblies.

XV-E-1—FUEL COSTS FOR TETR

We will only include the cost of routinely purchased materials such as tritium and deuterium. There are many others costs we could include such as operation of the fueling device, clean up systems, distillation towers, rad waste, etc., but these are included in the O & M costs for simplicity. Since this is intended to be a government facility, we also will follow the philosophy of only charging for that amount of tritium which is burned up or lost by decay. Presumably, the government would provide the initial inventory (~ 12 kg), and we would then only buy enough T_2 to replace the T_2 destroyed or decayed into He-3 (no credit is applied for resale of He-3 which amounts to about 700g per year).

The market price for tritium is probably the most uncertain factor in this assessment, and we have used a value of $5,000/gram which is reasonable considering the current capacity and operating costs of a major tritium-producing facility like Savannah River. The cost of deuterium has been recently set at $1,060/kg of D_2 in heavy water (Nuclear News, April 1977, p. 138), so we will use $1.06/gram for deuterium.

The fueling costs for tritium were then determined as follows:

1) The burn rate was established.
2) The annual flow rate was determined from the burn rate.
3) The inventory in the fuel cycle was determined by the residency time in one complete loop from injection, collection, purification and reinjection.
4) The inventory required for storage in the event of a component breakdown was established.
5) The total decay rate was determined from the total plant inventory.

Let us now briefly go over the above items one by one.

The tritium flow rate over the burn cycle is 4.55×10^{-2} gram atom/second, and at a 0.33% burn up per pass, the following amount of tritium is burned per year.

$$4.55 \times 10^{-2} \frac{\text{g atom}}{\text{sec}} \times \frac{3\text{g}}{\text{g atom}} \times 3.15 \times 10^{7} \frac{\text{sec}}{\text{year}} \times 0.7 \times 0.0033 = 9932 \text{ g/year.}$$

At $5,000 per gram, this amounts to an annual cost of $49,662,000.

The inventory in the fuel cycle is repeated in Table XV-E-1. It shows that with a six-hour cycle time for the cryopumps, there is approximately 1.52 kg of tritium tied up in those components alone. The short residency times in the distillation columns and injector vacuum pumps require much lower inventories in those components.

TABLE XV-E-1

TRITIUM INVENTORY - TETR

		kg
1)	Cryopump	1.52
2)	Injector vacuum pumps	0.012
3)	Distillation columns	0.188
4)	Storage - 1 day supply	9.760
		11.588
		~ 12 kg
	Decay of T_2 per year	0.587

It was also determined that we wish to have at least one day's inventory of tritium in storage to allow operation in the event of a temporary malfunction in the cleanup system. The number is somewhat arbitrary, but it is unlikely to be very far off, because running for say ten days without being able to extract the tritium would produce an inventory and decay costs which would be prohibitive (~100 kg!).

On the other hand, an inventory for only 0.1 day (2.4 hr.) is also probably unreasonable, because it would be very difficult to locate and repair malfunctions in such times. Since shutting down and starting up a reactor (from a thermal inertial standpoint) is not expected to be easy, we feel that prudent engineering analysis would suggest an inventory of approximately one day. This amount of tritium is 9,760 grams and the total inventory in the reaction is then approximately 12 kg.

The decay of the tritium in this ineventory is approximately 600 g per year, and the cost is approximately three million dollars per year.

The 'loss' rate of deuterium is 0.079 m-moles/sec reacted with tritium and 0.127 m-moles/sec lost up the stack with hydrogen. Hence, the total amount of deuterium consumed per year is

$$\frac{0.206 \text{ m-mole}}{\text{sec}} \times \frac{2\text{mg}}{\text{m-mole}} \times 3.15 \times 10^7 \frac{\text{sec}}{\text{year}} \times 0.7 = 9.08 \text{ kg/yr}$$

This only amounts to approximately $9,600/year.

The total fuel costs are listed in Table XV-E-2 and reveal that the major item is, as expected, the burnup of tritium (94%). The total cost is $52,607,000 per year.

TABLE XV-E-2

TOTAL ANNUAL FUEL COSTS TETR

	Dollars
1) Tritium Burned	49,662,000
2) Tritium Decayed	2,935,000
3) Deuterium	10,000
	52,607,000

XV-F—TOTAL OPERATING COSTS TETR

The total operating costs of TETR have been calculated to be $82,046,000 per year (see Table XV-F-1). The major cost items are listed below.

	% Total Operating
Burnup of T_2	58
Elec. for beams	24
Other elec.	7
Decay of T_2	3

TABLE XV-F-1

SUMMARY TOTAL ANNUAL OPERATING COST TETR

Item	Dollars
Fuel	52,607,000
Electricity	29,434,000
Other O & M	4,300,000
	85,114,000

It is obvious that two of the major design decisions have had a great impact on the operating costs of TETR. The decisions not to breed tritium and operate in the driven mode constitute 88% of the operating costs. The magnitude of these cost items features could be reduced by two not totally unreasonable governmental actions:

1) Association of TETR with a capitve hydroelectric station producing power at 3.3 mills/KWh.
2) Dedication of an existing thermal production reactor to the production of T_2 for TETR. This, associated with other cost-saving features, could lower the cost of Tritium. However, it is unlikely that the optimistic

combination of the above factors would reduce the annual operating costs by more than a factor of two to approximately $40,000,000/year.

XV-G--SUMMARY OF TETR COST ANALYSIS

We conclude that one TETR could be built without imposing any unrealistic demands on the United States or world resources. The total capital costs should be between $600,000,000 - $700,000,000, and the annual operating costs in the $85,000,000 a year level. Several key areas of TETR should be studied for the potential of reducing these costs; development of radiation damage resistant electrical insulators for magnets, low cost neutral beams, dedicated tritium-producing facilities and coupling with cheap hydroelectric power. We did not examine the construction schedule in detail, but it appears reasonable that such a facility could be built and operating in five to seven years after authorization.

XVI. Conclusions

In this chapter we have tried to distill some of the major conclusions from this study in order to put this work in perspective. These are by no means all of the conclusions one could have listed but represent only those which are unique. The statements are brief and the supporting information and arguments can be found in the Overview and body of the report.

XVI-A. Design Philosophy

. A materials and engineering test reactor operating on the DT cycle is a vital cornerstone of the timely construction of the first demonstration power reactor (DPR).

. In order to meet the desire to operate a DPR in the late 1990's such a Test Facility must be operating by the 1987-90 period. This means that the test facility must be designed with 1980 state-of-the-art technology.

. A useful test reactor must not only provide the appropriate neutron flux and spectrum but it must provide for a large in situ testing capability and a realistic operating environment (time of irradiation, temperature coolants, stress, etc.).

. The Tokamak Engineering Test Reactor (TETR) can satisfy the above needs in the time frame desired and at a cost which is reasonable.

XVI-B. Plasma Physics

. A DT plasma, operated in the TCT mode, can provide the necessary neutron flux and duty cycle required to simulate anticipated DPR operations.

. The major problem with the plasma design in TETR is the MHD stability in the vertical direction. Methods have been devised to control the instability in TETR.

. Both space-time and global model analysis of the plasma indicate that the temperature and density profiles are very peaked in the center. The low particle density at the edge of the plasma indicates that the divertor may not be very useful to screen particles which come from the first solid surfaces. However, the divertor will help to remove He and impurities from the plasma.

. Even though the trapped particle scaling laws predict very short energy and particle containment time ($\tau_E \sim$ 50 ms, $\tau_p \sim$ 31 ms), the plasma in TETR will be hot enough to produce the neutron fluxes desired; long values of τ_E would enhance neutron production but would require high beta equilibria. Longer particle containment times reduce tritium concentration and neutron production.

. An innovative vacuum pump design has allowed us to achieve a pumping speed of 1.94×10^6 liters/sec for D and T as well as 0.48×10^6 liters/sec for He with a ~57 m^2 area in the vacuum chamber.

XVI-C. Plasma Heating

. It is possible to provide 150 MW of neutral beam power to TETR at 150 keV with positive ion technology at ~48% overall efficiency. Such a system uses 12 beam lines with 7 positive ions per line and molecular ion extraction at 150 keV.

. Negative ion technology which may not be available at 150 keV by the early 1980's, could also heat the TETR at a much higher (73 to 81%) overall efficiency.

. The role of RF heating in TETR was investigated and it was found that only the low frequency fast Alfvén wave could make a contribution by the 1980's. However, with the present scaling laws (e.g., trapped ion scaling) used in TETR, the efficient use of the fast Alfvén wave to heat the electrons and provide more fusion output power from the neutral beam heated plasma is precluded.

XVI-D. Magnets

. Sixteen (16) cryogenically stable NbTi superconducting TF coils in the constant tension "D" shape can provide the necessary on axis field (42 kG) for successful operation of TETR. However, such coils must be magnetically shielded from the pulsed vertical fields by high purity Al.

. A series of safety protection circuits for the TF coils has been devised.

. Assuming that pulsed superconducting OH coils will not be available by 1980, an OH coil system which is cryogenically cooled high purity aluminum has been devised to provide the necessary breakdown and heating fields. However, the power required to cool these coils is very large (30 MW_e) and the capital investment in cryorefrigeration equipment is ~75 million dollars. This means that there is great incentive to return to superconducting OH coils if they can be developed by 1980.

. Room temperature copper VF coils can be used for TETR which have brazed joints for easy removal during a reactor repair. The major penalty with this approach is the ~80 MW of thermal power generated from the I^2R loss during the burn.

. A total of ~25% (~120 MW_e) of the time averaged electrical requirements for TETR are associated with the magnet system and only a maximum of 370 MW_e needs to be drawn from the line at the end of a burn.

XVI-E. Blanket and Shield

. The first wall of the TETR can be a steam cooled stainless steel tubular structure which operates at a maximum temperature of 300°C. The maximum stress in the tubes is 51 MPa (7400 psi) which is modest compared to the potential of steel at that temperature.

. The carbon curtain has enough thermal inertia to greatly reduce the thermal stresses in the tubular 316SS walls between burns. The maximum pressure change during the 12.5 second down time is 28 MPa (4124 psi).

. Quick accessibility to the test sections has been achieved by incorporating "swing away" shields so that the test sections can be inserted and removed from the outside of the reactor without ever breaking the vacuum in the plasma chamber. This should greatly improve the plant factor and allow replacing test specimens at reasonable intervals (several times per year if necessary).

XVI-F. Neutronics

. The neutron flux has been calculated in great detail around the test cells and reveals that it is possible to obtain a 1 MW-y/m^2 irradiation in a calendar year of operation.

. The damage gradient across the test cells is tolerable, on the order of 0.2 dpa/cm in the first 10 cm from the first wall.

. Leakage of neutrons up divertor slots and down neutral beam injector points produces damage rates ~10 times higher than predicted from 1-D calculations and requires additional shielding to meet the radiation damage and heating limitations of TETR.

. The neutron spectrum relaxes to that of the test cells within 5-10 cm of the blanket and shield and therefore can be typical of future reactor designs, not only of the particular design of the TETR blanket.

XVI-G. Thermal Hydraulics

. The removal of some 600 MW of heat from TETR can be accomplished with water, steam and helium coolants. The specimens are heated electrically or with gamma heating while the rest of the reactor components are all designed to operate <300°C.

. Heat loads to divertor collector plates in TETR will be more severe than in previous reactor designs because of the limited space available. One must also consider the possibility that the particle flux from the plasma will not be symmetrically removed from the four divertor slots and energy fluxes of 20 MW/m^2 may occur for short periods of time.

. A particle collection scheme has been designed which uses Ta-10W plates approximately placed with respect to the incoming beam. This design can handle average fluxes of 6.7MW/m^2 as well as 20 MW/m^2 for short periods of time. High speed, low temperature (45-70°C) water is used to remove the high heat fluxes.

. The carbon curtain used in TFTR can protect the first wall against plasma dumps of up to 1000 watts/cm^2 for up to 10 seconds before vaporizing. Such fluxes would cause serious damage to an unprotected first wall in 0.1 seconds.

XVI-H. Radiation Damage to TETR Components

- Analysis of the 316 SS structure reveals no obvious problem that would limit the lifetime of the structural component to less than 10 MW-y/m^2 at 300°C. Potential problem areas are the impact of more exact stress state analyses on the fatigue crack growth rates and the effect of helium on enhancing the dimensional changes up to ~100 dpa and 2000 appm helium content.

- The shrinkage (~8%) and expansion (~34%) of the carbon curtain during a 10 MW-y/m^2 exposure at 1200°C should be acceptable without compromising the plasma operation.

- Combined physical and chemical sputtering rates of up to ~0.5 mm/year can probably be accommodated by a thicker curtain design but the effect of such carbon erosion rates on the cryopumps of the vacuum system needs to be assessed.

- A severe problem exists in the Ta-10W divertor collection plates. Erosion rates of 0.6 mm/month will require replacement of the collector tubes in less than one month of operation. This is one of the most severe problems uncovered in the present design and further work is required.

- Radiation damage to the copper stabilizer and NbTi superconductor of the TF coils is acceptable to 10 MW-y/m^2 in all but a few locations near the divertor slots. Extra shielding and minor design changes can be incorporated to alleviate the "hot spot" problem.

- Radiation exposure of the mylar thermal insulation in the TF coils appears to make a 10 MW-y/m^2 lifetime somewhat questionable in certain "hot spot" areas. The epoxy fiberglass insulation should perform satisfactorily for the required lifetime.

- Radiation damage to the epoxy fiberglass electrical insulation of certain VF coils appear to be severe enough to require alternate materials. Inorganic ceramic insulators may have to be used in certain positions.

- No significant problems have been encountered in the W, B4C, Pb, and copper conductors of the VF coils. All of these materials should allow a full 10 MW-y/m^2 performance.

- It is felt that even though a few areas of concern have been expressed for the lifetimes of TETR components, the majority of the systems should give satisfactory performance based on today's information Allowing for some progress in the next 10 years, we feel that such a reactor could be reasonably operated in the late 1980's to provide valuable materials information for the Demonstration Reactor which may be built in the late 1990's.

XVI-I. Test Modules for Structural Materials

. It has been shown that there is ample testing space in TETR to provide solid experimental data from which to design the DPR in the early 1990's. More specifically, the current design of TETR provides more than 16 m^2 of high flux test area directly facing the plasma. These test stations also provide approximately 2 m^3 of high flux test volume which can be instrumented and closely controlled with respect to temperature, environment, and stress.

. The specific test matrix for primary DPR and backup DPR alloys reveals that more than 3000 in situ mechanical property tests can be conducted simultaneously. In addition, at least 2000 additional post irradiation samples can be irradiated at the same time.

. It is important to emphasize that the specimens in TETR are being tested in the "proper" radiation environment with the charactertistic transmutation, damage, and microstructural cascade features. In contrast to all other currently proposed test facilities, no "simulation" is involved with the TETR test program.

XVI-J. Lithium Test Modules

. Two distinct types of test modules pertaining to the use of Li and its compounds in a fusion reactor have been investigated.

. The first module has been designed to test the corrosive action of liquid Li under actual CTR conditions (i.e., neutrons, temperature fluctuations, magnetic field, etc.).

. The second module will examine tritium breeding and evolution in solid Li compounds. The effect of sintering high helium gas production and interaction with high pressure gaseous coolant are some of the areas that could be studied in the test assembly.

XVI-K. Tritium System

. The tritium inventory in TETR is ~1.8 kg in the active part of the reactor (fueling, cleanup, fuel preparation, etc.) and roughly 10 kg is required for storage if a 1 day's reserve is to be established.

. The main loss of tritium is through the Ta-10W divertor plate collectors and this amounts to ~8 g/day. A water coolant cleanup system has been devised to recover that tritium when the level reaches 60 curies/liter. Loss rates of tritium to other reactor coolants is <0.02 curie/day.

. A tritium reprocessing system to clean up tritium "spills" in the reactor hall has been devised which allows a 1 kg release to be removed in a matter of a few days.

. The tritium requirements due to burn up are 9.9 kg per year at 70% plant factor and an additional 0.6 kg per year is required to replace the tritium which delays from the inventory. Such amounts of tritium could be obtained from current production facilities in the U.S. if given the proper priority.

XVI-L. Radioactivity

. The use of tungsten for a shield material increases the short-term radioactivity in the shield by a factor of 203 over an all steel shield but the activity decays away within a year or two ($t_{1/2}$(max) => 5 days).

. The total activity in the blanket and shield of TETR is ~5 curies/watt at shutdown; after a few months of operation such high radioactivity levels represent a potential problem in the event of an accident in which the tungsten (or steel) could be volatilized and appropriate safety precautions need to be taken.

. The radiation dose outside the shield in the vicinity of the TF magnets ranges from ~700 to 1900 mrem/hr at shutdown depending on the structural material on the outside of the shield. The use of Al for the last 10 cm or so of the shield will allow the radiation levels from the reactor to drop to 3 mrem/hr after 1 week of decay so that hands-on-maintenance can be accomplished.

. Neutron leakage down divertor slots and neutral beam ports can result in much higher radiation levels than behind the normal shields. The "shadow" shielding which will be required to reduce these levels can be very expensive and difficult to incorporate in this compact design.

XVI-M. Plant Layout

. Underground siting of TETR can reduce the potential hazards associated with disruptive accidents emanating from external and internal sources.

. Much more attention needs to be given to the hot cell facilities to handle the radioactive test samples as well as reactor components which fail.

. It would be relatively easy to incorporate the ability to generate electricity in TETR if so desired. The increase in capital costs would be ~10% and as much as 80 MW_e could be produced on an intermittent basis.

XVI-N. Resource and Cost

. The resource requirements for TETR will not represent a great problem if only one device is built. Even the unusually large tungsten requirements could be met with today's capabilities.

. The capital cost of TETR is estimated to be 628 million dollars including indirect and contingency costs. The reactor is the major cost item (69%) and the shield accounts for 51% of that value. The major cost component of the shield is the W which accounts for 87% of the shield cost and 26% of the total reactor costs.

. The operating costs for TETR are estimated to be 85 million dollars per year which is mainly composed of tritium costs (61%) and electricity (34%).

. The capital costs of TETR coils can be greatly reduced by -

(1) Using superconducting OH coils, thus eliminating expensive refrigeration equipment.

(2) Finding electrical insulators in the magnets which can stand higher radiation damage and allowing more conventional shielding material to be used.

(3) By developing neutral beams which cost less than 40¢/watt.

. The operating costs of TETR could be greatly reduced by -

(1) Establishing a source of tritium for less than 5,000$/g.

(2) Using higher efficiency neutral beam injectors.

(3) Coupling TETR with a source of electricity which costs <10 mills/kWh (e.g., a hydroelectric facility).

Finally, we realize that this represents only the first step to an even more detailed design of such a test facility and we would recommend that such a study be initiated with industry, national laboratory and University participation as soon as possible.

Appendix A

We have included here the basis for some of the calculations that led to the detailed cost data of Table XV-C-3. The information is included in the order in which it appears in the above table, but no effort was made to completely document all the numbers used or to explain every assumption made.

A-1. Corrections Made for the Use of UWMAK-II Data

Many of the numbers for the balance of plant (accounts 21, 22, 23, 24 and 25) came from the UWMAK-II study (UWFDM-112) and the escalation factors were determined as shown below.

Basis - UWMAK-II Costs - 1974

1500 MW_e

Heat Rejected - 3500 MW_t - UWMAK-II

600 MW_t - TETR

Escalation - 8%/year to 1977

Escalation Factor $(1.08)^3 = 1.26$

Water System Factor $= (1.08)^3 \left(\frac{600}{3500}\right)^{0.59} = 0.45$

Cooling Tower Factor

200 MW_t Size $\rightarrow (1.08)^3 \left(\frac{200}{875}\right)^{0.59} \frac{1}{4} = 0.13$

80 MW_t Size $\rightarrow (1.08)^3 \left(\frac{80}{875}\right)^{0.59} \left(\frac{1}{4}\right)(2) = 0.15$

Power Level Factor $= (1.08)^3 \left(\frac{500}{5000}\right)^{0.59} = 0.32$

A-2. - Basis For Capital Cost Estimates

Account Number	Account Title & Estimating Philosophy	Quantity	Unit Cost	Total Cost
20	Land and Land Rights Same as for PWR	500 acres	2000	1,000,000
21	Structures and Site Facilities			
211	Site Improvements and Facilities (60% of UWMAK-II)			5,000,000
212	Reactor Building Reinforced Concrete	10,200 m^3	500	5,100,000
213	Cooling System Structures[a]			890,000
215	Reactor Auxiliary Building Reinforced Concrete	3200 m^3	400	1,280,000
218	Miscellaneous Buildings			
	Control Room Building (2 times PWR[a])			1,330,000
	Diesel Generator Building[a]			160,000
	Administration Building[a]			420,000
	Service Building[a]			1,500,000
	Helium Storage Building			100,000
	Miscellaneous[a]			550,000
219	Ventilation Stock[a]			500,000
22	Reactor Plant Equipment			
221	Reactor Equipment			
.1	Blanket			
	316SS First Wall-Fab.	18.1 MT	30,000	543,000
	Graphite Liner	300 m^2	$30	9,000
.2	Shield			
	304 SS	792 MT	15,000	11,880,000
	Tungsten	3310 MT	35,000	115,850,000
	B_4C	237 MT	13,000	3,081,000
	Pb	4560 MT	600	2,736,000
.3	Magnets			

(a) WASH-1230, Volume 1

Account Number	Account Title & Estimating Philosophy	Quantity	Unit Cost	Total Cost
.31	OH Coil			
	HP Al-Conductor	25.878 MT	10,000	259,000
	316SS Structure	40.87 MT	20,000	817,400
	Micarta Spacers	8 MT	10,000	80,000
	Superinsulation	150.9 m^2	90	14,000
	He Dewar - 316SS	2.95 MT	30,000	89,000
	Vacuum Dewar - Al Alloy	4.07 MT	20,000	8,000
	Installation Labor			771,000
221.32	VF Coil			
	OFHC Copper	159.52 MT	10,000	1,595,000
	Insulation-Silicate Impregnated Mica	2,500 m^2	150	375,000
	Installation Labor			966,000
.33	TF Coils			
	NbTi in Fab. OFHC Cu Coil	488.2 MT	15,000	7,323,000
	316SS Structure	330 MT	10,000	3,300,000
	Insulation Fiberglass Epoxy	15 MT	88,000	132,000
	Winding Labor	729.5 MT	5,500	4,012,000
	Al Alloy Bolts	700 kg	440	3,000
	Micarta Spacers	11.7 MT	10,000	117,000
	Epoxy Struts	1,200 kg	88	11,000
	Al Shield	25.4 MT	10,000	254,000
	He Dewar - 316SS	22 MT	30,000	660,000
	Vacuum Dewar - Al Alloy	34.5 MT	20,000	692,000
	Superinsulation	753 m^2	90	68,000
	Lateral Support Structure Cast Al	86 MT	44,000	378,000
	Central Sup. Struc. - 316SS	170 MT	10,000	1,700,000
	Superins. for CSS	50 m^2	90 m^2	5,000
	Dewars for CSS			95,000
	Assembly and Erection			6,841,000
.4	Neutral Beams (UCRL-521-73) - Neg. Ion	150 MW	400,000	60,000,000
.5	Test Modules			
	16 Test Modules	3570 kg	300	1,071,000
	12 Bayonet Modules	192 kg	300	58,600
	Test Equipment - In Situ			1,110,000
	Control Equipment - Test Mod.			14,800,000
	Control Equipment - Bayonet			600,000
0.6	Control Devices			18,000,000

Account Number	Account Title & Estimating Philosophy	Quantity	Unit Cost	Total Cost
222	Main Heat Transfer and Transport System			
.1	Primary Coolant System			
.11	Pumps and Motor Drives 6 @ 400 gpm + 1000 psi			210,000
.12	Piping (allowance)			180,000
.13	Heat Exchanger			750,000
.2	Divertor Coolant System			
.21	Pumping (9 @ 3600 gpm + 100 psi)			230,000
.26	Tritium Extract 10 n (mound)			4,000,000
.3	Magnet Cooling System			
.31	Pumps and Motor Drives (4 @ 3600 gpm + 100 psi)			102,000
223	Auxiliary Cooling System			
.11	Piping (same as UWMAK-II)			470,000
.2	Cryogenic Cooling System			
.21	Cryogenic System			
	120 kW @ 4.2°K	15 unit-8 kW ea.	3,000,000	45,000,000
	300 kW @ 77°K	6 unit-50 kW ea.	250,000	1,500,000
	Installation			11,625,000
122	Piping			
	Liq. He Trans. Line + Inst.			5,000,000
	LiQ N_2 Trans. Line + Inst.			2,500,000
.24	Tanks			
	Liq. He Tanks (100,000 ℓ)	4	300,000	1,200,000
	Liq. N_2 Tanks (100,000 ℓ)	2	250,000	500,000

Account Number	Account Title & Estimating Philosophy	Quantity	Unit Cost	Total Cost
225	Fuel Handling and Storage System			
.11	Fuel Purification System (mound laboratory)			1,276,000
.13	Fuel Fabrications			60,000
14	Fuel Inspection (UWMAK-II)			1,500,000
226	Other Reactor Plant Equipment			
.2	Ventilation Air Purification			17,200,000
226.11	Neutral Beam Vac. Equip.			
	Cryopumps (rev)	290 m^2	25,000	7,250,000
	Ducts - 304SS	20 MT	30,000	600,000
	Dry Compressors			153,000
.12	Core Vacuum System			
	Cryopumps (rev) 140 m^2	140 m^2	25,000	3,500,000
	Ducts - 304SS	10 MT	30,000	300,000
	Dry Compressors			72,000
.13	Miscellaneous			
	Dry Compressors + Ducts			500,000
	Magnet Vac. Sys.	26	10,000	260,000
24	Electric Plant Equipment			
2426	Station Service Equipment			
.3	Diesel Engine Generators (2000 kW)	2	1,470,000	2,940,000
.4	Diesel Auxiliaries (fuel tanks and fire prev.)			110,000
248	DC Convertor System			16,000,000
26	Special Materials			
261	Helium	400,000 ℓ	2.5	1,000,000
262	Nitrogen	200,000 ℓ	0.1	20,000

A-3. Philosophy Behind the Costing of Experimental Facilties in TETR

The fundamental philosophy for costing the experiments in TETR is to include the cost of the test module, the internal testing equipment and control instrumentation in the capital costs. The replacement modules (including new testing apparatus) would be included in the OHM costs.

Items not included in TETR are

- Specimens
- Personnel to monitor the tests
- Post irradiation testing equipment (hot cells are provided)

Cost Basis For Test Modules

The volume of the upper test module is 0.17 m^3 (1.2 m x 1 m x 0.14 m). The actual weight of fabricated 316 SS steel is 270 kg/module. At 300 $/kg of fabricated 316 SS the cost per module is$81,000.

The lower bayonet test sections occupy a volume of 0.01 m^3 and involve 16 kg of steel. These modules amount to $4800 a piece.

In situ testing equipment is difficult to determine because such devices will be highly specialized. Based on information in chapter X we estimate that the following costs will be incurred for the test devices:

Device	Number Per Module	Cost Per Device(a) $	Total Cost Per Module
Pressurized Tube Rack	100	100	10,000
Creep Rigs	1500	200	300,000
Fatigue Tests	100	300	30,000
Crack Propagation	50	300	15,000

a) including control leads to outside of reactor

We expect to have 2 fatigue modules, 2 creep modules, 1 crack propagation and 1 biaxial module. The total cost for the first reactor load is $685,000.

The control equipment has been costed as follows

Device	Control Equipment Cost Per Device	# of Devices	# of Modules	Total
Box of Pressurized Tubes	2000	100	1	200,000
Creep Rigs	4000	1500	1	6,000,000
Fatigue Tests	3000	100	2	600,000
Crack Propagation	3000	50	2	300,000
				7,100,000

The cost of testing equipment and control associated with the other 12 upper test modules is outlined below

Module #	Test	$/Module	$ For Test Device	$ Control	Total $
1.)	Fatigue-Struc.	81,000	30,000	300,000	411,000
2.)	Fatigue-Struc.	81,000	30,000	300,000	411,000
3.)	Creep	81,000	300,000	6,000,000	6,411,000
4.)	Crack Propagation	81,000	15,000	150,000	246,000
5.)	Crack Propagation	81,000	15,000	150,000	246,000
6.)	Biaxial Tubes	81,000	10,000	200,000	311,000
7.)	Surface Effects	30,000	10,000	50,000	90,000
8.)	Carbon	81,000	50,000	100,000	231,000
9.)	Li Loop	45,000	25,000	100,000	170,000
10.)	Defect Testing	60,000	50,000	100,000	210,000
11.)	Non Li Coolants	45,000	10,000	50,000	105,000
12.)	T_2 Breeder and N Multiples	60,000	50,000	100,000	210,000
13.)	Back-up Alloy-Fatigue-Creep	81,000	200,000	3,000,000	3,281,000
14.)	Back-up Alloy-Biaxial, Crack Propagation	81,000	15,000	200,000	246,000
15.)	Refractory Metals - Fatigue, Creep, Biaxial	81,000	150,000	2,000,000	2,231,000
16.)	Advanced Materials Fatigue, Creep, Biaxial	81,000	150,000	2,000,000	2,231,000
					17,091,000

The costs of the quick access bayonet sections have only been estimated at this time. Assuming the volume to be 4-5% of the upper cells we estimate the average cost of tests plus control to be (0.045×10^6 = 45,000/module). The total cost of the test control equipment for the 12 bayonet sections is then $840,000.

The final cost of the test sections, internal devices and external control equipment is then $17,631,000.